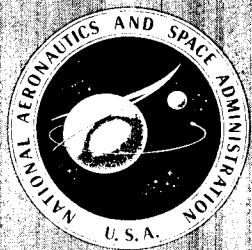


EIGHTH CONFERENCE ON
SPACE SIMULATION

(NASA-SP-379) EIGHTH CONFERENCE OF SPACE
SIMULATION (NASA) 859 p HC \$21.25 CSCL 14B

N76-11113
THRU
N76-11180
Unclas
H1/09 04034

A symposium held in
SILVER SPRING, MARYLAND
November 3-5, 1975



NATIONAL AERONAUTICS AND SPACE ADMINISTRATION

SPACE SIMULATION

The proceedings of a symposium held November 3-5, 1975
at the Sheraton Silver Spring Motor Inn
Silver Spring, Maryland

Sponsored by

Institute of Environmental Sciences
The American Institute of Aeronautics and Astronautics
The American Society for Testing and Materials
and the National Aeronautics and Space Administration

Prepared at Goddard Space Flight Center



Scientific and Technical Information Office

1975
NATIONAL AERONAUTICS AND SPACE ADMINISTRATION
Washington, D.C.

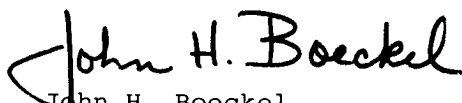
For sale by the National Technical Information Service
Springfield, Virginia 22161
Price — \$19.25

FOREWORD

The National Aeronautics and Space Administration has served as a co-sponsor of the Eighth Space Simulation Conference and has published the proceedings as a NASA Special Publication so that the information presented would be available as a permanent record and as a reference source for persons interested in the technologies.

This conference provided an international forum for the discussion of the state of the art in space simulation, contamination, biosciences, and flammability. It is through this forum that many persons with differing interests and responsibilities in the aerospace research, development, and testing programs have been brought together for the interchange of knowledge in areas which affect them all.

The NASA is again pleased to present, with the Institute of Environmental Sciences, American Institute of Aeronautics and Astronautics, and the American Society for Testing and Materials, this important material and to make it accessible to the greater scientific community as a NASA publication.

A handwritten signature in black ink that reads "John H. Boeckel". The signature is written in a cursive style with a large, stylized initial "J".

John H. Boeckel
Director of Systems Reliability
Goddard Space Flight Center

PREFACE

These proceedings document the Technical Program of the eighth in the series of space simulation conferences jointly sponsored by the Institute of Environmental Sciences (IES), the American Institute of Aeronautics and Astronautics (AIAA), and the American Society for Testing and Materials (ASTM). The National Aeronautics and Space Administration (NASA) was also a co-sponsor of the sixth, seventh, and eighth conferences.

Responsibility for organizing and conducting these conferences is rotated among the three sponsoring societies, which participate in this effort in order to:

- Afford a broad, international forum for the exchange of meaningful and useful information in this field
- Realize economies both to the societies and to the participants by consolidating the conference efforts on this subject, and reducing the number of conferences
- Provide a mechanism for the unified publication of timely technical papers.

A permanent Joint Policy Committee is maintained by the three sponsoring societies. This committee, comprising two representatives from each of the three societies, provides guidance and formulates general policy for the organization and conduct of the conferences, thereby assuring compliance with each society's rules and regulations for the conduct of meetings.

A General Conference Committee is appointed for each conference. This committee is responsible for arranging and conducting the meeting, providing publicity, guest speakers, social affairs, ladies' programs, and publishing the proceedings. A Technical Program Committee is also appointed for each conference, and is responsible for organizing the technical program, acquiring and presenting technical papers, establishing and staffing the technical sessions, and compiling the proceedings.

The Technical Committees of the sponsoring societies which are directly involved in space simulation assist in organizing the technical program of the conferences. The committees which have historically assisted are:

- IES - Solar Radiation Committee
- AIAA - Ground Testing and Simulation Committee
- ASTM - Committee E-21 on Space Simulation

The scope of the eighth conference was expanded to include related technologies as well as the application of the space simulation and testing technologies to non-space activities in addition to classic space simulation technology. Consequently, in addition to the above committees, the following committees assisted in the eighth conference technical program, and were represented on the program committee:

- IES - Bio-Sciences Division
- AIAA - Life Sciences and Systems Committee
- ASTM - Committee F-7 on Aerospace Industry Methods

The Eighth Space Simulation Conference was hosted by the Institute of Environmental Sciences, and was held at the Sheraton-Silver Spring Motor Inn, Silver Spring, Maryland, on November 3, 4 and 5, 1975. The committees for this conference are listed on the following pages. The proceedings were published by the National Aeronautics and Space Administration, which was a co-sponsor of this conference.

George J. Frankel
Grumman Aerospace Corporation
Technical Program Chairman

COMMITTEES FOR
EIGHTH SPACE SIMULATION CONFERENCE

GENERAL CONFERENCE COMMITTEE

General Chairman	- Eugene N. Borson The Aerospace Corporation
Technical Program Chairman	- George J. Frankel Grumman Aerospace Corporation
Manager of Conference for IES	- John D. Campbell Perkin Elmer Corporation
Publications Chairman	- Russell T. Hollingsworth NASA/GSFC
Facilities Chairman	- David H. Orbock Northrop Services, Inc.
Registration Chairman	- Joseph Stecher NASA/GSFC

PROGRAM COMMITTEE

Charles H. Duncan	- NASA/GSFC
Paul R. Gauthier	- Boeing Aerospace Company
Terry L. Hershey	- Spectrolab Division of Textron
R. E. "Zeke" King	- Hughes Aircraft Company
Raymond Kruger	- NASA/GSFC
Eldon B. Nicholas	- Department of Transportation
David H. Orbock	- Northrop Services, Inc.
Richard Piotrowski	- NASA/JSC
Thomas C. Shupert	- Martin Marietta Corporation
David R. Simonsen	- Eastman Kodak Company
M. Donald Sivinski	- Sandia Laboratories
Emil S. J. Wang	- McDonnell Douglas Corporation
George F. Wright, Jr.	- Sandia Laboratories

JOINT POLICY COMMITTEE

IES

John D. Campbell - Perkin Elmer Corporation
Russell T. Hollingsworth - NASA/GSFC

ASTM

Eugene N. Borson - The Aerospace Corporation
Charles Duncan - NASA/GSFC

AIAA

Charles G. Miller - Jet Propulsion Laboratory
Dwight H. Reilly - NASA/LeRC

TABLE OF CONTENTS

SESSION 1 CONTAMINATION I: CONTAMINATION MODELS AND SPACECRAFT EXPERIMENTS

Session Organizer - Raymond Kruger
NASA Goddard Space Flight Center

Session Chairman - Raymond Kruger
NASA Goddard Space Flight Center

Session Co-Chairman - John J. Scialdone
NASA Goddard Space Flight Center

<u>Paper No.</u>		<u>Page</u>
1	AESC Multinodal Free Molecular Contamination Transport Model, E. A. Zeiner, Aerojet Electro- Systems Company	1
2	Spacecraft Recontamination, J. Barengoltz, Jet Propulsion Laboratory, D. Edgars, The Bionetic Corporation	33
3	Helios Surface Materials, Test-Predictions and Test- Results of Orbit Conditions Compared with Mission Results, W. Winkler, GfW/DFVLR, PORZ-WAHN	51
4	Correlation of an Optical System Degradation with Contamination on a Critical Surface, J. J. Scialdone, Goddard Space Flight Center	63
5	Data From a Synchronous Altitude Satellite Quartz Crystal Microbalance Monitor, John F. Rogers, NASA/ Goddard Space Flight Center	73
6	Experiment to Measure Enhancement of Spacecraft Contamination by Spacecraft Charging, David F. Hall and E. N. Borson, The Aerospace Corp., and R. A. Winn and W. L. Lehn, Air Force Materials Laboratory. .	89

SESSION 2 SPACECRAFT AND SYSTEMS TESTING I

Session Organizer - R. E. King
Hughes Aircraft Company

Session Chairman - Emile S. J. Wang
McDonnell Aircraft Company

Session C-Chairman - R. E. King
Hughes Aircraft Company

<u>Paper No.</u>		<u>Page</u>
7	Skylab Parasol Material Evaluation, Stephen Jacobs and Thomas J. Ballentine, Lyndon B. Johnson Space Center	109
8	Development of a Thermal Prediction Model and Flight Data Evaluation and Comparison for the EOB Experi- ment of the Helios Solar Probe, K. Kramp, W. Ley, H. P. Schmidt, Space Simulation Institute	125
9	Lay Out, Test Verification and in Orbit Performance of Helios A Temperature Control System, W. Brungs, Helios Project Team	133
10	Analysis of the Response of a Bimetal Actuated Thermal Control Louver System by Computer Simulation, R. Mancuso, RCA Astro-Electronics Division, P. Hrycak, New Jersey Institute of Technology	137
11	Dosimetry of Low Energy Proton Beams for Use in Spacecraft Parts Testing, Charles G. Miller, Jet Propulsion Laboratory, California Institute of Technology	153
12	Thermal Scale Modeling of a Manned Spacecraft, Roger L. Shannen and Ronald C. Zentner, The Boeing Company	155

SESSION 3 THERMAL PROTECTION

Session Organizer George F. Wright
 Sandia Laboratories

Session Chairman George F. Wright
 Sandia Laboratories

Session Co-Chairman - Robert E. Shedahl
 Sandia Laboratories

<u>Paper No.</u>		<u>Page</u>
13	Thermostructural Testing Of Instrumented ATJ-S Graphite Nosetip Models in the AFFDL 50 MW Rent Facility, Charles L. Budde, Air Force Materials Laboratory	159
14	Thermostructural Test Facilities for Re-Entry Vehicle Nosetip Materials, Charles L. Budde, Air Force Materials Laboratory	161
15	A Method for the Evaluation of Damage on the Surface of Carbon-Carbon Ablation Samples, E. W. Heinonen, G. Y. Jumper, Jr., Air Force Materials Laboratory . .	163
16	Large Modular Graphite Radiant Heaters for Testing Space Shuttle Thermal Protection Systems, B. G. Cox, McDonnell Aircraft Company, H. E. Christensen, McDonnell Douglas Astronautics	175
17	Properties of Conductive Coatings for Thermal Control Mirrors and Solar Cell Covers, D. E. Joslin and H. K. A. Kan, The Aerospace Corporation	187
18	An Experimental Summary of Plasma ARC Exposures of Space Shuttle High-Temperature Reusable Surface Insulation Tile Array with a Single Missing Tile, S. A. Galanter, Rockwell International Space Division	195
19	A New Arc Heater Shroud Test Technique for Thermo-Structural Testing of Full-Scale, Nose-Tip Skirt Materials, R. R. Williams and J. W. Stultz, McDonnell Douglas Research Laboratories, R. J. Popp, McDonnell Douglas Astronautics Company	209

SESSION 4
SPACECRAFT AND SYSTEMS TESTING II

Session Organizer - R. E. King
 Hughes Aircraft Company

Session Chairman - R. E. King
 Hughes Aircraft Company

Session Co-Chairman - Emile S. J. Wang
 McDonnell Aircraft Company

<u>Paper No.</u>		<u>Page</u>
20	Spin Test on Helios Louver, F. Joó, Space Simulation Institute	223
21	Special Problems of the Thermal Simulation of Helios Experiment E6 — Test Results Compared with Flight Data, W. Hallmann, W. Ley, H. P. Schmidt, DFVLR, Space Simulation Institute	233
22	Helios Mission — Critical Assessment of Ground Test Results Versus Actual Orbit Performance, H. C. Benöhr and H. W. Prem, Messerschmitt-Bölkow- Blohm GmbH, Space Division	243
23	Combined Environmental Effects on Polymers, Lawrence Fogdall, Sheridan S. Cannaday, Boeing Aerospace Company	259
24	Functional and Dynamics Testing of the Flexible Solar Array for the Communications Technology Satellite, T. D. Harrison, R. Buckingham, F. R. Vigneron	261

SESSION 5 CONTAMINATION II: THE SPACE TRANSPORTATION SYSTEM

Session Organizer - Raymond Kruger
NASA Goddard Space Flight Center

Session Chairman - R. J. Naumann
NASA Marshall Space Flight Center

Session Co-Chairman - L. Leger
NASA Johnson Space Center

<u>Paper No.</u>		<u>Page</u>
25	Preliminary Evaluation of the Contaminant Induced Environment for the Space Shuttle Orbiter, L. E. Bareiss, R. O. Rantanen, and E. B. Ress, Martin Marietta Corporation, L. J. Leger, NASA, Lyndon B. Johnson Space Center	279
26	STS Contamination Control Requirements; Rational & Implication, R. Naumann, NASA Marshall Space Flight Center.	305
27	A Radiometer for Monitoring Column Densities of Infrared-Active Molecules, F. C. Witteborn, J. P. Simpson, L. S. Young, C. D. Swift and R. K. Melugin, NASA-Ames Research Center	307
28	The Outgassing Rate for a Shuttle Thermal Protective Surface Using RTV 560 Adhesive, D. W. Jex, E. L. Shriver, Marshall Space Flight Center.	321
29	Cryogenic Quartz Crystal Microbalance, D. McKeown, G. Sonnenschein and M. G. Fox, Faraday Laboratories Inc.	343

SESSION 6 THERMAL SIMULATION

Session Organizer - Richard J. Piotrowski
NASA Johnson Space Center

Session Chairman - Richard J. Piotrowski
NASA Johnson Space Center

Session Co-Chairman - Albert R. Lunde
Boeing Aerospace Company

<u>Paper No.</u>		<u>Page</u>
30	Analysis of Radiative Sources with Both Specular and Diffuse Characteristics in the Visible and Infrared Spectrum, Franklin U. Williams, Johnson Space Center	355
31	Satellite Thermal Modeling Using The Illuminographic Camera, S. J. Wiesner, Stanford University, B. Howland and D. M. Nathanson, Massachusetts Institute of Technology, Lincoln Laboratory	371
32	The Use of Solar Simulation Systems for Producing Artificial Global Radiation for the Purpose of Determining the Heat Load of Rooms, A. C. Kalt, DFVLR, Space Simulation Institute	387
33	High Energy Solar Beam Testing in the JPL 25-ft Space Simulator, J. W. Harrell, Jet Propulsion Laboratory	401
34	Performance and Operating Characteristics of a 4.88-M Diameter Solar Simulator for Viking Space Simulation Tests, R. P. Parrish, Martin Marietta Aerospace	409
35	Special Techniques of the Viking Lander Capsule Thermal Vacuum Test Program, T. Buna, Martin Marietta Aerospace	419
36	Thermoelastic Analysis of Solar Window of a Vacuum Chamber, C. L. Amba-Rao and S. R. Soni, Space Science & Technology Centre	435

SESSION 7 SPACE SIMULATION FACILITIES AND OPERATIONS

Session Organizer - Robert P. Parrish
Martin Marietta Corporation

Session Chairman - Robert P. Parrish
Martin Marietta Corporation

Session Co-Chairman - Paul R. Gauthier
Boeing Aerospace Company

<u>Paper No.</u>		<u>Page</u>
37	Transport of Liquid State Nitrogen Through Long Length Service Lines During Thermal/Vacuum Testing, F. A. Florio, General Electric Company	449
38	Leak Rate Measurements for Satellite Subsystems and Residual Gas Analysis During Space Environment Tests H. Nuss, LABG, Laboratory for Space Simulation	469
39	The Thermal System for an Environmental Chamber, K. Srinivasan, Engineer SC2, Space Science & Technology Centre ISRO Post, K. Badari Narayana, S. Srinivasa Murthy and M. V. Krishna Murthy, Department of Mechanical Engineering	487
40	Vacuum Considerations in the Design of a Space Simulator, S. Ramachandran, E.T.D. Project Vikram Sarabhai Space Centre	495
41	Facility and Test Support Equipment for the Manned Thermal-Vacuum Tests of the Apollo Soyuz Docking Module, O. L. Pearson, Johnson Space Center	505
42	Preparation, Control, and Use of Standard Operating Procedures in a Space Simulation Laboratory, R. P. Parrish, Jr., Martin Marietta Corp	533

SESSION 8 SPECIAL TOPICS

Session Organizer - David H. Orbock
Northrop Services, Inc., GSFC

Session Chairman - David H. Orbock
Northrop Services, Inc., GSFC

Session Co-Chairman - Thomas R. Amacher
Northrop Services, Inc., GSFC

<u>Paper No.</u>		<u>Page</u>
43	Design and Application of a Goniophotometer, M. W. Finkel, and J. B. Heaney, Goddard Space Flight Center and R. K. Brookshier	537
44	Scattering From Specular Surfaces, M. W. Finkel, Goddard Space Flight Center	549
45	Skylab Fluid Mechanics Simulations: Oscillation, Rotation, Collision and Coalescence of Water Droplets Under Low-Gravity Environment, Otha H. Vaughan, Jr., Aerospace Environment Div./Space Sciences Lab., NASA/Marshall Space Flight Center, R. J. Hung, The University of Alabama.	563
46	Size Distribution of Fragment Debris Produced by Simulated Meteoroid Impact of Spacecraft Wall, T. Dale Bess, NASA, Langley Research Center.	575
47	Application and Utilization of a Space Chamber for the Drying and Decontamination of Books, Documents and Other Materials to Prevent Biodeterioration, Martin G. Koesterer, Senior Microbiologist, and John A. Geating, Bioscientist, Biomedical Programs Operation, Space Systems Organization, General Electric Company	589
48	The High Current Transient Generator — Theory and Operation for Simulating Lightning Induced Voltages Into Aerospace Electrical Circuits, E. H. Schulte, McDonnell Aircraft Company	591

SESSION 9
CONTAMINATION III: SPECIAL FACILITIES AND EQUIPMENT
FOR DEFINING AND DEALING WITH CONTAMINANTS

Session Organizer - Raymond Kruger
NASA Goddard Space Flight Center

Session Chairman - C. B. Fischer
Aerojet ElectroSystems Company

Session Co-Chairman - E. A. Zeiner
Aerojet ElectroSystems Company

<u>Paper No.</u>		<u>Page</u>
49	A Study of Molecular Contamination, T. H. Allen, T. A. Hughes, McDonnell Douglas Corporation, B. C. Price, U.S. Air Force Materials Laboratory . . .	609
50	A System for the Study of Molecular Contamination, C. F. Dillow, T. H. Allen, and R. M. F. Linford, McDonnell Douglas Corporation, R. G. Richmond, NASA Johnson Space Center	623
51	Optical Measurements on Contaminated Surfaces, T. E. Bonham, R. J. Schmitt, and R. M. F. Linford, McDonnell Douglas Corporation	635
52	Spacecraft Contamination Under Simulated Orbital Environment, R. W. Phillips, L. U. Tolentino, and S. Feuerstein	645
53	A Laser Particulate Spectrometer for a Space Simulation Facility, R. J. Schmitt, B. A. Boyd, and R. M. F. Linford, McDonnell Douglas Corporation, R. G. Richmond, NASA Johnson Space Center	647
54	Particulate Size Distribution Cascade Analyzer for Space- Craft Contamination Monitoring, Donald A. Wallace, Engineering Manager, and Raymond L. Chuan, Assistant to the President, International BioPhysics Corp.	663
55	Development of a Laboratory Demonstration Model Active Cleaning Technique Device, R. L. Shannon and R. B. Gillette, The Boeing Company	665

SESSION 10
BIOSCIENCES/MANNED EFFECTS

Session Organizer - M. Donald Sivinski
 Sandia Laboratories

Session Chairman - M. Donald Sivinski
 Sandia Laboratories

Session Co-Chairman - Paul R. Gauthier
 Boeing Aerospace Company

<u>Paper No.</u>		<u>Page</u>
56	Walking in a Rotating Space Station: An Electromyographic and Kinematic Study, Randall L. Harris, Sr., Langley Research Center	689
57	Comparison of Two Methods of Predicting Characteristics of an Organism Which Develops Under the Condition of Free Fall, A. H. Brown, A. O. Dahl, D. K. Chapman, and L. Loercher, Plant Centrifuge Laboratory, University City Science Center and Biology Department, University of Pennsylvania	705
58	A Thermal Vacuum—UV Solar Simulator Test System for Assessing Microbiological Viability, Dennis S. Ross, Michael D. Wardle and Daniel M. Taylor, Jet Propulsion Laboratory, California Institute of Technology . .	711
59	Life Sciences Laboratory Breadboard Simulations for Shuttle, S. T. Taketa, R. C. Simmonds, and P. X. Callahan, Ames Research Center.	723
60	Metabolic Rate Control During Extravehicular Activity Simulations and Measurement Techniques During Actual EVAs, David J. Horrigan, NASA, Johnson Space Center	741
61	The Use of a Model of Human Thermoregulation During The Apollo and Skylab Programs, James M. Waligora, NASA, Johnson Space Center.	749

62	Evaluation of the Gravity Independent Miniature Analytical System, Larry D. Wallace, Carolyn S. Leach, and C. B. Lassiter, NASA, L. B. Johnson Space Center	759
63	Proposed Applications of Lower Body Negative Pressure to Cardiology, E. V. Schmidt, R. F. DeBusk, R. L. Popp, Division of Cardiology, The Biomedical Technology Transfer Team, Stanford University School of Medicine	769

SESSION 11

REMOTE SENSING RADIOMETRY AND SOLAR MEASUREMENTS

Session Organizer - Charles H. Duncan
NASA Goddard Space Flight Center

Session Chairman - Charles H. Duncan
NASA Goddard Space Flight Center

Session Co-Chairman - George E. Sweet
NASA Langley Research Center

<u>Paper No.</u>		<u>Page</u>
64	Calibration Source for Remote Sensors, J. T. McLean and A. McCulloch, Goddard Space Flight Center, E. I. Mohr, Columbia Union College	783
65	The Status of the Measurement and Transfer of the Absolute Spectral Response of Silicon Photodiodes, Edward Zalewski, National Bureau of Standards	797
66	Current Status and Future Plans for NBS Radiometric Source Standards, Henry J. Kostkowski, National Bureau of Standards	799
67	Solar Radiation Measurements by the Active Cavity Radiometer — Past, Present and Future, R. C. Wilson, Jet Propulsion Laboratory, California Institute of Technology.	807

68	Initial Solar Radiation Measurements from ERB, J. R. Hickey and F. J. Griffin, The Eppley Laboratory, Inc., D. T. Hilleary, NOAA/NESS	809
----	---	-----

SESSION 12
FLAMMABILITY; SMOKE SENSITIVITY, TOXICITY TESTING

Session Organizer - Eldon B. Nicholas
Dept. of Transportation, FAA

Session Chairman - Eldon B. Nicholas
Dept. of Transportation, FAA

Session Co-Chairman - Joe C. Spurgeon
Dept. of Transportation, FAA

<u>Paper</u> <u>No.</u>		<u>Page</u>
69	Quantitative Determination of Smoke and Toxic Product Potential of Materials with the Aminco [®] NBS Smoke Density Chamber, Samuel Greenberg, Applications Engineer, American Instrument Company	815
70	Fire-Resistant Aircraft Materials Development and Evaluation Program, Richard W. Bricker, and Robert N. Stuckey, NASA Johnson Space Center	833
71	Development of Fire Resistant Electronic Configurations for Use in Oxygen Enriched Environments, F. J. Smith, Martin Marietta Aerospace	855
72	A Relative Toxicity Ranking of Thermally Decomposed Aircraft Interior Materials, Joe C. Spurgeon, DOT/ FAA/NAFEC	859

AESC MULTINODAL FREE MOLECULAR CONTAMINATION TRANSPORT MODEL

E. A. Zeiner, *Aerojet ElectroSystems Company, Azusa, California*

ABSTRACT

This report focuses on the film formation effects of self-induced clouds and condensed films of volatile-condensable materials (VCMs) which outgas from such sources as paints, coatings, adhesives, and other non-metallic surfaces of satellites. A semi-empirical theory for the multiple scattering of free neutral molecules from dielectric surfaces which includes the effects of condensation and evaporation has been defined and a mathematical model of the process was developed. The formation rate of thin surface films is considered to be the net accumulation of two simultaneous, but independent, molecular processes; emission (evaporation) and adsorption (condensation).¹ The net formation rate is considered to be dependent upon the temperature of the surface nodes, the mass and temperatures of the gas molecules, and the total pressure of the incident molecular flux. For a given contamination source material which emits various VCMs, a saturation pressure versus temperature curve must be experimentally determined. A similar curve is required for the VCM in addition to the change in the average molecule weight versus temperature. Finally, the temperature dependency of the thermal accommodation coefficient must be experimentally obtained. Apparatus and procedures for measuring these parameters are presented.

The model was initially derived for a "regular" enclosure where all nodes "see" each other with about the same order of geometric view factors. This regularity admits an assumption of a uniform molecular flux magnitude (isotropic or scalar flux) on each nodal surface. Enough scattering occurs so that the flux motion is completely random. A second formulation introduces flux anisotropy by assuming a more general enclosure configuration where nodal sizes vary significantly and some nodes can not "see" others. In this case, a mass transfer analogy to radiation heat transfer methods can be introduced where geometric view factors couple the internodal fluxes. Enough scattering must occur to at least tangentially randomize the motion of the local flux.

For exterior surfaces, where insufficient scattering occurs to tangentially randomize the motion of the flux, Monte Carlo path-line tracing methods are generally required. However, a single scattering interaction could be approximated using a modification of diffuse emission to account for the directional character of the emitted flux.

INTRODUCTION

Concern has recently risen about the effects of molecular clouds and condensed films of VCMs which outgas from such sources as paints, coatings, adhesives, and other non-metallic surfaces of satellites. This report focuses on the film formation aspects of the problem. The objectives are to quantitatively predict the instantaneous film thickness and formation rate on a surface which is remote from the emitting source material. While aerodynamics and aerosol modeling techniques have good applicability to describe self-induced molecular clouds provided the source characteristics are valid, the aerosol technology is limited to noncondensing gases. A more general mass-transport model is therefore required if contamination control systems such as cold, condensing baffles ("cold-traps") are to be reliably designed. This more sophisticated transport model is also needed to quantitatively evaluate the use of local heaters to inhibit film-type contamination, and to identify the best locations on a satellite for positioning cold IR sensor detectors, windows, and radiators. In fact, without a transport model which accounts for the condensability of VCMs, contamination management for sensitive orbiting systems degenerates to guess work.

To quantitatively account for the VCM film formation phenomenon, a transport model must include the time and temperature dependency of the VCM source outgassing (evaporation, sublimation) and the adsorption (condensation) rates. It must further include the geometrical arrangement and temperatures of the nodal surfaces which define the boundaries of the system as well as the physical characteristics of the VCM molecules themselves. The model presented here is intended for practical engineering design application. Therefore, the parameters which characterize the emission and condensation of the VCM molecules must relate to practical materials and processes and be measurable in relatively simple laboratory configurations using conventional instrumentation and procedures. While atomistic derivation of condensation and evaporation probabilities relating to a given number of VCM-surface collisions can be broadly described by quantum mechanics,² workable results currently limit this approach to the simple known gas molecules. In the real world,

the VCM molecules are very complex and their chemistry is very uncertain at the present time.

One of the principle advantages of this semi-empirical approach is that the chemical identification of the VCM need never be known except for its average mass spectra as a function of temperature.

In this contamination transport model, the VCM from the source material is assumed to be diffusion-limited for short-term outgassing (several days) and is described in that period by a diffusion coefficient and an initial concentration; both being temperature dependent.³ After the short-term products (resins, moisture, etc.) have volatilized, a long-term emission follows where such VCMs as plasticizers and unpolymerized fractions are emitted at very low outgassing rates. This emission is best described as a Langmuir process where the mass loss is related to a source saturation pressure at each temperature. The free VCM is characterized by an average mass number (by averaging the mass spectra) at each temperature, by a VCM saturation pressure-temperature profile, and by a set of Knudsen thermal accommodation coefficients.⁴ In the initial steps of the model derivation, the sticking coefficient of the VCM is introduced. This coefficient can subsequently be eliminated from the equations of transport by observing that the difference between the molecular emission rate and the simultaneous condensation rate is linearly dependent on the difference between the VCM saturation vapor pressure and the local VCM kinetic pressure.⁵ This substitution of variables eliminates the need to measure sticking coefficients which can be quite arduous, and describes condensation and evaporation as pressure-dependent processes which are well established phenomena.

Synoptically, the paper initially presents assumptions and limitations of the model. This is followed by the derivation of the nodal pressures in terms of an incident molecular flux by applying kinetic theory. Next, a set of first order non-homogeneous differential equations were derived which describe the rates of change of the energy classes of the molecules within the bounding nodal enclosure. For the isotropic flux version of the model, the isotropy of the fluxes permits expressing the molecular density in terms of nodal pressures so that differential equations can be written in terms of the nodal pressures. The parameters which characterize the source and the VCM are in the elements of the coefficient matrices of the differential equations. Numerical integration is probably the most practical method to solve these equations when many surface nodes are involved. However, when the system configuration is simplified to only two or three nodes, closed form solutions to the differential equations of pressure are

practical. Procedures can then be established by which these parameters can readily be measured using a large ultra-clean high vacuum chamber, a nude ion gage, a 400 AMU mass spectrometer (RGA), and a quartz-crystal micro-balance (QCM). The apparatus, instrumentation, and procedures needed to make these measurements have been described. The simplified isotropic flux version of the model, which is applicable to the test configuration, is then generalized for "irregular" configurations by introducing geometric view factors between the nodes. The resulting equations are substantially more complex and as the derivation shows, digital computers must be used to solve these equations. To apply the model to the exterior surfaces of satellites, where, for the most part, the bounding enclosure is open space, Monte Carlo path-tracing methods are required since insufficient scattering occurs to generate a tangentially randomized flux over the nodes. First order approximations, assuming single nodal interactions, can be computed using emission geometry modified for non-diffuse emission.

ASSUMPTIONS

The first assumption is based on the phenomenology of the physical adsorption of molecules on clean surfaces.⁶ It was assumed that a sub-film always exists on all surface nodes and that the net mass evaporation and condensation rates are linearly proportional to the algebraic difference between the saturation vapor pressure at the node temperature and the local kinetic vapor pressure on the node. Thus evaporation will take place when the kinetic pressure is less than saturation (provided the VCM film thickness is greater than the sub-film) and condensation will take place when the kinetic pressure is greater than saturation. The linear proportionality follows from Langmuir's experiments. Experiments have shown that a very thin film is rapidly formed (milliseconds) on a clean surface at constant temperature and that its thickness is limited to only a few molecular layers until the exterior gas pressure reaches the saturation vapor pressure. The BET theory⁶ accounts for this sub-film formation which essentially saturates the surface Van der Waals forces so that the subsequent condensation process for pressures above saturation is independent of the surface properties.

A second assumption requires that the molecular density of the VCM at any location be low enough to insure that the free VCM can be considered Maxwellian. This rarified gas restriction requires the mean-free path to be in excess of any significant physical dimension. This precludes any significant intermolecular collisions within the VCM itself and the absence of any boundary layer

on the nodal surface (except the sub-film). When no fluid-boundary layer exists, experimental evidence indicates that the scattering of molecules following surface interactions is nearly diffuse regardless of the incident angle of the molecule,⁷ provided the mass of the molecule is greater than about 10 AMU. It is this scattering characteristic of a rarified gas that permits application of a thermal radiation mass analog using geometric view factors to account for the distribution of molecular flux among the system nodal surfaces. The VCM is considered to be constituted of as many energy or temperature "classes" of molecules as there are different nodal temperatures. Due to the lack of molecular intercollisions, each class exists independently with the Maxwellian velocity distribution corresponding to the class temperature.

A third, and perhaps the most restricting assumption, is that an average mass number must be designated for the VCM over the complete temperature range of all the nodal surfaces. A VCM at a given temperature is comprised of many different molecular species as evidenced by typical mass spectra data.⁸ This composition changes with the respective temperatures of the system nodes.

A final assumption was formulated which limited the thermokinetic response of a VCM molecular surface interaction. Associated with each surface collision, the incident molecule was assumed to have three subsequent possibilities. It could be "elastically" scattered whereby its temperature was unchanged and only its direction was altered. This is typical of very light inert gases on inactive surfaces. It could also be "inelastically" scattered although fully accommodated. This is the process typically associated with non-condensing gases of molecular weights greater than 20 AMU which come to thermal equilibrium with a surface, but do not adhere. Finally, the incident molecule may be permanently adsorbed on the nodal surface. The knudsen "thermal accommodation coefficient" indicates the probability of whether an elastic or inelastic scattering event occurs, while the "sticking coefficient" determines the probability of a fully accommodated molecule being permanently adsorbed.

A number of other assumptions are required when the general transport theory is specialized for differing geometric configurations. The most general approach would apply Monte Carlo path-tracing techniques which can easily incorporate any directional scattering probability desired. Recent outgassing experiments indicate that the outgassing has almost a cosine distribution about the surface normal.^{3,8} In the Monte Carlo technique, a molecular flux is not defined since each molecule is traced. Computational times and costs may be prohibitive. A significant

simplification results if it is assumed that over each node, the molecules of each class have been scattered enough times to be more or less tangentially randomized (i.e., molecules possess random motion in the plane parallel to each surface). The local value of the molecular density will vary among the nodes as predicated by the configuration, but a flux can be defined for each class of molecule incident on each node. For a configuration which has n nodes at different temperatures, this simplification results in n^2 first order differential equations with the inter-nodal flux coupling being described by geometric-view factors assuming diffuse (Lambertian) scattering and emission. While computer facilities are required to solve the equations, the operations are numerical integration and matrix manipulations which are well adopted for machine processing. Finally, if the areas of the nodal surfaces which bound the system are about the same size and uniformly configured, the molecular density of each class of molecule becomes uniform throughout the defined volume thereby creating a completely isotropic flux of equal magnitude on each node. This simplification eliminates the need for geometrical-view factors and reduces the model to n linear differential equations which can be easily integrated in a functional closed form when the configuration has only two or three nodes. This closed form solution is absolutely required to design the experimental geometry and instrumentation necessary to measure the source and VCM transport parameters.

In the derivations which follow, the isotropic (scalar) flux simplification was initially assumed for each class of molecule. The solution for a 2-node system with a small hole is then obtained which is applied to the test configuration. Then, the first level generalization to an anisotropic tangentially randomized flux is derived which is necessary for the generally irregular surface configurations such as are typical of the interior compartments and surfaces of orbiting satellites. A specialization is then made for non-diffuse emission and scattering processes which can be applied to the interior model, or to external "open" systems where insufficient scattering exists to develop tangential randomization. This non-diffuse emission process requires modified view factors to define the flux coupling.

NODES

Two unique types of nodes were identified in this transport model: source nodes and VCM nodes. A principal difference is the initial condition of the surface. A source node is initially covered with the VCM source material while the VCM node is clean except for the sublayer. The concentration of VCM in the

source material is far less than the relatively pure VCM film which condenses on a VCM node. Hence, the saturation pressure of the VCM for a source node will be substantially less than for a VCM node at the same temperature. This is a direct application of Raoult's Law.

A typical source node is shown in Figure 1a. The node is covered with the contamination source material of a specified thickness, h . If diffusion-limited short-term outgassing is to be considered, the VCM initial concentration, C_0 , and diffusion coefficient, D_0 , must be specified. These properties can be related to a time-varying saturation pressure, P_{ℓ} , by proper experimentation. For long-term outgassing, the Langmuir equation has been shown to be quite applicable. The emission flux from a source node is thus a short-term diffusion-limited³ process superimposed upon the long-term Langmuir outgassing process.

775-1267

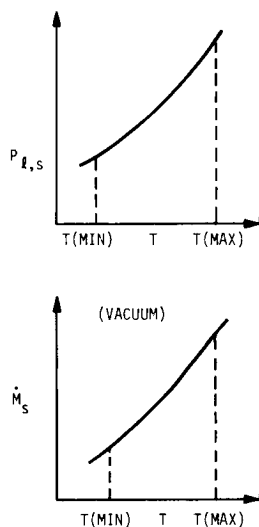
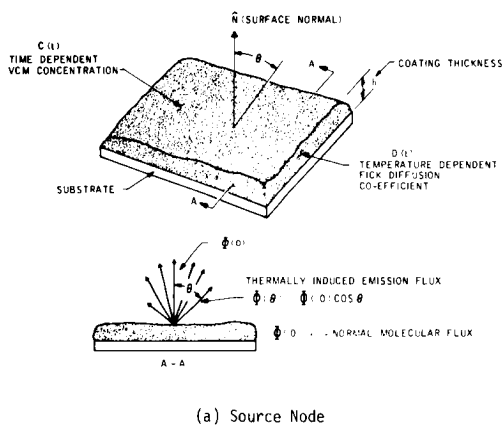


Figure 1. Characteristics of Typical Source Node

$$\phi_{e,s}(t) \cong C_0 \sqrt{\frac{D_0}{\pi t}} \left[1 + 2 \sum_{n=1}^{\infty} (-1)^n e^{-\frac{n^2 h^2}{D_0 t}} \right] + \frac{A_0 P_{\ell,s}}{\sqrt{2\pi R \bar{M} T_s}} \quad (1)$$

When a VCM flux is incident on a source node it is presumed that its volatility is characterized by the saturation pressure-temperature profile of the source node. The mass emission flux, in the absence of any incident flux (vacuum) for a source node, can be expressed in terms of the source emission curve parameters shown in Figure 1b. This is Langmuir's equation.

$$\dot{m}_{\text{source}} = \frac{A_o}{\sqrt{2\pi R}} \sqrt{\frac{\bar{M}}{T_s}} P_{l,s} \quad (2)$$

A VCM node does not require any parameter specifications.

VCM CHARACTERISTICS

While a formal chemical analysis of a VCM is not necessary to permit accounting for its transport properties, it is necessary to quantify the thermo-kinetic behavior of the VCM molecules as they interact with a surface. This requires the determination of three VCM properties as indicated in Figure 2. The average mass number, \bar{M} , of the VCM must be known throughout the temperature range of the system. This is indicated in Figure 2a where the lighter more volatile components are emitted at lower temperatures and the higher mass fractions are released at higher temperatures. Similar to the source node, a saturation pressure-temperature (P_l - T) profile is needed as sketched in Figure 2b.

775-1265

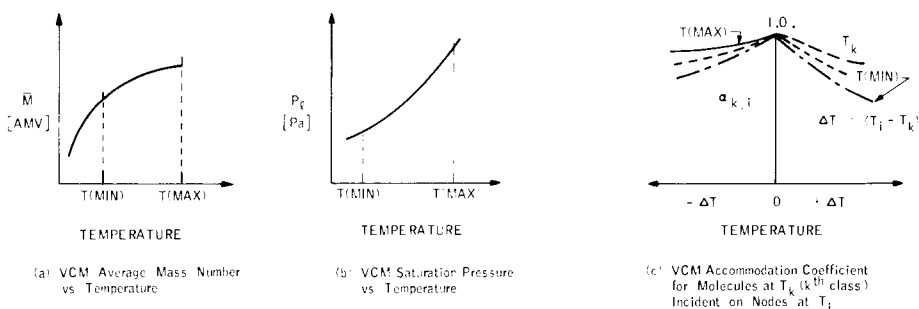


Figure 2. Typical VCM Thermo-Kinetic Properties

It has been noted that an incident VCM molecule can react in three ways and that this behavior is accounted for by defining two statistical probabilities. The one shown in Figure 2c is the

thermal accommodation coefficient, $\alpha_{k|i}$, which is the probability that an incident molecule of the k th class (i.e., one from the group of molecules with a Maxwellian distribution about T_k) will become "thermalized" during the interaction so that its temperature becomes the same as the surface node. The node temperature differs from the kinetic temperature of the molecule and the accommodation coefficient is in general not symmetrical about the parent node, T_k , where it is unity by definition. The other probability is the sticking coefficient, $\sigma_{k|i}$, which in this model is the probability that an incident molecule will be permanently adsorbed or condensed on the surface. This is a subset of the accommodation coefficient since it is assumed that an adsorbed molecule has been fully accommodated. However, the converse is not necessarily true as is the case with the non-condensables in the VCM. Figure 3 illustrates the application of these parameters in accounting for the scattering and adsorption of incident k th class molecules on a VCM nodal surface at T_i . The emission flux can readily be computed from the saturation pressure curve at T_i using the Langmuir equation.

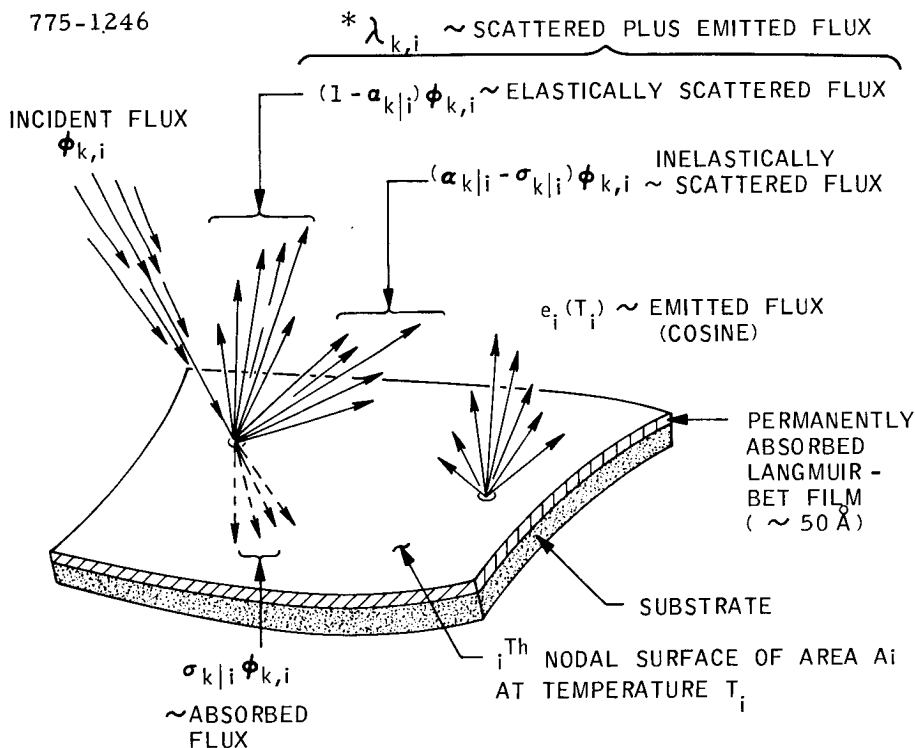


Figure 3. Flux Interactions on a VCM Node

BOUNDING ENCLOSURE

In order to predict the mass accumulation rates on a system of nodes, it is necessary to define the boundaries of the nodal system. When the source node clearly "sees" all the VCM nodes and these in turn "see" each other and are about the same size, the boundaries are self-evident and the enclosure is said to be "regular". A simple configuration is depicted in Figure 4, along with the description of nodal and VCM characteristics as are appropriate. Care in defining the bounding enclosure and identifying the nodes is required when repeated scattering will cause flux to strike nodes which are obscured from the source line of sight. Since the scattering is more or less diffuse, this can include surfaces which are quite remote from the source node.

775-1247

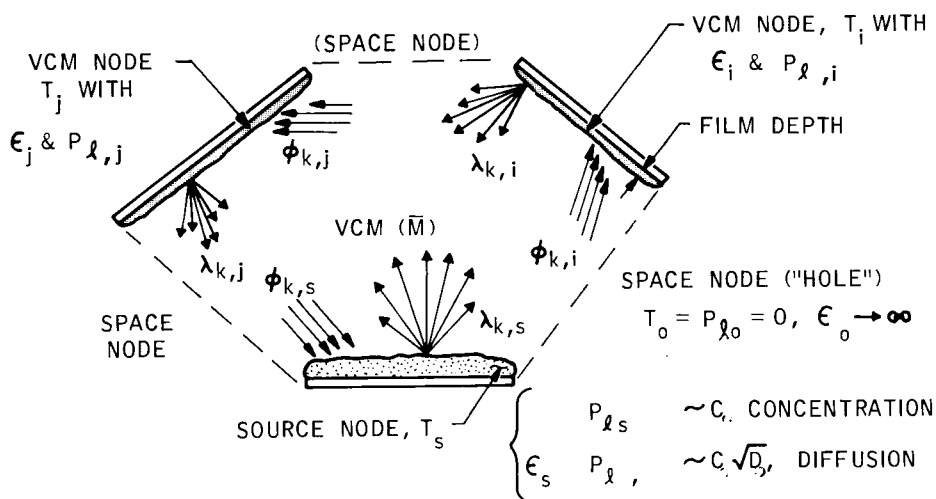


Figure 4. A Multi-node Bounding Enclosure

Once the bounding enclosure is established for a specified configuration, it is possible to define the total number of VCM molecules of a given class that are within the boundaries at any given instant of time. Since the bounding nodal surfaces are the only sources and sinks, the rate of change in this total number of molecules can be described in terms of the flux interactions at each surface. Mathematically, this is described as a set of linearly coupled ordinary first order non-homogeneous differential equations. It is a property of these systems that following a

step change in the nodal temperatures, a brief exponential transient occurs in the total number of molecules after which an equilibrium condition is established where the number of molecules emitted throughout the system is just balanced by the number being adsorbed or passing into space. This is simply a statement of the conservation of mass within the bounding enclosure.

If the system has a single hole (space node), all of the VCM which is available in the source will eventually pass through it into space. If there are no such nodes, all the VCM will eventually end up on the coldest surface. If all the VCM nodes possess temperatures equal to the source node (an isothermal container), then the source will outgas until saturation vapor pressure is obtained for the source material at that temperature. The number of molecules can be readily computed from the ideal gas law.

NODAL PRESSURES

The pressure on a nodal surface is the reaction force per unit area created by the change in the normal component of linear momentum per unit time of incident molecules which are scattered and adsorbed, and of the molecules which are thermally emitted.⁹ As mentioned previously, the completely general case requires an individual trajectory tracing (Monte Carlo) method which places no restriction on the motion of each molecule followed. If it can be assumed that enough scattering has occurred within a bounding enclosure so that incident flux on each node has been at least tangentially randomized (i.e., equal directional probability in the planes parallel to the surfaces), then the results of kinetic theory can be applied which relate the pressure to the incident flux.

For each class of molecules (say, the k th class) incident on a nodal surface (say, the i th node), the incident molecular flux ($\phi_{k,i}$) can be partitioned into three groups corresponding to the three-event probabilities following a surface interaction. Let the accommodation coefficient of the k th class molecules on the i th node be labeled $\alpha_{k|i}$, and the corresponding sticking coefficient be labeled $\sigma_{k|i}$. The elastically scattered fraction of the incident k th-class molecular flux is then $(1-\alpha_{k|i})\phi_{k,i}$. The fraction of incident flux which is inelastically scattered is $(\alpha_{k|i}-\sigma_{k|i})\phi_{k,i}$, and the fraction which is permanently adsorbed is simply $\sigma_{k|i}\phi_{k,i}$. Considering that the k th class molecules all possess temperature T_k (they were either emitted by or inelastically scattered from the k th node, or elastically scattered from the other nodes), then the pressure due to

the k th class tangentially randomized flux on the i th node (at temperature T_i) can be expressed according to kinetic theory.

$$P_{k,i} = \left\{ \frac{1}{A_o} \sqrt{2\pi R \bar{M} T_i} (1 - \alpha_{k|i}) + \frac{1}{2A_o} \sqrt{2\pi R \bar{M} T_i} \left[1 + \sqrt{\frac{T_k}{T_i}} \right] \right. \\ \left. (\alpha_{k|i} - \sigma_{k|i}) + \frac{1}{2A_o} \sqrt{2\pi R \bar{M} T_i} \sqrt{\frac{T_k}{T_i}} \sigma_{k|i} \right\} \phi_{k,i} \quad (3)$$

Equation (3) can be rearranged and summed over all the classes of molecules to give the pressure due to all incident molecular fluxes.

$$P_{\phi,i} = \frac{1}{2A_o} \sqrt{2\pi R \bar{M} T_i} \sum_{k=1}^n \left[\alpha_{k|i} + (2 - \alpha_{k|i}) \sqrt{\frac{T_k}{T_i}} \right] \phi_{k,i} \\ - \frac{1}{2A_o} \sqrt{2\pi R \bar{M} T_i} \sum_{k=1}^n \sigma_{k|i} \phi_{k,i} \quad (4)$$

Assuming that the thermally emitted flux from the i th node (ϵ_i) is more or less diffusely emitted (experiments indicate that a cosine directional probability is more precise), kinetic theory defines the pressure due to emission.

$$P_{\epsilon,i} = \frac{1}{2A_o} \sqrt{2\pi R \bar{M} T_i} \epsilon_i \quad (5)$$

The total pressure on the i th node is the sum of the pressure of the incident fluxes and the emission flux.

$$P_i = P_{\phi,i} + P_{\epsilon,i} \quad (6)$$

Experimental evidence¹⁰ indicates that the net evaporation rate of a volatile material from a surface is directly proportional to the excess of the saturation vapor pressure of that substance at the nodal temperature to the total vapor (VCM) pressure.

$$(P_{\ell i} - P_i) = \frac{1}{2A_o} \sqrt{2\pi R \bar{M} T_i} \left[\epsilon_i - \sum_{k=1}^n \sigma_{k|i} \phi_{ki} \right] \quad (7)$$

Equation (7) substitutes the saturation VCM pressure $P_{\ell i}$ for the more complicated series term with the sticking coefficients. This substitution represents a significant simplification in the experimental work needed to measure the transport parameters. The final expression for the i th nodal pressure is obtained by combining Equations (6) and (7).

$$P_i = \frac{1}{2} P_{\ell i} + \frac{1}{4A_o} \sqrt{2\pi R \bar{M} T_i} \sum_{k=1}^n \left[\alpha_{k|i} + (2 - \alpha_{k|i}) \sqrt{\frac{T_k}{T_i}} \right] \phi_{k,i} \quad (8)$$

NODAL MASS LOSS RATES

The principle expressed in Equation (7) permits direct computation of the net mass loss rate from a node. The net mass rate per unit area (mass flux), at which the previously adsorbed VCM is leaving the i th node, is the product of the average mass of VCM molecules and the net evaporation flux.

$$\dot{m}_i = \frac{\bar{M}}{A_o} \left[\epsilon_i - \sum_{k=1}^n \sigma_{k|i} \phi_{k,i} \right] \quad (9)$$

Then the total mass rate from the i th node can be expressed by substitution of Equation (7) in Equation (9) and multiplying by the nodal area.

$$\dot{M}_i = \frac{2A_o A_i}{\sqrt{2\pi R}} \sqrt{\frac{\bar{M}}{T_i}} (P_{\ell i} - P_i) \quad (10)$$

If $P_{\ell i} > P_i$, evaporation is occurring and \dot{M}_i is positive. Conversely when $P_{\ell i} < P_i$, condensation is occurring and \dot{M}_i is negative. When a node is in a perfect vacuum, no flux is incident on that node. The nodal pressure is then reduced to that of emission only by Equation (6). The pressure due to emission only then is obtained from Equation (8).

$$P_{e,i} = \frac{1}{2} P_{\ell i} \quad (11)$$

When this result is applied to Equation (10), the Langmuir equation for loss of material from a surface in vacuum is obtained.

DIFFERENTIAL EQUATIONS OF MOLECULAR DENSITY

In order to determine the instantaneous value of the nodal pressures and the mass loss rates, it is necessary to develop the differential equations which describe the rates of change in the total number of molecules of each class within the bounding volume. These changes occur at each node for each class of molecule. When deriving these equations for the case where non-uniform densities exists, the problem is complicated by the existence of n^2 fluxes which are coupled by geometric view factors, but only n differential equations describing the changes in the molecular densities. When the uniform density assumption is made, the nodal fluxes become independent of the system view factors so that there are exactly n independent fluxes associated with the n nodes of the system.

In a "regular" enclosure, at any instant of time, there are N_i molecules of the i th class. This number is continually being increased at the i th node by emission and by inelastic scattering of other incident class molecules. It is continually being decreased at remote nodes by inelastic scattering and adsorption. The rate of change of the total number of molecules of the i th class can be expressed as an ordinary non-homogeneous first-order differential equation with linear coupling of the fluxes.

$$\frac{dN_i}{dt} = A_i \epsilon_i + \sum_{k=1}^n \left[A_i (\alpha_{k|i} - \sigma_{k|i}) \phi_k - A_k \alpha_{i|k} \phi_i \right] \quad (12)$$

The sticking coefficients can be eliminated as before by substituting the saturation pressure relationship in Equation (7). When Equation (7) is combined with Equation (12), the i th class rate-of-change equation is expressed in terms of the nodal pressure.

$$\frac{dN_i}{dt} = \frac{2A_o A_i}{\sqrt{2\pi R \bar{M} T_i}} (P_{li} - P_i) + \sum_{k=1}^n (A_i \alpha_{k|i} \phi_k - A_k \alpha_{i|k} \phi_i) \quad (13)$$

DIFFERENTIAL EQUATIONS OF PRESSURE

Since the nodal pressures are thermodynamic experimental observables, it is appropriate to reformulate Equation (13) in terms of these pressures. It is recalled that when the uniform density condition is assumed ("regular" enclosure with scalar flux), the molecular fluxes are derived in terms of the corresponding molecular densities.

$$\phi_i = \frac{1}{4V} \sqrt{\frac{8RT_i}{\pi \bar{M}}} N_i \quad (14)$$

The nodal pressures of Equation(8) can also be expressed in terms of the molecular densities of the classes.

The molecular density rate equations are transformed into pressure differential equations in three steps. First, Equation (14) is introduced into Equation (13). Matrix notation is introduced for conciseness.

$$\frac{dN_i}{dt} = \frac{2A_o}{\sqrt{2\pi R \bar{M}}} A_{ii}(P_{\ell i} - P_i) - \frac{1}{\sqrt{2\pi R \bar{M}}} \left(\frac{R}{V}\right) B_{ij} N_j \quad (15)$$

(i=1, ..., n)

Secondly, the pressure vector is obtained by substituting Equation (14) into Equation (8).

$$P_i = \frac{1}{2} P_{\ell i} + \frac{R}{4A_o V} C_{ij} N_j \quad (i=1, \dots, n) \quad (16)$$

When Equation (16) is substituted into Equation (15), n non-homogeneous first-order differential equations for the nodal pressures result.

$$\frac{dP_i}{dt} = \frac{1}{V} \sqrt{\frac{R}{8\pi \bar{M}}} C_{ij} \left[(A_{ii} + B_{ij} C_{ij}^{-1}) P_{\ell i} - (A_{ii} + 2 B_{ij} C_{ij}^{-1}) P_i \right] \quad (17)$$

(i=1, ..., n)

Numerical integration, using digital computer routines, is a straightforward way to solve these equations when the elements of the coefficient matrices are known. However, these elements contain the accommodation coefficients of the system which must be determined experimentally, thus, a functional closed form solution to Equation (17) must be obtained. As with a single first order ordinary non-homogeneous differential equation, matrix calculus defines an integrating matrix or matrizant $H_{ij}(t)$ which can be derived from Sylvester's Theorem¹¹ which applies to the set of n differential equations.

$$H_{ij}(t) = \text{Exp} \left[\frac{1}{V} \sqrt{\frac{R}{8\pi \bar{M}}} C_{ij} (A_{ij} + 2 B_{ij} C_{ij}^{-1}) t \right] \quad (18)$$

If the determinant of the argument matrix of the matrizant is greater than zero, then the matrizant vanishes when $t = \infty$, and an equilibrium (steady state) exists. The requirement that the determinant of the argument matrix be greater than zero is always met provided at least one accommodation coefficient and one nodal temperature of the system are non-zero. When all accommodation coefficients are unity, the system is at uniform temperature, and the pressure is at saturation everywhere. Hence, no transient pressure exists. This is evidenced by the argument matrix degenerating to a null matrix. When the matrizant of Equation (18) is introduced into Equation (17) the pressure vector is an explicit function of time.

$$P_i(t) = H_{ij}^{-1} P_i(0) + \frac{1}{V} \sqrt{\frac{R}{8\pi M}} H_{ij}^{-1} \int_0^t H_{ij} C_{ij} (A_{ii} + B_{ij} C_{ij}^{-1}) P_{lj} dt \quad (i=1, \dots, n) \quad (19)$$

A steady state or equilibrium value of the pressure vector can be written directly from Equation (17) by noting that since the argument matrix of the matrizant is greater than zero, the vector (dP_i/dt) will vanish when time goes to infinity. Calculations indicate that this takes less than about 0.050 seconds for typical low outgassing materials at cryogenic temperatures.

$$P_i(\infty) = (A_{ii} + 2 B_{ij} C_{ij}^{-1})^{-1} (A_{ii} + B_{ij} C_{ij}^{-1}) P_{lj} \quad (i=1, \dots, n) \quad (20)$$

Using Equation (20), Equation (19) is integrated and exhibits the usual exponential transient pressure vector becoming asymptotic to the steady-state values of $t = \infty$.

$$P_i(t) = H_{ij}^{-1} [P_j(0) - P_j(\infty)] + P_i(\infty) \quad (i=1, \dots, n) \quad (21)$$

The transient net mass loss rates can be computed as before by applying Equation (10). The short transient times which are typical of many low outgassing materials used on satellites¹² indicate that the mass loss during the transient period is an insignificant amount. The system can thus be assumed to go from one steady state to another in a step-wise manner as the nodal temperatures are varied, provided that a rate of change to nodal temperatures does not exceed about 1 K/sec. This is a significant result when applying the model to orbiting satellites and

laboratory conditions. The computer logic flow diagram for Equations (19), (20), and (10) is shown in Figure 5.

LABORATORY MODEL

The solution of the differential equations of pressure, as shown in Equation (19), requires functional development of the matrixant which is quite tedious for more than 2 or 3 nodes.

However, the experimental laboratory configuration must be restricted to 3 nodes (one is an orifice) so that the number of accommodation coefficients which must be determined is equal to the number of independent measurements. There are $n(n-1)$ accommodation coefficients which have values of less than unity in a system of n nodes. Since the orifice is a space node, it does not create a third class of molecules so that the laboratory configuration will have two classes of molecules and thus two accommodation coefficients. The two independent measurements are a pressure measurement using a nude ion gage and a QCM which gives a net mass loss rate. A 400 AMU mass spectrometer was used to obtain the averaged VCM mass number.

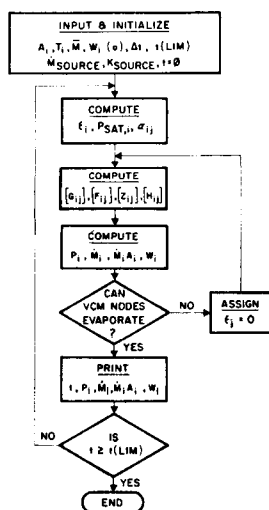


Figure 5. Logic Flow Diagram for Transient VCM Film Adsorption (Uniform Scalar Flux)

The transport model of the laboratory system was obtained by computing the elements of the matrices of Equations (20) and (21) with $n = 2$.

$$A_{ii} = \begin{bmatrix} A_1/\sqrt{T_1} & 0 \\ 0 & A_2/\sqrt{T_2} \end{bmatrix} \quad (22a)$$

$$B_{ij} = \begin{bmatrix} (A_2 \alpha_1 |_2 + A_3) \sqrt{T_1} & -A_2 |_1 \alpha_2 |_1 \sqrt{T_2} \\ -A_1 |_2 \sqrt{T_1} & (A_1 \alpha_2 |_1 + A_3) \sqrt{T_2} \end{bmatrix} \quad (22b)$$

$$C_{ij} = \begin{bmatrix} 2T_1 & [\alpha_2 |_1 \sqrt{T_2 T_1} + (2 - \alpha_2 |_1) T_2] \\ [\alpha_1 |_2 \sqrt{T_1 T_2} + (2 - \alpha_1 |_2) T_1] & 2T_2 \end{bmatrix} \quad (22c)$$

$$H_{ij}^{-1}(t) = \frac{1}{b} \begin{bmatrix} \frac{1}{2}(z_{22} - z_{11}) & -z_{12} \\ -z_{21} & \frac{1}{2}(z_{11} - z_{22}) \end{bmatrix} \sinh bt e^{-at} + \begin{bmatrix} 1 & 0 \\ 0 & 1 \end{bmatrix} \cosh bt e^{-at} \quad (22d)$$

where: z_{11} , z_{12} , z_{21} , z_{22} = elements of Z_{ij} ($i, j=1, 2$).

To obtain the source and VCM parameters, an orificed two-node laboratory system was manufactured as shown in Figures 6a and 6b. It consists of a hinged two-section Emission Crucible with full independent temperature controls on each segment. One segment is completely covered with the source material while the other is kept clean. The orifice is in the middle of the clean section with an area roughly 1/1000 of the source area, but always less than 1/10 of the expected mean free path. Typically, the orifice area is about 2 to 4 mm in diameter. A schematic of the Emission Crucible in the closed configuration is shown in Figure 6a. The tubulated inlet geometry on the RGAs are to measure directed flux when the crucible is open to thereby evaluate the non-diffuse directional emission characteristics. In the closed configuration, the ion gage determines source material saturation pressure while the RGA concurrently determines the mass spectra as the crucible is stepped through the temperature range. The QCM on the VCM (clean) node indicates the on-set of condensation on this node when the crucible is closed, and the maximum (vacuum) outgassing rate of the VCM when the crucible is open. Sufficient VCM must be condensed on the QCM in the closed mode prior to obtaining open-mode data. The open crucible configuration is schematically illustrated in Figure 6b. While the saturation-pressure measurements and the mass-spectra data are straightforward measurements, the two accommodation coefficients require procedures

which combine measurements taken in both the open and closed configurations for the same temperatures. The nude ion gauge (Bayard-Alpert) measures the total local molecular density. This reading can be directly related to the model parameters.

$$P_m = \frac{4A_o}{R} \left\{ \left[\frac{2T_2 - C_{21}}{4T_1 T_2 - C_{12} C_{21}} \right] P_1^{(\infty)} + \left[\frac{2T_1 - C_{12}}{4T_1 T_2 - C_{12} C_{21}} \right] P_2^{(\infty)} \right\} \quad (23)$$

where: C_{12}, C_{21} = Off-diagonal elements of C_{ij} in Equation (22c).

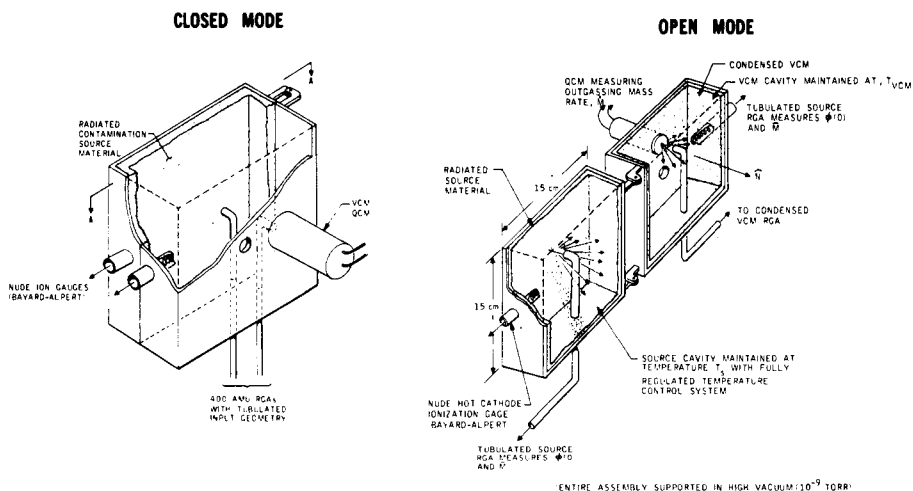


Figure 6. VCM Mass and Emission Crucible

The observable ion gauge reading can be generally expressed as a function of four of the system parameters for a given pair of temperatures, T_1 and T_2 .

$$P_m(T_1, T_2) = P_m[P_1^{(\infty)}, P_2^{(\infty)}, \alpha_{1|2}, \alpha_{2|1}] \quad (24)$$

The solution of the transport equations for the 2-node laboratory crucible in the closed configuration may be used to derive the functional dependency of the steady-state pressures on P_{l1} , P_{l2} , $\alpha_{1|2}$, and $\alpha_{2|1}$. These relations can be stated in a general non-linear functional form.

$$P_i^{(\infty)} = P_i(P_{l1}, P_{l2}, \alpha_{1|2}, \alpha_{2|1}) \quad (25)$$

By combining the functional forms derived from the transport equations in Equation (25) with the relationship of (24), the measured ion pressure gauge reading can generally be expressed as a function of four VCM parameters.

$$P_m(T_1, T_2) = P_m(P_{\ell 1}, P_{\ell 2}, \alpha_{1|2}, \alpha_{2|1}) \quad (26)$$

The P_m readings are physically meaningful only when the crucible is closed and at steady state. In the closed configuration, the condensing rate on the VCM node at T_2 , as measured by the QCM, is a function of the VCM parameters.

$$\dot{M}_{QCM}^{(closed)} = \frac{2A_o A_{QCM}}{\sqrt{2\pi} R} \sqrt{\frac{\bar{M}}{T_2}} [P_{\ell 2} - P_2(\infty)] \quad (27)$$

Again, using the functional forms of Equation (25), this mass-loss rate can be expressed as a general non-linear function of the same four VCM parameters as the ion gauge measurement.

In the closed configuration, $P_{\ell 1}$ may be measured directly by the ion gauge when $T_1 = T_2$. However, $P_{\ell 2}$ may be calculated by use of the Langmuir equation from the QCM mass-loss rate measurements of the VCM node when the crucible is open.

$$P_{\ell 2} = \frac{\sqrt{2\pi} R}{A_o A_{QCM}} \sqrt{\frac{T_2}{\bar{M}}} \dot{M}_{QCM}^{(open)} \quad (28)$$

The temperatures with the crucible open were set to be the same as when closed so that the values of $P_{\ell 1}$ and $P_{\ell 2}$ could be measured at all temperature combinations of T_1 and T_2 required to cover the system temperature range. The inverse forms of Equation (26) can be used to determine the two unknown accommodation coefficients.

$$\alpha_{i|j} = \alpha_{i|j} [P_m, \dot{M}_{QCM}^{(closed)}, P_{\ell 1}, P_{\ell 2}] \quad (29)$$

These implicit relations require the simultaneous solution of two non-linear algebraic equations. However, these equations have first order dependency with no transcendental forms, hence non-linear equation solving algorithms¹³ can be employed which are sufficiently powerful to evaluate the accommodation coefficients with high precision.

PROCEDURES (SOURCE NODE 1, VCM NODE 2)

- (1) Start with $T_1 = T_2$ in the closed crucible configuration. The source node will outgas giving a source saturation pressure, $P_{\ell 1}$, within 1% of the true value as measured directly by the nude ion gauge. The RGA, calibrated by the ion gauge, measures (\bar{M}) .
- (2) Lower T_2 gradually (transient effects last less than 0.1 sec) while holding T_1 constant. Take pressure, temperature, and mass spectra readings in about 50 F intervals. Monitor the QCM on node 2 to detect the VCM node temperature where condensation starts. As long as the VCM saturation pressure is greater than the pressure on the VCM node at T_2 , neither condensation nor evaporation can occur since this node is initially clean. The steady-state nodal pressures during this phase of cooling node 2 are given in their explicit functional form for the case where $P_{\ell 2} > P_2(\infty)$.

$$P_1(\infty) = P_{\ell 1}$$

$$P_2(\infty) = P_{\ell 2} + \left\{ \frac{\alpha_{2|1} [\alpha_{1|2} T_2 + (2 - \alpha_{1|2}) \sqrt{T_1 T_2}] + 2\alpha_{1|2} T_2}{\alpha_{1|2} [\alpha_{2|1} \sqrt{T_1 T_2} + (2 - \alpha_{2|1}) T_2] + 2\alpha_{2|1} \sqrt{T_1 T_2}} \right\} \quad (30)$$

Again, these parameters $P_1(\infty)$ and $P_2(\infty)$ are not measured quantities, but are applied to the P_m and the \bar{M}_{QCM} relationships.

- (3) Further cooling of T_2 will produce condensate on node 2 which is measured by the QCM as $\bar{M}_{QCM}(\text{closed})$. The ion gauge readings are taken at each set of temperatures T_1 and T_2 and are then expressed as general functions of the parameters $P_{\ell 1}$, $P_{\ell 2}$, $\alpha_{1|2}$, $\alpha_{2|1}$ using equations similar to Equation (30). The RGA is continuously monitored to give $\bar{M}(T_1, T_2)$.
- (4) When sufficient VCM condensate is formed on the QCM, the crucible is opened, and the vacuum mass loss rate of VCM from node 2 is measured so that the VCM saturation pressure, $P_{\ell 2}$, can be computed. Each value of T_2 during the non-condensing phase, as well as the condensing phase, must be set and \bar{M}_{open} measured. The open crucible will evaporate VCM about 20 to 30 times faster than the condensation processes so that an hour of condensate will be evaporated in about 2 or 3 minutes.

- (5) When all the values of T_2 have obtained for a constant value of T_1 , then T_1 is changed and the procedures over the entire T_2 range repeated. This repetition is necessary because the accommodation coefficients are generally not symmetric. If the range for both temperatures is from 400K (125C) down to LN₂ temperature (77K), then a typical test schedule would assign eight settings to T_1 at say 400K, 350K, 300K, 250K, 200K, 150K, 100K, and 77K. For each of these values of T_1 , there would be the same eight settings for T_2 . In other words, 64 (T_1 , T_2) combinations would be required. The accommodation coefficient temperature dependency can be plotted as shown in Figure 2C as an operational characteristic of the VCM.

FLUX ANISOTROPY

As mentioned earlier, the isotropic (scalar) flux restriction on VCM free molecule direction substantially simplifies the transport model by eliminating the dependency of the flux distribution on the view factors thereby creating equal fluxes on all the nodes.

Keeping the constraint of tangential randomness, but allowing the magnitude of the incident flux to vary among the nodes will permit a much more realistic enclosure configuration including nodes which cannot "see" the source nodes and thus receive scattered flux only. When deriving the transport equations for this case, the problem becomes complicated by the necessity to first derive n^2 flux-coupling equations in terms of the geometric view factors and expressing $n(n-1)$ of the fluxes as functions of the remaining n fluxes which are arbitrary. With this result, the n differential equations for the changes in the molecular classes can be expressed in terms of only the n arbitrary fluxes so that the equations become determinant.

FLUX COUPLING

The fraction of the flux, of say the k th class, which is scattered from the j th node and subsequently hits the i th node is dependent on the directional scattering probability of the molecules from the j th node and the configurational relationship between the i th and j th nodes. If the scattering is diffuse, then the fraction is directly proportional to the geometric view factor. Referring to Figure 3, let the total of the k th class of molecules leaving the j th node to be designated $\lambda_{k,j}$. For diffuse scattering, the total flux of the k th class incident on the i th node from

all the nodes (including the self-induced flux) can be stated by summing the geometrical factors.

$$A_i \phi_{k,i} = \sum_{j=1}^n A_j F_{ji} \lambda_{k,j} \quad (31)$$

Radiation interchange analysis¹⁴ shows that for diffuse scattering events, a reciprocity relation exists among the view factors.

$$A_j F_{ji} = A_i F_{ij} \quad (32)$$

When the reciprocity condition, Equation (32), is introduced into Equation (31), the basic flux coupling equation for diffuse scattering results.

$$\phi_{k,i} = \sum_{j=1}^n F_{ij} \lambda_{k,j} \quad (33)$$

This represents a set of n^2 equations which couples the n^2 fluxes through the geometric-view factors. The total molecular fluxes leaving the i th node have two defining relations.

$$\lambda_{k,i} = (1 - \alpha_{k|i}) \phi_{k,i} \text{ for } k \neq i \quad (34a)$$

$$\lambda_{i,i} = \epsilon_i + \sum_{k=1}^n (\alpha_{k|i} - \sigma_{k|i}) \phi_{k,i} \quad (34b)$$

The nodal pressures as derived in the initial sections of this report apply to the fluxes depicted in Figure 3. By using Equations (7) and (8), Equation (34b) can be reformulated in terms of the saturation pressures and the accommodation coefficients only.

$$\lambda_{i,i} = \frac{A_o P_{\ell i}}{\sqrt{2\pi R M T_i}} - \frac{1}{2} \sum_{k=1}^n (2 - \alpha_{k|i}) \sqrt{\frac{T_k}{T_i}} \phi_{k,i} \quad (35)$$

When Equations (33), (34a), and (35) are combined and expanded, the result is a set of n^2 non-homogeneous equations which linearly couple the n^2 nodal fluxes through the view factors, the accommodation coefficients, and the nodal temperatures. The constant terms in this set are simple algebraic functions of the view

factors, the average VCM mass number, the nodal temperatures, and the nodal saturation pressures. Symbolically, this is most concisely expressed as a matrix equation. To facilitate expressing the $n(n-1)$ of the fluxes in terms of n arbitrary fluxes, it is convenient to partition the $n^2 \times n^2$ coefficient matrix into an $n \times n$ array of $n \times n$ submatrices, $[d_{ij}]$. The corresponding n^2 fluxes and constant elements are partitioned into n n -element subvectors ψ_j and v_i , respectively.

$$D_{ij} \psi_j = v_i \quad (i=1, \dots, n) \quad (36)$$

Each of the submatrices of D_{ij} consist only of diagonal elements and a single row of elements which is designated by the second subscript of the submatrix index.

The rank of D_{ij} is $n(n-1)$, therefore $(n-1)$ flux subvectors can be expressed as functions of the remaining arbitrary n -element subvector¹¹, say ψ_n . Symbolically, this can be expressed using the previous matrix forms. This is the final form of the flux coupling equations.

$$\psi_i = D_{ij}^{-1} v_j - [d_{in}] \psi_n \quad (i=1, \dots, n-1) \quad (37)$$

The n arbitrary fluxes are determined for steady-state density equations on the assumption that the transient mass loss is negligible. There are then n homogeneous equations linearly coupling the fluxes.

$$\frac{dN_k}{dt} = \sum_{i=1}^n A_i (\lambda_{k,i} - \phi_{k,i}) = 0 \quad (k=1, \dots, n) \quad (38)$$

These n equations can be expanded in terms of the saturation pressures and the accommodation coefficients by applying Equations (33) through (35).

$$\sum_{k=1}^n \left\{ \left[\left(\frac{1}{2} A_i + A_k \right) \alpha_{i|k} + \frac{1}{2} A_i (2 - \alpha_{i|k}) \sqrt{T_i/T_k} \right] \phi_{i,k} - A_i \alpha_{k|i} \phi_{k,i} \right\} = \frac{A_o A_i P_{li}}{\sqrt{2\pi R \bar{M} T_i}} \quad (i=1, \dots, n) \quad (39)$$

Equation (39) can be rearranged to express the results in terms of the n flux subvectors.

$$\sum_{i=1}^n [g_i] \psi_i = \frac{A_o}{\sqrt{2\pi R M}} \left\{ \begin{matrix} A_1 P_{11} / \sqrt{T_1} \\ \vdots \\ A_n P_{n1} / \sqrt{T_n} \end{matrix} \right\} \quad (40)$$

Since Equation (37) can be used to obtain the $(n-1)$ subvectors in terms of v_i and the arbitrary subvector, ψ_n , then Equation (40) completely determines the steady-state values of the n fluxes in the arbitrary subvector. Thus, when ψ_n has been determined, the remaining $n(n-1)$ fluxes can then be computed by reapplying Equation (37). When all the fluxes have been computed, then the nodal pressures may be obtained by using Equation (8) and the net mass-loss rates using Equation (10).

This last section demonstrates that a fairly general mass-transport model, which allows for flux anisotropy, may be used to compute nodal mass accumulation rates by only using matrix algebra, which is readily adaptable for digital computer programming. The model is applicable to quite general spacecraft enclosures where a sufficient number of scattering nodes exist to generate tangential randomness. This model is probably most applicable to such structures as interior instrument bays or well-vented structures such as telescopes.

NON-DIFFUSE EMISSION

Source nodes, both internal and external, appear to outgas with a directional probability which can be approximated by a rotationally symmetric low-order cosine distribution measured from the node surface normal.^{3,15} For the external sources when repeated scattering does not occur, this non-diffuse emission can be accounted for by modification of the geometric view factors.

The total mass incident on the i th node due to a rotationally symmetric emission from the j th node can be expressed as a double integral.³

$$A_i \phi_i = \int_{A_j} \int_{A_i} \frac{\mu_j(\theta_j) \cos \theta_j \cos \theta_i}{r_{ji}^2} dA_j dA_i \quad (41)$$

For a low-order cosine emission characteristic, the directional intensity function can be expressed as a function of the total emission flux.

$$\mu_j(\theta_j) = \left(\frac{2+m}{2\pi} \right) \phi_j \cos^m \theta_j \quad (42)$$

When the order of the cosine function is zero, Equation (42) simplifies to the case for an isotropic diffuse emitter, and when n approaches infinity, the emission flux is collimated. Actual tests¹⁵, for thermally induced emission, indicated that $1 \leq n \leq 2$ is the most likely range of the exponent. Numerical integration of Equation (41) is straightforward when the order of the emission is known. If a typical edge dimension of the source and VCM nodes is less than about 1/3 of the distance between the nodes, the average value of the emission function can be applied where $\bar{\theta}_{ji}$ is the angle that the path line, joining the centroids of the two nodes, makes with the normal to the source node. Equation (41) then simplifies to a modified version of the geometric view factor.

$$A_i \phi_i \cong A_j G_{ij}(m, \bar{\theta}_{ji}) \phi_j \quad (43)$$

$$\text{where: } G_{ij}(m, \bar{\theta}_{ji}) = \frac{1}{2}(2+m) \cos^m \bar{\theta}_{ji} F_{ij}$$

The area reciprocity relationships are valid for this modified view factor.

$$A_i G_{ij} = A_j G_{ji} \quad (44)$$

It may be that the combined emission flux and scattered flux have a somewhat non-diffuse emission characteristic. This can be empirically evaluated during the testing procedures by orienting a tubulated ion gauge (or RGA) to measure only the normal intensity of the outgassing flux $\mu_i(0)$ when the emission crucible is in the open node (see Figure 6b). From the $P_{\ell i}$ measurements and the average mass number, \bar{M} , the total emission flux can be computed using Langmuir's equation. Then, the order of the non-diffuseness can be found by solving Equation (42) for $\bar{\theta}_{ij} = 0$.

$$m = 2 \left[\pi \left(\frac{\mu_i(0)}{\phi_i} \right) - 1 \right] \quad (45)$$

EXTERNAL SURFACES

In general, totally external satellite surfaces will require the application of Monte Carlo path-tracing methods incorporating the accommodation coefficients as event probabilities. However, if there is negligible geometric coupling between the exterior surfaces of a satellite (for example, convex surfaces), a comparatively simple approach is possible on the assumption of single source-VCM node interactions (i.e., no flux coupling). After computing the flux of the interior enclosure by solving the previous transport equations, the vents (space nodes of the internal enclosure) become VCM sources themselves with the appropriate non-diffuse emission. The modified geometric view factor of the venting surfaces to the external surface sections that are visible can then be used to determine the flux on each node. Since this incident flux is presumed to have only a single contact, the pressure calculated using Equation (8) should be reduced by the cosine of θ_{ij} [the angle that the ray joining the centroids of the source (vent) node and external VCM node makes with the VCM node surface normal]. The basic assumption is that molecules which do not stick are scattered to space without any further interactions.

SUMMARY

In summary, this report has presented an experimentally augmented theory for determining the rate at which thin films of condensable molecules form or evaporate from nodal surfaces within enclosures where scattering of molecules also occurs. The simplest form of the resulting transport theory was used to obtain closed function solutions to the transport phenomenon which can be applied to experimental procedures to obtain desired parameters. When the parameters are known, a more general model can then be used to account for behavior in a comparatively open enclosure typical of the internal bay, compartments, and telescope collimators of orbiting satellites. To evaluate the film accumulation on the external surfaces, a Monte Carlo approach, in general, is required. An approximate procedure is suggested by combining the "adsorption" fluxes of holes or vents computed using a transport model during the internal configuration analyses with the actual externally located source nodes. If only single encounters are assumed externally, and molecules which do not stick are scattered to space, then the view factors will give the local fluxes. If non-diffuse emission, and/or scattering is apparent as indicated by tests, then a simple modification of the geometric view factor is applicable.

REFERENCES

1. Buffham, B.A. et al., "A Theoretical Evaluation of the Sticking Co-efficient in Cryopumping," Transactions of the 9th Vacuum Symposium, American Vacuum Society 1962, N.Y.
2. Goodman, F.O., "Scattering of Atoms by Solid Surfaces," Surface Science 24 (1971) 667-699, North Holland Publishing Co.
3. Santeler, D.J. et al., Vacuum Technology and Space Simulation, NASA SP-105, 1966, Washington, D.C.
4. Knudsen, M., Annalen der Physik, 34, 593, 1911, "The Molecular Conductivity of Gases and Their Accommodation Co-efficients."
5. Langmuir, I., "The Evaporation, Condensation, and Reflection of Molecules and the Mechanisms of Adsorption," Physical Review, Ser. 2, Vol. 8, August, 1916.
6. Young, D.M. and Crowell, A.D., Physical Adsorption of Gases, Butterworths Publishing, Montreal, 1962.
7. Patterson, G.N., Molecular Flow of Gases, John Wiley & Sons, N.Y., 1956.
8. Shapiro, H. and Paxson, B.N., "A Mass Spectrometric Analysis of DC-704 Diffusion-Pump Oil Fragmentation," NASA TN D-3033, NASA, Washington, October 1965.
9. Kennard, E.H., Kinetic Theory of Gases with an Introduction to Statistical Mechanics, 1st Ed. McGraw-Hill, 1948.
10. Glasstone, S., Textbook of Physical Chemistry, 2nd Ed., Van Norstrand Co., N.Y., 1946.
11. Korn and Korn, Mathematical Handbook for Scientists and Engineers, 2nd Ed., McGraw-Hill Co., N.Y., 1961.
12. Buckley, P.H. and Johnson, R.L., "Evaporation Rates for Various Organic Liquid and Solid Lubricants in Vacuum to 10^{-8} mm Hg at 55° to 1100°F ," NASA TN P-2081, Lewis Research Center, Cleveland, Ohio, 1963.
13. Rabinowitz, P. (Edit), Numerical Methods for Non-Linear Algebraic Equations, Gordon and Beard Science Publishers, London, England, 1970.
14. Sparrow, E.M. and Cess, R.D., Radiation Heat Transfer, Brooks/Cole Publishing Co., Monterey, Calif., 1966.
15. Ready, J.F., Effects of High-Power Laser Radiation, Academic Press, 1971.

SYMBOLS

A_o	= Avogadro's Number, 6.023×10^{28} molecules/Kg-mole
A°	= Nodal surface area, m^2
C	= Concentration of VCM in source material, Kg/m^2
D	= Diffusion coefficient of VCM in source material, m^2/sec
F	= Geometric view factor between two nodes
$G(m, \bar{\theta})$	= Modified view factor for non-diffuse molecular interchange between two nodes
\bar{M}	= Average molecular weight of VCM, AMU
\dot{M}	= Nodal mass loss rate, Kg/sec
N	= Total number of molecules in bounding enclosure
P	= Instantaneous nodal surface pressure, Pa
$P(0)$	= Initial nodal pressure, Pa
$P(\infty)$	= Steady-state pressure, Pa
R	= Universal gas constant, 8.317×10^3 J/K-Kg-mole
T	= Nodal temperature, K
V	= Volume of bounding enclosure, m^3
a	= $1/2$ the trace of matrix Z_{ij}
b	= $\sqrt{a^2 - \det(Z_{ij})}$
$\det(Z_{ij})$	= Determinant of matrix Z_{ij}
h	= Thickness of source material on source node, m
m	= Order of cosine function in non-diffuse emission
\dot{m}	= Mass loss flux, $Kg/m^2\text{-sec}$
n	= Number nodes in the enclosure
\hat{n}	= Surface normal direction
t	= Elapsed time, sec
α	= Knudsen thermal accommodation coefficient
ϵ	= Thermal emission nodal flux, $molecules/m^2\text{-sec}$
θ	= Angle from surface normal to specified direction
$\bar{\theta}$	= Angle from surface normal to the path-line joining the centroids of two nodal areas
λ	= Total flux leaving a node, $molecules/m^2\text{-sec}$
μ	= Non-diffuse emission directional intensity, $molecules/m^2\text{-sec-sr}$
σ	= Sticking coefficient
ϕ	= Flux incident on a node, $molecules/m^2\text{-sec}$

SUBSCRIPTS

i	designates i th node or molecule class
j	designates j th node or molecule class
k	designates k th node or molecule class
l	designates saturation parameter

m	designates measurements by ion gauge
o	relates to source diffusion constants
s	designates source type node
QCM	designates measurements by quartz crystal micro- balances
ϵ	designates emission flux
ϕ	designates pressure due to all fluxes
1	designates source node in laboratory configuration
2	designates VCM node in laboratory configuration
3	designates pumping orifice in laboratory configuration
ij	indicates view factors from ith node to jth node
i, j	indicates ith molecular flux on jth node
i j	indicates accommodation and sticking coefficients of ith molecular class on the jth node
ϕ_i	indicates saturation value for the ith node
ϵ, s	designates emission flux to the source node
ϕ, i	designates total flux to the ith node
ϵ, i	designates emission flux to the ith node
1)	when a variable has a single literal subscript in an equation, and the symbol (=1,...,n) follows the equation, then the subscripted variable is an n-ele- ment vector
2)	(=.) reads "represents" or "stands for"

VECTORS AND MATRICES

$$A_{ii} = \begin{bmatrix} A_1/\sqrt{T_1} & & \\ & \ddots & \\ & & A_n/\sqrt{T_n} \end{bmatrix}, n \times n \text{ scalar matrix}$$

$$B_{ij} = \begin{bmatrix} \sum_{k=2}^n A_k \alpha_{k|i} \sqrt{T_1} & \dots & A_1 \alpha_{n|1} \sqrt{T_n} \\ \vdots & & \vdots \\ -A_n \alpha_{1|n} & \dots & \sum_{k=1}^{n-1} A_k \alpha_{k|n} \sqrt{T_n} \end{bmatrix}, n \times n \text{ matrix}$$

$$C_{ij} = \begin{bmatrix} 2T_1 & & \dots & [\alpha_{n|1} \sqrt{T_n T_1} + (2 - \alpha_{n|1}) T_n] \\ \vdots & & & \vdots \\ [\alpha_{1|n} \sqrt{T_1 T_n} + (2 - \alpha_{1|n}) T_1] & \dots & & 2T_n \end{bmatrix},$$

n x n matrix

$$C_{ij}^{-1} = n \times n \text{ inverse matrix of } C_{ij}$$

$$D_{ij} = \begin{bmatrix} [d_{11}] & \dots & [d_{1n}] \\ \vdots & & \vdots \\ [d_{n1}] & \dots & [d_{nn}] \end{bmatrix}, \quad n^2 \times n^2 \text{ flux coupling matrix}$$

$$[d_{ii}] = \begin{bmatrix} [(2-\alpha_{i|1})\sqrt{T_i/T_1} - \frac{1}{2}\alpha_{i|1}]F_{i1} \dots 0 & \dots & 0 \\ \vdots & & \vdots \\ - (1-\alpha_{i|1})F_{i1} \quad \quad \quad + (1+F_{ii}) \quad \quad \quad - (1-\alpha_{i|n})F_{in} \\ \vdots & & \vdots \\ 0 & \dots & 0 \quad [(2-\alpha_{i|n})\sqrt{T_i/T_n} - \frac{1}{2}\alpha_{i|n}]F_{in} \end{bmatrix},$$

typical $n \times n$ submatrix of D_{ij}

$$[g_i] = \begin{bmatrix} [(2-\alpha_{i|1})\sqrt{T_i/T_1} - \frac{1}{2}\alpha_{i|1}]A_1 \dots 0 & \dots & 0 \\ \vdots & & \vdots \\ A_i \alpha_{i|1} \quad \quad \quad A_i \quad \quad \quad A_i \alpha_{i|n} \\ \vdots & & \vdots \\ 0 & \dots & 0 \quad [(2-\alpha_{i|n})\sqrt{T_i/T_n} - \frac{1}{2}\alpha_{i|n}]A_n \end{bmatrix},$$

$n \times n$ matrix

$$H_{ij}(t) = \text{Exp } [Z_{ij}(t)], \text{ Sylvester's } n \times n \text{ matrizant}$$

$$I_{ii} = \text{identity matrix}$$

$$Z_{ij} = \frac{1}{V} \sqrt{\frac{R}{8\pi M}} C_{ij} (A_{ii} + 2B_{ij}C_{ij}^{-1}) \quad n \times n \text{ argument matrix of Sylvester's matrizant}$$

$$v_i = \frac{A_o}{\sqrt{2\pi R M}} \left\{ \begin{array}{c} F_{i1} P_{\ell 1} / \sqrt{T_1} \\ \vdots \\ F_{in} P_{\ell n} / \sqrt{T_n} \end{array} \right\} \quad \text{ith } n\text{-element constant subvector}$$

$$\psi_i = \left\{ \begin{array}{c} \phi_{i,1} \\ \vdots \\ \phi_{i,n} \end{array} \right\}, \quad \text{ith } n\text{-element flux subvector}$$

SPACECRAFT RECONTAMINATION*

J. Barengoltz, *Jet Propulsion Laboratory, California
Institute of Technology, Pasadena, California*
D. Edgars, *The Bionetic Corporation*

ABSTRACT

A computer simulation program to model the redistribution of particulate contaminants on a spacecraft after launch has been developed. The component models for particulate adhesion, meteoroid impact, and electrostatic forces are described and intermediate results are presented. The results of a sample calculation have shown that the recontamination process is important.

INTRODUCTION

Planetary quarantine is an international cooperative program concerned with the prevention of the contamination of another planet by terrestrial organisms. Such a contamination by an automated spacecraft could yield false positive results from its own life detection instruments and, if the terrestrial microbes grew and spread on the planet, would confuse all subsequent studies (Ref. 1).

In the implementation of a planetary quarantine program, a distinction is made between spacecraft which are intended to probe or to land on another planet and those which are designed to flyby or orbit outside its atmosphere (Ref. 2). Thus for a multiple element spacecraft to another planet, the allowed (and actual) microbial contamination of the non-incursive spacecraft components would be significantly larger than that of the others. The recontamination process is the redistribution of particulates, presumably associated with microbes, from a region on a spacecraft with a relatively large burden to a region that has been decontaminated. The objective of the study discussed in this paper is the development of the techniques to evaluate the probability of this process.

*This paper presents the results of one phase of research carried out at the Jet Propulsion Laboratory, California Institute of Technology, under Contract No. NAS 7-100, sponsored by the National Aeronautics and Space Administration.

The approach has been to study the effects of typical mission environments on the redistribution of particles on spacecraft surfaces both analytically and experimentally. This study consisted of three logical components, which have been reflected in the effort: (1) particle adhesion, (2) dynamic release mechanisms, and (3) particle transport. The effort in particle adhesion has been principally a particle release experimental program, together with analytical work and attempts to correlate other data found in the literature and elsewhere. Under dynamic release mechanisms, meteoroid impact and pyro firing have been modeled. The particle transport activity was an analytical effort which included the development of computer codes for spacecraft geometry and orientation, forces acting on released particles, and trajectory.

Finally, all of these components were assembled into an operational, integrated computer code. For a demonstration calculation with this computer code, a geometrical model of a dual element spacecraft and the spaceflight phase between Earth orbit and Mars encounter were chosen.

MODELS

Particle Adhesion

The four particle adhesion forces which play an important role in general are: Van der Waals or molecular, contact potential, Coulomb, and capillary or water surface tension. In the case of particulate contamination settled on a surface in air and then evacuated, the capillary force tends toward zero due to the loss of trapped water. In addition, the Coulomb forces due to static electrification during settling are considerably reduced by the particulate-surface system's passage through the corona discharge pressure region. Thus, the principal adhesive force is expected to be molecular and/or contact potential with a dependence on particle size d proportional to d or its $2/3$ power, respectively (Ref. 3). Under vacuum conditions, the dependence found is typically linear (Refs. 4 and 5).

To investigate this matter, a series of experiments on the adhesion of glass beads to a stainless steel surface was conducted. The beads were taken from samples with known size distributions; the mean values ranged from 22 to 110 μm . The specimens were seeded on the face of an accelerometer mounted on a metal diaphragm. The diaphragm, which closed off a vacuum flange, was stressed and impulsively released by a special hydraulic system. The actual number of beads before and after the run was determined by counting. The acceleration history was recorded from the accelerometer.

In order to model the data obtained in this experiment, a linear dependence on particle size (i. e., molecular adhesion) was assumed.

Thus, a characteristic force, F_0 , corresponding to a removal fraction of 0.5 was taken as:

$$F_0 = kd \quad (1)$$

or the characteristic acceleration a_0 :

$$a_0 = 6k/\pi d^2 \rho \quad (2)$$

where d is the diameter and ρ is the density of the particle.

The model must relate the applied force or acceleration to predict the removal fraction. Since a distribution of adhesion forces is expected even for a collection of identical particles because of the variation in microscopic surface conditions, a probabilistic model is indicated. The constant k of Eq. 2 was assumed to be log-normally distributed with a mean value of $\log k$ equal to m and a standard deviation σ_r . Then the removal fraction for a specific d is given by the probability that the applied force F^* exceeds the characteristic force F_0 . This probability may be written:

$$P(F^* > F_0) = \frac{1}{\sqrt{2\pi}} \int_{-\infty}^{(\log k^* - m)/\sigma_r} dt \exp(-t^2/2) \quad (3)$$

where

$$k^* = F^*/d = \frac{\pi d^2 \rho a^*}{6} \quad (4)$$

and a^* is the applied acceleration.

By inverting Eq. 4, for a given data point and an assumed value of σ_r , one can calculate an estimate for m . Such a collection of estimates for m may be averaged to provide a best estimate m_0 for the selected σ_r . There is also a standard deviation for this collection, σ_m , which should be minimized. The program for search over σ_r , treating the data, and minimizing σ_m has been incorporated into a computer code. The best fit to the data was obtained for $\sigma_r = 0.4$, $m_0 = -0.882$, and $\sigma_m = 0.52$. These values are consistent with MKS metric units; e.g., k^* and $10m_0$ have units of N/m.

The meaning of σ_m is such that if one calculates the removal fraction with $m = m_0 - \sigma_m$ and with $m = m_0 + \sigma_m$, substituted into Eq. 4 there is the usual 68% probability that a test result will fall between the two answers. If one is concerned only with an upper limit on the removal fraction, there is an 84 percent (50 + 34) probability that the prediction with $m = m_0 - \sigma_m$ will not be exceeded. These comments may be extended in the usual way.

A result of this data analysis and the data for 48 μm glass beads are shown in Figure 1. The most probable and the "conservative" ($m = m_0 - \sigma_m$) predictions of the model are included.

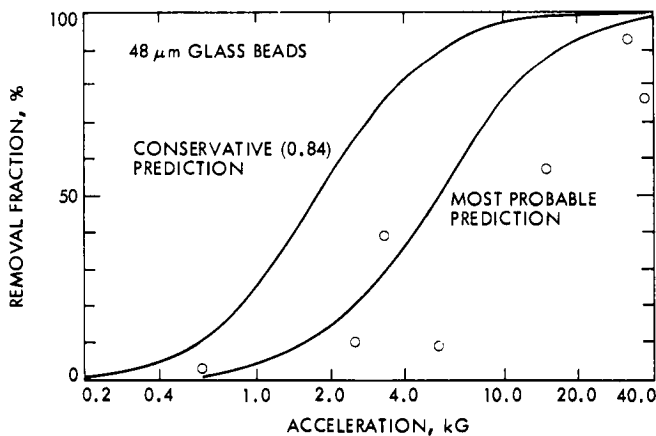


Fig. 1—Comparison of particle adhesion data with predictions of model

Meteoroid Impact

A model to predict the acceleration and velocity response of a surface struck by a meteoroid consists of a loading function and of a differential equation to be solved. The loading function model predicts a pressure P , in general a function of time t , and r , position on the surface relative to the center of impact, for a given meteoroid event. For simplicity, the positional dependence has been assumed to be Gaussian and factorable:

$$P(r, t) = P_0 e^{-r^2/s^2} f(t) \quad (5)$$

This choice was motivated by the existence of a closed-form solution velocity response for a thin plate subjected to a loading of this form with the impulse time function.

The function $f(t)$ has been chosen:

$$f(t) = \left(1 + \frac{t}{T_o}\right)^{-2} \quad (6)$$

This form has been derived along the lines of an analysis due to Ludloff (Ref. 6). This treatment takes into account the transport of molten target material in the crater region. The result depends on Ludloff's form for the crater radius; the crater is assumed to be hemispherical. The expression for the crater radius R in terms of the target material strength S , the projectile diameter d , density ρ_p and velocity v_o is:

$$\frac{R}{d} = \frac{1}{2} \left(\frac{\rho_p v_o^2}{S} \right)^{1/3} \quad (7)$$

The solution of the equation of motion leads to Eq. 6. The characteristic time T_o may be immediately identified as:

$$T_o = \frac{4}{3} \frac{d S^{1/6}}{v_o^{4/3} \rho_p^{1/6}} \left(1 + \frac{\rho_p v_o^2}{S} \right) \quad (8)$$

One may also identify $P_o = 2S$. In the formula for T_o , ρ_T is the target density and all other symbols have been previously defined. Ludloff, in keeping with his treatment of the molten target material, takes as the target material strength S , the product of the latent heat of fusion and the density (e.g., for aluminum, $S = 8.7 \times 10^8 \text{ N/m}^2$).

Finally, we have chosen for the parameter s in the loading function (Eq. 5), a value of $(1/3)R$, where R is the crater radius given in Eq. 7. At this point the loading function is completely expressed in terms of known parameters of a meteoroid impact.

The formal solution of the differential equation is straightforward. Classical plate theory provides a solution for the velocity response WDOT of a thin plate to an impulsive loading with a Gaussian shape factor (Ref. 7). The surface velocity \dot{w} and the surface acceleration \ddot{w} due to a general time function $f(t)$, e.g., Eq. 6, may be expressed by convolution integrals.

Since the precise time relative to meteoroid impact when a particle is released is unimportant, an adequate parameter of the surface response at a fixed r is the peak acceleration. The fraction of particles removed by a given meteoroid will depend on the peak acceleration as a function of r . Similarly, the variation in the velocity of release will depend more strongly on the radial (r) dependence than the time dependence for all but the largest particles released by the largest meteoroids. As these cases are disfavored by the actual environments, the release velocity has been characterized by the surface velocity for a fixed r at the time that the corresponding acceleration peaks.

An approximate algorithm has been devised to predict the time at which the acceleration will be maximum. With its use, only a few convolution integrals need be calculated at each value of r to find the peak acceleration. A considerable savings in computer cost has been realized. Additionally, the convolution integration was optimized for the limited range of the time variable (t).

A sample calculation of the meteoroid impact model is shown in Figure 2 for a simulation of an experimental run conducted elsewhere (Ref. 8). A comparison with a direct measurement of the release velocity for 50 μm glass beads (Ref. 8) is also indicated.

The meteoroid impact model was combined with the particle adhesion model to predict particle release due to a meteoroid impact. This combination provides removal fractions as a function of distance from impact, effective (r. m. s.) clearing radii, and release velocity distributions, all as a function of particle size. The removal profile predicted by a simulation of an experiment conducted elsewhere (Ref. 9) and a discrete data value are shown in Figure 3.

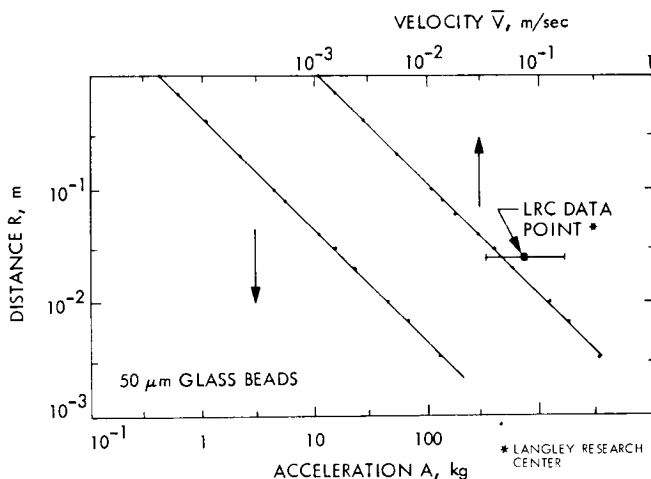


Fig. 2—Recontamination simulation of LRC run 6

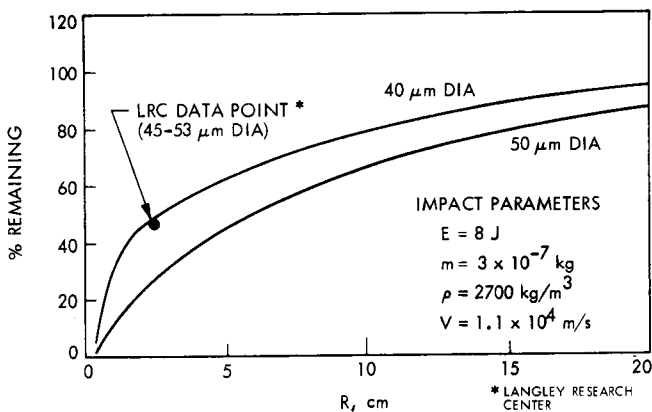


Fig. 3—Glass bead removal profile for simulation of LRC experiment

Particulate Transport

The purpose of the particulate transport analysis is to solve the equation of motion of a released particle in the vicinity of the spacecraft. Of the important forces acting on the particle, the electrostatic force due to the charge on the particle and the electric field of the spacecraft is most difficult to predict. The models for particulate charging and spacecraft electric field, both of which arise due to solar charged particle accretion and the photoelectric effect, will be described below.

The particle charging model deals with spherical particles for simplicity and consists of three special cases: illuminated particle, shaded (by the spacecraft) particle in the wake, and shaded particle outside the wake. Given the geometry of the particle and the potential-dependent currents flowing into it, one may express the charging rate in an implicit form.

For the illuminated particle, the charging rate $d\phi/dt$ is given by:

$$\frac{d\phi}{dt} = \frac{2.9 \times 10^{-9}}{R^2} \pi d \left[A_p + (1 - \alpha) A_e + A_\nu \right] \quad (9)$$

where

$$A_p = \frac{n_p v_o}{4} \quad \text{for } |\phi| \ll \frac{M v_o^2}{2e}$$

$$A_e = - \frac{n_e \bar{v}_e}{4} \begin{cases} \exp(e\phi/kT_e) & \text{for } \phi \leq 0 \\ \left[1 + 2e\phi/kT_e\right]^{1/2} & \text{for } \phi > 0 \end{cases}$$

In this equation, the proton flux A_p depends on the number density $n_p(m^{-3})$ and the directed velocity $v_0(ms^{-1})$ and the temperature $kT_e(eV)$. The photoelectron flux A_p is calculated from photoelectric yield data (Ref. 10) for the solar spectrum, material of the particle, and surface potential $\phi(V)$. A model for the secondary emission yield α (unitless) has also been incorporated (Ref. 11). The secondary emission affects $d\phi/dt$ only when $\phi < 0$. With A_p , A_e , and A_p in units of $m^{-2}s^{-1}$, the particle diameter d in m and the heliocentric distance R in AU, one obtains $d\phi/dt$ in Vs^{-1} .

For the shaded particle, the photoelectron flux A_p is zero. The electron flux A_e and the secondary emission yield α are essentially unchanged. The crux of the problem is the proton flux A_p . The proton accretion may be expected to depend only on the thermal motion of the protons, since there is no line of sight in the shade. It follows then that for this case:

$$A_p = \frac{\bar{n}_p \bar{v}_p}{4} \begin{cases} \exp(-e\phi/kT_p) & \text{for } \phi \geq 0 \\ \left[1 - 2e\phi/kT_p\right]^{1/2} & \text{for } \phi < 0 \end{cases} \quad (10)$$

where \bar{v}_p is the proton mean thermal speed and kT_p is the proton temperature.

This equation, an analog to the electron flux equation, is only approximate. The quality of the approximation depends largely on the value taken for \bar{n}_p , an effective proton number density in the shade. This value actually depends on the complete solution to the spacecraft potential problem. In the model, a conical wake was assumed, within which \bar{n}_p equals zero and outside of which \bar{n}_p assumes the ordinary value n_p .

Results of calculations with this model at $R = 1$ AU are shown in Figures 4 and 5. Note that equilibrium potentials may be inferred by the requirement $d\phi/dt$ equals zero (Figure 4). The model does not quite equilibrate in the shade, but a reasonable value is $-3 kT_e/e$ or $-60V$ for $kT_e = 20$ eV (Figure 5).

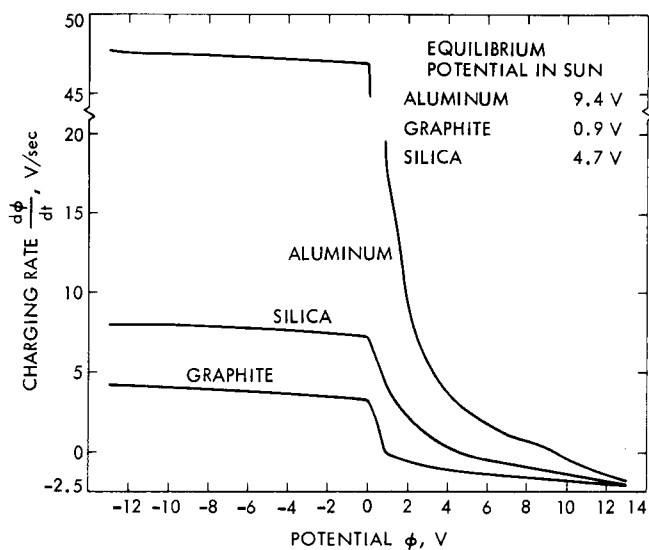


Fig. 4—Particulate charging in sunlight

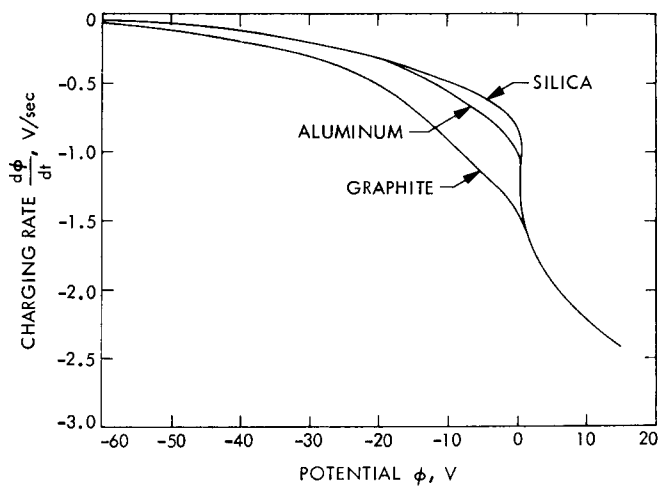


Fig. 5—Particulate charging in shade

An electric field model depends on the solution for the spacecraft/solar plasma potential problem. Because the relative directed velocities of the various plasma components are unequal, no solution exists even in the simplest three dimensional geometry. Thus, the approximate model adopted treats the near-field case by a one-dimensional approximation, considers the plasma velocity situation by a conical wake, and describes the far-field case by an equivalent sphere at rest in the plasma.

The solution to the one-dimensional problem of a plate exposed to solar illumination, electrons, and protons has been found in the literature (Refs. 12 and 13). In this solution the positional dependence of the electric potential in equilibrium was expressed implicitly in terms of the surface potential and the plasma parameters. An approximate explicit form for the potential based on this work has been developed by these authors which provides an approximate formula for the electric field as well (Ref. 14):

$$E = 4c_2 \left\{ -c_1 + \left[(\sqrt{\phi_o - \phi_m} + c_1)^{1/2} - c_2 x \right]^2 \right\} \\ \times \left[(\sqrt{\phi_o - \phi_m} + c_1)^{1/2} - c_2 x \right]$$

for the region:

(11)

$$x < \frac{(\sqrt{\phi_o - \phi_m} + c_1)^{1/2}}{c_2}$$

where c_1 , c_2 , and ϕ_m are calculated constants.

Following the authors of Ref. 12 and 13, two classes of solutions to the problem were found, noted as monotonic ($\phi_m = 0$) and non-monotonic. However, the quantity of interest here, the electric field in the vicinity of the plate, is virtually the same for two solutions. Some results for aluminum and silica are shown in Figure 6. The most striking feature of these results is a fall-off of the field with distance at a far faster rate than the field for the case with no photoelectric effect.

The e-folding distance in the latter case (the usual Debye length) is used with the assumed $-3 \text{ kT}_e/e$ shaded surface potential to model the near field for positions in the shade but outside the wake.

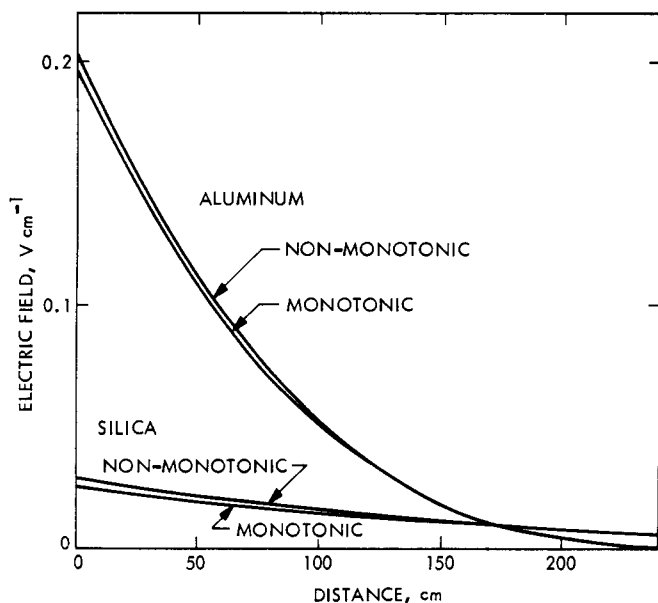


Fig. 6—One dimensional electric field

The electric field for the wake is approximate and basically depends on a potential model of the form:

$$\phi = \phi_o \left[J_o \left(2.4 \frac{r}{a} \right) \exp \left(-2.4 \frac{|z|}{a} \right) \right] \quad (12)$$

where (r, z) is the position in cylindrical coordinates, \bar{a} is the cone radius at height z , ϕ_o is the shaded surface equilibrium potential, and J_o is the zeroth order Bessel function. Corrections were made to approximately satisfy the boundary conditions of a conical geometry.

The electric field in the far field region is based on the usual potential solution for a uniform sphere in a plasma (at rest):

$$\phi(r) = \bar{\phi}_o \left(\frac{a}{r} \right) \exp \left(- \frac{(r-a)}{\lambda} \right) \quad (13)$$

In this equation the surface potential $\bar{\phi}_o$ of the equivalent sphere is an area-averaged value, as is the effective Debye length λ . The radius of the equivalent sphere a is based on the projected shadow of the spacecraft. It is also the radius of the base of the conical wake.

RESULTS

The recontamination computer program was synthesized from the preceding models. The details of the program and its calculations are contained in a comprehensive report (Ref. 15). The program estimates the following quantities:

- 1) The expected number of recontamination hits, particles released from contaminated area which strike uncontaminated (specified) areas.
- 2) The expected number of safe hits, particles released from contaminated areas which strike contaminated areas again.
- 3) The expected number of escapes, a polar distribution of the direction of escapes (referenced to sun/spacecraft axis), and the average velocity of all escaped particles.

For a demonstration calculation with this computer program, a geometrical model of a dual element spacecraft and the spaceflight phase between Earth orbit and Mars encounter were chosen. The results of this calculation are summarized in Table 1 for two meteoroid models and a pyro event simulation. The conservative model includes some high velocity impacts (groups 2 and 3 of Table 2) that would result from some choices of spacecraft trajectory. The other model represents a nominal trajectory selection by only low velocity impacts (group 1 of Table 2). The directional distribution of escaped particles is shown in Figure 7. Finally, the meteoroid group model, and the recontamination and safehit numbers as a function of meteoroid group are displayed graphically in Figures 8, 9, and 10.

Table 1—Summary of Results of Recontamination Analysis:
Sample Calculation

	Conservative Meteoroid Velocity	Nominal Meteoroid Velocity	Pyro Pyro
Recontamination Hits	33	10	1
Safehits	21,215	7281	849
Escapes	126,778	34,349	35,000
Average Escape Velocity	1.15 m/s	0.69 m/s	1.94 m/s
Meteoroid Impacts Pyro Events	28,279	18,842	4

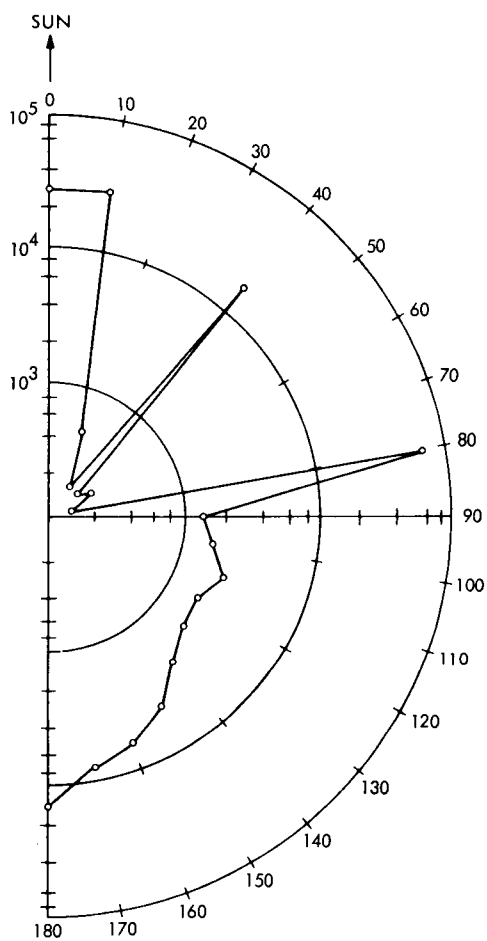


Fig. 7—Angular distribution of escaped particulates

Table 2—Micrometeoroid Mass and Velocity Groups

MASS GROUPS		VELOCITY GROUPS	
1	$10^{-15} - 3 \times 10^{-14}$ kg	1	$1.2 - 2.0 \times 10^4$ m/s
2	$3 \times 10^{-14} - 3 \times 10^{-13}$ kg	2	$2.0 - 2.8 \times 10^4$ m/s
3	$3 \times 10^{-13} - 3 \times 10^{-12}$ kg	3	$2.8 - 3.6 \times 10^4$ m/s
4	$3 \times 10^{-12} - 3 \times 10^{-11}$ kg		
5	$3 \times 10^{-11} - 3 \times 10^{-10}$ kg		
6	$3 \times 10^{-10} - 3 \times 10^{-9}$ kg		
7	$3 \times 10^{-9} - 3 \times 10^{-8}$ kg		
8	$3 \times 10^{-8} - 3 \times 10^{-7}$ kg		
9	$3 \times 10^{-7} - 3 \times 10^{-6}$ kg		

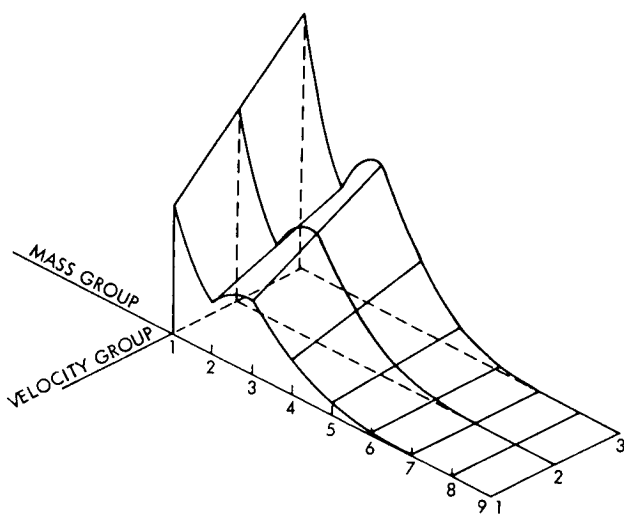


Fig. 8—Micrometeoroid fluence distribution over mass and velocity groups

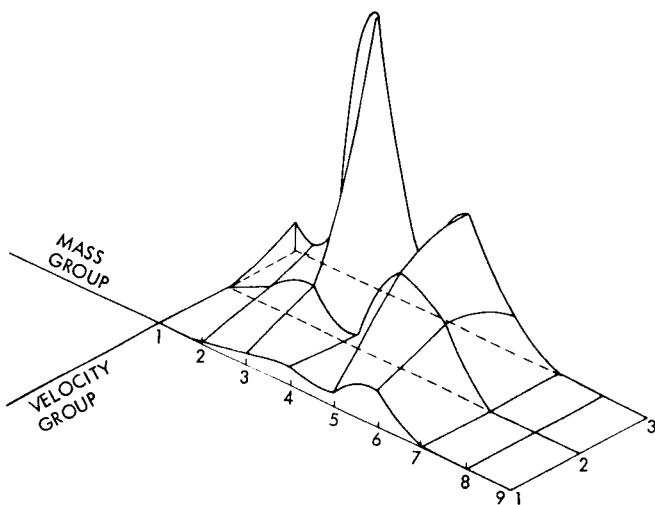


Fig. 9—Recontamination event distribution

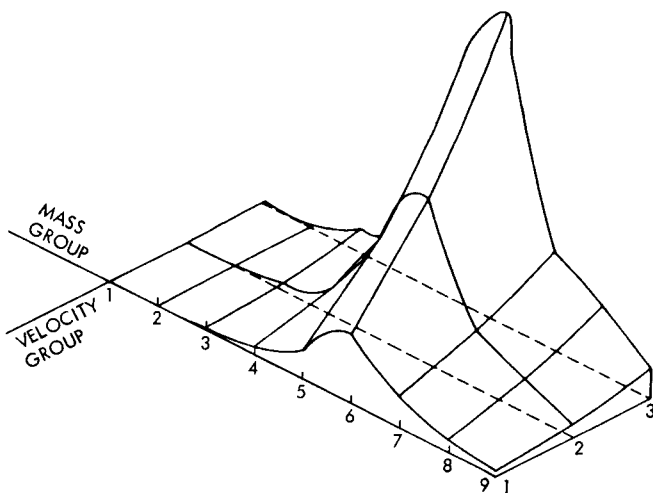


Fig. 10—Safe-hit event distribution

SUMMARY AND DISCUSSION

Although a direct verification of the recontamination model would be extremely difficult, several intermediate points may be checked. The particle adhesion model, for example, is based on experimental data. It is also interesting to compare these results with literature data. The coefficient k in the present (vacuum) model is 0.13 N/m. Corn (Refs. 4 and 5) used the same formula (Eq. 1) and obtained the following values (converted to MKS units): 0.17 N/m for the adhesion of pyrex particles to optical glass, 0.12 N/m for the adhesion of quartz particles to optical glass, and 0.075 N/m for the adhesion of quartz particles to pyrex glass. Since these data were obtained at 95% relative humidity, the agreement with our results must be considered somewhat fortuitous. An analysis of other data for ambient conditions also reflects a fair agreement.

From these comparisons and a consideration of the Vander Waals and capillary adhesion forces only, one may predict the trend of total adhesion between ambient pressure with 100% relative humidity and vacuum. As the relative humidity is decreased the capillary force decreases in a linear fashion (Refs. 4 and 5). As long as water is present, the Van der Waals force is reduced to a negligible factor by the molecular interaction with the interface water (Ref. 3). For small relative humidity (50%), there is a minimum adhesion. Finally, as the test system is evacuated, the capillary force becomes negligible and the Van der Waals force attains its maximum value. On the basis of the data, the adhesion force in vacuum is commensurate with that in air at 100% relative humidity and certainly exceeds values for low (but non-zero) relative humidity.

The meteoroid impact model contains an important assumption in the choice of $f(t)$ (Eq. 6). However, we have found that for reasonable forms, only the characteristic time T_0 of the impact was critical for the peak acceleration. Additionally, the combination of the particle adhesion and meteoroid impact models can reasonably predict experimental results.

The equilibrium values of the particle charging model are consistent with other analyses. The form of the one-dimensional electric field is also reasonable in terms of the expected effect of the photoelectrons. The unphysical synthetic solution renders the complete electric field very approximate. However, the trajectory integration should smooth the artifactual discontinuities.

Of the many assumptions in the geometrical model, the most serious is the assumption of a uniform spacecraft structure relative to meteoroid impacts. This simplification, necessary to decouple impact position from surface response, significantly reduced the computer cost of a complete analysis. The assumption of 0.32 cm (1/8 inch) aluminum plate should cause an over-estimate of the number of released particles. Thermal blankets, for example, would release very few particles under meteoroid impact.

All of the assumptions were chosen to be conservative (where the trend was known), so that the values for the various numbers of recontamination hits, safe hits, and escapes should be over-estimates. An appraisal of this factor indicates that the results shown may be an order of magnitude high. However, the probability of a recontamination by at least one particle is very near to unity, and the process of particle relocation in general is important.

REFERENCES

1. Hall, L. B. and Lyle, R. G., "Foundations of Planetary Quarantine," Planetary Quarantine Principles, Methods, and Problems, ed. L. B. Hall, Gordon and Breach (1971) p. 5.
2. Schalkowsky, S. and Kline, R. C., Jr., "Analytical Basis for Planetary Quarantine," *ibid*, p. 9.
3. Zimon, A. D., Adhesion of Dust and Powder, transl. M. Corn, Plenum Press (1969).
4. Corn, M., J. Air Pollution Control Assoc., 11, No. 11 (1961) p. 523.
5. Corn, M., J. Air Pollution Control Assoc., 11, No. 12 (1961) p. 566.
6. Ludloff, K. G., "A Hydrodynamic Model for Hypervelocity Impact," UCLA doctoral dissertation, University Microfilms (1967).
7. Sneddon, I. N., Fourier Transforms, McGraw-Hill (1951).
8. Goad, J. H., Jr., DiBattista, J. D., Robinson, D. M. and Chu, W. P., "Removal of Spacecraft-Surface Particulate Contaminants by Simulated Micrometeoroid Impacts," NASA TN D-7494 (1974).
9. Humes, D. H. et al., private communication.
10. Feurbacher, B. and Fitton, B., J. Appl. Phys., 43 (1972).
11. Knott, K., Planetary and Space Science, 20, No. 8 (1972).
12. Guernsey, R. L., and Fu, J. H. M., J. Geophys. Res., 75, No. 16 (1970).
13. Fu, J. H. M., J. Geophys. Res., 76, No. 10 (1971).

14. Barengoltz, J. and Bauerle, C., JPL Quarterly Technical Review, 3, No. 1 (1973).
15. Barengoltz, J. and Edgars, D., (to be published by Jet Propulsion Laboratory).

HELIOS SURFACE MATERIALS, TEST-PREDICTIONS AND TEST-RESULTS OF ORBIT CONDITIONS COMPARED WITH MISSION RESULTS

W. Winkler, *GfW/DFVLR, PORZ-WAHN, Linder Höhe Germany*

ABSTRACT

The severe HELIOS mission environment asked for an appropriate material selection for optical surfaces based on a good approach to predict degradation and contamination effects by analysis and an adequate verification by test. Analysis results will be compared with first flight data of the HELIOS-A mission.

INTRODUCTION

The HELIOS sunprobe mission with its extreme elliptic orbit (1.0 AU-0.3 AU) and the steep gradients of temperature, particle and radiation fluxes asked not only for an excellent design of thermal control and adequate test methods but also for an appropriate selection of surface materials such as answering the high quality and performance standards necessary for surviving this environment.

The material selection, however, is often burdened by unknown synergetic effects in space environment due to combined influences of particles, radiation, dust and temperatures and to interactions between exposed materials causing contamination and similar effects difficult to interpret correctly[1]. This paper will discuss a basic model for analyzing these effects on surface materials exposed to space and the resulting definition of test conditions for the best simulation of the HELIOS mission profile. These input data will be compared with results of the HELIOS-A flight. The evaluation and comparison of tests and mission will include the problems of testing synergetic effects and of accelerated testing.

Prediction and Test for Surface Materials

Environmental Model- HELIOS surface materials were expected to survive a mission covering wide ranges

of particle densities, radiation intensities and temperatures (-60°C to $+180^{\circ}\text{C}$). But these temperatures would have been even higher if the relevant optical parameters (α/ε) would change during the mission time (2 orbits, 190 days each) by degradation/contamination effects more than 50%. At first this number seemed to be quite unrealistic but first test results [2] and indications from MVM'73 tests [3] demanded for an improved environmental model and a better test definition for the simulation of the main expected stresses for surface materials :

- temperature
- proton fluxes
- UV-irradiation
- contamination
- synergetic effects

The energy input into the S/C is a function of the optical parameter α of the used surface materials. But this parameter itself is a function of time-dependent particle fluxes striking the surfaces, UV-intensities and the contamination effects by the surrounding, outgassing materials.

$$\alpha(t) = f[\phi_p(t), I_{UV}(t), C(\text{material})] \quad (1)$$

So the determination or at least a good definition of $\phi(t)$ for the whole mission profile, of $I_{UV}(t)$ and of a relevant contamination model as well as an evaluation of the expected interactions was the most urgent problem.

Following the technical outlines of the Boeing MVM'73 flux calculations [4] we calculated the maximum fluxes and the energy distribution for protons for one and two HELIOS orbits and defined test conditions for the used surface materials [1,5]. Assuming a pure $1/r^2$ - dependance of UV-intensity and of proton fluxes and fluences for the solar wind, assuming a quiet sun with a maximum of 40 events of solar flares $\phi(t)$ and $I_{UV}(t)$ were calculated using the following input data [6]

- solar plasma velocity : 3500 Km/sec.
- plasma density : $5p^+$ /cm³.
- average activity of the sun over the whole mission.
- linear dependance of radiation damage and proton energy in the range between 1 and 1000 KeV [1,7].
- validity of an orbit factor K for I_{UV} and $\phi(t)$ to derive mission flux data from near-earth data. $K=3.18$ for HELIOS.

Including a safety factor of 1.5 to cover also missions closer than 0.3AU to the sun, the fluence for the HELIOS-mission was calculated to be :

$$\Phi(\text{mission}) = 4 \times 10^{16} \text{ p}^+ / \text{cm}^2 \text{ and } \overline{E}_{\text{p}^+} = 10\text{KeV}$$

$$I_{\text{UV}} = 13000 \text{ ESH (1HELIOS orbit)}$$

p^+ of 10KeV were chosen because protons with lower energies did not damage surfaces covered by contamination layers as found during the MVM'73 - Boeing tests (up to 2000A⁰) [1,5]. Because of the linear dependance of damage and energy fluences of $4 \times 10^{16} \text{ p}^+ / \text{cm}^2$ were used to have a good simulation of the hard space environment.

For the UV-irradiation was assumed that a 16 UV-sun-source would provide the necessary ESH within a reasonable test time and without having measurable acceleration effects. This point has to be discussed in more details later.

As outlined in a previous paper [1] degradation and contamination effects on optical properties had to be treated as a whole and can not be separated from one another. So synergetic effects during the missions were expected. But the appropriate simulation was extremely difficult. All outgassing neighboring materials (paints, laquers and mainly RTV-type adhesives) were considered to be contamination sources and to react with the contaminated surfaces by physical and chemical processes at higher temperatures and under combined environment. Test results from MVM'73 and TRW-HELIOS [2,3,5] showed clearly that contamination could not be neglected and that there exists a clear dependance between the thickness of a contamination layer and the $\Delta\alpha$ [1]

So for our two series of Boeing tests we made a special screening set-up to protect all samples from cross-contamination by other neighboring samples and the chamber itself. Whitmess samples should monitor the tests to prove the efficiency of our protection set-up. []

For analyzing purposes we compared test results with and without screening and similar test results to come up with a worst case $\Delta\alpha$ which could be included in the termal balance calculations.

With: $\alpha_{\text{final}} = \alpha_{\text{initial}} + \Delta\alpha_{\text{cont.}} + \Delta\alpha_{\text{degr.}}$ (2)

and using different test results (HELIOS, MVM'73, see table 1.) we could derive from an $\alpha_{\text{initial}} = 0.06$ a $\Delta\alpha_{\text{cont.}} \approx 0,05-0,06$.

For all combined particle-, UV- and temperature tests special emphasis was laid on very low gradients all over the sample holder. So a sweeping beam for protons, monitored by Faraday-cups was used. The temperature could continuously be varied by cooling and heating GN_2 , pumped through the copper sample holder itself. The high IR-energy flux within the 16-suns-UV-beam was stopped by a quartz-distilled water-device placed between UV-source and sample plate [8].

To transform analysis data for the orbit into data to define test conditions we used acceleration factors K : $K_{\text{UV}} = I_{\text{UV}}(\text{test})/I_{\text{UV}}(\text{mission})$, I_{UV} ex-

pressed in UV-suns and the total energy in ESH and $K_{\text{p}^+} = \phi(\text{test})/\phi(\text{mission})$, ϕ expressed in

$\text{p}^+ / \text{cm}^2 \cdot \text{sec}$. These linear expressions seem to be valid only for the proton fluxes used in these tests but not for the UV intensities. But up till now hardly enough tests had been performed to set up an analytical relation between $I(\text{test})$ and $I(\text{mission})$ and calibration curves for the main surface materials. We intend to run these tests within the next future to improve the validity range of those combined tests, but we can already propose a calibration curve of the following type (figure 1). Here synergetic effects were not yet taken into account and for higher p^+ -fluxes certainly the linear dependance will be no longer valid, too. [12]

Materials under test and test results - Only a few materials could be used on HELIOS fulfilling the high technical standards asked for by the tight thermal design touching at the limits of the present state of art. So mainly quartz was used as second surface mirrors (SSM/OSR) with and without conductive coating (CC), or as coverslides to protect the solar cells. Only on places where flexible OSR-foils were unavoidable we used aluminized FEP.

A number of about 50 specimen of these materials were exposed to combined environmental tests, a number high enough to allow a statistical evaluation with a good confidence level. These tests were run at 175°C with a proton fluence of $4 \times 10^{16} \text{ p}^+/\text{cm}^2$ and a total UV dose of at least 7000 ESH. The temperature of 175°C was higher than the calculated mission average but we assumed that this elevated temperature did not cause additional unexpected or unexplainable physico-chemical damage mechanism nor special synergetic effects. If these assumptions were true or not could not be demonstrated for no theoretical evaluations for combined and accelerated effects and to few test data of combined tests were available at this time.

Table 1 summarizes the results of these tests. A typical degradation curve will be given in figure 2.

Figure 1a: HELIOS-orbit (schematic)

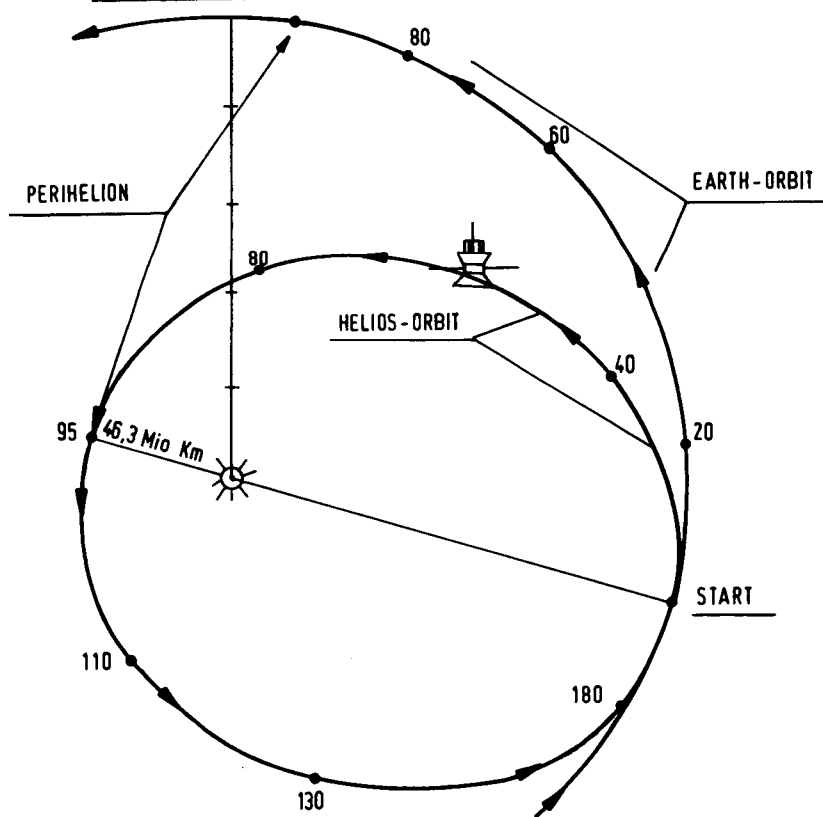


TABLE 1: $\Delta\alpha$ FOR HELIOS SURFACE MATERIALS . TESTRESULTS [1,5]

MATERIALS IN TEST FACILITY	Ag-FEP	Al-FEP	S S M	CC-SSM	Al - Plate as Contamination monitor
<u>T R W :</u> $p^+/\text{cm}^2: 4 \cdot 10^{16}$ ESH: 4000	0.08 (1) 0.09 (1)	0.07 (1)	0.09 (0.04) (3)	-	0.05
<u>E M R :</u> $p^+/\text{cm}^2: 5 \cdot 10^{15}$ ESH: 4000	0.15 (2) 0.16 (2)	-	0.19 0.22	-	unknown concentration
<u>BOEING-1:</u> $p^+/\text{cm}^2: 4 \cdot 10^{16}$ ESH: 19000	0.11 (1)	0.11 (1)	0.04 0.043 (0.03) (3)	0.041 (0.031) (3)	0.015
<u>BOEING-2:</u> $p^+/\text{cm}^2: 3 \cdot 10^{16}$ ESH: 13000	-	-	0.035 (0.03) (3)	0.057 0.044 (0.045) (3)	0.007

(1): becomes a white and diffuse reflector

(2): unknown but high contamination level

(3): average degradation level, contamination concentration of last column subtracted

These data allow the following conclusions :

- α - values of the TRW-test are higher than the Boeing-HELIOS results and similar to the Boeing-MVM'73 results [1,3] . Here $\Delta\alpha(\text{cont.}) = 0.05$ (see last column) could be derived. The corresponding $\Delta\alpha$ -values caused only by degradation are in good accordance with the Boeing-HELIOS results.
- SSM and CC-SSM show a very similar degradation behaviour. Only $\Delta\alpha = 0.01$ can be attributed to the degradation of CC [5] itself.
- The proton irradiation caused a higher damage rate and a higher $\Delta\alpha$ than UV only but a part of the α -values measured must result from combined effects.
- The contamination screening of Boeing was effective.

($\Delta\alpha \leq 0.01$) while at TRW the contamination monitoring system showed a $\Delta\alpha = 0.05$.

- e) Ag-FEP and to a smaller degree Al-FEP showed a white surface after tests at temperatures higher than 110°C but only under a combined environment [1] .

So taking into account contamination ($\Delta\alpha = 0.06$) and degradation (formula 2) using the results of Boeing tests the following data for the thermal balance analysis were accepted:

$$\alpha_{\text{FEP(Al)}} = 0.22; \alpha_{\text{SSM}} = 0.16; \alpha_{\text{CC-SSM}} = 0.17;$$

Figure 3 showed the resulting temperature curves (undegraded and degraded/contaminated) for the central body heat shields. Now mission data had to prove if the basic assumptions of these calculations were right and if the test results were in good accordance with mission data.

HELIOS - mission results

HELIOS measuring equipment - The main interesting solar plasma parameters and their distributions (velocity, temperature, propagation direction and density) were measured down to particles with low energies (some eV). This plasma experiment E1 allowed to compare the assumptions made before with direct environmental data from a mission orbit between 1.0AU and 0.3AU.

The temperatures of interesting surface points were monitored by thermistors and resistors collecting data from heat shields, solar arrays, antennas and boom-mounted experiments. So from these temperatures and known surface parameters

α_{final} and $\Delta\alpha = \alpha_{\text{final}} - \alpha_{\text{initial}}$ could be calculated.

To interpret these results in terms of degradation and contamination, results from the plasma experiment and data from a previous paper [1] as well as a contamination model [9] were used.

Environmental data - The prediction of the solar radiation intensity was rather exact so that the total time-depending heat flux was known. Only the recalculation of the orbit factor K for the final HELIOS-A-orbit revealed a difference. Test conditions were

based on a total of 13000 ESH but in reality this number must be corrected to be at least 14.600 ESH. Together with the deceleration effects in test (see above) a total intensity of about 16.000 ESH is much more adequate for the UV-simulation of one orbit.

The HELIOS-A mission covered a period of a very quiet sun and could serve as a basic calibration of the solar wind parameters, undisturbed by solar flare effects. This might change for HELIOS-B, at least for the second orbit, end of 1976. So the following first data could be derived from measurements :

- a) The plasma velocity, assumed to be nearly 500 Km/sec changed with the 27 days sun rotation period between 300 Km/sec and 850 Km/sec having an average value of 620 Km/sec.
- b) The average proton density, assumed to be $5p^+/\text{cm}^3$ in analysis, was also slightly higher, about $6p^+/\text{cm}^3$ but still within the given bandwidth of measurements [6]. Additional 5% of α -particles, having a 4 times higher energy, has to be simulated in tests. So a total fluence of the solar wind protons Φ (1st orbit) = $3.2 \times 10^{16} p^+/\text{cm}^2$ can be derived in good accordance with the test values, derived from worst case conditions.
- c) The average plasma temperature showed a normal behavior quite according to the predictions and this hold true also for the energy distribution curves. So a maximum deviation of 5% up to higher values can be assumed to be realistic.
- d) Solar flares could not been detected by E1 and therefore no data were available for direct comparison. But a recent documentation [9] showed that our assumptions which on the first view seemed to be rather high are even lower than other calculations [10]. So for an average sun (1978-80) an additional fluence of $\Phi_p + (\text{flares}) = 2 \times 10^{16}$ [1, 9] is not overestimated.

Temperature data and absorption coefficient changes
 - Figures 3 and 4 show typical measured temperature curves for the first orbit [11]. The measurement point is located on the heat shield of the center body covered with CC-SSM. Here the best case analysis based on an $\alpha = 0.18$ including the small gaps between the 2 x 2 cm mirrors. The worst case analysis

including the degradation was based on $\alpha = 0.23$. Comparing the measured data with the analysis we can see that from launch to the first perihelion and then to the first aphelion the measured data showed an increasing tendency to approach the upper curve. This proves clearly that a steady degradation/contamination occurred on the heat shields such causing increasing temperatures. If we derive from these temperature data the $\Delta\alpha$ -values as a function of probe-sun-distance and plot them using appropriate energy units we get a curve which shows a steady increase (fig. 5). After an initial jump from 0.18 to 0.19, probably due to primary contamination caused by a contamination layer of 500-800 Å [1], the slowly accelerating increase of $\Delta\alpha$ until perihelion and decelerating growth until 1st aphelion shows the expected and predicted shape. Comparing these mission data with the Boeing measured degradation curve and other test informations one can try to give a new improved expression for α_{final} using formula (2).

For the first orbit a α (degr) = 0.03 seems to be reasonable and a α (contam) = 0.02 can be derived. The first portion of 0.01 results from values measured during Boeing tests even under "clean" - conditions, and the second portion of 0.01 is due to "primary" contamination in orbit. So we get the following expression :

$$\alpha_{\text{final}} = \alpha_{\text{initial}} + \Delta\alpha(\text{degr}) + \Delta\alpha(\text{contam}) \quad (3)$$

$$0.22 = 0.17 + 0.03 + 0.02$$

Following this trend one can try to derive the α and the corresponding temperatures for the end of the second orbit, too, and compare such calculated numbers with data which will be received until end of this year.

Prediction for second perihelion

$$\alpha = 0.24 = 0.17 + 0.045 + 0.025 \quad (2\text{nd orbit}) \quad (3)$$

$$T \text{ (2nd perihelion)} = 121^{\circ}\text{C}$$

Conclusions

The performed environmental tests with combined and accelerated stress proved to be valid at least if a good preparation of basic data and good interpreta-

tion of basic effects are possible. Some assumptions had to be corrected, following the measured mission results, but not to the extent, that the derived test conditions must be regarded as not applicable. A worst case assumption for fluences prevented here from too high errors in test results and showed to be a good tool to overcome difficulties by unknown or not quite well understood effects.

New and improved studies had been forwarded to get more recent and improved data and to incorporate them into more modern synergetic theories. These effects could be found for HELIOS, for the whitening of metallized FEP is due to combined effects of particles, UV-irradiation and high temperatures such proving the validity of the proposed hypothesis [1]. But still more informations, mainly now for materials exposed to solar flares, are necessary. Then hopefully the whole picture of the interdependence between environmental factors themselves and environment and materials can be seen and will be correctly interpreted.

References :

- [1] WINKLER, W. "Kontamination und Degradation optischer Oberflächen unter HELIOS-Orbitbedingungen", Raumfahrtforschung, 18, S. 72-78, (1974)
- [2] LUEDECKE "Solar-Absorptionsvermögen an Werkstoffen bei UV- und Protonenbelastung" TRW-System Group Report 8526,72 (1972)
- [3] IPL internal data (May-July 1973) see 1, page 75-76
- [4] THOMAS, I.R. "MVM'73 Solar Proton Environment" BOEING-SRL 98124 (1971)
- [5] WINKLER, W. and STAMPFL, P. "Conductive Coating" Acta Astronautica, to be published (1975)
- [6] CUPERMANN, S. "Solar Wind" NASA-SP-308 (1971)
- [7] MILLER, R. and CAMPBELL, F. "Effects of low Energy Protons on Thermal Control Coatings" Proc. AIAA, Thermophysics (1965)
- [8] ERNO-VB 370-175-029 "UV- and Proton Degradation Tests on HELIOS-SSM", (1973)
- [9] BAEUERLEIN, R. "Berechnung der Strahlungsbelastung von Solarzellen und Strukturen aus KFK-Massen" RV21-V30/74-QH (1974) S. 16
- [10] ALLISON, J.F., Letter to GfW March 11, 1974
- [11] UNZ, SCHUERMANNS and BRUNGS HELIOS-A MISSION DATA Sheet for the 1st perihelion March 15, 1975, Thermal Analysis
- [8a] FOGDALL, L. and CANNADAY, S. "Radiation Effects on Second Surface Mirrors" Proc. CNES. Evaluation of Space Environment on Materials (1974)

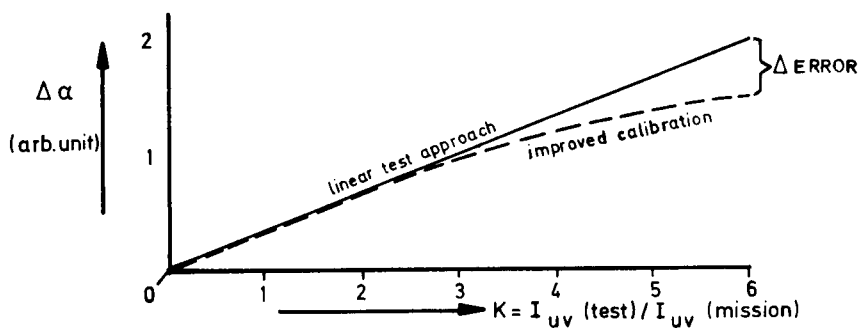


Fig.1: test error $\Delta\alpha = f(K)$ (schematic). K = acceleration factor

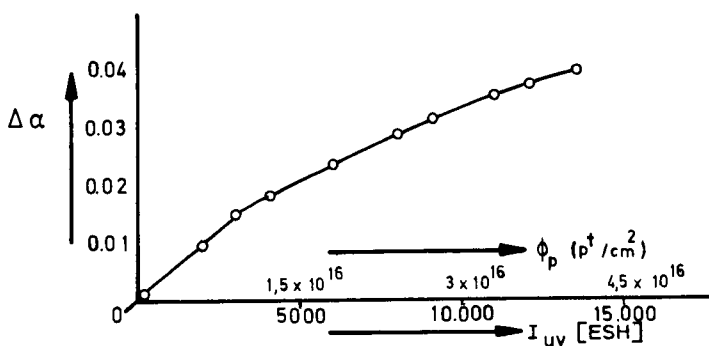


Fig.2: Typical degradation of quartz-SSM during Boeing-tests

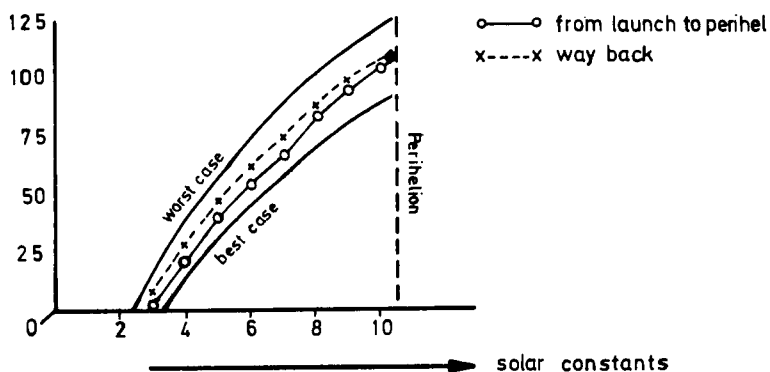


Fig.3: Analysis and mission data for heatshield temperatures

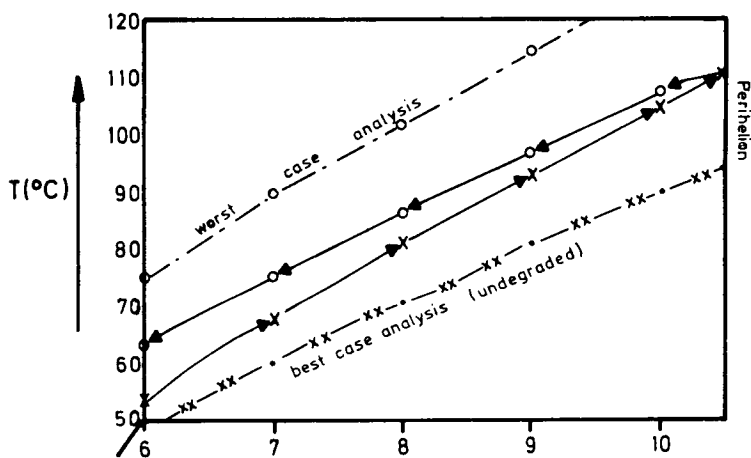


Fig. 4 Mission data and analysis (detail of Fig. 3)

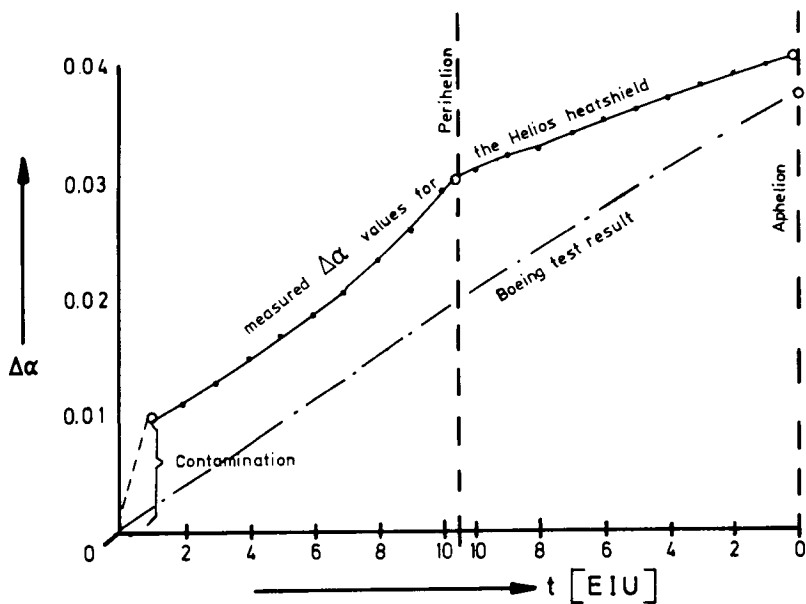


Fig.5 $\Delta\alpha$ values derived from measured temperature values

CORRELATION OF AN OPTICAL SYSTEM DEGRADATION WITH CONTAMINATION ON A CRITICAL SURFACE

J. J. Scialdone, *Goddard Space Flight Center, Greenbelt, Maryland*

ABSTRACT

A method to identify the reasons for the loss of sensitivity of a radiantly cooled radiometer during space operation has been investigated. A quartz crystal microbalance (QCM), mounted in the proximity of the instrument filter lens and held at its temperature, measured the contaminant at that location during a vacuum test. The temperature cycling of the lens and the QCM verified the contamination of the lens as the cause of the deterioration. Data on the instrument performance in space and in the chamber allowed estimation of the rate of contaminant accretion on the lens in space service. That rate was used to estimate the contaminant partial pressure. The nature of material was inferred by comparison of that partial pressure and the saturated vapor pressures of materials at the temperature of the contaminated surface. These data, in conjunction with data on fields of view of the lens, can be used to identify the sources of contamination. The experimental and analytical work reported here showed that contamination of the infrared (IR) filter lens of the radiometers on the spacecraft is the cause of instrument loss of sensitivity. The contaminant has an IR equivalent optical extinction coefficient of $4.23 \times 10^{-3} \text{ g/cm}^2$. The instrument degradation in space has a time constant of about 416 days. It is caused by materials accreting on the lens at a constant rate of $1.2 \times 10^{-10} \text{ g/cm}^2\text{s}$ and having saturated vapor pressures of less than $1.33 \times 10^{-7} \text{ Pa}$ (10^{-9} torr) at 233 K (-40°C). Materials meeting these requirements are hydrocarbons, phthalates, adhesives, plasticizers, and their combinations. The constancy of the contamination rate indicates that the sources may be oils from lubricated areas or long term sublimation of polymeric materials located near the lenses.

INTRODUCTION

Several causes have been postulated for the in-space degradation of some radiometric instruments. The most probable is contamination resulting from the condensation and adsorption of outgassing materials

on critical surfaces of the instruments. For optimum infrared (IR) performance, the IR detector must be at cryogenic temperatures. Adjacent surfaces will also attain cold temperatures. The contamination on these surfaces is difficult to prevent even for small contaminant fluxes.

This paper describes a test method to measure the contamination on a filter lens of the radiometer instrument during the spacecraft thermal vacuum test. The contamination was monitored by a quartz crystal microbalance (QCM) which was located near and held at the same temperature as the IR filter lens. The accretions and losses of materials, as measured by the QCM, were correlated with the performance of the instrument. The correlation confirmed that the instrument loss of sensitivity was attributable to contaminant material on the IR lens. It also provided data on the optical properties of this contaminant. These results, together with data on sensitivity loss versus time experienced in space operation, were used to estimate the contaminant magnitude, rate of change, and equivalent vapor pressure with time. These results are used to infer the origin of the contaminant.

EXPERIMENTAL

The spacecraft, which carries two radiometer instruments, was tested in a 7.3-m dia by 6.1-m (24-ft dia by 20-ft) vacuum chamber. The spacecraft solar panels were not included in this test. The chamber, which is equipped with two mechanical pumps and sixteen 0.8-m (32-in.) diffusion pumps, LN₂ baffled, maintained pressures of the order of 1.33×10^{-4} Pa (10^{-6} torr) during the test. The thermal arrays of the chamber walls simulated the orbit thermal conditions. Their temperatures were varied between 303 and 258 K (+30° and -15°C). Helium cooled targets, facing the radiators of the radiometer instruments, provided the means for attaining the cold temperatures they attain in space. The various surfaces of the radiometers were temperature controlled with heaters by closed-loop thermal servos. The performance of the radiometers were monitored periodically during the test, which consisted of stimulating the optics with a source of IR energy and measuring the voltage output of the radiometers.

The output voltages versus energy inputs are a measure of the instrument sensitivity. The data for these measurements are compared to those obtained with the instruments in a very clean small chamber. The radiometer instrument schematic is shown in Figure 1. It consists (References 1 and 2) of a two-channel line scan utilizing a common optical system. The temperatures attained at each surface in space are indicated. The 10.5- to 12.5- μ m filter lens, suspected of being the cause of degradation of the instruments and the object of this investigation, acquired a temperature of 231 K (-42°C) during the test. The

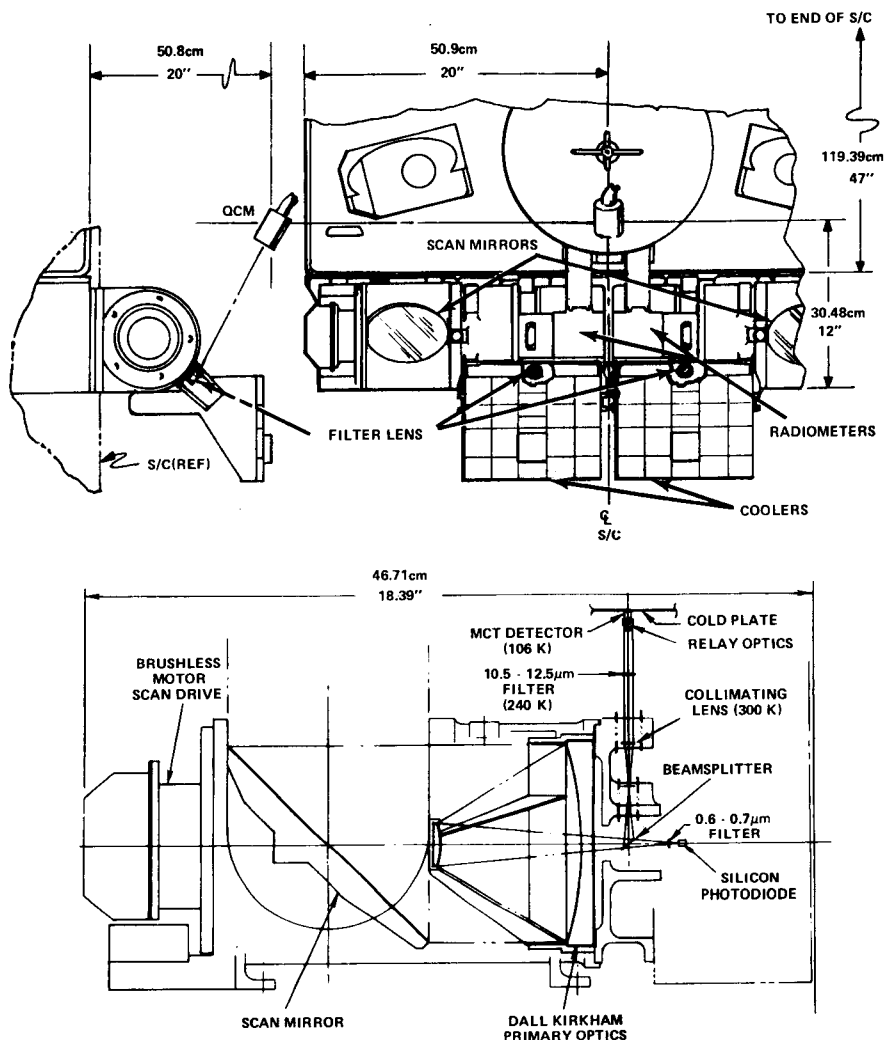


Figure 1. Location of QCM during test and schematic of radiometer detector, at a much lower temperature, was protected by cryogenic baffles which have proved effective against contamination. For the test, a QCM was mounted as shown in Figure 1, outside the well vented spacecraft, but as near as possible to the lens. Its temperature was controlled to reproduce the lens temperature at all times. The accretions registered by this instrument are shown in Figure 2 and measured in kHz ($1 \text{ kHz} = 4.5 \times 10^{-6} \text{ g/cm}^2$). This figure shows also the temperatures of the chamber walls, which were also attained by the spacecraft, and the measured degradation of the two radiometers. The correspondence between temperatures and accretion rates

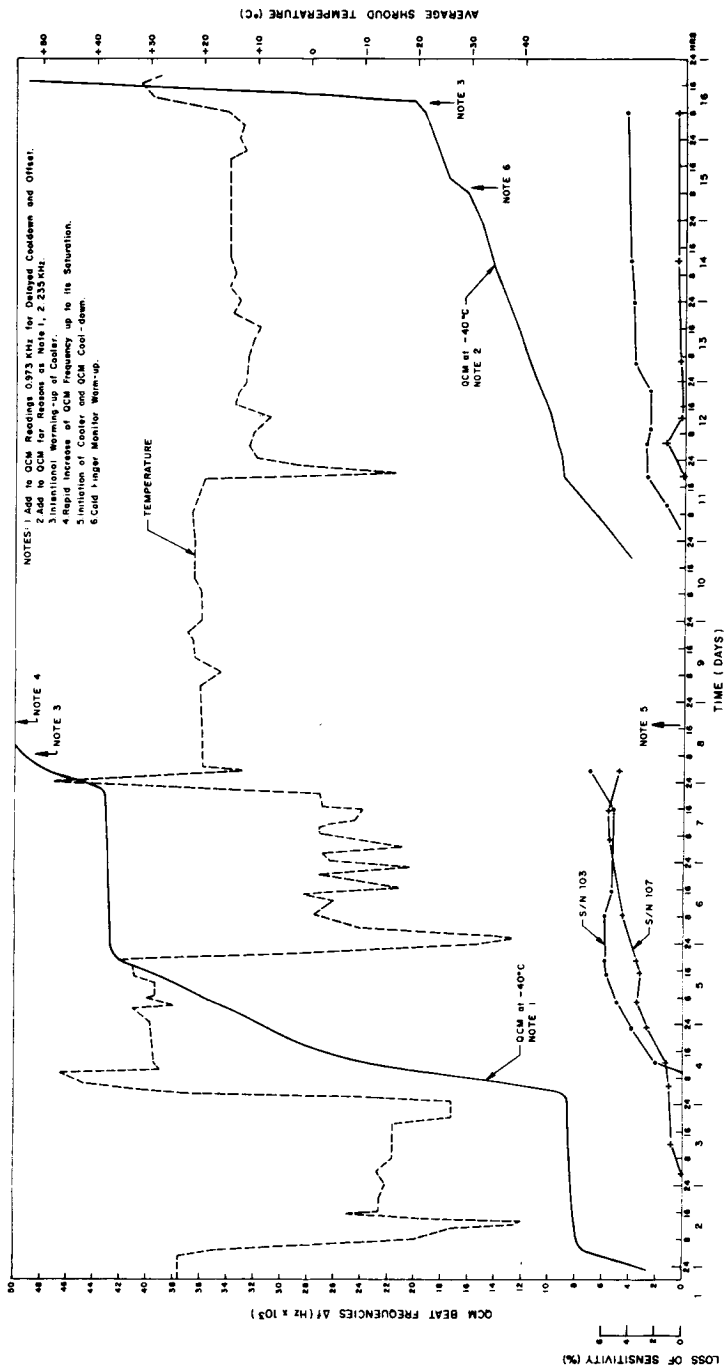


Figure 2. Thermal-vacuum test. Correlation QCM and radiometer filter lens contamination

on the QCM are well reflected by the curves. Decreased accretion rates with time for the same temperatures are not obvious from the plot; nevertheless, they occurred and reflected the depletion of the outgassing with time. The cyclic pumping and rejection by the chamber walls of the outgassing materials makes the determination of outgassing versus time difficult.

Midway during the test, when the radiometers indicated sensitivity losses of about 6 percent and the QCM indicated about 50 kHz, the radiometers were warmed up. The large amount of condensed material which was released was reflected by the sudden increase in beat frequency recorded by the QCM and its eventual saturation. The radiometers, after 32 hours at normal temperatures, were recooled and their calibrations rechecked. They showed restored sensitivities. Resumption of contaminant accretion, as recorded by the QCM, was reflected by gradual loss of sensitivity of the radiometers in proportion to the mass accreted. This loss of sensitivity and restoration by temperature cycling has been shown in other, subsequent tests (Reference 3).

The sensitivity loss versus QCM mass accretion is shown in Figure 3. The data include sensitivity for the two instruments, both before and after the restoration of performance. The scattering of data is a reflection of the difficulty of making accurate measurements. The curve fitting is discussed later. As indicated previously, data on accretion versus time as a measure of the strength of the contaminant source cannot be extracted easily by this test because of the cycling of the wall temperatures. However, a test could be made to establish this parameter. A better indication of the loss of sensitivity versus time is provided by the data shown in Figure 4. This was obtained from calibrations of four instruments on three different spacecraft in orbit (T. Heslin, private communication).

Some additional data from space operation are available, but they are very inconclusive, having been taken for very short periods of time and for changed conditions. In one case (Reference 2), a small heater was used to warm up the cold patch from 106 to 230 K when the instrument had degraded by about 20 to 25 percent. This increased the lens temperature by about 10 K. An improvement of 5 percent in sensitivity was obtained, but not a full restoration of sensitivity, probably because the heater was not large enough to remove the total amount of the contaminant. No accurate and consistent data on degradation in space has been taken. A reason for this may be that these radiometers slowly reach a degradation of about 30 percent during the life of the spacecraft. In the past, this degradation has been acceptable for these instruments. But, it may not be for longer spacecraft lives and for more sophisticated instruments of the future.

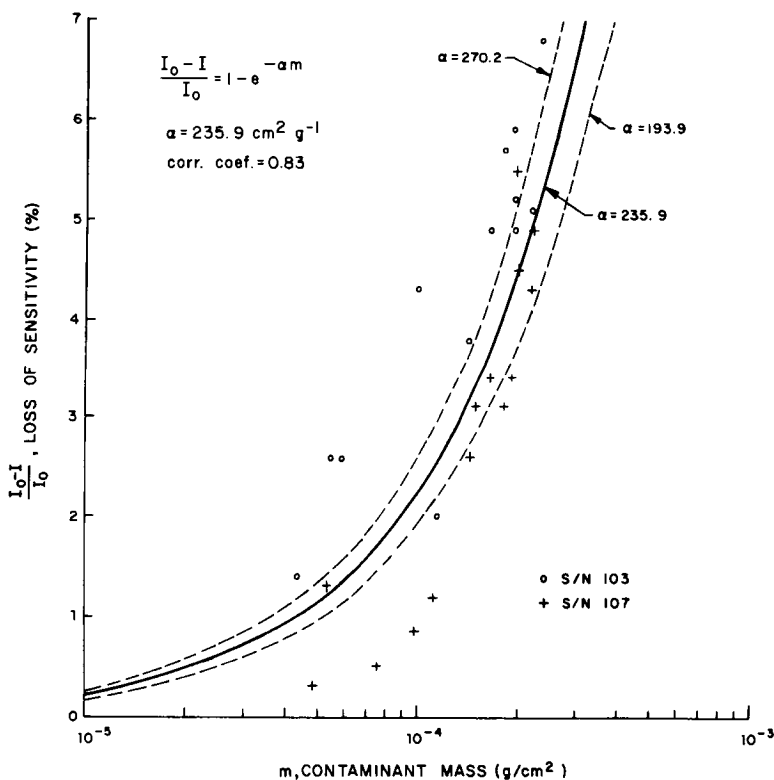


Figure 3. Sensitivity loss versus mass deposited on lens

ANALYSIS

The loss of radiometer sensitivity versus mass accreted on the lens during test, and the loss experienced with time with the instruments in orbit, form the basis of the analysis. The loss of sensitivity being a result of mass accretion on the lens is supported by the experimental evidence that sensitivity is restored following removal of the contaminant from the surface. The contaminant on the lens must absorb part of the energy. The absorption characteristic of a substance is expressed by a coefficient which depends on the wavelength of the incident energy and on the properties of the material. For a not very dense material, the absorption depends on the thickness and on the number of absorbing molecules or density of the material. The attenuation of the intensity I_0 passing through the material of thickness ℓ (cm) and density ρ (g/cm³) is then given by

$$I = I_0 e^{-\alpha \rho \ell} = I_0 e^{-\alpha m}$$

where α (cm²/g) is the molecular absorption coefficient and m (g/cm²)

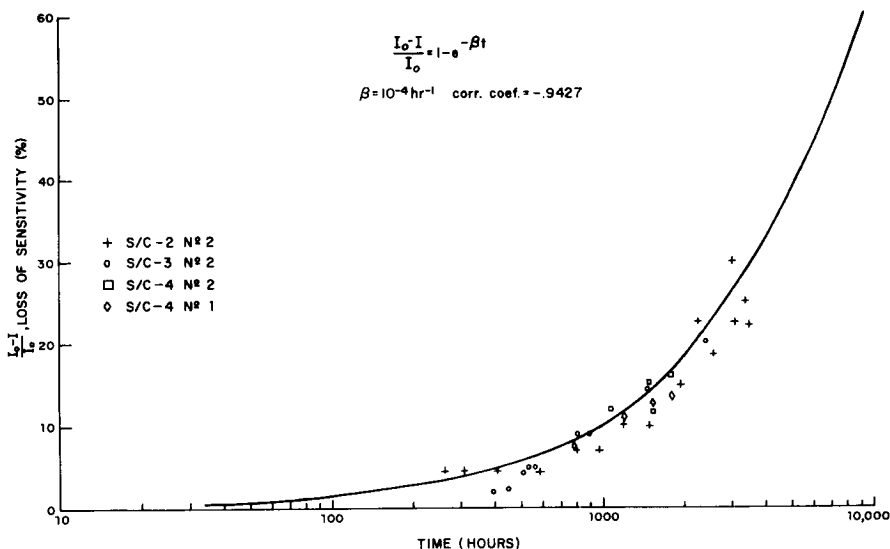


Figure 4. Sensitivity loss versus time in orbit

is the mass density per unit thickness of the material. This relation expressed in terms of percent loss of intensity or sensitivity is $I_0 - I/I_0 = (1 - e^{-\alpha m})$. The measurements on the loss of sensitivity of the two instruments versus mass have been fitted to this expression using the method of least square. The data for one of the instruments fitted the curve with $\alpha = 270 \text{ cm}^2/\text{g}$ with a correlation of 94 percent. The other fitted with $\alpha = 193.9$ with a correlation of 86 percent. The fitting of all the available data to one curve gave an $\alpha = 235.9 \text{ cm}^2/\text{g}$ with a correlation of 83 percent. The extinction coefficient, using this last value, is $1/\alpha = 4.23 \times 10^{-3} \text{ g/cm}^2$. This coefficient represents the mass of material on the lens required to produce a loss of 64 percent in sensitivity. In terms of thickness, this mass corresponds to about $50 \mu\text{m}$ of a hydrocarbon substance.

The loss of sensitivity with time during the vacuum test is the result of outgassing from surface temperatures of the chamber and spacecraft which were changed periodically from hot to cold and back. With this type of operation, part of the outgassing was being transferred from one surface to another. A characterization of contaminant source versus time is therefore representative of the test only.

In a future test, a constant cold chamber wall temperature should be used. The data on time dependence of the degradation obtained from space results are shown in Figure 4. It fitted best, with a correlation of 94 percent, the equation $I_0 - I/I_0 = (1 - e^{-\beta t})$, where $\beta = 10^{-4} \text{ hr}^{-1}$.

The time constant $\beta^{-1} = 10^4$ hr is the length of time required for the degradation to become 64 percent of the original undegraded performance. An attempt to fit the data with an inverse power of time also gave very small changes with time, but the correlation was less satisfactory.

The mass of contaminant accreted and its rate of accretion with time can be found by equating the two experimental equations derived above. In fact, equating $(1 - e^{-\alpha m})$ to $(1 - e^{-\beta t})$ the mass accretion with time is:

$$m = \frac{\beta t}{\alpha} \quad \text{g/cm}^2$$

and its rate is the constant:

$$\frac{dm}{dt} = \frac{\beta}{\alpha}$$

The net contamination rate in space service, is then 4.24×10^{-7} g/cm²hr (1.177×10^{-10} g/cm²s) using the values of α and β obtained experimentally. This rate is directly proportional to the contaminant flux and partial pressure as seen by the surface. The rate of evaporation of the contaminant can be disregarded. This is because at the temperature of the lens and for the total pressure involved, the rates of evaporation of accretable materials, polymers, hydrocarbons, phthalates, and silicone oils, are at least one order of magnitude lower than the above. This results from their low values of the saturated vapor pressure (10^{-8} to 10^{-10} Pa (10^{-10} to 10^{-12} torr)) at that temperature of 233 K (-40°C) (Reference 4). The impinging flux is the above rate, but multiplied by a condensation coefficient, α . Since a bulk material accretion is involved, this coefficient is very close to one because of the nature of the contaminant (heavy molecular weight), low energy (room temperature gas) and the relatively cold surface (233 K (-40°C)). The magnitude of the contaminant partial pressure can also be estimated without much of an error assuming the gases to have a molecular weight $M \approx 300$ to 500 g/mole and an average temperature of $T = 293$ K. In fact, with $\alpha = 1$, $M = 400$ g, $\dot{m} = 1.177 \times 10^{-10}$ g/cm²s, and $T = 293$ K, the Langmuir relation

$$\dot{m} = \alpha \frac{P}{17.4} \left(\frac{M}{T} \right)^{1/2} \quad \text{g/cm}^2\text{s}$$

indicates a partial pressure $P = 2.33 \times 10^{-7}$ Pa (1.75×10^{-9} torr). The magnitude of this pressure excludes contaminants on the lens, such as water and other gases, which have saturated vapor pressure greater than 10^{-7} Pa (10^{-9} torr) at 233 K (-40°C). Materials which have lower saturated pressures than these have been indicated above. It is of interest to note that in Reference 5, calculations on a similar radiometer indicated that an invariant partial pressure of about 3.99×10^{-7} Pa (3×10^{-9} torr) of Windsor lube $M = 430$ g existed in the radiometer

compartment as a result of lubricant leakage from both ends of the shaft of the speed reducer filter drive motor. Also a partial pressure of about 10^{-8} Pa (10^{-10} torr) was estimated for adhesive materials used to seal the edges of the insulation sheets.

CONCLUSIONS

A method to investigate the contamination on an optical surface has been developed. It utilizes a QCM mounted near and held at the same temperature of the surface. A record of the mass accretion versus the performance of the optical system can be used to calculate the equivalent optical property of the contaminant. Temperature cycling of the optical surface and QCM can be used to confirm contamination as the cause of deterioration. The vapor pressures of the contaminant can be estimated at various temperatures by recording the rates of frequency change of the QCM during warming up cycles. The loss of instrument sensitivity with time is also recorded in addition to the degradation versus mass. Equating the two parameters, one obtains the mass accreted with time, and, by differentiation of this, the rate of accretion with time is also known. The rate is directly related to the flux and partial pressure of the contaminant. Its change with time may serve as an identification of the contaminant source based on known outgassing behavior of materials with time. Furthermore, the magnitude of the partial pressure compared to the saturated pressure at the temperature of the contaminated surface, determines which materials may or may not deposit.

The experimental work and analysis reported here has shown that contamination of a filter lens is the cause of a radiometric instrument loss of sensitivity. The contaminant had an equivalent optical extinction coefficient (64 percent loss of transmission) for IR energy of 4.23×10^{-3} g/cm² (about 50 μ m of material with density of 0.8 g/cm³). In space operation, the degradation of the instrument follows an exponential law with a time constant of 10^4 hours (416 days). These data indicate that the contamination in space occurs at a constant rate of 1.2×10^{-10} g/cm²s, and the materials have saturated vapor pressures of less than 10^{-7} Pa (10^{-9} torr) at 233 K (-40°C). The materials which possess these low vapor pressures are hydrocarbons, phthalates, adhesives, plasticizers, and their combinations. The constancy of the contamination rate indicates that the source contaminant may be oil escaping from drive motors or a long term subliming polymeric material located near the lens.

ACKNOWLEDGMENT

The author wishes to acknowledge the cooperation of Mr. Jack O'Brien, the experiment technical officer, for having promoted the test and Mr. Ben Paxson for setting up the instrumentation.

REFERENCES

1. Aronson, A. I., "Very High Resolution Radiometer," RCA, Corporate Engin. Services, Reprint RE-20-1-18, 1974.
2. Donohoe, M. J., A. Sherman, and D. E. Hickman, "Radiant Coolers—Theory, Flight Histories, Design Comparisons and Future Applications," AIAA 13th Aerospace Sciences Meeting, Pasadena, Cal., January 20-22, 1975.
3. O'Brien, J., "VHRR, One Year in Orbit" in Significant Accomplishments in Science and Technology, NASA SP-361, 1973, p. 217.
4. Santeler, D. J., D. H. Holkeboer, D. W. Jones, and F. Pagano, "Vacuum Technology and Space Simulation," NASA SP-105, Washington, D. C., 1966, pp. 139, 153.
5. Scialdone, J. J., Appendix II in "Report of the Findings of the Radiation Cooler Task Group" DIRS 02-273-I-2-TR-239-032-215, Goddard Space Flight Center, Greenbelt, Md., September 1970.

DATA FROM A SYNCHRONOUS ALTITUDE SATELLITE QUARTZ CRYSTAL MICROBALANCE MONITOR

John F. Rogers, *NASA/Goddard Space Flight Center, Greenbelt, Maryland*

ABSTRACT

Results of one year's operation in orbit of the Quartz Crystal Microbalance Monitor on the ATS-6 satellite are presented. The data indicate a general decreasing trend for the first four and one-half months in orbit. At that time, a sudden increase in beat frequency occurred; this correlates in time with the firing of the North Cesium Ion Engine. A general increase in beat frequency is evidenced since that time. Laboratory tests conducted to investigate the phenomenon are described.

INTRODUCTION

The ATS-6 spacecraft has, as one of the experiment complement, a Very High Resolution Radiometer (VHRR). One part of the VHRR is a radiation cooler, a device which is exposed to space and allowed to radiatively cool to very low temperatures. Surfaces of this cooler have thermophysical properties which can be degraded by the deposition of contaminants. The Quartz Crystal Microbalance Monitor (QCM) was installed aboard the ATS-6 as a monitor for contaminants which might deposit on the VHRR cooler or other spacecraft sensitive surfaces. It was designed to operate at low temperature to simulate certain cooler surfaces and configured so that measurements of fluxes by the QCM can be related to other surfaces.

Data from the QCM could be used as a basis for modifying orbital operations in order to decrease contamination hazards and to obtain information as to the contamination environment of this spacecraft in orbit.

Spacecraft Configuration

The ATS-6 spacecraft was launched from Cape Kennedy at 13:00 G.M.T. on Thursday, 30 May 1974. The orbital configuration for ATS-6 is shown in Figure 1 with the solar arrays and the parabolic dish antenna deployed. The end-to-end distance of the extended solar arrays is

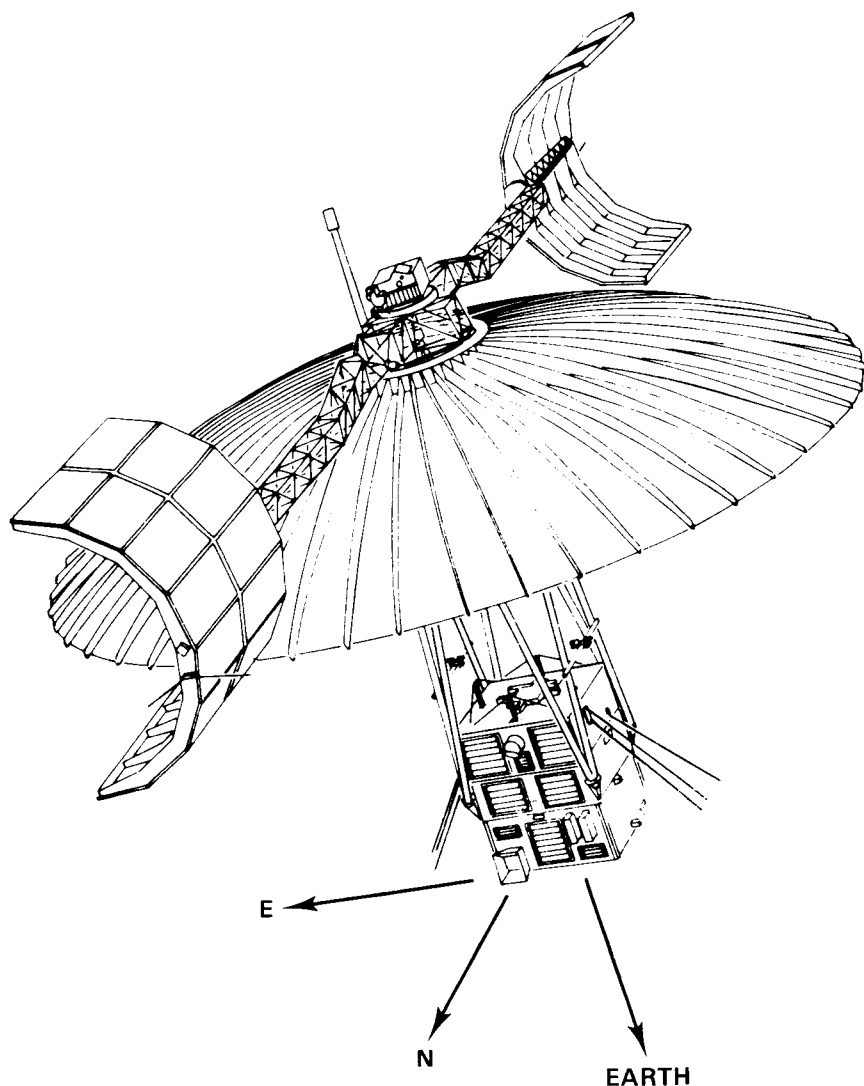


Fig. 1—ATS-6 spacecraft

1555 cm (51 feet). The overall height of the spacecraft is 823 cm (27 feet) from the earth-viewing surface of the Earth Viewing Module (EVM) to the top of the magnetometer. The erected parabolic antenna is 914 cm (30 feet) in diameter. The EVM basic structure is a near cube of 137 x 137 cm cross section and 165 cm high (54 x 54 x 65 inches). The spacecraft moves in the easterly direction at 3 km/s to maintain its fixed position above the earth at synchronous altitude. Three inertia wheels serve as prime torques in the attitude control subsystem. A hydrazine propulsion subsystem

provides for jet control of attitude and for orbital velocity control of the spacecraft. The initial orbital weight is approximately 1393 kg (3070 pounds). The Quartz Crystal Microbalance is located on the North panel of the EVM viewing the North direction. The solar array is at a distance of 808 cm (26.5 feet) from the QCM and is entirely within its field-of-view while only a segment of the dish antenna is within the field-of-view of the QCM. The EVM shown in Figure 2 is made up of three subsections. The lower subsection is designated the experiment module and contains most of the experiments and all of the earth viewing sensors. The middle section called the service module contains the electrical power subsystem, telemetry and command, and the attitude control subsystems. The top section is the communication module and houses the transponder and three experiments closely associated with the communications subsystem. The aluminum louvers shown are backed by Optical Solar Reflectors (OSR) used for active thermal control of the EVM. The Radiometer cooler views North and is shielded by a sun shade. The Polaris Star Tracker and two of the hydrazine thrusters are shown on the Experiment Module. The North engine of the Cesium Ion Engine Experiment is near the top of the Communication Module; a similar engine is mounted on the South panel. The QCM is mounted adjacent to the hydrazine thrusters near the top of the Experiment Module.

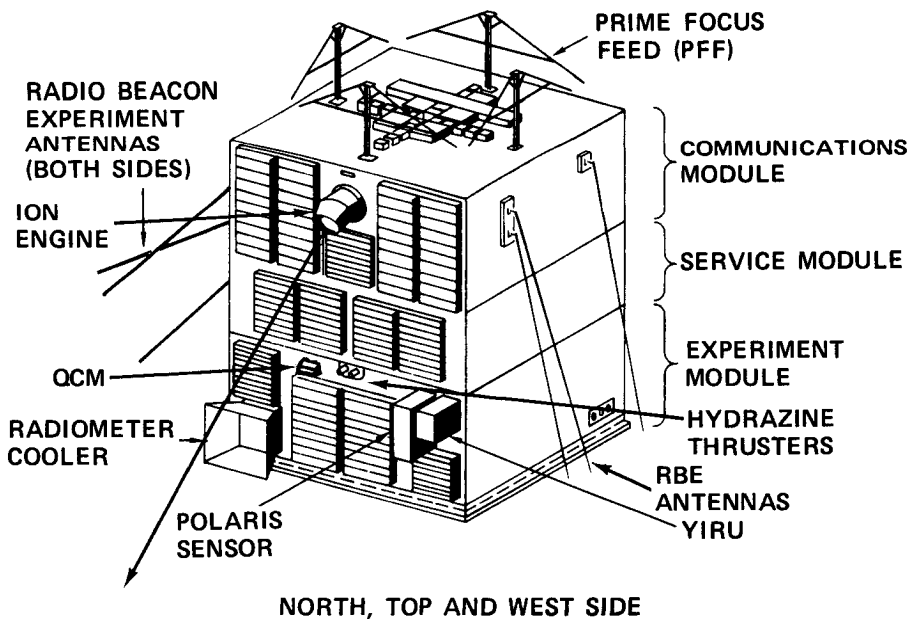


Fig. 2—Earth viewing module

QCM Description

The QCM consists of the sensor head mounted on the exterior of the North panel, as shown in Figure 3, with the electronics package on the interior of the same panel immediately behind the sensor head. The main elements of the sensor head are the crystal assembly and the mixer-oscillator (M/O) circuit. The M/O circuit is radiatively coupled to the spacecraft skin to maintain its temperature above -25°C while the crystal assembly is radiatively coupled to space to achieve a design goal of -70°C .¹ The entire housing uses OSR's for solar input decoupling and maximum thermal emissivity. Two stages of conductive isolation are used, one between the housing and the spacecraft skin and the other between the sensor housing and the crystal assembly. A solar simulation test with the flight unit at the worst sun angle indicated satisfactory thermal performance.

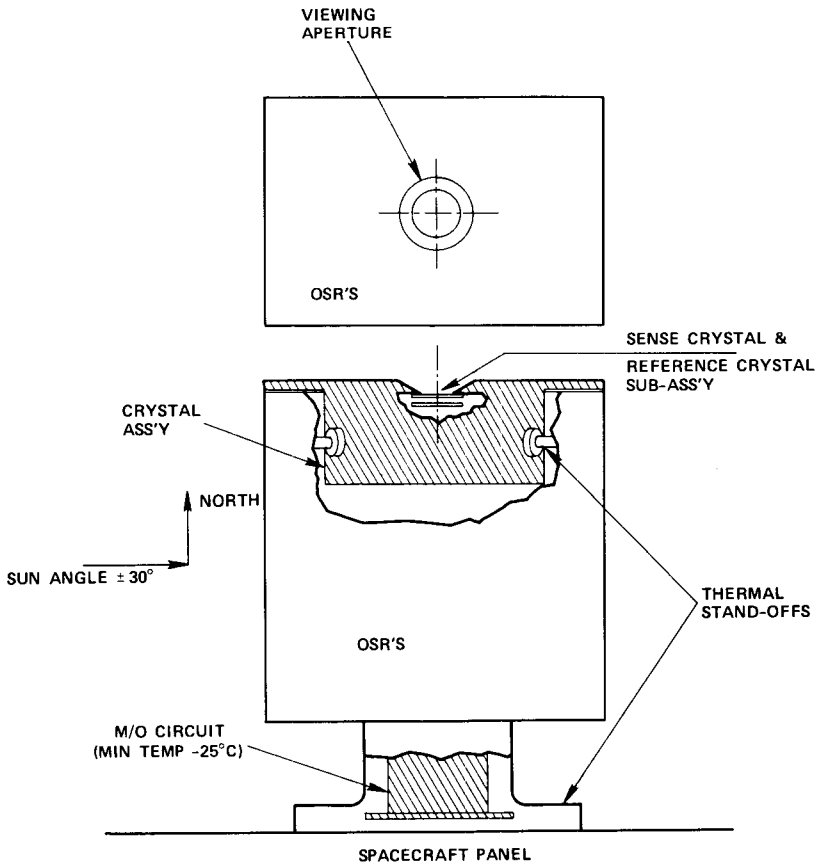


Fig. 3—Quartz crystal microbalance assembly

The electronic package provides regulated voltages for the M/O circuit, thermister data processing circuitry, and the crystal beat frequency-to-digital words conversion circuitry. The beat frequency is amplified to a square wave, counted, and held in registers for input to spacecraft telemetry. Two nine bit words are used for the maximum range of the beat frequency while maintaining a 1 Hz accuracy.

The crystals used are 10 MHz, AT cut, natural quartz with aluminum electrodes. The beat frequency temperature dependence is about 240 Hz from +25°C to -70°C.

QCM OPERATIONAL PERFORMANCE

The beat frequency at the completion of the thermal vacuum spacecraft system test was 1300 Hz. The first turn on of the QCM at Cape Kennedy showed about a 600 Hz increase (an equivalent of 2.7×10^{-6} g/cm²) since leaving Germantown, Maryland. It was decided that an attempt at cleaning the crystal(s) would introduce uncertainties due to residuals and therefore the QCM was flown as is.

The performance during the launch phase and the time to synchronous altitude is given in Figure 4. The first hour from lift-off is shown on an expanded scale with the periods of no telemetry marked. The lift-off phase, including payload fairing separation, is characterized by a decreasing beat frequency. The temperature for the first ten minutes after lift-off decreased from +20°C to around +13°C and further decreased to -12°C at the beginning of the thermal maneuvering phase. The beat frequency for the telemetry period 21 minutes after lift-off shows an increase and finally stabilizes at 1800 Hz. This performance would appear to agree with SKYLAB data.² The explanation given in the SKYLAB report of the sense crystal cleaning up at a faster rate than the reference crystal most likely applies to the data given here.

The orientation of the spacecraft during the thermal maneuvering phase is such that the sun sweeps across the crystal during each rotation of the spacecraft. The solar exposure causes the 200 Hz dips shown in Figure 4. The periods of no solar exposure do not indicate that any mass accretions are occurring during the thermal maneuvering phase. The temperature of the QCM has stabilized at -15°C from 1430 hr G.M.T. to 2000 hr G.M.T.

The first year's performance is given in Figure 5 where the beat frequency is on the right hand scale and the temperature is on the left hand scale. The technique of daily averages for the data presentation is used. The June to September 1974 period of decreasing beat frequency corresponds to a desorbing mass flux of 1×10^{-13} g/cm²s at a crystal temperature of -20°C. McKeown,³ using a quartz crystal microbalance on OGO-6, reports an evaporation rate of 1.2×10^{-13} g/cm²s at a temperature of +7°C. The constant value of the beat frequency during July

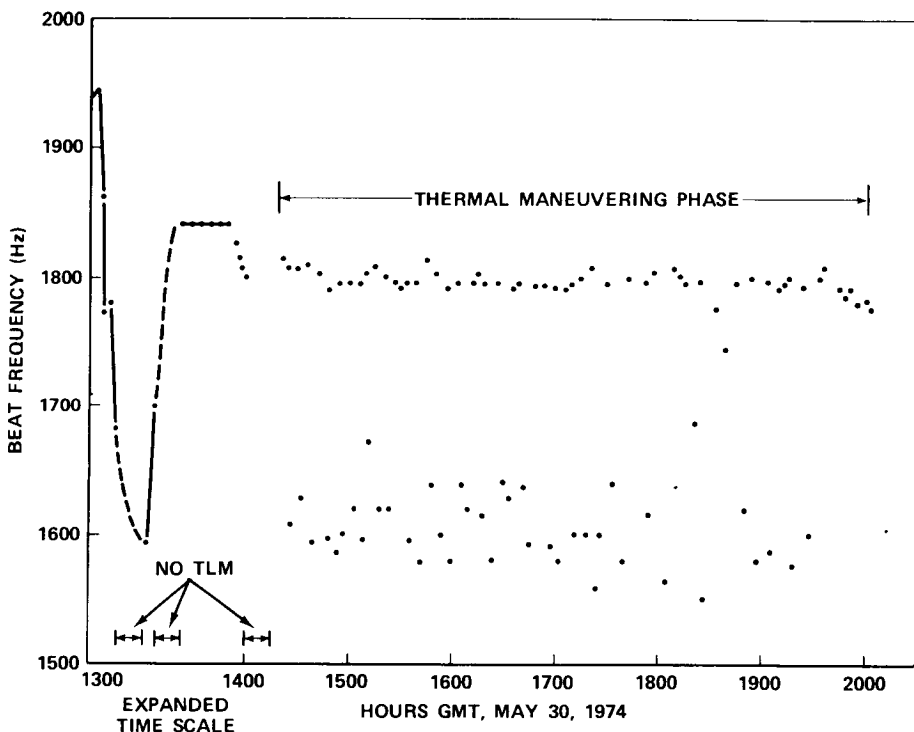


Fig. 4—Launch and thermal maneuvering phase

1974 departs from the general desorption rate and may indicate an equilibrium condition exists between the QCM and an external flux field. However, this condition has not been correlated with spacecraft activity as of this date. The hydrazine engines on the North side were fired in the order of milliseconds about every three days for inertia wheel unloading. A detailed examination of the data showed no time based correlation with the QCM. It has been reported that spacecraft static change in the kilovolt range was observed less than fifty percent of the days that the spacecraft passed through the shadow of the Earth.⁴ The QCM did not show any accretions during the ecliptic period which would correspond to the change phenomenon events.

The poor thermal performance of the QCM led to a decision to do a 24 hour heating cycle in the event that the thermal coatings had been contaminated. This was done on June 7, 1974. The +50°C heating period resulted in a decreased beat frequency but no improvement in the thermal performance. It is possible that inter-reflections from the thermal louvers, radiometer cooler sun shade, and other protuberances could increase the solar input to the equivalent 2 or even 3 solar constants.

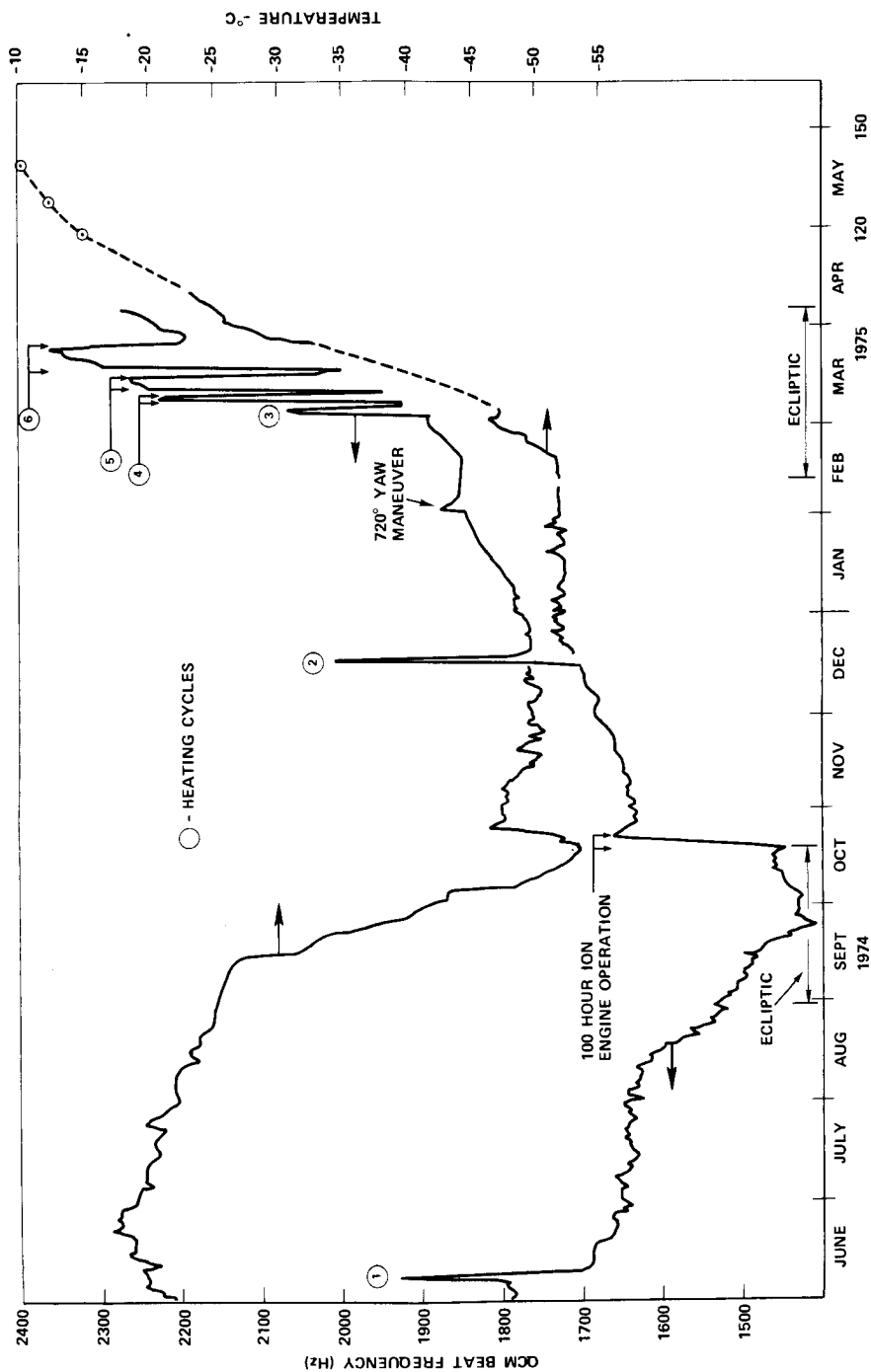


Fig. 5—ATS-6 quartz crystal microbalance first year's performance

Possible focussing effects of solar energy by the parabolic antenna may be contributing additional energy to the QCM radiator plate causing the higher than expected temperatures.

During the North Ion Engine firing (100 hours), an accretion rate indicated by a frequency change of 1.8 Hz/hr (corresponding to 1×10^{10} atoms/cm²s assuming cesium) is noted followed by an indication of slight mass desorption and finally a leveling off phase. Approximately 80 Hz of the total 240 Hz measured occurred in the two hours after engine turn-on. Appendix 1 contains a discussion of the Cesium Ion Engine exhaust plume characteristics and the QCM data.

The November 1974 to May 30, 1975 period is one in which the beat frequency is increasing at different rates. The total increase for this period is 1280 Hz or an equivalent 5.7×10^{-6} g/cm². An attempt was made on 17 December 1974 to clear the crystal of deposited contamination. The beat frequency did not show a drop as was experienced in June 1974 but rather indicated an increase after the heating period. The rate of increase is also slightly greater after the heating period than before. In March 1975 four additional heating cycles of one, two, four, and finally eight days was done in an attempt to clarify the 17 December performance. The results tended to conform to the earlier bake-out. "Quick-look" data shows the rate of increase to be 16 Hz/day for the period 20 to 30 May 1975 (not shown on the figure).

From November 1974 to mid-February 1975 direct sunlight does not impinge on the QCM housing resulting in a relatively stable temperature. The 17 December 1974 heating period resulted in an average 2° decrease in QCM temperature. The rising temperature profile corresponding to changing sun angle is somewhat masked by heating cycles of the QCM for the March–April 1975 period. The data for May 23 and May 30, 1975 (not on Fig. 5) show the temperature to be about -3.5°C. These results do not compare with the temperature of -20°C for a similar sun angle in 1974 nor was there a significant increasing temperature trend in 1974.

LABORATORY TESTING

Assuming the October 1974 response of the QCM to the Cesium Ion Engine operation is a valid in-flight measurement of charge-exchange atoms depositing on a cool, electrically unbiased surface, then, according to the vapor pressure data the cesium would re-evaporate rapidly when the QCM was heated. The in-flight bake-outs did not conform to the vapor pressure data and a laboratory test was performed to determine the reason. The details of the test are given in Appendix II. The cesium deposited on the prototype QCM would not re-evaporate at QCM temperatures up to 120°C. The vacuum was 4×10^{-4} Pa (3×10^{-6} torr) which can result in a monolayer formation of air in one second. It is therefore

possible for the cesium to combine with residual gases forming a cesium compound and which would not follow the cesium vapor pressure data. A test made with the QCM at +100°C and the shroud temperature at +20°C shows a 160 Hz/hour increasing beat frequency. This characteristic may be a measure of the gettering phenomenon associated with cesium.

CONCLUSIONS

At the temperature and sensitivity of the QCM there was no indication of the spacecraft outgassing flux interacting with the ambient molecules nor any measure of molecular self-scattering. The June to September 1974 period is one in which the spacecraft has maximum outgassing fluxes⁵ and the period during which the phenomenon may have been observed. The self-contamination models given in References 6 and 7, do not predict the spacecraft outgassing flux interacting with ambient molecules causing a measurable return to the North side of the ATS-6 spacecraft. The hydrazine engine operations did not show any time correlation with the QCM performance and no mass accretions occurred with the QCM at -20°C nor at -60°C. The solar arrays vary from about +60°C to below -50°C during the 24 hour orbit. The outgassing flux would thus cause a time dependent response of the QCM. No such time dependent response was apparent in the QCM data. The measured accretion rate during the 100 hour operation of the cesium engine of 1×10^{10} atoms/cm²s correlates with the analytic predictions of 1.3×10^{10} atoms/cm²s given by Lyon⁸ and of 3×10^9 atoms/cm²s given by Kemp.⁹ No definitive conclusions can be reached at this time for the November 1974 to May 1975 performance. Preliminary experimental work indicates a mechanism may exist for retention of the deposited contaminate and further a mechanism may exist for the contaminate to react with an external flux not detectable with the normal QCM sensitivity.

REFERENCES

1. Application Technology Satellite ATS-F Spacecraft Manual, X-460-74-154, Bernard J. Trudell, May 1974, Goddard Space Flight Center, Greenbelt, Maryland 20771.
2. MSFC SKYLAB Contamination Control Systems Mission Evaluation, TMX-64826, Skylab Program Office, May 1974, George C. Marshall Space Flight Center, Alabama.
3. Space Measurements of the Contamination of Surfaces by OGO-6. NBS-SP336, McKeown, D. and Corbin, W.E., Jr. Oct. 1970, Gaithersburg, Maryland.

4. Application Technology Satellite ATS-6 Experiment Check-Out and Continuing Spacecraft Evaluation Report X-460-74-340, Dec. 1974, Goddard Space Flight Center, Greenbelt, Maryland 20771.
5. The Outgassing and Pressures in A Spacecraft, John J. Scialdone, Proceedings of the Institute for Environmental Sciences, 28 April to 1 May 1974, Washington, D.C.
6. Self Contamination and Environment of an Orbiting Spacecraft, NASA TN D-6645, John J. Scialdone, May 1972, Goddard Space Flight Center, Greenbelt, Maryland 20771.
7. Contamination Assessment and Control is Scientific Satellites, NASA TN D-7433, Robert J. Naumann, October 1973, Marshall Space Flight Center, Alabama 35812.
8. Propellant Condensation on Surfaces Near An Electric Rocket Exhaust, W. C. Lyon, Dec. 1970, vol. 7, No. 12, pp 1494 to 1496, J. Spacecraft and Rockets.
9. Electrostatic Propulsion Beam Divergence Effects on Spacecraft Surfaces, TRW No. 11985-6003-RU-00, R. F. Kemp, D. F. Hull, E. E. Luedke, Sept. 1973, TRW Systems Group, California.
10. A North South Stationkeeping Ion Thruster System for ATS-F., R. Worlock, 17-19 April 1972, AIAA 9th Electric Propulsion Conference, AIAA Paper No. 72-439.
11. A Study of Cesium Exhaust from an Ion Engine and Its Effect Upon Several Spacecraft Components, HIT-399, June 1969, Hittmann Associates, Inc., Columbia, Maryland.
12. Determination of Adsorbate Structures on Metal Surfaces: Alkalies, Rare Gases, and Hydrogen on Tungsten, L. D. Schmidt, March 1972, pp. 882 to 889, (Vol. 9, No. 2), J. of Vacuum Science and Technology.
13. Use of the Quartz Crystal Microbalance for Outgassing and Contamination Measurements, D. A. Wallace, January 1972, Vol 9 No. 1, J. Vacuum Science and Technology.
14. Vapor Pressure of Caesium by the Positive Ion Method, Taylor and Langmuir, May 1, 1937, vol. 51, pp 753 to 760, Physical Review.
15. Charge Transfer Between Positive Cesium Ions and Cesium Atoms, Lawrence L. Marino, Dec. 1, 1962, vol. 128, No. 5. Physical Review.

APPENDIX 1

CESIUM ION ENGINE EXHAUST PLUME CHARACTERISTICS AND QCM DATA

The Cesium Ion Engine was one of the experiments aboard ATS-6. It's function was to demonstrate the application of ion thruster technology to the synchronous satellite North-South stationkeeping mission. A full description of the ion engine may be found in the literature.¹⁰

Cesium Exhaust Plume: General

The exhaust beam of the ion engine contains neutral atoms and charged positive ions. The ions are designated Groups 1, 2, and 4, depending on their characteristics. Group 1 ions are high energy ions which constitute most of the engine exhaust. These remain within the exhaust plume and do not interact with the spacecraft. Group 2 ions range in energy from a few electron volts up to the Group 1 ion energy. These are formed within the accelerating structure of the engine and are ejected at various angles with respect to the engine exhaust opening. Group 4 ions are low energy ions which are formed by charge exchange interactions in the exhaust plume external to the engine. For practical purposes, they leave the plume perpendicular to the exhaust direction. The Group 1 and Group 2 cesium ions in the engine exhaust are not considered as being measured by the QCM during the initial 100 hours of operation as no line-of-sight to the engine exhaust plane is possible. The neutral atoms leave the exhaust plane with roughly a cosine distribution and again are not measured by the QCM for the reason above. The Group 4 ions, then, are the primary source of a mass accretion measurement of the QCM. An estimate of other materials from the engine, such as sputtered aluminum, would require a knowledge of the amount leaving the engine and the respective charge-exchange cross-section. The analysis and measurement of charge-exchange cesium atoms are applicable to electrically unbiased surfaces. The QCM is not biased electrically and, therefore, an analytic prediction could be compared with the in-flight response.

Group 4 Cesium Ions

The arrival rate of Group 4, $N(r, x)$, per unit area at a distance, x , perpendicular to the exhaust plume centerline is given¹¹ as:

$$N(r, x) = [QD^2 n \mu'_0 (\pi m / 8 kT)^{1/2}] / [8 \times \{16(r/D)^4 + 8(r/d)^2 + 1\}] \quad (1)$$

with D = engine exhaust diameter
 μ'_o = neutral atom emission rate per unit area (at the engine)
 x = distance from exhaust plume centerline to surface receiving ions
 r = distance from exhaust plane along the thrust axis
 Q = charge exchange cross section
 n = ion arrival rate per unit area
 $(\pi m/8kT)^{1/2} = \frac{1}{v}$ = inverse velocity due to temperature of the neutrals.

For the QCM configuration, the Group 4 flux is 2.9×10^{10} ions/cm² s using the values of Lyon¹¹ for the parameters in Equation 1. This value was arrived at by using a mass utilization efficiency of 80%; recent indications are that 90% is more probably correct. The scaling relationship of:

$$\frac{N_1}{N_2} = \frac{(1 - \eta_1)(\eta_2)}{(\eta_1)(1 - \eta_2)}$$

results in a $N(r, x)$ of 1.29×10^{10} ions/cm² s.

The derivation of Equation 1 neglects the depletion of n and μ'_o and the $N(r, x)$ it predicts is too high by some amount. Lyon shows that the assumption of a constant n is valid within the numerical limits of the analysis, i.e., the removal of 1.67×10^{16} from the 8.28×10^{17} ions/sec will not change the calculated results significantly. He further calculates the ratio of the number of atoms remaining at a distance of 38 cm from the exhaust plane to those leaving the engine to be 0.88; i.e., Equation 1 is 10 to 15 percent too high. Using the same analysis for $r = 68$ cm (QCM value), the ratio is 0.86; the error is not great enough to be of consequence. An analysis was subsequently performed by Kemp⁹ using Equation 1 and updated values for the engine parameters resulting in a $N(r, x)$ of 3×10^9 ions/cm² s.

Cesium Vapor Pressure

To compute evaporation rates, cesium vapor pressures are needed. Several adequate references exist and are presently in use. Lyon recommends that the following equation be used for the vapor pressure of cesium:

$$\log_{10} P = \frac{-4053.30}{T} - 0.915282 \log_{10} T + 12.05025 \quad (2)$$

where P, the vapor pressure is in Pascals and T, the temperature in degrees Kelvin.

An alternate expression is based upon experimental data and is consistent with most of the data used in thermionic research is as follows.

$$\log_{10} P = \frac{-3920.38}{T} - 0.519781 \log_{10} T + 10.71914 \quad (3)$$

This equation leads to inconsistencies in the heat of condensation at 0°K. The use of Equation (2) has been recommended by Lyon for application to the ATS-6 configuration due to the large extrapolations to the colder temperatures of interest.

QCM Data Analysis

The accretion rate during the engine firing was 1.8 Hz/hour yielding 1×10^{10} atoms/cm²s. The accretion rate thus agrees favorably with predictions. The measurement of 240 Hz yields:

$$(240 \text{ Hz}) (4.45 \times 10^{-9} \text{ g/cm}^2\text{Hz}) \left(\frac{1.873 \text{ g/cm}^3}{2.655 \text{ g/cm}^3} \right)$$

$$\text{or: } 7.53 \times 10^{-7} \text{ g/cm}^2$$

for the total weight deposited. The total number of atoms deposited is:

$$(7.53 \times 10^{-7} \text{ g/cm}^2) \left(\frac{6.03 \times 10^{23} \text{ Molecules/Mole}}{133 \text{ g/Mole}} \right)$$

$$\text{or: } 3.41 \times 10^{15} \text{ atoms/cm}^2$$

Using the 2/3 root of the number density of the solid as an approximation for a monolayer surface coverage results in 4.22×10^{14} atoms/cm². The total equivalent monolayers is thus 8 layers.

The desorption energy for cesium on cesium is given as 0.81 eV and for low surface coverage of cesium on tungsten the activation energy is given¹² as being about 3.3 eV. Due to the small amount of cesium, possibly 8 monolayers, it was felt that the failure of the on-orbit bake-outs to adhere to the vapor pressure data may be attributed to the differences between thin films and thick films reported in Reference 13. However, this does not appear to be the case.

APPENDIX 2

LABORATORY TESTS

The test set-up utilized a one gram ampoule of cesium and the prototype QCM. The approach taken was to deposit cesium onto the QCM, initially at -60°C , and subsequently to heat the QCM to re-evaporate the cesium. The test was run in an oil diffusion pumped, LN_2 trapped and shrouded stainless steel vacuum chamber. The chamber pressure during the experiment was 4×10^{-4} Pa (3×10^{-6} Torr).

Both the cell and the prototype QCM were heated to $+100^{\circ}\text{C}$ for a period of 24 hours. The glass ampoule containing the cesium was broken during the cool-down phase during which the prototype unit was set to -60°C and the cell allowed to cool was approximately -100°C . The cell was at -10°C and the QCM at -40°C when the ampoule was broken. There was no measure of mass deposition at this time. Conditions were left stable for 20 hours and no mass depositions were noted. The cell was heated to $+90^{\circ}\text{C}$ and 17 equivalent monolayers (504 Hz) were allowed to deposit on the QCM. LN_2 was immediately applied to cool the cell and the QCM was simultaneously heated to $+50^{\circ}\text{C}$. The QCM was left at $+50^{\circ}\text{C}$ for 16 hours. The main emphasis of the experiment was to verify mass desorption from the crystal but this did not occur.

The QCM was then cooled to -61°C and remained at this condition for 64 hours. The beat frequency settled at 2420 ± 5 Hz during this phase. The mass loading procedure was again followed; an additional 295 equivalent monolayers was deposited (8746 Hz) and again there was no indication of mass desorption when heated. According to the vapor pressure data, the number of atoms leaving a surface at $+50^{\circ}\text{C}$ is 2×10^{15} atoms/ cm^2 s. The first mass deposition was equivalent to 7×10^{15} atoms/ cm^2 and therefore within 3.5 seconds should have desorbed from the crystal. Similarly, the second phase of the test has an equivalent 1.3×10^{17} atoms/ cm^2 and a calculated 66 second mass unloading period.

A different approach was next tried wherein the QCM temperature would be such that no mass accretions should occur. The cell temperature was set to 125°C and combined with the view factor resulted in a computed arrival rate at the crystal of 1.7×10^{14} atoms/ cm^2 s. The QCM was set to $+20^{\circ}\text{C}$ and according to the vapor pressure data 2×10^{14} atoms/ cm^2 s would be leaving the surface. An overnight run at the above conditions resulted in a net accretion rate of 2.3×10^{13} atoms/ cm^2 s. The mass loading at the end of this run was equivalent to 2,165 equivalent monolayers (64,200 Hz).

The QCM was heated to $+120^{\circ}\text{C}$ for three hours and then cooled to $+20^{\circ}\text{C}$ with no evidence of mass leaving. Stabilization at $+20^{\circ}\text{C}$ was maintained for a period of 14 hours with the beat frequency stable within ± 5 Hz.

The vapor pressure data of cesium is well documented^{14,15} so that the difficulties encountered must lie with the experimental set-up. The vapor pressure data generated by Marino¹⁵ was accomplished in a "stainless steel vacuum chamber pumped by mercury vapor pumps and liquid nitrogen-cooled traps." It was initially supposed that the addition of a LN_2 shroud would improve the experimental set-up, however, the results do not indicate this to be true. It may be that at 4×10^{-4} Pa (3×10^{-6} torr) the cesium is combining with residual gases and, therefore, would not behave according to published data.

A final test was made to investigate the gettering phenomenon associated with cesium with the chamber shroud at room temperature. The data is shown in Figure 6.

A decreasing beat frequency, approximately 1000 Hz is seen for the initial 64 hours. The two rises at 1200 on 5/10 and 1000 on 5/11 are associated with the LN_2 trap valve malfunctioning when the chamber pressure rose to about 6×10^{-2} Pa (5×10^{-4} torr). The QCM was then set to $+100^\circ\text{C}$. The initial 3000 Hz drop is normally associated with mass desorption. This was followed by a 160 Hz/hr increasing frequency. The QCM was subsequently cooled and reheated with the initial drop not repeating.

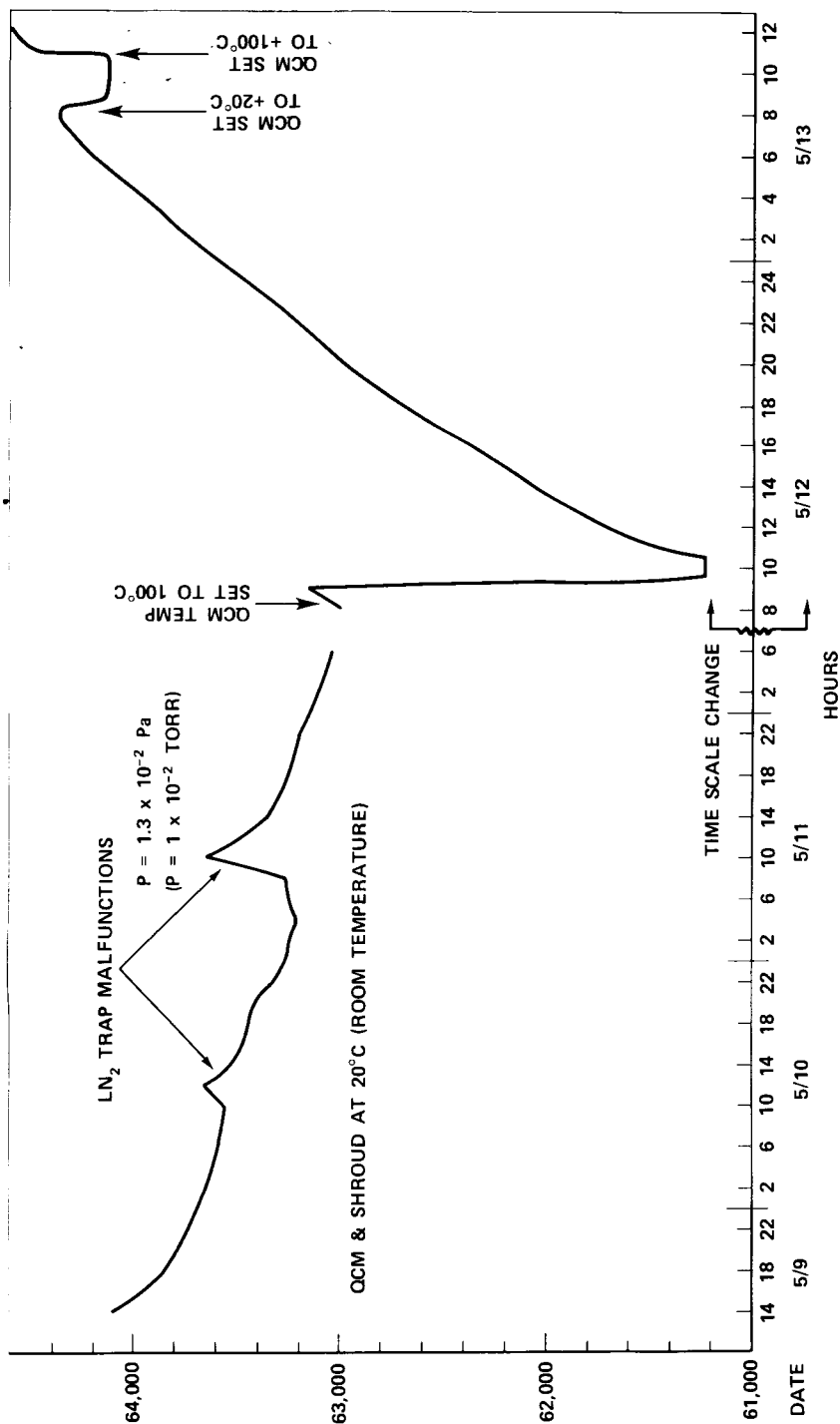


Fig. 6--Prototype QCM laboratory tests $P = 4 \times 10^{-4} \text{ Pa}$ ($3 \times 10^{-6} \text{ Torr}$)

EXPERIMENT TO MEASURE ENHANCEMENT OF SPACECRAFT CONTAMINATION BY SPACECRAFT CHARGING

David F. Hall and E. N. Borson, *The Aerospace Corporation, El Segundo, California* and R. A. Winn and W. L. Lehn, *Air Force Materials Laboratory, Wright-Patterson AFB, Ohio*

ABSTRACT

Temperature-controlled quartz crystal microbalances incorporated in retarding potential analyzers and surface thermal-property detectors will be used to measure contamination on the Spacecraft Charging at High Altitudes (SCATHA) Spacecraft.

1. INTRODUCTION

An ambitious effort to measure contamination on a highly instrumental spacecraft is being carried out. Spacecraft contamination enhancement by spacecraft charging is described in Section 2. A brief summary of the motivation for and the capabilities of the Spacecraft Charging at High Altitudes (SCATHA) Spacecraft is given in Section 3. In Section 4, the experimental approach is described and summaries are given of previous spaceflight experiments in which similar instrumentation has been used. Section 5 contains a description of the experimental flight hardware planned for SCATHA.

2. CONTAMINATION ENHANCEMENT BY SPACECRAFT CHARGING

When a material body is placed within a plasma, the potentials of its surfaces come to equilibrium values such that the net flow of charged particles between the body and the plasma is zero. Usually, these surface potentials are different from the ambient plasma potential, and transition region, called a sheath, forms between the surface and the undisturbed portion of the plasma. The sheath thickness increases with plasma temperature and decreases with plasma density. The potential diagram of a negative conducting sphere immersed in an idealized plasma is shown in Fig. 1. Factors that complicate the case of a synchronous altitude spacecraft are photo or secondary emission from the spacecraft, nonspherical shape, heterogeneous spacecraft surface materials, magnetic fields, reflection of incoming electrons over a finite distance within the sheath rather than at the sheath boundary, and anisotropic plasma properties.

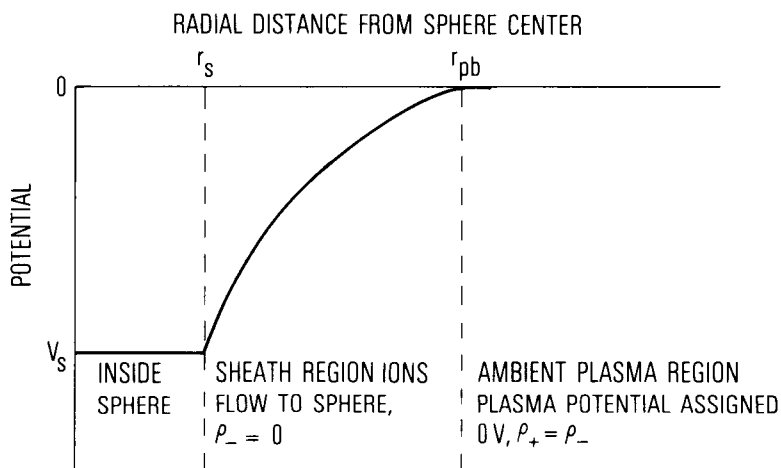


Fig. 1—Potential diagram of a stationary conducting sphere immersed in an idealized plasma.

Sunlit surfaces are generally slightly positive, and dark surfaces are negative (Fig. 1). At synchronous altitude, where plasma densities are often $1 \text{ electron cm}^{-3}$ or less and plasma temperatures 10 eV or more, sheath thicknesses will range from tens to hundreds of meters.

Neutral molecules outgassed by a spacecraft or released by a thruster that become ionized within the sheath of a negative spacecraft surface will be attracted by and returned to the spacecraft. Most ionization will occur several spacecraft radii or more from the spacecraft because the sheath volume increases with the cube of the distance from the spacecraft. Therefore, most ions return to the spacecraft at a point distant from their point of origin. If this return flux is significant, it will be much more troublesome than the line-of-sight mass-transport mechanisms usually considered in spacecraft design.

Cauffman¹ has estimated that ionization of large molecules by energetic space electrons and by energetic photons is about equally probable and that, if the plasma shielding length is 100 m, approximately 5×10^{-4} of the outgassed molecules will be returned if the spacecraft is -1 V with respect to the space plasma. The recapture coefficient would be even larger for a thicker sheath. Thicker sheaths are expected during magnetic substorms when electron temperatures and spacecraft surface potentials reach kilovolt magnitudes.²⁻⁵

A 7°C quartz crystal microbalance (QCM) viewing OGO-6 solar panels recorded a mass arrival rate⁶ that, when corrected for the QCM view factor with respect to the panels, indicated a minimum panel outgassing rate of

$$F_{og}(t) = 4.4 \times 10^{-5} \exp\left(\frac{-t}{41.6}\right) \quad (\text{g m}^{-2} \text{ sec}^{-1}) \quad (1)$$

where t is time from launch in days. The desorption energy of this contamination was 26 kcal (g mol⁻¹), a reasonable value for spacecraft contamination. If Eq. (1) is taken as typical of spacecraft outgassing rates and it is assumed that all returning molecules stick, the thickness buildup of contamination can be calculated from

$$Z(t) = \int_0^t \frac{\gamma F(t) dt}{\rho} \quad (2)$$

where

γ = fraction of outgassed molecules returned

ρ = density of material returned

when Eq. (2) is integrated and Cauffman's values of $\gamma = 5 \times 10^{-4}$ and $\rho = 10^6$ g m⁻³ are used,

$$Z(t) = 7.9 \times 10^{-8} \left[1 - \exp\left(\frac{-t}{41.6}\right) \right] \quad (m) \quad (3)$$

Thus, the entire spacecraft would eventually be covered with 790 Å, 500 Å of which would arrive within the first 42 days. Eight hundred angstroms is certainly enough to degrade critical optical surfaces and, perhaps, low-absorption thermal control materials as well.

Because of the many uncertainties regarding the production rate of recapturable molecules, i. e., ionization cross sections and sheath thickness, an experiment is planned to measure the rate at which ionized contamination returns to a typical spacecraft and to determine its thermo-optical effects. These measurements will be made on SCATHA.

3. THE SCATHA SPACECRAFT

A description of the SCATHA Program is given in Reference 3, but is summarized briefly here. The program is motivated by measurements of spacecraft charging events on the ATS-5 and ATS-6 Satellites and performance anomalies of other geosynchronous spacecraft that might be the result of charging events. Many of these anomalies occurred in the electronic circuits and could have been the result of electrical disturbances associated with discharges between spacecraft surfaces at different potentials. In some instances, unexplained degradation of thermal control coatings has occurred, and the rate of change of temperature is found to correlate with geomagnetic activity. The objectives of the SCATHA Program are to investigate in detail satellite charging and its effects on spacecraft performance and to evaluate the utility of various corrective techniques for the prevention of charging and differential charging.

SCATHA will be launched into synchronous orbit in the Spring of 1978. Its spin vector will be in the orbital plane and perpendicular to the sun line. The payload will consist of several charged-particle spectrometers, a plasma probe, and a magnetic-field monitor to measure the properties of the ambient plasma; an electron gun and an argon ion engine to permit artificial biasing of the spacecraft; electric field and spacecraft sheath detectors to measure the plasma sheath around the spacecraft; and a spacecraft surface potential monitor, a charging electrical effects analyzer, temperature-controlled quartz crystal microbalances (TQCM) in retarding-potential analyzers, and thermal control coating sample monitors to measure the effects of charging on spacecraft subsystem performance. The purpose of this paper is to describe the latter two sets of instruments and the contamination experiments planned for SCATHA.

4. SCATHA CONTAMINATION EXPERIMENTS

The objectives of the SCATHA contamination experiments are to:

1. Determine whether or not spacecraft charging increases its contamination rate, and if so, by what means.
2. Distinguish between degradation of selected thermal control coatings caused by contamination and that caused by environmental factors.
3. Determine the effects of the space environment, on spacecraft contamination, i.e., vapor pressure lowering, darkening, and removal.
4. Compare in-space thermal control coating degradation effects with the results of terrestrial and other in-space degradation experiments.
5. Provide contamination monitoring for other experiments.

4.1 Experimental Approach

The use of three types of devices capable of detecting contamination, i.e., QCMs, surface thermal property detectors, and charged-particle spectrometers, is planned. An electron gun and an argon ion engine will permit control of the spacecraft ground potential. The ground potential will be determined with respect to the ambient plasma potential from energy shifts in the spectra of spectrometers or the electric-field detector, which consists of Langmuir probes on the ends of 50-m booms, or both.

The two (radial and axial viewing) QCMs will be unique: the mass-sensing crystals will be behind retarding potential analyzer (RPA) grids and the crystal temperatures will be controlled at one of several commandable levels. The RPAs will permit the determination of the fraction of arriving mass that is charged except when spacecraft ground is more than -500 V.

Simultaneous measurement of the ion current and mass-deposition rate will permit the calculation of the average charge-to-mass ratio of these particles. However, the mass and electrical sensitivities of the instrument and the magnitudes of arriving particle fluxes will probably be such that some time integration will be required to make these measurements. Temperature control will enhance QCM stability and permit condensation of contaminants at low temperatures where contamination problems are more severe. Heating the crystals to a high temperature will evaporate condensed contaminants. In addition to cleaning the crystals, observation of the spectra of desorption temperatures of contamination will provide some indication its chemical identity.

Figure 2 illustrates how the RPA will be used. The RPA collector will be at spacecraft ground. In these examples, spacecraft ground is -100 V with respect to the ambient plasma potential, the result either of natural spacecraft charging or operation of the argon ion engine with its neutralizer biased. A positive ion formed at Location D by collision with an energetic photon would be collected if the retarding potential grid were set to 0 V (Curve C) or 10 V (Curve B), but not if set at 100 V (Curve A). Because the QCM (not shown in figure) will be behind a gridded aperture in the center of the collector, varying the retarding potential affects the number of charged particles reaching it as well.

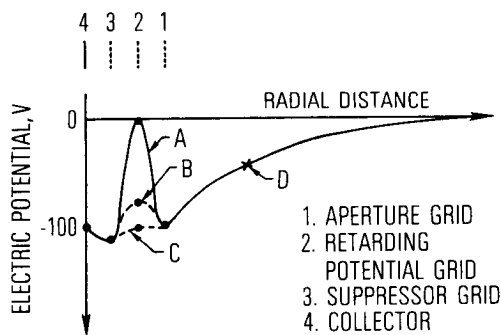


Fig. 2 — Potential Diagram of an RPA on a spacecraft at -100 V

The surface-thermal-property detectors will be improved versions of thermal control coating (TCC) experiments flown previously. TCC experiments permit the ratio of the solar absorptance α_s to hemispherical emittance ϵ_H (abbreviated α/ϵ) of a number of samples to be monitored in time. The technique will be to fit some of the sample positions on each of two radial-viewing TCC experiments with materials known to be very optically stable in space, e.g., fused-silica, second-surface

mirrors. If a change occurs in the α/ϵ of these samples and it correlates with an increase in the mass on the nearby TQCM controlled to the same temperature, the same contaminant probably will have been detected by both sensors. When the temperature of the TQCM is increased to above the TCC mirror temperature, the vapor pressure of the contaminant can be determined. Then the mirror temperatures will be increased with heaters to desorb the contaminant. If the α/ϵ returns to the clean value after the mirror is raised to the temperature at which the TQCM was cleaned, it will be concluded that the same material has been detected by both sensors. In addition, the change in the α/ϵ associated with a given mass of contaminant then will be known.

If the TQCM detects increased mass and there is no change in the α/ϵ , the implication will be that either the contamination is transparent in the solar region and has an infrared emittance similar to that of the mirror or that it has segregated on the mirror rather than forming a thin film. Another TCC sample will be highly polished aluminum, the emittance of which is approximately 0.05 that of fused silica, which will make it possible to distinguish between the two possibilities.

Stable, low- α samples on the TCC packages and the TQCMs also may permit detection of increases in the optical absorptance of a contaminant from exposure to the space environment. This effect has been produced on contamination films with vacuum ultraviolet exposures in the laboratory.⁷ An ideal sequence for this purpose would be a period of time of increased mass on the TQCM, e.g., when the spacecraft is negative, followed by a period of time when $dm/dt \leq 0$. If the α/ϵ were observed to increase with time even though the TQCM no longer detected an arrival rate of contamination, it could be concluded that the absorptance of the contamination would be increasing.

If the contaminant re-evaporation versus TQCM temperature characteristic changes as a function of time since deposition, it will be direct evidence of the lowering of vapor pressure by polymerization of the contaminant. If a contaminant is deposited on a constant-temperature TQCM and the indicated mass has the approximate form

$$M(t) = M_1 \exp\left(\frac{-t}{\tau_1}\right) + M_2 \exp\left(\frac{-t}{\tau_2}\right) + \dots + M_n \exp\left(\frac{-t}{\tau_n}\right) \quad (4)$$

where $\tau_1 < \tau_2 < \dots < \tau_n$, it will be evidence that water-vapor and low-molecular-weight fractions are evaporating, leaving low-vapor-pressure, high-molecular-weight residues.

The TQCM also can be used to detect mass removal by ion sputtering. The first step would be to elevate the crystal temperature so that high-vapor-pressure material on its surface will be desorbed. Subsequent mass loss could then be ascribed to sputtering, especially in cases where positively biasing the crystal reduced or stopped the mass loss. If the aluminum

crystal electrode were clean, the threshold sensitivity of the TQCMs for detection of sputtering would be

$$\Gamma_{s/c}^+ |_{\min} = \frac{1 \times 10^{13}}{S} \quad (\text{ions m}^{-2} \text{ sec}^{-1}) \quad (5)$$

where

$\Gamma_{s/c}^+$ = number of ions $\text{m}^{-2} \text{ sec}^{-1}$ arriving at the spacecraft surface

S = number of molecules sputtered by each ion

The arriving ions might be protons from the ambient plasma or ionized outgassed molecules from the spacecraft. However, even if the OGO-6 QCM data are representative and Cauffman's estimate of γ is correct, the initial outgassing rate will be too low to cause measurable sputtering. There are energetic protons in the space plasma, but measurements⁸ indicate that there are not nearly enough to meet the criteria of Eq. (5). Presumably, there are also cold ions in the ambient plasma with energies below the 50-eV detection limit on the ATS-5 instrument. When the spacecraft is biased hundreds of volts negative, the plasma sheath might be hundreds of meters in radius, thereby enabling it to collect a large enough ion current density on the spacecraft to produce measurable sputtering.

In addition to the TQCMs and TCCs, there will be several particle spectrometers on board for other purposes that probably will detect charged contamination molecules also. It will, of course, be necessary in interpreting spectrometer data to find a means by which contamination ions can be distinguished from low-energy ions from the ambient plasma. Two spectrometers are capable of determining mass per charge as well as energy per charge. Unfortunately, the mass range of both instruments is lower than the expected molecular weight of the condensable outgassed materials, although one resolves up to 150 a. m. u./charge. Therefore, ionized molecular fragments and multiple-ionized molecules will be observable at best. A second limitation of this instrument is a 100 eV/charge minimum particle energy. Thus, only when the spacecraft biases are larger than 100 V will this spectrometer be useful in detecting charged contamination.

4.2 Review of Previous QCM Spaceflights

Quartz crystal microbalances were used first in space as surface erosion sensors and thermometers. Discover 26 was launched into a 230 by 810-km orbit in July 1961 and carried QCMs made with matched and unmatched pairs of 10-MHz crystals.⁹ The beat frequency between a matched pair of thermally coupled crystals is relatively insensitive to temperature; therefore, if one of the pair (the reference crystal)

undergoes no mass change, the change in beat frequency is a measure of the mass change of the other crystal (the sensor crystal).

The mass-detecting QCM was oriented to receive ram air normal to its surface. After approximately four days of temperature and outgassing perturbations, it measured the constant, slow erosion of its gold electrode caused by sputtering. The temperature-sensing QCM was shielded from direct particle bombardment and recorded a cool-down to -110°C over a four-day period.

Later, similar measurements of the sputtering rates of surfaces orbiting at 200 km were successfully made on two Air Force satellites.¹⁰

Subsequently, a QCM was used in space as a detector in an experiment on OGO-6 (launched June 1969) to measure the energy transferred from ram air to metal surfaces.¹¹ However, the experiment also yielded valuable data concerning solar panel outgassing of condensables, Eq. (1). It also yielded indirect evidence that noncondensables outgassed from the spacecraft at a high rate during the first 72 hours of the 397- by 1098-km polar orbit.

Six matched, AT-cut, 10-MHz QCMs were on Skylab-1 (SL-1) launched in May 1973.¹² The AT cut minimizes the effect of temperature on crystal frequency. All QCMs showed some loss in mass immediately after launch. Then, all except the two sun-pointing apollo-telescope-mount (ATM) QCMs showed mass increases. The ATM QCMs continued to lose mass throughout the Skylab mission. Two QCMs showed mass gain attributable to backscattering of outgassed molecules from the ambient atmosphere.¹³ Hard docking of Skylab-2 (SL-2) with SL-1 resulted in a large increase in mass of one QCM, most of which disappeared within five days. Some deposition was observed on all QCMs when SL-2 performed the fly-around inspection prior to docking, but this material disappeared quickly from the ATM QCMs at 20°C .

Several Titan III launch vehicles have been instrumented with 5-MHz QCMs with a sticky coating on the sensor crystals.¹⁴ The coating makes the QCMs sensitive to particulates as well as condensables. With one QCM exposed to the total launch and orbital environment and another QCM protected until the payload fairing separated and with the output of both QCMs monitored from liftoff, it was possible to conclude that degradation of a thermal radiator was associated with separation of the solid rocket motor. The mass acquired during this event was very large, $2.7 \times 10^{-1} \text{ g m}^{-2}$.

A synchronous Air Force spacecraft was fitted with two AT-cut, 10-MHz QCMs because radiator contamination was the suspected cause of a steady increase in temperature experienced by certain components on previous flights. Efforts were made to get the QCM into the -150 to -50°C operating range of the radiator.

The QCM data are not completely reduced. Both QCMs experienced a 30- to 40-day initial outgassing phase, which was prolonged by their low operating temperatures. The beat frequency of QCM No. 1 remained nearly constant thereafter, whereas that of QCM No. 2 continued to drop for 140 days, passing through zero. This raises the question as to whether or not the reference crystal was contaminated or the sensor crystal was subjected to sputtering. The latter possibility is highly unlikely at 37,000 km unless the magnitude of bombarding particles was enhanced by spacecraft charging. These data demonstrate the importance of ensuring that contamination does not reach the reference crystal and of establishing the outgassing characteristics of the QCM before launch.

A radiatively cooled, 10-MHz TQCM on ATS-6 (launched into synchronous orbit in May 1974) monitored prelaunch, launch, and in-orbit contamination.¹⁵ Briefly, the average sensor temperature during the first three months in orbit was -20°C , not the desired -70°C . Subsequently, the instrument became completely shadowed from the sun, and the temperature dropped to approximately -52°C . However, "quick-look" data indicate that, when the instrument was again partially illuminated, the temperature increased to approximately -2°C . Apparently, the heat load from the spacecraft is higher than anticipated and the optical solar reflector (OSR) radiators have degraded. A 24-hr, 50°C crystal bakeout was started after eight days in orbit and approximately $4 \times 10^{-3} \text{ g m}^{-2}$ was desorbed. Although this also elevated the temperature of the main radiator, the subsequent operating temperature was unaffected.

The QCM acquired mass prior to but not during the launch. It outgassed during the first three months in orbit; thereafter, the frequency remained constant at -52°C . An approximately $9 \times 10^{-3} \text{ g m}^{-2}$ mass increase was recorded during a 100-hr firing (October 1974) of an ion engine on the same face of the spacecraft. Since that time, the mass on the crystal has been gradually increasing for reasons not understood. No correlation was noted between mass accumulation rates and spacecraft charging events;¹⁶ however, the OSR radiator surrounding the entrance aperture could have become charged and thereby deflected incoming ions.

4.3 Review of TCC Previous Spaceflight Experiments

A great deal of effort has been expended in the development and formulation of improved TCCs that have the required set of thermal radiation properties and have predictable performance in space. These coatings have been extensively tested in simulated operational environments. However, very little actual flight data exist to correlate laboratory results with orbital performance, particularly at synchronous altitudes. Furthermore, laboratory tests have been only moderately successful in predicting flight performance, probably because of contamination of flight samples. Therefore, there is considerable motivation

to obtain flight data on coatings at synchronous altitudes and on contamination effects.

The Air Force Materials Laboratory (AFML) conducted a low-altitude-flight experiments using techniques similar to those that will be used for SCATHA. The results of these experiments are reviewed here. A more general review of TCC flight data has been reported.^{17, 18}

The initial AFML TCC experiment was launched on the OV1-4 Satellite from the Western Test Range in March 1966 into a 547 by 478 nmi, 144-deg orbit. Unfortunately, data transmission ended after only three weeks as a result of a battery malfunction. The data obtained were of limited usefulness because (1) of the short time span, (2) scatter and dropouts in data could not successfully be smoothed because of the limited amount of continuous data obtained, and (3) spacecraft orientation with respect to the earth was not accurate enough to compute confidently earth input values.¹⁹

A second TCC experiment^{20, 21} was launched on the OV1-10 Satellite on 11 December 1966 into a nearly circular polar orbit of 415 by 345 nmi. The satellite produced six months of intermittent data before a tape recorder failure resulted in the termination of the transmission of usable data. Approximately 300 orbits of TCC data were obtained from the first 2900 orbits. Scatter in the data necessitated curve smoothing. From the data of 200 initial orbits, it was determined that the white paints initially degraded to a greater degree than expected. Laboratory and OV1-10 data for a typical white paint are compared in Fig. 3. Agreement appears to improve with time. Thin-film or multilayered coatings appeared to be relatively stable, but as with white paints, the initial solar absorptance values were considerably higher than anticipated.

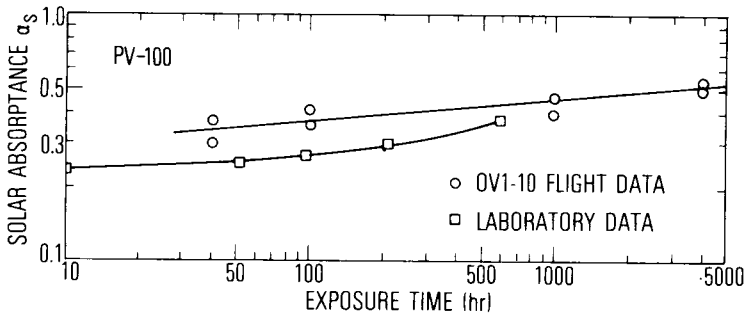


Fig. 3 - Comparison of solar absorptance data on a white paint vs space exposure obtained in a simulator and in space.

The OV1-17 Satellite was launched on 16 March 1969 into a nearly circular polar orbit of 215 by 250 nmi. The OV1-17 Satellite had a refined telemetry system, considerably improved over the OV1-10 system. However, the satellite did not achieve the necessary stabilized attitude condition, and data reduction attempts were not successful. Only general trends of optical degradation were obtained.²²

The ML-101 TCC spaceflight experiment was launched on 2 October 1972 on board the STP P72-1 Spacecraft into a polar (98-deg) sun-synchronous, nearly circular 409 by 398 nmi orbit. The satellite is still providing satisfactory TCC data after a total of more than 28 months in orbit. The results of the effects of the first 12 months exposure to the near-earth space environment on the various thermal control materials are shown in Fig. 4. As in the case of the OV1-10 data, the initial solar

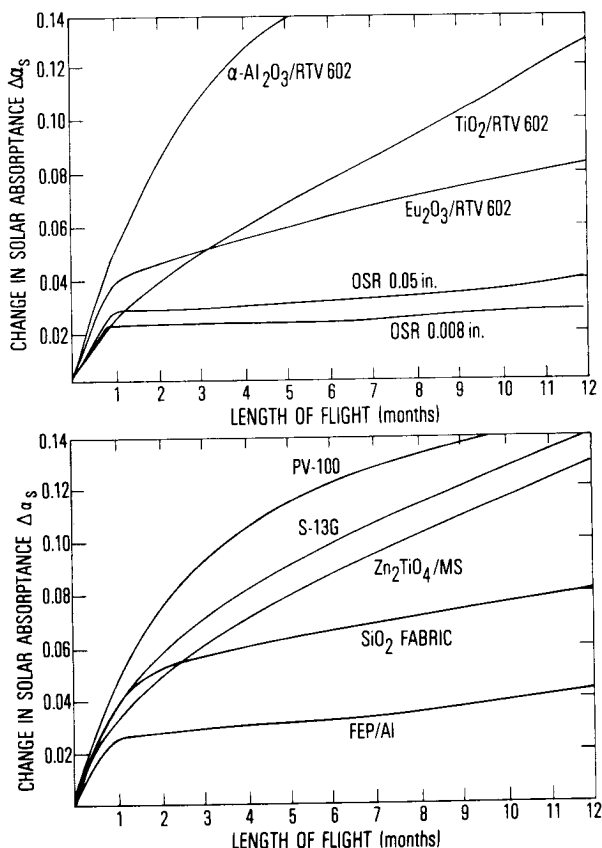


Fig. 4-Degradation of several thermal control materials measured by ML-101 experiment on the STP P72-1 Spacecraft.

absorbance values were considerably higher than anticipated. The high values are believed to result from surface contamination on the samples acquired during launch and early orbits. Contamination might come during launch from the hot fairing and during early orbits from spacecraft outgassing, which is then at maximum. The coatings that showed the greatest degradation in laboratory tests also showed the greatest degradation in space. A more detailed presentation of the data obtained from this experiment will be presented in the future.²³

Data obtained from the SCATHA TCC flight units will permit the evaluation of thermal control materials in a 20,000 nmi synchronous orbit as a function of exposure to the hostile space environment. With the additional contamination data from the RPA TQCM units and desorption data from the TCC units, it should be possible to determine the effects and contributions of launch and on-orbit contamination, including the effects of spacecraft charging on the observed degradation in thermo-optical properties. The data obtained will help delineate the mechanisms of degradation of these materials, permit comparison of laboratory simulation results with high-altitude data, and provide guidelines for the development of new and improved conductive, space-stable coating materials.

5. SPACEFLIGHT HARDWARE

5.1 TQCMs

The TQCMs will be radiatively cooled, and the temperatures will be maintained at the desired level with a controller regulated electrical heater. The TQCM construction and electrical connections are shown in Fig. 5. The radiators will use silvered, fused-silica, second-surface mirrors coated with electrically conducting indium oxide connected to the spacecraft ground. This will prevent electrostatic charge buildup on the

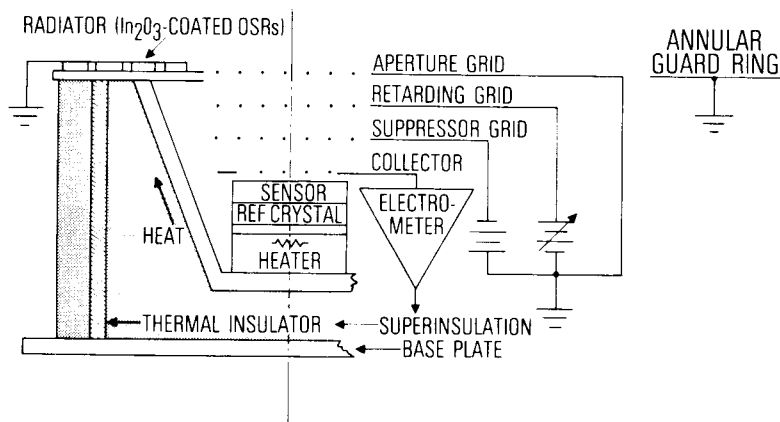


Fig. 5—One of two RPA TQCMs that will be flown on SCATHA.

radiator surface. The aperture grid and an annular guard ring surrounding the radiator will also be grounded to minimize defocusing incoming ions. The QCM sensor has a field of view of approximately 3.5 sr (50-deg half angle cone), and the RPA has a coaxial field of view of approximately 4.1 sr (59-deg half angle cone).

The QCM receives molecules through a gridded aperture in the RPA collector. Together the four RPA grids will intercept approximately 35% of the incident contaminant flux. The QCM sensor will use two AT-cut, 15 MHz, optically polished crystals with aluminum electrodes. The sensitivity will be $1.6 \times 10^{-5} \text{ g m}^{-2} \text{ Hz}^{-1}$; therefore, for the $\pm 1 \text{ Hz}$ telemetry resolution and an integration time of one hour, the net sensitivity expected is approximately $1.6 \times 10^{-5} \text{ g m}^{-2} \text{ hr}^{-1}$. This is equivalent to 7×10^{12} silicone molecules $\text{m}^{-2} \text{ sec}^{-1}$. The maximum mass loading for which the sensor crystal will still oscillate will be approximately 1 g m^{-2} .

During the early part of the mission, this sensitivity will permit mass detection of as few as 10^{-4} of the molecules outgassed by the spacecraft and reattracted to it as ions if the outgassing of condensables is described by Eq. (1). Cauffman¹ estimates the fraction returned will be 5×10^{-4} when a spacecraft is only slightly negative.

The crystals will be matched for a minimum frequency versus temperature change between -100 and $+100^\circ\text{C}$. Between -60 and $+60^\circ\text{C}$, the frequency change will be no more than $\pm 75 \text{ Hz}$.

The QCM heater will be commanded from the ground to control at one of five predetermined temperatures in the range of -60 to $+100^\circ\text{C}$. Controller off will be a sixth command state. Precision helium-filled, platinum, resistance thermometers which are linear to $\pm 0.5\%$, will indicate QCM temperature.

An approximately 1 cm^2 annular collector plate, immediately above the QCM, in combination with an electrometer and guard ring circuitry will measure currents in the range of 10^{-12} to 10^{-8} A with a resolution of $\pm 10^{-12} \text{ A}$. This is approximately 6×10^{10} to 6×10^{14} electrons $\text{m}^{-2} \text{ sec}^{-1}$ or the equivalent in ionized molecules. During the early part of the mission, this sensitivity will permit electrical detection of as few as 1×10^{-6} of the molecules outgassed by the spacecraft and reattracted to it as ions if the spacecraft outgassing is as described by Eq. (1). The electrometer will detect the arrival of both condensable and noncondensable ions.

The retarding potential grid will be commanded from the ground to one of the following potentials: $+500$, $+100$, $+10$, $+1$, 0 , -1 , -10 , and -100 V .

The radiator and entrance aperture will be covered from the conclusion of performance testing until commanded open on orbit to protect the radiator and TQCM from ground and launch-related contamination.

The TQCM sensors, including radiators and heaters, are being designed and constructed by Faraday Laboratories, Inc.,

La Jolla, California. The RPAs and electrometers are being designed and constructed in The Aerospace Corporation Laboratories.

5.2 TCCs

The TCC experiment will determine continuously the thermophysical properties of 14 coating samples so that the environmental and contamination effects can be observed. The thermophysical properties are determined by the measurement of coating sample temperatures and the incident solar flux. These values are used to solve the applicable heat-balance equation for ϵ_H and α_s .

As discussed in Section 4.1, two experiment packages will be used. Each package (Fig. 6), is comprised of a sample tray and a signal-processor unit. Eight individual 1.25-in.-diam thermal control coating sample holders are provided on each tray. The apparatus is constructed to minimize the heat interchange between the samples and the spacecraft and to precisely define the same area.²⁴ It will be calibrated in the laboratory so

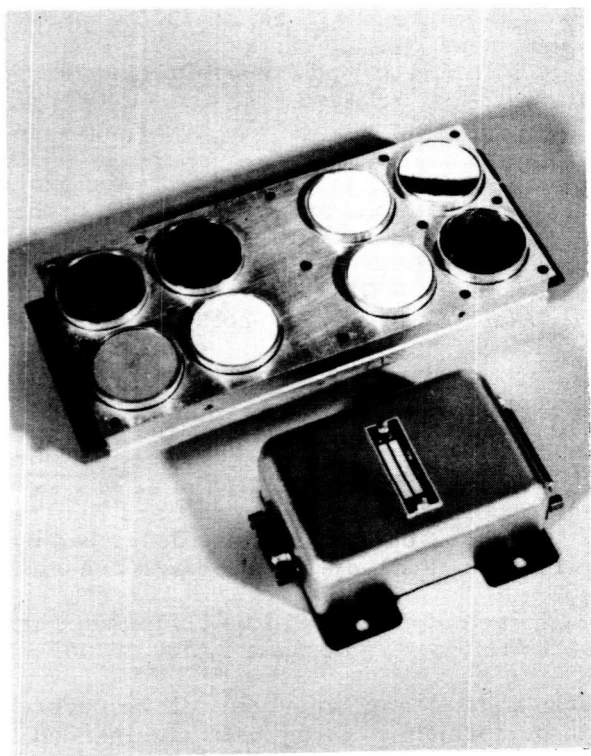


Fig. 6—One of two TCC packages that will be modified and flown on SCATHA.

that the small heat leakage that occurs can be calculated from the measured sample temperature and the measured temperature of the TCC frame. Incident solar flux is deduced from the temperature of the fifteenth and sixteenth sample positions (one on each sample tray), which are coated with a stable, black paint. When the samples are not illuminated, the sample temperatures are determined primarily by ϵ_H . This property is observed rarely to change from its (measured) prelaunch value unless contamination effects are present. When the samples are illuminated, α_s also affects sample temperature, and, since the emittance is determined independently, the absorptance value can be calculated from the heat-balance equation.

The utility of the TCC experiment will be extended with a contamination desorption capability. On ground command, several of the sample positions will go through a programmed temperature schedule by powering built-in calibration heaters. The schedule will consist of steps of increasing temperature separated by periods when no power is applied to the heaters. Thus, if a contaminant is observed to desorb, the approximate temperature required will be determined. By the use of sample materials of different optical properties and stabilities and the information from the TQCMs, it will be possible to distinguish between radiation damage and contamination effects.

The construction of an individual sample holder is shown in Fig. 7. The sample is mounted on a receiving disk that is

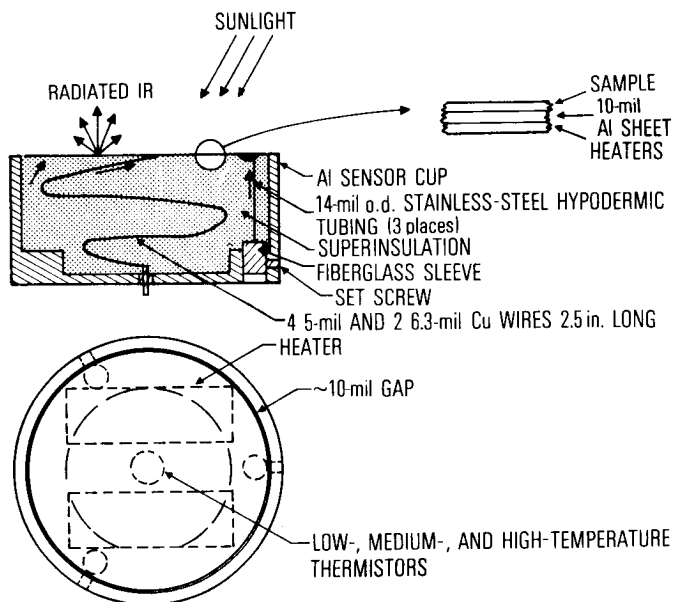


Fig. 7—Construction details of individual TCC sample holder. (Straight arrows indicate various heat paths.)

fitted with heaters and thermistors. To minimize thermal interchange between the sample and the tray, this disk is supported by three legs made of thin-walled stainless-steel tubing, and the electrical leads to the heaters and thermistors are long and of small diameter. The tubing and wires together give a $9 \times 10^{-4} \text{ W}^{-1} \text{ }^{\circ}\text{C}$ conduction coefficient. The volume enclosed by the disk and cup walls is filled with a combination of multi-layer and open-cell polyurethane insulation. The radiation coupling coefficient between the disk and cup is estimated²⁴ to be $1.4 \times 10^{-4} \text{ m}^2$.

This TCC experiment design evolved from that used in the earlier OV1 series of experiments.²⁵ These sample holders were 7.5-in. -diam aluminum trays in which were mounted six 0.937-in. -diam sample disks, supported upon 50 layers of superinsulation by a continuous Dacron cord under tension.

In addition to increased sample area and a contamination desorption capability, the SCATHA TCC experiment will feature better sample temperature measurement than earlier experiments. There are three thermistors on each sample disk, and each thermistor will cover a different overlapping range of approximately 100°F . Four sample disks can be installed in either of two angular positions so that low- and medium-temperature range thermistors are connected or medium- and high-temperature-range thermistors are connected. All three thermistors on the other four disks on each tray can be connected at a single position. Thus, samples that are expected to experience a wide range of temperature can be mounted in one of these eight positions.

Solar absorptance values will be calculated from preflight laboratory calibration and telemetered flight data by the equation

$$\alpha_s = \frac{(\epsilon A) \sigma (T_s^4 - T_o^4) - (FA_c) \sigma (T_c^4 - T_s^4) - (C)(T_c - T_s)}{GA} \quad (6)$$

where

α_s = solar absorptance

G = incident solar flux density

A = sample area

C = effective cup to sensor conduction coupling constant

FA_c = effective cup to sensor radiation coupling constant

ϵA = effective sensor to surrounds radiation coupling constant

σ = Stefan-Boltzmann constant

T_s = sensor temperature

T_c = cup temperature

T_o = surrounds temperature

In this equation, the factors ϵA , C , and FA_c are to be determined from the laboratory calibration. The remaining factors are known or are measured.

The uncertainty in the measured value α_s can be estimated by calculating the square root of the sum of the squares of the products of the partial derivatives of Eq. 6 and the uncertainties of the values of the independent variables. If only relative changes in absorptance are sought, factors unchanging in time and temperature can be omitted. On this basis, $\delta(FA_c)$, $\delta(c)$, and probably $\delta(\epsilon A)$ can be set equal to zero. The 8-bit conversion of the spacecraft's analog telemetry channels and the thermistor sensitivities yield $\delta(T_c) = 0.2^\circ\text{C}$. If it is assumed that T_o is within 1°C of absolute zero and that the incident solar flux is determined within 1.5%, the anticipated nonrepeatabilities of α_s can be computed. For $T_c = 38^\circ\text{C}$, $\delta(\alpha_s)$ ranges from approximately 0.004 for metals to approximately 0.02 for black paints. These values are diminished for lower values of T_c .

REFERENCES

1. Cauffman, D. P., Ionization and Attraction of Neutral Molecules to a Charged Spacecraft, TR-0074(9260-09)-1, The Aerospace Corporation, El Segundo, Calif. (August 1973).
2. DeForest, S. E., "Spacecraft Charging at Synchronous Orbit," J. of. Geophys. Res. 77, 651, (1972).
3. McPherson, D. A., Cauffman, D. P., and Schober, W., Spacecraft Charging at High Altitudes - The SCATHA Satellite Program, Paper No. 75-92, AIAA, New York, N. Y. (January 1975).
4. Bartlett, R. O., DeForest, S. E., and Goldstein, R., Spacecraft Charging Control Demonstration at Geosynchronous Altitude, Paper No. 75-359, AIAA, New York, N. Y. (March 1975).
5. Rosen, A., "Large Discharges and Arcs on Spacecraft," Astron. and Aeron. 13, 36, (1975).

6. McKeown, D. and Corbin, W. E., Jr., "Space Measurements of the Contamination of Surfaces by OGO-6 Outgassing and Their Cleaning by Sputtering and Desorption," Space Simulation, J. C. Richmond, editor, Special Publication 336, National Bureau of Standards, Washington, D.C. (October 1970).
7. Fleischauer, P. D., and Tolentino, L. U., "The Far Ultraviolet Photolysis of Polymethylphenylsiloxane Films on Quartz Substrates," Space Simulation, NASA SP-336, NASA Goddard Space Flight Center, Greenbelt, Md. (1973).
8. Deforest, S. E. and McIlwain, C. E., "Plasma Clouds in the Magnetosphere," J. of Geophys. Res. 76, 3587, (1971).
9. McKeown, D. and Fox, M. G., "Measurement of Surface Erosion from Discoverer 26," ARS J. 32, 954, (1962).
10. McKeown, D., et al., "Sputtering in the Upper Atmosphere," AIAA J. 2, 400, (1964).
11. McKeown, D. and Dummer, R. S., "Gas-Surface Energy Transfer Experiment for OGO-F," IEEE Trans. on Geosci. Electron. GE-7, 98, (1969).
12. Naumann, R. J. Quartz Crystal Microbalance Contamination Monitors on Skylab - A Quick Look Analysis, "NASA TMX-64778, NASA Marshall Spaceflight Center, Alabama (8 June 1973).
13. Naumann, R. J., Skylab Induced Environment, Paper No. 74-1225, AIAA, New York, N.Y. (1 November 1974).
14. Hetrick, M. A. and Ramine, G. L., Payload Contamination Environment for TIIC Launch Vehicles Using Launch Complex 40, MCR-75-118, Martin-Marietta Corp., Denver, Colo. (January 1975)
15. Rogers, J., "Data from a Synchronous Altitude Satellite Quartz Crystal Microbalance," Proceedings IES/AIAA/ASTM/NASA Eighth Space Simulation Conference, Silver Springs, Md. (November 1975).
16. Rogers, J., NASA Goddard Space Flight Center, personal communication (18 June 1975).
17. Neel, C. B., "Role of Flight Experiments in the Study of Thermal Control Coatings for Spacecraft," Prog. Astron. and Aeron. 20, 411, (1967).

18. McCargo, M., et al., Review of the Transient Degradation/Contamination of Thermal Coatings, LMSC-D177876, Lockheed Missiles and Space Co., Sunnyvale, Calif. (May 1971)
19. Frank, L. E. and Luedke, E. E., Data Reduction for Orbital Temperature Control Experiment - A Computer Program and Flight Results, TR-67-14, Air Force Materials Laboratory, Wright-Patterson AFB, Ohio (April 1967).
20. Boebel, C. P., Proceedings of the Joint Air Force - NASA Thermal Control Working Group, 16-17 August 1967, AFML-TR-68-198, Part I, Air Force Materials Laboratory, Wright-Patterson AFB, Ohio (March 1969).
21. Boebel, C. P., OV1-10 Thermal Control Coating Orbital Experiment, AFML-TR-68-392, Part I, Air Force Materials Laboratory, Wright-Patterson AFB, Ohio (March 1969).
22. Boebel, C. P., Air Force Materials Laboratory, Wright-Patterson AFB, Ohio, private communication (1969).
23. Prince, D. E., Air Force Materials Laboratory, Wright-Patterson AFB, Ohio, private communication (1974).
24. Luedke, E. E. and Kelley, L. R., Development of Flight Units for Thermal Control Coatings Space Experiments, AFML-TR-72-233, Part I, Air Force Materials Laboratory, Wright-Patterson AFB, Ohio (October 1972).
25. Bevans, J. T. and Luedke, E. E., Design and Construction of Sample Holders for Orbital Temperature Control Coatings Experiment, Vol. 1: Design, Analysis, and Test Results, Vol. 2: Calibration Data and Drawings, RTD-TDR-63-4269, Air Force Materials Laboratory, Wright-Patterson AFB, Ohio (April 1964).

ACKNOWLEDGMENTS

The authors have benefited from the many helpful discussions with D. A. McPherson, W. T. Chater, and F. A. Morse of The Aerospace Corporation and from D. McKeown of Faraday Laboratories. This work was supported in part by the Air Force Materials Laboratory Director's funds.

SKYLAB PARASOL MATERIAL EVALUATION

Stephen Jacobs and Thomas J. Ballentine, *Lyndon B. Johnson Space Center, Houston, Texas*

ABSTRACT

Results of experimental work to evaluate the degradation rate of a parasol that was used to alleviate thermal problems encountered soon after the launch of the Skylab 1 space vehicle are presented.

INTRODUCTION

A structural failure of the micrometeoroid shield on the Skylab orbital workshop occurred 63 seconds after launch of the Skylab 1 (SL-1) space vehicle. The initial failure caused premature deployment and, ultimately, separation of solar array system wing 2 from the orbital workshop. In addition, debris from the micrometeoroid shield prevented the normal deployment of solar array system wing 1. Loss of the micrometeoroid shield caused immediate and severe thermal problems inside the orbital workshop. Several proposals were considered to alleviate the thermal problems. A parasol was initially accepted to be the most feasible concept from mechanical, logistic, and installation standpoints. The SL-2 crew deployed the parasol thermal shield through the solar scientific airlock soon after initially manning the orbital workshop.

To determine the expected use life of the SL-2 nylon ripstop parasol material and to establish confidence in the satisfactory performance of the material throughout the SL-2 mission, a series of ultraviolet radiation degradation tests was initiated. The effects of ultraviolet exposure on the critical properties of the material were evaluated, and the optical and mechanical properties of the degraded material were compared to the properties of the unexposed material. The mechanical properties initially tested consisted of breaking strength and elongation and of tear strength. Because of the nature and importance of the initial investigation, a wide variety of additional material properties such as stiffness, shrinkage, shock loading, and total mass loss was also evaluated to ensure compliance with the flight requirements. The results of these tests, although in some cases extraneous to the overall qualification of the material, are reported for completeness.

MATERIAL DESCRIPTION

Several materials were considered for the SL-2 parasol; packaging characteristics, physical properties, and availability of the

material were of prime concern. The material finally chosen was a laminate consisting of orange nylon ripstop cloth weighing 37.1 g/m^2 . The cloth was laminated with a thick thermosetting polyester to an aluminized Mylar film (0.0125 millimeter), with the aluminized surface on the outside. The material, identified as batch 558, GT-76, had a total thickness of 0.08 millimeter and an average weight of 54.3 g/m^2 .

ULTRAVIOLET DEGRADATION GROUND TESTS

Ultraviolet/thermal-vacuum exposures of the SL-2 parasol material were initially performed at the NASA Lyndon B. Johnson Space Center (JSC) and the NASA George C. Marshall Space Flight Center (MSFC). Shortly thereafter, exposures were performed at TRW Systems, General Electric (GE), and NASA Langley Research Center (LaRC) facilities. At each of the five testing facilities, an attempt was made to simulate the vacuum, thermal, and ultraviolet space radiation environments likely to be encountered by the SL-2 parasol deployed in Earth orbit.

Test Conditions

Breaking strength and elongation measurements were made at the five facilities. The objective was to determine whether the material met basic strength requirements and also to determine the amount of degradation that would result from ultraviolet and thermal-vacuum exposure. Test conditions for the five facilities are summarized in Table 1 and in the discussions in the following sections.

Lyndon B. Johnson Space Center--Most ultraviolet exposures at JSC were performed in the chamber D facility (1.2 solar flux, xenon lamp) of the Space Environment Simulation Laboratory, where a 91.24- by

TABLE 1 — SUMMARY OF TEST CONDITIONS FOR ULTRAVIOLET RADIATION
DEGRADATION EXPOSURES

Exposure location	Sample size, cm	Solar ultraviolet irradiance	Duration, equivalent solar hr	Exposure temperature, K
JSC				
Chamber E	60.96 by 60.96	2.5	50	394
Chamber D	91.24 by 91.24	1.2	500	311 ± 5
MSFC	30.48 by 30.48	2.0	60, 80, 200, 300, 650	394
	30.48 by 30.48	3.5	50, 280	344 to 366
TRW	^a 2.54 by 15.24	5.4	650, 1260	327
		4.0	1260	350
GE	^a 2.54 by 20.32	5.0	3460	350 ± 5
LaRC	^a 2.54 by 20.32	3.5	686, 3316	355 ± 5

^a2.54- by 2.54-cm test section.

91.24-centimeter parasol sample was suspended (nylon side toward the lamp) and was instrumented with eight thermocouples evenly spaced along one diagonal of the material. One end of the parasol was mechanically flexed twice a day through a 12.7-centimeter range to roughly simulate motions that would be induced by the reaction control system engine plume impingement. Radiometers covered with the nylon material were also mounted at 45° angles to the nylon sample to detect changes in reflectance of the sample surface. The temperature of the parasol sample was maintained between 306 and 316 K by quartz heaters mounted below the aluminized side of the sample in addition to the xenon lamp. Sample conditions were recorded on video tape at selected intervals during the test by means of a black and white television camera mounted in the chamber. At the conclusion of the chamber D test, the sample was removed and the optical properties were measured on a Gier-Dunkle MS-251 reflectometer (solar absorptance) and a DB-100 emissometer (total emittance). The 91.24- by 91.24-centimeter sample then was cut into specimens for testing of various physical properties. In addition to the chamber D tests, a 60.96- by 60.96-centimeter parasol sample was exposed to carbon arc radiation at 2.5 solar flux for 50 hours in chamber E of the Space Environment Simulation Laboratory. Optical and mechanical properties also were measured after this exposure.

George C. Marshall Space Flight Center--In the MSFC tests (2.0 solar flux, xenon lamp), a 30.48- by 30.48-centimeter parasol sample was exposed. This sample was mounted on a water-cooled substrate plate. A high-conductivity, low-outgassing, hydrocarbon vacuum grease (FS-1281) was used to maintain good thermal contact between the sample and the substrate plate. Temperatures were maintained between 344 and 366 K. At the conclusion of the exposure, optical properties were measured using an MS-251 reflectometer (solar absorptance); then, mechanical properties were tested.

TRW Systems--For the TRW tests (1.35 solar flux, xenon lamp; 4.0 solar flux, xenon lamp; 5.4 solar flux, xenon lamp), performed under NASA Contract NAS 9-13523, the samples were exposed in two separate facilities, the combined environment facility and individual ion-pumped chambers located around a compact xenon arc lamp. In the first test, a holder for eight samples, each approximately 2.79 by 15.24 centimeters, was fabricated and installed in a high-vacuum test chamber, where the samples were exposed to 4.0 times solar ultraviolet irradiance for 315 hours (1260 equivalent solar hours) at a temperature of 349 K that was maintained during the test with a temperature-controlled circulation bath. The samples were attached to a 0.64-centimeter-thick copper mounting plate with a thin layer of Krytox 240-AC grease. The samples were enclosed in a "picture frame" cover that prevented curling at the edges. A sketch of the sample-mounting arrangement is shown in Figure 1. Another series of tests was started concurrently with the first test, and the samples were placed in six individually pumped vacuum tubes. The sample configuration was 2.79 by 15.24 centimeters, and the central 2.54- by 2.79-centimeter portion was used as the test section. The samples were cooled in the same manner as in the previous

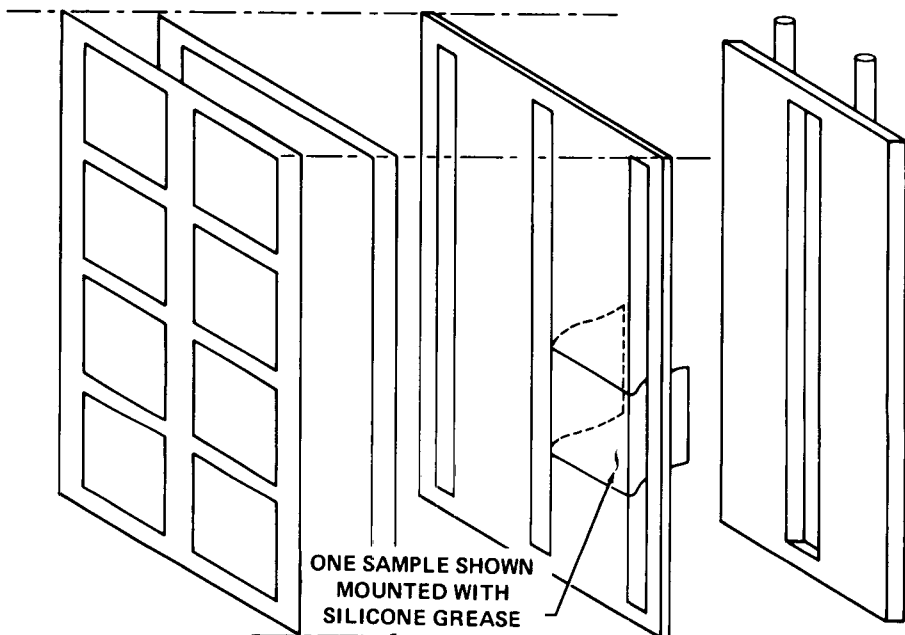


Fig. 1 — The TRW sample-mounting arrangement

test, but the temperature was "controlled" using laboratory tapwater, the temperature of which varied from 293 to 333 K. One sample was exposed at 1.35 times solar ultraviolet irradiance until an exposure of 400 equivalent solar hours was reached. Four samples were exposed at 5.4 times solar ultraviolet irradiance; three were measured after 650 equivalent solar hours, and exposure of the fourth was extended to 1260 equivalent solar hours. One vacuum tube failed. At the conclusion of the combined environment facility and small chamber exposures, the samples were removed and the optical properties were measured. Solar absorptance measurements were performed using an Edwards-type integrating sphere reflectometer on a Beckman DK-2A spectrophotometer. Reflectance measurements were taken at 15° from the normal plane in the wavelength region 0.28 to 2.5 micrometers; the spectral data were integrated over the solar spectral distribution to obtain the solar absorptance. Emittance measurements were made using a Gier-Dunkle emissometer, model DB-100. Breaking strength and elongation measurements were also performed on the samples after removal from the test chambers.

General Electric--The GE testing (5.0 solar flux, mercury/xenon lamp), performed under NASA Contract NAS 9-13593, was designed to irradiate the GT-76 material for long-term ultraviolet exposure at a high flux. The source used was a 5-kilowatt mercury/xenon lamp; solar intensity at the sample locations was calibrated at 5.0 solar ultraviolet irradiance using an Epply thermopile. Virgin material was supplied to GE, and eight 2.54- by 20.32-centimeter GT-76 sample strips were

cut and placed at the 5.0-solar-flux sample plane backed by a water-cooled (350 K) metallic plate simulating the configuration used by TRW. The test was continued until an exposure of 3460 equivalent solar hours was achieved on the GT-76 material. However, because of nonintimate contact between the cooled metal plate and the sample material, several burnthroughs occurred. Enough material was still available to enable measurement of breaking strength and elongation after removal of the material from the test chamber. Optical property measurements were not performed for these tests.

Langley Research Center--In the LaRC tests (1.0 and 3.5 solar flux, xenon lamp), 24 samples were mounted vertically in 2 vacuum chambers, each mounted on a water-cooled copper plate (8 at 1.0 solar flux, 16 at 3.5 solar flux). A high-thermal-conductivity, low-outgassing thermal grease was used between the test sample and the water-cooled plate to ensure good thermal contact. An aluminum frame was used to hold the samples in place during irradiation and to enable exposure of only 6.45 square centimeters of each sample to the simulated solar radiation. The samples in each chamber were maintained between 350 and 360 K by regulation of the cooling-water flow to each sample-mounting plate. Three thermocouples were attached to each sample plate, and the output of these thermocouples was monitored continuously by means of a temperature-compensating potentiometer having a strip-chart recorder. At 686 equivalent solar hours of exposure, nine of the test specimens were removed from the 3.5-solar-flux accelerated test for comparison with the specimens exposed for the same period at only 1.0 solar flux. These data were used to check the validity of the accelerated testing. The remaining seven specimens were tested for the full duration exposure of 3316 equivalent solar hours.

Test Results

The overall visual appearance of all samples from the five testing organizations was virtually the same; that is, the color had changed from bright orange to dull gold. No apparent physical degradation was noticed during a visual examination of the specimens. Because of anomalies during the TRW tests (outgassing of the Krytox 240-AC vacuum grease), bubbling of several specimens and subsequent overheating, including burnthrough, occurred in four of the eight samples exposed in the combined environment facility. Also, because of the GE-sample burnthroughs discussed earlier, data are reported for only three GE samples. Data for control samples are presented for comparison with posttest measurements and with measurements performed on a flight sample. In all cases, the degraded mechanical properties are compared to properties of the unexposed samples. Undoubtedly, in some cases, the degradation was due to both radiation and thermal exposure.

Optical properties--The only in situ data available on optical properties (as opposed to posttest data) were from the radiometers mounted in chamber D for the JSC tests. These data show a slight decrease in solar absorptance (0.40 to 0.35) at levels as high as 180 equivalent

TABLE 2 — SUMMARY OF OPTICAL PROPERTY DATA FROM ULTRAVIOLET DEGRADATION EXPOSURES

Exposure location	Solar ultraviolet irradiance	Duration, equivalent solar hr	Exposure temperature, K	Optical properties				Instrument used for absorbance measurement	
				Before exposure		After exposure			
				Absorbance	Emittance (a)	Absorbance	Emittance (a)		
JSC Chamber E Chamber D	2.5	50	394	0.36	0.85	0.44	0.85	MS-251	
	1.2	500	311 ± 5	.36	--	.44	--	MS-251	
MSFC	2.0	60	394	.39	--	.46	--	MS-251	
	2.0	80	394	.39	--	.46	--	MS-251	
	2.0	200	394	.39	--	.46	--	MS-251	
	2.0	300	394	.39	--	.46	--	MS-251	
	2.0	650	394	.39	--	.69	--	MS-251	
	3.5	50	344 to 366	.49	--	.62	--	Beckman DK-2A	
	3.5	280	344 to 366	.49	--	.66	--	Beckman DK-2A	
	TRW	4.0	1260	350 ± 5	.49	--	.52	--	Beckman DK-2A
		4.0	1260	350 ± 5	.49	.84	.56	--	Beckman DK-2A
		4.0	1260	350 ± 5	.49	.84	.51	--	Beckman DK-2A
4.0		1260	350 ± 5	.49	.84	.53	--	Beckman DK-2A	
5.4		650	327	.49	.84	.58	.85	Beckman DK-2A	
5.4		650	327	.49	.84	.58	.86	Beckman DK-2A	
5.4		650	327	.49	.84	.58	.84	Beckman DK-2A	
5.4		1260	327	.49	.84	.57	.86	Beckman DK-2A	
LaRC	3.5	686	355 ± 5	.49	.84	b .66	.85	Comparable to Beckman DK-2A	
	3.5	3316	355 ± 5	.49	.84	.55	.85	Beckman DK-2A	

^aAll measurements were performed with the Gier-Dunkle DB-100 portable emissometer.^bSample overheating.

solar hours. Recovery in absorbance to approximately 0.38 is shown at the test conclusion. The measured optical properties at the conclusion of these exposures are shown in Table 2. Figure 2 shows the change in solar absorbance with equivalent solar hours. General Electric did not perform optical property measurements.

Mechanical properties--Test data on mechanical properties include breaking strength, elongation, tear strength, and shrinkage.

The breaking strength and elongation testing at JSC was accomplished on a Scott CRE Tensile Tester in accordance with Federal Test Method Standard 191, Method 5102. Testing at TRW, GE, and MSFC was accomplished on comparable equipment and followed comparable test methods. In testing at LaRC, a somewhat different procedure was followed in that the mechanical properties were measured on a commercially available power-driven Instron testing machine having a constant rate of jaw separation. Figures 3 to 6 were prepared from the test data.

The tear strength of the nylon ripstop aluminized Mylar laminate was determined at JSC on the Elmendorf tear tester in accordance with Federal Test Method Standard 191, Method 5132. The results are shown in Table 3.

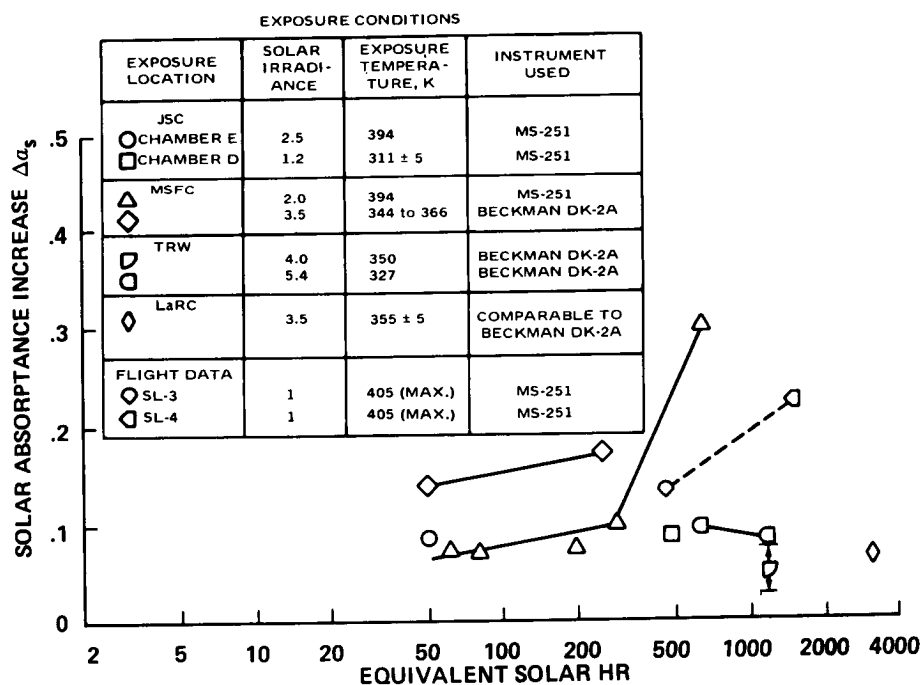


Fig. 2 — Increase in solar absorbance as a function of equivalent solar hours

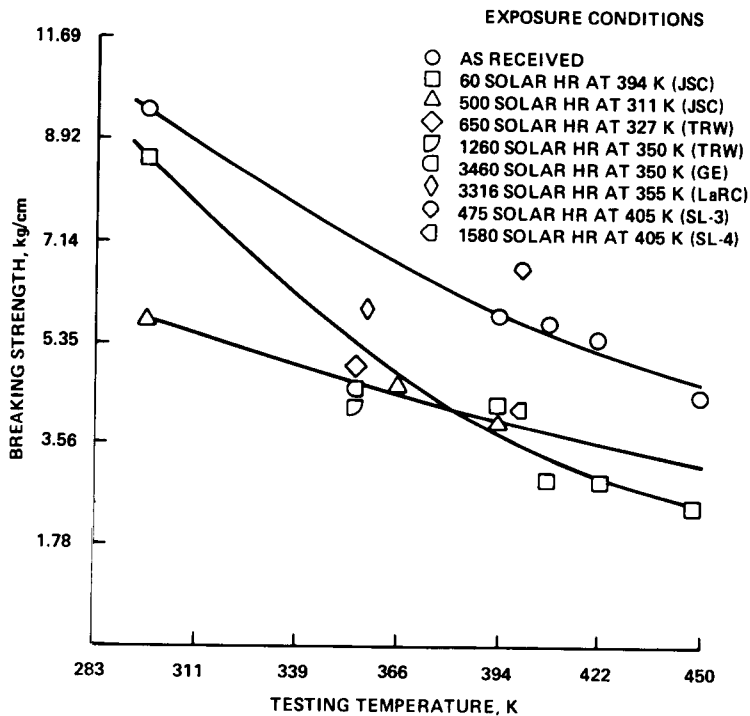


Fig. 3 — The ultraviolet-induced degradation of GT-76 breaking strength as a function of temperature

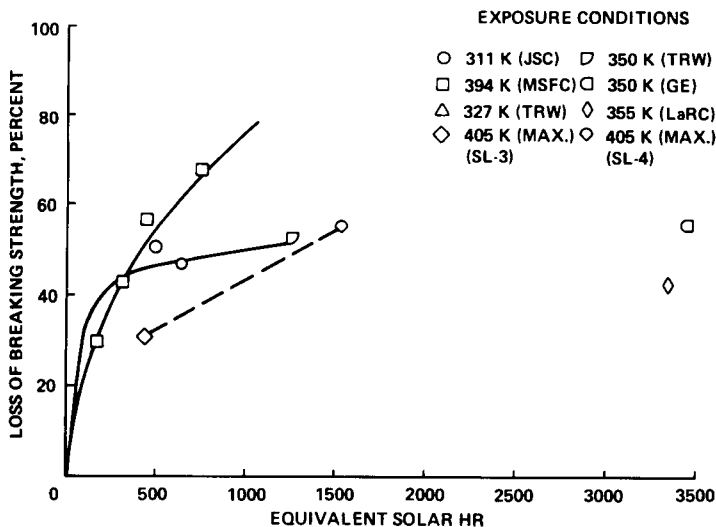


Fig. 4 — The ultraviolet-induced degradation of nylon/Mylar laminate breaking strength as a function of equivalent solar hours

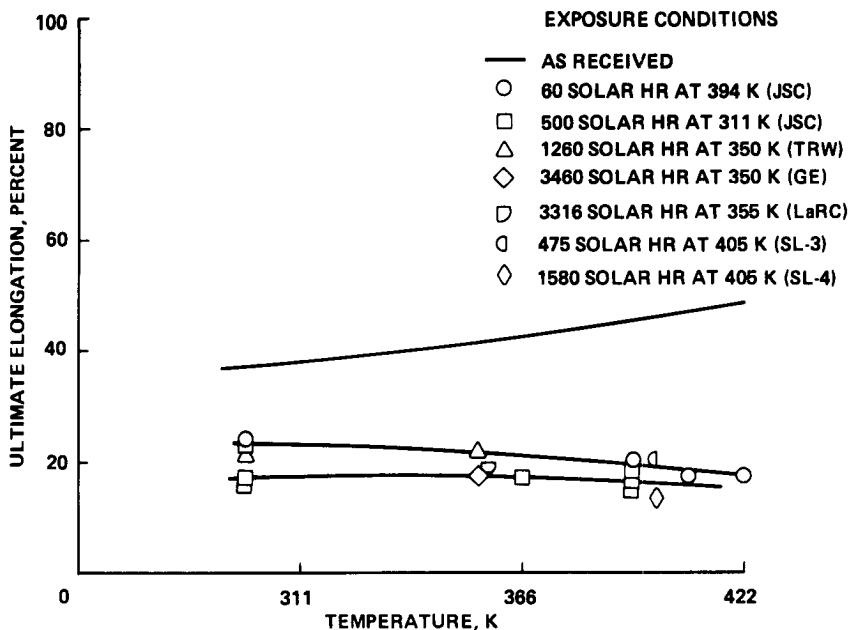


Fig. 5 — The ultraviolet-induced degradation of GT-76 elongation as a function of temperature

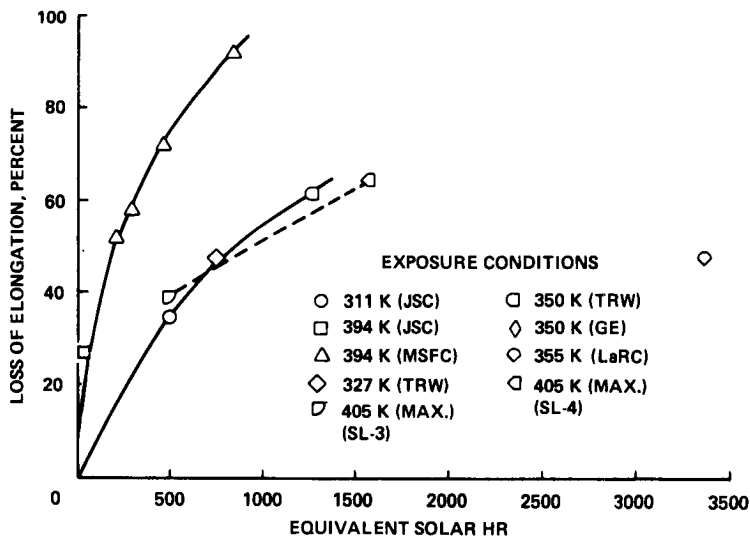


Fig. 6 — The ultraviolet-induced degradation of nylon/Mylar laminate elongation as a function of equivalent solar hours

TABLE 3 — SUMMARY OF TEAR STRENGTH DATA FROM JSC

Solar ultraviolet irradiance	Duration, equivalent solar hr	Exposure temperature, K	Test temperature, K	Tear strength, g
Before exposure	--	--	294 ± 5	4700
2.5	50	394	294 ± 5	500
1.2	500	311 ± 5	294 ± 5	1420

The shrinkage of the nylon ripstop aluminized Mylar laminate was determined at JSC after the material had been exposed to an ultraviolet/vacuum environment for 500 equivalent solar hours. The objective of the measurement was to determine whether the overall shrinkage of the parasol would cause any structural problems while in use. The dimensions of 40 squares of the ripstop material were measured in the longitudinal and transverse directions before and after exposure. The results show a 0.97-percent shrinkage in the longitudinal direction and a 1.6-percent shrinkage in the transverse direction.

Scanning electron microscopy--A scanning electron microscope (Cambridge Stereoscan S-4) was used at JSC to examine surface morphology of the nylon ripstop material as received, after 500 equivalent solar hours ultraviolet exposure, and after 1260 equivalent solar hours ultraviolet exposure. The appearance of dark spots on the 500-hour specimen is accompanied by a slight surface roughening and by the formation of a thin crust. Evidence of some embrittlement is seen on the cut end of the 500-hour specimen. The 1260-hour specimen shows a marked increase in surface roughness, and the surface crust is well defined. Increased embrittlement is indicated by marked surface cracking near the cut region. No evidence of flaking or lack of crust adherence was observed at these exposure levels.

Additional JSC test results--The following additional tests were performed on the parasol material and were independent of the ultraviolet radiation exposure tests.

Three corners simulating the parasol corners were tested to determine structural integrity. At each corner of the parasol was a polybenzimidazole (PBI) loop, which attached to the Skylab structure. Each end of the PBI cord was sewn to 1.27-centimeter Nomex webbing, and the webbing was sewn to each side of the corner. The corner was tested on the Scott Tensile Tester by placing a pin through the PBI cord loop and attaching the pin to a fixture on the load cell. Two 30.48-by 30.48-centimeter aluminum plates were used as bottom jaws to retain the ripstop cloth. The jaws and the crosshead were separated at a rate of 2.54 cm/min. The results show two types of failure mechanisms: failure of the PBI cord leading to a corner strength of 61.7 kilograms, and failure of the seam leading to a breaking strength ranging from 50 to 77.1 kilograms.

The relative stiffness of the laminate as a function of temperature was determined. The relative stiffnesses of several seam configurations were measured on 2.54- by 22.8-centimeter strips of material in a temperature-controlled ambient-pressure cabinet, and a balance was used to measure the extension force. The springback distance, expressed as a percentage of sample free length, and the force necessary to extend the sample to 90 percent of its free length were measured. These results are presented in Table 4.

TABLE 4 — STIFFNESS AS A FUNCTION OF TEMPERATURE

Sample description	Test temperature, K					
	200 ± 10		295 ± 4		395 ± 10	
	Springback distance, percent (a)	Force to 90-percent extension, g	Springback distance, percent	Force to 90-percent extension, g	Springback distance, percent	Force to 90-percent extension, g
GT-76 unseamed	86.5	0.06	81.5	1.85	--	--
GT-76 triple-lapped seam	46.7	28	54.5	25.6	41.0	25.5
GT-76 nylon tape edge seam	31.0	112	78.0	36.6	64.5	86
GT-76 Nomex tape edge seam	29.0	^b 156	82.0	^b 156	--	--
GT-76 double-lapped seam	--	--	--	--	54.5	12

^aPercent springback = measured springback divided by free length of the sample.

^bExceeded pull force of test equipment.

A shock-loading test was devised to investigate the effects of deployment and of other rapidly applied loads on the parasol material. A 61.0- by 2.54-centimeter sample was shock-loaded by a falling weight dropped from varying heights. The induced tensile force was measured by using a load cell (attached to the top of the sample) in conjunction with a high-speed oscillograph. The falling body weighed 1360 grams. The impact height was varied from 2.54 to 55.9 centimeters. The measured forces for specific drop heights varied from 12.9 to 21.5 kilograms.

An Ainsworth vacuum balance system was used for the evaluation of the outgassing characteristics of the parasol material. This system provides a continuous in situ measurement of mass loss. Figure 7 shows data on the total mass loss and the volatile condensable matter for the unexposed parasol material.

FLIGHT-SAMPLE MEASUREMENTS

Two 30.48- by 30.48-centimeter specimens of the parasol material were deployed by the SL-3 crew during the second extravehicular activity. One sample was returned by the SL-3 crew after approximately 475 hours solar exposure in the space environment. The second specimen was returned by the SL-4 crew after approximately 1580 hours solar exposure. Optical properties, breaking strength, and elongation were measured.

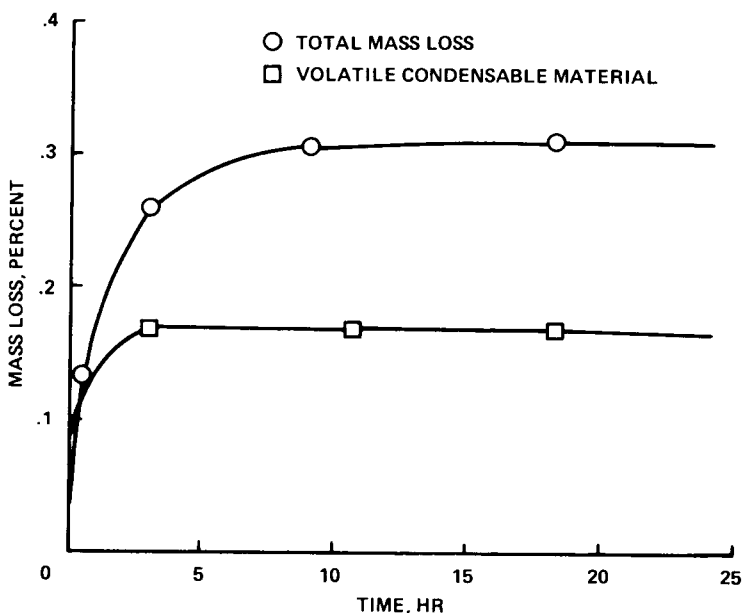


Fig. 7 — Volatile condensable material determination of GT-76 at 399 K and $1.33 \times 10^{-4} \text{ N/m}^2$

Optical Properties

The instrumentation used for the flight-sample optical property measurements was the same as that used for the ground test specimens, namely the MS-251 reflectometer for solar absorptance and the DB-100 emissometer for total emittance. For the SL-3 sample, solar absorptance increased from the preflight value of 0.36 to 0.49; for the SL-4 sample, to 0.58. Total emittance was virtually unchanged from preflight values for the two exposed samples. These data are shown in Table 5.

TABLE 5 — FLIGHT-SAMPLE MEASUREMENT RESULTS

Condition	Optical properties		Breaking strength, kg/2.54 cm of width	Elongation, percent	Duration, equivalent solar hr
	Absorptance (a)	Emittance (b)			
Before exposure	0.36	0.85	9.3	35.0	0
After SL-3	.49	.86	6.4	20.9	475
After SL-4	.58	.86	4.3	13.3	1580

^aMeasurements performed with MS-251 reflectometer.

^bMeasurements performed with DB-100 emissometer.

Mechanical Properties

As shown in Table 5, measurements of the flight samples indicated a sharp decrease in breaking strength and elongation. These changes in mechanical properties were due to the combination of ultraviolet radiation and elevated parasol temperature. Additional mechanical property measurements were not possible because of the limited amount of exposed material.

COMPARISON OF GROUND TEST AND FLIGHT DATA

When possible, ground test data were compared with flight test data to prove the validity of the ground simulations and to determine the expected flight life of the deployed parasol.

Optical Properties

The increase in solar absorptance of the parasol material due to ultraviolet radiation, as shown from ground test data and flight-sample measurements, was within the expected range and was found to be acceptable by the thermal analysis of the parasol and of the orbital workshop. No direct correlation was observed between increased ultraviolet solar intensity and increased solar absorptance. However, for the same solar intensity, an increase in equivalent solar hours led to an increased solar absorptance. No measurable change existed in total emittance from preexposure values for ground test or flight-sample measurements.

Mechanical Properties

Ground test results indicated that a decrease in breaking strength and elongation does occur as a result of radiation/thermal-vacuum exposure. After ultraviolet radiation exposure (ground simulation), testing at room temperature (295 K) revealed a degradation of 18 percent, whereas tests at 394 K indicated a degradation exceeding 50 percent. Measurements of the flight samples also indicated a sharp decrease in breaking strength and elongation (greater than 50 percent) after recovery of the SL-4 sample. As previously mentioned, this condition was due to the combination of ultraviolet radiation and elevated parasol temperature (calculated to be 327 to 409 K). This information compares well with ground test data.

Tear strength--A significant decrease in tear strength occurred after exposure to combined ultraviolet radiation/thermal-vacuum conditions. The material deterioration contributed to the decrease in tear strength, but most of the decrease was due to the thermal exposure, which improved the bonding between the layers of the laminate. Before exposure, the nylon ripstop and Mylar were not rigidly bonded; therefore, as the samples began to tear, the yarns in the fabric could move fairly freely. This freedom of movement allowed the yarns to absorb most of the energy of the swinging pendulum while tearing. The movement of the yarns in the exposed sample was inhibited because the fabric

adhered too rigidly to the Mylar. Consequently, a much lower tear strength resulted. The decrease of tear strength did not affect the structural integrity because of the minimum loading imposed in the flight environment.

Shrinkage--Shrinkage values indicate that the material contracted when exposed to the ultraviolet radiation. However, the maximum value of 1.6 percent was insignificant for this application.

DISCUSSION OF ADDITIONAL TEST RESULTS

Some results of additional tests in the areas of corner strength, stiffness, shock loading, and volatile condensable material are discussed in the following sections.

Corner Strength

Three samples simulating parasol corners (as previously described) were tested, but in only one case did the PBI loop break. With the other two samples, the seams broke initially, and the PBI loops eventually pulled out. However, the breaking strength values exceeded the design requirements.

Stiffness

The laminate generally was not unacceptably stiff over the temperature range from 200 to 394 K. However, the addition of reinforcing webbing at the edge seam caused a marked increase in stiffness, especially at cold temperatures. Nomex webbing was found to be exceptionally stiff when cold.

Shock Loading

The laminate was not sensitive to the strain rates encountered during deployment. A 61.0- by 2.54-centimeter section of the material withstood a 55.9-centimeter drop of the 1360-gram weight (which produced a tensile force of 21.5 kilograms and an onset rate of 547 kg/sec) without breaking.

Total Mass Loss and Volatile Condensable Material

Total mass loss and volatile condensable material were measured for the parasol material. Total mass loss (0.3 percent) was within the requirements specified in NASA SP-R-0022 (less than 1 percent), and volatile condensable material was slightly greater than the requirement of 0.1 percent. Although the volatile condensable material in the parasol was slightly above specified values, the figure was not considered to be sufficiently high to interfere with the performance of the Skylab parasol.

CONCLUDING REMARKS

The results of the evaluation program indicate that exposure of the Skylab parasol material to an ultraviolet radiation/thermal-vacuum environment causes degradation of the components of the parasol. The effects are pronounced in the mechanical properties and, less important, in the optical properties. Good correlation was achieved between measurements from flight samples and those from ground-based test data. Even these degraded properties, however, were acceptable for the parasol because of the minimum loading the material received in service. No visual evidence indicated that exposure to ultraviolet radiation caused the material to be undesirable in other ways such as particle generation. Other properties of the parasol material were also acceptable for the Skylab Program. The successful parasol deployment during the Skylab 2 mission and the subsequent satisfactory performance verified that the material selected for the parasol was appropriate and useful.

DEVELOPMENT OF A THERMAL PREDICTION MODEL AND FLIGHT DATA EVALUATION AND COMPARISON FOR THE EOB EXPERIMENT OF THE HELIOS SOLAR PROBE

K. Kramp, W. Ley, H. P. Schmidt, *DFVLR — Space Simulation Institute, 5 Cologne 90, F.R. Germany*

ABSTRACT

A thermal model for the EOB experiment has been developed, adopted to test data, and used to predict flight temperatures. These predictions are compared to flight data covering the period from launch until the first black-out.

SUMMARY

For the EOB experiment of the HELIOS solar probe in many investigations data were collected in the Space Simulation Institute, which could be used to set up a mathematical model for thermal control. This model was then adapted to the findings of a solar simulation test of the experiment and rearranged to the orbit conditions. In addition worst-case predictions were made taking into account the possibility of 75 % of the Parylen foil covering the experiment window being destroyed and all incoming solar energy being absorbed.

The predictions are compared with the flight data covering the period from launch until the first black-out (mid April, irradiation level at 2.5 SC).

It can be said that the mathematical model has predicted the orbit temperatures with good accuracy though only a part of the experiment could be used for the test (time-of-flight tube removed) and the simulation of the influence of the central compartment has not been perfect.

The degradation up to now has not become dangerous and the Parylen foil has not been destroyed remarkably.

INTRODUCTION

The EOB experiment of the HELIOS solar probe was designed by the Max-Planck-Institute for Nuclear Physics, Heidelberg, Germany. It is a mikrometeorite analyser measuring the distribution of masses, velocities,

and directions, and the chemical composition of the interplanetary dust particles.

During the development of the probe, special care had to be devoted to the thermal control; particularly the influence of the window was important for experiment and central compartment.

To learn more about that, tests were carried out in the High Intensity Solar Simulation Chamber and other facilities of the Space Simulation Institute of the DFVLR in Cologne, Germany. This was a cooperative work with MPI, Heidelberg, rfe, München, and GfW, Köln-Porz, and served for the following purposes:

- to measure thermal/optical qualities, especially the α/ϵ -ratio of the Al-coated Parylene foil (made by Union Carbide) covering the experiment window, and variation of that value caused by degradation. Also investigations have been made on different samples about the life time and the appearance of holes, resp. On the basis of these tests recommendations could be given to change the conical angle at the front ring, and the shutter in front of the input window has been introduced. For safety against excessive heat input through the window into the central compartment on principle is very important, because the whole thermal control can otherwise be endangered.
- to measure temperatures in a space simulation test in the complete experiment in order to correct the mathematical model set-up with the data from the previous investigations and adapt it to the test data.

After the verification of the model with the test data it was adapted to orbit conditions to produce flight temperature predictions. These predictions should take into account especially the worst-case that 75 % of the Parylene foil covering the input window are destroyed and all solar energy penetrating into the experiment is absorbed.

After launch of the solar probe, the flight data have been compared with the predictions and applicable conclusions were drawn.

PREPARATIONAL INVESTIGATIONS

During 1972 and 1973 the facilities of the Space Simulation Institute were used to carry out some tests to measure basic data 1, 2 .

Outgassing rates and products have been measured

which occur during the irradiation of Parylene foils with simulated solar radiation of different intensity (up to 16 SC). Also basic values of the mean solar absorptivity have been determined measuring the spectral reflectivity with a ZEISS spectral photometer (PQM 2 with RA3 cavity), calculating the absorptivity, and folding it with the Johnson spectrum. The values between 0.24 and 0.26 correspond well with the figures given by the manufacturer.

Qualification tests have also been carried through on samples of the foils. These samples differed by size, design, and construction of the fixture, and the method of fixing the foil to that fixture. During the tests different irradiation levels have been used for periods of different length. The increase of light transmission has been measured using solar cells behind the foils, the increase of the number of holes in the foils has been photographically registered.

At two samples which had been exposed to mean 13.1 SC for 200 hours later the solar absorptivity has again been determined in order to get an idea about the amount of degradation. Together with values measured by other authors these were the basis to consider degradation effects for the flight data prediction.

A final qualification test for the Parylene foils has been made in September 1973. The foil was already fixed in the same manner as in the later orbiting experiment. It was glued to a metal ring with oblique inner wall which was covered with SSM's. The irradiation level was 3, 8, 11, and 16 SC. The rotational motion of the probe was simulated using a shutter which opened for a short time corresponding to the spin rate. The slope of the inner wall was designed unfavorably as was seen during the tests. The number of holes increased more in a special region because the reflected radiation was concentrated there.

This result led to a recommendation to change the angle of the conical inner side of the front ring in order to prohibit this intensification of the solar radiation influence.

MODEL COMPUTATIONS, FLIGHT PREDICTIONS, AND ORBIT DATA COMPARISON

The EOB experiment consists of three main parts:
grid-target tube,
time-of-flight tube,
multiplier tube.

In addition there are two electronic boxes and the shutter with motor.

During the tests in the HISS facility, the time-of-flight tube had to be removed from the experiment. Otherwise the experiment could not be taken into the irradiated part of the chamber. This change was considered within the mathematical model. For the computation of the temperature distribution, 26 isothermal nodes have been introduced; these had been increased by 3 to take into consideration the environment. For the flight prediction the number was increased by 4 because part of the heat shield had to be added which is opposite the opened shutter.

For the computation of the heat exchange factors the isothermal coarse nodes were divided into 55 fine nodes in total within 5 thermal enclosures. For these fine nodes first the geometrical view factors were computed, after that the Gebhart factors which serve as input data for the proper temperature distribution.

The heat conductivity was first estimated. The mathematical model (without time-of-flight tube) was then fitted to the findings of the solar simulation test using an iterational process. Here especially the heat conductivity was changed which was only estimated previously. This fit was made for the measured values of the different irradiation levels which were used during the test. In the same way the different shutter positions were taken into account. In order to overcome some uncertainty in the amount of energy dissipated within the experiment during some test phases, different temperatures were used for the experiment case.

The ready checked model was later on extended to include the time-of-flight tube. The parameters referring to the surroundings were then adapted to orbit conditions to produce flight predictions.

Using different assumptions for the conditions of the foil, the model could also produce worst-case data thus making clear which connection exists between foil condition and heat flow from experiment EOB into the central compartment (see Fig. 1)

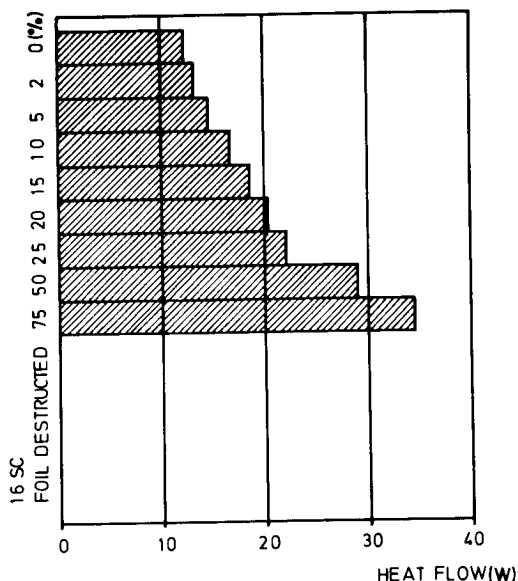


Fig. 1 - Heat flow into central compartment as a function of foil destruction

Fig. 2 and 3 give the interesting data for multiplier and grid electronic, respectively:

- measurement values from the solar simulation test in the HISS facility which produced at 11 SC two values because the experiment case was heated to two different temperatures in order to simulate two different amounts of dissipated energy (two measuring points at the multiplier)
- the predicted flight temperatures from the mathematical model of the experiment
- the flight prediction from the complete central compartment model of ERNO and the values interpolated by Space Simulation Institute computation for three different conditions:
 - a) nominal
 - b) without degradation
 - c) with degradation which is assumed for the time after the third perihelion
- the actual flight temperatures (slight deviations are probably caused by different switch-on/switch-off status).

It can be seen from these data that there is no

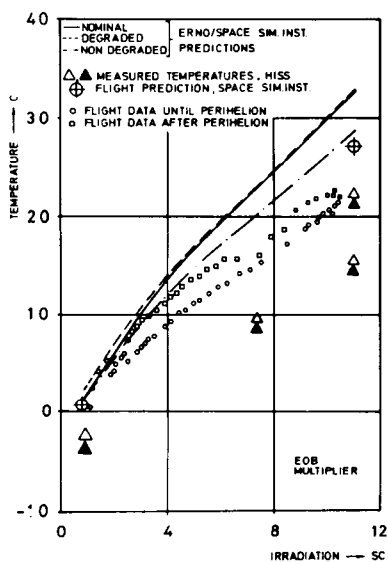


Fig.2 - EOB multiplier, temperature predictions and flight data

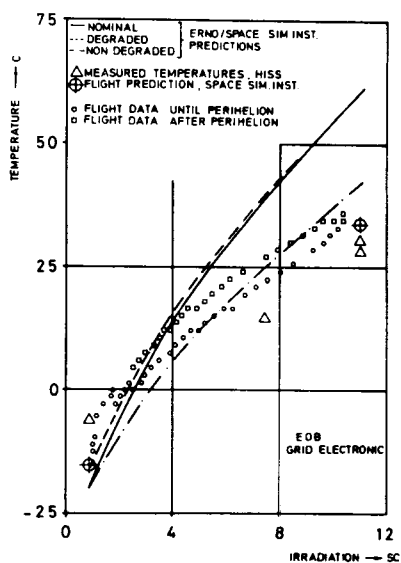


Fig.3 - EOB grid electronic, temperature predictions and flight data

dangerous degradation up to now.

The worst case prediction is given in Fig. 4. For 11 SC the temperatures are shown as a function of the percentage of the destructed foil area.

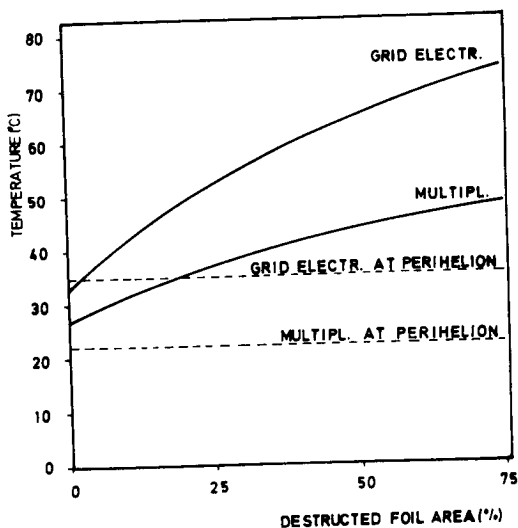


Fig.4 - Temperature predictions for 11 SC as a function of foil destruction percentage

Comparing with the temperatures of the first perihelion which are also indicated we conclude that there is no remarkable destruction of the foil.

As a concluding statement it can be said that

- the mathematical model has produced sufficient accurate predictions though the verification of the model was done using test data which were measured under unfavorable conditions;
- neither degradation nor percentage of foil destruction reached a dangerous level until the first black-out.

References

- | | | |
|---|--|---|
| 1 | H. Fuchs, F. Mühlhoff,
H.P. Schmidt | Parylene-Folien-Tests
IB 353-72/11 |
| 2 | K. Kramp, W. Ley | HELIOS-Komponenten-Tests
EOB, IB 353-73/27 |
| 3 | | ERNO TN 370-3-028/73 |
| 4 | H.P. Schmidt | Temperaturvorhersage der
Mission HELIOS A
IB 353-75/9 |

LAY OUT, TEST VERIFICATION AND IN ORBIT PERFORMANCE OF HELIOS A TEMPERATURE CONTROL SYSTEM

Dipl.-Ing. W. Brungs, *System Manager for Thermal Control in the HELIOS Project Team in Gesellschaft für Weltraumforschung mbH*

ABSTRACT

The HELIOS A solar probe has been launched on December 10, 1974, into a sun orbit with an orbit period of about 190 days. It successfully passed its first perihelion at 0.31 astronomical units sun distance on March 15, 1975.

Ten scientific experiments on board investigate the interplanetary space between earth and sun by measuring magnetic and electrical fields, the solar wind, cosmic rays and interplanetary dust. On its way to the 0.31 AU perihelion the spacecraft is subjected to solar intensities varying between 1 and 10.5 solar constants and to particle radiation changing accordingly. Therefore experiments and spacecraft parts especially the outer parts such as booms, antennas and solar arrays require a thermal design which provides adequate temperature control under these environmental conditions. The objective has been achieved by establishing an appropriate spacecraft configuration and applying most known active and passive means of temperature control (except heat pipes and phase change materials).

The proposed paper will describe the final lay out of the unique HELIOS temperature control system resulting from design and test efforts. The main design features and the impact of interactions between experiment, spacecraft system and temperature control system requirements on the design are discussed. The major limitations of the thermal design regarding a closer sun approach are given and related to test experience and performance data obtained in orbit. Some of these are:

- antenna system influence on radiator efficiency
- experiment aperture radiation heat inputs
- heater power availability
- problems related to specular coatings of most outside spacecraft surfaces
- power requirement versus solar array temperature.

More attention is given to the transfer of experiences gained during the extensive test program performed to verify the thermal design.

The test program performed consisting of:

- degradation tests on surface materials
- test on components e.g. louvers
- tests of subassemblies and spacecraft thermal model
- tests of prototype and flight spacecraft

is presented. Applied test techniques are described. In particular the importance of combined environment and space simulation testing for the development of the HELIOS spacecraft will be shown by reporting the unexpected problems found during testing. They resulted in a number of changes of the spacecraft as well as of the test facilities and set up.

The major problems uncovered were:

- increase of solar absorptance of flexible and rigid optical solar reflectors under HELIOS environment
- degradation of reflection properties of Ag Teflon and Al Teflon from specular to diffuse
- change of louver characteristics under spin environment
- backloading of louvered radiators by radiation inputs from antennas and antenna reflector
- radiation inputs into radiator of boom mounted search coil magnetometer combined with inefficiency of the insulation system resulting in a redesign of the temperature control system for the experiment
- influence of chamber wall reflections on test results at high radiative energy fluxes
- limitation of IR simulation test technique at high intensities (heated reflector dummy versus heated reflector).

Finally the validity of the test results achieved with prototype and flight spacecraft is evaluated by comparison between test data, orbit temperature predictions and flight data.

Also in orbit some upper temperature limits were unexpectedly reached or exceeded. This occurred on spacecraft parts which could not be subjected to a realistic space simulation test. However, it did not result in spacecraft malfunctions. Explanations for these deviations and changes will be dealt with, which may allow a sun approach of 0.28 AU equivalent to 12.75 solar constants intensity for HELIOS B (launch data in December 1975).

In essence the paper will be an attempt to spread experiences, ultimately supported by flight evidence, which were gathered during development of the thermal control system designed for what was the most severe environmental conditions to be encountered by a spacecraft to date.

ANALYSIS OF THE RESPONSE OF A BIMETAL ACTUATED THERMAL CONTROL LOUVER SYSTEM BY COMPUTER SIMULATION

R. Mancuso, *RCA Astro-Electronics Division, Princeton, New Jersey*

P. Hrycak, *New Jersey Institute of Technology, Newark, New Jersey*

ABSTRACT

The performance characteristics of a bimetallic coil actuated thermal control louver system have been simulated using a multinode mathematical computer model. There appears to be satisfactory agreement between space chamber data and calculations by the methods discussed below.

INTRODUCTION

The ability to predict the response characteristics of an active thermal control system¹ in spacecraft operations under changing environmental conditions has previously relied upon extensive on-the-ground testing^{2,3} and availability of space simulation facilities. This procedure has proven to be extremely costly and time consuming⁴. The purpose of this paper is to simulate accurately the performance of a bimetallic coil actuated louver system by computer analysis using a multinode thermal model of the system, in order to reduce substantially the amount of on-the-ground testing of the entire spacecraft. The particular nodes are linked by conductive and/or radiative coupling^{5,6,7}. Comparisons with actual test data are also made.

Statement of the Problem

Crucial in the present analysis is an accurate determination of the temperature of the bimetallic coil used to operate the louvers. In order to obtain accurate thermal predictions with an overall satellite thermal model using active thermal control, both the transient response and heat rejection capability (i.e. louver position) as a function of coil temperature must be determined for all environmental conditions. The two designs considered in this paper are a heater activated louver system and a louver system which relies on good thermal coupling to a mounting surface for actuation. The most important factor in the

heater activated design is the rate at which the louver may be actuated and subsequently cooled. The second design requires extensive evaluation of performance in terms of changing environmental conditions since systems of this type are subject to performance curve shifts as the external sink varies. Simulation of this shift is of primary importance in this paper.

System Description

The first louver design type consists of a bi-metallic coil driven by a heater sensor circuit. The coil is connected to a shaft which rotates a louver blade, thereby varying the view factor to space from the radiating surface behind the louver. A schematic representation of the louver unit is shown in Figure 1. Since a heating element is located on the bimetal, a remote sensor may be used to control louver position as a function of the temperature at any selected location.

The second louver type is similar in configuration to the first system but relies on the temperature of the surface to which it is mounted as the driving mechanism. This system is less expensive when thermal control over a wider range is acceptable. Previous louver systems used metallic louver blades driven by bimetallic coils or fluid actuation.⁸⁻¹³ The louvers in this design are made of polyurethane foam significantly decreasing system weight.

Thermal Model Description

The thermal network model of the louver system is shown in Figure 1. The multinode model simulated the louver system with respect to mass, specific heat capacitance, surface properties and material thermal conductivity. Surface optical properties were measured using a Gier Dunkle infrared reflectometer. Radiation couplings between system nodes and from system nodes to the surrounding environment (i.e. space and rear surface radiator) were computed using a radiative interchange configuration factor computer program. Since the radiative coupling between the louver blade and the environment changes as a function of blade position, several louver positions were examined and input to the main computer model as look up tables defining radiation coupling as a function of bimetal temperature. The relationships used in solving the radiation network are shown in Appendix A to this paper. The view factors

used in solving the radiation network were computed using a view factor computer program including blockage.⁷

Results

The first system to be considered was the heater driven louver. Test data for bimetal temperature response was available for room temperature (25°C) and liquid nitrogen (-185°C) environment testing for two different power inputs (i.e. 1 watt and 2 watts). For comparison, an average bimetallic coil temperature node was generated by proportionally conductively coupling each individual node to an artificial node which would then run at the weighted average temperature of all bimetal nodes. The computer predicted temperature response as compared with test data is shown in Figures 2 and 3. Computer predictions show the bimetal temperature rise to be 50°C and 80°C in sixty minutes with one watt and two watts of heater power respectively. Actual test measurements show temperatures rises of 55°C and 95°C for the two cases considered. The predicted cool down rates were 40°C and 50°C in sixty minutes as compared with 45°C and 60°C during actual test. Although these results show good correlation it was clearly understood that a prediction of transient temperature response for a system with very small couplings to space relies primarily on the ability to accurately determine the system masses and specific heat capacitance rather than accurate determination of thermal radiation and conduction couplings. Also, the heater activated system has an electronic set point adjustment which allows changing the point at which the louver opens in actual flight. These features minimize the dependence on knowing the system "offset" as a function of external sink temperature, the important variable which must be determined for the non heater activated design.

The second system considered was the design in which the heat generated by the body adjacent to the housing which surrounds the bimetallic coil is the actuation mechanism. Comparison and correlation of computer results with test data for this system was based on louver position as a function of bimetal temperature rather than temperature response. The parameters by which louver position were assessed were the total coil deflection (therefore rotation) and the "louver transmissibility ratio" (LTR). The LTR is defined as the ratio of total system heat

rejection with louvers to the total system heat rejection if the louvers are not present (i.e. a black cavity). Typical LTR values for the types of systems examined are 0.10 with louvers fully closed and 0.95 with louvers fully open (see Figure 4).

The computer results for this system used the model developed in the transient analysis and allowed the model to run to a steady state condition corresponding to a particular external sink temperature. At each temperature plateau the total angular coil rotation and louver blade position was computed. The total coil rotation is given by:

$$\Delta\theta = K_{DC} \Delta T(1) (1.8)/t \quad (1)$$

where: K_{DC} = deflection constant for the bimetallic coil
 ΔT = temperature variation for each bimetal node in $^{\circ}\text{C}$
 $\Delta\theta$ = angular deflection for each bimetal node in degrees
 l = length of bimetal node in cm.
 t = coil thickness in cm.

Since the amount of coil rotation is a function of the angular displacement of each bimetallic coil node, the total rotation is the summation of the individual node deflections. Coil rotation from full closed to full open occurs in 90 angular degrees. Computer results were generated for six (6) different sink temperatures ranging from 25°C to -185°C in order to determine if the system couplings were such that the offset would be correlated. As the temperature of the external environment was decreased, the louver blade, shaft and housing temperature decreased. The cooling of the shaft and blade cause heat to flow from the center coil of the bimetal and subsequently create an increasing temperature gradient in the bimetal from outer coil to inner coil. Since the driving mechanism is the temperature of the mounting surface, higher temperature levels are required to obtain the same bimetallic coil rotation therefore the "offset". Figure 5 shows the comparison of predicted results with test measurements. While absolute temperature levels were in error between 0.2°C and 0.8°C depending on sink temperature, the performance curve shift was reflected in the computer predictions. The errors obtained may be reduced by "fine tuning" the model in terms of

conduction and radiation couplings but similar modifications would be required when applying this scheme to any similar system.

During the course of this analysis and model development, relationships which are helpful in designing bimetal louver systems were developed from the basic bimetal equations¹⁴ and empirical measurements. These relationships will aid the designer in determining system sensitivity, torque, weight and size for almost any application. A summary of these relationships appears in Appendix B to this paper.

Summary

A valid and accurate simulation of a bimetal activated louver system using well known and defined thermal analysis modeling techniques has been accomplished. The problem of determining the shift or "offset" in louver performance for changing environmental conditions by extensive thermal vacuum testing can be greatly alleviated by correlating a mathematical model with relatively few data points. The test data used for comparison in this paper required approximately four weeks in a thermal vacuum facility. Modification of a mathematical model would require a fraction of that time. More detailed computer analysis is mandatory to develop this scheme to the confidence level stated but the goal of this paper, that of examining the feasibility of computer simulation for a relatively complex phenomenon has been achieved.

BIBLIOGRAPHY

1. Williams, R. J., "Frictionless Bimetal Actuated Louver System," ASME Vol. 71-AV-39, Life Support and Environmental Control Conference, July 12-14, 1971.
2. Hrycak, P., "Thermal Design of Telstar", Astronautics and Aerospace Engineering, pp. 44-49, December, 1963.
3. Hrycak, P. and Unger, B.A., "General Criteria for Simulation and Model Testing", Proceedings of the Institute of Environmental Sciences, pp. 257-263, 1964.
4. Strickberger, H.P. and Gordon, G.D., "Solar Simulation for Thermal Vacuum Testing Do We Need It?" Institute of Environmental Sciences Annual Techni-Meeting, 1964.

5. Sparrow, E.M., and Cess, R.D., "Radiation Heat Transfer," Brooks Cole Publishing Company, 1970.
6. Kreith, F., "Principles of Heat Transfer," International Textbook Company, Scranton, Pennsylvania, 1968.
7. Mancuso, R., "Analysis of the Response of a Bi-metal Actuated Thermal Control Louver System by Computer Simulation", M.S. Thesis, N.J. Institute of Technology, Newark, N.J., 1975.
8. Bannister, T. C. and Eby, R. J., "Pegasus Thermal Design," NASA Technical Note, NASA TN D-3625, NASA, Washington, D.C., November 1966.
9. Parmer, J. F., and Buskirn, O. L., "Thermal Control Characteristics of Interior Louver Panels," ASME and AICE, National Heat Transfer Conference, Seattle, Washington, August 1967.
10. Parmer, J. F. and Stepandic, E. L., "Thermal Control Characteristics of a Diffuse Bladed Specular Base Louver System," AIAA Third Thermophysics Conference, Los Angeles, June 1968.
11. Parmer, J. F. and Buskirn, D.L., "Thermal Control Characteristics of Spacecraft Temperature Control Louvers in the Solar Space Environment," AIAA Second Thermophysics Conference, New Orleans, April 1967.
12. Russell, L. W. and Leuten, R. C., "Experimental Studies of the Pagasus Thermal Control Louver System," AIAA Second Thermophysics Conference, New Orleans, April 1967.
13. Reusser, P. U. and Coeburgh, J. A. F., "High Performing Actuation System for Use with a Louver Array for Satellite Thermal Control," Presented at RCA AED, 1974, Engineers Management Consultants 25, Gruelstrasse, Zurich/Switzerland.
14. W. M. Chase Company Thermostatic Metals Catalog, Detroit, Michigan, 1973.

APPENDIX A

METHOD OF SOLUTION FOR RADIATION NETWORK COUPLINGS

The RIJ Computer Program used essentially solves the matrix equation:

$$R_{IJ} = \epsilon_I A_I F_{IJ} \{ I_N - \rho_I F_{IJ} \}^{-1} \epsilon_I$$

where: R_{IJ} = NxN matrix of radiative coupling factors

ϵ_I = NxN diagonal matrix of surface emissivities

A_I = NxN diagonal matrix of surface areas

F_{IJ} = NxN matrix of configuration factors

I_N = NxN identity matrix

ρ_I = NxN diagonal matrix of surface reflectivities defined as

$$\rho_I = I_N - \epsilon_I.$$

This matrix equation is derived as follows: If G_i is defined as the incident radiative power in watts/cm² on the i th surface of a radiative network of n gray bodies, the total power incident on the i th body is:

$$A_i G_i = \{ \epsilon_1 A_1 D_1 + \rho_1 A_1 G_1 \} F_{1-i} + \dots + \{ \epsilon_n A_n E_n + \rho_n A_n G_n \} F_{n-i} \quad (1)$$

where: A = surface area (cm²)

ϵ = surface emissivity

E = surface black body emissive power, σT^4 (watts/cm²)

ρ = surface reflectivity ($\rho = 1 - \epsilon$)

F_{j-i} = configuration factor evaluated from surface j to surface i

If a similar equation is defined for each of the n surfaces, the resulting set of n equations is:

$$A_1 G_1 = \{\epsilon_1 A_1 E_1 + \rho_1 A_1 G_1\} F_{1-1} + \dots + \{\epsilon_n A_n E_n + \rho_n A_n G_n\} F_{n-1}, \text{ etc.}$$

If all the $A_i G_i$ terms are grouped to the left of the equality sign, there results

$$A_1 G_1 \{1 - \rho_1 F_{1-1}\} - A_2 G_2 \rho_2 F_{2-1} - \dots - A_n G_n \rho_n F_{n-1} = \epsilon_1 A_1 E_1 F_{1-1} + \dots + \epsilon_n A_n E_n F_{n-1}, \text{ etc.}$$

which after a few simple transformations may be written in matrix notations

$$\{I_N - \rho_I F_{IJ}\}^T A_I G_I = F_{IJ}^T \epsilon_I A_I E_I \quad (2)$$

where $G_I = N \times 1$ column matrix of incident radiant powers.

$E_I = N \times 1$ column matrix of black body emissive powers.

Superscript T indicates a transposed matrix.

Multiplying both sides of the equation by

$$\{[I_N - \rho_I F_{IJ}]^T\}^{-1} = \{[I_N - \rho_I F_{IJ}]^{-1}\}^T;$$

$$A_I G_I = \{[I_N - \rho_I F_{IJ}]^{-1}\}^T F_{IJ}^T \epsilon_I A_I E_I \quad (3)$$

The radiative coupling factor (R_{ij}) is defined such that the net radiative heat transfer from surface i to surface j is: (5)

$$Q_{ij} = R_{ij} (E_i - E_j)$$

Therefore, the net heat absorbed by the i th surface is:

$$\epsilon_i A_i G_i = R_{1-i} E_1 + \dots + R_{n-i} E_n \quad (4)$$

If a similar equation is defined for each of the n surfaces, the resulting set of n equations is:

$$\epsilon_1 A_1 G_1 = R_{1-1} E_1 + \dots + R_{n-1} E_n, \text{ etc.}$$

or in matrix notation:

$$\epsilon_I A_I G_I = R_{IJ}^T E_I \quad (5)$$

Substituting equation (3) for $A_I G_I$ in equation (5) yields:

$$R_{IJ}^T E_I = \epsilon_I \left\{ [I_N - \rho_I F_{IJ}]^{-1} \right\}^T F_{IJ}^T \epsilon_I A_I E_I$$

or

$$R_{IJ}^T + \epsilon_I \left\{ [I_N - \rho_I F_{IJ}]^{-1} \right\}^T F_{IJ}^T \epsilon_I A_I \quad (6)$$

Since ϵ_I and A_I are diagonal matrices ($\epsilon_I = \epsilon_I^T$ and $A_I = A_I^T$), transposing both sides of the equation (6) yields:

$$R_{IJ} = A_I \epsilon_I F_{IJ} [I_N - \rho_I F_{IJ}]^{-1} \epsilon_I \quad (7)$$

APPENDIX B

BIMETAL COIL RELATIONSHIPS

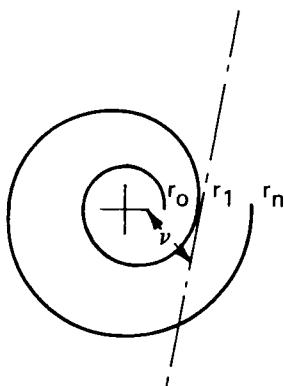
- A. Relationship Between Coil Radius and Length of Bimetal:

$$l_{r_o \rightarrow r_n} = \frac{r_n - r_o}{(\cos v)} = \frac{D_n - D_o}{(2 \cos v)}$$

Experimentally, it has been determined that for the coils used

$$v = 88.97^\circ \quad \therefore l_{r_o \rightarrow r_n} = (27.8) (D_n - D_o)$$

Also, $\cos v \cot v = 0.018$ here.



- B. Radius to any Point on Spiral may be expressed as ⁷

$$r_n = r_o \left\{ 1 + n z e^{nz} \right\} \quad \text{where} \quad \begin{aligned} z &= 2\pi \cot v \\ z &= 0.113 \end{aligned}$$

C. Distance Between Consecutive Spiral Elements:

$$r_n - r_{n-1} = r_o \sum e^{nZ} \{n - (n-1)e^{-Z}\}$$

Also $r_n - r_{n-1} = (S + t) (n-1) \rightarrow n$

where: S = spacing between consecutive bimetal coils

t = coil thickness

Minimum spacing occurs at coil inside at first turn when $n = 1$:

$$\therefore (s + t)_{0 \rightarrow 1} = (s + t)_{\min} = r_o (0.127)$$

For $r_o = 0.318$ cm

$$(s + t) = .041 \text{ cm}$$

D. Bimetal Weight:

$$Wt = (l) (t) (b) (\rho)$$

where: b = height of coil

ρ = density of material

t = thickness

l = length

For type 6650 material

$$\rho = 0.28 \text{ lb/in.}^3 \text{ (7838 Kg/m}^3\text{)}$$

E. Angular Deflection for Free Rotation:

$$\Delta\theta = \frac{K_{DC} \Delta T l (1.8)}{(t)}$$

where: K_{DC} = deflection constant for particular coil material

ΔT = temp change - $^{\circ}\text{C}$

$\Delta\theta$ = angular deflection in degrees

Units of l, t, b are cm.

F. Torque Developed by Coil:

$$\Delta\phi = K_{DC} K_{pc} \Delta T b t^2 \quad (1.8)$$

where: K_{pc} = coil torque constant for
particular coil material

ΔT = temp change - $^{\circ}C$

$\Delta\phi$ = torque in units of g-cm

G. Active Bimetal Length is Less Than Total Length
Due to Bonding and/or Compression of Outer Coils
When Installed Into the Bimetal Housing.

$$\text{Let: } l_{\text{active}} \approx l_{\text{total}} - \pi D_n$$

which allows for the outer coil to be shorted.

H. Rule-of-Thumb Good Practice for Power, Motor, or
Clock Springs Allow:

$$D_o \text{ (Shaft Size)} \leq 25 \text{ (t)}$$

$$\text{and } \frac{1}{5} \leq 7000$$

Values in excess of 10,000 will cause a jumpy
condition.

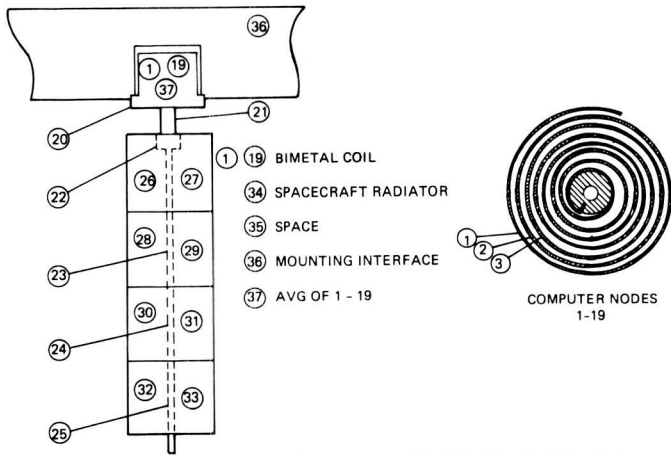


Figure 1. Bimetal Louver Multi-Node Model

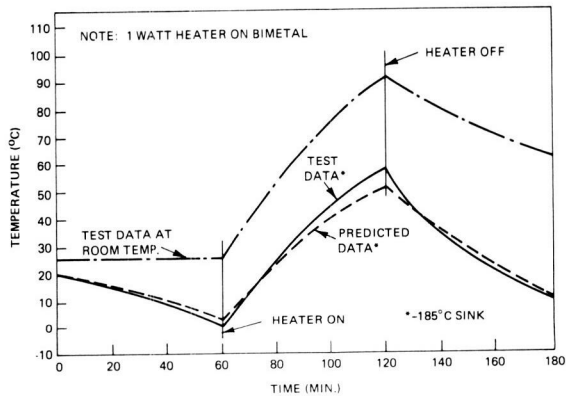


Figure 2. Predicted System Response vs Test Data (One-Watt Heater)

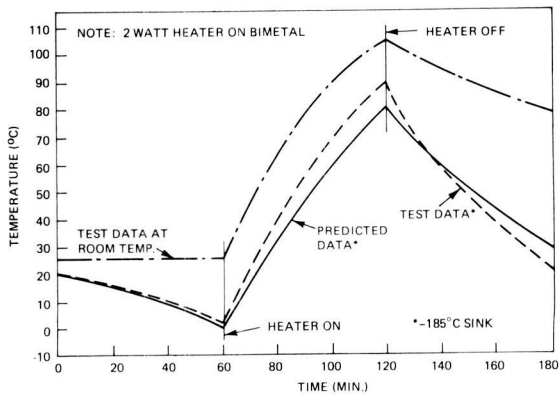
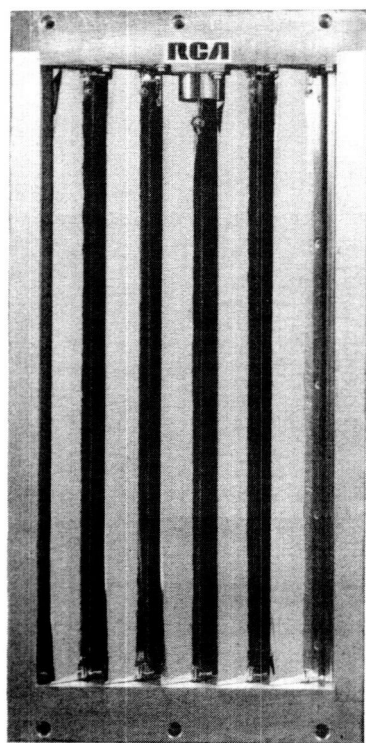
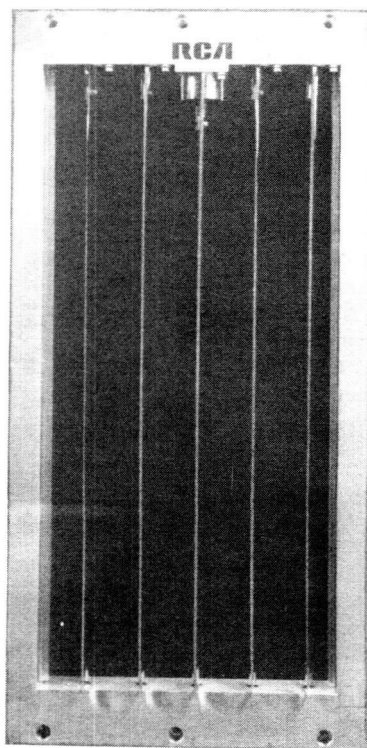


Figure 3. Predicted System Response vs Test Data (Two-Watt Heater)



(a)



(b)

Figure 4. Bimetal Louvers, (a) Partially Open, (b) Fully Open

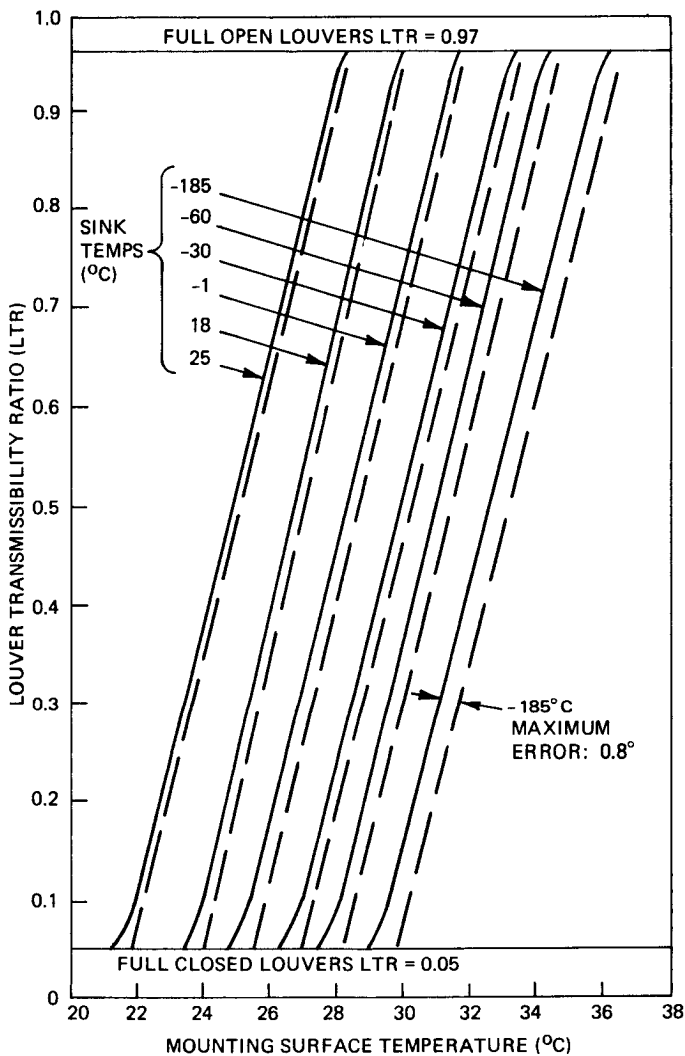


Figure 5. Predicted Response of Non-Heater-Activated System vs Test Data

DOSIMETRY OF LOW ENERGY PROTON BEAMS FOR USE IN SPACECRAFT PARTS TESTING

Charles G. Miller, *Jet Propulsion Laboratory, California Institute of Technology, Pasadena, California*

ABSTRACT

An extensive body of information exists concerning the use of Thermoluminescent Dosimeters (TLD) to measure penetrating gamma radiation. When programs were developed to measure the radiation commonly encountered in space, this experience was broadened to include the measurement of natural particulate radiation. These measurements studied electron beams using TLD, and at later dates, proton beam impingements were also measured by TLD. Reasonable agreement was found between gamma response and electron response, and also proton response as long as the proton beam energy was in the 20 MeV-and-above range.

When TLD were used to measure proton fluences consisting of 5 MeV or lower energies, the results were at variance with the corresponding gamma measurements. The results of our experiments on low energy proton dosimetry using LiF-in-teflon microrods (TLD-700 or LiF-7), will be presented. The findings may be summarized in the following points.

1. The thermoluminescent response is strongly dependent on the Linear Energy Transfer (LET) of the radiation. If the response is normalized to that for Co-60 gamma rays, the thermoluminescent response, which is over 90% for protons at 20 MeV, and 60% for 4 MeV, goes down to 25% for 2 MeV protons. For radiation with a higher LET, such as alpha particles, the response is only 15%.
2. The beginning of supralinearity is observed for Co-60 gamma rays to be at an absorbed dose of 500 rads, but for protons the beginning does not occur until 1000 rads, and for alpha particles the onset is over 2000 rads.
3. The peak in the ratio Thermoluminescence:absorbed dose, in LiF-in-Teflon microrods which occurs at 40,000 rads for gamma radiation, is shifted to 300,000 rads for protons, and is over 10^6 rads for alpha particles.

4. Because the 2 MeV protons are stopped by the first 10% of the thickness of the microrods, that is, 100 microns out of 1000 microns thickness, we can measure the effective absorption coefficient of the microrods to their own thermoluminescent radiation, and our preliminary value is $\mu = 1.098 \text{ mm}^{-1}$.

The implications of these findings on the dosimetry of low-energy proton beams will be discussed from the standpoint of characterizing the simulation environment for spacecraft parts testing.

THERMAL SCALE MODELING OF A MANNED SPACECRAFT*

Roger L. Shannon and Ronald C. Zentner, *Specialist Engineers, The Boeing Company, Seattle, Washington*

ABSTRACT

This paper describes a manned spacecraft thermal scale modeling program. The program consisted of the design, construction, instrumentation, testing, data correlation and associated analysis of a transient thermal scale model (TSM) of the Subsystem Test Bed (STB). The STB was chosen as a representative manned spacecraft for which detailed thermal vacuum test data were available. The STB is a cylindrical vehicle (15 ft diameter by 8.3 ft high) with four docking hatches and six windows. The pressure shell is insulated with multilayer insulation and protected by meteoroid shields. Four truss assemblies were used to support the STB during testing.

A thermal scale modeling study of the STB was made to determine the model scale ratio, scaling technique, thermal simulation technique, and design approach. This study showed the most promising scale modeling approach would be to use the temperature preservation scaling technique, solar simulation and a model scale ratio of approximately 1/5. The design approach was to establish a practical design for the basic pressure shell structure which satisfies both the scale modeling and pressure vessel requirements. The design of the other components would then be tailored to match the pressure shell design. A practical pressure shell design was established for a 1/5.5 scale model which uses stainless steel to simulate the STB aluminum structure.

Based on the results of the model study a 1/5.5 scale model of the STB was designed and constructed. The scale model included, in addition to the basic pressure shell, modeling of the meteoroid shield, multilayer insulation system, docking hatches, window-assemblies, sidewall heaters, ceiling and floor, air circulation system and truss support assemblies. The basic sidewall and bulkhead frames were welded. The bulkhead skin membranes were then brazed to the welded frames. The bulkhead assemblies are removable from the sidewall structure and the hatch closure

*Work supported under NASA Contract NAS9-8332

plates and window panes are removable from the pressure shell. The model was instrumented with 193 thermocouples. These were mostly located at positions corresponding to those on the STB. Other instrumentation provided for air flow rate and internal model pressure measurements.

The STB scale model was tested in NASA/MSC space chamber D. The test conditions simulated the test conditions of the STB tests which had been conducted in space chamber A. The scale model test time was a factor of 2.5 less than that of the STB. The thermal vacuum test included phases with the cabin depressurized and phases with the cabin pressurized. The depressurized phases included conditions with and without top sun solar simulation. The pressurized phases included conditions with and without forced convection. Various heater power levels were used in the different test phases.

Direct temperature correlations between scale model and STB showed that the pressure shell temperature differences between scale model and STB grouped about a mean difference to within $\pm 5^{\circ}\text{F}$ for 83 percent of the data and to within $\pm 10^{\circ}\text{F}$ for 98 percent of the data. The major differences between model and STB temperatures were caused by the model's more effective multilayer insulation. This resulted in a mean temperature difference between model and STB pressure shells of up to about 18°F for worst case conditions. Detailed data correlations showed other temperature differences to be caused by imperfect thermal similitude in test conditions, heater surface emittance, joint conductance and forced convection.

A thermal math model (TMM) was developed for the STB thermal scale model. This TMM, consisting of 639 nodes, was used to make pre-test predictions. Comparisons between TMM predictions and scale model data resulted in upgrading of the TMM. Correlations between the upgraded TSM TMM temperature predictions and the test results were quite good. The mean temperature of the pressure shell was predicted to within about 5°F and differences between predicted and measured values grouped about a mean to within $\pm 5^{\circ}\text{F}$ for 87 percent of the data and to within $\pm 10^{\circ}\text{F}$ for 96 percent of the data.

The upgraded TSM TMM was modified, taking into account the known scale modeling compromises, so that it represented the STB (STB TMM). This STB TMM was used to predict the STB test temperatures. Only one computer run was made and the predicted temperatures correlated well with the test results. The mean temperature of the STB pressure shell was predicted to within about 6°F and the temperature differences grouped about the mean to within $\pm 5^{\circ}\text{F}$ for 72 percent of the data and to within $\pm 10^{\circ}\text{F}$ for 91 percent of the data. The correlations for the heater regions where

free convection effects were important show the same discrepancies as the scale model analysis/test correlations. The meteoroid shield temperatures were predicted fairly well with the TMM. The correlations were slightly poorer than the scale model analysis/test correlations except for the solar heating phase where the STB analysis/test correlations were slightly better.

Based on the results of this thermal scale modeling study it was concluded that thermal scale modeling can be used as an effective thermal design/verification tool for manned spacecraft. Thermal analysis can be used in conjunction with scale model testing to provide a verified math model that can be applied to the prototype manned spacecraft.

THERMOSTRUCTURAL TESTING OF INSTRUMENTED ATJ-S GRAPHITE NOSETIP MODELS IN THE AFFDL 50 MW RENT FACILITY

Capt. Charles L. Budde, *Space and Missiles Branch, Systems Support Division, Air Force Materials Laboratory, Wright Patterson AFB, Ohio 45433*

ABSTRACT

Instrumented ATJ-S graphite shell nosetip models were tested in the AFFDL 50 MW RENT Facility. The inside surface of the models were instrumented with seven thermocouples and three clip-on extensometers. One thermocouple was located at the inside stagnation point and three thermocouples were located at 120 degree intervals on the aft portion of the skirt of the model. In addition, three thermocouples at 120 degree intervals plus three clip-on extensometers at 120 degree intervals offset 60 degrees from the thermocouples were located in the critical region. The outside surface temperature of the models was monitored in two locations by optical pyrometers. Finally, the tests were recorded by three high speed motion picture cameras. Pressure models and calorimeters were also tested in order to help define the flow field condition and heating distribution around the models.

A pre-test thermostructural analysis was conducted in order to design and locate the instrumentation for the ATJ-S graphite nosetip models. Preliminary test runs indicated that the flow field was relaminarizing on the conical portion of the test models. Therefore, for the post-test analysis, the heating distribution was adjusted to account for the relaminarization phenomenon. The surface thermochemistry and in-depth heat transfer solutions were obtained using the ASTHMA computer code. The thermal stress analysis was conducted using the DOASIS computer code. A temperature dependent orthotropic mixed-modulus deformation plastic material model was used in the analysis. Material property values used in the analysis were based on the recommended ATJ-S graphite data package published by Southern Research Institute. Analytical results correlated well with the temperature and strain values measured during the test runs. In addition, the test models fractured in the location predicted by the pre-test analysis.

The results of the 50 MW test program were highly significant. This was the first instance in which actual temperature and strain data had been obtained for a nosetip in a simulated re-entry environment. The development of this improved thermostructural testing capability has brought two important advantages to the Air Force. The first advantage is that a

quantitative assessment can be made of the thermostructural performance of re-entry vehicle nosetip materials. This will lead to the development of improved nosetip materials due to the improved understanding of their thermostructural response. In addition, a quantitative assessment can be made of potential nosetip designs. The second advantage is that the test data obtained from instrumented test series can be used to validate and justify future improvements in the present analysis capability. By having actual temperature and strain data of a nosetip in a simulated re-entry environment, the accuracy of current design analysis techniques can be determined and any shortcomings can be identified.

THERMOSTRUCTURAL TEST FACILITIES FOR RE-ENTRY VEHICLE NOSETIP MATERIALS

Capt. Charles L. Budde, *Space and Missiles Branch, Systems Support Division, Air Force Materials Laboratory, Wright Patterson AFB, Ohio 45433*

ABSTRACT

The Air Force has been engaged in the continuous utilization of a wide variety of thermostructural test facilities for use on re-entry vehicle nosetip materials. The need for nosetip thermostructural reliability is an obvious requirement for any re-entry vehicle system. The ultimate test that can be used to assess the thermostructural performance of a re-entry vehicle nosetip is to perform an actual flight test involving a full scale re-entry trajectory. However, if it were desired to obtain the required statistical verification of a particular nosetip design's thermostructural reliability, the required number of flight tests would be prohibitively expensive. In addition, flight tests are not feasible for testing the thermostructural performance of newly developed pre-prototype nosetip materials. To provide a more cost effective means of assessing the thermostructural performance of nosetip materials, the Air Force has developed and utilized two types of thermostructural facilities; ground simulation facilities and laboratory facilities.

The purpose of ground simulation facilities is to simulate as accurately as possible the re-entry environment. While it has not yet been possible to recreate the exact conditions of re-entry, the key aspects of re-entry are duplicated well enough to provide a highly useful tool to the nosetip designer or materials developer. Due to testing limitations, ground simulation facilities are operated in either an ablation testing mode or a thermostructural testing mode. There are currently three ground simulation thermostructural test facilities available to the Air Force; the Philco-Ford San Juan Capistrano Rocket Nozzle Facility, the AFFDL 50 MW RENT Facility, and the AFRPL ABRES Rocket Nozzle Facility. The Philco-Ford facility has been extensively utilized as a proof test facility. Survival of a Philco Ford test is a prerequisite before any prototype nosetip design will be committed to a flight test program. In addition, the Philco-Ford facility has been used to competitively assess a wide variety of pre-prototype nosetip materials. However it should be noted that there is only a limited amount of instrumentation available at the Philco-Ford facility. Thus very little quantitative data is available after a test. The AFFDL 50 MW RENT Facility is an arc heater which has been used to

test instrumented graphite nosetips. It is characterized by higher surface temperatures and lower side wall heating compared to rocket nozzle facilities. The primary advantage of the 50 MW facility is its instrumentation capability which provides temperature and strain data for comparison with analytical predictions. The AFRPL ABRES Rocket Nozzle Facility has only become operational in the last few years. Use of an improved propellant produces surface temperatures almost as high as those produced in the 50 MW facility. The ABRES facility also has an instrumentation capability comparable to the 50 MW facility. An additional advantage is that the ABRES facility has the capability of testing full scale models.

As a means of providing a more basic understanding of the thermo-structural response of re-entry vehicle nosetip materials, the Air Force has made use of several laboratory thermostructural test facilities. These facilities provide the capability for more extensive instrumentation than ground simulation facilities and also provide a well characterized and closely monitored heating environment. The laboratory thermostructural test facilities currently in use are the Southern Research Institute Temperature/Stress Test, the McDonnell-Douglas Astronautics Company RF Induction Heater, the AFML RF Induction Heater, and the TRW Thermoionic Electron Beam Heater. The first three named facilities are all induction heating facilities and operate in the same manner. The Southern Research facility has been the most widely utilized and has the best developed instrumentation capability. However it has a limited power capability which has restricted the expansion of its testing versatility. The McDonnell-Douglas facility has approximately twice the power of the Southern Research facility, but is much more limited in its instrumentation capability. The AFML RF Induction Heater is only recently operational and it has approximately five times the power of the Southern Research facility. The AFML facility is the only currently available facility with the capability for conducting biaxial and triaxial thermostructural testing. The TRW Thermoionic Electron Beam Heater can be used to provide either interior or exterior heating. It has a power capability roughly comparable to the Southern Research and McDonnell-Douglas facilities. Recently it has been extensively used for testing rocket nozzle materials. In addition, TRW personnel have been working to provide advanced instrumentation capabilities for their facility.

A METHOD FOR THE EVALUATION OF DAMAGE ON THE SURFACE OF CARBON-CARBON ABLATION SAMPLES

E. W. Heinonen, Capt, *USAF*, and G. Y. Jumper, Jr., Capt, *USAF*
Air Force Materials Laboratory, Wright-Patterson AFB, Ohio

ABSTRACT

The effect of weave geometry on the onset of transition from laminar to turbulent flow around a sample of an orthogonally woven fine weave carbon-carbon material tested in an arc-jet is investigated in this paper. Seventeen post-test models which had undergone only partial transition around the circumference were examined as to location of turbulent regions relative to the weave axes. It was statistically shown that the weave axes had the lowest probability of being a position of initial transition onset. The probability generally increased with distance from a major axis, with some rays, notably the 45° rays, showing better transition resistance than the adjacent rays. The incidence of initial transition onset correlated well with the number of X or Y fibers that the flow passes over from stagnation point to the shoulder.

Introduction

One of the critical criteria in the determination of the best materials for use on reentry vehicles is the altitude at which the boundary layer flow around the body experiences transition from laminar flow to turbulent flow. This transition involves an increase in the heating rate and a change in the heat transfer distribution about the nosetip which causes a change in shape from a laminar blunt to a turbulent biconic shape. In general, this transition to turbulent flow is detrimental because it increases the heating rate and thus the rate of recession of the nosetip material. This results in greater material loss and possibly in an asymmetric shape which may adversely affect vehicle dynamics. Information on transition is needed to determine the best flow conditions for optimum reentry.

Because of the expense and difficulty of flight-testing nosetip materials, methods have been developed to simulate reentry conditions by the use of plasma heated arc-jets. Although many materials experience full transition to turbulent shapes during this simulation, a few experience transition only on a portion of the circumference. It has been noted that post-test

models of carbon-carbon materials (carbon fiber preform with carbon filler) exhibit the beginning of transition on the shoulder, as evidenced by transition gouges, away from the orthogonal axes of the preform. This paper indicates the result of a systematic program to examine post-test samples with respect to transition gouges and the relationship of this damage to the weave orientation. In addition, this program also allows a determination as to whether the arc-jet might, due to misalignment, itself cause early transition in one area. A short description of both the materials and the arc-jet test is first presented, followed by results. The final section of the paper presents a discussion of a hypothesis, based on weave spacing, for the transition location.

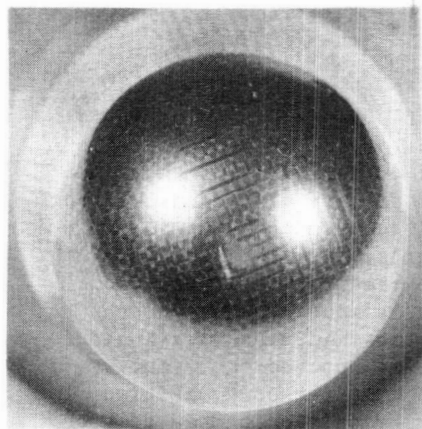
Materials

The carbon-carbon materials of interest for this study all fall into one primary design type. Each material is woven into billets from Thornel-50 yarns in a 3-D configuration along the principal orthogonal axes. The materials vary only in the ratio of yarns in each of the three directions and in various processing steps. Figure 1a is a top view of a model machined from a billet for a test. Reference 1 contains a brief description of the type of materials used in this study. Various samples are cut from a billet being careful to maintain the X-Y-Z axes. As tested, each sample has the Z axis aligned with the flow direction (Fig 1a).

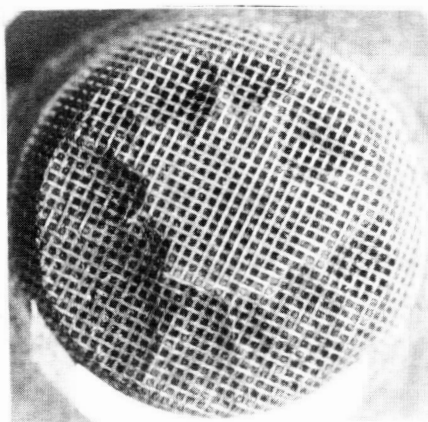
50 MW Arc Trajectory Mode

The data used in this study was generated in the Air Force Flight Dynamics Laboratory (AFFDL) 50 MW arc-jet (Fig 2). Nominally, the model is moved into the arc at a position 6.35 cm (2.5 inches) from the exit plane and "stored" there for two seconds to pre-heat the model. Then the model is moved forward at 1.524 cm (.6 inches) per second for 4 seconds until it reaches a point .254 cm (.1 inches) from the exit plane where it remains for .5 seconds until it is removed from the arc. This mode more nearly simulates the pressure and heating history of actual re-entry than any other ground test and is thereby chosen as the simulation mode in which these samples will be tested.

The models themselves are 1.27 cm (1/2 inch) radius hemispherical nosetips. As the model is moved forward in the arc simulating the change to a lower altitude, the heat transfer distribution is highest at the stagnation point which causes a blunting of the nosetip shape. The distribution in turbulent flow is highest at some angle away from the stagnation point. Transition, as evidenced by gouging, does not occur simultaneously around the tip, but rather in a "spotty" fashion around the circumference of an otherwise smooth blunt shape. As the Reynolds number increases, more shoulder area experiences gouging, and the leading edge of the damaged areas migrates towards the stagnation point.



(a)



(b)

Fig. 1 50-MW Samples. (a) Before Test (b) After Test.

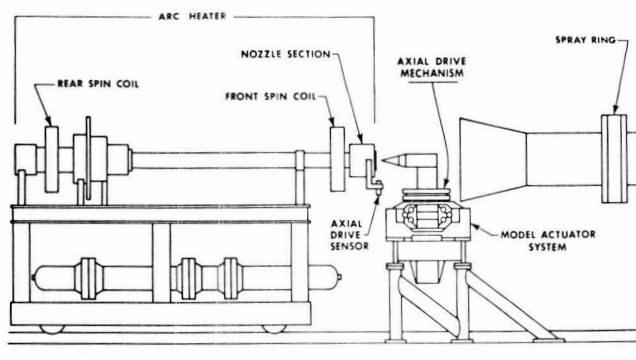


Fig. 2-RENT Test Leg Schematic.

Figure 1b shows the flattened top and gouging along the side of a post-test model.

Analysis

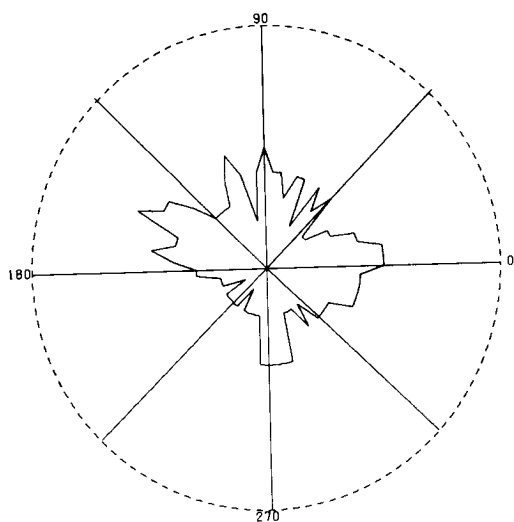
The first step in the analysis of post-test samples is to take high quality, close up photographs of the stagnation region of the model to clearly indicate weave orientation and the transition damaged areas. The top of the model, as placed in the arc, is marked and the axis of the weave closest to this top is designated the weave zero axis. Then the presence or absence of a damaged area is recorded every five degrees. This information, together with the type of material, the sample number, and the angular separation between the top of the sample as it is held in the arc and the closest weave axis, is punched on computer cards. This data is then input into a computer code entitled "DAMASES" which automatically averages transition damage at each angular location, and prints out these averages on a 0-10 basis. The code then automatically shifts each sample to the arc axis and performs a similar process. Finally, the code condenses the weave damage into a 45° segment which is an average of all data points.

The code contains several options to plot the results. The first plot option is to plot the 45° segment. This will indicate which ray has the most damage. The second plot option is a polar plot of damage vs angle. In both cases, the amount of undamaged area is plotted. Thus, the larger the radius at a location, the better it has resisted transition there.

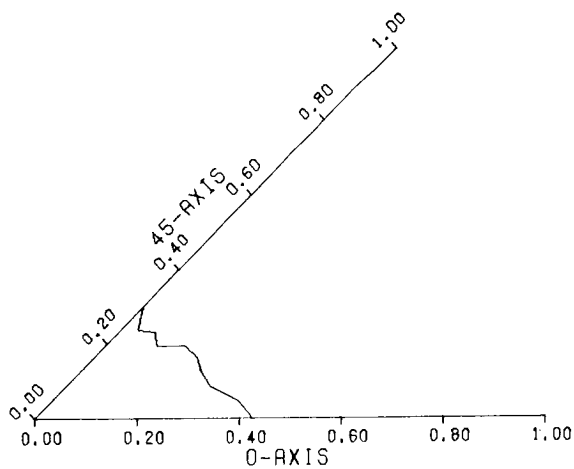
Results

Although there have been many materials tested in the RAMP mode, only the post-test samples from an Air Force Materials Laboratory processing study were available to be examined in detail for this study. There were 10 samples of identical fine weave carbon/carbon material of which 4 samples were treated with a special processing step and six were untreated. All samples were exposed to the same nominal arc conditions. Post-test photographs were taken and the presence or absence of transition induced damage was noted from both the photographs and the post-test models themselves. Indications from the test indicate that, except for one model which received extensive damage from particulate impact, the only damage done to the model surface was transition-induced. The laminar area of the impacted model was eroded away and thus did not affect the conclusion in any manner.

Figures 3a and 3b are the plots for all 10 samples in this study indicating the percentage of time transition damage did not occur at a given location. The longer a ray, the better resistant to damage it was. Figures 4a and 4b are the same plots for the 4 samples which were treated with the processing steps. These samples resisted transition better and began the transition at a later time, thus there was less gouging. It is very

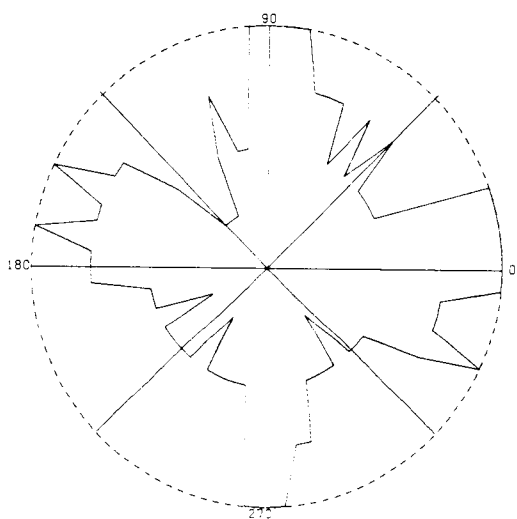


(a)

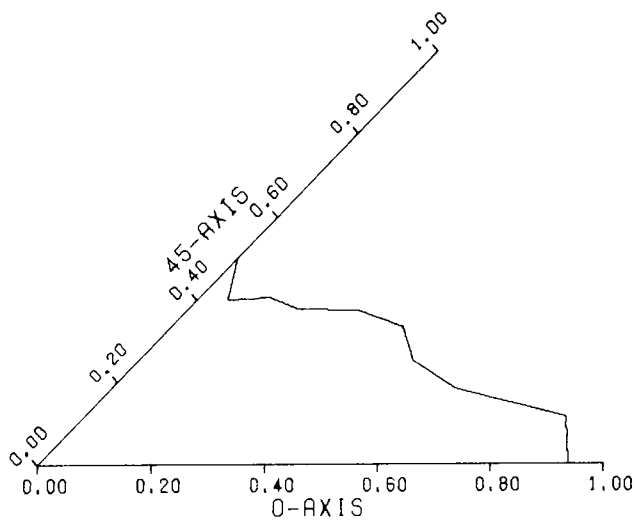


(b)

Fig. 3-Processing Study, 10 Samples, Weave Orientation (a) Polar
(b) 45° Segment.



(a)



(b)

Fig. 4-Processing Study, 4 Treated Samples, Weave Orientation
(a) Polar (b) 45° Segment.

apparent from Fig 4a, and slightly less so from Fig 3a, that the orthogonal axes are more damage resistant, that is, transition will not begin there as readily as off axis. The 45° segments in Figures 3b and 4b also indicate this and indeed show the 45° axis resists transition better than surrounding rays.

Although only this series is available for detailed analysis, several samples from an earlier test series were examined briefly to see if the trends held. All post-test samples not completely damaged around the circumference had the presence or absence of damage measured on the actual model and the same analysis as the above series was conducted. Although this measurement technique is not as accurate as above, Figures 5a and 5b indicate that indeed the axes have the best resistance to transition. The 45° ray is not more resistant to damage, but neither is it less resistant. Thus the trends, if not the exact results, are confirmed.

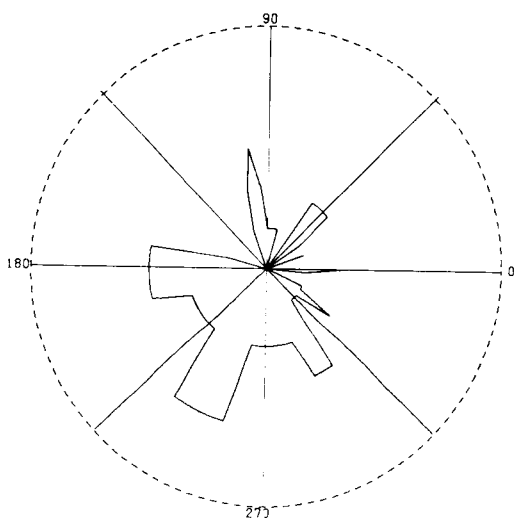
This program also has a capability to show whether the arc itself may bias the location of the beginning of transition. Fig 6a is a polar plot of the ten samples from the latter study, while Fig 6b is polar plot of the earlier series. It is obvious that there is little, if any bias in the Fig 6a, but a large bias in that Fig 6b has more transition damage in the 10° to 200° sector than in the rest.

Discussion

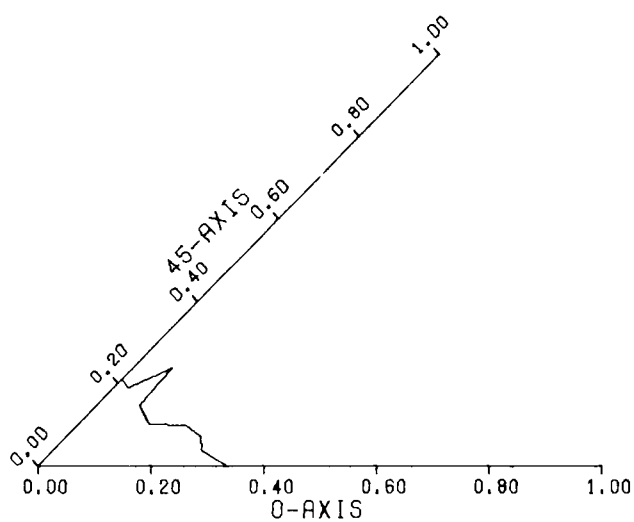
The ramp experiment yields a unique glimpse into the effects of surface geometry on transition. With a properly aligned arc-model system, the model geometry remains axisymmetric during the laminar heating portion of the test. The boundary layer edge pressure and enthalpy distribution should also have this axial symmetry. The ablation response of the carbonaceous material, that is surface temperature and blowing rate, should also be symmetrical. Therefore the test provides a transition experiment in which the surface geometry from ray to ray is the only parameter which is varied while all other parameters of interest remain equal.

The post test models exhibit a roughness pattern which is caused by preferential mass loss of the matrix material and the Z fibers compared to the X-Y woven fibers. At any instant the outermost surface will be composed of regions of predominantly X fibers or Y fibers as shown in Fig 7. These regions give the laminar surface a Moire' like appearance. The Z fiber and surrounding matrix depressions are deep enough that the non-predominant fiber orientation can also be seen. A scan along a ray from stagnation point to shoulder will typically pass over three to five regions. The depth of the depressions is about the same anywhere on the laminar face of the model.

It is possible that secondary flows in the channels between the predominant fibers could be generating vorticies which ultimately lead to transition. Hama, in his article "An Efficient Tripping Device" (Ref 2) reports that a row of equilateral

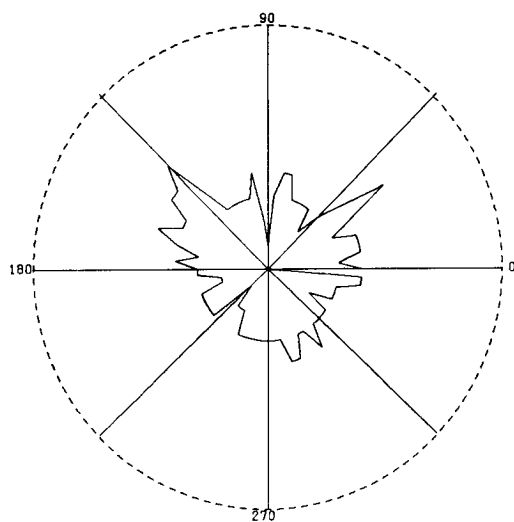


(a)

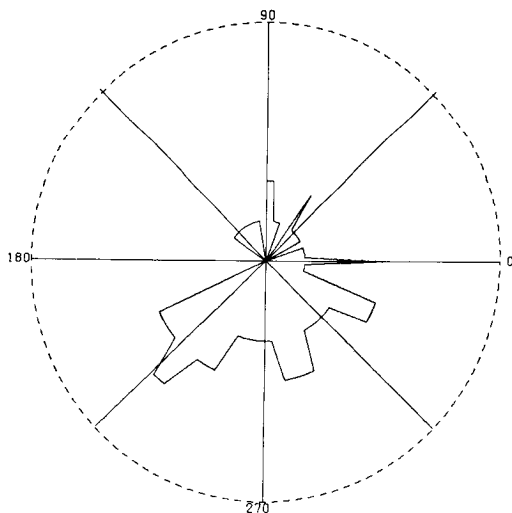


(b)

Fig. 5-Series M, 7 Samples, Weave Orientation (a) Polar
(b) 45° Segment.



(a)



(b)

Fig. 6-Polar of Arc Orientation (a) Processing Study, 10 Samples (b) Series M, 7 Samples.

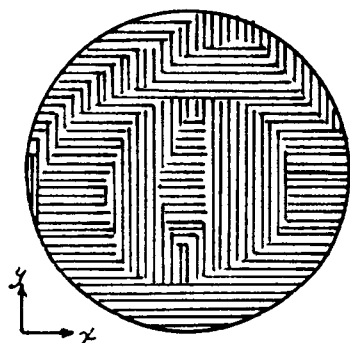


Fig. 7-Laminar Stagnation Region.

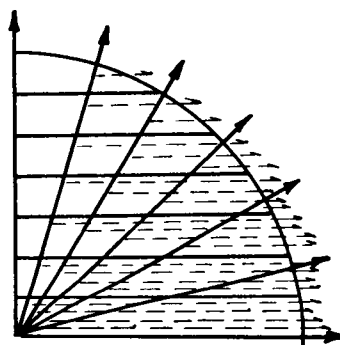
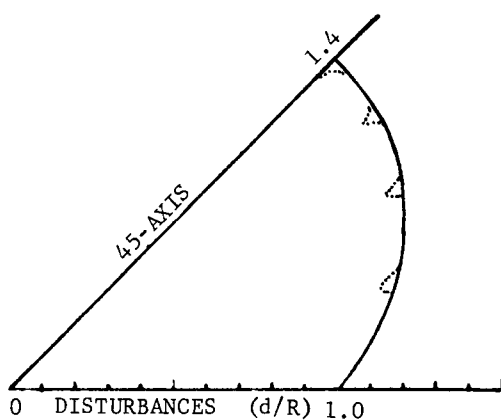
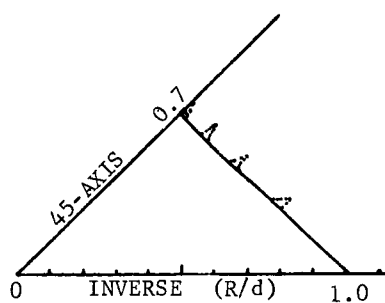


Fig. 8-Secondary Flows on a Unidirectional Grid.



(a)



(b)

Fig. 9-Disturbance Theory (a) Number of Disturbances (b) Inverse.

triangular patches with one apex pointing upstream tripped a boundary layer at a substantially lower Reynolds number than either a row of spheres or a trip wire. If strong secondary flows were established, as in Fig 8, the initial transition location would probably occur at some angle away from the primary axes. The fact that the predominant direction continues to change as the material ablates and the fact that a ray passes over many preferred orientation regions on the way to the shoulder complicates the straight forward application of this hypothesis.

A simple analysis conducted in this study does a fair job of correlating the observed results. The basis of the theory is that the flow is equally disturbed by each X or Y fiber (or bump) which it passes over. In this analysis all fibers are counted, not just the orientation which is predominant in a given region. In a continuum approximation, the sum of fiber encountered along any ray is

$$d = R (|\sin\theta| + |\cos\theta|)$$

where R is the number of fibers encountered along a primary axis and θ is the angle away from the primary axis. In any quadrant, this function is symmetrical about the diagonal; therefore all the information can be presented in a 45° segment. A correction to this approximation is to count an X-Y intersection as only one disturbance. A plot of the above equation with some allowance for X-Y intersections is shown in Fig 9. A comparison with Fig 3b shows that the equation does indicate the major trend that the probability of transition onset increases with distance from a major axis. The rays with significant X-Y intersections, listed in order of decreasing number of intersections are 45° , 26.5° , 14° , and 36.9° . The experimental data does indicate a lower incidence of transition onset near these rays.

Conclusion

The purpose of this study was to attempt to confirm visual observations that transition, as evidenced by gouging on the shoulder of a model, begins off the orthogonal axes, and to develop a theory to explain this. Although the number of samples exposed is too small for any definitive conclusion, results indicate that

1. Transition will begin at locations off the orthogonal axes.
 2. The probability of transition beginning at a certain ray is related to the location of that ray relative to the orthogonal axes.
 3. Because of its location on the axes, the 45° family of rays exhibits better resistance than surrounding families of rays.
- The results of this study should be considered by material developers in improving transition performance of their materials. This study has shown that roughness depends as much on weave

geometry as it does on peak-to-valley measurements. One conclusion of this study is that, if other factors are unchanged, a polar weave should have better resistance to transition than orthogonal weaves, and, perhaps more importantly, transition, when it finally occurs, should occur more nearly symmetrically about the surface. There will be some materials tested in the near future which possess higher symmetry in the X-Y plane. These must then be carefully analyzed to determine the effect this new weave orientation had on transition performance.

References

1. Ross, Eric M., The Carbon-Carbon Assessment Program - An Evaluation of Candidate Composite Materials for Reentry Vehicle Nosetips, Air Force Materials Laboratory, AFML-TR-74-39, September 1974.
2. Hama, Francis R., An Efficient Tripping Device, Journal of the Aeronautical Sciences, Vol 24, No. 3, pp 236, 237, March 1957.

LARGE MODULAR GRAPHITE RADIANT HEATERS FOR TESTING SPACE SHUTTLE THERMAL PROTECTION SYSTEMS

B. G. Cox, *McDonnell Aircraft Company, St. Louis, Missouri*

H. E. Christensen, *McDonnell Douglas Astronautics, St. Louis, Missouri*

ABSTRACT

A graphite radiant heating array, capable of heating a 5-ft span of Shuttle wing leading edge or a 4 x 8 ft flat panel through an entry thermal profile up to 3200°F, has been designed and built by McDonnell Douglas Corporation for NASA-Johnson Space Center. The unique, interchangeable, self-contained heater modules and their versatile support structure/coolant manifold are discussed along with the extensive thermal analysis that accompanied the design effort. A complete description of the geometric capabilities of the array, as well as the design details of the individual modules, is presented. Also discussed is the complete performance envelope of the array, including maximum temperature and gradients, heating uniformity, and the required utilities and support equipment.

INTRODUCTION

A large radiant heating array was developed and built by McDonnell Douglas Corporation (MDC) for Shuttle Thermal Protection System qualification programs at NASA-Johnson Space Center (JSC). The array is capable of imposing flight entry heating profiles around the leading edges of 5-ft long full-scale wing sections, or it can be rearranged into a flat array with a heated area of up to 4 x 8 ft. Modular graphite element heaters and energy absorbers mounted in an adaptable support structure are used to form the leading edge configuration. The absorber modules are used where the heat balance on the wing leading edge is predominately heat rejection to space. The flat array is comprised of the appropriate number of modular heaters arranged side by side. Both the heater and absorber modules have a variable length feature which permits tailoring the size of the heating array to the test article. The array operates in an inert atmosphere at near vacuum conditions as well as at sea level pressures.

The leading edge of the Shuttle wing experiences a variable heat flux and temperature profile around the moldline. During Shuttle entry at high angles of attack (30 degrees), the leading edge is heated on the lower surface then internally radiates energy to the upper surface where it is rejected. Extensive thermal analysis was necessary to determine the best arrangement of heaters and absorbers to obtain the entry profile. This analysis established power requirements for the individual modules and predicted how closely the heating array could reproduce theoretical entry profiles.

The performance criteria for the heater modules were as follows. Each module must have the ability to produce the maximum expected stagnation point temperature, plus some growth potential. This temperature was established as 3200°F. In addition, the spanwise heating uniformity must be adequate to simulate the real Shuttle wing heating environment. A heat flux uniformity of 85% over the span of

a 60-inch long test article was deemed acceptable. The heater modules (and array) must be sized for, and be compatible with, the facilities available at JSC. This included the coolant system, electrical power controllers, and the test chamber.

A thermal analysis program also guided the design and development of the heater modules. Heat transfer analyses were performed on various heater module configurations to predict their thermal performance. These predictions were verified and the thermal model was updated from performance tests conducted with a prototype heater module. The refined model was then used to finalize the array design.

Thermal Analysis of Entire Array

Thermal analyses were performed on typical leading edge test articles surrounded by heating arrays. Consider the analysis performed for the Shuttle leading edge at 67% semispan. A steady-state heat transfer analysis was performed to predict performance of the heating array surrounding this leading edge. This analysis was performed using a thermal model (Figure 1) implemented on MDC's HEATRAN

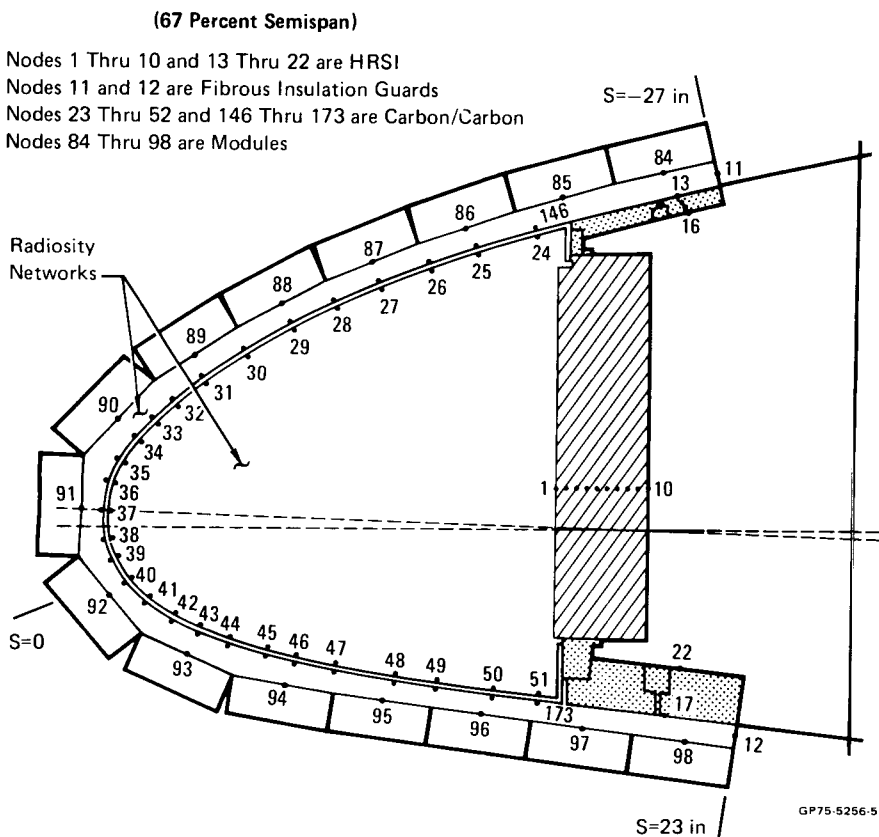


**FIGURE 1 COMPUTER MODEL OF HEATING ARRAY
AND SPACE SHUTTLE LEADING EDGE**

general thermal analyzer computer program, which considered heat conduction and radiation between various components of the test setup. Automated view factor calculations were used in a radiosity network solution for handling radiant energy exchange, including reflections. This model was employed to size the width of the modules, the spacing between the modules and specimen surface, and the arrangement of the modules around the specimen. An inverse solution thermal analysis was performed to determine power and heater element temperature. This consisted of specifying temperatures representing a typical Shuttle flight temperature distribution at peak heating conditions at various points around the leading edge and solving for the individual heater module temperature and power required to maintain that temperature. The power requirement included the waste heat absorbed by each heater module. Also the solution determined which modules were absorber modules. The calculated and desired leading edge temperature distributions are compared in Figure 2. The solid symbols are the control nodes for the heater modules and were specified in the thermal analysis. The open symbols represent calculated temperatures from the thermal model. The predicted heating element temperatures and input powers required to provide these temperatures are presented in Figure 3. The power shown for each module is on a unit area basis of 1 square foot. The negative powers indicate where energy absorbers are required. These analyses along with companion analyses indicated that the heating array would produce the environment required to test Shuttle leading edge sections.

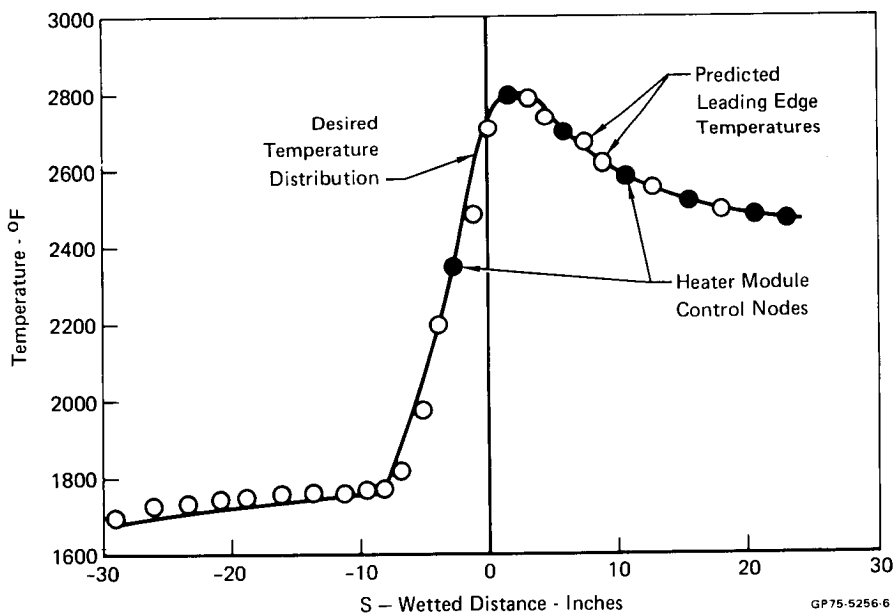


FIGURE 2 LEADING EDGE TEMPERATURES FOR THE EIGHT HEATER MODULE/SEVEN ABSORBER CONFIGURATION

- Steady State Analysis
- 2800°F Maximum Leading Edge Temperature
- XXX = Temperature (°F)
- (YYY) = Heat Flux (Btu/Ft² - Sec)

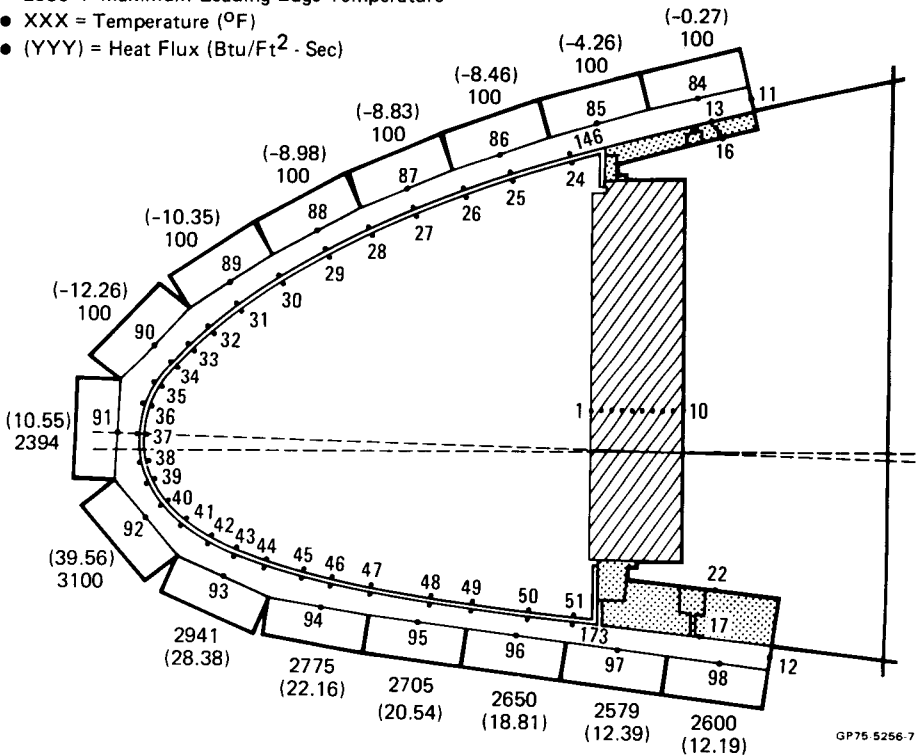


FIGURE 3 PREDICTED HEATING ARRAY TEMPERATURE AND POWER REQUIREMENTS FOR THE EIGHT HEATER MODULE/SEVEN ABSORBER CONFIGURATION

Thermal Analysis of the Heater Module

A prototype heater module, 36 inches long and 5 inches wide, was designed and fabricated to serve as a test bed for the design concepts to be used in the full-scale array. The significant features of the prototype module were serpentine graphite heater elements, gold-plated reflector panels, self-holding tapered heating element supports, and a lever system to prevent excessive element sag and compensate for thermal expansion of the element during heater operations. Gold-plated reflectors were used to increase heater operating efficiency and enhance the heat flux uniformity to the test articles. The prototype heater module was used to conduct performance tests to determine the effective reflectance of the gold-plated reflectors, map the incident heat flux uniformity provided to the test article, and substantiate detailed thermal predictions of the modules performance.

A test article, simulating a section of the wing leading edge, was constructed for use with the prototype heater module. The prototype test article and heater module were instrumented to measure incident heat flux on the specimen surface, energy absorbed by the heater module, power input to the heater module, and the test article surface and heater element temperatures.

An 83-node thermal model was implemented on HEATRAN to calculate heater module heat transfer characteristics and performance. This model considered heat generation in each of 19 heater nodes, 3-dimensional radiant heat transfer and a 38-node radiosity network between heater elements, test article, and reflectors, as well as thermal conduction within the heater elements and cooled supports. The thermal model was set up so that only a few hallmark dimensions needed to be changed to evaluate a different length heater module.

Values of effective reflectance for the reflectors was developed using measurements of test specimen and heater element temperatures while operating at various steady-state power levels. These data were then compared to analytical predictions based on various assumed values for reflectance. Under actual operating conditions, outgassing products from the test article deposit to some extent on the gold reflectors. The effective reflectance was measured both with clean reflectors and after a period of operation. A comparison of measured and predicted test specimen temperatures is shown in Figure 4. The measured data taken with clean reflectors shows an effective reflectance slightly greater than 0.80. Data taken after a period of operation indicates the effective reflectance decreases to 0.70. This is significantly higher than the effective reflectance of 0.55 for chrome-plated reflectors which we had used on previous heater designs. A similar comparison was made between measured and predicted heater element temperatures with the same results. Based on these tests, an effective reflectance of 0.80 describes the heater module performance when the reflectors are clean and 0.70 when deposits are allowed to accumulate on the reflector surfaces.

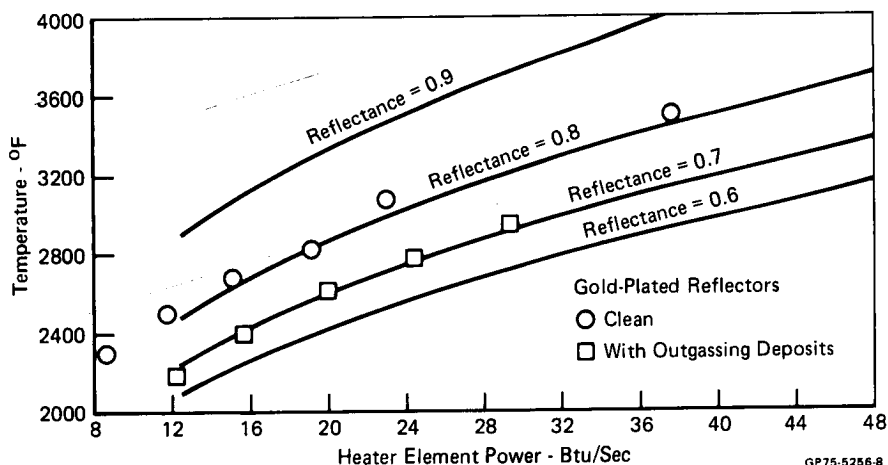


FIGURE 4 MEASURED AND PREDICTED TEST SPECIMEN TEMPERATURES FOR THE 36-INCH PROTOTYPE HEATER MODULE

The next series of prototype heater module performance tests measured the incident heat flux distribution along the span of the test article surface. A thermal analysis was performed to predict the heat flux uniformity for the prototype heater module using an effective reflectance of 0.80. To correlate the predicted uniformity versus the measured, the reflector panels were cleaned prior to all incident heat flux measurements. The measured heat flux uniformity from the performance test is compared with the predicted uniformity in Figure 5. Excellent agreement exists above the 80% uniformity level.

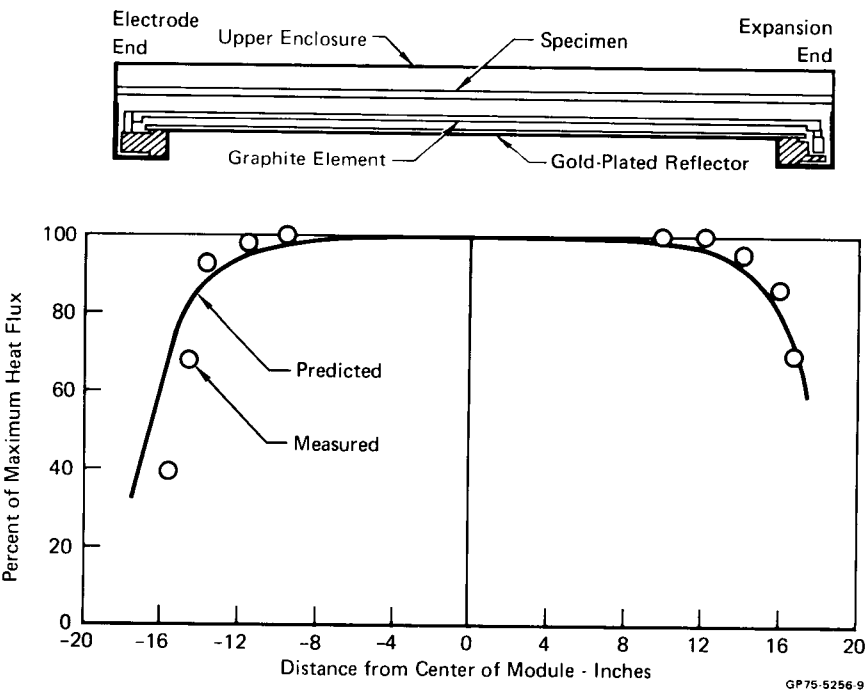


FIGURE 5 MEASURED AND PREDICTED HEAT FLUX UNIFORMITY FOR THE 36-INCH PROTOTYPE HEATER MODULE

The thermal model was then utilized to calculate how long the module should be to obtain 85% heat flux uniformity over a 60-inch span. The calculations indicated a 72-inch long module would suffice. Subsequently, a 72-inch module was fabricated and heat flux uniformity tests were conducted to verify the predicted performance. Figure 6 compares the measured heat flux versus that predicted. Although the prediction was not as good as it was for the 36-inch module, the 85% uniformity criterion was achieved for the 60-inch span.

The thermal model was refined by including the effects of varying element resistivity with temperature and test specimen heat losses. This refined model eliminated some of the discrepancies between predicted and measured performance on the 72-inch module. This improved model was subsequently used to finalize the design of the heating array.

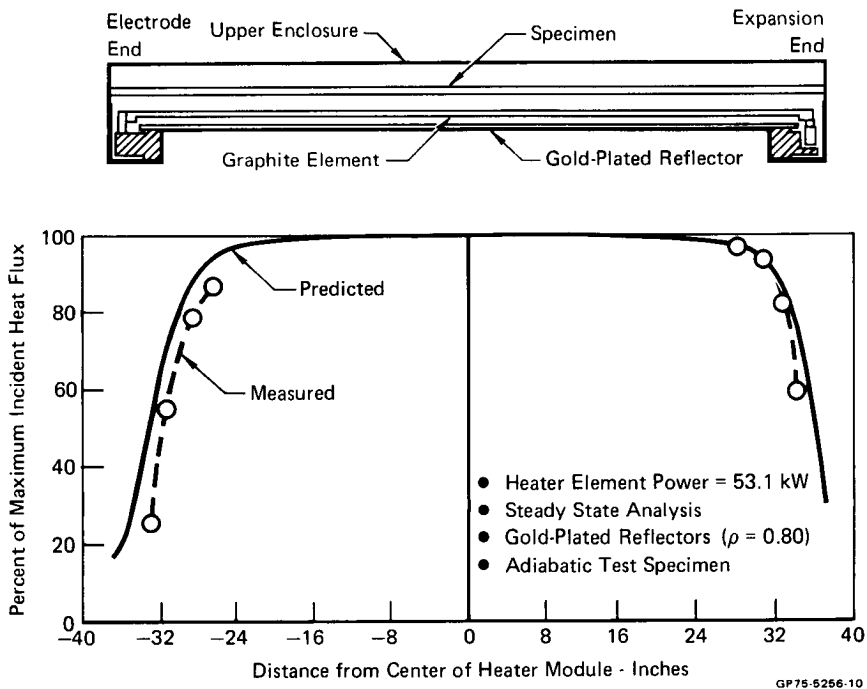
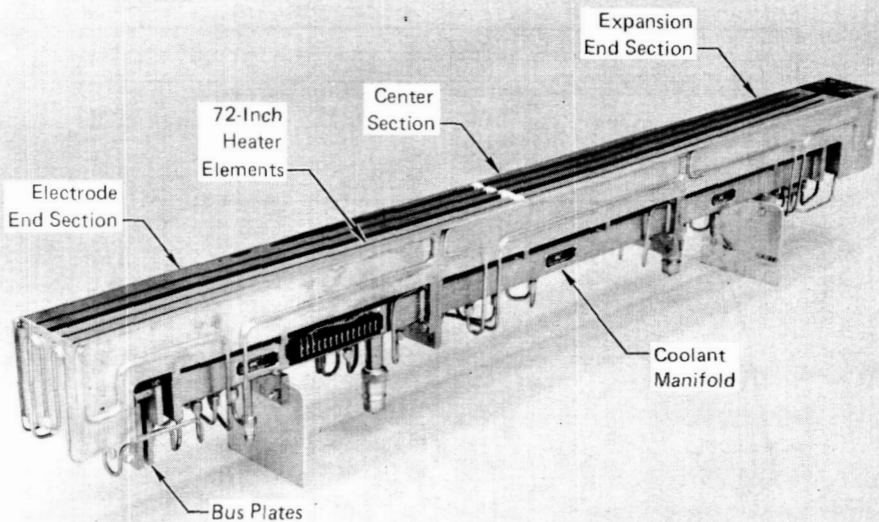


FIGURE 6 MEASURED AND PREDICTED HEAT FLUX UNIFORMITY FOR 72-INCH HEATER MODULE

Heating Array Description

The heating array was designed so that it could test Shuttle leading edge test articles, and also be arranged to form a large flat heated area up to 4 x 8 ft to test large flat panels. The array consists of a set of variable-length heater modules, a set of variable-length heat absorbing modules, an adaptable support structure to support these modules around a leading edge test article and in a flat array, and a set of special optical pyrometers for measuring test article surface temperatures without altering the test article surface.

One of the 22 variable-length heater modules is shown in Figure 7. It consists of three sections, the electrode end, the expansion end, and a center section, which can be removed to shorten the heater length from 72 to 48 inches. This variable-length design feature provides an efficient method of testing smaller size test panels. The heater module is approximately 5 inches wide and contains two two-pass serpentine graphite heater elements. The elements have constant cross-sectional dimensions throughout the heated length and are thickened on both ends for electrical power connections, and for the end supports. Coolant manifold tubes which distribute coolant to all the heater components also serve as the structural backbone of the heater. These manifolds are flanged to mate with the other heater sections. Brackets are attached to the manifolds to mount the heaters to the array support structure.



GP75-5256-11

**FIGURE 7 VARIABLE LENGTH HEATER MODULE
(72-INCH CONFIGURATION)**

The electrode end of the heater assembly is shown in Figure 8. Water-cooled tapered pegs retain one end of the heater elements and transmit power to the element. This mounting feature retains the element through friction and provides positive electrical contact to the graphite element. The electrical components are isolated from the heater frame by insulating sleeves and plates. Bus plates provide convenient attach points for water-cooled power cables.

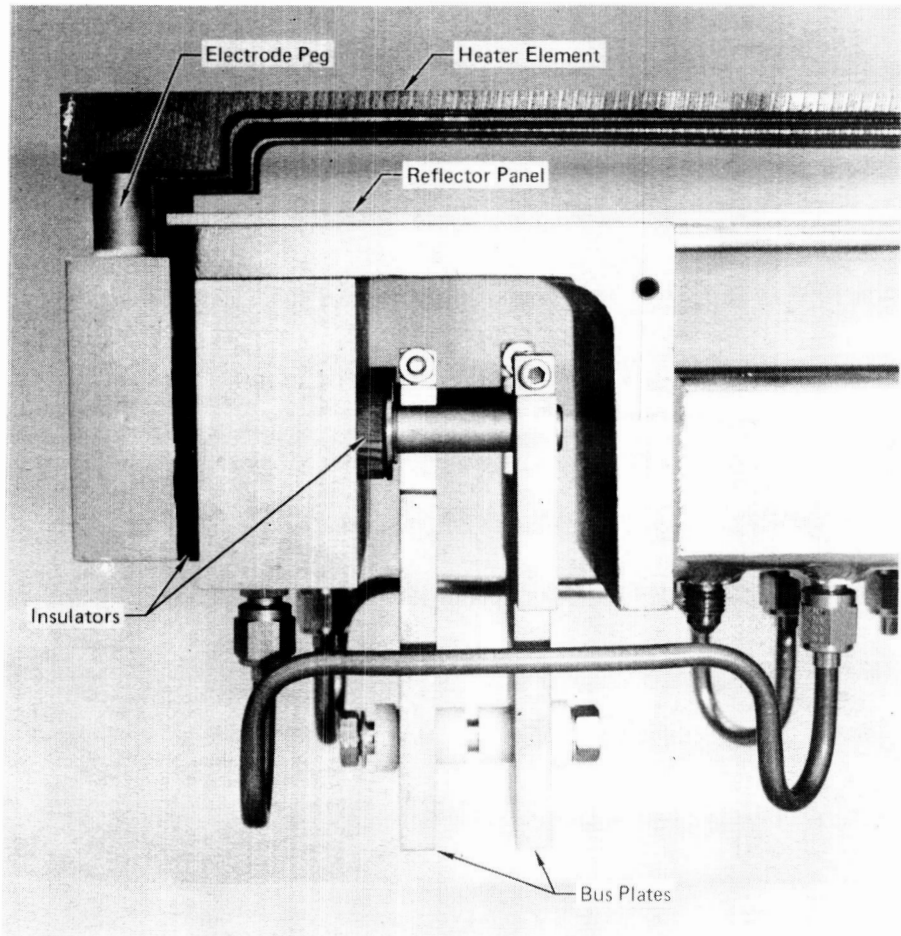
Figure 9 shows the details of the expansion end of the heater module which supports the other end of the heating elements and takes up thermal expansion of the elements during operation. It consists of graphite levers pinned at the bottom and tapered at the upper end to retain the elements. As the elements expand during heater operation, the levers pivot to allow for thermal expansion. As on the electrode end, electrical isolation is provided by insulating sleeves and plates.

Water-cooled gold-plated reflector panels surround the heated zone on five sides, leaving only the area above the elements open for radiating to the test article. Coolant circuits are attached to the outer surfaces of the reflector panels to remove waste energy. The coolant circuits on the side reflector panels are so situated that they nest with the circuits of the adjacent module in the array to provide closer packing. These side reflector panels can be removed so modules can be butted side to side to form a large flat heating array. In the flat array, the side reflectors are installed at the periphery to prevent stray radiation.

A special optical pyrometer was developed for use with graphite radiant heaters. These pyrometers fit into water-cooled mounting blocks fixed to the bottom reflector of the heater. The mounting block automatically aims the pyrometer to view the test article surface through the gaps between elements. Baffles within

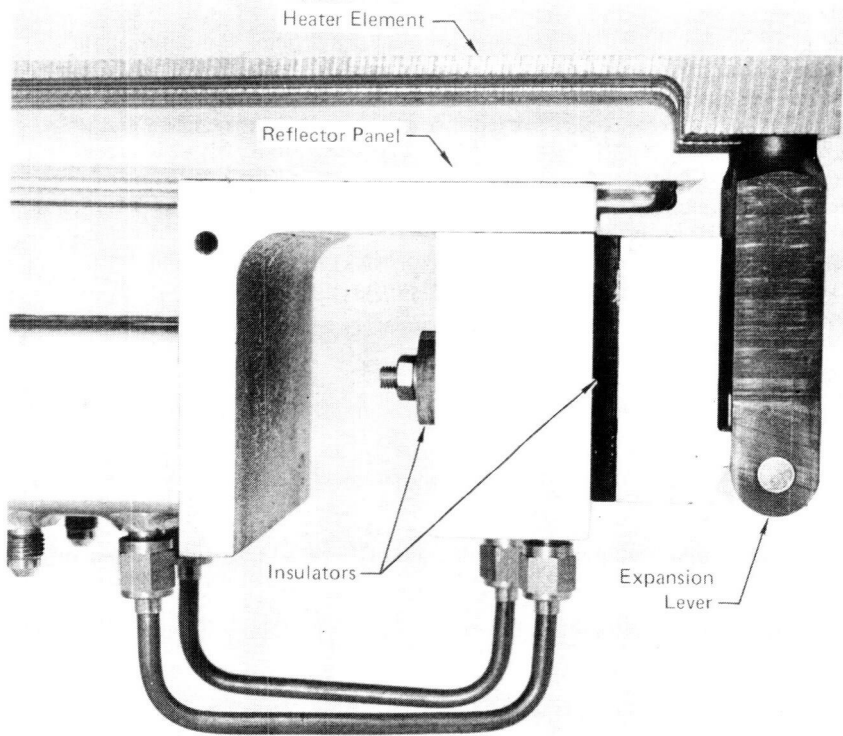
each instrument restrict the field of view and eliminate all stray radiation from the heater elements except that which reflects from the test article. These pyrometers give the test conductor a means of reliably monitoring the test article surface temperature without securing instrumentation to the test article.

The variable length concept is carried through to the absorber modules. An absorber is shown in Figure 10. It also consists of three sections, with the center section removable to shorten the overall length of the unit. The dimensions of the absorber are approximately the same as the heater module thereby making it interchangeable with a heater in the leading edge array. A water-cooled energy absorbing panel is mounted on each section of the absorber. As with the heater modules, each of the absorber module panels is equipped with a water-cooled mounting block for an optical pyrometer.



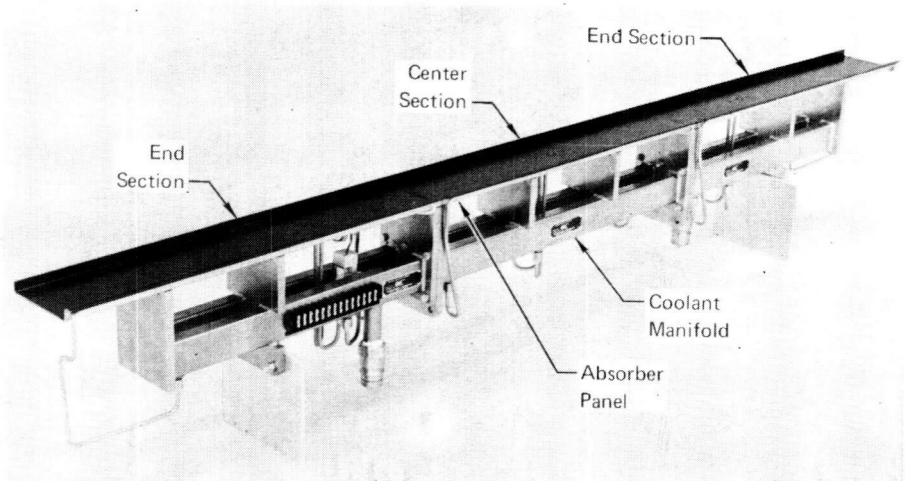
GP75-5256-12

FIGURE 8 ELECTRODE END DETAILS



GP75-5256-13

FIGURE 9 EXPANSION END DETAILS

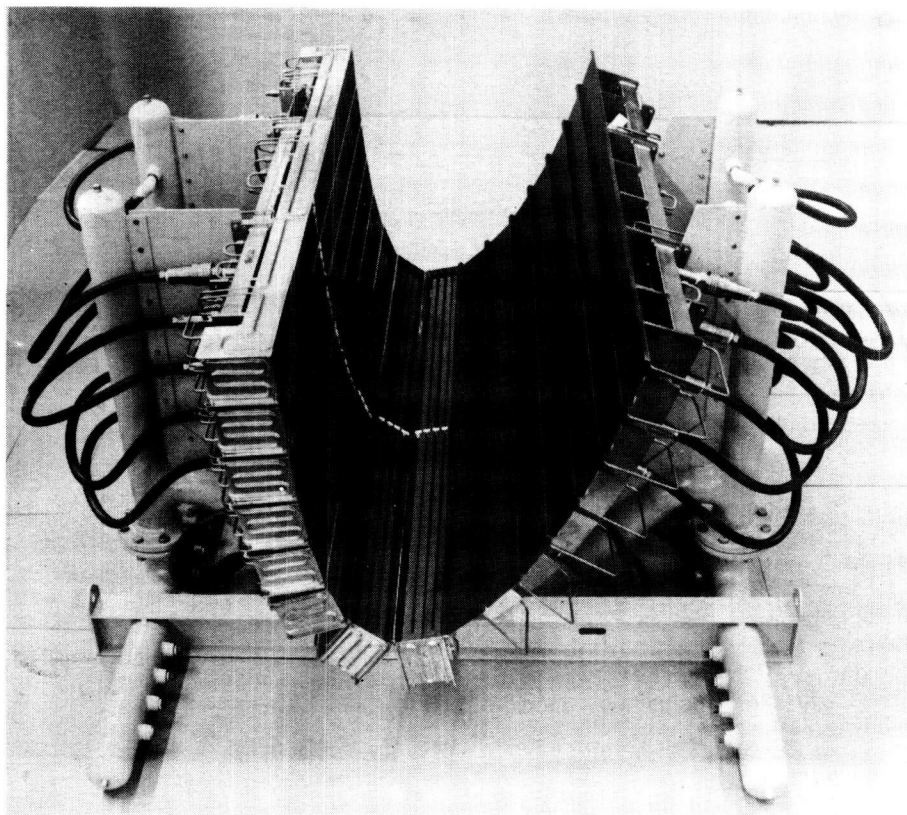


GP75-5256-14

**FIGURE 10 VARIABLE LENGTH ABSORBER MODULE
(72-INCH CONFIGURATION)**

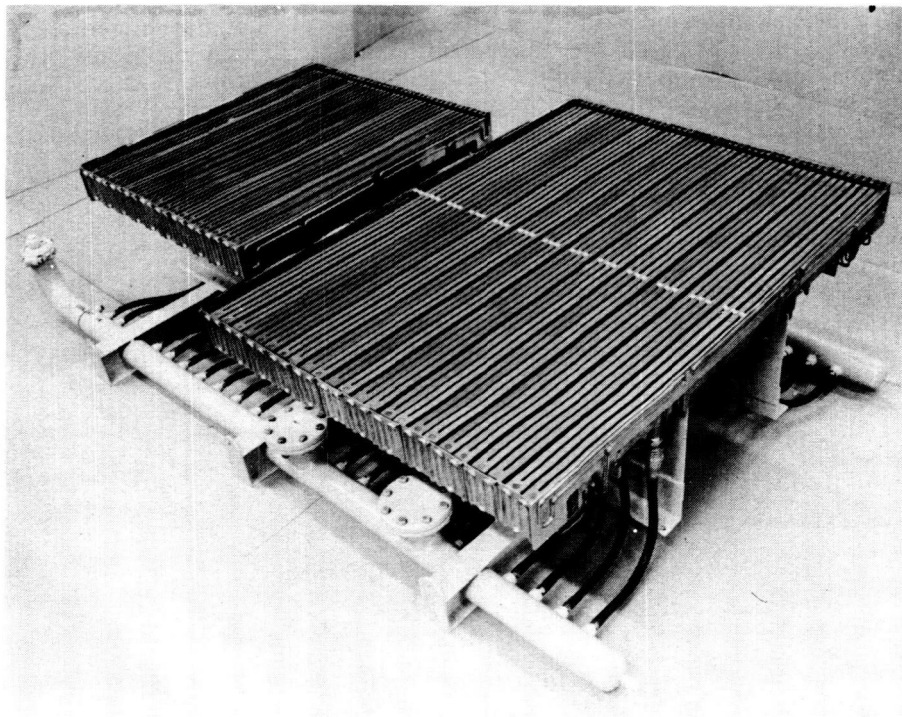
The heating array support structure can be converted to support the heater and absorber modules in either a leading edge configuration or a flat array configuration. This support structure was sized to fit inside the 10-ft diameter altitude chamber located in the Radiant Heat Test Facility at NASA-Johnson Space Center. When the support structure is in the flat configuration, up to 24 heaters can be arranged side-by-side to form a flat horizontal heating array. When the support is configured to test wing leading edge sections, heaters and/or absorbers are attached to mounting plates specially contoured for each test article. In either configuration, the heaters and absorbers are supplied coolant from integral manifolds in the support structure.

Figure 11 shows a leading edge heating array configuration consisting of eight 72-inch heater modules and seven 72-inch absorber modules. Figure 12 shows two flat array configurations. The larger flat array is composed of twelve 72-inch heater modules with the smaller array composed of ten 48-inch heater modules. The modules can be rearranged to suit the individual test requirements.



GP75-5256-15

FIGURE 11 HEATING ARRAY IN LEADING EDGE CONFIGURATION



GP75-5256-16

**FIGURE 12 HEATING ARRAY WITH TWO POSSIBLE
FLAT CONFIGURATIONS**

Heating Array Performance

The heating array performance characteristics meet or exceed all of the design criteria specified for testing Shuttle leading edge test articles. The array can sustain over 3400°F on the surface of a test article with thermal characteristics similar to the Shuttle leading edge. It is capable of providing a minimum heat flux along a 60-inch span of not less than 85% of the maximum heat flux during steady-state operation at peak temperatures. This is with the array in the 72-inch configuration. It has a high heating rate capability of 600°F per minute between 80° and 2800°F on a leading edge type test article. The array operates in an inert environment such as gaseous nitrogen to prevent oxidation of the graphite elements. The array is designed to operate at low pressures as well as one atmosphere, with operation demonstrated down to 0.5 torr. The voltage operating range of the heater modules is 0 to 100 volts, with power supplied by standard ignitron power controllers through 4:1 step-down transformers.

Acknowledgements

The sponsorship and program monitoring by W.D. Sherborne and J.C. Welch of NASA-JSC is greatly appreciated.

PROPERTIES OF CONDUCTIVE COATINGS FOR THERMAL CONTROL MIRRORS AND SOLAR CELL COVERS

D. E. Joslin and H. K. A. Kan, *The Aerospace Corporation, El Segundo, California 90245*

ABSTRACT

Conductive transparent coatings applied to the dielectric surfaces of a spacecraft offer the possibility of distributing charge uniformly over the entire spacecraft surface. Optical and electrical measurements of such a coating as a function of temperature are described. These results are used in considering the impact of a conductive coating on the absorptance of thermal control mirrors and on the transmittance of solar cell cover glass, which can be improved by the application of an antireflection coating.

INTRODUCTION

Thermal control mirrors and solar cell covers in a spacecraft must necessarily be exposed to the space environment. In both cases, the front surface is fused silica, which as an insulator has a tendency to be charged electrostatically in a space environment. The charging phenomena are quite complicated and are dependent on photoelectric effect and on the effect of electrons and protons from the space plasma. It is known that the electrostatic charging may cause significant operational problems such as the malfunction of electrical circuits and degradation in the mirror itself, particularly when discharge from dielectric breakdown occurs. These are also possible effects of charging on the transfer of contaminants. In some applications, it is desirable to dissipate the charge built up on these surfaces with, for example, a conductive coating. The coating, of course, should be such that the optical properties of the thermal control mirror and solar cells are not significantly degraded.

This report describes the result of an evaluation of the optical and electrical properties of one such commercial coating made by the Optical Coating Laboratory, which is designated OCLI conductive coating (CC). The composition of the coating nominally is indium oxide. This coating was originally developed for the US-German Helios space program where the interest was the performance at near-sun orbits (0.3 AU) and elevated temperatures. Test data had been obtained by NASA¹ and

Boeing.² NASA reported some uv-induced coloration in the coating but no observable effect by irradiation with low-energy electrons or protons. Boeing reported combined uv and low-energy protons resulted in some absorptance increase and negligible change in electrical resistance. The measurements to be reported here, made between +100°C and -160°C, do not consider radiation effects but are directed more towards obtaining data on the effect of the coating on low-temperature and low-absorptance applications.

Fused-silica silver mirror is currently the preferred thermal control surface where low solar absorptance and high thermal emittance are desired. It is possible to cool a device to the neighborhood of -100°C in space with this type of a passive surface. The solar absorptance of such a mirror, typified by the OCLI SI-100, is 0.06 to 0.07 for a 10-mil-thick mirror. A lower absorptance value of about 0.035 can be achieved using multilayer dielectric filters (OCLI MSI-100) to increase the reflectance in the spectral region of 0.35 μ m where silver has strong absorption. Because of differences in these two types of mirrors, the effect of the coating on solar absorptance is expected to be different.

The GEOS satellite that is due for launch in mid-1976 will establish the long-term behavior of particles and fields of geostationary orbit. The solar cell cover glass includes a conductive coating and a conventional uv-reflection filter that eliminates radiation below 400 nm. It was shown that, for this case, the output of solar cell will have a 1% to 2% loss.³ However, today, with the development of solar cells that have an extended blue response, it will be important to optimize transmittance of the cover glass that employs a conductive coating. This paper also considers the use of an antireflection (AR) coating over the CC to improve the transmittance in the wavelength region of 350 nm to 600 nm, as well as the impact of the insulating properties of an AR coating on the charge dissipation.

EXPERIMENTAL PROCEDURE

The coating samples, supplied by OCLI, consist of their standard coating on fused-silica silver second-surface mirrors (SI-100) and on plain fused-silica substrates. Transmittance and reflectance measurements were made on a Cary 17 spectrophotometer. The reflectance measurements were made with a W-V Strong-type reflectance attachment that permits absolute reflectance measurements of specular surfaces. Low-temperature optical measurements were made in vacuum. Limited thermal cycling data were obtained with the samples cycled in air. Electrical resistance measurements were made between weld-tabs integral to the mirror as shown in Fig. 1.

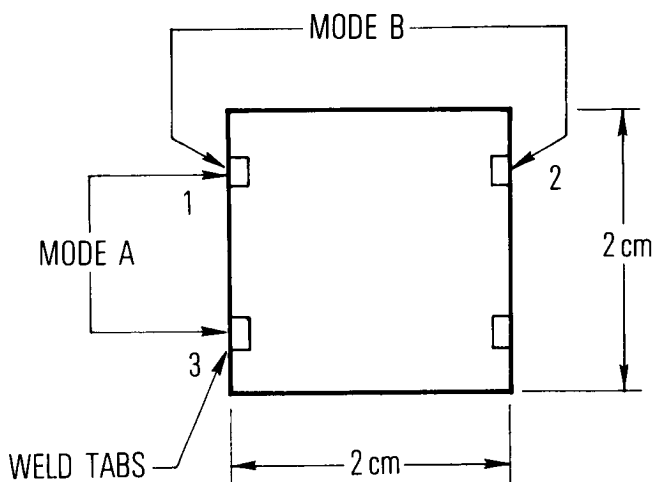


Fig. 1—Electrical contact configuration on the OCLI conductive transparent coating. Resistance measurements made between contacts 1 and 3 are referred to as mode A. Measurements between contacts 1 and 2 are referred to as mode B.

RESULTS AND DISCUSSION

Since the thermal control mirrors may reach quite low temperatures, it is important to measure the temperature dependence of the electrical resistance of the coating. The results of such measurements are shown in Fig. 2 where it is seen that the temperature dependence of the resistance is negligibly small. The most resistive sample shows a thermally activated conductivity, as is frequently observed in polycrystalline semiconducting oxides. The activation energy, however, is quite small especially among the more conductive samples, and the temperature dependence of most samples may in effect be neglected.

Since thermal control mirrors are generally exposed to an elevated temperature, e.g., during the curing of the bonding adhesive, the effect of heating cycling between 100°C and -160°C was determined in a limited fashion. After four complete cycles in air, the resistance was observed to decrease by 1.5% to 8%. Since the tolerance requirement for resistance is not expected to be strict and since a resistance decrease is not detrimental, the effect of thermal cycling is not considered to be significant.

In evaluating the optical properties of the CC, the primary interest was to determine the change in absorptance that may occur with decreasing temperature and the effect of the CC absorptance on the second surface mirrors. The transmission

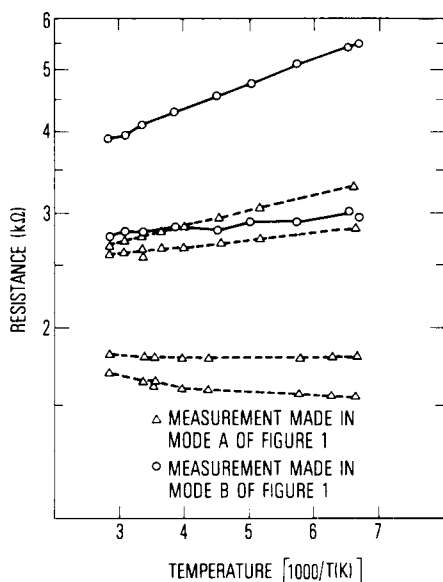


Fig. 2—Resistance versus temperature of six different OCLI conductive transparent coating samples

curves in Fig. 3 demonstrate the effect of low temperature on the CC absorptance. There are reflection losses in these curves that include the sample surfaces and the windows of the dewar in which the sample is mounted. The absorptance of the coating in practically the entire solar spectrum is not measurably affected by lower temperature except for the very small change in the uv. The small shift is consistent with the behavior of the absorption edge of most materials, i. e., the fundamental absorption edge usually shifts towards higher energy with lower temperatures.

For thermal control application, the important parameter is the absorptance of the coating. The transmittance of CC on fused silica is shown in the lower curve of Fig. 4 and includes the effect of reflection loss at both the CC-air interface and the fused silica-air interface. The absorptance spectrum, as determined from the measured transmittance and reflectance data, is shown in Fig. 5. Based on the data in this figure, a value of $\alpha_s = 0.004$ was calculated for the coating in the spectral region of 330 to 540 nm and $\alpha_s = 0.007$ in 290 to 540 nm. The short wavelength limits are approximately the 50% reflectance points of the SI-100 and MSI-100 mirrors, respectively.

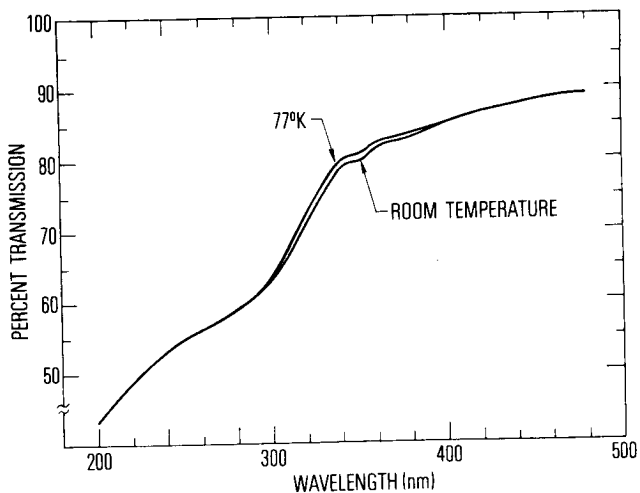


Fig. 3—Transmission of an OCLI conductive transparent coating at room temperature and 77° K including loss because of the dewar windows

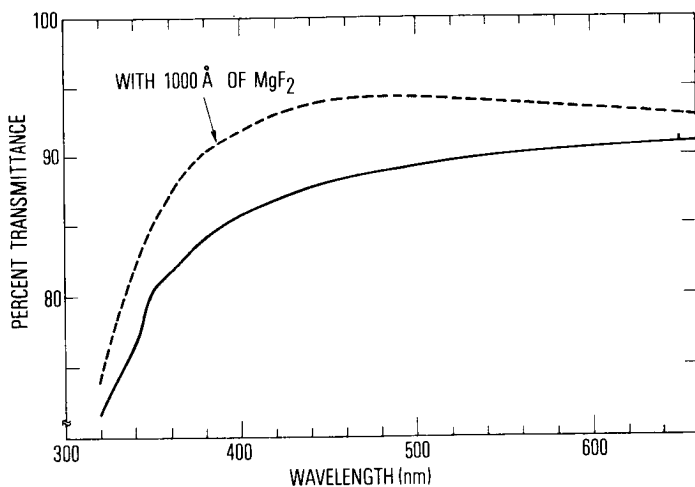


Fig. 4—Transmittance of an OCLI conductive transparent coating in air with and without an antireflection coating of MgF_2

Since the absorptance of a coated MSI-100 mirror has not been reported, for the purpose of an estimate, a calculation was made to determine the effect of a coating (Fig. 5) on two sample mirrors for which reflectance data were available. The sample mirrors had nominal $\alpha_s = 0.057$ (SI-100) and $\alpha_s = 0.042$ (MSI-100); $\Delta\alpha_s$ calculations were made in the two wavelength intervals mentioned above. It was found that the conductive coating would increase the mirror absorptance by $\Delta\alpha_s \approx 0.006$ for SI-100 type mirrors and $\Delta\alpha_s \approx 0.011$ for MSI-100 type mirrors.

The conclusion is that the coating would cause some increase in the solar absorptance for both mirrors but that the effects would be more severe in MSI-100, which has a lower absorptance than SI-100. The reason the increase in absorptance is larger for MSI-100 is that the absorption of the coating lies in a spectral region where MSI-100 mirrors have a high reflectance.

It was determined from the transmittance (Fig. 4) that the CC on fused silica caused a large loss because of the reflection at the CC-air interface. A solar cell with extended blue response covered in this manner would generate much less power. It was predicted that the reflection loss could be reduced by application of an antireflection (AR) coating of MgF_2 to the CC without inhibiting its conductive properties. A computer calculation indicated that 1000 Å of MgF_2 would maximize the transmittance of an optical stack of MgF_2 -CC- SiO_2 in the wavelength region from 350 to 600 nm. As a result, samples of CC on fused silica whose electrical conductivity and transmittance had been measured were coated at 232° C with 1000 Å of MgF_2 . The transmittance was measured subsequently and is also shown in Fig. 4. There is a noticeable improvement in the transmittance

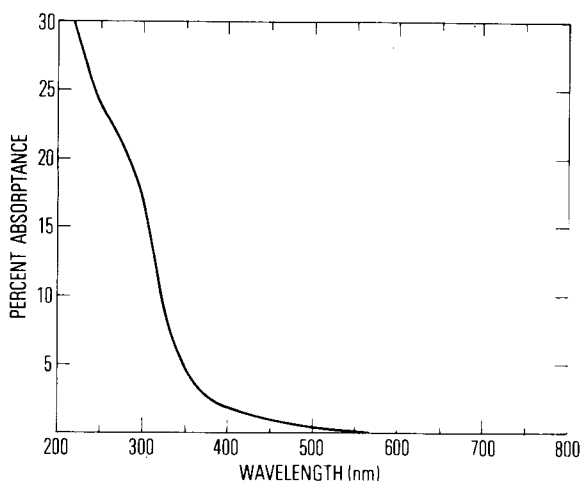


Fig. 5—Absorptance of an OCLI conductive transparent coating

at the peak of the solar intensity spectrum (460 nm). However, the CC absorptance is still evident below 420 nm. The electrical measurements after the deposition showed a 32% increase in the conductivity of the CC. Both these measurements indicate that an AR coating of MgF_2 would make the CC more desirable for use on a solar cell cover glass.

The remaining question of whether the AR coating would accumulate charge on its surface and render the CC ineffective was investigated by examining the time constant for the dissipation of charge deposited in the MgF_2 . One-keV electrons that have a calculated⁴ range of 144 Å in MgF_2 were swept across the MgF_2 surface. The resulting decay current was collected by the underlying CC with the sign of the charge deposited being positive. This indicated the secondary electron emission coefficient at this energy was greater than one. The observed time constant for the decay was one second; with this value as well as the estimated capacitance⁵ for a 1000-Å film of MgF_2 , the film resistance was calculated to be 10^9 to 10^{10} Ω/cm². Though this is a large resistance, it is not certain that it precludes the use of an AR coating on the CC. It will be necessary to consider a particular space environment and the electrical properties of the MgF_2 film in more detail.

ACKNOWLEDGMENTS

The authors wish to thank Dr. D. A. Lilly for his computer program that permitted calculation of the optimal AR coating thickness.

REFERENCES

1. Fry, J. and Nicoletta, C. A., "Ultraviolet and Charged Particle Irradiation of Proposed Solar Cell Cover Slide Materials and Conductive Coatings for the Helios Spacecraft," X-765-72-205, June 1972, Goddard Space Flight Center, Greenbelt, Md.
2. Fogdall, L. B. and Cannaday, S. S., "Proton and Ultraviolet Degradation Tests on Helios Spacecraft Materials," D180-17868-2, April 1974, Boeing Co., Seattle, Wash.
3. Kostlin, H. and Atzei, A., "Present State of the Art in Conductive Coating Technology," Photon and Particle Interactions with Surfaces in Space, R. J. L. Grard(ed.), D. Reidel Publishing Co., Dordrecht, Holland, 1973, pp. 333-341.
4. Feldman, C., "Range of 1-10 keV Electrons in Solids," Phys. Rev., Vol. 117, No. 2, 1960, pp. 455-459.
5. Weaver, C., "Dielectric Properties of Evaporated Films," Advances in Physics, Vol. 11, 1962, pp. 83-201.

AN EXPERIMENTAL SUMMARY OF PLASMA ARC EXPOSURES OF SPACE SHUTTLE HIGH-TEMPERATURE REUSABLE SURFACE INSULATION TILE ARRAY WITH A SINGLE MISSING TILE (Conducted at the Ames Research Center)

S. A. Galanter, *Rockwell International Space Division, Downey, California*

ABSTRACT

A Space Shuttle high-temperature reusable surface insulation (HRSI) tile array with a single missing or "lost" tile was exposed to a hot gas simulated reentry environment to investigate the heating conditions in and around the vicinity of the missing HRSI tile. Heat flux and pressure data for the lost tile condition were obtained by the use of a water-cooled lost tile calibration model.

The maximum aluminum substrate temperature obtained during the simulated reentry was 128°C (263°F). The lost tile calibration data indicated a maximum heat flux in the lost tile cavity region of 63 percent of the upstream reference value. This test was conducted at the Ames Research Center in the 20-MW semielliptical thermal protection system (TPS) pilot plasma arc test facility.

INTRODUCTION

HRSI is the TPS baseline material used on the Space Shuttle orbiter in areas where surface temperatures in the range of 640°C (1200°F) to 1260°C (2300°F) are expected. The baseline HRSI is a coated, high-purity silica material, fabricated into 15.4-cm (6-in.) square tiles. The tile thickness is established by the local aeroheating environment. Each tile is coated with a high-temperature ceramic on the top surface and down each side to improve handling, to control water absorption, and to provide a high surface emittance ($\epsilon = 0.85$). HRSI tiles are bonded with a silicone elastomer to a nylon felt strain isolator pad (SIP). The SIP is, in turn, bonded to the aluminum airframe structure with the same silicone elastomer. The maximum design allowable temperature for the aluminum structure is 177°C (350°F). The performance of the remaining TPS and the environmental impact on the orbiter were to be evaluated in the event that a tile was lost during flight.

The local heating environment was documented with the use of an instrumented, water-cooled, lost tile calibration model. The water-cooled calibration model is capable of enduring long exposures to the hot gas reentry environment without altering (melting) its geometry. Heat flux and pressure data were obtained throughout the simulated reentry to map the surface conditions of this unique geometry.

Figure 1 shows the predicted reentry bottom centerline peak heating distribution on the Shuttle orbiter for Trajectory 14040. Two body point locations were selected as test points for a lost tile test series because the regions have representative tile thicknesses of 5.08 cm (2 in.) and 7.62 cm (3 in.). A time history of the cold wall heating rate for Body Point 1220—5.08 cm (2 in.) tiles—is shown in Figure 2. This paper is a summary of the activities and results obtained from the Body Point 1220, 2-inch-thick tile lost tile test series conducted at NASA's Ames Research Center. A second model simulating the conditions at Body Point 1040 where the tile thickness is 7.62 cm (3 in.) is planned for testing at the Johnson Space Center.

NASA'S AMES TEST FACILITY DESCRIPTION

NASA's Ames Research Center 20-MW pilot TPS plasma arc facility was used for this test series (Figure 3). The arc jet

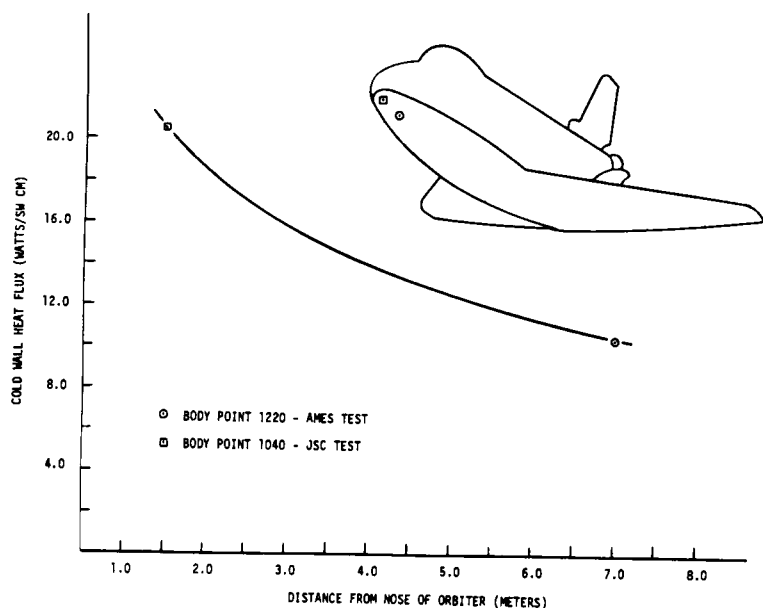


Fig. 1—Centerline peak heating distribution

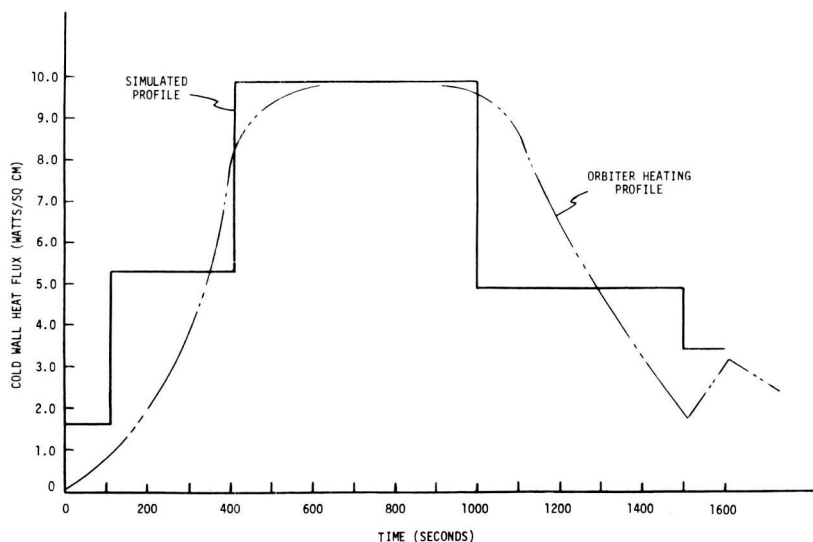


Fig. 2—Lost tile cold wall reentry heat flux history

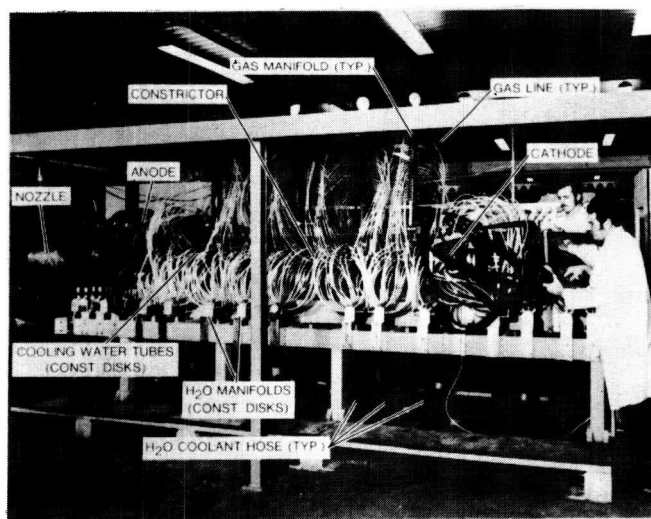


Fig. 3—NASA Ames 20-MW arc heater

is of the constricted arc design, consisting of a column of segmented water-cooled disks, which constitute an arc length of about 2.5 m (8.2 ft) and an inside diameter of 6 cm (2.36 in.). Air, heated by the arc, is accelerated through a semielliptical supersonic nozzle. The nozzle has an exit width of 43.2 cm (17 in.) and a peak height of 10.8 cm (4.25 in.). The exit Mach number is 5.5. At the nozzle exit, the test article is mounted on a table with three adjustable leveling screws to match the bottom flat surface of the nozzle. The table can be adjusted to vary the incident angle of attack. The higher the angle of attack, the higher the heating rate is. Other parameters that affect the heat transfer rate are electrical energy to the arc heater, mass flow rate, and test chamber pressure. By varying these parameters, one can select the test conditions at the model's surface that best match flight conditions. Once the flow travels past the test surface, it enters a diffuser where it is drawn from the test chamber by a large vacuum pumping system. Figure 4 shows the lost tile calibration model in test position. At the left is the semielliptical nozzle, in the center is the calibration model, and to the far right is the diffuser inlet.

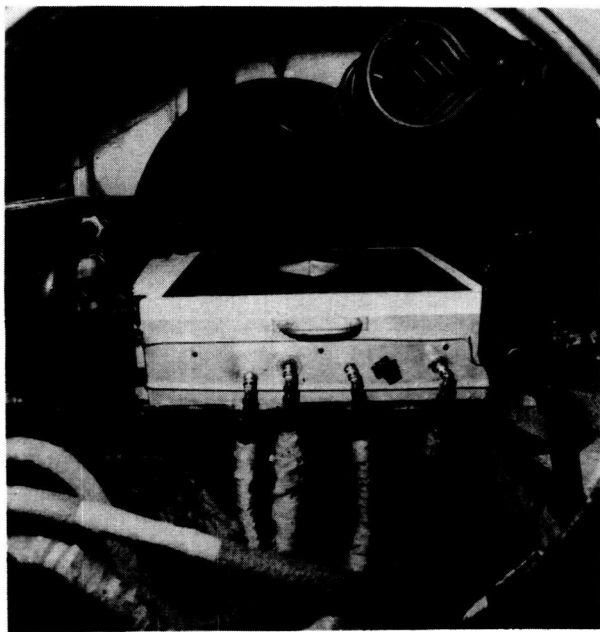


Fig. 4—Test chamber (semielliptical nozzle at left, calibration model in the center, and diffuser inlet at right)

TEST ARTICLE DESCRIPTION

Water-Cooled Lost Tile Calibration Model

The water-cooled lost tile calibration model is a geometric duplicate of the lost tile HRSI test article. It is constructed of individually water-cooled blocks of aluminum that are fastened to an aluminum base plate. Instrumentation consists of 12 asymptotic calorimeters (heat rate sensors) and 10 pressure ports. Three calorimeters were located upstream of the lost tile cavity; four were in the cavity floor; two were placed in the downstream cavity walls; and three more were positioned downstream of the lost tile cavity. Pressure ports were located next to each calorimeter with the exception of the sidewall calorimeters which had none. The location of each calorimeter is shown in Figure 5. Figure 6 shows the calibration plate prior to installation in the test chamber. The tubes in the front of the model connect the pressure ports to remote pressure transducers.

HRSI Test Article

The 61- by 61-cm (24- by 24-in.) HRSI test article was constructed of HRSI tiles 5.08 cm (2 in.) thick bonded to a thick representative substrate. The tiles were bonded to the aluminum

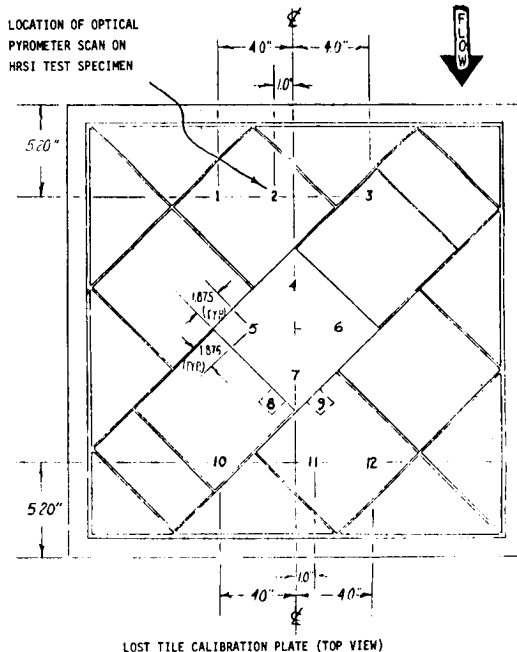


Fig. 5—Calibration plate calorimeter locations

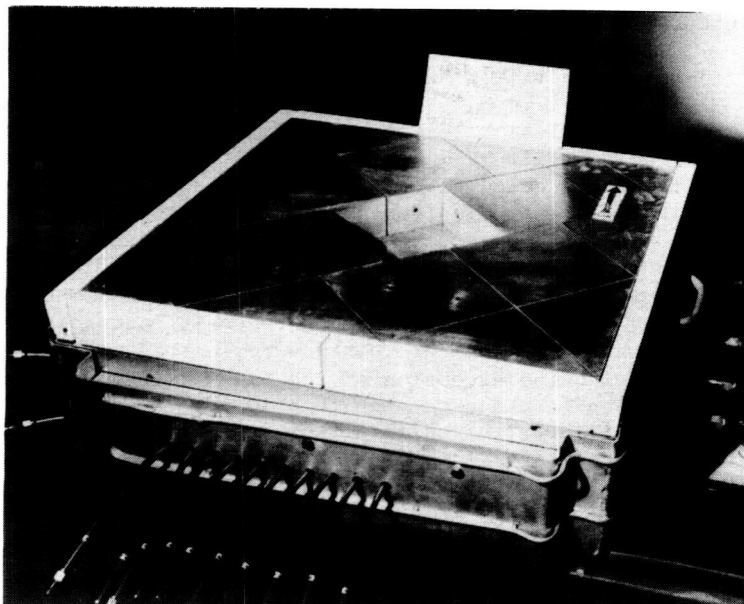


Fig. 6—Lost tile calibration model prior to installation in test chamber

substrate in the exact manner that they are to be installed in the Shuttle. The ceramic coating on most of the tiles was Lockheed 0042 formulation (original Shuttle baseline coating) except for three tiles located downstream of the lost tile cavity, which were coated with darker Lockheed 0050 coating (the new baseline coating). The SIP was bonded with the silicone elastomer to the floor of the lost tile cavity and then coated, again with silicone elastomer, on its top surface. This was done to simulate a tile separation at the silicone elastomer-HRSI bond line. Figure 7 shows the HRSI test article prior to testing. Instrumentation consisted of 26 thermocouples mechanically staked to various locations on the aluminum substrate. No thermocouples were located in the HRSI tiles.

An optical pyrometer was used to measure the surface temperature of the HRSI throughout the test. The pyrometer target on the HRSI test specimen corresponded to the location of Calorimeter No. 2 on the lost tile calibration model. (See Figure 5.)

EXPERIMENTAL PROCEDURE

To establish the baseline target heat flux values, as specified in Figure 2, data were gathered on a flat calibration plate before the lost tile calibration model was installed. This

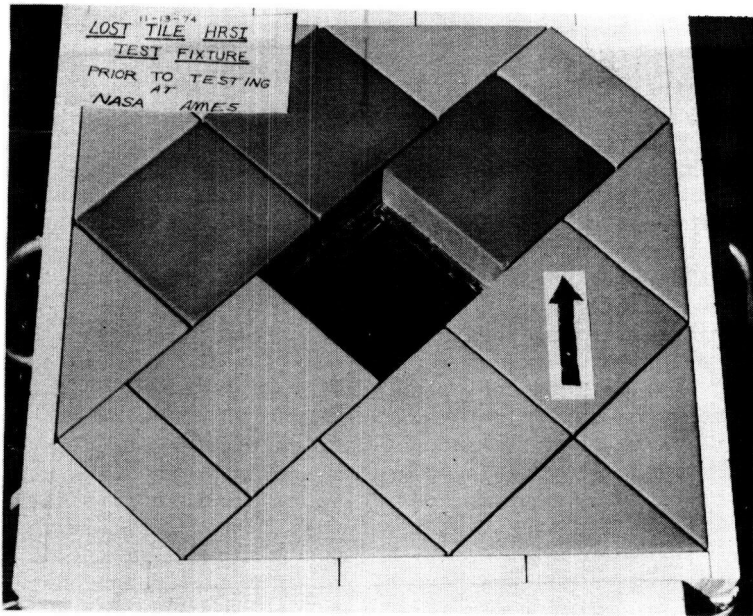


Fig. 7—HRSI test article prior to testing

plate was used for basic facility calibration and was provided by the Ames Research Center. The facility parameters (i.e., chamber pressure, mass flow rate, electric current, etc.) necessary to establish the target heating rates were recorded and used to establish subsequent operating conditions. The lost tile calibration plate was utilized to fine-tune the tunnel settings to closer agreement with the target heat flux values and to obtain heating rates throughout the lost tile cavity. Linking all the test points together for the necessary lengths of time subsequently formed the simulated reentry step profile shown in Figure 2.

It was desired that the tunnel settings, once fixed, remained the same from one run to the next. A tolerance of ± 10 percent was specified, and "repeatability" runs were performed to verify satisfactory operation. This was necessary because no real-time monitoring of heat flux was possible during the testing of the HRSI specimen. By fixing the tunnel settings (established from the calibration plates) and demonstrating repeatability, the proper HRSI heating rates during testing could then be inferred. After the above preparation, the HRSI test specimen was subjected to the established heating conditions.

RESULTS

Lost Tile Calibration Model

Results show that the heating rate on the floor of the lost tile cavity is much lower than the reference heating values shown in Figures 8 and 9. Figure 10 displays a nondimensional heat flux (with respect to Calorimeter No. 2) far less than unity (0.10) for those areas on the upstream tile cavity floor. The downstream floor region experiences a somewhat higher ratio (approximately 0.60).

The calorimeters located on the downstream tile cavity walls experience a heating rate somewhat higher than the reference value (Figure 11). It is interesting to note that the heating distribution is nonsymmetric on the cavity walls. This may be due to the orientation of the tile gaps at that particular location on the array. If the flow tends to follow the gaps, then the heating would indeed be nonsymmetric. But, because pressure port data are not available for these two locations, it is difficult to verify this possibility.

Localized heating downstream of the tile cavity approaches a value of about 0.7 of the reference value. However, at the location directly downstream of the aft tile apex, the heating rate is closer to the reference value, indicating the possibility of induced turbulence caused by the lost tile cavity (Figure 12).

The pressure data indicate that the pressure decreases as the distance from the nozzle exit plane increases. The exception is Pressure Port No. 9, corresponding to Calorimeter No. 11. Both indicate higher values than the general distribution, probably because of the presence of the lost tile cavity (Figure 13).

HRSI Test Fixture

Figure 14 shows centerline thermocouple locations as a function of temperature. The region located on the substrate and underneath the tile cavity yields higher temperatures than areas protected by the HRSI. Maximum substrate temperatures are in the downstream lost tile cavity region, as expected. The maximum substrate temperature (128°C or 263°F) occurred 1160 seconds into the reentry cycle. A single localized area was scanned with an optical pyrometer at a location equivalent to the site of Calorimeter No. 2 on the lost tile calibration model. This location yields a maximum surface temperature of 862°C (1580°F) at 450 seconds into the reentry. A time-temperature history is presented in Figure 15.

Comparison of Figures 7 and 16 illustrates the contrast between the HRSI tile array before and after plasma arc exposure. The white material on the outside regions of the HRSI tile array (Figure 16) is from the water-proofing material which is sprayed over the tiles after manufacturing to seal regions of the tile that are closest to the aluminum substrate and below 314°C (600°F).

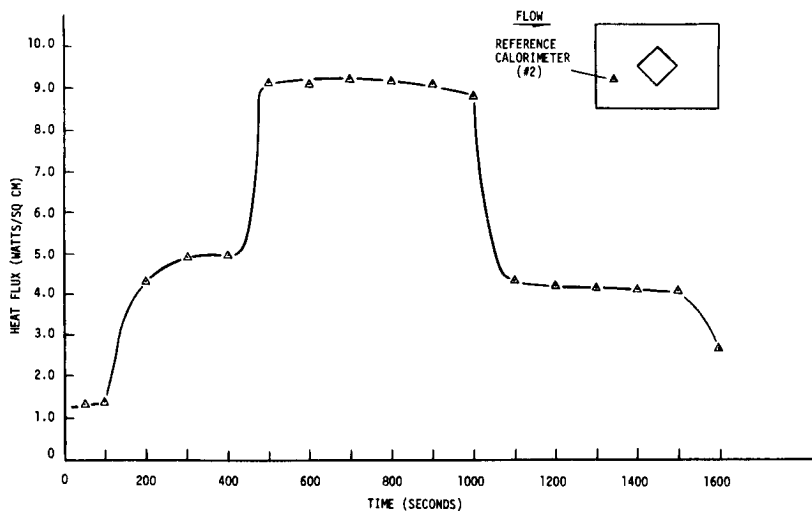


Fig. 8—Reference heat flux time response

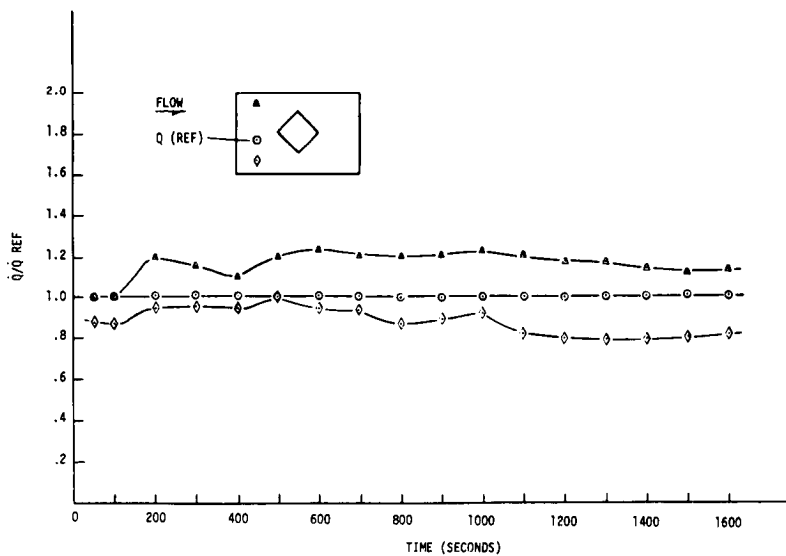


Fig. 9—Upstream nondimensional heat flux time response

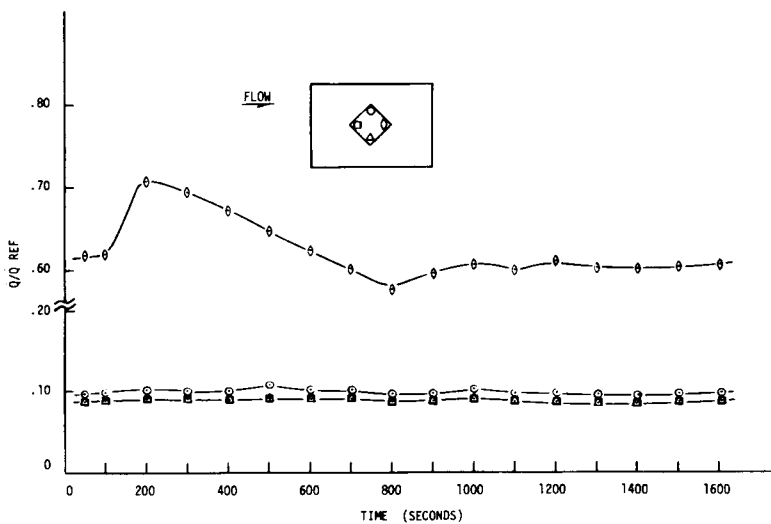


Fig. 10—Cavity floor nondimensional heat flux time response

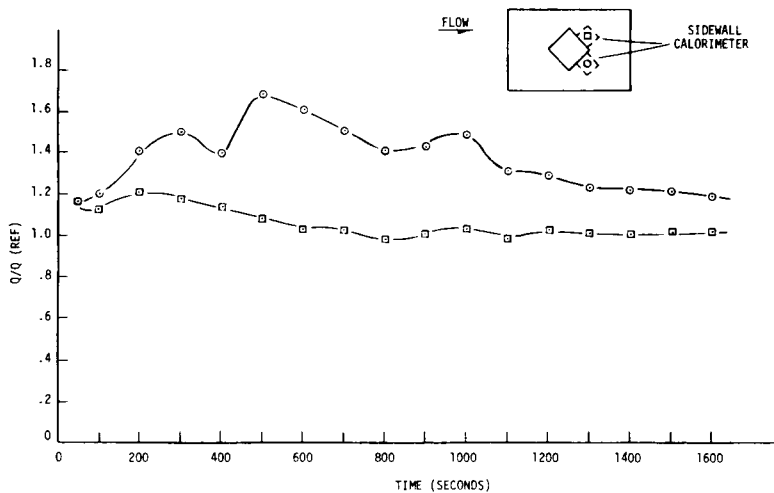
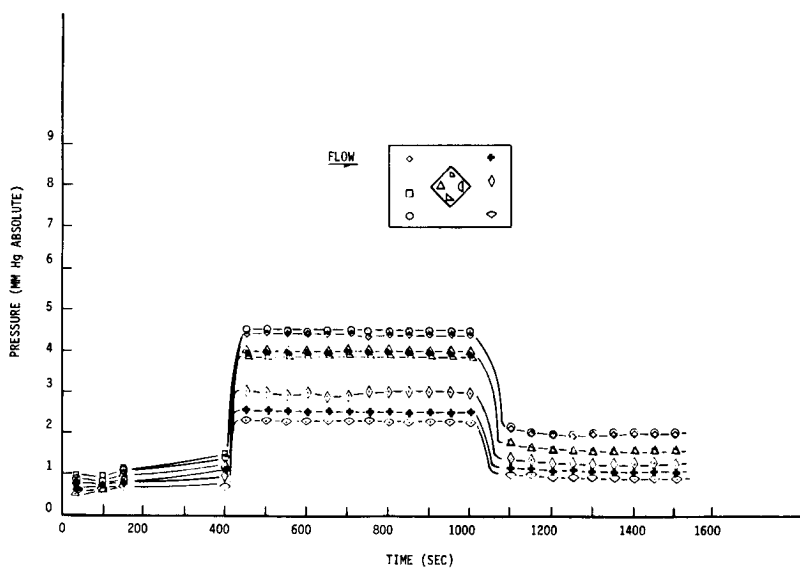
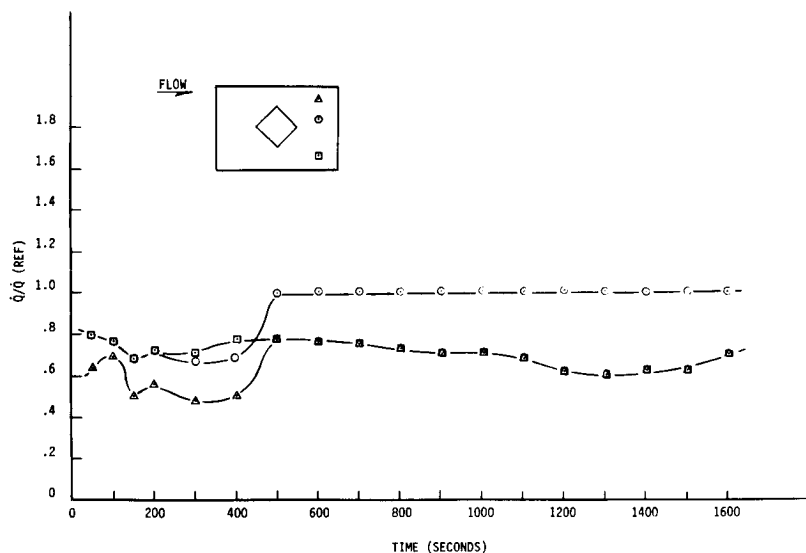


Fig. 11—Cavity sidewall nondimensional heat flux time response



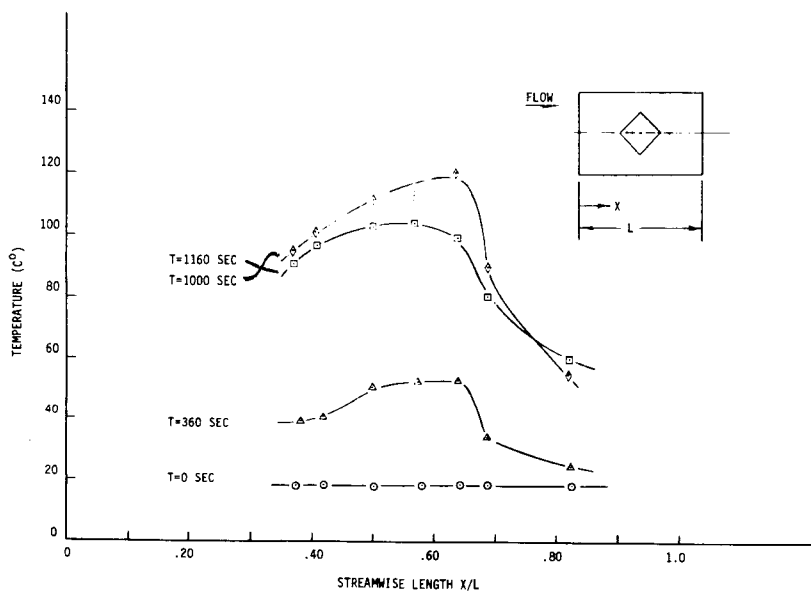


Fig. 14—HRSI substrate temperature versus centerline location

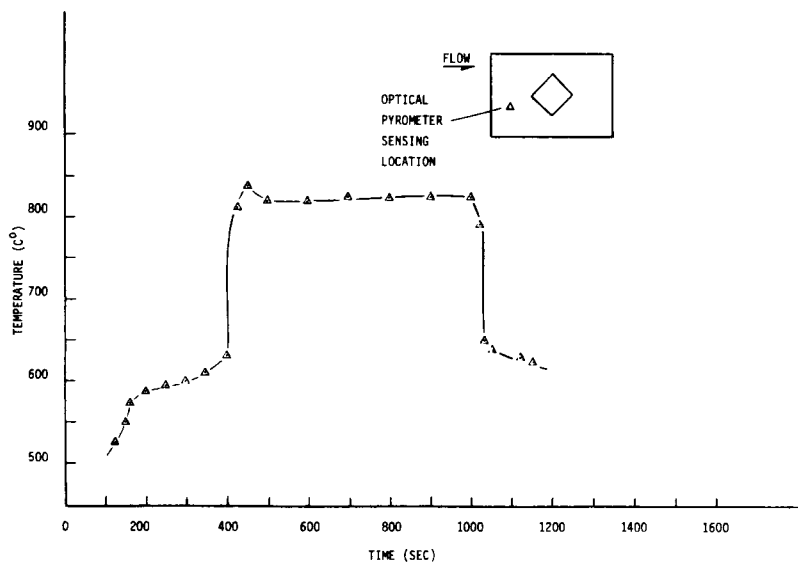


Fig. 15—HRSI surface temperature-time response

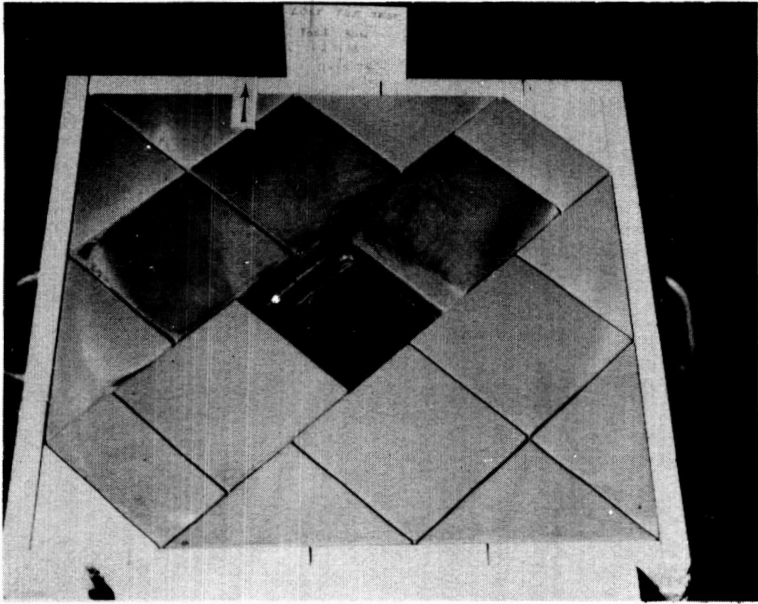


Fig. 16—HRSI test article after simulated reentry

A NEW ARC HEATER SHROUD TEST TECHNIQUE FOR THERMO-STRUCTURAL TESTING OF FULL-SCALE, NOSE-TIP SKIRT MATERIALS

R. R. Williams and J. W. Stultz, *McDonnell Douglas Research Laboratories*, and R. J. Popp, *McDonnell Douglas Astronautics Company, St. Louis, Missouri 63166*

ABSTRACT

A new arc heater shroud test technique has been developed for thermostructural testing of full-scale, missile nose-tip skirt assemblies. Reentry trajectory simulation is provided by changing the arc heater operation in a prescribed manner through manual and automatic controls. Excellent test repeatability allows screening of materials by direct comparison of test results. Continuous recordings of model surface temperature, pressure, heat flux, and model internal temperatures are made at several locations during the test.

INTRODUCTION

The development of improved missile nose-tip skirt materials involves evaluation of the ablative/insulative performance and the mechanical properties of each material at flight temperatures. Relatively inexpensive, arc heater facility material tests using sub-scale wedge samples are suitable for material screening. Several programs¹⁻³ of this type have been conducted in the McDonnell Douglas Research Laboratories (MDRL) High Impact Pressure (HIP) arc heater facility.⁴ However, because these wedge samples are only sections of the skirt, the thermal stresses developed during testing are relieved by expansion of the sample. Thus, the stresses developed during flight in the full 360 deg skirt are not duplicated.

In the past, thermostructural data have been obtained by testing full-scale nose-tip assemblies in the more expensive rocket engine test facilities.⁵ The new MDRL shroud test technique provides a means of obtaining the desired simulation for material thermal and structural evaluation at flight temperatures with economical arc heater facility tests. In this method, a shroud is used to confine the high-temperature, high-pressure air produced by the arc heater along the surface of the full-scale nose-tip skirt. The shroud contour is tailored to the model contour to provide simulation of reentry flight conditions along the surface of the skirt. Model surface and in-depth temperature data are obtained during the tests, as well as surface heat flux and pressure measurements.

DESCRIPTION OF EQUIPMENT

The shroud thermostructural test technique was developed in the MDRL HIP arc heater facility. The equipment involved included the MDC-200 arc heater,⁶ the shroud assembly, the nose-tip skirt model assemblies, the calibration model, and the associated facility and model instrumentation. The following sections describe these items and their interaction.

MDRL HIP Arc Heater Facility

The MDRL HIP arc heater facility was built primarily to provide reentry simulation for missile systems. In this capacity, it has been used to test various nose-tip plug materials, antenna window materials, skirt materials and other heat-shield materials. The MDC-200 arc heater is capable of providing a model impact pressure greater than 200 atm, the highest pressure available in any arc heater facility. When testing nose-tip plug materials, a laser-controlled servosystem, the Model Surface Recession Compensator⁷ (MSRC) system is used to maintain constant test conditions on the model throughout the test. This is done by moving the model upstream as the surface recedes because of thermochemical and/or mechanical material removal. Past HIP facility tests of nose-tip skirt materials and antenna window materials as well as other heat-shield materials have exposed wedge or inclined plane models to the test stream. These models are positioned at an angle-of-attack near the exit plane of a rectangular nozzle such that the flow impinges on the test surface at the desired location. Good ablative/insulative material performance data are obtained in this manner.

Shroud Assembly

The shroud developed for the thermostructural test program was designed specifically for use with the MDC-200 arc heater and a 0.75 in. radius hemisphere nose tip, 7 deg half-angle cone skirt model. The shroud-model assembly takes the place of the supersonic nozzle normally attached to the exit of the arc heater. Figure 1 shows the arc-heater/shroud-assembly and the model assembly which has been withdrawn from the shroud to show its characteristics. During the test, the model is completely inside the shroud so that only the phenolic shield surrounding the sting support is visible. Flow is from left to right in this photograph. As can be seen in Fig. 2, the minimum flow area is provided by the shroud liner and the model nose-tip. The shroud liner and model nose-tip are water-cooled copper to provide stable arc heater performance independent of skirt surface recession. The shroud liner provides 12 instrumentation pass-throughs, three equidistant in each of four axial planes. The axial station farthest upstream is in a region of structurally stable walls and serves as a check on test condition repeatability. The remaining three axial stations are in the skirt material region and are used to provide skirt performance and test condition histories.

The shroud stainless-steel housing is designed to mount directly to the arc heater exit. The skirt model assembly is mounted on one arm of the model actuator system. This arrangement allows assembly and mounting of the model outside the shroud and then insertion and alignment of the model in the shroud.

Model Assemblies

The test model, Fig. 3, is a representative-size plug nose-tip section. The tip of the graphite plug has been replaced for test by a water-cooled tip to provide an unchanging contour at the sonic point. Analysis indicates that the presence of the cooled tip and its water supply tubes do not significantly alter the tungsten or graphite temperatures. This graphite spacer also has a typical nose-tip plug contour at the skirt interface to simulate flight hardware. The remainder of the skirt is backed by a tungsten sub-tip. The entire assembly, including internal thermocouples, was bonded using Epon 956.

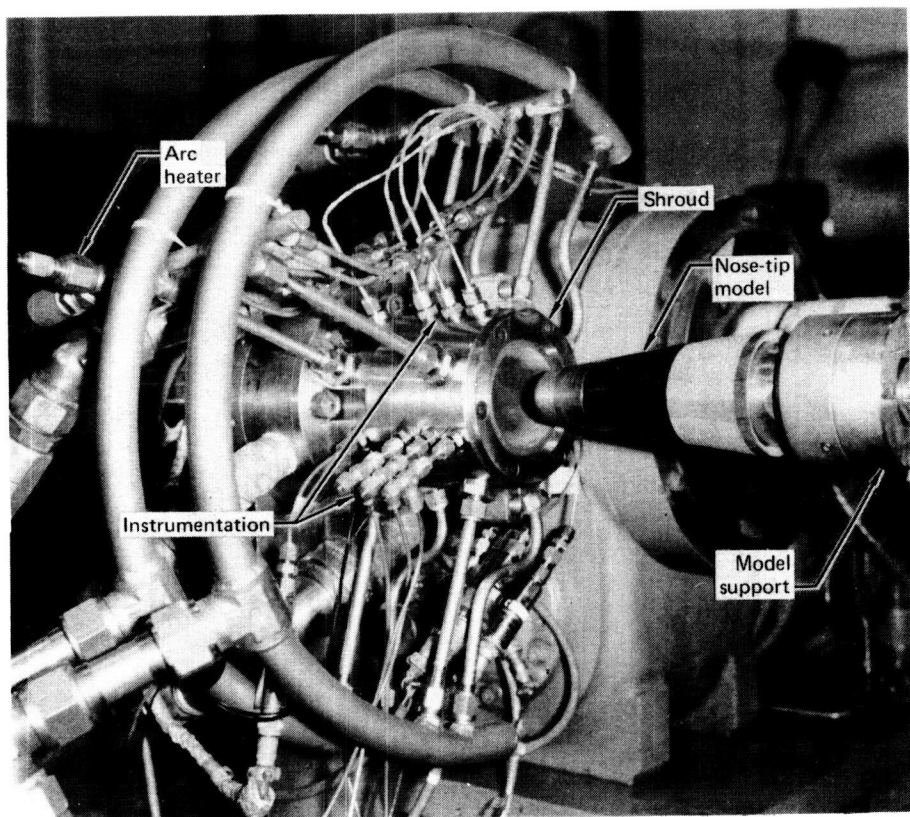


Fig 1 Arc-Heater/Shroud-Assembly

GP75-0652-10

As shown in Fig. 3, the skirt models have nine internal thermocouples carefully located to assist in the post-test thermostructural analysis. Thermocouples 1 and 9 were platinum/platinum-10% rhodium; the remainder were chromel/alumel. Additional thermocouples and/or other locations are possible.

A water-cooled copper model was used for calibration of the system during the initial phase of the program. This model had the same external size and shape as the skirt model and, in addition, contained a pressure port at the stagnation point. Use of this model allowed checkout of the system and technique and provided cold-wall calibration data.

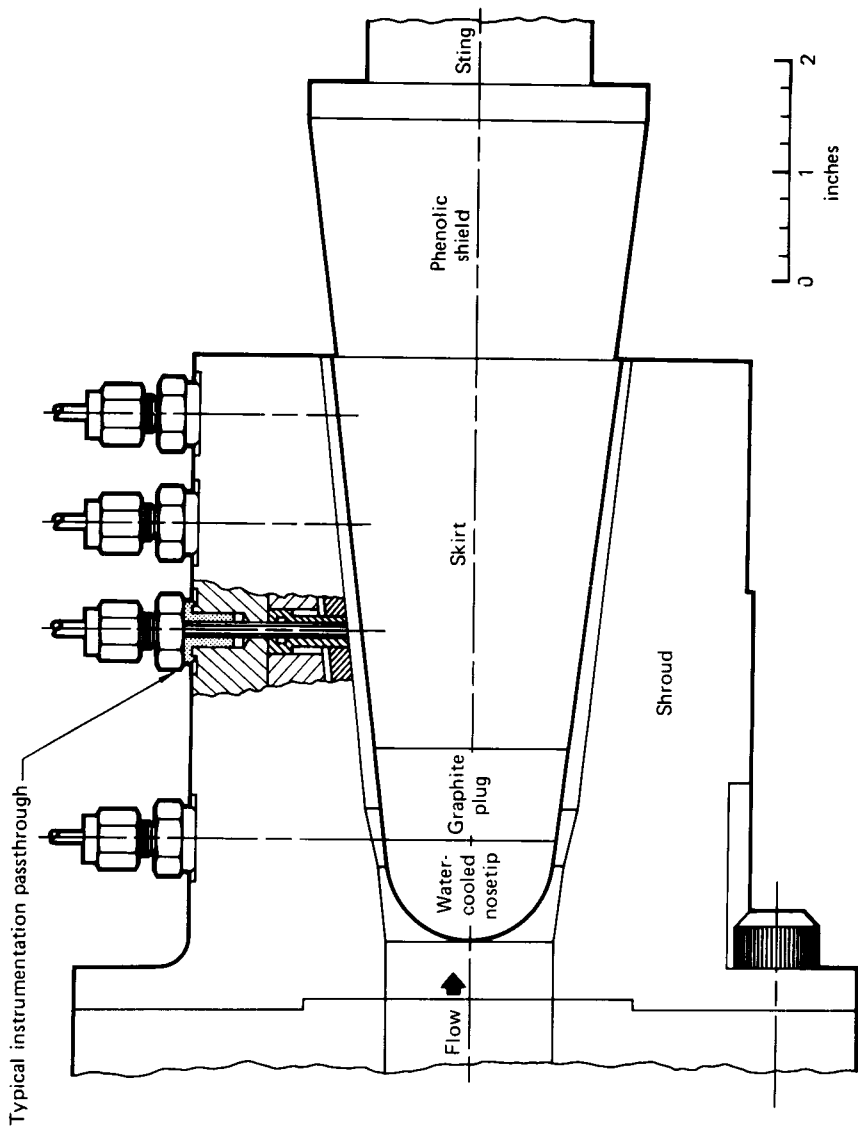


Fig 2 Model position in shroud during test

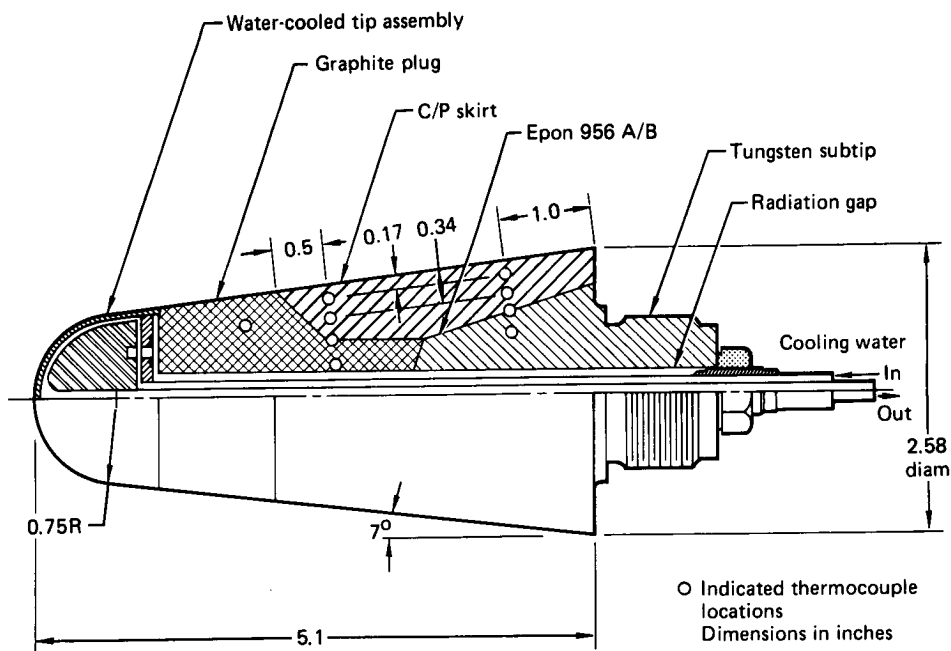


Fig 3 Thermostructural test model

GP75-0652-3

Instrumentation

Each of the shroud assembly instrumentation pass-throughs was designed to accept a 0.125 in. diam probe. One pass-through at each axial location was angled to provide flush sensor alignment at the shroud-liner inside surface. This was necessary for the calorimeters since they could not be formed to the shroud liner contour. The other pass-throughs were perpendicular to the shroud assembly centerline. The pressure probes were hand formed to be flush with the liner inner contour, and the fiber optic sensors were positioned approximately 0.5 in. from the inner surface.

The shroud instrumentation consists of pressure sensors, calorimeters, and photovoltaic pyrometers to sense the model surface temperatures. The water-cooled, Gardon-type calorimeters were made by Thermogage, Inc., to MDRL specifications. Each sensor is individually cooled and provides local heat flux data throughout the test. Calorimeter data obtained from tests using the calibration model are attributed to stream heating, while those obtained during an ablation model test include additional heating resulting from radiation from the hot ablating surface.

The model surface temperature is monitored throughout the test using gas-purged, fiber-optic probes to provide an optical path to silicon detector photovoltaic pyrometers. Each of these 0.125 in. diam probes provides local model surface temperature data directly across the instrumentation pass-through. The effective spot size of the probes is 0.020 in. and the spectral response of the detectors is centered around $0.8 \mu\text{m}$.

The static pressure in the flow annulus was sensed using 0.065 in. diam ports and pressure transducers mounted near the shroud housing to enhance the overall response.

During the calibration phase, four calorimeters and eight pressure probes were used to obtain axial heat flux and pressure distributions. Since measurement of the water-cooled calibration model temperature was unnecessary, the normal temperature sensing pass-throughs were occupied by additional pressure sensing systems to allow a symmetry check by measurement along two stream lines.

During the skirt model tests, the pressure sensing systems at stations 2, 3, and 4 were replaced with fiber-optic probes. A pressure symmetry check remain at station 1 located in the water-cooled nose-tip region.

The standard HIP facility instrumentation was used to monitor the performance of the arc heater and associated subsystems. All pertinent data were recorded on the MDRL Digital Data Acquisition System which utilizes a Varian 620f computer.

THERMOSTRUCTURAL SIMULATION

The main function of the shroud is to confine the high-temperature, high-pressure arc heater exhaust along the model surface. Without this confinement, the flow would expand to ambient pressure, and the resultant skirt surface pressure and heat flux would be low in comparison with the flight environment. In addition, the shroud provides efficient application of the test stream energy in the skirt area of the model.

Figure 4 presents the trajectory selected for simulation. This typical skirt re-entry environment was selected based on requirements of the initial materials program⁸ using the MDRL shroud test technique. Other trajectory simulations are possible within the limits of the arc-heater/shroud capabilities. The pressure experienced by the skirt during this reentry is below the level required to affect the material performance through mechanical material removal. Also, for the materials of interest in this program,⁸ the chemical reactions are not pressure dependent. Thus, the prime consideration was to simulate the flight heat-flux to enthalpy ratio trajectory at conditions sufficient to produce the surface temperatures associated with material ablation. For example, a constant heat flux test would provide a high initial heat-flux to enthalpy ratio with subsequent high material loss.

Although not included as a direct part of the work reported herein, some mention of material performance analysis is appropriate. For most ablation materials, the effective heat of ablation is a function of enthalpy; this function varies for different materials according to

$$H_{eff} = \frac{\dot{q}}{\dot{m}} = f(h), \quad (1)$$

or

$$\dot{m} = \frac{\dot{q}}{f(h)}, \quad (2)$$

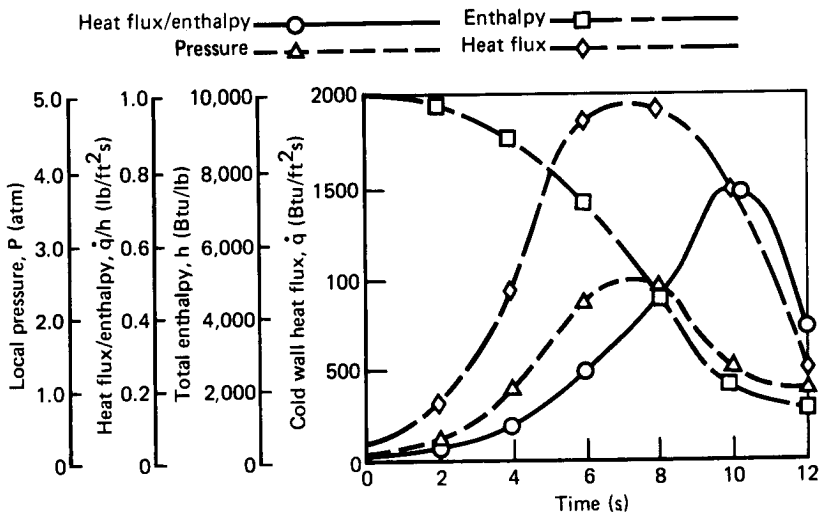


Fig 4 Typical RV skirt reentry environment

GP75-0652-1

where H_{eff} = effective heat of ablation,
 \dot{q} = heat flux,
 \dot{m} = material mass loss rate, and
 h = enthalpy.

Thus, by simulating the proper \dot{q}/h ratio trajectory, a mass-loss history can be produced that is similar to that experienced during flight. These data can then be used to verify earlier-derived thermal models, and the material performance during flight can be calculated using these thermal models.

EXPERIMENTAL PROCEDURE

Comparative analysis of the material performance based on data from different tests is greatly simplified if the test conditions are repeatable. This was not entirely possible, but the experimental procedure was established with test repeatability as a prime consideration. An automatic air flow-rate control system was installed to provide automatic control of two air flow-rate levels, the time at each level, and the slope of the ramp between the two levels. The other factor affecting repeatability was the arc power level, or more specifically the arc current, which was controlled manually. Early difficulties in arc current control were overcome with increased arc heater operator experience. Overall repeatability of the heat-flux to enthalpy ratio achieved was $\pm 5\%$.

Figure 5 shows some of the arc heater performance data for a typical test. Only the arc current, air flow-rate, chamber pressure and enthalpy are plotted to illustrate the experimental procedure and the resultant simulation. As can be seen in Fig. 5, the arc current, once initiated, rapidly attained the desired level and was maintained fairly constant. After the arc power was activated, and main air valve was opened, and the air flow-rate was increased to the first pre-set level. As the arc heater operator increased the arc current to the desired level, a set-point relay was closed which in turn initiated two timers. The first timer controlled the test time at

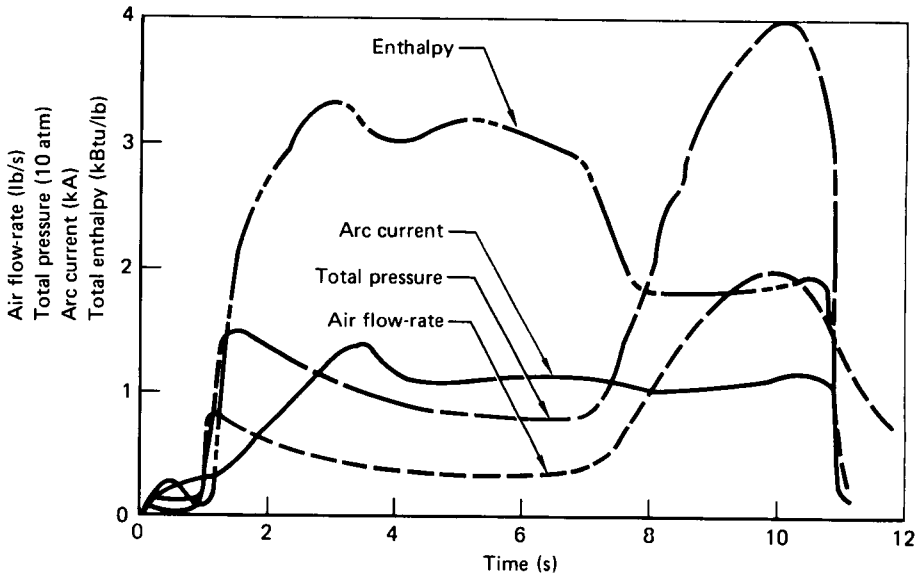


Fig 5 Typical arc heater shroud performance during trajectory simulation test

GP75-0652-4

the lower air flow-rate condition, and the second timer controlled the total test time. When the first timer expired, the automatic air flow-rate system started to increase the air flow-rate at a predetermined rate to the pre-set higher level. The air flow-rate was maintained at this higher level until the second timer expired and then quickly reduced to the lower level. At this time, the arc current was rapidly decreased and the test was terminated.

Immediately after test shutdown on ablation model tests, the main air valve was closed to minimize the amount of cold gas flowing over the hot model. Data acquisition was continued until maximum model internal thermocouple responses occurred. Physical measurements and several photographs were taken of each model before and after testing. The model bulk surface recession was determined in this manner on a minimum of three rays.

The reported results are from tests using the water-cooled calibration model. The purpose of these tests was to provide cold-wall calibration data. Typical test condition histories are shown in Fig. 6 (see Fig. 5 also). The heat flux and static pressure shown are the average values from stations 3 and 4. The data from station 2 calorimeter during these tests were intermittent. Smooth transition is exhibited in all parameters during the trajectory simulation.

The good repeatability of the shroud test conditions is shown in Fig. 7 where the stream enthalpy, model surface pressure, and heat flux are shown as functions of stream total pressure. The data are from two tests which differed somewhat in initial and final programming in order to better fit the target trajectory. This can be seen primarily in the stream enthalpy and the model surface heat flux. The majority of the two tests, however, were similar and exhibit good repeatability.

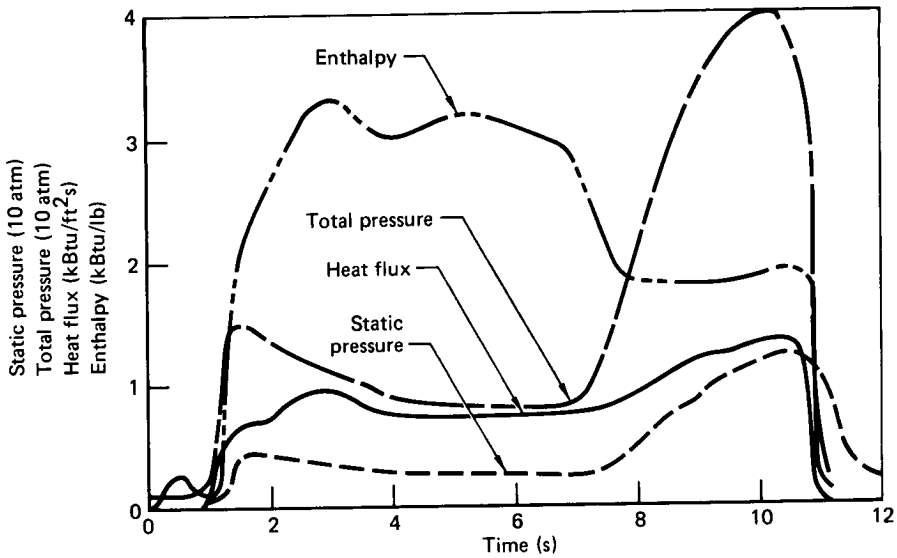


Fig 6 Test conditions in skirt region during trajectory simulation test

GP75-0652-5

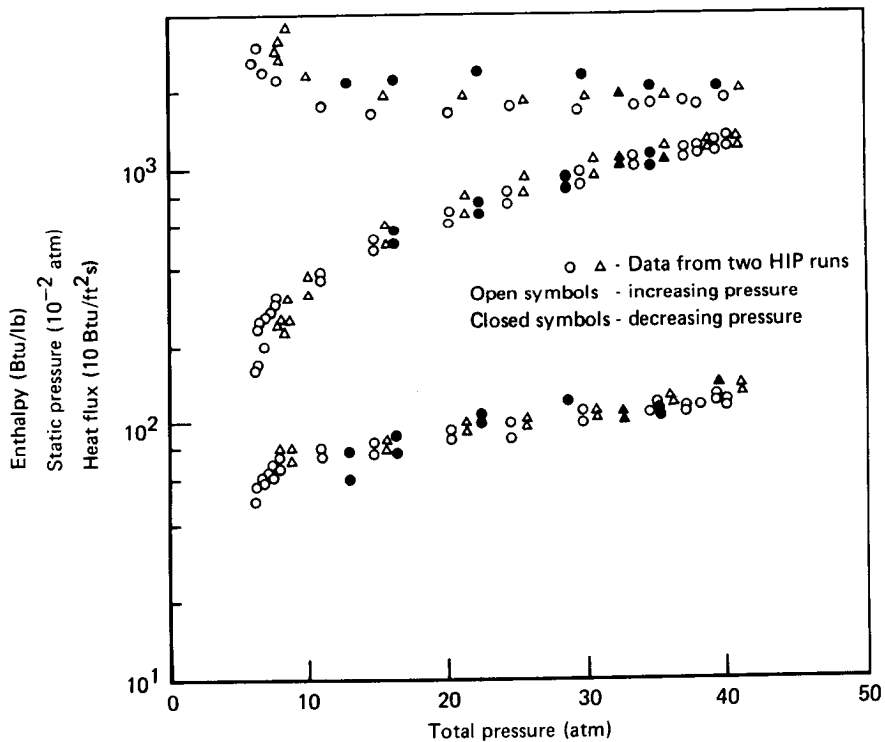


Fig 7 Test condition repeatability

GP75-0652-6

The heat flux to enthalpy ratio is the environmental parameter to which the test material is most responsive. This ratio in the two tests is presented in Fig. 8 and compared to the target trajectory. The response of a typical carbon phenolic skirt material, R6300, to the test environment was calculated and compared with the predicted response of the same material to the flight trajectory. These responses, shown in Fig. 9, agree and assure a good test of the skirt material.

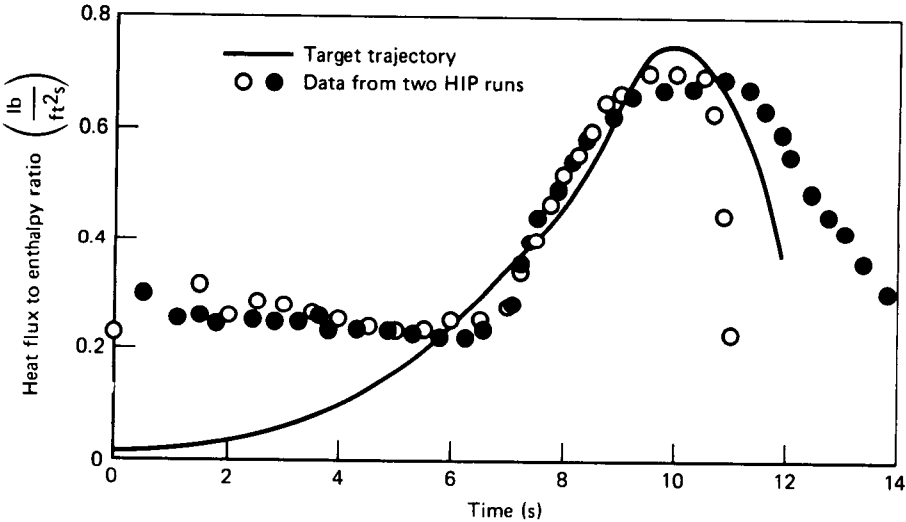


Fig 8 Trajectory simulation

GP75-0652-7

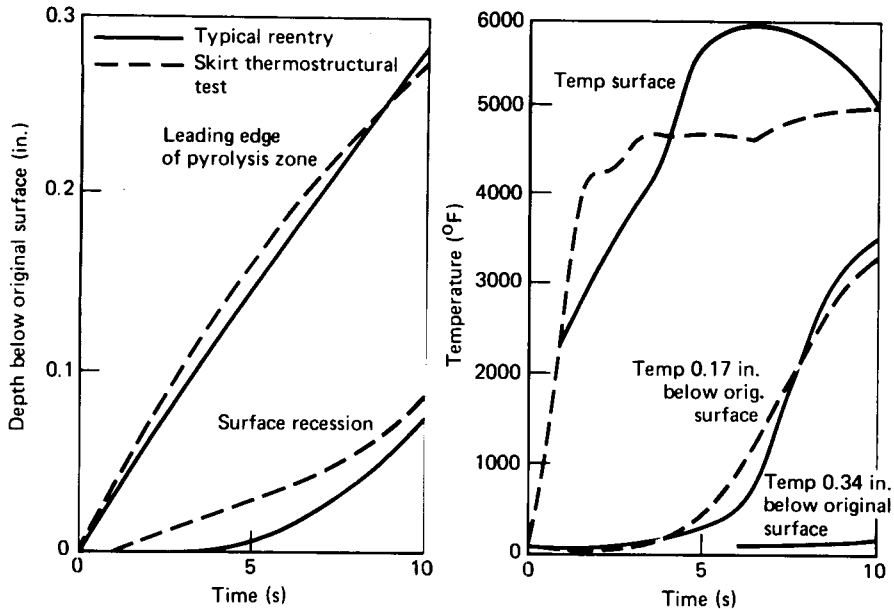


Fig 9 Nominal skirt response during reentry and test

GP75-0652-2

CORRELATION OF RESULTS

The surface heat flux and pressure produced at the model surface using the shroud technique were predicted assuming turbulent flow in an annulus. Calculation of heating rates were based on the McAdams' equation:⁹

$$Nu = 0.023 (Re)^{0.8} Pr^{0.4} \quad (3)$$

where Re is the Reynolds number and Pr is the Prandtl number.

The actual data as seen in Fig. 10 show a slightly higher than expected heating rate. Parameters not taken into account in the initial prediction and which could result in the slight discrepancy of Fig. 10 are surface roughness, heat flux distribution, and departure from equilibrium flow upstream of the model surface.

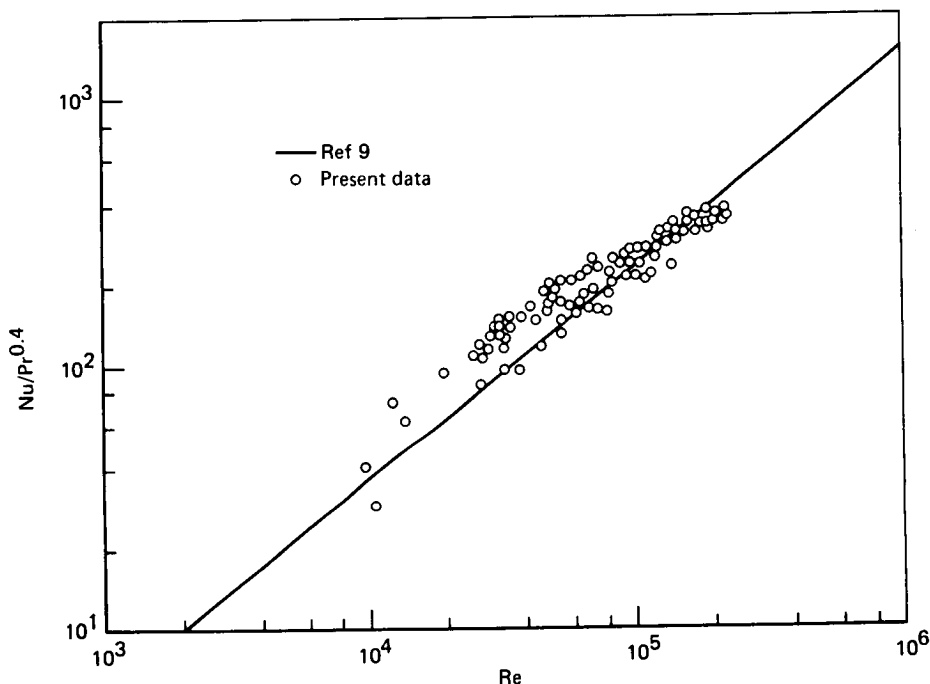


Fig 10 Heat transfer correlation

GP75-0652-8

The stream total properties obtained from the arc heater operating characteristics were combined with the measured model surface conditions to determine the capability envelope for the shroud. Figure 11 shows the resultant simulation capability of the shroud test technique. Within the limits of facility response times, all trajectories which fall within this envelope can be simulated. Also shown in Fig. 11 are the data from the two trajectory simulation tests.

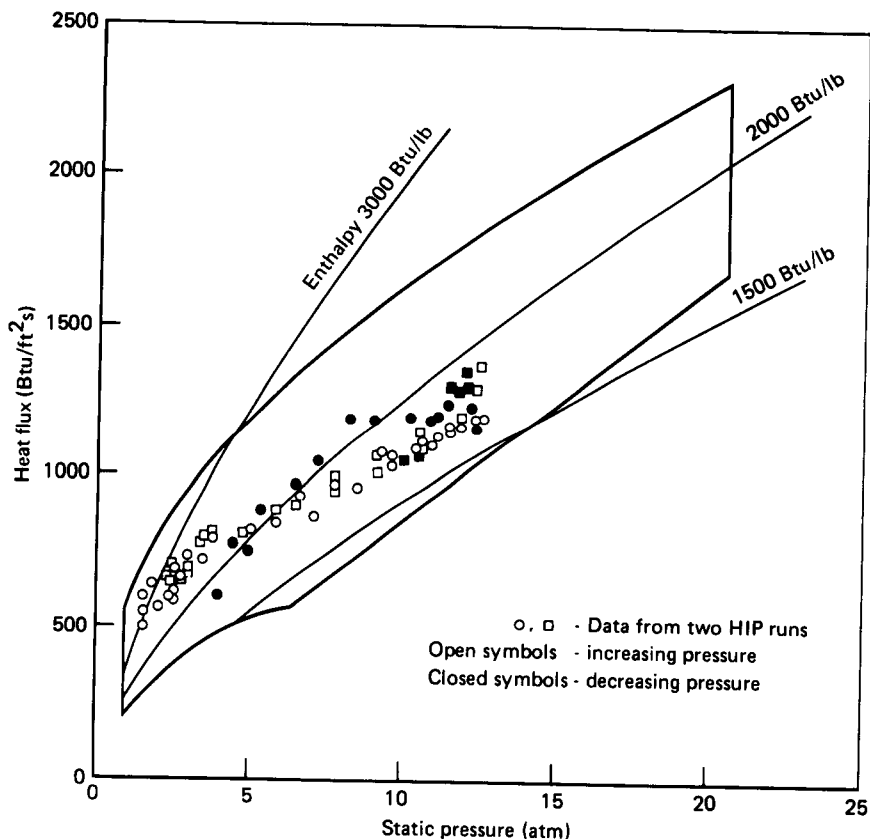


Fig 11 Shroud capability envelope

GP75-0652-9

CONCLUSIONS

An economical arc-heater/shroud test technique has been developed to provide thermostructural simulation for nose-tip skirt development testing. Inspection of the test results show the simulation to be repeatable and uniform in the skirt region. The flowfield is turbulent and fully developed in the model skirt region. Based on the shroud test results obtained to date and previous arc heater performance, a capability envelope has been calculated which provides a wide range of model surface conditions. Although the simulation presented was developed to test RV nose-tip skirts, the facility is attractive for other applications:

- Heat-shield material performance documentation - the facility provides uniform, nearly parallel, flowfield (unlike splash-type wedge tests), trajectory simulation, and continuous record of test environment.
- Subscale thermostructural test of ring antenna,
- Thermostructural tests of rocket motor throats and their coatings - this is accomplished by a water-cooled center piece with the test material and extension of the shroud.

REFERENCES

1. R.J. Popp, Engineering Improvements for Heat Shield, McDonnell Douglas Report MDC E0874, July 1973.
2. R.R. Williams, Metallic Materials Ablation Tests in the MDRL HIP Facility, McDonnell Douglas Report MDC Q0516, February 1974.
3. R.R. Williams, MK400 Nose Plug, Heat Shield and Antenna Window Material Ablation Tests in the MDRL HIP Facility, McDonnell Douglas Report MDC Q0524, April 1974.
4. W.A. Rinehart, J.H. Painter, R.R. Williams and R.A. Williamson, High Impact Pressure (HIP) Arc Heater Facility, 17th Annual IES Technical Meeting, Los Angeles, California, April 1971.
5. Aeronutronic Engineering Rocket Motor Test Facilities, Philco-Ford Corporation, Aeronutronic Division Publication No. U5022, April 1972.
6. J.H. Painter, R.J. Ehmsen and R.B. Helm, Development of the MDC-200 Arc Air Heater, McDonnell Douglas Report MDC Q0432, July 1972.
7. R.A. Williamson, W.A. Rinehart and R.R. Williams, Laser Activated, Model Surface Recession Compensator System for Testing Ablative Materials, AIAA Paper No. 73-380, March 1973.
8. Low Recession Woven Carbon Fiber/Resinous Plastic Skirts for Reentry Missile Plug Nose Tips, USAF Contract F33615-74-C-5048, 1 May 1974.
9. W.H. McAdams, Heat Transmission, McGraw-Hill, New York, 168, 1942.

SPIN TEST ON HELIOS LOUVER

F. Joó, *Space Simulation Institute, 5 Köln 90, F. R. Germany*

ABSTRACT

The task of the qualification test described was to investigate how the spin motion of the solar probe modifies the characteristic of the louver, i.e. the dependency of the blade position on temperature.

INTRODUCTION

In the course of planning and construction of HELIOS solar probe special attention has been paid to thermal control. Since the radiation energy absorbed by the spacecraft shows a great variation along the orbit, an "active" regulator (louver) has been designed by ERNO, Bremen, for regulating temperatures.

As the spin axis of the probe is perpendicular to the ecliptic plane the top and bottom plates cannot be irradiated by the sun. Therefore they are very suitable to emit the heat energy from the central compartment into space. So the louvers are located on these plates.

On the top plate the louver consists of a number of blades arranged in ring shape. This ring is assembled from 8 separate units containing 6 blades each, which can be turned around their radially directed shafts. Further two units are mounted underneath the antenna.

On the bottom plate 5 of such units are placed.

The blades are manufactured from aluminium honeycomb material. Each of them is fitted with a bimetal spiral spring coupled to its axis, which turns the blade into a position depending on the temperature.

The springs are so calibrated that the blades stand perpendicularly ($\alpha = 90^\circ$) to the plate at a temperature of $+18^\circ\text{C}$ allowing a free heat radiation. At -8°C approximately the blades are parallel to the plate ($\alpha = 0^\circ$) forming a closed ring surface with

reduced emission. The emissivity of the louver amounts to $\epsilon = 0.80$ in opened position ($\alpha = 90^\circ$) and to $\epsilon = 0.10$ in closed position ($\alpha = 0^\circ$).

A given temperature causes a blade position with emissivity between the two boundary values mentioned above.

The characteristic of the springs, i.e. the dependency of the blade position α on the temperature T is linear. Pretests with ERNO have proved this behavior during standstill.

$$\alpha = \frac{\pi}{2(T_2 - T_1)} (T - T_1)$$

T_1 and T_2 are the temperatures at $\alpha = 0^\circ$ and $\alpha = 90^\circ$, respectively.

The task of the qualification test described below was to investigate how the spin motion of the spacecraft modifies the characteristic of the louver.

Two louver units were used as test articles. There were slight differences in the designs of the spring mechanism.

Test set-up and procedure

The test was performed in the thermal vacuum chamber of the DFVLR Space Simulation Institute. This chamber has a completely closed thermal shroud. A vacuum down to 10^{-6} Torr and ambient temperatures between -70°C and $+80^\circ\text{C}$ could be maintained. The temperature fluctuation with time was less than $\pm 0.5^\circ\text{C}$. During the test the pressure was approximately $1 \cdot 10^{-5}$ to $5 \cdot 10^{-5}$ Torr (see Figures 1 and 2).

A rotation table designed for the spin simulation was carrying the two louver units in the same distance from the axis as on the spacecraft. It was driven by a regulable motor so that speed could be continuously changed. The number of revolution was controlled with an accuracy of 2 rpm. At both louver models the temperature was measured by means of 7 platinum resistors. The signals from the rotating table were fed via slip rings into a small data acquisition system. By this system which operated under computer control, the signal voltages were measured every ten minutes, then converted into temperatures and printed out.

The accuracy of temperature measurements was approximately $\pm 0.1^\circ\text{C}$.

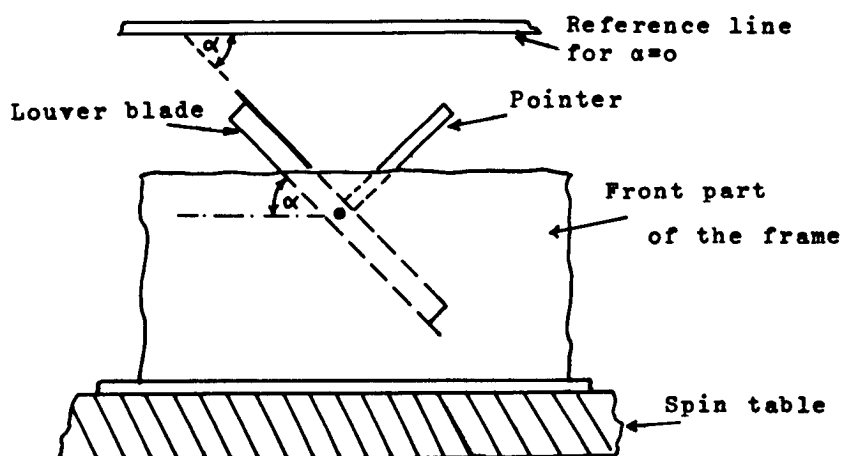
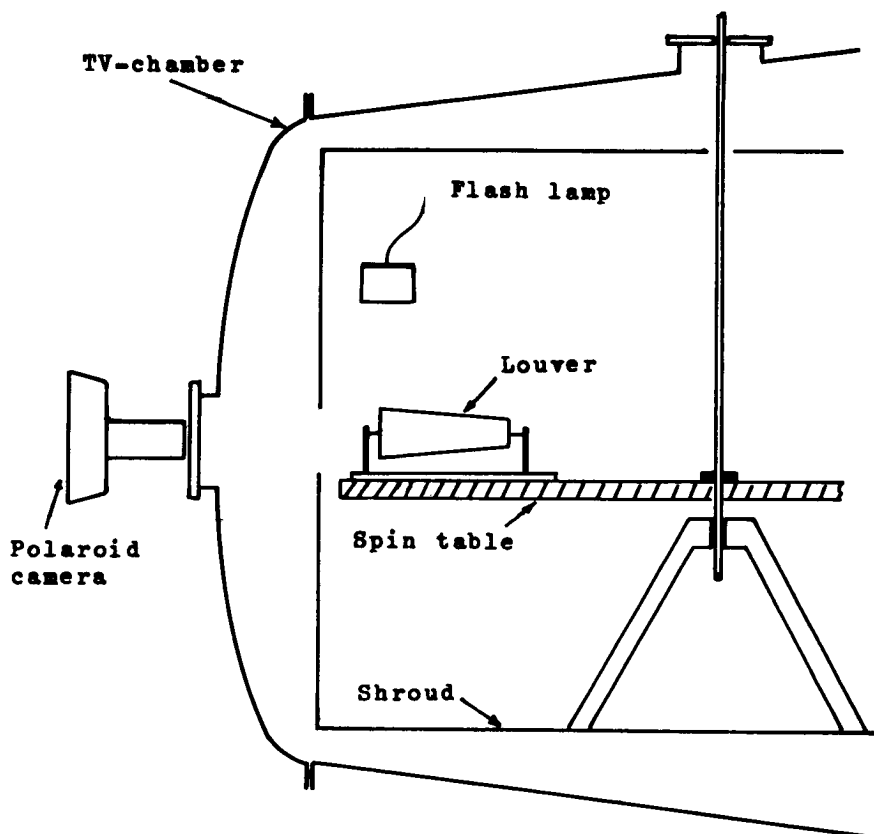


Fig. 1 - Test set-up

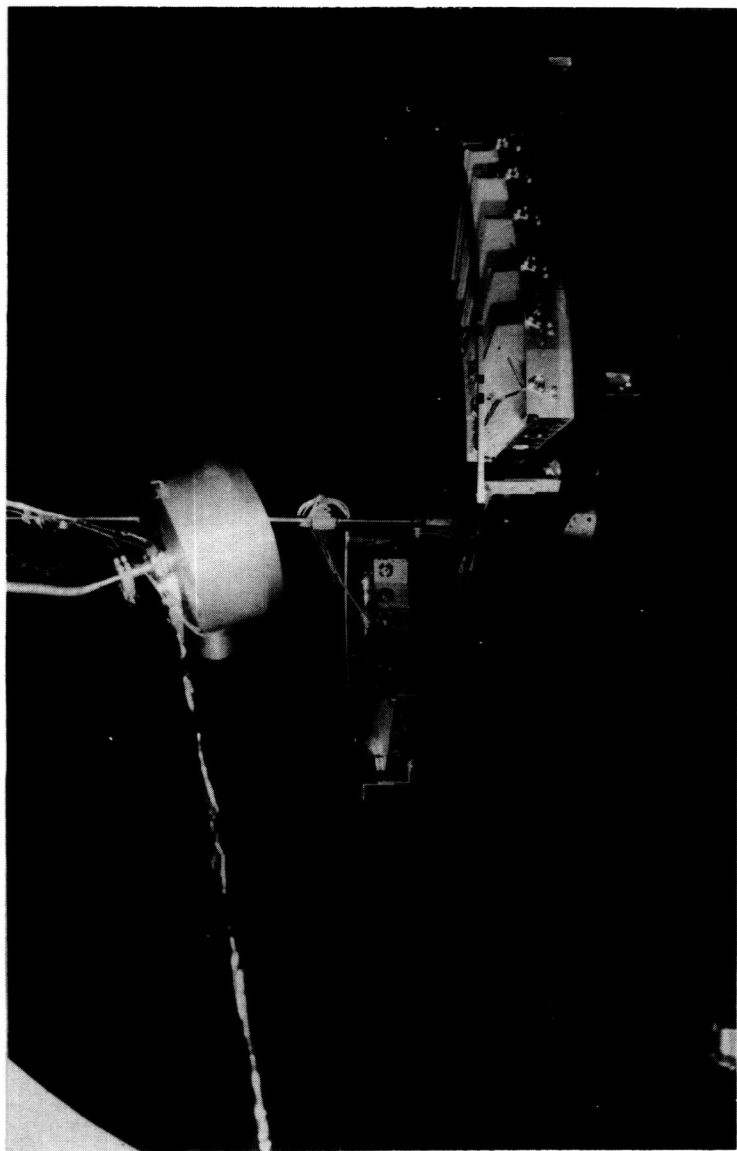


Fig. 2 - Spin table with louver units
(The cables from the Pt-resistors are fed through the shaft to the slip rings which run in atmosphere)

The determination of the blade position depending on the temperature during the spin motion was carried out by means of photographic registration. This method allows in a simple way to find out the blade position without any mechanical contact, i.e. without perturbation.

A polaroid camera supplied with a telephoto lense was used to photograph each louver blade. The test specimen was illuminated by flash light triggered on the desired blade position. For the correct determination of the angle at the photos it was necessary to photograph the blades exactly in frontal view.

At small angles the louver blades disappeared behind the front part of the frame. In order to be able to register the angle also in this position, each blade was provided with a perpendicular pointer. These pointers consisted of a very thin aluminium foil and were sufficiently light (0.2 g), not to change the characteristic.

The accuracy of the determination of the position on the photo was ± 1 degree.

To find out first the temperature versus angle characteristic at standstill, a temperature cycle has been performed without rotation.

One cycle means a stepwise cooling-down/warm-up process between $+ 25^{\circ}\text{C}$ and $- 15^{\circ}\text{C}$. At every step equilibrium temperature was waited for ($T \leq 0.5^{\circ}\text{C}$ per hour) and all 12 blades were photographed.

Thereafter the same procedure has been performed twice under rotation of 60 rpm.

Test results

The measurements (Fig. 3) verify the linear characteristic at standstill and give only one line for cool-down and warm-up.

Under rotation, however, the louvers show a modified behavior. The position does not only depend on temperature T , but also on spin speed ω : $\alpha = f(T, \omega)$; additionally there are two different curves for the cool-down and warm-up part. That means: a kind of hysteresis occurs.

The nonlinear dependency $\alpha = f(T, \omega)$ can be easily explained by calculating the torques acting on a blade during rotation. In the laboratory system (x, y, z) the constant spin vector ω points into the z -direction. The motion of a blade can be simplest described in a coordinate system (x_1, x_2, x_3) moving with the body

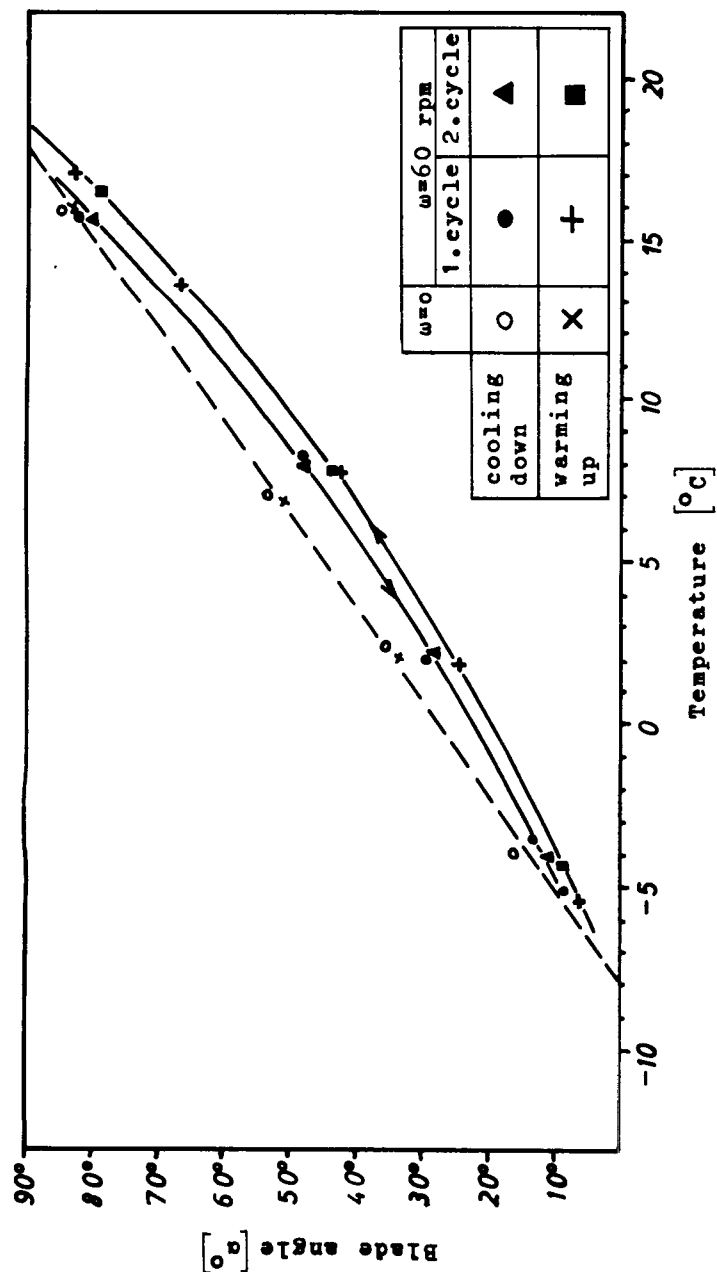


Fig. 3 - A typical louver characteristic

and attached to its center of mass (Fig. 4).

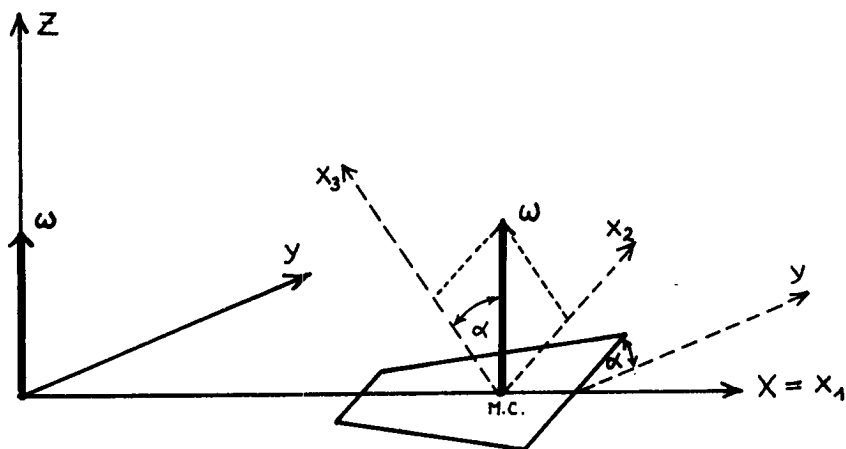


Figure 4

The Euler equations of a rigid body are:

$$M_1 = I_1 \cdot \dot{\omega}_1 - (I_2 - I_3) \omega_2 \cdot \omega_3$$

$$M_2 = I_2 \cdot \dot{\omega}_2 - (I_3 - I_1) \omega_3 \cdot \omega_1$$

$$M_3 = I_3 \cdot \dot{\omega}_3 - (I_1 - I_2) \omega_1 \cdot \omega_2$$

As no external torques are acting, the components are $M_1 = M_2 = M_3 = 0$. The components of the angular velocity are:

$$\omega_1 = \dot{\alpha}, \quad \omega_2 = \omega \cdot \sin \alpha, \quad \omega_3 = \omega \cdot \cos \alpha$$

$I_1 < I_2 < I_3$ are the principal moments of inertia of the blade.

The first one of the Euler equations yields the differential equation for the revolution around the x_1 -axis

$$I_1 \cdot \ddot{\alpha} = - (I_3 - I_2) \omega^2 \sin \alpha \cos \alpha = - \frac{I_3 - I_2}{2} \omega^2 \sin 2\alpha$$

This means, however, that due to the rotation of the spacecraft a torque

$$\bar{M}_1 = - \frac{I_3 - I_2}{2} \omega^2 \sin 2\alpha$$

is induced. This tends to decrease the inclination angle α of the blade and has to be added to the spring torque.

Thus the linear characteristic is destroyed.

$$\alpha = \frac{\pi}{2(T_2 - T_1)} (T - T_1) + c \cdot \bar{M}_1$$

C is a constant factor resulting from the friction of the ball-bearings, and T_1 and T_2 mean the temperatures for $\alpha = 0^\circ$ and $\alpha = 90^\circ$ respectively, given by the characteristic at standstill.

The relation between angle α , temperature T, and spin ω is therefore described by

$$2\alpha + B \cdot \omega^2 \sin 2\alpha = \frac{\pi}{T_2 - T_1} (T - T_1)$$

The positive constant factor $B = C \cdot (I_3 - I_2)$ can be calculated from the above-mentioned function by inserting the temperature T* for $\alpha = 45^\circ$, which is determined by the measured curve.

The table below shows a comparison between calculated and measured temperatures for Fig. 3.

measured		calculated		
α°	$T_m^{\circ}C$	$T_c^{\circ}C$	$T_c - T_m$	
1. cycle	82.5	+ 15.6	16.11	+ 0.51
	48	+ 8.1	7.84	- 0.26
	29.5	+ 2.0	2.26	+ 0.26
	13	- 3.6	- 3.35	+ 0.25
	8.5	- 5.1	- 4.95	+ 0.15
2. cycle	80	+ 15.5	15.58	+ 0.08
	48	+ 8.0	7.84	- 0.16
	28	+ 2.2	1.77	- 0.43
	10.5	- 4.1	- 4.23	- 0.13

Thus the explanation for the nonlinearity of the characteristic under spin motion has been found.

The other interesting phenomenon, the appearance of hysteresis, has not been investigated in detail, as the small difference does not exceed the tolerance limit.

A possible reason is the increased friction of the ball-bearings, which is induced by the centrifugal forces in radial direction.

SPECIAL PROBLEMS OF THE THERMAL SIMULATION OF HELIOS EXPERIMENT E6 - TEST RESULTS COMPARED WITH FLIGHT DATA

W. Hallmann, W. Ley, H. P. Schmidt, *DFVLR, Space Simulation Institute, 5 Cologne 90,
F. R. Germany*

ABSTRACT

The maximum solar energy (16 Solar Constants) irradiating experiment orifice E6 intermittently during the mission of space probe HELIOS has been reproduced in a High Intensity Component Test Facility. A detailed comparison is given between test results and flight data evaluation.

INTRODUCTION

The HELIOS experiment E6 serves for measuring cosmic radiation, especially particles of cosmic radiation of medium and higher energies, and of the solar X-ray radiation. The experiment has been designed by the Institute for Nuclear Physics of the Kiel University (F. R. Germany).

E6 is placed in the central compartment, its weight is 7.15 kg and its electrical power consumption is 4.48 Watts.

A preliminary thermal test should answer the question how the orifice of experiment E6 will behave during sun approach to 0.25 AE (astronomical units). The test set-up and the thermal simulation test have been conducted in the High Intensity Component Test Chamber (HISS) of the Institute of Space Simulation (DFVLR, Cologne-Porz, F.R. Germany).

Thermal Simulation as Component Test

During the mission, the probe rotates with 60 min^{-1} around its longitudinal axis. The facility does not allow rotations of the experiment and the test box at an irradiation of 16 SC. Therefore solutions had to be found to offer the experiment the same amount of energy per time unit [2].

The absorbed energy in space of the experiment orifice A may be deduced by the energy balance of one HELIOS rotation.

$$1) \dot{Q}_w = \frac{P \cdot S \cdot A \cdot \int_{-\pi/2}^{\pi/2} \cos \varphi d\varphi}{\pi} = \frac{P \cdot S \cdot A}{\pi}$$

$$P = 1.353 \text{ kW/m}^2 \approx 1 \text{ SC}$$

S = Number of Solar Constants in the test plane

The amount of \dot{Q}_w of eq. 1 has to be realized during the tests. The best way to do that will be described in the following.

The fixed original orifice A will be intermittently irradiated in the HISS-chamber at an intensity of 16 SC.

Therefore:

$$2) \frac{P \cdot S \cdot A}{\pi} \cdot T = P \cdot S \cdot A \cdot t$$

T = Time in space related to one rotation

t = Time of irradiation at simulation

Thus:

$$3) \frac{T}{t} = \pi$$

The proposed theoretical solution has been transformed into a practical solution by means of a rotating chopper.

The necessary chopper aperture (formed as circular sector) has been calculated to:

$$4) T = \frac{2\pi}{\omega_c} ; t = \frac{\varphi}{\omega_c}$$

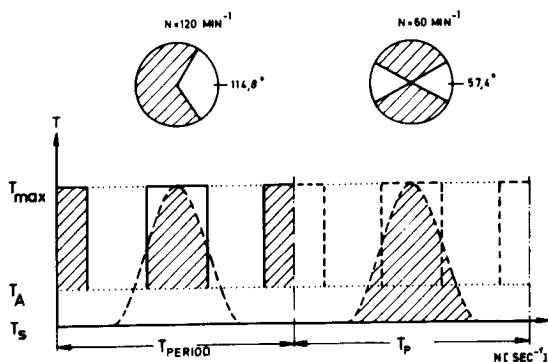
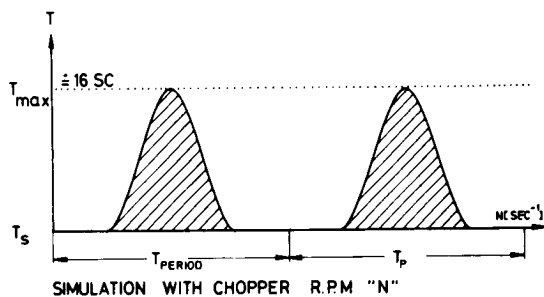
$$\frac{T}{t} = \frac{2\pi}{\varphi} = \pi,$$

$$\varphi = 2, \text{ or } \varphi = 114,8^\circ$$

The sectors in the chopper may be varied by changing the chopper r.p.m.

Figure 1 shows the relations of the

- energy load in space for experiment E6
- energy load during simulation at chopper rotational speeds s .



The figures refer to two rotations of the probe. For a better general view the occurring temperatures of the experiment instead of the amounts of energy are plotted. T_s is identical with the space temperature 4K, T_A is identical with the ambient temperature = chopper temperature during simulation.

As shown in Fig. 1 the experiment orifice will collect the space temperature $T_s = 4K$ during mission if it is not irradiated by the sun. For economical and constructive reasons, these ambient temperatures will not be simulated during test in the High Intensity Component Test Facility. Usual ambient temperatures are about 80 K.

The test set-up, the position of the chopper, and the additional cold walls are shown in Figure 2.

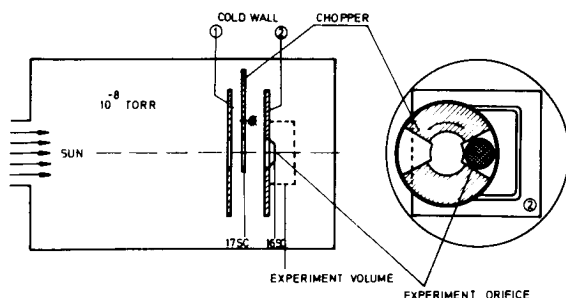


Fig. 2 - Chopper and cold wall 1 and 2

If the experiment orifice is covered by the chopper, the chopper itself will be irradiated by the simulated sun and heated up to a temperature T_A (as seen by the experiment E6).

In this position the chopper will cause an additional infrared irradiation of the experiment E6 because of the chopper temperature.

An optimization calculation will give the best top surface covering (α/ϵ -ratio) for the chopper or, expressed in another way, the amount of infrared energy emitted by the chopper should be as low as possible.

The best solution to solve this problem is the following:

- Chopper sector directed to the sun: aluminized Teflon foil,
- Chopper sector directed to E6 : aluminium polished,
- Chopper facing cold wall 1 and 2 : black colour.

The ratio of $\dot{Q}_{\text{Chopper}}/\dot{Q}_{\text{Sun}}$ is very low for this combination of top surface covering and has a value of 0.139 %, whereas 45.82 Watts by the sun and 0.0636 Watts by the chopper are offered to experiment E6.

The occurring chopper temperature amounts to some 206 K.

Simulation Test

The thermal model TM E6A has been constructed by DORNIER SYSTEM. The thermal qualities are identical with the flight unit.

The space simulation test under extreme thermal loads (0.9; 6; 11.1 and 16 SC) has been carried out to prove and verify the thermal computer model of E6A. Besides this test should give an answer about the energy absorption caused by the sensor. New results were gained of:

- the influence of the boundary between the orifice and the heat shield
- the energy absorption of the orifice
- the energy absorption of the reflector
- the heat conductivity of the materials and contact surfaces
- the temperatures of the detectors
- the compatibility of the materials and the surfaces

The alternating radiation load caused by the probe spin has been simulated by a system described in section 2. The experiment was installed in a chopper box (sprayed totally black) to simulate the experiment ambient in the HELIOS probe (s. Fig. 3). The circle sector in the front side has been equal to the irradiated contour of the experiment area (s. Fig. 4).

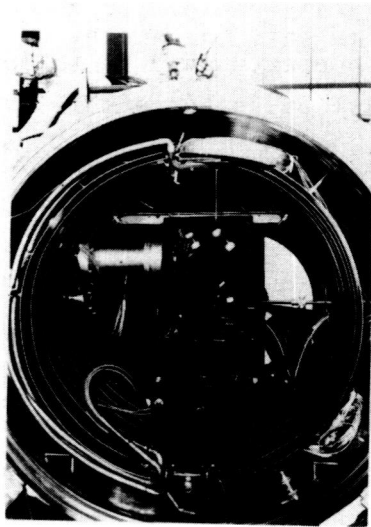


FIG.3 MOUNTING OF HELIOS E6A -
EXPERIMENT

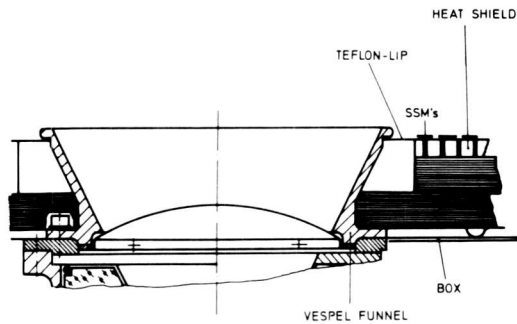


Fig. 4 - Heat shield HELIOS E6A-experiment

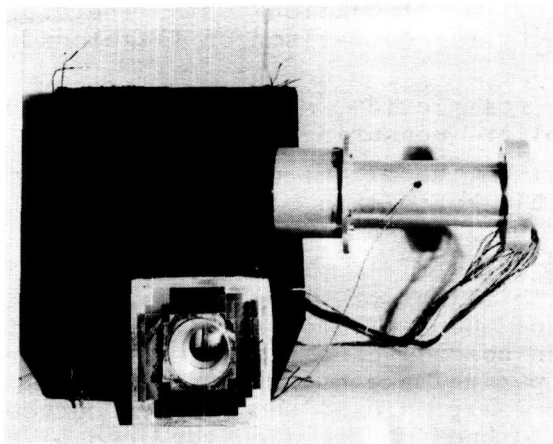


FIG.5 FRONT VIEW OF HELIOS E6A -
EXPERIMENT WITH HEAT SHIELD
AND TEST BOX

By means of 7 independent heating conductors for the 7 independent heating plates of the chopper box the requested temperature could be regulated. 18 Cu/Co-thermocouples served as temperature control of the chopper box.

The heat shield - made out of honeycomb - has been covered for a diameter of 150 mm Ø with Second Surface Mirrors. The connection between the experiment orifice and the SSM's was produced by an adapted Teflon lip. Between the heat shield and the front plate of the test box two layers of superinsulation foils - each consisting of 19 layers - has been attached.

At a vacuum pressure in the range of 10^{-7} Torr and a temperature of the cold wall of -188°C the uniformity of the different irradiation values ranged between $\pm 1\%$.

During the tests the temperatures of the experiment have been measured and registered by means of 28 Cu/Co-thermocouples [3].

Test Results compared with Flight Data

During the mission of HELIOS A housekeeping - temperatures are measured at different positions of the experiment E6A. These measuring points are all inside the electronic- and sensor boxes. Against that, all thermocouples have been installed outside

the boxes during the simulation tests. Therefore a problem arises by the comparison of flight data and test results.

Under this restriction, a comparison will be made for the multiplier (measuring point 17).

Figure 6 gives the flight data of the multiplier up to the 1st blackout (15th of March, 1975). A temperature distribution can be seen unmistakably after the 1st perihel.

Moreover the flight preliminaries - resulting from the heat balance model of the whole compartment [4] - are plotted. In nominal case the predicted degradations up to the 3rd perihel are considered. Besides the limiting curves of the predicted temperature curves for the non-degraded and the degraded surfaces of the probe are registered.

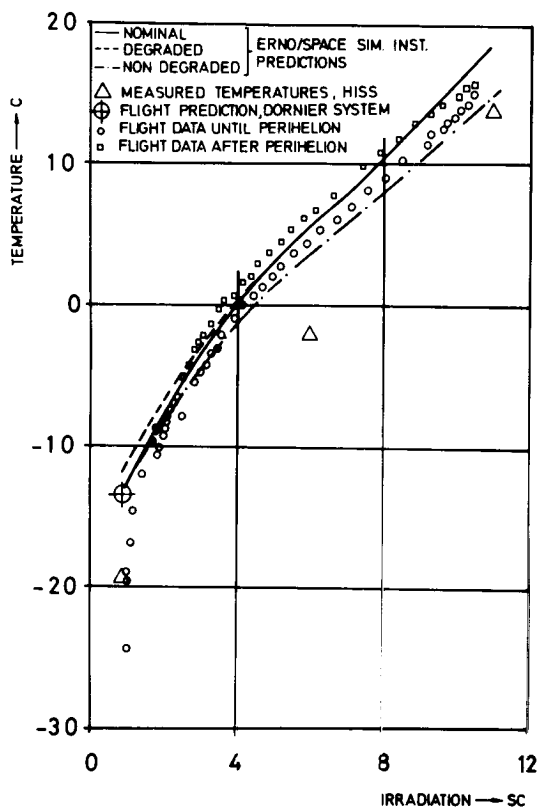


Fig. 6 - Temperature comparisons

Beneath those actual data and predictions - given by the mathematical model covering the heat balance of the compartment - Fig 6 includes the experimental results for the measuring point 17 of the simulation test. The temperature measured during the simulation tests are altogether too low.

This discrepancy may result from the following different possibilities:

1. The actual compartment temperatures do not agree with those given for the test as foundation of the test box temperatures.
2. The heat dissipation in the experiment (0.7 Watts) has not been simulated during the tests.

These temperature differences cannot be referred to experimental errors, but to nonuniform predictions.

By means of these test results DORNIER SYSTEM performed a flight prediction for the experiment at 0.9 and 16 SC on the basis of the estimated limiting conditions at this time.

The outcome at 0.9 SC is plotted likewise in Fig. 6. The conformity to the actual flight data is quite good.

For the development of the heat balance of a system, it is logical to conduct simulation tests under simplified limiting conditions, which allow an extrapolation to the orbital limiting conditions.

Literature:

- [1] Projekt HELIOS, Presseinformation,
Teil B, Gesellschaft für Weltraum-
forschung mbH in der DFVLR, Porz-
Wahn, Germany

- [2] HALLMANN, W. Lösungen für die thermische Simu-
LEY, W. lation des HELIOS-Experimentes E6
Raumfahrtforschung Heft 6/1974,
p. 285-289

- [3] LEY, W. HELIOS-Komponententest Experiment
E6, DFVLR, Köln-Porz, Institut für
Raumsimulation
IB 353-73/31

- [4] SCHMIDT, H.P. Projekt HELIOS
Temperaturvorhersagen der Mission
von HELIOS A
DFVLR, Köln-Porz, Institut für
Raumsimulation
IB 353-75/9 April 1975

HELIOS MISSION – CRITICAL ASSESSMENT OF GROUND TEST RESULTS VERSUS ACTUAL ORBIT PERFORMANCE

H. C. Benöhr and H. W. Prem, *Messerschmitt-Bölkow-Blohm GmbH, Space Division,
Ottobrunn, Fed. Rep. Germany*

ABSTRACT

Results of ground tests on the Helios spacecraft are correlated to orbit performance of Helios A. In-orbit failures and corrective actions for Helios B are summarized.

INTRODUCTION

The Helios Project comprises development, manufacturing, launch, and operation of two space probes. Helios A was launched on 10 December 1974 and since that time is performing a very successful mission, with the scientific objective to investigate the properties of the interplanetary space and physical processes in the vicinity of the sun down to 0.31 AU.

Helios B is scheduled to be launched on 8 December 1975 during a period of increasing solar activity and is expected to reach a 0.29 AU perihelion.

The Helios schedule (see fig. 1) already indicates a significant prolongation of the "Design and Development Phase" brought on by the thermal problems encountered during this phase.

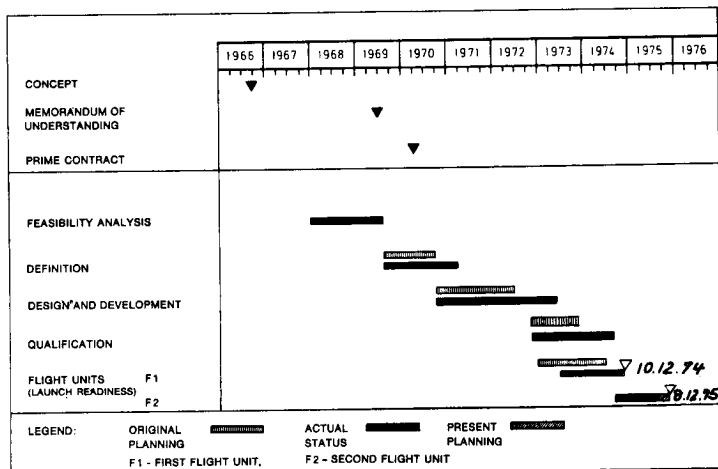


Fig. 1: Helios Schedule

Therefore, among the major problem areas emphasized in this report are the thermal problems which definitely set an upper limit to the scientific return of this solar mission. Furthermore, the Helios transponder and antenna performance will be outlined. Failures observed in orbit and the relevant corrective actions in respect to Helios B will be discussed; the adopted philosophy for determining vibration input levels based on flight loads analysis is summarized.

Helios Mission

The Helios mission is characterized by two spacecraft positions of major interest which can be clearly demonstrated in a fixed earth-sun line coordinate system. Fig. 2 shows for a 10 December launch date besides time and distance between spacecraft and sun the so-called blackout periods, whenever the spacecraft location on a line of sight from the earth is in front of or behind the sun. Prior and after such a line-up position behind the sun, telemetry signals have to penetrate the solar corona, and the order of magnitude of the monitored Faraday rotation of these signals is used to determine magnetic fields of the near sun area. Furthermore, predicted relativistic effects will be verified by time delays of telemetry signals measured.

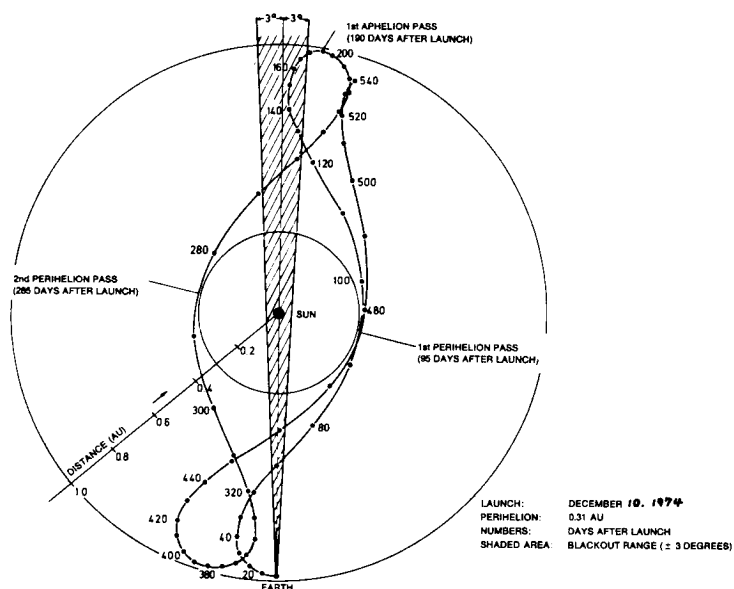


Fig. 2: HELIOS orbit for fixed earth-sun line.

The orbit segment of primary scientific interest is the perihelion phase. The proton, electron and alpha particle density within this near sun domain is considered to be extremely different from other interplanetary regions. Therefore experimenters involved in these investigations try to reach a perihelion as close as possible. Thermal constraints, together with launch energy considerations, dictate the minimum perihelion.

Helios Thermal Subsystem

Design Criteria and Spacecraft Layout - The two extremes for which the Helios thermal concept had to be designed are summarized in Fig. 3. At perihelion 0.3 AU (equivalent to 11 SC) the insolation for a spacecraft of this size reaches approximately 75 kW. All except 0.27 kW (more than 99%) of the energy impinging upon the spacecraft is reflected or emitted from the Helios outer surface or the rear side of the conical solar arrays.

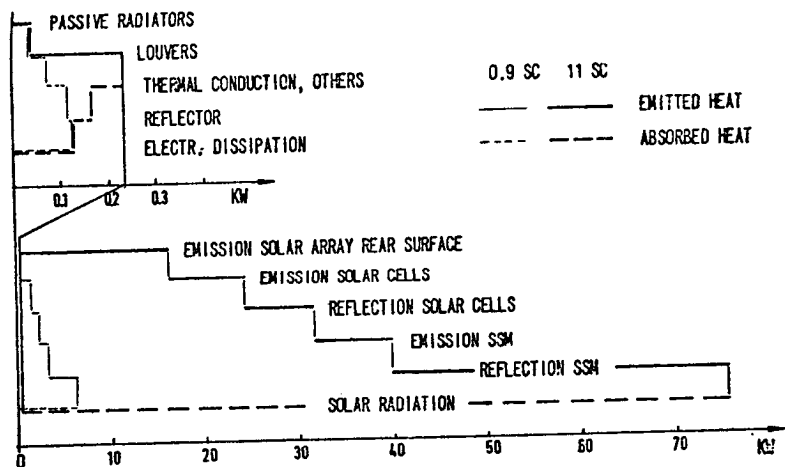


FIG. 3 HEAT BALANCE AT 11 AND 0.9 SOLAR CONSTANTS

Louvers, passive radiator areas and thermostats switching relevant heaters are dealing with the remaining 0.27 kW (mainly internal dissipation) in the hot case and 0.13 kW in the cold case.

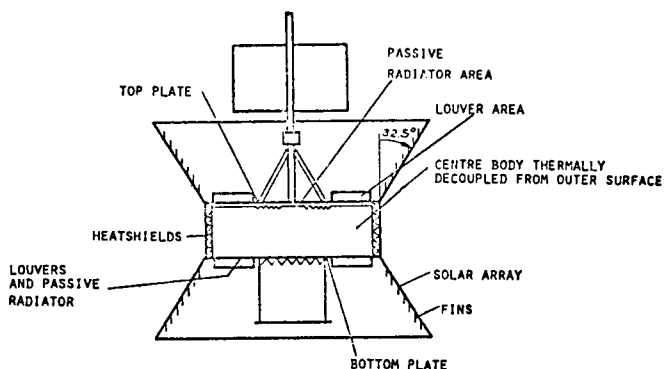


FIG. 4 PRINCIPAL CONCEPT OF HELIOS THERMAL SUBSYSTEM

The basic thermal concept is characterized by the following principal parameters:

- The spacecraft spin reduces effective insolation by a factor of π .
- Angle of attack between solar array plane and sun vector reduces effective solar intensity for the array by a factor $\cos 32.5^\circ$. In addition to this input reduction, the view angle of the solar array rear side to space is increased and radiation from the solar array rear side is directed parallel to the spin axis to space by the fins.
- Except for the solar array (50% second surface mirrors (SSM's), 50% solar cells) all surfaces illuminated by the sun are protected by rigid SSM's with an absorptivity of $\alpha = 0.07$ to 0.1 .
- Furthermore, the Center Body is thermally decoupled from the outer surfaces (ie. solar array, heatshield).
- Radiation areas of the Center Body to space are the top and bottom plate.

Test Temperatures (JPL) versus Orbit Temperatures - The Helios thermal concept had to be developed and tested at a time at which no solar simulation test facility existed for extremely high intensities. Therefore design changes of the Helios thermal concept had to be verified with an infrared test technique (see ref.1) in Germany, but this test technique - infrared simulation of the solar heat input - left open problems especially in the high intensity area. A solar simulation test at JPL using the Helios thermal model became absolutely necessary as a calibration test for the infrared test technique. The maximum achievable intensity at that time was 4.5 SC, and we were very fortunate that since 1972 continuous improvements of the

JPL chamber finally permitted an 11 SC test of the prototype in May 1974. Fig. 5 demonstrates in principle the test set-up of this valuable prototype test, which verified that Helios is able to fly a 0.3 AU (11 SC) solar mission.

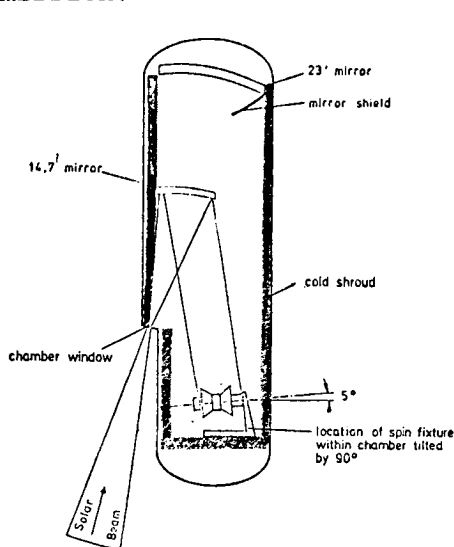


FIG. 5 HELIOS P-TEST AT JPL MAY 74

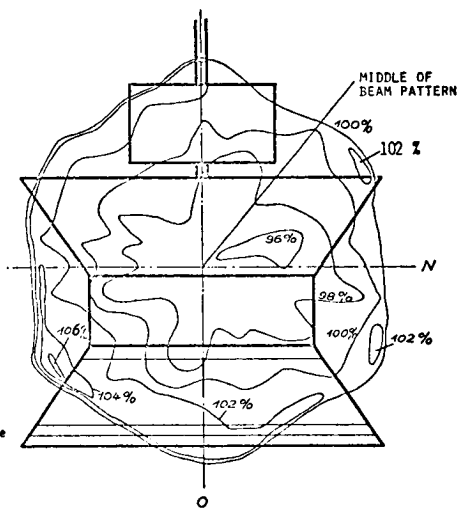


FIG. 6 INTENSITY DISTRIBUTION DURING 11 SC JPL TEST

Temperatures given in fig. 7 to fig. 9 are test temperatures of the 11 SC Prototype Solar Simulation Test compared to Flight Unit temperatures measured in orbit at 10.4 SC.

Fig. 6 summarizes the intensity distribution during the 11 SC test. The beam pattern does not fully illuminate the Helios outer shape, for instance in the lower solar array and antenna area. Nevertheless the relative position of Helios within the beam pattern has been chosen such that the antenna-reflector heat input to the top plate is correctly simulated and the relatively good agreement of test temperatures with orbit temperatures indicate the validity of this test in spite of all test constraints.

The major temperature trends observed:

- central compartment in orbit 10 to 6°C cooler than during test
- adapter experiments in orbit 5 to 12°C warmer than during test

are explained by test conditions and changes implemented as a result of the prototype test.

Deviations between test and orbit conditions are:

- Reduced orbit intensity (10.4 SC) compared to test (11 SC)
- Partly illuminated spacecraft due to facility constraints during test.

Based on the results of the JPL test, the following changes were implemented for Helios A:

- The temperature/angle characteristic of 9 (out of 15) louver assemblies was changed in order to get fully opened louvers in the hot case. This change is equivalent to a temperature reduction in the hot and the cold case.
- The heater power for the adapter experiments has been increased due to low temperatures indicated during the P-test. This change is equivalent to a shift of the overall temperature level to higher temperatures.

Although these changes have not been verified by ground testing, the observed temperature trends in orbit indicate expected trends.

Based on these valuable P-test results, the Helios perihelion of 0.30 ± 0.01 AU has been selected.

Degradation of outer surfaces - Temperature measurements in the heatshield area versus solar intensity are plotted in figure 10. Due to degradation/contamination effects, temperatures measured during the first approach to the perihelion deviate somewhat from those temperatures taken during the departure from the perihelion.

The correlation between absorptivity (α) and equivalent sun hours (ESH) for second surface mirrors flown on Helios A is given in fig. 11. These results have been determined during environmental testing of SSM's at Boeing (ref. 4).

A first approximation for correlating orbit temperature differences measured and absorptivity is described by the following equation:

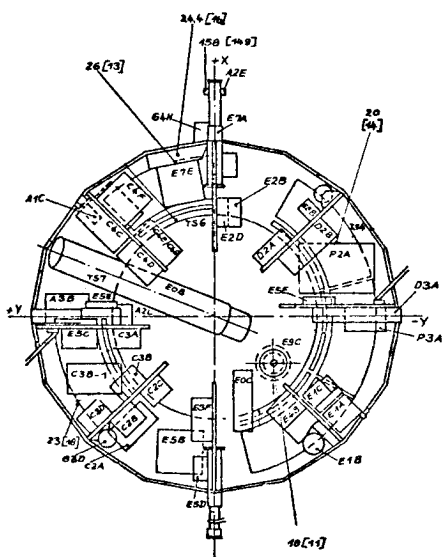


FIG. 8 TEMPERATURES MEASURED AT BOTTOM PLATE
11 SC TEST/(ORBIT)

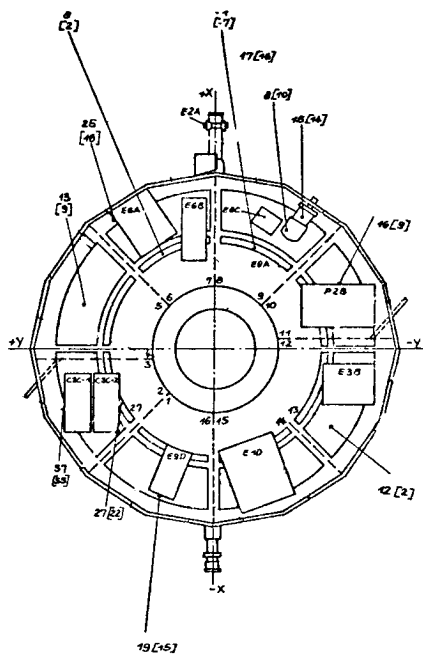


FIG. 7 TEMPERATURES MEASURED AT TOP PLATE
11 SC TEST/(ORBIT)

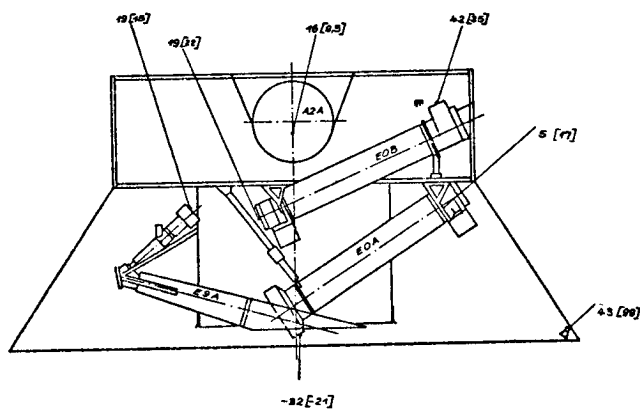


FIG. 9 TEMPERATURES MEASURED AT ADAPTER EXPERIMENTS
11 SC TEST/(ORBIT)

$$\alpha_2 = \alpha_1 \left(1 + 4 \frac{\Delta T}{T_1}\right) \text{ or } \Delta \alpha = \alpha_1 \cdot 4 \frac{\Delta T}{T_1}$$

Based on heatshield temperatures, the change in absorptivity for one Helios orbit is determined to be 0.014 which nearly agrees with predicted degradation of $\Delta \alpha = 0.017$ to 0.02 measured during the Boeing test (see fig. 11). Therefore predictions including degradation for the second and third perihelion have been based on these valuable ground test results.

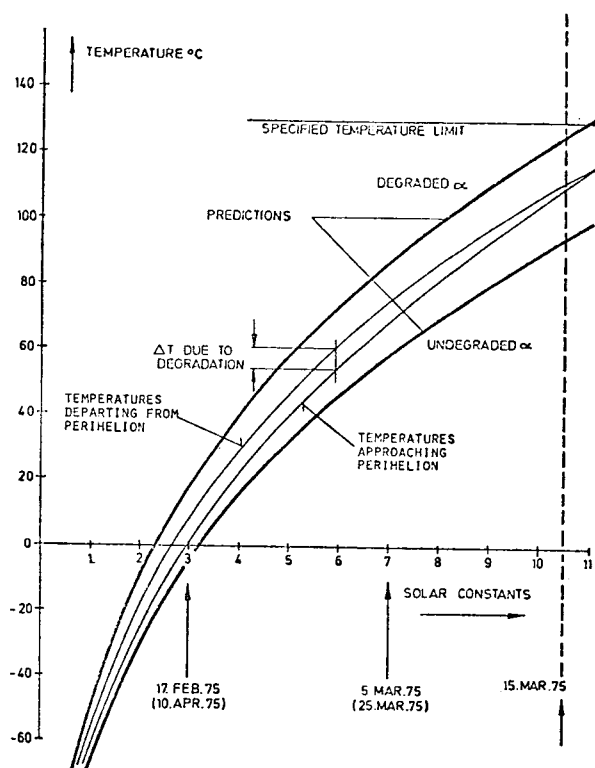


FIG. 10 HEATSHIELD TEMPERATURES

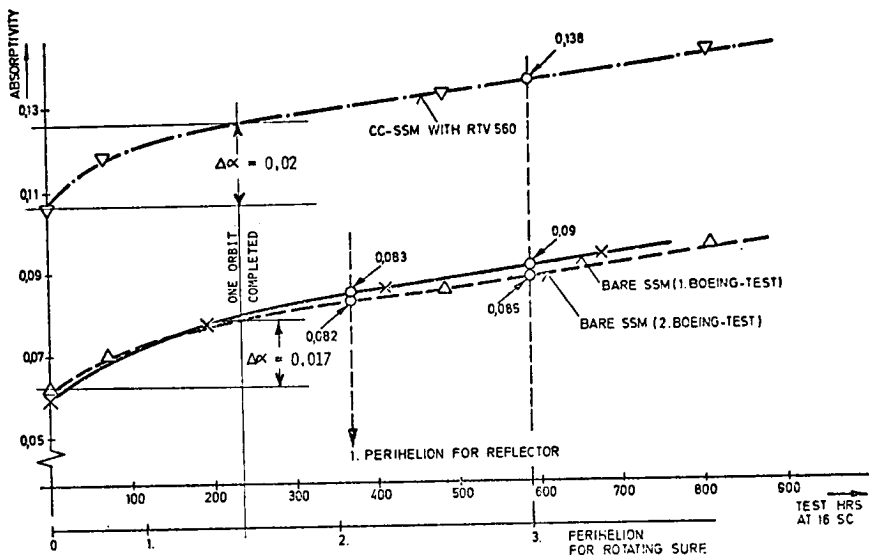


FIG. 11: ABSORPTIVITY VERSUS EQUIVALENT SUN HOURS

Telecommunication

The Helios telecommunication subsystem is designed to be compatible with the NASA S-band deep space network. The transponder is the very first S-band transponder with phase-locked-loop ever built in Europe. Coherent operation (up/down link) and ranging capability are provided. Because of development problems, the earlier concept of a parametric preamplifier was abandoned in favour of a transistorized unit. A maximum of 20 Watts RF power for telemetry is provided by a TWT amplifier.

The data system is capable of operating at bit rates ranging from 8 bps to 4096 bps with 6 different telemetry formats for transmission, in selectable combinations of engineering, real time science and stored science data. A core storage with a capacity of 0.5 Megabits has been incorporated for protection of science shock data, blackout data and engineering data from ascent phase. For reliability reasons the system is equipped with adequate redundancy. Possible "single point failures" have been carefully eliminated.

From launch through the first perihelion up to the end of the Helios A primary mission (first superior conjunction) transponder and data system operated well within their specified and expected limits and no redundant units were needed. Actual link performance

turned out to be better than expected. During operation of the high gain antenna an unexpected disturbance of the plasma and solar wind experiments was observed, which could subsequently be identified in the laboratory and which will be eliminated on Helios B by a change in the antenna slot configuration.

Helios A Link Performance - Based on actual orbit and ground station performance data the original assumption of an SNR threshold of 9.6 dB for all bit rates turned out to be too conservative. Depending on bit rate and carrier suppression the SNR could be reduced considerably. Note: The telemetry subcarrier is phase modulated on the carrier with a peak modulation of 0.733 radians (low carrier suppression) or 0.953 radians (high carrier suppression).

Low carrier suppression leads to an improvement of the carrier stability at weak signal levels (phase jitter). It is commanded if the bit rate has to be reduced to 32 bps or below due to large communication distance and/or limited antenna gain.

Table 1 gives a comparison between predicted and actual link performance.

Secondary Electron Generation by High Gain Antenna - It is well known that RF systems in vacuum may experience a voltage breakdown due to a cascade of secondary electron generation processes (see for example ref. 3). This effect is known as "Multipacting Breakdown" and it has been studied carefully on various RF-systems. The Helios transponder system has been designed such that any degradation in RF performance due to multipacting is carefully avoided and that an adequate safety margin is guaranteed. Although no degradation in RF characteristics has been observed in orbit, it was found that two highly sensitive experiments, namely the solar wind and plasma experiments, were disturbed during operation of the Helios high gain antenna. Subsequently a series of trouble-shooting tests have been performed at the JPL RF breakdown test facility, using Helios prototype hardware and the highly sensitive electron detectors of Helios experiment 1. It was found that secondary electrons may be generated at a level much below the classical breakdown threshold. Electron currents are extremely low and no impact on RF performance could be observed. It is obvious that for scientific satellites like Helios new safety limits have to be established. Based on these tests, the slot geometry for the Helios B high gain antenna has been modified in order to reduce the critical strength of the electrical RF field (see fig. 12).

Table 1: Helios A Link Performance (transmitter in high power mode)

Ground Station (disk diameter)	S/C Antenna (HGA/MGA)	Distance (AM)	Bit rates (bps)			SNR threshold (dB)
			required	Predicted (adverse)	Actual	
26 m	HGA	0.4	2048	1024	2048	2.5
26 m	HGA	1.3	128	128	256	2.5
26 m	HGA	1.6	64	32	128	4.0
26 m	HGA	2.0	8	8	64	5.0
26 m	MGA	0.3	128	32	256	2.5
26 m	MGA	0.4	64	16	128	4.0
26 m	MGA	0.8	8	-	32	3.0
64 m ⁺	HGA	0.4	2048	4096	2048 ⁺⁺	2.5
64 m ⁺	HGA	1.3	128	2048	2048	2.5
64 m ⁺	HGA	1.6	64	2048	1024	2.5
64 m ⁺	HGA	2.0	8	256	512	2.5
100 m	MGA	0.3	2048	2048	2048	2.5
100 m	MGA	1.3	128	32	128	4.0
100 m	MGA	1.5	64	16	64	5.0
100 m	MGA	2.0	8	-	32	3.2

+) including 100 m Effelsberg station

++) Helios A to be operated only up to 2048 bps

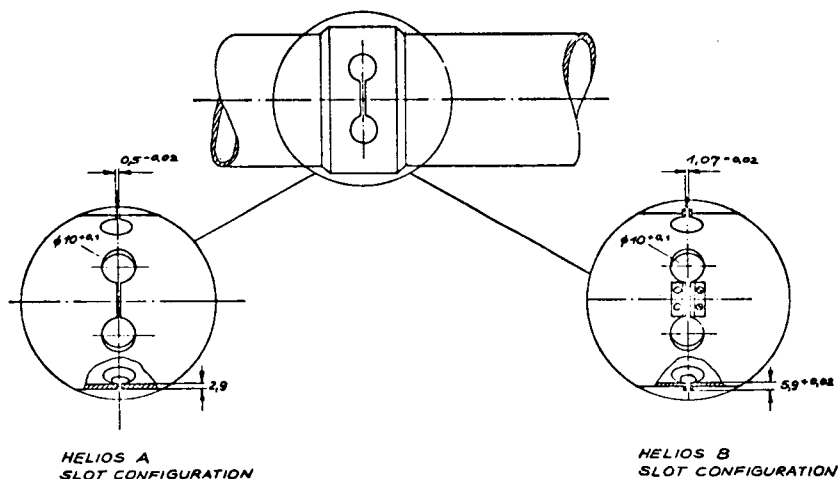


Fig.12: High gain antenna (HGA) SLOT configuration

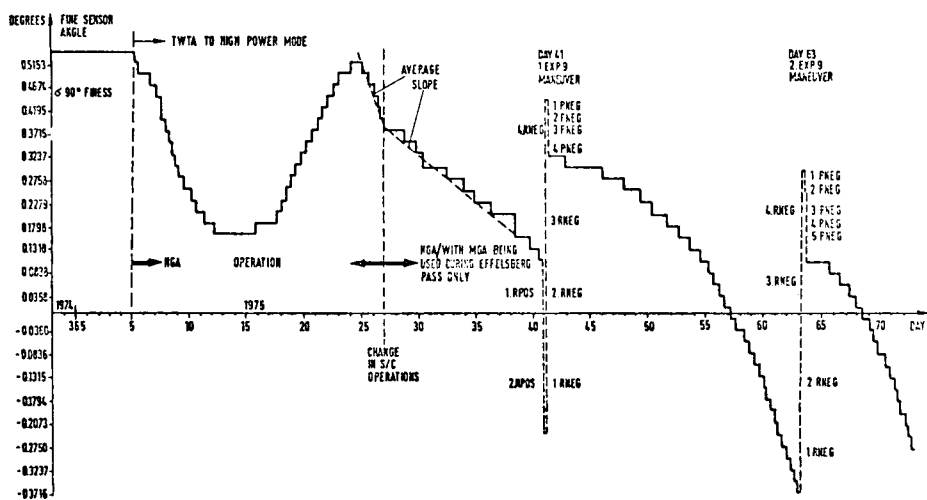


Fig.13: Solar Aspect Angle versus Mission Time

Failures in Orbit and Corrective Actions

Radio wave antenna failure, design changes, and performance verification during ground testing - For the Plasma and Radio Wave Experiment, two 15 m long antennas (overlapping tubular extendable element) are on board Helios and were deployed radially from the center body. The very first part of this antenna is shielded by an ion guard, which is folded within the antenna box in the stowed position. During deployment the antenna element and the ion guard move together in the radial direction. In this phase the ion guard transfers tension and torsion loads to the antenna element. After the ion guard has reached its final length, the antenna element will continue to deploy to the full length of 15 m.

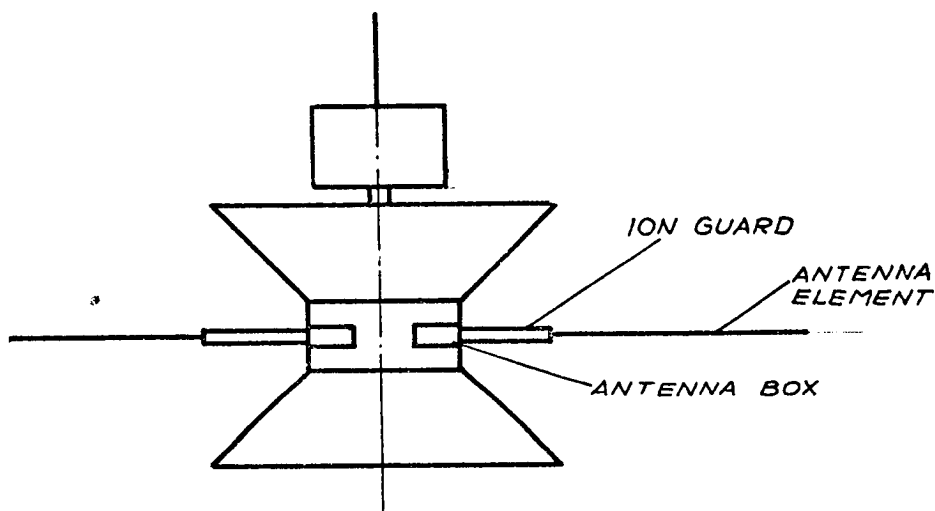


Fig. 14: Principle of Helios Radio Wave Antenna

During deployment of one antenna, torsion transferred from the deploying ion guard on to the antenna element caused increased friction between the antenna element and a guide piece (ply). Since the element in its flattened out state cannot sustain compression forces, the element folded up and jammed in the mechanism.

For Helios B, a conducting and rigid ion guard is now foreseen. The antenna element has therefore been decoupled loadwise from the ion guard in order to prevent similar failures.

During operational spin, the antenna element can now be extended at least to the length of the rigid

ion guard, which protects the antenna against air forces. Ground test results are so far positive and we therefore do not expect problems for Helios B.

Anomaly in Solar Aspect Angle - During the initial phase of the Helios A mission, an anomalous drift in solar aspect angle was observed which exhibits a considerable deviation from the anticipated drift as caused by the solar pressure in conjunction with roll/pitch cross coupling (rotating coordinate system). Figure 13 shows the fine sun sensor angle versus mission time. So far the pattern between day 5 and day 25 (1975) cannot be explained in a satisfactory way. However, there is some indication that this anomaly is closely related to the HGA operation and possibly to the secondary electron generation mechanism as already described.

- o Electron generation and anomalous drift started simultaneously on day 5 (1975) when the TWTA was switched to high power mode while using the directional (despin) high gain antenna (HGA).
- o For protection of experiment 1 and 5 scientific data, the spacecraft operation was changed on day 27 (1975) by using the medium gain antenna (lower bit rate, no secondary electrons) during the Effelsberg pass. This resulted in a corresponding change in average slope of the drift curve (see fig. 13).

Although the correlation between drift anomaly and HGA operation seems to be obvious, no quantitative verification could so far be established. This may be due to the fact that generation of secondary electrons was variable in time due to unknown effects. After the 4 April 1975, multipacting stopped altogether, and since then the drift in solar aspect angle can be easily explained.

Unexplained Power Drop Event - The Helios power supply system is designed to protect itself in case of an unexpected overload. Non-essential loads (experiments) are switched off by opening the master relays of the non-essential bus. Switching status of all further relays behind the master relays shall remain unchanged. This feature has been tested successfully on ground without any anomaly.

On day 104 after launch (24 March 1975) the non-essential load was dropped. However, in addition to the master relays switch off, random switching of various other relays on the power control and distribution unit has been found. It was concluded that this event was due to a spike on command lines. The source of this

spike could not be positively identified. Possible, it is located in the Helios experiment package with experiment 10 (micrometeoroid analyser), being most suspect.

Flight Loads Analysis and Application of Results for Vibration Testing

For Titan-Centaur-Launch Vehicle including the Helios payload, flight load calculations have been performed in order to determine the maximum load to which Helios has to be tested.

As a result of the TC-1 flight a new load case predominant to all other load cases has been detected, which occurred just after ignition of the solid rocket motors. Best reconstruction of this forcing function for the dynamic model was an unsymmetric pressure wave reflection from the umbilical tower which forced pitch plane vibration.

The currently predicted maximum separation plane bending moment at a frequency of 6 Hz for a 380 kg spacecraft mass is 193 000 cm kp. During spacecraft system vibration tests in lateral direction, the test input at the spacecraft basic resonance frequency (13 Hz) is notched in order not to exceed the maximum calculated moment.

This principal philosophy cannot be followed strictly due to late detection of this "unsymmetric pressure wave" load case. The successfully launched Helios A spacecraft has been tested up to 158 000 cm kp, whereas the Helios B spacecraft has been subjected to the highest level the spacecraft can take (177 000 cm kp).

In spite of this discrepancy between theoretical prediction and capability, a successful Helios A launch was performed with a measured maximum bending moment of 100 000 cm kp. The difference between load capability and measured bending moment seems to provide an adequate safety margin for a successful Helios B launch.

CONCLUSIONS

The main aspects of the Helios in-orbit performance have been compared with ground test results. Especially thermal test results for the total spacecraft system, as well as on component level (degradation tests), turned out to describe orbit performance very accurately. Transponder, antenna, data handling and electrical distribution system performance demonstrate the expected or even a better behaviour than that shown during environmental testing. Preventative changes for the Helios B high gain antenna have been implemented to avoid the secondary electron generation effect discovered during the very first phase of the Helios A mission. The failure of one antenna of

the plasma and radio wave experiment is thought to be corrected for Helios B by using a rigid ion guard. This change for Helios B is expected not only to reduce noise level for the antenna but also increase possibilities for reasonable and cost effective deployment tests in air.

Finally, it can be concluded that the extensive ground test program, including the subsequent corrective actions is reflected by a successful Helios A mission.

REFERENCES

- (1) J. Gülpen, W. Lorenz: Infrared test techniques developed for the Helios spacecraft.
2nd ESTEC Seminar on "Structural and Thermal Test, their Evolution and Present Trends", 1973.
- (2) J. Gülpen, W. Lorenz: Method and results of infrared testing of the Helios Solar Probe, Space Simulation, NASA SP-336, 1973.
- (3) R. Woo: Final Report on RF voltage breakdown in coaxial transmission lines, JPL Technical Report, 32-1500, (October 1, 1970).
- (4) L.B. Fogdall, S.Canaday: Radiation effects on second surface mirrors, Proceedings Cnes, Symp. Evaluation of Space Environment on Materials, p. 549-560, 1974.

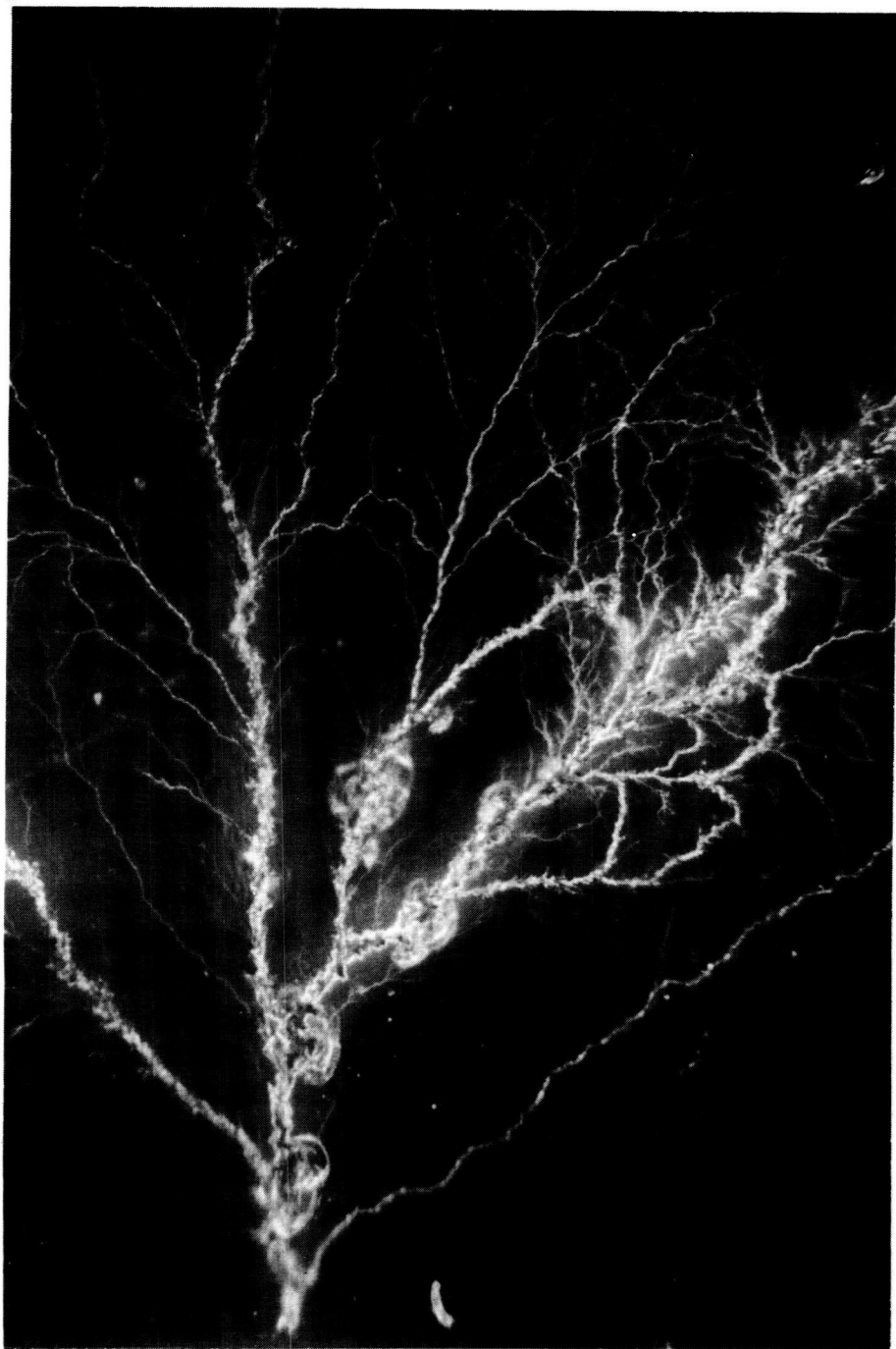
COMBINED ENVIRONMENTAL EFFECTS ON POLYMERS*

Lawrence B. Fogdall and Sheridan S. Cannaday, *Boeing Aerospace Company, Seattle, Washington 98124*

ABSTRACT

A series of space simulation tests on FEP Teflon and other polymeric thermal control coatings has been conducted using UV, electrons, protons, and Lyman-alpha wavelength vacuum UV radiation. Interest was centered on simulating synchronous altitude radiation environment conditions. Ultraviolet radiation was at or near the real-time space rate (0.14 watt/cm^2 for one Astronomical Unit, air mass zero) in each test, whereas test conditions for electron and proton fluxes ranged from 2×10^8 to 3×10^9 particles/ $\text{cm}^2\text{-sec}$. Proton energies were 40 to 50 keV, and electron energies ranged from 50 to 115 keV. This resulted in wide-ranging conditions of charge buildup and particle penetration in the dielectric materials investigated. In FEP Teflon, optical property degradation was quite rate dependent, implying a relationship with dielectric properties. At the higher electron exposure rates complete dielectric breakdown was observed. Physical changes in materials included loss of specularly and introduction of a high density of photographable tracking defects on a microscopic scale. An example shows the discharge of trapped electrons when dielectric strength is exceeded. This leaves a portion of the Teflon volume no longer clear, but diffusely transmitting and reflecting. Thermophysical changes included degradation of solar absorptance coefficients as much as five-fold. The situation that prevails here for earth orbit will be contrasted with polymer performance in the solar wind (such as HELIOS orbital conditions). Discussion will include generation of an α_s "performance envelope" for FEP Teflon that allows comparison with fused silica second surface mirrors. This work strongly suggests that conductive overcoatings be developed for polymers and other flexible materials, comparable or superior to those available for fused silica SSMs.

*Work performed in part under Contract NAS1-13530, NASA-Langley Research Center; Contract CSC-IS-556, Communications Satellite Corp. as Management Services Contractor for INTELSAT; and Boeing Co. independent research.



Electron Discharge in FEP Teflon. Magnification: 240X

**FUNCTIONAL AND DYNAMICS TESTING OF THE FLEXIBLE SOLAR
ARRAY FOR THE COMMUNICATIONS TECHNOLOGY SATELLITE**

T. D. Harrison,* R. Buckingham,** F. R. Vigneron***

ABSTRACT

The paper describes the test objectives, test methods, thermal environmental simulations, and test results, for a series of combined dynamic, thermal, and vacuum environmental tests on a Deployable Solar Array for the Communications Technology Satellite. Six major resonant structural modes were observed over an excitation range of 0.1-1.0 Hz. Corresponding modal damping factors were found to be between 0.001 and 0.01. Variation of temperature environments between -125°C and 42°C did not significantly affect the characteristics of the fundamental modes, but did influence some of the higher modes. Superharmonic response behaviour was observed. The tests also verified functional mechanical performance of the solar array under thermal and vacuum conditions.

INTRODUCTION

The Communications Technology Satellite(CTS), is a 3-axis stabilized experimental SHF communications spacecraft which is scheduled to be launched into geosynchronous orbit in December, 1975. The project is a joint effort between Canada(DOC) and the United States (NASA). The European Space Research Organization(ESRO), is also participating by supplying certain communications components and, significant to this paper, supporting the development of the solar cells and flexible substrates for the Deployable Solar Array(DSA) (Reference 1).

During launch the two DSA's are stowed on the north and south panels of the spacecraft. The DSA's are deployed after the CTS has achieved geostationary orbit(Figure 1). For the major part of the spacecraft's two year mission, the central body of the spacecraft(with the SHF antennas) remains earth pointing while the two DSA's rotate relative to the spacecraft body such that their solar cell areas are always maintained normal to the sun except during eclipse periods. _ _ _ _ _

* Research Engineer

** Consulting Engineer

*** Research Scientist, Member AIAA

mounted solar cells and associated bus wiring)*, a single BISTEM stainless steel boom, an inboard pallet, an outboard pressure plate, and related substructure**; configured as shown in Figure 2. Internal to the spacecraft there is a drive and track mechanism for maintaining the DSA normal to the sun, a deployment actuator, a slip ring assembly, and other associated equipment. The portion of a DSA which protrudes from the spacecraft is structurally flexible, and has a total mass of approximately 19kg. The blanket substrate is a composite fabric 76 μ m thick, made up of a kapton layer bonded to a glass fibre reinforcing layer. Solar cells, coverglasses, and adhesives, having a thickness of 440 μ m, are

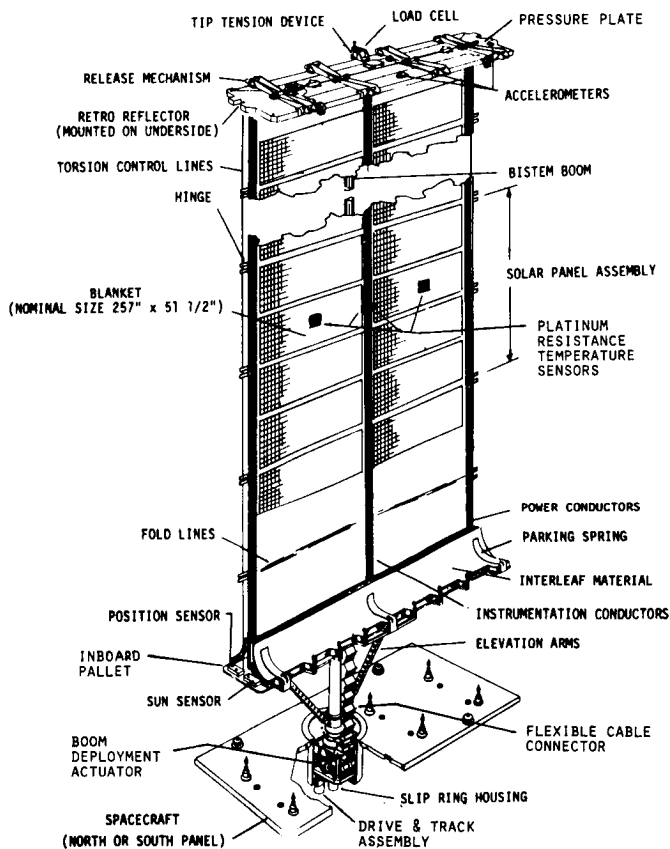


Figure 2 CTS Deployable Solar Array (DSA)

* The blanket was designed and built by AEG-Telefunken, Hamburg, Germany.

** The mechanical portions of the DSA were designed and built by SPAR Aerospace Products Ltd., Toronto, Canada.

bonded to the substrate. Electrical power and instrumentation flexible bus lines are located at the edges and at the centerline of the blanket. At the inboard end these bus lines connect, via a diode board, to a flexible connector cable which in turn connects to the spacecraft electrical subsystem via a slip ring assembly. The blanket is structurally supported by a 3.40cm diameter deployable BISTEM which is offset from the blanket approximately 6.3cm as shown. The ends of the blanket are supported by the inboard pallet and the outboard pressure plate. During launch the pallet and plate serve as a protective sandwich structure for the stowed blanket. The deployed blanket is maintained at a nominal tension of 35.6 N via a constant force spring mechanism located at the outboard end of the boom. To provide torsional stiffness, at each edge of the blanket there is a thin stainless steel line tensioned to a constant force of 1.33 N. The outboard parts rotate relative to the spacecraft, via a drive and track mechanism which is energized by a stepper motor. The DSA is normally rotated at a rate of 1 revolution per day. In addition, a capability exists to rotate at a rate of 35.7°/minute (the hardware evaluated in the test program had a rate capability of 15°/minute, rather than 35.7°/minute), which will be used during sun acquisition (at initial startup and when the spacecraft comes out of an eclipse). An autotrack feedback control system which utilizes an analog sun sensor mounted on the inboard pallets of the DSA's can be used to automatically step the DSA. A fuller description of the DSA is given in Reference 2 and 3. Structural parameters of the array are given in Table 1.

Instrumentation- The DSA instrumentation is illustrated in Figure 2. Three accelerometers (Systron Donner Servo type) with a range of ± 100 milli g's, are mounted on the outboard pressure plate of each flight DSA. The accelerometers will enable in-flight measurement of acceleration normal to and in the plane of the blanket. However, in the testing program discussed herein, the flight accelerometers were replaced with similar accelerometers of equal weight, which have a range of ± 500 milli g's.

Each DSA is equipped with a deflection sensing system, which will enable measurement of deflection of the outboard pallets relative to the spacecraft central body during flight. The sensors were not available for the test program described herein.

Five platinum resistance thermometer temperature sensors with measurement range of -200°C to 120°C are mounted on the blanket.

A load cell, with a specially designed strain gaged sensing beam, is incorporated into the DSA at the outboard pallet. The device will enable measurement of DSA tension over the range of 0 to 110 N under zero-g on-orbit conditions.

A number of sensors are provided with each DSA to support operational functions for the spacecraft, namely a digital position encoder (in the drive and track assembly), an array-mounted sun

sensor, extension arm microswitch, and potentiometer in the tip tension negator spring mechanism.

TABLE 1 : CTS SOLAR ARRAY PARAMETERS (Qualification Model as Tested)

Parameter Description	Nominal Value or Range	Units
length of boom	7.209	m
length of blanket	6.502	m
width of blanket	1.311	m
mass per length of boom	0.292	Kg/m
mass per length of blanket	1.06	Kg/m
mass of tip pallet	4.42	Kg
mass of inboard pallet	3.40	Kg
moment inertia of pallet about		
- x axis - torsion	1.356	Kg/m ²
- y axis - parallel to blanket	.03	Kg/m ²
- z axis - perpendicular to blanket	1.356	Kg/m ²
boom centre line to blanket centre line	.061	m
distance from boom centre line to pallet CM	.150	m
boom root stiffness out-of-plane	1356-2712	N-m
boom root stiffness in-plane	2034-4068	N-m
stiffness of elevation arms(in-plane)	1220	N-m/rad
spring constant at blanket-tip-(in-plane)	1356	N-m
array tensioning spring force (Nominal)	35.6	N
bending stiffness of boom out-of-plane	867-1033	N-m ²
bending stiffness of boom in-plane	950-1033	N-m ²
torsional stiffness constant of boom	.0454	N-m/rad
torsion control line force (Nominal)	1.33	N

PREVIOUS CTS DSA TESTING & ANALYSIS

This paper reports specifically on the structural dynamics and functional testing performed on a deployed flight representative(flight spare)DSA, which was completed in January 1975. This work was the culmination of a comprehensive test development and analysis program which was begun in 1973 by CRC(Reference 4,5, & 6). In the course of the preliminary work, a dummy(no solar cells)DSA was first tested, followed by tests on the CTS preliminary DSA. Analytical work was being done throughout this time period, to obtain information regarding the applicability of ground test(one-G

environment) results and to obtain a fundamental understanding of the structural dynamic characteristic of CTS type flexible solar array configurations.

Thermal vacuum behaviour had also been previously determined by a series of tests at NASA Lewis Research Center's vacuum facilities, Cleveland, Ohio. During these tests, the DSA's were deployed along a horizontal track in a vacuum chamber under a thermal simulation environment, as described in Reference 7.

Other tests on the DSA are noted and described in References 2 and 3.

TEST OBJECTIVES

The overall objective was to determine the structural dynamic and operational behaviour of a DSA in its fully deployed state, in a vacuum with a thermal environment roughly simulating temperatures obtained under: a) on-orbit solar exposure, b) on-orbit eclipse, and c) laboratory ambient conditions. Testing was performed to determine:

- i) natural frequencies and mode shapes;
- ii) modal damping;
- iii) response to dynamic inputs which simulated attitude acquisition maneuvers, thruster firings, and other specialized mission events;
- iv) automatic sun acquisition and tracking performance;
- v) rotation-per-command performance.

TEST EQUIPMENT, CONFIGURATION, AND CONTROL

Vacuum Facility - The tests were performed in CRC's vertical 3m diameter x 9m high vacuum chamber (Figure 3). The chamber has a vacuum capability of $<10^{-2}$ torr under room temperature conditions, and adequately eliminates aerodynamic effects for purposes of dynamic testing. Four movable cryogenic panels each can be located in the vacuum chamber, and via a LN_2 cryogenic system they can be lowered in temperature to $-196^{\circ}C$ in approximately 2 hours. Heat input may be produced by an assembly of quartz halogen lamp bulbs which may be arranged to illuminate the full length (one side) of the DSA. The lamps do not give a true solar spectrum; however the power level to the lamps may be adjusted to induce temperatures on the DSA, which correspond to analytically predicted temperatures for an orbital solar and vacuum environment.

Configuration of DSA, Support Instrumentation, and Hardware - A schematic diagram of the test setup for room temperature tests is shown in Figure 3. No attempt was made to compensate for gravity (by use of counter-weights, etc.), since it was judged to be possible, through the use of analytical methods, to interpret dynamic results obtained in a 1-G field and draw conclusions regarding performance in zero-G (Reference 6).

The DSA was mounted to an interface structure at the top of the vacuum chamber and allowed to hang down freely. This mounting interface was attached to a linear bearing rack and pinion

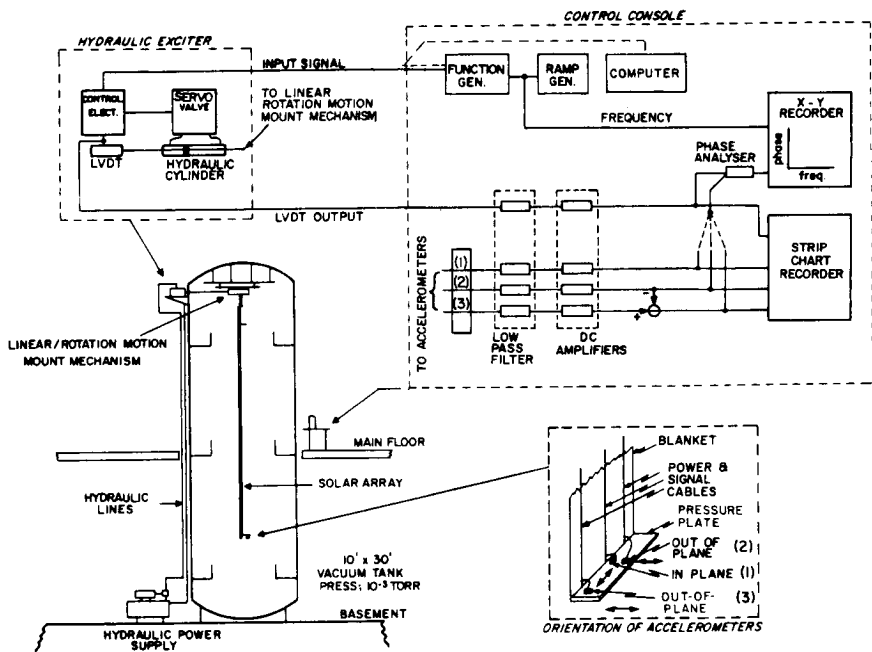


Figure 3 Block Diagram of Test Set-up

mounting mechanism(Figure 4) which was coupled, via a driver bar which penetrated the chamber wall, to an external hydraulic-actuator excitation system. The system may be operated with input waveforms supplied by a function generator or an on-line PDP-9 computer. By this setup it was possible to input sinusoidal, sinusoidal sweep, or computer calculated non-sinusoidal excitations to base of the DSA. The base of the DSA could be excited in out-of-plane linear, in-plane linear, or torsional, directions.

The DSA was mounted so that its' requirement to seek and acquire an artificial sun via an analog sun sensor, and to rotate by command at various rates, could be functionally tested. An electrical test set allowed an operator, external to the vacuum chamber, to send commands and receive instrumentation output. This enabled simulation of the various rotational command modes of the DSA. The accelerometers on the pressure plate of the DSA sense accelerations along three axis(Figure 3):(1) parallel to the blanket and through the center of gravity of the pressure

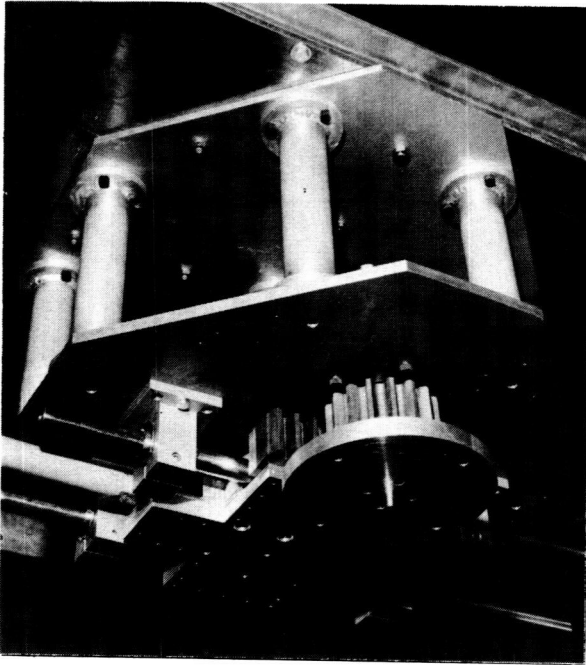


Figure 4 Linear and Rotational Drive Mechanism and Mount for Base of DSA

plate (in-plane accelerometer); (2) perpendicular to the blanket and through the center of gravity of the pressure plate(out-of-plane centerline accelerometer); (3) perpendicular to the blanket and through a point offset from the center of gravity by 61 cm (out-of-plane edge accelerometer). By subtracting out-of-plane centerline accelerations from out-of-plane edge accelerations, torsional accelerations were obtained. The signals from the accelerometers were fed through the tank wall to the control console, where they were conditioned by filters and amplifiers, and then recorded. The phase of the accelerometer output with respect to the input signal(the linear variable differential transformer (LVDT) output signal) was measured by the phase analyzer and recorded on the x-y recorder. At resonance, the phase angle between the acceleration of the base and the acceleration of the tip of the array shifts by 90° . For lightly damped systems this phase shift occurs over a narrow frequency range, and the phase analyzer enables one to find the resonant frequency easily and accurately. A more complete explanation of the test methods and equipment is given in Reference 5.

Thermal Control- Four thermal environments were imposed on the DSA:

- (a) Laboratory Ambient condition with constant temperature

of 20°C.

- (b) Semi-Cold condition, achieved by arranging the cryogenic panels in a V-shape behind the array, and providing heat input from the front-facing chamber wall, as shown schematically in Figure 5. The blanket temperature stabilized at about -40°C in this configuration.
- (c) Eclipse condition, achieved by addition of an encapsulating superinsulation sheath to the above-noted Semi-Cold configuration(Figure 5). The blanket temperature stabilized at about -125°C in this configuration.
- (d) Irradiated condition(induces blanket temperatures expected on-orbit, with full sun), achieved by addition of illumination via the lampbank, to the above-noted Semi-Cold configuration(Figure 5). The blanket temperature on the cell side stabilized at 42°C in this configuration.

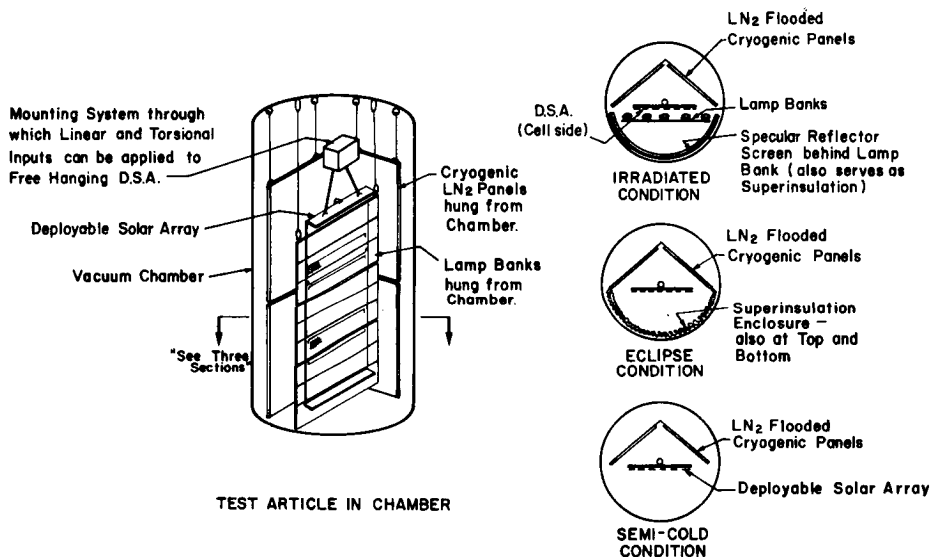


Figure 5 Thermal Environmental Configurations:semi-cold condition, eclipse condition, and irradiated condition

Thermal instrumentation on the DSA consists of 5 platinum wire resistance thermometers, as previously noted. However, to establish precise details of the above thermal conditions(i.e., temperature distribution of DSA, cryogenic panels, and chamber walls) preliminary thermal trials were conducted, in which the DSA and chamber were instrumented with thermocouples. The additional thermocouple lead wires on the DSA were removed prior to dynamic testing, to ensure that they would not influence dynamic

response and damping measurements.

TEST METHODS AND RESULTS

Functional and structural dynamics tests performed on the DSA are summarized in Table 2, identifying direction of excitation, form of excitation, and thermal condition for the dynamic and functional tests performed.

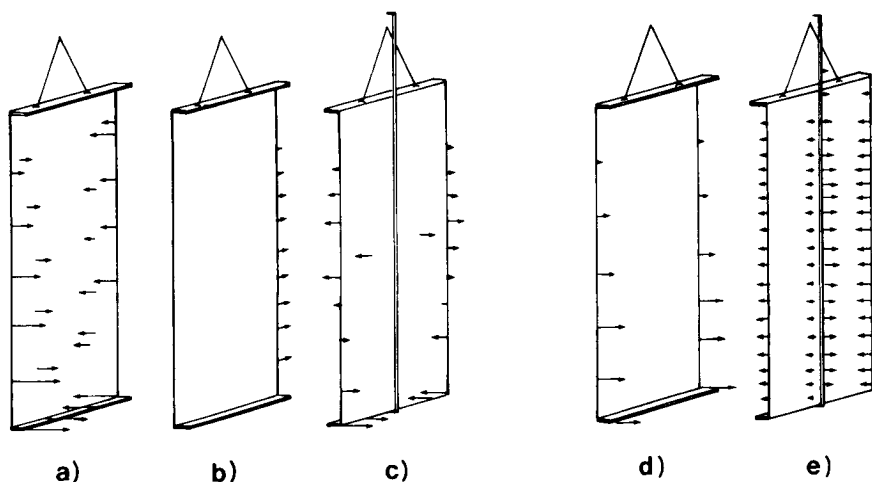
TABLE 2 - SUMMARY OF COMBINED ENVIRONMENT TESTS

Thermal-Vacuum Environment Chamber Setup	Laboratory Ambient: Room Temperature & Pressure (Pre-Test Checkout)	Laboratory Ambient (Room Temperature & 10 ⁻² torr vacuum)	Semi-Cold (blanket = -40°C , 10 ⁻² torr vacuum)	Eclipse Condition (blanket = -125°C, 10 ⁻² torr)	Irradiated Condition (blanket = +42°C vacuum = 10 ⁻² torr)
Test Performed					
<u>Resonance and Damping Tests</u>					
(a)In-Plane Sinusoidal Input	X	X	X	X	X
(b)Torsional Sinusoidal Input	X	X	X	X	X
<u>Non-Sinusoidal Torsional Excitation</u>					
(a)Attitude acquisition simulation	X	X			
(b)Momentum dumping		X			
(c)Special excitations associated with Solar Array Tech- nology Experiment (Reference 8)		X			
<u>Functional Tests</u>					
(a)24 Hour Continuous Stepping For One Complete Cycle		X			
(b)Simulated Sun Acquisition and Autotrack	X	X			
(c)Fast and Slow DSA Stepping, Exercising Various Functional Commands	X	X	X		X

Resonance and Damping Tests- The resonant frequencies of the DSA were determined by exciting the base of the array with a constant amplitude, sinusoidal motion. The excitation frequency was swept linearly at a rate slow enough to allow the resonance to build up. Modal damping was obtained by abruptly stopping the shaker at each resonant point and observing the decay rate (Reference 5). The damping coefficient, ζ , is that defined via the relation

$$\zeta = \frac{1}{2\pi N} \ln \left[\frac{A_o}{A_n} \right]$$

where N is the number of cycles, A_o is the initial amplitude, A_n is the amplitude after N cycles, and ζ is the damping coefficient. Five major resonances and one localized blanket resonance were identified. The results obtained are given in summary form in Table 3. A sampling of detailed cases is given in Table 4. A sketch of the significant mode shapes is given in Figure 6.



a	First IN-PLANE / Torsion Resonance (.26Hz)
b	Second IN-PLANE / Torsion Resonance (.51Hz-.46Hz)
c	Third IN-PLANE / Torsion Resonance
d	First OUT of PLANE Resonance
e	Second OUT of PLANE Resonance

Figure 6 Major Resonant Mode Shapes

The major mode shapes appear in 3 basis categories: out-of-plane, in-plane, and torsion, with intercouplings occurring, particularly between torsion and in-plane. The naming of the categories of the modes (in-plane/torsion, and out-of-plane) follows a

TABLE 3: SUMMARY OF DYNAMICS TEST RESULTS

Mode and Environment	Frequency (Hz)		Damping Coefficient	
	by in-plane excitation	by torsional excitation	by in-plane excitation	by torsional excitation
1st. In-plane/ torsion				
hot	-	.26	-	coulomb
ambient	-	.26	-	coulomb
semi-cold	-	.26	-	coulomb
cold		.26		coulomb
2nd. In-plane/ torsion				
hot	.51 - .48	.51 - .46	.012 - .008	.011 - .008
ambient	.51 - .46	.51 - .46	.011 - .008	.010 - .008
semi-cold	.51 - .48	.51 - .46	.013 - .009	.010 - .008
cold		.51 - .46		.010 - .008
3rd. In-plane/ torsion				
hot	.74	.68	-	highly damped
ambient	.78	.76	.005	.012 - .008
semi-cold		-	-	
cold		.73		coulomb
1st. Out-of- plane				
hot		.27	-	.002 - .0012
ambient	.27	.27	.0017	.003 - .0015
semi-cold		-	-	
cold		.27		.005 - .0012
2nd. Out-of plane				
hot	.90	.78		.008 .006
ambient	.83	.82	.005	.004 .003
semi-cold	.83			
cold	.81		.005 - .004	

TABLE 4 - DETAIL TEST RESULTS

No.	Type of Excitation	Range of Sweep (Hz)	Sweep Rate (Sec/Hz)	Excitation Amplitude	Resonant Frequency (Hz)	Description of Resonance	Response Amplitude	Damping Coefficient	Thermal Environment	Comment
1	in-plane	.2- .62	8,200	.25 cm	.47	2nd in-plane/torsion	1.27 cm		ambient temp.	
2	in-plane	.58- 1.0	15,000	.25 cm	.78	3rd in-plane/torsion	-		"	
					.83	2nd out-of-plane	-		"	
					.91	blanket				
3	in-plane	No sweep	-		.27	1st out-of-plane		.002	"	decays at .51 hz.
					.45	2nd in-plane/torsion		.008		
					.78	3rd in-plane/torsion		.005		
					.83	2nd out-of-plane		.005		
25	torsion	.1- .5	14,500	.34°	.51	2nd in-plane/torsion			hot	excited at .108hz.
					.51	2nd in-plane/torsion			hot	excited at .17 hz.
					.27	1st in-plane/torsion				
					.27	1st out-of-plane				
					.46	2nd in-plane/torsion				
27	torsion	No sweep			.78	2nd out-of-plane		.008-.006	hot	highly damped
					.68	3rd in-plane/torsion		-		
					.51	2nd in-plane/torsion		.0108-.008		
					.26	1st in-plane/torsion		coulomb		
					.27	1st out-of-plane		.002-.0012		

convention established in References 5 and 6; the convention is illustrated in Figure 6. The frequency of the 1st in-plane/torsion mode was found to be .26 Hz. The damping appears to be coulomb in nature(the decay envelop was linear, not exponential, Figure 7).

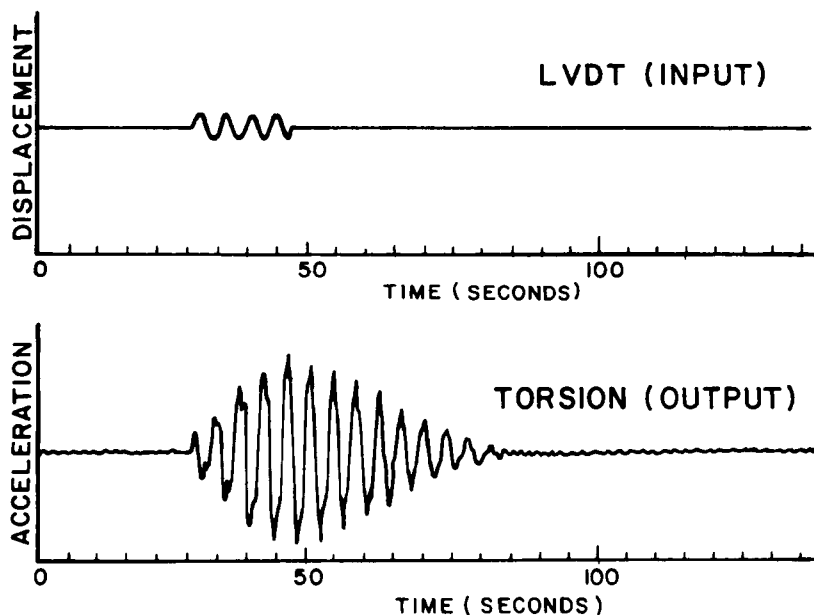


Figure 7 Decay of 1st In-plane/torsion Resonance

The resonant frequency and damping did not change with temperature. The second in-plane/torsion resonance was found to be at .51Hz for small amplitudes(0.64cm) and .46-.48Hz for larger amplitudes(1.2-5cm) which indicates a degree of non-linear behaviour. No appreciable coupling with torsion was noted. The mode shape is shown in Figure 6. The blanket behaved as a rigid plate with the elevation arms flexing to allow movement. Neither the frequency nor the damping coefficient of this resonance varied with temperature. The 1st out-of-plane resonance was found to be .26Hz(Figure 6). Its mode was such that the boom appeared to be in a 1st cantilever mode with the blanket remaining flat. A very small amount of torsion motion was noted. The resonant frequency and the small amplitude damping coefficient did not change with temperature. The large amplitude damping coefficient appears to increase as the temperature decreases. The 3rd in-plane/torsion and the 2nd out-of-plane resonances had large variations in the resonant frequency and the damping coefficient for different test set-ups. These resonances and damping coefficients also varied in an uncorrelated manner with temperature changes. The third in-plane/torsion resonance decayed in a "coulomb like" manner for hot and cold cases and in a viscous manner for ambient temperature. It is noted that both of these resonances have a predominant blanket motion.(Based on the limited testing done, conclusive remarks can not be made

about these latter two resonances and their temperature dependence).

Thermal flutter of the DSA was not observed during any of the tests. Thermally induced static blanket distortion was observed, in which the 3 wiring areas were deflected relative to the solar cell areas by as much as 6cm in the out-of-plane direction. This distortion was most severe under the eclipse conditions.

The tests reported herein (and also in Reference 5) also showed that fundamental array modes could be excited substantially by excitation at frequencies which are fractions of the modal frequencies (superharmonic vibration). This phenomenon is usually attributed to non-linearities in structural stiffness or damping.

Non-Sinusoidal Torsional Excitation- Non-sinusoidal wave forms were input to the base of the array in this series of tests. They were derived by analysis for the purpose of simulation and demonstration of the flexible body dynamics effect on the DSA of spacecraft thruster firings and other disturbances primarily associated with the attitude acquisition phase of the CTS mission. The waveforms were generated by a PDP-9 computer and recorded on magnetic tape. The tape was examined for the presence of spurious input data, and if acceptable, then played through the attenuator directly to the hydraulic actuator (in some cases the hydraulic actuator was driven directly from the PDP-9, in a real-time mode). The non-sinusoidal waveforms were input to the DSA while it operated in its various modes (one rev/day rotation, 15° /minute rotation, autotrack, and stationary state).

The tests did not excite the array to any appreciable amplitude. The 1st and 2nd in-plane/torsion resonances were excited to a small amplitude when the stepper motor started and stopped stepping slews. The largest response, about 1° to 3° , occurred when the stepper motor started and stopped at regular intervals at the resonant frequency of the DSA. The array survived 200 cycles of torsional special excitation with a triangular wave of maximum amplitude of 0.312° without damage.

Functional Tests- A special test set was designed and built in order that the DSA could be commanded via hardwiring with identical commands as will be used on the spacecraft. As previously described, output data was obtained via the three accelerometers, the digital position encoder, and visual and TV monitoring through the vacuum chamber ports.

The functional tests included operation for 360° at the nominal stepping rate, and for multiple full revolutions at the fast stepping rate. Sun acquisition and the ability of the DSA to autotrack, that is to cease stepping on acquiring the sun, was tested. An artificial sun (a 150W light) was set up in the chamber and the DSA stepped until the light came into the sun sensor's field of view. The DSA then stopped. Various override commands were then exercised.

The DSA operated well under the various environments. No serious anomalies were observed during stepping or simulated sun

acquisition tests.

CONCLUSIONS AND REMARKS

The DSA functional testing was completed with no major problems or unexpected anomalies.

Some variations in resonant frequency and damping coefficients with temperature were observed, but no significant large temperature dependent trends were evident. The damping coefficients were found to range between 0.001 and 0.01. The results of the tests were used to validate and substantially improve an analytical dynamics model of the response of the array under test (one-g) conditions. Results calculated using the same analytical model, with the effect of gravity eliminated, indicate that a DSA will have all modes of vibration higher than 0.1 Hz.

Thermal flutter was not observed. Some thermal induced blanket distortion was noted.

Superharmonic response behaviour and certain types of blanket membrane modes, which were not expected or predicted via analysis, were found by testing.

The testing technique described herein, appears to be practical from a spacecraft engineering point-of-view, and is expected to be applicable for future large solar arrays and other flexible appendages.

ACKNOWLEDGEMENTS

The authors express their sincere appreciation to K.Ogilvie, T.McPherson, R.Bonnycastle, R.Bilodous, E.G.Williams and S. Thompson for technical and facilities support associated with the tests. They also wish to thank R.Vetrone for the loan of NASA LERC's lampbank equipment, and N.A.Harrison for numerous suggestions and final review of the manuscript.

REFERENCES

1. C.A.Franklin and E.H.Davison, "A High Power Communications Technology Satellite for the 12-and 14-GHz Bands", Progress in Astronautics and Aeronautics, Vol.32, The MIT Press, Cambridge, Massachusetts, 1974.
2. R.Buhs, "Layout and Technology of the CTS Solar Array Blanket". presented at the Photovoltaic Specialists Conference, IEEE, Palo Alto, 1974.
3. E.Quittner, S.Sachdev, and D.Gossein, "Mechanical Design of a Deployable Flexible Solar Array System for a Communications Satellite", CASI/AIAA Joint Meeting, Toronto, Ontario, 30 and 31st Oct. 1974.
4. Private Communication by T.D.Harrison, "Solar Array Testing Program. Report on Phase 1", October, 1973, CRC File Number CRC 6666-15-1-6.
5. T.D.Harrison, "Communications Technology Satellite Deployed Solar Array Dynamics Tests", CRC Report No.1264, Department of Communications, Ottawa, Jan. 1975.
6. F.R.Vigneron, "A Structural Dynamics Model for Flexible Solar Arrays of the CTS Class", CRC Report No.1268, Department of

Communications, Ottawa, March, 1975.

7. J.S.Smith, S.S.Sachdev, and J.A.Hunter, "Testing of the Communications Technology Satellite Deployable Solar Array Subsystem", Paper No.2.1, 11th IEEE Photovoltaic Specialists Conference, Pheonix, Arizona, May 6-8, 1975.
8. F.R.Vigneron and R.A.Millar, "Plan For Flight Evaluation of Attitude Stabilization And Flexible Solar Array Dynamics For The Communications Technology Satellite", accepted for presentation at the 26th International Astronautical Federation Congress, September, 1975, Lisbon, Portugal.

PRELIMINARY EVALUATION OF THE CONTAMINANT INDUCED ENVIRONMENT FOR THE SPACE SHUTTLE ORBITER*

L. E. Bareiss, R. O. Rantanen, and E. B. Ress, *Martin Marietta Corporation, P. O. Box 179, Denver, Colorado 80201*; L. J. Leger, *NASA, Lyndon B. Johnson Space Center, Houston, Texas 77058*

ABSTRACT

Contamination control of the induced environment during all operational phases of the Space Transportation System (STS) will be an important consideration in ensuring overall satisfactory performance of many of the envisioned ultrasensitive payloads to be flown. A preliminary evaluation of the on-orbit induced environment from those identified major sources of contamination for the STS Shuttle Orbiter is presented. These sources are the external nonmetallic material outgassing/offgassing, flash evaporator vents, cabin atmosphere leakage, Vernier Control System (VCS) 25-lb thrust engines, and the return flux from these sources as a result of gas-gas interactions of the contaminants with the ambient atmosphere. The paper discusses a contamination computer mathematical model that was used to develop the description and predictions of the induced environment along with the extent and physical makeup of the molecular induced environment from these sources. The predicted induced molecular environment from each source is evaluated against current Space Shuttle Program on-orbit contamination control criteria. The flash evaporator vents and the VCS 25-lb thrust engines are shown to significantly exceed applicable contamination control criteria and were the subject of extensive evaluation. Preliminary conclusions concerning the contaminant potential of these sources along with recommendations for various measures of contamination control regarding the Shuttle Orbiter design and operational activities are made.

INTRODUCTION

Unlike preceding space programs, the Space Shuttle Program has planned multiple launchings extending over the next two decades for many of its payloads and Shuttle Orbiter vehicles. As

* This paper is related to work performed under NASA Contract NAS9-14212.

a result of this, the Space Shuttle Program will require proper contamination control measures to maintain payload integrity and ensure the quality of the acquired scientific data. Of particular concern will be the induced molecular and particulate environment generated by the Shuttle Orbiter during its on-orbit operational phase. It is during this phase that all aspects of contamination control must provide an adequate environment for the successful operation of payloads. Because of the wide diversity of considerations involved in contamination assessment, many disciplines must participate in decisions for final requirements and approaches to contamination control. Such is the function of the Particles and Gases Working Group (PGWG) at the Lyndon B. Johnson Space Center, Houston, Texas. The PGWG is comprised of those technical disciplines required to provide contamination assessment of the Shuttle Orbiter and its potential impact on payload systems. Key elements in establishing effective contamination control are the identification and understanding the nature of the contaminant sources, development of the physics of interactions of the contaminants, and the capability to perform in a consistent manner a detailed system analysis of the contaminant environment. Results of the analysis can then be related to given criteria and can be used in all overlapping design and operational approaches for contamination control through the direction of the PGWG.

This paper presents results of a preliminary evaluation of the on-orbit molecular induced environment for the STS Shuttle Orbiter.¹ This evaluation was established to understand the nature and extent of the on-orbit contaminant induced environment emitted from the Shuttle Orbiter, and subsequently to identify those areas where the contaminant induced environment can be minimized through proper design considerations and operational procedures. A contamination computer mathematical model being developed by the Denver Division of Martin Marietta Corp. under contract to NASA was used to establish detailed contamination systems analysis of the Shuttle Orbiter induced environment. Included in this paper is a general outline of the modeling approach indicating some of the important physical considerations used in the modeling to develop the description of the induced environment. A flow diagram indicating the logic of the model, the formulation of some of the basic model relationships along with computer drawn graphic displays are presented to show versatility and utility of the model. In addition to the description of the induced environment, characteristics of the sources that contribute to the induced environment and the extent and physical makeup of the induced environment are presented. Those major Shuttle Orbiter contaminant sources evaluated were outgassing (long term weight loss characteristic of nonmetallic materials), offgassing (short term weight loss characteristics of nonmetallic materials), flash evaporator vents, cabin atmosphere leakage, the Vernier Control System (VCS) 25-lb thrust engines, and the return flux of these sources

as a result of gas-gas interaction with the ambient environment.

The induced environment is evaluated against current on-orbit contamination criteria.² These criteria are:

- 1) fewer than 1 particle larger than 10 microns in a 4-arc minute half angle field-of-view per orbit within 1 km;
- 2) column density less than 10^{12} polar molecules/cm²;
- 3) background brightness from scattering or emission less than 20th magnitude/arc sec in the near ultraviolet;
- 4) return flux of less than 10^{12} molecules/cm²/sec;
- 5) no more than 1% absorption from IR through UV by condensibles on optical surfaces.

Of these criteria, criteria 2) and 4) were used to establish a basic evaluation of the predicted molecular induced environment.

MODEL DESCRIPTION

The following discussions present brief descriptions of some of the major considerations in development of the Shuttle Orbiter Contamination Model. These discussions present a general description of the model, the modeled Shuttle Orbiter geometry, the established lines-of-sight for contamination impact evaluations, and the major contamination sources considered in development of the predicted induced environment for the STS Shuttle Orbiter.

General Model Description - The model has been developed for use on a CDC series 6000 computer using a Scope 3.4.1 operating system. The Shuttle Orbiter Contamination Model consists of a series of data files, main program logic, and subroutines to facilitate handling. The model incorporates a specific Shuttle Orbiter geometric configuration and those previously mentioned contamination sources. A Shuttle Orbiter configuration has been synthesized using a mass transport analog to thermal radiation phenomena for surfaces that act as Lambertian emitters of mass flux (e.g., outgassing, offgassing, and cabin atmosphere leakage). The geometric relationships for point sources (e.g., evaporator vents and VCS) or interactions with the orbital ambient environment are determined from a modified thermal radiation program. The flow fields and contamination assessments are established as subroutines in the model. Figure 1 presents a logic flow diagram of the Shuttle Orbiter contamination computer model used to establish the results presented in this paper.

Without the subroutines, the model uses approximately 105K core of the computer. Several reasons for maintaining the basic model in the general format as presented in the logic flow diagram of Fig. 1 are:

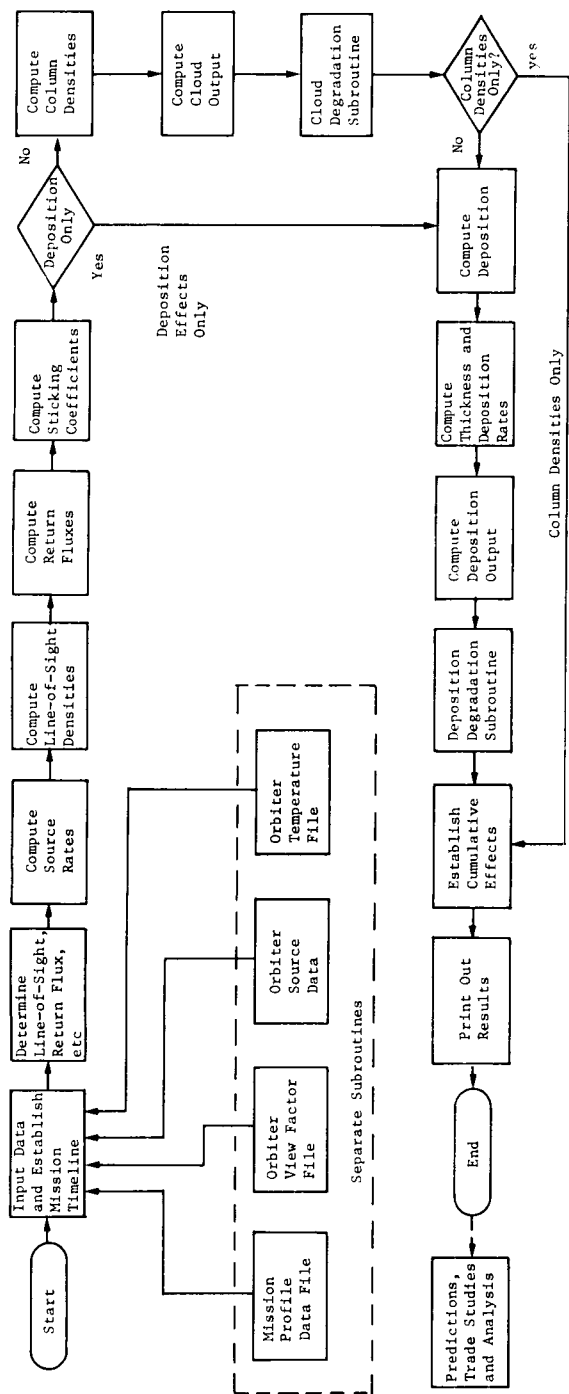


Figure 1. Basic Shuttle Orbiter Contamination Mathematical Model Preliminary Flow Diagram

- 1) Improved fidelity of the Shuttle Orbiter configuration (additional surfaces) will increase the total computer core requirements.
- 2) Sources such as the evaporator, VCS, and return flux do not use a radiation analog for their characteristic source description; therefore, they require different subroutines for computation.
- 3) Timelining of and positioning on the Shuttle Orbiter of the sources identified in 2) have not been firmly established.
- 4) Identification of mission profiles, temperature data, beta angles, mission duration, etc have not been discretely defined and will require additional core storage for these data arrays as the data becomes available.
- 5) The total size required, ultimate usage, and necessary streamlining has yet to be determined for the computer model.
- 6) At this point of the model development, it has been shown that using specific subroutines rather than a large complex computer program is more cost effective in performing timely trade studies.

As can be seen from Fig. 1, four data files are used to develop the model input data. These are mission profile, Shuttle Orbiter geometry (view factors), Shuttle Orbiter contamination sources, and Shuttle Orbiter surface temperatures. Depending upon the detail and nature of the contaminant induced environment to be evaluated, portions of or all of these files are used to establish a mission and mission timeline. The lines-of-sight to be evaluated and return flux characteristics (which are functions of instrument/payload/critical surface characteristics) are established. The contaminant source rates are then calculated and their contributions to selected lines-of-sight, return flux characteristics, and sticking coefficients for the return flux of contaminant are determined. The deposition potential or extent of the induced environment (column density) or both are defined. The deposition and column densities are used as inputs to subroutines that establish degradation factors as required. The cumulative effects are established as a function of orbital time and are summed to establish mission duration influences.

Three different computer data list matrices are developed with respect to the configuration modeling. These listings provide important tabular visibility to all the geometric considerations used in establishing the contamination model and resulting output. These listings are:

- 1) input data matrix;
- 2) view factor data matrix; and
- 3) geometric relationship data matrix.

The input data matrix consists of all necessary input data required to completely describe the geometrical surfaces and configurations analyzed. This matrix contains surface number, geometric surface type (e.g., rectangle, disc, cylinder, etc), surface shadowing capability, surface ability to be shadowed, surface rotation about the major axis system, point input data (e.g., three-dimensional input with respect to program axis system), and surface name and description. The view factor data matrix presents all the modeled Lambertian surfaces including third surface shadowing between the source and receiver capable of impinging upon susceptible surfaces of interest.

The geometric relationship data matrix supplies the computer output information of geometrical relationships between all Shuttle Orbiter surfaces capable of viewing each other. This data is also used in conjunction with closed form mathematical source characteristics for sources other than Lambertian to determine fluxes at surfaces of interest. This matrix includes such things as surface areas, distance between surface center points, perpendicular vector (X,Y,Z components) normalized to the surface area and the angle made by the radius between surfaces with the surface normal vectors.

This computer modeling method was shown on Skylab to be an effective tool in contamination evaluation and assessment. This technique, as in the case with any analytical approach to a problem, is highly dependent upon quality of input data, such as nonmetallic material characteristics, mission profiles, surface temperatures, vent characteristics, and development of the physics involved in establishing how the induced environment will interact with critical surfaces or lines-of-sight in question. These types of limitations are inherent in all forms of modeling. However, they do not detract from the overall utility of such an approach. An assessment of this type allows basic parameters to be identified, geometric considerations to be established, and formulates, in a systematic perspective, the trends that evolve from variations of important physical parameters.

Shuttle Orbiter Model Geometry - The Shuttle Orbiter has been described geometrically by 60 basic surface shapes. These surfaces have been further subdivided into a total of 194 nodes. By inputting the geometry into the computer, the area of each nodal surface, surface location, distance between nodal surfaces, angular relationships, geometric shadowing between nodal surfaces, and fraction of mass leaving each surface impinging on another surface can be established. The physical shapes of the surfaces that are used as inputs to the computer are drawn graphically by scale cathode ray tube displays. These are used to verify location and geometrical shape of any specific surface or relationship between surfaces or contamination sources before finalizing input to the contamination computer model. Figure 2

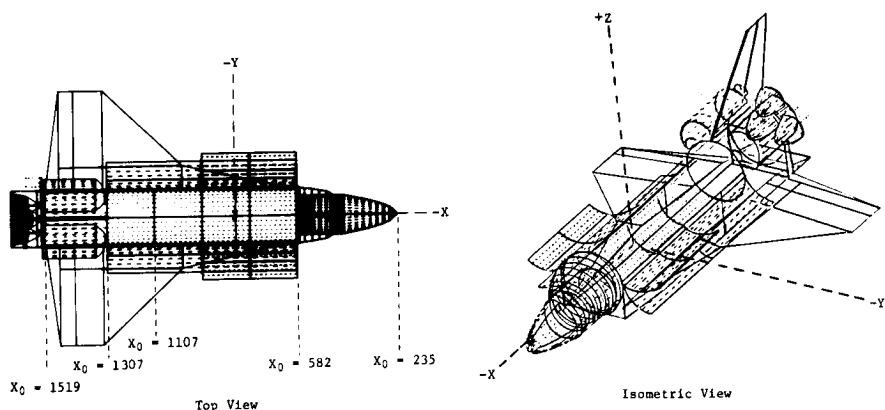


Figure 2. Graphic Displays of the Current Modeled Shuttle Orbiter

presents two computer-drawn graphic displays of the modeled Shuttle Orbiter configuration. This figure presents a top view and a three-dimensional view of the Shuttle Orbiter with its payload bay doors open.

An additional important aspect in the development of the Shuttle Orbiter model is that selected surfaces can be displayed whether they are a source or a receiver and spatial interactions can be developed without addressing the entire configuration. This latter point is useful in surface mapping a configuration for surface and/or material categorization and surface location studies before integrating it into the contamination model for assessment.

The axis system depicted in Fig. 2 is consistent with the current reference axis system being employed by the Space Shuttle Program. Key reference station numbers are presented in Fig. 2 to indicate relative locations of various contamination sources and lines-of-sight to be discussed in the following sections of this paper. Microfilm records are developed and are kept on file for reference and/or additional copies as required.

Baseline Shuttle Orbiter Lines-of-Sight - To evaluate the contaminant induced environment and its impact upon sensitive surfaces or instruments within the payload bay, nine lines-of-sight (originating at $X_0 = 1107$) were established to encompass a 100 deg conical viewing volume within the upper hemisphere of the Shuttle Orbiter. These lines-of-sight encompass the viewing requirements of the majority of identified Shuttle Orbiter payloads, and were also selected to include viewing angles through the anticipated maximum induced environment regimes. This includes those regions directly above the Shuttle Orbiter wings

and those near various aft located point sources. These lines-of-sight are depicted in Fig. 3 and are identified as:

- LOS 1 - parallel to +Z axis;
- LOS 2 - 50 deg off +Z towards +Y;
- LOS 3 - 25 deg off +Z towards +Y;
- LOS 4 - 50 deg off +Z towards ± 45 deg towards +X;
- LOS 5 - 50 deg off +Z towards -X; and
- LOS 6 - 50 deg off +Z towards +X.

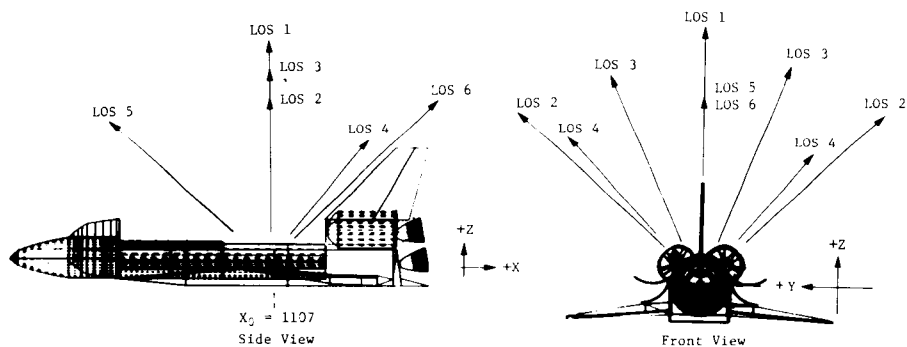


Figure 3. Baseline Lines-of-Sight

To establish the contaminant environment along a line-of-sight, the model uses the view factors and geometric relationships between the Shuttle Orbiter sources and selected points along the line-of-sight. The contaminant mass flux and density (flux/velocity) at each of the selected points are calculated for the individual Shuttle Orbiter sources considered. Integration of these points along the line-of-sight results in mass column density (MCD) in g/cm^2 . By knowing the physical makeup of the contaminants (e.g., H_2O , O_2 , N_2 , N_2O_4 , CO_2 , etc) for each source, mass column density is converted to molecular number column density (NCD) in molecules/ cm^2 for each known constituent. This is also true for defining return flux in grams or molecules/ cm^2/sec of the contaminants as they interact with the ambient atmosphere.

The return flux is calculated directly from the mass column or molecular number column density interaction with the ambient environment. The collision cross section and frequency assume a hard sphere interaction. The scattered molecules are assumed to scatter as a diffuse distribution from the point of collision with respect to the direction of the ambient atmosphere drag vector. For the baseline predictions presented in this paper, return flux has been calculated for a representative payload surface with a physical field-of-view of 28 deg (0.19 steradians). With certain limits, the return flux to surfaces

with larger or smaller physical fields-of-view can be obtained by multiplying the presented results by the ratio of the involved solid angles. In many instances, a surface may have a larger field-of-view over which the mass column density varies significantly. Also, the off axis portions of an instrument such as a cooled baffled system may be susceptible to contamination. Coupled with these possibilities, the density of the induced environment does not decrease uniformly with distance along a line-of-sight. These considerations rule out simple analytical approaches to the return flux calculation and require geometrical relations to be established by additional computer configuration modeling to accurately assess the return flux capability.

Major Shuttle Orbiter Contamination Sources - Analysis of the Shuttle Orbiter configuration has resulted in identification of nonmetallic materials outgassing/offgassing, cabin atmosphere leakage, flash evaporator vents, and 25-lb thrust VCS engines as well as the return flux from these sources as being the major on-orbit Shuttle Orbiter contamination sources. Figure 4 schematically presents the locations and relationships of these major sources.

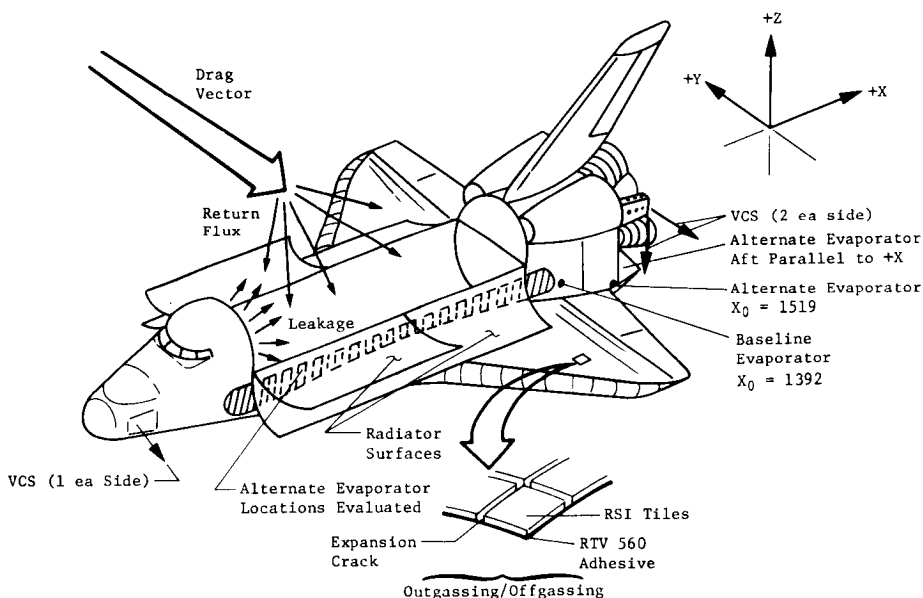


Figure 4. Major Shuttle Orbiter Sources Locations

Table I presents parametric descriptions used in modeling these major sources. It includes source durations/frequencies, flowrates, constituents, plume shape functions (Lambertian-cos

Table I. Major Shuttle Orbiter Sources Summary

Major Sources	Duration/Frequency	Flowrate	Constituents	Plume Shape Function	Velocity	Size Parameter
Outgassing	Continuous	$5.0e^{-t/4100}$ $e^{(T-100)/29}$ $\times 10^{-10}$ g/cm ² /sec	Hydrocarbon chain fragments KIV's, etc.	$\cos \theta/r^2$	$12.9 \sqrt{T} \text{ (}^\circ\text{K)} \text{ m/sec}$	Molecular Avg. M = 100 (assumed)
Offgassing	Continuous for first 100 hours on-orbit	$3.87e^{-0.14t}$ $3.0e^{-0.055t}$ $e^{(T-100)/29} \times 10^{-9}$ g/cm ² /sec	Water Light gases Volatiles	$\cos \theta/r^2$	$30.4 \sqrt{T} \text{ (}^\circ\text{K)} \text{ m/sec}$	Molecular Avg. M = 18 (assumed)
Evaporator *(2)	As required	13.64 kg/hr total	Water	$\cos^6 (1.01 \theta)/r^2$ $[0^\circ < \theta < 36.8^\circ]$ $\frac{e}{r^2} - 0.0773(\theta - 36.8^\circ)$ $\frac{e}{r^2} [36.8^\circ < \theta < 148^\circ]$	1012 m/sec	Molecular M = 18
Cabin Atmosphere Leakage	Continuous	3.18 kg/day	O ₂ N ₂ CO ₂ H ₂ O	$\cos \theta/r^2$	$2220 \sqrt{\frac{T}{M}} \text{ m/sec}$	Molecular Avg. M = 29
RCS Vergier Engines	As required	40.8 g/min	H ₂ O N ₂ H ₂ CO CO ₂ H	$\left(\frac{\cos(\frac{\theta}{2})}{r^2} \right)^{8.65}$ $\frac{e}{r^2} [0^\circ < \theta < 40^\circ]$ $\frac{e}{r^2} 0.0467(\theta - 40^\circ)$ $\frac{e}{r^2} [40^\circ < \theta < 140^\circ]$ $\frac{e}{r^2} - 4.67$ $\frac{e}{r^2} [140^\circ < \theta < 180^\circ]$	3505 m/sec	Molecular
Ambient Reflection	~10 to 30 min per orbit	Varies with above sources & orbital attitude	Any of the above sources	$\cos \theta/r^2$ from collision points	Varies with all above sources Max = 7.65 km/sec	Varies with all above sources

* Plume reflections off of structural surfaces (e.g. wings, experiment bay doors) are equivalent to a source equal to the plume impingement rate with a $\cos \theta/r^2$ distribution and a velocity of $30.4\sqrt{T}$ m/sec from the surface where T = surface temperature (°K).

** RCS plume reflections off of structural surfaces are assumed to have a rate equal to the plume impingement rate with a $\cos \theta/r^2$ distribution and a velocity equal to $129\sqrt{\frac{T}{M}}$ where T = surface temperature (°K).

M = Molecular weight
T = Temperature (°C unless noted)
t = Time (hours) of vacuum exposure
θ = Angle (degrees) off surface normal or plume centerline
r = Distance (cm) from emitter to receiver

θ/r^2 or other), velocities as a function of temperature (T) $^{\circ}\text{K}$ and molecular weight (M), and size parameter. Each source is handled uniquely and is a function of numerous variables. A brief summary of each source follows.

The mass loss of Shuttle Orbiter nonmetallic materials is considered as the sum of materials outgassing (which comes from the bulk material characteristics and is long term in nature) and materials offgassing (which includes release of adsorbed and absorbed volatiles, gases, and liquids, and decays to below the outgassing rate after approximately 50 to 60 hours of vacuum exposure depending on temperature and on duration of on-orbit exposure). For presentation purposes, both the outgassing and offgassing rates are identified at the 100°C temperature. However specific temperature relationships are used in the model to establish resulting outgassing rates as a function of surface temperature. The primary nonmetallic material contamination source is the Reusable Surface Insulation (RSI) of the Shuttle Orbiter Thermal Protection System (TPS) tiles which emit outgassed and offgassed products from the RTV 560 TPS adhesive as well as other components of the RSI system through the expansion cracks. (See Fig. 4.) Recent testing of a representative RSI tile configuration at MSFC³ yielded weight loss data that is used in the model and reflected in Table I for outgassing at time zero and 100°C . Source rates for outgassing and offgassing are modeled as a function of surface temperature (T) in $^{\circ}\text{C}$ and time of vacuum exposure (t) in hours.

Cabin atmosphere leakage is considered to be that amount of cabin atmosphere that will leak from the one atmos. pressurized crew quarters through structural seams, cracks, and seals. All leakage is assumed to be emitted from the entire surface area of the forward bulkhead of the payload bay in a diffuse manner because it is within this area that the largest number of penetration points exist.

The evaporator vent system can flash evaporate approximately 142 kg of water/day as produced by the Shuttle Orbiter fuel cell system. The baseline locations for these vents are at $X_0 = 1392$, $Y_0 = \pm 113$, and $Z_0 = 323$ (Fig. 4). Several alternative vent locations have been analyzed for this source in an attempt to minimize its potential contamination impact. These will be covered later under minimization studies. Test data⁴ for evaporator vent flowfields were modeled using a closed-form analytical approach developed by Simons⁵ describing the plume as a function of separation distance (r) and angle (θ) off the vent centerline. An additional concern for the two evaporator vents at the baseline location is their increased contamination potential caused by vent plume reflections off of the Shuttle Orbiter wings. Plume reflections off of the Shuttle Orbiter wings are assumed to have a source rate equal to the plume impingement rate with a $\cos \theta$ distribution and a velocity

distribution based upon thermal accommodation with the wing surfaces.

The VCS consists of 6 monomethyl hydrazine/nitrogen tetroxide (MMH/ N_2O_4) 25-lb thrust hypergolic engines used for vehicle attitude control during payload operations. Two forward engines are canted at 35 deg from -Z towards +Y using a scarfed nozzle resulting in an effective 45 deg thrust angle for these engines. Two of the four aft engines fire in the -Z direction and the remaining two aft engines fire in the +Y direction. These are also modeled using the Simons⁵ approach modified to include the test data of Chirivella and Simon⁶ at angles greater than 140 deg from the engine centerline. As with the evaporator source, wing reflections (from the 4 aft engines) significantly impact the induced environment. These engines operate on an as-required basis with total usage a function of orbital altitude, attitude, and payload pointing (deadband) requirements. Extensive minimization studies have been conducted on the VCS 25-lb thrust engines and will be discussed later.

Although not a unique source in itself, the return flux of emitted contaminant species is also considered. This results from the interaction of contaminant molecules with the ambient molecular flux causing them to be reflected back to sensitive Shuttle Orbiter/payload surfaces. This phenomena is modeled as a function of a variety of parameters including size and mass of contaminant and ambient molecules, orbital and contaminant velocities, orbital altitude, surface field-of-view and orientation with the drag vector, and contaminant and ambient molecular densities.

BASELINE INDUCED ENVIRONMENT PREDICTIONS

The induced environment predictions for major Shuttle Orbiter contamination sources are presented in Tables II through VI for the identified lines-of-sight (LOS 1 - LOS 6). Depicted in each table are predicted mass column density (MCD), number column density (NCD), and maximum return flux to a 0.19 steradian surface for three representative orbital altitudes (700, 435, and 200 km). The maximum return flux corresponds to periods when ambient atmosphere flow is perpendicular and into the surface of interest. These baseline tabular results can be evaluated against current applicable contamination control criteria, criteria 2) and 4), presented in the Introduction. A brief evaluation and discussion of baseline predictions follows.

Outgassing Predictions - Table II includes predictions for outgassing, based upon vehicle attitude and orbital positions, for the maximum and minimum anticipated vehicle surface temperatures. As indicated, NCD predictions meet current criteria of 10^{12} polar (infrared active) molecules/ cm^2 . The return flux at 200 km is attenuated to approximately zero because at this

Table II. Outgassing Induced Environment Predictions
for the Shuttle Orbiter Configuration

Predicted Parameters		MCD (g/cm ²)	NCD (mol/cm ²)	Return Flux (Max) (mol/cm ² /second)		
Line-of-Sight/ Temperature Extreme				700 km	435 km	200 km
LOS 1	Max	3.1(-11)*	2.0(11)	3.4(9)	9.1(10)	~0
	Min	1.4(-12)	8.8(9)	1.5(8)	4.1(9)	~0
LOS 2	Max	2.2(-11)	1.4(11)	2.4(9)	6.7(10)	~0
	Min	1.4(-12)	8.8(9)	1.5(8)	4.1(9)	~0
LOS 3	Max	2.7(-11)	1.7(11)	2.9(9)	7.9(10)	~0
	Min	1.4(-12)	8.8(9)	1.5(8)	4.1(9)	~0
LOS 4	Max	2.8(-11)	1.7(11)	3.0(9)	7.9(10)	~0
	Min	1.2(-12)	7.2(9)	1.3(8)	3.5(9)	~0
LOS 5	Max	2.4(-11)	1.5(11)	2.7(9)	7.3(10)	~0
	Min	1.3(-12)	8.1(9)	1.4(8)	3.8(9)	~0
LOS 6	Max	3.8(-11)	2.4(11)	4.1(9)	1.1(11)	~0
	Min	1.1(-12)	6.6(9)	1.2(8)	3.1(9)	~0

Table III. Offgassing Induced Environment Predictions
for the Shuttle Orbiter Configuration

Predicted Parameters		MCD (g/cm ²)	NCD (mol/cm ²)	Return Flux (Max) (mol/cm ² /second)		
Line-of-Sight/ Temperature Extreme				700 km	435 km	200 km
LOS 1	Max	6.5(-11)*	2.1(12)	1.3(9)	4.0(10)	2.0(12)
	Min	3.0(-12)	9.9(10)	6.0(7)	1.8(9)	9.0(10)
LOS 2	Max	4.7(-11)	1.6(12)	9.3(8)	2.8(10)	1.4(12)
	Min	2.9(-12)	9.8(10)	5.7(7)	1.7(9)	8.7(10)
LOS 3	Max	5.5(-11)	1.8(12)	1.1(9)	3.1(10)	1.7(12)
	Min	3.0(-12)	9.9(10)	6.0(7)	1.8(9)	9.0(10)
LOS 4	Max	6.0(-11)	2.0(12)	1.2(9)	3.3(10)	1.8(12)
	Min	2.6(-12)	8.5(10)	5.3(7)	1.5(9)	7.7(10)
LOS 5	Max	5.0(-11)	1.7(12)	1.0(9)	3.0(10)	1.6(12)
	Min	2.8(-12)	9.0(10)	5.7(7)	1.6(9)	8.3(10)
LOS 6	Max	8.0(-11)	2.7(12)	1.6(9)	4.7(10)	2.3(12)
	Min	2.3(-12)	7.5(10)	4.7(7)	1.3(9)	6.7(10)

Table IV. Leakage Induced Environment Predictions
for the Shuttle Orbiter Configuration

Predicted Parameters		MCD (g/cm ²)	NCD (mol/cm ²)	Return Flux (Max) (mol/cm ² /second)		
Line-of-Sight				700 km	435 km	200 km
LOS 1		1.0(-9)*	2.2(13)	1.2(10)	3.7(11)	1.9(13)
LOS 2		9.9(-10)	2.2(13)	1.2(10)	3.7(11)	2.0(13)
LOS 3		1.1(-9)	2.3(13)	1.3(10)	3.9(11)	2.1(13)
LOS 4		8.8(-10)	1.9(13)	1.1(10)	3.2(11)	1.7(13)
LOS 5		1.6(-9)	3.5(13)	2.0(10)	5.6(11)	3.1(13)
LOS 6		8.6(-10)	1.9(13)	1.1(10)	3.2(11)	1.7(13)

*(-11) = 10⁻¹¹

Table V. Shuttle Orbiter Baseline Evaporator, $X_o = 1392$, Induced Environment Predictions

Predicted Parameters Line-of-Sight/ Evaporators		MCD (g/cm^2)			NCD (mol/cm ²)	Return Flux (Max) (mol/cm ² /second)		
		Direct Impingement	Wing Reflection	Total		700 km	435 km	200 km
LOS 1					Total			
-Y Evaporator	0		2.6(-9)	2.6(-9)	8.7(13)	5.3(10)	1.4(12)	7.9(13)
+Y Evaporator	0		2.6(-9)	2.6(-9)	8.7(13)	5.3(10)	1.4(12)	7.9(13)
Both	0		5.2(-9)	5.2(-9)	1.7(14)	1.1(11)	2.9(12)	1.6(14)
LOS 2								
-Y Evaporator	3.3(-9)*		6.3(-9)	9.6(-9)	3.3(14)	1.9(11)	5.3(12)	2.8(14)
Opposite Evaporator**	0		2.6(-11)	2.6(-11)	8.5(11)	5.3(8)	1.4(10)	7.6(11)
Both	3.3(-9)		6.3(-9)	9.6(-9)	3.3(14)	1.9(11)	5.3(12)	2.8(14)
LOS 3								
-Y Evaporator	4.6(-10)		6.3(-9)	6.8(-9)	2.3(14)	1.3(11)	4.0(12)	2.0(14)
Opposite Evaporator**	0		4.9(-10)	4.9(-10)	1.6(13)	9.9(9)	2.8(11)	1.4(13)
Both	4.6(-10)		6.8(-9)	7.4(-9)	2.4(14)	1.4(11)	4.3(12)	2.1(14)
LOS 4								
-Y Evaporator	1.7(-9)		9.8(-9)	1.1(-8)	3.8(14)	2.2(11)	6.3(12)	3.3(14)
Opposite Evaporator**	0		4.4(-12)	4.4(-12)	1.4(11)	8.6(7)	2.4(9)	6.6(9)
Both	1.7(-9)		9.8(-9)	1.1(-8)	3.8(14)	2.2(11)	6.3(12)	3.3(14)
LOS 5								
-Y Evaporator	0		1.3(-9)	1.3(-9)	4.1(13)	2.5(10)	6.9(11)	3.6(13)
+Y Evaporator	0		1.3(-9)	1.3(-9)	4.1(13)	2.5(10)	6.9(11)	3.6(13)
Both	0		2.6(-9)	2.6(-9)	8.2(13)	5.0(10)	1.4(12)	7.3(13)
LOS 6								
-Y Evaporator	0		2.4(-9)	2.4(-9)	7.9(13)	4.6(10)	1.3(12)	7.3(13)
+Y Evaporator	0		2.4(-9)	2.4(-9)	7.9(13)	4.6(10)	1.3(12)	7.3(13)
Both	0		4.8(-9)	4.8(-9)	1.6(14)	9.2(10)	2.7(12)	1.4(14)

* (-9) = 10^{-9}

**Opposite Evaporator corresponds to the evaporator on the opposite side of the Shuttle Orbiter with respect to the line-of-sight

Table VI. Shuttle Orbiter VCS (25 lb thrust)
Induced Environment Predictions

Predicted Parameters Line-of-Sight & Engine Flux Direction	MCD (g/cm ²)			NCD (mol/cm ²) Total	Return Flux (Max) (mol/cm ² /second)		
	Direct Impingement	Wing Reflection	Total		700 km	435 km	200 km
LOS 1							
Aft -Z*	2.4(-10)***	1.8(-8)	1.8(-8)	4.4(14)	2.7(11)	7.6(12)	3.9(14)
Aft Y*	1.9(-9)	6.3(-9)	8.2(-9)	2.0(14)	1.2(11)	3.4(12)	1.8(14)
Forward Y/Z*	1.6(-10)	0	1.6(-10)	3.9(12)	2.3(9)	6.6(10)	3.4(12)
LOS 2							
Aft -Z	7.3(-10)	3.3(-8)	3.4(-8)	8.3(14)	4.9(11)	1.4(13)	7.3(14)
Aft -Z** _{opp}	0	3.0(-10)	3.0(-10)	7.3(12)	4.4(9)	1.2(11)	6.6(12)
Aft Y	2.0(-8)	1.0(-8)	3.0(-8)	7.3(14)	6.8(11)	1.2(13)	6.6(14)
Aft Y _{opp}	0	2.9(-10)	2.9(-10)	7.1(12)	4.1(9)	1.2(11)	6.3(12)
Forward Y/Z	1.3(-9)	0	1.3(-9)	3.2(13)	1.9(10)	5.4(11)	2.9(13)
Forward Y/Z _{opp}	0	0	0	0	0	0	0
LOS 3							
Aft -Z	3.4(-10)	3.4(-8)	3.4(-8)	8.3(14)	4.9(11)	1.4(13)	7.3(14)
Aft -Z** _{opp}	0	2.7(-9)	2.7(-9)	6.6(13)	3.9(10)	1.1(12)	5.9(13)
Aft Y	6.2(-9)	8.9(-9)	1.5(-8)	3.7(14)	2.2(11)	6.3(12)	3.2(14)
Aft Y _{opp}	0	3.5(-9)	3.5(-9)	8.5(13)	5.1(10)	1.5(12)	7.6(13)
Forward Y/Z	4.5(-10)	0	4.5(-10)	1.1(13)	6.6(9)	1.9(11)	9.8(12)
Forward Y/Z _{opp}	0	0	0	0	0	0	0
LOS 4							
Aft -Z	5.4(-10)	5.8(-8)	5.9(-8)	1.4(15)	8.5(11)	2.4(13)	1.3(15)
Aft -Z** _{opp}	0	7.9(-11)	7.9(-11)	1.9(12)	1.1(9)	3.2(10)	1.7(12)
Aft Y	2.2(-8)	1.3(-8)	3.5(-8)	8.5(14)	5.1(11)	1.5(13)	7.6(14)
Aft Y _{opp}	0	6.3(-11)	6.3(-11)	1.5(12)	9.3(8)	2.7(10)	1.4(12)
Forward Y/Z	6.4(-10)	0	6.4(-10)	1.6(13)	9.3(9)	2.7(11)	1.4(13)
Forward Y/Z _{opp}	0	0	0	0	0	0	0
LOS 5							
Aft -Z*	2.1(-11)	7.4(-9)	7.4(-9)	1.8(14)	1.1(11)	3.2(12)	1.6(14)
Aft Y*	2.9(-10)	3.0(-9)	3.3(-9)	8.1(13)	4.9(10)	1.4(12)	7.3(13)
Forward Y/Z*	1.1(-10)	0	1.1(-10)	2.7(12)	1.6(9)	4.6(10)	2.4(12)
LOS 6							
Aft -Z*	1.4(-10)	3.2(-8)	3.2(-8)	7.8(14)	4.7(11)	1.3(13)	7.1(14)
Aft Y*	3.1(-9)	7.1(-9)	1.0(-8)	2.4(14)	1.5(11)	4.1(12)	2.2(14)
Forward Y/Z*	0	0	0	0	0	0	0
* Due to symmetry of this line-of-sight with respect to verniers, contributions to it from opposite side verniers are equal to values presented.							
** Contribution to line-of-sight from vernier on opposite side of vehicle $\left[Z_{opp}, Y_{opp}, Y/Z_{opp} \right]$							
***(-10) = 10 ⁻¹⁰							

altitude, the mean free path of the outgassed molecules is essentially so short (less than 1 meter) that the molecules are unable to travel far enough into the ambient drag vector to be reflected back to the evaluated surface. The return flux is inversely proportional to mean free path (MFP) and directly proportional to mass column density (MCD) so that return flux is proportional to the MCD/MFP. Therefore, as ambient density increases with a decrease in altitude, the mean free path decreases causing an increase in return flux. However, as the mean free path decreases, the chance of a molecule intercepting a line-of-sight decreases when the ambient drag vector is oriented such that it carries it away from the line-of-sight. The net result is that the mass column density decreases faster (after some decreasing altitude is reached) than the collision frequency increases. There will be a point near 250 to 300 km when return flux of outgassed molecules for a given mass column density is a maximum.

Offgassing Predictions - Offgassing induced environment predictions are depicted in Table III for maximum and minimum temperature extremes after 10 hours on-orbit vacuum exposure. The 10 hour point was chosen for evaluation assuming that this would be the elapsed time after launch when on-orbit operations might be expected to commence. After initial Shuttle Orbiter flights, the offgassing rate at the 10 hour point may be considerably less than predicted values. Offgassing as opposed to outgassing will demonstrate a return flux capability at the lower orbital altitudes (down to 200 km) because the mean free path for the offgassants at these altitudes is considerably longer than that of the larger outgassing molecules. In some cases, the offgassing number column density and return flux approach and/or exceed applicable contamination control criteria. This source is considered not to present a major contamination problem unless early on-orbit usage of cryogenic systems is contemplated. Even in this case, proper operational timelining and attitude selection will minimize the effect from this source for those susceptible payloads.

Cabin Atmosphere Leakage Predictions - Table IV depicts induced environment predictions for cabin atmosphere leakage. Leakage source rates are not temperature dependent; therefore, no maximum or minimum relationships are included. All predicted NCDs fall within the low 10^{13} molecule/cm² range. Approximately 2% of the leakage effluents are polar (infrared active), which brings the NCD levels within the applicable criteria. In contrast, the return flux predictions at 200 km significantly exceed the 10^{12} molecule/cm²/sec criteria for all lines-of-sight. Return flux impacts resulting from this source can be minimized through proper choice of vehicle attitudes that avoid the ambient drag vector being perpendicular to the sensitive surfaces in question. Additionally, fields-of-view smaller than 0.19 steradians would reduce the amount of return flux received by a surface.

Evaporator Predictions - Table V presents the predicted evaporator induced environment. For lines-of-sight LOS 1, 5, and 6, the contributions from each evaporator is the same because of symmetry considerations. For lines-of-sight LOS 2, 3, and 4, the -Y evaporator contribution corresponds to the evaporator on the same side of the (X,Z) plane as the line-of-sight. Opposite evaporator is the evaporator on the opposite side of the Shuttle Orbiter. At this location, the evaporator exhaust also reflects off of the Shuttle Orbiter wings and is a significant contributor to all lines-of-sight. For lines-of-sight in the (X,Z) plane, the wing reflection is the only contribution from the evaporator.

The molecular number column densities are seen to vary between 10^{13} and 10^{14} molecule/cm² for the baseline evaporator location, and the return flux criteria is exceeded at all altitudes below approximately 450 km. Because the evaporator's contribution to all the established lines-of-sight exceeds the applicable contamination control criteria, other locations have been evaluated to determine if a more suitable position could be found to minimize this contaminant source.

Vernier Control System (VCS) 25-lb Thrust Engine Predictions - Table VI presents the induced environment predictions for the VCS engines. Each engine contribution is delineated because each may fire independently. The duration of each engine pulse and firing frequency is highly dependent on the orbital altitude and vehicle attitude requirements. Table VI includes contributions of the VCS engines from both sides of the vehicle to the payload lines-of-sight. Values presented for the forward VCS engines result only from the backflow portion of the engine plume. The molecular number, column density, which varies between 10^{12} to 10^{14} molecule/cm² and the return flux, exceed the applicable criteria for almost all thrusters and orbital altitudes evaluated. As in the case of the evaporator, minimization studies for the VCS engines were conducted to determine if their contribution to the lines-of-sight could be significantly reduced.

OTHER CONSIDERATIONS

This section addresses other areas of evaluation in addition to the induced atmosphere predictions for payload lines-of-sight. Included are induced environment density as a function of distance along LOS 1 for each of the major sources evaluated and for all sources combined, and the potential of surface deposition for certain situations as related to important Shuttle Orbiter surfaces.

Induced Environment Density Variations - An additional utility of modeling the induced environment as presented herein is that contaminant induced environment density (g/cm³) can be determined at points along any given line-of-sight. This is extremely

useful in conducting specific trade studies, compatibility analyses, and determining MCDs between specific points along a line-of-sight when evaluating boom-mounted instruments or subsatellite systems. Figure 5 illustrates the extent of the induced

environment by presenting predicted maximum densities along LOS 1 for each of the Shuttle Orbiter major sources, as well as the total for all major sources evaluated. Data is presented for distances from the Shuttle Orbiter X axis starting at the entrance aperture of the previously mentioned representative surface located at $X_0 = 1107$ and extending out to a distance where all source densities approach a $1/r^2$ characteristic (approximately 80 meters). By using a series of such plots, an isodensity profile about the Shuttle Orbiter can be developed to show the spatial variation for each major source and all the sources combined.

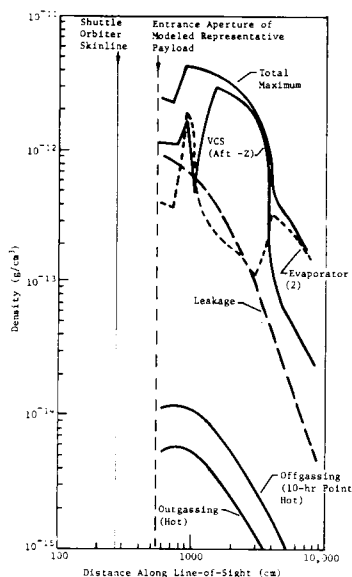


Figure 5. Density as a Function of Distance Along LOS 1 for Major Shuttle Orbiter Sources

representative surface is located at the Shuttle Orbiter skinline 4.9 m forward of the payload bay aft end, parallel to the X axis viewing towards +Z. If this rate continued for 7 days, the total impingement would be on the order of 6×10^{-7} g/cm², which equates to approximately 60Å deposit of contaminants for unit density and unit sticking coefficient. It is unlikely that this high rate will continue for all of the vacuum exposure time. It depends on sunlight exposure per orbit and Shuttle Orbiter attitude. However, this maximum rate is possible for specific mission profiles and could impact some critical surfaces located at this position.

The outgassing rate assumed here is the steady-state rate for RTV 560 (plus the tile configuration) at 100°C. If the initial mass loss period during early vacuum exposure has a higher emission rate of condensible species, the contamination potential could significantly increase. Since this is one of the few Shuttle Orbiter surfaces that view directly into the payload bay, the use of RTV 568 in place of RTV 560 should be

Tail Outgassing Into Payload Bay -

The leading edge of the Shuttle Orbiter tail has a direct line-of-sight into the payload bay. The outgassed flux, from the tail, on a representative surface in the payload bay is approximately 10^{-12} g/cm²/sec for an outgassing rate of 5×10^{-10} g/cm²/sec at 100°C. The representative

considered because RTV 568 reportedly has a lower outgassing rate. Testing for condensible species during the early vacuum exposure period for RTV 560 is being planned by JSC. This high rate will occur for the first Shuttle Orbiter mission or for missions on which the tail leading edge surface has been replaced. Continued vacuum exposure on subsequent flights will reduce the contamination potential of this surface.

Shuttle Orbiter Radiator Degradation - Portions of the radiator surfaces of the Shuttle Orbiter can receive direct line-of-sight flux from the $\pm Y$ facing aft VCS engines, the $\pm Y$ facing Reaction Control System (RCS) 900-lb thrust engines and outgassing from the Orbital Maneuvering System (OMS) pod structure. Additionally, the OMS 6000-lb thrust engines and the RCS engine effluents, along with the Shuttle Orbiter outgassing effluents can impinge on the radiator surfaces through interactions with the ambient atmosphere (return flux). These four sources (VCS, RCS, and OMS engines, and outgassing) result in deposits that are long term in nature especially in the presence of ultraviolet radiation, and even, in some cases, proton and electron fluxes. A preliminary prediction of the potential radiator degradation from these sources is presented here to indicate the magnitude of the potential contamination problem.

The portion of the radiator surfaces that have the greatest degradation potential from the $\pm Y$ VCS and RCS engines is the outer-aft door radiator surfaces, (See Fig. 4.) The deposition rate per second of engine firing is approximately 2.1×10^{-10} g/cm²/sec and 3.3×10^{-9} g/cm²/sec for the VCS and RCS engines, respectively. For typical mission VCS and RCS engine requirements, the solar absorptivity of the radiator surfaces can degrade to 0.21 and 0.11, respectively, from an original solar absorptivity of 0.08. The actual degradation is a strong function of engine fuel consumption for a given mission.

The portion of the radiator surfaces that have the greatest degradation potential from the OMS pod structure outgassing is also the outer-aft door radiator surfaces. For an outgassing rate of 5×10^{-10} g/cm²/sec at 100°C, the flux rate on this surface is 2.0×10^{-11} g/cm²/sec. Because the radiator surfaces operate over a wide range of temperatures, the fraction depositing will vary. Early vacuum exposure periods may exhibit a higher rate of condensibles. If this is borne out through testing, consideration should be given, for the OMS pod structure, to replacing the RTV 560 tile adhesive with RTV 568 which reportedly has a lower outgassing rate.

The return flux of outgassing and RCS and OMS engine effluents will be a strong function of altitude and attitude. Based on a typical mission RCS and OMS engine requirements, the radiator degradation (change in solar absorptivity) could be 0.14 and 0.24, respectively, from an original solar absorptivity

of 0.08. These sources would impact the total radiator surface area. The return flux of outgassing from the Shuttle Orbiter additionally depends on temperature relations between Shuttle Orbiter external surfaces and radiator surfaces.

In summary, the sources considered can potentially degrade Shuttle Orbiter radiator surfaces. Direct impingement from the VCS engines, RCS engines, and the OMS pod structure outgassing primarily impact one-fourth of the radiator surface area. The return flux of the RCS engines, OMS engines, and Shuttle Orbiter outgassing impact the entire radiator surface area.

The OMS engine and RCS engine impact can be eliminated or minimized by closing the payload bay doors during the periods when these engines are required to operate. The degradation potential of the sources presented are being reassessed as specific mission profiles are defined in detail and test results are evaluated.

MINIMIZATION STUDIES

As a result of exceeding certain aspects of the current contamination control criteria for baseline locations, minimization studies were performed for the VCS engines and the evaporator vents. The approach taken was to evaluate relocation and canting of the VCS engine nozzles and evaporator vent nozzles from their baseline locations. Data from these evaluations were used to select optimum locations from an overall vehicle standpoint (e.g., guidance and control, structures, thermal, etc).

Vernier Control System (VCS) 25-lb Engines - The baseline aft VCS engine location is shown in Fig. 4. At this location, the effects of canting the engine and the wing elevon were investigated in an attempt to reduce the wing reflected and direct flow contributions to payload lines-of-sight. For all of the situations analyzed, the predicted molecular number column densities were in the 10^{13} to 10^{14} molecule/cm² range. Relocation of all of the VCS engines to a forward location was investigated for comparison to the baseline locations. At the forward location, the -Z firing aft engine must be repositioned to fire along +Z to maintain the same attitude control. The VCS engines were also canted down (-Z) and forward (-X) to determine the resultant effect to payload lines-of-sight at this location. The molecular number column densities exceeded 10^{12} molecule/cm² in all cases² and were typically in the range of 10^{13} to 10^{14} molecule/cm².

For all locations and orientations (canting angles) evaluated, the VCS engines exceed both the number column density and the return flux criteria. For payloads sensitive to VCS engine

effluents, consideration could be given by payloads to using Control Moment Gyros (CMGs) for maintaining attitude control. Gimballed payloads could also minimize VCS engine requirements for specific attitudes. Another alternative is to select deadband, attitude, and altitude requirements that result in minimum usage of the VCS engines.

Evaporator Vent System - Because the evaporator vents can be a near-continuous source and have the capability to be located at more positions than other major sources, they have undergone the most extensive analysis of the sources modeled to date. The evaporator vents were investigated at positions beginning at approximately $X_0 = 600$ back to $X_0 = 1519$ and also at an aft location facing $+X_0$, (See Figure 4.)^o

A program ground rule was that the evaporator vents could not be located in high temperature areas produced during re-entry such as the underside of the Shuttle Orbiter. At some acceptable locations (from a contamination viewpoint), the evaporator vents will produce forces and torques on the Shuttle Orbiter by impinging on adjacent surfaces. Because of these forces, the VCS systems would be required to fire more frequently. Therefore, even though a specific evaporator vent location may reduce its contamination contribution, it could increase the overall contamination environment because of the VCS coupling.

The molecular flux from the evaporator impinging on cold adjacent Shuttle Orbiter surfaces may allow condensation. This potential ice buildup could later become an undesirable source of particulates during on-orbit operations. Preliminary analysis shows that the flux rate of the evaporator exhaust exceeds the sublimation rate of ice at the anticipated cold surface temperatures for locations under the payload bay door and at $X_0 = 1519$. It was assumed that ice buildup occurs when the flux rate exceeds the sublimation rate. The surfaces where ice buildup can occur for these areas are the door underside and the trailing edge of the wing.

Results of the evaporator analyses are presented in Table VII. Included are the location, coordinates, LOS 1 contribution, forces generated, and the advantages and disadvantages for each of the evaporator vent locations investigated. The aft evaporator vent location, employing a single nozzle facing along $+X_0$, is the best location from a contamination threat consideration. Out of all positions evaluated, this location impacts the smallest fraction of payload lines-of-sight. If the thrust produced by this location causes an increase in VCS engine usage, its status as an acceptable location should be re-evaluated.

The next most favorable location is the $X_0 = 1519$

Table VII. Supersonic Evaporator Nozzle Summary

Evaluated Evaporator Positions and Flow Rates	NCD (mol/cm ²) LOS LA	Forces	Advantages	Disadvantages
$X_0 = 594$ to 845 $Y_0 = \pm 104$ $Z_0 = 353$ 6.8 kg/hr per nozzle	5.5×10^{11} to 1.1×10^{12}	2.18 N +Z direction on payload bay door	NCD less than 10^{12} mol/cm ² without payload bay door hinge line sealed - no wing reflections	Door impingement produces Z forces and ice buildup on payload bay door underside which can produce undesirable ice particles.
$X_0 = 924$ to 1124 $Y_0 = \pm 104$ $Z_0 = 353$ 6.8 kg/hr per nozzle	1.9×10^{12} to 1.6×10^{14} for door hinge line open 5.2×10^{11} to 1.6×10^{14} for door hinge line sealed	0.62 N to 0.71 N + Z force at locations between $X_0 = 900$ to $X_0 = 950$	From a contamination viewpoint there are no advantages	NCD in excess of 10^{12} mol/cm ² ; door impingement produces Z forces and ice buildup on payload bay door underside; wing reflections exist for evaporator exhausts.
$X_0 = 1392$ $Y_0 = \pm 113$ $Z_0 = 323$ 6.8 kg/hr per nozzle	1.7×10^{14}	1.86 N -Z direction on orbiter wings	From a contamination viewpoint, there are no advantages.	NCD in excess of 10^{12} mol/cm ² for all lines-of-sight - wing impingement produces -Z forces.
$X_0 = 1519$ $Y_0 = \pm 126$ $Z_0 = 285$ 6.8 kg/hr per nozzle	0	Undetermined small X force on trailing edge of wing	NCD less than 10^{12} mol/cm ² for significant portion of payload viewing directions; NCD is zero for lines-of-sight within ~ 5 degrees of (X, Z) plane - no appreciable forces generated.	NCD exceeds 10^{12} mol/cm ² for lines-of-sight greater than 30 degrees off of Z axis towards Y at $X_0 = 1107$ and for lines-of-sight viewing aft and over the wings for angles greater than 25 degrees off Z towards Y.
$X_0 = 1525$ $Y_0 = 0$ $Z_0 = 323$ 13.61 kg/hr	0	3.2 N + X(aft) direction	Provides the largest number of payload viewing directions that have zero contribution to NCD for all evaporator locations evaluated in this table; no wing reflections; entire forward and side viewing lines-of-sight have zero NCD.	X force of ~ 3.2 N; for lines-of-sight greater than 10 degrees off Z axis in (X, Z) plane NCD exceeds 10^{12} mol/cm ²

location. The assumption here is that the evaporator vents can be positioned low enough in the aft corner so that exhaust reflections from the top of the Shuttle Orbiter wings are eliminated. Under this assumption, a large fraction of the payload viewing directions has number column densities less than 10^{12} molecule/cm². The forces generated would also be minimized because the only surface impingement of the exhaust plume of any consequence would be on the trailing edge of the elevon. The next favorable positions from an induced mass or molecular column density viewpoint are the locations between $X_0 = 594$ and $X_0 = 950$, assuming a covering or boot could be employed for the payload bay door/Shuttle Orbiter hinge line. However, the potential for ice buildup in this region may result in undesirable ice particle generation during on-orbit operations. Any other location along the X axis between $X_0 = 950$ and $X_0 = 1500$ allows significant wing reflection contributions to all lines-of-sight that exceed 10^{12} molecule/cm².

Fundamentally, there are very few evaporator vent locations that meet contamination control criteria and do not impact other considerations. One basic option always exists for those payloads particularly sensitive to the effluents of the evaporator -- to store the evaporator effluents during their critical periods of operation. However, this means a loss in current heat rejection capability and would be a prime consideration in overall mission design. Until final design and test of the evaporator system and location of the vents has been accomplished, results of this analysis should be used as guidelines, where applicable, in identifying the effect of the evaporator upon the on-orbit induced environment.

CONCLUSIONS

These conclusions are intended to briefly summarize those major areas investigated during this activity.

1) Major Shuttle Orbiter Sources

- a) Evaporator Optimum Location - From contamination considerations, the optimum evaporator vent locations evaluated in order of least impact are aft facing +X location, $X_0 = 1519$ facing +Y, and various X positions between 600 and 950 facing +Y. These positions will have the least impact upon the majority of lines-of-sight evaluated during this study. All of the locations investigated contributed in excess of 10^{12} molecule/cm² to all lines-of-sight considered.
- b) VCS Engine Location and Orientation - For all locations and orientations (canting angles) evaluated, the VCS engines exceed molecular column density and return flux criteria. For payloads

sensitive to VCS engine effluents, consideration should be given for the use of Control Moment Gyros (CMGs) for maintaining attitude control. Another alternative is to select deadband, altitude, and attitude requirements that use minimum fuel usage for the VCS engines. Gimballed payloads could also minimize VCS engine requirements for specific attitudes.

- c) Outgassing Molecular Number Column Densities and Return Flux - Molecular number column densities for all lines-of-sight considered are less than the maximum criteria of 10^{12} molecule/cm². The return flux values for this source are highly dependent upon the viewing angle and orbital altitude and, in some cases, exceed criteria of 10^{12} molecule/cm²/sec. The number column densities and return flux for outgassing will tend to decrease with vacuum exposure time for a given Shuttle Orbiter.
 - d) Offgassing Molecular Number Column Densities and Return Flux - At a 10 hour on-orbit point, the molecular number column densities exceed the criteria of 10^{12} molecule/cm² for all lines-of-sight. After 24 hours on orbit, the molecular column densities are less than the maximum criteria of 10^{12} molecule/cm² for all lines-of-sight. The return flux for this source is dependent upon the viewing angle and altitude and, in some cases, exceeds the criteria of 10^{12} molecule/cm²/sec. The contribution to the induced environment by offgassing will also tend to decrease as does outgassing with vacuum exposure time. The rate of decrease will depend upon the orbital temperatures and prelaunch conditions (e.g., refurbishment, clean room control, and launch pad environment).
 - e) Cabin Atmosphere Leakage Molecular Number Column Densities and Return Flux - The molecular number column densities of the CO₂ and H₂O components of the leakage sources (polar molecules) are less than the maximum criteria of 10^{12} molecule/cm² for all lines-of-sight considered. However, the return flux of the total leakage effluents exceeds the 10^{12} molecule/cm²/sec criteria. This is based upon a specified maximum leak rate with all the leakage emitted from the forward payload bay bulkhead in a diffuse manner.
- 2) Other considerations
- a) Evaporator Ice Buildup Potential - For those evaporator vent locations evaluated, the evaporator effluents may impinge on cold adjacent Shuttle

Orbiter surfaces. The potential for ice buildup has been identified. This occurs when the flux rate of evaporator water vapor exceeds the sublimation rate of ice at the temperature of the surface impinged upon. The on-off cycle of the evaporator could reduce some of the long term ice buildup at specific locations. However, a potential source of particles exists where an accumulative ice buildup could occur. Testing will be required to assess this potential problem.

- b) Evaporator Forces - Between $X_0=600$ and $X_0=950$, the evaporator vents produce net +Z forces. At $X_0=1519$, the evaporator vents produce small -X forces. At the aft location (facing +X), the evaporator vent produces -X forces. For locations between $X_0=950$ and $X_0=1392$, the evaporator may produce a zero net Z force but would be unacceptable from a contamination viewpoint because of mass column density contributions. The forces generated may require additional VCS usage to maintain attitude control that will tend to increase the contaminant potential from the VCS.
- c) VCS Engine Usage Frequency - The duty cycles of the VCS engines varies from almost continuously to once or twice per orbit. The rate is highly dependent upon attitude, altitude, and deadband requirements.
- d) Tail Outgassing Into Payload Bay - The leading edge of the tail is one of the only major surfaces that views directly into the payload bay. Depending on the early vacuum exposure outgassing rate, the leading edge of the tail could degrade sensitive payload surfaces.
- e) Radiator Degradation - The Shuttle Orbiter radiator surfaces can be degraded from direct line-of-sight impingement of VCS and RCS engines and the OMS pod structure surface outgassants. Additionally, the radiator surfaces can degrade from the return flux of Shuttle Orbiter outgassing, RCS engine plumes, and OMS engine plumes. The extent of degradation is a strong function of VCS, RCS, and OMS engine usage, the relative temperatures of Shuttle Orbiter and radiator surfaces, and the vehicle attitude and altitude.

In comparing the predicted induced environment for the identified major Shuttle Orbiter sources against current applicable on-orbit contamination control criteria, it has been shown that from a preliminary analysis and design consideration certain aspects of these sources will not meet the given criteria. This is not to say that the induced environment from

these sources cannot be effectively dealt with from a contamination control viewpoint. It does indicate that in some cases just design control influences, such as location and directional considerations, will not be adequate to meet the contamination control criteria. As a result, certain on-orbit operational controls will also be required to minimize the contaminant potential of these sources in their present configuration. This is particularly true for both the flash evaporator (when at $X = 1392$) and the 25-lb thrust VCS engines. These on-orbit operational controls will not be limited to the Shuttle Orbiter itself, but will depend strongly upon the nature of the particular payload being flown. Consequently, it is envisioned that as the Shuttle Program develops, on-orbit operational controls will be required to be developed in conjunction with the payloads to provide the necessary contamination controls.

The assessment presented in this paper has established basic contamination parameters of concern for the identified major Shuttle Orbiter contamination sources. As a result, it has been indicated that through basic design consideration complete contamination control can not meet the applicable criteria. To achieve necessary contamination control will require operational considerations for both the Shuttle Orbiter and many of its proposed payloads.

REFERENCES

1. "Payload/Orbiter Contamination Control Assessment Support." MCR 75-13, June 27, 1975, Contract NAS9-14212, Martin Marietta Aerospace, Denver Division.
2. "Space Shuttle Program Space Shuttle System Payload Accommodations." JSC 07700 Volumes X and XIV, Revision C, July 3, 1974, Lyndon B. Johnson Space Center.
3. Naumann, R. J.: "Shuttle TPS Panel Tests Preliminary Results" Working Paper. Space Sciences Laboratory, MSFC, January 16, 1975.
4. Summerhays, R.: "MRS Plume Test." LTV, Dallas, Texas.
5. Simons, G. A.: "Effect of Nozzle Boundary Layers on Rocket Exhaust Plumes." AIAA Journal, Volume 10, No. 11, November 1972.
6. Chirivella, J. E. and Simon, E.: "Molecular Flux Measurements in the Back Flow Region of a Nozzle Plume." JANNAF 7th Plume Technology Meeting, April 1973, Redstone Arsenal, Huntsville, Alabama.

STS CONTAMINATION CONTROL REQUIREMENTS; RATIONAL & IMPLICATION

R. Naumann, *NASA Marshall Space Flight Center, Huntsville, Alabama 35812*

ABSTRACT

The requirements for controlling the induced particles and gases environment in and around the Space Transportation Systems (STS) are presented and discussed in terms of their necessity for utilizing the full scientific potential of the system. A cursory estimate of the design and operational constraints imposed by these requirements is given. It is shown that current technology and experience is sufficient to meet the majority of the requirements, but that additional data is required on material outgassing as a function of temperature is needed to assure that some of the more stringent astronomical requirements can be met. Also, it appears that the attitude control thrusters will have to be inhibited during certain observational periods. This implies that an instrument pointing system or attitude control system will be required that does not depend on thrusters.

A RADIOMETER FOR MONITORING COLUMN DENSITIES OF INFRARED-ACTIVE MOLECULES

F. C. Witteborn, J. P. Simpson, L. S. Young, C. D. Swift, and R. K. Melugin, NASA-Ames Research Center, Moffett Field, CA 94035

ABSTRACT

If infrared astronomical telescopes are to be used to their full advantage on the Space Shuttle, the column density of gas above the Shuttle payload bay must not exceed 10^{12} infrared-active molecules cm^{-2} . H_2O is the molecule of greatest concern because of its abundant offgassing from the Orbiter and its strong rotational and vibration-rotational spectrum which spans the infrared spectral range. Other molecules such as CO_2 and NO also contribute significantly to the IR background. In addition to the molecular line radiation there will be continuum radiation from the zodiacal light, stars, and contaminant dust particles. A cryogenically cooled radiometer with a 10 to 35 cm aperture, an array of 10 to 18 low noise detectors at the focal plane, a rotating, cold chopper-filter, and a well baffled enclosure could detect column densities of water at 270 °K as small as 10^{10} cm^{-2} . By measuring the intensities of two bands of water with different temperature dependency both the column density and temperature can be determined. The information obtained by such an instrument will be very helpful in determining the most desirable operational modes of the Shuttle not only for IR astronomy but for sensitive UV and visible observations as well.

INTRODUCTION

When astronomers were asked to consider using the Space Shuttle as a platform for telescopes, one of their first concerns was the infrared radiation from the contaminant environment of the spacecraft. This radiation will be emitted primarily by water vapor and to a lesser extent by CO_2 and other gases which will come from the Orbiter by outgassing, leakage, deliberate venting and rocket firings. IR radiation will also be emitted by particulates such as dust and ice flakes which can come from vents, leaks and dirty surfaces. A limit on the column density of infrared active molecules of 10^{10} to 10^{12} cm^{-2} has been recommended in order to not impair the capabilities of a 1-meter-diameter, cooled, infrared telescope. A limit on particulates 5

microns and larger to one sighting per orbit in a 15 arcminute field-of-view has been requested. The column densities are of concern to UV astronomers, as well, because of absorption and scattering. The particles are of general concern in astronomy because of their contribution to the background, particularly on the sunlit side of the orbit. A sensitive monitor is needed on early Shuttle flights not only to determine to what extent the Shuttle contamination goals have been met, but also how the contaminant environment will be affected by different operational modes of the Orbiter. Measurements must be made as functions of altitude, time in orbit, thruster firing frequency, and vent operation. The effects of these and other conditions on the contaminant environment must be verified and understood in order to optimize the usefulness of the Shuttle for astronomical observations.

A small radiometer, 10 to 35 cm in diameter, will be capable of measuring infrared backgrounds as low as those required by the most sensitive payloads proposed for the Shuttle. Knowledge of the H_2O emission spectrum permits determination of column densities and temperature from the IR background. In this report the required sensitivity and measurement techniques are described.

Infrared Spectral Characteristics of the Contaminant Atmosphere

The spectral features of water vapor are prominent throughout the infrared. We will limit our attention to the 3 to 100 micron range which is most susceptible to background radiation problems. The infrared spectra of H_2O and CO_2 were discussed by Herzberg (1945). McClatchey et al. (1973) give band and line wavelengths and strengths of both molecules. The vibration-rotation bands dominate at wavelengths below 16 microns and the pure rotation lines of H_2O are the major source of IR contaminant radiation beyond 16 microns. CO_2 has strong vibration-rotation bands centered at 4.2 microns and 15 microns. Some of the bands are indicated in figure 1 which also shows natural background sources. If it is assumed that the molecules are in equilibrium, the column densities and temperatures may be determined from comparison of the intensities of different bands or lines. These arise from transitions between different energy levels whose populations vary with temperature in accordance with the Boltzmann distribution. The temperature dependence of radiation intensities in several bands is shown in figure 2.

Water vapor leaving the Shuttle Orbiter will soon be out of equilibrium. Upper energy levels of most of the molecules will be depleted as they move into the cooler radiation environment dominated, in the IR, by blackbody radiation from the earth's lower stratosphere. On the other hand, collisional excitation by the ambient atmosphere moving past the Orbiter at about 8 km/sec will populate the higher energy levels, thus tending to raise the temperature. However, the column density will drop to less than half beyond 100 meters from the Orbiter (Rantanen, 1975), while the mean free path will be on the order of kilometers at

altitudes above 300 km, so that only a very small fraction of molecules will be excited in this manner. Order of magnitude estimates of departures from equilibrium by radiative decay and by collisional excitation have been made by Simpson and Witteborn (1975). These indicate that the 15 micron band from contaminant CO_2 molecules will remain near the equilibrium value at the Orbiter surfaces, but the 4.3 micron band will come into radiative equilibrium almost immediately, with an excitation temperature of 300°K on the sunlit side of the orbit and 273°K on the dark side. The vibration-rotation lines of H_2O may be excited to radiate several times more strongly than H_2O in equilibrium with the surface. Temperatures on these surfaces will vary with orientation relative to sun and earth; values from 201°K to 366°K are expected, and at this time 273°K appears to be an appropriate average over surface area and time. The flash evaporator will vent water at 280°K , but molecules from this source will have to undergo one or more collisions before coming into the field-of-view and are expected to comprise less than one-third of the column density.

Dust particles are expected to have a continuum spectrum, possibly with some broad features characteristic of their composition. For our purposes their spectrum can be approximated by a 300°K blackbody for wavelengths between 5 and 30 microns. Air drag will sweep them across the field-of-view of a radiometer with crossing times on the order of one second; therefore, individual particle crossings will be readily identified because of the sudden brightening and dimming of the background intensity. Nearby particles will be out of focus so that their images will be distributed over an extended area of the focal plane. They will be easily distinguished from stars which have point images in the focal plane and have quite different spectra. Cool interstellar dust clouds such as those associated with HII regions will be distinguished easily by their broadband spectra.

Spectral Characteristics of the Natural Background

It is important that any instrument which monitors the IR radiation from contaminants be able to measure the natural IR background as well, and be able to distinguish one from the other. The natural background has not been determined yet in the IR, but may be as important as contaminant radiation to astronomical instruments. It consists of radiation from interplanetary dust (zodiacal light), radiation from that part of the earth's upper atmosphere still above the Shuttle, and radiation from unresolved stars and galaxies.

The zodiacal light is brightest along the ecliptic and decreases in intensity with increasing angular distance from the sun. Even though it is visible from the earth's surface to the naked eye and can be explained in terms of scattering of sunlight by small particles, the size distribution and composition of the particles are uncertain. These uncertainties limit the accuracy of predictions of the IR intensity to an order of magnitude.

Estimates of the zodiacal light intensity in the infrared were made by Jarecke and Wyett (1975) based on a model by Peterson (1963). In the worst (brightest) case the particle temperature was assumed to be as high as 304°K at earth's orbit and the emissivity was assumed to be 0.7. This is the case shown in figure 1 for an angle of 80° from the sun along the ecliptic. At larger angles from the sun, and out of the ecliptic plane, the radiation decreases further, but by no more than a factor of 3. Closer to the sun, near the ecliptic plane, the intensity is higher. From figure 1 it is clear that the zodiacal light intensity may exceed that from the contaminant water vapor out to about 30 microns, so that radiometer measurements in this region must be able to discriminate spectrally between the two.

Infrared emission from ions, atoms and molecules will be a function of Orbiter altitude. It also depends on the temperature of the upper atmosphere which varies between night and day and with solar activity. Intensities of the brightest lines seen from 350 km, assuming the average upper atmosphere temperature of 1000°K , are: $3.7 \times 10^{-15} \text{ W cm}^{-2}\text{deg}^{-2}$ for the 63.1 micron line of OI, $1.1 \times 10^{-16} \text{ W cm}^{-2}\text{deg}^{-2}(\text{daylight})$ for the 5.3 micron vibration-rotation band of NO, $4.8 \times 10^{-18} \text{ W cm}^{-2}\text{deg}^{-2}(\text{daylight})$ for the 4.27 micron vibration-rotation band of NO^+ , and $9.2 \times 10^{-17} \text{ W cm}^{-2}\text{deg}^{-2}$ for the 147 micron OI line (Simpson, 1975). The intensity of NO is very uncertain because its abundance has not been measured above 170 km.

The average background radiation from stars and galaxies is considerably lower than that predicted for zodiacal light and from the main water vapor features. However, the zodiacal light may be much fainter than the prediction, so that starlight may be important at short wavelengths. The background starlight intensity curve in figure 1 is based on the average background star density. It is a factor of 2 to 3 higher in the galactic plane and lower near the poles. A temperature of 5500°K was used as representative of the average star contributing radiation in this region of the spectrum. It is likely that cooler stars make a larger contribution than this temperature implies, but this is not important since the possibility of a strong zodiacal light background already makes it necessary to discriminate spectrally against continuum backgrounds to measure the contaminant molecules. Occasionally a bright star or planet will move through the field-of-view of the radiometer. It can be distinguished from other sources easily because it will have a point image in the focal plane. An array of detectors would see extended sources such as zodiacal light and contaminant molecules in all detectors at once. Nearby dust would show up in several or all detectors at once. Stars bright enough to be measured at all would show up in only one detector at a time.

Measurement Technique: A Multiband, Cryo-Cooled Radiometer

Cryogenically cooled telescopes ranging in aperture from 10 cm to 35 cm have been built for rocket flights to measure celestial

objects in the infrared. Such a system could be adapted for use as a column density monitor with proper modification of the focal plane. In this section we first determine the sensitivity to H_2O column density that could be achieved with a 35 cm diameter radiometer using detectors with noise equivalent power (NEP) of $10^{-15} \text{ W Hz}^{-1/2}$. For background radiation this is roughly equivalent to using a 10 cm diameter radiometer with detectors having $10^{-16} \text{ W Hz}^{-1/2}$ NEPs. The larger system enables us to use conservative estimates of available detector capabilities. It will also be more effective in detecting dust particles.

The power P , reaching the detector is proportional to the collection area A , the field-of-view Ω , the bandpass $\Delta\lambda$ at wavelength λ , the system transmission $T(\lambda)$, and the background intensity $I(\lambda)$. Thus $P = A \Omega T(\lambda) I(\lambda) \Delta\lambda$, provided the radiometer is properly cooled and baffled so that internal radiation and scattering of external, off-axis light are reduced below the lowest required signal level. A field-of-view of one square degree per detector is the largest that can be used without sacrificing desired spatial (relative to Shuttle fixed coordinates) resolution that may be needed to locate contaminant sources and gradients in radiation intensity. The unobscured collection area of a 35 cm diameter radiometer (see figure 3) is roughly 800 cm^2 .

Assuming thermodynamic equilibrium at 273 K, the intensity from the whole $6.3\mu H_2O$ band is $3.6 \times 10^{-15} \text{ W cm}^{-2} \text{ deg}^{-2}$ so with reasonable transmission, say $0.2 = T(6.3\mu)$, it is readily detectable provided that it can be distinguished from the zodiacal light. In order to produce an easily amplified signal, the input to IR detectors will be modulated. For measuring very extended radiation this modulation is usually done with a cold blade chopper so that the detector sees alternately full background and zero (provided the blade is cold enough). This is called total chopping and will be used for most of the detectors in the radiometer focal plane so that the total radiation background can be measured in enough bandwidths to thoroughly cover the continuum. However, to distinguish the H_2O from the continuum a different kind of modulation is required. By replacing the open part of a blade chopper with a filter that transmits in one of the peaks of the 6.3 micron band and by replacing the opaque part with a filter that transmits in the dip, the modulated signal will be proportional to the H_2O emission only, with continuum subtracted out. If the continuum has a steep slope, as is expected for zodiacal light, it is better to use three bands: two for water, with the continuum in between, or vice versa. In either case the continuum is subtracted out to the extent that it can be approximated by a linear function. The modulation arrangement is shown in figure 4. It is combined with the total blade chopper so that only one moving part is needed for modulating the signals to all the detectors in the array. When the cracks between the filters cross through a detector's field-of-view, the signal must be electronically suppressed. Thus the chopping efficiency will be less than 0.50 expected for a perfect chopper. 0.40 will be assumed. Losses in the filters near 6 microns decrease the

signal by another factor of 2 so that $T(6-7\mu) = 0.20$. From figure 1, for $T = 273^\circ\text{K}$ and column density $= 10^{12}$ H_2O molecules cm^{-2} , the intensity between 6.0 and 6.1 microns is $2.9 \times 10^{-15} \text{ W cm}^{-2} \text{ deg}^{-2} \mu^{-1}$ and between 6.4 and 6.5 microns it is $5.7 \times 10^{-15} \text{ W cm}^{-2} \text{ deg}^{-2} \mu^{-1}$. The intensity $I(\lambda)$ used in the equation for P is the average of these two bands. The continuum band is chosen to be 6.2 - 6.3 microns where the water intensity is a factor of 10 lower. Using the values obtained above in the equation for power, the result is $P = 6.9 \times 10^{-14} \text{ W}$ to the detector. The signal-

to-noise is $S/N = \frac{P t^{\frac{1}{2}}}{\text{NEP}} = 690$ in 100 seconds of integration for a detector $\text{NEP} = 10^{-15} \text{ W Hz}^{-1/2}$. Even a column density of 10^{10} cm^{-2} would give $S/N = 6.9$ in 100 seconds near $T = 273^\circ\text{K}$. The signal-to-noise increases at higher temperatures and decreases at lower temperatures.

A similar technique will be used to measure the intensities of two rotational bands, possibly those at 23.7 - 24.0 microns and at 28.0 - 29.0 microns. These also provide adequate S/N . The ratios of the intensities of the different bands vary with temperature (see figure 2). Assuming that the strongest rotational lines which contribute to the bands chosen in the pure rotation spectrum are in thermodynamic equilibrium, their relative intensity determines the rotational temperature. The column density is then determined by comparing the measured intensity of either band with the calculated equilibrium intensity for the measured rotational temperature. In thermal equilibrium temperature may be determined from the vibration-rotation spectrum using the ratios of the 6.0 - 6.1 plus 6.4 - 6.5 bands to either rotational band. This may yield a different "temperature" if collisional excitation causes a significant departure from equilibrium. In that case the column density determined from the rotational band ratios and the intensity measurement for the vibration-rotation band may be used to determine the vibration-rotation temperature. Column densities down to 10^{10} cm^{-2} of H_2O at temperatures down to 270°K can be detected by this method. Errors rise linearly with lower column densities and faster with lower temperature, but in these cases the information would not be as important.

While the H_2O contribution to background radiation is very important to astronomers, their concern is with the total background spectrum. It can be measured directly by a totally chopped array of detectors filtered for the following bands: 3.5 - 4.0 μ for continuum, 4.2 - 4.4 μ for CO_2 , 5.0 - 5.9 μ for NO , 9 - 12 μ for continuum, 14 - 16 μ for CO_2 , 17 - 19 μ for continuum, 20 - 30 μ , 30 - 40 μ , 50 - 100 μ . The last four bands are intended to measure the general shape of the background which is expected to be dominated by water emission beyond 30 μ . A separate band for the 63.1 micron line of OI may be required. Analysis of these bands can provide the zodiacal light spectrum, approximate values of CO_2 column density and temperature, and further checks on the rotational temperature and column density of H_2O .

A multiband radiometer with continuous monitoring of signal outputs is an ideal tool for monitoring particulates released from the Orbiter. An estimate of the smallest sphere visible in the 9 - 12 μ band ($T_\lambda = 0.2$) follows: Let the sphere have radius a , temperature $T = 300^\circ\text{K}$, emissivity = 1, and be at distance r from the telescope primary whose aperture diameter is $D = 35$ cm and effective area $A = 800$ cm² used before. The energy reaching the primary in the 9 - 12 μ band is $7.27 \text{ W} \times \frac{a^2}{r^2}$. If the detector has field of view of diameter θ then for $r \leq \frac{D}{\theta}$ the fraction of power reaching the detector is $T_\lambda \frac{\theta^2 r^2}{D^2}$. Thus the power reaching the detector is $P = 7.27 \text{ W} \frac{a^2 \theta^2}{D^2} T_\lambda$ for $r \leq \frac{D}{\theta} = r_o$.

For larger values of r all of the energy falls on the detector (i.e. the image is in focus) and the power drops as r^{-2} . For $\theta = 1$ deg, $r_o = 20$ meters. If a 2×10^{-4} cm (the smallest size of concern to the 1 meter cooled telescope)

$$P = 7.27 \text{ W} \times \frac{4 \times 10^{-8} \text{ cm}^2}{35^2 \text{ cm}^2} \times \frac{0.2}{57.3^2} = 1.4 \times 10^{-14} \text{ W}.$$

In one second the proposed radiometer will detect this tiny dust particle with a signal-to-noise ratio 14 to 1 in the absence of other background. Since an S/N of 3 is adequate, detection to 40 meters is likely. Note that the particle is detected equally well on the night or day side of the orbit.

Detectors suitable for the specified bandwidths are primarily doped silicon photoconductors. Shortward of 30 microns the best available detectors will operate at 8°K or higher which is quite compatible with the use of supercritical helium. Supercritical helium has been used for extended periods in space before and does not suffer from phase separation problems in zero gravity. Detectors for the wavelengths beyond 30 microns may require lower temperatures which could be provided by expanding some of the gas through a Joule-Thomson valve.

The cooled (20°K) optics will be protected from back-scattered contaminant molecules and the ambient atmosphere by a continuous helium gas purge (using the cryogen boil off) which will maintain the pressure in the radiometer tube near 10^{-5} torr. A low emissivity door will close automatically whenever the radiometer points near the sun or earth or when the contaminant level is excessive.

A simple, rugged pointing system which holds the radiometer at fixed angles relative to the Orbiter will be adequate for contaminant background monitoring. It is desirable to locate the entrance of the radiometer as close as possible to the top of the payload bay.

Data from the radiometer must be recorded continuously and correlated with Orbiter inertial attitude, altitude and sun angle.

This will permit determination of the radiometer pointing direction in stellar coordinates so that occasional sightings of astronomical sources will not be confused with contaminants.

Comparison with Other Methods

There are several alternate methods that might be considered for determining the infrared environment of the Shuttle. Measurement of deposition of condensible species provides indirect information on column density if one has a reliable model for the returned molecular flux versus distance from Orbiter. However, this method does not provide any hint at all of the temperature of gas and thus fails to measure the infrared background. Observation of laser excitation of various contaminants has the advantage of being applicable to many species for measuring column density. However it is not sensitive to the temperature of the gas and thus also fails to measure the infrared background. Measurement of the solar spectrum to determine H_2O features suffers from requiring an inertial guidance system and from being operable during only half the orbit. Since the rotational lines are so narrow and absorption is less than 1% for $10^{12} \text{ H}_2\text{O cm}^{-2}$, this method would not be nearly as sensitive as the proposed radiometer. None of these alternate methods is capable of detecting the particle environment.

Conclusion

A 35 cm diameter, cryogenically cooled radiometer would be capable of accurately measuring the infrared background from 3.5 to 100 microns and the column density of H_2O for the low values specified for the Orbiter. In addition it could detect 2 micron radius particles at distances up to 40 meters in both day and night.

References

- Allen, C. W. 1973, "Astrophysical Quantities," 3rd ed. Athlone Press, London.
- Herzberg, G. 1945, "Infrared and Raman Spectra of Polyatomic Molecules," Van Nostrand and Company, Inc., New York.
- Jarecke, P. J. and Wyett, L. M. 1975, Hughes Aircraft Company Interdepartmental Correspondence 27735/180.
- McClatchey, R. A., Benedict, W. S., Slough, S. A., Burch, D. E., Calfee, R. F., Fox, K., Rothman, L. S., and Garing, J. S. 1973, "AFCLRL Atmospheric Absorption Line Parameter Compilation," AFCLRL-TR-73-0096, Bedford, Massachusetts.
- Peterson, A. W. 1963, Astrophys. J., 138, 1218.
- Rantanen, R. 1975, Martin Marietta Corp., Denver, Colorado, private communication.
- Simpson, J. P. 1975, in preparation.
- Simpson, J. P. and Witteborn, F. C. 1975, in preparation.

Figure Captions

Figure 1.- Intensity of background radiation versus wavelength. The emission spectrum of H_2O assumes thermal equilibrium at a temperature of $273^\circ K$ and a column density of 10^{12} molecules/cm². A column density of 2×10^{11} molecules/cm² and a temperature of $295^\circ K$ is assumed for the CO_2 emission at 15 microns. The emission from NO at 5.3μ is for the sunlit side of the earth. An altitude of 350 Km is used for all the molecular contributions.

Zodiacal light intensity is based on radiation from dust with an absorbtivity of 1.0, an emissivity of 0.7, a temperature of 304° , and at 80° elongation. This spectrum turns up near 3 microns due to reflected sunlight. The contribution from starlight is based on the average star distributions given by Allen (1973) and an approximated temperature of $5500^\circ K$.

Figure 2a & 2b.- The emission intensity of H_2O at several wavelengths is given as a function of temperature. A column density of 10^{11} molecules/cm² is used for these calculations.

Figure 3.- A conceptual drawing of the radiometer is shown. It is expected that the diameter of the primary mirror in the radiometer will be approximately 30 centimeters.

Figure 4.- This figure shows details expected to be included in the spectral chopper and detector array.

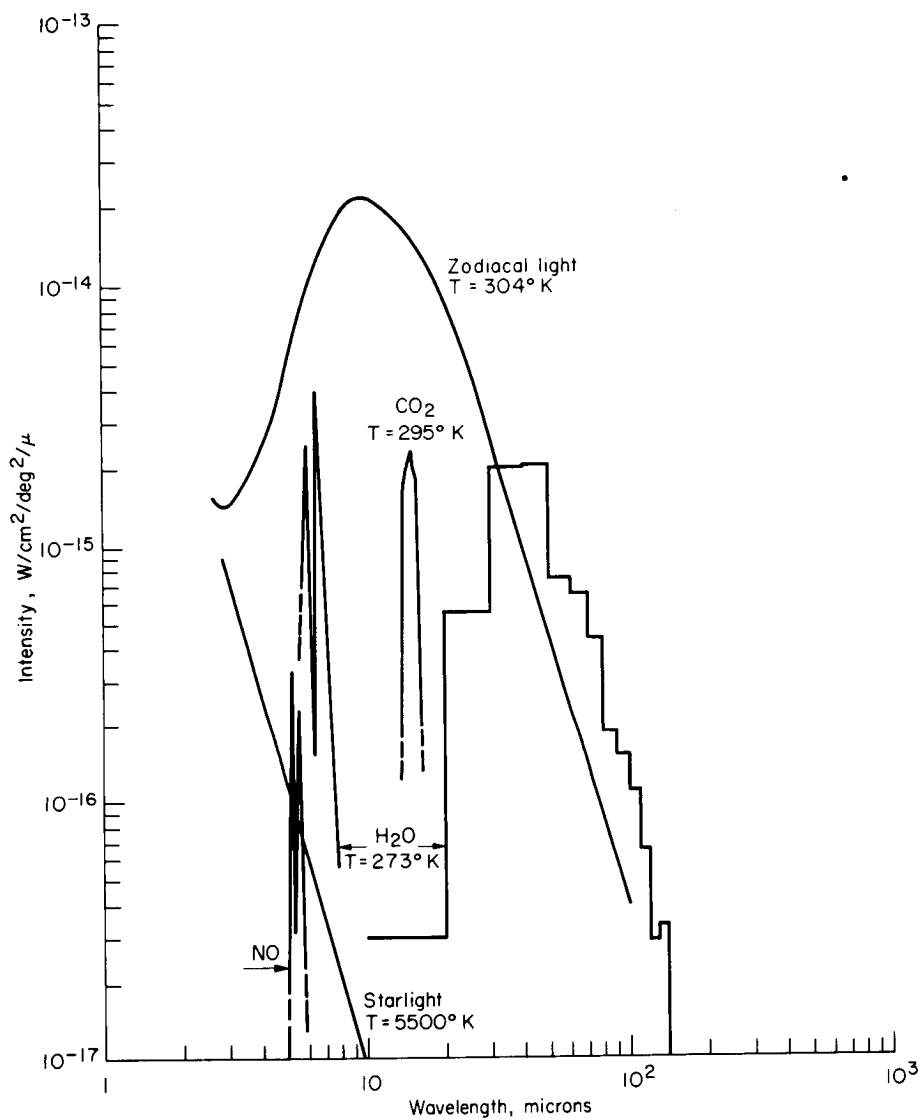


Figure 1.

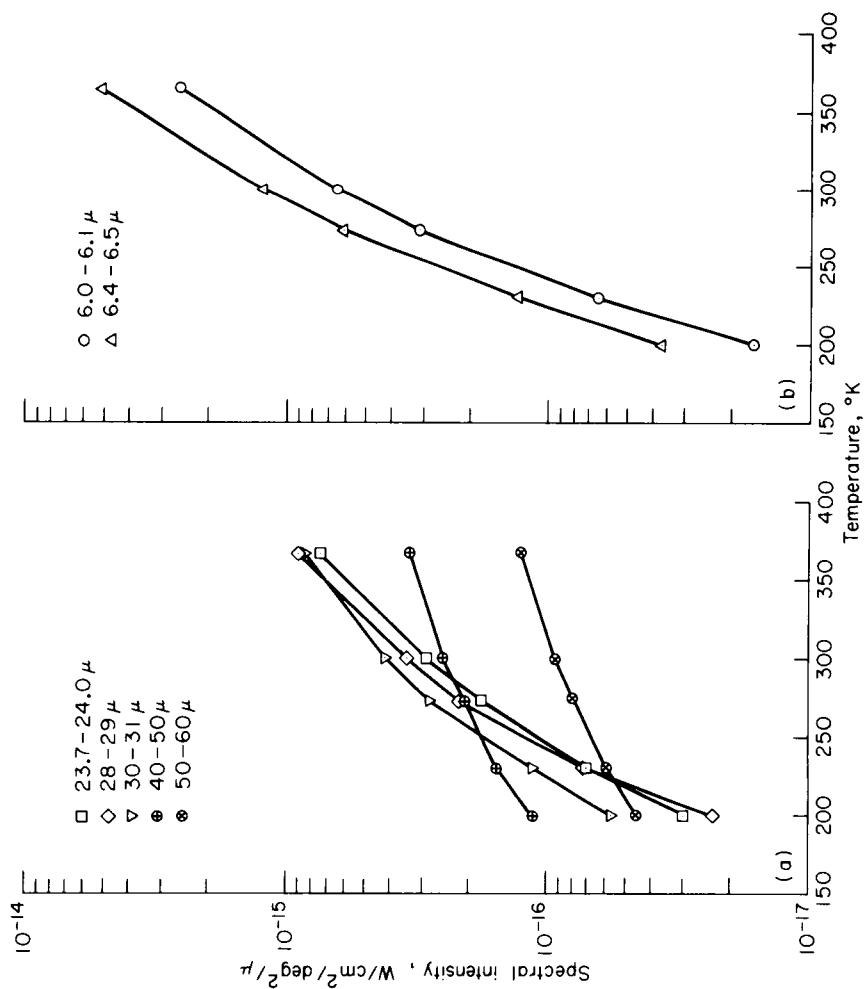


Figure 2.

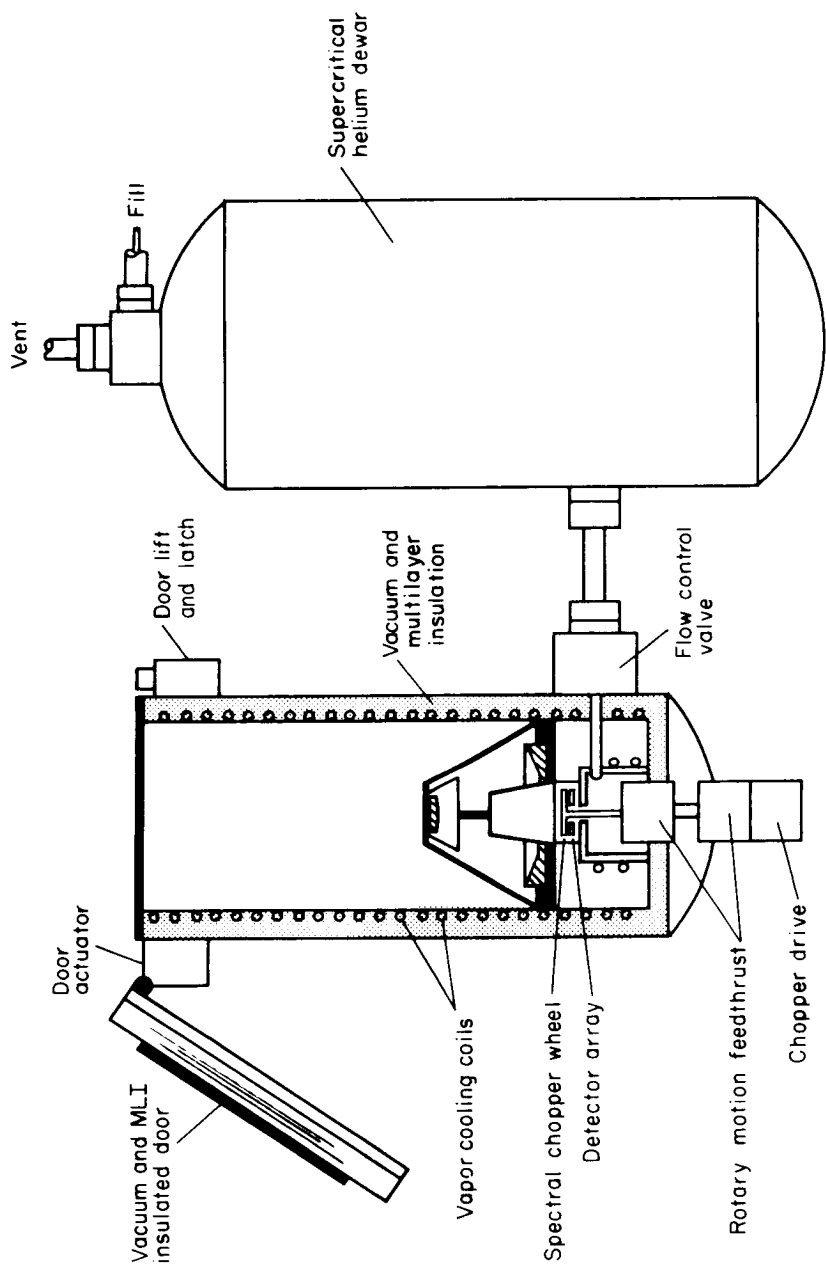


Figure 3.

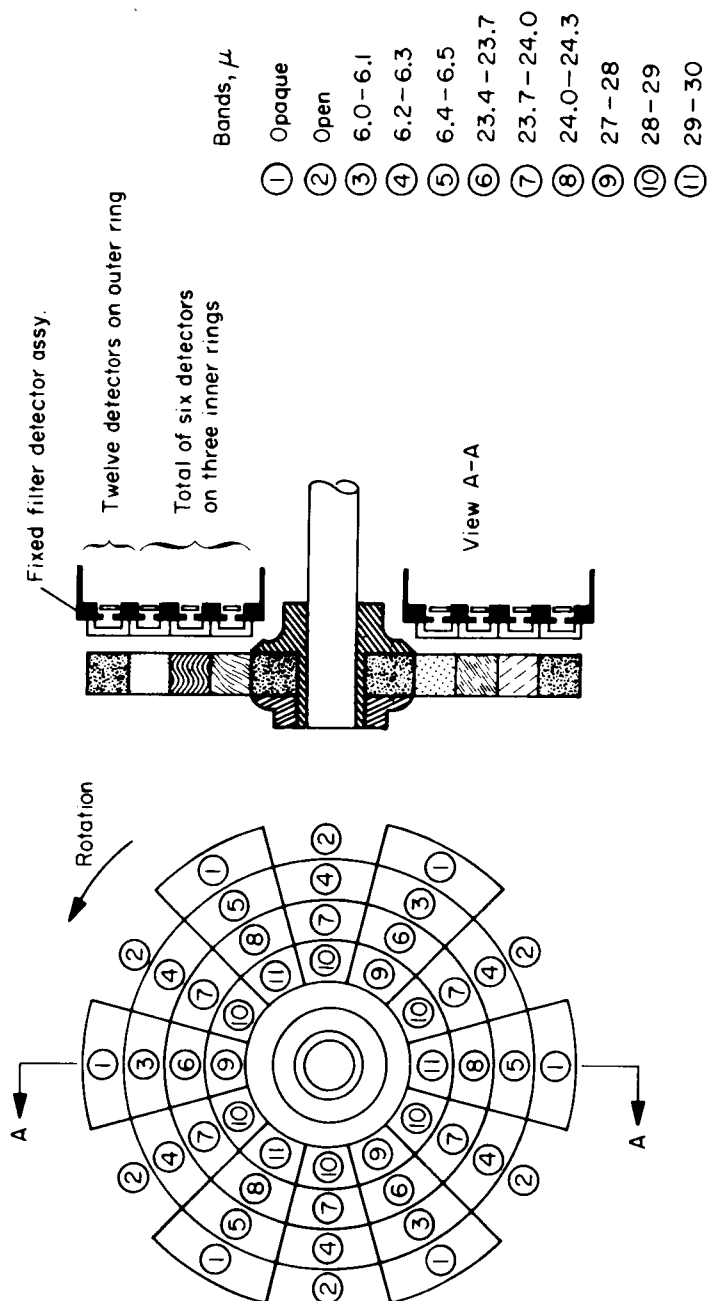


Figure 4.

THE OUTGASSING RATE FOR A SHUTTLE THERMAL PROTECTIVE SURFACE USING RTV 560 ADHESIVE

D. W. Jex, *Marshall Space Flight Center, Huntsville, Alabama*

E. L. Shriver, *Marshall Space Flight Center, Huntsville, Alabama*

ABSTRACT

An experimental program has been conducted to identify the outgassing rate for a Shuttle baseline thermal protective surface (TPS) which utilizes room temperature vulcanizing (RTV) 560 adhesive.

INTRODUCTION

The Shuttle is the first launch vehicle designed to be reusable for payload transport from ground based stations to earth orbit. The development of such a system presents many engineering challenges and situations never before encountered. Technology developed through past experience and investigation are essential buoys. They outline known or previously traveled avenues and channels that can be used to reach new understanding.

To achieve the desired goals of this vehicle, one of the candidate methods for the Shuttle baseline construction incorporates a metal substrate structure covered with six inch square tiles, much like a kitchen floor. This construction enables the vehicle to be repaired or modified by removal and replacement of certain tiled areas. It also means low maintenance cost and fast turn-around time between flights.

The tiles are installed by use of an adhesive on the back of the tile such that a protective paper can be removed and the tile attached to the substrate like a decal. There is a felt pad between the tile and the substrate to provide strain relief during the extremely high temperatures encountered during launch and re-entry. There is also a gap left between adjacent tiles to allow for expansion during these phases of the mission.

Many of the tiles are extremely light weight and porous. The adhesive presently proposed is a room temperature vul-

canizing (RTV) adhesive designated as RTV 560.

It was known from previous experience that RTV 560 has some unacceptable short term outgassing characteristics. However, the long term time history and specific measurement of these parameters for the use intended had not been determined. Dr. Lubert Leger, chairman of the Particles and Gases Working Group, discussed with Dr. Robert Naumann the possibility of using instruments and techniques developed at MSFC over the last few years to research and document information that would help provide guidelines upon which recommendations could be made by this group to Shuttle management.

TEST PARAMETERS

A panel simulating the High-temperature Reusable Surface Insulation (HRSI) portion of the outer Thermal Protective Surface (TPS) of the Shuttle was prepared by Rockwell International Corporation on August 8, 1974. The panel was constructed using twelve tiles 15 cm (6") square and 1.5 cm thick laid in a 3 by 4 rectangular matrix on an aluminum substrate. A gap of .32 cm was left between adjacent tiles. A photograph of a portion of this panel is shown in figure 1. The placement of thermocouples used to monitor the temperature of the panel is also shown.

This panel was subjected to a series of 4 vacuum tests in the stainless steel test fixture in SSL (ES33) at MSFC. The four tests and pertinent events between test are listed below:

Background test with all instrumentation except the panel

- (1) Initial outgassing test (~ 143 hours)
Panel was baked at 191°C (375°F) for 30 minutes to simulate re-entry conditions
- (2) Second outgassing test (~ 53 hours)
Panel was baked at 177°C (350°F) for 30 minutes
- (3) Solid particle generation test
Panel was baked at 177°C (350°F) for 30 minutes
Panel was subjected to vacuum for 2 hours
Panel was baked at 204°C (400°F) for 35 minutes
- (4) Third outgassing test (~ 99 hours)

The outgassing tests were to gain data concerning some characteristics of the outgassing contaminants. While the solid particle generation test was to gain data on the size and number of solid particles that might be generated under 4 typical shock

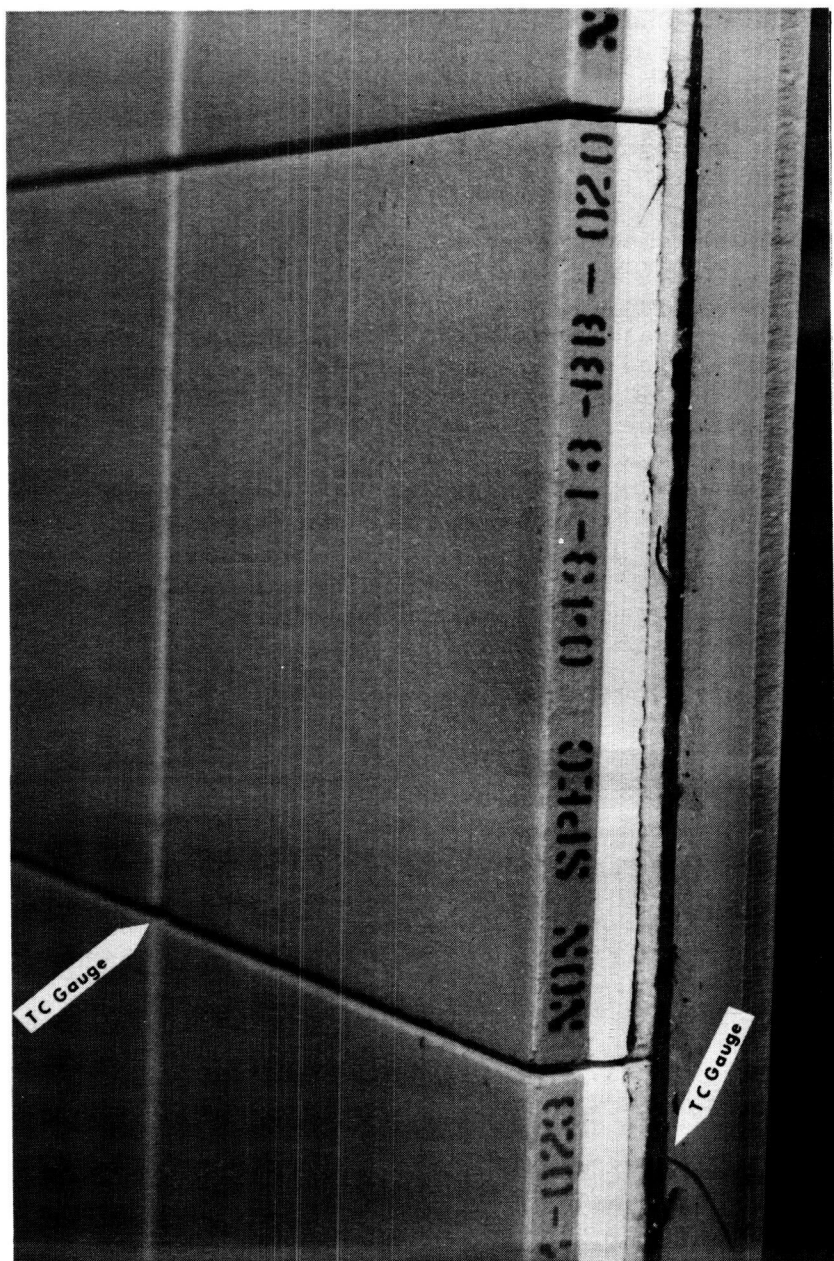


FIGURE 1: PHOTOGRAPH OF A PORTION OF TPS PANEL

conditions. The four shocks employed were:

- (a) A thermal shock to simulate thermal cycling
- (b) An electrostatic shock to simulate charge buildup and discharge
- (c) A gas impingement shock to simulate RCS and other motor plume impingements
- (d) A mechanical shock to simulate impulse loading

The instrumentation used for the outgassing tests included two Thermoelectric Quartz Crystal Microbalance (TQCM), and a UTI quadrupole mass analyzer. The TQCM's were used to measure outgassing and deposition rates as a function of time and temperature. The quadrupole was used to identify and monitor the amount of outgassing constituents as a function of time and temperature.

The instrumentation used for the particle generation test included a laser beam tailored as a thin rectangle and a filtered photomultiplier. The installation of the panel was so that a solid particle dislodged over the beam by any of the 4 shock conditions would fall through the beam and the scattered light would be detected by the photomultiplier.

TEST RESULTS

Background Test:

A chamber background measurement was taken using a dummy panel before committing the actual panel to the vacuum chamber. The chamber was pumped down to 10^{-7} torr and then a solar simulator was turned on. Both TQCM's showed a large initial deposition immediately after the simulator was turned on. After 18 minutes, the rate reversed itself and an evaporation followed for the next 12 minutes at about the same rate as the deposition. The following 48 minutes showed a small but steady accumulation of $6 \text{ to } 10 \times 10^{-11} \text{ gm/cm}^2/\text{sec}$ at collecting surface temperatures below 20°C .

It was believed this steady rate was due to condensible materials being sublimed off of the liquid nitrogen cold shroud which was cold at the time the solar simulator was initially turned on. Therefore, a procedural change called for the solar simulator to be turned on for at least 20 minutes before the cold shroud was filled and the TQCM to remain at high temperatures during this period.

This background measurement was repeated with these modifications and the result was that no accumulation was measured over a period of 6 hours at collecting surface temperatures as low as -60°C .

Discussion of the Initial Outgassing Test:

The panel was mounted in a vacuum chamber which was equipped with 3600 watts of quartz lamps with reflectors to direct most of the energy onto the top surface of the panel. These lamps were employed as the solar simulator.* There were strip heaters located underneath the panel to heat the substrate directly if necessary to achieve the desired temperatures. This chamber can easily reach and maintain pressures of 4×10^{-7} torr.

Some difficulty was encountered in roughing the chamber below 200 microns because of heavy panel off-gassing, but after a few minutes the chamber pressure began dropping rapidly.

The TQCM's were brought on-line 20 minutes after the test was initiated and both TQCM's showed an accumulation rate of approximately 15 Hz/min. There were three oscillations of the panel temperature around 43.3°C (110°F) as the solar simulator was adjusted. These identical oscillations were reflected in the accumulation and re-evaporation rates of the TQCM's. This confirms the fact that the accumulation is derived from the panel.

In analyzing the data, it was assumed that only the slots in the panel act as sources and that each element of area along the slot can be treated as a Lambertian source. The TQCM viewing factors for the slots are computed to be .0320 and .0590 since the two TQCM's were oriented differently.

To establish the accumulation rates, the procedure was to start with the collecting surface hot (above 70°C) and then lower it in increments until the rates at various temperatures were confirmed. Then return the collecting surface to the high temperature to clean it and begin a new sequence. Following this

*The measurements of the output of the solar simulator were made with a radiometer that cuts off at 4.5 microns. Since the solar simulator is an incandescent lamp, the actual radiation flux of one solar constant of the lamp is somewhat higher than the sun. However, temperature is the important parameter here, not true simulation of the sun.

procedure, a collecting surface temperature at which outgassing products begin to accumulate can be established. In addition, this procedure will indicate the temperature at which the sticking coefficient for the outgassing components becomes unity, since from that temperature down the accumulation rate will remain constant and be equal to the outgassing rate.

It was found that outgassing products from the panel at a temperature of approximately 45°C began to accumulate on a collecting surface slightly lower than 45°C . This was confirmed on 4 separate runs and is not surprising, but does confirm the fact that the TQCM's are measuring the accumulation of panel outgassing products.

The temperature at which the sticking coefficient essentially becomes unity appears to be between -15°C and -25°C . This correlates with the data obtained by Dr. Rodney M. F. Lindford during his "Investigation of Contamination Effects on Thermal Control Surfaces"¹ for the Air Force. In this study the data shows outgassing products of S-13G paint (which uses an RTV binder) and RTV 602 to have sticking coefficients of unity between -12°C and -24°C on S-13G and aluminized teflon collecting surfaces.

The accumulation rates measured by the TQCM's at temperatures below -25°C can be used to establish the total panel outgassing rate, since the sticking coefficient at these temperatures is unity, and the total outgassing rate multiplied by the view factor of the collector is equal to the accumulation rate measured,

$$\text{Total Panel Outgassing Rate} = \frac{\text{Accumulation Rate}}{\text{View Factor of Collector}}$$

The time history of the accumulation rates indicate very high outgassing rates (greater than $2.3 \times 10^{-8} \text{ gm/cm}^2/\text{sec}$) for the first 24 hours at a panel temperature between 43.3°C (110°F) and 60°C (140°F). At 26 hours into the test, a problem developed with the TQCM heat sinks and the solar simulator had to be employed at values that caused the panel temperature to go as high as 77.8°C (180°F). This problem was not remedied until 42 hours into the test, so that a gap in the data exists between $t = 26$ hours and $t = 42$ hours.

¹"Investigation of Contamination Effects on Thermal Control Materials," T. A. Hughes, T. H. Allen, R.M.F. Lindford, T. E. Bonham, Contract F33615-73-C-5091, Report AFML-TR-74-218, January 1974.

When regular procedures were reestablished, it was found that the TQCM's would not clean up to their original state. A residue of some material that would not come off at temperatures as high as 80°C remained on both TQCM's. The amount of residue on TE-1 was $8.4 \times 10^{-6} \text{ gm/cm}^2$ and $2.3 \times 10^{-6} \text{ gm/cm}^2$ on TE-4. The outgassing rates at this time were down to $2.73 \times 10^{-9} \text{ gm/cm}^2/\text{sec}$.

This nominal outgassing rate of $2.73 \times 10^{-9} \text{ gm/cm}^2/\text{sec}$ at a panel temperature between 43.3°C (110°F) and 60°C (140°F) decreased very slowly over time. During the entire test period, the decreasing outgassing rate was broken by several sporadic releases of volatile, condensible materials as reflected by sudden increases in both accumulation rates and chamber pressure.

It is not clear whether such events were caused by bubbles of volatile material reaching the surface of the TPS bond line or whether this was material dumped by temperature fluctuations of the LN_2 door shroud. The automatic fill valve on the chamber door sometimes does not open and a manual over-ride procedure must be used. Since the door shroud temperature was not monitored, time correlation is not possible. However, the fact that the nominal rates of the TQCM's track one another by a factor of approximately 2 (the view factor ratio is 1.84) and the sporadic releases measured by the TQCM's have a ratio of 2 indicates that the sporadic releases are bubbles of volatile material from the panel rather than fluctuation in the door shroud temperature. (the ratio of view factors for the door shroud is close to 1).

After an elapsed time of 110 hours, the outgassing rate was down to $9.1 \times 10^{-10} \text{ gm/cm}^2/\text{sec}$ and seems to approach an asymptote of $9.0 \times 10^{-10} \text{ gm/cm}^2/\text{sec}$. In fact the rate at 141 hours is the same value as at 110 hours or $9.1 \times 10^{-10} \text{ gm/cm}^2/\text{sec}$. Plotting the log of these three outgassing rate values vs. time suggests that the steady state is reached close to an elapsed time of 70 hours as shown in figure 2.

After this test was terminated, the TQCM collecting surfaces were cleaned with solvents to their initial frequencies and the collected solute was submitted for analysis. Photographs of the residue as it appeared on the TQCM collecting surfaces before cleaning are shown in figure 3.

In both photographs there are dark brown spots of solid material that are from tenths of microns to microns in size.

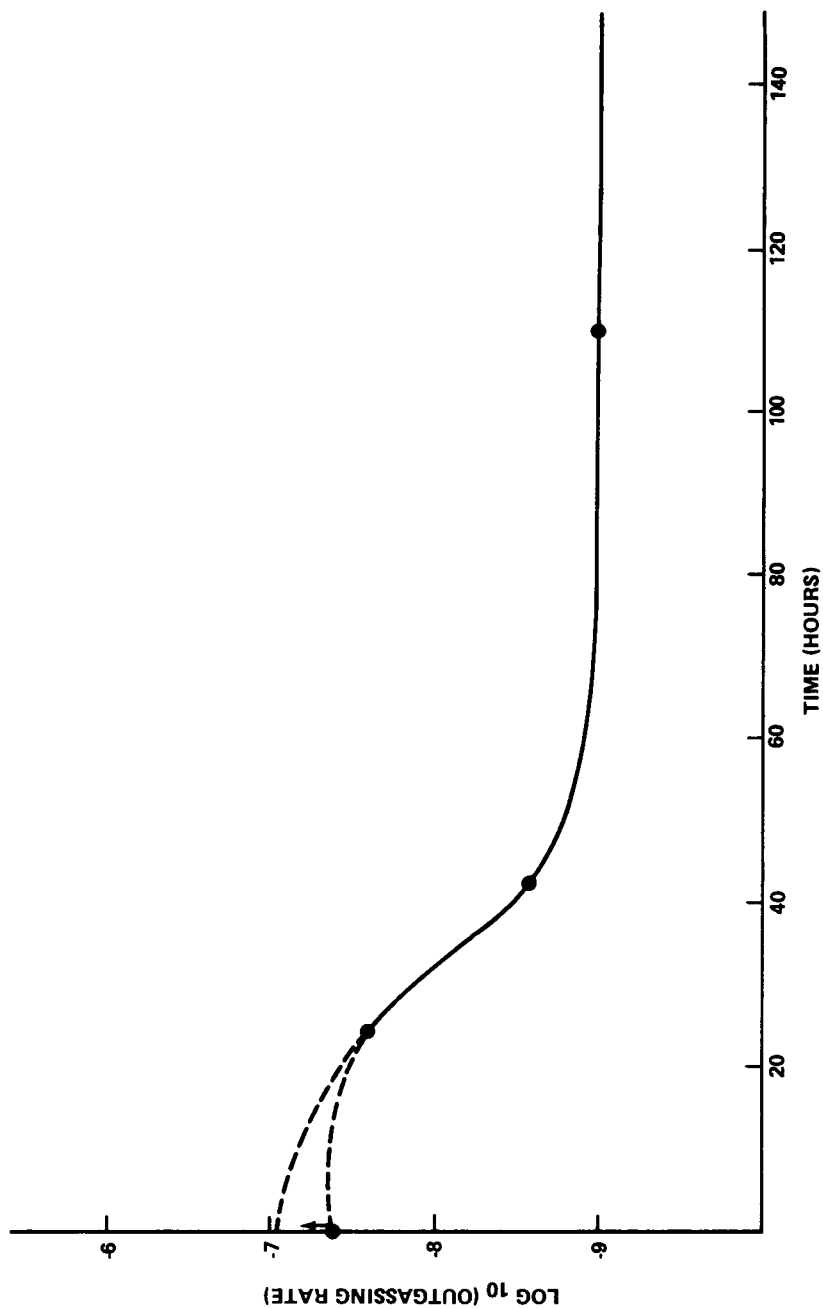


FIGURE 2: PLOT OF THE LOG_{10} (OUTGASSING RATE) VS. TIME DURING TEST I.

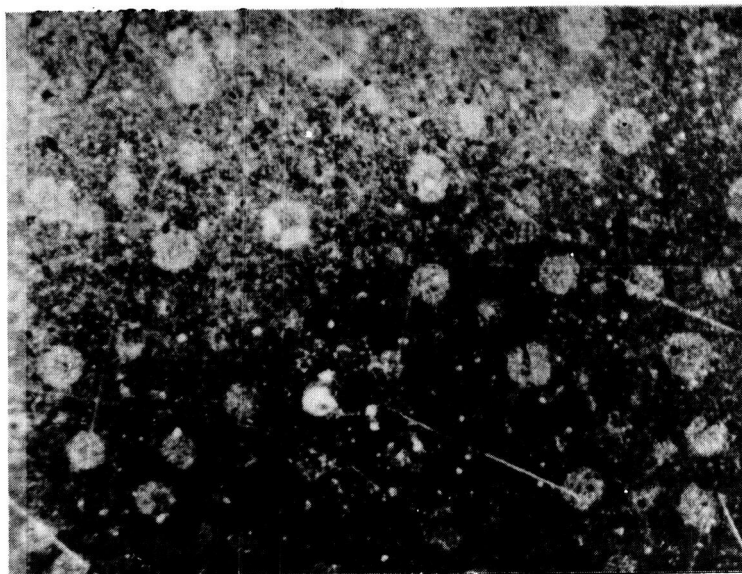


FIGURE 3: PHOTOGRAPHS OF THE RESIDUE
ON TQCM SURFACE.

They are irregular and randomly distributed over the surface. Another feature was a yellow material which was distributed in circles in the top photograph and in waves in the bottom photograph. This same residue was also found on the top of the tile surfaces and the door shroud.

A sample was removed from the tile surface and the shroud using cotton swabs. These swabs and a strip of the RTV from the panel was sent to Walter C. McCrone Associates, Inc. Excerpts from the letter from Dr. Richard E. Stevens explain the results of their analysis.

"The first sample, labeled 'Sample no. 1A, Tile no. 1, Nov. 25, 1974' contained an organic solid identified by infrared spectroscopy as a silicone polymer.

The second sample, material collected on a cotton swab and labeled 'door shroud at panel end' has also been identified as a silicone polymer. Particulates consist of thin, brittle yellow flakes.

Examination of cut sections of the cured RTV rubber submitted for comparison showed numerous voids (at least 5 per section), . . . and all containing a lump of uncured silicone.

.....

It is this material that volatilized to produce the observed deposit. This is in basic agreement with your letter of 10 December 1974 in which you state 'we believe the material contained in these specimens are outgassing products of this adhesive when raised to a temperature approximately equal to 150^oF'.

In a separate experiment, we examined RTV rubber prepared from materials which you supplied (RTV 560 monomer and curing catalyst dibutyl tin dilaurate). This artificially prepared sample appears free of voids and the previously observed monomer particles."

.....

In summary, it was found that outgassing products from the TPS panel which was at a temperature between 43.3^oC (110^oF)

and 60°C (140°F) began to show a net accumulation when the collecting surface was near 45°C and that the sticking coefficient of these products approaches unity between -15°C and -25°C.

The outgassing rate goes from an initial value above 2.3×10^{-8} gm/cm²/sec after 24 hours through 2.73×10^{-9} gm/cm²/sec at 42 hours to an asymptote of 9×10^{-10} gm/cm²/sec after 110 hours. A plot of the log of these rates vs. time indicates a minimum of 70 hours of elapsed time before a steady state outgassing rate of 1×10^{-9} gm/cm²/sec is reached.

A nonvolatile residue of silicone polymer is given off by the panel at temperatures somewhere between 43.3°C and 78°C within the first 42 hours. This residue will collect and remain on collecting surfaces which are 10 to 13 cm from the panel and as hot as 80°C. There will also be sudden sporadic jumps in the outgassing rates as bubbles of volatile material reach the surface of the TPS bond line.

Discussion of Outgassing Test 2:

The same chamber and equipment used in test number 1 was used in test number 2. There was no alteration of the respective elements of the test set-up.

Pumpdown proceeded rapidly to the low 10^{-7} torr region. With the panel operating at 43.3°C (110°F), the initial source rate was 7.6×10^{-9} gm/cm²/sec and appeared to gradually decrease to a value of 3.4×10^{-9} gm/cm²/sec at the end of the first 48 hours. Some volatile components were present in the accumulated material as evidenced by the fact that the observed deposition rate declines as the material accumulates because of increased evaporation. No large fluxes of volatile material such as observed in Test 1 was observed at any time during Test 2. No residual accumulation that did not desorb at higher temperatures was collected.

After 48 hours the volatiles seemed to disappear and the outgassing rates were similar to those observed near the end of Test 1.

Near the end of this test, the TQCM's were set to -60°C and the panel temperature was varied to determine the source strength as a function of temperature. The results are shown in Figure 4, which is a plot of the natural log of the accumulation

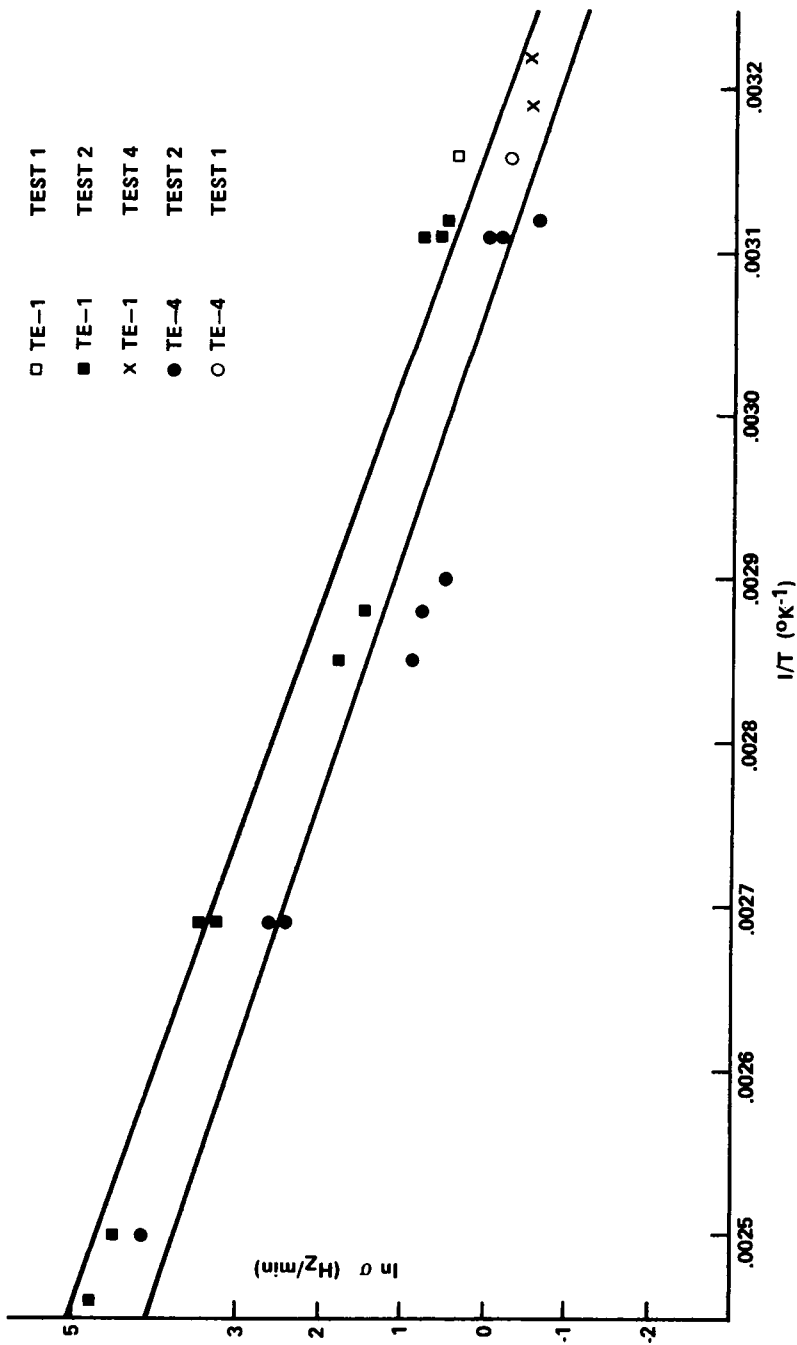


FIGURE 4: PLOT OF COLLECTION RATE AS A FUNCTION OF THE RECIPROCAL OF ABSOLUTE TEMPERATURE.

rate as a function of the reciprocal of absolute temperature. Since vapor pressures of most substances are related to $\exp(-H/RT)$, the result should plot as a straight line on such a plot and the heat of vaporization can be obtained from the slope. The temperature range for which the accumulation rate could be reliably measured is limited on test 1 and a slope can not be determined accurately from that test, but the data are plotted for comparison. Evaporation rates for higher temperatures were obtained at the end of the second test and these are used to determine the slope of the line.

The fact that the data are consistent when extrapolated to the temperatures in test 1, suggests that the steady state outgassing rate did not change significantly between the end of test 1 and the beginning of test 2 even though the panel was baked for 30 minutes at a temperature of 191°C (375°F).

The evaporation rate can be expressed theoretically by

$$\dot{m}_{\text{evap}}^{\circ} = \frac{\sigma_0}{\tau_0} \exp(-H/RT)$$

where σ_0 is the surface density of molecular leaving the surface, τ_0 is the time required for a molecule to escape from the lattice which is on the order of a vibrational period (10^{-12} sec), H is the binding energy or heat of vaporization, and R is the gas constant (1.98 cal/mole/degree).

Using the facts that

$$\dot{m}_{\text{evap}}^{\circ} (\text{Hz/min}) = 5.833 \times 10^{-11} \dot{m}_{\text{evap}}^{\circ} (\text{gm/cm}^2/\text{sec})$$

and

$$\ln \dot{m}^{\circ} = \ln \left(\frac{\sigma_0}{\tau_0} \right) + (-H/R) (1/T)$$

we can use the slope and intercept of figure 4, to find

$$\dot{m}^{\circ} = .168 \exp(-6905/T)$$

therefore, with a detector sensitivity of $3.5 \times 10^{-9} \text{ gm/cm}^2 - \text{Hz}$

$$\sigma_0 = 1.68 \times 10^{-13} \text{ gm/cm}^2$$

and

$$H = 13,672 \text{ cal/mole}$$

The normal surface density of molecules with a molecular weight of 100 gms and $\rho = 1 \text{ gm/cm}^3$ is $6.023 \times 10^{21} \text{ molecules/cm}^2$. When the molecular weight of 100 gms is converted to grams/molecule and divided into $\sigma_0 \text{ (gm/cm}^2\text{)}$ the result will give the number of molecules per square centimeter. In this case, the value is $1 \times 10^9 \text{ molecules/cm}^2$. This suggests that the volatile outgassing molecules diffusing to the surface and 1×10^9 the available sites are vacated by outgassing molecules.

The deposition rates of TE-4 were consistently between .4 and .8 times those measured by TE-1. The calculated view factors predict that TE-4 should collect .5 times that of TE-1 if the source is a Lambertian source. It is, therefore, reasonable to assume the panel slots do behave as Lambertian sources.

The steady state outgassing rate of the panel between 43.3°C (100°F) and 60°C (140°F) is $7.6 \times 10^{-9} \text{ gm/cm}^2/\text{sec}$ and decreases to a value of $3.6 \times 10^{-9} \text{ gm/cm}^2/\text{sec}$ at the end of 48 hours. The total area of the panel in these tests was 2782 cm^2 .

This test was terminated on December 5, 1974, after 53 hours of continual testing. After completion of this test, the panel was baked at 177°C (350°F) for 30 minutes to simulate a second bond-line temperature cycle during re-entry.

Discussion of Test 3:

The purpose of test 3 was to determine some general conditions under which solid particles originating from the panel might be generated or dislodged, and also to determine the size and number of such particles.

To support this objective, the panel support was turned 180° , so that instead of the panel being located at the bottom of the chamber with the panel surface facing up, it was at the top of the chamber with the panel surface facing down. A laser beam was tailored to make a rectangular beam 5.08 cm wide and .635 cm thick which was parallel with the panel surface and 11.5 cm below it.

Any particle dropping from the panel and passing through this beam would scatter light. A selected de-

tection area (12 cm^2) was monitored by a photomultiplier (PM) tube which was filtered to pass only the laser wave length. The height of the pulse given by the PM tube was assumed to be related to the size of the particle and the duration of the pulse to be proportional to the time the particle remains in the detection region.

The method of calibrating the system was to randomly drop glass spheres of a known diameter through the detection volume. The table below lists the results.

Diameter of Glass Sphere	Total Pulses Recorded	Average Millivolt Signal	Standard Deviation	Minimum Signal
20	177	.75	.28	.40
60	116	1.03	.37	.60
90	116	1.10	.24	.80
105	47	1.21	.22	.90

Using the results, a regression analysis (least square fit) was performed to relate the detected signal to the sphere diameter. The resulting equation is

$$X = \frac{y - .669}{.005} \text{ for average signal relationship, with } r^2 = .96$$

$$X = \frac{y - .269}{.006} \text{ for minimum signal relationship, with } r^2 = .99$$

where X is the diameter of the sphere in microns and y is the signal amplitude in millivolts.

The panel was placed in a vacuum of 10^{-6} Torr and subjected to 4 types of shocks:

(1) a thermal shock

This was accomplished by raising the temperature as quickly as possible using front surface heating from the solar simulator and then turning off the light source and allowing the temperature to drop as rapidly as possible.

(2) an electrostatic shock

This was applied by reversing a supply voltage (300 volts) which was applied to the aluminum substrate from plus to minus every 15 seconds.

(3) a gas impingement shock

In this case a 10 cm^3 volume of helium gas was released through an orifice .1 cm in diameter which was located 9 cm from the tile surface and allowed to impinge on the same surface.

(4) a mechanical shock

This shock was induced by dropping a 90.4 gram weight suspended 5.5 cm above the aluminum substrate on the side opposite from the tile surface.

Each shocking mechanism was applied several times allowing sufficient time between each application for any particles generated to fall through the detection volume.

There were no observed particles on repeated applications of the first three types of shocks. However, there were a total of 30 particles observed on 8 applications of the mechanical shock. The distribution and size of these 30 particles is given below (the size was calculated using the average signal equation):

Shock Application

Size of Particles in Micron	1	2	3	4	5	6	7	8	TOTAL
0-100	3	3	3	2		1	1	1	14
101-200		1		2	3	1		1	8
201-300	1	1						1	3
301-400	1				1				2
401-500	1								1
501-700		2							2
Over 700									0
Total	6	7	3	4	4	2	1	3	30

There is the expected trend toward fewer and smaller particles on successive applications, but some particles are generated on each and every application.

The area of the panel subtended by the detection volume was 0.4% of the total panel area. The subtended area included the tile intersection point directly opposite the point where the mechanical shock was applied.

There is insufficient data to present specific conclusions concerning the size and distribution of particles that may have been produced for any shock condition over the total panel, but the conclusion that particles of a rather significant size are generated by a mechanical shock is obvious.

Upon the completion of this test series, the panel was again baked at 177°C (350°F) for 30 minutes, submitted to a vacuum of 10^{-7} torr for 2 hours, and later baked at 204°C (400°F) for 35 minutes before being submitted for the final test.

Discussion of Test 4:

The panel was again mounted in the stainless steel fixture used on test 1 and 2. The TQCM's were oriented so that they were both at a 90° angle to the normal from the tile surface. An additional change was made. The entire test set-up was oriented so that the tile surface was parallel to the inlet plane of the UTI quadrupole for direct access to the quadrupole by the outgassing molecules. The new view factors for TE-1 and TE-4 were essentially the same in this test and were equal to .0133.

This test lasted for 4 days and measurements were taken between 8:00 A.M. and 4:30 P.M. each day. During the evening, the data recording rates were slowed down and the solar simulator was turned off so that the system would "coast" during the night. Each temperature to which the panel was subjected (10°C , 38°C , and 65.5°C) was repeated to verify results.

The results showed an outgassing rate of 3.6×10^{-10} gm/cm²/sec at a temperature of 10°C (50°F), 2.8×10^{-9} gm/cm²/sec at a panel temperature of 38°C (100°F), and 5.6×10^{-9} gm/cm²/sec at a panel temperature of 65.5°C .

(150° F). These rates are on the same order as the steady state rates established in test 1 and test 2. In fact, the rates established lay on the extrapolated line in figure 4, which is the plot of $\ln \sigma$ (Hz/mn) vs. $1/T$ (°K⁻¹).

The total time that the panel was subjected to simulated solar radiation was 24 hours. During this time a UTI model 100C quadrupole mass analyzer was used to monitor the gases in the vacuum chamber during the TPS outgassing tests. The mass analyzer was mounted on the wall of the test chamber with a gate valve between the mass analyzer and the test chamber. A 20 to 60 liter per second vac ion pump was used to pump out the mass analyzer so that it could be kept under vacuum at all times.

During this test, a series of four two inch diameter baffles with 1/2 inch holes were mounted in front of the inlet port of the mass analyzer to limit the field of view of the instrument to a specified area of the surface of the TPS panel. An ion gage was mounted in close proximity to the mass analyzer and was baffled in the same manner to monitor total pressure during the test.

A "fingerprint" spectrum of RTV 560, the adhesive used on the TPS panels, was supplied by Raymond Kruger of Goddard Space Flight Center (GSFC). This data was taken on a Finnegan model 400 quadrupole residual gas analyzer. The major peaks in the fingerprint occurred at 73, 91, and 135 AMU. These peaks were those which were used as identifiers for RTV 560 in the TPS tests.

The data from Test 4 was used to obtain the time history of the decay rates. Figure 5 presents the data for mass peaks 73, 91, and 135 AMU. As can be seen from the figure the curves all follow a similar trend. The number of molecules is high when the pressure is higher, immediately after the panel temperature has stabilized, and then decays even though the panel temperature remains constant. This same trend was obtained for mass peaks at 18, 56, 57, 58, 77, 78, and 79 AMU.

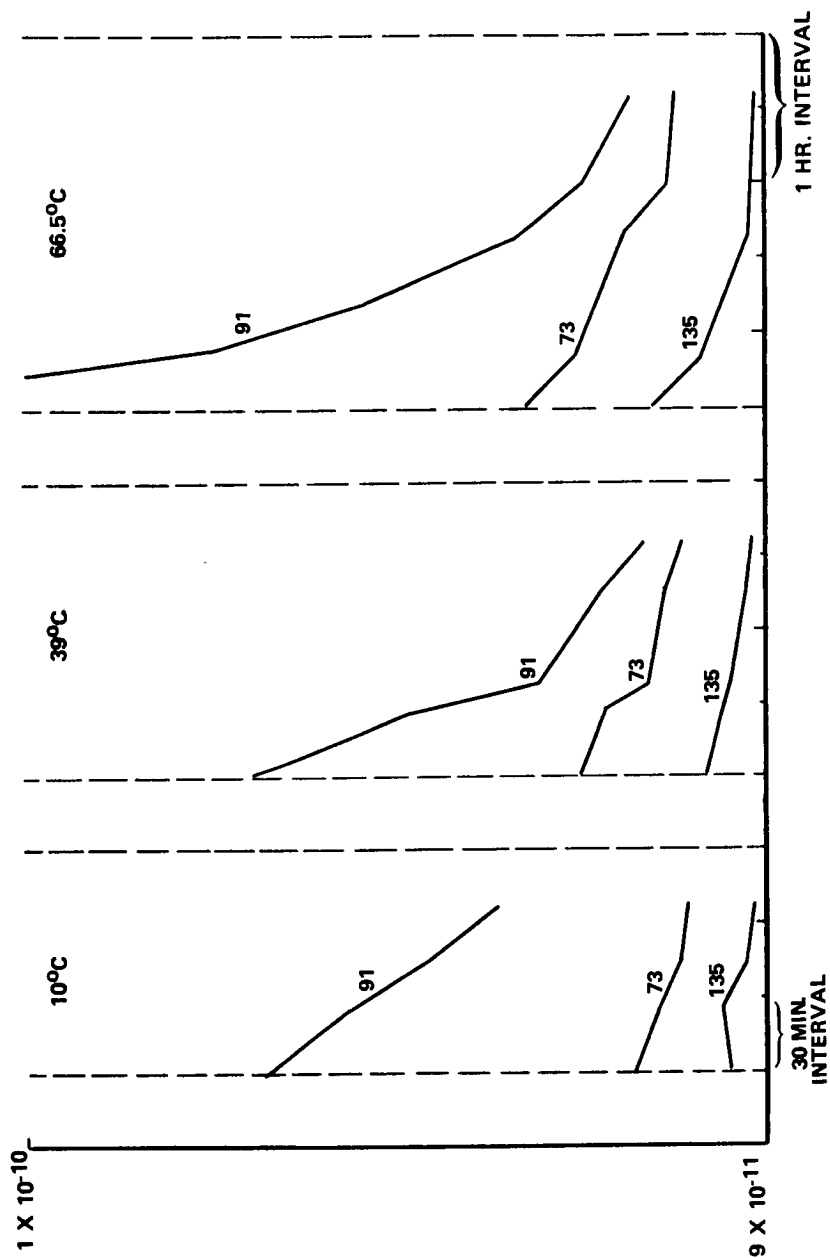


FIGURE 5: QUADROPOLE PLOTS OF RTV560 FINGERPRINT MASS PEAKS 73, 91, 135 AMU.

CONCLUSIONS

As might be expected, initial exposure of the TPS panel to simulated orbit temperatures produces copious quantities of outgassing products, most of which are quite volatile. These products begin to accumulate on surfaces as warm as 45°C (113°F). If the collecting surface is as cold as -25°C (18°F) the accumulation rate will be equal to the outgassing rate since the sticking coefficient at this temperature is essentially unity.

With no initial bake-out procedure, the outgassing rate of the TPS structure at temperatures between 43°C (110°F) and 60°C (140°F) could begin as high as $6.5 \times 10^{-8} \text{ gm/cm}^2/\text{sec}$, diminish to $2.3 \times 10^{-8} \text{ gm/cm}^2/\text{sec}$ after 24 hours, and approach an asymptotic rate of $2.73 \times 10^{-9} \text{ gm/cm}^2/\text{sec}$ after 70 hours.

Even with a bake-out procedure using temperatures as high as 204°C (400°F), the outgassing rates will be around $1 \times 10^{-9} \text{ gm/cm}^2/\text{sec}$ because this rate represents the long term steady state outgassing rate for elapsed times of 220 hours at simulated orbit temperature.

After reentry, the TPS surface will absorb some materials which will increase the outgassing rate by a factor of 2 during the first few hours of subsequent flights. After this initial rate the steady state rate of $1 \times 10^{-9} \text{ gm/cm}^2/\text{sec}$ will be approached and maintained.

If the temperature of the TPS surfaces, which utilize RTV 560, go as high as 78°C (180°F) during the first 42 hours, a non-volatile, silicone polymeric residue will collect on surfaces as hot as 80°C and will remain until physically or chemically removed.

No conclusions on the water outgassing can be drawn from this test since the background water vapor in the chamber was of the same order of magnitude as the panel outgassing.

The probability of generating solid particles from RCS or other motor gas impingements, electrostatic charging and discharging of the substrate, and thermal stressing is lower than the probability of generating them by mechanical shock. It is recommended that extreme care be

taken in moving pallets in the bay area, manipulating the extension arms, and/or performing other activities that may result in an impact being delivered to the vehicle structure. Such an impact has a high probability of generating particles several hundreds of microns in diameter that would interfere with experimental observations.

CRYOGENIC QUARTZ CRYSTAL MICROBALANCE*

D. McKeown, G. Sonnenschein and M. G. Fox, *Faraday Laboratories Inc., La Jolla, California*

ABSTRACT

A radiatively cooled Cryogenic Quartz Crystal Microbalance has been designed to monitor highly volatile contaminants on Shuttle. Measurements will be made with two 15-MHz microbalances having removable, optically polished sensors mounted in a radiant cooler. One sensor operates below the freezing point of water and monitors contamination including that of water vapor. The second sensor is heated and monitors the contamination background. It provides a reference from which the density of the water vapor cloud enveloping Shuttle can be determined. The mass measurement range of each sensor is 1.6×10^{-9} to 2.0×10^{-4} g/cm². The temperature of each sensor is monitored between 130 and 310°K. The design incorporates a low-power dissipation oscillator, heaters for ice removal and a new method for attaching second-surface mirrors to the radiator employing an indium type solder instead of an RTV.

INTRODUCTION

Water vapor contamination of optical systems operating at cryogenic temperatures presents a serious problem to Shuttle experimenters. At temperatures below about 140°K, water vapor is adsorbed as ice and will progressively degrade an optical system with time. Visentine, Ehler and Roberts¹ have explored the problem in the laboratory to determine the flux caused by dumping water generated during fuel cell operation. These measurements show water vapor fluxes of 1.4×10^{-7} g/cm²-sec. Fluxes of this magnitude will result in contamination remote from the source by back streaming.

Donohoe, Sherman and Hickman² have surveyed flights of infrared radiometers, spectrometers and radiant coolers that operate at temperatures below 100°K. Significant degradation in the operation of these instruments has been observed with time. The most probable cause was by water vapor contamination.

Water vapor contamination can be easily monitored by cooling a QCM to cryogenic temperatures and observing its mass loading rate. In the laboratory, cooling of the QCM is usually done with

* This work supported under NASA Contract NAS8-31110

liquid nitrogen or helium. On spacecraft, radiative cooling is the most practical method to attain cryogenic temperatures because of the lack of cryogenic fluids. We have recently completed the design of a radiatively cooled Cryogenic Quartz Crystal Microbalance (CQCM) to monitor water vapor contamination on Shuttle that I would like to present here.

THERMAL MODELING

Before a radiatively cooled CQCM can be built, its design must be thoroughly analyzed to assure that the 140°K operating temperature will be attained. A simple analysis of a radiant cooler gives a false picture of its ability to cool a CQCM because an isolated surface with unity emissivity will radiate a large amount of power into deep space. The amount of power, W , radiated is defined by

$$W = \epsilon \sigma (T_1^4 - T_0^4) \quad (1)$$

where ϵ is surface emittance, σ the Stefan-Boltzman constant ($5.67 \times 10^{-8} \text{ W/m}^2\text{K}^4$) and T_1 and T_0 are respectively the surface temperature and the temperature of space in °K.

The power radiated by a surface (140°K) into space (4°K) is 2.8 mW/cm². For a 100 cm² radiator, suitable for cooling a CQCM, the power is 218 mW. In practice, the effective cooling is much less, only about 20 mW, because

- a) Surface emittance is less than unity
- b) Back side of the radiator will absorb heat from the spacecraft
- c) Conduction of heat from the spacecraft to the QCM
- d) Oscillating quartz crystal sensors dissipate power

To determine the operating temperature of the CQCM, a thermal model was made. A computer modeling program previously developed for the OGO-6 Energy Transfer Probe⁵ was used and the basic approach will be described. The term thermal model refers to the physical parameters of a system which influence its temperature within a given environment, such as, mass, specific heat, conduction, radiation and geometric shape.

The CQCM was divided into parts called nodes. This is done on the basis of isothermality. Those parts of the CQCM which have a common temperature, due to high internal conduction paths, are lumped together. The degree of accuracy of the calculation procedures is dependent on the number of nodes considered. The thermal modeling program as now constituted can handle up to 200 nodes having a maximum of 400 conductive paths and 100 radiative paths.

Temperature is a measure of the stored energy of an object. The process of computing temperature as a function of time is an energy balance between the following heats gained or lost by

- a. Conduction to or from another node
- b. Conduction to the spacecraft
- c. Radiation exchange between nodes
- d. Radiation exchange to the spacecraft
- e. Radiation exchange to space
- f. Dissipation of electrical power

When the above factors are summed, they produce a net gain or loss of energy to the node. Energy gained is stored in the mass of the node and results in positive change of temperature. This change of temperature is proportional to the product of the mass and specific heat of the node. Energy lost to the node results in a negative change of temperature with the same constant of proportionality.

Conduction

The heat which is exchanged by conduction is computed using:

$$Q_{c(j)} = \frac{K(j) A_{c(j)}}{L(j)} [T_{a(j)} - T_{b(j)}] \quad (2)$$

where m values of conductivity (K), a conductive path cross section (A_c), path length (L), and the integers (a) and (b) are entered as inputs for conductive paths number $j = 1 - m$. The integers (a) and (b) denote the numbers of nodes (i) linked by the conductive path at (j).

Radiation

Heat which is exchanged by radiation between nodes is computed using

$$Q_{r(k)} = \sigma F_{(k)} A_{c(k)} [T_{c(k)}^4 - F_{d(k)}^4] \quad (3)$$

where m values of script F and the integers c and d are entered for each radiative path $k = 1 - n$ in the same manner as for conductive paths. Script F is the combined shape-emissivity factor for radiative heat transfer calculations. The values of F are obtained from a special computer program when an internal radiosity network is involved. External radiation to space is found by

$$F_{(i)} = \psi_{(i)} \epsilon_{(i)} \quad (4)$$

where ψ is the geometric view factor of node (i) for space.

CQCM

Several computer runs were made on CQCM models⁴ using various materials for its construction and different levels of power dissipations in the crystal sensors. The final design CQCM package, shown in Fig. 1, consists of a Sensor Head unit and Controller unit. Package weight is approximately 1 kg.

The Sensor Head contains the radiant cooler, two removable mass sensors, oscillators and output amplifiers. One sensor is called the Water Vapor Monitor (WVM) and operates below the freezing point of water in vacuum. The other sensor is called the Water Vapor Reference (WVR), operates above the freezing point of water and monitors contaminants other than that of water.

The Controller contains the voltage regulator, signal conditioner and heater power supplies and signal outputs. The regulator takes the $+28 \pm 4$ Vdc spacecraft power and provides $+20 \pm 0.1$ Vdc CQCM power. Controller operating power is approximately 470 mW. Sensor outputs are frequency-mass, analogue-mass and analogue-temperature. Power is supplied continuously to heat the WVR to 156°K to keep ice from adsorbing on it. Power commands are provided for cleaning ice from the WVM sensor and radiant cooler.

Sensor Head

A detailed drawing of the CQCM Sensor Head is shown in Fig. 2. The radiant cooler is an inverted truncated hexagonal structure of aluminum. The sensors are mounted on a plate attached to the radiator. The mirrors have a solar absorptance $\alpha \sim 0.06$ and a thermal emittance $\epsilon \sim 0.80$. Similar spectral properties are obtained for sensor and reference sensor crystals by Al plating and MgF_2 overplating. The radiator is attached to the base plate by three high-strength fiberglass-epoxy laminate standoffs. The two electronic units are connected to the crystal sensor by 0.05 mm diameter stainless steel leads to provide thermal isolation.

Radiative heat exchange from spacecraft to the radiator is minimized using a stack of 20 multilayer superinsulation of gold plated Kapton.

A plot of the cool down of the sensors with time is shown in Fig. 3. A 13 mW heater power is required to maintain the reference sensor at 156°K . The minimum temperature of the water vapor sensor is approximately 130°K and is reached in 10 hours.

Analysis was made using a foam insulating material instead of super insulation. Foam was discarded because heat conducted through the foam to the sensors limited the minimum operating temperatures to about 180°K , well above the freezing point of water in vacuum.

Analysis was made assuming the crystal oscillators were located on the radiator. The oscillators added 14 mW per sensor. Mounting the oscillators on the radiator was discarded because the additional power would result in sensor temperatures greater than 140°K .

Radiant Cooler - The successful operation of a CQCM requires lowering the temperature of the WVM sensor to below 140°K by use of a radiant cooler. Radiant coolers are usually fabricated with spectrally selective paints, such as S-13G/Lo or Z-93, or adhesive coatings of metallized plastics (Schjeldahl). Review of the outgassing characteristics of these materials precluded their use in CQCM design.

The search for a more favorable radiator surface has led to metallized quartz wafers called second-surface mirrors. They are normally bonded to the radiator structure by means of RTV silicone adhesives such as GE 566 or Dow "Silgard". This technique has two major drawbacks with regard to CQCM design. The RTV will outgas when the radiator views the sun and it interposes a thermal resistance between the second-surface mirrors and the radiator structure. We have developed a bonding technique using an indium type solder that eliminates the outgassing problem and significantly increases the heat conduction from the radiator structure to the mirrors. Fig. 4 shows a second-surface mirror soldered to an aluminum substrate. The radiant cooler will be composed of a mosaic of these mirrors with an effective surface area of about 160 cm².

Removable Crystal Sensor - To minimize the power load of the electronics on the radiator, the removable crystal sensors are mounted in the radiant cooler remote from the electronics (see Fig. 2). The sensor design is shown in Fig. 5.

The mass sensor consists of two high-sensitive 15-MHz quartz crystals. The beat frequency between the crystals is proportional to mass loading. Mass sensitivity is 1.6×10^{-9} g/cm²Hz which is more than twice as sensitive as previously flown 10-MHz QCM's. (Only 0.1 cm² area in the center of the crystal is mass sensitive and the absolute mass sensitivity is 1.6×10^{-10} g.) The sensor can measure a maximum loading of about 2.0×10^{-4} g/cm². Frequency-temperature characteristics are matched to minimize temperature instability.

The temperature sensor is a helium filled precision platinum thermometer. It is linear to $\pm 0.5\%$ and will be used to readout temperature to $\pm 1^\circ\text{K}$ between 130 and 300°K.

A major advantage of the removable CQCM mass sensor is that it can readily be changed with a clean one prior to launch. A clean sensor will minimize the problem of contamination absorbed during pre-launch test.

Quartz Crystals - Optically-polished quartz crystals will be used in the CQCM to minimize crystal power dissipation and improve measurement accuracy. Rough polished crystals commonly used in QCM's require significantly more power to oscillate because of low Q. Also, rough crystals give different readings for a contamination mass flux because the effective surface area of a rough crystal varies from crystal to crystal while the area of optically-polished crystals is minimal and well defined.

When oscillated, rough finished crystals develop about 0.4 V

to 1.0 V between the crystal electrodes. The motional resistance for a semi-polished crystal at resonance is about 5 ohms. The crystal power dissipation (V^2/R) ranges between 30 mW and 200 mW depending on drive level. This is a significant amount of power because it is generated in a small area in the center of the crystal where the electrode is plated and creates a hot spot. The generation of heat is troublesome when monitoring water vapor contamination.

Trouble arises because the hot spot is located exactly on the mass sensing region of the crystal (only the oscillating portion of the crystal is mass sensitive). The heat generated is either radiated into space or conducted to the crystal holder by the quartz blank. Radiation is low because the spot is metal plated which has a low emissivity. The conduction of heat to the holder is small because of the poor heat conduction properties of quartz. Consequently, a large temperature gradient will be set up between the center and edge of the crystal.

Making water vapor contamination measurements with rough crystals required that a QCM be cooled well below the condensation temperature of water vapor to take into account the elevated temperature of the active portion of the crystal. If the crystal is not cooled sufficiently, water condensing in the center of the crystal will flow to its cooler edge. When freezing occurs beyond the motional area of the crystal, inaccurate measurements result.

Optically-polished crystals have significantly larger Q's compared to rough finished crystals. $Q = 2\pi fL/R$ where f is the oscillation frequency, L the crystal effect electrical inductance and R its resistance. Q is a quality factor for a crystal and is the ratio of total oscillation energy of the crystal to the energy lost per cycle. For a high- Q crystal, only a fraction of its oscillating energy is lost per cycle. Optically-polished crystals dissipated only between 0.1 and 1 mW when oscillated and its larger active area precludes formation of a hot spot because the higher the Q , the less the energy will be that is dissipated in the crystal.

The difference in Q for crystals of different size and finish is shown in Fig. 6. A 1.27 cm dia optically-polished crystal has a Q about 10 times that of the same size rough crystal. Decreasing the diameter of a polished crystal by 1/2, degrades its Q to that of the rough crystal showing that a large diameter optically-polished crystal should be used for mass measurements at cryogenic temperatures.

The crystal used in the QCM is oscillated in the first overtone. Oscillating the crystal on a higher overtone increases mass sensitivity Δm .

$$\Delta m = k\Delta f/nf^2 \quad (5)$$

where k is a constant, Δf the frequency change from mass loading, f the crystal fundamental frequency and n the overtone. Crystals can be oscillated actively on the 3rd, 5th or 7th overtone. Only

odd overtone oscillations are possible because the crystal electric dipole can only be excited in odd multiples. The disadvantage of overtone oscillation is the crystals are highly temperature dependent and cannot be used over a wide temperature range.

Electronics

The goal of the electronics design was to minimize power dissipation in the CQCM so as not to excessively load the radiant cooler. The complete electronics design has been previously reported⁵ and the basic circuits will be described here.

Oscillators - Oscillators are designed with a wide-band width to operate crystal sets having fundamental frequencies between 10-MHz and 30-MHz to provide CQCM sensitivity in the range of 3.9×10^{-10} to 3.5×10^{-9} g/cm². The power dissipation for the CQCM oscillators is 5 mW.

Beat Frequency - The oscillators drive a mixer-beat-frequency operational amplifier having a low impedance high-gain output. The total power dissipation of the CQCM oscillators and operational amplifier is only 14 mW and represents a reduction of better than 2/3 over the best QCM now available. The frequency output of the amplifier is proportional to the contamination loading of the CQCM. This frequency is provided as an output for direct monitoring of contamination. The frequency is also fed into a converter to provide an analogue output for spacecraft telemetry.

Frequency Converter - The analogue output of frequency is provided by a digital-phase-locked loop (PLL) frequency/analogue (F/A) converter. A voltage analogue of frequency is generated by using a voltage controlled oscillator (VCO) internal to the PLL. The sensitivity of the PLL is 50 μ V/Hz.

Log-Amplifier - For space application, the output voltage from an F/A converter must be limited to 0 - 5 Vdc for telemetry. The low frequency end requires expansion to enhance threshold sensitivity for detection of the first monolayers of contamination adsorbed. This is accomplished by feeding the PLL output into a Log-Amplifier for further signal conditioning. CQCM calibration is shown in Table 1.

Temperature Bridge - The temperature of CQCM sensors is monitored by a precision helium-filled platinum thermometer linear to 0.5%. The temperature output is provided by a bridge whose output is 23 mV/°K. The bridge is designed for an eight bit telemetry system that can transmit voltages of 19.5 mW. The temperature of each sensor will be readout between 130 and 310°K to $\pm 1^\circ$ K and corresponds to a 0 to 5 Vdc output change from the bridge.

CQCM ΔF Hz	F/A Converter V	Log-Amp V	Total Mass Loading 10^{-9} g/cm ²
<1	<0.50005	<0.1	<1
12	0.5005	1	19.2
149	0.505	2	238.4
1,639	0.55	3	2,622
16,149	1.0	4	25,838
126,149	5.5	5	201,838

Table 1 CQCM Calibration

Regulator - The spacecraft voltage of 28 ± 1 Vdc is not stable enough to operate the CQCM. A voltage regulator provides the 20 ± 0.1 Vdc required for operation.

The regulator also provides the power required for heaters in the sensors and radiant cooler for the removal of ice.

CONCLUSIONS

The design study of a CQCM has shown that the heat load to the radiant cooler must be minimized to attain operating temperatures below 140°K . The sources of electrical power, such as the voltage regulator and electronic oscillators, must be located remote from the radiant cooler. High-Q optically-polished crystals should be used to reduce power dissipated in the cooler and minimize the temperature of the mass sensitive region in the center of the crystal to assure accurate measurements. Multilayers of super insulation should be used instead of foam to thermally isolate the cooler from the spacecraft.

REFERENCES

1. Visentine, J.T., Ehlers, H.K.F. and Roberts, B.B., "Determination of High-Velocity Water-Vapor Plume Profiles in a Thermal-Vacuum Environment", AIAA Paper No. 60, Presented at 7th Space Simulation Conference, Los Angeles, CA (1973).
2. Donohoe, M.J., Sherman, A. and Hickman, D.E., "Radiant Coolers - Theory, Flight Histories, Design Comparisons and Future Applications", AIAA Paper 75-184, Presented at AIAA 13th Aerospace Sciences Meeting, Pasadena, CA (1975).
3. McKeown, D. and Dummer, R.S., "Gas-Surface Energy Transfer Experiment for OGO-F", IEEE Geoscience Electronics, GE-7, pp 98-106, (1969).
4. McKeown, D. and Sonnenschein, G., "CQCM Radiative Cooler Design", FAR-D-002-75, Faraday Laboratories Inc., La Jolla, CA (1975).
5. McKeown, D. and Fox, M.G., "CQCM Electronics Design", FAR-D-003-75, Faraday Laboratories Inc., La Jolla, CA (1975).

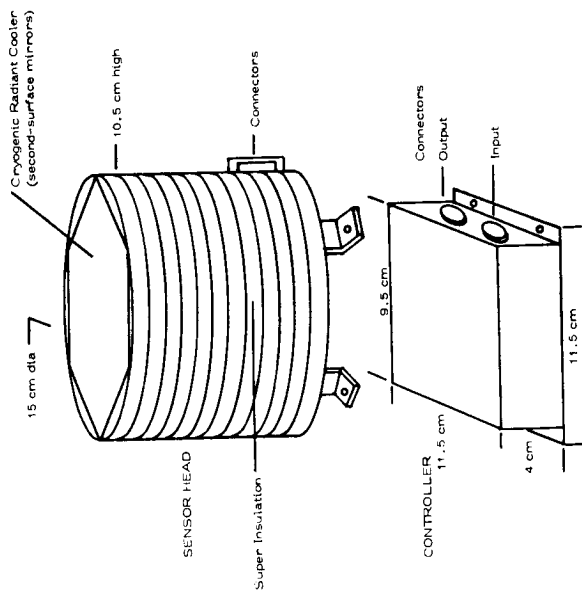


Fig. 1 CQCM Package

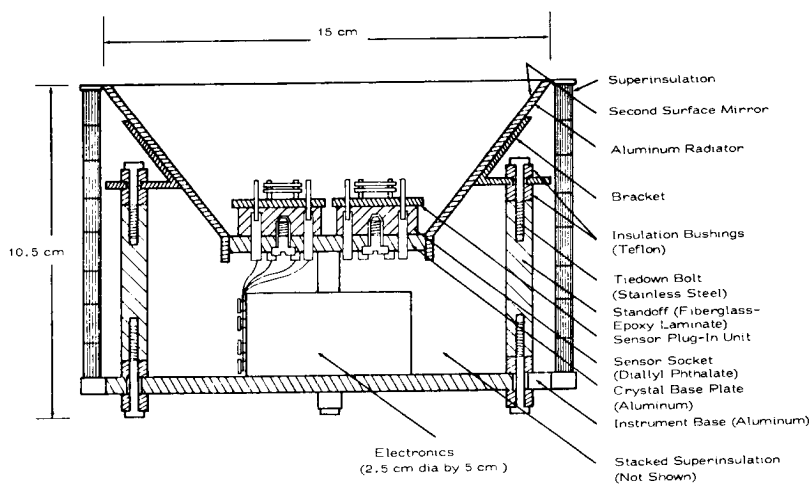


Fig. 2 CQCM Sensor Head

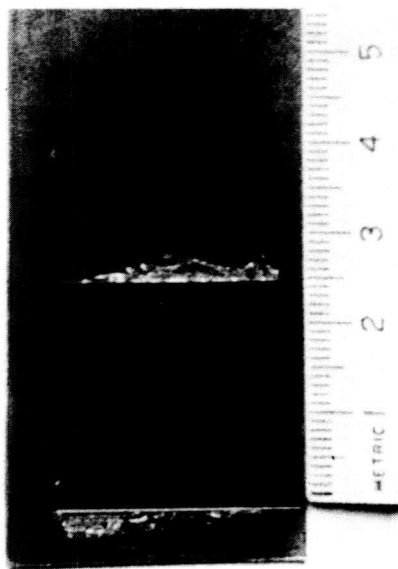


Fig. 4 Second-surface mirror soldered to aluminum

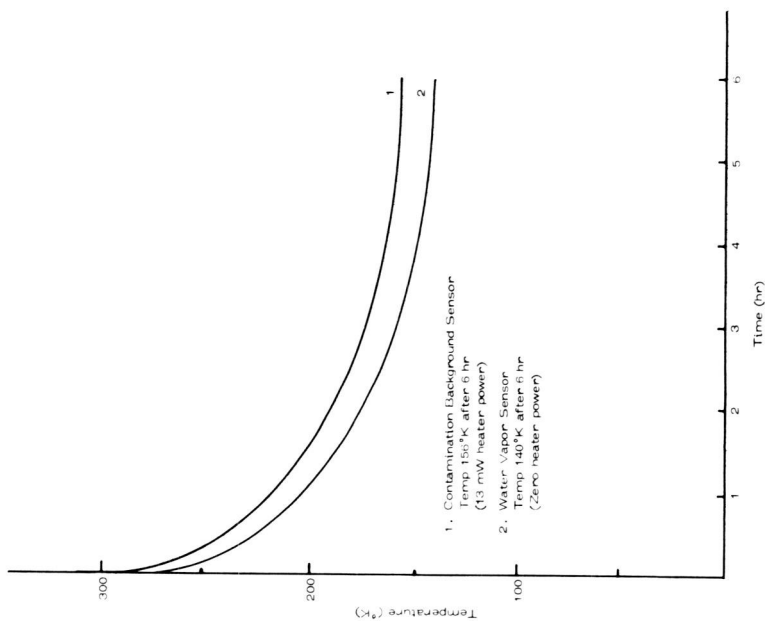


Fig. 3 Temperature of CQCM Sensors with time after pointing into deep space

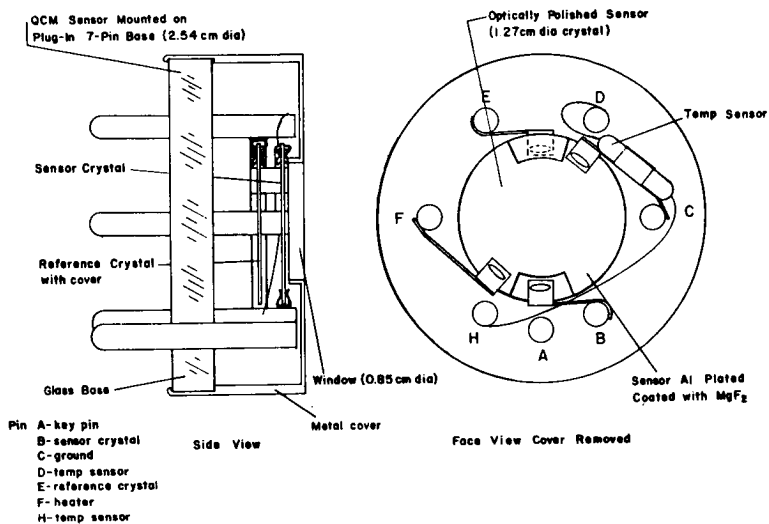


Fig. 5 CQCM Mass Sensor

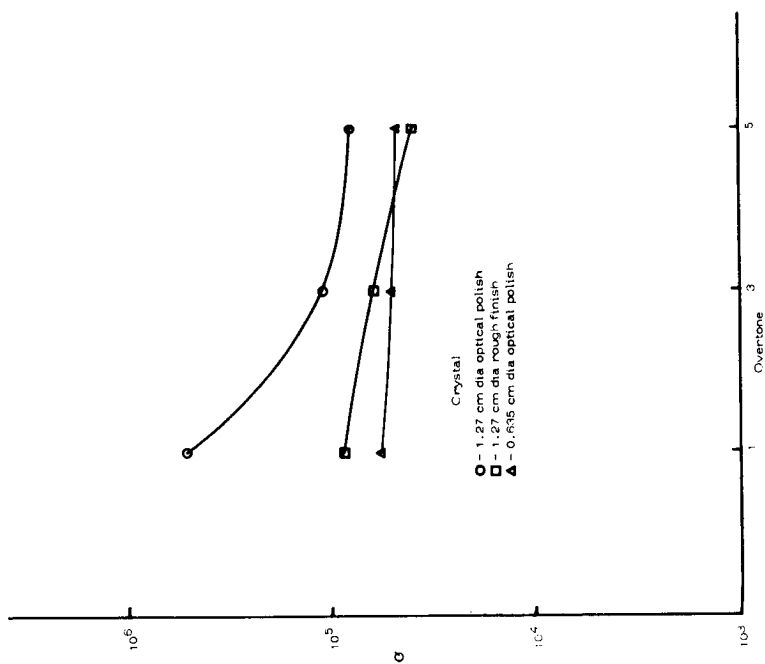


Fig. 6 Quartz crystal Q as a function of overtone in vacuum

ANALYSIS OF RADIATIVE SOURCES WITH BOTH SPECULAR AND DIFFUSE CHARACTERISTICS IN THE VISIBLE AND INFRARED SPECTRUM

Franklin U. Williams, *Johnson Space Center, Houston, Texas*

BACKGROUND

A joint United States/Union of Soviet Socialist Republics manned space mission is planned for July 1975. The U.S. Apollo command module and the U.S.S.R. Soyuz spacecraft will rendezvous and dock for approximately 2 days while exchange visits between the U.S. astronauts and U.S.S.R. cosmonauts will be televised to the Earth.

The Apollo Soyuz docking module (ASDM) will accommodate the docking system of both spacecraft, contain experimental equipment and an integral life support system, and control its internal temperature between 289 and 300 K for variable thermal conditions. The source of these variable conditions will be metabolic, equipment, and the external thermal stimuli of Earth orbit.

Simulation of these external thermal stimuli was one of the major test objectives during the manned tests of the ASDM conducted during the June to October 1974 period in chamber B of the Space Environment Simulation Laboratory at the Johnson Space Center in Houston, Texas.

INTRODUCTION

The purpose of this paper is to describe the application of analytical concepts which were developed to facilitate the design and analysis of the thermal simulator for the ASDM thermal-vacuum test series. (See figs. 1 and 2.)

Four functions were used to mathematically formulate the irradiance from a quartzline lamp and its reflector. The algorithmic expressions for the lamps

and for the surfaces of the ASDM zones provided the nucleus for a computer program.

The four functions used to mathematically formulate the irradiance from a quartzline lamp and reflector will be described with examples of application to simple geometries. The calculated and measured values obtained during the design phase will be compared. Additionally, general information will be denoted for utilization of the functions in computer or calculator programs with approximate computer storage and statement requirements.

LAMP FUNCTIONS AND THEIR APPLICATION

A number of analytical concepts can be applied to calculate the resultant irradiance from an array of lamp elements. One of the most elegant but demanding methods is to functionally describe each component of the lamp assembly diagrammatically shown in figure 3 and calculate the resultant irradiance for the interdependent effect of elements a, b, and c. The elegance and complexity of this method can be appreciated from the functional relationships:

1. $I_T = f(I_a, I_b, I_c)$
2. $I_a = G(x, y, z, \bar{n}, \alpha, \epsilon, \rho, T, P, \lambda)$
3. $I_b = H(x, y, z, \epsilon, \alpha, \tau, t, \bar{n}, T, \lambda, P)$
4. $I_c = J(x, y, z, \alpha, \epsilon, \rho, \bar{n}, T, \lambda)$

where x, y, z, \bar{n} are position coordinates and surface normals, respectively; $\alpha, \epsilon, \tau, \rho$ are absorptivity, emissivity, transmissivity, and reflectivity, respectively; T is the temperature of the element; t is the quartz thickness; P is the power applied; λ is wavelength; and I_T symbolically represents the irradiance at the point of interest. Obviously, the analytical solution by this method is an awesome task.

To provide a simpler method, a functional relationship was assumed to exist of the form

$$I_n(A, B, d, P) = f(A)G(B)H(d)J(P)$$

where A and B are the angles shown in figure 4, d is the distance from the lamp assembly's geometric center to the small surface area irradiated, P is the

power applied, and I_n is the incident flux density at the small surface area (S_n) normal to the vector from the lamp assembly's geometric center to the small surface area. Thus, once this functional relationship was confirmed and empirical equations developed for the explicit functions, $f(A)G(B)H(d)J(P)$, incident flux density on S_n was the product of the scalar quantities for the functions at values of A, B, d, P corresponding to the position of S_n relative to the lamp geometric center and the power applied to the lamp.

From lamp test data the explicit functions for the 40.6 cm lamp were empirically determined by curve fitting to be as follows:

1. $f(A) = 1 - 4.229 \times 10^{-3} |A| + 2.0918 \times 10^{-4} A^2 - 3.176 \times 10^{-6} |A|^3, A \text{ in degrees.}$
2. $G(B) = 1 + 4.08889 \times 10^{-3} |B| + 8.6667 \times 10^{-5} B^2 - 2.8395 \times 10^{-6} |B|^3, B \text{ in degrees.}$
3. $H(d) = 4.285 \exp(-0.03182415d), d > 38 \text{ cm.}$
4. $J(P) = 32.5563 - 16.7523I + 4.2582I^2 + 4.0935I^3, I \text{ in amps.}$

These functions are presented in the final form that was used to design the thermal simulator and to calculate flux densities for the Apollo Soyuz Test Project thermal-vacuum tests. The functions are the result of several refinements of the equations, reexamination of test data, and review of initial assumptions.

To calculate the resultant flux density at points on an arbitrary surface, the dot product of a unit vector for the surface at the point of interest (\bar{S}) and a unit vector from that point to each lamp assembly's geometric center (\bar{C}) were used in the application of the explicit functions in the computer program. Hence

$$I_T = \sum_{j=1}^k I_n(A_j, B_j, d_j, P_j) \bar{C}_j \cdot \bar{S}, j=1, 2, 3, \dots, k$$

where I_T was the resultant flux density in W/m^2 from k lamp assemblies at a point on an arbitrary surface.

The calculated values were compared to the design requirements. When calculated values were not within design tolerance, the designer would select new values

for each affected lamp's position and rotation (6 degrees of freedom) relative to the test article and the power applied (7th degree of freedom) until design requirements were calculated to have been achieved.

A simplified example of application to a plane surface (fig. 5) is as follows:

1. $\bar{L} = h\bar{k}$ where h is the fixed lamp height.
2. $\bar{W} = x\bar{i} + y\bar{j}$ and (x, y) is the point of interest.
3. $d\bar{C} = x\bar{i} + y\bar{j} + h\bar{k}$ where d is distance from lamp center to the point of interest and \bar{C} is the unit vector from the point of interest to the lamp center.
4. $\bar{s} = \bar{k}$ is the unit vector normal to the xy plane.

By inspection it can be seen that

5. $A = \tan^{-1} (y/h)$
6. $B = \tan^{-1} (x/h)$
7. $d = \sqrt{x^2 + y^2 + h^2}$

and

$$8. \quad \bar{s} \cdot \bar{C} = h/d.$$

For lamps translated from the origin

$$9. \quad A = \tan^{-1} \left(\frac{Y - Y_L}{h} \right), \text{ etc.}$$

where Y_L , X_L are position coordinates of the lamp. Rotation of the lamp about the "x" axis in figure 5 either adds or subtracts from the computed value of A . Rotation about the Y axis affects B similarly. Rotation about the Z axis requires transformation of the x, y coordinates.

Analogously, an example of application to a cylinder (fig. 6) is as follows:

1. $\bar{L} = (R+h) \cos \theta \bar{i} + (R+h) \sin \theta \bar{j} + Z_L \bar{k}$ where " θ " is the lamp angle from the "x" axis, R is the cylinder radius, h is the lamp height, and Z_L is the location of the lamp on the Z axis
2. $\bar{W} = R \cos \phi \bar{i} + R \sin \phi \bar{j} + Z \bar{k}$ where ϕ, z are variables which determine the point of interest on the cylinder surface.
3. $d\bar{c} = [(R+h) \cos \theta - R \cos \phi] \bar{i} + [(R+h) \sin \theta - R \sin \phi] \bar{j} + (Z - Z_L) \bar{k}$ where \bar{c} is a unit vector and d is the scalar distance to the lamp center.
4. $\bar{s} = \cos \phi \bar{i} + \sin \phi \bar{j}$ is the unit vector normal to the surface at the point of interest.

It can be shown that

$$5. A = \tan^{-1} \left[\frac{R \sin (\phi - \theta)}{h + R - R \cos (\phi - \theta)} \right]$$

$$6. B = \tan^{-1} \left[\frac{Z - Z_L}{R + h - R \cos (\phi - \theta)} \right]$$

$$7. d = \left[R^2 + (R+h)^2 + (Z_L - Z)^2 - 2R(R+h) \cos (\phi - \theta) \right]^{1/2}$$

$$8. \bar{s} \cdot \bar{c} = \frac{(R+h) \cos (\phi - \theta) - R}{d}$$

When $\bar{s} \cdot \bar{c} \leq 0$, the computed value of I_n must not be included in the summation to calculate I_T^n .

MEASURED AND CALCULATED IRRADIANCE

The lamp data used to develop the explicit functions were obtained in tests of individual lamp assemblies in the small thermal-vacuum chambers of the Space Environments Effects Laboratory. The test configuration is shown in figure 7. The radiometers were normal to the lamp assembly's center and positioned to obtain data at distances of 45.7, 61, 76.2, and 86.4 cm and B angles of 0, 20, 40, and 60 degrees as the lamp assembly was rotated about its long axis to A of 0, 10, 20, ..., 70, and 80 degrees. Data were obtained for the 40.6, 25.4, and 12.7 cm lamps. Data were obtained at current settings from 0 to 5 amp in 0.5 amp steps for the 40.6 cm lamp assembly, etc.

The data were normalized for fixed values of all of the independent variables at some arbitrary point. Plots of the normalized curves were reviewed to determine the validity of the assumption that explicit functions could be formulated. For example, the existence of an explicit function $f(A)$ was verified by

$$\frac{f(A)}{f(A=0)} = \frac{f(A)G(B=a)H(d=b)J(P=c)}{f(A=0)G(B=a)H(d=b)J(P=c)}$$

where the numerator values to the right of the equality sign were measurements as the argument A was varied and B,d,P were fixed. The denominator was the measured value at the normalizing position. By this method each explicit function was shown to be independent within an acceptable mean average.

The functions were evaluated further by conducting a test in chamber D of the Space Environments Effects Laboratory to correlate the calculated with the measured irradiance from an array of lamps on a cylinder and plane. The test configuration for the cylindrical surface is shown in fig. 8.

The lamp assemblies were positioned and power was applied in accordance with the conditions used in the calculations. The radiometers were indexed to positions corresponding to points on the surface where values had been calculated.

Correlation of the cylindrical surface data (table I) was performed by tabulating the ratio of measured to the calculated values of irradiance. The

mean average for all points was 1.03 with a standard deviation of 0.097. The ratio data at positions -99 and +99 had the largest deviation and were suspected to have been the result of the extraneous influence of surfaces near the end points.

However, the measured data also had included the effects of variances between lamp assemblies, radiometer errors, positioning errors, and applied power errors. These error sources were estimated to have a mean average of 0.0222 with a standard deviation of 0.0255. Thus for the intended application the "close" correlation of ratios was deemed to have validated the usefulness of the functions.

CALCULATOR/COMPUTER PROGRAMS

Both calculator and computer programs were developed for use during the ASTP design phase. A simplified flow chart is shown in figure 9.

A program for a 9830A Hewlett Packard calculator with extended memory was developed for up to 42 lamps and simple geometries. Run time for 20 lamps was approximately 20 minutes versus approximately 4 hours for 42 lamps.

A larger program was developed for the Univac 1108 computer with the capability of 100 lamps and complex geometries which included the effect of shadowing by intervening surfaces. Run time without the shadowing was approximately 20 minutes versus 1 hour with shadowing. The program required approximately 700 Fortran statements utilizing 40×10^3 memory locations.

CONCLUSION

In conclusion, the explicit functions originated at the Johnson Space Center were the basis for substantially reducing the design cost of the thermal simulator for the Apollo Soyuz Test Project in comparison with the design cost of the thermal simulators used in other test programs. In the future the concept of explicit functions will be extended to provide analysis of other types of radiative sources. This extension in conjunction with an adaptation of the computer program could be used effectively by other organizations for thermal simulator design as it will be used by the Space Environment Simulation Laboratory.

TABLE I.- RATIO OF MEASURED TO CALCULATED
FLUX DENSITY, CYLINDRICAL SURFACE,
CASE 13, CHAMBER D

		Radiometer								
		1	2	3	4	5	6	7	8	9
Z-axis in cm	99	1.20	1.55	1.26	1.26	1.35	1.15	1.07	1.22	1.17
	83.8	.98	1.28	1.12	1.12	1.22	1.04	1.00	1.12	1.17
	68.6	.97	1.00	.95	.99	.98	.96	.91	.96	1.06
	53.3	.99	1.02	.99	.99	.89	.97	.94	1.00	1.06
	38.1	1.00	1.02	1.00	.97	.93	.96	.94	1.02	1.05
	22.9	1.02	1.03	1.02	.97	.93	.96	.96	1.03	1.06
	7.6	.99	1.02	1.01	.97	.92	.97	.96	1.02	1.04
	-7.6	.99	1.02	1.01	.97	.95	.99	.97	1.01	1.02
	-22.9	1.01	1.03	1.02	.97	.97	1.01	.98	1.01	1.03
	-38.1	.98	1.02	1.01	.96	.97	1.00	.99	1.02	1.01
	-53.3	.95	1.02	1.01	.96	.96	1.02	1.00	1.04	1.02
	-68.6	.90	.98	.99	.96	.97	1.01	.99	1.08	1.02
	-83.8	.95	1.10	1.08	1.00	1.10	1.04	1.11	1.29	1.12
	-99	1.03	1.04	1.02	1.04	1.11	1.07	1.19	1.32	1.17

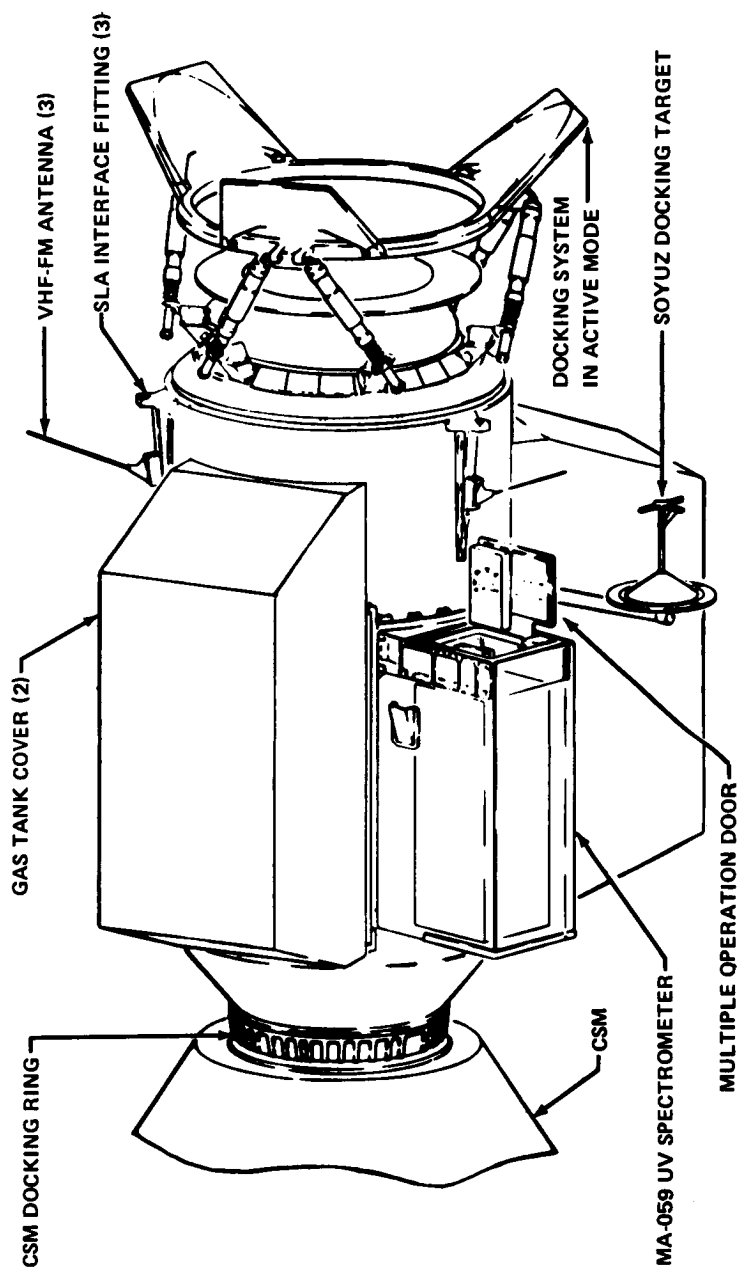


Fig. 1 - Outboard profile of DM

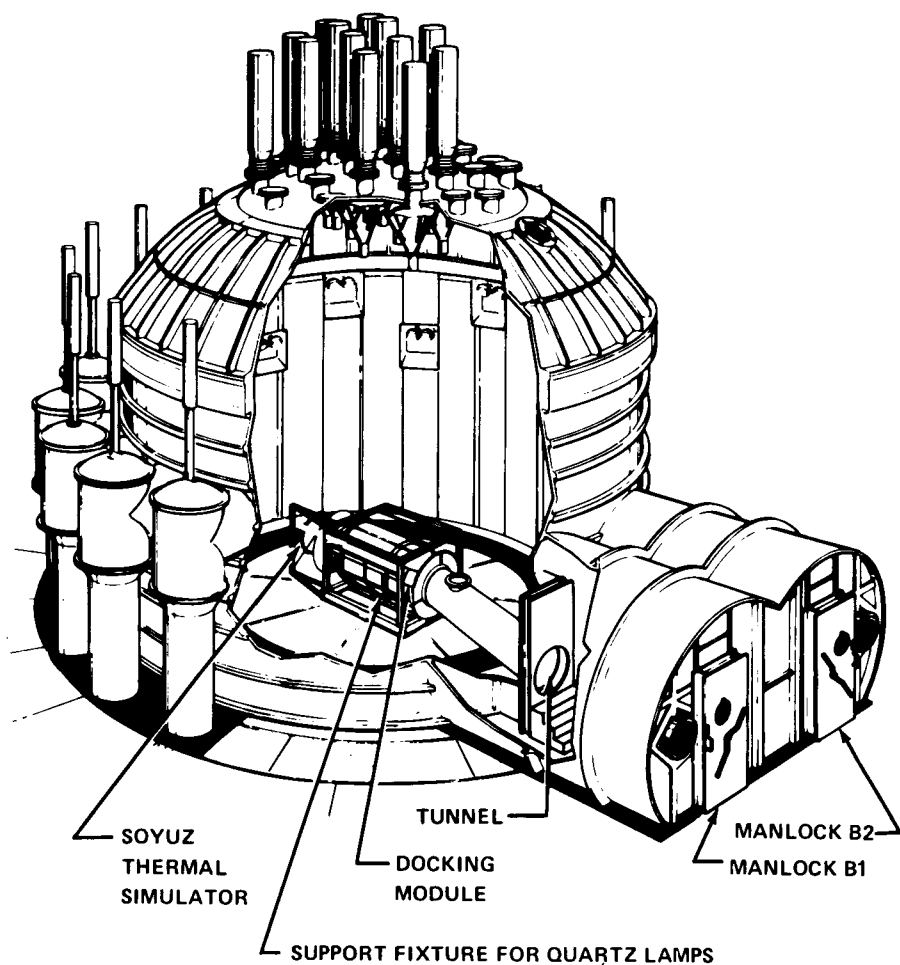


Fig. 2 - Docking module thermal vacuum test

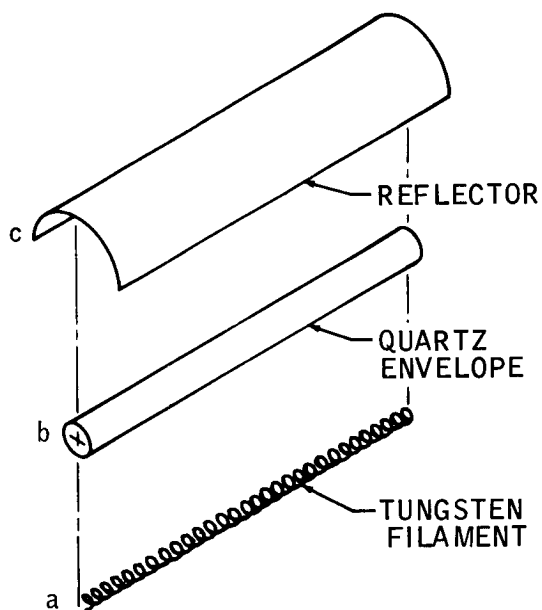


Fig. 3 - Lamp assembly

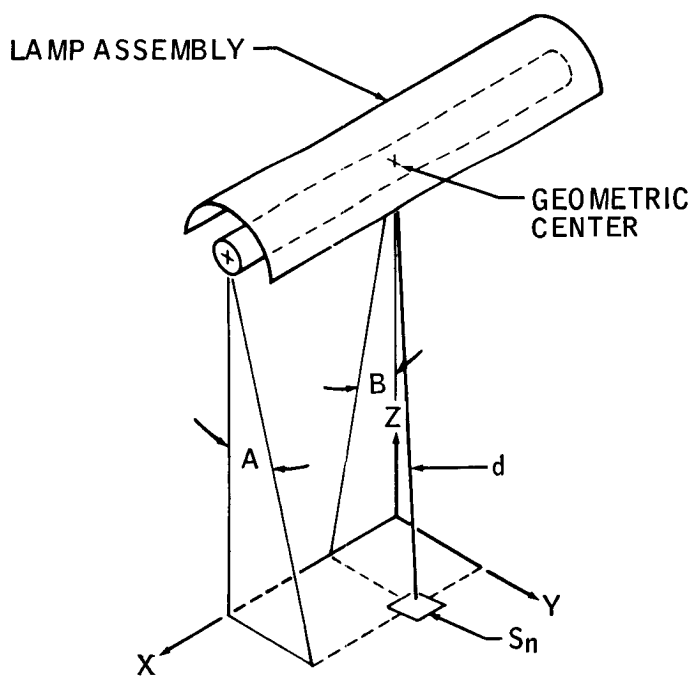


Fig. 4 - Coordinates for explicit functions

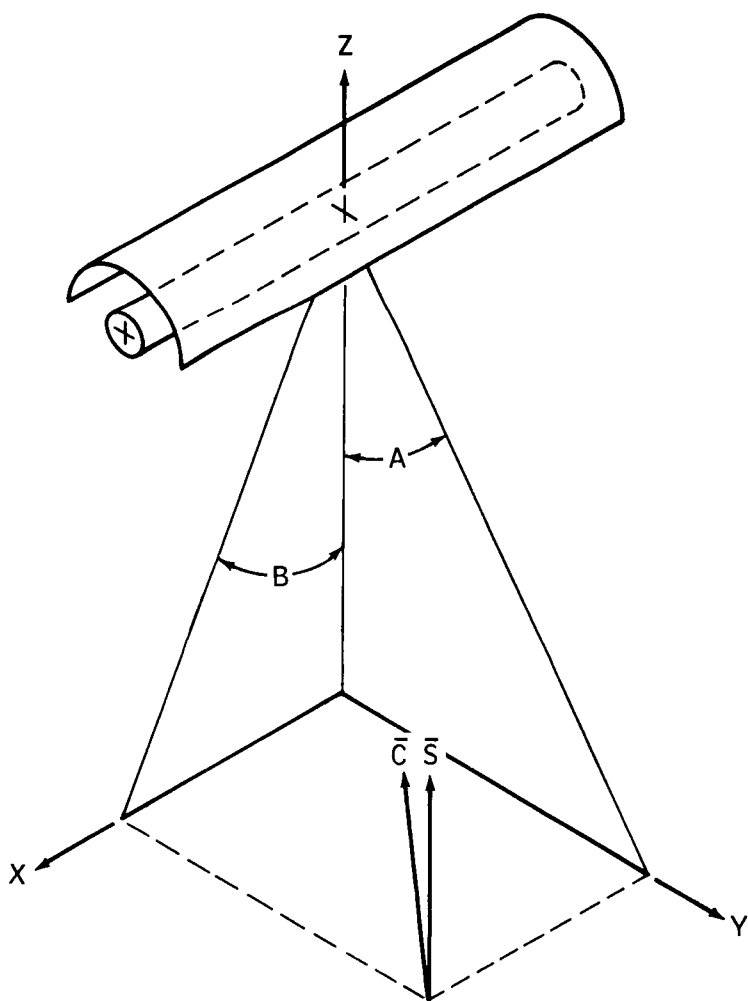


Fig. 5 – Application to a plane surface

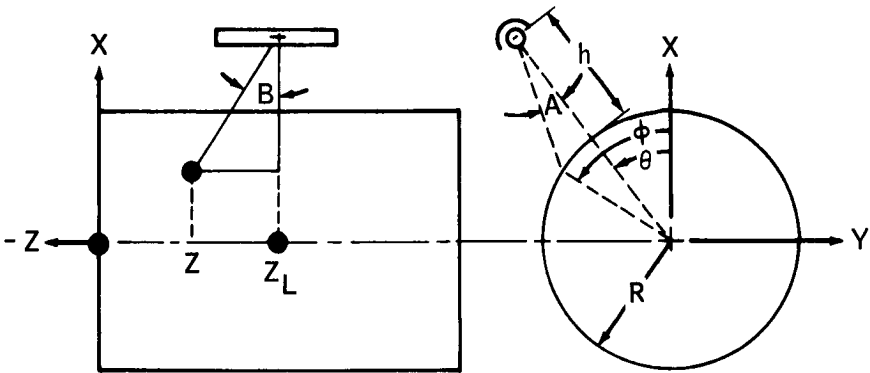


Fig. 6 - Application to a cylinder

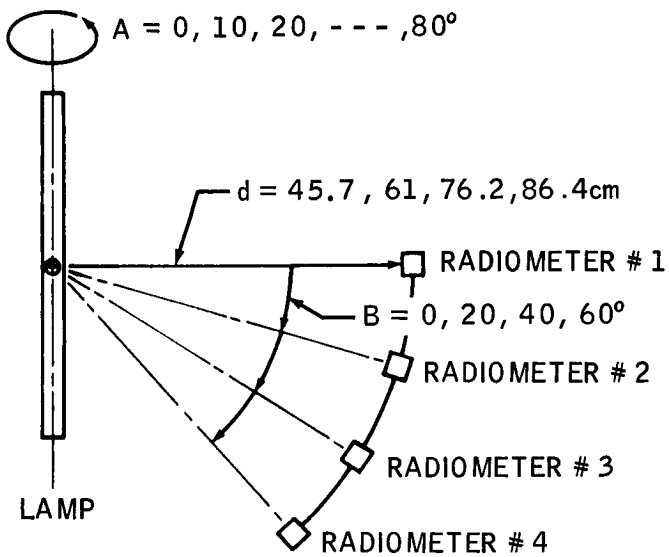


Fig. 7 – Individual lamp test

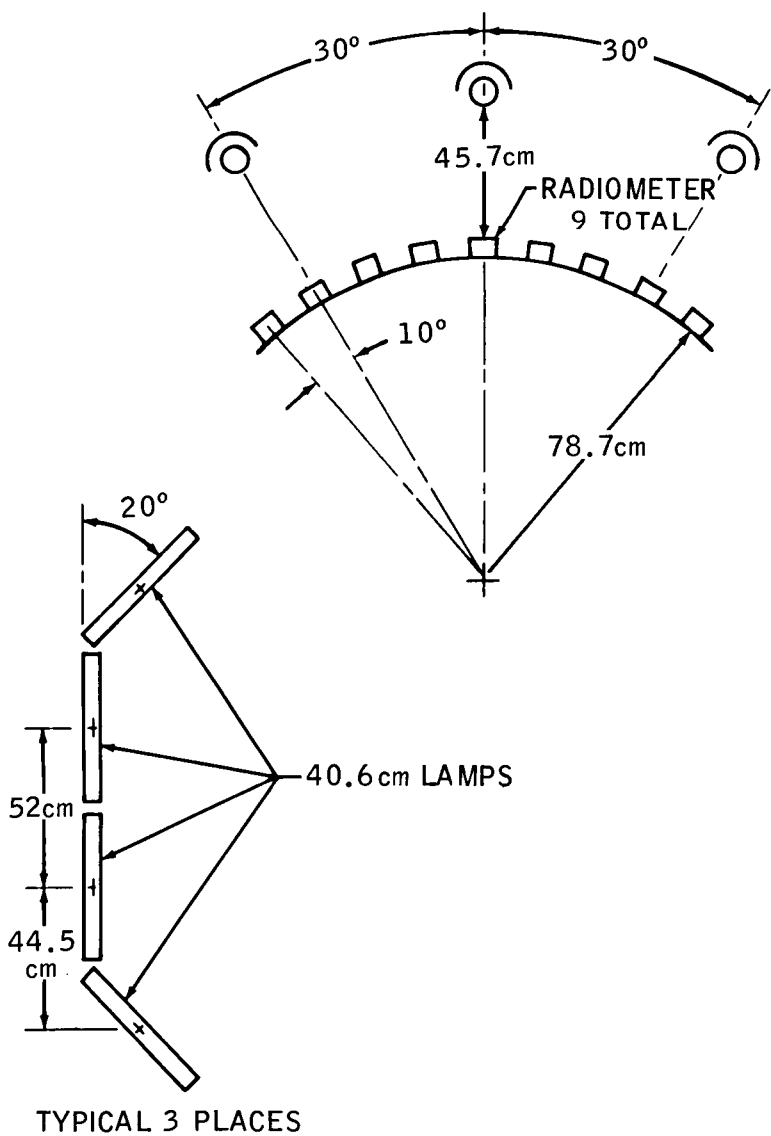


Fig. 8 - Cylindrical surface case 13, chamber D 12 lamp array

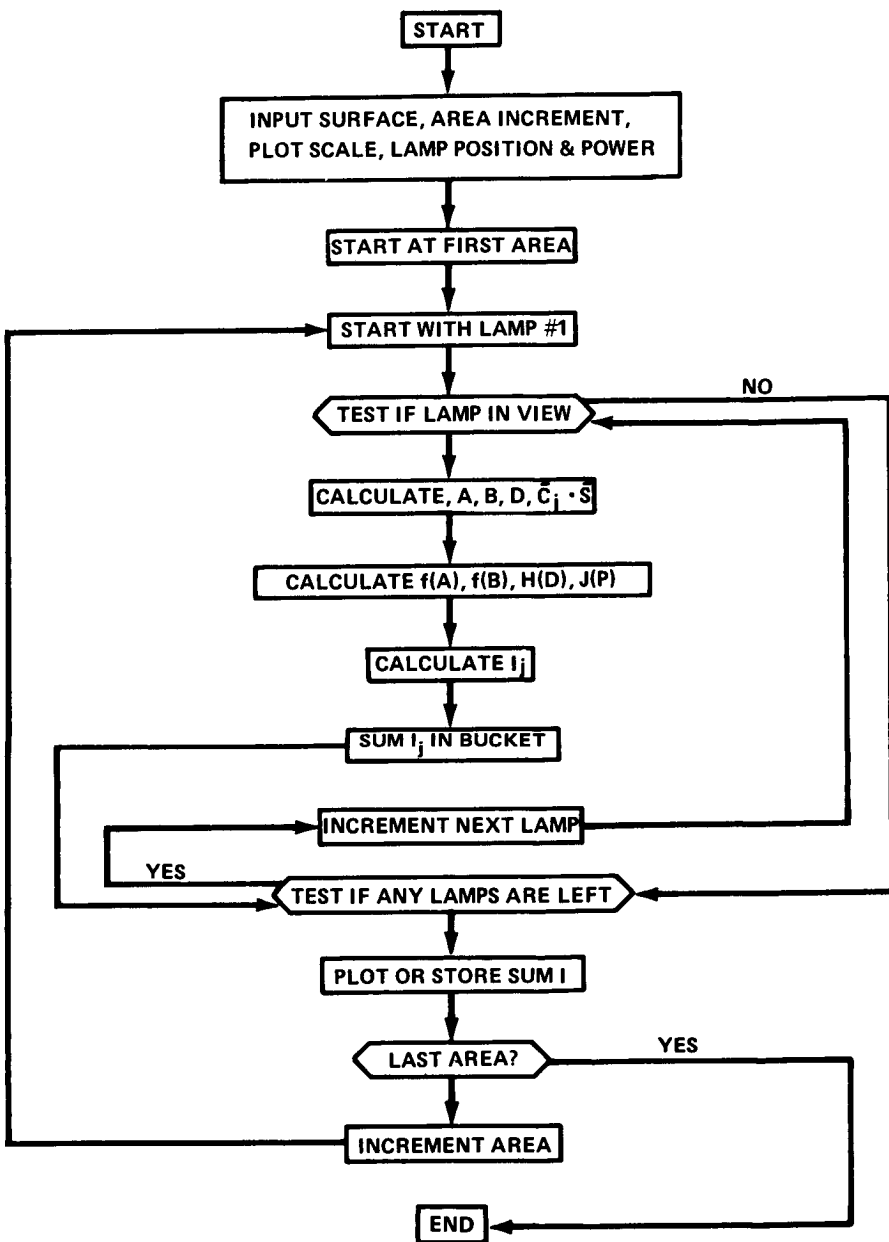


Fig. 9 – Simplified flow chart

SATELLITE THERMAL MODELING USING THE ILLUMINOGRAPHIC CAMERA*

S. J. Wiesner, *Stanford University, Palo Alto, California*, B. Howland and D. M. Nathanson, *Massachusetts Institute of Technology, Lincoln Laboratory, Lexington, Massachusetts*

ABSTRACT

This paper discusses the application of illuminographic camera techniques to the measurement of radiative form factors for satellite modeling applications. The equation for the illuminographic mirror is derived, and the advantages of the method are discussed. Proximity error for the illuminographic mirror is defined, and estimates of this error as a function of the scale factor of the model are given, together with a method for halving this error.

Two designs for new illuminographic mirrors are presented: the first provides a further threefold reduction in proximity error; the second permits the estimation of thermal radiation transfer coefficients to interior regions of otherwise inaccessible volumes. Finally, reflex Polaroid camera techniques appropriate to the relatively small size of the illuminographic mirror are described.

INTRODUCTION

Two differing empirical techniques for assessing the form factors governing radiative heat transfer have been described in the literature.^{1,2,3} The two devices, termed the form factometer and the illuminographic camera, are similar in that both produce an image of the half space, as reflected by an aspheric mirror. They differ in the shapes of the aspheric mirrors and the techniques used to derive form factors by optical imaging. Although both methods lend themselves to the convenience of photographic survey for satellite thermal modeling, there are disadvantages to each method which encourage the development of improved techniques to assist the thermal specialist.

This paper compares the two methods to elucidate advantages and disadvantages of each and describes and improves techniques which make use of the fundamental properties of the illuminographic camera to provide for quick, accurate, and convenient determination of form factors. The mathematical formulation of the

*This work was sponsored by the Department of the Air Force.

illuminographic technique is presented and forms the basis for design improvements using a hyperhemispherical mirror system.

Comparison of Methods

A. Form Factometer--The form factometer method, utilizing an inverted paraboloid of revolution, is illustrated in Fig. 1;

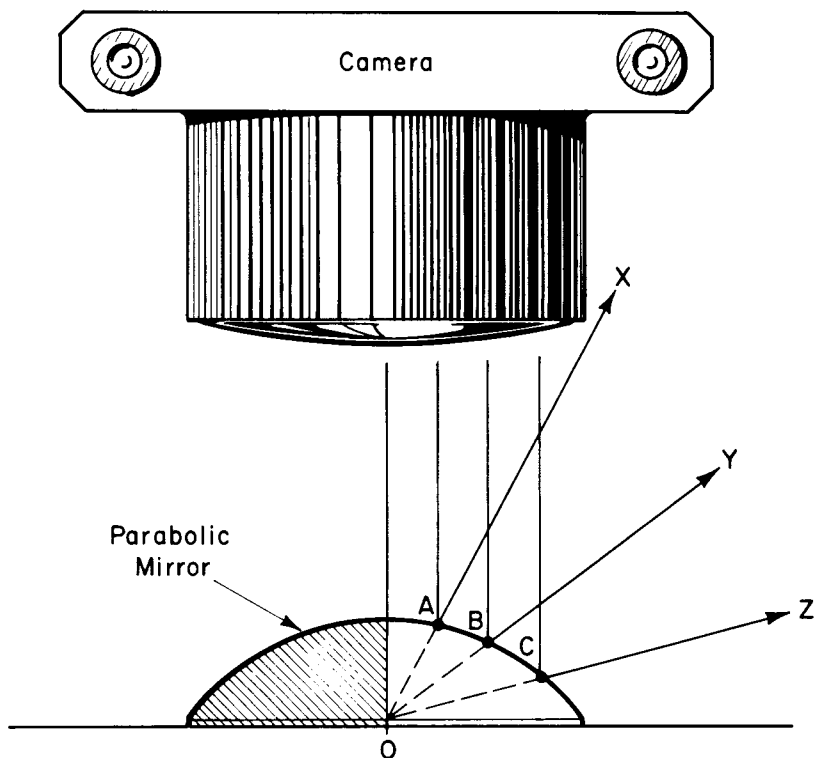


Fig. 1 Illustrating geometry of the form factometer, which utilizes a parabolic mirror. (Distance to camera here greatly foreshortened.)

the distance from the camera to the paraboloid is in practice large, and is here not shown to scale. We note that the well-known geometric property of the paraboloid (that parallel rays are brought to a focus) has been utilized to provide a mathematically precise viewing point, as follows: Rays AX, BY, CZ are the reflections of a pencil of parallel rays assumed to emanate from the camera, intersecting object points X, Y, and Z. If these rays are projected back through the mirror, they must intersect the

optical axis of the mirror at the focus of the paraboloid, 0, which point we have termed the viewing point of the system. This fixed point is that from which the picture reflected by the mirror and photographed by the camera may be said to have been taken. Since point 0 lies on the surface of the model from which the radiation is being modeled, no correction for the distance of the objects to which the radiation transfers will be necessary, i.e., near and far objects which image similarly in the photograph will have equal radiative form factors.

This important geometrical property of the form factometer must be weighed against the disadvantage that a radial nonlinear transformation of the areas mapped in the photograph is necessary in the course of rendering the data into usable radiative transfer coefficients. (Equal areas of the photograph in general do not correspond to equal form factors.) This non-linear radial weighting transformation may be executed in a number of ways, such as the use of a specially designed transparent overlay having non-uniform sized subdivisions which are counted, or more recently, with the use of computer graphics.^{3,4}

B. Illuminographic Camera--The illuminographic camera was designed to solve problems in illumination engineering which are mathematically equivalent to the thermal radiation problem. It utilizes a camera, located at a distance, which photographs a mirror especially shaped so that the areas of the objects as they appear in the photograph will be directly proportional to the corresponding radiative form factors. Thus, simple planimetry of the photograph is all that is required to recover the data. As we shall show, in return for this desideratum, there is a concomitant disadvantage which we have termed the proximity error; objects which are relatively near to the mirror will, in general, produce an image proportionally smaller than their corresponding radiative form factors. It is important to note that the original illuminographic camera was designed to be used for full scale measurements to determine illumination levels in classrooms, drafting rooms, etc. Here it is possible to use a mirror as large as several inches in diameter, and still have the size of the mirror small in comparison to the relevant dimensions of the model space. Thus, in its original application, we can agree with Benford, with respect to the proximity error that "this error is insignificant, and may be ignored".

Proximity errors notwithstanding, we felt that the illuminographic camera could contribute to improved satellite modeling techniques once the mathematical formulation was determined and level of proximity errors defined. We based this judgment not only on the fact that retrieval techniques could be simplified, but that a superior optical image would be produced by the uniform magnification offered by the illuminographic technique.

For our satellite modeling experiments, it was first necessary to decide on an appropriate size for the mirror, and then to determine its equation, as we did not choose to use a graphical method of the sort used for the original illuminographic camera.

For simplicity, we assumed the camera to be located at infinity corresponding to the so-called telecentric view, and we scaled the mirror to a diameter of two inches (5.08 cm), twice the size of the original form factometer.

Illuminographic Mirror

The shape of the illuminographic mirror together with a tracing of some rays through the system is shown in Fig. 2. The

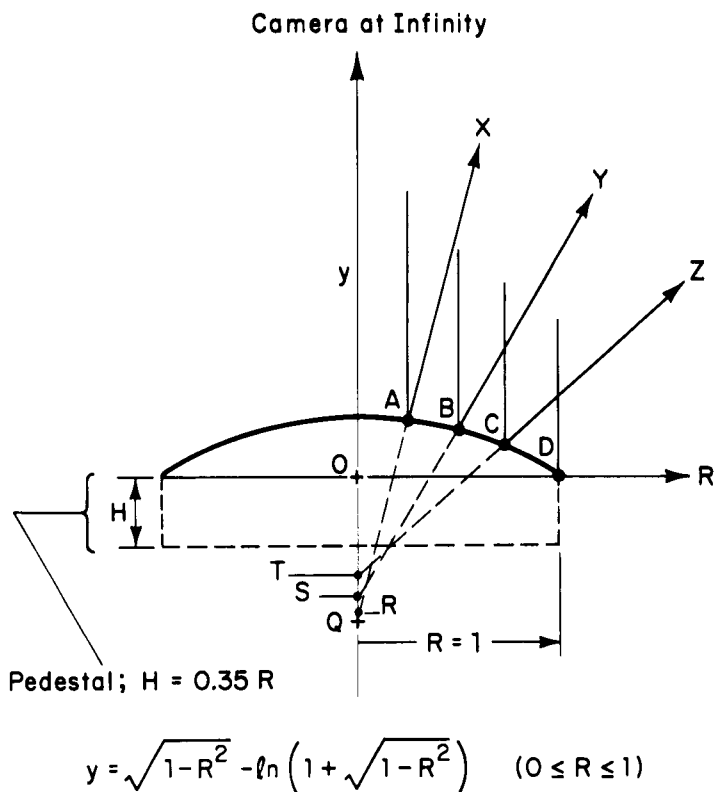


Fig. 2 Cross section of theoretical illuminographic mirror, for camera location at infinity.

intersections of rays ZC, YB, and XA with the optical axis of the mirror are shown as points T, S, and R, respectively. The locations of these intersections determine effective viewing points of the system. Rays reflecting from objects located normal to the mirror will intersect the axis at the focal point, Q.

The equation for the mirror, a surface of revolution, for the case of the camera located at infinity is given by Eq. 1:

$$y = \sqrt{1-R^2} - \ln\left(1 + \sqrt{1-R^2}\right) \quad (0 \leq R \leq 1) \quad (1)$$

where R is the radius and y is the height above the surface. Several models of this mirror surface having radius one inch (2.54 cm.) were made for us from aluminum alloy, machined and hand polished, and were tested with a specially constructed three foot diameter optical protractor to verify their accuracy.⁵ For ease in aligning the camera system normal to the axis of the mirror, a small dot was drilled in the center of each mirror; the reflected image of the lens of the camera is centered accordingly.

In Figs. 3a and 3b we show comparison photographs of essentially the same objects taken with the illuminographic camera and the form factorometer respectively; it is seen that the illuminographic camera provides a considerable magnification of the regions of the angular space near the normal to the plane, and a corresponding demagnification of the objects located elsewhere. Our purpose was to determine the net view factor from the reference surface to truss tubes shown. View factors were analyzed in the case of the illuminographic technique by taking the ratio of area occupied by tube sections as found by tracing on transparent sheets, having Cartesian squares, to the total area of the mirror image. In the case of the form factorometer method a scaled overlay having non-uniform sized subdivisions was used and the total number of subdivisions covering tube areas was counted. View factors compared within 5%.

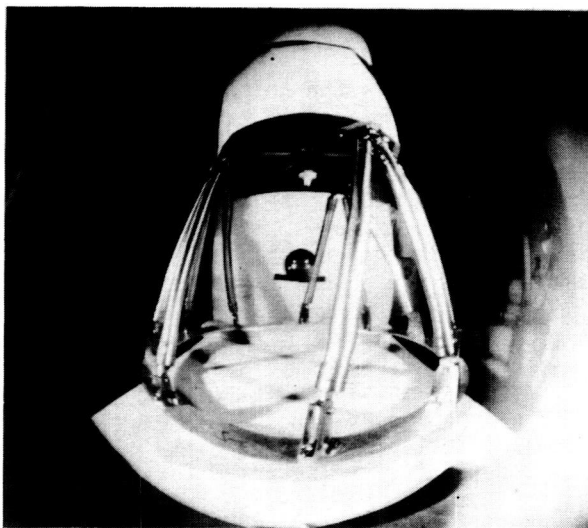
Photographs taken using the illuminographic mirror can also be analyzed with the use of the planimeter, ratios being taken with respect to the area of the mirror, or by counting squares with an overlay of Cartesian squares, scaled such that there are exactly 1000 squares for the radiative half space.

Although the two-inch illuminographic camera mirror has been used satisfactorily for full-scale modeling experiments, an estimate of the proximity error is necessary if the method is used for smaller scale modeling.

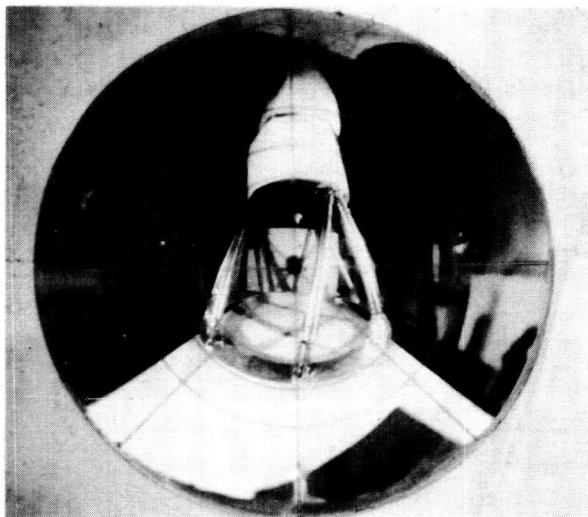
Proximity Error of the Illuminographic Mirror

Referring to Fig. 2, we note that rays reflecting from objects nearly normal to the surface will intersect the axis at the focal point, Q , which is located a distance below the apex of the mirror surface equal to half the radius of the tangent sphere. By differentiating, one determines the radius of the tangent sphere at this point to be two inches. Thus, the location of the viewing point, Q , is one inch below the apex of the mirror, or approximately 0.7 inches below the measurement plane.

A nearby object N , located at distance D above the surface is, in effect, viewed from point Q , and will thus appear to be smaller in angular size by the ratio $(D/D+0.7R)$; the correction to the form factors is given in Eq. 2:



3A



3B

Fig. 3 (A and B) Comparison photographs of satellite truss assembly: Fig. 3A shows the image reflected by the illuminographic mirror; Fig. 3B shows the same scene as reflected by the form factometer.

$$\frac{F_{\text{corr}}}{F_{\text{meas}}} = \left(\frac{D+0.7R}{D} \right)^2 \quad (2)$$

where F_{meas} is the form factor determined from the photograph, F_{corr} is the corrected form factor, and R is the radius of the illuminographic mirror. The percentage error E due to this cause is given by Eqs. 3 and 4.

$$E = 100 (F_{\text{corr}}/F_{\text{meas}} - 1) \quad (3)$$

or, approximately,

$$E = \frac{140R}{D} \text{ for } D \gg R \quad (4)$$

Thus, if we set an upper limit to the proximity error of 2% in the size of any single object in the photograph, the nearest that this object can safely be located to the two inch (5.08 cm) diameter mirror is 70 inches (178 cm), if no correction for this effect is to be made. We note that the sign of the error is always the same, thus some error balancing is possible. Raising our mirror on a pedestal of height equal to 0.35 inches (0.9 cm), would thus reduce the maximum error by half.

It is apparent that, if extensive corrections to the form factors determined by planimetry of the photographs must be made, much of the original advantage of the illuminographic camera method will be lost. Therefore, we conclude that in its original form the illuminographic camera method is best suited for measurements on models for which the relevant distances of the objects are large compared to the size of the mirror.

Photographic Techniques Used For These Experiments

The illuminographic camera finds its greatest utility when used in conjunction with Polaroid photography. In Fig. 4 we show a camera system which we have used to photograph either the form factometer, or the illuminographic mirror. This camera utilizes a Nikon-F 35 mm reflex camera body, with a 200 mm f/4 telephoto lens, together with one or two lens-extender units.⁶ Attached to the body of the camera is a Speed Magny unit, which provides an additional image amplification, and allows the use of Polaroid film in either of two formats.⁷ Attached to the front of the sliding sunshade of the telephoto lens is a series-7 female screw-thread adapter, into which an achromatic closeup lens, having diameter of two inches (5.08 cm) and a choice of four possible focal lengths is screwed.⁸ Also shown is a waist-level magnifier, to facilitate viewing of either a Type E ground glass with ruled

markings for centering, or a similarly ruled fibre optic viewing screen, for improved resolution and focusing.^{9,*}



Fig. 4 Showing the combination of the Nikon-F camera with waist-level magnifier, Speed Magny Polaroid unit, 2X lens extender, and closeup lens mounted to sliding sunshade, which can be used to photograph either of the two mirrors.

In Table I we list the total magnification which this system provides with the Speed Magny 100 unit (8 cm \times 11 cm format), i.e., image size: object size for various combinations of closeup lens and camera configuration.

The predominating features of this camera assembly are its very large effective focal length, together with ease of focusing and framing. The focusing of the camera is effected in a somewhat unusual manner, to preserve constancy of image size as follows: The camera lens is set to infinity, and the sliding

* The fibre-optic viewing screen is an experimental development in which we have substituted a thin sheet of optically polished fibre-optic faceplate material for the ground glass surface. The new screen gives considerably enhanced resolution at the small camera-aperture settings (large f-numbers) that we constrained to use.

Table I
Image Magnification Table for Speed
Magny 100 ($3\frac{1}{2}" \times 4\frac{1}{2}"$ Format)

Lens Combination	Focal Length of Closeup Lens				
	15"	20"	24.5"	30"	40"
	38.1 cm	50.8 cm	62.23 cm	76.2 cm	101.6 cm
200 mm lens	1.68 ⁺	1.26 ⁺	1.03	0.84	0.63
200 mm lens plus one 2X-telextender	3.36 [*]	2.52 [*]	2.06	1.68 ⁺	1.26 ⁺
200 mm lens plus two 2X-telextender	6.72	5.04	4.12	3.36 [*]	2.52 [*]

Notes: ^{*} Combinations recommended for photographing one-inch diameter form factor.

⁺ Combinations recommended for photographing two-inch diameter illuminographic mirror.

sunshade, to which the closeup lens is attached, is set at the midpoint of its approximate two inch range of linear travel. The camera, mounted on a tripod, is then positioned vis-a-vis the mirror so that centering with respect to the mark on the mirror, and approximate focus, are attained. The final focal adjustment is made by sliding the sunshade (and closeup lens) towards or away from the mirror until exact focus is obtained. This method, which utilizes the principal of the optical collimator, guarantees that the size of the image is invariant with respect to focal setting, thus a single set of transparent overlays will suffice for data reduction. Measurements of the Polaroid photographs taken with this system indicate a pincushion distortion of several percent. This distortion is principally due to the use of the Speed Magny unit.

Design for Improved Illuminographic Mirror

In Fig. 5 we show a new design for an illuminographic mirror which exhibits one third the proximity error of the original illuminographic mirror. Also shown in the figure are the backwards projection of a number of rays, AX, BY, and CZ, and their intersections with the optical axis; the limiting viewing point, Q, lies a distance of 0.22R below the surface.

This design utilizes a second-surface, aspheric mirror, having a hyperhemispheric front lens, fashioned from a high index, low dispersion glass, for example LaSF-1, having a refractive index of 1.803 and a reciprocal dispersion of 46.8.¹⁰

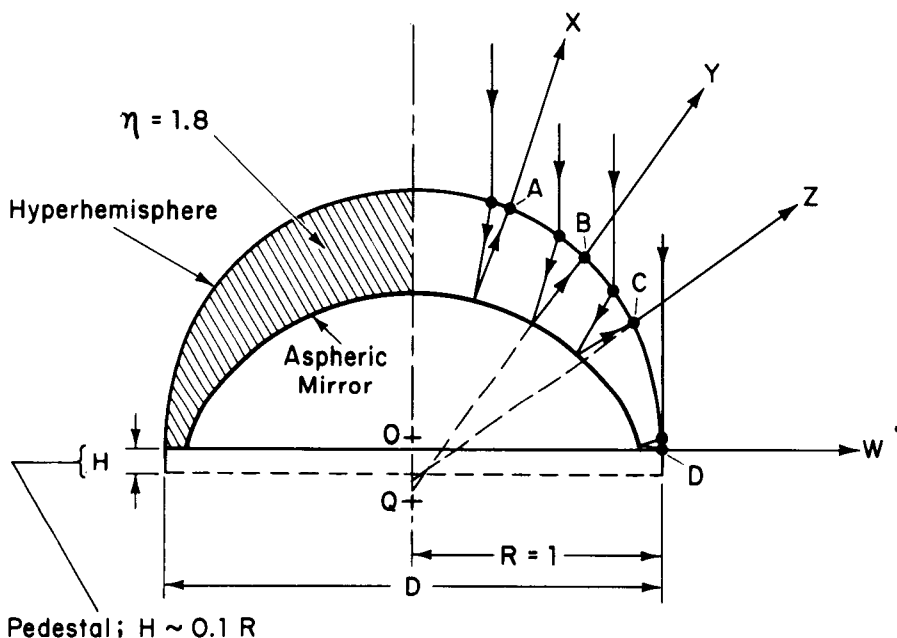


Fig. 5 Cross section of hyperhemispheric, second-surface aspheric illuminographic mirror, which exhibits a threefold reduction in proximity error.

Calculation of the Equation of the Aspheric Surface

The design of the aspheric surface was obtained with the aid of a PDP-8 computer as follows: A polar coordinate system was chosen to be concentric with the outer, hyperhemispherical surface, for which $\rho = 1$. The aspheric inner surface, a surface of revolution, was represented by ten terms in a Fourier series approximation, Eq. 5.

$$\rho = \sum_{n=0}^9 K_n \cdot \cos(n\theta) \quad (5)$$

where ρ is the radius and θ is the angle measured from the normal to the surface. Result from a preliminary graphical analysis were used to set the first coefficient, $K_0 = 0.9$, (this number sets the thickness of the lens at the base, where it contacts the surface under measurement) and also to set $K_1 = -0.3$.

The computer was programmed to trace thru the system ten rays, assumed parallel, emanating from the camera, equally spaced in the numerical aperture of the mirror, and to compute the mean squared error in the departure of their exit angles from the

theoretical value for an illuminographic mirror, as required by the double projection algorithm of Benford.¹ Coefficients $K_1 - K_9$ were initially set to zero, and were then iteratively adjusted until further significant reduction in the mean square error was marginal. Finally, the location of the center of the hyperhemisphere was determined by tracing the extreme ray for $R = 1$ through the system.

In Table II we give the coefficients describing this aspheric surface approximation, which has a residual mean squared error

Table II
Parameters of New Illuminographic Mirror

- A. Refractive Index: $\eta = 1.8$
 B. Outer Surface: $\rho = 1$
 C. Inner Surface: $\rho = \sum_0^9 K_n \cos(n\theta)$

where:

$K_0 = 0.9$	$K_5 = -0.00031$
$K_1 = -0.3171$	$K_6 = -0.00037$
$K_2 = 0.0002$	$K_7 = -0.00005$
$K_3 = 0.0045$	$K_8 = 0.000115$
$K_4 = 0.0023$	$K_9 = 0.000020$

in the exit ray angles of 2.5 milliradian. With this design, configured to a one-inch (2.54 cm) radius, the maximum displacement of the viewing point is 0.22 inches (0.56 cm) from the surface, corresponding to a proximity error of one third that of the original illuminographic mirror. With a pedestal of height 0.11 inch (0.28 cm), this error can again be halved. Thus, with a mirror of two inches diameter mounted on a pedestal, and an error limit of 2% for the form factor of any object, correction is unnecessary for objects which are no closer than 12" (30 cm) to the mirror; with a one inch (2.54 cm) diameter mirror (the same size as the original form factometer), the objects may be as close as six inches (15 cm) from the mirror.

The chromatic errors which are introduced by refractions at the lens surface in front of the mirror have been estimated by ray tracing with a slightly differing index of refraction; the effect is evidently not serious, but for highest precision results the photograph should be taken through an orange filter. If color

coding is used to identify the reflected images of the objects in the model, a second exposure without the filter may be necessary.

Possible Variations in the Design

It is interesting to note that the radius of the inner aspheric surface differs from a sphere by only 1.5%. Thus, two further possible constructions are suggested: (a) The aspheric surface may be put instead on the outside, and the inner surface could be made spherical, with little likely qualitative change in configuration or performance. The advantage to be gained from this recomputation of the design would be a one-third reduction in fabrication cost. (b) Both inner and outer surfaces could be made aspheric, with the aim of further reduction and probable elimination of the proximity error. However, both the difficulties of computation and the cost of fabrication would be considerable.

New Mirror Configuration for Looking into the Satellite

In Fig. 6 we show a new design for an inverted illuminographic mirror which permits one to determine the radiative transfer to an enclosed volume by means of a hole drilled into the surface of the model. This design could be useful when the internal physical configuration of the model is such that it is impossible to place the camera opposite the surface under measurement.

Conclusions

The use of the illuminographic camera to derive form factors for satellite thermal modeling has been described and compared to techniques using parabolic mirror systems. The illuminographic technique permits quick and convenient determination of form factors by simple planimetry since the mirror is shaped so that areas of objects are directly proportional to the corresponding radiative form factor; the total area of the mirror image having a form factor of one. Photographic techniques which make use of the conveniences of Polaroid photography have been described.

The equation for the illuminographic mirror has been derived and proximity errors were defined. For the 2 inch (5.08 cm) diameter illuminographic mirror machined for our experiments, it was shown that in order that the proximity errors for a particular object be limited to 2%, the mirror should be located no closer than 70 inches (178 cm) to the object. Raising the mirror on a pedestal of 0.35 inches (0.9 cm) reduces the proximity error by half, thus allowing the distance between mirror and object to be 35 inches (90 cm) for allowable 2% error. We therefore conclude that, in its original form, the illuminographic camera is limited to models for which the relevant distances to the objects are large as compared to the scale of the mirror.

Improvements to the illuminographic technique which reduce proximity errors to 1/3 that of the original illuminographic mirror can be achieved by producing a mirror design having a second

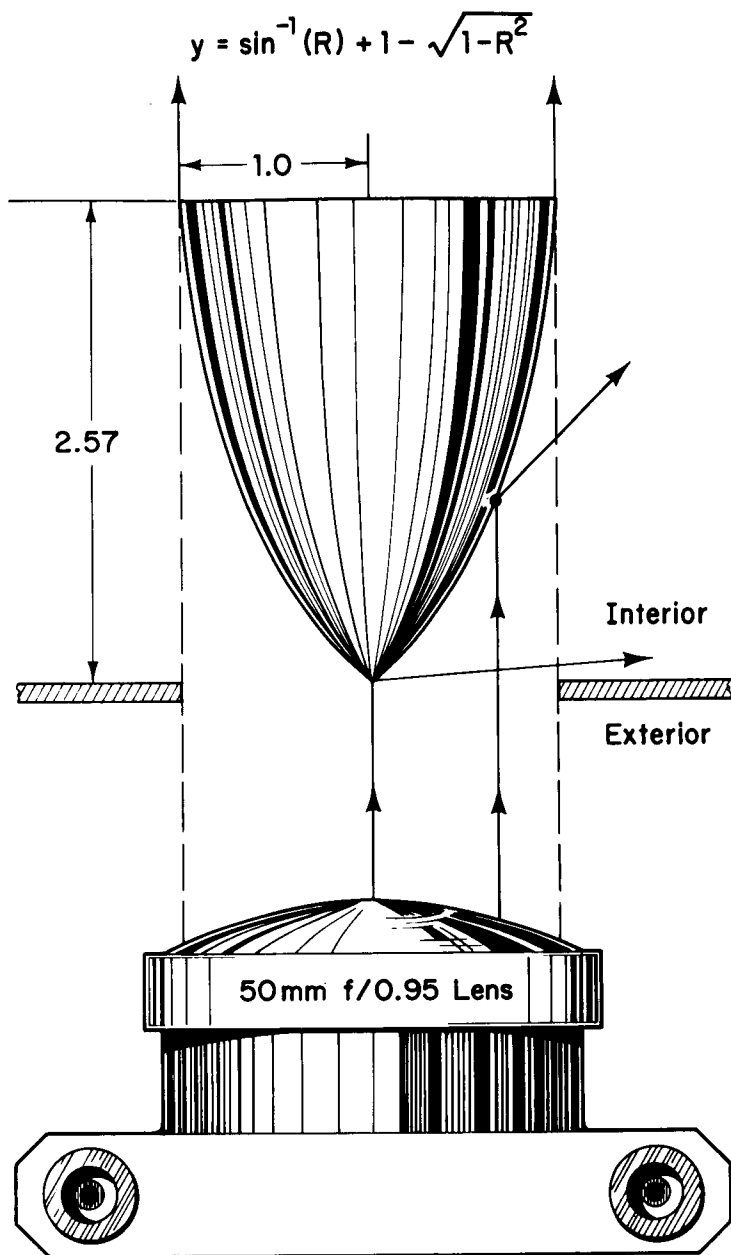


Fig. 6 Novel form of inverted illuminographic mirror for determining the radiative transfer coefficients to interior of an enclosed volume. (Distance to camera here greatly foreshortened.)

surface aspheric mirror and hyperhemispheric front lens made from a high refractive index, low dispersion glass. A 2-inch (5.08 cm) diameter mirror having this design can be used up to 12 inches (30 cm) from the object with no more than 2% proximity error when used with a pedestal. Alternatively, a 1-inch (2.54 cm) diameter hyperhemispheric second-surface mirror can be used at distances as close as 6 inches (15 cm).

Finally, techniques have been described which allow determination of view factors within enclosed volumes through the use of an inverted illuminographic mirror. It is felt that the development of these techniques can provide a unique set of instruments to assist the thermal specialist in deriving form factors for satellite thermal modeling.

Acknowledgement

We wish to thank the support from the technicians and computer programmers at Lincoln Laboratory who have greatly assisted us with these measurements and with the reduction of the data. We thank Mr. Frank Cooke, Optician, for his helpful discussions regarding design improvements which would facilitate manufacture and reduce cost of fabrication. We also thank Prof. Howard C. Howland, of the Cornell University Section of Neurobiology and Behavior, for suggesting the method for the determination of the aspheric surface, using orthogonal polynomials, and for writing and debugging the program.

References

1. F. Benford, "An Illuminographic Camera", J. Optical Soc. Am., 33, No. 8, p. 440.
2. R. S. Hickman, "The Measurement of Radiation Configuration Factors with Parabolic Mirrors", Jet Propulsion Laboratory Report (1961).
3. Instruction Manual for the Form Factometer, Rev. A, 1962, Thermospace Corporation, Altedena, CA.
4. T. Ishimoto and J. A. Moses, "Optical Shape Factor Data Processing Through Computer Graphics", AIAA Progress in Astronautics and Aeronautics: Thermal Design Principles of Spacecraft and Entry Bodies, J. T. Bevens, ed., Vol. 21, Academic Press, N. Y., 1969, pp 31-34.
5. Tech Ridge Inc., Chelmsford, MA. 01824.
6. Vivitar 2X Extender, distributed by Ponder and Best Inc., Santa Monica, CA. 90406.
7. Ehrenreich Photo Optical Industries, Garden City, N. Y. 11530.
8. Available from A. Jaegers, Lynbrook, L. I., N. Y., 11563.

9. Fibre-optic faceplate material available from Fibre Optics Division, American Optical Co., Southbridge, MA. 01550.
10. Schott Glass Works, distributed by the Fish-Sherman Co., New Rochelle, N. Y.

THE USE OF SOLAR SIMULATION SYSTEMS FOR PRODUCING ARTIFICIAL GLOBAL RADIATION FOR THE PURPOSE OF DETERMINING THE HEAT LOAD OF ROOMS

A. C. Kalt, *DFVLR - Space Simulation Institute, 5 Cologne 90, F.R. Germany*

ABSTRACT

Certain climatic tests which require solar and sky radiation can be carried out in the laboratory by using simulated global radiation. The advantages of such a method of measurement and the possibilities and limitations resulting from the simulation of global radiation are described.

Experiments concerning the thermal load in rooms have been carried out in order to test the procedure. In particular, the heat gain through a window with sunshade was discussed, a venetian blind between the panes of a double-glazed window being used in most cases.

1. The problem: The investigation of air conditioning data by laboratory experiments.

1.1 Previous procedures for the determination of certain air conditioning data, like transmission factors, storage factors, etc.

For the heat flow Q_A entering a room of a building from outside we may write:

$$(1) \quad Q_A = Q_{WA} + Q_T + Q_S \quad W$$

The instantaneous radiant heat flow through windows Q_S is primarily dependent on the total radiation.

$$(2) \quad Q_S = (FF \cdot I \cdot a + FA \cdot IDIFF) \cdot b \quad W$$

In this equation we have:

FF = window area on which solar radiation falls

FA = window area in the shade

I = total radiation through a window which has single glazing

IDIFF = diffuse radiation onto window area on which sunlight does not fall since it is shaded by projections in the buildings or by neighboring

- buildings
 b = transmission factor of the window including
 sunshade, related to a single-glazed window
 a = correction factor

According to the relation

$$(3) \quad QKA = QWA + QT + (FF \cdot I_{\max} \cdot a + FA \cdot IDIFF_{\max}) \cdot b \cdot S \cdot W$$

the actual instantaneous external cooling load QKA is still dependent on the storage factor S, which takes into consideration the storage part of the energy penetrating through the window with respect to time and quantity.

A number of measurements have been carried out in the past to determine the transmission factor b and the storage factor S. Since both factors are dependent on a large number of parameters, results have only been determined for certain conventional combinations of these parameters.

All investigations of this nature were carried out using natural solar and sky radiation. When natural solar and sky radiation are used difficulties are encountered in investigations of the type mentioned, since the desired radiation conditions are hardly ever available in reality. The investigator has to accept the conditions on the location and at the time of measurement. The intensity of radiation is given, not variable and not constant.

Furthermore it is very difficult - if at all possible - to take into consideration certain local conditions which influence the radiation impinging on the window (e.g. reflection of solar radiation from neighboring buildings). On the other hand, such conditions may interfere with measurements in a particular location.

However, the main disadvantage when natural radiation is employed is that the experimental conditions are not reproducible.

1.2 Possible future procedure

Thanks to the rapid development of analogue and digital computers, the largely analytical treatment of air-conditioning problems will become more widespread. Mathematical processes of this nature require, however, initial or characteristic data determined initially by measurement. And to obtain these data experiments are necessary.

Experimental investigation is also logical and conventional for checking results obtained by analysis.

In order to eliminate difficulties encountered when natural solar and sky radiation are used, it is proposed that experimental investigations of this type be carried out in the laboratory using artificially produced global radiation.

This requires a source of radiation which permits simulation of solar and sky radiation on an adequately large area. Solar simulation equipment such as has been built for space projects is suitable for this purpose.

Equipment of this type permits the reproducible setting of all radiation intensities required for air-conditioning investigations and can be used throughout the year.

1.3 Proof of the practicability and practicality of such investigations in the laboratory

Taking as an example investigations into the heat load of rooms as a consequence of radiation through windows the practicability of such experiments in the laboratory using artificially produced global radiation should be proved.

The measurements are further intended to show that because of the good reproducibility of the experimental conditions permitted by the proposed method of investigation, it is possible to vary single parameters involved in the problem. For instance, by varying the colour of the venetian blind, the influence of this on heat gain through the window could be determined.

If this procedure is used to determine the thermal response of experimental rooms, then for example, by varying the furnishings in the room the change in the heat storage in the walls can be investigated, all other experimental conditions particularly the heat gain through the window, being unchanged.

2. Possibilities and limitations for carrying out investigations of this nature in the laboratory

2.1 Characteristics of solar simulation equipment

Of the range of solar simulation equipment available, only large equipment can be entertained for the investigations projected; the equipment must be able to irradiate at least an area having a side length of about 1 m. The equipment used is designed for irradiating a vertical surface and was therefore particular-

ly suitable for the investigations carried out. A detailed description is given [1].

Irradiated area:	circular, 1.4 m diameter
Radiation intensity range:	$60 \text{ W/m}^2 - 1000 \text{ W/m}^2$
Maximum variation of the radiation intensity over the irradiated surface:	$\pm 5 \%$
Constancy:	$\pm 1 \%$
Operating life with one set of lamps:	250 h
Semi angle of divergency:	9°

Table 1 - Characteristic of the solar simulation equipment used

2.2 Simulation of global radiation

In addition to the direct solar radiation entering the room through a window, the diffuse radiation from the sky also makes a contribution to the heat gain. The sum of these two components, referred to a horizontal surface, is termed global radiation.

The short-wave radiation from outside on a window consists of global radiation directly impinging on the vertical surface and part of the global radiation which is reflected from the ground or objects in the vicinity. The sum of these two components is termed total radiation.

Solar simulation equipment normally produces directed radiation. Since the major proportion of the total radiation is direct solar radiation, in other words directed radiation, it was decided only to simulate directed radiation. During times of day when the diffuse radiation from the sky predominates, in order to better simulate this, it was decided not to simulate the actual sun/wall azimuth angle, but to irradiate the window with an azimuth angle of 0° . To take into consideration the dependence of the diffuse radiation on the angle of elevation of the sun, the actual angle of elevation of the sun was also set for these periods.

The spectral distribution of global radiation depends on a number of factors, but as a first approximation it may be considered as being independent on the angle of elevation of the sun, therefore it can be considered as constant.

Fig. 1 compares the mean values for global radiation according to Schulze [2] and Albrecht [3] with the radiation produced by the solar simulation equipment. Since the difference appeared to be acceptable, further attempts at exact matching were not made for the purpose of the experiments. However, such matching is quite possible by using further selective filters.

2.3 Positioning of the experimental object with respect to the setting of angle of elevation of the sun and azimuth angle

The location of the sun relative to the outer wall of a building or to a window can be described by the angle of incidence of the radiation. The angle of incidence depends on the angle of elevation and the azimuth angle, which change between sunrise and sunset. Since the position of the solar simulation equipment cannot be changed, the experimental object has to be moved relative to the solar simulation equipment. To simulate the irradiation conditions in Germany (latitude 50° north, provision must be made to vary the angle of elevation of the sun between 3° and 63° and the wall azimuth angle by $\pm 90^{\circ}$.

A positioning device was therefore built to vary the attitude of the experimental object. The device built is shown in Fig. 2.

It is designed for experimental objects with a surface area of up to $2\text{ m} \times 2\text{ m}$ and weighing up to 2.500 kp . The angles are set manually. Because of the inherent inertia in thermal processes it did not appear necessary to provide a device for continuous adjustment.

The positioning device is designed so that the angular movement takes place about the centre point of the irradiated surface of the experimental object. This reduces the errors arising due to the divergence of the radiation of the solar simulation equipment used.

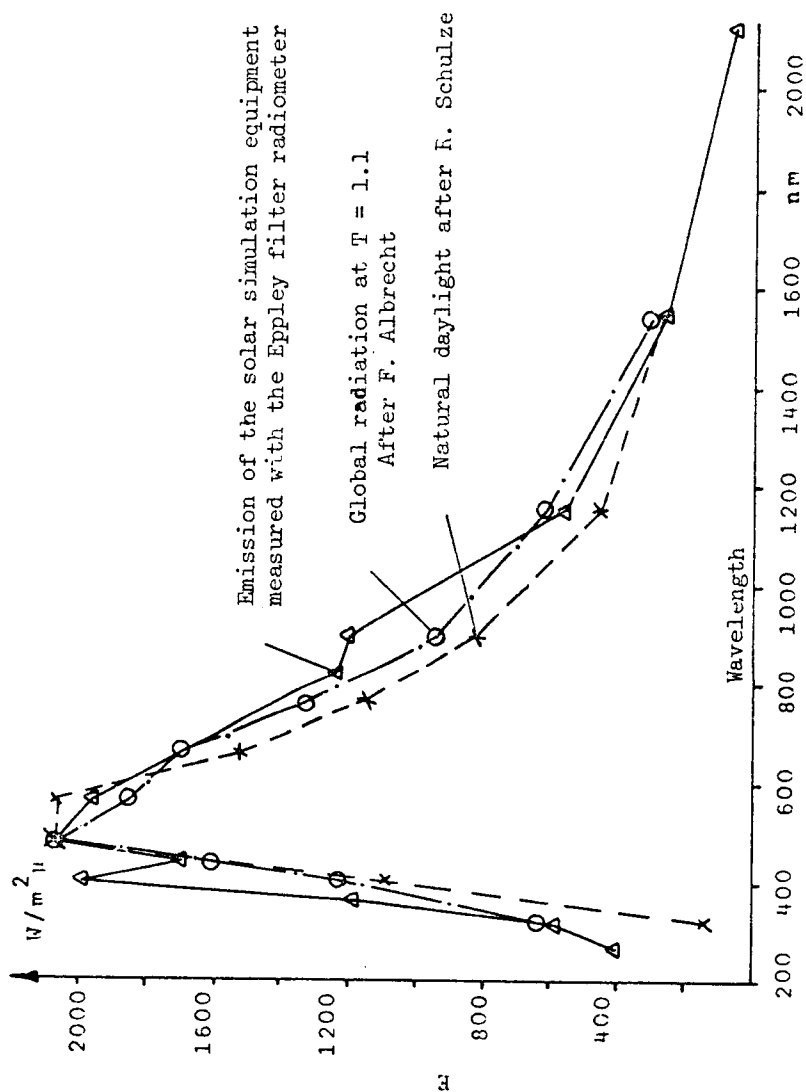


Fig. 1: Spectral emission of the solar simulation equipment compared with the global radiation.

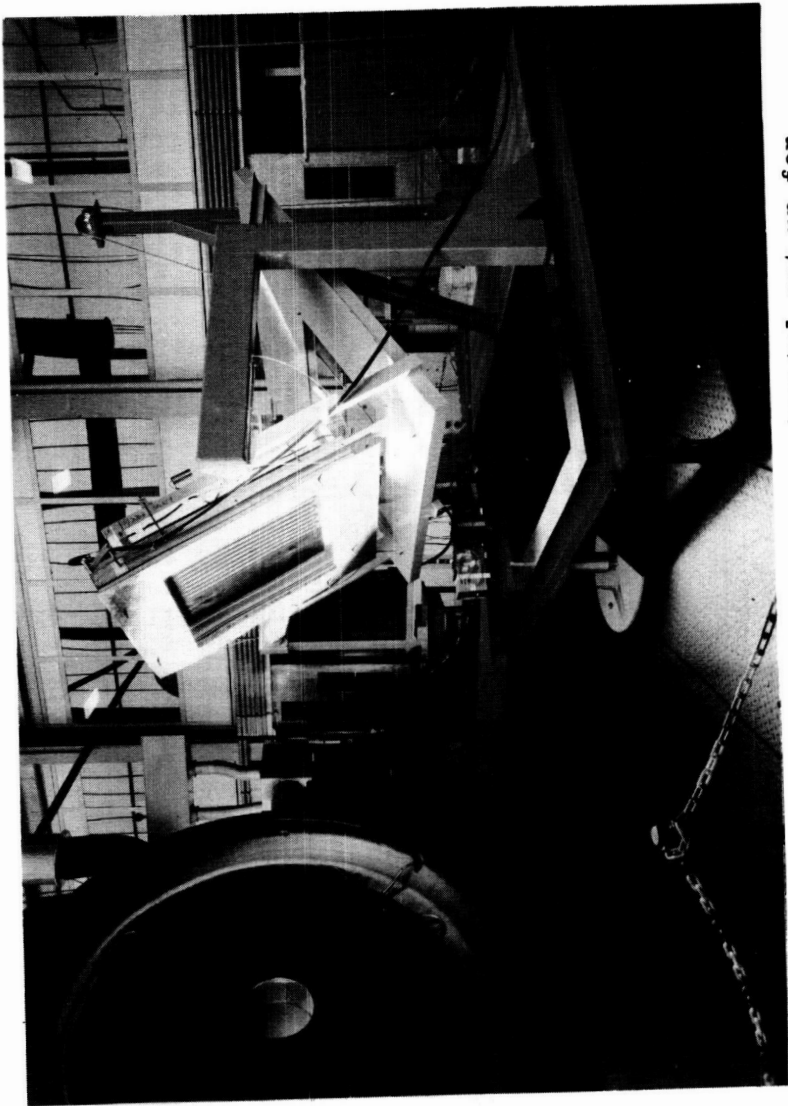


Fig. 2 - Positioning device with experimental set-up for determining the heat gain through a window incorporating a sunshade

2.4 Factors limiting the size of the experimental object

The maximum size of the window of the experimental object is given by the area that can be irradiated. A square window having sides of 1 m can be irradiated with the solar simulation equipment employed here. It will only be possible to apply the experimental results to real conditions if certain size factors are transferable. The use of standard sunshade devices, e.g. a venetian blind, presupposes that the number and width of the slats do not vary too much from standard conventional data.

2.5 Deviations from natural conditions due to simulation of global radiation by means of solar simulation equipment

Solar simulation equipment cannot completely simulate natural global radiation. In particular, deviations occur in the following characteristics of the radiation:

Spectrum;

Uniformity of the intensity of radiation on the irradiated area;

Directional dependence of the impinging radiation.

The errors to be expected as a result of these factors and possible measures to reduce their effects are now discussed.

Major differences in the spectrum of the radiation produced as compared with the natural global radiation would cause marked errors. The reason is the dependence of the degree of reflection, degree of absorption and the degree of transmission of the different wavelength.

The spectral matching of the radiation from solar simulation equipment is carried out according to the spectral distribution of extra-terrestrial solar radiation. This essentially differs from the global radiation by the fact that more powerful radiation is present in the range from 250 nm up to 400 nm. Since ordinary window glass does not start to transmit until 300 nm is reached and rises up to 400 nm, a window pane is additionally heated by absorption of radiation in this range. The result is an increased heat gain in an experimental room due to an increased heat flow from the inner pane into the room. This can be avoided by additionally filtering the global radiation produced by using a filter of window glass.

Local variations of the intensity cannot be avoided on an area irradiated by solar simulation equip-

ment. However, these variations may be kept relatively small and hardly exceed a value of $\pm 5\%$ related to the mean radiation intensity. The mean flux impinging on the surface can, however, be approximated to a large extent to the set value if the radiation intensity is measured at a sufficiently large number of positions on the surface, and the mean value used in calibration.

With solar simulation equipment it is not possible to simultaneously produce directed and diffuse radiation. However, the normally produced directed radiation can be used if in case of prevailing diffuse radiation a corresponding positioning of the experimental object is chosen.

Because of the large distance of the sun from earth, the direct solar radiation may be regarded as a parallel beam. The solar simulation equipment employed by the author produced a beam with a semi-angle of about 9° . In contrast to natural solar radiation, this results in different radiation intensities on parallel surfaces at different distances from the solar simulation equipment. In addition, surfaces may receive radiation which would not be received from natural solar radiation and vice versa. In order to eliminate or keep as small as possible errors due to this source, the following aspects must be borne in mind.

The axes of the rotary motion for setting the angle of elevation of the sun and the azimuth angle must intersect at the centre of the surface of the experimental object to be irradiated. For the equipment used here we then have a maximum deviation of 0.7% for the mean radiation intensity.

Further deviations from the natural conditions also result when a venetian blind is used as a sunshade. Because of the smaller inclination to the horizontal of the rays striking the upper part of the window, more radiation can penetrate between the slats than can penetrate between the slats lower down. Marked differences result above all when the blind is fully opened. However, to a first approximation the total proportion of the radiation penetrating between the slats in the experimental layout described here corresponds to the total for parallel radiation despite divergent radiation.

3.6 Measurements carried out for determining the heat gain through a window

Two kinds of measurement were carried out.

The first type of measurement was taken for given times of day and settings of venetian blind, when the combination of window and calorimeter had reached the steady state.

In the second type of measurement the hours of global radiation between 7.00 and 17.00 hours were simulated by suitably continuously changing the angle of elevation of the sun, the azimuth angle and the radiation intensity.

4.1.1 Influence of the colour of the blind as an example for possible measurements

As an example for the different measurements carried out the influence of the colour of the blind will be presented. If the absorption of the total radiation by the blind is high, for example when dark coloured blinds are employed, particularly unfavorable conditions result.

For a medium-blue blind, the temperature of the blind rises to as much as 94°C . On the average it is 17° higher than for the white blind. Accordingly, the pane temperatures are also higher. As Fig. 3 shows, the heat gain through the window using the medium-blue blind between the panes is greater for all slat positions than when the white blind is used. On the other hand, the quantity of light entering the room is much smaller even when the blue blind is fully opened.

3.2 Reproducibility of the measurements

One of the main advantages of the method of measurement employed here is intended to be the good reproducibility of measured results.

In order to check the degree of reproducibility similar measurements were carried out on two different days. Only very small differences were observed, the reason of which lying in instabilities of the blind fastening.

4. Comparison of the author's results obtained with simulated global radiation with those of other authors

Table 2 compares these results with those obtained by other authors. In the case of the venetian blind arranged between two panes of glass, the author's measured data are between those of the ASHRAE and the CSTB and those given in the VDI Guidelines. In the case of the venetian blind arranged outside a single

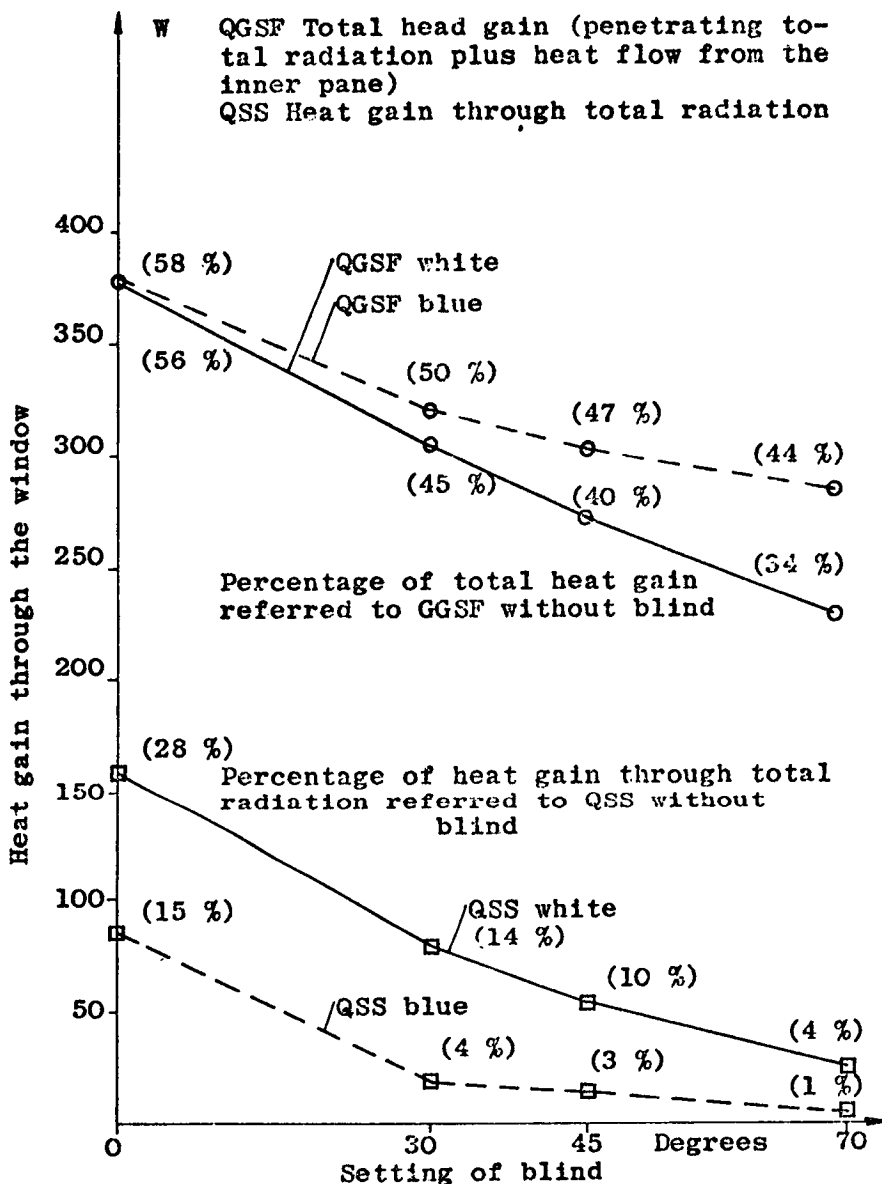


Fig. 3 - Influence of colour of venetian blind on heat gain. Blind between double-glazing.
Date: September 22, Time 11.00/SOH 39°/AZIM 19°
Facing south, 50° latitude north.

Location of blind	Between double-glazing				Outside single pane		
	open	half-closed	closed		open	half-closed	closed
Setting of blind	0°	45°	70°		0°	45°	70°
Measurements by <u>Caemmerer</u> [4], metal blind	74 %		46 %		45 %	14 %	10 %
Measurements by the Centre Scientifique et Technique du Batiment (CSTB), metal blind [5]		37 %	31 %			15 %	10 %
Measurements by the American Society of Heating, Refrigerating and Air-conditioning Engineers (ASHRAE) [5]		37 %				15 %	
Author's measurement, white blind, 12.00, Angle of elevation of sun 40°, sun/wall azimuth 0°	59 %	40 %	34 %		40 %	21 %	15 %
Author's own measurement, blue blind, 11.00, Angle of elevation of sun 39°, sun/wall azimuth 19°	58 %	47 %	44 %				
VDI Guidelines 2078 [6]		50 %				15 %	

Table 2: Reduction of the total heat gain for a window by using a blind as sunshade (author's measurements and the measurements of other authors).

pane, the author's own measurements show a higher heat gain. The causes are probably found in the different construction of the windows. By fitting the venetian blind in a frame with which the blind was in close contact when lowered, in the author's case ventilation of the space between blind and pane on both sides was made more difficult.

5. Summary

It could be shown that air-conditioning investigations can be carried out when using artificially produced global radiation.

The results of the measurements show adequate agreement with the results of other workers who undertook their investigations with natural global radiation. The differences observed are apparently attributable to a different experimental set-up and not to the use of artificially produced radiation.

The main advantage of the procedure, the reproducibility of the experimental conditions, was proved. Further investigations into the thermal response of an experimental room, e.g. in respect to heat storage in the walls, which have been carried out thereupon using the investigation procedure described, have also indicated its advantages for problems of this character.

A number of investigations which are difficult or impossible to carry out theoretically, or which require reproducible experimental conditions can therefore be carried out in the laboratory.

Examples:

Influence of the colour of the internal walls, the equipment in the room, routing of the air, etc. on heat storage processes and on the cooling load in an experimental room.

Problems in connection with temporary air-conditioning. Checking results obtained theoretically.

The procedure described can therefore be an extension to and an improvement on previous investigation procedures. Since the investigations can be carried out any time, it may also contribute towards more rapid treatment of any problem on hand.

6. References

- [1] Kalt, A. Die Planung des Sonnensimulationsgerätes für die große Weltraumsimulationsanlage der DVL.
(Designing the solar simulation equipment for the large space simulation plant of DVL)
DLR-Mitteilung 66-15 (1966)
- [2] Schulze, R. Zur Spektralverteilung natürlicher Beleuchtung
(On the spectral distribution of natural illumination).
Lichttechnik 2 (1950), pp. 155 and 159.
- [3] Albrecht, F. Intensität und Spektralverteilung der Globalstrahlung bei klarem Himmel
(Intensity and spectral distribution of global radiation with clear skies)
Arch.Met.Geoph.Bickl.Vol. III.
- [4] Caemmerer, W. Beitrag zum Problem des Sonnenschutzes von Fenstern.
(A contribution to the problem of the sun-screening of windows)
Gesundheitsingenieur 83 (1962), pp. 349-357.
- [5] Caemmerer, W. Testing of sunbreaks in Germany, Sunlight in Buildings
Rotterdam: Bouwcentrum International (1967), p. 211 and 216.
- [6] VDI-Richtlinien 2079, Berechnung der Kühllast klimatisierter Räume (1970).
(VDI Guidelines 2078, Determination of the cooling load of air-conditioned rooms (1970)).
- [7] Kalt, A. Ermittlung der Wärmebelastung von Räumen infolge Sonneneinstrahlung durch Fenster im Laborversuch unter Verwendung künstlich erzeugter Globalstrahlung.
DLR-FB- 73-73 (1973)
Investigation of the thermal load of rooms as a result of solar radiation through windows by laboratory experiments using simulated global radiation.
Technical Translation ESRO TT-92 (1974).

HIGH ENERGY SOLAR BEAM TESTING IN THE JPL 25-FT SPACE SIMULATOR

J. W. Harrell, *Jet Propulsion Laboratory, Pasadena, California*

ABSTRACT

Solar-thermal vacuum tests have been performed on Mariner and Helios class spacecraft at intensities up to eleven solar constants. Many improvements were made to individual components in the solar simulation system to enhance their performance. An increase in lamp power from 20 KW to 30 KW was required. This necessitated improved lamp life and performance. The depressurizable 20/30 KW Hanovia lamp life has been extended to 900 hours plus at 20 KW and 300 hours at 30 KW. Increased life, of course, results in reduced operating costs.

A family of solar beams from eight to 18.5 feet in diameter can be provided at intensities related to beam size with a maximum intensity of 12 solar constants over a 9 ft. diameter. 1.1 megawatts of simulated solar energy is available in the lamp array. Moderate size beams can be operated at 1 solar constant for several thousand hours.

Helios, a spin stabilized solar probe was tested in the 9-ft diameter beam at eleven solar constants in May of 1974.

The vacuum vessel is a right circular cylinder 85 feet high and 27 feet in diameter. It is diffusion pumped to a pressure level of 5×10^{-7} torr. A liquid nitrogen shroud can be temperature controlled from -320°F to $+200^{\circ}\text{F}$.

The unique work which was required to achieve the foregoing performance and cost savings is described in this paper.

INTRODUCTION

The JPL 25-Ft Space Simulator has been in operation for solar-thermal vacuum testing since 1962. Such programs as Ranger, Surveyor, Mariner Venus, Mariner Mars, Mariner Venus/Mercury (MVM'73) and Viking have been tested in the simulator as well as several non-JPL projects.

Modifications were completed in 1966 which replaced the original cassegrain solar simulator with an off-axis optical system (Fig. 1). An array of 37-20 KW Xenon arc lamps was provided as the energy source for the integrated beam. Each lamp is housed in a 27-inch ellipsoidal water cooled collector. The energy passes through a nineteen channel optical mixer or integrating lens unit. From the mixer the energy is projected through the chamber penetration window onto a 23-ft collimating mirror in the top of the chamber and reflected back down into the test volume. This off-axis system was capable of producing solar intensities in excess of that at the planet Venus over a 15-foot diameter area.

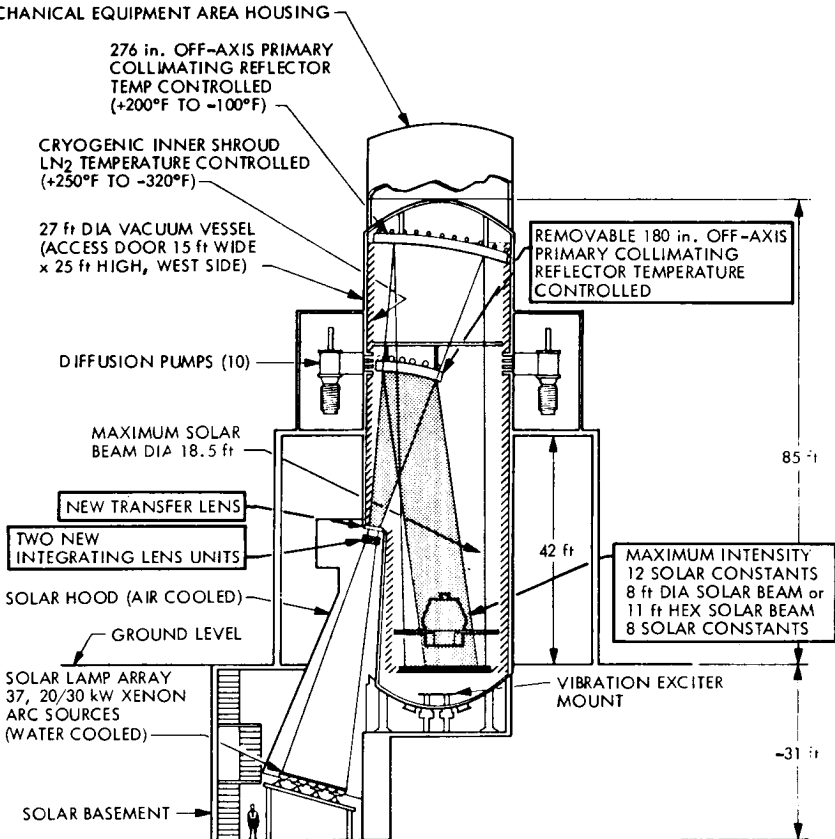


Fig. 1-JPL 25-Ft Space Simulator

High Energy Large Beam Testing

Further facility modifications were made in 1972 to enhance the solar simulation capabilities. Testing of the Mariner Venus/Mercury '73 spacecraft required an eleven foot diameter beam capable of producing 4.8 solar constants. Helios, a spin stabilized solar probe built by the West German Government required test capabilities up to eleven solar constants. These capabilities were provided by the 1972 modification.

Solar System Modifications

The solar source array was not changed. Improvements were made to the power supply cooling which allows lamp operation up to 30 KW.

Two new optical mixers were built. One produced an 11-ft diameter beam and the other a 9-ft diameter beam.

A new Optosil flat penetration window was fabricated and installed to reduce window temperatures and stresses.

A second collimating mirror was built for installation on a removable support system below the existing 23-foot diameter collimator. The smaller 15-ft diameter mirror also has a spherical curvature and is structurally similar to the 23-foot mirror.

Solar Simulator System Performance & Test Results

The versatility of the off-axis solar simulator is apparent in view of the variety of solar beams and intensity levels available as described in Table 1.

CURRENT SOLAR SIMULATOR PERFORMANCE CAPABILITIES

Mixer and Beam Diameter (Feet)	Lamps Available	Maximum Operating Solar Intensity (SC) All Lamps at 25 KW (a)	Collimator Size (Feet)
SSB-15	37	4.3	23
SSB-15.5	37	4.1	23
SSB-18.5	37	2.7	23
SSB-8	7	2.6	23
SSC-9	37	12.0	15
SSC-11	37	8.0	15

SC - 1 Solar Constant = 126 w/ft²

- (a) Test duration and power reserve requirements will effect the ability to operate at these solar intensities.

TABLE 1

The highly successful Mariner Venus/Mercury '73 spacecraft was tested at intensities up to 4.8 solar constants in the solar simulator (Fig. 2). The spacecraft recently completed its third and final flyby of the planet Mercury. The Mission has now been terminated due to the exhaustion of the on-board gas supply for attitude stabilization. Thermal conditions of the spacecraft systems were within specified design limits. The satisfactory thermal performance was achieved as a result of analysis and design changes resulting from the solar simulator tests.

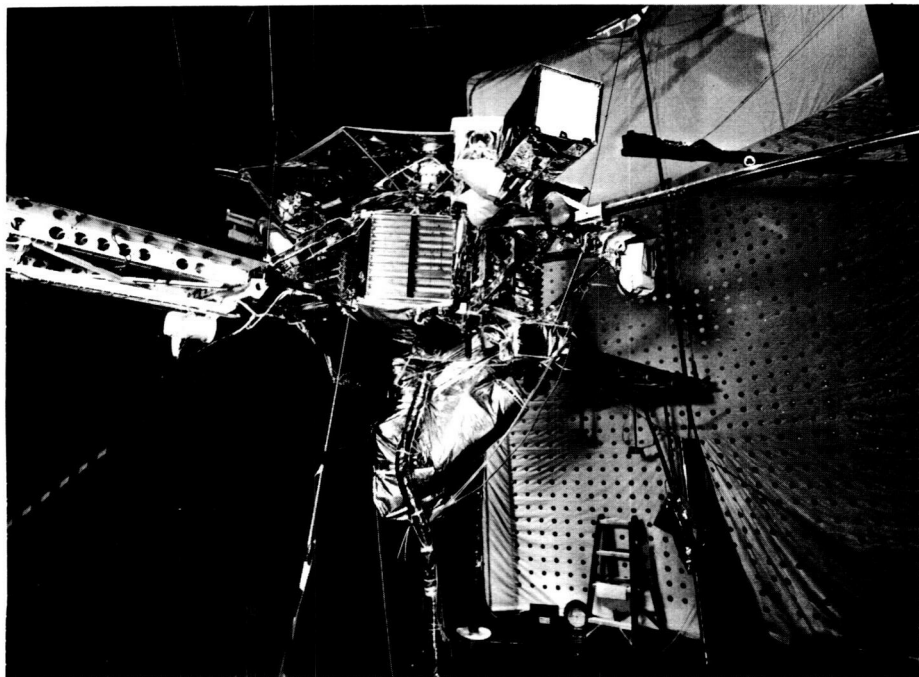


Fig. 2-Mariner Venus/Mercury Spacecraft

The Helios A mission is a West German solar probe launched by NASA from the Kennedy Space Center on December 10, 1974. The spacecraft is spin stabilized at a nominal 60 RPM. The first Perihelion was experienced on March 15, 1975 at 0.3094 AU. The solar intensity at perihelion was 10.4 solar constants.

The spacecraft was tested at JPL in the 9-ft diameter beam at a maximum of 11 solar constants (Fig. 3).

The thermal subsystem performance was excellent. The solar array temperatures varied between 125 and 130°C (predicted values). The fuel tank was 9.5°C, the spacecraft adapter was -19°C. Most temperatures on the vehicle were between 5 and 15°C below predictions for 11 solar constants. The probable cause for these discrepancies was (1) the predicted values used "worst case" surface thermal properties (accumulated degradation

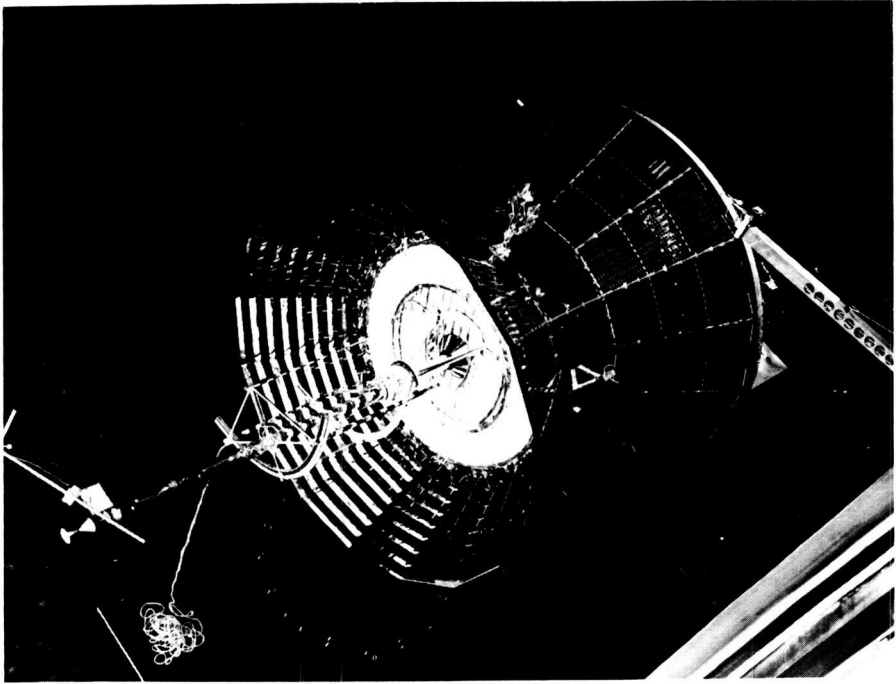


Fig. 3-Helios Prototype Spacecraft

for 3 orbits), (2) a better spin alignment was achieved than that assumed in analysis. These facts assuredly contributed to the reduced temperatures measured at perihelion.

Temperatures of the solar arrays, heatshields, precession thrusters and high gain antennas with reflectors are in agreement with predictions. The medium gain antennas and radial booms were warmer than expected but are still within specified limits. It is interesting to note that those items located on the radial arms which were above predictions were not tested in a solar simulator due to spacecraft/facility configuration limitations.

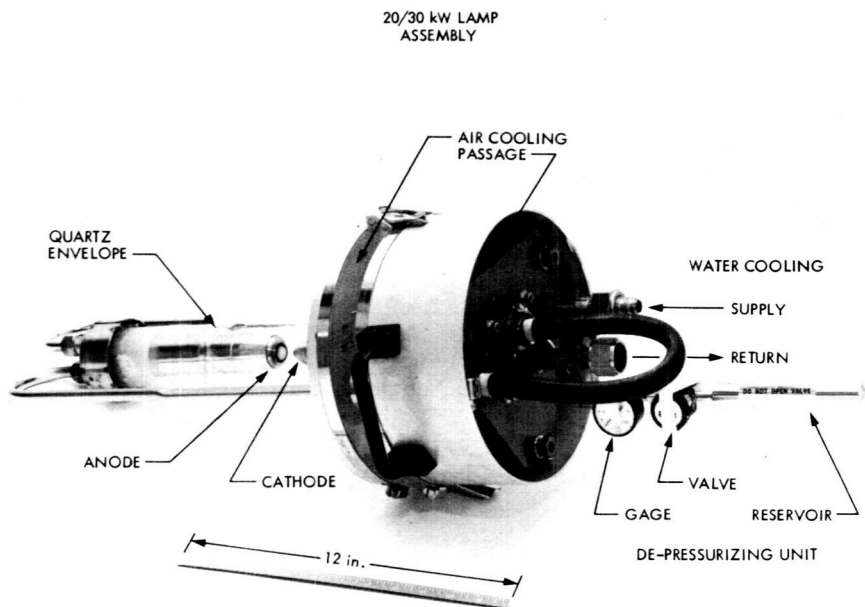
The favorable thermal data received thus far has prompted optimism for a closer approach on subsequent flights. Helios Mission B is anticipating a 0.28 AU perihelion equal to 12.75 solar constants. Some minor changes in thermal shields and radiator area are recommended for Mission B to further enhance its thermal properties.

Solar Simulator System Refinements

The off-axis optical system was designed to utilize compact arc lamps with a power rating of 20 KW. In order to accomplish the Helios test objective of eleven solar constants it would be necessary to operate the lamp array at a minimum of 25 KW/lamp.

Further, to compensate for system degradation, the power would have to be increased towards 30 KW to maintain a constant intensity in the test volume through the course of the test. Lamp performance had to be improved and lamp life extended beyond that previously experienced in order to achieve the Helios test objectives.

The depressurizable 20/30 KW Hanovia lamp which is utilized in the array is supplied by Canrad Precision Industries (Fig. 4). Several improvements were made in the manufacturing process. A higher purity quartz was selected. A better technique for extrusion and envelope forming was established which provided a more uniform product. Better quality control procedures were initiated and improved inspection practices incorporated. As a result of these improvements, equatorial stresses which cause envelope fractures have been eliminated almost entirely. The lamps are rigorously inspected upon arrival at JPL for defects. An inspection report is made and individual lamp histories are maintained and evaluated. Frequent inspections are made of each lamp in service for changes in stress patterns, gas pressures, tungsten deposition inside the envelope, voltage changes and anode cratering. Experience has indicated that the life of the gas seal on the lamp stem is extended by allowing the envelope to remain pressurized except during inspection and handling periods. This also facilitates monitoring the Xenon gas pressure gage on each lamp.



JUNE 1975

Fig. 4-20/30 KW Arc Lamp

The air cooling of the lamp envelope was increased to a flow rate equal to about twice that specified by the manufacturer. The anode/cathode water cooling was doubled by reducing the back pressure on the water circuit. The high back pressure was established at a time when a thin copper anode lamp was in use. The present solid tungsten configuration utilizes reduced pressure, high volume cooling water. These changes in air and water cooling have contributed to increased lamp life.

Through the course of the high energy solar testing accomplished on the MVM'73 and Helios programs, we have experienced lamp life up to 900 hours at 20 KW (500 over warranty) and 300 hours at 30 KW (100 over warranty). This success is attributable to the combined effect of the improvements described. Conscientious inspection and recordkeeping have proven to be essential in controlling quality and performance.

Kilowatt hour costs for a lamp that survives to only its warranted life at 20 KW are \$0.23. As a result of extending the life to 900 hours the cost per kilowatt hour has been reduced to \$0.10. At 30 KW the costs have been reduced from \$0.31/KWh to \$0.21/KWh. These figures represent lamp replacement costs only and do not include other system operation costs.

Reference:

1. Morgan, N. R., "The 7.63-Meter Space Simulator Modification," JPL TM 33-639, dated Sept. 1, 1973.

PERFORMANCE AND OPERATING CHARACTERISTICS OF A 4.88-M DIAMETER SOLAR SIMULATOR FOR VIKING SPACE SIMULATION TESTS

R. P. Parrish, *Martin Marietta Aerospace, Denver, Colorado*

ABSTRACT

The solar simulator met the solar radiation requirements of the two and a half year Viking test program, but not without some interesting problems and experiences. Operating characteristics of the simulator, the system maintenance program and the test program all contributed to the performance of the system.

INTRODUCTION

When considering the operational performance of any system, the main interest should be in how well the system does the job for which it was designed. The cost for providing a simulated space environment for qualifying the thermal design of a spacecraft and the potential loss of the spacecraft if the thermal design proves inadequate makes the quality of the thermal simulation of space of paramount importance.

Three configurations of the Viking spacecraft were tested in simulated thermal environments: cruise, post-separation, and landed. To produce these thermal environments, solar simulation, chamber pressure, cold wall (sink) temperature, and gas composition were controlled simultaneously.

The most difficult part of the thermal environment to simulate is the radiation from the sun because solar radiation has several significant characteristics. These are the level of intensity, the uniformity of intensity, the spectral distribution and the subtense or decollimation angle. Of these characteristics the uniformity, spectral distribution and subtense angle are the most difficult to closely simulate.

Building a system that will produce a radiation beam closely simulating these characteristics and large enough to irradiate an entire spacecraft within the financial and state-of-the-art constraints is challenging to say the least. Operating and maintaining the system while minimizing the probability of failure is only slightly less challenging and is still expensive. However, we have significantly reduced the operating cost with improve-

ments to the system performance, component reliability, operating procedures, and maintenance techniques.

This paper is a review of the solar simulators' performance characteristics, operation and maintenance of the system, and the use of solar simulation in the test program.

THE TEST PROGRAM

The Viking test program consisted of nine major systems tests. Chart I depicts these tests with some description and the nominal solar requirements.

CHART I

Test Designation	Description	Solar Intensity Requirements (W/M)
RTG Cruise	All simulated	None
TETM-Cruise	Equipment simulated-vehicle controls and structure are flight configuration	567
TETM-Post Separation		567
TETM-Mars Surface		643, 1090
PTC-Post Separation		567
PTC-Mars Surface	Qualification Article	567, 1090
Flight Article 1 - Cruise	Workmanship Verification	567
Flight Article 2 - Cruise	Workmanship Verification	567
PTC-Biology PV	Experiment Systems Test	567

RTG - Radioisotope Thermoelectric Generator

TETM - Thermal Effects Test Model

PTC - Proof Test Capsule

PV - Performance Verification

Solar Simulator Performance

- Test Volume -

Except for the solar panels, for which thermal simulators were made, the solar test volume met the program requirements.

- Intensity -

Since each one of the 19 source modules illuminates the entire test volume and 16 can provide one earth solar constant, the hot extreme of 1.7 times the Mars solar constant was easily obtained with 14 source modules. Three radiometers (Hy-Cal P8400) with calibrations traceable to NBS were used to control and monitor the intensity.

- Uniformity -

The uniformity in the volume occupied by the vehicle was even better than in the entire test volume. This is because the edges of the test volume vary most from the average intensity. Three measurements and two alignments assured maintenance of at least the original quality.

- Spectrum -

The system held to the original closely matched spectral distribution of radiation as compared to the real sun. This was verified three times during the test program with a Beckman linear grating spectroradiometer.

- Subtense Angle -

Although there was not a specific requirement for a close simulation of the subtense angle, the $\pm 2^\circ$ of this system provided close shadow effects for the landed configurations.

Test Schedule

The intermittent nature of the test schedule allowed the laboratory to repair equipment, perform preventive maintenance, and calibrate the system without interfering with the test program.

The longest continuous period of the total 500 hours of solar simulation was a 216 hour TETM cruise test. Most of the other periods followed a Martian day-night of 12.3 hours on and 12.3 hours off. Special tests utilizing solar simulation requiring from a few minutes duration to over 40 hours duration made up the rest of the program.

THE SOLAR SIMULATOR

The solar simulator is a part of a 8.84m diameter by 19.81m high space simulation facility in Martin Marietta's Space Simulation Laboratory. The capabilities of the solar simulator are based on specifications in keeping with MIL-STD-810B-517-1, Class I solar simulator. The fidelity of the solar simulator is rated on its five main performance characteristics. These are; spectral distribution of illumination, beam uniformity, beam test volume size, range of intensity level, and beam subtense angle. Values of these characteristics are:

- o Beam Test Volume Size 4.9m high by 4.9m diameter
- o Range of Intensity Levels 0 to 1800 watts/m²
(0 to 1.25 solar constants)

- | | |
|--|--|
| o Spectral Distribution of Illumination | Close match to NASA Standard (Ref. NASA SP-298). Meets Class I of MIL-STD-810-517.1. |
| o Beam Subtense Angle | $\pm 2^\circ$ |
| o Beam Uniformity (4 cm ² sensor) | $\pm 2.0\%$ in plane of best uniformity from set point. |

Of perhaps equal importance is the system's reliability for maintaining the levels of the performance characteristics, especially when a long period of time is required for the spacecraft to reach thermal equilibrium. Significant improvements in reliability have been made to an already reliable system. Modifications have been and still are being made as preventive maintenance measures to facilitate repairs and equipment upkeep during operation.

Also, improvements to the system and components are effecting a reduction in the cost of consumables such as the Xenon arc lamps. A cost comparison of the use of the solar simulator versus an infrared lamp cage is presented in Figure 1. The lamp cage estimate is a 20 zone cage with 56 lamps per zone that is large enough to illuminate a 4m diameter spacecraft.

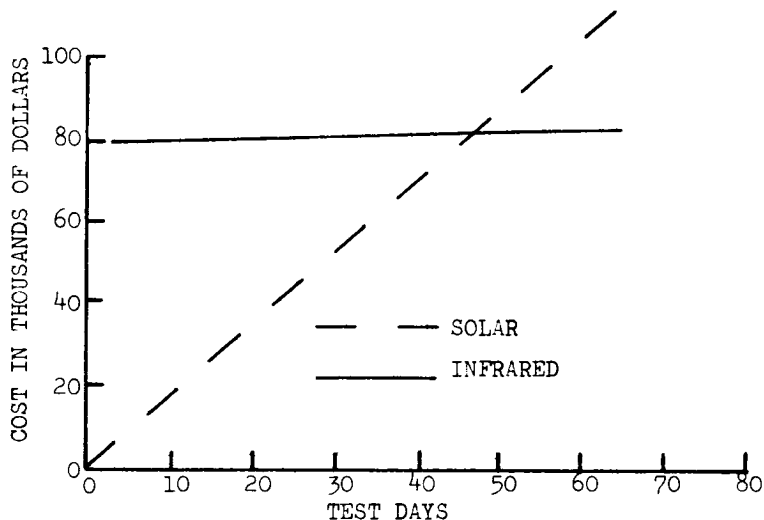


Fig. 1 - Cost Comparison of Solar and Infrared Simulation in the 8.84m x 19.81m Space Simulation Facility

Although performance is the major aspect of any system, the physical makeup is also of interest. The solar simulator has nineteen source modules each of which contains a lamp, an aconic collector, a lamp starter, and cooling lines for the lamp, collector, and starter. Each of the lamps is powered by a power supply rated at 52 KW which, in turn, is controlled by a Module Controller. Current or light control of each individual lamp is also available. The radiant energy from each source module is focused on a lenticular transfer optics system that mixes or integrates the energy. This optics system projects the beam into the vacuum chamber to a 7m diameter collimating mirror which reflects a 4.88m diameter collimated beam down the centerline of the chamber.

Operation

- Procedure -

A standard operating procedure was prepared, reviewed, and approved through the normal channels before the test program began. However, revisions to the procedure are still being made three years later as we discover and develop better ways of operating the system.

- Personnel -

The operating personnel also maintain the solar simulator, thus providing the laboratory with operating personnel who know the system well and can respond correctly to the equipment malfunctions. The laboratory initiated practice of always having at least one engineer and one technician on each work shift who were certified for operation of the system.

The laboratory did not require formal training for the operators except for test discipline. All of the operators were familiar with the system due to previous test experience and were certified on the basis of their knowledge and experience.

Control

Once the system has become operational, control of the system may be completely accomplished at a control console. Controllers for each of the source modules and system control panels have malfunction alarms that shutdown the system or the particular module to prevent damage from an out-of-tolerance condition. Audible and visual signals give indication of a malfunction or warning condition. Rather than shut the system down, the warning signals simply alert the operator and turn on a light with a legend showing the warning condition.

An additional panel has been added adjacent to the control console to provide data on pressures, flow rates and conductivity

of the cooling water. This has been a valuable aid to the operation because previously, the operators had to obtain this data from several places in the laboratory.

In general, the system controls were well designed to provide a good control capability with minimum manpower.

Instrumentation

With the exception of the cooling water system panel mentioned above, the instrumentation has also been adequate. The critical system parameters are indicated on a recorder, meter, or gauge. All the malfunction and warning lights are labeled so that a parameter going out of tolerance can quickly be identified.

Much of the system consists of temperature control subsystems, especially cooling, so that thermocouples make up most of the instrumentation.

Subsystems

One of the more difficult aspects of the solar simulator is keeping the many subsystems going. These subsystems consist of the facility cooling water system, the thermal control unit for the 23-ft diameter collimating mirror, the environmental control unit for the lamphouse air, and the coolant conditioning unit for the source modules and power supplies. These subsystems are checked every two hours to help anticipate and correct problems before they can cause a shutdown. Many system shutdowns were avoided during the test program as a result of the walkthroughs.

Maintenance

- Preventive -

Much reliability was built into this system but a good preventive maintenance effort is required to maintain this reliability.

One of the first things learned in operating a solar simulator is to protect the first-surface aluminum optics from contamination and damage. Denver is fortunate to have dry and rather clear air which causes little contamination. The cases of damage to these aluminum optic surfaces have resulted from failures and contamination. As a whole, the laboratory's contamination control has been effective in protecting the mirrors.

Another problem area for contamination is in the cooling water systems. Closer monitoring of the filters while keeping contaminants out of the system has essentially solved this

problem. Monitoring the conductivity, pressures, and flows at the control console has also helped.

One of the best things the laboratory did was to operate the system for about two hours several days prior to test start. This can be especially important if several weeks or more elapse between tests. Problems were uncovered in a few of these check-outs that would have definitely delayed the test. Fortunately, we were able to make the necessary repairs before the test started.

Other preventive measures include cleaning the vacuum window/lens prior to each test, removing all the source modules in order to clean the collectors of dust once and of water spots a second time, bleeding the cooling water into the source modules, and visually checking the large collimating mirror for contamination.

- Corrective -

A system as complex and unique as this is going to experience failures during operation. The laboratory's approach was to do everything within reason to facilitate repairs. An instruction manual and a full set of drawings were obtained with the system and were adequate in most cases. A big effort was made to stock spares for all components the laboratory felt might fail. Another effort was made to provide redundancy in the facility cooling water system with backup pumps, filters, and cooling towers. The next step was to become as familiar as possible with the system and this was primarily accomplished by working closely with the contractor (Spectrolab) during the design, construction, checkout, and alignment of the system. An extremely detailed acceptance test helped familiarize the personnel with the system operation.

Many repairs such as changing lamps can be accomplished with the system operating, but are usually postponed until after the test unless absolutely necessary. Almost all repairs for this program were accomplished during normal down times because there was always a risk of inadvertently shutting the system down while making repairs.

Malfunctions and Problems

Probably the most difficult part of the system to maintain is the cooling water system with its deionized water. Fittings fail, flow switches stick or leak, carbon steel parts corrode when installed in the system, and leaks develop in general. These are just some of the problems encountered with the water system. Only the redundancy and having spare modules kept the system operational during the test program.

Maintenance of the 7m diameter collimating mirror caused as much concern as anything else in the system. The high cost of stripping and realuminizing the surface in addition to the time involved causes the mirror to be one of the most critical items in the system.

One untoward incident occurred during the test program. A small amount of oil inadvertently fell on the top of the mirror. During the next pumpdown this oil was redistributed to the bottom reflective mirror surface and small projections were noticed from the pits on the mirror while the mirror appeared hazy with coloring like an oil film. The subsequent analysis revealed the projection to be moth wings and identified the contaminant as oil. The laboratory was fortunate because pumpdown into high vacuum with an LN₂ cooled contamination plate while elevating the mirror temperature to +125°F removed both the oil and the wings. RGA scans verified complete removal of the oil from the chamber.

Strict control of contaminants such as freons and other halogens and the cleanliness level in the building also help protect the reflective surfaces.

The xenon arc lamp usage represents a major cost in the operation of the system. In the past few years though, this cost has been steadily decreasing. Most lamp failures (12 lamps to date) can be attributed to malfunction in the lamp coolant system. Improvements in this system has decreased the lamp failure rate. Most of the lamps in the system have more than 500 hours of accumulated burn time and one has 852 hours.

SUMMARY

The solar simulator worked extremely well in meeting the program requirements. This is especially true when the complexity of the system and the limited operating experience of the personnel at the beginning of the program are taken into account. All the program solar simulation requirements were met. Improvements to the system, the operating procedure and the maintenance program have greatly increased the mean time between failures.

REFERENCES

1. T. Buna and T. C. Shupert, "Cost Effectiveness as Applied to the Viking Lander Systems-Level Thermal Development Test Program." 1974 Proceedings of the Institute of Environmental Sciences, Washington, D. C., April 1974.
2. T. R. Tracey and T. Buna, "Thermal Testing of the Viking Lander Capsule System." ASME - presented at the Inter-

society Conference on Environmental Systems, Seattle, Washington. July 29-August 1, 1974.

3. T. Buna, T. R. Tracey, T.W.E. Hankinson, "Thermal Testing of the Viking Lander in Simulated Martian Environments." Presented at the AIAA/ASTM/IES/NASA Symposium on Space Simulation held in Los Angeles, California, November 1973.
4. T. L. Hershey, T. J. Shohfi, "Design and Performance of the Martin Marietta Corporation 16-Foot Solar Simulator." Presented at the 17th Annual Technical Meeting of the IES in April 1971, at the Biltmore Hotel in Los Angeles, California.

SPECIAL TECHNIQUES OF THE VIKING LANDER CAPSULE THERMAL VACUUM TEST PROGRAM*

Tibor Buna, *Martin Marietta Aerospace, Denver, Colorado*

ABSTRACT

Techniques employed to reduce chamber time and improve data capabilities on the Viking Lander Capsule thermal test program are described.

INTRODUCTION

The Viking Lander Capsule (VLC) thermal test program at the systems level, with emphasis on novel objectives, major facility requirements, and overall approach has been described in a series of recent papers ^{1,2,3}. The purpose of the present paper is to describe four techniques employed at the detailed test operations level to improve the overall effectiveness of the thermal vacuum test program.

Two of the techniques are aimed at reducing the required chamber times associated with the high thermal impedance of the VLC in its cruise and post-separation (deorbit) configurations. They include the use of chamber repressurization in combination with shroud temperature control to achieve accelerated cooling, and a one-node approximation technique for the prediction of final equilibrium temperatures from cooling (or heating) transients with sufficient confidence to permit early termination of a test.

The other two techniques described are related to thermal measurements. Experience with thermal imaging used on an experimental basis on the program is discussed, and the use of heat flow gauges as environmental sensors for the characterization of the complex chamber environment during Mars surface simulation is evaluated. Although motivated by the requirements and peculiarities of the VLC test configurations, the techniques are sufficiently general to be of potential value to future programs.

The detailed discussion of the techniques just outlined is preceeded by a test program overview presented in the next section, in order to familiarize the reader with applicable nomenclature, and as a general reference. The overview also serves to update the major test sequences previously reported.

*Work performed under Contract NAS1-9000.

TEST PROGRAM OVERVIEW

The thermal vacuum test matrix of the VLC is depicted on Figure 1, relating test configurations and power sequences with the development (DEV), qualification (QUAL) and acceptance (FA) phases of the program. Also shown is an exploded view of the major subassemblies comprising the Viking spacecraft and the VLC test articles. The three test configurations represent the thermally most significant phases of the mission--excluding dry heat sterilization², which is outside the scope of this paper. The cruise phase begins in Earth orbit after ejection of the Bioshield Cap and ends in Mars orbit where the VLC separates from the orbiter (and Bioshield Base). The post-separation configuration is maintained through the entry phase, which is followed by aeroshell jettison, aero-deceleration, terminal descent, and landing. The investigations on the Martian surface are carried out by the lander in its deployed configuration. During the tests, the orbiter and the Martian ground were simulated by the Orbiter Thermal Effects Simulator (OTES) and the Martian Ground Plane Simulator (GPS), respectively. The latter was mounted on a two axis gimbal to permit variations of solar angles during Mars surface simulation.

The tests comprised two major categories: those during which the vehicle configuration, power sequences, and chamber environments were matched to simulate a given sequence of the mission; and those during which they were not. In the latter case a mission phase was either partially simulated, or bracketed by "artificial" test conditions. Tests in the former category are designated by the abbreviation SIM in the Test Sequences column on Figure 1. The second category played an important role during the acceptance phases of the test program, where, for reasons of economy, a single test configuration was used.

A unique feature of the program was the inclusion of the Science End-to-End Tests (SEET), with the objective to verify the capability of the complete lander system with the science team in the loop to acquire, analyze, and interpret Mars surface data. Some of the special provisions required to conduct SEET are indicated on Figure 2, which shows the qualification test article (with its soil acquisition boom extended) in the chamber during ambient checkout. SEET provisions not shown include a retractable nozzle and associated gas system to produce wind stimuli for the lander's meteorology sensor assembly. The four soil boxes (only one shown on Figure 2) contained prepared samples for soil acquisition and analysis by the lander, and were equipped with remotely controlled lids to prevent the soils that had a tendency to erupt during evacuation to deposit on the vacuum window of the solar simulator. Such deposits could have resulted in local overheating and potential implosion of the glass.

The bulk of the Science End-to-End Tests were conducted in a simulated nominal Martian environment with the ground simulator held in a horizontal position. This resulted in a distortion of the solar component of the simulated environment (see subsequent

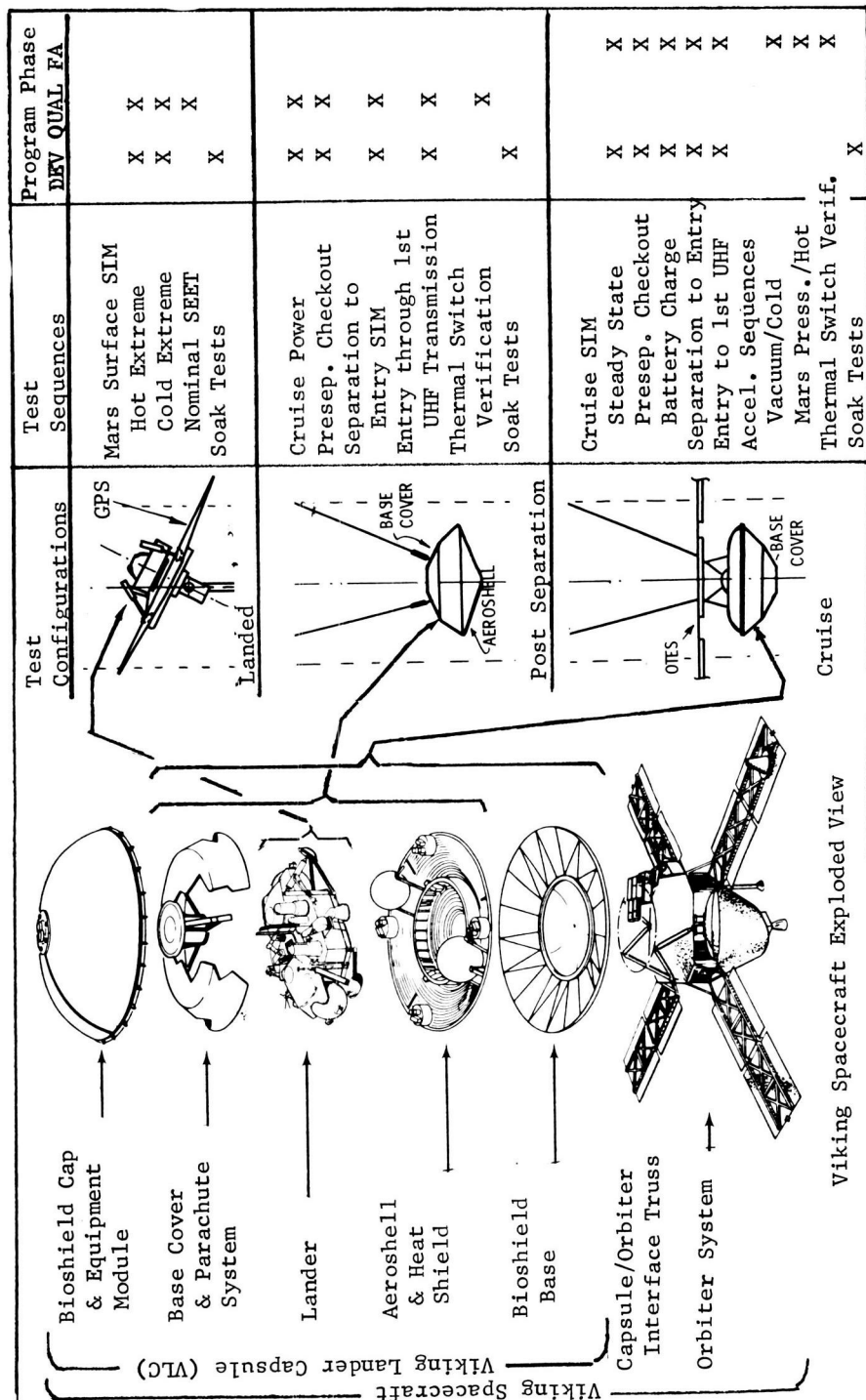


Fig. 1 - VLC thermal vacuum test program overview

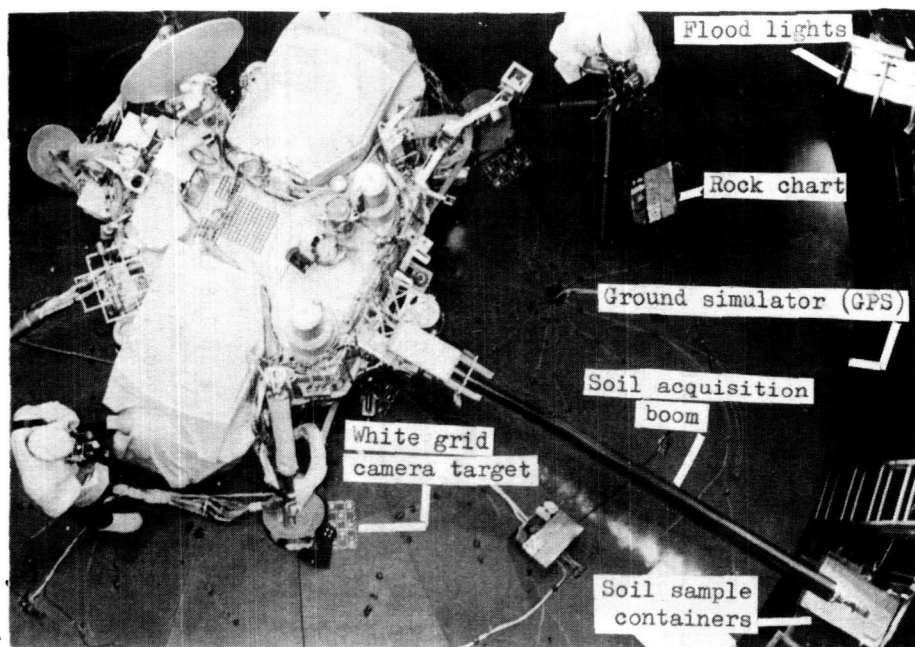


Fig. 2 - Ambient checkout prior to SEET

discussion and Figure 10), which was acceptable; however, for the purposes of these tests.

ACCELERATED COOLING

The large thermal impedance of the VLC in its cruise and post separation configurations and in the interplanetary environment, is associated with relatively rapid internal heating during intense power transients and extremely slow cooling to steady-state equilibrium levels at moderate (constant) or zero internal power dissipation. Furthermore, the equilibrium temperatures so obtainable are too high for some of the special tests contemplated to verify lander equipment performance in the cruise or post-separation configurations but under cold temperature conditions to be encountered on the Martian surface. These considerations pointed to the need for techniques that would provide rapid cooling to the desired levels, thereby reducing the chamber time required for transitions from test to test, and contributing to the feasibility of the contemplated special tests.

The technique successfully employed consisted in establishing a conductive/convective coupling between the internal equipment of the lander and the chamber shroud by repressurizing the chamber with nitrogen or carbon dioxide, while increasing the shroud temperature to a sufficient level to protect the external (to the lander) equipment from exceeding their lower temperature

limits. A typical combination of parameters is shown on Figure 3. The temperature profiles shown are those obtained during the thermal switch setpoint verification test on Flight Article No. 2. The somewhat irregular shroud temperature profile reflects the attempts of the operator to provide as low a heat sink temperature as possible consistent with the lower limits of the VLC equipment, whose response lagged considerably behind the shroud transients. The controlling components were the deorbit propulsion system propellant tanks, whose temperatures during interplanetary flight are maintained by heaters and thermostats, and multilayer insulation. The performance of the multilayer insulation rapidly decays with increasing pressures and was found quite ineffective at pressures above seven microns.

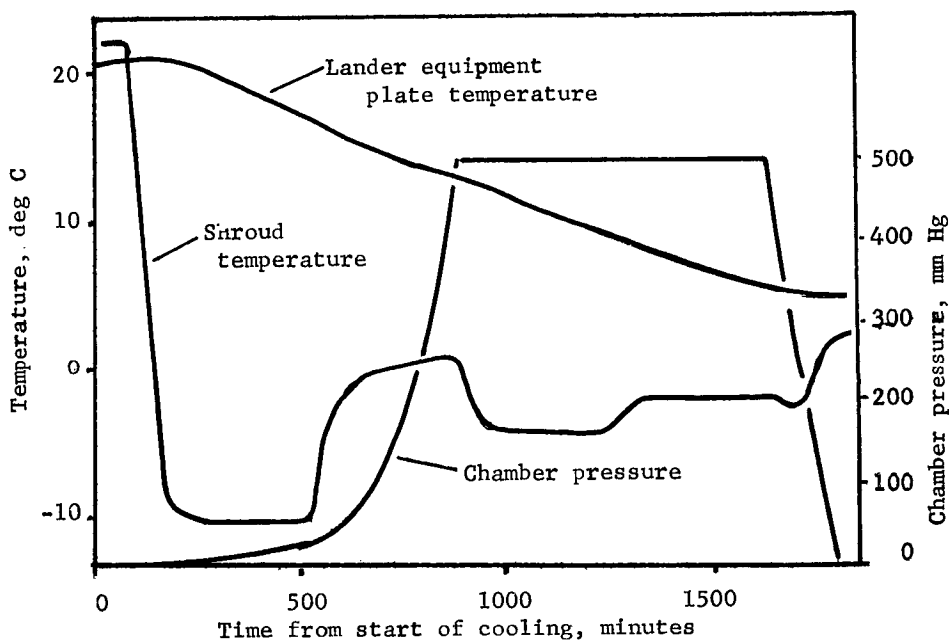


Fig. 3 - Accelerated cooling transients

Note on Figure 3 that the continuously decreasing temperature difference between the equipment plate and the shroud is compensated by the simultaneously increasing pressure, resulting in a nearly linear equipment plate temperature profile. The average cooling rate of 11 C/1000 minutes to a minimum temperature of 5 C obtained with this technique compares favorably with 0.5 C/1000 minutes cooling rate to 15 C obtainable with liquid

nitrogen shroud and the chamber at high vacuum.

ONE-NODE APPROXIMATION OF THE APPROACH TO STABILIZATION

During the final stages of the VLC cruise simulation tests, the measured cooling rates of the equipment mounting plate of the lander ranged from one degree to a fraction of a degree per day at temperature levels still several degrees above their predicted equilibrium values. Yet the determination of the final cruise temperatures was considered important because they represent the initial conditions for the critical preseparation checkout transients at the end of the cruise phase. These observations indicated the need for an analytical technique that could be used to extrapolate the equipment cooling transients to their asymptotic values with sufficient confidence to justify an early termination of the tests.

The technique successfully tried hinges on the assumption (which, as it will be shown, can be verified by the data) that during its approach to stabilization, the equipment plate "behaves" as an isothermal mass thermally coupled to a sink at unspecified but constant temperature T_o . It was further assumed that the time-dependent temperature of the "isothermal" mass was equal to the average temperature of the plate and that its coupling with the heat sink was either by radiation or by conduction. It should be noted that isothermal behavior was not a priori indicated by the data, since a temperature spread of 3 to 6 C was maintained by the plate throughout its cooling transient. With these assumptions, the following equations apply:

Radiation Coupling

$$(mc) \, d\bar{T}/dt = Q - K_R(\bar{T}^4 - T_o^4) \quad (1)$$

where (mc) is the effective thermal mass of the plate (including mounted equipment); \bar{T} is its average temperature in degrees absolute, t is the time from an arbitrary data point; Q is the total internal heat dissipation in watts, K_R is an effective radiative conductance, and T_o is the sink temperature in degree absolute. Let \bar{T}_f represent the final (equilibrium) temperature of the plate. With $d\bar{T}/dt=0$ when $\bar{T} = \bar{T}_f$, Equation (1) may be recast into the form

$$(mc/K_R) \, d\bar{T}/dt = \bar{T}_f^4 - \bar{T}^4 \quad (2)$$

For a time period from t_1 to t_2 , Equation (2) integrates into

$$(2\bar{T}_f^3 K_R/mc)(t_2 - t_1) = \phi_2 - \phi_1 \quad (3)$$

where $\phi = \tan^{-1}(\bar{T}/\bar{T}_f) + \coth^{-1}(\bar{T}/\bar{T}_f)$, $\bar{T} > \bar{T}_f$ (cooling) (4a)

and $\phi = \tan^{-1}(\bar{T}/\bar{T}_f) + \tanh^{-1}(\bar{T}/\bar{T}_f)$, $\bar{T} < \bar{T}_f$ (heating) (4b)

Since \bar{T}_f , K_R , and (mc) are constants in any given situation, it follows from Equation (3) that the function ϕ is linear in t if the underlying assumptions of the analysis are valid. Thus, for any three points on an empirically determined cooling curve $\bar{T}(t)$ that are equally spaced, so that $t_3 - t_2 = t_2 - t_1$, the correct value of \bar{T}_f must satisfy the test

$$\phi_3 - \phi_2 = \phi_2 - \phi_1 \quad (\text{for } t_3 - t_2 = t_2 - t_1) \quad (5)$$

and can be found by an iterative process. The requisite calculations may be programmed on a small computer, such as a pocket or desk calculator. Once the correct value of \bar{T}_f is determined, the "best" curve going through the three experimental points may be constructed by substitutions into Equations (3 and 4), and the adequacy of the extrapolation technique checked by its superposition on the experimental curve. The result of such a procedure is illustrated on Figure 4, which represents the equipment plate cooling transient during the Flight Article No. 2 cruise simulation test.

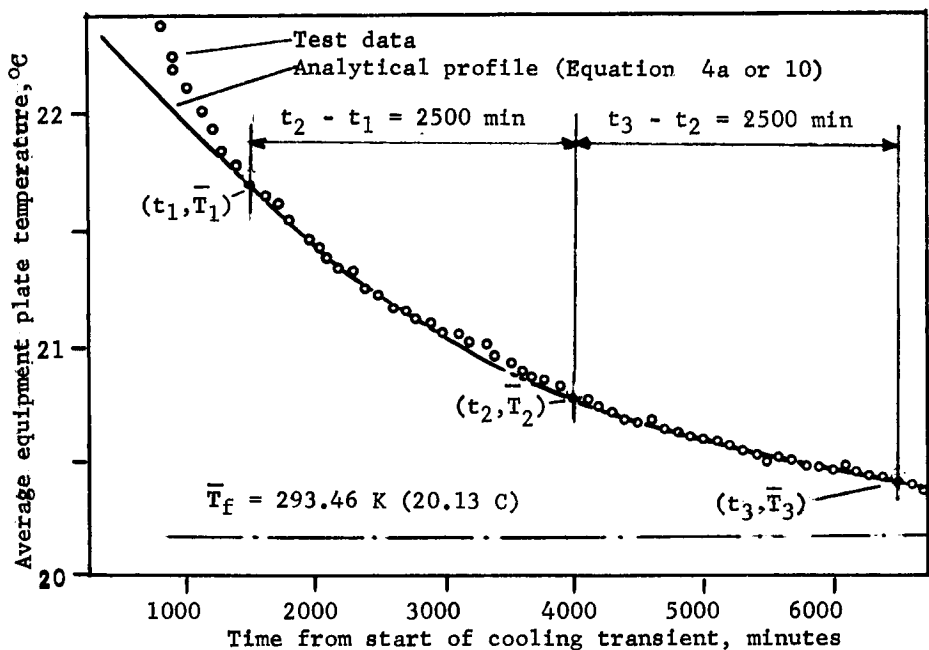


Fig. 4 - Asymptotic approach to stabilization

Conduction Coupling

The heat balance now takes the form

$$(mc) \frac{d\bar{T}}{dt} = Q - K_C (\bar{T} - T_O) \quad (6)$$

where K_C is an effective linear conductance, and the other symbols are as above. With $d\bar{T}/dt = 0$ at $\bar{T} = \bar{T}_f$, Equation (6) becomes:

$$(mc/K_C) d\bar{T}/dt = \bar{T}_f - \bar{T} \quad (7)$$

which, for the time period from t_1 to t_2 integrates into

$$-(mc/K_C) \ln \left[(\bar{T}_2 - \bar{T}_f) / (\bar{T}_1 - \bar{T}_f) \right] = t_2 - t_1 \quad (8)$$

Thus for any three points equally spaced on an experimentally determined cooling curve:

$$\bar{T}_f = (\bar{T}_2^2 - \bar{T}_1 \bar{T}_3) / (2\bar{T}_2 - \bar{T}_1 - \bar{T}_3), \text{ (for } t_3 - t_2 = t_2 - t_1 \text{)} \quad (9)$$

from which \bar{T}_f can be determined explicitly. The analytical curve satisfying (9) may be constructed by first solving Equation (8) for (mc/K_C) , and then re-writing the equation into the form

$$(T_1 - T) / (T_1 - T_f) = 1 - \exp \left[-(t - t_1) / (mc/K_C) \right] \quad (10)$$

where (mc/K_C) represents the familiar concept of a "time constant". The curve fit can be verified by superimposing a plot of Equation (10) on the experimental points. In the sample problem illustrated on Figure 4, Equations (10 and 4a) gave virtually identical curves. This is not surprising since for the temperature levels and ranges under consideration, a fourth-power difference may be closely approximated by the linear expression:

$$\bar{T}^4 - \bar{T}_f^4 = 4\bar{T}_f^3(\bar{T} - \bar{T}_f) \quad (11)$$

Note that the curve-fitting techniques described above only use measured times and temperatures as inputs, and no quantitative knowledge is required of (mc) , K_R , K_C , Q and T_0 .

The conditions for isothermal behavior

The question yet to be resolved is under what conditions do Equations (1) or (6) apply to the cooling of a non-isothermal body. More specifically, what are the requisite temperature distributions for isothermal "behavior". For the answer, let a non-isothermal body of arbitrary temperature distribution be divided into n elements of equal thermal mass $(mc)_i$, but generally at different temperatures T_i . Let the subset j of the n elements be associated with internal heat distributions q_j , and a subset k be conductively coupled to k heat sinks at arbitrary but constant temperatures T_{ok} through conductances K_{ck} . The n elements are, by definition, thermally coupled to each other. The heat balance equation becomes:

$$\sum_n (mc)_i dT_i / dt = \sum_j q_j - \sum_k K_{ck} (T_k - T_{ok}) \quad (12)$$

The solution to our problem is to find a temperature distribution $T(\bar{T})$ such that, when substituted into Equation (12), it can be recast into the form of Equation (6). It may be shown by substitution that the general form of the temperature distribution sought is

$$T_i = a_i + b_i \bar{T} \quad (13)$$

where a_i and b_i are constants. The variables and constants of Equation (6) may, then, be expressed as follows:

$$\bar{T} = n^{-1} \sum T_i \quad (\text{by definition}) \quad (14)$$

$$(mc) = \sum (mc)_i = n(mc)_i \quad (15)$$

$$Q = \sum q_j \quad (16)$$

$$K_c = \sum K_k b_k \quad (17)$$

$$T_o = (\sum K_k T_{ok} - \sum K_k a_k) / \sum K_k b_k \quad (18)$$

It is seen that the averaging procedure for the temperature and internal heat dissipation is straightforward, whereas that for the conductance and heat sink temperature is not.

There are two cases of special interest. For

$$a_i = 0, b_i = 1, i = 1, 2, 3 \dots n \quad (\text{isothermality}) \quad (19)$$

the body is truly isothermal. For

$$a_i = 0, b_i \neq 0, i = 1, 2, 3 \dots n \quad (\text{self-similarity}) \quad (20)$$

the cooling (or heating) process is self-similar⁴. During a self-similar process, the ratios of temperatures at arbitrarily selected points are preserved; hence, the number of measurements that are necessary to characterize the process can be drastically reduced.

It may be shown by an analysis similar to that just described that the necessary condition for isothermal behavior during radiation cooling or heating is that the process is self-similar.

Compliance with Equation (13) has been verified for the measurements comprising the cooling transient shown on Figure 4 for that part of the curve between t_1 and t_3 .

An example of self-similar behavior will be given in the next section.

THERMAL IMAGING

Thermal imaging by infrared photography and/or television type scanning systems is extensively used in industry, medicine, and defense; however, there have been no apparent published accounts on its applications to thermal vacuum testing.

IR imaging was used on an experimental basis on the Viking test program, and some typical results are described in this section to illustrate its merits and limitations.

The instrument used was an AGA "Thermovision" system, consisting of a real-time infrared scanning camera linked by a coaxial cable to a cathode ray tube display unit. The thermal picture is displayed with a gray scale, and one has the option of displaying one or two isotherms selected by the use of the gray scale, either by themselves or superimposed on the thermal picture. Temperatures can be calculated in degrees C by the use of a calibration curve if the temperature of a reference point with known emissivity is in the field of view of the camera. The displayed thermal image and the isotherms can be photographed with a polaroid camera. The detector is sensitive to total infrared radiosity in the 2 to 5.6 micron range, and suitable corrections must be applied to account for emissivities and reflected infrared radiation when calculating temperatures.

The camera was installed on the 12.5 m-level catwalk of the chamber as shown on Figure 5, and imaging was accomplished through a viewport equipped with sapphire window transparent in both IR and visual wavelengths. The axis of the viewport is pointed upwards at 45 degrees towards the center of the collimating mirror of the solar simulator; and viewing of the test article, usually located in the lower half of the chamber, is accomplished through a gimbaled mirror inside the chamber with remotely controlled tilt angle. This viewport is one of four installed at the same level, all equipped with tilting mirrors, and two with sapphire windows. A visual picture of the lander, approximately as it would appear through the viewport of the IR camera, is shown on Figure 6. (A careful examination of the relative locations of external equipment will reveal that the lander shown on Figure 6 is a mirror image of the lander shown on Figure 2). Indicated on this figure are several locations on the test configuration which are featured on the thermal pictures of Figures 7, 8, and 9, so that the IR and visual images may be cross-referenced.

Figure 7 shows a series of thermal pictures of one of the two ETG (Electrical-Thermoelectric Generator) windshields during a shutdown cooling transient. (The ETGs were used to simulate the Radioisotope Thermoelectric Generators during the tests). The purpose of this series of pictures was to provide an illustration of self-similar cooling discussed in the previous section. One of the properties of self-similar behavior implied by Equation (20) is that the points connected by an isotherm during one stage of the cooling process will be connected by isotherms, necessarily of identical size and shape, throughout the process. Conversely, preservation of isotherm geometry during a cooling (or heating) process is a necessary and sufficient condition of thermal self-similarity. Pictures 7a and 7b were taken approximately at the same time ($t=0$), the former showing a "gray" image of the wind cover, the latter only showing two

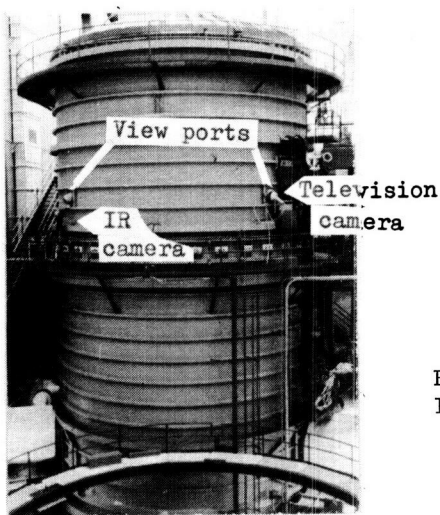


Fig. 5 - Thermal vacuum chamber

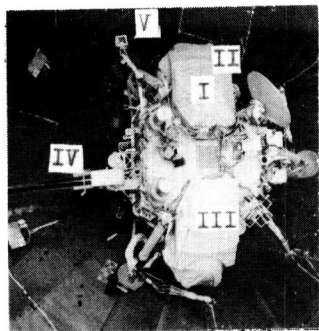
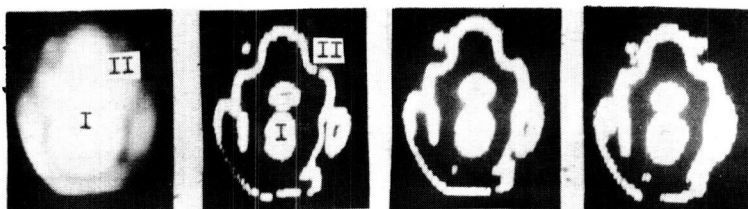


Fig. 6 - Visual image of lander thru IR viewport. Reference locations :

- I :Top,ETG Windshield 2
- II :Side,ETG Windshield 2
- III:Top,ETG Windshield 1
- IV :Soil acquisition boom
- V :Ground Simulator (GPS)



a. $t=0$ b. $t=0$ c. $t=135$ min d. $t=245$ min
 Gray image $T_I = 51.6$ C $T_I = 42.8$ C $T_I = 31.9$ C
 $T_{II} = 45.7$ C $T_{II} = 38.5$ C $T_{II} = 29.5$ C
 Fig. 7 - Self-similar cooling of ETG Windshield

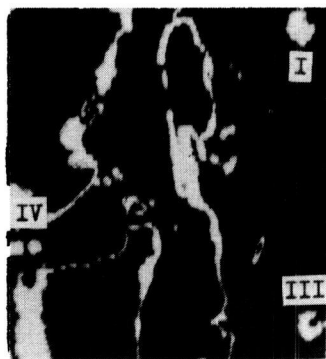
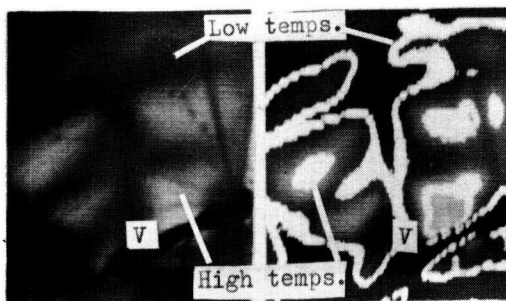


Fig. 8 - Boom temp. survey



a. Gray picture b. Isotherm survey
 Fig. 9 - GPS temperature survey

arbitrarily selected isotherms. Isotherm I represents a "hot spot" on the top of the windshield, and was used as a reference for temperature measurements, since it coincided with the location of a thermocouple. Isotherm II was selected for its somewhat intricate geometry. Both isotherms retained their shapes during subsequent stages of the cooling process, as shown on Figures 7b and 7c. The slight but progressive broadening of the iso-lines indicated by these pictures was due to the decreasing resolution of the selected "isotherm width" at the lower temperatures.

Figure 8 depicts a pair of isotherms used to determine the temperature of the extended soil acquisition boom during SEET. Isotherm I represents the top of the windshield as before, and Isotherm IV goes through the extended boom, as well as other portions of the lander. Because of its rolled-up configuration when stowed, the boom is inaccessible to thermocouple instrumentation. Its predicted temperatures - when extended - are relatively high because of the high solar absorptivity to emissivity ratio of the heat treated nickel steel used for its construction. With the requisite corrections for emissivity, the boom temperature determined from Isotherm IV was 174 C (345.2 F), which is within expectations in the nominal Martian environment.

Figure 9 depicts a portion of the ground simulator (GPS) during SEET, at a time of the simulated Martian day associated with maximum ground temperatures. Local variations of the GPS temperatures are indicated on both the "gray" (Figure 9a) and isotherm (Figure 9b) representations. These were a consequence of spot-bonding (and differential expansion) of the heater blankets on the aluminum substrate, and caused some concern regarding the performance of the ground simulator. The isotherm survey has shown, however, that the temperature non-uniformity as indicated by the "high" and "low" temperature isotherms (Fig. 9b) did not exceed 5°C.

The three examples discussed above illustrate the unique capabilities of thermal imaging in providing information that would be difficult or impossible to obtain by conventional instrumentation. The principal limitations include the fact that imaging quality deteriorates markedly at temperatures below approximately 0 C, and that the surveys are limited to the external surfaces of the object.

HEAT FLOW GAUGES AS ENVIRONMENTAL SENSORS

The local environment in the chamber during Mars surface simulation is characterized by the superposition of its radiative and convective components. The former can be evaluated in a straightforward manner by available techniques. A mapping of the convective process, on the other hand, would involve measurements of both temperature and flow; and that is too cumbersome to be practical during a systems-level test. Also, there are no available analytical techniques or empirical correlations by which the heat transfer rates could be related to their (controlled)

forcing boundaries. These considerations pointed to the need for novel approaches to the measurement and characterization of simulated planetary environments.

One approach particularly suited for thermal control test applications is to measure the environment by its capability to dissipate heat as a function of source temperature. This was accomplished on the Viking program by the use of commercial heat flow gauges equipped with temperature sensors. The gauge provides information of the form:

$$f(q_{tr}, T_s, t, \alpha, \epsilon) = 0 \quad (21)$$

where f represents the function symbol, q_{tr} is the heat flow through the gauge per unit area exposed to the environment, T_s is the gauge temperature, t is time, and α and ϵ are the solar absorptivity and emissivity, respectively, of the gauge surface. In the case of a passive gauge mounted on the external surface of, and having the same optical coating as the vehicle, the measured q_{tr} is representative of internal heat dissipation and can be used for the dual purpose of measuring the environment and evaluating vehicle heat balance. An illustration of this application is presented in Reference 1. An active gauge mounted on a controllable patch heater and installed close to the vehicle surfaces (to properly account for the main convective flow surrounding the vehicle) can be used to produce a much broader mapping of the environment, such as illustrated on Figure 10. These measurements were taken at the indicated times of the simulated Martian day to provide a comparison among the hot-, nominal-, and cold environments used during SEET. The gauge was painted black for this application, and it is shown as installed on the ground simulator near the "science side" of the lander on Figure 11.

The adequacy of the simulation approach may be verified by either passive or active gauges, by comparing the function f (Equation 21) as measured in the chamber with the "required" function determined by analysis from the properties of the gauge and the planetary environmental model.

The heat flow sensors used during the Viking tests were of the wafer type, which measure the temperature gradients caused by heat flowing through them by a thermopile, and provide a self-generated millivolt output proportional to the heat flow rate. Gauge sensitivities ranged from 0.04 to 0.05 millivolts per watts per square meter, which is typical of heat flow sensors under 1000 ohm impedance--a requirement imposed by compatibility with the facility's data system.

CONCLUDING REMARKS

The special techniques described in this paper have been implemented by the use of readily available equipment, and are believed to have had contributed significantly to the economy and quality of the VLC thermal test program. Accelerated cooling,

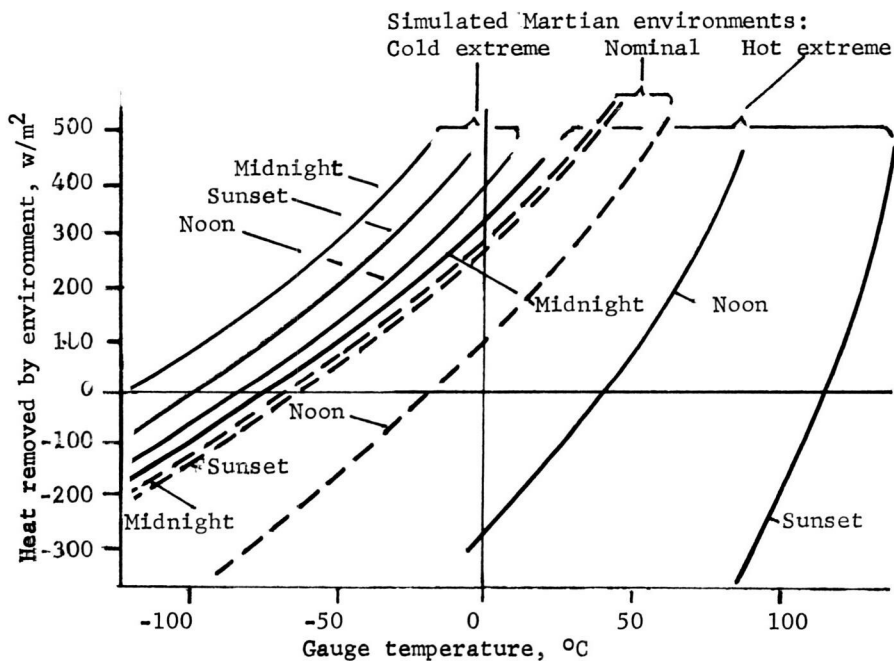


Fig. 10 - Comparison of SEET environments

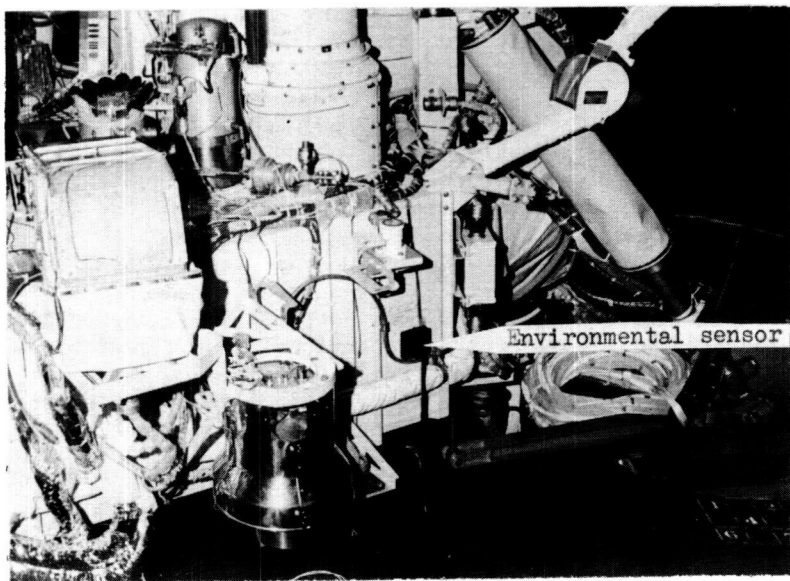


Fig. 11 - Sensor location for
characterization of SEET environments

which depends on the availability of shroud temperature control, resulted in savings of several days of chamber time. It has also contributed to the feasibility of total vehicle checkout in the cruise configuration during the FA tests.

The one-node approximation technique is related to the familiar concept of "time constant", but with a much broader application extending to both linear and non-linear (radiation) heat transfer and providing two tests for its applicability: the curve fitting techniques incorporated into Equations (1) through (11), and the linear temperature distribution criterion defined by Equation (13). The relation between isothermal behavior and self-similarity requires further exploring, especially with regard to its potential to reduce the required instrumentation on future test programs.

Thermal imaging emerged as a powerful technique for the acquisition of data inaccessible to conventional instrumentation. The technique of using heat flow sensors for environmental measurements was found to be highly cost-effective, and was the only means available to evaluate natural convective effects independently from the response of the test article in the chamber. Its potentials as a general instrument for the characterization of simulated planetary environments requires further evaluation.

REFERENCES

1. Buna, T., Tracey, T. R., and Hankinson, T. W. E.: "Thermal Testing of the Viking Lander in Simulated Martian Environments", 7th Space Simulation Conference Proceedings, NASA SP 336, p. 41, November 1973.
2. Tracey, T. R. and Buna, T.: "Thermal Testing of the Viking Lander Capsule System", ASME Paper 74-ENAS-34, July/August 1974.
3. Buna, T. and Shupert, T.: "Cost Effectiveness as applied to the Viking Lander Systems-Level Thermal Development Test Program" - IES Proceedings, January 1974.
4. Section 15.9 Self-Similarity in Handbook of Fluid Dynamics, V. L. Streeter, Editor-in-Chief, McGraw-Hill Book Company, Inc., New York, 1961; pp 15-17 through 15-25.

THERMOELASTIC ANALYSIS OF SOLAR WINDOW OF A VACUUM CHAMBER

C. L. Amba-Rao* and S. R. Soni**, *Space Science & Technology Centre, Vikram Sarabhai Space Centre, Trivandrum-695022, India*

ABSTRACT

It has been noted during space simulation test programmes that the chamber penetration window becomes the limiting factor as the solar intensity increases. The high intensity levels cause very high center to edge temperature differences. The temperature at the center of the window normally attains a level of 550°C , while the edge temperature remains at about 35°C . The stresses produced by this thermal gradient combined with the atmospheric pressure are studied within the framework of classical theory of elasticity, treating the window as a three dimensional medium. The solution for the problem is obtained by solving the static uncoupled thermoelastic equations for a circular blank, subjected to nonuniform heat on one face, by introduction of two auxiliary variables. The displacements are expressed in terms of Bessel functions and parameters of interest are computed at various mesh points of the window. The maximum principal stresses thus obtained show that even with steep temperature gradient, the safety factor is acceptable, though reduced significantly.

INTRODUCTION

A thermo vacuum chamber is used to simulate the deep space environmental conditions in the laboratory. The chamber is under vacuum conditions while solar energy radiation, close to Johnson's curve, impinges through a window. The quartz or fused silica window is of uniform thickness and is subjected to intense nonuniform heat inputs on one face.

*Head, Structures and Aerodynamics Divisions; also Project Leader Environmental Test Facilities Development Project.

**Scientist, Physics and Applied Mathematics Division.

To obtain a circular window of uniform thickness without any air bubbles or striations is extremely difficult and can be expensive. It is not easy to prescribe the limitations on the size of the defects (see Section 8.7 and Ref. 1). So also, are the scratches on the window. It will be extremely interesting and useful to calculate the stress distribution in the window, treating it as an ideal three-dimensional elastic body. Later on, one can introduce a certain stress concentration factor to increase the stress levels in the proximity of the defects and see whether the stress levels are acceptable and lie within the prescribed safe limits for the material.¹

Even in a recent space simulation conference, great concern has been expressed regarding the seriousness of the problem,² viz., thermal gradients in the Lens material.

As already stated, the window is a very expensive item, and any analysis made regarding the possible failure criteria with an emphasis to salvage it, is worth the effort. With the above motivation, this investigation has been undertaken, and is a preliminary effort in such a programme.

This study deals with the general problem of steady-state thermoelastic stress distribution in a flat circular glass slab due to a parabolic surface temperature distribution on one face, while the slab is subjected to vacuum conditions on a parallel face. The theory used is that of a three-dimensional classical elasticity. The edge is assumed to be at room temperature and in a stress free state. The temperature at the center of top face of the window is assumed to be 515°C above the stress free ambient state of 35°C (Ref. 2).

Various authors³⁻⁹ have analytically described the thermoelastic behaviour of half space or thick plate extending to infinity. The solution of a thick circular plate of finite dimensions with elastic restraint at the boundary with thermal and mechanical loads is not available in the open literature. The motive of the present investigation is to present a model for the analysis and determine those parameters which can be adjusted to optimize and control the window failure.

We consider a thick circular plate of finite thickness, with elastic restraint all around the boundary. We impose a second degree parabolic temperature distribution and a uniformly distributed mechanical load of one atmosphere (to take the effect of vacuum conditions on the vacuum side of the window) on one face and the second parallel face is a free unloaded boundary (see Fig. 1).

Assuming the thermal and mechanical problems are uncoupled, (a valid realistic assumption for engineering analysis) we can solve the linear stationary heat conduction equation. Then, using the known temperature inputs, the equations of elasticity enable us to solve for the stress and strain distribution within the body, treating it as a three-dimensional elastic medium.

BASIC THERMOELASTIC EQUATIONS

Consider an elastic thick circular plate of radius a , thickness $2h$, referred to cylindrical polar coordinates, in which a temperature field $T_0(1 + T)$ is established, where T_0 is the temperature of the plate in a state of zero stress and strain. Since the thermal and mechanical loads are radially symmetric, deformations also are axisymmetric and hence we restrict our attention to an axisymmetric problem about the z -axis. The hard crystalline plate is treated as a linearly elastic, isotropic, homogeneous, brittle and continuous medium. Coupling between thermal and elastic behaviours is neglected. Further, thermal and mechanical properties are assumed to be independent of temperature. Taking " a " as the unit of length, T_0 as the unit of temperature and μ rigidity modulus as the unit of stress, the thermoelastic equilibrium equations in their usual notations can be written as¹⁰

$$\frac{\partial \sigma_r}{\partial r} + \frac{\partial \tau_{rz}}{\partial z} + \frac{\sigma_r - \sigma_\theta}{r} = 0 \quad (1)$$

$$\frac{\partial \tau_{rz}}{\partial r} + \frac{\partial \sigma_z}{\partial z} + \frac{\tau_{rz}}{r} = 0 \quad (2)$$

where

$$\begin{aligned} \sigma_r &= (\beta^2 - 2)\Delta + 2 \frac{\partial u}{\partial r} - bT \\ \sigma_\theta &= (\beta^2 - 2)\Delta + 2 \frac{u}{r} - bT \end{aligned} \quad (3)$$

$$\sigma_z = (\beta^2 - 2)\Delta + 2 \frac{\partial w}{\partial z} - bT$$

$$\tau_{rz} = \frac{\partial u}{\partial z} + \frac{\partial w}{\partial r}$$

$$\beta^2 = 2(1 - \nu)/(1 - 2\nu)$$

$$b = (3\beta^2 - 4) T_0 \alpha$$

$$\Delta = \frac{\partial u}{\partial r} + \frac{u}{r} + \frac{\partial w}{\partial z}$$

α = coefficient of linear expansion.

The temperature distribution is assumed to be generated by electromagnetic radiation and has the form

$$T = 2 \sum_{i=1}^{\infty} \bar{\phi}_i J_0(r \xi_i) / J_1^2(\xi_i) \quad (4)$$

where

$$\bar{\phi}_i = A \sinh \xi_i z + B \cosh \xi_i z$$

$$A = (1 - \tau) 9 J_2(\xi_i) / \xi_i^2 \sinh \xi_i h$$

$$B = (1 + \tau) 9 J_2(\xi_i) / \xi_i^2 \cosh \xi_i h$$

and ξ_i are the +ve roots of $J_0(\xi_i) = 0$. The foregoing temperature distribution is obtained by solving the axisymmetric steady state heat conduction equation in terms of cylindrical polar coordinates (axisymmetric) with the following boundary conditions:

$$T(r, h) = f(r), T(r, -h) = \tau f(r), T(1, z) = 0$$

Here τ represents the transmittance of the medium, $f(r)$ the temperature input function and is taken to be equal to $9(1 - r^2)$. The above boundary conditions are based upon experimental observations.

The window is considered partially fixed (Fig. 1) all around the boundary and uniformly distributed mechanical load of one atmosphere (to account for the effect of vacuum conditions) acts on one face and the other face is a free unloaded boundary. These requirements become:

$$w(1, z) = \sigma_z(1, z) = 0 \quad (5)$$

$$\sigma_z(r, h) = \tau_{rz}(r, \pm h) = 0 \quad (6)$$

$$\sigma_z(r, -h) = -q/\mu \quad (7)$$

where q is the atmospheric pressure.

Assuming weak coupling between thermal and mechanical loads, the orders of magnitudes of stress distributions were calculated and we arrived at the conclusion that the mechanical load (vacuum) effect may be ignored as compared to thermal load from an engineering point of view.

SOLUTION

To solve the equilibrium Equations 1 - 3, we introduce the displacement potentials ψ and ϕ (Ref. 9)

$$u = \frac{\partial \phi}{\partial r} - \frac{\partial \psi}{\partial z}, \quad w = \frac{\partial \phi}{\partial z} + \frac{1}{r} \frac{\partial}{\partial r} (r \psi) \quad (8)$$

Substitution of Equation 8 into Equations 1 and 2 yields

$$\begin{aligned} \beta^2 \frac{\partial}{\partial r} [\nabla^2 \phi - b_1 T] - \frac{\partial}{\partial z} [\nabla_1^2 \psi] &= 0, \\ \beta^2 \frac{\partial}{\partial z} [\nabla^2 \phi - b_1 T] + \frac{1}{r} \frac{\partial}{\partial r} [r \nabla_1^2 \psi] &= 0 \end{aligned} \quad (9)$$

where $b_1 = b/\beta^2$

$$\nabla^2 = \partial^2/\partial r^2 + \partial/(r \partial r) + \partial^2/\partial z^2$$

$$\nabla_1^2 = \nabla^2 - 1/r^2$$

Equation 9 can be rewritten in the following form

$$\beta^2 \frac{\partial \phi_1}{\partial r} - \frac{\partial \psi_1}{\partial z} = 0, \quad \beta^2 \frac{\partial \phi_1}{\partial z} + \frac{1}{r} \frac{\partial}{\partial r} (r \psi_1) = 0 \quad (10)$$

$$\nabla^2 \phi - b_1 T = \phi_1, \quad \nabla_1^2 \psi = \psi_1 \quad (11)$$

It can be seen that $\phi_1 = \psi_1 = 0$ represents trivial solutions of Equation 10. In this case it was found that Equation 11 did not yield requisite number of arbitrary constants to prescribe the desired boundary conditions at the faces $z = \pm h$, and therefore a nontrivial solution was sought. For this purpose, Equation 10 was solved by the use of usual variable separable technique to give ϕ_1 and ψ_1 as:

$$\phi_1 = -\frac{1}{\beta^2} \sum_i \{ A_i \sinh \xi_i z + B_i \cosh \xi_i z \} J_0(r \xi_i) \quad (12)$$

$$\psi_1 = \sum_i \{ A_i \cosh \xi_i z + B_i \sinh \xi_i z \} J_1(r \xi_i)$$

where A_i and B_i are arbitrary constants.

To determine the auxiliary functions ϕ and ψ , we solve the differential Equation 11, with Equation 12 as right hand side, by using Bessel Fourier Expansions of ϕ and ψ in terms of $J_0(r \xi_i)$ and $J_1(r \xi_i)$ respectively. The substitution of these expansions yields ordinary differential equations in terms of z -coordinate (r -coordinate is eliminated) whose solutions are well known.

The final solutions of Equation 11 are given by

$$\begin{aligned}\phi &= \sum_i \left[\left\{ \left(\bar{A} - \frac{A_1}{\beta^2} \right) \frac{z}{2\xi_i} + A_2 \right\} \cosh \xi_i z + \left\{ \left(\bar{B} - \frac{B_1}{\beta^2} \right) \frac{z}{2\xi_i} + B_2 \right\} \right. \\ &\quad \left. \sinh \xi_i z \right] J_0(r \xi_i) \\ \psi &= \sum_i \left[\left(A_3 + \frac{B_1 z}{2\xi_i} \right) \cosh \xi_i z + \left(B_3 + \frac{A_1 z}{2\xi_i} \right) \sinh \xi_i z \right] J_1(r \xi_i) \\ \bar{A}, \bar{B} &= 2(A, B)b/J_1^2(\xi_i)\end{aligned}\tag{13}$$

where A_i, B_i ($i = 1, 2, 3$) are arbitrary constants and are to be determined from boundary conditions at the faces $z = \pm h$. It can be shown that the boundary conditions of Equation 5 are satisfied by the solutions of Equation 13. The substitution of solutions (Eq. 13) in Equation 8 leads to

$$\begin{aligned}u &= - \sum_i \left[\left\{ (\bar{A} + \lambda_2 A_1) \xi_i z + B_1 + 2\xi_i^2 (A_2 + B_3) \right\} \cosh \xi_i z \right. \\ &\quad \left. + \left\{ (\bar{B} + \lambda_2 B_1) \xi_i z + A_1 + 2\xi_i^2 (B_2 + A_3) \right\} \sinh \xi_i z \right] J_1(\xi_i r) / 2\xi_i \\ \lambda_2 &= 1/(1 - 2\nu)\end{aligned}\tag{14}$$

$$\begin{aligned}w &= \sum_i \left[\left\{ (\bar{A} + \lambda_2 A_1) \xi_i z + \left(\bar{B} - \frac{B_1}{\beta^2} \right) + (A_2 + B_3) \xi_i^2 \right\} \sinh \xi_i z \right. \\ &\quad \left. + \left\{ (\bar{B} + \lambda_2 B_1) \xi_i z + \left(\bar{A} - \frac{A_1}{\beta^2} \right) + (B_2 + A_3) \xi_i^2 \right\} \cosh \xi_i z \right] J_0(r \xi_i) / 2\xi_i\end{aligned}$$

To determine the arbitrary constants, we recall the boundary conditions at the surfaces; the two pertinent nondimensional stresses are:

$$\sigma_z = (\beta^2 - 2)(\phi_1 + b_1 T) + 2 \frac{\partial w}{\partial z} - bT\tag{15}$$

$$\tau_{rz} = \frac{\partial u}{\partial z} + \frac{\partial w}{\partial r}\tag{16}$$

The substitution of values of ϕ_1, T, w and u from the preceding section and the use of boundary conditions ($\sigma_z(r, h) = \tau_{rz}(r, \pm h) = 0$ and $\sigma_z(r, -h) = -q/\mu$), and some algebra lead to the following values of arbitrary constants for our problem:

$$\begin{aligned}
A_1 &= -\bar{A}/\lambda_2 - 2q \cosh \xi_i h / \mu \xi_i \lambda_2 (\sinh 2\xi_i h - 2\xi_i h) J_1(\xi_i) \\
B_1 &= -\bar{B}/\lambda_2 + 2q \sinh \xi_i h / \mu \xi_i \lambda_2 (\sinh 2\xi_i h + 2\xi_i h) J_1(\xi_i) \\
C_1 &= B_2 + A_3 = -(\cosh \xi_i h + \xi_i h \sinh \xi_i h)(A_1 \lambda_2 + \bar{A})/2\xi_i^2 \cosh \xi_i h \\
D_1 &= A_2 + B_3 = -(\sinh \xi_i h + \xi_i h \cosh \xi_i h)(B_2 \lambda_2 + \bar{B})/2\xi_i^2 \sinh \xi_i h
\end{aligned} \tag{17}$$

In determining the above values of arbitrary constants, a finite Hankel transform was employed to the equation representing the normal stress σ_z at $z = -h$. The other boundary conditions reduced to the form

$$\sum_i f(\xi_i h) J_n(\xi_i r) = 0$$

which would be true for all values at r only if $f(\xi_i h) = 0$. This argument provided us the requisite number of equations to determine required arbitrary constants. It can be seen from Equations 13 and 14 that there are six arbitrary constants A_i, B_i ($i = 1, 2, 3$); but $A_3 + B_2$ and $B_3 + A_2$ are taken as C_1 and D_1 respectively. Thus the solution of the problem is complete and the parameters of interest, i.e., stresses, strains and displacements, at any point can be computed with the help of Equations 14 and 17.

EXAMPLE AND DISCUSSIONS

The nondimensional temperature distribution given by Equation 4 is given in Figure 2. Using Equations 14 and 17, displacements, strains and stresses are computed, at a grid of points, for a chamber window with the following properties:

Radius of the window	$a = 12 \text{ inch (30.48 cm)}$
Thickness	$2h = 2 \text{ inch (5.08 cm)}$
Poisson's ratio	$\nu = 0.16$
Rigidity modulus	$\mu = 4.5 \times 10^6 \text{ psi}$ $(316.4 \times 10^6 \text{ gm/cm}^2)$
Temperature in the state of zero stress and strain	$T_0 = 100^\circ\text{F (38}^\circ\text{C)}$
Maximum temperature at the Centre	$T_1 = 400(100)1000^\circ\text{F (150-705}^\circ\text{C)}$

Coefficient of thermal
expansion

$$\alpha = 0.55 \times 10^{-6} / ^\circ\text{F} (0.3056 \times 10^{-6} / ^\circ\text{C})$$

Normal pressure

$$q = 14.7 \text{ psi } (1033.56 \text{ gm/cm}^2)$$

The normalized displacements, strains and stresses appear in Figures 3-9 for $z = -h, 0, h$. During computation of results, it was seen that the series represented by Equation 14 and their derivatives with respect to r and z are rapidly convergent. There was no significant difference in the results when the number of terms in these series was more than eight. For the calculation of results shown in Figures 2-10, the number of terms was fixed at 12. Figures 8 and 9 show that the stresses σ_r and σ_θ on the central line of the plate $r = 0$, are equal and comprehensive with magnitude 2430 psi (171 kg/cm^2) for maximum temperature input of 550°C .

For the range of parameters used in this analysis tensile and compressive stress states exist within the regions $0.8 \leq r \leq 1.0$ and $0 \leq r \leq 0.8$ respectively, such that only the major principal stress be used to predict failure. In the case σ_θ appears to play major role, because it is compressive at the center and tensile at the edge. If we concentrate on the maximum allowable tensile stress criterion to predict failure, σ_θ is the parameter of interest. Thus the failure can occur either at the center or at the edge of the window. The maximum acceptable compressive and tensile stresses for a fused silica material are $11,250 \text{ kg/cm}^2$ and 492 kg/cm^2 respectively. Figure 10 depicts the maximum tensile and compressive stresses for the maximum temperature input range $150 \leq T_1 \leq 705^\circ\text{C}$ for $z = -h, h$. Since the shear stress τ_{rz} on the lower and upper faces of the window was taken to be zero (boundary condition), the stresses σ_r and σ_θ shown in Figures 8 and 9 represent principal stress at the face $z = \pm h$. The examination of Figures 8 to 10 reveals that the principal stresses caused due to such a steep temperature lie within the acceptable safety factor range. From Figure 9, it would seen that no airbubbles or scratches are permitted in the annualr space $0.76 \leq r \leq 1$ as thermal tangential stresses alone are critical.

REFERENCES

1. Handbook of Solar Simulation for Thermal Vacuum Testing, Section 8, Ed. Griffith, J. S., Institute of Environmental Sciences, 1968.
2. Harrell, J. W., Large Solar Beam Testing at Planet Mercury and Greater Intensities in the JPL, 25-Ft Space Simulator, p. 716, Seventh Conference on Space Simulation NASA SP-336 (1973).
3. Sneddon, I. N., "Boundary Value Problems in Thermoelasticity," Proceedings of a Symposium on Boundary Problems in Differential Equations, The University of Madison Press, Madison, 1960.

4. Martin, C. and Payton, R. G. , "Thermoelastic Stresses in a Slab," *Journal of Mathematics and Mechanics*, Vol. 13, 1964, pp. 1-30.
5. Sneddon, I. N. and Lockett, F. J. , "On the Steady State Thermoelastic Problem for the Half Space and the Thick Plate," *Quarterly of Applied Mathematics*, Vol. 18, 1960-61, p. 145.
6. Sternberg, E. and McDowell, E. L. , "On the Steady State Thermoelastic Problem for the Half Space," *Quarterly of Applied Mathematics*, Vol. 14, 1957, pp. 381-398.
7. McDowell, E. L. , "Thermal Stresses in an Infinite Plate Arbitrary Thickness," *Proceedings of 3rd Midwestern Conference of Solid Mechanics*, 1957, pp. 72-85.
8. Akoz, A. Y. and Tauchert, T. R. , "Thermal Stresses in an Orthotropic Elastic Semispace," *Journal of Applied Mechanics*, March 1972, pp. 87-90.
9. Sve, E. and Miklowitz, J. , "Thermally Induced Stress Waves in an Elastic Layer," *Journal of Applied Mechanics*, March 1973, pp. 161-167.
10. Sneddon, I. N. , "Mixed Boundary Value Problems in Potential Theory," *John Wiley & Sons Inc.* , New York, 1966, p. 11.

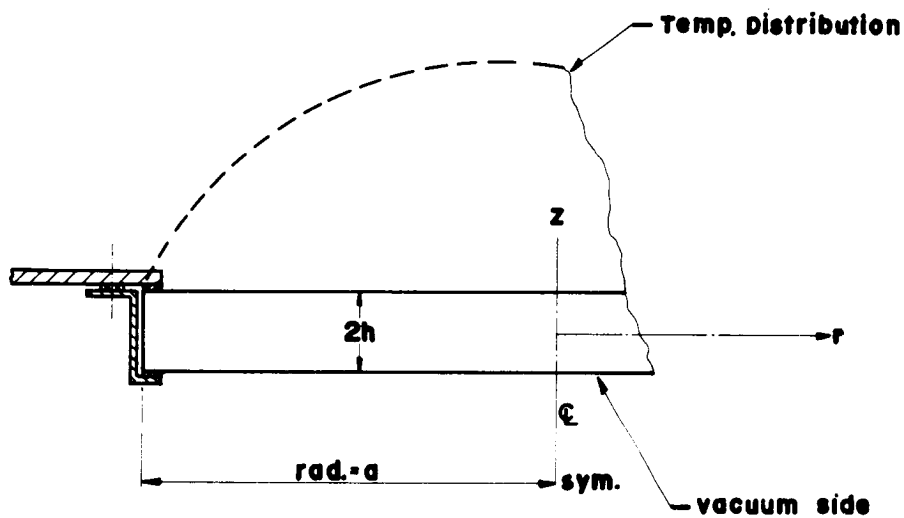


Figure 1. Solar Window of a Vacuum Chamber with Coordinate System

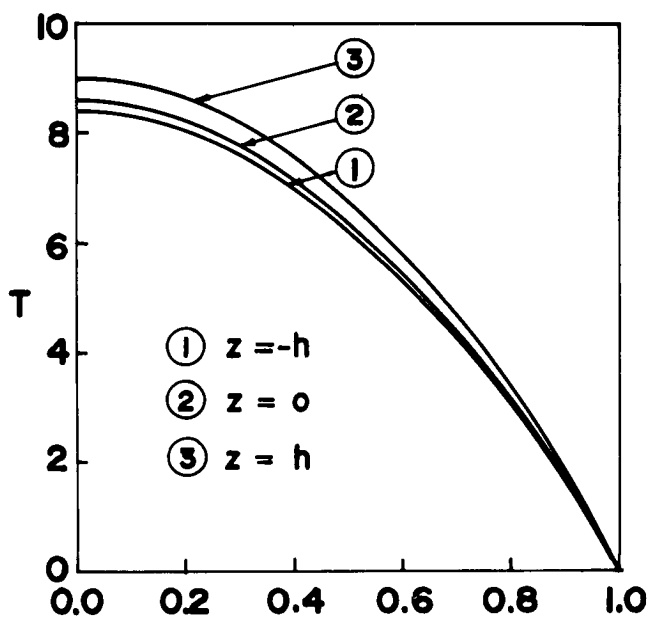


Figure 2. Non-dimensional Temperature T vs. r

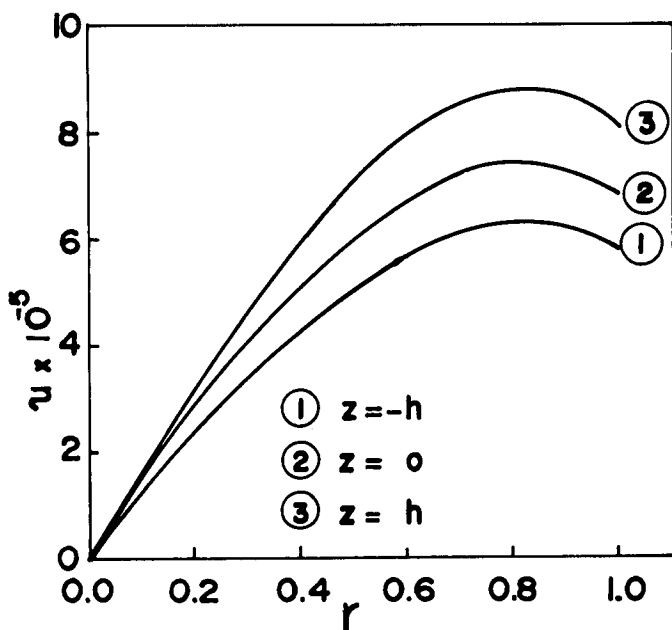


Figure 3. Non-dimensional Radial Displacement U vs. r

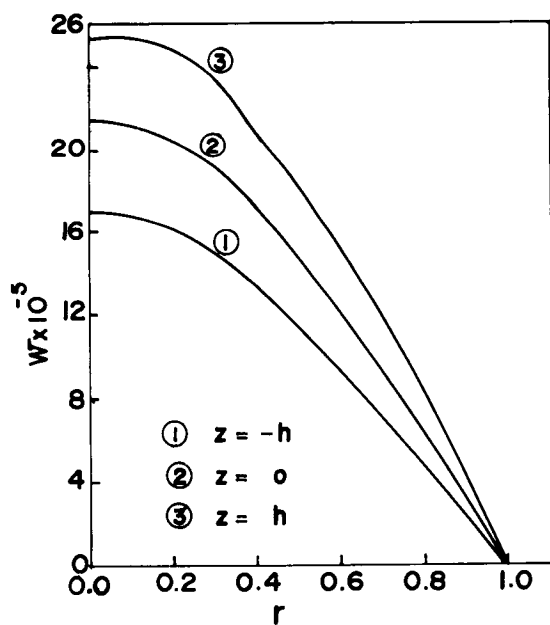


Figure 4. Non-dimensional Transverse Displacement W vs. r

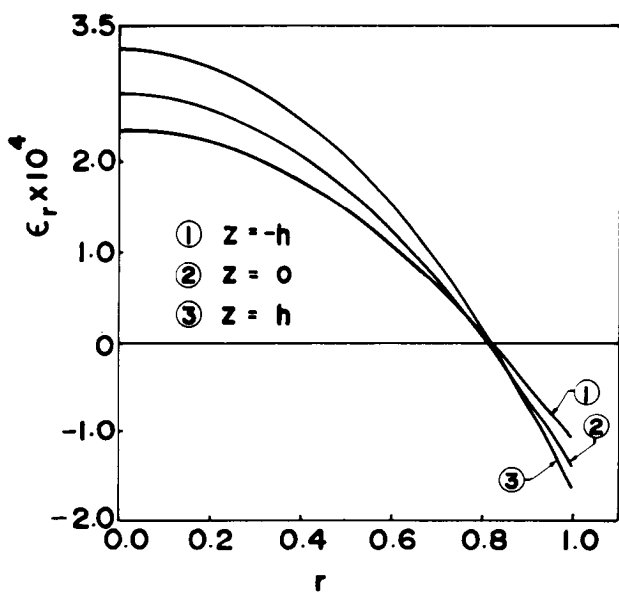


Figure 5. Non-dimensional Radial Strain
 ϵ_r vs. r

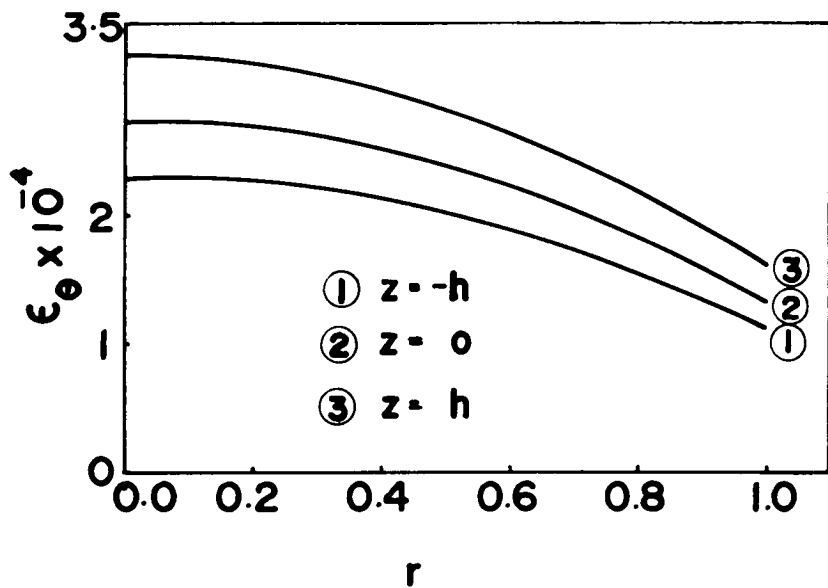


Figure 6. Non-dimensional Tangential Strain ϵ_θ vs. r

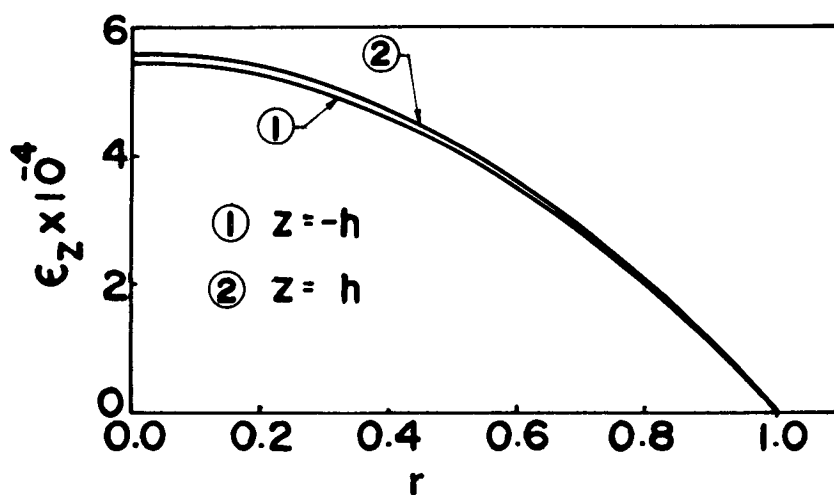


Figure 7. Non-dimensional Transverse Strain ϵ_z vs. r

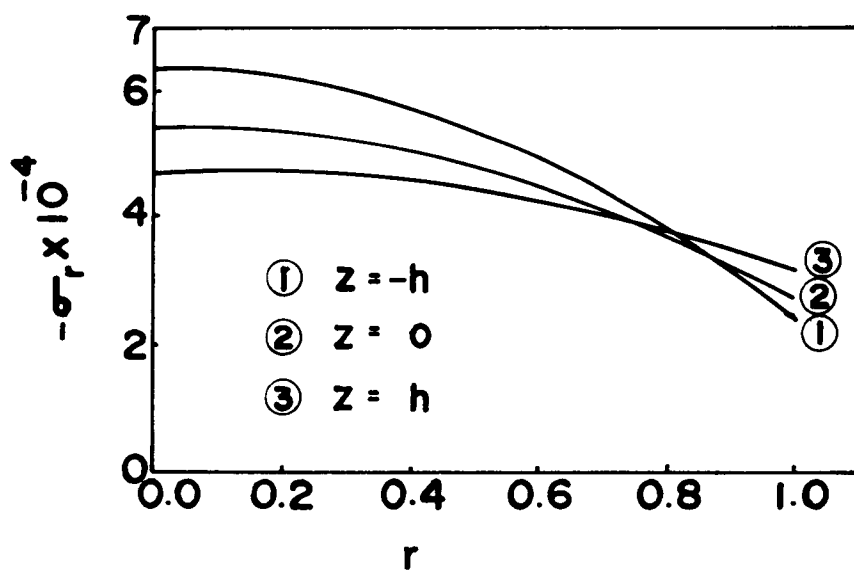


Figure 8. Non-Dimensional Radial Stress σ_r vs. r

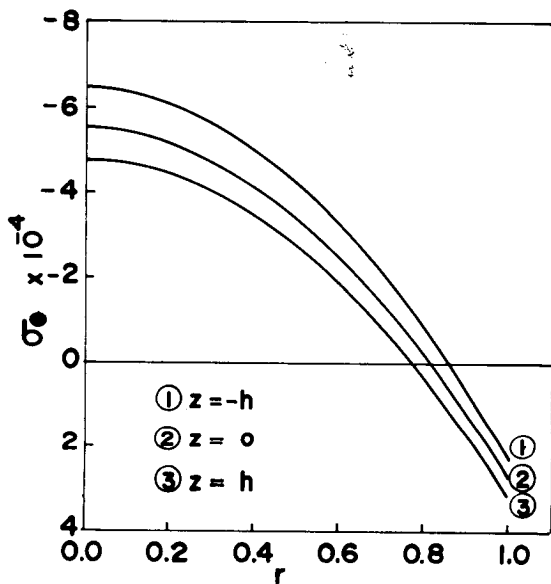


Figure 9. Non-Dimensional Tangential Stress σ_θ vs. r

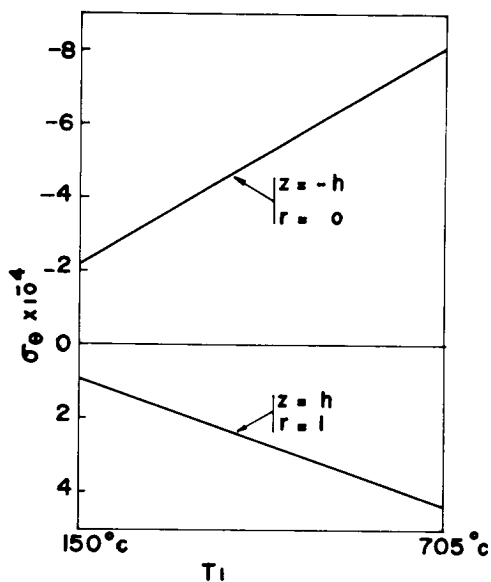


Figure 10. Maximum Non-dimensional tangential Stress σ_θ vs. Maximum Temperature T_1

TRANSPORT OF LIQUID STATE NITROGEN THROUGH LONG LENGTH SERVICE LINES DURING THERMAL/VACUUM TESTING

F. A. Florio, *General Electric Co., King of Prussia, Pennsylvania*

ABSTRACT

Physical and analytical aspects associated with the transport of liquid state nitrogen through long length service lines in a thermal/vacuum environment are presented. Included with this is a definition of the problems and difficulties imposed by the servicing of a typical solid cryogen system, as well as a discussion of the transport requirements and of the rationale which governed their solution. Accordingly, a successful detailed transport configuration is defined, and the application of established mathematics to the design approach is demonstrated. Thus, the significance of head pressure, pressure drop, line friction, heat leak, Reynolds number, and the fundamental equilibrium demands of pressure and temperature are examined as they relate to the achievement of liquid state flow. Performance predictions are made for the transport system, and several analytical quantities are tabulated. These data are analyzed and compared with measured and calculated results obtained while actually servicing a solid cryogen system during thermal/vacuum testing.

INTRODUCTION

An increasingly popular design innovation employed by manufacturers of optical experiments for meteorological spacecraft involves the use of solid cryogens to maintain thermal control of low temperature detectors. Basically, the in-orbit principle of operation depends on continued sublimation and overboard venting of the cryogens to provide the cooling required to offset any reasonable heat leak into the material from the surrounding spacecraft structure. Accordingly, a constant heat sink temperature for the detector is thereby maintained. This is the equilibrium temperature of the cryogens at the design pressure.

Ground handling of the solid cryogens, however, presents some significant problems, since ambient heat leaks into the cryogen dewar are continually attempting to disturb the thermodynamic balance, and in this circumstance it is generally considered undesirable for the cryogens

to sublime directly into the immediate environment. The basis for this viewpoint is the fact that many of the cryogenics are toxic and dangerous. In addition, collection of the vented cryogenics is cumbersome due to thermodynamic constraints, while extensive use of a vacuum pump to support sublimation and protect environmental concerns is also frowned upon because of logistics problems. Furthermore, replenishment of the cryogenic stores on a regular basis can also prove expensive. Thermodynamic conditions at ambient are therefore maintained in such a way that no significant sublimation is allowed to take place. Instead, the cryogen temperature is continually raised by the ambient heat leaks. It follows then that at some suitable point in time, the cryogenics must be re-cooled and hardened before a critical temperature is reached where liquefaction and pressure rise would be significantly accelerated.

RECOOL REQUIREMENTS

Thermal/Vacuum testing of the Nimbus F spacecraft included ground support of the *LRIR solid cryogen dewar. Figure 1 presents a functional sketch of the dewar or cryocooler as it is commonly termed. The cryogenics stored in this container are solid methane and ammonia. A 0.63 centimeter (1/4 in.) coolant line with flexible corrugated plastic sections is provided within the dewar to permit circulation of liquid nitrogen for cooling the cryogenics. In short, this line performs as a heat exchanger. It also serves by its fixed dimensions to limit the amount of liquid flow which it will transfer for any given head pressure.

In all ground testing of the LRIR experiment the temperature of the solid methane was permitted to vary between 78°K and 85°K , and the ammonia between 82°K and 138°K . A red line temperature of 85°K for the methane defined the permissible upper limit before re-cooling was required. To accomplish the recool, a ground handling system had to be devised which would result in coolant temperatures

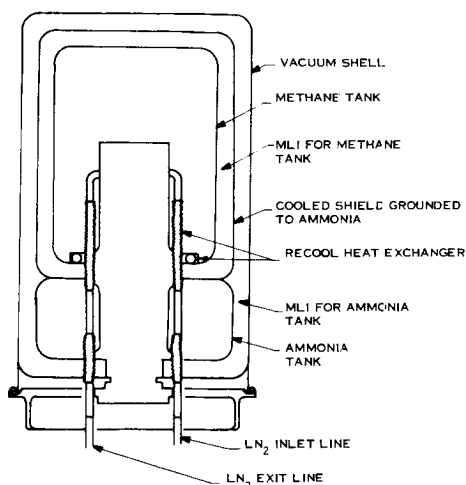


Fig. 1-Basic Configuration of Honeywell Solid Cryogen Cooler¹

*Limb Radiance Inversion Radiometer, Mfg., by Honeywell, Inc., Lexington, Mass.

CL
in the range of 80°K to 82°K within the cryocooler. In the case of the Nimbus F thermal/vacuum test, this requirement presented a significant problem, since test facilities necessitated that an excessive length of transport line be used to deliver the liquid nitrogen to the LRIR experiment.

In addition to constraints imposed by the requirement to maintain certain liquid state temperatures, a further limitation was placed on the transport system head pressure since the plastic sections of the cryocooler internal corrugated line were rated for a limited burst pressure. The implications were: 1) that the head pressure for pumping liquid nitrogen through the transport line not exceed 4218 kgf/M^2 gauge (6 psig) as a safe upper limit, and 2) that the heat transfer and consequent vaporization rate of liquid nitrogen in the transport line be closely controlled such as to preclude any accidental build-up of excessive pressure. It is obvious that with an expansion ratio of 648 (gas to liquid volume at standard conditions), it would be relatively easy for the trapped liquid - given the right amount of heat - to vaporize and cause a rupture of the corrugated lines. This fear resulted in still a further requirement that the liquid state nitrogen be delivered to the cryocooler within three minutes after the recool procedure has started. This left little time for cooling the transport line itself once the recool procedure is initiated.

THERMAL/VACUUM RECOOL CONFIGURATION

The thermal/vacuum configuration for the Nimbus F spacecraft is generally defined in Figure 2. Essentially, the 1.5 meter (5 ft.) diameter, 3.0 meter (10 ft.) high spacecraft was placed at the approximate vertical centerline of an 11.9 meter (39 ft.) spherical thermal/vacuum chamber. Because of the location of the spacecraft with respect to available chamber feed-through fittings, a minimum line length of 13.1 meters (43 ft.) was required to circulate liquid nitrogen through the cryocooler. The length of coolant line within the cryocooler itself provided an additional 1.5 meters (5 ft.) to this length. Prior to the thermal vacuum test, any attempt at recooling the cryogens in ambient air with line lengths greater than about 2.1 meters (7 ft.) resulted in flow blockage by condensed solids and excessive back pressure. Since the 82°K requirement for the liquid nitrogen implied a maximum gas pressure of approximately 6749 kgf/M^2 gauge (9.6 psig), it was immediately obvious that the heat leak to the liquid nitrogen carrying lines had to be kept to a minimum. To support this requirement, a double walled transport line was devised which would make use of two separate liquid nitrogen supply sources: 1) for the transfer of liquid nitrogen through the cryocooler, and 2) for cooling the annulus which surrounds the transport line.

The double walled line was formed simply in inserting a 0.63 centimeter ($1/4$ in.) tube inside of a 1.6 centimeter ($5/8$ in.) tube. Since both

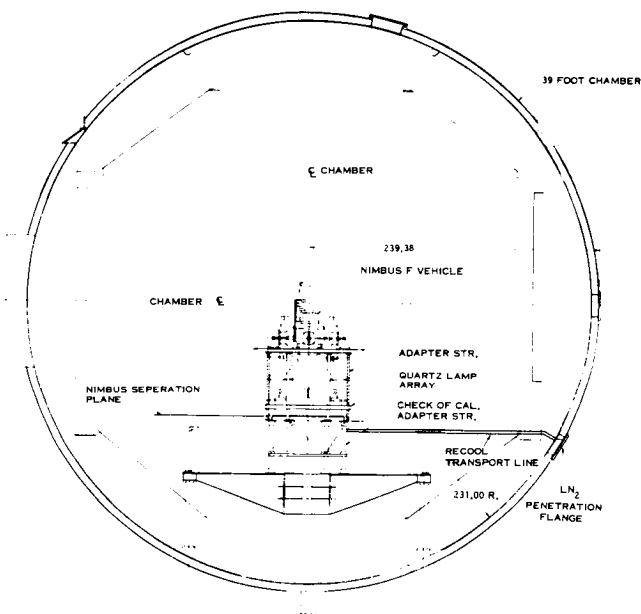


Fig. 2-Nimbus F S/C Installation in 39' T/V Chamber

tubes were to be maintained at liquid nitrogen temperatures, it mattered little that they might be touching at various points. Break-away junctions were achieved by the use of tee fittings, with the 0.63 centimeter (1/4 in.) tube leaving the tee by means of the run and the 1.6 centimeter (5/8 in.) tube leaving by means of the branch. Diameter reductions for the outer tube were achieved by utilizing standard stock reducer fittings. All tube joints involved the use of sweat fittings so that a pressure tight seal might be achieved between the inner and outer tubes. Copper was chosen as the tube material because of its high thermal conductivity, availability as sweat type fittings, and ease of attachment. Figure 3 presents a functional schematic of the recool system. In addition to plumbing hardware, the configuration reveals an electrical isolator fitting (Figure 4) at both the inlet and outlet ports of the cryocooler. This fitting served to prevent any variation of the electrical ground potential with respect to the spacecraft via the LRIR; it also minimized heat flow from the cryocooler to the liquid nitrogen sink. A possible source for heat leak to the nitrogen coolant was present in the form of a 0.63 centimeter (1/4 in.) copper tube which served to provide a pressure tap at the inlet to the cryocooler.

To protect against heat leak, the liquid nitrogen lines downstream of the electrical isolator fittings were wrapped with multilayer superinsulation blankets. It was considered impractical to attempt to fabricate a

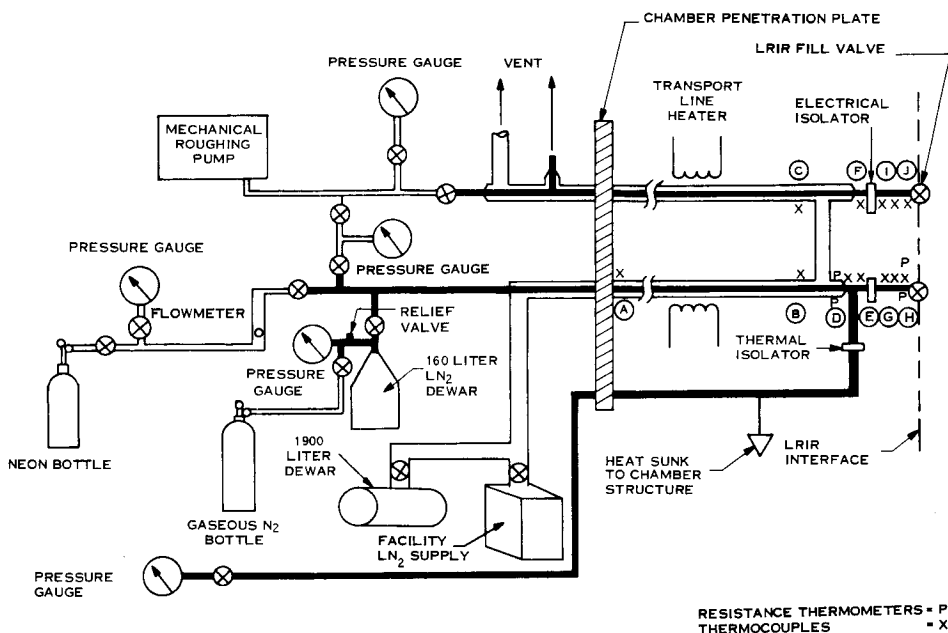


Fig. 3-Functional Schematic of Recoil Configuration

double walled line on the LRIR side of the isolation fittings because of the electrical requirement and because of the complicated configuration of the fitting itself and of the lines which interfaced with the LRIR experiment. Furthermore, it was felt that the blankets would serve as a satisfactory means of minimizing heat transfer to the liquid nitrogen coolant from the immediate environment. Subsequent calculations showed that only about 1 Watt of heat was admitted to the liquid nitrogen via the superinsulated section during the recoil procedure. The superinsulation blankets consisted of 20 layers of crinkled 6.35×10^{-3} millimeter (1/4 mil) aluminized mylar shaped in rectangular patterns. The long dimension of the rectangle coincided with the length dimension of the tube

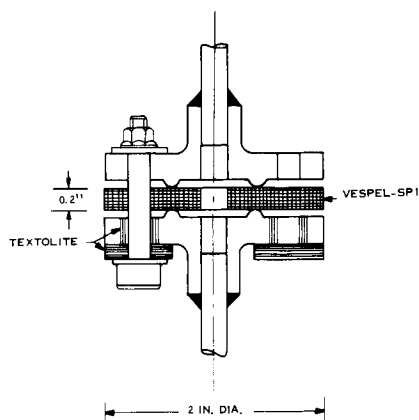


Fig. 4-Electrical Isolator Fitting²

run. The blankets were wrapped around the liquid nitrogen coolant lines in an overlap fashion (Figure 5) and fastened in place with aluminized mylar tape. A 0.05 millimeter (2 mil) outer layer of aluminized mylar was used to add a certain degree of stiffness to the assembly. Adjacent blanket sections were also overlapped and taped to protect the joint interface from exhibiting excessive heat leakage.

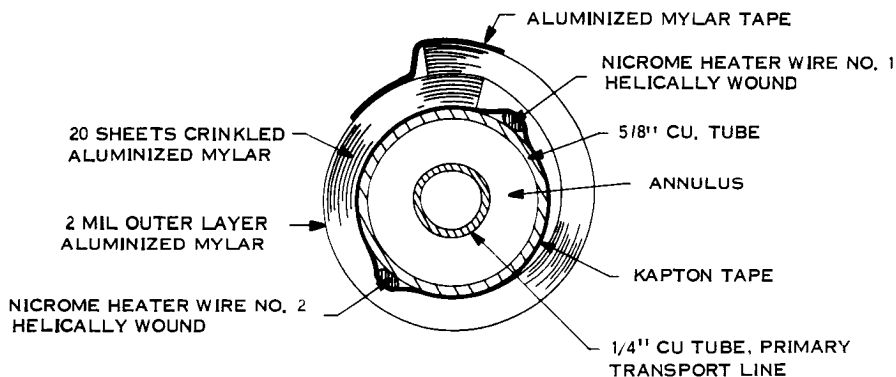


Fig. 5-Liquid Nitrogen Transfer Line and Superinsulation Configuration

Liquid nitrogen was pumped through the transport lines (including annulus) by means of a static head pressure at the supply containers. Individual supply sources and not the plant facility were used in the recool process so that liquid nitrogen could be supplied in a supercooled condition. The plant facility liquid nitrogen supply pumps nitrogen under a head pressure of approximately 24607 kgf/M² gauge (35 psig). Accordingly, the liquid state nitrogen at the supply can be relatively warm (as high as 89°K) and requires that much expansion and vaporization take place before a temperature in the range of 82°K can be achieved. Rather than rely on the evaporation mechanisms, separate liquid nitrogen supply containers were installed to service the primary transfer line and the annulus surrounding it. The vapor pressure at the primary transfer line supply vessel was maintained at 0 N/M² gauge (0 psig) right up to the time of recool. An artificial head pressure of 1406 kgf/M² gauge (2 psig) was then used to pump liquid nitrogen through the cryocooler. Use of the separate liquid nitrogen supply minimized the amount of expansion and cooling which would have been required with the plant facility supply, thereby insuring relatively quick delivery of liquid nitrogen at low temperature (77°K to 79°K) to the cryocooler.

Identical considerations also applied to the liquid nitrogen which was circulated in the annulus surrounding the primary transfer line. The heat transfer rate between the primary tube and annulus liquid was so large that the annulus liquid had to also be below 82°K in order to achieve required coolant temperatures in the cryocooler. Accordingly, liquid

nitrogen from the facility supply was used only to precool the annulus, and a second liquid nitrogen supply vessel was employed for supplying liquid to the annulus during the LRIR recool process. As before, the annulus liquid source was also stabilized at 0 N/M² gauge (0 psig) pressure prior to the recool procedure so that a supercooled liquid might be available.

Figures 6, 7 and 8 show the liquid nitrogen supply vessels as they were positioned to support the Nimbus F thermal/vacuum test. The 0.16 cubic meter (160 liter) bottle was used to supply nitrogen to the cryocooler; the 1.9 cubic meter (1900 liter) vessel contained liquid for cooling

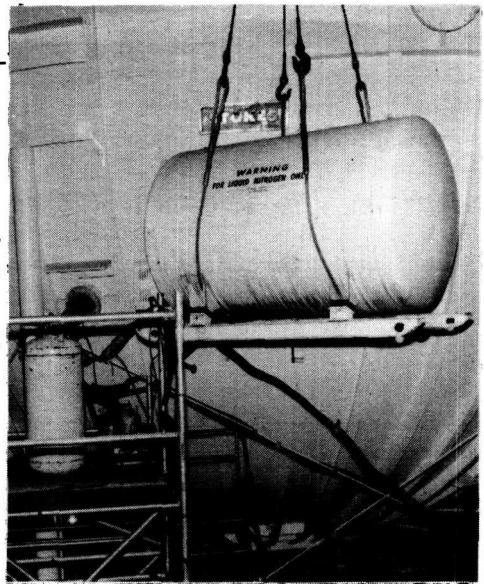


Fig. 6-Positions of Liquid Nitrogen Supply Vessels

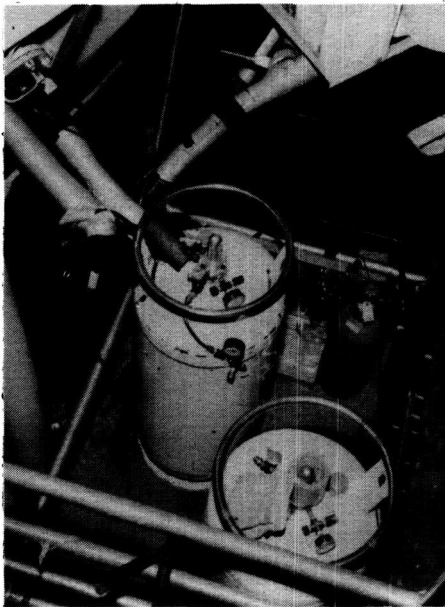


Fig. 7-Transport Line Configuration on Outside of T/V Chamber

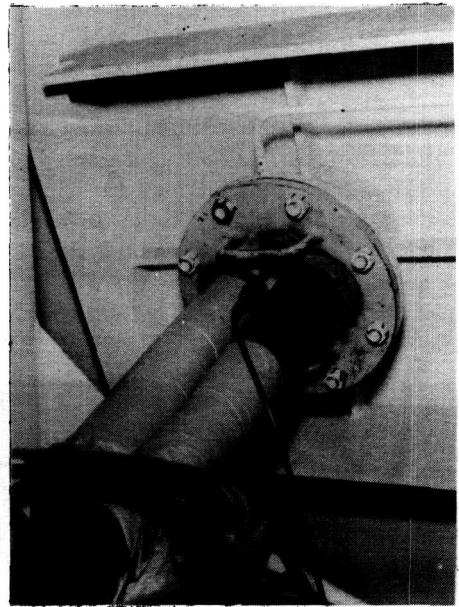


Fig. 8-Insulation Coverings on Transport Line Sections Exposed to Ambient Air

the annulus. The 1.9 cubic meter (1900 liter) tank was supported by an overhead crane with the aid of a Hydraset so that the weight of liquid usage might be recorded. The scaffold and supporting crane are indicative of the care taken to assure that the line lengths to the chamber wall be kept at a minimum. Note (Figure 8) the heavy insulation [7.6 centimeters O.D. (3 in.)] that was used to minimize ambient air heat transfer effects. This insulation is a flexible foam; it was fastened in place by the use of fabric backed pressure tape. Because of the contour of the thermal vacuum chamber, the approach taken by the transport lines toward the chamber was slightly upward. The loss in head pressure effected by this rise was calculated to be approximately 281 kgf/M^2 absolute (0.4 psia). For all practical purposes, the liquid nitrogen transport lines within the chamber were run parallel to the horizontal and in the same plane as the cryocooler fill valves. This, of course, was done to minimize gravitational effects and thereby the head pressure required to pump the liquid nitrogen.

To facilitate data taking during the test, platinum resistance thermometers and copper constantan thermocouples were installed at various strategic locations along the transport line, including the vicinity of the LRIR inlet and exit ports. This was done to provide an indication of the coolant temperature throughout the circulation path especially at that point where the coolant is about to enter the cryocooler. The annulus coolant temperatures between the chamber wall interface and the exit port were also measured with the aid of the temperature monitors.

The platinum resistance thermometers were supplied with a ceramic overcoat. The thermometers were bonded to the copper tubing using silver filled epoxy adhesive. The lead lines of the platinum thermometers were first insulated with thin plastic sleeving to preclude electrical shorting. Finally, the assembly was wrapped with kapton tape and covered over with the superinsulation blankets. Instrumentation lead lines were also taped to the copper tubes to prevent temperature read-out error resulting from heat transfer down the leads to the thermometers. A voltage divider circuit was used for resistance measurement and the results read out on a digital voltmeter. Prior to the test, the platinum resistance thermometers were calibrated in a liquid nitrogen bath.

To supplement the platinum resistance thermometers, copper-constantan thermocouples were placed at other locations on the coolant lines. The thermocouples were primarily intended to provide indications of temperature trends and to add additional credence to the observed performance of the entire recool system. The output of the copper-constantan thermocouples was fed into a Keinath data plotter which provided a continuous graph of temperature versus time for each thermocouple.

Finally, attention was directed to the residual liquid that remains in the transport line when the LRIR recool is completed. Since subsequent heat leak and excessive pressure build-up can be detrimental to the structural integrity of the cryocooler, it was essential that the liquid

nitrogen be completely expelled from the transport system under a controlled pressure. Furthermore, at the end of recool the liquid nitrogen supply had to be disconnected without resulting in a backflow of ambient air, which can introduce all sorts of contaminating materials to the system.

Accordingly, a liquid nitrogen evacuation procedure was devised which was charged with making sure that all of the liquid nitrogen has been vaporized and expelled from the transport system. A gaseous purge operation was then activated to prevent contaminants from entering the line. Electrical heating in the form of Nicrome heater coils wrapped around the surface of the outer tube in the double jacketed transport line (Ref. Figure 5) was used to effect the liquid vaporization. Neon gas served as a medium for safety purging and reconditioning the transport line in preparation for subsequent high vacuum pumping.

THERMAL ANALYSIS

The basic challenge regarding the recooling of the LRIR cryogens involved the actual achievement of liquid nitrogen flow for the transport tubing I. D. and lengths required. Accordingly, the main task was to prevent excessive pressure build-up in the transport line. This was accomplished by keeping all external heat leaks to a minimum with the use of insulation barriers and transport line jacket cooling, and by maintaining all line segments at the shortest possible lengths. Referring to pressure-temperature dependence data for liquid nitrogen, it is seen that an 82°K (or lower) liquid temperature can be achieved at the inlet to the cryocooler provided the vapor pressure is less than 6749 kgf/M² gauge (9.6 psig). Thus, if the flow resistance presented by the cryocooler and transport line is sufficiently small and the maximum permitted 4218 kgf/M² gauge (6 psig) head pressure results in a basically liquid state flow, then the vapor pressure would be somewhat less than 4218 kgf/M² gauge (6 psig) and low temperature liquid nitrogen (less than 82°K) would flow through the cryocooler.

The feasibility of single phase flow was demonstrated by an application of the Darcy-Weisbach equation

$$-\left(\frac{dp}{dL}\right)_f = \frac{f \rho V^2}{2 Dg} \quad (1)$$

The main difficulty in using this equation involves a determination of a suitable estimate for the friction factor f . By enabling evaluation of the pressure gradient the equation provides essential information as to what the liquid nitrogen temperature could be at any point along the recool line. To minimize pressure drop in the LRIR recool set-up specially manufactured refrigeration tubing was selected for use in constructing the transport line. The tubing was manufactured "plug draw" and was

furnished, as a result, with relatively smooth inside walls. Extrapolation of the data defining relative roughness for small diameter tubing showed the 0.63 centimeter (1/4 in.) tube to be on the asymptotic part of the performance curve (Figure 9). However, a relative roughness equal to 1.8×10^{-4} was indicated and this pointed to a friction factor of approximately 0.028³. A further calculation of friction effects was performed by making use of the relationship⁴

$$f = 0.184 \text{ Re}^{-0.2} \quad (2)$$

And still further by the equation⁵

$$f = 0.0056 + 0.5 \text{ Re}^{-0.32} \quad (3)$$

Results of equations (2) and (3) indicated friction factors of 0.026 and 0.028 respectively, which are acceptable duplications of the previous estimate. It is a well known

fact that the friction factor is dependent on the Reynolds number. With 4218 kgf/M² gauge (6 psig) head pressure, a Reynolds number of 17,000 was determined as being representative of a turbulent condition of flow.

Application of the Darcy-Weisbach equation to the liquid nitrogen transport condition with 4218 kgf/M² gauge (6 psig) head pressure indicated that a pressure drop of about 633 kgf/M² (0.9 psi) could be expected between the pressure head and the entrance to the LRIR cryocooler. Accordingly, this equation showed that delivery of liquid nitrogen at approximately 80°K to the inlet port of the cryocooler was entirely feasible. The importance of delivering liquid state nitrogen to the inlet of the cryocooler is paramount to the success of the recool operation, since it is the liquid itself which serves as the heat transfer medium for the cryogenics. However, to examine the liquid flow further, it is essential that the heat leak along the transfer line and in the LRIR experiment itself also be evaluated.

The heat absorbed by the recool system originated primarily from two separate and distinct sources: (1) the environment surrounding the liquid nitrogen transport line from the supply source through the ambient air and the thermal/vacuum chamber to the exit port, and (2) the cryogen dewar itself, where stored heat is actually removed from both the methane and ammonia masses. For all practical purposes, the principal heat

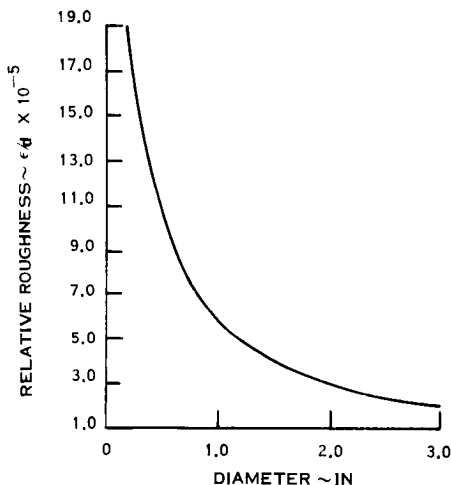


Fig. 9-Effect of Tube Diameter on Relative Roughness

leak into the transport line occurs at the ambient portion of the transport system; namely, at the 0.762 meter (2-1/2 ft.) section between the storage container and the chamber wall. Calculation established the 0.762 meter (2-1/2 ft.) inlet line loss at 17 watts. The heat leak was minimized by the use of thick walled foam insulation coverings over these lines. In addition, other heat leaks on the outside of the thermal vacuum chamber included the dewar storage container, pressure measurement and purge plumbing, and exhaust lines from the transport system. The total heat leak from all external sources was evaluated at 41 Watts.

Within the thermal vacuum chamber, the heat loss was considerably less despite the fact that the lines were much longer. This was a result mainly of the jacketed segment which represented approximately 80 percent of the total length. In relation to the other leaks in the transport system, the heat leak via the jacketed lines was effectivity zero, since the heat represented by all conductive and radiative couplings was absorbed by the coolant flowing in the annular part of the line. The heat leaks presented by the superinsulated sections of line and the foam insulated lines within the optical portion of the experiment were calculated to be approximately 15 Watts. These heat leaks were a result of conductive ties within the experiment and radiative couplings to the experiment and spacecraft.

The final heat leak to be considered was that absorbed within the cryocooler during the cryogen recooling and hardening process. Here, the calculation simply involved an accounting of the total heats absorbed by the cryogens and the dewar structure prior to recool, causing a rise in temperature from the desired levels to the level at the time of recool. Conductive losses via the cryocooler were ignored for this calculation since they were insignificant as compared to the heat capacities of the cryogens themselves. The heat absorption required to recool the cryogens and cryocooler structure was estimated to be 12 Watts.

The addition of heat to the recool system, no matter how small, eliminated the possibility of achieving totally single phase flow. Actually, the flow through the return leg of the transport line must necessarily be two phase in nature. Considering the calculated heat leak in conjunction with the anticipated mass flow rate under 4218 kgf/M² gauge (6 psig) head pressure, it was estimated that approximately 93 percent of the liquid nitrogen flow would pass through the transport system without vaporization taking place. Application of a correction factor of $(1 + G/Li)$ to account for the gaseous component in the Darcy-Weisbach equation showed that the pressure drop through the system would be increased by less than 7 percent. Table 1 gives the predicted performance of the recool system under a head pressure of 4218 kgf/M² gauge (6 psig). Heat capacity estimates involving those items of transport system hardware preceding the LRIR experiment indicated that approximately 0.9 minute duration would be required before liquid nitrogen arrived at the inlet to the cryocooler.

Table 1. Predicted Versus Observed Recool Performances

	Predicted				Observed During T/V			
					No. 1		No. 2	
Head pressure $\sim \text{kgf/M}^2$ gauge (psig)	4218	(6)	1406	(2)	1406	(2)	1406	(2)
Δp (@ cooler inlet - 19.5') $\sim \text{kgf/M}^2$ (psi)	1153	(1.64)	654	(0.93)	* 612	(0.87)	* 773	(1.10)
Δp (@ 17.5') $\sim \text{kgf/M}^2$ (psi)	1090	(1.55)	619	(0.88)	584	(0.83)	612	(0.87)
Δp (@ exit port) $\sim \text{kgf/M}^2$ (psi)	2039	(2.90)	1104	(1.57)	1019	(1.45)	1076	(1.53)
$Q \sim \text{cubic meters/hr} \times 10^{-3}$ (liters/hr)	43.5	(43.5)	5.0	(5.0)	* 3.7	(3.7)	* 3.4	(3.4)
$W \sim \text{grms/hr}$ (lb/hr)	35154	(77.5)	4037	(8.9)	* 2994	(6.6)	* 2722	(6.0)
$V_{Li} \sim \text{M/sec}$ (ft/sec)	0.66	(2.17)	0.21	(0.70)	0.18	(0.60)	0.16	(0.54)
$V_G \sim \text{M/sec}$ (ft/sec)	-		5.7	(18.7)	5.2	(17.2)	5.0	(16.5)
Re_{Li}	17000		2050		1400		1260	
Re_G	-		16000		15600		15100	
LN_2 temp. @ cooler inlet $\sim ^\circ K$	79.8		78.3		* 78.1		* 77.7	
$q \sim \text{Watts}$	70		70		70		66	
$\Delta t \sim \%$	3.6		30.9		41.6		44.1	
$\Delta p \sim \%$	2.94		1.25		1.15		0.74	
$\Delta \theta$ (deliver LN_2 @ inlet) $\sim \text{min.}$	0.9		8.6		* 3.0		++	

*measured data
**data not available

The encouragement provided by the results of these calculations led to an investigation of the minimum pressure head required by the recool system, since the anticipated amount of liquid flow showed that only a small portion of it would actually be used for cooling. However, before going on with this discussion, it might be appropriate to backtrack to the frictional aspects of the recool system and re-examine them in terms of the total hardware including valves, fittings and bends in the transfer line. To support this, use was made of the correlation³

$$\psi = (0.106)\left(\frac{r}{D}\right)^{-2.5} + (2000)f^{2.5} \quad (4)$$

which gives the fractional velocity head loss associated with tube bends and other resistances. Values of ψ were also determined for two ball type shut-off valves used at the inlet and outlet ports of the LRIR experiment. The pressure loss provided by the frictional aspects of all hardware in the transport line was determined in terms of equivalent tube length.

$$Le = \frac{\psi D}{f} \quad (5)$$

Calculations showed a total increase of 2.4 meter (7.8 ft.). Applying the Darcy-Weisbach equation once again a pressure drop of 872 kgf/M² (1.24 psi) was indicated at the inlet to the cryocooler, thus preserving the feasibility of cooling the cryogenes under a 4218 kgf/M² gauge (6 psig) head pressure.

Returning to the determination of the minimum pressure head required for recooling the cryogenes, reference is made to the method of Jacobs⁶ as described by Timmerhaus⁷. Although this method was apparently conceived with an application to much larger transfer line diameters, it was rationalized that the basic physical principles are equally applicable to small diameters, as long as a predominantly liquid flow can be achieved. Development of a flow equation for the transport system takes the following form

$$\frac{P_i}{P_o} = \frac{4L\tau}{Dp_o} + \exp \left\{ \frac{\lambda}{RT_o} \left[1 - \frac{1}{\frac{T_i}{T_o} + \frac{q}{W C_p T_o}} \right] \right\} \quad (6)$$

This equation relates the frictional and thermal aspects of the system and contains the basic definition that the minimum pressure ratio is equivalent to the frictional effect plus the thermal effect. By direct comparison with equation (6), this is written

$$\Pi p = \Pi f + \Pi t \quad (7)$$

Generally, it is expected that Πf should be the significant term if the flow rate and line length are large and the diameter small, and Πt the significant term, when the heat leak is large and the flow is small.

With further development and the incorporation of a few simplifying assumptions, Jacobs was able to express the frictional and thermal parameters by the relationships

$$\Pi f = (3.266) \left(\frac{L}{D^3} \right) \left[C_1 \left(\frac{Q}{D} \right)^2 + C_2 \left(\frac{Q}{D} \right)^{1.68} \right] \quad (8)$$

and

$$\Pi t = \exp \left[\frac{\lambda}{RT_o} \left(1 - \frac{1}{1 + \frac{q}{W C_p T_o}} \right) \right] \quad (9)$$

The constants C_1 and C_2 are functions of the specific properties of a given fluid and have been evaluated for liquid nitrogen⁸.

Before utilizing equations (8) and (9), it must be reiterated that the derivation only applies to single phase flow. Now, it has already been shown that there exists throughout the LRIR recool system a significant amount of heat leak which must necessarily be absorbed by the vaporization of liquid nitrogen. Accordingly, the flow, in reality, will be two phase in nature, with the ratio of gaseous to liquid phases increasing as the pressure head and mass flow rate are decreased.

Nevertheless, an attempt to use Jacob's equations was made by basically considering only the liquid flow region of the transport line. In this connection, it was hypothesized that if the heat leaks and flow rate as well as the friction effects are small enough, a stratified type of flow might be achieved where the liquid phase would be somewhat laminar and clinging to one side of the transport line. It might then be appropriate to apply Jacob's equations to the liquid region as a separate entity considering the hydraulic diameter of the effective liquid cross-section. In this way, the frictional parameter can be determined for the liquid component, since this has a significant bearing on the pressure drop and with that defines the minimum head pressure required for liquid flow. In the case of two phase flow where no appreciable radial static pressure difference exists, the total pressure drop may be considered equivalent to the pressure drop of the liquid phase alone.

Let us assume that the nitrogen flow in the transport system consists of two separate and distinct regions: 1) a gas phase, which was initially liquid and which absorbs all of the heat leaks in the system turning entirely to vapor by the time it reaches the exit port; and 2) a liquid phase, which absorbs no heat as it passes through the transport system. Since the total heat leak to the transport system is known, it is a simple matter to calculate the quantity of liquid flow that is required to absorb this heat. The flow rate was calculated to be $1.55 \times 10^{-3} \text{ M}^3/\text{hr}$ (1.55 liters/hr).

Applying equation (8) to the liquid phase, the frictional parameter is then calculated to be 0.19. Since the heat leak is assumed to be zero, the thermal parameter is simply equal to 1.0. The total pressure ratio is 1.19, which implies that the minimum head pressure required for liquid state flow is approximately 1898 kgf/M² gauge (2.7 psig). This number was interpreted as being indicative of the fact that a pressure head less than 4218 kgf/M² gauge (6 psig) and in the range of 1400 to 2100 kgf/M² gauge (2 to 3 psig) would result in liquid state nitrogen flow through the recool system.

Assuming that the static pressure drop for liquid and gas are equal, the two phase pressure drop may be determined from the relationship.

$$\left(\frac{\Delta p}{\Delta L}\right)_{TP} = \left(\frac{f \rho V^2}{2 D g}\right)_{Li} = \left(\frac{f \rho V^2}{2 D g}\right)_G \quad (10)$$

This equation showed that for a head pressure of 1406 kgf/M² gauge (2 psig), the two phase pressure drop would be approximately 844 kgf/M² (1.2 psi). The calculated pressure drops for liquid and gas respectively were 822 kgf/M² (1.17 psi) and 879 kgf/M² (1.25 psi). The Reynolds number for liquid flow was established at 2050 and the total mass flow rate through the system at 4037 gms/hr (8.9 lb/hr).

Having established a minimum tentative head pressure of 1406 kgf/M² gauge (2 psig) for the recool system operation, a check on the accuracy of the entire rationalization was now attempted by using the method of Martinelli and Nelson⁹ for two phase flow. This method is an amplification of a correlation applicable to isothermal, two component flow, with no vaporization of liquid to gaseous state. The two phase pressure drop is given as

$$\Delta p_{TP} = \Delta p_\ell \left(\frac{\Delta p_{TP}}{\Delta p_\ell} \right) + \frac{C_m M^2}{g} \quad (11)$$

where the factors $[\Delta p_{TP}/\Delta p_\ell]$ and C_m are determined graphically. Based on the expected quality of fluid flow and mass flow rate as determined previously, values for the unknown factors of equation (11) were determined. However, some difficulty was encountered in establishing a reliable friction factor for the determination of the pressure gradient $(\Delta p/\Delta \ell)_0$ under the assumption that the flow is totally liquid. For this condition the flow can be considered in a transitional state with an applicable friction factor as low as 0.018 or as high as 0.03. Using these values for f , the Martinelli-Nelson relationship indicated that the two phase pressure drop was somewhere in the range between 1336 kgf/M² (1.9 psi) and 2250 kgf/M² (3.2 psi). These pressure drops are in fairly good agreement with previously calculated data, thus adding further credence to the assumption that a head pressure of less than 4218 kgf/M² gauge

(6 psig) would result in liquid nitrogen flow and that this flow would be of a stratified, somewhat laminar nature.

The predicted performance of the recool operation with 1406 kgf/M² gauge (2 psig) head pressure is also presented in Table 1. The loss of liquid nitrogen due to flashing is a result of heat absorption along the transport line and within the cryocooler and of the frictional effects provided by the total line length including fittings and other hardware. Considering the cooldown dynamics which takes place at the beginning of the recool procedure, it was estimated that a time duration of approximately 8 minutes would be required before delivery of liquid nitrogen could be achieved. To preclude any time difficulties, it was specified that a 4218 kgf/M² gauge (6 psig) head pressure would be used at the outset of the recool procedure and later changed to 1406 kgf/M² gauge (2 psig) after approximately 30 minutes of the recool has elapsed.

RECOOL RESULTS

During the course of the fourteen day Nimbus-F thermal/vacuum test, ambient heat leak into the LRIR solid cryogen dewar made it necessary to recool the cryogens on two separate occasions. Figures 10 to 13 present temperature-time data corresponding to various points (Figure 3) along the transport line, covering the time periods before, during, and after the first recool operation. Notice the response of the transport line to precooling prior to the recool operation. The lowest temperature attained in the annulus during the precool was about 82°K as determined by the use of platinum resistance thermometers. This temperature was accomplished with the plant facility liquid nitrogen supply. The 1.9 M³ (1900 liter) supply was admitted to the annulus about 20 minutes before the recool was initiated. During this period the annulus temperature dropped from 83°K to 79°K.

The temperature of the superinsulated sections of transport line between the electrical isolator fittings and the cryocooler were significantly warmer than the precooled sections. These temperatures ranged from about 170°K at the isolator fittings to 235°K at the inlet connections to the LRIR experiment. Although no temperature monitor was available for the transport line segment within the experiment itself, it was reasoned that the temperature should reflect the environmental condition, and this was established with the help of other spacecraft monitors to be about 273°K. Once the recool is started the occurrence of liquid nitrogen flow is evidenced by a sudden drop of temperature at all instrumented points. A short duration spike in the temperature curve (return leg of transfer line) just prior to liquid flow indicates initial passage of a relatively warm gas. The time required for liquid delivery at the inlet to the cryocooler under 4218 kgf/M² gauge (6 psig) pressure was measured to be 3 minutes maximum. With the occurrence of liquid flow, all points of transport line instrumentation leading up to the LRIR experiment

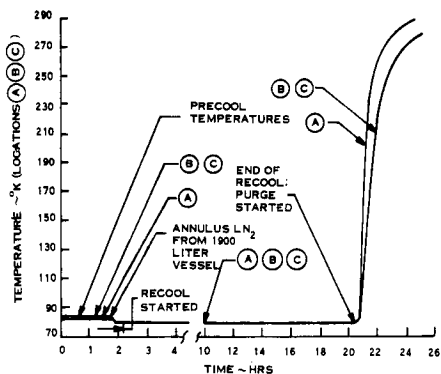


Fig. 10-Temperature Profiles for Transport Line Outer Jacket

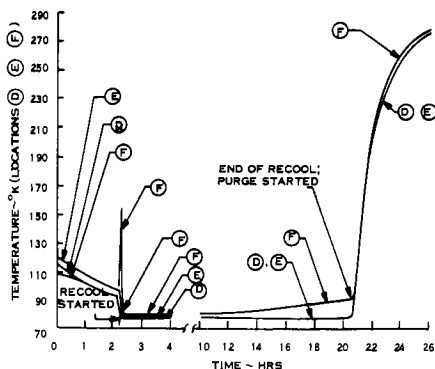


Fig. 11-Temperature Profiles at Extremities of Non-Jacketed Transport Line

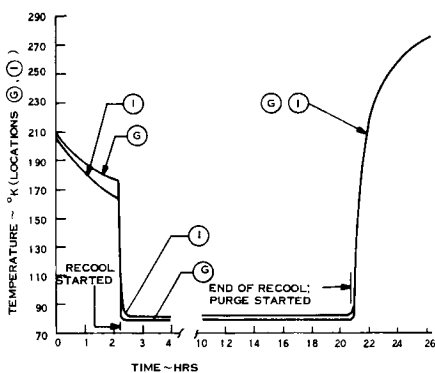


Fig. 12-Temperature Profiles at LRIR Side of Electrical Isolator Fittings

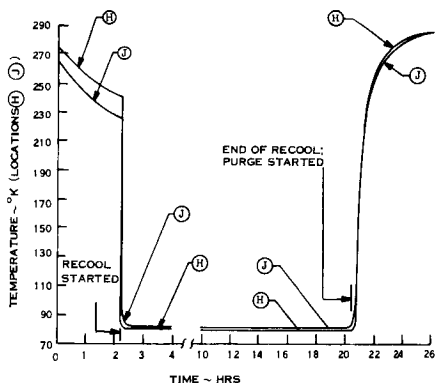


Fig. 13-Temperature Profiles at Inlet/Outlet Connectors of LRIR Experiment

showed themselves to remain at liquid nitrogen temperatures (80°K or lower) until the end of the recool.

Examining the response of the solid cryogen dewar to the recool operation, it is seen that a total time period of approximately eighteen hours was required to complete the cooling and hardening process. This is about the same time duration that is required to achieve similar results in ambient air when the cooling supply source is placed in close proximity [2.1 meters (7 ft.)] to the LRIR experiment. Graphs of cryogen tank temperature versus time are provided in Figures 14 and 15. This data shows an initial rise in the Methane tank temperature lasting for about 4 minutes duration followed by a steady decrease to a final temperature near 78°K . The initial temperature rise is a result of the relatively warm gas which precedes the liquid flow and passes down the tube after having absorbed the heat content of the transport line upstream of the cryocooler. The data shows that the Methane tank is first to cool and that the cooling period is relatively quick. The ammonia tank, on the other hand, requires the full eighteen hours in cooling from an initial temperature of 137°K to 82°K . Reasons for this difference are attributed to the larger thermal capacity associated with the ammonia tank and to the more efficient heat exchange that takes place between the Methane tank and the internal coolant tubing.

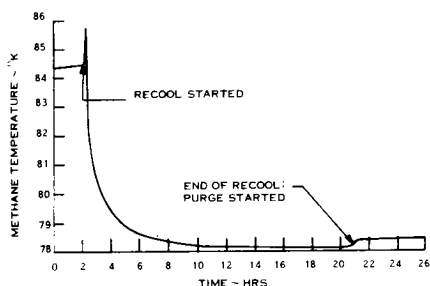


Fig. 14-Temperature Profile for Solid Methane During Recool No. 1

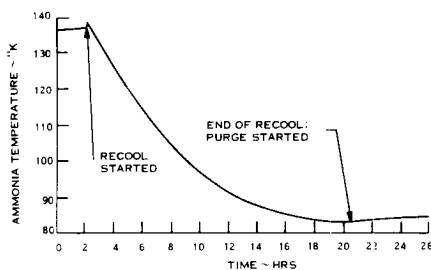


Fig. 15-Temperature Profile for Solid Ammonia During Recool No. 1

Transport line and solid cryogen temperatures corresponding to the second recool were essentially the same as those obtained in recool No. 1. Accordingly, temperature graphs are not presented for this recool, but comparison data is offered in Table 1 for the purpose of verifying the initial recool results.

Since the recool system was primarily constructed to service the LRIR experiment, measurement of physical flow data was performed on a limited basis wherever it did not interfere with the recool configuration or procedure. These data are presented in Table 1 for both recools along with the predicted performance. The remaining data listed under both 1406 kgf/M² gauge (2 psig) recool operations was calculated using the measured data as known quantities in the analytical relationships previously presented.

Comparison of the performance obtained with the LRIR recool to that predicted by analysis indicated that the flow rates and velocities were generally reduced with the actual recool. This is probably linked to an analytical underestimation of the friction forces and pressure drops within the system. In addition, error was introduced with the calculations involving the Darcy-Weisbach equation which did not include any expansion effects taking place at the transfer line exit port, where the pressure in fact is reduced to ambient. Considering the type of error historically involved in the prediction of cryogenic two phase flow, it is concluded that the observed performance of the LRIR recool system was fairly well predicted by the accepted mathematical techniques. The largest inconsistency occurred with the calculation that attempted to predict the time required for liquid state flow to arrive at the inlet to the cryocooler. It is felt in this case that closer results are obtainable with a more detailed mathematical model which would include the conduction paths and heat capacities of all components involved in the cooldown. This includes elements of the thermal vacuum chamber, spacecraft structure, and various filling and purging equipments which maintain a conductive link on the outside of the chamber.

At the end of the recool procedure, care had to be taken to assure that the liquid nitrogen flow could be stopped and the coolant lines returned to a high vacuum condition without endangering the cryocooler. This meant that all trapped liquid in the transfer line had to be completely evacuated without introducing a significant amount of heat or contaminants to the cryocooler. An electrical input power of 130 Watts was found to produce liquid nitrogen vaporization and subsequent evacuation at a safe rate. Figures 10 through 15 show the temperature-time response throughout the transport system during the heating cycle and for about 5 hours after it. Heat leak to the methane and ammonia tanks in this period is evidenced by the small temperature rises shown in the cryogen data curves of Figures 14 and 15. Fortunately, these heat inputs represented minimum levels only. Concurrent with the heating cycle the

transfer line was purged with Neon and Nitrogen gases to assure the removal of all liquids and possible contaminants. The total heating and purge procedure lasted for a duration of approximately 20 minutes. Subsequent to this, the transfer line was returned to the high vacuum condition.

LIST OF REFERENCES

1. "Limb Radiance Inversion Radiometer, Protoflight Model Final Report", R. W. Drozewski, J. C. Gille, J. R. Thomas, K. J. Twohig, R. R. Boyle, Honeywell Radiation Center, Lexington, Mass.
2. Keough, J. T., PIR 1R42-NF-261, "Electrical Isolator Fitting Used in the T/V LRIR Recool Plumbing", May 8, 1975.
3. Kent's Mechanical Engineers' Handbook, John Wiley and Sons, Inc., 1954.
4. Kreith, Frank, "Principles of Heat Transfer", International Textbook Co., 1963.
5. Koo, E. C., Ph. D. Thesis in Chemical Engineering, Massachusetts Institute of Technology, Cambridge, Mass., 1932.
6. Jacobs, R. B., "Single Phase Transfer of Liquified Gases", NBS Circular 596, 1958.
7. Vance, R. W., and Duke, W. M., "Applied Cryogenic Engineering", John Wiley and Sons, Inc., 1962.
8. Jacobs, R. B., NBS-CEL, Unpublished Calculations, 1957.
9. Martinelli, R. C., and Nelson, D. B., "Prediction of Pressure Drop During Forced Circulation Boiling of Water", Trans. Am. Soc. Mech. Engrs., 70, No. 8 (1948), 695.
10. Brown, A. I., and Marco, S. M., "Introduction to Heat Transfer", McGraw-Hill Book Co., Inc., 1958.
11. Scott, R. B., "Cryogenic Engineering", D. Van Nostrand Co., Inc., 1962.

NOMENCLATURE

p	= pressure	C_p	= heat capacity
Δp	= pressure drop	Π_p	= pressure ratio
T	= temperature	Π_f	= friction parameter
D	= hydraulic diameter	Π_t	= thermal parameter
L	= length	Q	= volumetric flow rate
ΔL	= increment of length	C_m	= momentum correction factor
f	= friction factor	M	= Weight flow rate per unit area
ρ	= density	g	= gravitational constant
V	= velocity	Δt	= LN_2 flashing loss due to thermal effects
Re	= Reynolds number	Δp	= LN_2 flashing loss due to pressure effects
G	= gas volume	$\Delta \theta$	= time increment
Li	= liquid volume		

ψ = fractional velocity head loss SUBSCRIPTS

r	= tubing bend radius	i	= inlet
L_e	= equivalent length	o	= outlet
τ	= shearing stress	TP	= two phase
λ	= latent heat of vaporization	Li	= liquid
R	= gas constant	G	= gas
q	= absorbed heat	ℓ	= liquid only
W	= mass flow rate		

**LEAK RATE MEASUREMENTS FOR SATELLITE SUBSYSTEMS AND
RESIDUAL GAS ANALYSIS DURING SPACE ENVIRONMENT TESTS**

H. Nuss,* *LABG, Laboratory for Space Simulation, D 8012 Ottobrunn, West-Germany*

ABSTRACT

The measuring and evaluation procedure for the determination of leak rates of satellite subsystems with a quadrupole mass spectrometer and the results of the residual gas analysis during space environment tests are described. The method selected for leak rate determination was placing the system into a vacuum chamber and furnishing the chamber with a mass spectrometer and calibrated leaks. The residual gas of a thermal vacuum test facility, in which for the thermal balance test radiation input was simulated by a heated canister, was analysed with the mass spectrometer in the atomic mass unit range up to 300 amu. In addition to the measurements during the space environment tests mass spectrometric studies with samples of spacecraft materials were performed. The studies were carried out during tests for the projects HELIOS, AEROS B and SYMPHONIE.

INTRODUCTION

Various ways for a leakage evaluation of a satellite system, subsystem or component have been considered in the past [1]. The method selected for the tests to be described in the following was placing the system in a vacuum chamber and measuring the leaking into the chamber with a mass spectrometer. In addition to the high sensitivity this method has the preference when performed during thermal vacuum or solar simulation tests to display the variation of the leak rate within the specified temperature limits. A number of techniques have been developed to detect molecular contamination of spacecraft, subsystem and experiments [2]. As possible test facility as well as possible spacecraft outgassing sources have to be taken into consideration supplementary investigations must be accomplished additionally to the measurements during the test in order to identify the outgassing sources.

*Present address: NASA Johnson Space Center, Space Environment Test Division, Houston, Texas 77058, where the author is working as an ESRO fellow. The paper involves work done at IABG and was written at JSC.

In the following the procedures for leak rate determination and residual gas analysis carried out with a Balzers QMG 101 quadrupole mass spectrometer are described.

1.0 LEAK RATE

1.1 Determination Procedure: The measuring set-up for leak rate determination is to establish the system to be investigated in a vacuum chamber and to furnish the chamber with the quadrupole mass spectrometer and a calibrated leak.

For steady-state conditions the leak rate of the system Q_s results in a partial pressure p_s and the calibrated leak effects a partial pressure p_e . The mass spectrometer responses H_s and H_e , respectively, are proportional to the number density of the particles i.e. at constant temperature conditions to the partial pressures:

$$\frac{H_e}{H_s} = \frac{p_e}{p_s} \quad (1)$$

With an effective pumping speed S_{eff} for the gas Equations (2) and (3) hold:

$$p_e = \frac{Q_e}{S_{eff}} \quad (2)$$

$$p_s = \frac{Q_s}{S_{eff}} \quad (3)$$

Assuming a constant pumping speed S_{eff} the following relationship results from Equations (1), (2) and (3):

$$\frac{Q_e}{Q_s} = \frac{H_e}{H_s} \quad (4)$$

In the actual measurement procedure for the peak height of calibrated leak H_e and of the system H_s the mass spectrometer response can result from additional sources (for instance chamber background) and therefore, the peak height of calibrated leak and chamber H_{e+k} and peak height of system and chamber H_{s+k} will be measured.

As the total mass spectrometer signal is a sum of the responses for the different partial pressures resulting from the different sources i.e. the total mass spectrometer response is an additive function of the responses for the different sources, the following relationships hold according to Equation (4):

$$\frac{Q_s}{Q_e} = \frac{H_{s+k} - H_k}{H_{e+k} - H_k} = \frac{H_{s+k} - H_k}{H_{e+s+k} - H_{s+k}} = \frac{H_{e+s+k} - H_{e+k}}{H_{e+s+k} - H_{s+k}} \quad (5)$$

H_{e+k} : Peak height for calibrated leak and chamber

H_{s+k} : Peak height for system and chamber

H_{e+s+k} : Peak height for calibrated leak, system and chamber
 H_k : Peak height for chamber

A comparison of the three parts of Equation (5) shows that using part 2 or 3 of the equation for the determination of Q_s/Q_e has the advantage that only one quantity (H_k or H_{e+k}) has to be measured before the actual environmental test.

An analysis of the measuring error by differentiating Equation (5) and calculating the expression $\Delta Q_s/\Delta Q$ shows with the assumption that the different peak heights can be measured in the optimum measuring range, the minimum error holds for:

$$H_{s+k} \text{ and } H_{e+k} \gg H_k \quad \text{and } H_e = H_s$$

This indicates that the measuring error is small when the response of the mass spectrometer due to the chamber background at the amu to be determined is small and leak rate of calibrated leak and of the system are in the same order of magnitude.

Equation (5) is valid for constant values of pumping speed S_{eff} and of characteristic parameters of mass spectrometer (high voltage, resolution). In addition, the dependence of the mass spectrometer signal from total pressure has to be analyzed to assure that the pressure variation occurring during the experiments does not affect sensitivity of the mass spectrometer.

In case the characteristic parameters of the mass spectrometer cannot be maintained constant throughout the measurements the following method is applicable:

According to Equation (4):

$$Q_s = Q_e \frac{H_{s+k}}{H_{e+k} - H_k} - Q_e \frac{H_k}{H_{e+k} - H_k} \quad (6)$$

$$Q_s = Q_{s+k} - Q_k \quad (7)$$

From Equation (6) and (7) follows, that the characteristic parameters of the mass spectrometer have to be constant during the determination of Q_{s+k} and during measurement of Q_k but can be different in both cases.

According to Equation (4) the following expressions can be derived:

$$\frac{Q_{s+k}}{Q_e} = \frac{H_{s+k}}{H_{e+k} - H_k} \quad (8)$$

$$\frac{Q_{e+k}}{Q_e} = \frac{H_{e+k}}{H_{e+k} - H_k} = \frac{H_{e+k}}{H_{e+s+k} - H_{s+k}} \quad (9)$$

$$\frac{Q_{e+s+k}}{Q_e} = \frac{H_{e+s+k}}{H_{e+k} - H_k} = \frac{H_{e+s+k}}{H_{e+s+k} - H_{s+k}} \quad (10)$$

$$\frac{Q_k}{Q_e} = \frac{H_k}{H_{e+k} - H_k} \quad (11)$$

From Equation (5) follows:

$$Q_s = Q_{s+k} - Q_k = Q_{e+s+k} - Q_{e+k} \quad (12)$$

According to Equation (8) to (12) the following relationships hold if the numbers 1 and 2 refer to different characteristic parameters of mass spectrometer:

$$Q_s = Q_e \frac{H_{s+k}}{H_{e+k} - H_k} \Bigg|_1 - Q_e \frac{H_k}{H_{e+k} - H_k} \Bigg|_2 \quad (13)$$

$$Q_s = Q_e \frac{H_{s+k}}{H_{e+s+k} - H_{s+k}} \Bigg|_1 - Q_e \frac{H_k}{H_{e+k} - H_k} \Bigg|_2 \quad (14)$$

$$Q_s = Q_e \frac{H_{e+s+k}}{H_{e+s+k} - H_{s+k}} \Bigg|_1 - Q_e \frac{H_{e+k}}{H_{e+k} - H_k} \Bigg|_2 \quad (15)$$

A comparison of Equation (13) to (15) shows that the application of Equation (14) or (15) for determining Q_s is to be preferred Equation (13) because of the number of measurements for the calculation of Q_s . Additionally Equation (13) does not correspond to the experimental conditions, because different mass spectrometer parameters generally are used for measurements with and without the system. Using Equation (15) has the advantage that the values to be measured are greater than in Equation (14) and therefore, the measuring error is smaller if the measuring range cannot be changed optimumly.

Concerning the test requirements four cases have to be considered:

1. Leak rate determination of a subsystem filled with a gas for which the mass spectrum is known and a calibrated leak is available.
2. The leak rate has to be determined equivalent to a Helium leak rate, because the system leak rate is specified for Helium. The subsystem contains a gas filling, whose spectrum is known and a calibrated leak is available.
3. The subsystem gas filling's spectrum is unknown, there is no calibrated leak of the gas filling available and the leak rate has to be determined in a rate equivalent to a Helium leak rate.

4. The subsystem is filled with a gas mixture (for instance a Helium-Nitrogen mixture) and the leak rate has to be determined for pure He gas.

Case 1: The subsystem leak rate $Q_{s, He}$ can be determined by application of Equation (5) or Equation (15).

Case 2: There are three possibilities. Assuming the system is filled with Argon and $Q_{s, A}$ and $Q_{s, He}$ are the system leak rates for Argon and Helium, respectively, the following equations [6] hold for constant temperature conditions (index A and He referring to Argon and Helium, respectively):

For molecular flow conditions

$$Q_{s, He} = Q_{s, A} \sqrt{\frac{M_A}{M_{He}}} \quad (16)$$

M: Molecular weight

For laminar viscous flow conditions

$$Q_{s, He} = Q_{s, A} \frac{\eta_A}{\eta_{He}} \quad (17)$$

η : Viscosity of gas

$Q_{s, A}$ can be determined according to Equation (5) or (15) and $Q_{s, He}$ can be calculated with the aid of Equation (16) or (17). For practical applications it is difficult to decide whether molecular flow or laminar viscous flow conditions have to be considered (see Case 4). The second possibility is to use Equation (5) or (15) for determination of $Q_{s, A}$ and measure the expression:

$$\frac{Q_{s, A}}{Q_{s, He}} = \frac{Q_{n, A}}{Q_{n, He}} = \frac{H_{n+k, A} - H_{k, A}}{H_{n+k, He} - H_{k, He}} \quad (18)$$

$Q_{n, A}, Q_{n, He}$: Leak rate of a needle valve for Argon and Helium, respectively.

H_{n+k} : Peak height for needle valve and chamber. The subscripts A and He refer to Argon and Helium, respectively.

The measurement is carried out by gas inlet of He and A through the constant opening of a needle valve, which has a leak rate in the same order of magnitude as the system to be detected. From Equation (18):

$$Q_{s, He} = Q_{s, A} \frac{Q_{n, He}}{Q_{n, A}} \quad (19)$$

From Equation (5), (18), (19):

$$Q_{s, He} = Q_{e, A} \frac{(H_{s+k, A} - H_{k, A})}{(H_{e+k, A} - H_{k, A})} \cdot \frac{(H_{n+k, He} - H_{k, He})}{(H_{n+k, A} - H_{k, A})} \quad (20)$$

The third possibility for the determination of the subsystem leak rate equivalent to a Helium leak rate $Q_{s, He}$ follows by considering the needle valve was calibrated with a calibrated He leak:

$$Q_{s, He} = \frac{Q_{s, A}}{Q_{n, A}} \cdot Q_{n, He} = \frac{Q_{s, A}}{Q_{n, A}} \cdot Q_{e, He} \frac{(H_{n+k, He} - H_{k, He})}{(H_{e+k, He} - H_{k, He})} \quad (21)$$

From Equation (5) and (21):

$$Q_{s, He} = Q_{e, He} \frac{H_{n+k, He} - H_{k, He}}{H_{e+k, He} - H_{k, He}} \cdot \frac{H_{s+k, A} - H_{k, A}}{H_{n+k, A} - H_{k, A}} \quad (22)$$

Comparing Equation (20) and (22) indicates that Equation (20) can be applied for the determination of $Q_{s, He}$ by calibrating the needle valve by a calibrated A leak, Equation (22) by using a calibrated He leak. Equation (22) has the advantage that it can be used when no calibrated leak for the subsystem gas filling is available.

Case 3: The system leak rate $Q_{s, He}$ can be determined by inlet of the gas whose spectrum is unknown through a needle valve and measurement of the characteristic peaks with the mass spectrometer. Then Equation (22) can be applied for calculation of $Q_{s, He}$ by following the measurement procedure, which leads to Equation (22).

Case 4: If the subsystem leak rate is measured for a gas mixture, (for example a He/N₂ mixture) the extrapolation to the subsystem leak rate for the pure gas is possible by the following procedure: For molecular flow conditions ($Q < 10^{-8}$ torr ls⁻¹, [3], [4]) for the measurement conditions (partial pressure in subsystem p_1 , leak rate $Q_1 He$) Equation (23) is valid:

$$Q_1 He = \frac{V_{He}}{4} \alpha A (p_1 - p_k) \quad (23)$$

V_{He} : mean velocity of gas molecule

α : probability for molecule emerging the leak

A: leak area

p_k : chamber pressure

If the system filling is pure Helium (pressure p_2 , leak rate $Q_2 He$) the following relationship holds:

$$Q_2 He = \frac{V_{He}}{4} \alpha A (p_2 - p_k) \quad (24)$$

For p_1 and $p_2 \gg p_k$ and constant temperature conditions:

$$Q_2 He = Q_1 He \frac{p_2}{p_1} \quad (25)$$

For laminar viscous flow conditions ($Q > 10^{-5}$ torr ls⁻¹, [3], [4]) for the measurement conditions (total leak rate Q_{tot} , leak rate for He $Q_{1\text{ He}}$ and for N₂ Q_{N_2}) the following expression can be derived from the basic relationship [6] for laminar viscous flow:

$$Q_{tot} = Q_{1\text{ He}} + Q_{N_2} = \frac{k}{\eta_{\text{He N}_2}} (p_{1\text{ He}} + p_{N_2} - p_k) (p_{1\text{ He}} + p_{N_2} + p_k)$$

(26)

$\eta_{\text{He N}_2}$: viscosity for He-N₂ mixture

$p_{1\text{ He}}, p_{N_2}$: partial pressure of He and N₂, respectively

$k = \frac{\pi r^4}{16 l}$, r: radius of the leak, l: length of the leak

For viscous flow the partial flows for He and N₂ $Q_{1\text{ He}}$ and Q_{N_2} , respectively, are a linear function of the concentration and therefore Equation (27) holds:

$$\frac{Q_{1\text{ He}}}{Q_{N_2}} = \frac{p_{1\text{ He}}}{p_{N_2}} \quad (27)$$

If the subsystem gas filling is pure Helium (pressure $p_{2\text{ He}}$) for the leak rate $Q_{2\text{ He}}$ the following relationship is valid:

$$Q_{2\text{ He}} = \frac{k}{\eta_{\text{He}}} (p_{2\text{ He}} + p_k) (p_{2\text{ He}} - p_k) \quad (28)$$

From Equation (26), (27) and (28) and with the assumption

$p_k \ll p_{1\text{ He}} + p_{N_2}$:

$$\frac{Q_{2\text{ He}}}{Q_{1\text{ He}}} = \frac{\eta_{\text{He N}_2} p_{2\text{ He}}^2}{\eta_{\text{He}} (p_{1\text{ He}} + p_{N_2}) p_{1\text{ He}}} \quad (29)$$

From Equation (29) assuming the experimental conditions $p_{2\text{ He}} = p_{1\text{ He}} + p_{N_2}$ the relationship of Equation (30) can be derived:

$$\frac{Q_{2\text{ He}}}{Q_{1\text{ He}}} = \frac{\eta_{\text{He N}_2}}{\eta_{\text{He}}} \cdot \frac{p_{2\text{ He}}}{p_{1\text{ He}}} \quad (30)$$

For the viscosity of a mixture (He - N₂) Equation (31) holds: (see [1])

$$\eta_{\text{He N}_2} = \eta_{\text{He}} \frac{p_{1\text{ He}}}{p_{1\text{ He}} + p_{N_2}} + \eta_{N_2} \frac{p_{N_2}}{p_{1\text{ He}} + p_{N_2}} \quad (31)$$

Because $\eta_{\text{He}} \approx \eta_{N_2}$ [7] from Equation (31) can be derived:

$$Q_2 \text{ He} \approx Q_1 \text{ He} \frac{P_2 \text{ He}}{P_1 \text{ He}} \quad (32)$$

Comparing Equation (25) and (32) indicates that for the measurement of leak rates for gas mixtures and extrapolation to pure gas conditions for molecular flow and laminar viscous flow the same relationships are applicable if the above mentioned assumptions are valid for the specific experimental conditions.

It must be pointed out that because of different pressure conditions and leak geometry of the subsystem leak and the calibrated leak flow conditions can also be different. It is feasible for one leak to be in the viscous flow while a second leak which passes an identical gas flow under the same pressure conditions could be in molecular flow. With change in pressure conditions the flow of gas through the two leaks will become widely different. The existence of the different flow conditions is basically caused by different leak geometry, specifically by different radius to length ratios. [1] [3] [4]

1.2 Experimental Results: In this chapter leak rate determination during the projects HELIOS, AEROS B and SYMPHONIE will be described. It will be shown, which problems existed, calculating leak rates according to the relationships mentioned in Chapter 1.1.

1.2.1 HELIOS Experiment E2: For this experiment the leak rate of the subsystem E2A, which contained n-Heptane $\text{CH}_3(\text{CH}_2)_5$, had to be determined in a leak rate equivalent to a Helium leak rate. According to Case 3 of Chapter 1.1 the characteristic peaks of n-Heptane were identified. Peaks were found for $m/e = 27, 29, 31, 41, 43, 57, 71$. This result is in agreement with other measurements [5]. The subsystem leak rate equivalent to a He leak rate $Q_{s, \text{He}}$ was determined according to Equation (22). To lower the measurement error for the peak height of n-Heptane with chamber H_{s+k, NH} the peak heights for the different m/e values were added. The results are shown in Table 1. The total chamber pressure was $p_k < 8 \times 10^{-6}$ torr.

$H_{k, \text{He}}$ was found to be negligible compared to $H_{n+k, \text{He}}$ and $H_{e+k, \text{He}}$ and with Equation (22) the following test results shown in Table 2 were calculated.

Though the results of the three measurements show good agreement an additional test filling the subsystem with He did not agree with the results of Table 2. This indicates the difficulty of leak rate determination for m/e values mentioned above, for which partial pressures can also result from other materials of the system to be studied. A measuring error can also be caused by contaminating other parts of the system during filling the subsystem. The first problem can be solved by measuring the chamber background peak height with the not with n-Heptane filled subsystems or by application of a longer evacuation time.

TABLE 1

Test	$\frac{H_{s+k}, \text{NH}}{\text{mm}}$	$\frac{H_k, \text{NH}}{\text{mm}}$	$\frac{H_{n+k}, \text{NH}}{\text{mm}}$	$\frac{Q_{e, \text{He}}}{\text{Torr ls}^{-1}}$	$\frac{H_{e+k}, \text{He}}{\text{mm}}$	$\frac{H_{n+k}, \text{He}}{\text{mm}}$
First leak test	177					
Chamber test		85	138	1.3×10^{-5}	15	990
Second leak test	175					
Third leak test (with LN_2 - cold trap)	125					
Chamber test (with LN_2 cold trap)		40				

TABLE 2

Test	$\frac{Q_{s, \text{He}}}{\text{Torr ls}^{-1}}$
First leak test	1.5×10^{-3}
Second leak test	1.4×10^{-3}
Third leak test	1.4×10^{-3}

1.2.2 AEROS B Flight Unit: During the space environment test of AEROS B Flight Unit three components were pressurized with three different gases (He, A, Kr) and the leak rates were determined with the quadrupole mass spectrometer and calibrated leaks. Table 3 indicates that the relative magnitude of the different measuring values result in a small measuring error. The values for the peak heights are given in arbitrary units. The chamber pressure during the measurements was $p_k < 5 \times 10^{-7}$ torr.

TABLE 3

System	Gas	m/e	H_k	H_{n+k}	H_{s+k}	H_{n+s+k}
1	He	4	2	2700	9	1500
2	A	40	13	630	90	3000
3	Kr	84	20	27×10^4	75	1500

From Equation (5), (21) and (22) the leak rates of the different components $Q_{s1, He}$, $Q_{s2, He}$, $Q_{s3, He}$ are given by the expression:

$$Q_{s, He} = Q_{n, He} \left(\frac{H_{s+k}}{H_{n+s+k} - H_{s+k}} - \frac{H_k}{H_{n+k} - H_k} \right) \quad (33)$$

The results were for $Q_{n, He} = 2.5 \times 10^{-3}$ torr ls⁻¹:

$$Q_{s1, He} = 1.3 \times 10^{-6} \text{ torr ls}^{-1}$$

$$Q_{s2, He} = 2.2 \times 10^{-5} \text{ torr ls}^{-1}$$

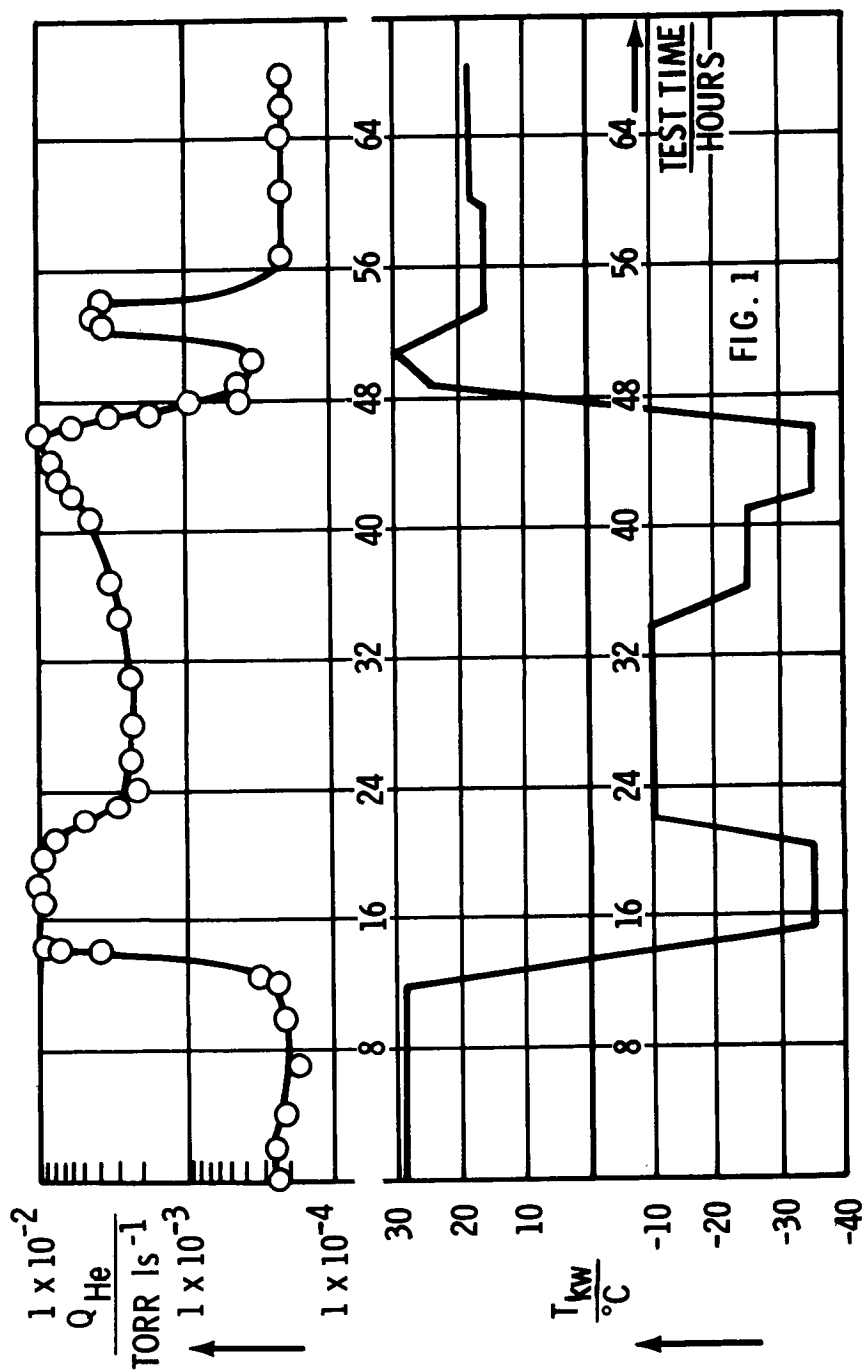
$$Q_{s3, He} = 1.3 \times 10^{-4} \text{ torr ls}^{-1}$$

These measurements show that the leak rates of three different subsystems could be determined during one test by using different gas filling He, A, Kr for the components and measuring the peak heights with a quadrupole mass spectrometer.

1.2.3 HELIOS Flight Unit: During the thermal vacuum test of HELIOS Flight Unit the leak rate of the cold gas system, which was filled with a mixture of He and N₂ in a ratio 1:5, was determined. The evaluation of the measurements was accomplished according to Equation (5) and (32). In Fig. 1 and 2 the leak rate of the cold gas system Q_{He} is shown as a function of test time and also the shroud temperature as a function of test time is plotted. The leak rate changes from 2×10^{-4} to 1×10^{-2} torr ls⁻¹ as a function of the shroud temperature, which corresponds to a changing subsystem temperature. The leak rate increases with decreasing shroud and subsystem temperature. Additionally, the leak rate rises when the temperature is changed, which indicates the dependence of the leak rate from a temperature gradient in the subsystem.

1.2.4 SYMPHONIE Prototype: The leak test required the determination of leak rates of the subsystems Hot Gas System (fluid part and high pressure part), Cold Gas System and Apogee Motor (fluid part and high pressure part) during one test using four different gases in the subsystems. According to earlier measurements carried out in the same facility with the satellite AEROS A this should have been possible also by filling the different subsystems not by pure gases but with the less expensive noble gas-nitrogen mixtures with a ratio 2:98.

The test results however indicate that for the achievable chamber pressure $p_k < 8 \times 10^{-6}$ torr and the used gas mixture ratio for Kr/N₂ and Ne/N₂ a high measuring error existed. This high measuring error was caused by the fact that the mass spectrum in the range of $m/e = 84$ and $m/e = 22$ has changed comparing chamber background measurement and leak test not only by the subsystem gas filling but also by other materials of the spacecraft. Therefore, it was necessary to extrapolate from the increase of the peak heights for m/e values in the range of $m/e = 84$ and 22 to the increase of the peak height for $m/e = 84$ and 22, which was caused by these



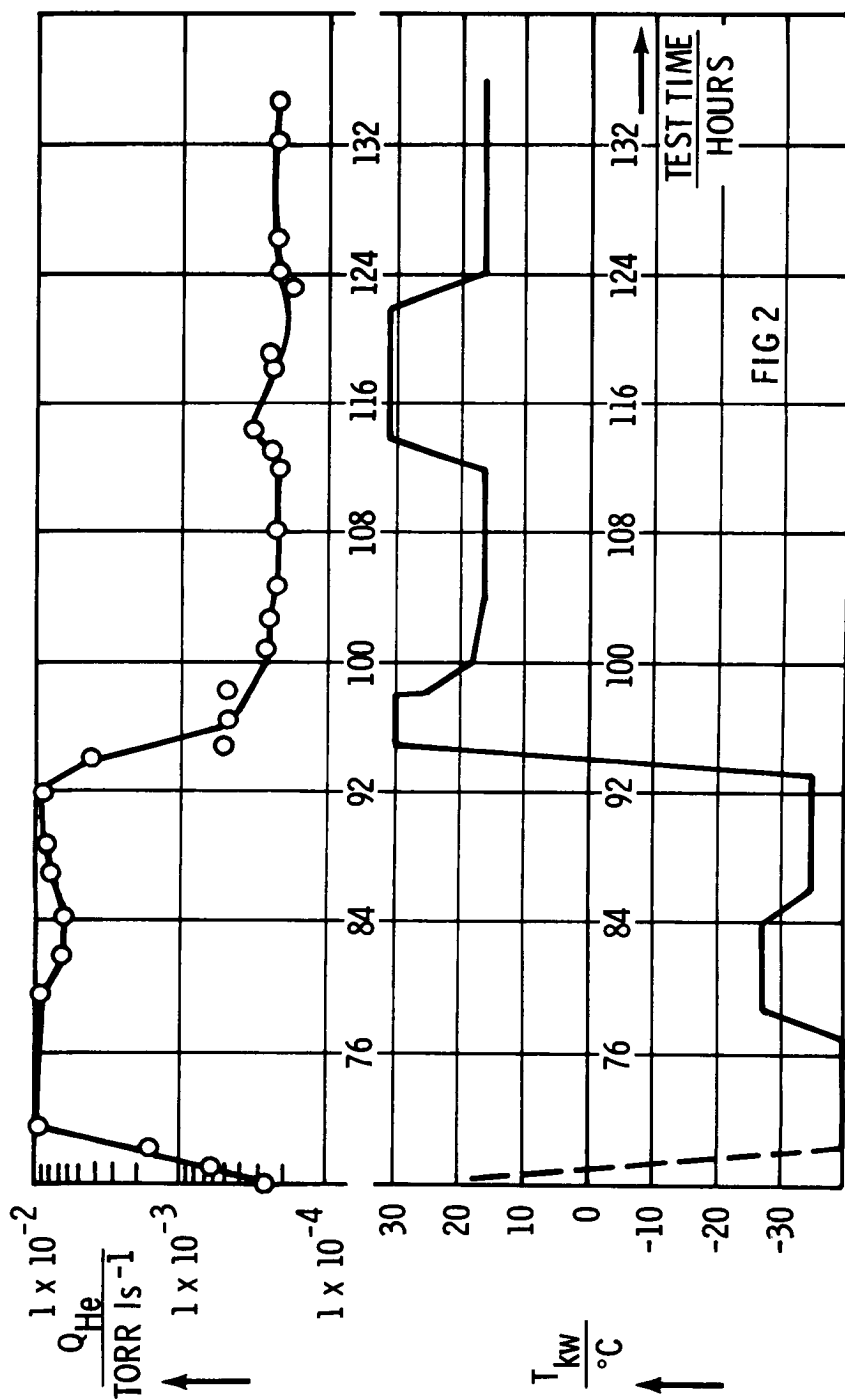


FIG 2

other materials and calculate the peak heights of the background during test. These tests indicate comparable difficulties as the measurements described in chapter 1.2.1. By using a higher amount of noble gas in the gas mixture or by reducing the background spectrum in a longer evacuation time the above mentioned measuring error could be decreased. Because both possibilities were cost intensive the leak test was carried out in three test phases pressurizing different subsystems during the three phases. The results are shown in Table 4. The evaluation was accomplished according to Equation (33).

TABLE 4

System	Gas	$Q_{s, He}$
		Torr ls ⁻¹
Hot Gas	He	$(7.6 \pm 6.0) 10^{-5}$
	Freon	$(2.5 \pm 2.5) 10^{-3}$
Cold Gas	He	$(1.8 \pm 0.4) 10^{-3}$
Apogee Motor	He	$(8.3 \pm 3.0) 10^{-4}$
	Ne/N ₂	$(0.5 \pm 9.3) 10^{-3}$

2.0 RESIDUAL GAS ANALYSIS

2.1 Determination procedure: The thermal vacuum chamber, in which the tests were carried out, was operated with two diffusion pumps with liquid nitrogen cooled baffles. Though due to the present construction of the chamber the quadrupole mass spectrometer was located in the space between cold shroud and chamber wall and not in the actual test volume, characteristic mass spectrometer peaks resulting from the test article and from the facility could be identified. Distinguishing between facility and spacecraft as outgassing source is based on the results of the chamber background measurement, of the mass spectrometer data in transition phases when shroud and spacecraft temperature are different, and of the sample measurements in a small vacuum chamber with materials used in the spacecraft (RTV 560, RNF 100 - 1, Aluminum - Magnesium Compound AlMg 3).

The partial pressures for the different m/e values were calculated by means of the total pressure and the ratios for the specific peak heights. This is an approximation, because the calculation does not consider different ionization probabilities.

2.2 Results and discussion:

2.2.1 Thermal vacuum test of HELIOS prototype: Measurements and evaluation was accomplished together with ESTEC [8], which in addition to the Balzers mass spectrometer QMG 101 or 311 operated by IABG measured with a Riber QML 51 mass spectrometer. Some of the following results include information due to discussions with ESTEC or due to other measurements carried out by ESTEC [9], [10], [8].

During the thermal vacuum test the temperature of the shroud was changed in the range -70°C and 45°C , the total pressure was $p_k < 7 \times 10^{-6}$ torr, the partial pressure for $m/e > 50$ was $< 10^{-8}$ torr for $T_{sh} = 25^{\circ}\text{C}$ and $< 10^{-9}$ torr for $T_{sh} = -35^{\circ}\text{C}$.

In Table 5 a typical change of the partial pressures during test due to different temperatures is shown for a peak which has its origin in the spacecraft (mean partial pressure p_1 for $m/e = 70$ and 78) and peaks which are caused by the facility (mean partial pressure p_2 for $m/e = 111$ and 149). T_{sh} is the shroud temperature, T_s the maximum spacecraft temperature.

TABLE 5

Test Time Hours	T_{sh} $^{\circ}\text{C}$	T_s $^{\circ}\text{C}$	p_1 Torr	p_2 Torr
30	30	35	1.5×10^{-9}	3×10^{-10}
48	-10	-10	2.5×10^{-10}	6×10^{-10}
52	-35	15	1.5×10^{-9}	8×10^{-11}
180	25	70	7×10^{-10}	8×10^{-10}
232	-45	-5	2×10^{-11}	2×10^{-11}
280	45	45	1.5×10^{-9}	1×10^{-9}

The temperature dependence of the partial pressure indicates an increase of p_1 , when the spacecraft temperature was raised from $T_s = -10^{\circ}\text{C}$ to $T_s = 15^{\circ}\text{C}$, whereas p_2 decreases when the shroud temperature is decreased from $T_{sh} = -10^{\circ}\text{C}$ to $T_{sh} = -35^{\circ}\text{C}$. These results agree with the information of the sample measurements and [9], [10]: The peaks for $m/e = 70, 78$ originate from RTV 560, the peaks for $m/e = 111, 149$ can be attributed to diffusion pump oil. $m/e = 149$ is found for phthalate, which is contained in diffusion pump oil, but is also used in plasticizers.

In a similar way the other measured peaks were identified:
 $m/e = 70, 78, 135, 147, 197$: RTV 560

$m/e = 69, 71$: Possible source is pump oil and RNF 100 - 1

$m/e = 73$: Silicone grease

$m/e = 87, 156$: Appears not during background test, so it has to be attributed to spacecraft.

m/e = 91: Origin is black paint, the peak is higher during test than in background measurement.

m/e = 105: RNF 100 - 1

2.2.2 Infrared Simulation Test of HELIOS Flight Unit: In this test the heat input to the spacecraft was simulated by a heated canister [11], the shroud temperature was $T_{sh} = -175^{\circ} \text{C}$. Figure 3 shows the dependence of the partial pressures for m/e = 70 and 78 and m/e = 111 and 149. At the time t_1 the shroud temperature has reached a constant value of -175°C and the canister heating was started. Figure 3 indicates the origin of the peak for m/e = 70, 78 in the canister or the spacecraft (partial pressure increasing with raising the temperature of the canister) whereas the partial pressure of m/e = 111 and 149 decreases with increasing test time and therefore indicates a source in the facility. At the time t_2 the simulated heat radiation was changed from a value corresponding to 6.6 solar constants to a value of 0.9 solar constants. At the time t_3 the temperature of the spacecraft and of shroud was increased to prepare repressurization of the chamber. The constituent of the masses m/e > 65 is 5×10^{-10} torr. Following additional peaks were measured:

m/e = 70, 78, 135, 147, 197: RTV 560

m/e = 73, 147, 191, 207: Silicone grease

m/e = 69, 71, 105, 235: RNF 100 - 1

m/e = 201, 203, 205, 217, 219, 233, 249, 250, 252, 267: No satisfactory explanation for these peaks was possible. Partial pressure is in the 10^{-12} torr range.

2.2.3 Outgassing Test of Thermal Canister for HELIOS F1 and Vapor Pressure of Al-Mg Compounds:

Before the infrared test for HELIOS flight unit the thermal canister was outgassed in a test during which the maximum canister temperature reached values of 230°C . The supporting structure used for the canister during this test consisted of an Aluminum-Magnesium compound Al-Mg 3, Material No. 3.3535. Because parts of the canister were built from a similar compound and no quantitative data about outgassing of this compound at different temperatures were available, the vapor pressure of Al-Mg 3 was determined using sample measurements in a small vacuum chamber. In the temperature range 40°C to 250°C the partial pressure of Magnesium was measured to be 2 to 3×10^{-9} torr and increased to approximately 10^{-7} torr for sample temperatures of 350°C . During the outgassing test of the canister the vapor pressure of Magnesium caused a visible change of the black painted grooved cold shroud surface on small areas. Chemical analysis of the deposit on the shroud and on the cryopanel also indicates Magnesium. HELIOS spacecraft used an Aluminum-Magnesium compound with a lower Magnesium content as Al-Mg 3. The vapor pressure of Magnesium measured during thermal vacuum testing of HELIOS prototype was in the 10^{-10} torr range, during TV test of HELIOS flight unit in the order of magnitude 10^{-10} to 10^{-11} torr, chamber background measurements showed pressures in 10^{-11} torr range. For all measurements the location of the mass spectrometer (Chapter 2.1) has to be considered. The results propose the consideration of vapor pressures in the mentioned

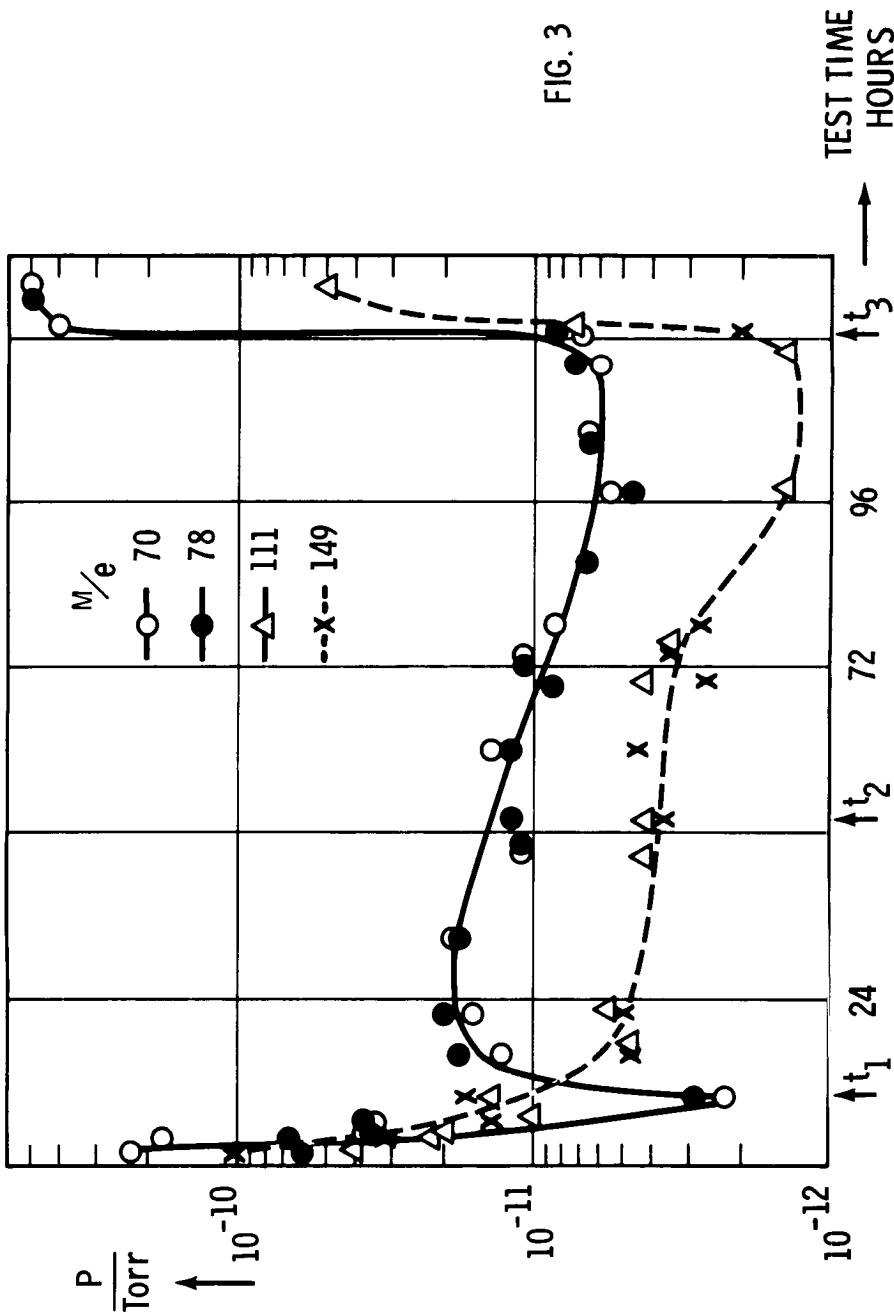


FIG. 3

to 10^{-11} torr, chamber background measurements showed pressures in 10^{-11} torr range. For all measurements the location of the mass spectrometer (Chapter 2.1) has to be considered. The results propose the consideration of vapor pressures in the mentioned order of magnitude 10^{-9} to 10^{-11} torr for sensitive experiments during tests and during the mission.

3.0 CONCLUSIONS

The applicability of leak rate measurements in the order of magnitude of the mentioned test requirements is shown. Difficulties concerning m/e values for which outgassing of spacecraft is super-imposed are discussed. Residual gas analysis in a test facility in the space between shroud and chamber wall has the capability to measure relative changes in vapor pressures and to distinguish between spacecraft and facility outgassing considering sample measurements and temperature dependence. Problems caused by Mg vapor pressure of Al-Mg compounds are indicated.

ACKNOWLEDGMENTS

The author wishes to acknowledge the diligent work of IABG personnel L. Krammer, P. Lau and J. Streuff in measuring with the mass spectrometer and in accomplishing data reduction.

The contribution of ESRO during the fellowship and the hospitality of NASA Johnson Space Center, Space Environment Test Division, is appreciated with gratitude.

REFERENCES

- [1] J. W. Marr: NASA CR - 952, 1968 , Leakage Testing Handbook
- [2] J. C. Goldsmith, E. R. Nelson: AIAA/ASTM/IES 5th Space Simulation Conf., 1970, p. 1
- [3] D. J. Santeler, Vac. Sympos. Trans., 1955, p. 31
- [4] D. J. Santeler, T. W. Moller, Vac. Sympos. Trans., 1956, p. 29
- [5] American Society for Testing and Materials, Index of Mass Spectral Data, 1969, p. 15
- [6] S. Dushman, Scientific Foundations of Vacuum Technique, John Wiley, Inc., 1962
- [7] J. H. Perry, Chemical Engineering Handbook, Section 5, McGraw Hill Book Co., New York, 1950
- [8] G. Sanger, Private Communication
- [9] G. Sanger, A. K. Franz, ESRO SP - 95, 1972, p. 383
- [10] G. Sanger, W. A. Shickle, ELDO/ESRO Scientific and Technical Rev. 1971, p. 507
- [11] J. Gulpen, W. Lorenz, ESRO SP - 95, 1972, p. 301

THE THERMAL SYSTEM FOR AN ENVIRONMENTAL CHAMBER

K. Srinivasan, *Engineer SC2, Space Science & Technology Centre ISRO Post, Trivandrum-22, INDIA*

K. Badari Narayana, S. Srinivasa Murthy and M. V. Krishna Murthy, *Department of Mechanical Engineering, I.I.T., Madras-600036, INDIA*

ABSTRACT

The design of a cooling and heating system for obtaining temperatures in the range of -60°C to $+120^{\circ}\text{C}$ on a thermal shroud is described. The proposed temperature control uses mechanical refrigeration with Freon-22 as the primary refrigerant, methanol as the secondary coolant for low temperatures and electrically heated ethylene glycol for high temperatures. The system is designed to give the following time-temperature characteristics:

- Lowering the temperature from $+30^{\circ}\text{C}$ to -60°C in 1.5 hours,
- Maintaining the temperature at -60°C for a period of 6 hours,
- Heating from -60°C to $+120^{\circ}\text{C}$ in 3 hours,
- Maintaining the temperature at $+120^{\circ}\text{C}$ for a period of 6 hours,
- Colling from $+120^{\circ}\text{C}$ in 1.5 hours.

A description of the system and its operation are given.

INTRODUCTION

Environmental testing to qualify flightworthiness of space bound components has attained a significant role in space research. When one considers the enormous cost of launching a space probe, it is absolutely imperative that the qualities and performance of each component and the spacecraft as a whole should be established beyond all reasonable doubt. One such environment is the space vacuum and temperature extremes likely to be encountered. Thus, over the past decade innumerable thermal vacuum chambers have been built for testing of spaceborne systems. While there is much choice left with designer for selecting a suitable vacuum system thermal engineer is faced with problems of selecting a refrigeration and heating medium to meet the specific requirements. The temperature range normally encountered is -60°C to 120°C . The lower limit is beyond the normal commercial regrigeration temperature range and yet falls too short of cryogenic range. Obviously the choice of cooling

medium plays a vital role. This problem has been analysed by Crane and Truman¹ who have compared the relative performances of a gaseous nitrogen system using liquid nitrogen injection into the stream, a brine-nitrogen system and a mechanical refrigeration method.

In the United States many thermal vacuum chambers work on the GN₂/LN₂ system. According to Monroe and Mac Swain² the advantages of such systems are low cost, availabilities of experience and equipment. However, in some cases when temperatures encountered are in the range -60°F (about -51°C) solid carbon dioxide has been used.³ The above reported works pertain to lower temperatures only. But, designing of a system for the whole range of -60°C to +120°C without GN₂/LN₂ poses some problems. This paper describes the advantages of a commercial refrigeration system using a secondary coolant for low temperature operation. The selection criteria for cooling and heating media are enumerated. The design details of the thermal system are included.

SELECTION OF HEAT TRANSFER MEDIA

A typical temperature cycle for design of thermal system is shown in Figure 1. The range of temperature is so large that gaseous nitrogen system with liquid nitrogen injection and heating could have been advantageous. However, in view of non-availability of bulk quantities of liquid nitrogen storage and transfer facilities, mechanical equipment and relative cost it is found that a commercial refrigeration system is more suitable. Further, refrigeration plants down to -60°C are satisfactorily operating in seafood industries and reliability for long term operation is established. On the other hand blowers for pumping dense gaseous nitrogen in the temperature range of interest are not indigenously available. Further, in order to achieve close temperature control of $\pm 2^\circ\text{C}$ it is essential to use large quantities of gaseous nitrogen which obviously needs pressurization. Another disadvantage is that certain quantity of gaseous nitrogen should be constantly removed from the system so that system pressure remains constant. This results in wastage of refrigeration effect. Leakage problem in the shroud is more severe for high pressure gas flow. Thus, it has been found to be highly feasible to go in for conventional refrigeration system to obtain low temperatures.

The possibility of allowing directly expanding refrigerant in the thermal shroud was explored. Though this method allows lower temperature limits, it is uneconomical where the chamber is located at a distance from the refrigeration system. Freon-22 is selected as refrigerant in view of its higher evaporating pressures at -60°C compared to Freon-12 or ammonia. Reverse cycle operation to enable the system to work as a heat pump for obtaining shroud temperatures above ambient was considered. It was observed that temperature control on the shroud becomes too difficult and the system design becomes complicated due to

the additional condenser required. Further close temperature variation is practically impossible with such a system. The evaporator of the reverse cycle needs special care in design and construction.

Consequently it was decided to use a secondary heat transfer medium. It is very difficult to find a single liquid which operates satisfactorily in the entire temperature range of interest. Probable fluids are aqueous solutions of inhibited glycols. Operation with the fluids below -60°F is not recommended⁴ as the viscosity of the fluids increases enormously at very low temperature and large pumping powers will be required. However, above ambient temperature operation with inhibited glycols is reported to be satisfactory. In the present design methyl alcohol is selected for operating in the range -60°C to $+30^{\circ}\text{C}$. The viscosity even at -60°C is sufficiently low and freezing point also is much below the limits of interest. Ethylene glycol is selected as secondary heat transfer medium for operation between 30°C and 120°C . Since the flow channels for both fluids are same it is necessary to check the compatibility of two fluids. It has been established⁴ that the two fluids namely methyl alcohol and ethylene glycol are miscible. It may be observed that there is ample overlap between the range of operation of the two fluids (i.e., from -20°C to $+30^{\circ}\text{C}$) in which zone either of the fluids may be selected.

DESIGN OF THE SYSTEM

The design specification of the thermal system include, the details of thermal shroud, transient period, the details of the components to be tested and shroud temperature limits. The temperatures indicated in Figure 1 are shroud temperatures. The design sequence is: (a) calculate the heating/cooling load, (b) determine the flow rate of secondary heat transfer fluid, pump capacity and line size, (c) select a suitable refrigerant compressor, calculate evaporator dimensions and (d) design the heating circuit.

Cooling load is calculated for transient and steady state cases. The transient load comprises of cool-down of shroud, connecting pipe lines, secondary fluid, the container, and test specimen. The steady state load is calculated based on conduction and radiation heat transfer from vacuum chamber to shroud, heat leak to the system through insulation etc. Since transient load is invariably larger than the steady state load the design should be based on transient heat load. Sufficient margin (20%) of safety is allowed to make sure that the transient conditions are satisfied. The net design heat load for the case under study is 1.5 tons at -66°C .

The secondary fluid flow rate in case of methyl alcohol has been calculated based on allowable temperature drop of 3°C though the shroud and 6°C in case of ethylene glycol. The mass flow rate is based on transient load due to shroud. The temperature uniformity over the shroud is expected to be better under steady state conditions.

A two stage compound compression refrigeration system is selected to cool the alcohol tank. The cycle is shown in Figure 2. Since the maximum permissible shroud temperature is -58°C , alcohol at the tank should be below this temperature. Use of good insulation on the pipe lines can restrict temperature rise to 1°C . From this, temperature rise due to pump work is subtracted to obtain alcohol temperature. Allowing for an overall temperature difference of 3.5°C between alcohol and refrigerant (R-22) in the coil the evaporating temperature is fixed at -66°C . The evaporating pressure for this temperature⁵ is about 0.27 kgf/cm^2 . Condensing temperature is selected at 40°C which is about 10°C above peak ambient temperature. A water cooled condenser is selected to handle the anticipated heat load.

The selected compressor capacity at 66°C is found to be 1.91 tons, by reducing the speed of compressor the capacity also may be brought down to designed range. However, condenser and evaporator are designed to handle full rated capacity of compressor. A flash type inter cooler is provided for cooling of refrigerant between low and high stages. All the refrigeration pipe lines have been designed in accordance with guide lines laid down by ASHRAE.⁴

Design of the evaporator coil posed a major problem. The evaporator coil made of 16 mm o.d. soft drawn copper tube is immersed in a well insulated methyl alcohol tank. This cooling unit is taken as a shell and coil type heat exchanger. The heat transfer coefficient in the tube for R-22 is calculated based on nucleate boiling correlation for boiling of outside horizontal cylinders given by Giarratano and Smith⁶ which is reduced form of correlation given by Breen and West water.⁷ Heat transfer coefficient on alcohol side is calculated based on natural convection correlations.⁸ Properties of methyl alcohol are obtained from Reference 9. The evaporator is designed for steady state heat load. However, the length of the coil so obtained is checked to suit the transient load as well.

Heating circuit design did not pose many problems. Electrical immersion type heaters are suggested to heat up ethylene glycol in the tank. Since mixing of the cold and hot fluids is to be avoided as far as practicable, the heating capacity is dispersed through the fluid so that each heater can be cut off or on. Further the heater voltage is controlled through a dimmerstat. Thus, close heating control becomes inherent in the system.

Since warm-up of the system from -60°C to ambient is likely to take a lot of time if left without external heating, the methyl alcohol tank is provided with immersion type multiple electrical heaters so that rapid heating takes place. However, suitable controls are provided to cut off the heater when the alcohol has attained a temperature of about 30°C . Similarly the ethylene glycol tank is incorporated with a chilled water coil to bring down the temperature from 120°C to 30°C . Temperatures in between -60°C and $+30^{\circ}\text{C}$ can be obtained by adjusting the thermostatic expansion valve of the refrigeration circuit and heaters in the alcohol tank.

Similarly if any temperature in between 30°C and 120°C is needed the heater voltage is ethylene glycol tank can be controlled. At the same time the chilled water coil can also be activated.

The schematic thermal system is shown in Figure 3. The valves in the secondary fluid circuit enable draining of shroud during transferring operation from cold to hot side or vice versa.

CONCLUDING REMARKS

The environmental chamber using two secondary heat transfer media, namely ethylene glycol for above ambient and methanol for below ambient temperature operations is expected to give the desired temperature in the range -60°C to +20°C. A commercial refrigeration system with Regrigerant-22 as medium in compound compression can effectively meet the cooling requirements, while electrical heating can meet the heating requirements. A close temperature control is inherent in this design.

REFERENCES

1. T. H. Crane and J. A. F. Truman, "Thermal Control Systems for Space Simulators," Proceedings of Institute of Environmental Sciences, pp. 449-455, (1963).
2. K. W. Monroe and W. F. Mac Swain, "Environmental Control System for F-111 Low Temperature Proff Load Chambers," Proceedings of Institute of Environmental Sciences, pp. 207-214, (1972).
3. R. W. Carr, "Automatic Temperature Control of Cryogenically Cooled Space Simulation Shrouds," Proceedings of the Institute of Environmental Sciences, pp. 200-206, (1972).
4. ASHRAE Hand book of Fundamentals. Publication ASHRAE, Inc. New York (1972).
5. A. V. Kletskii, "Thermophysical Properties of Freon-22," Israel Programme for Scientific Translations, Jerusalem, (1971).
6. P. J. Giarratano and R. V. Smith, Adv. Cry. Engg., 11, p. 492, (1966).
7. B. P. Breen and J. W. Westwater, Chem. Engg. Prog., 58, p. 67, (1962).
8. Hand book of Heat Transfer, Eds: W. M. Rohsenow, and J. P. Hartnett McGraw-Hill Book Comp. (1973).
9. Handbuch der Kaltetechnik, Ed: R. Planck, Springer-Verlag, Berlin, Vol. 4, (1962).

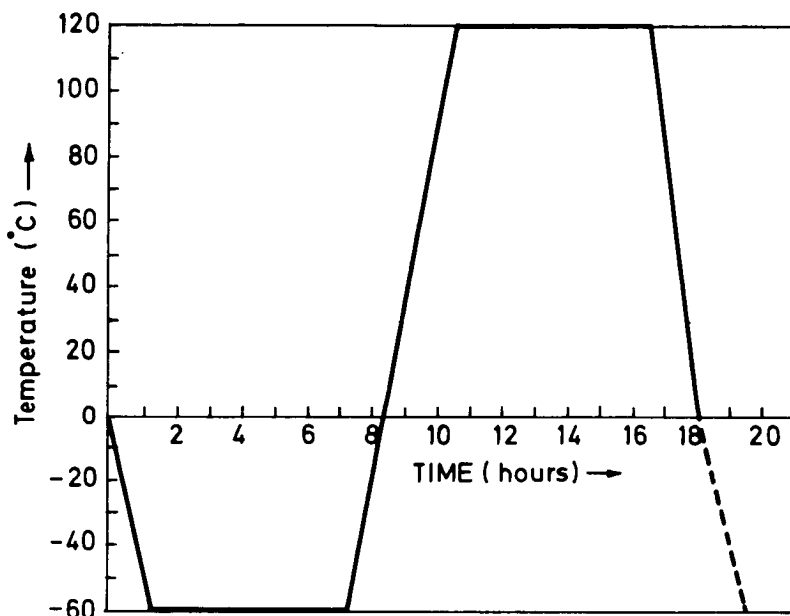


Figure 1. Time-Temperature Characteristics

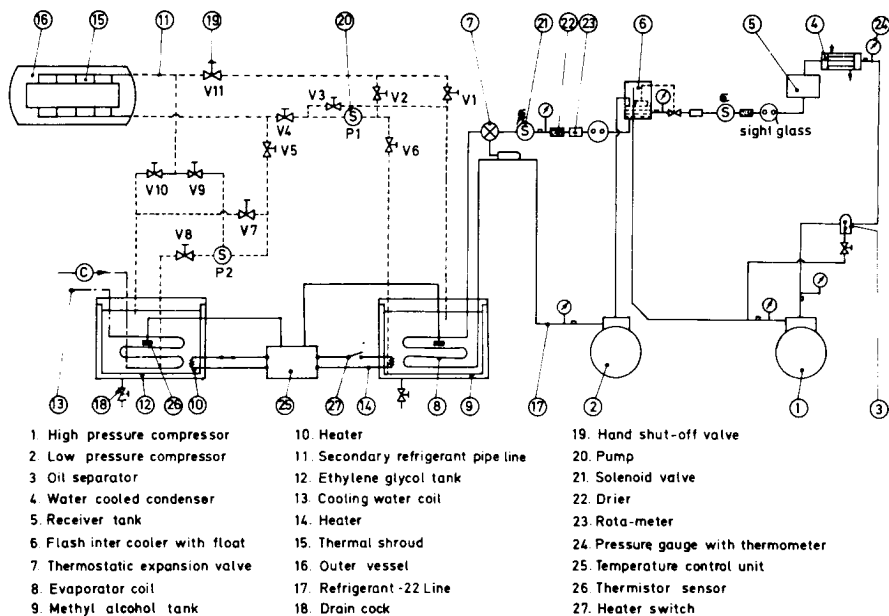


Figure 2. Schematic Arrangement of the Thermal Environmental System

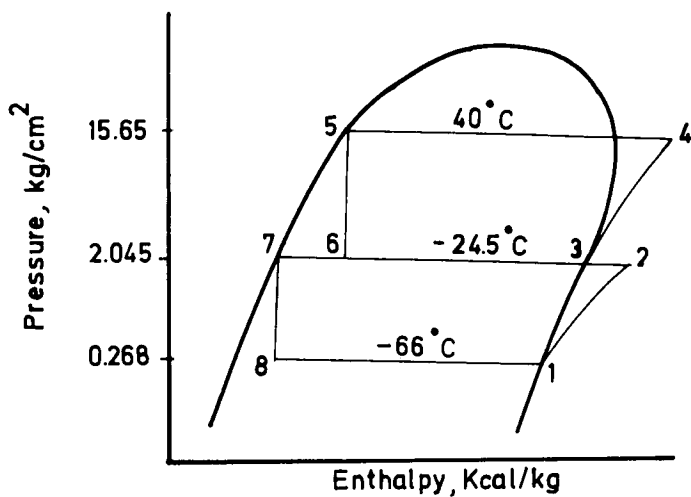


Figure 3. Pressure-Enthalpy Diagram for System in Figure 2

VACUUM CONSIDERATIONS IN THE DESIGN OF A SPACE SIMULATOR

S. Ramachandran, *E.T.D. Project, Vikram Sarabhai Space Centre, Trivandrum*

INTRODUCTION

The space environment is entirely different from the environment that is found on earth. It is characterized by an atmosphere whose density (Fig. 1) is much lower and whose chemical composition is different. In addition, intense solar and cosmic radiation, ions, electrons and meteorites are present. Vacuum plays a prominent role in simulating the effects of above environmental factors in a space simulator.

The design details of a particular type of space simulator depends on the particular type of environmental conditions to be simulated and tests to be conducted. Test chambers vary from small laboratory type chambers to system chambers with diameters of over 100 feet. Pressure vary from 10^{-2} to 10^{-14} Torr and the amount of auxiliary simulation equipment vary from none to large complex multienvironment facilities.

Today the Vacuum Engineer has at his disposal a wide selection of well designed and reliable vacuum products. Also, there is a wealth of established practice to aid him in setting up a functional system to meet the exact requirements of each specialized application. Even with all this available background data and reliable information, our industry is faced with host of new problems because of widening field for application of vacuum. The techniques of design, construction, and testing of equipment for each vacuum application is different from that of a conventional system. It is true, especially, in the areas of space simulation which are not so familiar and a careful interpretation of requirements and application of sound design are necessary for the functional success of the system.

This paper gives a brief account of some of the vacuum considerations in the techniques for design, fabrication and testing of a space simulator. Much stress is given to one using a diffusion pump—Rotary Pump combination for the vacuum system.

VACUUM ASPECTS OF A SPACE SIMULATOR

In a space simulator it is the effects of the spatial environment that is simulated and not the actual environment.

A pressure in the range of few torr will simulate the gross pressure effects of the outer space. But the thermal conductivity of the gas at this pressure is nearly the same as at ambient pressure. To attain a good simulation of the thermal environment of outer space, the pressure should be reduced to a point where the thermal conductivity of the gas is very small compared to the radiant heat transfer. Test vehicles operating at normal temperature range require a pressure of 10^{-5} Torr.

At 10^{-5} Torr glow discharge phenomena may pose problems. A reduction of pressure to a level of 10^{-6} Torr permits voltage in the KV range to be used without complications.

Another consideration is the outgassing of materials in a manner equivalent to that of outer space. To reduce the probability of molecules returning to the vehicle in a space simulator the wall should retain the molecules impinging on them. To achieve this, the walls are cooled to very low temperatures.

Walls cooled to liquid nitrogen temperatures condense out hydrocarbons, carbon dioxide and water vapor. At liquid hydrogen temperature all gases except Helium, Neon and Hydrogen are condensed out. At liquid helium temperature all gases except helium are condensed. Thus, these cooled walls besides simulating the conditions of outer space acts as cryopump to remove gasses by condensation on cooled walls.

Simulation of the environmental characteristics are a function of the test item and purpose of the test. For verification of thermal balance calculations and other investigations a vacuum of the order of 10^{-5} Torr are required to eliminate heat transfer by conduction and convection. Areas of test evaluation and study such as radiant heat transfer, corona, material evaporation, surface sensitive electrical and mechanical properties, etc. necessitates the vacuum of 10^{-8} Torr or lower.

CHAMBER DESIGN DECISIONS

The major decisions regarding the chamber design are

1. Chamber configuration - A decision must be made between single walled and double walled vacuum chambers. Single walled chambers are simple, accommodate feed throughs very easily and can readily be leak checked. Double walled chambers are made attractive for bake out, can provide shorter operating schedules, and far more tolerant of the leaks. If more weightage is given to simplicity and low cost, decision has to be taken in favour of single walled chamber.
2. Chamber seals - Access door, feed throughs and major joints require seals. In each case the designer must compromise between the ease of assembly and disassembly, likelihood of leaks and cost. On the whole welded seals are preferred where disassembly is not a frequent requirement.

BASIC STEPS IN THE SYSTEM DESIGN

The first step is to study the basic character of the experimental piece in terms of the adsorbed gases. The physical cleanliness is also another important factor.

The second step is to study the test procedure which may affect the system pressure—in the thermal performance test, during hot soak there will be considerable evolution of gases from the chamber walls and test load.

Third step is the factor of system economics. Vacuum systems and equipment intended for simulation system should be capable of maintaining a pre-determined role during test operation. Its failure to fulfill the basic requirement will lead to erroneous results. It is just as unwise to overdesign the system and equipment as it is economically disastrous to minimize or under estimate the actual requirements. The combined data from step one and two, vacuum to be maintained during the simulator test, together with the data from step three form the key to both the selection of vacuum equipment and system components.

Figure 2 represents the schematic diagram of the vacuum system for a space simulation. A complete and sound specification properly orients the manufacturer and helps him to proceed in an intelligent way.

SELECTION OF PUMPS

The vast region of pressure are divided as:

Vacuum:	760 Torr	- 0 Torr
Coarse vacuum:	760 Torr	- 1 Torr
Medium vacuum:	1 Torr	- 10^{-3} Torr
High vacuum:	10^{-3} Torr	- 10^{-6} Torr
Ultra high vacuum:	$< 10^{-6}$ Torr	-

Figure 3 shows different vacuum pumps operating in the above ranges.

Steam ejectors are available in wide range of types and capacities and are adapted to applications where large quantity of water vapor and other condensables are evolved during the process cycle.

In the medium vacuum range we have oil sealed rotary pumps which gives a pressure as low as 5×10^{-3} Torr. With booster in combination the pressure can still be reduced to 10^{-4} Torr. When equipped with controlled gas ballast these pumps can handle condensable vapors within the limits defined by the equipment manufacturer. Besides the primary pumping action, oil sealed mech. pumps act as a backing pump to booster pump, oil diffusion pump and ion pump.

The diffusion pump backed by a suitable rotary pump is the conventional assembly for the high vacuum range. There is a considerable

overlap both in the pumping speed and ultimate pressure attainable with booster ejector, diffusion ejector and fractionating ejector type of available pumping units. Selection of optimum unit is governed by such factors as desired pumping speed at a given pressure level.

Ionization type of pumps are best suited for non cyclic operation. In operation both ion pump and system is first evacuated to a pressure of the order of 10^{-2} Torr using an oil sealed rotary pump. Since no backing pump is required for ion pumping the oil sealed pump can be isolated from the system by means of a valve.

While selecting the pump it should be kept in mind that the published data relative to the curves for the pumping speed are based on the unvalved units and in the case of diffusion pump such data should be interpreted as pumping speed and pressure at the inlet flange.

The connection of vacuum components such as valves and piping between the chamber to be evacuated and pump inlet can reduce the pumping speed considerably.

SIZE AND CAPACITY OF PUMPS

Two conditions which govern the calculation of the pumping capacity for a system are:

1. Assume a tight system containing only air or other noncondensable gases at atmospheric pressure
2. Assume a known rate of evolution of gas from the chamber. The main sources of gases include outgassing of walls of the chamber, decomposition products from the pump, leaks through seals, and gas evolved from experimental piece within the chamber.

Inherent leakage, gas bursts or other contingencies suggests the application of a system factor, especially where exact conditions are not known. However, caution must be exercised in the application of the system factor, otherwise they tend to overdesign the system.

INFLUENCE OF CONDENSABLE VAPORS

The presence of large amount of condensable vapors reduce the overall efficiency of the pumping equipment. This is true when the operating pressure falls below 1 Torr.

Limited amount of condensable vapors are handled by a rotary pump with the addition of a gas ballast. Vapor handling capacity of a particular pump can be had from manufacturers data.

In large system which involve large rotary pump use of oil circulation and purification equipment have proved more useful.

In the high vacuum application the inclusion of a cold trap in the suction manifold is the effective means of removing vapor from the pump. A

mechanically refrigerated trap is effective in the range 0 to -40°C , dry ice over the range -40°C to -78°C and liquid nitrogen -80°C to -180°C .

SIZE AND DESIGN OF HIGH VACUUM PIPING

The factors to be decided when designing the piping are:

1. Lines should be as short as possible, and of adequate size to insure against the restriction to gas flow. When the pumping system includes diffusion pump the ideal assembly is to place the pump adjacent to the chamber without interconnected piping whatsoever.
2. Employ all welded constructions with flanged connections and these held to a minimum, valve designed for high vacuum applications and gauge connections at strategic points to permit "trouble shooting" when leakage is suspected.
3. Eliminate the leaks in the component piece of the overall assembly by suitable leak test before installing in the system.
4. All the areas exposed to vacuum should be cleaned.

The selection of diameter of the piping is based on the following equations for the conductance of gas flow for air at 20°C . They are accurate within $\pm 5\%$.

In the high pressure (Medium vacuum) range of viscous flow $D\bar{P} > 500$

$$C = 0.182 \frac{D^4}{L} \bar{P} \quad (1)$$

In the intermediate range or transition pressure range ($15 < D\bar{P} < 500$)

$$C = 0.182 \frac{D^4}{L} \bar{P} + 12.2 \frac{D^3}{L} \left(\frac{1 + 0.256 D\bar{P}}{1 + 0.316 D\bar{P}} \right) \quad (2)$$

In molecular range or high vacuum range ($D\bar{P} < 15$)

$$C = 12.2 \frac{D^3}{L} \quad (3)$$

where

C = Conductance in litres/sec.

D, L = Dia. and length of the pipe in cms

\bar{P} = Average pressure in microns of mercury

$$\bar{P} = \frac{P_1 + P_2}{2} \text{ where } P_1 = \text{Pressure at the suction side of the pump} \\ \text{and } P_2 = \text{operating pressure at the vacuum chamber.}$$

Now the pumping speed for the pumping system is determined

$$\frac{1}{S} = \frac{1}{SP} + \frac{1}{C} \quad (4)$$

where

S = net pumping speed in litres/sec

SP = speed of the pump in litres/sec

C = conductance of the piping in litres/sec

FABRICATION

For the high vacuum piping and vacuum chamber, all welded joints are designed for full penetration of the weld. Trapped volume and crevices in which contaminants may collect must be avoided. All the welds should be done in an inert atmosphere. Wherever possible flanged joints are recommended for pipings. The surface exposed to vacuum should be clean and should have a good surface finish.

TEST METHODS

When a vacuum system is assembled it is always better to check each component for leakage before assembly. If this procedure is followed, then any leakage registered in the system after assembly is due to leakage at the joints unless the component has been damaged by the application of excessive torque or thermal stress. It is further suggested that it is better to check the leak tightness of the system after each component is added and assembly proceeds.

It is always a good practice to make a permanent repair of leaks found during leak hunting. Temporary repairing only when the system is operated for a short time.

The manufacturer of vacuum component and equipment regard the helium type mass spectrometer method of testing techniques as the optimum means of leak detection and determination of tightness. The prospective users specification for both the components and the complete equipment should specifically require test by this method.

CONCLUSIONS

Investigation usually proves that the basic failure of the vacuum equipment is due to pumping system failure. Further the prospective users of the space simulation system have a tendency to submit their requirements for bid to conventional process equipment manufacturers. A well qualified and reliable vacuum equipment supplier has a caution born of experience in both engineering design and construction. His bid price will reflect in its higher cost figure the added cost of designing for efficient vacuum operation. To differentiate the two bid prices one should have a sound knowledge of vacuum system design and its application to space simulation systems.

ACKNOWLEDGMENT

The author wishes to thank Dr. C. L. Amba-Rao, Project Leader ETD, for his kind help and encouragement in preparing the paper.

REFERENCES

1. Santler, D. J., Jones, D. W., Holkeboer, D. H. & Pagano, F., Vacuum Technology and Space Simulation, Scientific and Technical Information Division, NASA, 1966.
2. Dennis, N. T. M. and Hippel, T. A., Vacuum System Design Chapman and Hall Ltd - 1968.

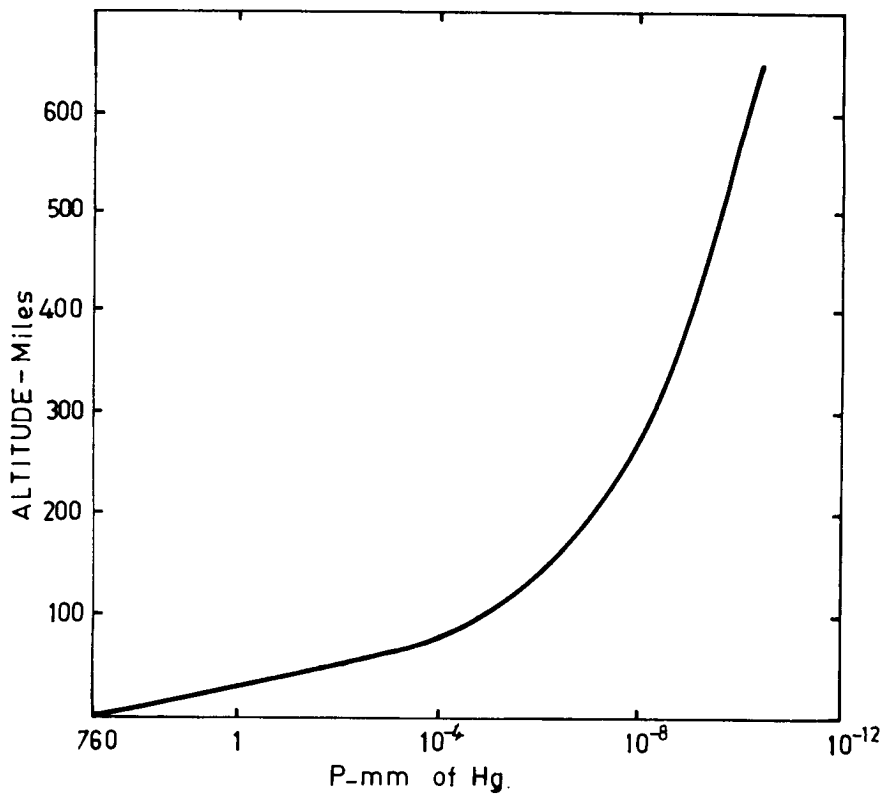


Figure 1. Variation of Pressure with Altitude

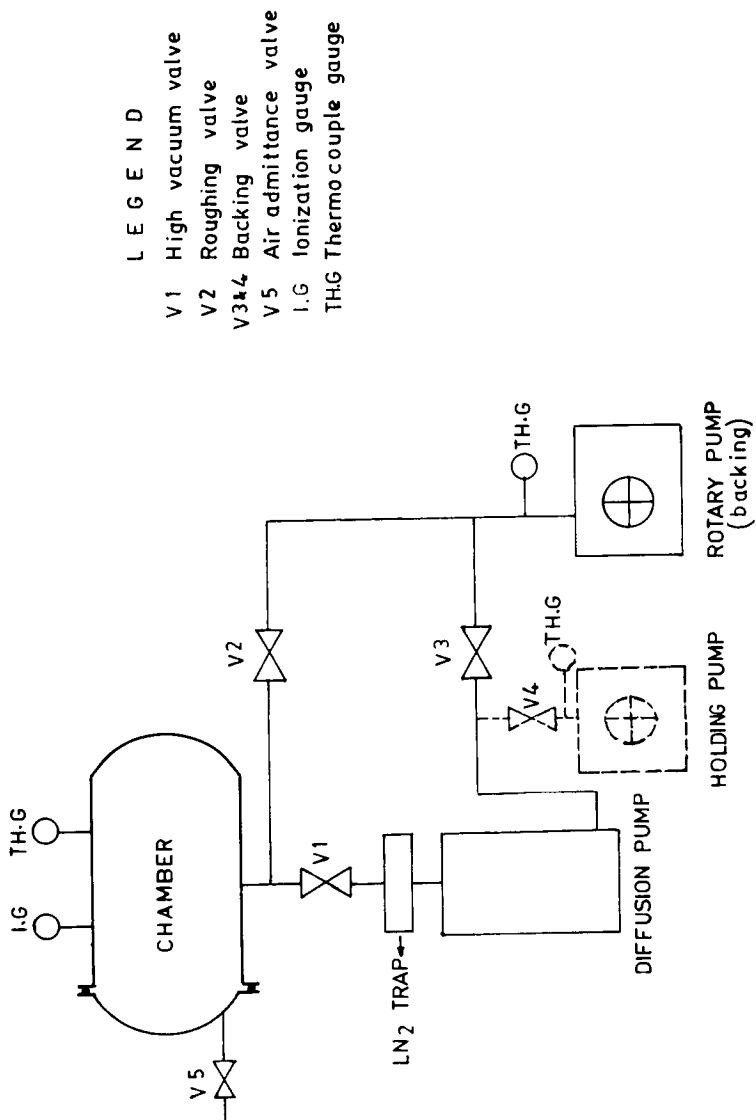


Figure 2. Vacuum System for a Space Simulator (Schematic)

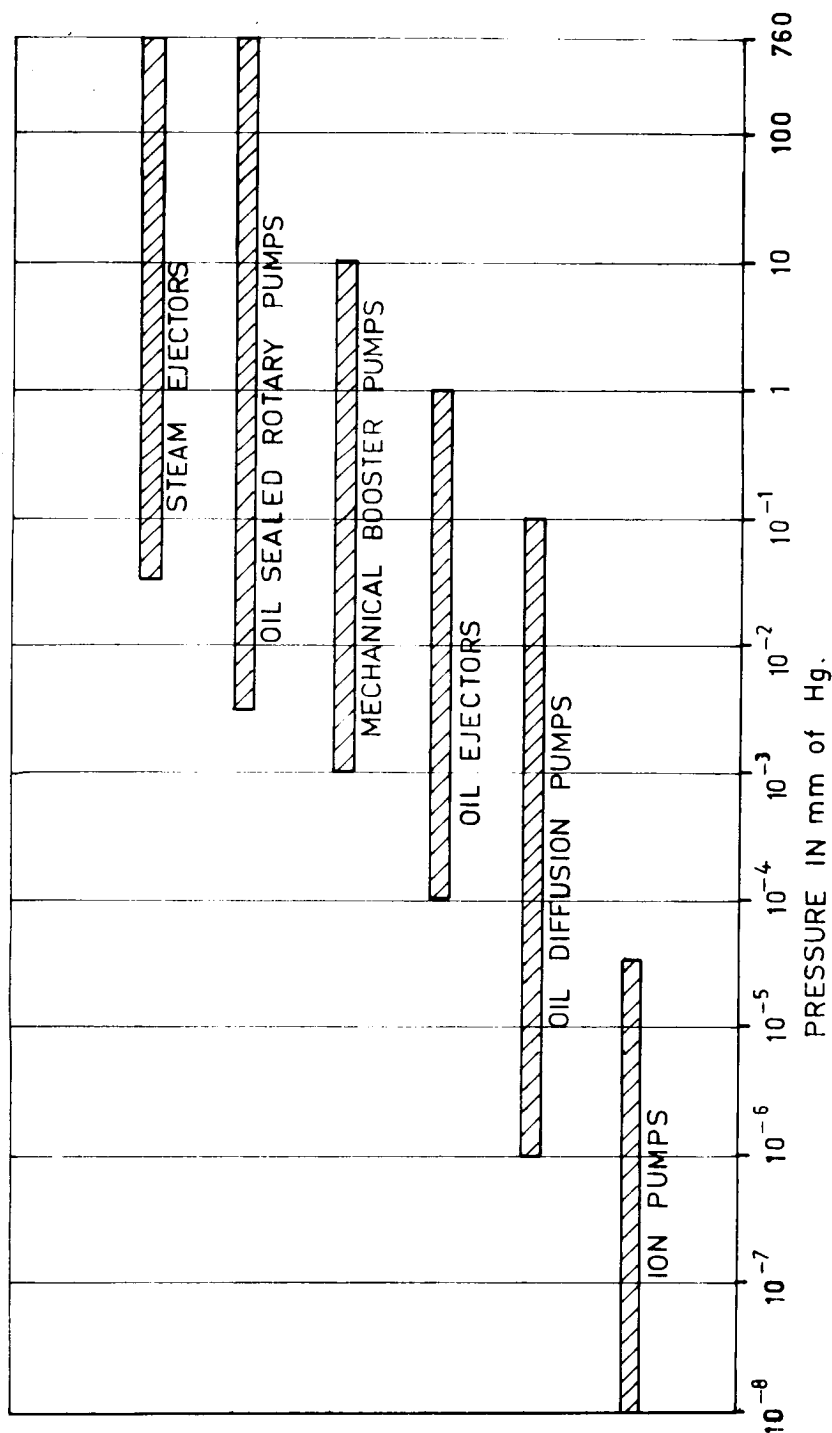


Figure 3. Range of Application for Vacuum Pumps

**FACILITY AND TEST SUPPORT EQUIPMENT FOR THE MANNED
THERMAL-VACUUM TESTS OF THE APOLLO SOYUZ DOCKING MODULE**

O. L. Pearson, *Johnson Space Center, Houston, Texas*

SUMMARY

In order to accommodate manned thermal-vacuum (TV) testing of the Apollo Soyuz Docking Module (ASDM), modifications to the facility, cleanliness and access control, and special test equipment were required.

Facility modifications included the following:

1. The addition of an oxygen supply system.
2. The modification of manlock (ML) piping for cleaning and access controls.
3. The addition of a nitrogen diluent system.
4. The removal of manlock internal lights and the addition of external lights as well as fusing all power circuits over 10 watts.
5. The removal/containment of flammable materials.
6. The upgrading of a ML fire suppression system.
7. The addition of a garment donning station for cleanliness control.

Special test equipment included the following:

1. An access tunnel for crew ingress/egress.
2. A support device for the Docking Module (DM) and simulators.
3. A Command Module (CM) thermal simulator.
4. A DM infrared (IR) simulator.
5. A Docking System (DS) IR simulator.

6. A metabolic heat load simulator.
7. A television camera simulator.

This paper describes the facility modifications, cleaning and inspection techniques, and the special test equipment used for the DM test. Also included is a brief summary of the test activities.

INTRODUCTION

As of this writing, a joint United States and Russian manned space mission is planned for July, 1975. A CM attached to the ASDM will rendezvous and dock with the Soyuz spacecraft. For about two days, United States and Russian crewmen will exchange visits which will be televised to earth.

The ASDM must maintain 289 K to 300 K (60° F to 80° F) while subjected to the internal metabolic and equipment heat loads and the external thermal extremes of earth orbit. The thermal balance of the ASDM is therefore sensitive to spacecraft attitudes, crew occupancy, equipment heat loads and duty cycles, solar radiation, earth albedo and thermal energy from the CM and the Soyuz.

In order to attain the same high level of confidence in this, the first manned international spaceflight, as was attained on earlier Apollo spaceflights, a manned test of the ASDM was performed June - October 1974, in chamber B of the Space Environment Simulation Laboratory at the Johnson Space Center in Houston, Texas.

The ASDM backup flight article was placed near the center of the chamber and was subjected to the simulated TV environment of earth orbit. (See figs. 1 and 2.) The purpose of the test program was to verify that the DM and DS during a simulated mission TV timeline would maintain design temperatures and pressures. The DM was tested in both the docked and the undocked configuration. The primary test objectives were to certify the DM/DS thermal control system including insulation, thermal control coatings, low conductance mountings and the use of DM components as thermal control heat sources, to verify the DM/DS thermal analytical model, and to demonstrate the DM capability to maintain crew comfort. All test objectives were accomplished. Total chamber test time was 571 hours which included 49 hours of manned test.

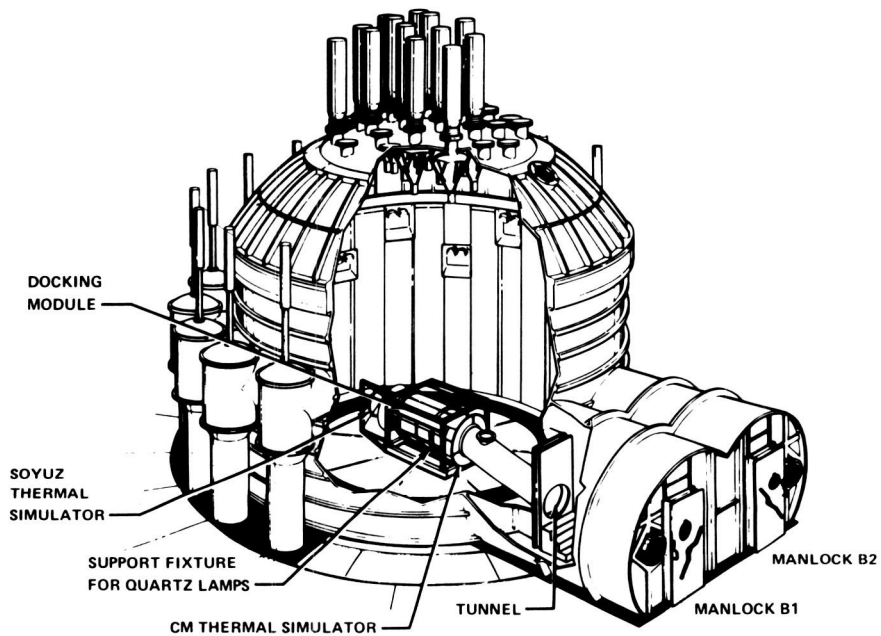


Figure 1.- Cutaway view of test setup.

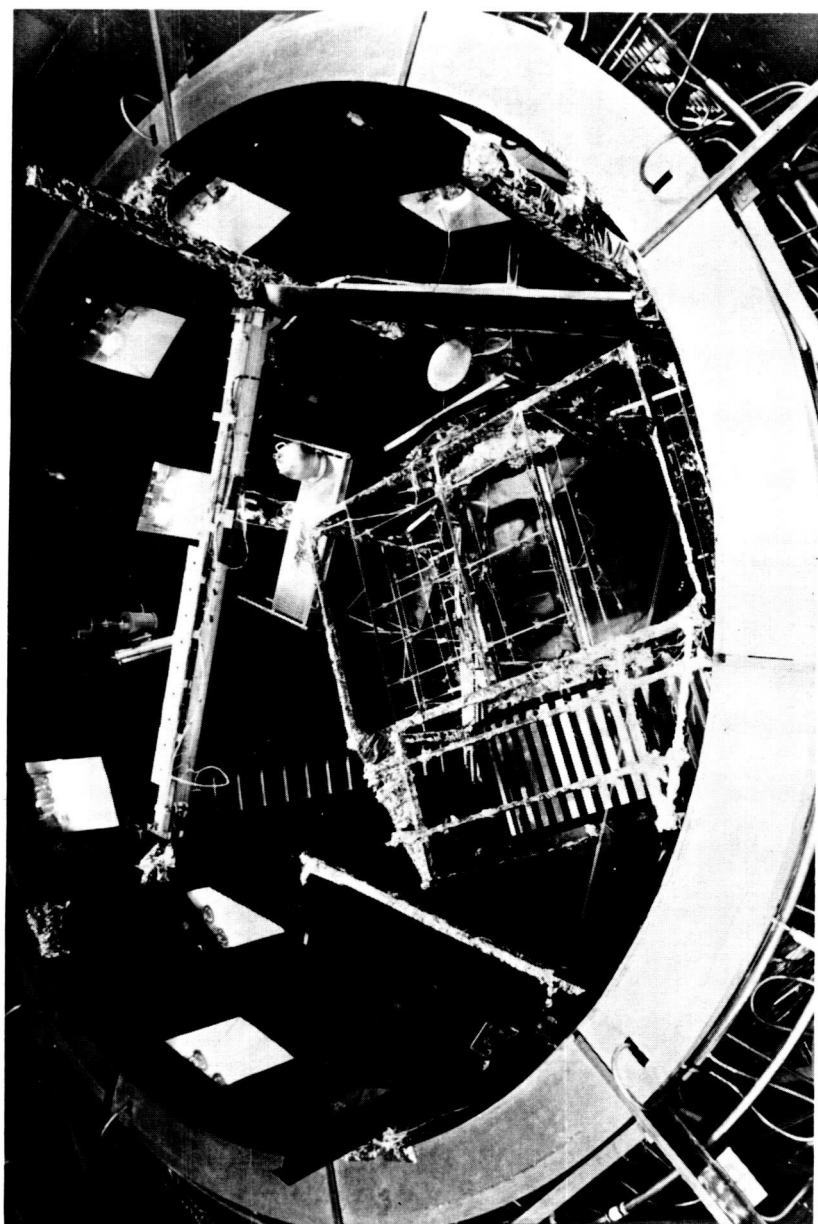


Figure 2.- View of test setup through top of chamber B.

Manned test considerations are shown in appendix B and abbreviated crew transfer procedures are shown in appendix C.

DM DESCRIPTION

The DM was a cylindrical pressure vessel with an internal diameter of 1.42 m (56 inches) and an overall length of 3.15 m (124 inches). (See fig. 3.) There was a hatch near each end of the DM and the internal distance between hatches was 2.07 m (81.5 inches). The gross internal volume was 3.79 m³ (133.9 cubic feet). With both hatches closed the DM was a self contained pressure vessel.

FACILITY DESCRIPTION

Chamber B is a 10.7 m (35 feet) diameter stainless steel vessel that has an overall height of 13.1 m (43 feet). Access to the chamber for large test articles is by removal of the top head which includes a Xenon solar simulator system. The test volume is shielded from the chamber walls by liquid nitrogen cooled panels. Further details of the facility capabilities are given in references 1 and 2.

The chamber has two interconnecting manlocks at the chamber floor level. Each ML has an internal length of 4.0 m (13 feet) and an internal diameter of 3.4 m (11 feet).

ML1 simulated either the CM or the Soyuz internal environment, depending upon the test phase, and ML2 was used as an "elevator" for the crew. (See app. C.)

FACILITY MODIFICATIONS

Manlock Oxygen System

A stainless steel pipe which was 1.27 cm (0.5 inch) in diameter transported oxygen from a tube trailer through a control valve to ML1 and also to a set of umbilicals which could be placed inside the DM by the crew to purge the DM. Ambient air was inbled to dilute the oxygen to the desired mixture and the ML pumps were used to achieve the desired pressure. ML1 instrumentation included total pressure, partial pressure of oxygen, partial pressure of carbon dioxide, relative humidity and temperature.

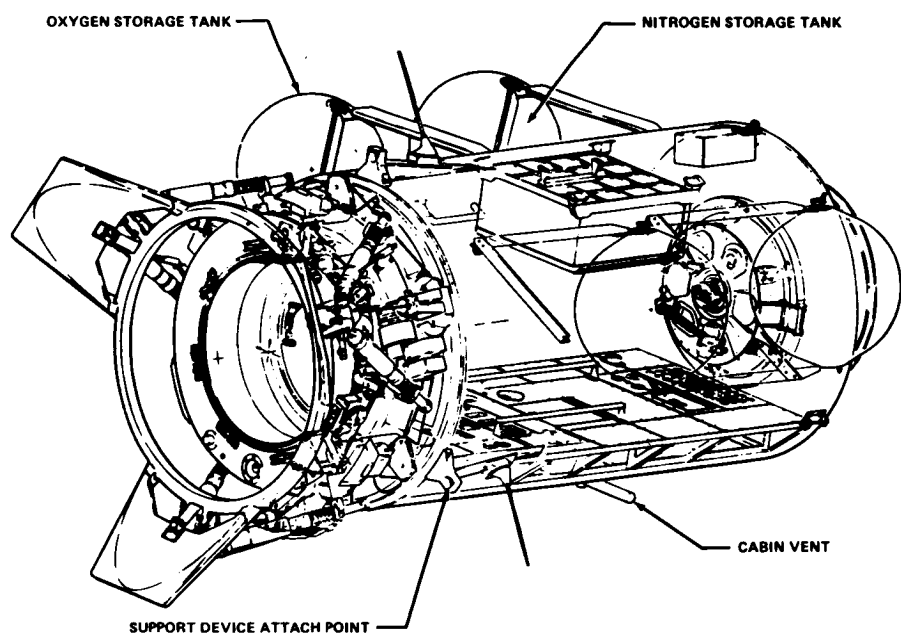


Figure 3.- Inboard profile of Docking Module.

ML Piping

The ML1 pumping train had originally been designed with welded rather than flanged fittings in order to decrease the number of potential air leaks. With the increased fire hazard because of the elevated oxygen partial pressure it was necessary to clean and inspect all areas of ML1 and its associated piping that would be exposed to the enriched oxygen atmosphere. Several sections of the piping were cut and refitted with bolted flanges for accessibility.

Nitrogen Diluent System

A nitrogen diluent was added into the pumping train along with a partial pressure of oxygen sensor to limit oxygen concentration within the pumping train. After the modification of the ML piping and the addition of the nitrogen diluent, all areas of ML1 and the associated piping could be cleaned and inspected or else the enriched oxygen environment was diluted to approximate the equivalent of air.

Ignition Sources

Because of the enriched oxygen atmosphere, special care was taken to remove the potential ignition sources and to remove or contain the flammable materials. All existing electrical devices (lights, mantrapped alarm, door closure microswitch, etc.) were removed.

ML lighting was provided by placing a 400 watt lamp which generated 46,000 lumens outside an existing ML viewport with forced convective cooling on the viewport glass. An aluminum reflector panel was placed inside the ML to disperse the light. Lighting was adequate for direct and television viewing of the crewmen at all times.

A communication system was installed which was similar to that previously qualified for enriched oxygen service in the Skylab Program.

All electrical circuits exposed to the oxygen rich environment of either ML1 or the DM were fused at 125 percent of their average load if the source capability exceeded 10 watts.

Materials

A detailed survey was conducted to identify all materials which would be exposed to the enriched oxygen atmosphere. A board of technical experts examined each material and application to insure that any potential fire would be restricted to minimum and well defined isolated areas without propagation paths in accordance with reference three, "Flammability, Odor, and Offgassing Requirements and Test Procedures for Materials in Environments that Support Combustion." All materials which were not self-extinguishing in the enriched oxygen atmosphere were either removed, isolated or attached to a suitable heat sink.

Fire Suppression System

The original chamber B fire suppression system is described in reference 1. ML1 was upgraded to conform to the requirements of reference 4, namely for a water flow of 0.034 m^3 (7.5 gallons) per minute for each 0.093 m^2 (square foot) of floor surface area with nozzles to impinge from all directions on all surfaces of chamber, equipment, and occupants. For ML1 and the ingress/egress tunnel, a water deluge system was installed which had a flow capability of 5.91 m^3 (1,300 gallons) per minute through 94 nozzles. (See fig. 4.) The system could be activated from the Test Director Console in the chamber B control room, from directly outside ML1 or from inside ML1. In addition, a water hose was installed beneath the tunnel floor which could be used to spray water inside the DM.

Garment Donning Station

A temporary structure was erected at the entrance to ML2 which consisted of an aluminum framework covered with a nonparticulate generating plastic and having an outward opening spring closure door. An existing air handling unit with a 3×10^{-7} meter (0.3 micron) filter caused a positive air flow from inside the DM to ML1 to ML2 to the donning station to outside the chamber and helped to prevent the introduction of particulate matter into the test volumes.

A motor operated shoe brush was used prior to entering the station. After entering the station, personnel donned a lint free outer garment, head covering, clean shoes, and gloves.

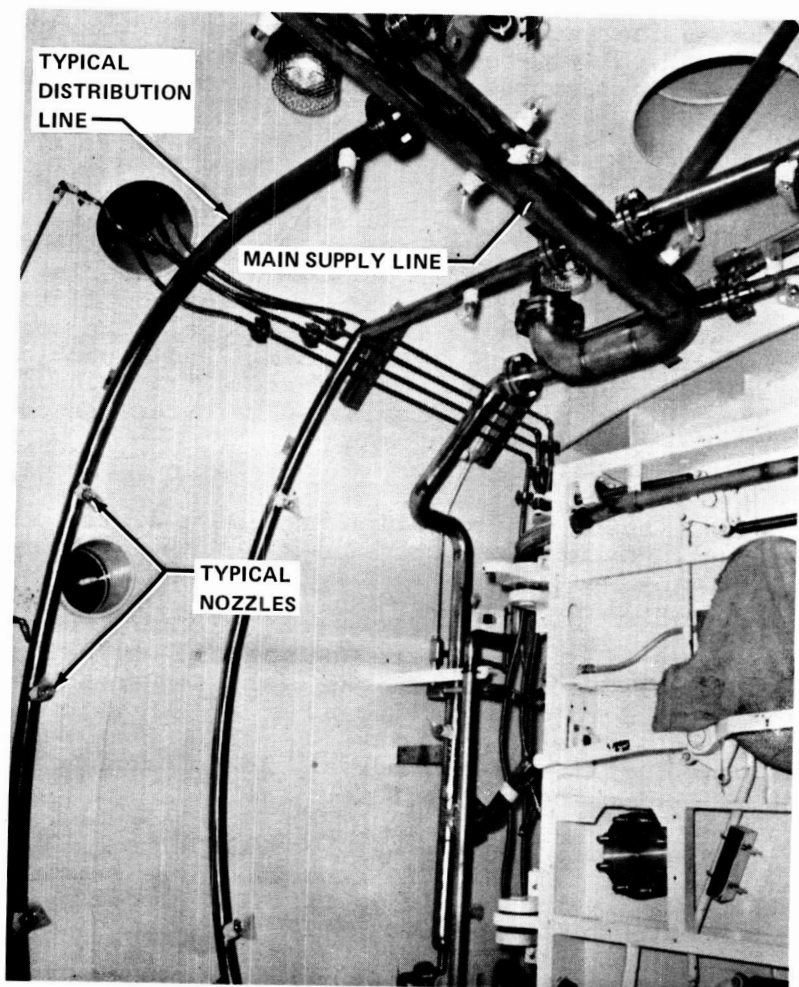


Figure 4.- Manlock B1 fire suppression system.

ML2

Although an enriched oxygen atmosphere was not required in ML2, it was recognized that there would be some mixing of the atmosphere from ML1 while the interconnecting door was opened to allow ingress/egress. Calculations indicated that the ML2 oxygen content could reach up to 30 percent during the time that the interconnecting door was open. For this reason, ML2 was treated identically to ML1 with respect to ignition sources, flammable materials, and cleanliness.

CLEANING AND INSPECTION

Cleaning of the areas which would later contain the oxygen enriched atmosphere was accomplished by using a vacuum cleaner followed by washing with detergent and water. Next a freon-soaked lint free cloth was used to wipe the entire area. The area was then inspected for both film and particulate contamination using both visible and ultraviolet light. Any areas found to be contaminated were recleaned.

SPECIAL TEST EQUIPMENT

The test configuration and most of the special test equipment utilized is illustrated in fig. 1.

Access Tunnel

Since the DM is to be manned while in earth orbit, simulation of the flight timelines required that hardware be developed for access to the DM while the DM was in the simulated TV environment. For realistic simulation, extraneous thermal loads could not be induced by the access hardware.

An access tunnel was installed from ML1 to the DM. (See fig. 5.) The ML1 inner door was removed and replaced by a 5 cm (2 inch) thick aluminum slab to which the tunnel was welded. The 1.27 cm (0.5 inch) thick aluminum tunnel was 1 m (39 inches) internal diameter and 3.96 m (13 feet) long with a flat floor and an upward slope of 11 degrees. The tunnel had an electrical penetration plate for DM power and signal wires and a viewport for illumination of the tunnel interior. Outside the viewport, in the chamber, three individually controlled incandescent filament lamps provided tunnel illumination. A CM docking mechanism was bolted to the end of the tunnel for mating with the DM.

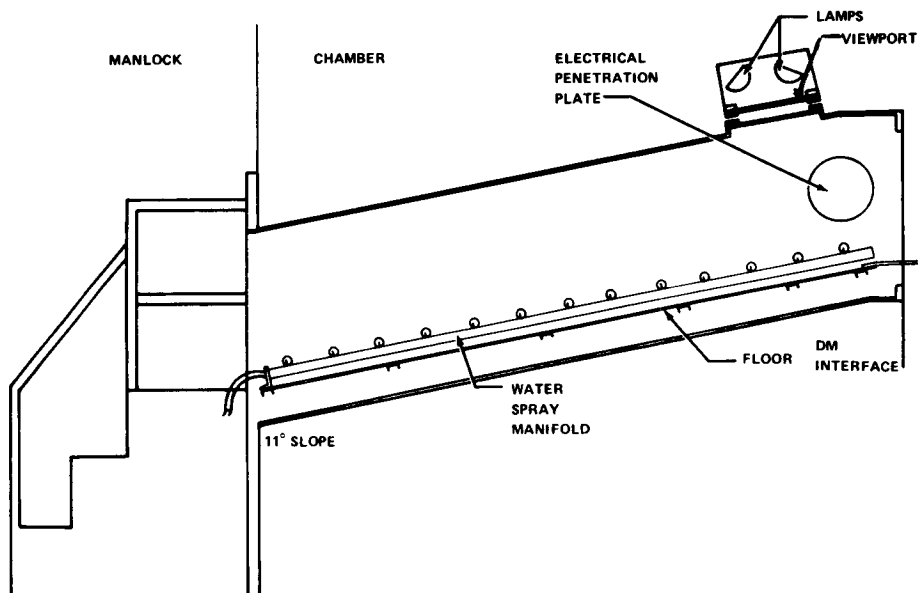


Figure 5.- Side view of DM to manlock access tunnel.

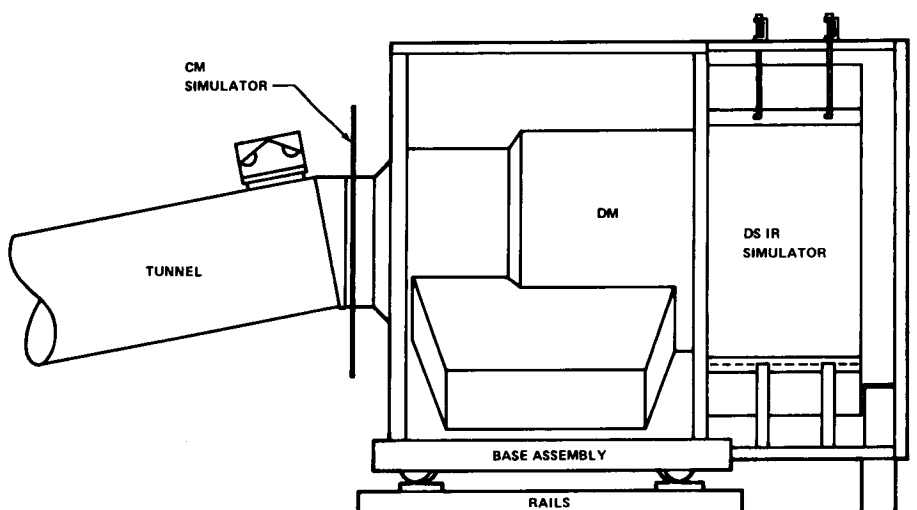


Figure 6.- Side view of the DM support device.

Superinsulation and electrical heaters together with thermocouples for temperature monitoring were used to maintain the tunnel/DM interface at $294\text{ K} \pm 6$ ($70^{\circ}\text{F} \pm 10$) to prevent extraneous thermal loads from occurring at the tunnel/DM interface.

Support Device

The DM was rigidly attached to the end of the tunnel (which was bolted to the ML door frame) by the docking mechanism. Because the combined weight of the DM and the simulators exceeded the design limits for moment on the docking mechanism in a one "g" field, a device was required to support the DM, the DM IR simulator and the DS IR simulator and to limit relative motions between them. Also at various times the device supported an additional 6672 Newtons (1500 pounds) for pressurization gases, the crew, extra equipment, and the DS and Soyuz simulators. The ML door frame to chamber floor radial beam dimensions change approximately 1.27 cm (0.5 inch) in various planes during vacuum and TV conditions. Thus the support device was required to accommodate changes in dimensions and changes in weight without imposing excessive moments upon the DM.

The support device consisted of an aluminum framework which was balanced at four places on levers with rollers at the fulcrums. (See figs. 6 and 7.) By applying suitable counterweights, the variation in test configuration loads were accommodated without inducing excessive moments into the docking mechanism/tunnel interface. The counterweights were readjusted as required between each TV test. The framework was wrapped with several layers of superinsulation to prevent excessive thermal gradients from warping the structure. The framework was instrumented with thermocouples.

CM and Soyuz Thermal Simulators

A CM thermal simulator and a Soyuz thermal simulator were required to approximate the view factors, the radiation surfaces, and the various temperatures of each.

The CM thermal simulator was a circular plate 2.64 m (104 inches) in diameter. (See fig. 8.) The DM side of the simulator was covered with the same reflective coating that is to be used on the CM. The simulator consisted of four symmetrical, independent quadrants with temperature control provided by nichrome

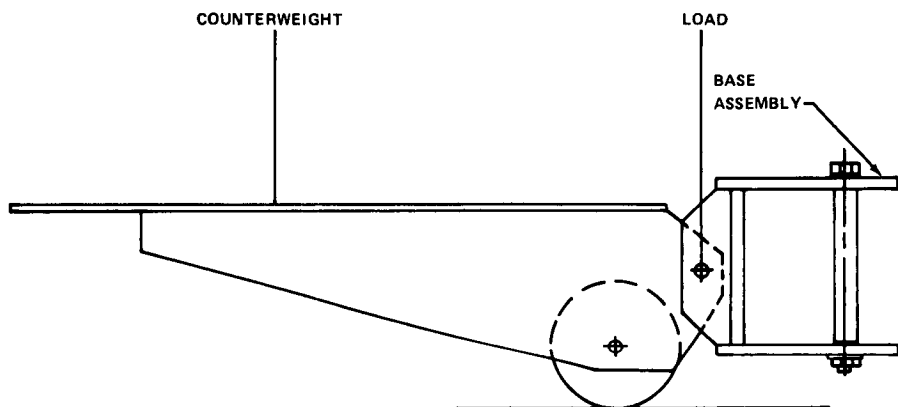


Figure 7.- DM support device balancing levers.

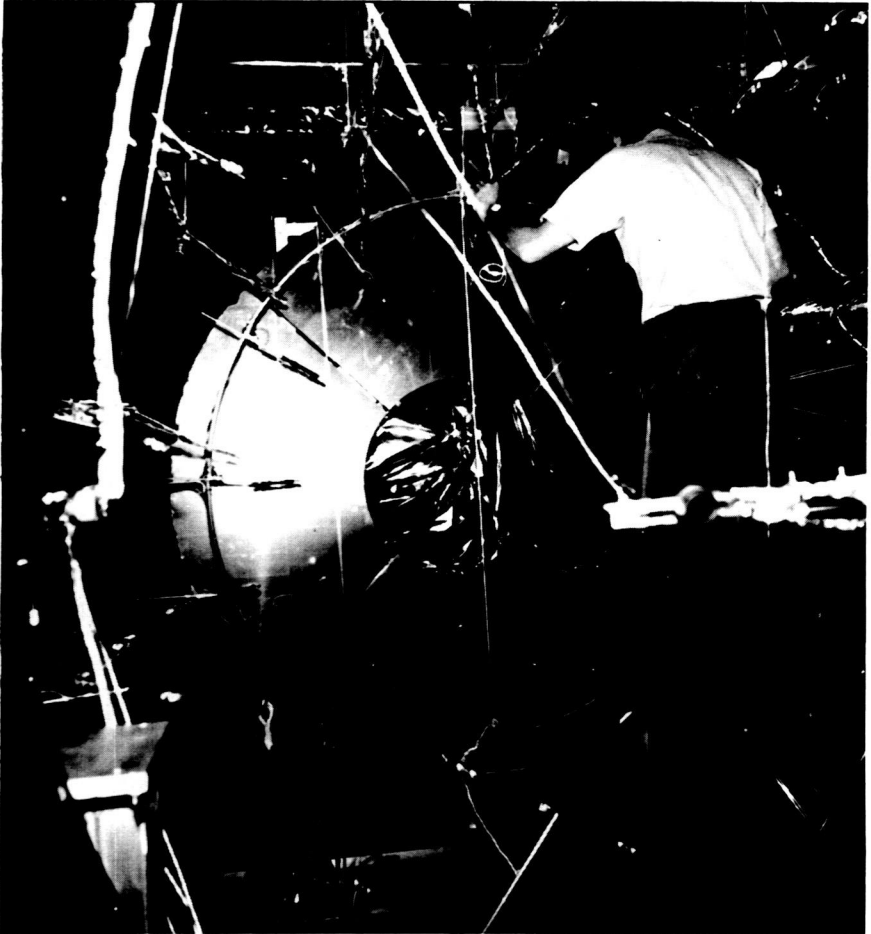


Figure 8.- CM thermal simulator and portion of the DM IR simulator.

REPRODUCIBILITY OF THE
ORIGINAL PAGE IS POOR

steel electrical heaters using d.c. power supplies and radiative cooling.

The Soyuz thermal simulator was a circular plate 2.06 m (81 inches) in diameter. (See fig. 9.) The DM side of the simulator was anodized aluminum. The simulator consisted of four symmetrical, independent quadrants with temperature control provided by silicone rubber encapsulated electrical heaters using d.c. power supplies and radiative cooling.

DM IR Simulator

It was required that the DM be irradiated over 48 different zones with each zone temperature individually controlled at temperatures varying from 214 K to 404 K (-75° F to +268° F).

The skin temperatures were controlled by means of radiative cooling with heating provided by 99 quartz lamps mounted in reflectors which were adjustable in seven degrees of freedom. Portions of the lamps and supporting structure can be seen on figures 2 and 8. Preliminary lamp locations were determined by computer calculations with final locations established by testing. Each lamp was individually controlled by a manually operated power supply and was operated at a maximum of one-half rated voltage to increase reliability.

DS IR Simulator

It was required that the DS be irradiated over six different zones with each zone temperature individually controlled at temperatures varying from 210 K to 344 K (-81° F to +160° F).

Cooling was accomplished by radiation to the chamber cold walls. Because of the highly irregular shape of the DS, heating was provided by a combination of quartz lamps and electric resistance heaters. The electric heaters were attached to the outside of an aluminum cylinder that was 2.44 m (8 feet) in diameter, 1.22 m (4 feet) high and 0.64 cm (0.25 inch) thick. (See fig. 10.) The cylinder was painted black inside and outside to speed radiative cooling and was divided into four quadrants, each with individual temperature control. Both radiometers and thermocouples were used for monitoring.



Figure 9.- Soyuz thermal simulator. (The center circular thermal blankets were attached with Velcro to provide rapid access to the DM for rescue.)

REPRODUCIBILITY OF THE
ORIGINAL PAGE IS POOR

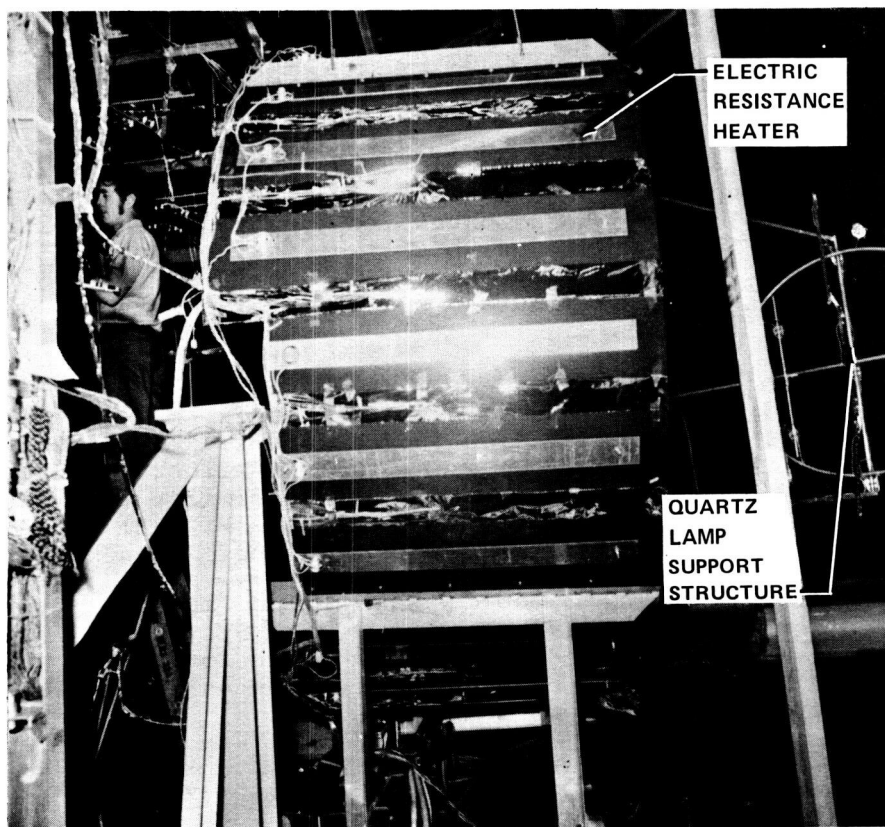


Figure 10.- DS infrared simulator.

REPRODUCIBILITY OF THE
ORIGINAL PAGE IS POOR

Metabolic Heat Load Simulator

In order to simulate manned occupancy for a 16-hour and also for a 48-hour period of thermal design mission transfers without subjecting the crew to extended work periods, a simulator was required that would generate a known thermal input similar to that of either one or two crewmen. The simulator was also required to operate safely within the enriched oxygen atmosphere and to cool to touch temperature within 30 minutes for removal by the crew.

Specific requirements were to dissipate either 175.86 watts (600 Btu/hr) or 351.72 watts (1,200 Btu/hr) over as large a volume as practical and still be removable through the hatch, to operate at less than 506 K (450° F) to prevent ignition of other DM equipment, to cool to touch temperature of 318 K (113° F) in less than 15 minutes, and to weigh less than 133 Newtons (30 pounds).

The unit was an aluminum cylinder 45.7 cm (18 inches) in diameter and 91.4 cm (36 inches) high. (See fig. 11.) It was mounted on four Teflon legs to prevent direct thermal contact with the DM floor. Four silicone rubber encapsulated heaters similar to those previously qualified for the Skylab Program were vulcanized to the inside of the cylinder. Each heater was controlled by a separate power supply. Any three of four heaters could supply the maximum test requirement of 351.72 watts (1,200 Btu/hr). The heaters were covered with beta cloth for additional safety. The outside of the cylinder was painted black to shorten the cooldown time.

The unit weighed 80 Newtons (18 pounds), the maximum operating temperature was 325 K (126° F) and the unit cooled to touch temperature in less than 2 minutes.

Television Camera Simulator

Two special flight television cameras were not available for the test. In order to provide a more realistic mission thermal profile, a simulator was required that would dissipate 35 ± 5 watts during selected phases of the tests in lieu of the flight cameras. In addition, it was required that the unit have the same mass as the flight cameras which was 57.8 Newtons (13 pounds) and operate below 318 K (113° F).

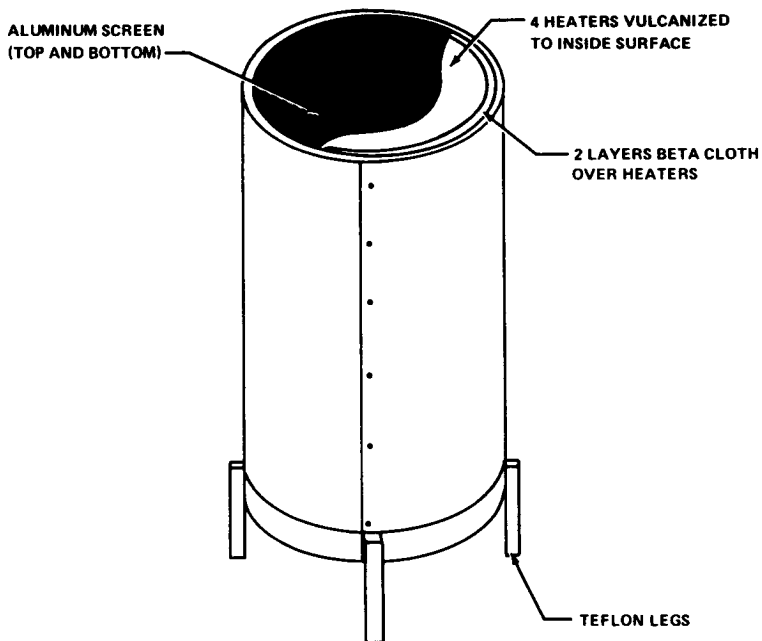


Figure 11.- Metabolic heat load simulator.

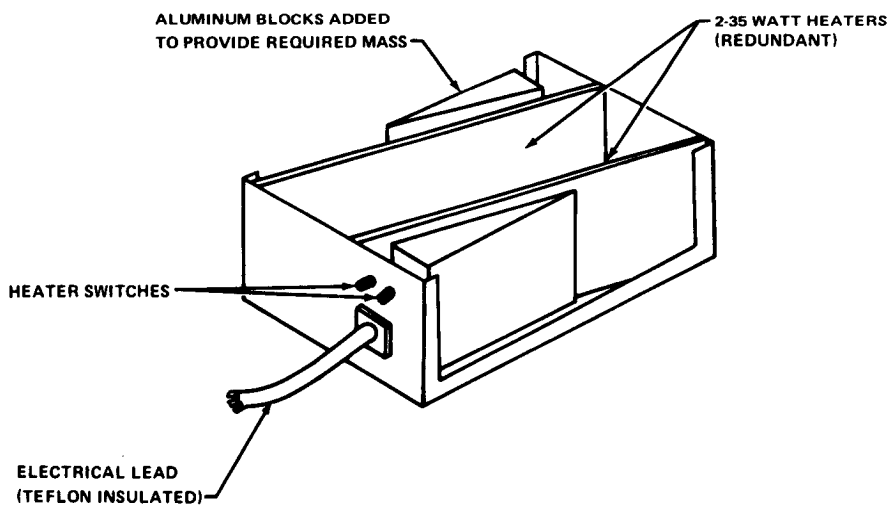


Figure 12.- Television thermal simulator.

The simulator consisted of an aluminum box 25.4 cm (10 inches) by 15.2 cm (6 inches) by 9.14 cm (3.6 inches) containing two redundant silicone rubber encapsulated electrical resistance heaters vulcanized to aluminum plates with aluminum blocks added to provide the thermal mass requirements. (See fig. 12.) Switches were provided on the box to select either heater should one fail. The heater power source was 28V d.c. from the DM and could not be adjusted.

Each heater dissipated 35.32 watts and the maximum operating temperatures was 316 K (109° F).

ASTP TEST PROGRAM

Five tests were performed to insure the readiness of the facility and the special test equipment (STE) for the DM thermal-vacuum tests.

The first test was to verify the capability to repressurize chamber B to 41,368 Pascals (6 psia) in 30 seconds or less or to ambient in 90 seconds or less. Also tunnel/chamber leak rates were measured and visibility data were obtained.

The second test was to verify the functional capabilities and operating procedures of the remainder of the STE as well as measure the support device movements relative to the tunnel.

The third test was to certify the ML1/tunnel for oxygen compatibility and to certify and calibrate the MHLIS and the television camera simulator in the enriched oxygen environments.

The fourth test was to demonstrate the structural and vacuum integrity of the DM, tunnel, manlocks, and chamber.

The fifth test was to calibrate the in-chamber thermal simulators to obtain predicted DM and DS surface temperatures for simulating various earth orbital thermal profiles. A secondary purpose was to verify facility and DM instrumentation and operation of all equipment prior to beginning a long series of thermal-vacuum tests.

All five tests were completed satisfactorily prior to the DM TV test. The DM was first tested in the undocked configuration, then in the docked configuration, and then manned.

CONCLUDING REMARKS

The successful manned operations of the DMTV tests bear evidence that the facility modifications, the cleanliness controls and the special test equipment were satisfactory.

REFERENCES

1. Pearson, O. L.; Gauthier, P.R.: Manned Operations for the Apollo Lunar Module in a Simulated Space Environment. NASA TN D-5760.
2. Thermal-Vacuum Laboratories, NASA, Johnson Space Center, National Aeronautics and Space Administration.
3. NHB 8060.1, Flammability, Odor, and Offgassing Requirements and Test Procedures for Materials in Environments that Support Combustion, NASA.
4. National Fire Protection Association Standard 56E, "Hypobaric Facilities."

APPENDIX A

ACRONYMS AND ABBREVIATIONS

ASDM	Apollo Soyuz Docking Module
Btu	British Thermal Units
CM	Command Module
cm	centimeter
d.c.	direct current
DM	docking module
DS	docking system
F	Fahrenheit
g	gravity
hr	hour
IR	infrared
K	Kelvin
m	meter
MHLS	metabolic heat load simulator
ML	manlock
NASA	National Aeronautics and Space Administration
psia	pound per square inch absolute
STE	special test equipment
TRRB	Test Readiness Review Board
TV	thermal-vacuum
V	volts

APPENDIX B

MANNED TEST CONSIDERATIONS

Minimum safety criteria for manned ground testing either at total oxygen pressures less than 14.7 psia or at partial oxygen pressures greater than 3.1 psia were incorporated into the JSC Safety Manual in May 1967. The chamber in which the DM tests were conducted conformed to all requirements of the safety manual which are summarized as follows:

1. Hardware design must include fail-safe features, backup systems, and adequate controls to minimize the possibility of injury to personnel.

2. Certification of test-team personnel must include demonstration of a thorough knowledge of duty-station operations, training in high-altitude physiology, and familiarization with the hazards of oxygen-enriched fires. Test personnel also must be certified as physically and mentally qualified.

3. A safety group, separate from the test organization, must review and approve the test activities.

4. Standard procedures for configuration control, calibration, technical review, and readiness approval for testing must be used.

5. A quality-control group, separate from the test organization, must use well-defined procedures to assure compliance with documented requirements.

6. System analysis to include failure modes and cleanliness requirements of all test hardware must be performed.

7. Test personnel shall not be subjected to a test environment in which a credible single-point failure will result in injury.

8. Medical surveillance of test subjects is required, as is the provision of appropriate emergency treatment equipment, including hyperbaric facilities. The surveillance includes the authority to terminate the test.

9. A rigid material-control plan must be established, hazardous material must be kept to the

minimum, and the use of flammables must be analyzed carefully for safety considerations.

10. Test checkout operations must include personnel briefings, ambient dry runs, simulated emergencies, and an unmanned environmental test to exercise personnel and equipments prior to manned tests.

11. Detailed test procedures approved by medical, quality, safety, and other personnel must be developed for normal and emergency operations.

All test operations in the laboratory were conducted according to detailed step-by-step procedures. Critical system procedures were accomplished under quality-control surveillance. Provisions were made to revise the procedures if necessary. The detailed step-by-step actions to be taken in the event of credible emergencies were preplanned, approved, verified, and practiced during simulated emergencies.

A specific document was prepared which contained test rules for each series of tests. The purpose of the test rules was to provide preplanned actions to be accomplished in the event of off-normal conditions arising during the tests. The order of priority upon which the rules were based was (1) personnel safety and (2) prevention of damage to equipment.

In addition to the normal supervisory review and approval cycle, investigative and review groups monitored the test activities prior to vehicle arrival at the JSC through post-test operations. These review groups are described immediately below.

Test Safety Review Committee

Senior technical experts from outside the test organization ascertained and certified the operational readiness of the laboratory. Consideration was given to the adequacy of design, training, documentation, quality control, configuration control, failure-effects analysis, support services, spares, and safety provisions. All tasks recommended by the Test Safety Review committee were resolved satisfactorily.

The JSC Manned Test Operation Office

In accordance with the JSC Safety Manual, test safety officers participated in all phases of manned

test activities. The test safety offices were knowledgeable in the operations of the test facility and the test article. The officers reviewed and approved test plans and procedures and had the authority to order discontinuance of any test operations deemed to be unsafe.

Industrial Safety at the JSC

The normal hazards expected around a large industrial complex, such as cryogenic handling, flammable storage areas, and high-pressure fluids, were kept under surveillance by the JSC industrial safety group. Periodic inspections were made of the entire laboratory complex to ensure that safe practices were maintained.

Contractor Safety Groups

Both the vehicle contractor and the laboratory operating contractor established safety groups whose activities were coordinated by the NASA. Each group reviewed laboratory practices, plans, procedures, equipment, and so forth to assure safe operations. Under NASA direction, each contractor organized fire-control and rescue teams and held periodic unscheduled emergency drills to ensure team proficiency.

Test Readiness Review Board

Within the week prior to performing the series of TV tests, a test readiness review was conducted. The purpose of the review was to evaluate the spacecraft, the crew equipment, and the ground-support equipment, the data-acquisition system, and the test facility readiness to achieve the test objectives safely.

The Test Readiness Review Board (TRRB) was composed of senior officials of the JSC organizations involved in the test.

The TRRB reviewed work accomplished after the Test Safety Review discussed previously, and reviewed the status of discrepancies and open work. In addition, the TRRB determined the qualification/certification status of the facility and the test article and specified the actions necessary prior to testing. Only after final approval by the TRRB could the testing begin.

APPENDIX C

ABBREVIATED CREW TRANSFER PROCEDURE

Notes:

1. CM environment is 34,580 Pascals (5 psia) and 75 ± 5 percent oxygen.
2. Soyuz environment is 69,160 Pascals (10 psia) and 35 ± 2 percent oxygen.
3. Inside observers using portable oxygen breathing masks enter ML2 with crew and remain in ML2. After the crew enters ML1, ML2 pressure is changed to remain near that experienced by the crew.
4. The flight procedures are followed as closely as possible for all transfers.

Procedure

1. Verify crew has prebreathed a minimum of 2 hours.
2. With ML1 at CM environment, crew enters ML2 using portable oxygen breathing masks.
3. ML2 is evacuated to CM pressure and crew enters ML1.
4. After ML1 oxygen content is verified at 75 ± 5 percent, crew removes mask, verifies ML communications, equalizes DM with ML1 and opens DM hatch.
5. Crew places oxygen umbilicals into DM and purges DM to at least 21,950 Pascals (3.2 psia) partial pressure of oxygen.
6. Crew enters and activates DM, removes oxygen umbilicals and closes DM hatch.
7. DM and ML1 pressurized to Soyuz environment.
8. Crew enters ML1 and simulates Soyuz stay.
9. Crew re-enters DM, closes hatch and opens oxygen purge valve (DM pressure relieves to

chamber) until 75 ± 5 percent oxygen level is reached.

10. ML1 is evacuated and backfilled to CM environment and DM is depressurized (to chamber) to the CM environment.

11. Crew equalizes DM with ML1 and egresses to ML1.

12. ML1 and ML2 are equalized, crew enters ML2 which is repressurized to ambient.

PREPARATION, CONTROL, AND USE OF STANDARD OPERATING PROCEDURES IN A SPACE SIMULATION LABORATORY

R. P. Parrish, Jr., *Martin Marietta Corp., Denver, Colorado*

ABSTRACT

The degree of success in the operation of a space simulation laboratory is a direct function of the role of its standard operating procedures. Their proper use in a thermal vacuum test will help effect a well-run test program.

INTRODUCTION

A standard operating procedure developed for use with laboratory equipment and systems serves several purposes. The procedure can be a valuable tool for training personnel to operate the equipment or system. As an operational check list it can help prevent an unsafe condition resulting from personnel error or an oversight. One of the most important functions of the standard operating procedure is to identify potential hazards with caution and warning notes. Necessary information such as value schedules, graphs and equipment settings may also be given. Changeover of personnel and determination of equipment or system status are both facilitated with signed off procedural steps.

One of the first questions to arise in the preparation of a standard operating procedure is whether a procedure is really required. Meters, recorders, and most shop equipment are examples where only skilled operators are required. Skilled operators may feel they can operate the more complex equipment without a procedure, but having it just for a checklist and training aid is worth the initial preparation effort.

The procedural control system must assure that all affected departments approve the procedure and all updates.

Management must assume the responsibility for the procedures being properly used.

PREPARATION

Writer

Once a decision has been made that a procedure is necessary,

the next step is to decide who the writer should be. If a professional technical writer is available he is probably the best choice, especially if he can consult with the engineers and technicians that are most familiar with the equipment and the way it should be operated. An acceptable second choice may be one of the laboratory engineers; even though many good engineers are not especially good at writing procedures.

Format and Content

One of the best aids in preparation of a standard operating procedure is a good standard format. The following is an example of the format followed for all of our laboratory standard operating procedures:

Cover Sheet - The standard format followed for the cover sheet is shown in the abbreviated example:

MARTIN MARIETTA CORPORATION Denver Division Space Simulation Laboratory Operating Procedure (Procedure Number)			
NAME: (Name of Procedure)		Effectivity: All programs	
	APPROVAL	DATE	
(Example)			
Prepared by			
Operations Lead			
Personnel Safety			
Systems Safety			
Quality Control			
etc.			
REVISIONS			
PCN	DESCRIPTION	DATE	APPROVED

The Procedure Change Notice (PCN) (which is not shown here) will have at least the same approvals as on the original procedure.

A Table of Contents usually follows the cover sheet to facilitate use of the procedure.

After the Table of Contents there may be four or more major headings of which the first three are standard format; and are designated as follows:

1.0 Scope

The scope tells what the procedure will encompass or involve as an operational entity.

2.0 Support Requirements

This section is composed of such categories as equipment, facilities, reference documents, and utilities.

3.0 Special Considerations

In this section are included requirements and information such as blanks designated for information (i.e., names and phone numbers of key personnel); descriptions of Warnings, Cautions, and Notes; definitions of abbreviations, and special instructions regarding safety.

The fourth section may be entitled Operations or Preparation and may be divided up as the writer wishes.

An important item for inclusion in the Operations section is sign-off blocks with spaces for the operator to include the date, the time, and his initials. This is a valuable aid for determining operational status and personnel involvement and identification.

One problem that should try to be avoided in the standard operating procedure is ambiguous statements. Solutions to this problem that are effective are good editing and thorough reviews. General statements may sometimes be necessary in the procedure, but they tend to be ambiguous. Specific, concise statements are conducive to the clarity of the procedure.

Corrective or preventive maintenance are not generally covered in the standard operating procedure, but steps are included to verify the system is operating properly.

Safety aspects of the procedure should include the information necessary to prevent a hazard to the operator or the equipment and should be emphasized. The words CAUTION and WARNING are used to emphasize to the operator that the following information is given to prevent endangering equipment or personnel.

Information helpful to the procedural operation such as notes, charts, and graphs may be utilized freely in the procedure.

A final item for the preparation of the standard operating procedure is the skill level for which the procedure will be written. Operators may be trained in the operation and maintenance of the equipment prior to the writing of the standard oper-

ating procedure. Thus the procedure may be written for a skilled operator who knows how to operate the equipment and uses the procedure as an aid.

PROCEDURE CONTROL

The level of control for any particular standard operating procedure is determined by the laboratory manager.

Procedure Approval

Procedure approval includes approval by personnel safety, systems safety and a responsible laboratory engineer. Most procedures are also approved by the quality control department and the laboratory manager. Occasionally other groups will be requested to approve the procedure if their area is involved. As a part of the approval effort, table-top reviews are held for the more involved procedures and are attended at a minimum by those on the approval list.

Procedure Changes

Changes to the procedure fall under the same approval requirements as the procedure itself. However, in some circumstances, a responsible engineer or supervisor may "red-line" a procedure for a unique situation. He makes the desired changes and initials them and the changes are valid for that particular copy of the procedure only.

Procedure Use

Laboratory supervision must see that the procedures are properly used. Periodic checks will assure that they are being followed, signed off, and that the operator is aware of the status of the equipment and the test.

As stated above, the procedures may be written for use by skilled operators. This means the laboratory management must see that all operators are trained before using the procedure to operate the equipment for a test.

Procedures are used for reference only during maintenance and calibration of the equipment as normal startups, operations, and shutdowns, procedures are not followed.

DESIGN AND APPLICATION OF A GONIOPHOTOMETER

M. W. Finkel, and J. B. Heaney, *Goddard Space Flight Center,
Greenbelt, Maryland* and R. K. Brookshier

ABSTRACT

The optical design of a goniophotometer is discussed. Several interesting features such as polarization, signal-aperture interaction, and backscattering about the normal are also treated. A simplified method of integrating the total reflectance is illustrated.

INTRODUCTION

In principle at least the goniophotometer is a rather simple instrument. Yet its utility is almost inversely proportional to its simplicity. In its primary role, determining the distribution function of scattered radiation, its realm of application is quite extensive. There exists today a very rich literature associated with scattering. Indeed, scattering measurements have become an indispensable tool for such diverse investigations as optical constants, molecular weights, inhomogeneity and surface parameters⁽¹⁾. Our principal interest, somewhat more prosaic, concerns the radiative properties of materials, particularly as they relate to the thermal control of spacecraft. Hence, our emphasis has been almost exclusively, with reflectance measurements. The goniophotometer to be described here was designed primarily for bidirectional reflectance measurements in the solar region. Some of the instruments novel features are treated in some detail. A simple method of integration is also discussed. The paper concludes with some illustrative examples.

Optical System

The optical scheme of the goniophotometer is shown in Figure 1. Briefly, the system consists of a source, monochromator, transfer optics M_1 and M_2 and detector optics M_3 and M_4 . Mirrors M_1 and M_2 are plane, M_3 is spherical and M_4 ellipsoidal. A_1 and A_2 are a set of variable stops, either circular or square. For the ultraviolet and visible portion of spectrum a xenon arc source is paired with a U.V. enhanced silicon photodiode. For the near infrared a zirconium source and lead sulfide detector are paired. Variation of the angle of incidence is realized by rotating the sample holder.

Hemispherical zones are scanned at variable speeds in the polar direction at some preselected azimuthal angle. A set of neutral density filters is available for attenuating the primary beam. The output of the detector is amplified and displayed on a strip chart recorder equipped with an integrating disk attachment. The output of the shaft angle encoder is digitally displayed.

We will now take a closer look at some of the essential features of the goniophotometer. Clearly the only surface in the transfer optics that contributes to the aberration function $\Delta(\rho, \phi, h)$, where ρ and ϕ are polar coordinates in the exit pupil and h is the object distance as measured from the optical axis, is the spherical mirror M_2 ($f = 34$ cm). But with the exit slit of the monochromator and the sample effectively located in the plane containing the center of curvature of M_2 the aberration function reduces to a single third order term,

$$\Delta(\rho, \phi, h) = a^2 \rho^2 h^2 \cos^2 \phi / R_0^3 \quad (1)$$

where a is the radius of the exit pupil and R_0 is the radius of curvature of M_2 . It can be shown, moreover, that throughout most of the solar region, providing the magnitude of the scattered intensity allows for a prescribed $F\#$, the Marechal tolerance can be satisfied.⁽²⁾ This very simple configuration thus assures us that the primary beam arriving at the sample will be contained in a very well defined bundle of rays.

The detector optics containing the off axis ellipsoid is, of course, axial stigmatic. Furthermore, if we neglect transmission losses, the intensity law of geometrical optics tells us that all the radiant flux passing through the aperture A_2 will be intercepted by the detector. It is apparent then that the resolution limit of the photometer is essentially determined by the scattered intensity contained in the solid angle subtended by A_2 . The secondary focus of M_4 is 32 cm and the demagnification is 6:1. This demagnification has several important implications. To begin with the critical figures of merit of a detector are invariably optimized with small area detectors. In addition, the problem of non-uniform local responses associated with most detectors can in large measure be mitigated by reducing the spot size imaged on the detector. In our case the radius of the spot size is about 0.17 mm.

An accompanying problem is the detector angular response, $F(\theta)$ which can be expressed as,⁽³⁾

$$F(\theta) = \frac{1 - R_0}{1 - R_\theta} \quad (2)$$

where R_0 and R_θ refer to the normal and oblique reflectances. We can determine the angular subtense at the detector from (see Figure 1),

$$d\phi = \left(\frac{1 + e^2 + 2e \cos \phi}{1 - e^2} \right) d\alpha \quad (3)$$

where e is the eccentricity of the ellipsoid.⁽⁴⁾ Depending upon the stop, A_2 equation (3) indicates in our case a half angle of less than 15° . Consequently, for $0^\circ < \theta < 15^\circ$, we conclude that the angular response is nearly flat.

And now a few general comments about detector performance. Since the modulation frequency is optional, we have chosen a chopping frequency well past the $1/f$ region in order that the signal to noise ratio might be optimized. We have also taken the added precaution to assure ourselves that the RMS value of the waveform generated by the chopper is maximized with respect to the peak-to-peak amplitude of a squarewave by placing the chopper at the entrance slit of the monochromator.

We need only refer to the Fresnel equations to appreciate the importance of polarization. The usual answer to this problem necessitates a separate determination of the parallel and perpendicular components. Alternatively, we could negate any polarization induced by the optical system and yet allow for sample polarization by depolarizing the incident beam. As a matter of expedience, we have chosen the latter approach. We have therefore introduced a pile of lithium fluoride plates in the path of the transfer optics and oriented the stack with aid of a Glan-type prism polarizer so that the incident beam arriving at the sample is completely unpolarized. The zero-displacement arrangement of the plates is shown in Figure 1. The detector optics M_3 and M_4 are arranged so that they tend to mutually cancel any further polarization.⁽⁵⁾

Another problem that warrants some concern is scattering measurements about the normal. Although we can approach to within 3° of the normal before obstructing the primary beam, the extrapolation to 0° often remains ambiguous. Our answer to this problem was to introduce an auxiliary segmented mirror M'_3 which can be rotated into the position formerly occupied by M_3 . The optical scheme is illustrated in Figure 2. The normally incident flux passes through the clear segments of M'_3 and is incident upon the sample. The backscattered flux is then intercepted by the matched conjugate segments and relayed to the detector. So in a sense, the segmented mirror, plays the role of a beam splitter, except that it has about twice the efficiency.

Let us now examine the general question of scanning. Suppose we consider the scanning aperture A_2 , which is almost always circular, and for simplicity the reflectance from a specular surface. We can interpret this interaction as a convolution of two circular functions $\Pi(R)$ and write,⁽⁶⁾

$$\Pi(R) * \Pi(R) = (2\cos^{-1}R/2a - R/a \sqrt{1-R^2/4a^2}) a^2 \quad (4.)$$

Now let us compare this with the convolution of two rectangular functions $\Pi(X)$ which can be expressed as,

$$\Pi(X) * \Pi(X) = \Lambda(X) \quad (5.)$$

where $\Lambda(X)$ is the well known triangle function. The two convolutions are shown in Figure 3. It is apparent that scattering about the specular peak can be more clearly distinguished with rectangular apertures. Hence, when advantageous, the circular stops are replaced by rectangular stops.

The alignment of the instrument is rather straight forward. As suggested by Figure 1, we begin with the transfer optics. Placing a plane mirror in the sample holder, M_1 and M_2 are aligned by passing the return beam through A_1 . The M_2 plane mirror is then removed and the detector optics M_3 and M_4 are aligned. The coaxial rotation of the detector optics about the sample can be verified by returning the plane mirror to the sample holder and requiring the angle of incidence equal the angle of reflection.

Measurements

We can define the radiant power incident on some elementary area, dA and contained in some very small wavelength interval λ , (Reference 7)

$$dP_i = N(\theta_i, \phi_i) \cos \theta_i \sin \theta_i d\theta_i d\phi_i \quad (6.)$$

Where the radiance N is the power incident per unit solid angle in the direction θ_i, ϕ_i per unit projected area. Similarly, we will define the radiant power reflected by merely changing the subscripts and write,

$$dP_r = N(\theta_r, \phi_r) \cos \theta_r \sin \theta_r d\theta_r d\phi_r \quad (6.a)$$

It follows then that the radiant reflectance can be expressed as, (see Figure 4)

$$d\rho = \frac{N(\theta_r, \phi_r) \cos \theta_r \sin \theta_r d\theta_r d\phi_r}{N(\theta_i, \phi_i) \cos \theta_i \sin \theta_i d\theta_i d\phi_i} \quad (7.)$$

In terms of the distribution function,

$$\rho(\theta_i, \phi_i; \theta_r, \phi_r) = \frac{N(\theta_r, \phi_r)}{N(\theta_i, \phi_i) \sin \theta_i \cos \theta_i d\theta_i d\phi_i} \quad (8.)$$

$d\rho$ can be expressed as,

$$d\rho = \rho(\theta_i, \phi_i; \theta_r, \phi_r) \cos \theta_r \sin \theta_r d\theta_r d\phi_r \quad (9.)$$

For the special case which is applicable to goniophotometer we can treat the active sample area as point like. Consequently, we can recast the above expressions in terms of radiant intensity $J(\theta, \phi)$ which we define as the radiant power per unit solar angle. In addition, the projected solid angle is simply $\sin \theta_r d\theta_r d\phi_r$. So that,

$$\rho = \int_0^{2\pi} \int^{\pi/2} J(\theta_r, \phi_r) \sin \theta_r d\theta_r d\phi_r / P_i \quad (10.)$$

Only rarely as in the case of a perfect diffuser will the distribution function be a constant. So that generally, we must reconcile ourselves to a rather tedious numerical integration if we are to evaluate the total reflectance. This implies that we rewrite Eq. (10) as a double summation,

$$\rho = \sum_{m=1}^M \sum_{n=1}^N J(\theta_n, \phi_n) \sin \theta_n \Delta \phi_n \Delta \phi_m / P_i \quad (10.a)$$

where the radiant intensity $J(\theta_n, \phi_m)$ is understood to be $\partial P / \partial \omega$ where P is the radiant flux contained in the solid angle ω subtended by the scanning aperture A_2 . The incident flux P_i is readout directly. Although several methods for evaluating Eq. (10.) have been suggested in the literature, for most laboratory workers it remains a vexing problem. It is our intent to show that with a relatively inexpensive disk integrator attachment to a standard strip chart recorder the evaluation of the total reflectance is readily realized.

To illustrate the procedure suppose we consider Figure 5 which represents a polar scan of a sodium chloride sample for azimuthal angles $\phi = 0$ and $\phi = 30^\circ$. The total count in the disk integrator trace, given that each traversal equals 100 counts, is 16516 for the $\phi = 0$ scan and 14656 for the $\phi = 30^\circ$ scan. The ratio of the scan is 0.887 which indicates that sodium chloride is quite Lambertian. If we were to assume that sodium chloride was indeed a perfect diffuser, then the error is about 2%. Now, let us endeavour to evaluate the total reflectance. In Figure 6 we have plotted counts per scan in the polar direction versus azimuthal angle for a sodium chloride sample, $\lambda = 5700\text{\AA}$ and $\theta_i = 45^\circ$. From Table I we calculate the total count to be 160090. The angular increment $\Delta \phi$ for this run was 6.4×10^{-2} radians. Now scaling for a $\Delta \phi$ of 10° or 0.1745 radians, we multiply the total count by 2.72. Further, allowing for the lower quadrants means doubling the total count. So we have $2 \times 2.72 \times 1.6 \times 10^5 = 8.7 \times 10^5$. The count for the incident flux was 8.60×10^5 . The calculated total reflectance is then 101%, which is about 5% higher than the value obtained with an integrating sphere reflectometer.⁽⁸⁾ We should bear in mind, however, that this error is distributed over 2π steradians. In addition, we should note that this method of integration affords us a quick look at the flux distribution.

TABLE I

Counts Per Polar Scan as a Function of Azimuthal Angle

ϕ	Counts/Polar Scan
5°	15150
15°	14750
25°	13920
35°	12300
45°	9750
55°	6900
65°	4330
75°	2300
85°	645

 $\Sigma 1.6 \times 10^5$

As a sampling of some recent efforts we will briefly review a few goniophotometer studies. Identifying specular and diffuse components is a fairly common problem. Figure 7 are polar plots exhibiting the azimuthal dependence of a zinc oxide, methyl silicone white paint. The specular peak, though massive is nearly all contained in the plane of incidence. The remaining flux is quite diffuse.

The pursuit of an optical black is the subject of Figure 8. Samples A, B, and C are carbon black pigmented flexible urethane composition base paint doped with hollow glass microballoons with mean diameters of 20 μ (A), 44 μ (B), and 63 μ (C). As a comparison, we have included a familiar 3M black velvet sample (D). It is clear that the specular component, particularly near grazing incidence, is a very strong function of surface roughness.

Conclusion

The goniophotometer described here is capable of generating bidirectional reflectance measurements throughout the solar region. The optical configuration and a few of the instruments special features which should be quite utilitarian where treated in some detail. A simplified method of integration accompanied by several illustrations was included. In summation, it has been demonstrated that the instrument can be a vital asset for generating pertinent measurement for thermophysical

applications.

References

1. Munis, R. H., and Finkel, M. W., "Goniometric Measurements of Infrared Transmitting Materials," Applied Optics 7 (10), 2001-2004, 1968.
2. O'Neill, E. L., "Introduction to Statistical Optics," Reading-Mass.: Addison-Wesley Publishing Company, 1963.
3. Schaefer, G. J., "A Study of the Angular Response of Lead Sulfide Photoconductors," Applied Optics, 1(5): 637-641, 1962.
4. Hart, P. J., "Distribution of Radiation from Elliptical and Parabolic Mirrors," J. Opt. Soc. Amer. 48, 637 (1958).
5. Shurcliff, W. A., "Polarized Light," Cambridge, Mass.: Harvard University Press, 1962.
6. Papoulis, A., "Systems and Transforms with Applications in Optics,": New York: McGraw-Hill Book Co., 1968.
7. Nicodemus, F., "Directional Reflectance and Emissivity of an Opaque Surface," Applied Optics 4 (7): 767-773, 1965.
8. Finkel, M. W., "Integrating Sphere Theory," Optics Communications 2 (1): 25-28, 1970.

27

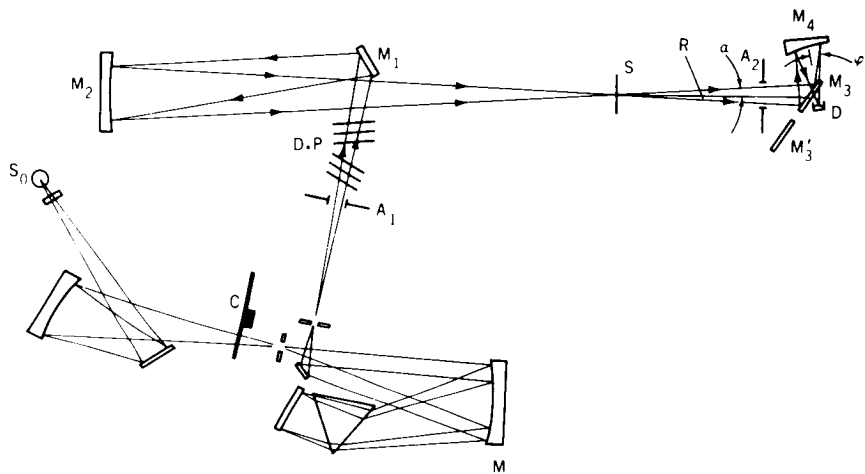


Figure 1 — Optical System: S_0 , source; M, monochromator; C, chopper; A_1 and A_2 , aperture; D.P., depolarizing plates; M_1 and M_3 , plane mirrors; M_2 , spherical mirror; M_3' , segmented mirror; M_4 , ellipsoidal mirror; S, sample; R, rotatable arm; D_1 detector.

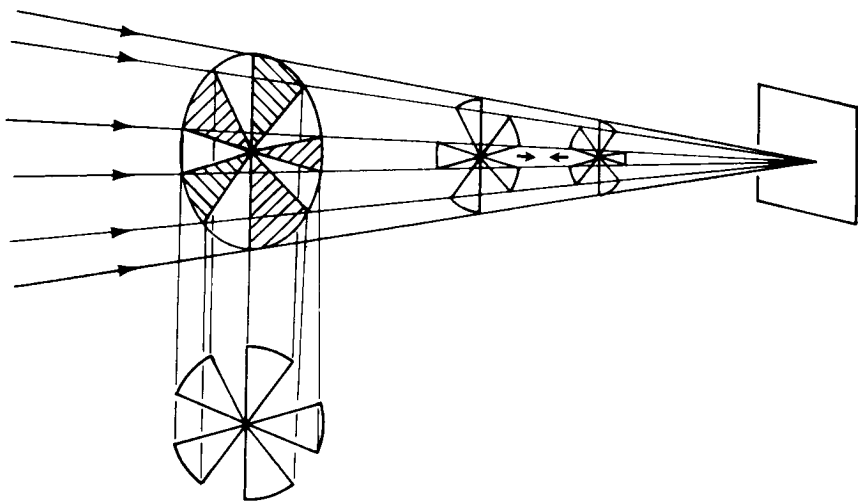


Figure 2 — Segmented Mirror.

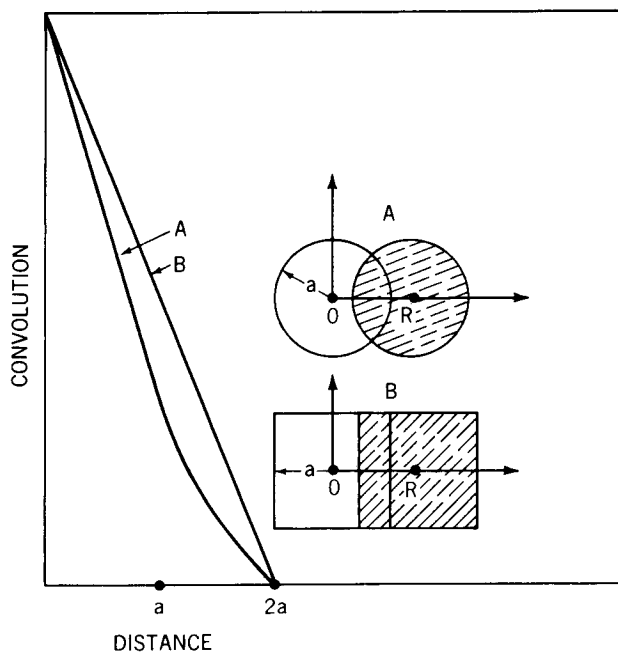


Figure 3 — Signal-Aperture interaction.

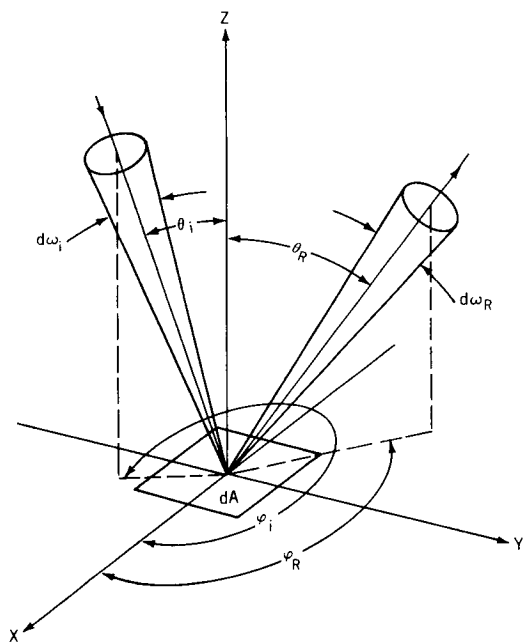


Figure 4 — Radiation geometry.

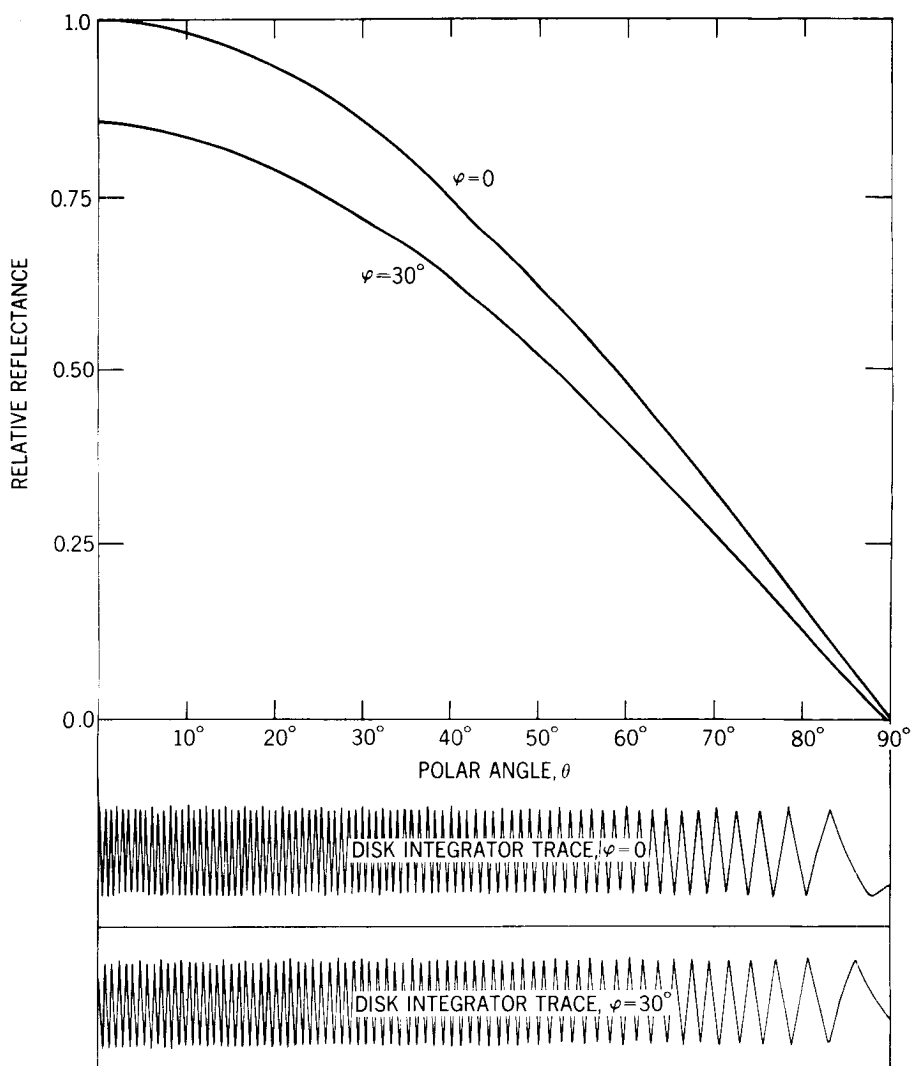


Figure 5 — Bidirectional Reflectance of NaCl, $\lambda = 0.570\mu$.

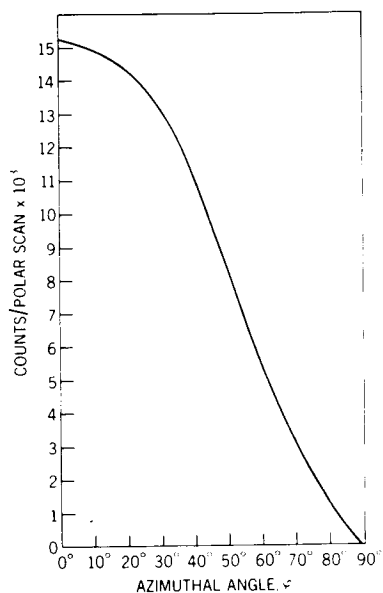


Figure 6 — Polar scan count versus Azimuthal Angle.

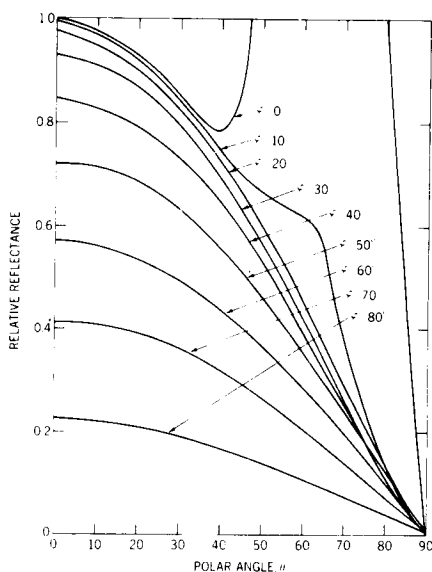


Figure 7 — Azimuthal dependence of a zinc oxide, methyl silicone white paint, $\lambda = 1.8\mu$, $\varphi_i = 63^\circ$.

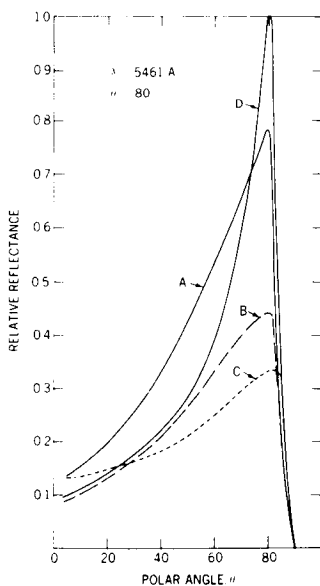


Figure 8 — Bidirectional Reflectance of a carbon black paint doped with microballons with mean diameters 20μ (A), 44μ (B), 63μ (C) and a 3M black velvet sample (D).

SCATTERING FROM SPECULAR SURFACES

M. W. Finkel, *Goddard Space Flight Center, Greenbelt, Maryland*

ABSTRACT

Diffraction by nearly specular Gaussian surfaces is discussed according to the Beckmann treatment and Fourier Optics. It is shown that the fundamental parameters σ , the RMS roughness and T , the correlation distance can be readily determined by scattering measurements.

INTRODUCTION

Optically polished metal surfaces, aluminum for example, exhibit random distributions of surface irregularities engendered by the very polishing process. Our special interest in these presumed specular surfaces relates to their spacecraft application. Optically, scattering from surface irregularities introduces stray light. Thermophysically, it may manifest itself as a critical power input. In the first part of this paper we shall in the main follow Beckmann's comprehensive treatment of scattering by rough surfaces. We have made a few small modifications so that it will be more amenable to our purposes. In the second section we have attempted to reformulate the problem according to Fourier Optics. Our principal concern will be the two parameters, the RMS roughness, σ and the correlation distance, T , and as we shall show, both can readily be determined by scattering measurements. The main import of the theory is given these two parameters we can completely characterize a surface. Throughout we shall use the terms coherent and specular, incoherent and diffuse, synonymously.

At this point we will write down a few underlying assumptions:

1. The incident wave is harmonic, plane and unpolarized.
2. Measurements of the scattered wave are made in the Fraunhofer region.
3. Multiple scattering, polarization, shadowing and edge effects can be neglected.
4. The surface roughness is isotropic and composed of a large number of elementary scatterers.
5. The scale roughness, σ/λ is much less than one.
6. We assume the reflectance, RR^* is known.

LIST OF SYMBOLS

A	projection of the active area
E ₁	incident scalar field
E ₂	scattered scalar field
g	$\sigma^2 V_Z^2$
J ₀	zero order Bessel function
\vec{k}	propagation vector
\vec{N}	normal vector
P	observation point
\vec{P}	$\vec{k}_1 + \vec{k}_2$
P(Z ₁ Z ₂ ;τ)	probability density
R ₀	distance from origin to P
\vec{R}	radius vector
S	active area
sinc X	sin X/X
T	correlation distance in which correlation coefficient, ρ attains the value e ⁻¹
\vec{V}	$\frac{\vec{k}_1 - \vec{k}_2}{\sqrt{V_X^2 + V_Y^2}}$
V _{XY}	
X, Y, Z	cartesian coordinates
ζ	ζ (X,Y)
θ ₁	angle of incidence
θ ₂	longitudinal scattering angle
θ ₃	lateral scattering angle
λ	wavelength
μ	mean value
ρ	correlation coefficient
ρ _s	normalized specular reflectance
ρ _d	normalized diffuse reflectance
σ	rms roughness
τ	separation parameter
φ	local angle of incidence
χ	characteristic function
< >	mean value
R	reflection coefficient

Diffraction by a Gaussian Surface

Following Beckmann⁽¹⁾⁽²⁾ we accept the solution of the Helmholtz integral,

$$E(P) = \frac{1}{4\pi} \iint (E \frac{\partial \Psi}{\partial N} - \Psi \frac{\partial E}{\partial N}) dS \quad (1.)$$

with Kirchhoff's approximation of the boundary conditions as,

$$E(P) = i e^{ikR_0/4\pi R_0} \iint (R\vec{V} - P) \cdot \vec{N} e^{i\vec{V} \cdot \vec{R}} dS \quad (2.)$$

Since we shall be principally concerned with scattering in the plane of incidence, we define the above vectors as (see Figure 1),

$$\bar{V} = \bar{k}_1 - \bar{k}_2 = k \{ (\sin\theta_1 - \sin\theta_2) \hat{x}_0 - (\cos\theta_1 + \cos\theta_2) \hat{z}_0 \} \quad (3.a)$$

$$\bar{P} = \bar{k}_1 + \bar{k}_2 = k \{ (\sin\theta_1 + \sin\theta_2) \hat{x}_0 + (\cos\theta_2 - \cos\theta_1) \hat{z}_0 \} \quad (3.b)$$

$$\bar{N} = -\sin\beta \hat{x}_0 + \cos\beta \hat{z}_0 \quad (3.c)$$

$$\bar{R} = X \hat{x}_0 + \zeta (X) \hat{z}_0 \quad (3.d)$$

Also, the projected area of a surface element is,

$$dS = dXdY \sec\beta \quad (3.e)$$

Tentatively assuming that the obliquity factor is independent of the coordinates and expressing the random variable, ζ by its average value the radiant flux at some field point, P can be written as,

$$\langle E_2 E_2^* \rangle = \left[\frac{(\bar{R} \cdot \bar{V} - \bar{P}) \cdot \bar{N}}{4\pi R_0} \right]^2 \sec^2\beta. \quad (4.)$$

$$\int_{-X}^X \int_{-Y}^Y \int_{-Y}^Y e^{iV_x(X_1 - X_2) + iV_y(Y_1 - Y_2)} \cdot \\ \langle e^{iV_z(\zeta_1 - \zeta_2)} \rangle dX_1 dX_2 dY_1 dY_2$$

Now let us introduce the characteristic function,

$$\chi(V_z, -V_z; \tau) = \int_{-\infty}^{\infty} \int_{-\infty}^{\infty} P(Z_1, Z_2; \tau) e^{iV_z(\zeta_1 - \zeta_2)} dZ_1 dZ_2 \quad (5.)$$

where $P(Z_1, Z_2; \tau)$ is some probability density. Almost invariably, however, surfaces tend to be normally distributed. So that it is entirely reasonable that we consider a bivariate normal distribution with means, $\mu_{Z_1} = \mu_{Z_2} = 0$ and standard deviation, $\sigma_{Z_1} = \sigma_{Z_2}$. We can then write the density as, ⁽³⁾

$$P(Z_1, Z_2; \tau) = \frac{1}{2\pi\sigma^2 \sqrt{1 - \rho^2}} \exp\left\{ -\frac{Z_1^2 - 2\rho Z_1 Z_2 + Z_2^2}{2(1 - \rho^2)\sigma^2} \right\} \quad (6.)$$

with the correlation coefficient, ρ given by, ⁽⁴⁾

$$\rho = e^{-\tau^2/T^2}$$

Before proceeding, it is necessary that we separate the characteristic function and with it the resulting fields into coherent and incoherent parts. There are several points of view we might adopt. If we turn to the joint density function it means separating out the marginal density. Or, if we think about it in quite general terms of correlation, it means distinguishing between periodic and random components. Alternatively, we could follow Beckmann and relate the mean scattered power to the variance. In any event we are lead to,

$$\chi(V_Z) \chi^*(V_Z) = e^{-g} \quad (7.a)$$

where $g = \sigma^2 V_Z^2$ and

$$\chi_2(V_Z, -V_Z) \chi(V_Z) \chi(V_Z) = e^{-g} \sum_{m=1}^{\infty} \frac{g^m}{m!} e^{-m \tau^2 / T^2} \quad (7.b)$$

where we associate (7.a) with the coherent field which, of course, implies constant phase and zero correlation, and conversely (7.b) with the incoherent field. Putting things together with reference to equations (4) and (7.a) we can express the mean relative power specular reflection coefficient for $g < 1$ as,

$$\langle E_2 E_2^* \rangle_S = \left[\frac{(\overline{RV} - \overline{P}) \cdot \overline{N}}{4\pi R_0 \cos \beta} \right]^2 e^{-g} \quad (8.)$$

$$| \int_{-X}^Y \int_{-X}^Y e^{iV_X X + iV_Y Y} dX dY |^2$$

From Figure 1 we conclude that

$$\begin{aligned} \theta_1 &= \phi_1 + \beta \\ \theta_2 &= \phi_2 - \beta \end{aligned}$$

Then the sum and difference of the propagation vectors dotted into \overline{N} reduce to,

$$\overline{P} \cdot \overline{N} = -k (\cos \phi_1 - \cos \phi_2)$$

$$\overline{V} \cdot \overline{N} = -k (\cos \phi_1 + \cos \phi_2)$$

If we presume local specularity, which is tantamount to saying that our surface is composed of a large array of elementary facets, then $\phi_1 = \phi_2$, and,

$$\overline{P} \cdot \overline{N} = 0 \quad (9.)$$

$$\overline{V} \cdot \overline{N} = -2k \cos \phi$$

Consequently, for normal incidence

$$\langle E_2 E_2^* \rangle = A^2 (R R^*) \frac{e^{-g} \text{sinc}^2 V_X X \text{sinc}^2 V_Y Y}{\lambda^2 R_0^2} \quad (10.)$$

Subsequently, we shall refer to the normalized specular reflectance which can be defined as,

$$\rho_s = \langle E_2 E_2^* \rangle / |E_{20}|^2$$

where $|E_{20}|^2$ is the flux from an otherwise identical but perfectly smooth surface. But realizing that now $V_X = V_Y = 0$ and of course, $g = 0$,

$$\rho_s = e^{-g} \operatorname{sinc}^2 V_X X \operatorname{sinc}^2 V_Y Y \quad (11.)$$

Turning now to the diffuse component and expressing the variable points $X_{1,2}$ and $Y_{1,2}$ in terms of the separation parameter, τ ,

$$X_1 - X_2 = \tau \cos \phi$$

$$Y_1 - Y_2 = \tau \sin \phi$$

we can rewrite (4) after inserting (7.b) as,

$$\langle E_2 E_2^* \rangle_D = \left[\frac{(\overline{RV} - \overline{P}) \cdot \overline{N}}{4\pi R_0 \cos \beta} \right]^2 A \int_0^\infty \int_0^{2\pi} \quad (12.)$$

$$e^{iv_X \tau \cos \phi + iv_Y \tau \sin \phi} e^{-g - \tau^2/T^2} \tau d\tau d\phi$$

Integrating with respect to ϕ yields,

$$\int_0^{2\pi} e^{iv_X \tau \cos \phi + iv_Y \tau \sin \phi} d\phi = 2\pi J_0(V_{XY}, \tau)$$

where J_0 is the zero order Bessel function and

$$V_{XY} = k (\sin^2 \theta, -2 \sin \theta_1 \sin \theta_2 \cos \theta_3 + \sin^2 \theta_2)^{1/2}$$

Then evaluating the integral,

$$\int_0^\infty J_0(V_{XY}, \tau) e^{-\tau^2/T^2} \tau d\tau = T^2/2 e^{-V_{XY}^2 T^2/4}$$

In a very real sense the above integral is a high point of this development. Not only does it reflect the implicit symmetry, but it transforms, as it should, one Gaussian into another. Once again imposing local specularly,

$$\overline{P} \cdot \overline{N} = 0$$

$$(\overline{V} \cdot \overline{N})^2 = 4k^2 \cos^2 \phi$$

$$\text{and } g = [4\pi(\sigma/\lambda) \cos \beta \cos \phi]^2$$

we find that the relative mean power diffuse reflection coefficient is,

$$\langle E_2 E_2^* \rangle_D = \sigma^2 k^4 T^2 A (RR^*) / \pi R_0^2 \cdot \cos^4 \phi e^{-(g + V_{XY}^2 T^2/4)} \quad (13.a)$$

We can restate (13.a) by letting $e^{-g} \rightarrow 1$ as $g \rightarrow 0$ and substituting $\phi = \theta_2/2$ for normal incidence and write,

$$\langle E_2 E_2^* \rangle_D = 16\pi^2 \sigma^2 / \lambda^4 (RR^*) \left(\frac{1 + \cos \theta_2}{2} \right)^2. \quad (13.b)$$

$$(\pi A T^2) (e^{-V_{xy}^2 T^2 / 4}) R_0^{-2}$$

which is in full agreement with Beckmann. For a one dimensional surface, that is a surface invariant in the y direction, we need only replace V_{xy}^2 by V_x^2 and $\pi A T^2$ by $\sqrt{\pi A T}$ so that (13.b) now reads,

$$\langle E_2 E_2^* \rangle_D = 16\pi^2 (\sigma^2 / \lambda^4) (RR^*) \left(\frac{1 + \cos \theta_2}{2} \right)^2. \quad (13.c)$$

$$\sqrt{\pi A T} e^{-V_x^2 T^2 / 4 / R_0^2}$$

The question as to whether a surface is one or two dimensional can be readily resolved by goniophotometric measurements in and out of the plane of incidence. For measurement out of the plane of incidence we need only replace $\cos^4 \phi$ by,

$$G(\theta_1, \theta_2, \theta_3) = \left(\frac{1 + \cos \theta_1 \cos \theta_2 - \sin \theta_1 \sin \theta_2 \cos \theta_3}{2} \right)^2$$

Fourier Optics

It should be instructive to arrive at the above formulation via Fourier Optics. In approaching the problem from another point of view we might, perhaps, gain added insight. Let us begin by asserting that the diffraction pattern of a non-periodic object is the Fourier transform of that object. All that follows merely flows from this fundamental statement. In our case the object happens to be a rough surface. Once again we will assume that our surface is bivariant and that $g \ll 1$. For simplicity we will consider a one dimensional rough surface. We can easily extend our final results to include a two dimensional isotropic surface by referring to equation (13). Also, since we are primarily concerned with the parameters σ and T , we can, without loss of generality, limit ourselves to normal incidence.

We first consider the specular component which we recall implies zero correlation. The distribution then reduces to a marginal density. But bearing in mind that our presumed infinite distribution really only extends over a finite range suggests that we introduce the rectangular function, Π and write,⁽⁵⁾

$$P(X, Z) = \frac{1}{\sqrt{2\pi}\sigma} e^{-Z^2/2\sigma^2} \cdot \frac{1}{2L} \Pi \left(\frac{X}{2L} \right) \quad (14.)$$

Now we know that the transform of the autocorrelation function is the power density spectrum (Wiener). Moreover, we can express a two dimensional auto correlation function as,

$$\phi(X, Z) = \int_{-\infty}^{\infty} \int_{-\infty}^{\infty} f(X', Z') g(X + X', Z + Z') dX' dZ'$$

Consequently,

$$\phi(X, Z) = \frac{1}{8\pi\sigma^2 L^2} \int_{-\infty}^{\infty} \int_{-L}^{L-x} e^{-Z'^2/2\sigma^2} \quad (15.)$$

$$e^{-(Z+Z')^2/2\sigma^2} \Pi\left(\frac{X'}{2L}\right) \Pi\left(\frac{X+X'}{2L}\right) dX' dZ'$$

$$= \frac{1}{8\sqrt{\pi}\sigma^2 L^2} e^{-Z^2/4\sigma^2} (2L - |X|)$$

for $-2L \leq X \leq 2L$

Now transforming the auto correlation function,

$$F(\phi) = \frac{1}{8\sqrt{\pi}\sigma L^2} \int_{-\infty}^{\infty} \int_{-2L}^{2L} e^{-Z^2/4\sigma^2} \quad (16.)$$

$$(2L - |X|) e^{-iV_X X - iV_Z Z} dX dZ$$

$$= e^{-\sigma^2 V_Z^2 \text{sinc}^2 V_X L} = e^{-g \text{sinc}^2 V_X L}$$

But the intensity distribution must be proportional to the incident intensity which means that in our case we can introduce a factor, (6)

$$M_0 = (RR^*)A/\lambda^2 R_0^2$$

So that now we have,

$$\langle E_2 E_2^* \rangle_S = \frac{A(RR^*) e^{-g \text{sinc}^2 V_X L}}{\lambda^2 R_0^2} \quad (17.)$$

which is the one dimensional form of equation (10) in the previous section.

Let us pause for a moment and review this development. Obviously, e^{-g} and $\text{sinc}^2 V_X L$ are transforms of the marginal distribution and the Π function. This, of course, suggest we could have proceeded by another route by appealing directly to the convolution theorem.

In terms of convolution the Π function, whose physical significance is entirely reminiscent of diffraction from a slit, can be interpreted as the instrument function. And just as with the slit, as we narrow the distribution, so do we spread the diffraction pattern.

Now let us turn to the diffuse (noncoherent) component. The characteristic function associated with diffuse component, equation (7.b) for $g \ll 1$ is,

$$\chi_2(V_Z, -V_Z) - \chi(V_Z)\chi(V_Z) = g e^{-g - \tau^2/T^2}$$

Furthermore, we can determine the auto correlation function, $\phi(\tau)$ from

$$\partial^2 \chi / \partial^2 v_z |_{v_z=0}$$

So that,

$$\phi(\tau) = \sigma^2 e^{-\tau^2/T^2} \quad (18.)$$

And once again transforming, we find that for a one dimensional surface,

$$F(\phi(\tau)) = \sigma^2 \sqrt{\pi} T e^{-v_x^2 T^2/4} \quad (19.a)$$

For a two dimensional surface,

$$F(\phi(\tau)) = \sigma^2 \pi T^2 e^{-v_{xy}^2 T^2/4} \quad (19.b)$$

According to the convolution theorem we must now determine the transform of the Π function. Only now the isotropy of the problem dictates that we introduce the circular function $\Pi(R)$, whose Fourier Bessel transform is given by,

$$B\{\Pi(R/L/2)\} = \left(\frac{L^2}{2}\right) \frac{J_1\left(\frac{\pi v_{xy} L}{2}\right)}{v_{xy} L/2}$$

Expanding the Bessel function for small arguments,

$$J_1(X) \rightarrow X/2$$

Therefore,

$$B\{\Pi(R/L/2)\} = \pi L^2/4. \quad (20.a)$$

This implies that since $T < L$ the incoherent scattering is essentially due to the surface roughness rather than the truncation of the Gaussian distribution. The intensity will, therefore, be,

$$B\{\Pi(R/L)\}^2 = \pi^2 L^4/16. \quad (20.b)$$

Consequently, from (19.b) and (20.b) we find that

$$\langle E_2 E_2^* \rangle_D = C \pi^2 \sigma^2 \pi T^2 e^{-v_{xy}^2 T^2/4}$$

where C refers to some amplitude.

Up to this point our treatment has been quite general. Nothing explicitly has been said about the wave nature of light. We can reconcile this matter by including in the constant, C the inclination factor,

$$K(\theta) = -i/2\lambda (1+\cos\theta)$$

as required by the Fresnel theory.

Again introducing, Mo and normalizing we find that,

$$(21) \quad \langle E_2 E_2^* \rangle_D = \frac{16 \pi^2 \sigma^2 (RR^*)}{\pi A T^2 (e - V_{xy}^2 T^2 / 4)} \left(\frac{1 + \cos \theta_2}{2} \right)^2 / \lambda^4 R_o^2$$

Which agrees with (13.b).

So we see that essentially our final result is composed of three factors. There is the $\Pi(R)$ function which plays and analogous role to the $\Pi(X)$ function, the transform of one Gaussian into another and the inclination factor necessitated by physical optics.

As an aside, we cannot help but note the Rayleigh-like character of these expressions. We have in mind the λ dependence and the appearance of $2\pi\sigma/\lambda$ which translates in the Rayleigh case to the size parameter, $\frac{2\pi R}{\lambda}$. If we care

to stretch matters a bit, it is tempting to compare our results with the scattered intensity from an inhomogenous solid.⁽⁷⁾ The similarity, although not unexpected, is quite striking.

Thus far we have been concerned with scattering from an elementary area. But we know that a great many such areas participate in the scattering process. The extension is straight-forward. According to a well known theorem in probability, if all directions have equal probabilities, the length of the resultant vector is \sqrt{N} . We, therefore, anticipate that the total power scattered should go as N times that of single surface element.⁽⁸⁾

Measurements

We return now to the key parameters σ and T . Because of the statistical nature of the problem we will not present a deluge of measurements. Rather, we are content to demonstrate the applicability of the theory and show that by fairly conventional measurements both the RMS roughness and the correlation distance can be determined. A very obvious method for making these measurements is the goniophotometer. The underlying assumption is, we repeat, given these two parameters we can with some confidence completely characterize a surface.

Looking back at equations (10) and (13) we note that the specular component has a λ^{-2} while the diffuse component has a λ^{-4} dependence. Consequently, σ can be determined less ambiguously at longer wavelengths. In the specular direction with $V_x = V_y = 0$ equation (11) reduces to

$$\rho_s = e^{-g}$$

or expanding the exponential,

$$\rho_s = 1 - (4\pi\sigma/\lambda \cos \theta_1)^2$$

For most goniophotometers it is simplest to select an angle of incidence of about 10° and perform a series of measurements varying λ . Figure (2) is a plot of ρ_s versus scale roughness, σ/λ , in which we have tacitly accepted nearly specular to mean that g is something less than 0.1. Typical values for ρ_s at 1μ for an aluminum (6061) surface overcoated with vacuum deposited aluminum when compared to a quartz substrate standard with an identical coating hovered about 98%, which means that σ is typically about 120\AA .⁽⁹⁾

We now consider the remaining parameter, T . Clearly, for this parameter it is advantageous to use a shorter wavelength, say 5000\AA . Suppose we scan in the θ_2 direction and ratio the scattered flux in two adjacent directions, θ_2 and θ_2' . Then from (13.c)

$$\frac{\langle E_2 E_2^* \rangle}{\langle E_2 E_2^* \rangle} \bigg|_{\theta_2} = \frac{(1 + \cos \theta_2)^2}{(1 + \cos \theta_2')^2} e^{-\pi^2 T^2 / \lambda^2 (\sin^2 \theta_2 - \sin^2 \theta_2')}$$

from which we can readily determine T . The results of two such measurements and their correlation distance are shown in Figure (3). The lap and polishing agent for curve A was bee wax and Linde 0.05, and bee wax and tin oxide for curve B. Again, the surface was aluminum 6061 overcoated with V.D.A. We note in each case the towering specular peak broadening as predicted by equation (10), then merging with the diffuse component. Instead of exhibiting the hoped for precipitous behavior of a delta function, the sinc function spreads the specular component over an extended range. Indeed, the figure shows that the specular component survives out to about 30° . This means that the determination of T must begin past the specular component and extrapolated back as shown by the dashed portion of the curve in Figure (3). The Gaussian character of equation (13) as shown in Figure (3) spreads the diffuse component over the entire forward space. Moreover, there is no apparent method of arresting this spread.

This brings us to an interesting question. According to theory, Kirchhoff approximations are valid for $T > \lambda$. Yet we find that the essential features of the theory are preserved for $T \approx \lambda$. But this is not necessarily a contradiction if we recall that diffraction gratings behave in a very predictable manner even with grooves of the order of a wavelength. As a further aside, it should be possible to extract further information from the theory, such as the width of the irregularities, and the number of scattering centers.

Finally, let us briefly indicate how these measurements might be employed thermophysically.⁽¹⁰⁾ Given that we have determined the mean power reflection coefficients we now essentially know the reflection distribution function. And knowing the distribution function we can determine the radiance. We can then express the power reflected by one surface element and intercepted by another in terms of the radiance.

Conclusion

We have presented two treatments of diffraction by nearly specular surfaces. The first, according to Beckmann, was slightly modified to include local specularity. The second, somewhat more physical, concerns diffraction from a truncated Gaussian distribution. We have seen that the parameters σ and T readily submit to experimental determination. Typically, we observe the massive specular component broadening and flowing into the diffuse component. We note with special interest that the essential features of the theory are preserved by extending Kirchhoff's approximation to $T < \lambda$.

References

1. Beckmann, D., and Spizzichino, A., "The Scattering of Electromagnetic Waves from Rough Surfaces," New York: MacMillan Co., 1963.
2. Beckmann, D., "Scattering of Light by Rough Surfaces," in: Progress in Optics ed. by E. Wolf, Amsterdam: North-Holland Pub. Co., 1967, pp. 55-69
3. Korn, G. A., and Korn, T. M., "Mathematical Handbook for Scientist and Engineers," New York: McGraw Hill Book Co., 1961.
4. Feinstein, J., "Some Stochastic Problems in Wave Propagation," Transactions I.R.E., AP-2: 23-30, 1954.
5. Bracewell, R., "The Fourier Transform And Its Applications," New York: McGraw Hill Book Co., 1965.
6. Levi, L., "Applied Optics," New York: John Wiley and Sons, 1968.
7. Debye, P., and Bueche, A. M., "Scattering by an Inhomogenous Solid," J. Applied Physics, Vol. 20: 518-525, June 1949.
8. Born, M., and Wolf, E., "Principles of Optics", New York: MacMillan Co., 1964.
9. Bennett, H. E., and Porteus, J. O., "Relation Between Surface Roughness and Specular Reflectance at Normal Incidence," J. Optical Soc. of America, Vol. 51, No. 2: 123-129, Feb. 1961.
10. Nicodemus, F., "Directional Reflectance and Emissivity of a Opaque Surface", Vol. 4, No. 7: 767-773, July 1965.

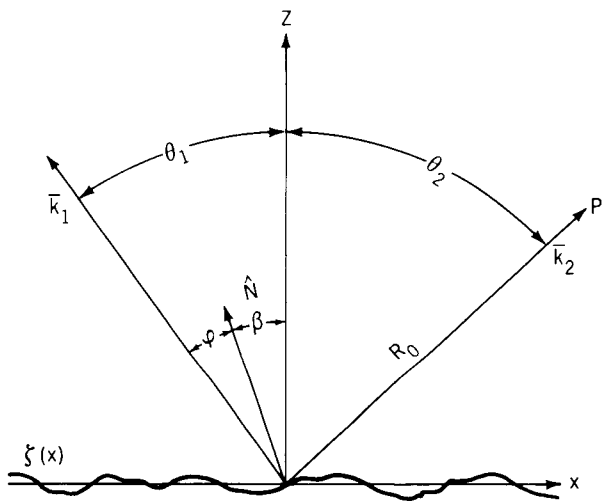


Fig. 1 - Scattering geometry.

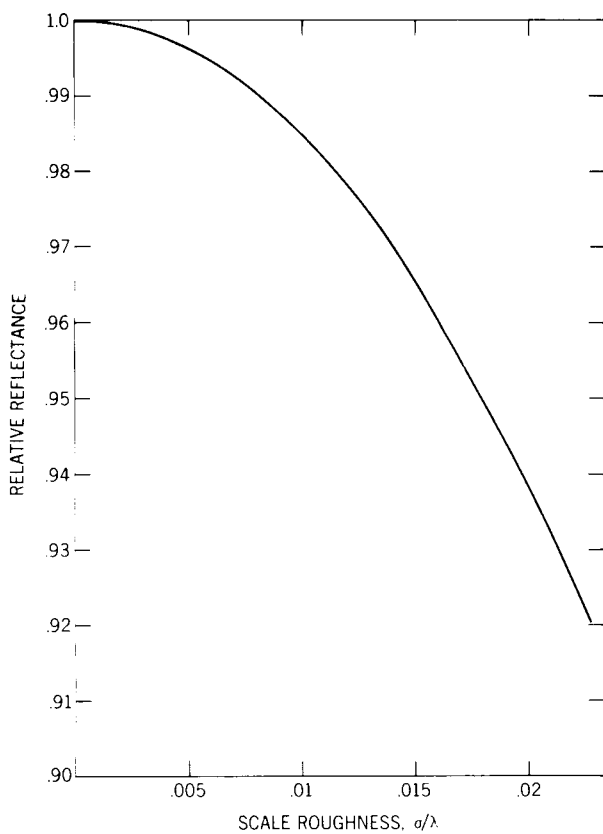


Fig. 2 - Normalized specular reflectance, ρ_s .

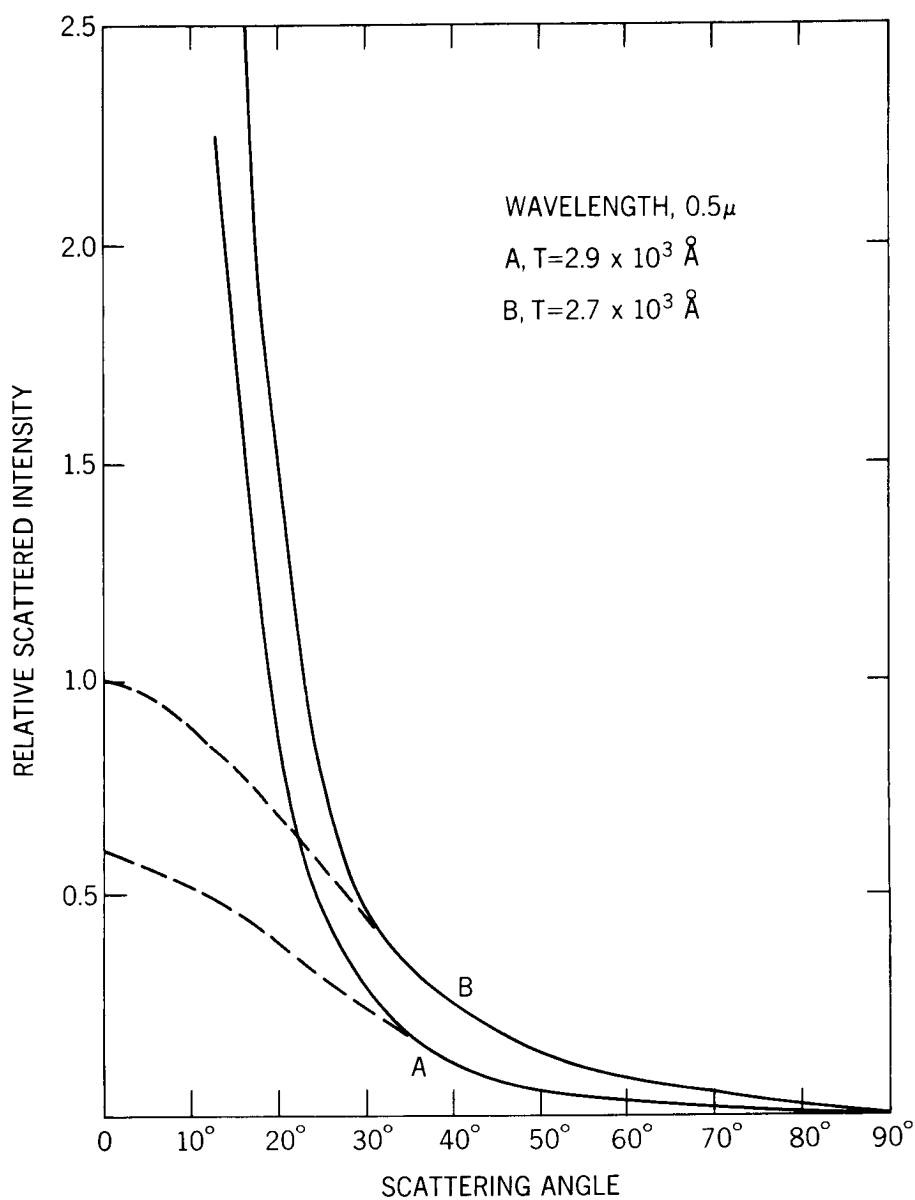


Figure 3 — Diffuse Reflectance at normal incidence for two aluminum samples. The correlation distance, T is determined from Eq. (13,c).

SKYLAB FLUID MECHANICS SIMULATIONS: OSCILLATION, ROTATION, COLLISION AND COALESCENCE OF WATER DROPLETS UNDER LOW-GRAVITY ENVIRONMENT

Otha H. Vaughan, Jr., *Aerospace Environment Div./Space Sciences Lab., NASA/Marshall Space Flight Center, Alabama 35812*

R. J. Hung, *The University of Alabama in Huntsville, Alabama 35807*

ABSTRACT

Studies of the dynamics of water droplets has been one of the most interesting areas in the fields of atmospheric microphysics, nuclear physics, astrophysics, fluid mechanics, mechanical engineering, and chemical engineering. Skylab 4 crew members performed a series of demonstrations showing the oscillations, rotations, as well as collision coalescence of water droplets which simulate various physical models of fluids under low gravity environment. The results from Skylab demonstrations show that these demonstrations have provided much interesting information and illustrate the potential of an orbiting space-oriented research laboratory for the study of more sophisticated fluid mechanic experiments.

I. INTRODUCTION

Recently, the dynamics of oscillation, rotation, collision and coalescence of water droplets has triggered the imagination of researchers in various fields of physical sciences, such as meteorology, nuclear physics, astrophysics, fluid mechanics, mechanical engineering and chemical engineering. Lord Rayleigh (1879) first investigated mathematically the various modes of oscillation of fluids. Since then there have been many investigations concerning the dynamics of liquid drops, yet the mechanics of the oscillation (particularly nonlinear oscillation), rotation (particularly rotation breakup), and the coalescence processes still remain poorly understood.

To study and observe the dynamics of liquids in the terrestrial laboratory, artificial supports are required to eliminate the gravitational force and to provide for longer observational time. The levitation apparatuses which are available today are the vertical wind tunnel, electrostatic potential, high frequency acoustic waves (ultrasonic waves), and high energy level laser beams. Although these are useful techniques, their use tends to mask other types of minute forces and disturbs their effects which might confuse the experimental

observations. Experiments performed in an orbiting spacecraft with its low gravity environment offer a technique to study fluids and observe their modes of oscillation without the side effects of artificial suspension techniques.

Prior to the Skylab program various studies had been performed in wind tunnels to observe the oscillations, rotations and coalescence of liquid drops (e.g., Beard and Pruppacher, 1971). However, many of the oscillation modes could not be detected or recorded because they were being masked by the aerodynamic forces. To understand how water droplets will oscillate, rotate and collide, and to see how fluids will behave under the low gravity environment, a series of simple science demonstrations were proposed for the Skylab mission. The demonstrations were designed to provide a data base for the design of a fluid mechanics and a cloud physics type laboratory to be flown as a part of the Spacelab Shuttle program. The Skylab 3 and 4 crews were requested to perform these science demonstrations so that the mechanics of collisions, coalescence, rotation, natural oscillations and techniques for manipulation and positioning of fluids in low gravity could be simulated and studied.

In the present paper, we have limited ourselves to a discussion of the following three branches of fluid mechanics simulation under low-gravity environment: (1) oscillation of droplet which characterizes the nuclear oscillation in nuclear physics, bubble oscillation of two phase flow in chemical engineering, and water drop oscillation in meteorology; (2) rotation of droplet which characterizes nuclear fission in nuclear physics, formation of binary stars and rotating stars in astrophysics, and breakup of water droplet in meteorology; and (3) collision and coalescence of droplets which characterize nuclear fusion in nuclear physics, and processes of rain formation in meteorology.

II. EXPERIMENTAL ARRANGEMENTS

The hardware used in the Skylab fluid mechanics demonstrations consisted of on-board medical type syringes, pieces of tape attached to drinking straws, marker pen writing ink, grape drink, strawberry drink, pieces of thread, the teflon coated flat surface of the ED 52 "web formation in zero gravity" spider cage, reflection mirror, etc., and the on-board color TV camera. The water used in the demonstration was colored, to enhance the photography, by adding a small amount of marker pen ink, grape drink mix, or strawberry drink mix to each drop. Movies of the dynamics of oscillations, rotations, collisions and coalescence of water droplets under low gravity environment were recorded on-board TV cameras. These series of color films are identified as Fluid Mechanics Demonstrations - TV 107.

The films taken with the on-board TV cameras were later analyzed. Measurements of the characteristics of the drop oscillations, rotations, collisions and coalescence were made by using a Vanguard film analyzer. The amplitude and wavelength of the oscillations were determined directly from the film using appropriate scale factors. The frequency of oscillation and angular velocity of rotation were determined by counting the number of frames that were observed during the time interval and then dividing this count number by the TV camera framing rate.

In this paper, techniques and results of space simulation will be discussed. The theoretical analysis and comparison of the Skylab demonstration data with existing theory is out of the scope of the paper but it is published elsewhere (Vaughan, et al., 1974a; Vaughan, et al., 1974b; Hung, et al., 1974).

III. SKYLAB FLUID MECHANICS SIMULATIONS

The Skylab science demonstration/simulation TV 107 (Fluid Mechanics Demonstration) has created much interest among the researchers in various fields, such as meteorology, nuclear physics, astrophysics, fluid mechanics, mechanical engineering and chemical engineering. In particular, fluid demonstration of oscillation, rotation, collision and coalescence of water droplets simulate some physical models of interests which may contribute toward the solutions of a great number of unsolved problems.

Some selected frames of oscillation, rotation, collision and coalescence of water droplets from TV 107 will be presented in this paper.

A. Oscillation of Water Droplet - Study of nuclear oscillations has been one of the major topics in nuclear physics in the last forty years. In particular, nuclear physicists are mostly interested in the investigation of nuclear deformation energy surfaces. To study these phenomena, a model of an incompressible liquid drop with charges uniformly distributed throughout the volume and a uniform surface tension is generally assumed (Cohen, et. al., 1974).

Atmospheric microphysics studies deals with droplet and droplet-droplet interactions. Particularly, oscillation of water droplet and oscillation breakup of droplet are closely correlated to the mechanism of rain formation (Mason, 1971).

Stability of bubble oscillation is very important for the study of two-phase flow in chemical engineering. Furthermore, chemical engineers are also very interested in the study of the dynamics of the contact line between the fluid and solid surface as the water droplet oscillated (West, 1911; Huh and Scriven, 1971).

These physical models of interests were very well simulated and are shown in the Skylab Fluid Mechanics Simulation. Figure 1 shows some selected frames of the various modes of water droplet oscillation. The numbers on the pictures in the figure show the

sequence of TV camera frames taken in the Skylab demonstration. Picture number 1 shows a water droplet with the diameter of 2.67 cm touched on opposite sides by two soda straws. Picture number 7 shows that two soda straws were plucked outward from the water droplet causing the water droplet to oscillate. We observe various modes of oscillation until the decay of oscillation occurs due to its internal damping. Picture number 9 shows the oscillation of a water droplet in longitudinal direction and picture 17 indicates the oscillation of a water droplet in transverse direction. Pictures number 22 and 24 show the transition of droplet oscillation from transverse direction to longitudinal direction. Pictures number 33 and 36 show the transition of droplet oscillation from longitudinal to transverse direction. Picture number 42 shows the recovery of the oscillation of a water droplet to its original shape due to damping effect.

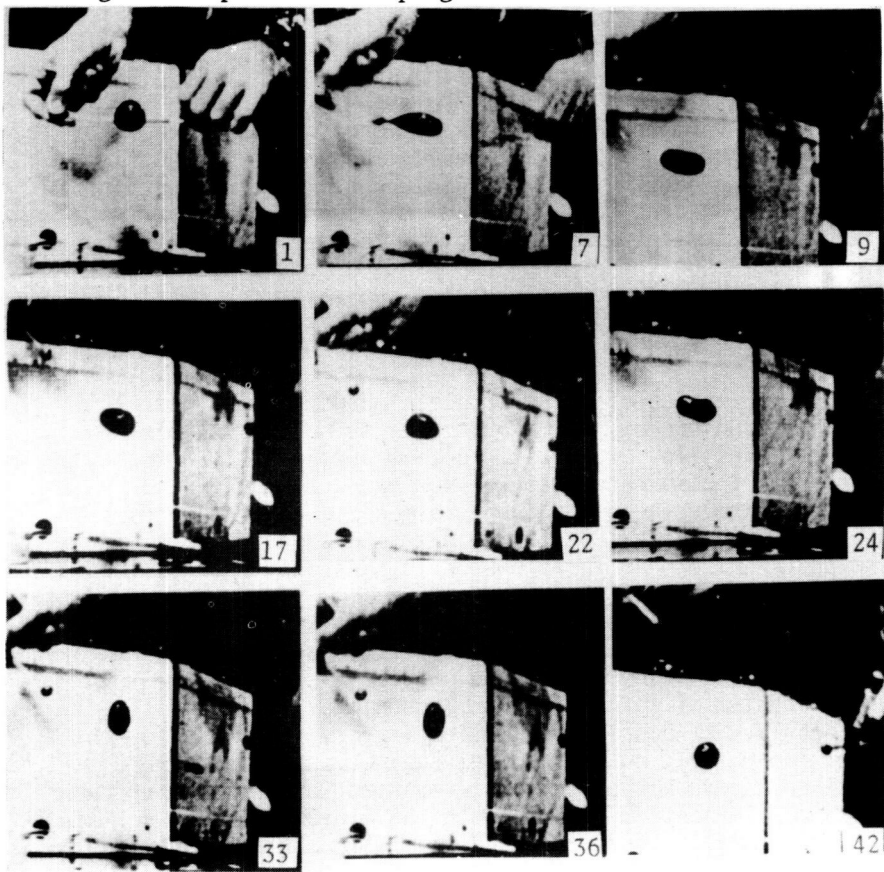


Figure 1. Skylab Fluid Mechanics Demonstration - Free Oscillation of Water Droplet.

Figure 2 shows selected frames of the various modes of the oscillating water droplet attached to the flat surface. This is very useful for the study of droplet oscillations and the dynamics of contact line between the fluid and solid surface as the water droplet oscillated. Picture number 1 shows a drinking straw being inserted into the center of a water droplet attached to the flat surface. Pictures number 3 and 10 show the soda straw being pulled out of the water drop. Picture number 17 shows the oscillation of water droplet as it reaches its maximum amplitude right after the soda straw left the surface of the droplet. Pictures number 22 and 26 shows the water droplet decreasing its amplitude, and picture number 29 shows the oscillation of a water droplet descending to its minimum amplitude. Picture number 31 shows the increasing amplitude of a water droplet, and picture number 39 shows the proximate moment when the water droplet just completed one cycle of oscillation and returned to its maximum amplitude.

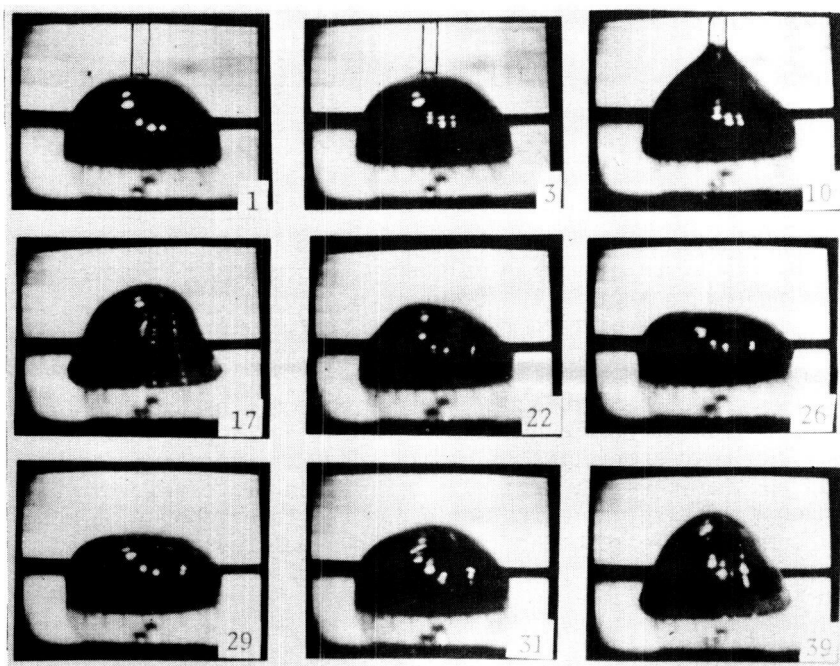


Figure 2. Skylab Fluid Mechanics Demonstration - Oscillation of Water Droplet Attached to the Flat Surface.

The dynamics of the droplet oscillation is governed by the boundary condition given by the Young-Laplace relation (Landau and Lifshitz, 1959). Solution of Young-Laplace relation leads to the relation of droplet oscillation (Rayleigh, 1879)

$$\omega^2 = \frac{\alpha \ell (\ell-1) (\ell+2)}{\rho R^3} \quad (1)$$

where α denotes surface tension; ρ , the density of fluid; R , the radius of unperturbed liquid droplet; ω , the circular frequency of oscillation; and $\ell = 0, 1, 2, \dots$, the integer numbers. Equation (1) shows that $\ell = 0$ and 1 correspond only to rigid body oscillations, and the fundamental mode corresponds to $\ell = 2$. In general, the oscillation for each mode ℓ , there are $2\ell+1$ oscillations along different directions. These oscillations with the same mode ℓ have the same frequency. If we consider only the characteristics of the mode and not the type of oscillations in the various directions, the shape of the drop is (Hung, et al., 1974)

$$r = R + \sum_{\ell} a_{\ell} P_{\ell} (\cos \theta) \quad (2)$$

where P_{ℓ} is the ℓ th order Legendre polynomial; (r, θ, ϕ) , the axes of spherical coordinates; and the coefficients a_{ℓ} are functions of time t :

$$a_{\ell} = R_e [b_{\ell} e^{-i\omega t}] \quad (3)$$

where ω is given by Equation (1), and b_{ℓ} is some amplitude of the oscillations.

Skylab Fluid Mechanics Demonstration provides us a good opportunity to study how well the theory stands.

B. Rotation of Water Droplet - About half the stars in the sky are binary stars. The fission theory, proposed by Poincaré in 1885, attempted to explain the occurrence of binary stars by a natural process of evolution of a single star. Unfortunately, recent investigation showed that the results were adverse to Poincaré's picture. A newer fission theory of rotating liquid drops has been proposed to study these problems (Chandrasekhar, 1969). Experimentally, the dynamics of rotating liquid drops simulate the characteristics of binary stars and rotating stars.

In nuclear physics, mechanics of fission process is the area which draws a great attention among the researchers. A model of an incompressible rotating liquid drop simulates the dynamic evolution of the stability of the mechanics of nuclear fission process (Cohen, et al., 1974).

In meteorology, dynamic of the breakup of water droplet is closely related to the warm cloud processes. The Skylab demonstration of rotating droplet is also of particular interest in large precipitation drop breakup.

Figure 3 shows some selected frames of the sequences of rotating drops exhibiting "dog bone" or "dumb bell" shape. To get the drop of water to rotate in the "dog bone" or "dumb bell" shape the astronaut conceived a simple technique which he used to produce initially a prolate spheroid by asymmetric excitation of the outer surface of the drop of water. After a few applications of this asymmetric excitation force the drop is caused to rotate at a higher rotational speed which produced an unstable oscillation

mode and the drop then tears into two separate drops. Picture number 1 shows the drop of water rotating in the "dog bone" shape. Picture number 2 shows a drop being initially touched with the rotation tool. The astronaut touches the drop and later he causes it to begin to rotate. Each time the astronaut touched the drop at its outer surface with a rotating motion he caused it to rotate at a slightly higher rotational rate. After a number of encounters with the drop, it was then allowed to rotate until it began to breakup by itself. Picture number 136 shows the drop still in contact with the tool and being excited - note the start of the prolate sphere shape now occurring. Picture number 165 shows the drop now free of the tool but in a rotating/oscillating mode. Pictures number 747 thru number 752 show how the drop began to reach the unstable mode as it begins to rotate faster until it begins to neck down and breakup into two distinct drops. In future space flights, a demonstration should be performed in the low gravity environment to illustrate the case of the oblate spheroid rotating at increasing angular velocity until a ring of fluid similar to a "donut" is produced.

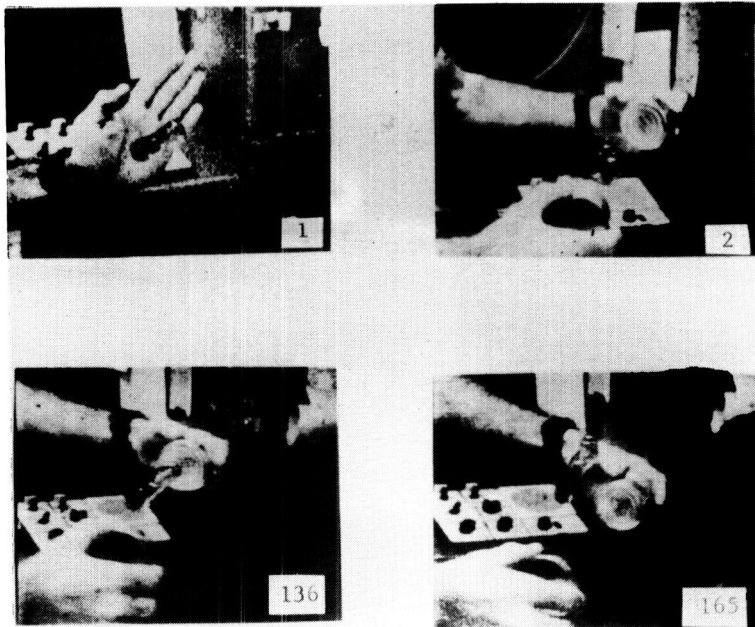


(Figure 3 to be Continued)

(Figure 3 Continued)

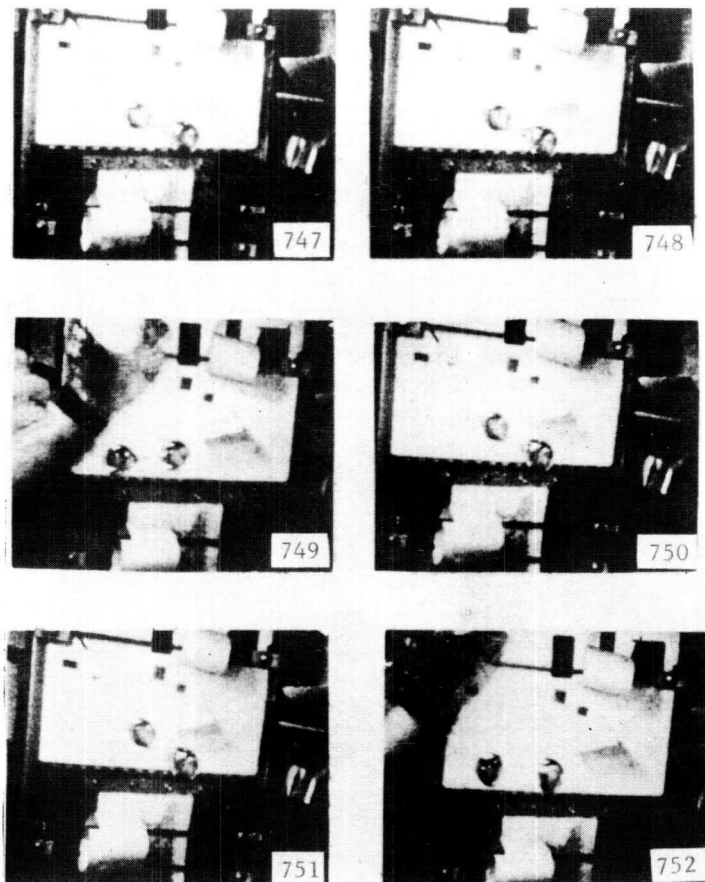


Figure 3. Skylab Fluid Mechanics Demonstration - Rotation of Water Droplet.

Based on the original work by Plateau (1866), Chandrasekhar (1965) extends the work and investigated various modes of oscillation on the stability of rotating drops. For an axisymmetrical form and uniform density, the figure of equilibrium depends on the value of the non-dimensional parameter ξ (Chandrasekhar, 1965)

$$\xi = \frac{1}{8\alpha} \rho \Omega^2 a^3 \quad (4)$$

where Ω denotes the angular velocity of rotation; a , the equatorial radius of the distorted drop; ρ , density of drop; and α ,

the surface tension. As ξ decreases the figure tends to the oblate spheroid, and degenerates into a sphere as $\xi = 0$. However, as ξ increases, the figure rapidly departs from the spheroidal form. The polar regions are flat as $\xi = 1$; as ξ increases beyond 1, the drop develops a dimple; and finally the breakup occurs.

The theory of time dependent evolution of rotating stability of liquid droplets has been a very active research field for many years. It is because of a conspicuous lack of experimental evidence to backup the boundary conditions assumed in numerical computation which makes the computer simulation still not completely explored. In this respect, the Skylab demonstration of a rotating droplet has enhanced the understanding of rotational stability of liquids.

C. Collision and Coalescence of Water Droplets - Recently studies of the dynamics of the collision and coalescence of water droplets has been widely used in simulating the mechanism of nuclear collision and nuclear fusion. These dynamic studies are considered to be a significant step in understanding fusion process of nuclear physics (Cohen, et al., 1974).

In cloud physics, the precipitation process is solely dependent on growth of droplets and ice crystals which is governed by the following three stages: (1) growth by nucleation process, this process includes condensation, ice deposition, and freezing of water droplets and ice crystals on the surface of foreign substances or of the same substances as nuclei; (2) growth by diffusion process, after a droplet or ice crystal has been nucleated and has surpassed the free energy barrier or critical radius, it enters a stage of growth by diffusion; and (3) growth by collision and coalescence process, the growth by diffusion process is negligible compared with that by coalescence process as the size of droplets is greater than 40 microns (μ) radius (Byers, 1965). This implies that the collision and coalescence process is one of the key processes of rain formation.

Figure 4 shows some selected frames of the collision and coalescence of two water drops. Picture number 1 shows the dark colored droplet moving toward the stationary pink colored droplet. The volumes of the two droplets are the same, 30 cm^3 , or a sphere with a 3.85 cm diameter. Picture number 5 is at the moment when the two colliding droplets reached the critical separation distance, and suddenly the distance between two colliding droplets was bridged and coalescence then proceeded rapidly. Pictures number 7, 14, 19 and 20 show how two of the coalescence droplets fused into one, and how the nonlinear wave-wave interaction oscillated in the longitudinal direction. Pictures number 26 and 31 show how the nonlinear wave-wave interaction oscillated in the transverse direction. Pictures number 39, 51, 59 and 72 show the continuous nonlinear oscillations and how the nonlinear damping effect overcomes the nonlinear growth rate. Pictures number 93, 132 and 151 show the typical small amplitude oscillations of a water droplet.

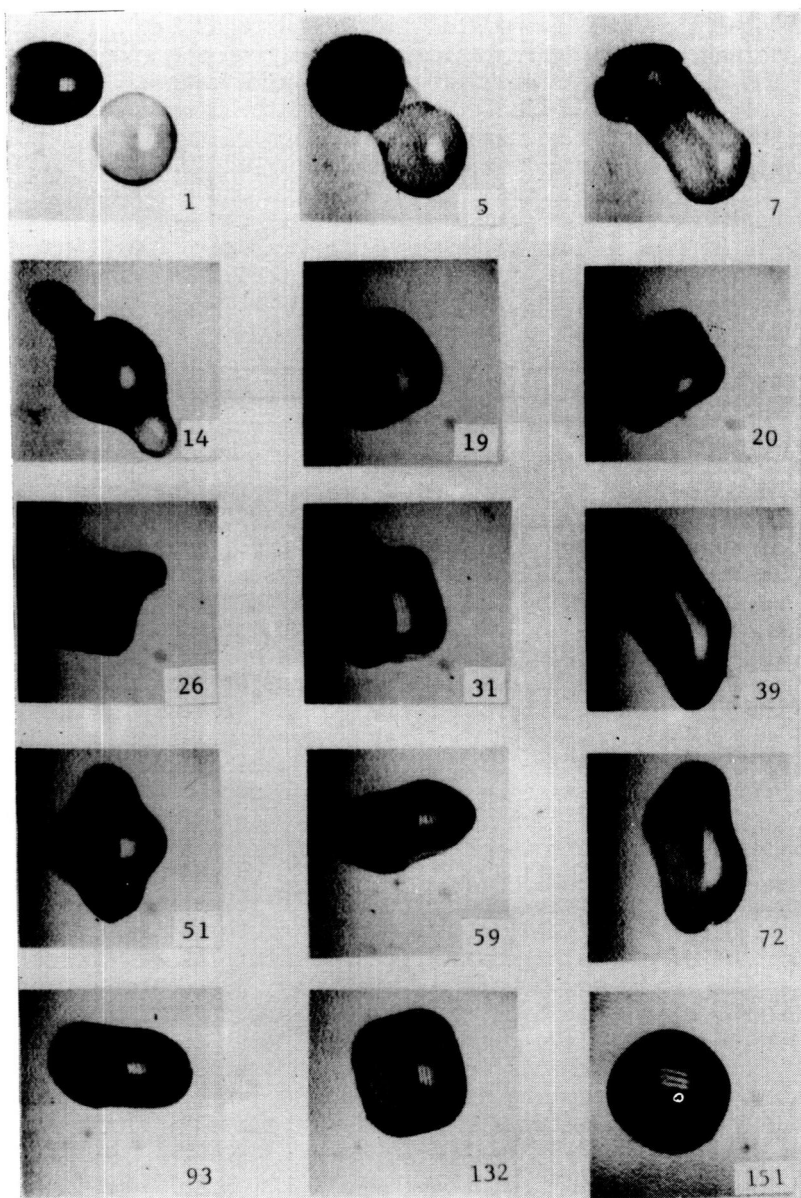


Figure 4. Skylab Fluid Mechanics Demonstration - Collision and Coalescence of Water Droplets.

The basic numerical techniques for studying collision and coalescence of an incompressible viscous fluid are those of the Marker-and-Cell (MAC) method which were developed by the Los

Alamos group (Harlow and Welch, 1965). The MAC method solves the finite difference form of Navier-Stokes equations with the velocity components and pressure defined over a staggered Eulerian mesh. The surface tension effects given by Young-Laplace relation serves as the boundary condition for the free surface. To apply boundary conditions at the edges of the collision (contact point of droplets), further experimental evidence must be obtained to justify either the condition of zero tangential stress or free-slip condition and/or other conditions to confirm the validity of numerical computations. In this sense, Skylab demonstrations of the collision and coalescence of water droplets has helped in our understanding of this phenomena.

IV DISCUSSIONS AND CONCLUSIONS

The study of droplet dynamics has been, for many years, one of the most interesting topics in the fields of atmospheric microphysics, nuclear physics, astrophysics, fluid mechanics, mechanical engineering, and chemical engineering. The Fluid Mechanics Demonstrations (TV 107 Series) performed during the Skylab missions produced excellent photographic data showing the oscillation, rotation, collision and coalescence of water droplets which simulate various physical models of interests under low gravity environment. Also, these TV 107 series of films provide interesting observations and illustrate the potential beneficial use of the low gravity environment for various branches of research. Particularly, scientific and technical evaluations have been provided by Skylab demonstrations to support the Zero-Gravity Atmospheric Cloud Physics Laboratory project in the future missions of Spacelab/Space Shuttle.

During the Skylab missions, special equipment was not available and video recording was used for data collection. These video tapes were subsequently transferred to 16 mm movie film which was then supplied to the researchers for analysis. In this respect, because of the restriction of speed of video recording, a laboratory type controlled experiment was not performed in the Skylab missions. However, qualitative in nature, these films have provided much interesting information and illustrate the potential of an orbiting research laboratory to provide data beneficial to terrestrial research problems.

ACKNOWLEDGEMENT

R. J. Hung wishes to acknowledge the support of NASA/ Marshall Space Flight Center through Contract No. NAS8-30247 and NAS8-31321. In addition, we would like to express our appreciation to the Skylab 4 astronauts, Bill Pogue and Ed Gibson, for performing the interesting fluid mechanics science demonstrations.

REFERENCES

- Beard, K.V. and H. R. Pruppacher, J. Atmos. Sci. **28**, 1445, 1971.
- Byers, H. R., Elements of Cloud Physics, Univ. of Chicago Press, Chicago, Ill., 1965.
- Chandrasekhar, S., Proc. Roy. Soc. (London) **A 286**, 1, 1965.
- Chandrasekhar, S., Ellipsoidal Figures of Equilibrium, Yale University Press, New Haven, Conn., 1969.
- Cohen, S., F. Plasil, and W. J. Swiatecki, Ann. Phys. **82**, 557, 1974.
- Harlow, F. H. and J. E. Welch, Phys. Fluids **8**, 2182, 1965.
- Huh, C. and L. E. Scriven, J. Coll. and Interf. Sci. **35**, 85, 1971.
- Hung, R. J., O. H. Vaughan, Jr., and R. E. Smith, AIAA Paper No. 74-1256, 1974.
- Landau, L. D. and E. M. Lifshitz, Fluid Mechanics, Pergamon Press, London, 1965.
- Mason, B. J., The Physics of Clouds, Clarendon Press, London, 1971.
- Plateau, J., The Annual Report of the Board of Regents of the Smithsonian Institution, pp. 255, Government Printing Office, Washington, D.C., 1866.
- Rayleigh, L., Proc. Roy. Soc. (London) **29**, 71, 1879.
- Vaughan, O. H., R. E. Smith, and R. J. Hung, Proc. Conf. on Cloud Phys., pp. 408, Am. Meteor. Soc., 1974a.
- Vaughan, O. H., R. E. Smith, R. J. Hung and S. T. Wu, Proc. International Colloq. on Drops and Bubbles, Jet Propulsion Lab., 1974b.
- West, G. D., Proc. Roy. Soc. A **86**, 28, 1911.

SIZE DISTRIBUTION OF FRAGMENT DEBRIS PRODUCED BY SIMULATED METEOROID IMPACT OF SPACECRAFT WALL

T. Dale Bess, NASA, Langley Research Center, Hampton, Virginia

ABSTRACT

A laboratory experimental program was conducted to determine the amount of fragment debris produced and its size distribution when simulated spacecraft walls are penetrated by hypervelocity projectiles. Two tests were made in which a spacecraft wall was struck with a small steel and an aluminum projectile, respectively. Results show that most of the fragment debris were irregularly shaped flat plates. The fragment data follow a cumulative number distribution law of the form $N = am^b$ where m is fragment mass and a and b are constants. Orbital lifetimes of most of the fragments were very short, being on the order of a few days.

INTRODUCTION

Should an orbiting spacecraft be hit by a meteoroid traveling at high velocity, cratering of the spacecraft wall will take place. Depending on a number of factors some of which are wall thickness, meteoroid velocity, and meteoroid density, the wall could be completely penetrated. If this happens other spacecraft components could be hit. In either case spacecraft debris will be produced.

From a meteoroid hazard point of view, extensive research, both theoretical and experimental, has taken place in recent years to explain the phenomena which occur when hypervelocity projectiles strike a spacecraft wall. Most of the research has been primarily directed toward finding penetration laws for different materials and methods of protecting spacecraft should a hit occur.

Some of the first theoretical work on penetration laws for thick targets was done by Bjork (Refs. 1,2). Theoretical work on penetration of thin plates has been treated by a number of people including Walsh (Ref. 3) and Riney (Ref. 4). Probably the most popular spacecraft protective device is the meteoroid bumper concept, as attested to by the many publications appearing on the subject in recent years (Refs. 5,6,7). A summary of much of the work on this subject, theoretical and experimental, can be found in Reference 8.

Although extensive research has taken place on the damage created by hypervelocity impact, no material could be found pertaining to the amount of fragment debris produced or its size distribution.

The present investigation was undertaken in an effort to determine the amount of fragment debris produced, its size distribution, and the expected orbital lifetime of the debris when a hypervelocity projectile strikes a spacecraft wall. The results are based on data from two hypervelocity projectile impact tests.

SYMBOLS

A_x, A_y, A_z	Projected cross-sectional areas to direction of flight when rotating about the three axes, cm^2
$\bar{A}_x, \bar{A}_y, \bar{A}_z$	Average of A_x, A_y, A_z
L	Fragment length, cm
M	Total weight of a sample, g
m	Average weight of the fragments, g
N	Cumulative number of fragments
n	Number of fragments from a sample
s	Average surface area of the fragments, cm^2
$W_{A_x}, W_{A_y}, W_{A_z}$	Weights assigned to cross-sectional areas
ω	Average width of fragment, cm
ρ	Mass density of a fragment, g/cm^3
θ	Angle through which fragment rotates

The Experiment

To determine the size distribution of fragments that result when a spacecraft wall is penetrated by a high velocity meteoroid, a simulated spacecraft wall was impacted with hypervelocity projectiles. The experiment utilized an accelerated reservoir light gas gun with a 22-caliber launch tube. Two such tests were made. In the first test the gas gun fired a 1.65-gram, 0.56-centimeter-diameter steel cylinder into the spacecraft wall. The velocity was measured to be 3 kilometers per second. In the second test the gas gun fired a 0.369-gram, 0.56-centimeter-diameter aluminum cylinder into the spacecraft wall. The velocity was not measured but thought to be approximately 4.5 kilometers per second.

Shape of Fragments

Visual estimates of sample fragments show that most of the fragments were irregularly shaped flat plates. About 15% had a length-to-width ratio of approximately 5. The other 85% had a length-to-width ratio of about 2. In both cases the thickness was about one-fourth the width. Some of the sample fragments are shown in Figure 4.

For the longer fragments the mass is given by

$$m_1 = (5\omega)(\omega)(\omega/4)\rho = 5/4 \omega^3 \rho$$

and the total surface area is

$$s_1 = 2(5\omega)(\omega) + 2(5\omega)(\omega/4) + 2(\omega)(\omega/4) = 13\omega^2$$

where ω is the average width of a sample fragment that will pass through a particular mesh size, and ρ is the density of a fragment, estimated to be 2 grams per cubic centimeter. For the short fragments the mass is given by

$$m_2 = (2\omega)(\omega)(\omega/4)\rho = 1/2 \omega^3 \rho$$

and the total surface area is

$$s_2 = 2(2\omega)(\omega) + 2(2\omega)(\omega/4) + 2(\omega)(\omega/4) = 11/2 \omega^2$$

The average weight of a fragment from a sample is

$$m = 0.15 m_1 + 0.85 m_2$$

The average surface area of a fragment from a sample is

$$s = 0.15 s_1 + 0.85 s_2$$

The average number of fragments from a sample is

$$n = M/m$$

where M is the total weight of a sample.

After the number of fragments from each sample has been determined, a distribution of fragment numbers, equal to or greater than a particular mass, can be obtained. A primary purpose of the following analysis was a determination of mass distribution.

Fragment Velocities

Velocities of the fragments that were produced by the projectile impact were very low as compared to the projectile velocity. The fragment velocities were estimated to be between about

A photograph of the simulated spacecraft wall is shown in Figure 1. This particular photograph was taken after the first test had been completed. The spacecraft wall consisted of an insulated fiberglass wall on the outside, in back of which was located a number of electronic components. The electronic components were made of resistors, capacitors, and so forth in an attempt to simulate an actual spacecraft. The simulated wall was placed on a table and positioned in front of the gas gun. A plywood enclosure surrounded the experiment in order to contain the debris. The events taking place during impact were photographed.

A photograph from the first test showing the simulated spacecraft wall positioned in front of the light gas gun is shown in Figure 2. Figure 2(a) was taken before gun firing. Figure 2(b) is just after gun firing. Some of the fragment debris is evident in Figure 2(b). Figure 3 is an enlarged picture of the simulated wall looking from the back. The steel cylinder penetrated the first electronic box. The cylinder deviated from its straight-line trajectory and penetrated the fiberglass wall to the left of the second electronic box.

The setup for the second test was similar to the first except that an electronic box was removed from the rear of the spacecraft wall, and solar cells were mounted in front of the wall.

The first test produced 13.85 grams of debris from the penetration of the spacecraft wall by the steel cylinder. In the second test the aluminum cylinder penetrated one electronic box but stopped before reaching the fiberglass wall and solar cells. A total of 8.20 grams of debris was recovered from the second experiment.

Debris Samples

In each experiment the debris was separated into five samples according to size. The size of fragments in each sample is based upon an average diameter of a gridded sieve which will allow all fragments of that sample to pass through. If the size of fragments from a sample is known, then the number of fragments is found by dividing the total weight of the sample by the average weight of a fragment from the sample.

The mesh diameters of the gridded sieves used were 0.0105 centimeter, 0.0438 centimeter, 0.1396 centimeter, and 0.5188 centimeter, respectively. The smallest sieve would pass any fragment with dimensions less than 0.0105 centimeter, that is, with an average diameter of 0.0052 centimeter. Fragments from the second sample had dimensions between 0.0105 and 0.0438 centimeter, that is, an average diameter of 0.0271 centimeter. Average diameter of fragments from the third sample was 0.0917 centimeter. Average diameter of fragments from the fourth sample was 0.3292 centimeter. The fifth sample consisted of only a few fragments greater than 0.5188 centimeter. Therefore, dimensions and number of fragments could be determined directly.

10 meters per second to 30 meters per second. The estimates are based on measurements from a 400-frame-per-second film that showed fragment movement.

Results of Analysis

In the first test, penetration of a spacecraft wall produced 13.85 grams of fragment debris. In the second test 8.20 grams of fragment debris were produced. The debris from each of the two tests were separated into five samples according to size.

Five data points were available for each test. The number of fragments in each sample was plotted as a function of average mass. Data from both tests showed a linear trend when plotted on logarithmic coordinate paper. Table 1 gives a summary of data collected from the five samples of each test.

Data from both experiments were fitted by the method of least squares to a power law of the form

$$N = am^b \quad (1)$$

where a and b are constants, m is the average fragment mass, and N is the cumulative number of fragments with a mass equal to or greater than m . For the first experiment the solution to Equation (1) is

$$N = 6.90415 m^{-0.80202}$$

with a residual standard error in the dependent variable of ± 0.07908 . For the second experiment the solution to Equation (1) is

$$N = 3.91543 m^{-0.83713}$$

with a residual standard error in the dependent variable of ± 0.13253 .

The solutions for the two experiments are shown in Figure 5 where fragment cumulative number is plotted versus fragment mass. It can be seen that fragment debris size ranges from about 1 gram to about 10^{-7} grams when fragment number ranges from 1 to 10^6 . Thus, an isolated meteoroid impact of a spacecraft wall is expected to produce a large number of fragments. However, most of these fragments are very small. Only about 100 fragments exist with a mass greater than 10 milligrams.

Nearly all of the fragments are too small to penetrate spacecraft walls but can cause other types of damage to sensitive parts such as pitting of lenses, thermal coatings, and other sensitive components. However, the possibility of damage by these small fragments is reduced when the fragments have short lifetime orbits. These fragment orbital lifetimes, which are calculated next, are influenced by the area-to-mass ratio of the fragments and the fragment orbital elements.

Fragment Area-to-Mass Ratio

The majority of the fragment particles from the meteoroid impacts have approximately the dimensions $L \times L/2 \times L/8$ where L is the fragment length. These fragments may be oriented in a particular direction or they may be rotating about some axis so that the projected cross-sectional area changes. It is desired to determine a mean cross-sectional area for these fragments and thus a mean area-to-mass ratio.

A sketch of one of these fragments with coordinate axes is shown in Figure 6. If the fragment is rotating about the x-axis, the projected cross-sectional area is

$$A_x = L^2/2 \cos \theta + L^2/8 \sin \theta$$

where θ is the angle measured from the direction of flight in the plane perpendicular to the x-axis.

The average of A_x is

$$\bar{A}_x = \frac{1}{\theta_2 - \theta_1} \int_{\theta_1=0}^{\theta_2=\pi/2} (L^2/2 \cos \theta + L^2/8 \sin \theta) d\theta = \frac{5}{4\pi} L^2$$

Likewise,

$$\bar{A}_y = \frac{9}{8\pi} L^2$$

$$\bar{A}_z = \frac{3}{8\pi} L^2$$

if the fragment is rotating about the y-axis and z-axis, respectively.

If these average cross-sectional areas are assigned weights, where weight is proportional to the average cross-sectional area, then $\bar{W}_{\bar{A}_x} = 1$, $\bar{W}_{\bar{A}_y} = 0.9$, and $\bar{W}_{\bar{A}_z} = 0.3$ where the weight of

\bar{A}_x is arbitrarily set to unity. The average cross-sectional area of the fragment is then

$$\bar{A} = \frac{\bar{A}_x + 0.9 \bar{A}_y + 0.3 \bar{A}_z}{3} = L^2/3.97$$

The mass of one of these fragments is

$$m = \rho V = \rho \frac{L^3}{16}$$

where ρ is the density of the fragment. For an average density of 2.0 g/cm^3 the mass is,

$$m = L^3/8$$

The mean area-to-mass ratio is thus,

$$\frac{\bar{A}}{m} = 2.01 \frac{1}{L}$$

Figure 5 shows that the fragment masses range from about 1 gram down to about 10^{-7} grams. Based on the fragment shape, the characteristic length, L , ranges from about 2 centimeters down to 0.01 centimeter. Thus, the mean area-to-mass ratio ranges from approximately 1 for the large fragments to 200 for the smaller fragments.

Orbital Lifetime of Fragments

Orbital lifetime calculations have been made using a modification of the RAND satellite lifetime program (Ref. 9). This program computes the secular orbit perturbations caused by gravitational attraction of the moon and sun, atmospheric drag, solar radiation pressure, and higher harmonics of the earth's gravitational potential. Lifetimes in various circular orbits and noncircular orbits have been calculated for a suitable range of fragment area-to-mass ratios. Orbit elements were arbitrarily set to $\omega = 120^\circ$, $\Omega = 90^\circ$, and $i = 30^\circ$.

Time of launch was 1969, a period of high solar activity which gives short lifetime estimates. During periods of low solar activity, such as the mid 1960's, lifetime estimates would increase.

Results of the lifetime calculations are shown in Figure 7, where mean area-to-mass ratio versus lifetime in days is given for a range of circular and noncircular orbit altitudes. Figure 7(a) shows that for circular orbits almost all fragments are characterized by having short orbital lifetimes. For instance, at a mean area-to-mass ratio of 100, no fragment is expected to survive in orbit longer than about 50 days. The larger fragments (which are few in number) can survive from 2 to 5 years when they are in high orbit altitudes of 700 to 800 kilometers. For a noncircular orbit of eccentricity 0.1, the orbital lifetimes are still relatively short for the smaller fragments. This is shown in Figure 7(b). For a mean area-to-mass ratio of 200, the smallest fragments have lifetimes not exceeding about 200 days. However, a larger fragment with an area-to-mass ratio of 20 has an expected lifetime of about 16 years for a 700-kilometer orbit.

Use of Size Distribution Law: An Example

The distribution law was used to estimate the size distribution of debris from a sample of reusable surface insulation material (thermal insulation to be used on space shuttle) which was struck by a small aluminum projectile at 5 kilometers per second. This sample of reusable surface insulation was one of several samples that were tested at Langley to access the damage to the thermal insulation caused by meteoroid type impacts.

The thermal insulation material has a density of 0.24 gram per cubic centimeter and the debris from the sample had a weight of about 2.5 grams compared to a density of 2.0 grams per cubic centimeter and a debris sample weight of 8.2 grams for the material on which the distribution law is based.

If the debris from the thermal insulation has the same slope as the distribution law, and cumulative number is proportional to material density and debris sample weight, then number versus size distribution for the thermal insulation debris is over an order of magnitude lower than the distribution shown in Figure 5. The largest piece of debris would have a mass on the order of 0.10 gram and an orbit lifetime of only a few days.

CONCLUSIONS

Two tests of hypervelocity projectile impacts to simulated spacecraft walls were conducted to determine number and size distributions of the debris produced by the impacts.

Inspection and analysis of the data show that the first test produced 13.85 grams of debris, and the second test produced 8.20 grams of debris. Most of the fragments were irregularly shaped flat plates with a length-to-width ratio of about 2, and a thickness of about one-fourth the width. The cumulative number distribution law versus mass fits a power law of the form $N = am^b$ where a and b are constants. For this distribution, the fragment masses from the debris range from about 1 gram to 10^{-7} grams when the number ranged from 1 to 10^6 . Velocities of fragments were very low (~10 to 30 meters per second).

Orbital lifetime calculation of these debris fragments for various circular and noncircular orbits and for a suitable range of area-to-mass ratios shows that almost all fragments have short lifetimes of a few days.

REFERENCES

1. Bjork, Robert L.: Review of Physical Processes in Hypervelocity Impact and Penetration. In Proceedings of the Sixth Symposium on Hypervelocity Impact, Vol. II, Part 1, Aug. 1963, pp. 1-58.
2. Bjork, R. L., et al.: Analytical Study of Impact Effects as Applied to the Meteoroid Hazard. NASA CR-757, 1967.
3. Walsh, J. M., and Johnson, W. E.: On the Theory of Hypervelocity Impact. Proceedings of the Seventh Hypervelocity Impact Symposium, Vol. II, Feb. 1965.
4. Riney, T. D., and Heyda, J. F.: Hypervelocity Impact Calculations. Proceedings of the Seventh Hypervelocity Impact Symposium, Vol. II, Feb. 1965.

5. McMillan, A. R.: Experimental Investigations of Simulated Meteoroid Damage to Various Spacecraft Structures. NASA CR-915, 1968.

6. Humes, Donald H.: Influence of the Bumper and Main Wall Material on the Effectiveness of Single Meteoroid Bumpers. NASA TN D-3104, 1965.

7. Nysmith, Robert C.: Penetration Resistance of Double-Sheet Structures at Velocities to 8.8 km/sec. NASA D-4568, 1968.

8. Frost, V. C.: Protection Against Meteoroids. NASA SP-8042, 1970.

9. Brooks, David R., Gibson, Gary G., and Bess, T. Dale: Predicting the Probability That Earth-Orbiting Spacecraft Will Collide With Man-Made Objects in Space. International Astronautical Federation (I.A.F.), XXVth Congress, Amsterdam, Sept. 30-Oct. 5, 1974.

TABLE 1

SUMMARY OF DATA COLLECTED FROM EACH IMPACT TEST

FIRST TEST

SAMPLE	TOTAL SAMPLE MASS, g	AVERAGE MASS OF FRAGMENTS, g	AVERAGE WIDTH OF FRAGMENTS, cm	NUMBER OF FRAGMENTS	AVERAGE SURFACE AREA OF FRAGMENTS, cm ²
1	0.33	1.722×10^{-7}	5.200×10^{-3}	1.916×10^6	1.792×10^{-4}
2	0.80	2.411×10^{-5}	2.710×10^{-2}	3.318×10^4	4.813×10^{-3}
3	1.90	9.477×10^{-4}	9.170×10^{-2}	2.004×10^3	5.591×10^{-2}
4	2.90	4.402×10^{-2}	3.290×10^{-1}	6.600×10^1	7.239×10^{-1}
5	7.92	8.800×10^{-1}	8.956×10^{-1}	9.000×10^0	5.316×10^0

SECOND TEST

1	0.30	1.722×10^{-7}	5.200×10^{-3}	1.742×10^6	1.792×10^{-4}
2	0.60	2.411×10^{-5}	2.710×10^{-2}	2.488×10^4	4.813×10^{-3}
3	1.50	9.477×10^{-4}	9.170×10^{-2}	1.582×10^3	5.591×10^{-2}
4	3.30	4.402×10^{-2}	3.290×10^{-1}	7.500×10^1	7.239×10^{-1}
5	2.50	5.000×10^{-1}	7.418×10^{-1}	5.000×10^0	3.647×10^0

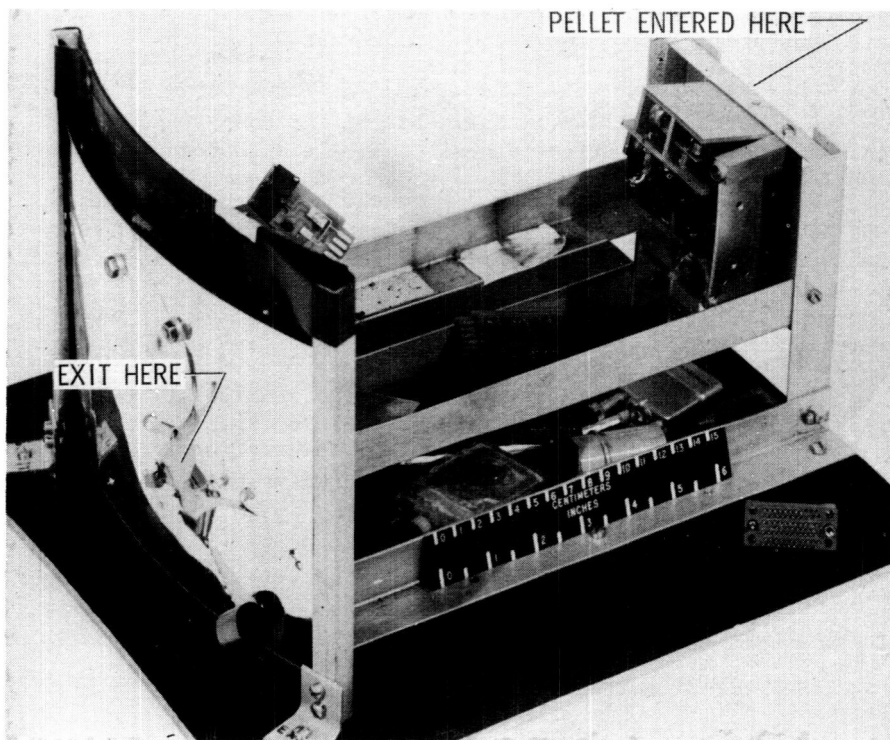


Fig. 1—Simulated spacecraft wall

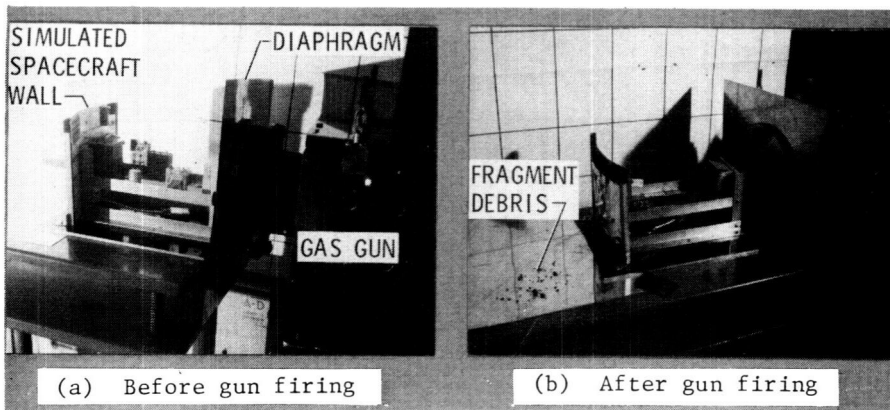


Fig. 2—Spacecraft wall in front of gas gun

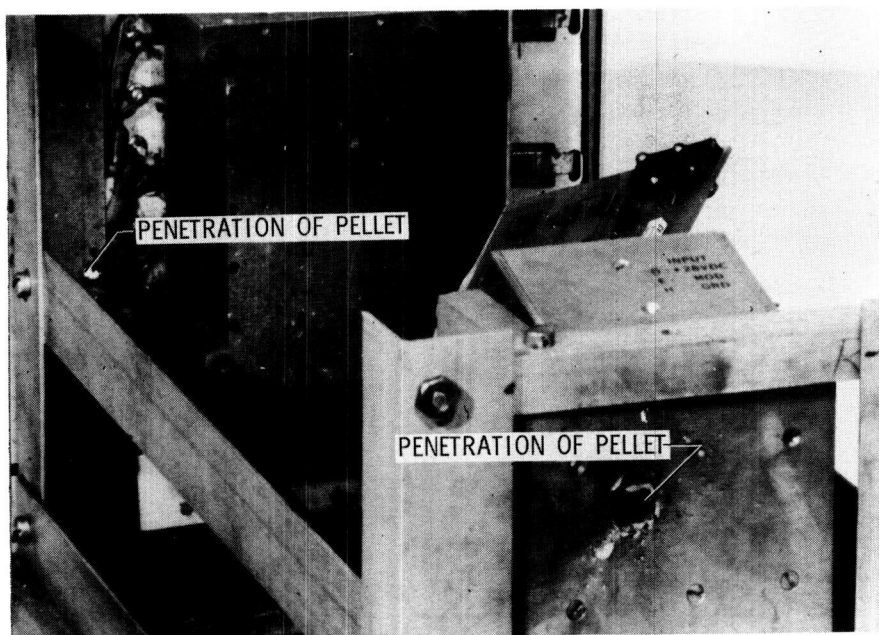


Fig. 3—Spacecraft wall showing pellet penetration

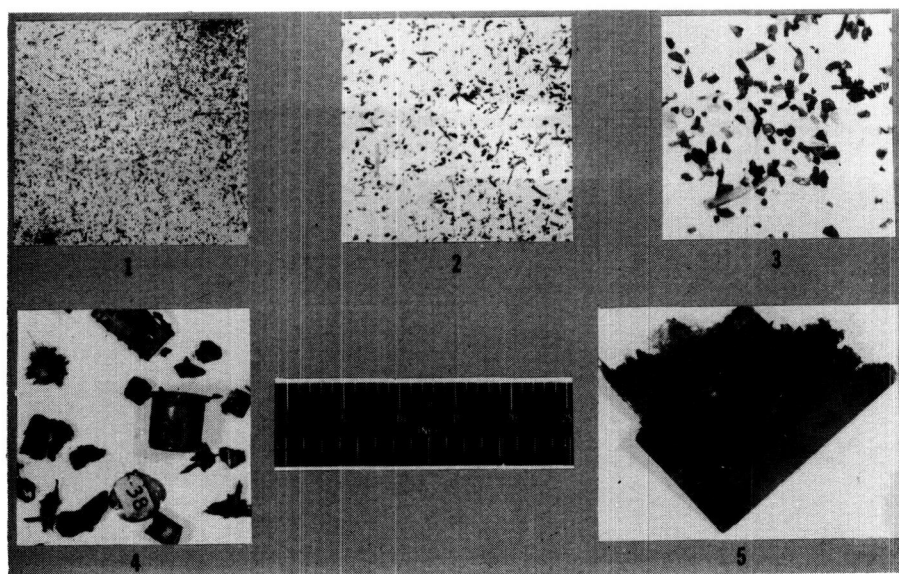


Fig. 4—Size of fragments from five samples

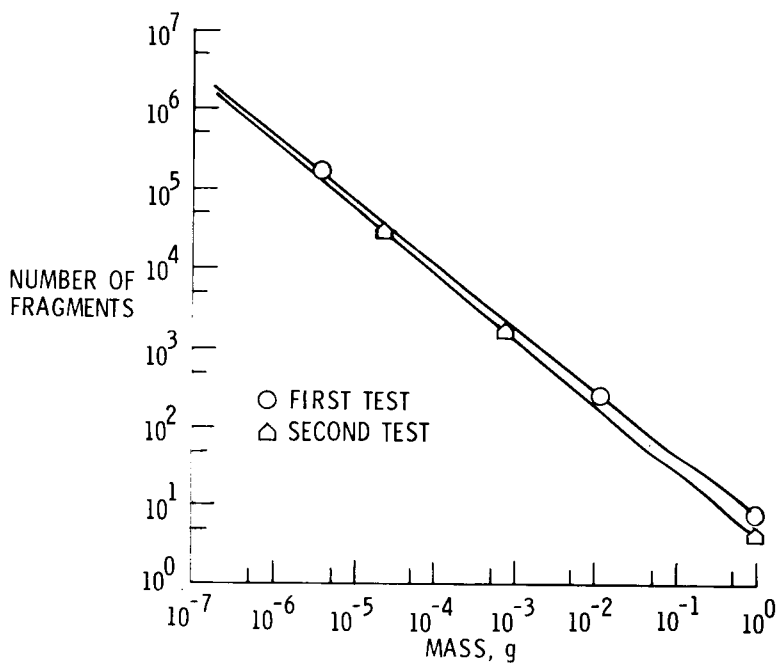


Fig. 5—Fragment distribution from meteoroid impact of spacecraft wall

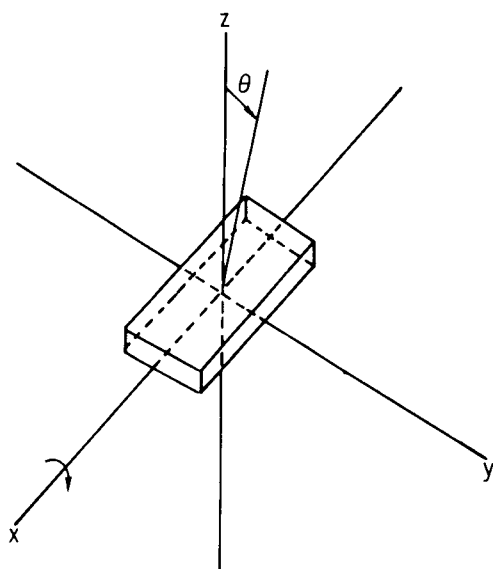
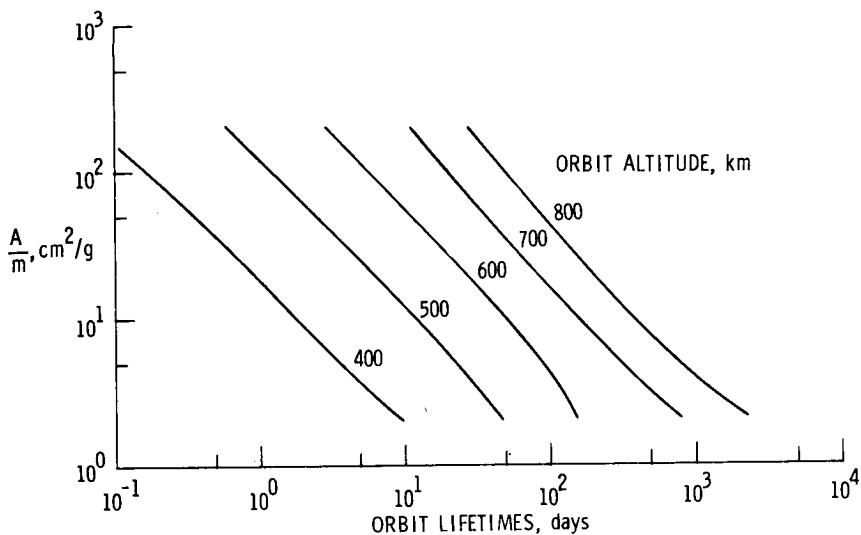
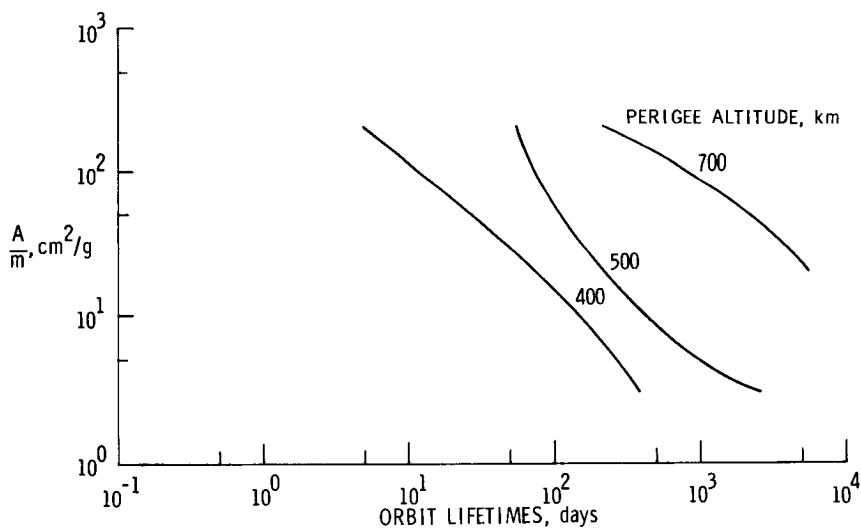


Fig. 6—Sketch showing fragment geometry for determining projected cross-sectional area



(a) Circular orbits

Fig. 7—Fragment orbit lifetimes for varying area-to-mass ratios



(b) Noncircular orbits, eccentricity of 0.10

Fig. 7—Concluded

APPLICATION AND UTILIZATION OF A SPACE CHAMBER FOR THE DRYING AND DECONTAMINATION OF BOOKS, DOCUMENTS AND OTHER MATERIALS TO PREVENT BIODETERIORATION

Martin G. Koesterer, *Senior Microbiologist*, and John A. Geating, *Bioscientist, Biomedical Programs Operation, Space Systems Organization, General Electric Company, Valley Forge Space Center, King of Prussia, Pennsylvania*

ABSTRACT

Truckloads of materials such as rare books, papers, engineering drawings, blue prints, art work; leather objects such as shoes; and clothing have been successfully dried, decontaminated and impregnated against future infestation by microorganisms in a large 12 x 24 foot vacuum chamber designed originally for testing unmanned spacecraft. The process is unique in that it allows either frozen or wet material, soaked by some catastrophic event to be dried and sterilized in the same chamber with a minimum of handling and transportation. This means that materials, especially invaluable paper records, soaked by flooding, whether from severe storms, water-line rupture, or fire-fighting equipment, or wetted by moisture in high humidity environments can be recovered and used again. The addition of a residual antimicrobial chemical is an option which may be exercised depending upon predicted future conditions for storage of the material.

The drying is accomplished under vacuum by evaporating the water in the material and then re-freezing it out of the system on a cryogenic panel. Evaporation of the water is aided by the use of an extensive network of controlled-temperature heaters throughout the shelving which contain the material to be dried. The decontamination is accomplished by admitting ethylene oxide and holding for up to 24 hours after the ice has been removed from the cryogenic panel. The residual antimicrobial chemical (thymol in trichlorethane) is admitted as a gas while the material is under vacuum.

Biological Sterility Indicators (paper strips containing spores of Bacillus subtilis var. niger) have been inserted between the pages of thick books, etc., and has shown the process to be completely effective. Depending upon packaging, handling and subsequent storage, materials so treated have been preserved from any further biodeterioration. In one case where books were dried and sterilized, but not chemically treated, it has been discovered that fungi are growing again. No deleterious effects have been observed on materials treated to date with the process.

The technological blending of a large vacuum chamber designed for testing spacecraft and antimicrobial/sterilization knowledge has allowed for the economical recovery of severely wetted materials, and the retardation (perhaps even elimination) of microbial deterioration of susceptible items. It opens a new door, allowing for the "spin-off" application for the processing of other materials.

THE HIGH CURRENT TRANSIENT GENERATOR - THEORY AND OPERATION FOR SIMULATING LIGHTNING INDUCED VOLTAGES INTO AEROSPACE ELECTRICAL CIRCUITS.*

E. H. Schulte, *McDonnell Aircraft Company, St. Louis, Missouri*

ABSTRACT

Because of the difficulty, hazard, and cost of simulating full-scale lightning currents on flight vehicles, a nondestructive test technique using reduced-scale lightning currents is often used to determine if threat level voltages will be induced into aircraft electrical circuits in the event the aircraft is actually struck by lightning. The reasoning and theory of selecting a particular simulated lightning waveshape and magnitude is given, showing that extrapolations of induced waveforms over several orders of magnitude should be avoided. The operation of new high-current transient generators and hardware are described along with typical applications. The means by which voltages are generated, induced, and measured, as well as possible sources of error, are discussed.

INTRODUCTION

Lightning is a potential threat to all aerospace vehicles (including spacecraft during launch and entry), whether they are airborne or on the ground.¹⁻⁷ In addition to the threat to structures, fuel, and crew, electrical and electronic systems may be subject to dangerously high induced transient voltages and currents if the vehicle is struck by lightning. Because lightning damage to other than electrical systems is quite localized, vulnerability and protection of those systems can be evaluated by the use of component level laboratory tests. However, since both electrical wiring and lightning currents, accompanied by magnetic fields, traverse the entire vehicle, the response of the electrical and attached electronic systems becomes a very complex function of vehicle geometry and shielding effectiveness. In light of the new generation of solid state control avionics systems, which are susceptible to upset and damage from low-level electrical interference, it becomes necessary to consider full-scale operational vehicle testing for lightning-induced transients in the electrical system.

The cost, complexity, and risk to the vehicle associated with generating full-threat level lightning currents (up to 200,000 amps peaking in 2 microseconds) is generally considered to be prohibitive. Therefore, a technique using reduced-scale (nondamaging) simulated lightning currents has been used to predict, by extrapolation, the level of induced transients to be expected from a severe strike.

The extrapolation technique has been utilized throughout the lightning test community for several years in cases where threat level currents could not be readily generated because of equipment limitations. However, in recent years, the technique has been extended to full-scale aircraft, employing very low driving currents on the

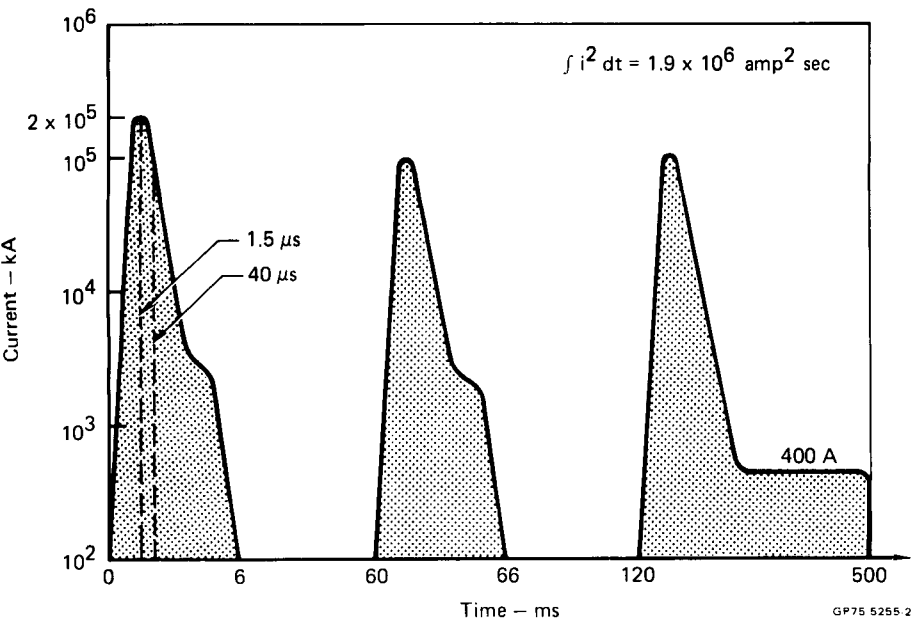
*This effort is supported in part by AF Contract No. F33657-70-C-0300

order of a few hundred amps,^{8,9} and more recently, to spacecraft, using driving currents of a few thousand amps.¹⁰

The purpose of this paper is to evaluate the effectiveness of this transient analyzer, or more properly, transient generator technique, and to present the results of scaled tests conducted with higher driving currents (requiring less extrapolation) at the McDonnell Aircraft Company's Lightning Simulation Laboratory. The discussion of the transient generator technique and equipment will be preceded by a brief review of the natural lightning environment, and the general interaction of the lightning currents with the aircraft electrical system.

Natural and Simulated Lightning Currents

Natural lightning currents are rather complex because of their individuality, i.e., no two lightning strokes are identical. Extensive efforts have been devoted to understanding and classifying the various lightning strike parameters such as peak current, rate-of-rise of the peak current, etc.^{11,12,13} Because of the wide variety of parameters in the lightning current, it is advisable to select some of the more damaging parameters and use these to simulate a "worst case" lightning strike, although the probability of such a strike may be low. Such a "worst case" lightning threat has been proposed by Pierce,¹² Figure 1, and is considered as a basis for the new SAE Aerospace Recommended Practice for lightning simulation testing.¹⁴ A worst case has also been proposed for Shuttle Lightning Protection¹⁵ using the same model. It can be seen that since the first current peak of 200kA is the highest current component and it has the highest value of di/dt , it is probably the most hazardous to electrical systems.

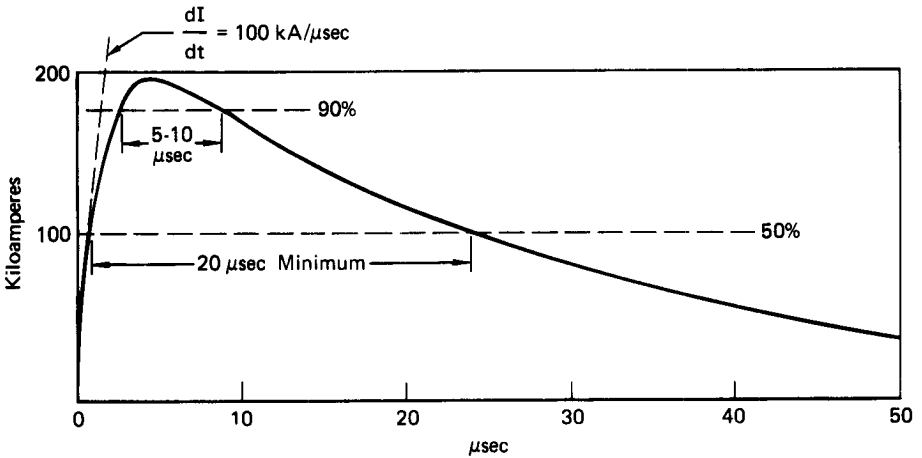


From Reference 12

GP75 5255-2

FIGURE 1 TIME HISTORY OF SEVERE (APPLIED) LIGHTNING MODEL

Therefore, where electromagnetic coupling is of concern, the lightning strike current waveform to be simulated usually is one which rises to a peak in only a few microseconds and has a relatively long exponential decay such as that specified in Reference 14 and in MIL-B-5087B.¹⁶ Although the MIL-B-5087B waveform has been used for over a decade, it is not well defined and it is often interpreted as being similar to that shown in Figure 2.⁹

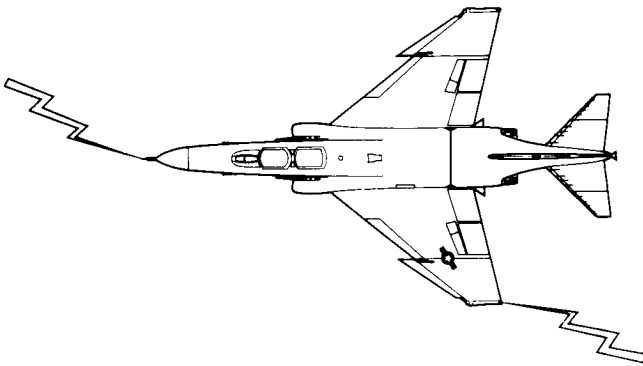


GP75-5255-4

**FIGURE 2 LIGHTNING CURRENT WAVE SHAPE
FOR SAFETY OF FLIGHT AS PER MIL-B-5087B.**

Induced Voltages

The aircraft extremities are generally the attachment points for lightning.¹⁷ When an aircraft is struck, it becomes a part of the electrical flow path of the lightning current. An example is the sketch in Figure 3 where entry and exit points for the lightning current are the nose and the wing tip. If the aircraft has an all metallic fuselage and metallic wing skins, most of the current will remain in the aircraft skin. However, the lightning current will cause other voltages or currents to be induced or directly coupled into the aircraft electrical circuits.



GP75-5255-20

FIGURE 3 LIGHTNING ATTACHMENT TO AIRCRAFT

Voltages or currents appearing in aircraft electrical circuits, as a result of a lightning strike to the aircraft, have all been classified as indirect effects,¹⁴ although for this paper, we will further divide these effects into two general categories, depending upon how the voltage was caused. These are:

- (a) direct attachment coupling and
- (b) indirect coupling.

A direct coupled voltage or current would probably become obvious by an associated physical damage. For example, referring to Figure 3, if the wing tip light lens were punctured by a lightning current and the lightning current attached directly to the electrical wiring, then physical damage to the lens would be evident and large currents and voltages would appear in the aircraft wiring to the light. Aircraft wiring is always maintained within the confines of the aircraft, but antennas, lights, and probes provide potential entry paths to the interior regions. Once inside the skin, additional circuits can be affected by field coupling. Therefore, these points of entry should be carefully protected by surge arrestors if they are in a strike zone.

Indirectly coupled voltages are not so obvious as the directly coupled voltages, and to help understand the problems the wiring in the aircraft can be classified into two general categories:¹⁸

- (1) Airframe return circuits - if the airframe is utilized as a common ground return path, it becomes a part of the signal carrying circuit loop. Induced voltages then result from:
 - (a) voltage drops resulting from the lightning current traveling through the metal airframe, ($e = iR$)
 - (b) magnetic flux linkage to the signal carrying circuit loop ($e = -d\phi/dt$).
- (2) Two wire circuits - the signal circuit may be grounded at the supply bonding point but not at the remote component location. Induced voltages or potential differences then result from:
 - (a) common mode potential differences because the airframe is carrying the lightning current and the signal leads are not,
 - (b) common mode magnetic flux linkage to the wire/airframe loop (open circuit voltage), and,
 - (c) differential voltages produced by flux linkage between the two wires of the pair.

For twisted pair circuits (c) is minimal, but (b) may be critical because the voltages from signal leads to ground may be very large and appear directly at the receiving end of the system. For example, if a common mode voltage of 1000 volts is induced into the twisted pair of wires, each of the signal leads has the same amplitude and polarity, and the net differential signal at the receiving end will be zero. However, if these wires pass thru an electrical connector whose shell is grounded, the 1000 volts will appear between each wire of the twisted pair and the metal of the connector frame, and may be sufficient to cause arc over, essentially shorting the circuit to ground.

Magnetic coupling results because the aircraft skin does not provide perfect electromagnetic shielding for the aircraft wiring. As a result, the lightning current conducted by the aircraft sets up a nonuniform magnetic field inside the aircraft which couples to the aircraft wiring. Magnetic coupling can be broken down into aperture coupling and diffusion coupling. An obvious example of aperture coupling would be coupling to the electrical circuits in the cockpit of an aircraft. Aperture coupling could also occur at the attachment of metallic skins to rib sections or at access doors or similar nonuniform mechanical points. An example of an aperture coupled open circuit voltage and the driving current is shown in Figure 4. Note that the maximum voltage occurs when dI/dt is greatest, i.e., at the start of the current,

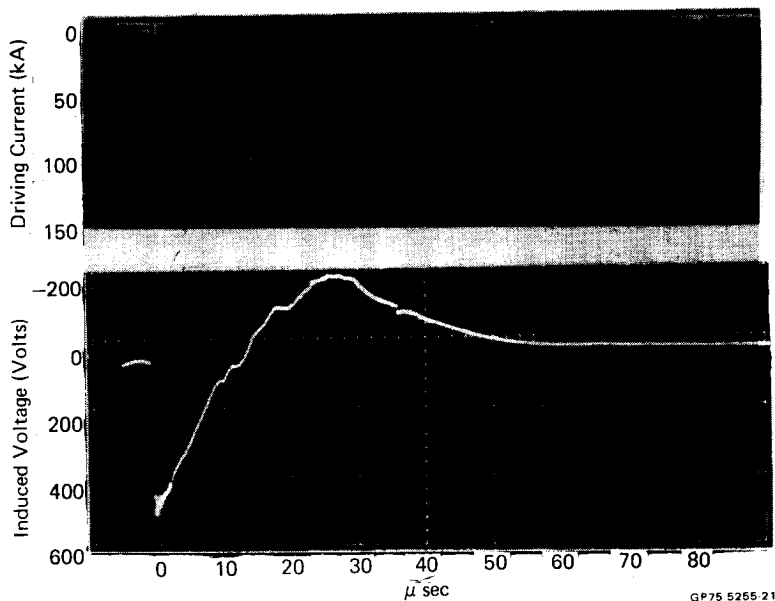


FIGURE 4 EXAMPLE OF APERTURE COUPLED VOLTAGE

and the induced voltage is zero when the current reaches its peak (100kA) because $di/dt = 0$. The occurrence of irregularities in the induced voltage waveform are due to the magnetic field set up by the test equipment switching which was initiated at approximately $t = 12$ microseconds.

Because of the initial high rate-of-rise of current in the lightning strike, the lightning current is initially confined to the outer surface of the aircraft skin because of the skin effect; however, as the current continues to flow, the lower frequency components diffuse through the skin, and the magnetic field inside the aircraft increases accordingly. As a result, the induced voltage from diffusion coupling will be delayed and will be less than that which would have occurred if the metallic skin had not been there. An example, of the delay in an induced voltage in a completely enclosed copper cylinder subjected to a lightning transient, has been computed by Burrows¹⁸ and is shown in Figure 5.

Because of the complexity of aircraft wiring and cable routing, and because of the complex mechanical assembly of the aircraft structures, it is extremely difficult, at best, to calculate the voltage and currents which would appear as the result of a lightning strike. It is seen therefore that a transient test is needed to at least assess the maximum voltages which could appear in critical circuitry. Although it is desirable to subject the whole aircraft to the simulated lightning currents (because some of the electrical wiring is routed over devious paths and is thus susceptible to diverse fields), sometimes this is not possible and only subassemblies containing the part to be tested are utilized. However, a full vehicle test should be conducted when possible.

Since most transistor and solid state circuits are sensitive to polarity, currents, rates of change of currents, voltages, and rates of change voltage, knowing the open circuit voltage only is not sufficient. Sometimes the input circuitry of a particular equipment can be easily simplified to determine the effects of a particular induced transient; however, the shape of the induced transient is usually difficult to predict.

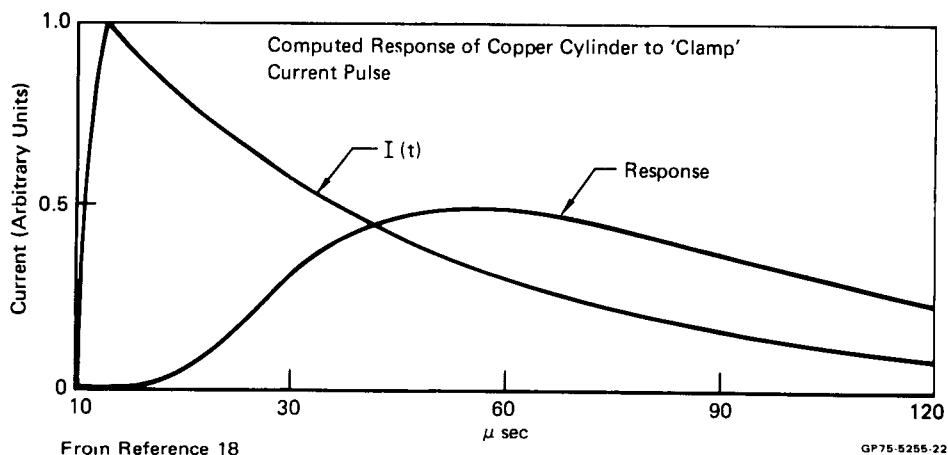


FIGURE 5 EXAMPLE OF DIFFUSION COUPLED VOLTAGE

This is another reason for performing a test utilizing simulated lightning currents and actual vehicle hardware.

As an example of this type of test, consider the oscillograms shown in Figure 6. These are voltages which were induced into the circuitry of an F-15 aircraft anti-collision light installed in the tail section. The transient generator driving current waveforms are shown in Figure 7, and generally fall in the 2 to 10 kiloamp range. The anti-collision light is generally a flashing red light and is mounted near the upper tip of the tail. The flasher unit is an aircraft unit employing solid state circuitry.

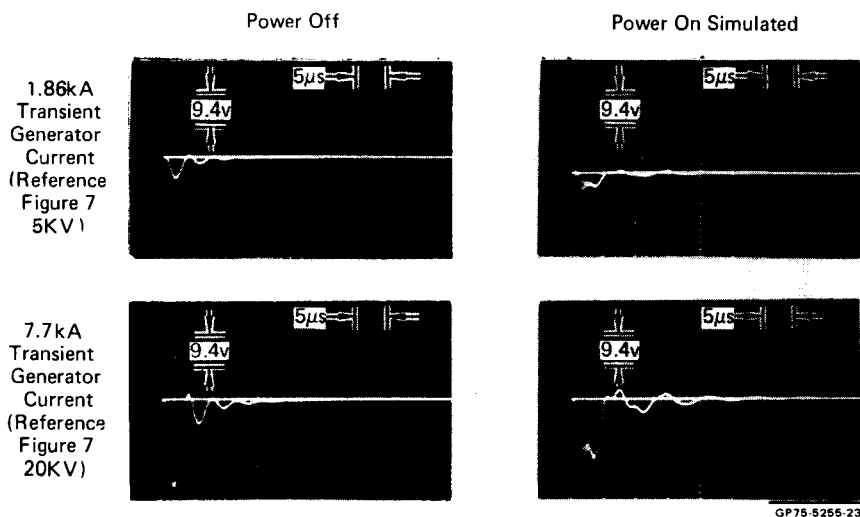
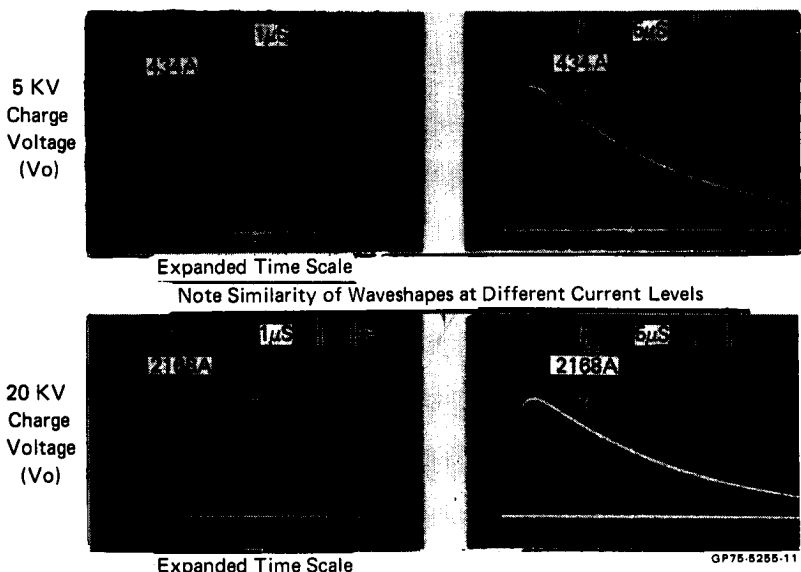


FIGURE 6 TYPICAL 'POWER OFF' AND 'POWER ON' VOLTAGES INDUCED IN TAIL ANTICOLLISION LIGHT CIRCUIT



**FIGURE 7 TYPICAL TRANSIENT GENERATOR CURRENT WAVEFORMS
(USED FOR TESTING F-15 FLIGHTS)**

Tests were performed at four different driving current levels under these conditions:

- (1) Power off - simulating unpowered aircraft on ground or combat flying conditions.
- (2) Power on - the light was operating in a flashing mode.
- (3) Simulated power on - power in a flashing mode was simulated to simplify induced voltage measurement. It was determined that the induced voltage waveshape was almost identical in shape to that in (2) above, although the absolute magnitude was slightly different.

The peak induced voltages are plotted in Figure 8 and it is seen that these voltages must be extrapolated or "scaled" to a 100kA peak driving current. (The 100kA level is specified in MIL-B-5087B for nonsafety of flight items.)¹⁶ This test shows that if the light were struck by lightning with a 100kA peak and having a leading edge waveform similar to that shown in Figure 7, a peak induced voltage of 184 volts could be expected for a power on condition; 303 volts would be produced in a power off condition, because of different circuit loading characteristics. It is noted that the induced voltage in the power on condition is lower than that obtained for the simulated power on condition. This is believed to be due to the impedance loading effects of the flasher unit and the 400 ~ power supply, which are slightly different when the units are operating normally and when the operation is simulated. Because of observed differences such as this, it is recommended that induced voltage testing be conducted when the subject equipment is operating normally.

It has been seen that for the circuit data shown in Figure 8, a linear extrapolation of the induced voltage seems reasonable; but, when extrapolating the voltages to full scale lightning levels, care must be taken to assess any possible nonlinearities, either as a result of equipment change of state or from altered lightning current flow

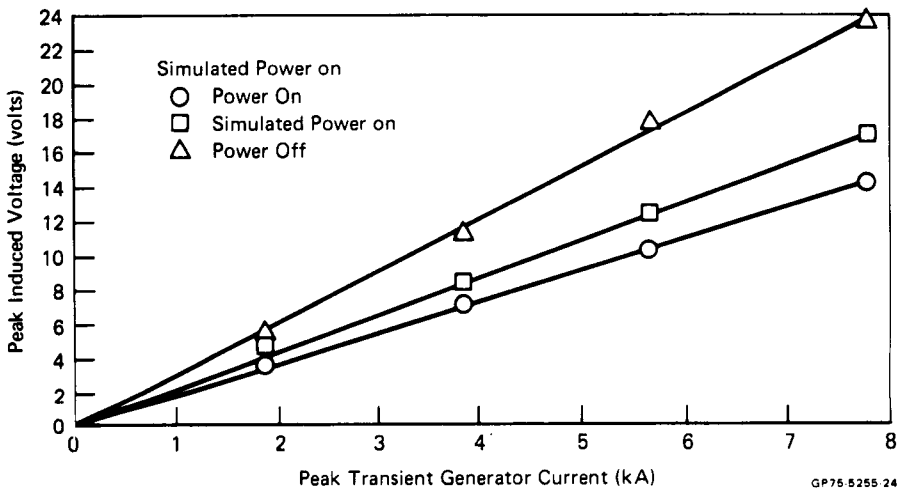


FIGURE 8 ACTUAL INDUCED VOLTAGES INTO TAIL ANTICOLLISION LIGHT CIRCUITRY

paths in the structure which may result due to arcing. Because of these latter conditions, it is generally desirable to test at the highest practical current level. The reduced level tests conducted at McDonnell are generally collaborated by a threat level high current test. The threat level waveform does not have the fast rate-of-rise of the transient generator waveform and this factor must be accounted for in the comparison. In addition, the threat level test may be destructive on an unproved system, and therefore does not generally allow repetitive testing. The higher peak current may generate sparking which alters the current flow pattern and therefore the induced signal levels. Generally speaking, however, it has been assumed that the 10 kiloamp level is high enough to overcome most nonlinearities on the subassembly level. We presently have no data to indicate that this is always true; but, efforts are currently underway to clarify the minimum confidence level for extrapolation.

Reduced Scale Lightning Currents

Since most voltages induced into the aircraft by lightning currents are magnetically coupled, it is easily seen that the fastest rising current would produce the greatest change in the magnetic field and thus induce the greatest voltage.

If we are going to scale down the lightning current to some lower level, we certainly must know what parts of the waveform we need to scale down. For example, consider the lightning current waveshape designated for testing and shown in Figure 2. At first glance it is not immediately obvious which portions of this waveform besides the peak are scaled down. In order to have a simple linear "scaling factor", the peak is reduced, but the time to peak and the rest of the waveform remain the same, as shown in Figure 9. If the amplitude of the simulated wave from time $t = 0$ to $t = t_f$ is different by other than a constant from the specified wave, then its frequency content will differ. This can be shown to be true by using a Fourier Analysis¹⁹ (see Appendix for example). If the frequency content is different, then the induced voltages may not be proportional. Shortening the time for the current to reach peak has the effect of increasing the high-frequency content of the wave, while stretching out the

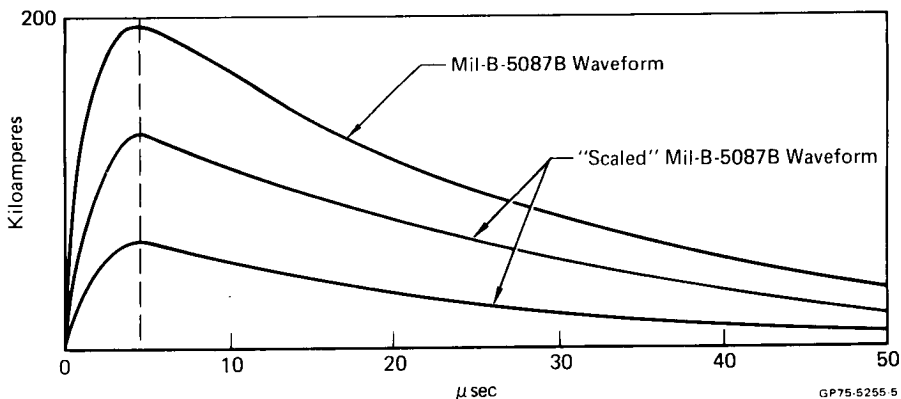


FIGURE 9 SCALED MIL-B-5087B WAVEFORM

decaying portion of the waveform has the effect of increasing the low-frequency content. Because aperture coupling generally poses the greatest threat, the leading edge of the current waveform is more important than the long decay.

Principle of Operation of the Transient Generator

The transient generator is basically an RLC circuit similar to that shown in Figure 10, which is designed to produce a scaled down version of a lightning strike current. In operation the switch S1 should be closed to charge capacitor C to some predetermined voltage V_0 ; then S1 would be opened and S2 would be closed, thus discharging the capacitor into the circuit resistance R and inductance L. There are basically three general waveshapes of current which may result from the capacitor discharging into the circuit shown: they are:

- (1) Underdamped case. If $1/LC > R^2/4L^2$, then the current will be oscillatory and will gradually be damped out.
Where: C = capacitance (farads)
R = resistance (ohms)
t = time (seconds)
L = inductance (henry)
- (2) Critically damped case. If $R = 2\sqrt{L/C}$, the circuit is said to be critically damped (the circuit current will not oscillate through zero as for the underdamped case).
- (3) Overdamped case. If $R > 2\sqrt{L/C}$, the circuit is said to be overdamped. As with the critically damped case, the circuit current will not oscillate.

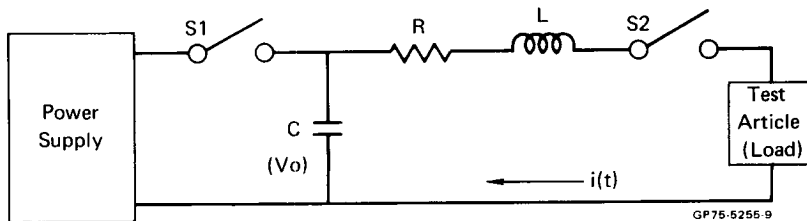


FIGURE 10 BASIC TRANSIENT GENERATOR SCHEMATIC

In order to approach the current waveshape specified in MIL-B-5087B, we will, for most practical cases, restrict ourselves to the overdamped case because of the very fast initial rise of current and the relatively long decay of current after the peak has been reached.

When the transient generator is connected to a load (test article) as shown in Figure 10, it is seen that the current does not exactly follow the theoretical prediction because of several reasons:

- (1) distributed inductance
- (2) distributed capacitance
- (3) mutual coupling between the various circuit components
- (4) temperature sensitive components in the circuit
- (5) reflections in either or all of the circuit components.

Since the transient generator is used to induce voltages and currents in electrical systems, the generator should have a clean waveshape and have linear characteristics so that the induced voltage can be linearly extrapolated to its maximum value. Because a large percentage of the induced voltages in aircraft wiring are magnetically induced, the initial rate-of-rise of the current waveform is critical. A relatively simple check on the linearity and rate-of-rise of a transient generator can be accomplished by plotting the initial charge voltage (V_0) on the capacitor (c) vs peak discharge current (I_p) at several settings. This should yield a straight line which goes through the origin if the system is linear, as shown in Figure 11. A second check would be to plot the peak current vs the extrapolated or "scaled" rate-of-rise of the current as shown in Figure 12. The "scaled" rate-of-rise of current is obtained by multiplying the actual rate-of-rise of current by the scaling factor (ratio of desired peak current to actual peak current).

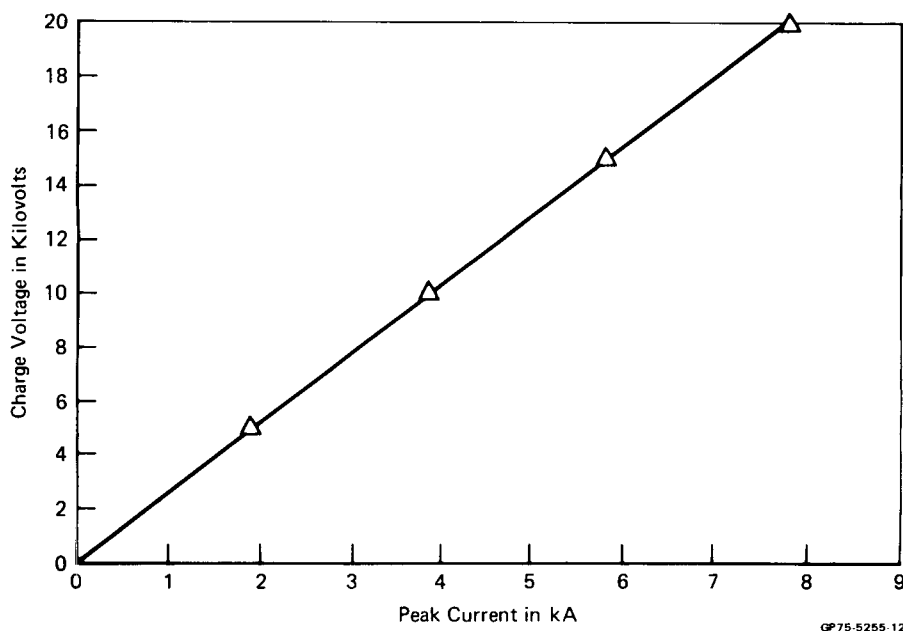
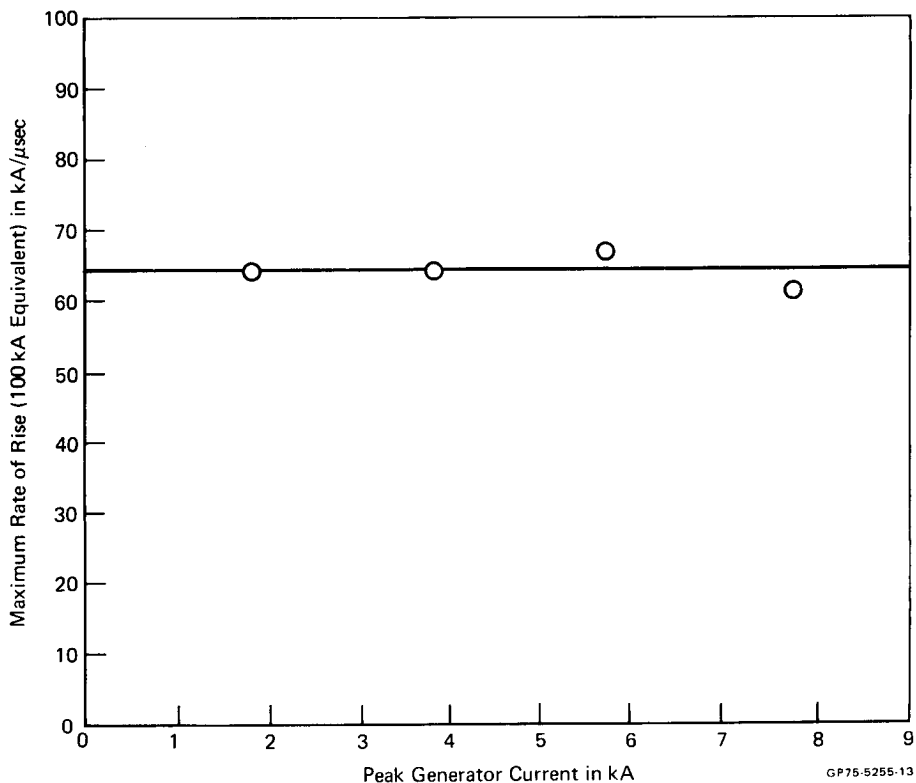


FIGURE 11 TRANSIENT GENERATOR CALIBRATION



**FIGURE 12 TRANSIENT GENERATOR RATE-OF-RISE CALIBRATION
SCALED TO 100 kA (USED FOR F-15 FIN TIP LIGHTS)**

The principal advantage of these two plots providing they are linear, as shown in Figures 11 and 12, is that any observed nonlinearity in the induced voltage and current data can be shown to be a true nonlinearity due to the circuit under test and not an anomaly introduced because of the nonlinearity of the transient generator current.

There is another approach to the use of a transient generator for induced voltage coupling which utilizes a damped oscillatory current (underdamped case). The advantage of the oscillatory technique is that no limiting impedances are present to restrict the magnitude of the driving current, so that considerably higher peak current levels may be realized. Although useful, this approach is not considered to be as desirable for simulating lightning induced transients because:

- (a) the damped oscillatory waveforms have limited frequency content
- (b) energy storage elements such as capacitors which may be included in electronic equipment input and output filtering circuitry may unrealistically limit the induced voltage transients resulting from the high-frequency oscillatory current waveform
- (c) induced voltages resulting from the high-frequency diffusion currents probably will become unrecognizable.

Transient Generator Hardware

A transient generator can be as elaborate or as simple as one desires. One of the first transient generators (called a transient analyzer), utilized for simulating lightning induced voltages into aircraft circuits, was that constructed by G.E.⁹ This transient analyzer was capable of a peak current of several hundred amps when simulating the scaled down version of MIL-B-5087B.

A more elaborate semi-portable transient generator, the capacitor bank of which is shown in Figure 13, has recently been constructed at McDonnell Aircraft and is designed principally for testing full size aircraft or large aircraft assemblies. This transient generator (designated the "Full Wave Lightning Transient Generator") has a maximum open circuit output voltage of approximately a half million volts and a maximum safe short circuit current of approximately 30,000 amps. When simulating a scaled version of MIL-B-5087B, peak currents greater than 10kA are possible. This generator consists of 20 stages (24kV/stage, 21 μ f/stage) in a Marx-Surge configuration. Because of the large amount of energy to be dissipated in the waveshaping resistor when the capacitor bank is discharged, the resistor currently used is a copper-sulfate water solution with a resistance of nominally 50 Ω . This type resistor exhibits an undesirable characteristic for this application in that its resistance is temperature sensitive; therefore, it must be monitored during a series of tests to be certain that it does not change value. Hard resistors are currently being designed to eliminate this problem. The full wave lightning transient generator is designed so that the same waveshape can be produced at peak currents as low as 100 amps or as high as 10kA. The polarity of the generator can readily be reversed. Also, if the situation arises, the output of the generator can be +240kV and -240kV with the midpoint of the generator grounded. The advantage of an installation such as this is that the test article can be maintained at essentially ground potential during testing. The advantage of using a high-output resistance (50 Ω) is that the impedance of the test article will not significantly affect the driving current amplitude and waveshape.

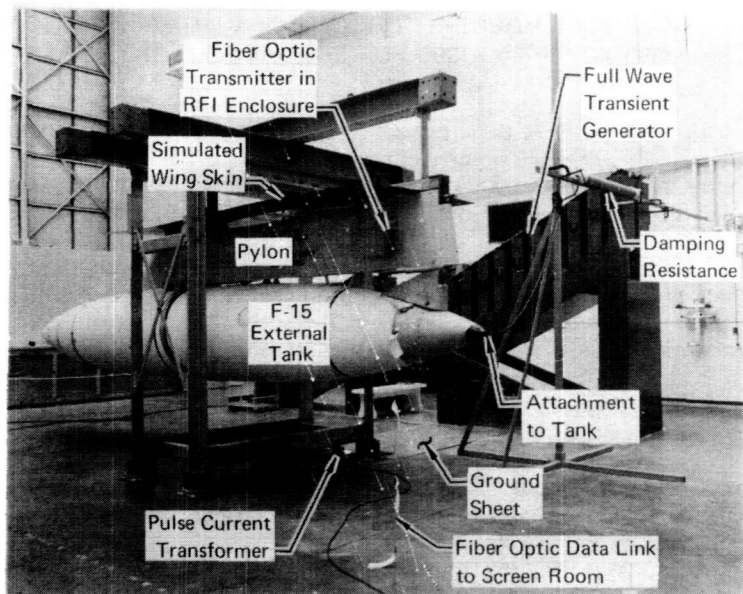


FIGURE 13 F-15 TANK TEST SETUP TO TRANSIENT GENERATOR

Application of the Transient Generator

For our applications, the purpose of the transient generator is to cause lightning type currents to flow throughout an aircraft or portion thereof in a manner similar to that caused by natural lightning currents. The current entry and exit points are therefore those that have been determined by either actual lightning strikes to similar aircraft or those determined by model attach point studies as described in Reference 17. The electrodes from the transient generator are normally attached securely to the desired current entry and exit points, and should be connected so as to duplicate the lightning arc attachment free field magnetic conditions outside the aircraft. This implies that the current leads from the aircraft are relatively long and oriented in the direction of probable arc attachment. This point is important for aperture coupling where aircraft wiring is close to the attachment point.

In order to minimize the inductance in the leads from the generator to the test vehicle, wide sheets of conductive foil, heavy gauge wires, or a series of spaced parallel wires are used. For example, in the test setup shown in Figure 13 (F-15 External Tank Test), a very heavy gauge lead was used and the ground return was a wide sheet of aluminum, although a 10 gauge wire could have easily carried the current surge. As another example, in testing the Apollo Soyuz Test Project¹⁰ spacecraft, a coaxial feed system was utilized. A schematic representation of this setup is shown in Figure 14.

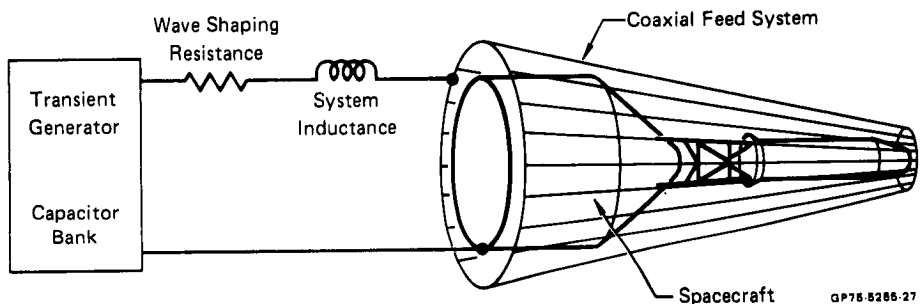
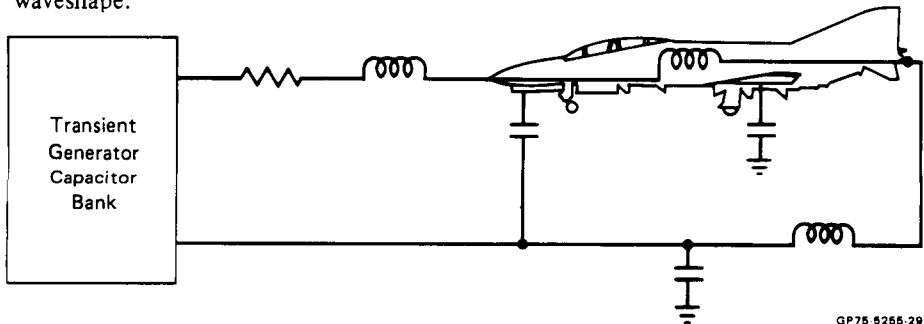


FIGURE 14 SOYUZ TEST SETUP SCHEMATIC

In any test setup involving the use of a transient generator, unwanted resonances exist which can complicate the generation of a "clean" simulated lightning current waveshape. For example, consider the setup illustrated in Figure 14. The spacecraft and the coax feed system wires constitute what could be classified as a section of coaxial transmission line, the impedance of which is a function of the inner conductor (spacecraft) and the outer conductor (coax feed system wires). If we assume that the impedance remains constant over the length of the spacecraft, then we still must consider the terminations at the ends of the spacecraft. If the "shorted" end of the coax feed system/spacecraft is not terminated in its characteristic impedance, then energy will be reflected resulting in a distortion of the waveshape. Such distortions complicate the analysis of test results. If there is a mismatch between the generator and the simulated coax cable load, then it is possible for the measured current in the generator line to be different from that in the vehicle under test.

As another example, consider the case of a small aircraft setting on the floor of a hangar and connected to a transient generator⁸ as shown in Figure 15. The aircraft can be seen as constituting one-half of a single turn loop inductance with an appropriate resonance. But it also comprises a part of a parallel plate transmission line with terminations at the nose and tail of the aircraft. With such a complex operating mode, some distortion of the leading edge of the simulated lightning waveshape is highly probable and it is very time consuming to determine a configuration which minimizes this distortion. Also, in this case, the simulated current waveshape will probably appear as a high-frequency damped waveform riding the leading edge of the desired waveshape.



GP75 5255-29

FIGURE 15 SCHEMATIC OF AIRCRAFT TEST SETUP

It was mentioned that minimizing the distortion on the leading edge waveshape can be very time consuming. Then how much can be tolerated? There is no hard and fast rule which can tell us the answer to this question since it will obviously depend upon the resulting magnetic fields and how these fields affect the electrical systems under test. If the electronic equipment under test is resonant near the "distortion frequency", some upsetting results may be obtained. Certainly, if the oscillograph trace of the current waveform reveals that the amplitude of the "distortion frequency" is larger than the amplitude peak of the desired waveform, then some re-evaluation probably should be undertaken. It has been our experience at MCAIR that tests in which a transient generator was used, the linearity of the induced voltages was directly related to the linearity and "cleanliness" of the driving current waveform.

Instrumentation

Voltage – Of prime importance is the accurate measurement of the induced voltage which is usually monitored on an oscilloscope. Although this sounds simple enough, in actual practice it becomes quite difficult for several reasons:

- (1) The measurement leads, from the pickoff point of the electrical circuit under test to the voltage readout instrumentation, are probably being subjected to some of the same electromagnetic fields which induced the voltage in the first place.
- (2) The readout instrumentation may also be subjected to some of the same high-magnetic fields.
- (3) Ground loops may exist between the desired article under test and the readout instrumentation.
- (4) Ground loops may exist between the transient generator and the readout instrumentation or its associated power supplies.
- (5) Possible loading effect caused by the readout instrumentation and associated cables on the electronic circuit under test.

Some of the above problem areas are interrelated and although it is not always possible to eliminate all the above problem areas completely, they at least must be minimized in order that confidence in the measured parameters is assured. In addition, the oscilloscope must have adequate bandwidth, extending to at least 5 MHz. The various problem areas can be minimized in several ways, including the following:

- (1) Double shielded wire for the instrumentation cable.
- (2) Double shielded duplex cable and differential readout instrumentation to eliminate common mode voltages.
- (3) Install readout instrumentation in an RFI enclosure such as a screen room.
- (4) Completely floating battery powered instrumentation (elimination of ground loops).
- (5) Fiber optics to isolate the readout instrumentation from both the electrical circuit under test and the transient generator (elimination of ground loops).
- (6) Fiber optics and very short instrumentation cables to minimize loading effect on the test circuit.
- (7) Isolation resistors at the pickoff voltage point to minimize the loading effects on the circuit under test.

Even after all these precautions have been taken, the induced noise in the measurement instrumentation system should be verified. This can generally be easily accomplished by delivering the transient current to the test object while monitoring the readout instrumentation with the leads disconnected from the electrical circuit under test. This should be done under two conditions:

- (1) with the disconnected measurement leads open circuited, and,
- (2) with the disconnected measurement leads shorted.

If this induced noise in the instrumentation readout system is significant when compared to the signal measured when connected to the electrical circuit under test, then additional "cleanup" should be done.

Current – It is also important to obtain accurate current waveforms as explained previously; whether it be the driving current or the induced current. Most of the precautions listed above are also applicable to the current measurement. The wide-band pulse current transformer has been found to be very good for these measurements.

CONCLUSIONS

The operational principles underlying the use of the transient generator as the pulse current source for simulating lightning currents and inducing voltages and currents into aerospace electrical systems has been given. It is concluded that the transient generator technique is an excellent nondestructive diagnostic technique which can be an invaluable aid in the determination of the susceptibility of aircraft electrical systems to lightning induced transients. However, sufficient details have also been given to show that the technique must be well controlled and used with care; the installation of the generator and measurement instrumentation, and the interpretation of data will require considerable attention to detail. In order to have confidence in the results, peak currents as high as possible should be used to overcome any nonlinearities in the system response.

APPENDIX

Theory of Waveform Analysis

The purpose of this section is to demonstrate why the waveform shown in Figure 2 is reduced in the manner illustrated in Figure 9. To do this we will utilize the Fourier analysis to show the relationship between a given waveshape and frequency. Because the waveshape shown in Figure 2 is rather complex, we will utilize a simpler waveshape to demonstrate the basic theory and infer from this argument the necessary changes required to reduce the waveshape shown in Figure 2 to that given in Figure 9.

Any periodic function (bounded, piecewise-continuous) could be represented as a sum of sinusoids and a constant. Or put another way, the periodic function can be broken down into a constant plus discrete sinusoidal frequencies; each frequency having its own amplitude and phase relationship to a reference frequency. For example, consider the "square" wave shown in Figure 16. It can be shown that this waveform can be represented by the Fourier series

$$P_1(t) = \frac{A}{2} + \frac{2A}{\pi} \cos\left(\frac{2\pi t}{\tau}\right) - \frac{2A}{3\pi} \cos\left(\frac{6\pi t}{\tau}\right) + \frac{2A}{5\pi} \cos\left(\frac{10\pi t}{\tau}\right) - \dots \tag{1}$$

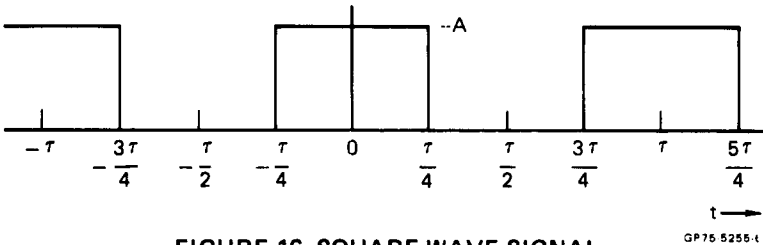
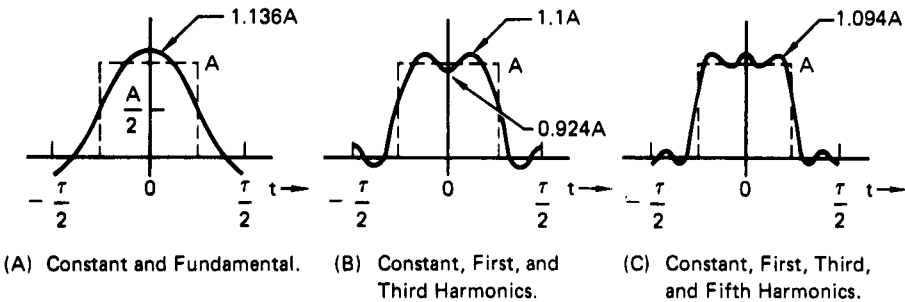


FIGURE 16 SQUARE WAVE SIGNAL

To appreciate how these sinusoidal frequencies combine to form the original "square" wave, refer to Figure 17 showing three waveforms. Figure 17a shows the constant and the fundamental, i.e., the first two terms to the right of the equal sign in equation (1). Figure 17b shows the constant, first and third harmonics (first three terms) and Figure 17c shows the sum of the constant, first, third, and fifth harmonics. The figures clearly indicate that as more and more terms are added to the series, the waveform more closely approaches the original "square" wave.



From Reference 19

GP75-5255 7

FIGURE 17 RECONSTRUCTED SQUARE WAVEFORM

Although it is realized that the transient waveform we are primarily interested in is not periodic as the square wave shown in Figure 16, you can realize that if a portion of a periodic waveform can be broken down into discrete frequencies without regard to the information occurring before time $-\tau/2$ and after $+\tau/2$, then, we can surely expect the same to be true for one single pulse occurring in time.

Next consider a square wave having the same period as that previously considered in Figure 16 except now the amplitude is $A/2$ rather than A . The Fourier series of this new waveform is:

$$P2(t) = \frac{A}{4} + \frac{A}{\pi} \cos\left(\frac{2\pi t}{\tau}\right) - \frac{A}{3\pi} \cos\left(\frac{6\pi t}{\tau}\right) + \frac{A}{5\pi} \cos\left(\frac{10\pi t}{\tau}\right) - \dots$$

which can be written

$$P2(t) = \frac{1}{2} \left[\frac{A}{2} + \frac{2A}{\pi} \cos\left(\frac{2\pi t}{\tau}\right) - \frac{2A}{3\pi} \cos\left(\frac{6\pi t}{\tau}\right) + \frac{2A}{5\pi} \cos\left(\frac{10\pi t}{\tau}\right) \dots \right]$$

but it noted that the terms inside the brackets = $P1$

$$\therefore P2(t) = \frac{1}{2} [P1(t)]$$

Here it is seen that only reducing the amplitude has reduced the amplitude of each term by the corresponding amount but the frequency of the fundamental and its harmonics have remained the same.

Although the lightning current waveshape specified in MIL-B-5087B is not a "square" wave but is closer to a double exponential waveform, the amplitudes, frequencies and phasing are different from those of the square wave, but it can now be realized that if the pulse is to be "scaled down," it must be done with careful attention to the waveshape. If the amplitude of the simulated wave from time $t=0$ to $t=t_f$ is different by other than a constant from the specified wave, then its frequency content will differ. For additional analysis the reader is referred to Reference 19.

REFERENCES

- ¹Air Force Systems Command Design Handbook, DH1-4DN 7A1, First Edition, 10 Jan 1969.
- ²Plumer, J.A. and Perry, B.L., "An Analysis of Lightning Strikes in Airline Operation in the USA and Europe," 1975 Lightning and Static Electricity Conference (L&SEC) 14-17 April 1975, Culham Laboratory, England.
- ³NASA MSC Design and Procedural Standard No. 138, "Lightning Protection Design."
- ⁴Kester, F.L., Gerstein, M. and Plumer, J.A., "A Study of Aircraft Fire Hazards Related to Natural Electrical Phenomena," NASA CR-1076, June 1968.
- ⁵Robb, J.D., Stahmann, J.R., and Boekland, L.A., "Lightning Electrical Hazards to Flight Vehicles," USAF (AL) TR-69-269, Dec 1969.

- ⁶Perry, B.L., "British Researches and Protective Recommendations of the British Air Registration Board," USAF (AL) TR-68-290, 1968 Lightning and Static Electricity Conference, May 1969.
- ⁷Wilson, H.Z. and Robb, J.D., "B-1 Lightning and Electrification Program," 1972 Lightning and Static Electricity Conference, USAF (AL) TR-72-325, p 242, Dec 1972.
- ⁸Plumer, J.A., "Lightning Effects on the NASA F-8 Digital Fly-by-Wire Airplane," 1975 Conference on Lightning and Static Electricity, 14-17 April 1975, Culham Laboratory, England.
- ⁹Walko, W.C., "A Test Technique for Measuring Lightning-Induced Voltages on Aircraft Electrical Circuits," NASA CR-2348, Washington, D.C., Feb 1974.
- ¹⁰Blount, R.L., Gadbois, R.D., Suiter, D.L. and Zill, J.A., "ASTP Simulated Lightning Test Report," NASA, Lyndon B. Johnson Space Center, JSC-09221, Nov 1974.
- ¹¹Uman, M.A., "Lightning," McGraw Hill, New York, 1969.
- ¹²Cianos, N. and Pierce, E.T., "A Ground-Lightning Environment for Engineering Usage," Stanford Research Institute Technical Report 1, SR1 Project 1834, August 1972.
- ¹³Pierce, E.T., "Natural Lightning Parameters and their Simulation in the Laboratory," 1975 Conference on Lightning and Static Electricity, 14-17 April 1975, Culham Laboratory, England.
- ¹⁴"Aerospace Recommended Practice: Lightning Effects Tests on Aerospace Vehicles and Hardware," SAE Committee AE4, Special Task F, 8 October 1975.
- ¹⁵"Space Shuttle Lightning Protection Criteria Document," MSC-07636, National Aeronautics and Space Administration, Lyndon B. Johnson Space Center, Houston, Texas.
- ¹⁶MIL-B-5087B, "Bonding, Electrical, and Lightning Protection for Aerospace Systems," 6 Feb 1968.
- ¹⁷Clifford, D.W., "Scale Model Lightning Attach Point Testing," 1975 Conference 1975 Conference on Lightning and Static Electricity, 14-17 April 1975, Culham Laboratory, England.
- ¹⁸Burrows, B.J.C., "Induced Voltages, Measurement Techniques and Typical Values," 1975 L&SE Conference, Culham Laboratory, England, 14-17 April 1975.
- ¹⁹"LaPlace and Fourier Transforms for Electrical Engineers," Edward J. Craig, Holt, Rinehart and Winston, Inc., 1964.

A STUDY OF MOLECULAR CONTAMINATION

T. H. Allen, T. A. Hughes, *McDonnell Douglas Corporation, St. Louis, Missouri*
Lt. B. C. Price, *U.S. Air Force Materials Laboratory, Wright Patterson AFB, Ohio*

ABSTRACT

Contamination kinetics of typical spacecraft materials were studied* using several techniques, including ellipsometry. Data was obtained on contaminant deposition rates, sticking coefficients, and reevaporation of the contamination. Materials studied included silicone sealants, a thermal control paint and a graphite laminate as contaminant sources, and gold coated surfaces, a thermal control paint and a second surface mirror material as the contamined. Both deposition and reevaporation rates were found to be non-linear with time, and followed an exponential decay. A hypothesis is presented that the non-linear behavior was a result of disproportionation of the molecular weight fractions of the polymers. The measured sticking coefficients were found to vary substantially with temperature over narrow ranges. Simulated space radiation was found to reduce the evaporation rates of contaminants by several orders of magnitude.

INTRODUCTION

Potentially serious problems exist on satellites and spacecraft when outgassed products from organic materials condense on thermal control surfaces and sensitive optical components, and seriously degrade their performance. Further complicating effects may be expected from subsequent space radiation impinging on the contaminated surfaces. The contamination of a second-surface mirror thermal control surface has been identified as the source of a serious heat-up problem on an Air Force satellite, and is suspected as the probable cause of malfunction of other satellites. Analysis of the DO-24 experiment on Skylab (a thermal control material evaluation to compare space exposure data with ground simulated exposure data) was seriously hampered by contamination during relatively brief space exposure. The quartz crystal microbalances contamination monitors of Skylab also revealed very high levels of contamination.

Sources of contamination include the outgassed products of organic polymers such as sealants, adhesives and coatings. Considerable effort has been devoted to the proper selection of such materials to eliminate the problem, however, as long as organic materials are present, some potential for contamination exists.

The Air Force Materials Laboratory has instituted a program (Contract F33615-73-C-5091) for a broad study of the effects of contamination on thermal control surfaces and optical components. This paper summarizes the results on one phase of that program, the kinetics of contamination, and in particular, outgassing rates, sticking coefficients, reevaporation rates, and effects of radiation for selected typical contaminants. The other aspects of the program are described in Reference (1).

*Work supported under Contract F33615-73-C-5091, "Investigation of Contamination Effects on Thermal Control Surfaces".

Previous work in this area has included considerable screening evaluations such as the NASA sponsored test that determines percent weight loss and percent volatile condensable material (VCM). McPherson (Reference 2) employed a microbalance technique and concluded that after an initial variable rate period, outgassing rates were constant with time. McKeown, et al (Reference 3) contaminated a QCM with a roughing pump vacuum oil and obtained a desorption rate that was essentially a first order reaction rate, i.e., the desorption was a function of the amount of oil remaining on the crystal. The investigators interpreted the data as representing the effect of increasing bonding forces as the number of monolayers decreased. Jaffe and Rittenhouse (Reference 4) have reviewed much of the data current at that time (1961), but the thrust of their review was not contamination but life expectancy of polymers based on weight loss. Further, the data was based on extrapolations from temperatures far above the normal decomposition temperatures of polymers.

Experimental Approach

Four materials were employed in the kinetics study as contaminant sources, and three materials as the sensitive contaminees. The sources used were RTV-602 silicone sealant, S-13G thermal control paint, RTV-566 silicone sealant and a graphite-epoxy laminate. The surfaces upon which the outgassed products were condensed were a gold mirror (vapor deposited gold on an aluminum substrate), aluminized Teflon (FEP) second surface mirror, and S-13G thermal control paint.

Three separate measurement techniques were used to measure the deposition rates and subsequent evaporation rates of the molecular contaminants. The most precise of these techniques was ellipsometry which was used extensively throughout this program for measuring the properties of contaminants deposited on gold mirrors. A quartz crystal microbalance (QCM) was also used for a limited number of measurements. The QCM was capable of making accurate measurements, but it was limited by the required substrate temperatures. Since ellipsometric measurements are limited to optically smooth surfaces, an electrobalance was used for making measurements with the optically rough surfaces of S-13G paint and FEP-A1. Measurements with the microbalance showed that its accuracy was at least an order of magnitude poorer than the ellipsometer or QCM.

Ellipsometry is an optical technique which measures the change in the state of polarization of monochromatic light reflected by an optical surface; an optically smooth reflecting surface is a requirement of the technique. In the case of a film-free surface, this technique can be used to measure the intrinsic optical constants, e.g., refractive index and absorption constant. When the surface is covered with a nonabsorbing thin film, the thickness of the film can be determined. The high sensitivity of ellipsometry in detecting and measuring the thickness of thin films and its adaptability to real time in-situ measurements made it an excellent technique for studying the kinetics of thin films.

The parameters measured by the ellipsometer are Δ (degrees), and ψ (degrees), which correspond to the changes in phase and reflected amplitude of the electric field vectors, respectively, caused by the optical boundaries. In this case of a contaminated surface, the measured Δ and ψ values can be used to determine the film thickness using the classical optical equations (Reference 5). The ellipsometer employed in this study used monochromatic light from a He-Ne laser ($\lambda = 0.6328 \mu\text{m}$) and all measurements were made using a compensator azimuth of -45° and an angle of incidence of 70° . The diameter of the light beam incident on the mirror surface was typically 0.2 cm diameter. The change in phase and reflected amplitude could be measured with a precision of $\pm 0.02^\circ$, which corresponds to a change in

film thickness of about $\pm 0.4\text{\AA}$ in the case of an organic film. The overall accuracy for a film thickness of $<200\text{\AA}$ was estimated to be $\pm 2\text{\AA}$.

The test arrangement consisted of a vacuum sample chamber and a commercial ellipsometer as shown in Figure 1. The chamber was equipped with specially designed windows to permit in-situ optical measurements and additional ports for radiation exposure of contaminated samples. The radiation sources included UV (3.6 UVSC), electrons (15 KeV) and protons (5KeV). A high-speed turbomolecular pump was used to provide 10^{-6} torr vacuum and to minimize sample contamination through hydrocarbon backstreaming.

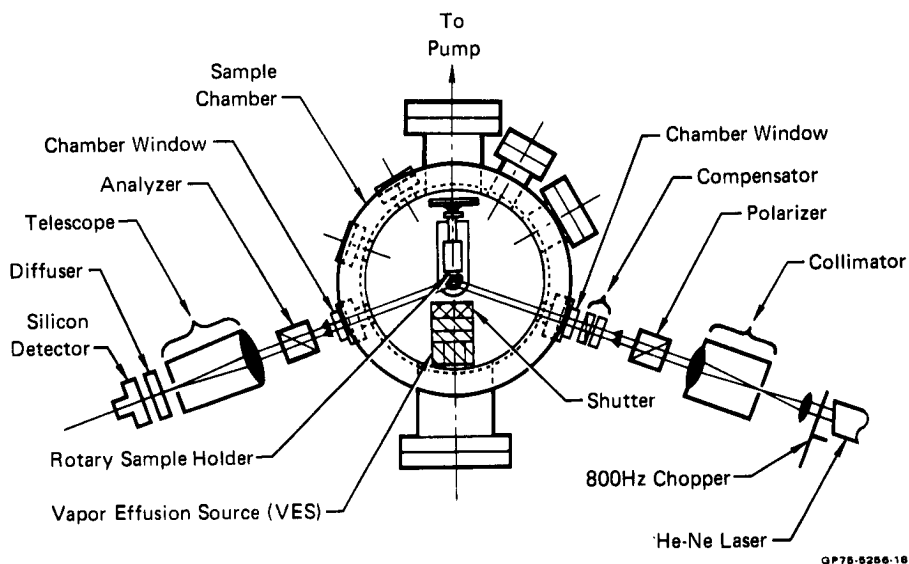


FIGURE 1 OPTICAL ARRANGEMENT OF ELLIPSO-METER AND SAMPLE CHAMBER

Of prime importance in a study of this type was the deposition of uniform thin films in a controlled and reproducible manner. This was accomplished by using a heated vapor effusion source (Knudsen cell) to direct a molecular beam at the contaminee. The VES was mounted within the vacuum chamber directly in front of and 7.36 cm from the test substrate. The nozzle of the VES consisted of 10 small orifices, 0.05 cm in diameter, equally spaced, on the circumference of a 0.81 cm diameter circle. The multi-orifice nozzle provided a more uniform thickness of deposit over a larger sample area than a customary single orifice nozzle. A mechanical shutter-manifold was used to control the deposition period. This special shutter-manifold was fitted with a vapor by-pass extending from the front of the shutter to the vacuum pump port. This feature was designed to minimize contaminant build up within the chamber while the shutter was closed. A view of the test arrangement within the vacuum chamber is shown in Figure 2.

The test substrate was mounted on an aluminum heater spool which was, in turn, mounted on a copper reservoir of liquid coolant. This arrangement permitted controlling the substrate temperature over the range from -198°C to 40°C .

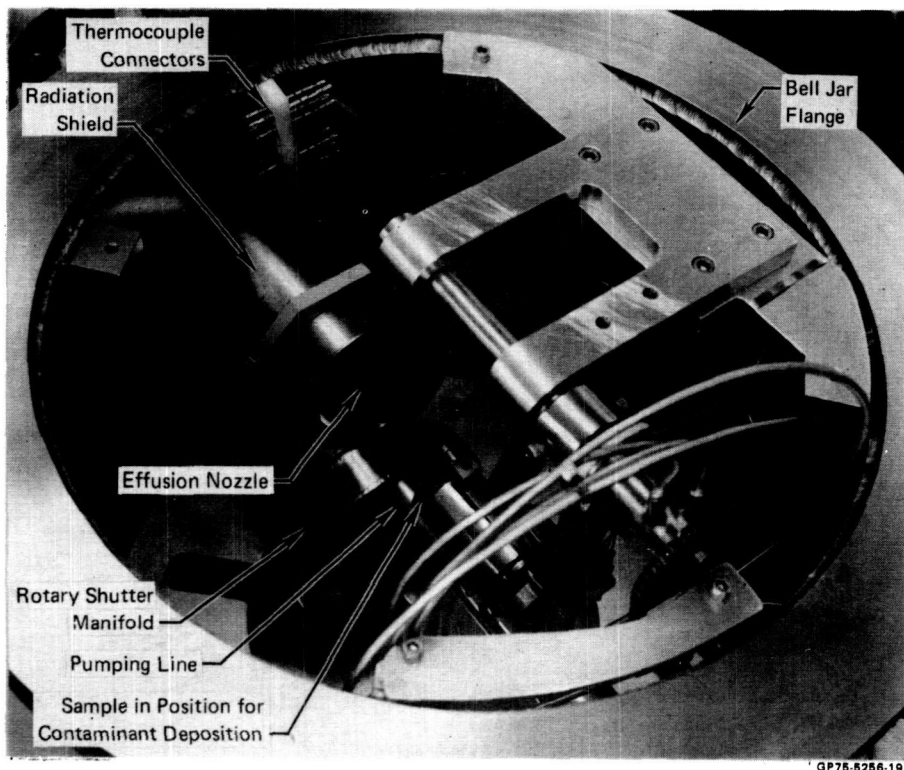


FIGURE 2 VES INSTALLED IN VACUUM CHAMBER

Deposition rate measurements were made by determining the rate of increase in thickness of the contaminant layer on the substrate with the shutter open to expose the substrate to the molecular beam from the VES. The evaporation rate of the deposited contaminant was measured by the rate of change of thickness of the contaminant with the shutter closed.

The probability that an impinging molecule will be incorporated on a surface is called the "sticking" or "condensation" coefficient. Since all measurements were made with a surface already covered with the contaminant, the term "self sticking coefficient" would be a more descriptive definition of the measured quantity discussed in this paper. It can be measured experimentally by determining the ratio of the material to the total amount impinged per unit of time, at a specific substrate temperature. The molecular weight of the contaminant was not known, therefore the total impingement rate could not be computed (Reference 6) analytically. This problem was resolved by reducing the substrate temperature until the deposition rate was constant, which usually occurred at about -20°C . This temperature independent deposition rate was assigned a sticking coefficient of unity and was used for determining values at higher temperatures. It was also necessary to normalize the deposition rates to a constant time to obtain valid data as it was found early in the program that the deposition rates were a function of age of the source.

Results

Initial measurements with RTV-602 were made with the ellipsometer using a gold mirror as a substrate and a VES temperature of 140°C. Because we were more interested in the outgassing products that would be emitted over a long lifetime in space, rather than those lost during and shortly after launch, the RTV-602 was preconditioned for 12 hours at normal vacuum chamber operating conditions. This was considered adequate to more closely simulate spaceborne material which had already lost the low molecular weight constituents.

Measurements with preconditioned RTV-602 clearly demonstrated that both the deposition and evaporation rates were not constant, but decreased with elapsed test time, as shown in Figure 3, for a constant substrate temperature. It was found that the decay or aging of both rates could be mathematically expressed as:

$$\beta = Ke^{-nt}$$

where β is the measured rate at time t , and K and n are constants.

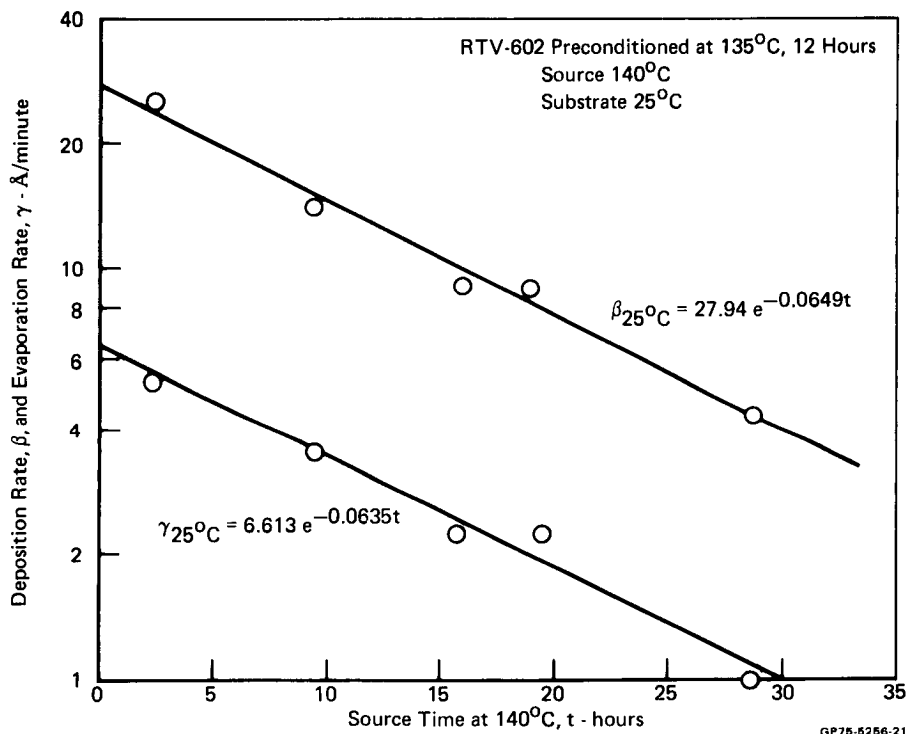
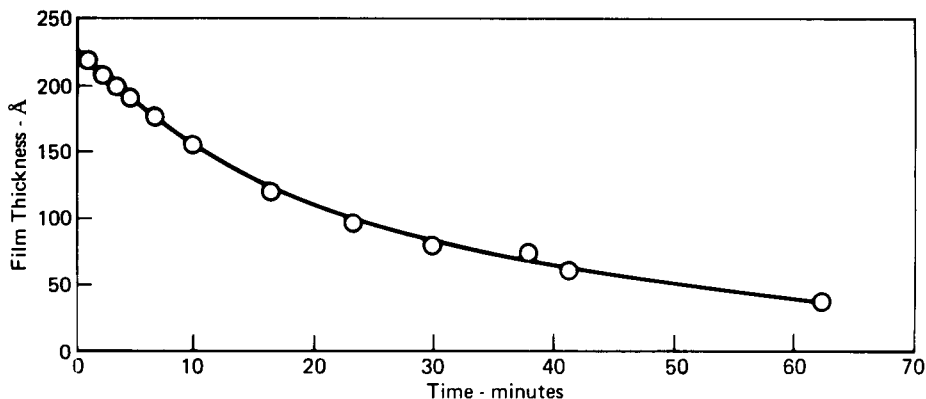


FIGURE 3 AGE EFFECT ON THE DEPOSITION AND EVAPORATION RATES OF CONTAMINATION FROM RTV-602

This exponential decay is again illustrated in Figure 4 which shows the thickness of a deposited contaminant film allowed to freely evaporate, as a function of time at a constant substrate temperature of 25°C. Data analysis indicated that the evaporation rates could be expressed as a constant function of the residual film thickness, and thus the remaining film thickness, as a function of time, followed an exponential curve.



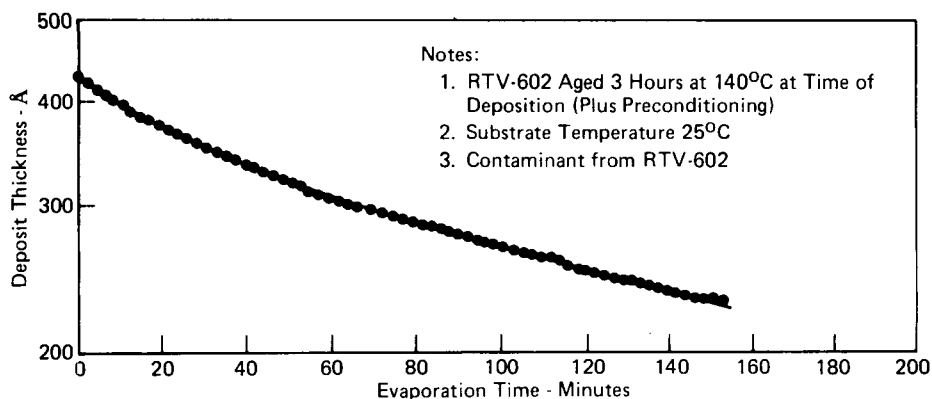
GP75-5256-20

FIGURE 4 EVAPORATION OF CONTAMINATION FROM RTV-602

To further verify the exponential change in evaporation rates with time, the evaporation of contaminant from RTV-602 was measured with a quartz crystal microbalance and the evaporation was closely observed. The results are shown in Figure 5, and confirm the trend of the results obtained with the ellipsometer. Differences in absolute values were expected due to the difference in the nature of the surfaces: an optically smooth gold mirror in one case, and an rough quartz crystal surface with the QCM. However, another influence was also apparent in the QCM data, in that the results could be best represented as the sum of two exponential equations:

$$A = 59.5e^{-0.381t} + 368e^{-0.000312t}$$

where A is the film thickness in angstroms and t is the elapsed measurement time (min). The first term on the right accounts for the initial higher rate which after a short period of time is insignificant in comparison to the second term, which then becomes dominant. Similar results were obtained with the ellipsometer. The data shown in Figure 4 were also found to be best expressed as the sum of two exponentials.



GP75-5256-24

FIGURE 5 EVAPORATION OF A THICK FILM DEPOSITED ON THE RECEIVER OF A QCM

Figure 6 shows the evaporation rates from another test with the contaminant deposited from RTV-602 onto a gold mirror, in which the substrate temperature was varied for determining sticking coefficients and evaporation rates as a function of temperature. The evaporation rate data at 25°C from Figure 3 is included for comparison. The expected strong dependence of evaporation of the contaminant on substrate temperature is clearly evident.

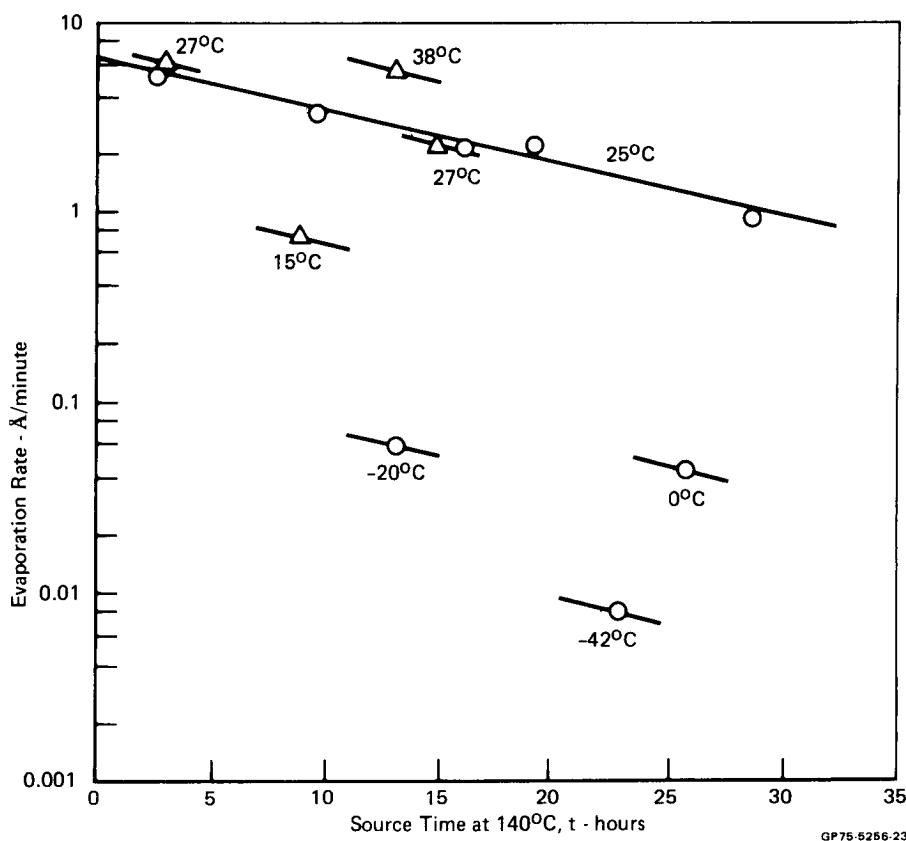


FIGURE 6 EFFECT OF SUBSTRATE TEMPERATURE ON EVAPORATION RATE OF CONTAMINANTS FROM RTV-602

The sticking coefficients of contaminant from RTV-602 as a function of substrate temperature are shown in Figure 7. Noteworthy is the dramatic change in sticking coefficients at about 25°C. This is the temperature at which the collector operates in the typical VCM test and may explain some problems in reproducibility of results.

Similar tests were conducted with S-13G thermal control paint as the contaminant source, using the gold mirror as the substrate and the ellipsometer to measure the contaminant thickness. Deposition rates and reevaporation rates are shown in Figure 8 and the sticking coefficients in Figure 7. The S-13G was used as-cured in these tests.

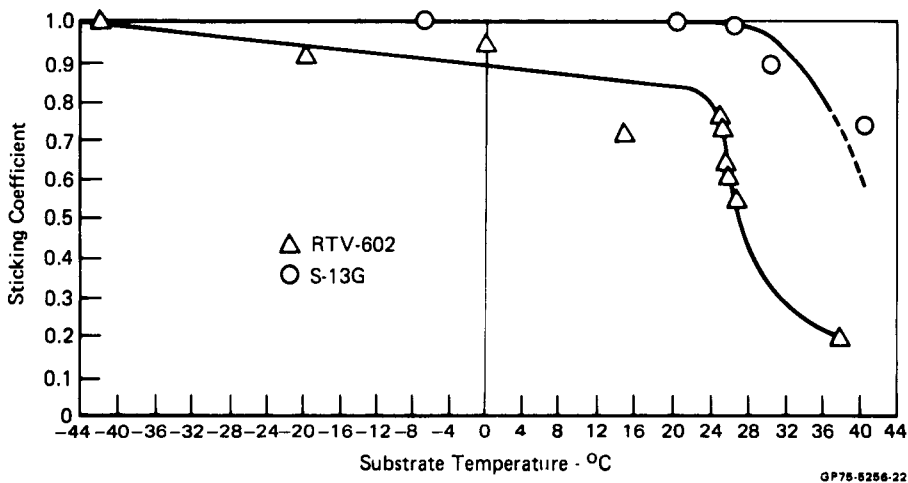


FIGURE 7 STICKING COEFFICIENTS FOR CONTAMINANTS FROM RTV-602 AND S-13G

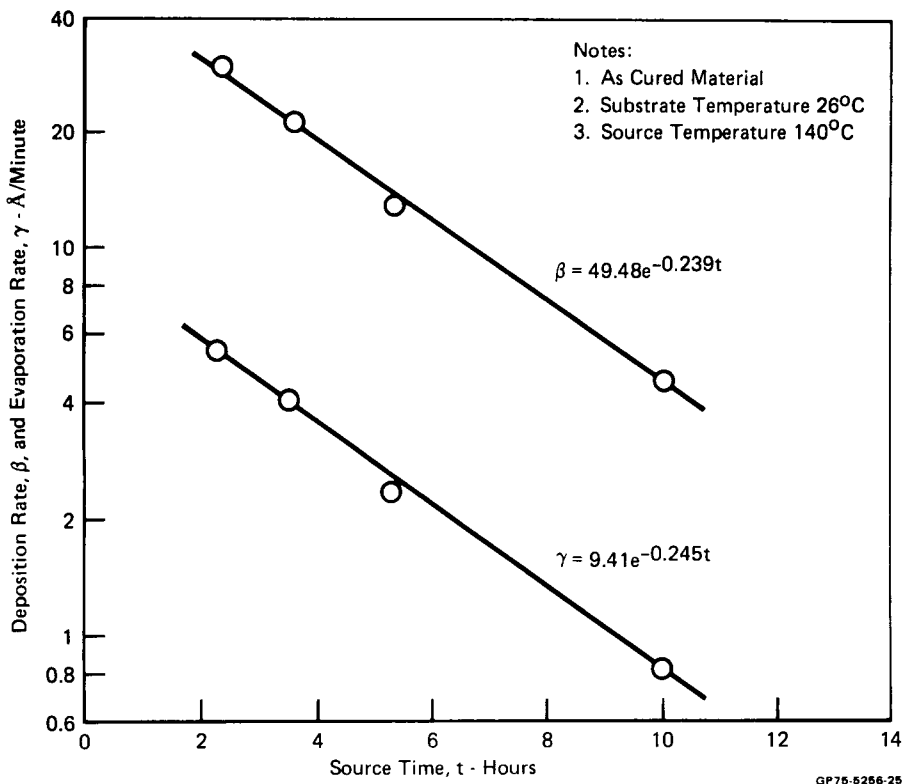


FIGURE 8 DEPOSITION AND EVAPORATION RATES OF THE CONTAMINANT FROM S-13G

Tests with RTV-566 were conducted on room temperature cured material without any elevated temperature preconditioning. In order to obtain a measurable rate of deposition from the RTV-566, it was necessary to operate the VES at an inordinately high temperature. The temperature was so high that the character of the outgassed products could be reasonably questioned as to whether they were normal outgassing products or decomposition products. While RTV-602 deposited about 25 Å/min (initially) with the VES at 140°C, RTV-566 deposited only 2.3 Å/min with the VES at 250°C. The subsequent evaporation rate for the deposited film (27°C) was approximately 0.02 Å/min. The deposition test with RTV-566 was repeated with the gold mirror at -40°C to assure complete capture of the incident material. This result was identical with the initial test. Such extremely low deposition rates prevented a realistic determination of sticking coefficients.

Tests, with the GY-70 graphite fiber/904 epoxy resin in the VES at 160°C, failed to produce a measurable amount of contamination on the gold mirror. The test specimen had originally been autoclave cured and postcured at 177°C prior to our tests. Because of the negative results, no further tests were made with the graphite-epoxy composite.

The results of deposition of contaminants on the S-13G thermal control paint and on aluminized Teflon, will be summarized here only. Complete details are contained in Reference 1. Due to a lower order of precision of the microbalance measurements, as compared to the ellipsometer, there was a much greater scatter in the microbalance data. Two of the significant findings with the microbalance data were that the sticking coefficients were affected by the nature of the surface (Figure 9), and the rate of evaporation of contaminants from the Teflon surface of aluminized Teflon was only about one-third the rate from a gold surface.

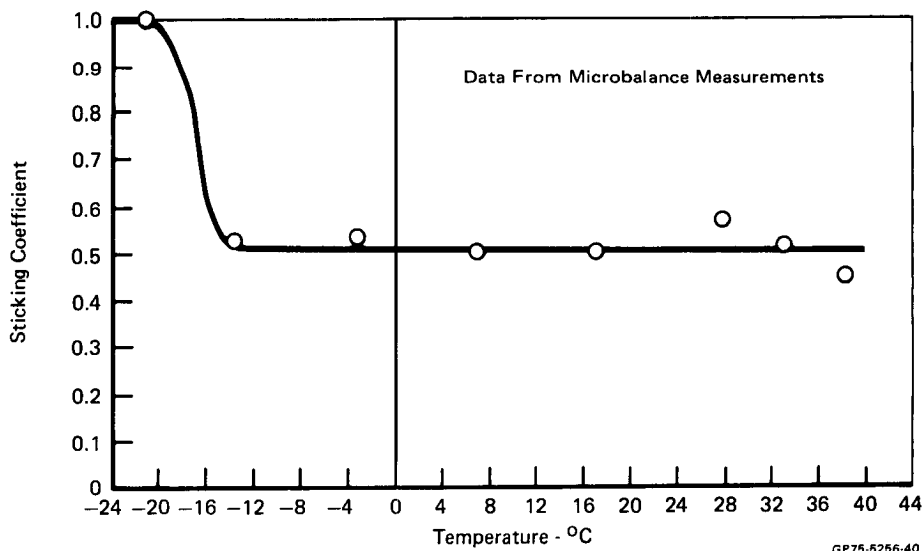


FIGURE 9 STICKING COEFFICIENTS FOR CONTAMINANTS FROM S-13G DEPOSITED ON ALUMINIZED TEFLON

The estimated relative total accumulation of the various contaminants on the various substrates is shown in Table 1. These estimates are based on the experimental values determined with the contaminant source at 140°C except where indicated, and the substrate at 25°C. All of the data shown were derived by integration of the deposition rate data over the time periods shown, after altering the equations to consistent time units. The values for RTV-602 without preconditioning were determined by virtue of the fact that the preconditioning procedure was nearly identical with the test conditions for measurement of deposition, with the assumption that time zero was -12 hours, based on the deposition time base. It may be noted that most of the accumulations occur early, with additional time providing only smaller additional increments. This is a natural result of the exponential decay rate.

It should be emphasized that this table should not be considered as absolute values, but only for relative comparisons. Any accumulation of contaminants will also be controlled by the source temperature, as well as geometry and viewing angles.

TABLE 1 RELATIVE ACCUMULATION OF CONTAMINANTS ON VARIOUS SUBSTRATES

Source 140°C, Substrate 25°C

Time - Hours	Total Accumulated Thickness μm								
	Gold Substrate			FEP Substrate			S-13G Substrate		
	1	10	100	1	10	100	1	10	100
Source									
RTV-602 Not Preconditioned	3.2	4.28	5.62	9.05	10.2	10.5	259	260	260
RTV-602 Preconditioned	0.16	1.23	2.58	0.25	1.36	1.75	0.58	1.66	1.69
RTV-566*	0.003	0.003	0.003	—	—	—	—	—	—
S-13G	0.26	1.13	1.24	0.47	1.33	1.34	0.33	0.88	0.89
Graphite-Epoxy**	0.0006	0.0006	0.0006	—	—	—	—	—	—

*Source at 250°C

GP75 5256 41

**Source at 160°C

Identification of Molecular Contaminants

The molecular structure of the deposited contaminants were studied using infrared internal reflectance spectroscopy. Measurements were made by deposition of contaminants on the surface of a KRS-5 internal reflectance cell using the VES. The contaminated cell was then removed and examined for characteristic infrared absorption peaks over a wavelength range of 2.5 to 15.0 μm . These measurements showed that the contaminants from RTV-602, RTV-566, and S-13G were all polydimethylsiloxanes. The data also indicated that the deposit from RTV-566 was a cyclic polymer by the absence of the absorption bands associated with $\text{Si}(\text{CH}_3)_3$ terminal groups, while the RTV-602 and S-13G deposits contained linear chains as indicated by the presence of the terminal groups. The latter two contaminants may also contain cyclic groups. While RTV-566 is reported by the manufacturer to be "based on a phenyl containing polymer," no absorption bands characteristic of phenylsiloxane linkage were found in the absorption spectra of the condensable material from RTV-566.

Effects of Space Radiation on Molecular Kinetics

Measurements to determine the effects of simulated space radiation on the kinetics of the contaminants from RTV-602 and S-13G were made by irradiating contaminated gold substrate with UV radiation, electrons and protons in separate experiments. Gold coated aluminum was used for the substrate since it can be rapidly cooled to cryogenic temperatures and is optically stable in the radiation environments. All measurements were made at chamber pressures of 10^{-6} torr.

The measurement sequence consisted of depositing a contaminant film (typical thickness $\sim 200\text{\AA}$) on the substrate at ambient temperature and measuring the pre-irradiation evaporation rate. The substrate was then rapidly cooled to cryogenic temperatures (-180°C) and held at this temperature during the irradiation period. Precautions were taken to prevent any accumulation of extraneous contamination during the cryogenic test period by surrounding the sample with liquid nitrogen cooled baffles. After radiation exposure, the substrate was again warmed to ambient temperature for post-exposure evaporation rate measurements. The purpose of cooling the contaminated substrate to the cryogenic temperatures was to simulate the equilibrium temperatures experienced by certain satellites and which had an added bonus of inhibiting both evaporation and ageing during the radiation exposure. A summary of these results are shown in Table 2.

TABLE 2 EVAPORATION RATES AT ROOM TEMPERATURE BEFORE AND AFTER IRRADIATION

Contaminant From	Evaporation Rates - $\text{\AA}/\text{Minute}$					
	RTV-602			S-13G		
Type of Irradiation	UV	e^{-}	p^{+}	UV	e^{-}	p^{+}
Before Irradiation	6.2	4.0	3.42	3.8	0.61	1.99
After Irradiation	0.04	0.00	0.02	0.00	0.05	0.00

Fluences: UV 160 EUVSH (3.6 UVSC)

e^{-} $1 \times 10^{16} e/\text{cm}^2$ (15 kev)

p^{+} $1 \times 10^{16} p/\text{cm}^2$ (5 kev)

GP75-5256-42

It is seen that the relatively modest radiation exposure had a profound influence on the molecular kinetics. It is assumed that reduction in evaporation rate is due to radiation-induced polymerization of the contaminant.

Further evidence that changes in the morphology of the contaminant had occurred during the low-temperature irradiation period came from detailed ellipsometric measurements during the warm up after irradiation. The results of these measurements, Figure 10, show that the film was optically active during this period resulting in large fluctuations in the measured optical phase, Δ . The cause of these changes is not certain, but it is believed to be due to devitrification of the contaminant (in this case, from RTV-602) during the prolonged exposure (70 hours) to temperatures of -180°C . Similar optical activity did not occur during a normal cool-down and warm-up with a hold at -180°C for only 1 hour. The process of devitrification, during the 70-hour exposure to -180°C , is suggested by the significant changes in the optical activity during warm up in the region of the glass transition temperature for silicones, -123°C (Reference 7), and the melt temperature, -65 to -85°C (Reference 7). Further support for this hypotheses is that it is

time-temperature sensitive, characteristic of the devitrification process. This implies that the optical activity was a result of long-term exposure to a temperature below the crystallization temperature, and not due to radiation. The latter, of course, was responsible for the change in kinetics.

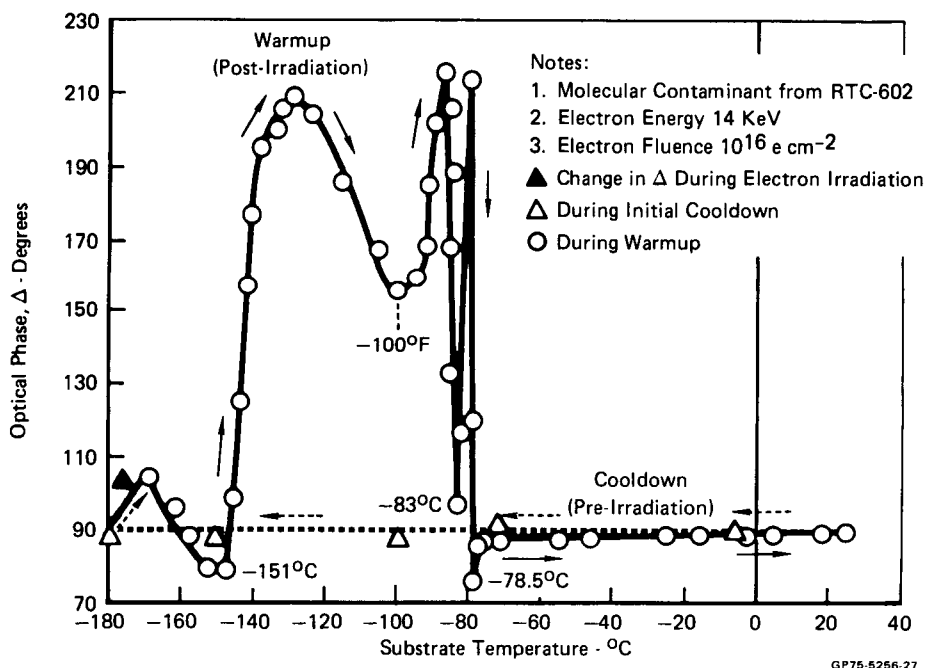


FIGURE 10 CHANGES IN OPTICAL PHASE DURING COOLDOWN AND WARMUP OF A CONTAMINATED GOLD MIRROR

Discussion

Deposition and evaporation measurements made in this study were consistently characterized by exponential decay with time, and in some cases by the sum of multiple exponentials. Santeler (Reference 8) also observed this latter characteristic among some materials he studied. He suggested that the two exponential slopes he observed might be due to changes in binding energies as the thickness changed: that at greater thicknesses the binding energy appropriate to bulk fluid properties controlled the evaporation, and at lesser thicknesses, binding energies associated with monolayer thickness was a controlling factor. Our previous experience (Reference 9) with a monomeric silicone diffusion pump oil, DC-704, shows this concept to have some merit except that the evaporation of DC-704 was linear with time (constant rate, irrespective of thickness above $\sim 20\text{\AA}$) and at thicknesses below $\sim 20\text{\AA}$, a different and smaller constant evaporation rate was observed. These results are at odds with the current data, and we believe the difference to be caused by the basic differences in monomers and polymers, and a possible mechanism is described below.

The contaminants studied in this program were polymers, which implies that the outgassing products (or decomposition fragments) were not of fixed molecular weight, but rather a mixture of homologs with a wide range of molecular weights. Typically, the vapor pressure of any species is a strong inverse function of chain length and molecular weight. This has the effect that the lower molecular weight fractions will have a higher vapor pressure and a higher evaporation rate, and result in a disproportionation in the molecular weight distribution of the unevaporated residue. Certainly all fractions are evaporating simultaneously but at much different rates. With the relatively high rates of the lowest molecular weight species, it will be exhausted first, leaving the next higher molecular weight species to be the temporarily dominant evaporant.

The effect of molecular weight on the evaporation rate of pure polydimethylsiloxanes can be estimated by the classical Langmuir evaporation equation. By substituting the Clausius-Clapeyron type equation for the vapor pressure term of the Langmuir equation, and using the data of Wilcock (Reference 10) to provide the Clausius-Clapeyron vapor pressure constants in terms of molecular weight, we have obtained:

for linear compounds –

$$w = \frac{1,570,650 (1.0139)^M \exp - \left(\frac{22.26M + 4387}{RT} \right)}{17.14} \sqrt{\frac{M}{T}}$$

for cyclic compounds –

$$w = \frac{11,745,720 (1.00826)^M \exp - \left(\frac{18.21M + 5450}{RT} \right)}{17.14} \sqrt{\frac{M}{T}}$$

where

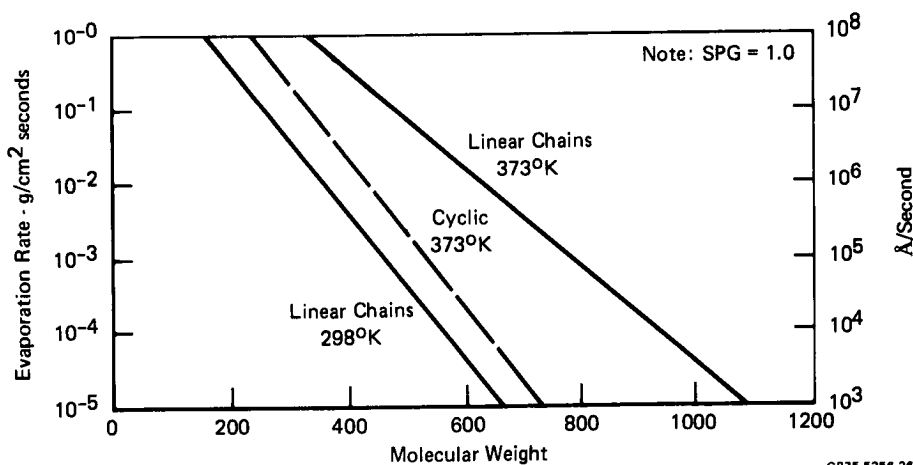
w = evaporation rate g/cm² sec

M = molecular weight

R = gas constant, 1.987 cal/mol K

T = temperature, K

A plot of these equations is shown in Figure 11, and shows the strong dependence of evaporation rate on molecular weight.



GP75-5255-26

FIGURE 11 CALCULATED EVAPORATION RATES OF POLYDIMETHYLSILOXANES

Our data has indicated that the slopes (exponents) of deposition rate curves and reevaporation rate curves were essentially identical. This could be explained by the molecular weight hypotheses, as the deposition at any given time would be rich in a specific molecular weight range, and the evaporation of that condensed fraction would be in proportion. A deposition at a later age would reflect a different "cut" and again the evaporation would be in proportion. Thus the two curves should parallel each other.

We are of the opinion therefore that in the case of polymeric materials, a "constant rate" period, as such, does not exist if measurements are made with sufficient accuracy, and that rates of deposition and evaporation of this type material will markedly decrease with time. It should be noted however, that by operating with a source at 140°C, we undoubtedly greatly accelerated the disproportion of molecular weight distribution. At lower (and more representative) temperatures, the decay rate would be expected to be less.

REFERENCES

- ¹T.A. Hughes, T.H. Allen, R.M.F. Linford, T.E. Bonham, "Investigation of Contamination Effects on Thermal Control Materials", AFML-TR-218, January 1975.
- ²D.G. McPherson, "Apollo Telescope Mount, Extended Applications Study Program – ATM Contamination Study," Contrac NAS w-1386, CR 61173, May 1967.
- ³D. McKeown, W.E. Corbin, R.J. Nauman, Thermoelectrically – Cooled Quartz Crystal Microbalance, presented at Seventh Conference on Space Simulations, AIAA, ASTM, IES, NASA, Los Angeles, November 1973. NASA SP-336.
- ⁴L.D. Jaffe, J.B. Rittenhouse, "Behavior of Materials in Space Environments," JPL-CIT Technical Report 32-150, November 1961.
- ⁵R.J. Archer, Ellipsometry, Gaertner Scientific Co., 1968.
- ⁶V.W. Hughes, H.L. Schultz, Methods of Experimental Physics (Academic Press, New York, 1967) 4, A, pp. 157-167.
- ⁷G. Odian, Principles of Polymerization, McGraw-Hill, 1970.
- ⁸D.F. Santeler, "Outgassing Characteristics of various Materials", 5th National Vacuum Symposium, October 1958, (Pergamon Press)
- ⁹T.H. Allen, "The Study of Molecular Kinetics Using Ellipsometry", AIAA/NASA/ASTM/IES 7th Space Simulation Conference, November 1973.
- ¹⁰D.F. Wilcox, "Vapor Pressure – Viscosity Relations in Methpolysiloxanes," JACS 68, 4, 691-696, April 1974

A SYSTEM FOR THE STUDY OF MOLECULAR CONTAMINATION*

C. F. Dillow, T. H. Allen, and R. M. F. Linford, *McDonnell Douglas Corporation, St. Louis, Mo.*; R. G. Richmond, *NASA Johnson Space Center, Houston, Texas*

ABSTRACT

An experimental capability has been developed for studying contamination kinetics and the degradation of optical surfaces by thin contaminant films.

INTRODUCTION

As the duration of space missions has increased and payloads have become more complex, contamination of optical surfaces on spaceborne systems has become a significant problem. Outgassed contaminants from non-metallic materials on a spacecraft generate an artificial atmosphere around the vehicles, and these contaminants can subsequently recondense on exposed or cooled surfaces. The problem is compounded if the condensed contaminants are exposed to energetic radiation (solar ultraviolet, electron and proton radiation), because such exposure can "fix" or polymerize the films and inhibit the natural reevaporation processes, which might otherwise reduce the build-up of contaminant films.

Most space vehicles are subject to prelaunch testing in space simulation chambers, and during testing there is risk of contamination from outgassing of polymeric materials in the chamber and from backstreaming of vacuum pump oils.

Optical surfaces are particularly sensitive to the effects of contaminant deposition, and lenses, mirrors, detectors and windows can all be significantly degraded by thin organic films. The most serious effects are experienced by systems operating at ultraviolet wavelengths, where absorption and scattering of the optical radiation is significant, even with contaminant films just a few hundred angstroms thick.

Cleaning of surfaces contaminated during space simulation testing is often difficult and expensive, and refurbishing surfaces contaminated in space is usually impossible. Therefore, it is important that the dynamics of contaminants and their effects be studied and understood, so that the design and testing of space vehicles can be modified to reduce the risk of degradation.

As part of an ongoing program to study contamination phenomena, an experimental vacuum chamber was designed and fabricated to provide a wide range of experimental capability. This Work Chamber Assembly (WCA) was conceived to establish the proof-of-principle of various techniques for studying the kinetics of contaminants and their effects. It incorporates the capability for depositing both optical and contaminant films on temperature-controlled samples, and for in-situ measurements of the vacuum ultraviolet reflectance. Ellipsometer

*Work conducted under NASA Contract NAS9-13606

optics are mounted on the chamber for film thickness determinations, and other features include access ports for radiation sources and instrumentation.

This paper includes a description of the design and fabrication of the WCA, and of a vacuum ultraviolet reflectometer that was assembled and integrated with the system.

Design Requirements

The Work Chamber Assembly (WCA) was designed to provide the capability to study the optical effects and degradation mechanisms associated with thin contaminant films on optical surfaces. The following experimental capabilities were included in the WCA design:

- Vacuum deposition of thin optical films onto a sample surface, with precise control of the film thickness.
- Measurement of the thin film growth rates using ellipsometry.
- Deposition of thin organic contaminant films on the sample surface in a controlled manner.
- Determination of the effects of contamination on the reflectance of an optical surface using a NASA-furnished vacuum ultraviolet scanning monochromator.
- Evaluation of sample cleaning techniques such as ion bombardment and substrate heating.
- Irradiation of samples with ultraviolet and particulate fluxes to simulate the natural space radiation environment.

Main Vacuum Chamber

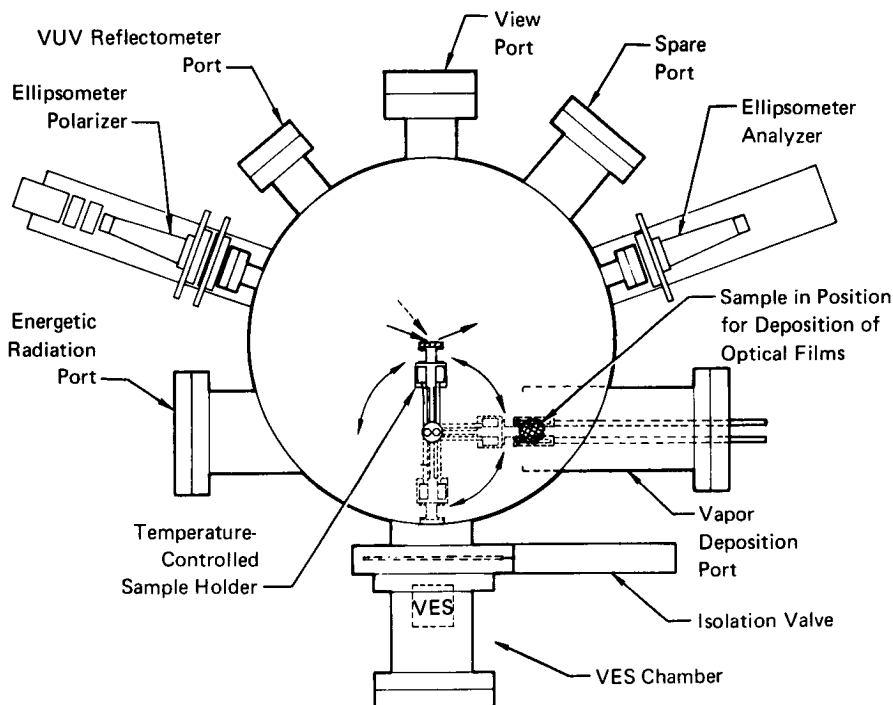
A diagram of the main chamber is shown in Figure 1. It was designed around a 24-inch diameter, 16-inch high stainless steel cylinder with a 7/8-inch thick base. A 24-inch Wheeler flange welded to the top of the cylinder mates to a similar flange on the chamber top plate. For added flexibility, the Wheeler flange on the chamber was designed to accept an elastomer O-ring to seal to an aluminum top plate. This feature provides for quick turnaround time at the expense of a decade or so of ultimate vacuum. A 6-inch diameter low profile viewing window is mounted on the chamber top plate.

Eighteen penetrations are provided around the chamber wall and in the base of the chamber, for various pumping systems, for interfacing with other equipment and for miscellaneous instrumentation. Varian Conflat flanges were selected to provide metal seals so that the system can be baked up to 350°C.

After assembly, the chamber was cleansed by immersion in an organic solvent and then in an alkaline cleaning bath. To passivate the internal surfaces to reduce virtual leaks, the chamber was immersed in a 50% nitric acid bath. A final polished finish was given by hand, using a series of abrasive and buffing compounds. The chamber was then sealed with blank flanges and leak checked with a helium mass spectrometer.

A combination of pumps are used to evacuate the WCA from atmospheric pressure to ultra-high vacuum. To reach the ultimate vacuum, a gas aspirator pump is run to remove 80% of the gas load and reduce the system pressure to 150 torr. This allows the sorption pumps to be used in an efficient manner to further reduce the pressure to the 10^{-3} torr range.

An Ultek 400 ℓ -sec $^{-1}$ ion pump is isolated from the main chamber by a pneumatically operated gate valve so that it can be run continuously without troublesome starting procedures. To equalize the pump and chamber pressures prior to opening the valve, a low-conductance bypass line is provided.



GP 75-5371-4

FIGURE 1 WCA PLAN VIEW

Vapor Effusion Source

Of prime importance in the study of thin film molecular contamination of optical surfaces is the deposition of uniform thin organic films in a controlled and reproducible manner. This is accomplished using a vapor effusion source, consisting of a heated oven to produce molecular vapors and an effusion nozzle to direct the molecular vapors toward the substrate. A source was designed which made possible deposition of spatially uniform contaminant films with a minimum of main vacuum chamber contamination.

The vapor effusion source is housed in an isolated annex to the main chamber. This VES Annex is illustrated in Figure 2. The annex is attached to the main WCA vacuum chamber by a 2-inch gate valve. An 8-inch flange, modified to include an elastomer seal, provides a removable end plate for the annex. All the internal fittings for the annex are supported on this end plate so that they can be removed easily for cleaning and recharging the VES.

The inclusion of the gate valve, connecting flanges and liquid nitrogen baffles results in an 8-1/2 inch separation between the VES nozzle and the sample to be contaminated. To limit the field angle of the molecular beam, a single orifice nozzle and aperture system are used. A combination of three apertures limits the cross section of the molecular beam to the diameter of the sample. The first aperture is a beam skimmer, the primary function of which is to deflect the outer portions of the beam to facilitate their immediate removal from the annex via the pumping port. Two cryogenically cooled baffles further limit the beam area and reduce the stray contamination entering the main WCA chamber. A picture of the completed VES is included as Figure 3.

Although the VES has been primarily designed for use with high molecular weight organic materials, it can, with slight redesign, be used with other molecular gases such as ammonia, nitrogen and oxygen.

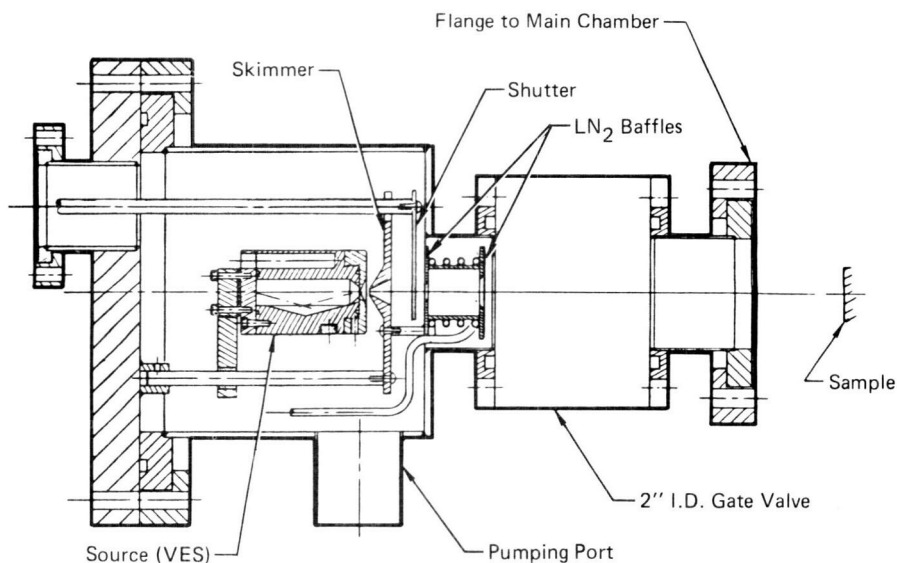


FIGURE 2 VES ANNEX

GP75-5371-2

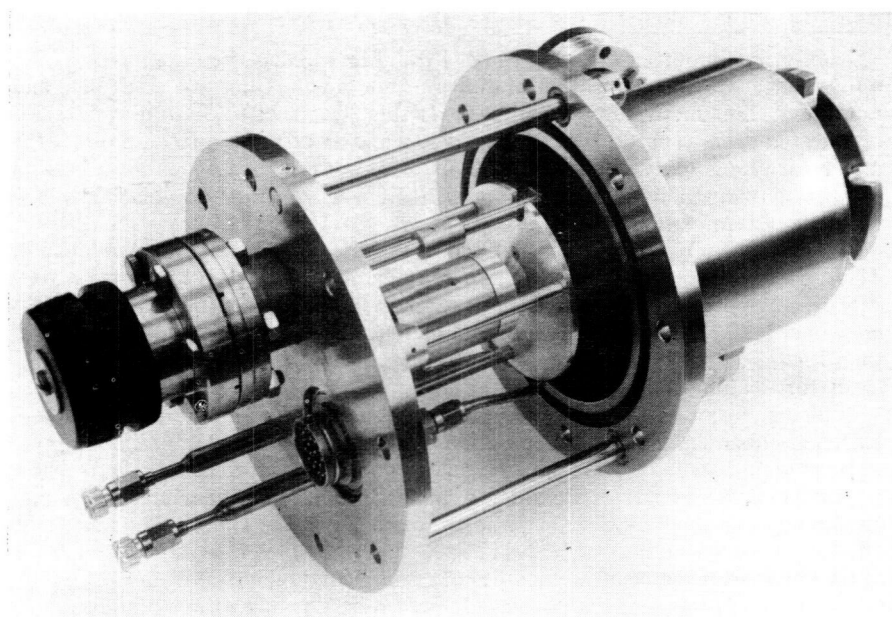


FIGURE 3 PHOTOGRAPH OF ASSEMBLED VES

Sample Holder

A multi-purpose sample holder was designed for the WCA. It features an electrically isolated, temperature controlled, instrumented sample mount which can be rotated through 270° . As shown in Figure 1, four sample positions are available as follows:

- Opposite the Vapor Effusion Source (VES) chamber for deposition of contaminant films.
- Over the vapor deposition boats for fabrication of optical coatings.
- Opposite the view port for simultaneous ellipsometric and vacuum ultra-violet reflectance measurements.
- Opposite the energetic radiation port for exposure to electrons, protons or solar radiation.

When the sample is in position for vapor deposition of optical films, it is tilted into the horizontal plane using a lever arm on a bellows pass thru.

The sample rotation assembly is supported on two ball bearings and is driven by a worm gear through a bellows rotary feedthrough. The 100:1 reduction of the worm allows precision, repeatable positioning of the sample assembly. A mechanical counter mounted on the feedthrough registers each $1/10$ of a revolution of the worm, equivalent to a movement of 20 arc minutes of the sample holder. Liquid nitrogen is supplied to the sample reservoir via two 12-inch long, $1/4$ -inch diameter stainless steel flexible bellows.

Details of the sample holder are shown in Figure 4. A 1-inch diameter, $1/4$ -inch thick sample is mounted on a hinged section, in thermal contact with the temperature control system. The sample temperature is controlled between -150° and $+100^\circ\text{C}$ by balancing the power input to a small nichrome heater, against the cooling effect of liquid nitrogen circulating through the small reservoir. Sample temperatures can be controlled within $\pm 0.5^\circ\text{C}$, using this method.

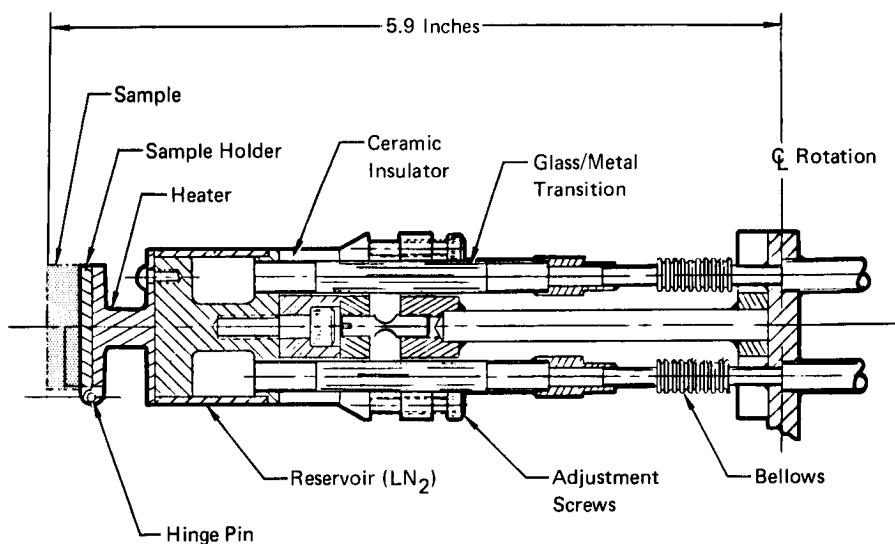


**FIGURE 4 DETAIL OF SAMPLE HOLDER ASSEMBLY
SHOWING THERMAL CONTROL SYSTEM**

A ceramic insulator and two glass-to-metal transitions in the liquid nitrogen circulation system provide electrical isolation of the sample for glow discharge cleaning and other experiments. Minature stainless steel bellows are included in the cooling lines to prevent damage to these transitions due to differential thermal expansions or contractions.

A picture of the completed sample holder is shown in Figure 5.

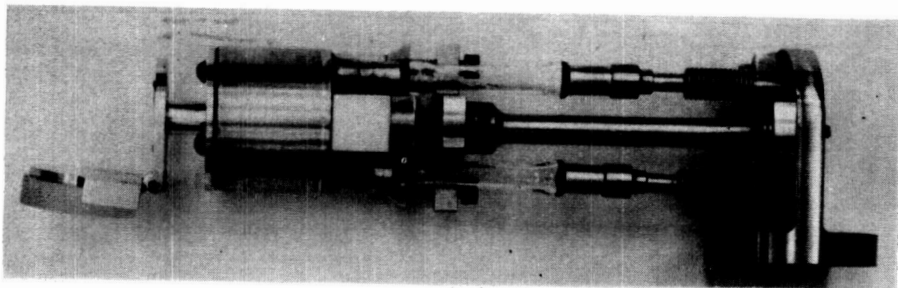


FIGURE 5 ASSEMBLED SAMPLE HOLDER

Ellipsometer

In recent years ellipsometry has been used extensively in our labortory¹ for measuring the optical constants, n and k , of vapor deposited optical coatings and the thickness of contaminant films on their surfaces. Measurements of films as thin as 1 \AA are routinely performed. Ellipsometer optics were mounted on the WCA to provide these capabilities. Standard Gaertner Scientific Corp. ellipsometer optics, with a helium-neon laser source modulated at 800 Hz and synchronously detected, are mounted on rigid platforms attached to the WCA and view the sample at 70° angle of incidence. An ellipsometer data reduction program was written for an HP-9830 programmable calculator to permit rapid data reduction.

Vacuum Ultraviolet Reflectometer

Thin contaminant films can severely degrade the reflectance properties of optical surfaces, especially at vacuum ultraviolet and ultraviolet wavelengths. The capability for studying such phenomena was to be included in the WCA design, and a reflectance study was undertaken as a basis for selecting the design parameters.

In the experiment, the effect of a DC-705 film on the specular reflectance of an overcoated aluminum mirror was investigated in the wavelength range of 120 nm to 600 nm. The effect of a 400 \AA film of DC-705 on this mirror is shown in Figure 6. The contaminant film is seen to severely degrade the optical performance of the mirror throughout the spectral region.

Visual inspection of the sample suggested that the degradation in reflectance of the contaminated samples was caused by scattering rather than by absorption of radiation. To confirm this phenomenon, the hemispherical reflectance of a contaminated sample was measured on a Beckman DK-2A spectrophotometer equipped with an integrating sphere. Results of these measurements are illustrated in Figure 7 and it is apparent that the hemispherical reflectance was barely influenced by a 400 \AA film of DC-705, yet the specular reflectance was halved, indicating that scattering was the predominant mechanism degrading mirror performance.

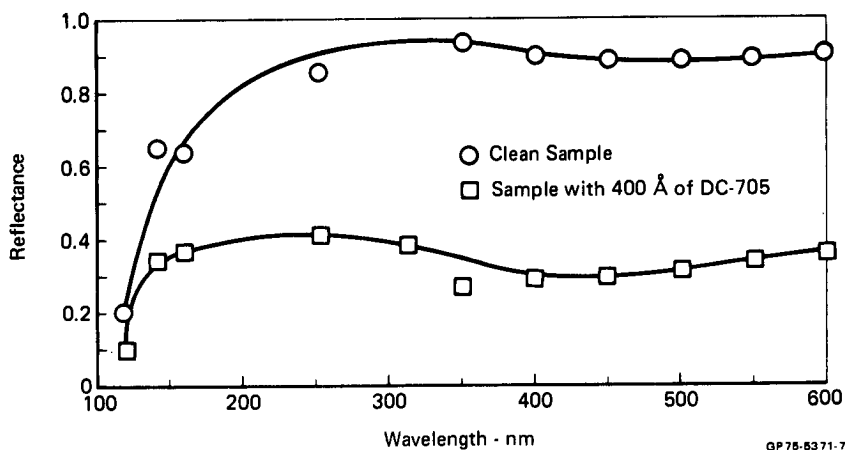


FIGURE 6 EFFECT OF A DC-705 FILM ON THE REFLECTANCE OF A 1/2 - WAVE MgF_2 OVERCOATED ALUMINUM MIRROR

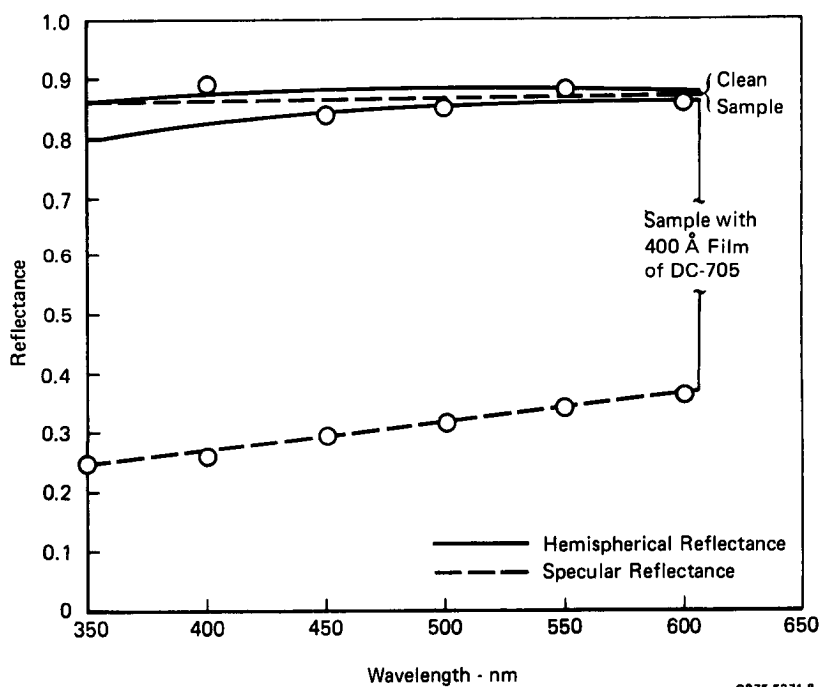


FIGURE 7 EFFECT OF A DC-705 FILM ON THE SPECULAR AND HEMISPHERICAL REFLECTANCE OF 1/2 - WAVE MgF_2 /AL MIRROR

The angular distribution of scattered 490 nm radiation was investigated using a rotating photomultiplier detector with an acceptance angle of approximately 3° . The result of such a measurement is shown in Figure 8 and the distribution of the scattered radiation is indicative of scattering by large particles, possibly several microns in diameter. Results of recent experiments on related McDonnell Douglas programs have confirmed this scattering effect.

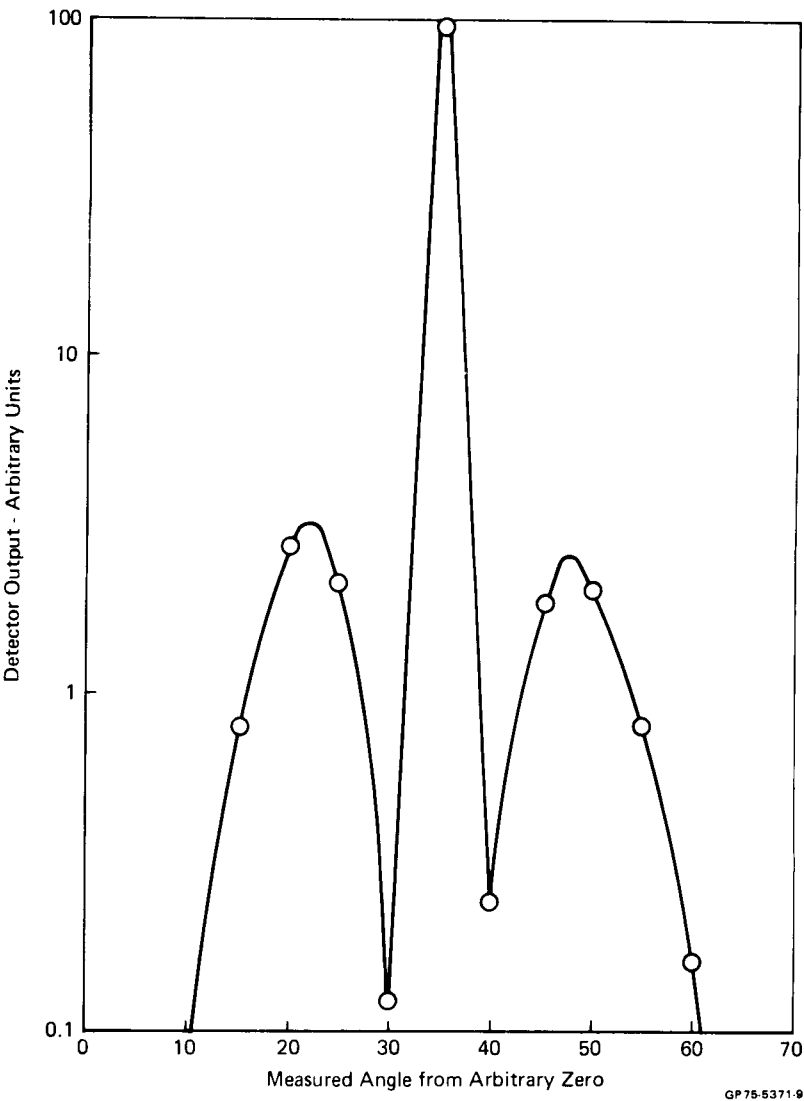
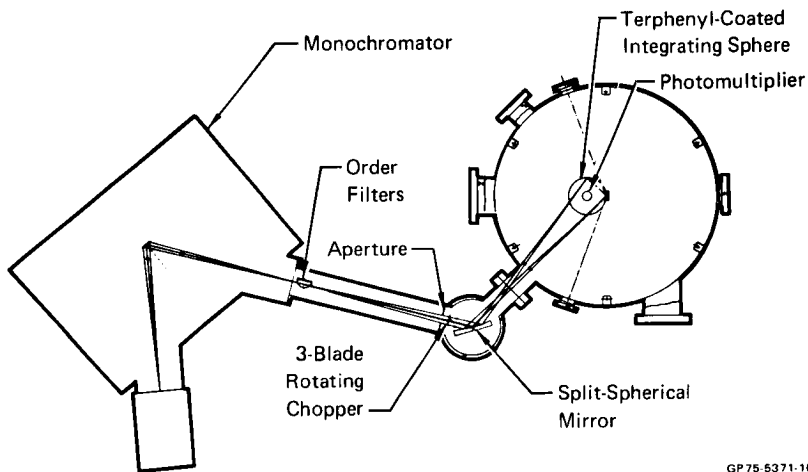


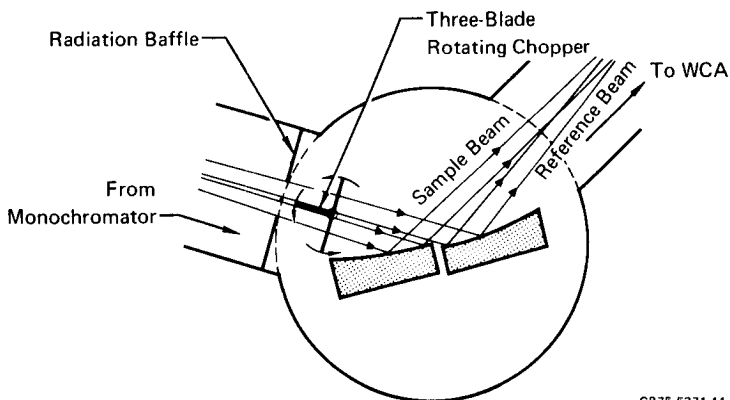
FIGURE 8 ANGULAR DISTRIBUTION OF 490 NM SCATTERED RATION FROM 1/2 - WAVE MgF_2/Al MIRROR CONTAMINATED WITH 400 Å OF DC-705

Both the results of the optical measurements and the experience gained during the study influenced the design of the WCA and of the VUV reflectometer. The optical design of the reflectometer is shown in Figure 9 and the key elements of the design are illustrated in Figure 10. Radiation from the monochromator passes through an order filter, a radiation baffle and a three-blade rotary chopper before illuminating a 1/2-meter focal length platinum-coated, split spherical mirror. This split mirror focusses the sample beam onto the sample and the reference beam onto the wall of the integrating sphere, wherein the two beams are alternately detected by a photomultiplier.



GP 75-5371-10

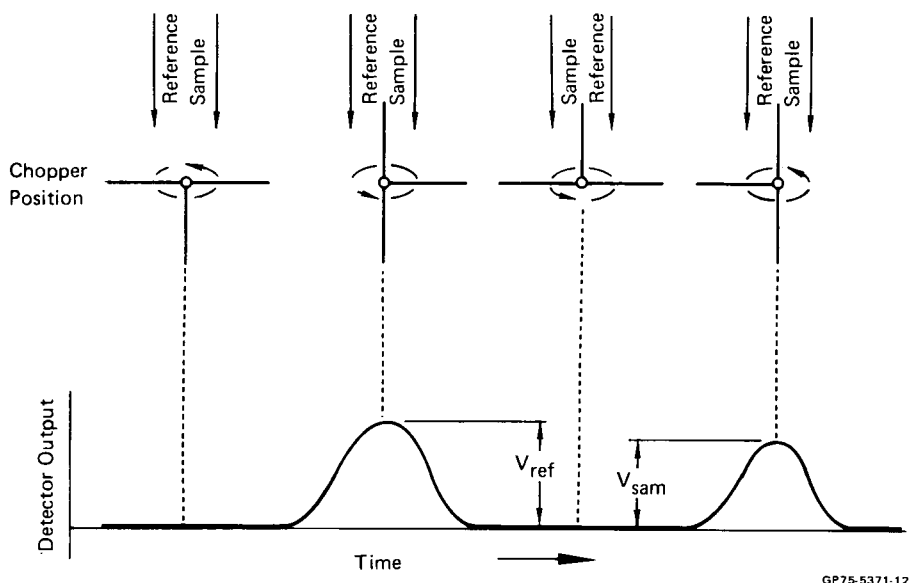
FIGURE 9 LAYOUT AND OPTICAL DIAGRAM OF VUV REFLECTOMETER



GP 75-5371-11

FIGURE 10 KEY ELEMENTS OF THE VUV REFLECTOMETER OPTICAL SYSTEM

A key element is the three-blade rotating chopper that is driven by a 200 rpm synchronous motor through a bellows-sealed rotary pass thru in the base of the mirror chamber. As illustrated in Figure 11, this chopper successively blocks both beams, opens the reference channel, blocks both, then exposes the sample channel.



GP75-5371-12

FIGURE 11 OUTPUT OF VUV REFLECTOMETER DETECTOR FOR EACH POSITION OF ROTATING CHOPPER

Another feature of the design is the fluorescent integrating sphere. A 4-inch diameter stainless steel sphere was first painted with an opaque coating of barium sulphate paint, chosen for its vacuum quality and its excellent diffuse reflectance throughout the visible spectrum. A coating of fluorescent para-terphenyl ($\sim 3 \text{ mg cm}^{-2}$) was vacuum deposited onto the painted surface. An EMI 9635A photomultiplier is mounted in the bottom of the sphere.

The optical system results in a detector output like that shown in Figure 11. The detector current output is fed directly into a McPherson Model 782 Logarithmic Radiometer where it is synchronized with the electronic logic circuitry. Reference pulses at 6.6 Hz are generated by an optical switch coupled to the drive shaft of the three-blade chopper. The switch consists of a slotted circular plate attached to the drive shaft passing through a Monsanto MCA-81 Optical Switch. The radiation baffle, order filters, split spherical mirror and 3-blade chopper are located in a small chamber which is mounted onto the WCA and provides the necessary vacuum interface between the VUV monochromator and the main chamber.

In order to verify the performance of the VUV reflectometer, the reflectance of an aluminum mirror was measured as shown in Figure 12. The selected spectral range was from 200 nm to 300 nm so that scans from other available instruments could be used for comparison. The data taken with the VUV reflectometer is seen to agree quite well with that obtained from other systems.

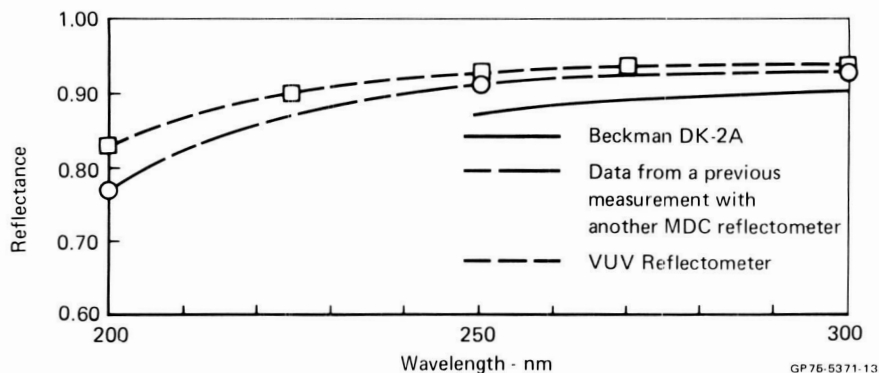


FIGURE 12 REFLECTANCE OF AN ALUMINUM MIRROR AS MEASURED WITH THE VUV REFLECTOMETER

Conclusions

A sophisticated and versatile capability has been developed which will provide for a wide range of experiments on contamination, oxidation and gas kinetics. The complete system is shown in Figure 13.

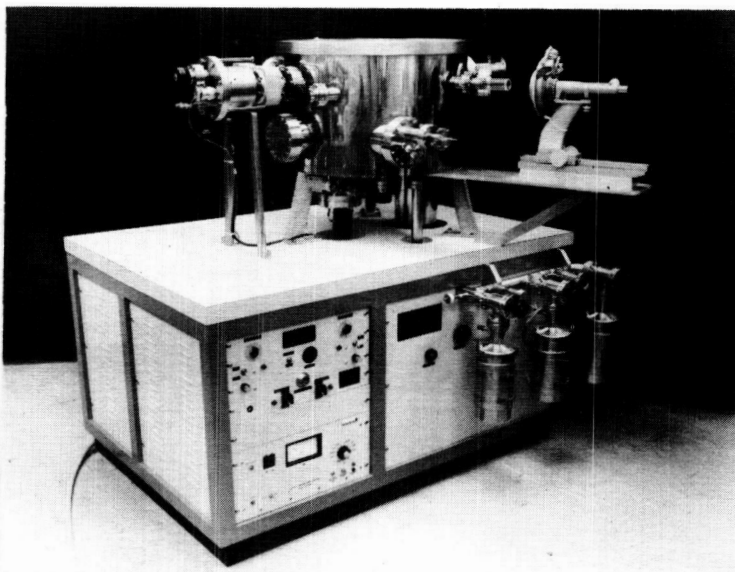


FIGURE 13 COMPLETED WCA

REFERENCES

- 1) T. H. Allen, "The Study of Molecular Kinetics Using Ellipsometry", AIAA/NASA/ASTM/IES 7th Space Simulation Conference, Nov 1973.

OPTICAL MEASUREMENTS ON CONTAMINATED SURFACES*

T. E. Bonham, R. J. Schmitt, and R. M. F. Linford, *McDonnell Douglas Corporation, St. Louis, Mo.*

ABSTRACT

A bidirectional reflectometer system has been developed for in situ measurements of the changes in spectral reflectance of surfaces contaminated with films of organic materials. The system permits experiments with films of controlled thickness in an environment that simulates the thermal, radiation, and vacuum conditions of space. The mechanical and optical construction of the reflectometer are discussed in detail, and actual data curves are used to illustrate its operation and performance.

INTRODUCTION

Because the surfaces of a spacecraft are often at cryogenic temperatures, they readily condense films of outgassed products from such sources as sealants, coatings, and adhesives used in the spacecraft construction. The presence of this molecular contamination poses a significant threat to systems which depend on optical properties for their performance. In particular, the thermal balance of a spacecraft may be seriously affected if thermal control surfaces become contaminated and thereby suffer a degradation of reflectivity. Moreover, additional changes in optical properties may be induced by the interaction of natural space radiation with the contaminant film.

In order to study these effects in a controlled manner, a system has been developed to permit in situ measurements of changes in optical properties of contaminated surfaces in a simulated space environment. The system incorporates several radiation sources and a bidirectional reflectometer integrated with a vacuum ellipsometer chamber. The design and operation of the reflectometer are discussed in detail in this paper; the vacuum ellipsometer has been described elsewhere.¹

System Requirements

For optical measurements on contaminated surfaces, before and after exposure to radiation, a variety of capabilities are required as follows:

Physical:

- i) vacuum controlled to 10^{-6} torr;
- ii) controlled deposition of contaminant films;
- iii) accurate determination of film thickness;
- iv) sample temperature control $\pm 1^\circ\text{C}$ from $+50^\circ\text{C}$ to -140°C ;
- v) low buildup of stray contamination throughout experiments of up to 100 hours duration.

*Work conducted in conjunction with Air Force Contract F33615-73-C-5091

Radiation:

- i) electron irradiation
- ii) proton irradiation
- iii) solar ultraviolet simulation

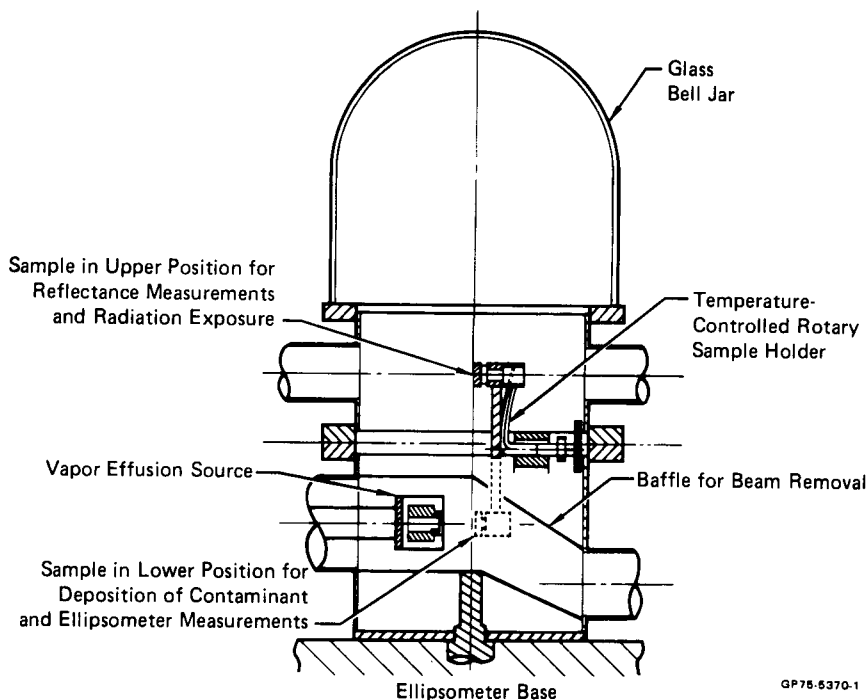
Reflectometer:

- i) wavelength range – 0.25 to 2.3 μm ;
- ii) sensitivity to changes in spectral reflectance of $\pm 1\%$;
- iii) repeatability and stability throughout experiments of up to 100 hours duration;
- iv) semi-automatic operation to facilitate data acquisition and reduction.

Many of these requirements were satisfied by a vacuum ellipsometer already in use¹, and the reflectometer was integrated by modifying this basic system.

Deposition of organic films is accomplished with a vapor effusion source mounted in a vacuum chamber equipped with a turbomolecular pump. The films are deposited on samples mounted on a holder provided with both liquid nitrogen cooling and a balancing heater for precision temperature control. Film thickness measurements are accomplished with an ellipsometer² operating at 632.8 nm with a HeNe laser source.

The original system is illustrated in the lower half of Figure 1. This figure also shows the modifications made to incorporate the reflectometer. The primary modification was a vacuum collar fabricated to mount on the top flange of the ellipsometer vacuum chamber with the enclosure completed by a pyrex bell jar. This arrangement has several advantages including economy and the capability for removing the collar when the system is to be used for other experiments.



GP75-5370-1

FIGURE 1 ELLIPSOETER VACUUM CHAMBER MODIFIED FOR REFLECTOMETER

C-6
Included in the collar are access ports for the radiation sources and windows for the reflectometer. For measurements on a contaminated surface, the sample holder is rotated from the lower chamber to the upper collar on an externally-controlled arm. Liquid-nitrogen cooled baffles around the sample restrict stray contamination.

Bidirectional Reflectometer

The reflectometer was designed to be sensitive to small changes in reflectance over periods of several days, at the expense of being capable of absolute reflectance measurements. To achieve this performance requires a combination of three functions. First, a dual-beam optical system is employed in which the sample reflectance is always compared to that of a reference reflector, the reference being used to balance the electro-optical system for each measurement. This reference reflector is replaced for each experiment and is selected to optically match the fresh sample. The reflectometer operates over the wavelength region 0.2 to 2.3 μm , covering 96% of the solar spectrum.

Second, the signal from the photodetectors must be amplified and conditioned for extraction of the spectral reflectance data. This is achieved by means of a dual-channel, dual-frequency, synchronous ratiometric amplifier system in conjunction with an instrument computer.

Third, data reduction is accomplished by means of a Hewlett-Packard 9810 programmable desk calculator.

Each of these functions is described in detail in the sections that follow.

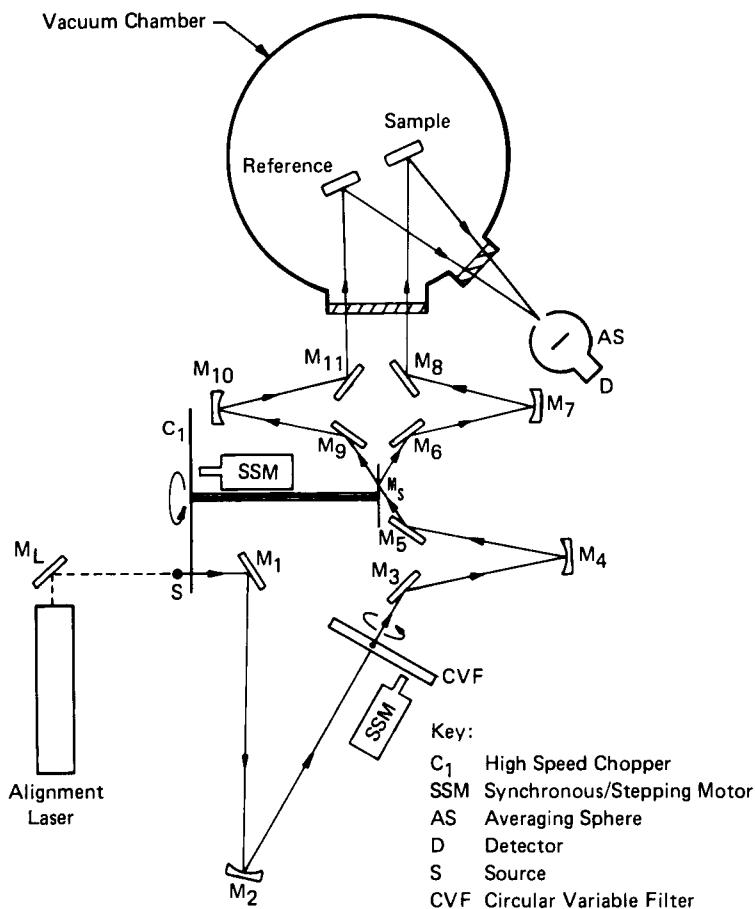
Optics Design and Physical Arrangement

Figure 2 shows the physical layout of the optical components. Key elements in the design are the switch mirror M_6 and the high-speed (220 Hz) chopper blade C_1 , which rotate on a common shaft. M_5 is a semi-circular mirror which switches the light between mirrors M_6 and M_9 ; thus the beam is time-shared equally between the sample and reference channels. An optical switch on the common shaft provides a low frequency reference signal and an optical switch also driven by C_1 provides a high frequency reference signal.

Optical radiation from the source S is modulated by the chopper C_1 and is focused by mirror M_2 onto the circular variable filter, CVF. The image is then transferred by M_3 , M_4 and M_5 onto the switch mirror M_6 . Mirrors M_7 and M_{10} focus the image on the sample and reference reflector, respectively inside the vacuum chamber, and the reflected beams are focused onto the inner wall of the detector averaging sphere.

The laser shown in Figure 2 is used for alignment of the optical paths. A tungsten-halogen lamp powered by an NJE Corporation Model CR-36-50 power supply was used as the light source for the spectral measurements in the 0.2 to 2.3 μm range.

Two separate detectors and two spectral filter systems were used to cover the complete wavelength range. For the wavelength region from 0.2 to 0.65 μm , an EMI Model 9601B photomultiplier tube was used; for the region from 0.65 to 2.5 μm , a Beckman lead sulfide detector was substituted. Because of the differing detector geometries, sensitivities and areas, and the position-sensitive responses of the detectors, an averaging sphere was coated internally with Kodak barium sulfate paint and the detectors were mounted so as to be interchangeable. The loss of overall signal level resulting from the use of the sphere is more than offset by the available gain of the detector preamplifiers.



GP75-5370-2

FIGURE 2 BI-DIRECTIONAL REFLECTOMETER OPTICAL SYSTEM

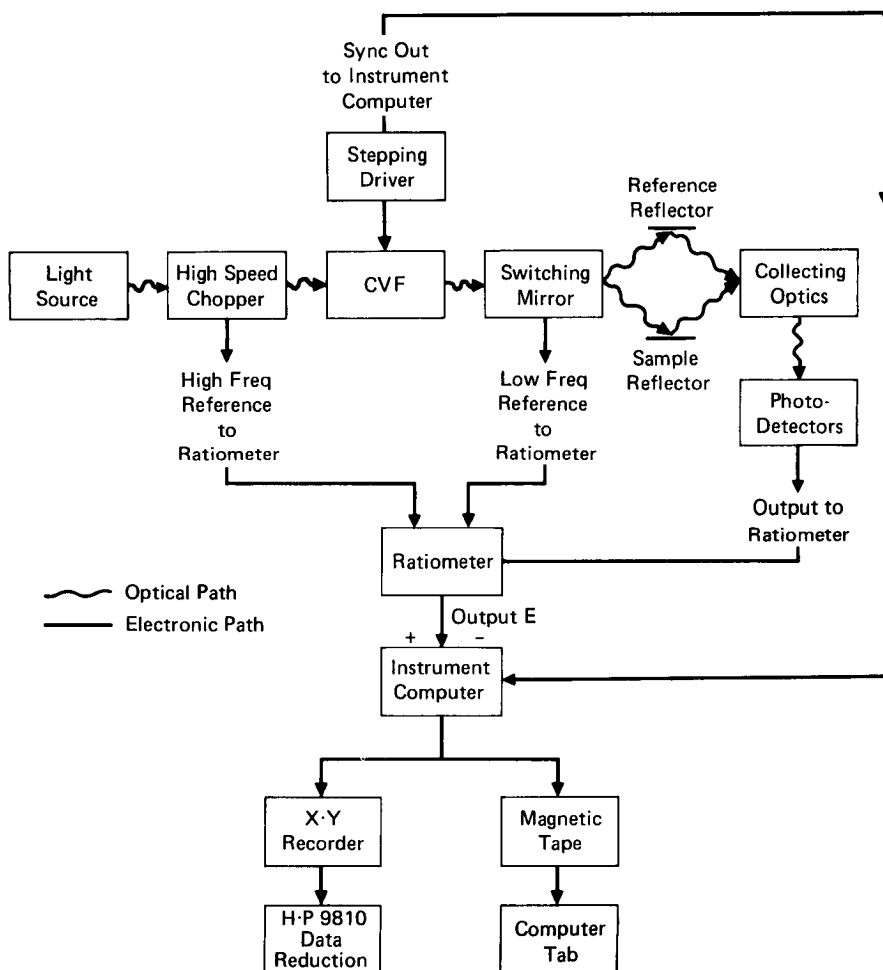
An OCLI* circular variable filter (CVF) is used as the main spectral element over the 0.45 to 2.3 μm range. This item consists of a wedge interference filter in the form of three pie-shaped segments of 90°, 90° and 180°, mounted on a shaft driven by a synchronous/stepping motor. Special circuitry was developed to drive the CVF and provide address advance pulses to the instrument computer recording the data; an optical switch on the drive shaft ensures that the advance sequence is initiated at the correct point, thus preserving the wavelength calibration of the system. At the onset of the program, the computer address is calibrated for wavelength using a series of narrow band interference filters. With this system a wavelength resolution of approximately 2% was obtained.

For wavelengths in the 0.23 to 0.37 μm range, a set of eight discrete narrow band interference filters on a sliding mount replaces the CVF and the data is recorded manually. There is a short gap in the data wavelengths between 0.37 and 0.45 μm .

*Optical Coating Laboratories Inc., Santa Rosa, California

Electronics Design

A block diagram of the reflectometer electronic system is shown in Figure 3. The output of the photodetector consists of a series of pulses whose amplitude is proportional to reflectivity. In the optical system, the switching mirror alternately directs the 220 Hz modulated light source to the sample reflector or allows the unreflected beam to strike the reference reflector. This occurs at a rate of 11 Hz. Thus, the photodetector output consists of 10 pulses containing reference channel information followed by 10 pulses containing sample channel information. Figure 4 is a diagrammatic illustration of this output. The pulse train must be demodulated to obtain useful analog signals and demultiplexed to separate the sample and reference channels for subsequent processing. This is the function of the ratiometer electronics, a block diagram of which is shown in Figure 5. This system was developed around a modified Ithaco Model RA353 lock-in amplifier.



GP75-5370-3

FIGURE 3 BLOCK DIAGRAM OF BI-DIRECTIONAL REFLECTOMETER

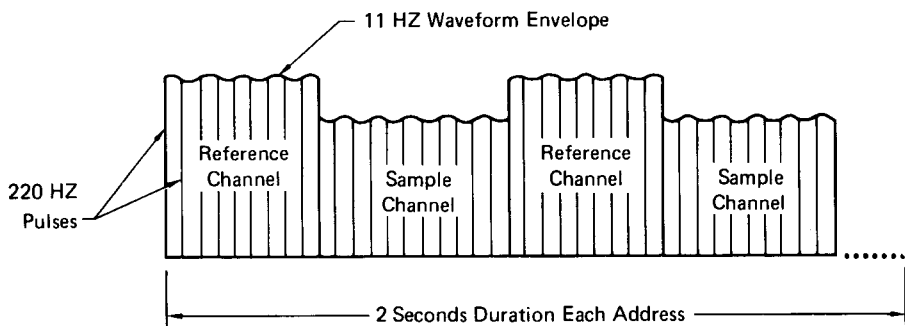
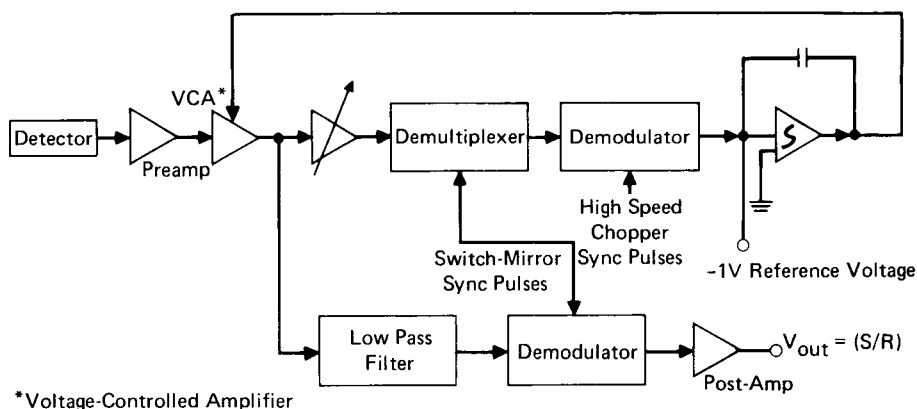


FIGURE 4 PHOTODETECTOR SIGNAL OUTPUT

GP75-5370-4



*Voltage-Controlled Amplifier

GP75-5370-5

FIGURE 5 BI-DIRECTIONAL REFLECTOMETER
SIGNAL PROCESSING SYSTEM

Because both the intensity of the light source and the photodetector sensitivity are a function of wavelength, these effects must be compensated before further signal processing can take place. In the bidirectional reflectometer, this is accomplished by using a voltage controlled amplifier (VCA) to control the amplification of the input to the ratiometer circuit. The gain of the VCA is automatically and continuously adjusted by a control voltage derived from the high frequency component of the signal. This is achieved as follows. A switching circuit driven by the low frequency reference gates the demultiplexer circuit shown in the block diagram, to pass only the reference channel reflectance signal to the demodulator. An amplifier tuned to the high frequency reference demodulates the pulses, and a signal proportional to the pulse amplitude becomes the input of a summing amplifier. This proportional signal is added to a -1 volt reference, and the output of the summing amplifier equals this sum (including sign) times the gain of the amplifier (typically $10^5 - 10^6$). This voltage output in turn, is fed back to the VCA, and the loop automatically and continuously seeks an equilibrium such that the input to the summing amplifier totals zero. This continual gain adjustment compensates the signal parameters that might not be constant since the circuit parameters in this loop do remain constant.

The gain of the VCA, g , is inversely proportional to the signal in the reference channel. That is, if the reference channel reflectance signal decreases relative to the -1 volt reference at the summing amplifier, then the summing amplifier output (and hence g) will increase. Then

$$g = C/R' \quad (1)$$

where C is the proportionality factor and R' is the signal in the reference reflector channel. Parallel to the gain loop is a low pass filter and demodulator. The low pass filter passes only the 11 Hz envelope of the photodetector signal, so the filter output voltage (E) is proportional to the difference in reflectivity between the reference and sample. Thus,

$$E = gm (R' - S'), \quad (2)$$

where S' is the signal in the sample reflector channel, m is the proportionality factor, and g represents the fact that the photodetector output was amplified by the VCA. (Note that g may be less than one.) Then

$$E = mC/R' (R' - S') \quad (3)$$

or

$$E = k (1 - S'/R') \quad (4)$$

which is the demodulator output, and where k is a lumped gain constant.

Data Analysis

The signal in either optical channel is the product of the reflectivity of each surface encountered by the light beam. Thus, by referring to Figure 2 it can be seen that:

$$S' = M_1 M_2 F M_3 M_5 M_6 M_7 M_8 S \text{ (RAS)} M_4 \quad (5)$$

and

$$R' = M_1 M_2 F M_3 M_5 M_9 M_{10} M_{11} (R) \text{ (RAS)} M_4 \quad (6)$$

where M_j is the reflectivity of the j -th mirror, F is the filter transmission, RAS is the reflectivity of the averaging sphere, S is the sample reflectance and R is the reflectance of the reference mirror. The ratio of equations 5 and 6 gives:

$$\frac{S'}{R'} = \frac{M_6 M_7 M_8 M_S}{M_9 M_{10} M_{11} R} \quad (7)$$

thus, from equations 4 and 7:

$$E = k \left[1 - \frac{(M_6) (M_7) (M_8) (M_S) S}{(M_9) (M_{10}) (M_{11}) R} \right] \quad (8)$$

The unknowns are eliminated in this equation by performing three separate measurements. First, the ratiometer output is measured with the sample beam blocked, thus simulating a sample reflectivity of zero. In this case:

$$E = E_0 = k \quad (9)$$

Second, the reference reflector is inserted into both beam paths, thus equating R and S . In this case:

$$E_R = E_0 \left[1 - \frac{M_6 M_7 M_8 M_S}{M_9 M_{10} M_{11}} \right] \quad (10)$$

or

$$\frac{M_6 M_7 M_8 M_S}{M_9 M_{10} M_{11}} = 1 - \frac{E_R}{E_0} \quad (11)$$

Third, the measurement of E_S with the reference and sample reflectors in their respective beams and making appropriate substitutions of equations 9 and 11 in equation 8.

$$\frac{S}{R} = \frac{E_0 - E_S}{E_0 - E_R} \quad (12)$$

These three determinations are made at each wavelength of interest.

In the procedure of taking data for the experiments, the output from the ratiometer is routed to a Fabri-Tek Instruments, Inc., Model 1072 instrument computer. The stepping motor which rotates the CVF is driven by a logic circuit which also advances the memory address of the instrument computer. The dwell-time per filter element and address is 2 seconds, thus permitting the instrument computer to signal average the ratiometer output before storing a data point. This procedure permits smoothing the noise in the electrical signal and improves the signal-to-noise ratio.

For each measurement E_O , E_R , and E_S , an entire wavelength scan is made for whatever filter element is used, and the data stored. The memory of the computer is then transferred to an x-y plotter and to magnetic tape compatible with large digital computers.

The data reduction is performed using a Hewlett-Packard 9810A programmable desk calculator with a Model 9864A digitizer and 9862A calculator plotter. The data x-y recording is digitized point-by-point, and the 9810A performs the necessary arithmetic on the values and drives the plotter to graph the result. Each plotted graph shows $\Delta R/R$ versus wavelength, with wavelength versus address having been previously calibrated by using known filters in place of the CVF.

The value S/R is the ratio of the reflectance of the mirror in the sample position (S) to that of a reference mirror (R). During the test runs the spectral values of S/R were determined three times; initially with the clean sample mirror, then with the contaminant deposited on the sample mirror, and finally after irradiation of the contaminated sample mirror. In all cases, the data was referenced to a common reference mirror. To determine the ratio of the reflectance of the contaminated sample mirror (or contaminated and irradiated) to its initial clean state, it was only necessary to divide the appropriate S/R 's for each wavelength and deduct from unity:

$$\frac{S_{\text{contam}}/R_{\text{ref}}}{S_{\text{clean}}/R_{\text{ref}}} = \frac{S_{\text{contam}}}{S_{\text{clean}}}$$

and

$$1 - \frac{S_{\text{contam}}}{S_{\text{clean}}} = \frac{S_{\text{clean}} - S_{\text{contam}}}{S_{\text{clean}}} = \frac{S}{S_{\text{clean}}}$$

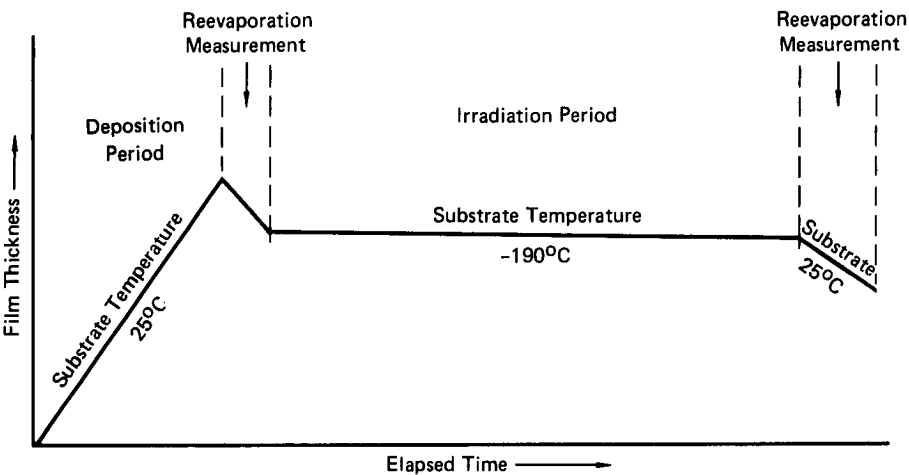
System Operation and Performance

To illustrate the operation and performance of the bidirectional reflectometer, the results of measurements taken with S-13G thermal control paint and RTV-602 silicone adhesive films deposited on a gold sample are presented. The sample was an optically polished, gold-coated aluminum substrate. The metal substrate was chosen for its thermal conductivity, and the vacuum deposited gold is highly stable in the radiation environment used and is chemically inert to the effects of the contaminant film. Gold-coated silica mirrors were used as reference reflectors since it was not necessary to provide cooling for them.

Typical of experimental procedures used in making measurements is the time profile shown in Figure 6. Optical measurements were made before and after contaminant deposition, at frequent intervals during the irradiation sequence, and at the completion of the irradiation sequence.

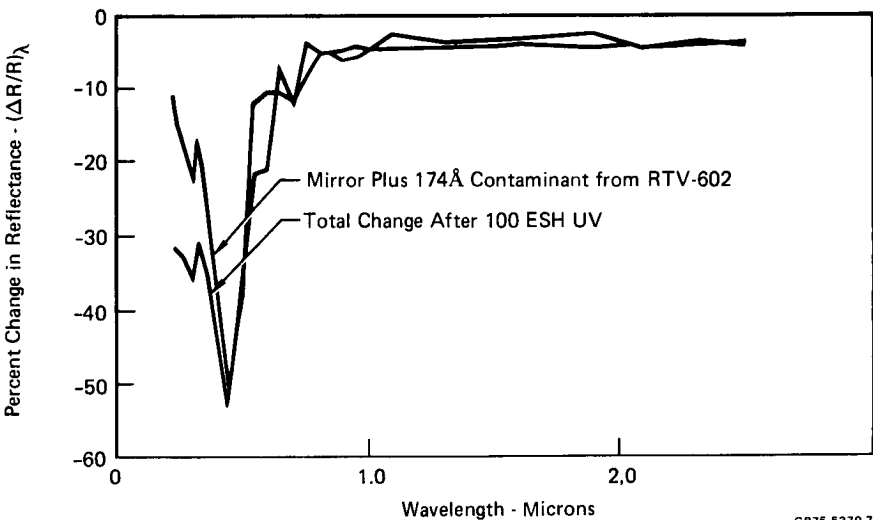
Figures 7 and 8 show the data taken on films of S-13G paint and RTV-602 silicone on gold substrates. The greatest change in optical properties occurs at $0.45 \mu\text{m}$, with little apparent effect above $0.75 \mu\text{m}$ for films of these thicknesses. Also note that S-13G films show more susceptibility to degradation by UV than do films of RTV-602 under the same conditions. An apparent periodic structure in the spectral

reflectance is also visible in this data. This is probably due to interference phenomena in the thin dielectric contaminant film on the surface of the gold.



GP75-5370-6

FIGURE 6 EXPERIMENTAL SEQUENCE



GP75-5370-7

FIGURE 7 CHANGE IN SPECTRAL REFLECTANCE OF A GOLD MIRROR DUE TO CONTAMINATION BY RTV-602 AND SUBSEQUENT UV EXPOSURE

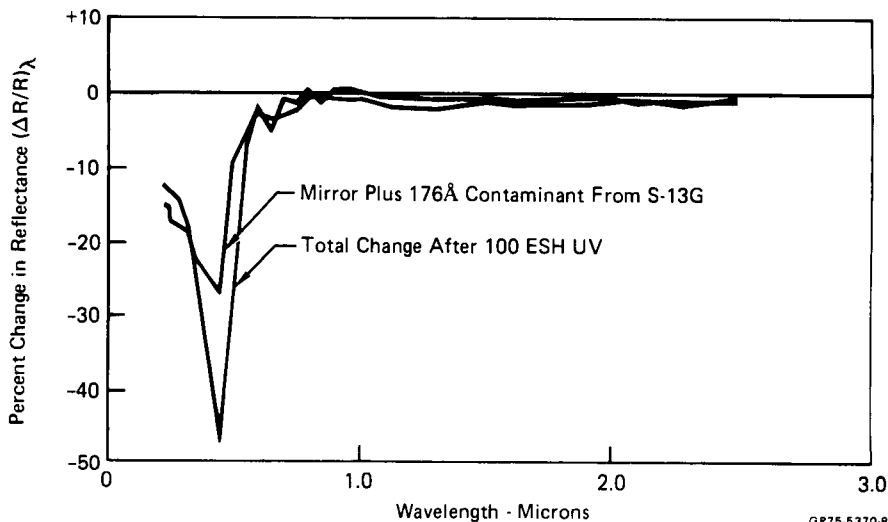


FIGURE 8 CHANGE IN SPECTRAL REFLECTANCE OF GOLD MIRROR DUE TO CONTAMINATION BY S-13G AND SUBSEQUENT UV EXPOSURE

Conclusions:

The sensitivity and stability of the reflectometer design utilized for these optical measurements are demonstrated well by the data shown in Figures 7 and 8. Changes in reflectance of 1% are readily observed in the graphs. The large reflectance minimum is evident, even though the absolute reflectance of the gold substrate is falling off rapidly in this wavelength region. Indeed the absolute reflectance of gold decreases from 50.4% to 22.5% over the wavelength region from 0.5 to 0.2 μm .

The interference effects produced by an irradiated contaminant film have been observed before³. The stability of the instrument allows the small interference effect in this case to be detected after an experiment that required nearly 48 hours to complete. Note also that the observed effects reported here are not influenced by film thickness differences since precision measurement and accurate deposition have produced films of nearly identical thickness.

REFERENCES

1. T. H. Allen, T. A. Hughes, and B. C. Price, "A Study of Molecular Contamination," 8th Space Simulation Conf., Nov. 1975
2. Gaertner Scientific Corporation, Model L119 Ellipsometer.
3. R. B. Gillette and B. A. Kenyon, Applied Optics, 10, 545 (1971).

SPACECRAFT CONTAMINATION UNDER SIMULATED ORBITAL ENVIRONMENT

R. W. Phillips, L. U. Tolentino and S. Feuerstein

ABSTRACT

Volatile condensible material (VCM) measurements on a number of spacecraft materials have shown that contamination rates onto surfaces at subambient temperatures cannot be predicted from standard outgassing tests, especially where long term exposure is involved. Contamination rates may depend markedly on the temperature differential between source and collector, the collection temperature and the exposure time. In addition, contamination rates may also be influenced by solar irradiation and/or spacecraft charging. The results of this study were obtained on a new VCM facility which overcomes many deficiencies experienced in earlier designs. Advantages of the present system include an oil-free high vacuum chamber (10^{-8} – 10^{-9} Torr), source temperatures from ambient to 120°C , collection temperatures from -140°C to $+50^{\circ}\text{C}$, in-situ VCM mass measurements using an internally temperature compensated quartz crystal microbalance, in-situ vacuum UV irradiation of either the sample or the VCM, and infrared identification of the VCM using frustrated multiple internal reflection techniques. The system also features automated data acquisition and data processing. An analysis of the present results is discussed and comparison made to previously published data. For each material, an equation is developed which can be used to predict the absolute outgassing rate at any given time.

A LASER PARTICULATE SPECTROMETER FOR A SPACE SIMULATION FACILITY*

R. J. Schmitt, B. A. Boyd, and R. M. F. Linford, *McDonnell Douglas Corporation, St. Louis, Mo.;*
R. G. Richmond, *NASA Johnson Space Center, Houston, Texas*

ABSTRACT

A Laser Particulate Spectrometer (LPS) System was developed to measure the size and speed distributions of particulate contaminants. Detection of the particulates is achieved by means of light scattering and extinction effects using a single laser beam to cover a size range of 0.8 to 275 microns diameter and a speed range of 0.2 to 20 meters/second. The LPS System was designed to operate in the high-vacuum environment of a space simulation chamber with cold shroud temperatures ranging from 77 to 300°K.

INTRODUCTION

The increasing complexity of space-vehicle designs and experiment payloads, coupled with increasing mission durations, has resulted in stringent cleanliness requirements for space environmental testing and simulation facilities. It is known that particulates are often found in the large high-vacuum chambers used in space simulation, and that these fluxes constitute a potential source of contamination to test articles placed inside such chambers. Studies have been conducted at NASA-JSC to determine the history of suspended particulates in a space simulation chamber during the entire cycle of thermal-vacuum testing, i.e., during pretest at one atmosphere, during early pumpdown, while at high vacuum, during chamber repressurization, and in the post-test period at one atmosphere.

These studies pointed out the necessity for an instrument which can measure and display in a convenient way the distributions of particle sizes and speeds. With such an instrument, details of particulate distributions can be defined.

This paper contains a description of the design, fabrication and performance of a Laser Particulate Spectrometer (LPS) System to operate in a space simulation chamber. This instrument measures the size and speed distributions of particulates (dusts, aerosols, ice particles, etc.) passing through the laser beam by detecting both the light scattered by the smaller particles and the laser beam intensity fluctuations due to larger particles. Details are presented of the system design which resulted in the development of an instrument sensitive to particles from 0.8 to 275 μm diameter moving through the laser beams at speeds between 0.2 and 20m/sec. A significant feature of the LPS design is the capability for operation at pressures ranging from room ambient to ultra-high vacuum and for operation within vacuum chamber cold shrouds which range in temperature from 77 to 300°K.

*Work conducted under NASA Contract NAS9-14171

The LPS System is designed to be compatible with the Hewlett-Packard 5401B/9810 Multi-Channel Analyzer/Programmable Calculator System. The LPS Electronics System was designed and assembled to provide the required compatibility. Special computer programs were developed to permit automatic acquisition and recording of LPS data via digital cassette tape and X-Y Plotter.

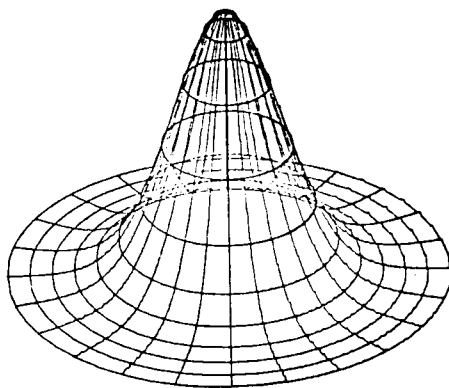
Optical Design of the LPS

In any optical system designed to detect and analyze particle size and velocity distributions, lasers are strong candidates for selection as the primary source of illumination⁽¹⁻⁵⁾. The laser provides a very intense, well collimated light beam which allows the use of low-voltage silicon detectors for scattering measurements, and forms a well defined particle probe volume. Acting as a light amplifier, the laser is a very sensitive system for extinction measurements. Several of the laser parameters can be varied to optimize the sensitivity of the system to detect particle fluxes. These include:

- The laser mode pattern
- The laser beam waist diameter
- The intensity of the light incident on the particle

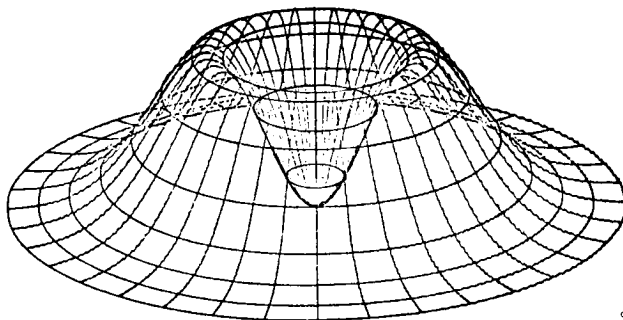
The effect of varying each of these parameters was evaluated and the results are summarized below.

Mode Pattern - A laser is capable of operating in one or more of many transverse mode patterns. The most common laser mode is the TEM_{00} or lowest order Gaussian mode. In this mode the laser beam has a peak in intensity on the beam axis which then drops off radially as is shown in Figure 1. This mode is unsuitable for detecting and sizing particles by scattering or extinction because a large particle passing through the edge of the beam can produce the same size pulse as a smaller particle passing through the center of the beam. For this reason, a higher order mode, the TEM_{01} * degenerate mode, was studied. This mode, shown in Figure 2, has a minimum at the center of the pattern, reaches a maximum and then falls off radially from the axis. A particle traversing the area within the ring of maximum intensity will produce a double pulse the amplitude of which will be dependent on the particle size. Suitable electronic logic can then be devised to detect double pulses and discriminate against single pulses produced when a particle passes through the edge of the beam.



GP75 0369.1

FIGURE 1 TEM_{00} MODE INTENSITY DISTRIBUTION



GP75 5369 2

FIGURE 2 TEM₀₁* MODE INTENSITY DISTRIBUTION

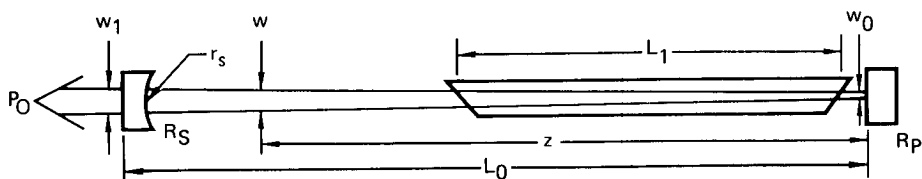
Beam Waist Diameter - A hemispherical laser resonator cavity consisting of a plane mirror and a spherical mirror forms a laser beam within the cavity which has a very small intense spot or waist at the plane mirror, and a large, less intense spot at the spherical mirror. For a given laser plasma tube, various beam diameters can be obtained by varying the length of the resonant cavity and the focal length of the spherical mirror. This in turn has an effect upon the peak intensity of the mode pattern and the size range of particles which can be measured by either scattering or extinction.

Figure 3 shows the major physical parameters of a laser cavity. Given a laser tube of length L_1 , with a certain He-Ne gas mixture which determines the gain (g_0), the only variable parameters are: L_0 , the overall cavity length, r_s , radius of the spherical mirror; and R_p and R_s , the reflectances of the plane and spherical mirrors respectively. The beam radius at any point within the cavity is given by:(6)

$$w(z) = w_0 \sqrt{1 + \left(\frac{\lambda z}{\pi w_0^2} \right)^2} \quad (1)$$

where λ is wavelength of light, w_0 is the beam waist radius and z is the axial distance from the plane mirror. The waist radius is determined by:

$$w_0 = \frac{L_0 \lambda}{\pi} \left(\frac{g}{1 - g} \right)^{1/4} \quad (2)$$



L_0 = Cavity Length

L_1 = Plasma Tube Length

R_S = Reflectance of Spherical Mirror

R_P = Reflectance of Plane Mirror

P_0 = Output Power

r_s = Radius of Curvature of Spherical Mirror

z = Axial Distance Along Cavity

w_0 = Waist Diameter

w_1 = Output Beam Diameter

w = Beam Diameter at Particle Probe Volume

g_0 = Unsaturated Gain of Active Medium

GP75 5369 3

FIGURE 3 LASER CAVITY PARAMETERS

Figure 4 shows the effect on beam radius of varying the radius of the spherical mirror in a cavity of fixed length. Results of an extinction analysis (presented below) imply that to size particles up to $300\mu\text{m}$ diameter, a beam radius of about $500\mu\text{m}$ is needed. From Figure 4 it is seen that two mirror radii, 60cm and 500cm, give a beam radius of approximately $500\mu\text{m}$. A 60cm radius mirror was used in the LPS as the resultant tapered beam more closely matched the bore of the laser plasma tube.

The reflectances of readily available commercial laser mirrors are 99.9% for the plane mirror and 97.5% for the spherical mirror; when combined with a plasma tube length of 30cm and an unsaturated gain coefficient of 10%, such mirrors result in a cavity power of 34mW, with a nominal 3mW output beam power level.

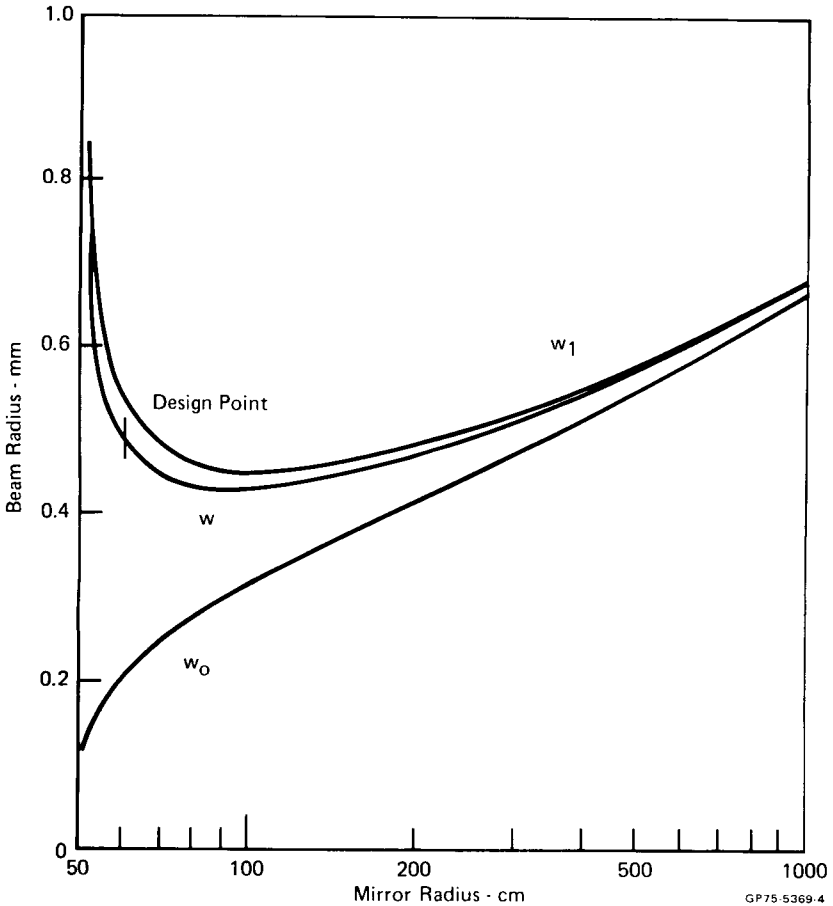


FIGURE 4 LASER CAVITY BEAM DIMENSIONS FOR A 50cm CAVITY

With the laser constrained to oscillate in the TEM_{01} mode, the intensity of the intracavity beam on the peak isophote is $2.63 \times 10^4 \text{ Wm}^{-2}$, in the absence of a particle. The average irradiance incident on a particle in the beam is a function of both the particle diameter relative to the beam radius and of the degree

of extinction of the laser cavity power due to the perturbing presence of the particle in the cavity. The effect of the geometrical parameters alone is illustrated in the upper curve in Figure 5; above $100\mu\text{m}$ the average irradiance drops off as the particle diameter approaches the dimensions of the laser beam. The lower curve in Figure 5 demonstrates the extinction effect, caused by the reduction of laser cavity gain due to the particles. The laser beam is completely extinguished by particles larger than $275\mu\text{m}$ diameter. Above $10\mu\text{m}$ the average irradiance on the particle is such a steep function of particle diameter that an intracavity scattering system would be inappropriate for particles larger than $10\mu\text{m}$. It is apparent from Figure 5 that the intracavity laser extinction mode should be used for the 10 to $275\mu\text{m}$ diameter range.

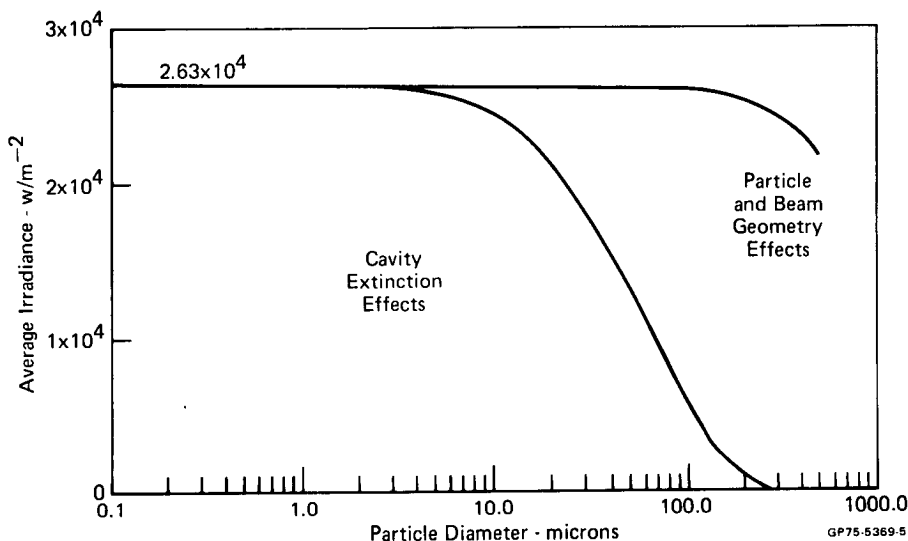


FIGURE 5 AVERAGE IRRADIANCE OF LASER LIGHT INCIDENT ON PARTICLE

A Mie Scattering computer program was run assuming an incident intensity on the particle of $2.63 \times 10^4 \text{ Wm}^{-2}$ to compute the scattered power incident on a lens system with annular collection angle between 8.5° and 31° .⁽⁷⁾ Figure 6 shows the collected power plotted as a function of particle size for four refractive indices. Except for the region between 1.0 and $2.0\mu\text{m}$ diameter, the effects of refractive index are rather small. If particles of known refractive index, e.g. water droplets ($n = 1.33$), are being analyzed the ambiguities in the 1.0 to $10\mu\text{m}$ range can be tolerated. However, if a particle flux of unknown refractive index is incident upon the scattering spectrometer, some uncertainty will result in the size determination.

For particle sizes less than $0.6\mu\text{m}$ diameter, the scattered power drops below the 10^{-9}W noise equivalent power level for a silicon detector with a 2MHz bandwidth.

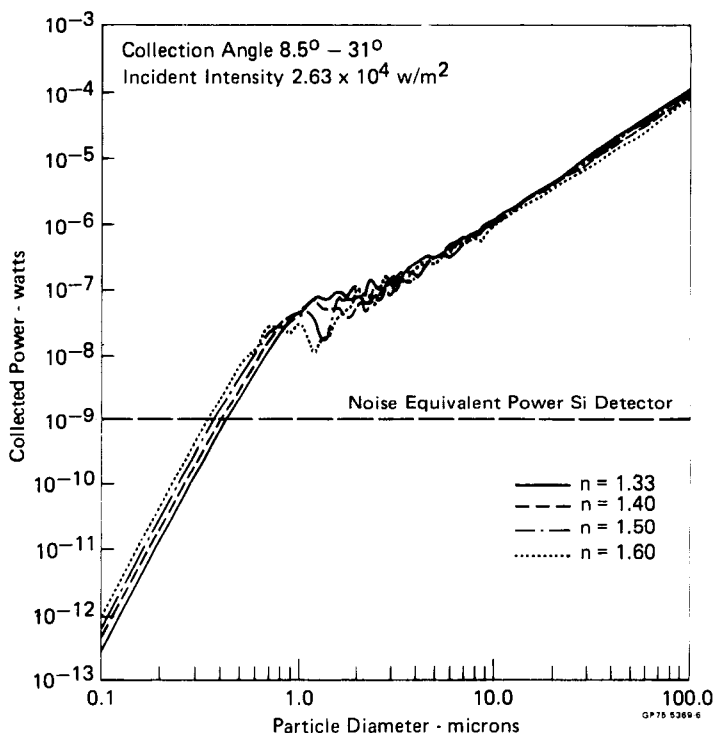


FIGURE 6 COLLECTED SCATTERED POWER (MIE THEORY)

The theoretical design analysis resulted in a design for the LPS Sensor Head with the following values for the key parameters:

- lasing medium - helium-neon gas
- overall cavity length - 50cm
- spherical mirror radius - 60cm
- mirror reflectances - 99.9% and 97.5%
- lasing mode - TEM_{01}^*
- output power (extra-cavity) - 3mW Nominal
- cavity power (intra-cavity) - 34mW
- peak incident intensity (intra-cavity) - $2.63 \times 10^4 \text{ Wm}^{-2}$
- beam parameters:
 - $w_0 = 212\mu\text{m}$
 - $w_1 = 520\mu\text{m}$
 - $w = 277\mu\text{m}$ at $z = 45\text{cm}$
- scattered power (intra-cavity)
 - $0.1\mu\text{m} \sim 10^{-12}$ watts
 - $1.0\mu\text{m} \sim 2 \times 10^{-8}$ watts
 - $10.0\mu\text{m} \sim 10^{-6}$ watts
- extinction power (normal output power = 3.0mW)
 - $10.0\mu\text{m} \sim 2.8\text{mW}$
 - $100\mu\text{m} \sim 0.6 \text{ W}$
 - $275\mu\text{m} \sim 0.00$ (laser oscillation ceases)

LPS System Design

A block diagram of the LPS system is shown in Figure 7. The Sensor Head which contains the laser, scattering optics and detectors, is designed to operate in a vacuum chamber. Pulses from the scattering and extinction detectors are processed by the LPS Electronics System to produce standard width pulses for the H-P Model 5401B Multichannel Analyzer (MCA). The H-P Model 9810 Programmable Calculator controls the functions of the MCA and formats the data into particle size and speed spectra suitable for display via x-y plotter.

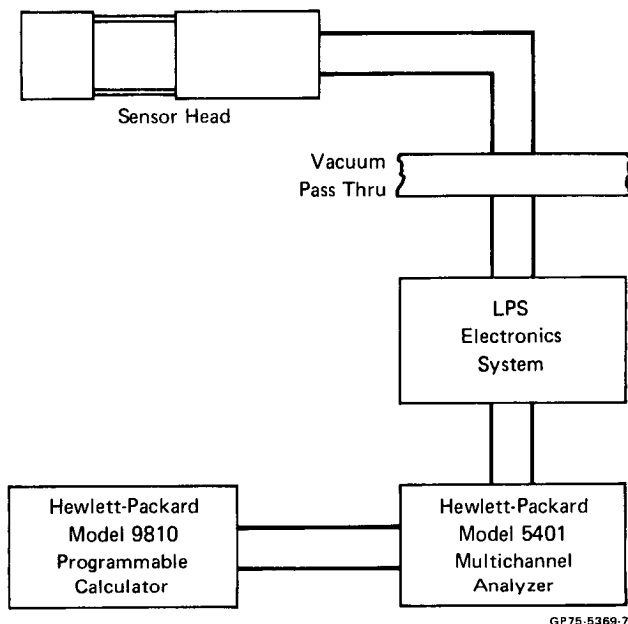


FIGURE 7 LPS SYSTEM BLOCK DIAGRAM

Figure 8 shows a schematic representation of the Sensor Head optical system. The highly collimated laser output beam passes through holes in lenses L1 and L2 and is directed onto the extinction detector by the small plane mirrors M1 and M2. The probe volume, the length of which is defined by two conical aluminum baffles is coincident with the focus of lens L1. Particles which traverse the probe volume scatter light into lens L1, which functions as a collimator. Lens L2 re-focuses the scattered light onto the scattering detector. The laser plasma tube and the plane laser resonator mirror are located within a hermetic enclosure to prevent corona discharge problems during vacuum chamber pump-down. The laser beam passes through a compensating double Brewster window attached to the hermetic enclosure. The second Brewster window removes the translational offset produced by the first window to maintain the laser beam congruent with the mechanical axis of the Sensor Head.

Sensor Head Mechanical Design - The majority of the mechanical design effort was concentrated on the Sensor Head. A number of mechanical design considerations were determined by the selection of the Hughes Model 3184H He-Ne laser. This laser consists of a glass plasma tube which is mounted in a

1.75-inch OD x 12.5-inch long aluminum tube using a flexible potting compound. This laser was selected after reviewing the range of commercially-available models, because the aluminum tube could be conveniently clamped to a heat sink with small probability of mechanical stress on the glass plasma tube and because the cavity mirrors could be detached from the metal tube for intracavity work.

The dimensions of the laser and the system requirements defined in the thermal analysis established the size of the laser hermetic enclosure and, to a large extent, the overall size of the entire Sensor Head. A basic cylindrical geometry was selected for the Sensor Head for simple design and ease of fabrication.

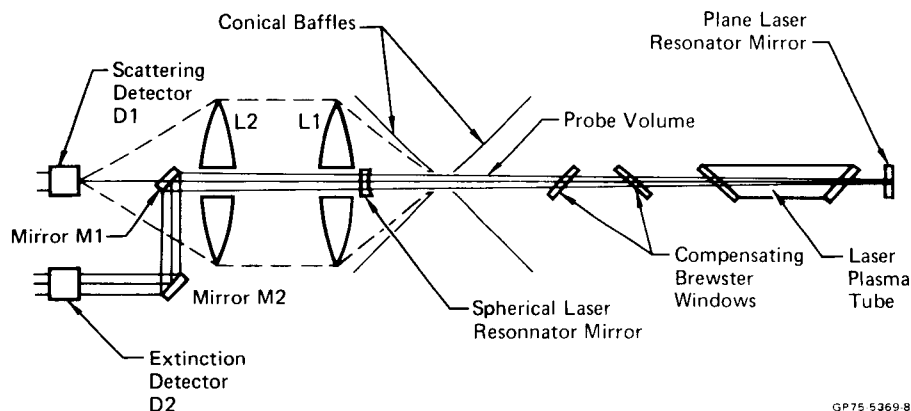
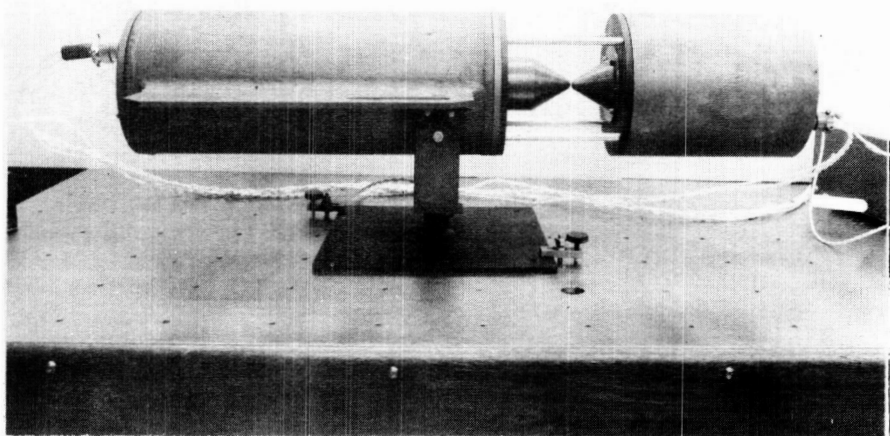


FIGURE 8 SENSOR HEAD DETAILS

A photograph of the LPS Sensor Head is shown in Figure 9. The design of the mounting structure for the laser plasma tube incorporates the dual requirements of providing a heat sink for the plasma tube and a high thermal conductance path to the cylindrical shell. The heat sink contains a semi-cylindrical machined groove into which the laser is clamped. Deep penetration heliarc welds were used to attach the heat sink to the 7-inch OD cylindrical shell. Two rectangular fins, integral to the heat sink, were included to increase the radiating surface area of the Sensor Head hermetic enclosure. The result of this design was to produce a combined heat sink-radiator assembly which permits efficient rejection of waste heat produced by the laser plasma tube and the laser high-voltage power supply.

The ends of the cylindrical shell are closed by aluminum end plates which mate with internal flanges. The rear plate carries a flat window through which the laser beam exits allowing a view of the resonant mode of the laser cavity during alignment of the LPS system. A valve is provided on the rear end plate for pumping and backfilling the hermetic enclosure with dry gas (nitrogen or helium). The front end plate carries the double Brewster window, which is located inside the laser resonant cavity.

The conical aluminum baffles are employed to define the length of the LPS probe volume (~ 1 mm). Proper spacing between the tips of the baffles is maintained by four low thermal expansion Invar rods which also support the scattering optics and detector assembly. The two lenses which comprise the scattering optics are carried on adjustable mounts supported on three alignment rods. Four additional rods carry the circuit card for the two photodiode detectors and preamplifiers and the end plate on which the electrical connectors and heater are mounted. The weight of the Sensor Head is approximately 40 pounds.



GP75-5369-9

FIGURE 9 LPS SENSOR HEAD

LPS Electronics System Design - Figure 10 shows a block diagram of the LPS Electronics System. Three separate functions are provided by this system, viz, supplying power to the laser, control of the Sensor Head temperature, and interfacing between the detectors and the H-P 5401B MCA. Several of the components of the electronics system are packaged in Nuclear Instrumentation Modules (NIM).

Silicon photodiode detectors are employed to measure the scattering and extinction signals. The preamplifiers convert detector current pulses into voltage outputs and drive these pulses through the LPS Cable System. Each detector/preamplifier combination has a line driver which converts the current pulses from the detectors into voltage pulses and provide sufficient current drive capability to power 150 feet twinax cables. One hundred feet of cable are located inside the vacuum chamber while the remaining 50 feet are located outside. The vacuum feedthrough consists of hermetic electrical connectors mounted on a plate attached to a port of the vacuum chamber.

The Channel Select Module contains line receiver amplifiers which provide high rejection of common-mode signals which under some circumstances may accompany the detector output pulses. Additional circuitry monitors the pulses in the two channels, selects pulses from either the scattering or the extinction channel and passes them to the Signal Conditioning Module (SCM).

The Signal Conditioning Module contains the circuitry required to produce pulses proportional in height to the particulate size and transit time across the laser beam. A Double Pulse Discriminator (DPD) circuit accepts double pulses generated by particles which pass through the axis of the laser beam and rejects single pulses produced by particles which make grazing encounters with the laser. A Time-of-Flight (TOF) circuit measures the duration of the double pulses to

yield the particulate transit time through the laser beam, while a Dead-Time-Counter (DTC) circuit provides the means for resetting the LPS Electronics System when a single pulse is encountered. A Reset/Memory Routing/Clock circuit generates reset pulses, 2MHz clock pulses for the TOF circuit, and the memory routing pulses required by the H-P 5401B MCA for operation in the "external memory routing" mode.

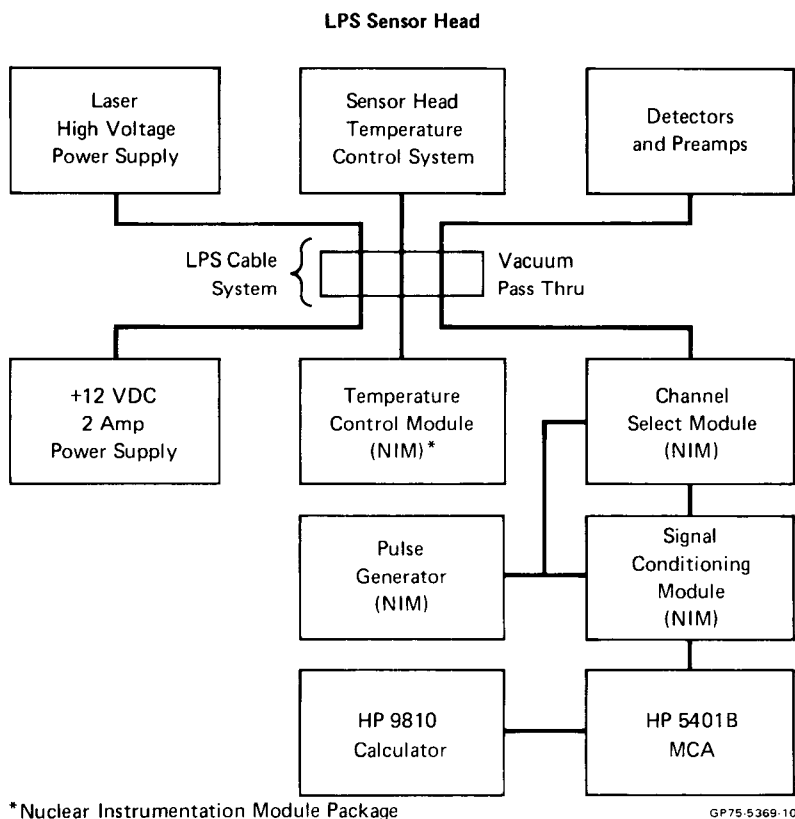


FIGURE 10 LPS ELECTRONICS SYSTEM BLOCK DIAGRAM

The Electronics System of the Laser Particulate Spectrometer is designed to utilize the capabilities of a Hewlett Packard 5401B Multichannel Analyzer - 9810 Programmable Calculator System for pulse height analysis of the spectrometer size and speed data, for displaying size and speed spectra via CRT monitors and x-y plotter, and for storing spectral data on a digital magnetic tape cassette. The LPS supplies size and speed data continuously to the 5401B which operates as a pulse height analyzer (PHA). The functions of the PHA (accumulation of spectra, display, and storage of data) can be controlled either manually via the PHA front panel controls or automatically under program control via the 9810 Programmable Calculator. The PHA/Programmable Calculator System has no direct control of the functions of the LPS which operates continuously once the laser and the LPS Electronics Systems are powered.

The operating temperatures of the laser, detectors preamplifiers and line drivers contained in the Sensor Head are controlled by the Temperature Control System (TCS) which consists of the Temperature Control Module (TCM), thermistor sensors, thermostats and cartridge heaters. In vacuum chamber tests this system successfully maintained the laser temperature in the range of 280 to 320°K.

Various types of pulse outputs for checking and aligning the LPS Electronics System are provided by the Pulse Generator. This unit produces simulated double and single pulses for aligning the scattering and extinction circuits of the Channel Select Module.

LPS System Calibration

Calibration of the LPS System is conceptually straightforward. Particles of known size are introduced into the probe volume and the resulting PHA spectra are recorded. The electronic gains of the scattering and extinction channels are then adjusted to obtain the desired calibration curve relating particle size and/or speed to LPS output voltage levels. However, there are major problems in the calibration: obtaining particles of known size; and generating sufficiently high fluxes of these particles for introduction into the LPS probe volume.

Scattering Channel Size Calibration - The scattering channel calibration was accomplished by introducing polystyrene latex particles of known size into the probe volume. A Royco Particle Generator was used to produce a stream of dry latex particles from a liquid suspension. A specially designed nebulizer produced an aerosol consisting of small water droplets and latex particles. This aerosol is passed through a drying column which evaporated the water particles and left an exiting stream of dry latex particles.

The particle size spectrum in Figure 11 was generated by the calculator-controlled x-y plotter under program control. The large peak at approximately 0.5V appearing in this spectrum is due to numerous small incompletely evaporated water aerosol droplets. This was verified by operating the Royco generator with

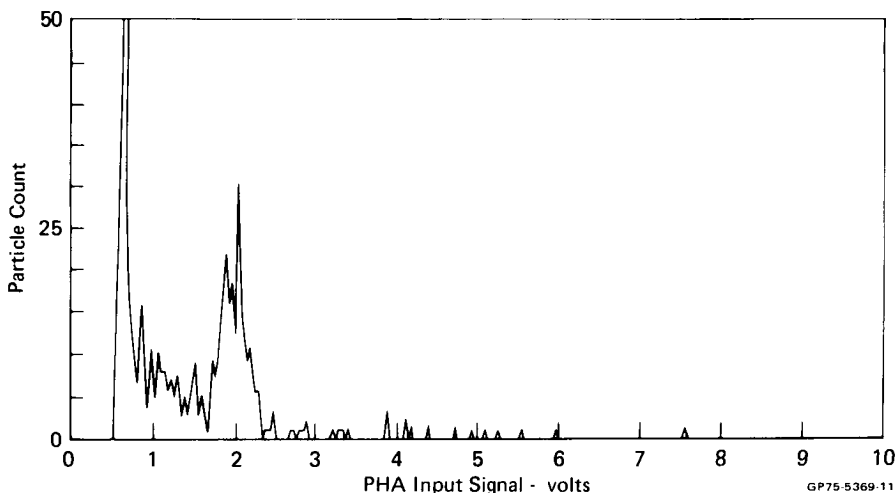


FIGURE 11 SCATTERING CHANNEL SIZE SPECTRUM
2.68 Micron Diameter Latex Particles

distilled water minus the latex particles. The threshold level of the scattering discrimination was set to approximately 0.3V to eliminate background noise due to small dust particles ($<0.5\mu\text{m}$ diameter) in the laboratory environment. The low-voltage side of the large peak is due to the action of the discriminator.

The scattering channel calibration data is summarized in Figure 12. The two curves are derived from Mie scattering theory applied to the inter-cavity laser design used in the LPS System. The curve for refractive index $n = 1.5$ applies to latex particles, while the $n = 1.33$ curve typifies water particles. These curves, which were scaled such that a $10\mu\text{m}$ diameter particle corresponds to a 10V pulse from the LPS, represent theoretical calibration curves for the LPS scattering channel.

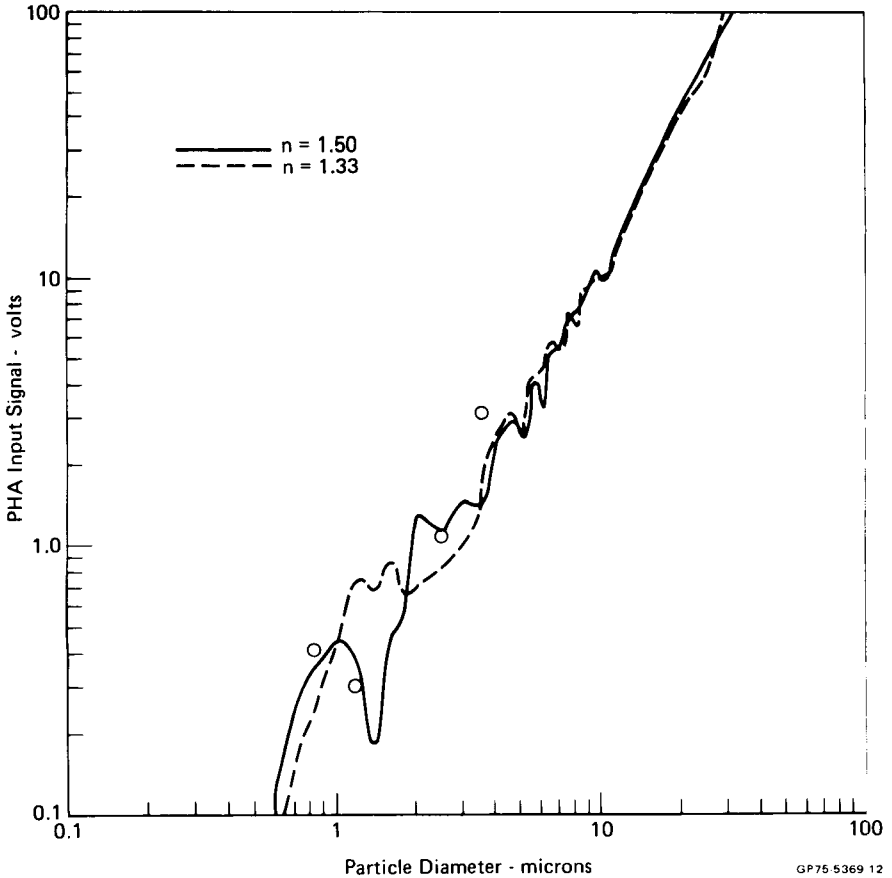
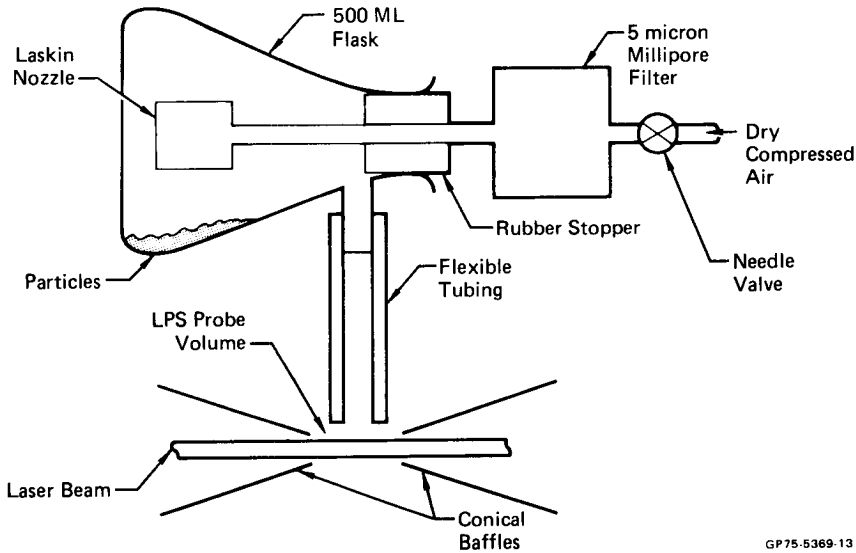


FIGURE 12 SCATTERING CHANNEL CALIBRATION CURVE

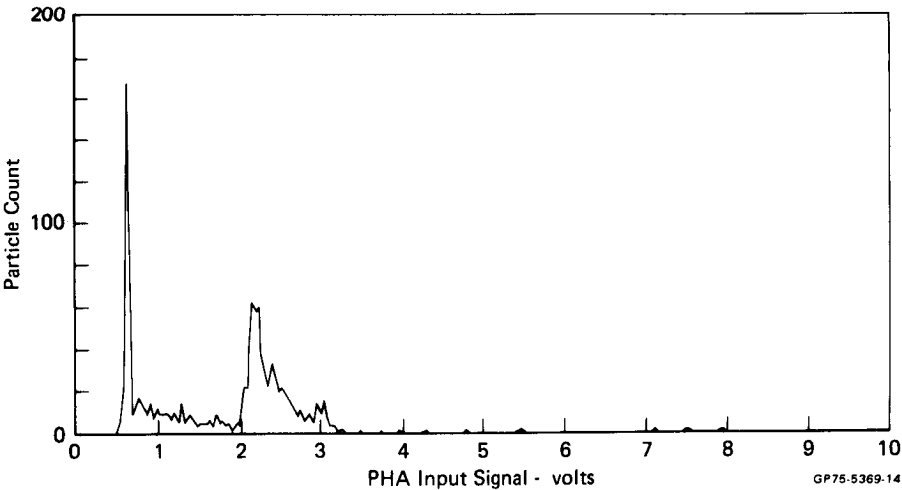
Extinction Channel Size Calibration - The extinction channel calibration was obtained using spherical glass beads obtained from the Cataphote Corp., Jackson, Mississippi, and the dry particle generator shown in Figure 13. A typical extinction spectrum is shown in Figure 14. The large peak in this spectrum centered at approximately 0.5V is due to multiple coincidence effects which reduce the laser beam

intensity sufficiently to cause the extinction channel noise level to rise above the discriminator threshold level. The coincidence problem is caused by random "bursts" of particles, unavoidable in this type of particle generator, which momentarily cause large fluctuations in the intensity of the laser beam.



GP75-5369-13

FIGURE 13 DRY PARTICLE GENERATOR



GP75-5369-14

FIGURE 14 EXTINCTION CHANNEL SIZE SPECTRUM
44-45 Micron Diameter Glass Beads

The extinction channel calibration derived from this data is shown in Figure 15. The boxes were constructed using the width (volts) of the PHA peak at half-height and the size range (microns) in which 90% of the particles are located. The lower limit for this channel lies between 15 and 20 μ diameter while the upper limit extends to approximately 275 μ diameter.

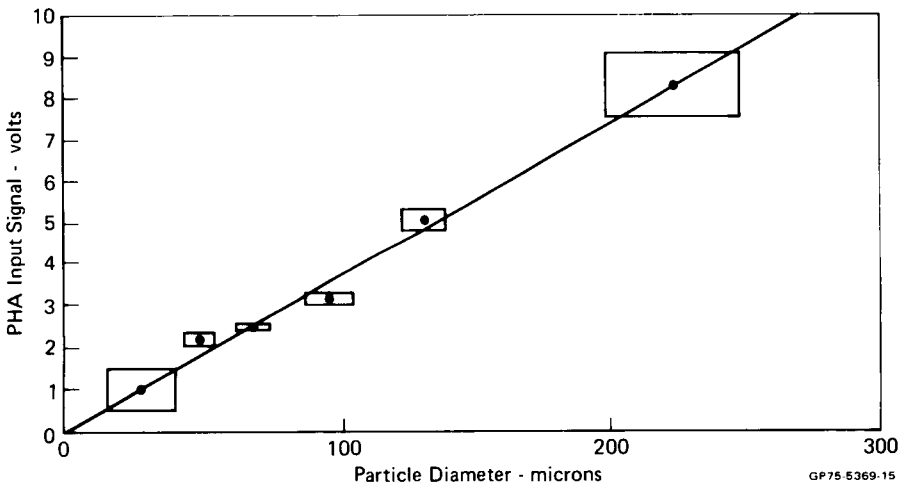


FIGURE 15 EXTINCTION CHANNEL SIZE CALIBRATION

Transit Time Calibration - Calibration of the scattering and extinction transit time spectra can be obtained in absolute terms since these spectra rely on the 1MHz internal clock in the Time-of-Flight (TOF) circuit. The TOF circuit output is +5 volts for zero transit time and decreases in a linear fashion to zero volts for a transit time equal to 8192 μ s (See Figure 16).

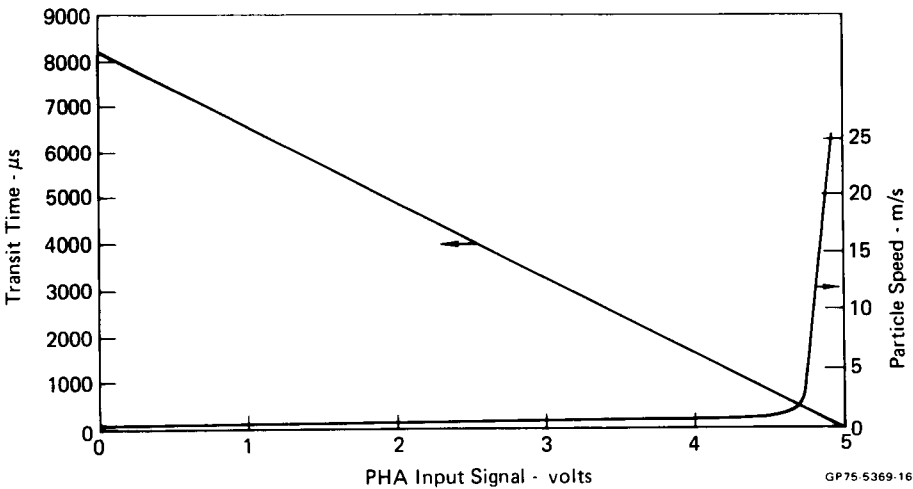


FIGURE 16 LPS TRANSIT TIME AND PARTICLE SPEED CALIBRATION

In terms of particle speed, the PHA 0-5 volt scale is highly non-linear. Linearization can be accomplished via the calculator software once the realtime data is recorded.

REFERENCES

1. Knollenberg, R. G., "An Active Scattering Aerosol Spectrometer", Atmos. Tech., No. 2 (June 1973).
2. Proctor, T. D., "A Laser Technique for the Measurement of Aerosols", J. Phys. E1, 631 (1968).
3. Schehl, R., Ergun, S., and Headrick, A., "Size Spectrometry of Aerosols Using Light Scattering from the Cavity of a Gas Laser", RSI 44, 1193 (1973).
4. Schleusener, D. A., "Automatic High Speed Particle Sizing Using a Gas Laser", RSI 39, 1916 (1968).
5. Schuster, B. G., and Knollenberg, R., "Detection and Sizing of Small Particles in an Open Cavity Gas Laser", Appl. Opt. 11, 1515 (1972).
6. Siegman, A. E., An Introduction to Lasers and Masers, McGraw-Hill Co., New York, 1971.
7. Dave, J. V., "Subroutines for Computing the Parameters of the Electromagnetic Radiation Scattered by a Sphere", Report 320-3237, IBM Scientific Center, Palo Alto, California, (1968).

PARTICULATE SIZE DISTRIBUTION CASCADE ANALYZER FOR SPACECRAFT CONTAMINATION MONITORING

Donald A. Wallace, *Engineering Manager*, and Raymond L. Chuan, *Assistant to President*,
International Biophysics Corp., Subsidiary of Ceresco Industries, Costa Mesa, California 92626

ABSTRACT

Contamination detection and control is imperative on spacecraft systems such as Space Shuttle and Spacelab where sophisticated optical instrumentation packages are involved. The experiment package may suffer from contaminating sources while housed inside the vehicle in an ambient spacecraft environment or after exposure to full vacuum condition.

A Cascade Particulate Analyzer has been developed for nearly real time measurement of the contaminating particulate size distribution in the spacecraft interior ambient environment and as a real time total impacting particulate mass monitor under vacuum conditions.

The analyzer has four stages, the first stage is a basic 10 MHz quartz crystal microbalance used widely on spacecraft (such as Skylab) for contamination monitoring purposes. In this application the front sensing crystal is coated with a low vapor pressure adhesive grease which captures impacting particles. This first stage has a wide viewing angle and measures total particulate mass impacting the crystal while the unit is exposed to the vacuum environment. The remaining three stages form an aerodynamic impaction cascade with individual quartz crystal microbalances at each stage acting as accumulated mass sensing elements. The aerodynamic nozzles used in each stage are designed using well established impaction theory and have 50% cutoff points of 5, 1 and 0.3 microns. These three stages thus give relative mass distribution of particulates in three ranges, particles having effective diameter greater than 5 micron, particles between 1 and 5 micron diameter and particles 0.3 to 1 micron diameter. Since the cascade requires airflow to carry the particles through the various stages, the size distribution is only valid when the analyzer is in an approximate atmospheric environment inside the spacecraft. The sensing QCM module uses 10 MHz matched crystals in a design which is flight proven. The vaned pump, motor and motor controller are flight qualified hardware. Each stage of the analyzer contains a dual oscillator and mixer hybrid chip, the crystals of the QCM being active elements in the oscillator circuit. Mass is sensed as a decrease in sensing crystal frequency and an increase in beat frequency

from the mixer. The mixer frequency outputs from the four stages are processed in a Signal Processing module resulting in zero to 5 volt telemetry signals of beat frequency and differentiated beat frequency (rate). The first stage crystal temperature is also available as an analog voltage as well as the unprocessed stage frequency.

Laboratory test results of measured size distributions under various environmental conditions are presented.

DEVELOPMENT OF A LABORATORY DEMONSTRATION MODEL ACTIVE CLEANING TECHNIQUE DEVICE

R. L. Shannon and R. B. Gillette, *The Boeing Company, Seattle, Washington*

ABSTRACT

A laboratory demonstration model of a device for removing contaminant films from optical surfaces in space has been developed.

INTRODUCTION

Contaminant film deposition can occur on surfaces in both vacuum chamber and space environments. Contaminant film deposition has been measured on manned (Skylab)¹ and unmanned (OGO-6)² spacecraft. A review of the spacecraft contamination problem is presented in Reference 3. Some aspects of optical contamination problems in vacuum chamber testing are reported in References 4, 5, and 6. Contamination is expected to remain a problem for sensitive surfaces during long-term space missions or vacuum test chamber exposures. Consequently, there exists a need for developing an in-situ or active cleaning technique (ACT) for use in both space and vacuum chamber applications.

Exposure to an oxygen-plasma has restored the reflectance of both radiation-damaged white paint^{7,8} and organic-film-contaminated telescope mirror surfaces⁶. More recently, two interrelated active cleaning technique studies have been conducted. One study was aimed at determining the feasibility of using plasma exposure as an active cleaning technique and the other involved the development of a laboratory demonstration device. During the feasibility study, a facility was developed for depositing contaminant films and subsequently performing plasma cleaning experiments. This facility includes: test chamber, vacuum pumping system, contaminant gas source, ultraviolet light source and proton accelerator system for contaminant film deposition, and plasma generator system. Later in the program, an in-situ monochromator/reflectometer was incorporated to make measurements while maintaining the test specimen in a vacuum environment. Results of the feasibility study, re-

ported¹⁰ in an earlier paper⁹ and in the first annual report¹⁰, show that oxygen-plasma exposure removes hydro-carbon contaminant films from typical spacecraft optical surfaces. In these early plasma cleaning experiments it was thought that atomic oxygen was responsible for the cleaning effects. It was postulated that the hydro-carbon contaminants were converted to volatile products by a series of oxidation reactions. Further results of the feasibility study show that this postulated cleaning-mechanism is incorrect. These¹¹ results are presented in the program final report¹¹ and are discussed in the present paper in conjunction with the development of a suitable plasma tube design.

The development of a laboratory-demonstration-model active cleaning technique device is the subject of the present paper. The details of this development are presented in the design study report¹² and final report¹³ for the program. The development of a plasma tube, which would produce the desired cleaning effects under high vacuum conditions, represented the major problem in the program. This plasma tube development is discussed first and then the resulting laboratory-demonstration-model device is described.

INITIAL PLASMA TUBE DEVELOPMENT

Background

The basic plasma tube configuration used in the feasibility study consisted of two concentric quartz tubes (4 mm and 10 mm I.D.'s) with the annulus sealed at the downstream (vacuum environment) end. Electrodes were provided by diametrically opposed wires placed in the annulus. A plasma discharge was generated in oxygen gas, flowing through the inner tube, by a 13.56 MHz radiofrequency (rf) power supply attached to the electrodes. A nominal upstream plasma tube pressure of about 4 torr was required to maintain the discharge. This resulted in an oxygen flow rate of about 50 STD cc/min and a vacuum chamber pressure on the order of 10^{-3} torr. Under these conditions a plasma discharge also existed throughout the chamber ("chamber discharge"). Also, in normal operation, the rf power supply was tuned to establish an intense discharge in the gas plume exhausting into the vacuum chamber ("ignited plume").

Since an active cleaning technique cannot rely on background gas pressure effects, a plasma tube configuration had to be developed which would provide the cleaning effects under high vacuum conditions. This

requires matching of the plasma tube design to the vacuum system pumping capabilities. The proposed NASA test facility for the laboratory demonstration model uses a 400 liter per second Varian-type noble ion pump. This pumping system limits the oxygen flow rate to 0.18 STD cc/min for a maximum chamber pressure of 10^{-5} torr.

Initial Plasma Tube Design

The initial plasma tube design for the laboratory demonstration model was based on the assumption that atomic oxygen is responsible for the plasma cleaning effects. The basic design concept was to add a flow restriction (capillary) at the downstream end of the plasma tube (See Figure 1). This capillary allows passage of atomic oxygen while maintaining sufficient upstream pressure for an rf discharge at low flow rates. The detailed analysis for sizing the capillary is given in the design study report¹³. Basically, Knudson flow regime calculations¹⁴ were made to determine the capillary sizes (lengths and diameters) as a function of upstream pressure for an oxygen flow rate of 0.18 STD cc/min. An analysis was then made to determine the atomic oxygen attenuation for the various capillary sizes. This analysis used an atomic oxygen wall recombination coefficient of 2×10^{-4} (Coefficients for pyrex, silica and quartz walls from 2×10^{-5} to 2×10^{-4} have been reported¹⁵). The sizing analysis showed an upstream pressure of 4 torr requires a capillary diameter of less than 0.02 cm to keep the atomic oxygen attenuation below 1 percent. Fabrication of a quartz tube with this small capillary diameter appeared to be a difficult and costly problem. Consequently, means of establishing a lower pressure rf discharge was needed in order to use a larger diameter capillary.

The low pressure operation limit on the original 4 mm diameter plasma tube is due to the electron-oscillation-amplitude limit. At low pressures, the electrons are swept to the tube wall on each half-cycle of the imposed rf field. This places a practical lower pressure limit on achieving an rf discharge at a given frequency and tube size (electrode spacing). This limit may be overcome by increasing either the frequency or tube size. Since the available power supply had a fixed 13.56 MHz frequency, experiments were conducted to determine the discharge breakdown voltage as a function of pressure for different diameter tubes using diametrically opposed electrodes. Based on the results of these breakdown voltage ex-

periments, capillary sizing analysis, and available quartz tubing sizes, two plasma tubes were designed and fabricated. These tubes are identical with the exception of capillary dimensions. Both use an inner 17 mm ID plasma discharge tube and an outer 30 mm ID shield tube as shown in Figure 1. One tube has a capillary sized (0.05 cm diameter by 0.2 cm length) to give an oxygen flow rate of 0.18 STD cc/min at an upstream pressure of 0.4 torr. The other has a capillary sized (0.1 cm diameter by 0.4 cm length) to give 1 STD cc/min flow at a pressure of 0.5 torr. Both were sized for an atomic oxygen attenuation of less than 1 percent. The plasma tube with the larger capillary was used for the tests discussed in the following paragraphs.

Plasma Cleaning Tests Using Initial Design

Initial plasma cleaning tests using soot coated specimens were conducted under various conditions of flow rate, power input, exposure time, and sample distance from the capillary. No visible cleaning of the specimens was observed in any of these tests. These cleaning tests were repeated using a magnesium fluoride overcoated aluminum mirror onto which 200-300 Å of carbon was vacuum desposited. After an exposure of six hours at oxygen flow rates of $\frac{1}{4}$ up to 2.5 STD cc/min, chamber pressures up to 2×10^{-4} torr, and distances from capillary down to 1.3 cm, there was no visible cleaning of the specimen. However, when the flow rate was increased such that the chamber pressure rose to 10^{-3} to 10^{-2} torr the "chamber discharge" and "ignited plume" phenomena were initiated and the carbon coating was rapidly removed. A final cleaning test was conducted using a quartz-crystal-microbalance (QCM), Sloan Model DTM-4. The quartz crystal was gold coated and then contaminated with a 1,3 butadiene film deposited in the presence of ultraviolet radiation. This contaminated crystal (mounted in the QCM assembly) was placed 2.5 cm from the capillary. Four hours exposure at an oxygen flow rate of 1 STD cc/min and a chamber pressure of 10^{-5} torr resulted in no measurable cleaning. (The threshold of detection was estimated to be about 4×10^{-12} gm/cm²-sec.) The flow rate was then increased to the point of achieving a "chamber discharge". In this operational mode a cleaning rate of about 2×10^{-9} gm/cm²-sec was measured. When the mode of operation changed to the "ignited-plume" mode, the cleaning rate increased to about 10^{-8} gm/cm²-sec. Since all attempts at plasma cleaning failed at low chamber pressure, further tests

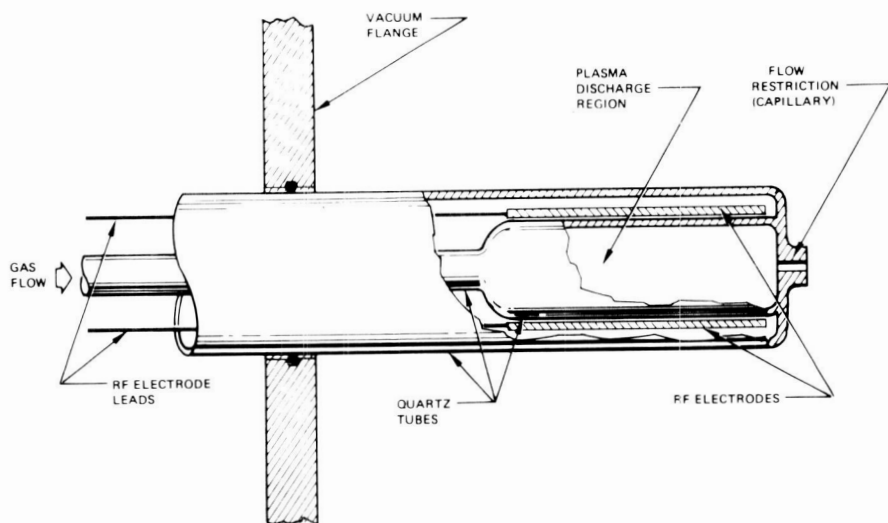


Figure 1: INITIAL PLASMA TUBE CONFIGURATION

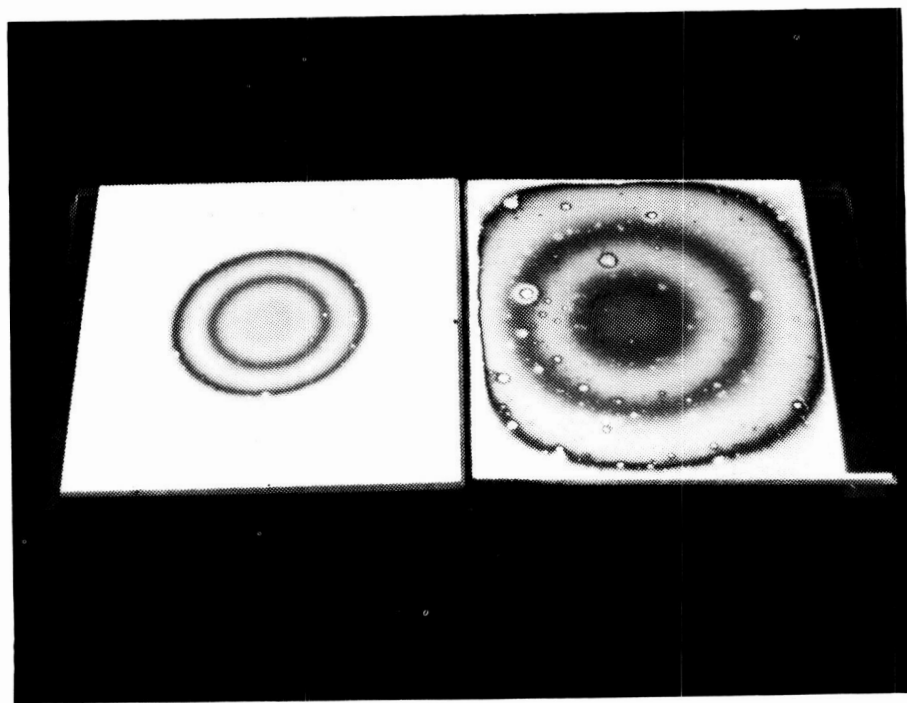


Figure 2: SILVER OXIDATION PATTERNS

were conducted to determine whether or not the plasma tube was producing atomic oxygen at low chamber pressures.

Silver Oxidation Tests Using Initial Plasma Tube

Since silver is readily oxidized by atomic oxygen, silver coated surfaces were used to detect the presence of atomic oxygen. Figure 2 shows oxidation patterns on two 5.08 cm square silver coated mirrors which were exposed to the plasma tube. The mirror with the smaller circular interference pattern was placed 1.3 cm from the capillary and exposed five minutes at an oxygen flow rate of 1 STD cc/min. The other mirror was placed 2.5 cm from the capillary and exposed five minutes at an oxygen flow rate of 2.5 STD cc/min. A quantitative measurement of the silver oxidation rate was attempted by using glass plates coated with 1700-2600 Å of silver except for a bare strip left in the center of the plates. This bare surface was to serve as a reference plane for post-test interferometry measurements. When these samples were exposed to the oxygen plasma, circular interference patterns resulted similar to those shown in Figure 2. However, the silver along the edges of the bare strips showed little, if any, oxidation. This "edge effect" can be seen in Figure 2 on the mirror with the larger interference pattern. The edge opposite the uncoated edge was masked by the sample holder. However, truncation of the circular pattern along the other edges show this "edge effect". The slower silver oxidation near the edges may be due to stronger binding of the surface atoms at the edges.

Successful determination of the silver oxidation rate was made using silver coated crystals in the QCM. The QCM was placed 2.5 cm from the capillary and exposed at an oxygen flow rate of 1 STD cc/min and vacuum chamber pressure of 7×10^{-5} torr until the silver was completely oxidized. The QCM frequency change corresponded to the addition of enough atomic oxygen to oxidize a silver surface 1670 Å thick. This agrees to within about 10 percent of the manufacturer's reported silver thickness of 1500 Å. Post-test x-ray diffraction analysis showed the oxide layer to consist primarily of Ag₂O with a trace of Ag₂O₃. Figure 3 shows the rate of atomic oxygen flux reacting with the silver as a function of the amount of reaction already taken place. Assuming the oxygen flux produced by the plasma tube to be constant, the atomic oxygen flux produced is greater than 0.625×10^{15} atoms/cm²-sec. A possible explanation of the oxidation rate behavior

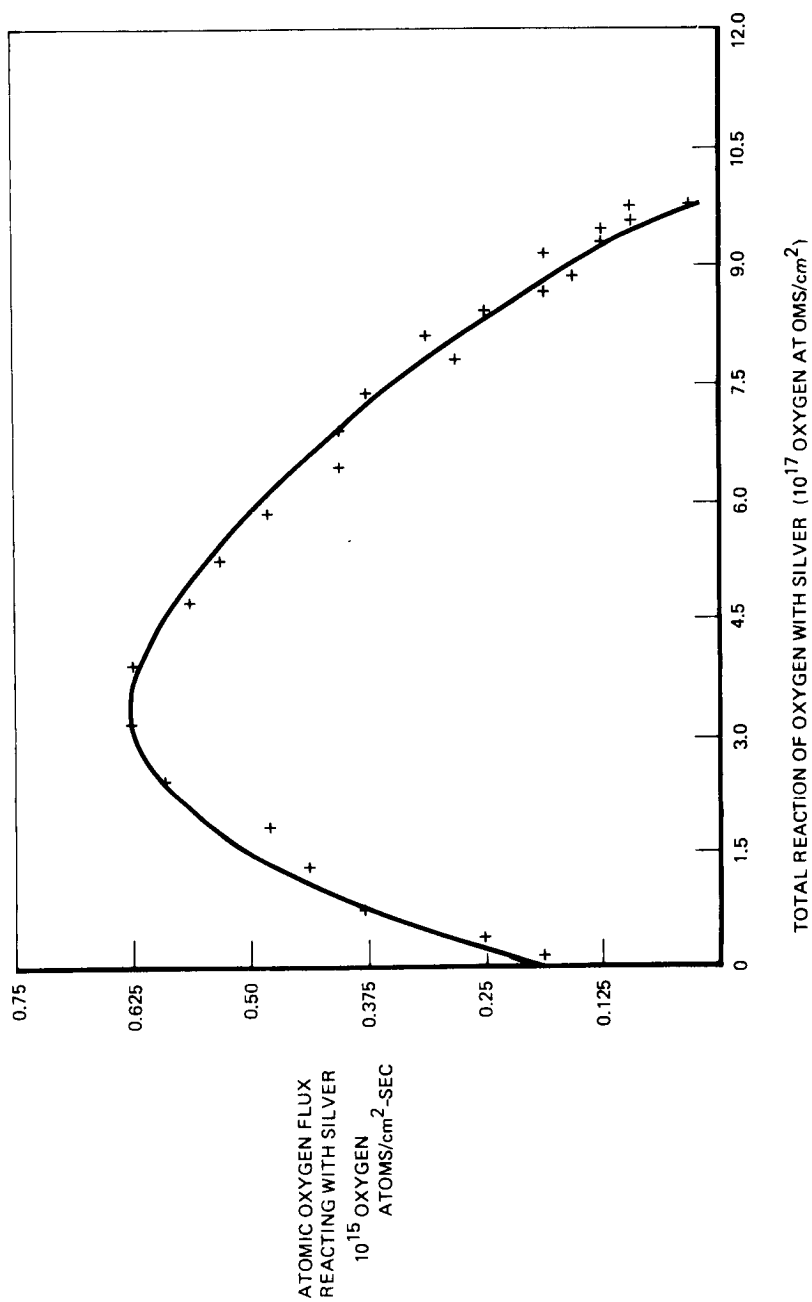


Figure 3: RATE OF SILVER OXIDE FORMATION

is that initially, with a clean silver surface, the oxygen atoms have a short residence time at the surface and the probability of an oxidation reaction is small. As the oxide layer builds, the residence time increases and the probability of a reaction increases. Finally, as the layer continues to build, the probability of oxygen atoms recombining with each other before reaching the silver surface increases. This would explain the decrease in oxidation rate as the oxide layer continues to build.

These silver oxidation tests showed that the initial plasma tube design was successful in producing silver oxidation at low vacuum chamber pressures. This oxidation was attributed to atomic oxygen produced in the plasma discharge (Ozone and excited molecular oxygen may have also contributed to the oxidation). These results show that the postulated oxidation-cleaning mechanism is incorrect. This conclusion is reinforced by the results of plasma cleaning tests using other gases.

Plasma Cleaning Using Various Gases

In-situ contamination/cleaning experiments were conducted to compare the cleaning effects produced by an argon plasma with those produced by an oxygen plasma. These experiments utilized gold coated mirrors which were contaminated with 1,3 butadiene in the presence of ultraviolet radiation. The contamination and subsequent plasma cleaning effects were determined by measuring the uv reflectance of the mirrors with the in-situ monochromator/reflectometer. Plasma cleaning was accomplished by operating in the "chamber discharge" and "ignited plume" mode of plasma tube operation. Figure 4 shows the reflectance data for a gold coated mirror before and after contamination and after exposure to an oxygen plasma. This same mirror was then recontaminated and cleaned using an argon plasma. Figure 5 shows the reflectance data for this test. These tests show that argon is as effective as oxygen in producing plasma cleaning effects.

Further experiments were conducted to compare helium and hydrogen with oxygen in plasma cleaning of vacuum deposited carbon. These experiments used a QCM with a gold coated quartz crystal overcoated with 200 Å of carbon. Figure 6 shows the results of these experiments. The reduction in QCM frequency indicates removal of carbon (removal of one microgram/cm² corresponds to a frequency change of about 50 Hz). All exposures used the "ignited plume" mode of operation. The initial series of tests (dashed lines) showed

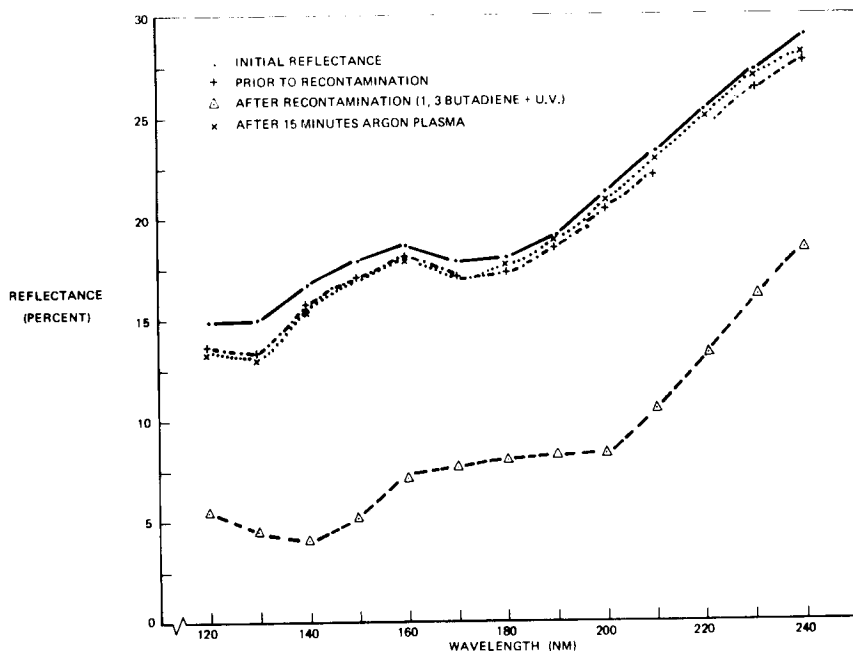


Figure 5: ARGON CLEANING OF GOLD COATED MIRROR

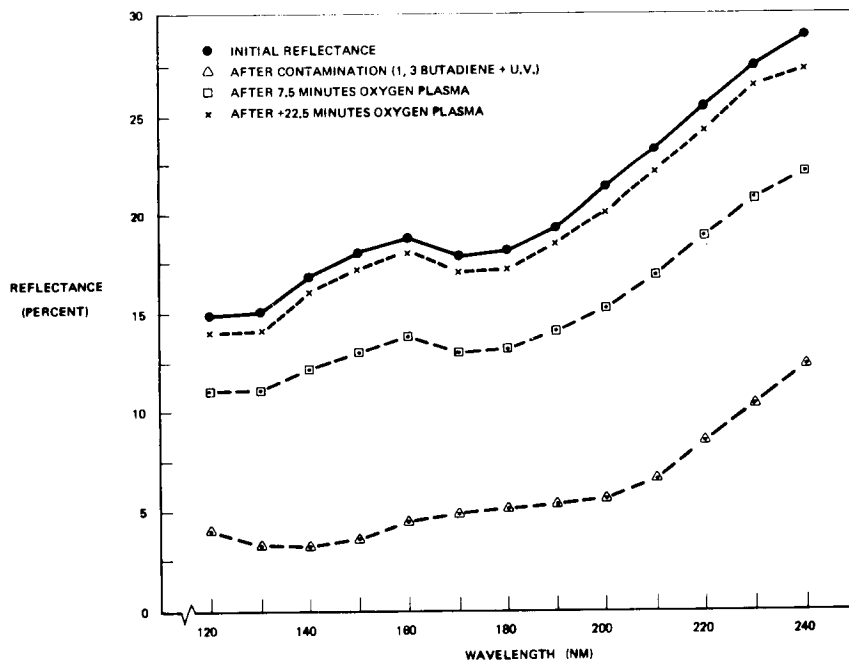


Figure 4: OXYGEN CLEANING OF GOLD COATED MIRROR

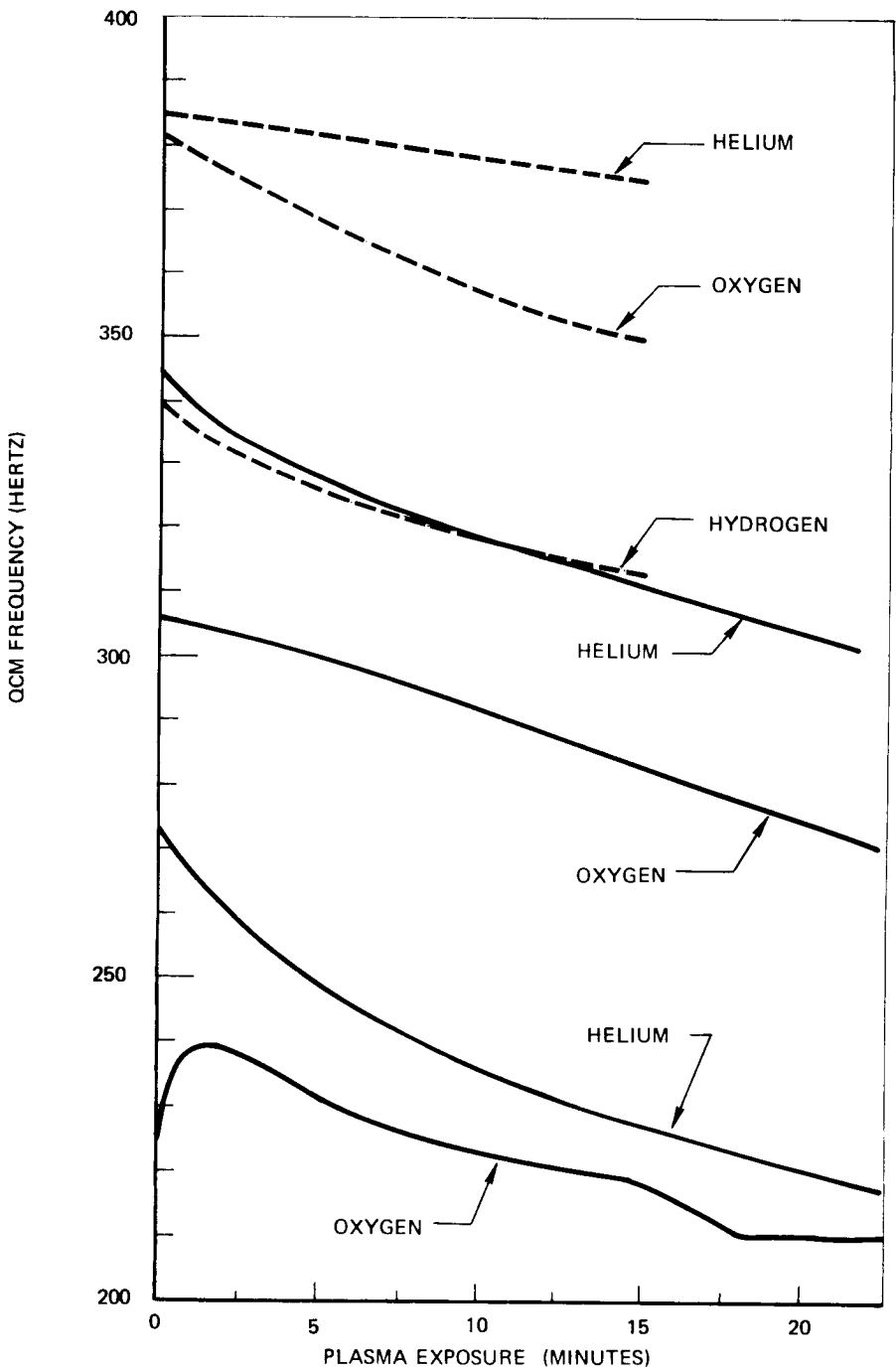


Figure 6: PLASMA CLEANING OF CARBON COATED QCM

hydrogen to be as effective as oxygen in removing the carbon. Helium appeared to be somewhat less effective. To check this result, a second series of tests (solid lines) was made to compare helium with oxygen. These tests indicated that helium was as effective as oxygen in removing carbon. The final oxygen exposure (lowest curve in Figure 6) removed the remaining carbon from the crystal.

These plasma cleaning tests along with the silver oxidation tests show that the postulated atomic oxygen cleaning mechanism was invalid. Consequently, a change in philosophy was necessary for the plasma tube development.

FURTHER PLASMA TUBE DEVELOPMENT

Development Philosophy

The initial plasma tube design produced silver oxidation at low chamber pressures, however, plasma cleaning was produced only at higher chamber pressures in the "chamber discharge" and/or "ignited plume" mode of operation. In all of the plasma cleaning tests, cleaning was always accompanied by a visible glow in the region of the test specimen. Consequently, the plasma tube development philosophy was to produce a visible plume at low vacuum chamber pressures. This allowed rapid evaluation of plasma tube configurations and operating conditions without time consuming cleaning tests.

Preliminary Experiments

A visible plume was established at low chamber pressures with a dc discharge through the plasma tube capillary. A tungsten wire probe placed inside the plasma tube was used as the high voltage electrode and a brass screen placed just downstream of the capillary was used as the ground electrode. Cleaning tests using this mode of operation showed contamination of the test specimen with electrode material. An rf discharge was established through the capillary by applying the rf voltage to the plate electrodes and the wire probe. The vacuum chamber acted as the ground electrode. This rf discharge mode also resulted in a visible plume. Cleaning tests indicated that simultaneous contaminant film removal and electrode material deposition resulted in this mode of operation. These tests showed that a visible plume can be produced at low chamber pressures and confirmed the need to have the electrodes outside the discharge region to prevent contamination.

Further experimentation with rf electrodes outside of the discharge region failed to produce satisfactory results. Consequently, experiments were conducted using a 4 mm ID quartz tube with no capillary. Figure 7 shows the configuration for this prototype plasma tube. Initial tests showed that: (1) an axial discharge and visible plume could be established at low chamber pressures; (2) the shape and position of the discharge were dependent on the gas flow rate and the relative positions of the electrodes; and (3) the axial symmetry of the visible plume appeared to be dependent on the routing of the rf leads. Subsequent cleaning tests using a carbon-coated QCM showed cleaning when the QCM was located in the visible plume and no cleaning outside of the visible plume. Further experiments using this plasma tube are described in Reference 11.

Laboratory-Demonstration-Model Plasma Tube

The laboratory-demonstration-model plasma tube development was based on the prototype plasma tube shown in Figure 7. The major problem in this development was housing the rf electrodes and leads in a 30 mm ID quartz shield tube so that a symmetric discharge could be maintained at the downstream end of the inner 4 mm ID tube. During the development tests, it became apparent that the power requirements (about 100 watts) using a frequency of 13.6 MHz were too large. The power requirements were greatly reduced by using a different power supply (Microdot Model 406A) which has a 50-200 MHz frequency range. The results of the development experiments showed that: (1) the production of a visible plume is enhanced by having the downstream electrode placed a short distance from the end of the plasma tube; (2) best operation occurs with a discharge downstream of the rf electrode as well as in between the electrodes; (3) the upstream portion of the inner tube must be shielded from the rf field to prevent an upstream discharge; and (4) tuning the rf power supply for proper operation requires observation of the discharge.

The plasma tube configuration which resulted from these development experiments is shown in Figure 8. This configuration provides adjustable electrode positions, rf shielding of the upstream gas, and light pipes to transmit light from the discharge to the outside of the plasma tube assembly. The upstream ground electrode is brazed to a tube which shields the upstream gas and provides the ground lead. The downstream electrode is connected to the rf power by means

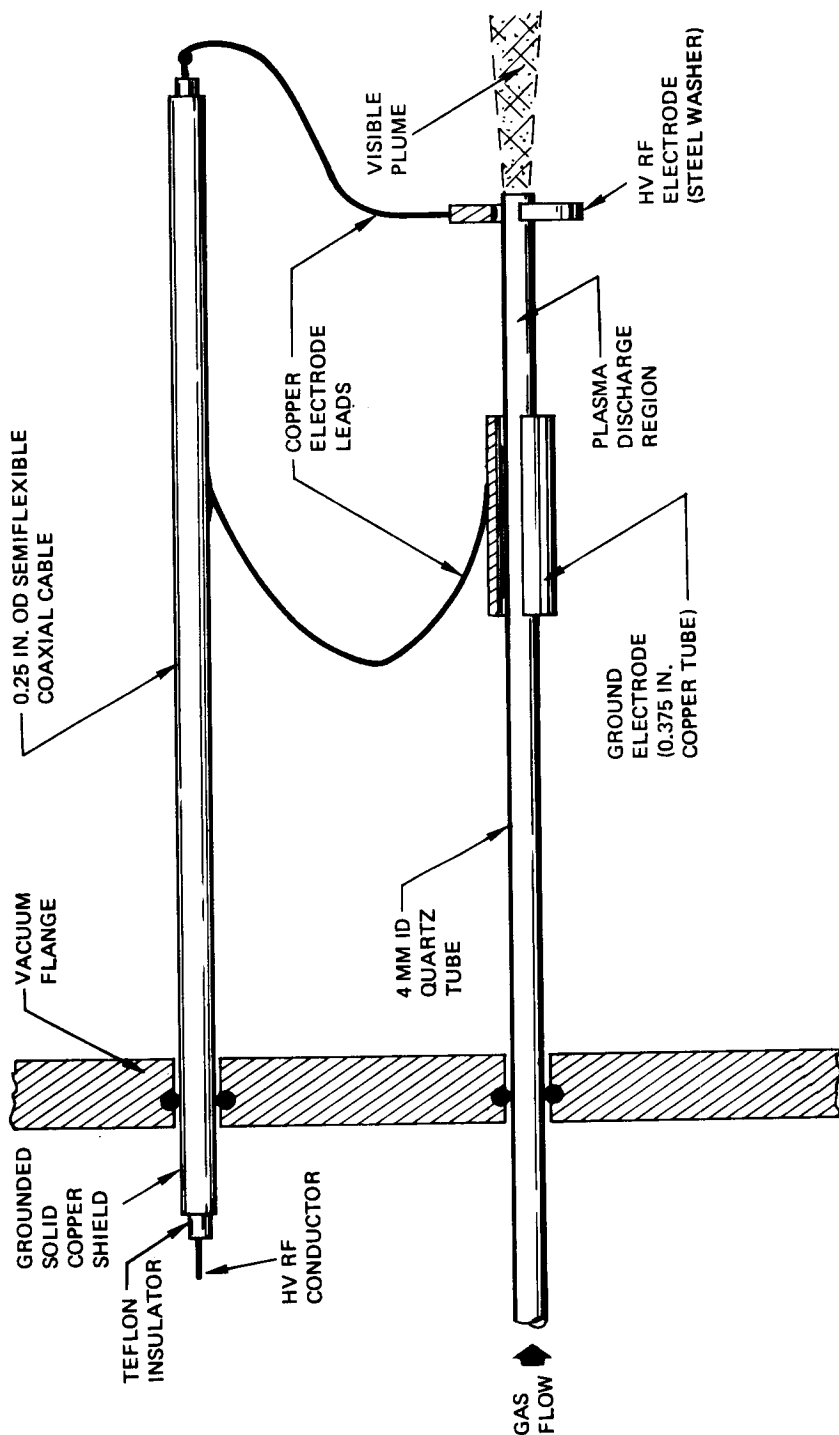


Figure 7: PROTOTYPE PLASMA TUBE CONFIGURATION

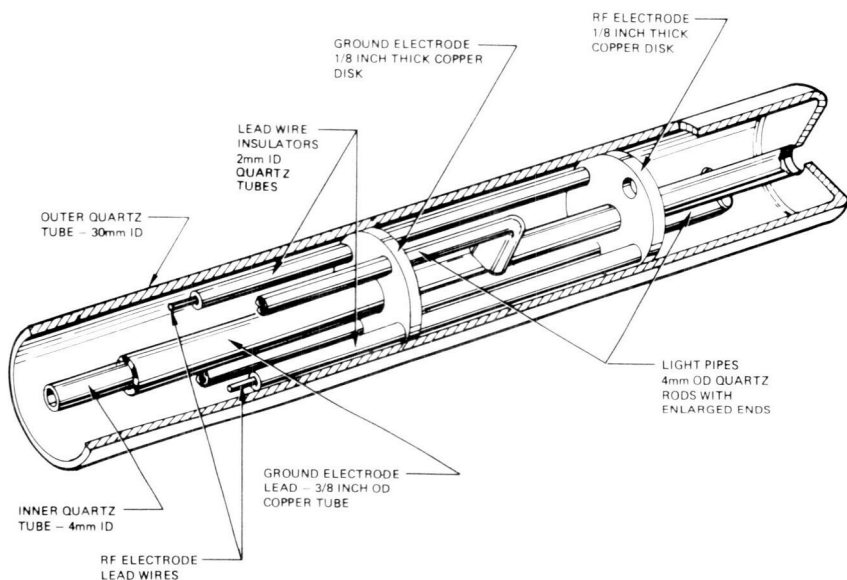


Figure 8: PLASMA TUBE CONFIGURATION

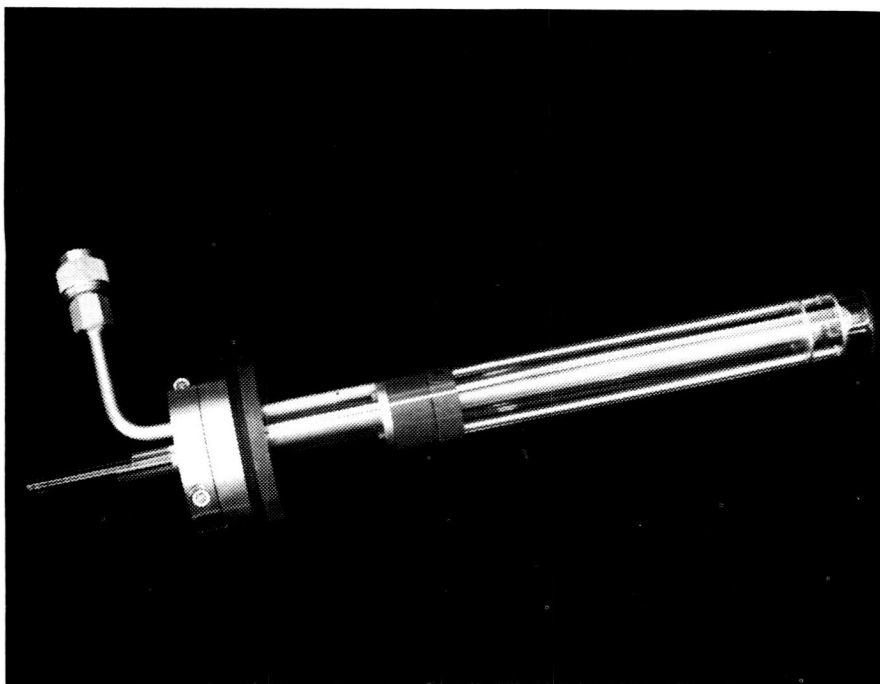


Figure 9: PLASMA TUBE ASSEMBLY

of two diametrically opposed leads. These leads are insulated by routing them through lengths of quartz tubing which pass through clearance holes in the ground electrode. Two light pipes, made from quartz rod, pass through clearance holes in the electrodes and view the discharge regions. Figure 9 shows a photograph of the plasma tube assembly.

LABORATORY-DEMONSTRATION-MODEL DEVICE

General Description

The laboratory-demonstration-model device consists of control console, cable bundles, plasma generator enclosure, plasma tube assembly, and ion accelerator assembly. The design was based on the following specifications:

- (1) The device was to be capable of operating in a plasma cleaning mode with an optional ion sputtering mode.
- (2) Device must be compatible with operation in NASA test facility.
 - (a) Nominal oxygen flow rate of 0.18 STD cc/min (based on 400 $\frac{1}{5}$ liter/sec Varian-type noble ion pump at 10^{-5} torr pressure).
 - (b) Plasma generator enclosure must mount with Varian-type vacuum flange on a 6-inch (15.2 cm) diameter port.
 - (c) RF shielding must be provided.
- (3) Plasma generator enclosure must be capable of remote mounting inside a vacuum chamber.
- (4) Plasma tube extension length must be adjustable from 9.7 to 17.3 cm with respect to mounting flange.
- (5) Remote operation of device from a control console required.

Figure 10 shows an overall schematic of the device and Figure 11 shows a photograph of the device during checkout tests. The control console contains the gas supply, rf power generator, high voltage power supply, plasma discharge sensor meters, and gas supply and plasma tube pressure gauges. The plasma generator

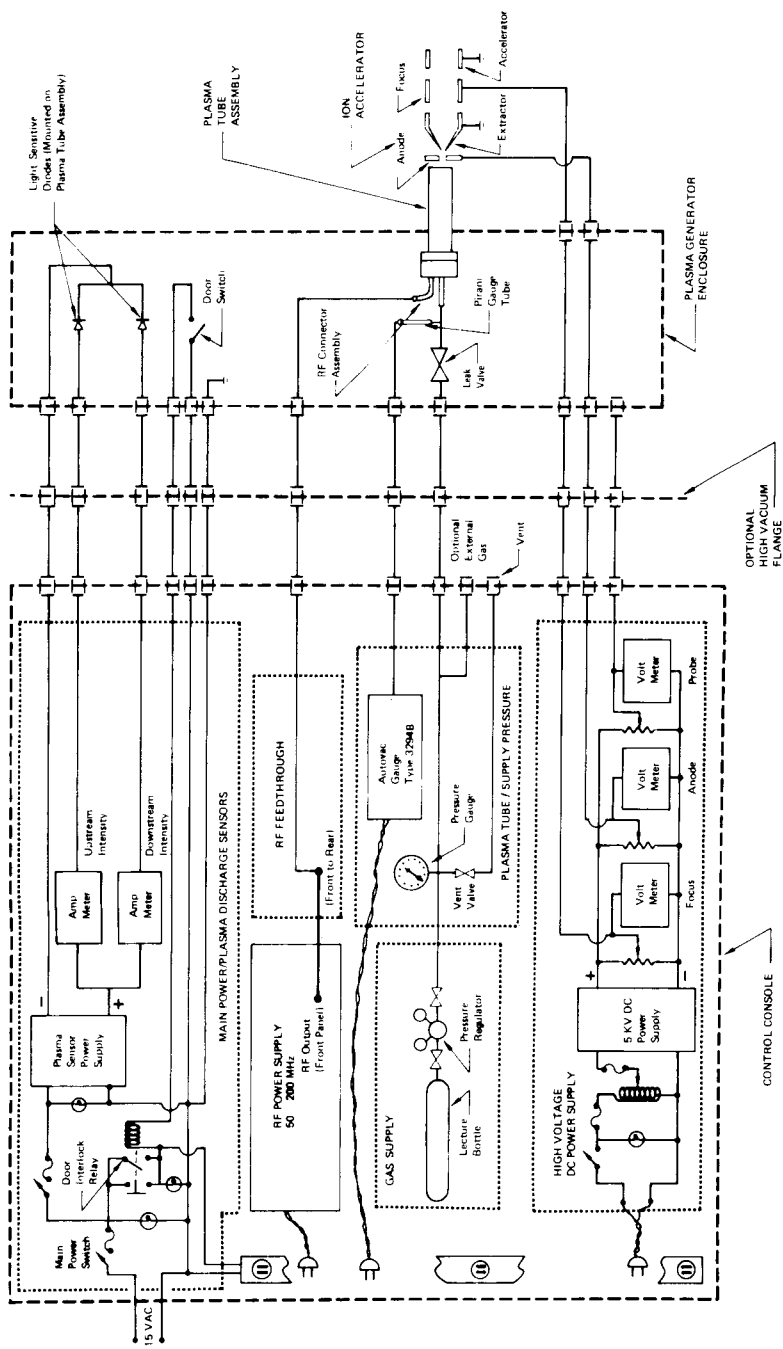


Figure 10: LABORATORY DEMONSTRATION MODEL SCHEMATIC

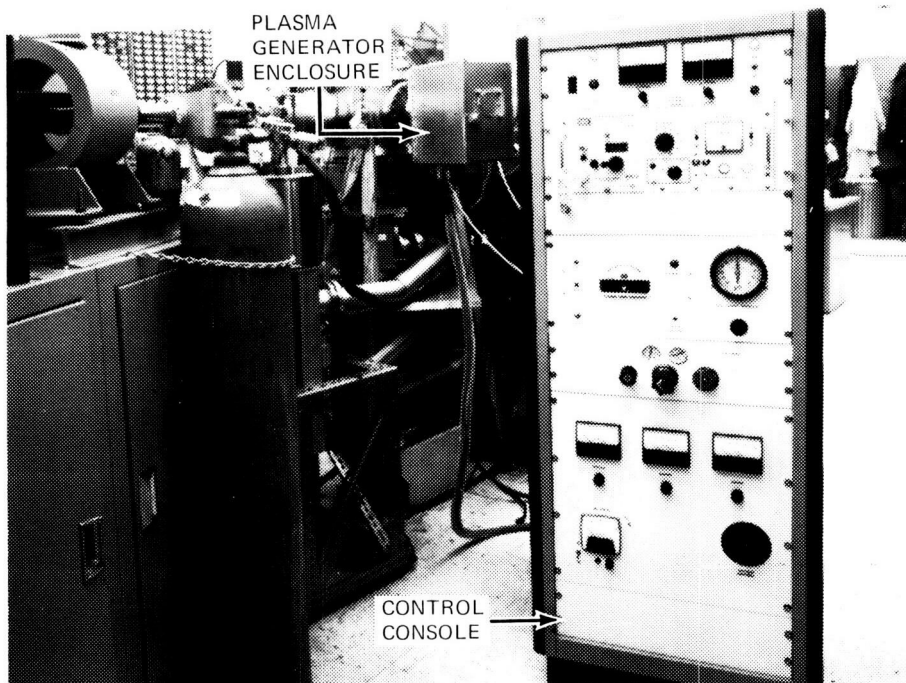


Figure 11: LABORATORY DEMONSTRATION MODEL

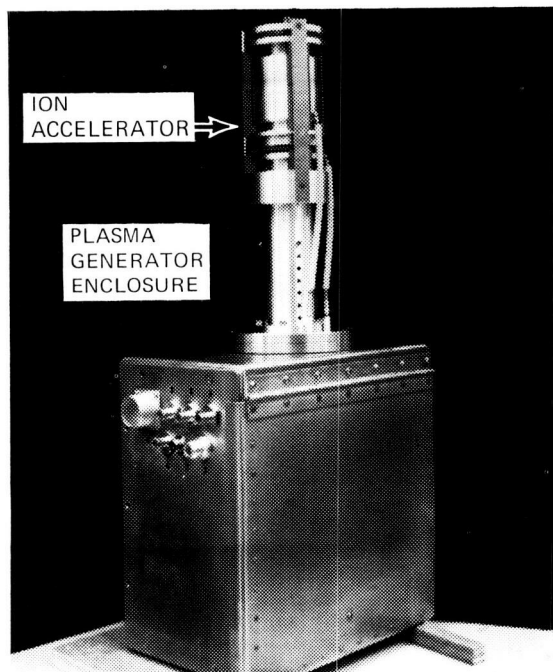


Figure 12:
PLASMA GENERATOR
ENCLOSURE/ION
ACCELERATOR

enclosure houses the plasma tube assembly and provides the required rf shielding. The enclosure also houses the light sensors, Pirani vacuum gauge tube, and variable leak valve. A photograph of the plasma generator enclosure with the ion accelerator attached is shown in Figure 12. The Gap-Einzel ion accelerator removes as a unit for operation in the plasma cleaning mode. A complete description of the laboratory-demonstration-model device and operational procedures is given in reference 16.

Operation

The desired gas flow rate is set by opening the variable leak valve (housed in the plasma generator enclosure) to the appropriate value and then fine adjusting with the upstream pressure regulated at the control console. The plasma tube pressure (Pirani gauge readout at the control console) provides the gas flow rate value by means of a calibration curve. After establishing the gas flow rate, the plasma discharge is initiated by adjusting the output, frequency and coupling of the rf power supply. The plasma discharge is monitored with the plasma discharge sensors that measure the current through light sensitive diodes mounted on the plasma tube light pipes. These sensors are used to detect the initiation of the discharge and to determine when the rf power supply is adjusted such that a visible plume is produced. When the ion acceleration is being used, the high voltage dc power supply at the control console is adjusted to the desired accelerating voltages.

Carbon Cleaning Tests

A carbon coated quartz-crystal-microbalance (QCM) was used to determine the carbon removal rate produced by the laboratory-demonstration-model. The QCM was mounted approximately on centerline 5 cm downstream of the plasma tube. The carbon removal rate was determined by measuring the rate of QCM frequency change for various oxygen flow rates and rf power levels. For the limited amount of data taken, the carbon removal rate appears to be primarily dependent on the forward rf power input. Figure 13 shows the correlation between carbon removal rate and forward rf power. The gas flow does not appear to have a significant effect on the cleaning rate. It was expected that the higher flow rates would provide a higher cleaning rate. This might still be the case if the plasma tube configuration be optimized for each flow rate.

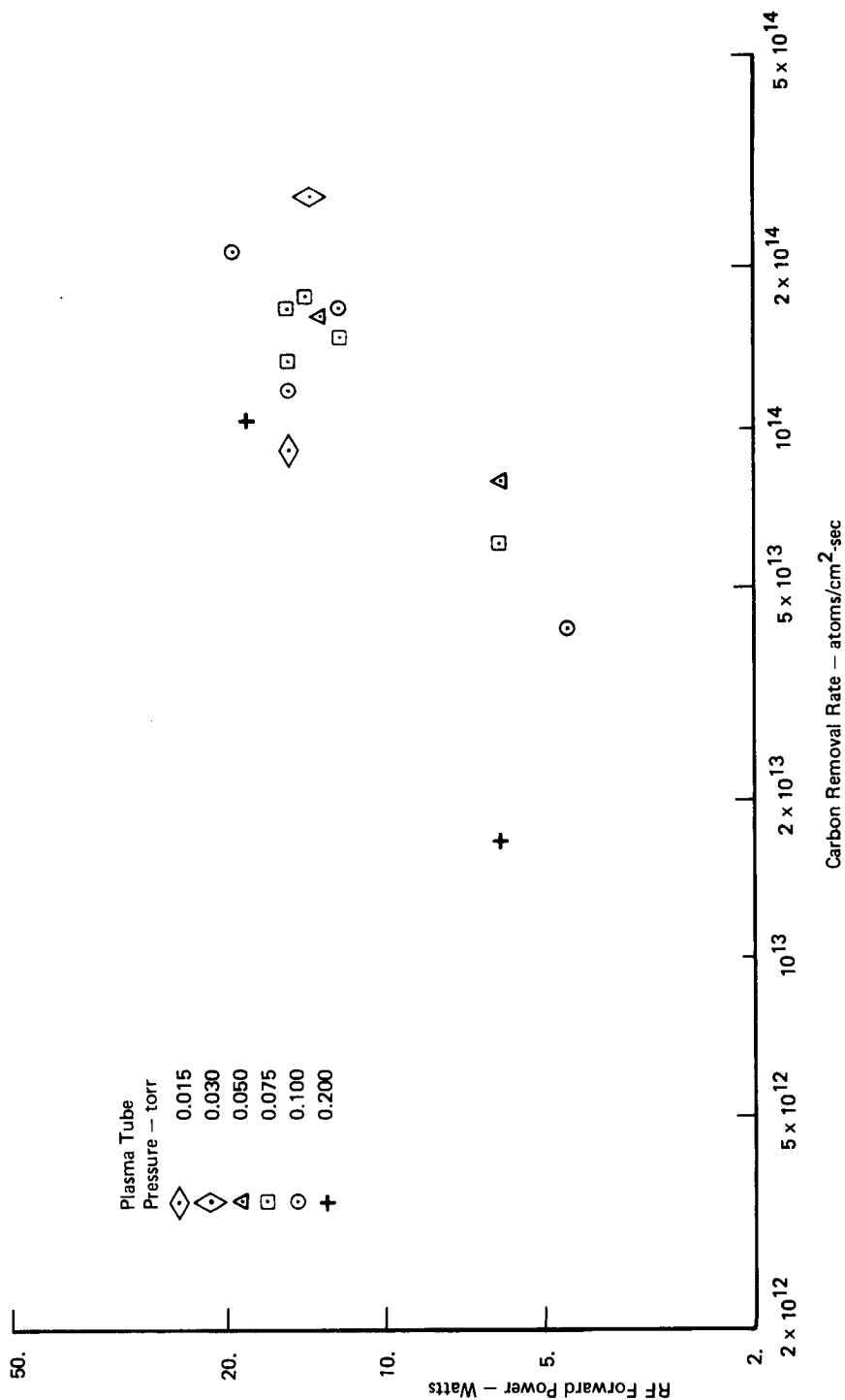


Figure 13: RATE OF CARBON REMOVAL - 5CM FROM PLASMA TUBE

Ion Accelerator Tests

A Faraday cup, mounted on centerline approximately 5 cm downstream of the accelerator, was used to measure the ion flux produced by the laboratory-demonstration-model. The ion current to the Faraday cup was measured for various oxygen flow rates, rf power levels, and accelerating voltages. During these tests the anode and focus voltages were set to the same level. In most cases only a slightly larger ion flux could be achieved by optimizing the focus voltage for a given anode voltage. The maximum accelerating voltage that could be used was about 3KV. At higher voltages the plasma discharge was adversely affected and was sometimes extinguished.

As was the case for the carbon removal rate, the ion flux appears to be primarily dependent on the forward rf power input level. Figure 14 shows the correlation between ion flux and rf forward power. The ion flux is not greatly affected by either gas flow rate or accelerating voltage in the 1-3 KV range. At lower accelerating voltage the ion flux increases with increasing voltage.

CONCLUSIONS

A laboratory-demonstration-model in-situ cleaning device has been developed. This device provides laboratory demonstration of cleaning of contaminant films from optical surfaces in a space environment. Further development of in-situ cleaning devices, for spacecraft and vacuum chamber applications, can be based on the laboratory-demonstration-model development.

Experiments conducted during development of the plasma tube show the need for further research on plasma cleaning. In particular, the mechanism responsible for the cleaning effect needs to be determined.

ACKNOWLEDGEMENT

This work was supported by NASA Contract NAS8-28270.

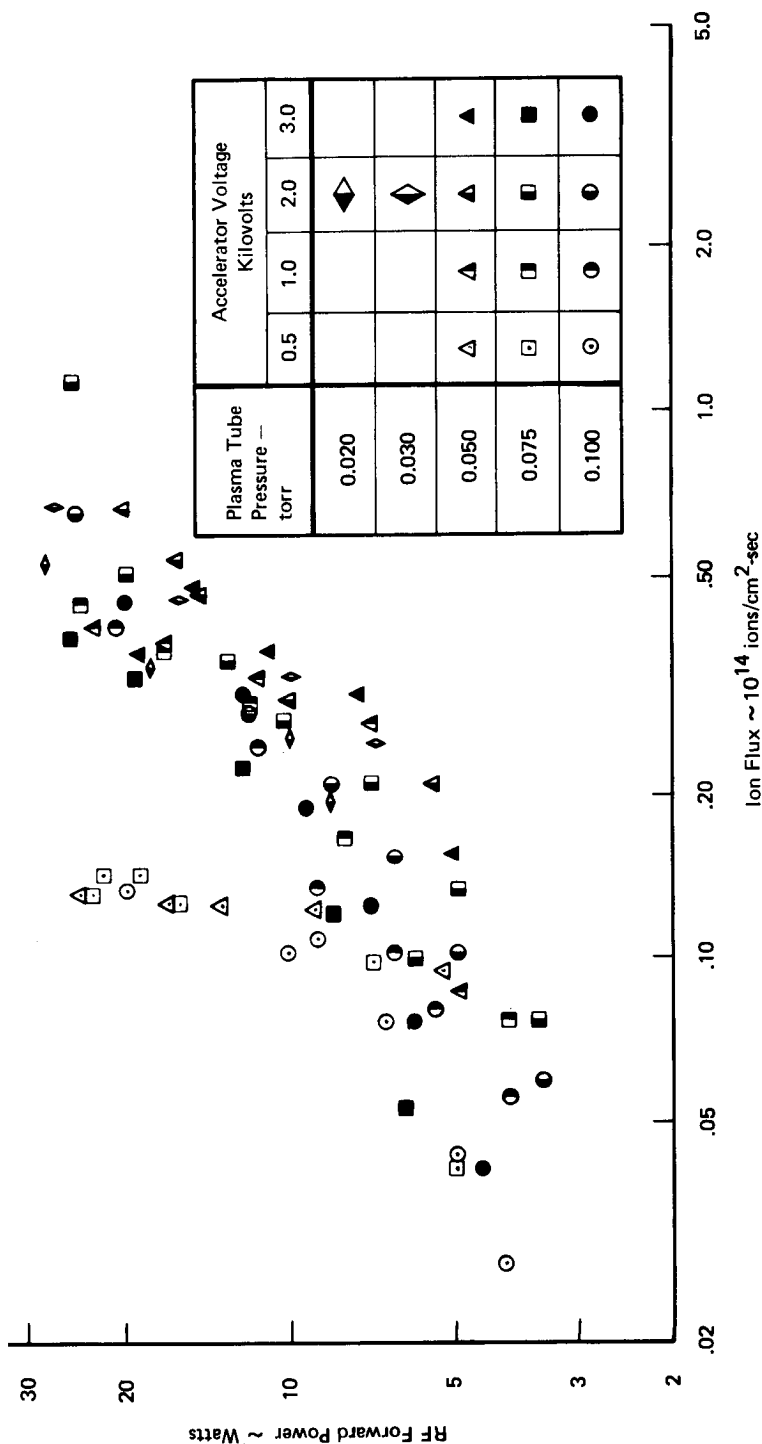


Figure 14: ION BEAM FLUX - 5 CM FROM ACCELERATOR

REFERENCES

1. Naumann, R., W. Moore, P. Nisen, W. Russell, and P. Tashbar, "Quartz Crystal Microbalance Contamination Monitors on Skylab - A Quick-Look Analysis," NASA TMX-64778, June 1973, George C. Marshall Space Flight Center, Marshall Space Flight Center, Alabama
2. McKeown, D., and W. E. Corbin, "Removal of Surface Contamination by Plasma Sputtering," AIAA Paper No. 71-475, April 1971, Tullahoma, Tennessee
3. Cothran, C. A., M. McCargo, and S. A. Greenberg, "A Survey of Contamination of Spacecraft Surfaces," AIAA Paper No. 71-457, April 1971, Tullahoma, Tennessee
4. "Optical Contamination During Thermal Testing in Vacuum," NASA Tech Brief 70-10659, December 1970
5. Kruger, R. and H. Shapiro, "Experiments on the Effect of Ultraviolet on Contamination in Vacuum Systems," X-322-71-165, April 1971, NASA
6. Gillette, R. B., and B. A. Kenyon, "Proton-Induced Contaminant Film Effects on Ultraviolet Reflecting Mirrors," Journal of Optical Society of America, Vol. 10, No. 3, March 1971, pp. 545-551
7. Gillette, R. B., J. R. Hollahan, and G. L. Carlson, "Restoration of Optical Properties of Surfaces by Radiofrequency - Excited Oxygen," Journal of Vacuum Science and Technology, Vol. 7, No. 5, Sept./Oct. 1970, pp. 534-537
8. Gillette, R. B. and W. D. Beverly, "Restoration of Degraded Spacecraft Surfaces Using Reactive Gas Plasmas," AIAA Progress in Astronautics and Aeronautics: Fundamentals of Spacecraft Thermal Design, Vol. 29, The MIT Press, Cambridge, Mass., 1971, pp. 167-185
9. Beverly, W. D., R. B. Gillette and G. A. Cruz, "Removal of Hydrocarbon Contaminant Film from Spacecraft Optical Surfaces Using a Radiofrequency-Excited Oxygen Plasma," AIAA Progress in Astronautics and Aeronautics: Thermal Control and Radiation, Vol. 31, The MIT Press, Cambridge, Mass.,

10. Gillette, R. B., W. D. Beverly and G. A. Cruz, "Active Cleaning Technique for Removing Contamination from Optical Surfaces in Space," Annual Report No. 5, Contract NAS8-26385, D180-14971-1, March 1972, The Boeing Company, Seattle, Wash.
11. Shannon, R. L., R. B. Gillette and G. A. Cruz, "Active Cleaning Technique for Removing Contamination from Optical Surfaces in Space," Final Report, Contract NAS8-26385, D180-17610-1, August 1973, The Boeing Company, Seattle, Wash.
12. Shannon, R. L. and R. B. Gillette, "Active Cleaning Technique Device - Design Study Summary Report," Contract NAS8-28270, D180-15454-1, March 1973, The Boeing Company, Seattle, Wash.
13. Shannon, R. L. and R. B. Gillette, "Laboratory Demonstration Model Active Cleaning Technique Device," Final Report, Contract NAS8-28270, D180-18031-1, March 1974, The Boeing Company, Seattle, Wash.
14. Dushman, S. and J. M. Lafferty, Scientific Foundations of Vacuum Technique, 2nd Edition, John Wiley and Sons, Inc., New York, 1962
15. Venugopalan, M. and R. A. Jones, Chemistry of Dissociated Water Vapor and Related Systems, John Wiley and Sons, Inc., New York, 1969, page 377
16. Shannon, R. L., "Operation Manual for Laboratory Demonstration Model Active Cleaning Technique Device," Contract NAS8-28270, D180-18030-1, March 1974, The Boeing Company, Seattle, Wash.

WALKING IN A ROTATING SPACE STATION: AN ELECTROMYOGRAPHIC AND KINEMATIC STUDY

Randall L. Harris, Sr., Ph.D., *Langley Research Center, Hampton, Virginia*

ABSTRACT

A simulation test program was conducted to investigate the influence of gravity level upon the walking characteristics and patterns of muscular activity in a rotating space station.

INTRODUCTION

The purpose of this report will be to study specifically the area of the biomechanics of locomotion in a rotating environment like that of a space station at various gravity levels. Comparisons were made of the walking gait patterns and the amplitudes of various leg muscle electrical outputs at different gravity levels. The results of these tests should be applicable to planning future space missions by providing a part of the information that will be needed to determine the type of vehicle and the gravity level to be provided for the astronauts if it is decided that artificial gravity is to be utilized.

SIMULATION EQUIPMENT AND TESTS

Simulation Technique

The Rotating Space Station Simulator (RSSS) (Fig. 1) at the Langley Research Center used what has been termed the inclined plane technique to simulate hypogravity levels. What is meant by inclined plane is that the sagittal plane of the test subject is rotated until the fraction of earth's gravity component in the sagittal plane is the level required. In the case of a rotating space station, zero gravity was obtained by a 90° inclination of the test subject relative to the local vertical. The test subject was supported on his side by a series of slings and cables attached to various body members and supported from an overhead boom and trolley (see Fig. 2). With the inclined plane technique, the test subject was limited to three degrees of movement: two linear motions and one rotary motion in the sagittal plane. It was felt that the primary effects on walking patterns would be elicited with this technique. The subject walked in a plane perpendicular to the axis of rotation. One drawback to this simulation was that the earth's gravity still exerted its influence on

the test subject. However, it was acting from side to side on the subject (similar to laying on your side in bed) instead of from head to foot. The test subjects very quickly adjusted to the sideways world and found that their movements became very much like that of walking in earth gravity.

Space Station Simulator

The simulator was a cylinder, 12.2 meters in diameter, of steel framework and plywood wall of 1.8 meters high along the periphery which served as the floor for the test subject (Fig. 1). Artificial gravity was obtained by rotation of the station. The cylinder was rotated by a variable speed 15 horsepower d.c. motor attached to the center shaft of the cylinder through a magnetic clutch. The motor was capable of driving the station at constant angular rates from 0 to 17 rpm, producing a maximum gravity level of two times earth gravity at the outer edge of the station acting perpendicular to the rotation axis. Attached to the center drive shaft was a boom made of aluminum trusses that extended from the center to the edge of the station and was servo controlled by hydraulic actuators to remain directly over the subject as he walked along the station floor. This servo mechanization removed inertia and wind drag effect of the boom from the test subject. The trolley that supported the test subject moved freely along this boom in response to the subject's radial movements.

Subjects and Testing Technique

Eight subjects participated in these tests. They were all healthy male subjects with no known medical problems or history of muscular disorders. They ranged in ages from 23 to 35 years. Their heights ranged from 168 to 183 centimeters and their weights were in the normal range for their heights and ages.

The subjects wore flight coveralls for the tests. Four pairs of Beckman miniature ECG electrodes were placed on the subjects' legs. They were placed in pairs 2 to 3 centimeters apart over the particular muscle of interest and were secured to the skin by adhesive collars. The hair was first shaved off at the skin and then the area was cleaned with rubbing alcohol. The skin resistance at the area of electrode placement was lowered to 1K and 2K ohms.

The test subjects were then taken out to the simulator and goniometers were applied to the hips, knees, and ankles so that their axes of rotation were located over the respective joints. The goniometers were taped to the subjects' legs over the flight coveralls with 5-centimeter-wide adhesive tape. Care was taken that they were not wrapped so tightly that they might cut off the circulation of the blood, yet tight enough to hold the goniometers securely in position. After joint freedom of movement was checked, the test subject was placed into the slings of the simulator and was ready for the testing.

The test subjects performed approximately 40 tests walking at different speeds covering a distance of a little less than 20 meters. The subjects were asked to walk in what they felt to be the most natural manner at each of four gravity levels: 0.17, 0.33, 0.5, and 0.75 times earth gravity. The subjects always walked in the direction of station rotation, a counterclockwise direction when viewed from above. The effective gravity level at the subject's center of gravity varied with his walking speed (Fig. 3). For example, with the station rotating at the 0.5 gravity level and the test subject walking at 2 meters per second the total gravity level on the subject would be 0.96 times earth gravity. It was felt that the increase in gravity level was acceptable for these tests since a similar increase in gravity would be encountered in an actual station of comparable diameter. (A decrease in gravity level would be experienced if locomotion was performed in a direction opposite that of the rotation.) For the remainder of this report the gravity levels mentioned will be that gravity level experienced by a stationary subject in the station.

INSTRUMENTATION AND DATA REDUCTION

All data were recorded on a 14-channel tape recorder at 19 centimeters per second which had a frequency response that was flat (± 3 dB) from d.c. to 3000 hertz.

For comparison purposes, it was desired to record the activity of two pairs of antagonist muscles, the right tibialis anterior and gastrocnemius, and the left biceps femorus and rectus femorus. Four electromyogram amplifier units were constructed that had a frequency response that was flat within ± 3 dB between 5 and 2500 hertz. The output of these amplifiers was recorded on the tape recorder.

The goniometers for measuring joint positions were made of two brass bars each about 12 centimeters long, 2.5 centimeters wide, and 0.5 centimeter thick (Fig. 4). One leg of the goniometer held the potentiometer and the other was fastened to the shaft of the potentiometer. For the ankle measurement, a slight variation was used to allow some freedom of rotation of the ankle (Fig. 5). One leg of the goniometer, which held the potentiometer, was fastened to the lower leg and an aluminum piece was fitted under the arch of the subject's shoe, held on by elasticized strips of Velcro. The aluminum brace was fastened to the shaft of the potentiometer through a fairly stiff spring 1.5 centimeters long. This allowed some freedom of movement of the foot while still being able to record the ankle flexion and extension. The brace was small enough that it was not noticeable under the normal street shoes of the test subject when he stood or walked. The output from each joint position transducer was fed to an amplifier unit similar to the electromyogram signal conditioning units and recorded on the tape recorder.

The velocity of the test subject was assumed to be the same as the velocity of the overhead boom. The output of the boom

tachometer was fed to one channel of the tape recorder. Movies of the test subject taken during some of the tests from a camera located on the overhead boom showed that the boom indeed tracked the subject so that its speed gave a good estimate of the subject's walking speed.

Digital Computer Analysis

Position Data—The recorded joint position data were converted to digital formatted data with a sample rate of 100 samples per second for analysis on a digital computer. A linear curve was then fitted to the peak-to-peak fluctuations of position versus walking speed by the method of least squares for each gravity level and test subject. A linear curve was selected because the data appeared linear and since it was desired to check for gross changes in the walking gait, a linear curve would show this even though the true relationship might be slightly complex. A mixed three-way analysis of variance was then performed on the slope and intercept coefficients of the fitted curve. Two factors and one interaction factor could be tested for their effects on the mean values of slope and intercept: gravity level, side of test subject (left and right), and the interaction of gravity and side factors.

Electromyogram Data—The electromyographic data were treated in a little different manner. The recorded electromyogram signals were played back through an analog computer that full wave rectified and low pass filtered the signals. This filter arrangement would take a sine wave signal and convert it into a d.c. signal whose amplitude would be proportional to the amplitude of the sine wave input signal. The sine wave signal input and output waveforms are shown graphically in Figure 6. The output looks somewhat like the typical isometric muscle tension response of a muscle to a train of supermaximal stimuli. This signal and the walking velocity were converted to digital formatted data at a sample rate of 100 samples per second for subsequent computer analysis.

The observation has been made by other investigators that the special filter arrangement used in these tests should only be used under isometric conditions (Ref. 1) because a change in muscle length causes a change in the amplitude of electromyogram. However, this filtering technique should provide a good indication of relative activity where there is a pattern of movement such as in walking, as well as changes in relative amplitude or phases of muscular activity.

The specially filtered electromyogram signals were analyzed by finding the average amplitude for each test walk. This average was not a conventional time average but an average over the accumulated activity time of the particular muscle. A linear curve was fitted to this average electromyogram amplitude versus walking velocity by the method of least squares for each subject at each gravity level. The linear curve was used for the electromyogram

data analysis for the same reasons listed for the joint amplitude analysis. A mixed two-way analysis of variance was performed on the slope and intercept coefficients of the fitted curves to determine if there were significant differences in their average value due to a change in gravity level.

RESULTS

Limb Positions

Typical time histories for hip, knee, and ankle positions are shown in Figure 7. When the oscillatory amplitudes of these time histories are plotted against the walking velocity, a straight-line relationship is observed for each of the three joint positions. The line of least squares had a correlation coefficient that was generally better than 0.75.

The average amplitude of hip rotation for one test subject is shown in Figure 8 plotted against the walking speed. This same type of linear relationship was exhibited for all three joint positions for all test subjects at all gravity levels.

The intercept of the fitted straight lines does not pass through the origin for each of the three joints. Therefore, both the slope and the intercepts will be analyzed with a mixed three-way analysis of variance test (ANOVA). The average slopes and intercepts for each joint are plotted against the simulated gravity level in Figure 9.

As determined by the ANOVA test, the only factor affecting the average linear increase of hip position with walking velocity was the sides of the test subjects ($p < 0.05$). All of the other factor levels were not significant. It would not be expected a priori that the left side would have a greater slope than the right (0.31 versus 0.25). This difference would most likely indicate an influence of the simulator and, perhaps, the suspension system of the legs. This will be discussed in more detail later. The average slope of the hip position versus velocity was 0.28 radian per meter per second.

The zero velocity intercept of the hip position amplitude, however, showed a significant variation ($p < 0.05$) with gravity level. This means that a constant increase in hip position amplitude at all walking speeds is caused by an increase in gravity level.

The slope of the knee amplitude of oscillation with respect to velocity was affected by none of the factor levels that could be tested. The average value of the slope of knee amplitude with walking velocity was 0.15 radian per second per meter per second. The ANOVA test showed a significant difference in average knee oscillation amplitude intercept due to sides ($p < 0.05$), the right side was greater than the left side. The average intercept of the knee position amplitude was 0.82 radian. Figure 9 also shows the slope and intercept of the knee plotted against simulated gravity level. The slope and intercept of the knee position are not influenced by gravity level.

The slope of the ankle oscillation amplitude versus walking velocity and the intercept did not vary significantly with gravity level or sides according to the ANOVA test. The average slope of ankle position amplitude was 0.26 radian per meter per second and the average intercept was 0.36 radian.

Electromyogram

The average amplitude of the specially filtered electromyographic signals were averaged and plotted against walking velocity. These average amplitudes also exhibited a monotonic increase with walking velocity. The least-square slopes and intercepts of these data for the different test subjects and gravity levels were analyzed in a mixed two-way analysis of variance (ANOVA) test for the four muscles studied in these tests. Typical time histories of the specially filtered electromyograms of the rectus femorus, biceps femorus, tibialis anterior, and gastrocnemius muscles are presented in Figure 10 which will be referred to later in the discussion.

Biceps Femorus—Although the ANOVA test did not show a significant effect of gravity level on either the slope or the intercept of the biceps femorus electrical output, it will be noted in Figure 11 that the slope of the biceps femorus electrical output does show a small average increase with gravity level.

Rectus Femorus—The ANOVA analysis showed that the gravity level affected both the slope ($p < 0.05$) and intercept ($p < 0.05$) of the rectus femorus electrical output. Both the slope and intercept showed a slight increase with increase of gravity levels (Figs. 11 and 12), doubling over the range of gravity levels simulated.

Gastrocnemius—The ANOVA test indicated that the slope of the gastrocnemius electrical output with respect to walking velocity was significantly affected by the gravity level ($p < 0.05$). Figure 11 does show a linear increase in the slope with gravity level, increasing by more than a factor of 2 over the gravity levels simulated. The intercept of the gastrocnemius electrical output had only a slight indication of variation with gravity level ($p < 0.25$). In fact, the graph in Figure 12 shows no overall consistent tendency for the intercept to increase or decrease with gravity level. These tests tend to agree with those of Mitarai (2) who noted that while a subject was standing the amplitude of the gastrocnemius electromyogram reduced as the simulated gravity level decreased. The gravity level was simulated by immersing the subject in various levels of water using the buoyant force to reduce the subject's apparent weight supported on his legs.

Tibialis Anterior—The average slope of the tibialis anterior electrical output versus walking velocity as indicated by the

ANOVA test showed only a slight chance of change ($p < 0.25$) due to gravity level change. In Figure 11 the slope is seen to have a definite increase with gravity level, increasing almost by a factor of 3 over the range of gravity levels simulated. The ANOVA test also showed that the average intercept of the tibialis anterior electrical output varied significantly with gravity level changes ($p < 0.25$). It looks as if the electrical intercept (Fig. 12) decreases only slightly as gravity level is increased. For all practical purposes, the changes in the intercept of the electrical output of the muscles were small enough to be ignored.

DISCUSSION

Muscle Phasing

This discussion will be concerned with the phasing of muscle involvement in gait patterns as observed in these hypogravity tests. The muscle phasing discussion will be qualitative in nature since no data analysis was performed. Many plots of filtered electromyogram and leg position were observed on microfilm and the following discussion is based on these observations. Typical time histories of the rectus femorus, biceps femorus, tibialis anterior, and gastrocnemius filtered electromyogram are presented in Figure 10 and should be referred to during this discussion along with Figure 7. The muscle patterns were consistent in all gravity levels and at all walking speeds.

Biceps Femorus—The biceps femorus muscle showed only one period of activity during a stride cycle. The activity period began during the forward swing of the hip, reaching a peak before the heel of that leg touched the ground and ending almost at the instant of heel touchdown. This agrees with results of Inman et al., 1953 (1), and Liberson (3).

Rectus Femorus—The rectus femorus functioned with two periods of activity during a stride. The first period of activity began as the hip was about to reach its full extension and lasted through the start of the flexion of the hip. This activity would seem to be involved with initiating the forward swing of the hip. The second peak occurs shortly after heel touchdown during the smaller flexion of the knee. The rectus femorus tends to restrict this secondary knee flexion and extends the knee joint to the standing position, thus helping to absorb the shock associated with placing the foot on the ground. This agrees with the phasing described by Inman et al. (1).

Gastrocnemius—The gastrocnemius was singly peaked during each walking stride. The peak activity occurred shortly before ankle extension or about the time of heel off and ended just before toe off. This was the same pattern shown by Inman et al. (1), and Liberson (3). This gastrocnemius activity also parallels the

activity pattern outlined in the eight phases of the human gait as presented by Schwartz (4).

Tibialis Anterior—The tibialis anterior seemed to be doubly peaked during a stride cycle, however, this did not appear consistently in all runs. The most predominant peak occurred after heel touchdown as the ankle was being extended due to the heel touchdown. This activity is probably a reflex pattern for the gait because of the sudden presumably passive extension of the ankle after heel touchdown. This action of the tibialis anterior would try to oppose the extension of the ankle at this instant. A second peak sometimes would be associated with the dorsiflexion of the foot after toe off and during the forward swing of the hip. It would usually carry over to the first peak mentioned above. Inman (1) also shows this second peak as being of very small amplitude compared to the other peak. The activity of the tibialis anterior followed the phases described by Schwartz (4). However, he did not show that the activity at heel touchdown was of greater amplitude.

Joint Position Amplitude

There were two primary factors involved in the variability of the human gait. Obviously, the test subject is one of the influencing factors on the gait characteristics each having differing leg lengths and slightly different idiosyncrasies. The second factor, which has not received the attention that it should have in the past, is the speed of locomotion. The hip, knee, and ankle joint amplitudes of oscillation increased monotonically with walking speed. This increase appears to be a linear function of walking velocity. Therefore, in order to get a more accurate estimate of the human gait characteristics this effect should be taken into account, otherwise the amount of variation in the data will be much larger than that due to the test subjects alone. More extensive tests should be made in earth gravity to delineate the exact nature of this variation with walking speed.

Simulator Effects

It was previously stated that the side of the subject influenced the average values of the slope of the amplitude of hip oscillation (left greater than right) and knee and ankle intercept (right greater than left).

Several factors taken together might cause the test subjects to overreact and cause the observed effect on his position, however, the alinement of the subjects might cause each leg to share the support weight unevenly. Special care was exerted to try to verify that the subjects looked all right and felt all right while suspended in the slings. One clue that the weight was shared unevenly is given by the amount of secondary knee flexion occurring during heel-floor contact. In fact, the left side secondary

knee flexion was higher. These differences from side to side were less than 5 percent of the total oscillation amplitude and for the purposes stated in this report they could be considered negligible. It is, however, interesting that these differences could be detected. No one has indicated thus far that there are not differences in the amplitude of oscillation of various subjects in which case it would not be a limitation of the simulator.

Subjective Observations

The subjects very quickly adapted to the rotating environment and were able to walk at any of the gravity levels with no effort or seemingly no required learning. The consensus of the test subjects was an expressed preference for either the one-third or one-half-earth-gravity level. The one-sixth-gravity level was too low for satisfactory walking in the direction against rotation which caused an extremely low gravity level hindering the subject's ability to come to a stop. If the walking speed exactly matched the rotating speed, the subject could lose all traction and float away from the floor. The three-fourth-gravity level was considered too great for walking, especially with the short radius of the simulator because it caused a change in gravity level with walking speed and with the rotation of the legs that was more noticeable than at the other gravity levels. This caused an uncomfortable feeling in the legs while walking, as if lead weights were added to them and gave the subjects a false indication of the gravity level.

In the pretest practice sessions the subjects walked on a 2.5-meter section of the RSSS floor which was straight. Walking on the first half was like walking up hill and on the last half was like walking down hill. These feelings were because the artificial gravity vector was perpendicular to the straight floor only at its middle and farther from perpendicular the farther the distance from the center of the straight portion of the floor. Walking along the regular curved floor section felt as if one was walking through the bottom of a gully only it continued with each step. After a while this feeling of continuous walking through a gully diminished and probably given sufficient time it would not be noticeable.

CONCLUDING REMARKS

The joint position data indicate that the gait of locomotion in a simulated rotating space station was hardly affected by the gravity level. The subjects preferred a gravity level of either one-third or one-half earth gravity. The electromyograms showed that the pattern of muscular usage remained unchanged for all gravity levels, however, the amplitude decreased with decreasing gravity level. This would seem to indicate a reduced effort and metabolic cost of locomotion at reduced gravity levels. Thus the final decision as to gravity level would probably be determined

by other factors than having to design for an environment suitable for locomotion since a subject should be able to adjust easily to a wide range of gravity levels.

REFERENCES

1. Prosthetic Devices Research Project, Institute of Engineering Research, University of California, "The Pattern of Muscular Activity in the Lower Extremity During Walking," A presentation of Summarized Data to the Advisory Committee on Artificial Limbs, National Research Council, at University of California, Berkeley, California, September 1953. Series II, Issue 25.
2. Mitarai, G.; Mano, T.; Mori, S.; and Jijiwa, H., "Electromyographic Study on Human Standing Posture in Experimental Hypogravic State," The Ninth International Symposium on Space Technology and Science, pp. 1135-1142, 1971.
3. Liberson, W. T., "Biomechanics of Gait: A Method of Study," Arch. of Phys. Med. and Rehabil., 46: 37-38, 1965.
4. Schwartz, R. P.; Trautman, O.; and Heath, A. L., "Gait and Muscle Function Recorded by the Electrobasograph," J. Bone and Joint Surg., 18: 445-454, 1936.

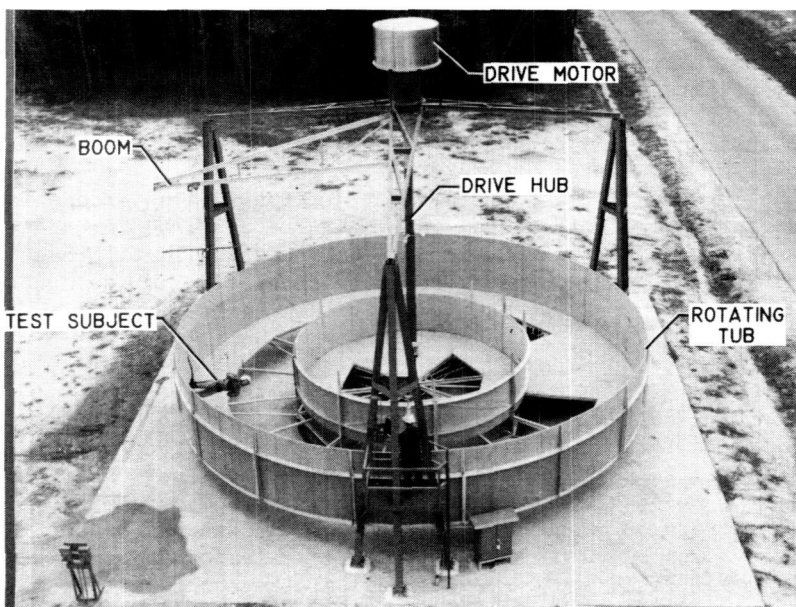


Fig. 1—Overall view of the Langley Rotating Space Station simulator

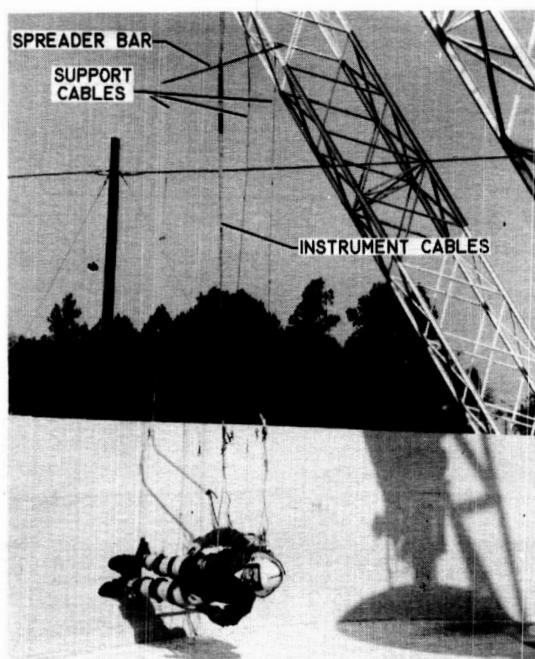


Fig. 2—An overall view of the test subject and the support system

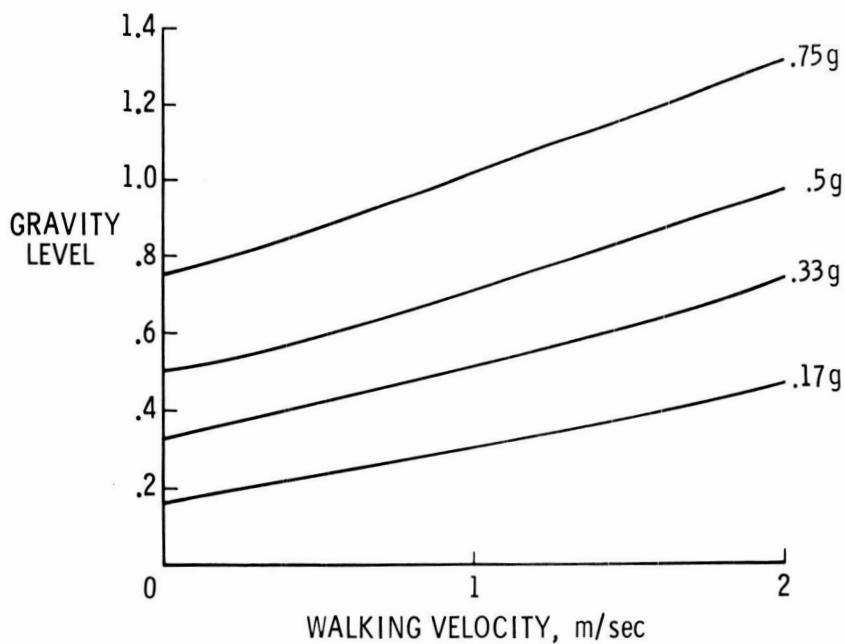


Fig. 3—Variation of simulated gravity level with walking velocity at the test subject's center of gravity

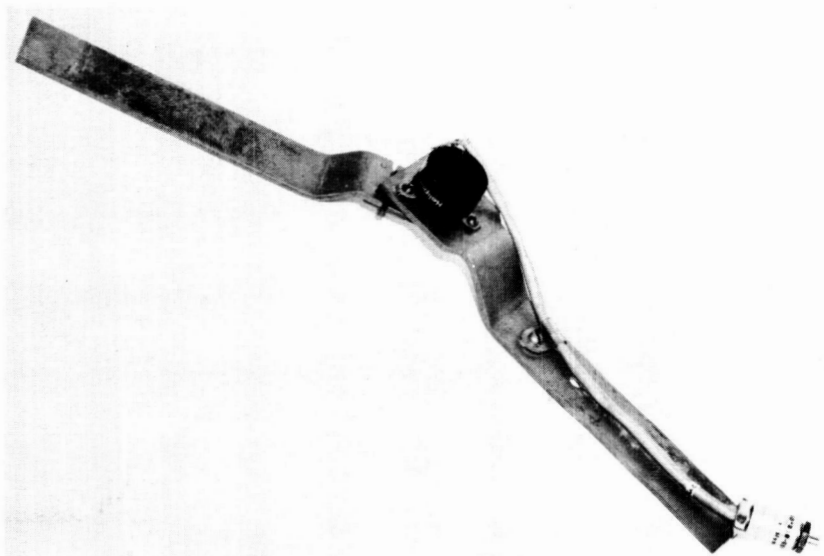


Fig. 4—Hip and knee goniometer

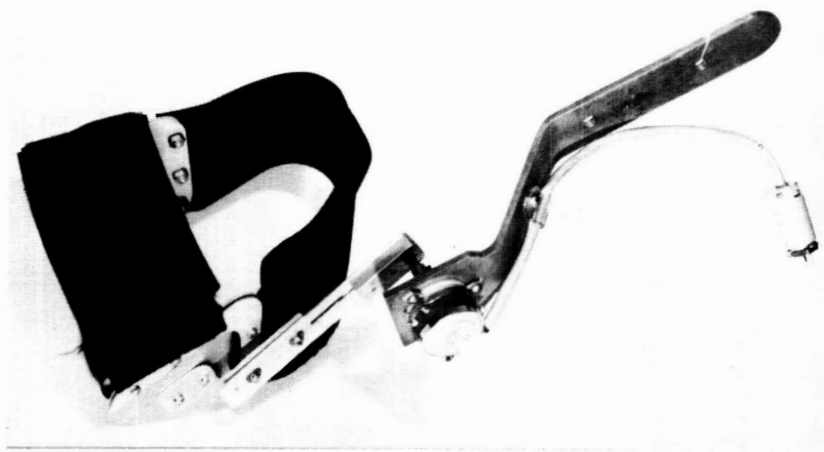


Fig. 5—Ankle goniometer

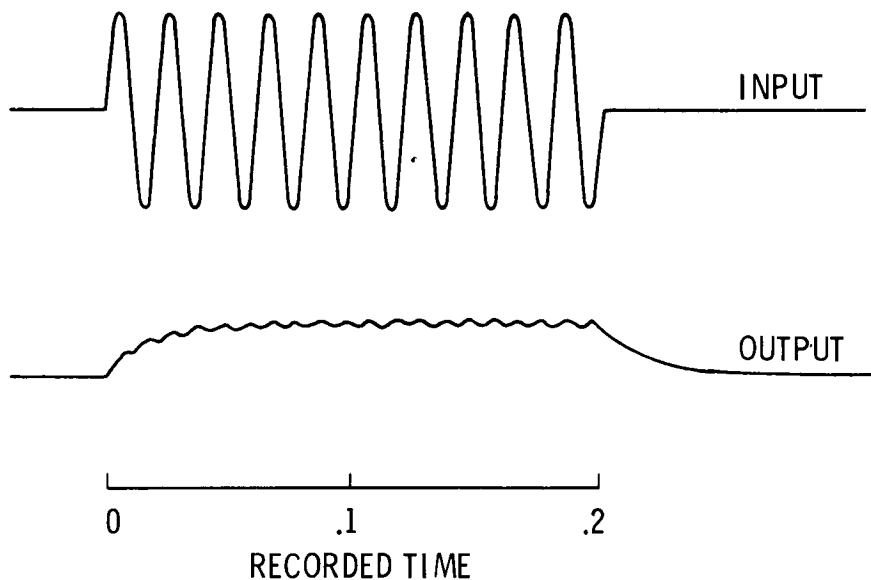


Fig. 6—Input and output of electromyogram filter

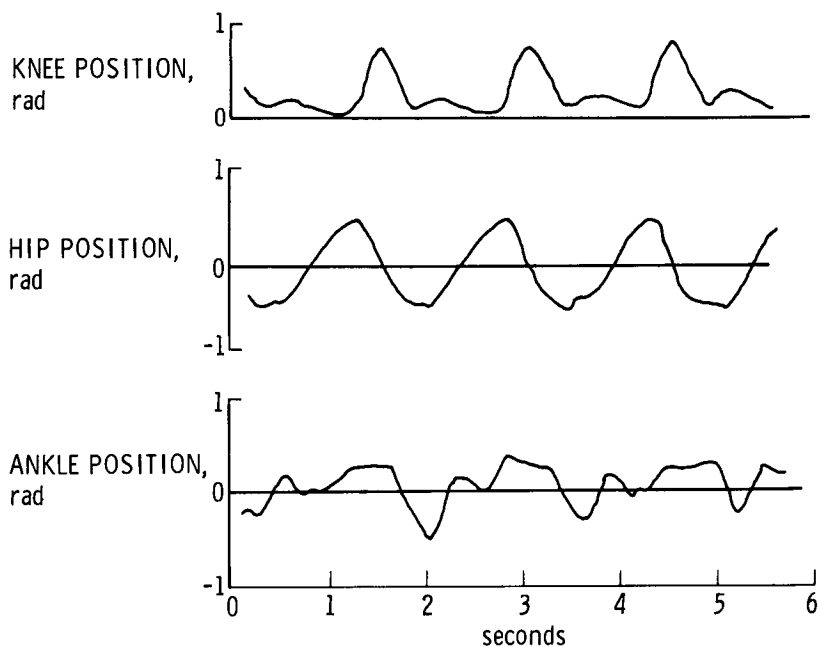


Fig. 7—Typical time histories of leg joint positions
(knee, hip, and ankle)

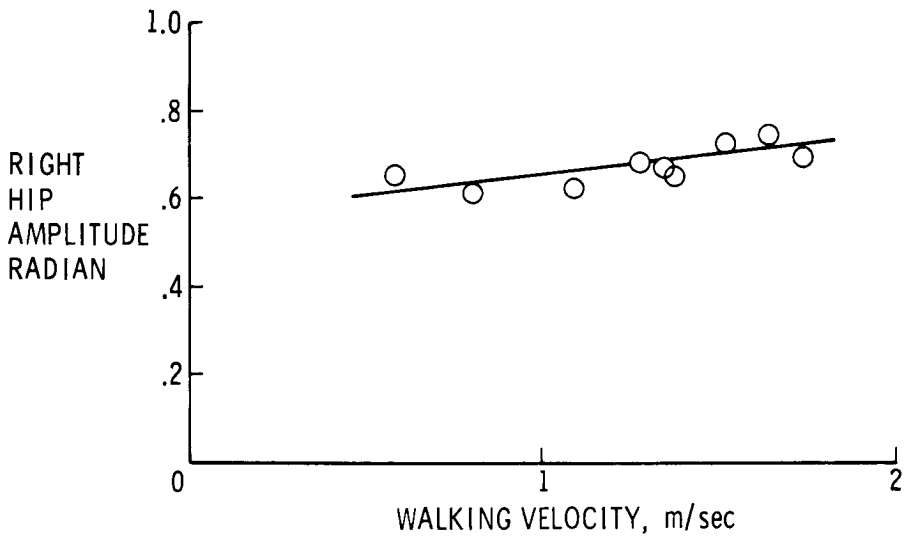


Fig. 8—Right hip position amplitude of oscillation at various walking velocities for test subject EL during three-fourth earth gravity tests. The slope for this test subject was 0.09 radian per meter/sec with a correlation coefficient of 0.86

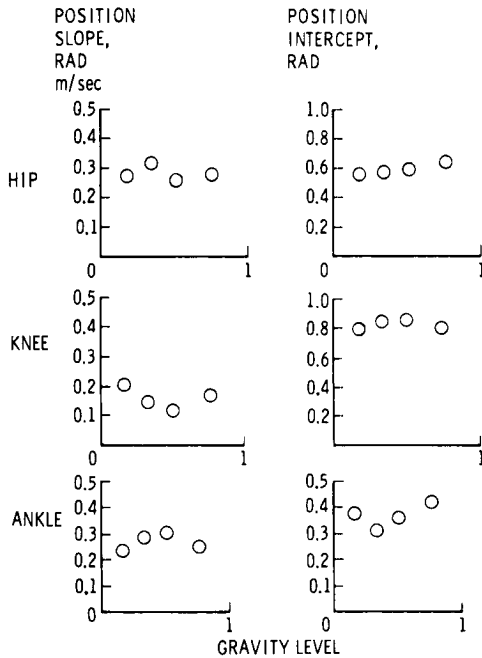


Fig. 9—Variation of straight line coefficients with gravity level

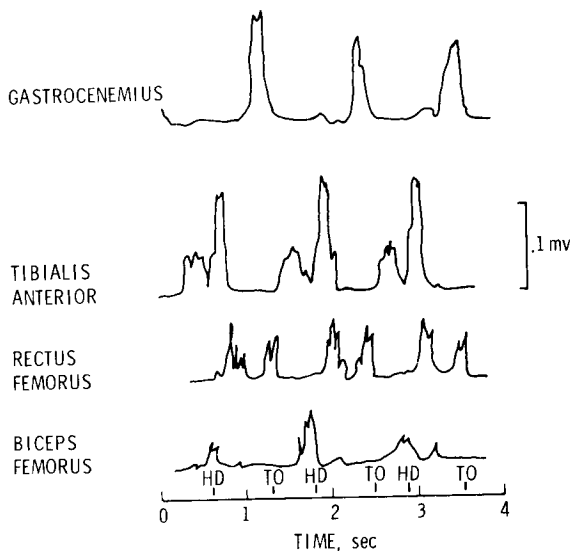


Fig. 10—Typical time histories of the biceps femorus, rectus femorus, tibialis anterior, and gastrocnemius filtered electromyograms. HD stands for the time at which the heel touches the ground and the TO represents the time at which the toe lifts off the ground

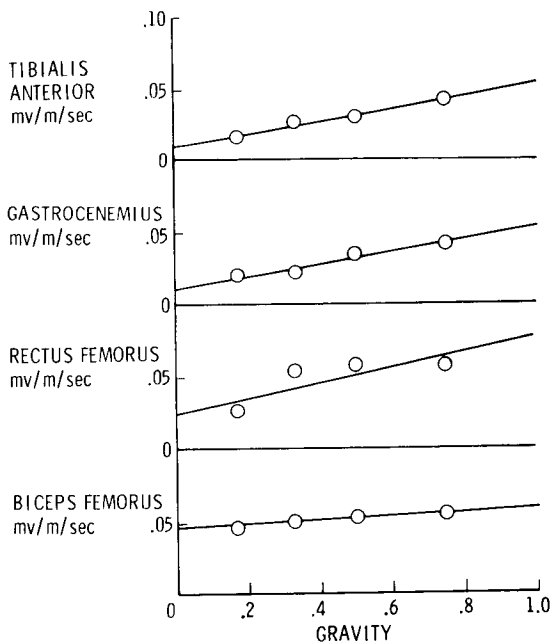


Fig. 11—The average slope of the four filtered electromyogram outputs with respect to walking velocity at various simulated gravity levels

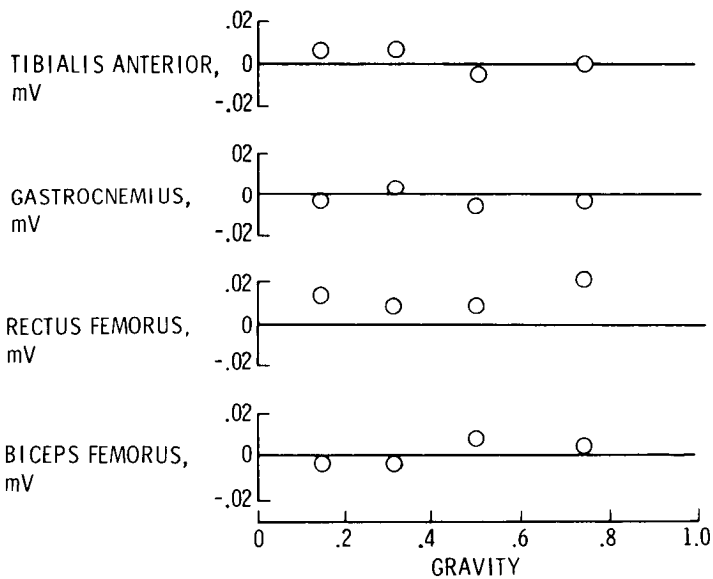


Fig. 12—The average outputs of the four filtered electromyograms extrapolated to zero walking velocity for various simulated gravity levels

COMPARISON OF TWO METHODS OF PREDICTING CHARACTERISTICS OF AN ORGANISM WHICH DEVELOPS UNDER THE CONDITION OF FREE FALL

A. H. Brown, A. O. Dahl, D. K. Chapman, and L. Loercher, *Plant Centrifuge Laboratory, University City Science Center and Biology Department, University of Pennsylvania, Philadelphia, Pa.*

ABSTRACT

Five morphological characteristics of Arabidopsis thaliana were measured on plant populations grown under continuous centrifugation. In separate tests different g-levels were used. For each character studied a linear g-function was calculated and extrapolated to zero-g. In other tests Arabidopsis plants were grown on horizontal clinostats after which the same set of characters was measured. Growth on a clinostat might simulate growth at zero-g. However, the zero-g predictions by the two methods did not agree consistently. The results were significantly different for three of the five characters for which comparisons were made. Therefore either the extrapolation method or the clinostat method should be considered unreliable as a means of predicting plant growth characteristics in the weightless environment of an earth satellite laboratory.

INTRODUCTION

Higher plants contain sensitive localized, bioaccelerometers with which they are able to sense the gravitational acceleration vector. They also employ transduction and internal communication devices which enable them to respond readily to environmental information supplied to them from their g-sensors. By processing that information plants can respond through differential growth (geotropism) within minutes and over longer periods they can use the information to control in part tissue differentiation and organ development (morphogenesis).

Plant physiologists have investigated intensively some of the responses which plants exhibit as a consequence of diverse gravitational stimulations. Most experimentation has concentrated on the nearly ubiquitous "righting reaction" (geotropic response)

when test plants were inclined from the vertical. Many studies have employed clinostats and a smaller number have reported on the use of centrifuges to alter the gravitational environment of the experimental organisms. However, it has been the inevitable consequence of earth-bound biology that in all such experimental manipulations of the g-vector direction or intensity the ideal control situation -- zero g-input -- has not been attainable in an earth laboratory.

Now that we have the technical capability to perform biological experiments in a satellite laboratory, it has become possible to study plant morphogenesis under essentially zero-g conditions. Several exploratory experiments of that nature have been proposed. Our laboratories are developing just such an experiment in which we plan to examine the morphology of plants grown from seed to maturity in earth orbit. In the course of background studies relating to that research and development project we have attempted to predict some of the characteristics of plants which, for the first time in their evolutionary history (perhaps ca. 10^6 years), individuals of the test species will have developed without significant inputs of g-vector information. We considered two ways, different in principle, by which such predictions could be approached. We tried both methods and compared the results.

MATERIALS AND METHODS

Experimental Organism

Our choice of a test organism was Arabidopsis thaliana (L.) Heynh., a member of the mustard family, the same species we are planning to use in flight experiments. Grown aseptically on nutrient agar gel under our culture conditions the life cycle is about three weeks. Its unusually short generation time has made Arabidopsis a favorite for plant genetic experiments and that also was partly responsible for our choice of this plant for the study of morphogenesis at zero-g.

The seed stock was traceable to Prof. G.P. Redi, Univ. of Missouri, and was derived from an Arabidopsis strain identified as 294-187-F. In all experiments reported here seed from the same harvest was used. It was stored at 2°C until needed. Although our studies extended over a 26-month period, periodic tests of the seed lot's germination and growth potential provided assurance that no significant deterioration had occurred during that interval.

Plants were grown in individual Pyrex glass

modules at $24^{\circ} + 1^{\circ}$ C under continuous illumination from Sylvania Wide Spectrum GroLux fluorescent lamps. The energy incident on the plants was $6.1 \pm 0.5 \times 10^3$ erg cm² sec⁻¹ which corresponded to 150 foot candles. Light intensity was monitored with Clairex CL605 photoconductive cells and was maintained within 5% of the nominal 150 foot candle level throughout each test. Further details of the experimental conditions and procedures can be found in a NASA Contractor's Report (1).

Experiments using protracted centrifugation.

Measurements of plant development at g-levels above unity were carried out with the 17.6 meter diameter "Biosatellite Centrifuge" at the NASA Ames Research Center. The centrifuge was operated continuously for the three-week period of test plant growth. In separate tests three different centrifuge rotation rates were used. The *Arabidopsis* plant modules were located in compact arrays at appropriate distance from the center of rotation (between 2m and 8.5m radius). Useful data were obtained at g-levels: 1,2,4,6,8,16 and 20. For each g-level above one about 24 plants were included in our measurements.

At the conclusion of each 21-day test the plants were chemically preserved by flooding each plant module with a solution of cytological fixative. This procedure was carried out as rapidly as possible after the centrifuge had been stopped. Later a number of morphological endpoints of development along with various cytological characters were measured on each plant in the populations of test material representing the results of growth at several different g-levels.

On the assumption that it may be valid to extrapolate the g-function of any morphological character of *Arabidopsis* to its value at zero-g, it was possible to arrive at a quantitative prediction of that character for a plant to be grown in the condition of weightlessness. Therefore, it can be argued that the extrapolation method should provide a reasonable basis for estimating what may occur during a space experiment.

Experiments using clinostats.

In principle a clinostat is a turntable which slowly rotates the plant about its longitudinal axis. It has been used in plant physiological studies for about a century. We used horizontal clinostats which maintained the axis of each rotating plant at an angle of 90° to the plumb line. The rotation rate was 0.5 rpm. Since the minimal time interval for plants to

show a detectable geotropic or righting response to lateral g-vector stimulation is of the order of a few minutes (at one g), the plants' accelerometers would experience essentially omnilateral stimulation over each two-minute interval. On such a clinostat the plant shows no tendency to depart from its horizontal orientation, although the modified g-stimulation does result in certain behavioral and developmental aberrations. Various authorities have referred to the condition experienced by a plant on a clinostat as "gravity compensation" (2) and others have stated that the clinostat effectively simulates the condition of free fall (weightlessness) (3,4,5).

RESULTS

Five gross morphological characters were chosen for the present comparison. These included leaf size and number, plant height, and length of the hypocotyl. The sets of measurements of these characters obtained from experiments with plants on the centrifuge were used to calculate by the method of least squares the best fitted linear function relating each character to the resultant g-force at which the plants were grown. Table I, columns I and II show the results of those calculations.

It is immediately evident that none of the regression lines had a very steep slope; i.e., the g-level was not an important determinant of the value of any of the characters we measured.

Column III of Table I gives the value of each g-function extrapolated to zero. The indicated standard errors for the respective values were calculated according to Ezekiel (6).

The alternative method for predicting zero-g characteristics of an Arabidopsis plant by the use of the clinostat gave the results shown in column IV of the Table. For certain characters the mean measurement of a clinostated population differed substantially from what was obtained when test plants were in the normal, upright, stationary position; however, the significant comparisons for our present purpose are those between values obtained on clinostated plants (column IV) the extrapolated values at zero-g from the centrifuge tests (column III). When those comparisons were made, predictions by the two different methods disagreed significantly for three of the five morphological characters which were considered.

DISCUSSION AND CONCLUSIONS

We undertook to compare the two methods for

TABLE I. RELATIONS BETWEEN EXTRAPOLATED VALUES OF MORPHOLOGICAL CHARACTERS OF ARABIDOPSIS GROWN OVER A RANGE OF G-LEVELS, COMPARED WITH VALUES OBTAINED FROM PLANTS GROWN ON HORIZONTAL CLINOSTATS.

Morphological Character	Data From Plants Grown on the Centrifuge Over a Range of G-Levels			Data From Plants Grown on Horizontal Clinostats		Significance of Difference (III-V)
	I	II	III	IV	V	
	no. of measurements	Regression coef.	Value by extrapolation to zero-g	no. of measurements	mean value	probability that difference was due to chance alone
Leaf length, mm	584	$-.044(\pm .016)^1$	$10.41(\pm .15)$	105	$8.12(\pm .30)$	$< 0.01\%$
Leaf blade width, mm	584	$-.009(\pm .003)$	$2.82(\pm .03)$	105	$2.47(\pm .09)$	$< 0.02\%$
Number of leaves	117	$-.016(\pm .012)$	$5.79(\pm .11)$	21	$5.43(\pm .23)$	NS ²
Hypocotyl length, mm	117	$+.035(\pm .028)$	$4.58(\pm .28)$	21	$5.93(\pm .35)$	$< 0.3\%$
Flower stem length, mm	117	$+.226(\pm .270)$	$45.94(\pm 2.31)$	21	$34.0(\pm 6.6)$	NS

¹

Numbers in parenthesis are standard errors.

²

NS = not significant; probability $\geq 5\%$

predicting properties of a plant grown in an artificial satellite without having any convincing reason to believe either method must be valid. Nevertheless, if the predictions obtained by both methods had coincided, we might have been somewhat encouraged to feel that the predicted characters of a plant to be grown under true weightlessness might not be entirely irrational. We should then have been even more eager to learn the results of our satellite experiment to determine whether those predictions were confirmed.

We did not attempt to bias the result by selecting only some morphological characters and not others; we used what data we had from the three separate tests with the A.R.C. Biosatellite Centrifuge and all the clinostated control plants which were grown at the same time as were those on board the centrifuge.

In view of the lack of agreement between the two predictive methods we believe it would be conservative to conclude that one or the other method must be unreliable for predicting the morphology of a plant cultured at zero-g. In fact, it may turn out that neither method will prove valid. Confirmation will be furnished only when comparable results have been obtained from plants grown in an orbiting satellite.

REFERENCES CITED

- (1) Brown, A.H., A.O. Dahl, and L. Loercher. 1974. Effects of prolonged acceleration with or without clinostat rotation on seedlings of Arabidopsis thaliana (L.) Heynh. Laboratory Report ARCENT-1, 32 pp + 9 Figs., 31 July 1974.
- (2) Gordon, S.A. 1964. Gravity and plant development: bases for experiment. in Gilfillan, F.A. (ed.) Space Biology - Proceedings of the Twenty-Fourth Annual Biology Colloquium. Oregon State Univ. Press, Corvallis. pp 75-105.
- (3) Anon. 1970. Space Biology. Report of study convened by the Space Science Board (Santa Cruz, Calif., 1969), National Academy of Sciences, National Research Council, Washington, D.C.
- (4) Lyon, C.J. 1968. Growth physiology of the wheat seedling in space. Bioscience 18:633-638.
- (5) Lyon, C.J. 1968. Wheat seedling growth in the absence of gravitational force. Plant Physiol. 43: 1002-1007.
- (6) Ezekiel, M. 1941. Method of Correlation Analysis. 2nd Edition, John Wiley & Sons, New York. Vide pp 128-158 and pp 312-340.

Research supported by NASA grants NGR 39-010-104 and NGR 39-030-010 and contracts NAS 2-2432 and NASW-2208.

A THERMAL VACUUM—UV SOLAR SIMULATOR TEST SYSTEM FOR ASSESSING MICROBIOLOGICAL VIABILITY

Dennis S. Ross, Michael D. Wardle and Daniel M. Taylor, *Jet Propulsion Laboratory, California Institute of Technology, Pasadena, California 91103*

ABSTRACT

Microorganisms were exposed to a simulated space environment in order to assess the photobiological effect of broad spectrum, non-ionizing solar electromagnetic radiation in terms of viability. A thermal vacuum chamber capable of maintaining a vacuum of 1.33×10^{-4} n/m² and an ultraviolet rich solar simulator were the main ingredients of the test system. Results to date indicate the system to be capable of providing reliable microbiological data.

BACKGROUND AND INTRODUCTION

The effect of monochromatic ultraviolet radiation on microorganisms has been intensively studied by numerous workers. However, data is sparse on the effect of broad spectrum solar electromagnetic radiation (wavelengths ranging from the vacuum UV through the infrared) on microorganisms irradiated under thermal vacuum conditions approximating those seen by a craft in space. Such data is of interest in light of planetary quarantine constraints that may be imposed on a spacecraft.

The aim of Planetary Quarantine is to prevent the introduction of terrestrial life forms to planets of biological interest where such could interfere with the scientific objectives of present or future missions. The space simulation system under discussion was designed to provide representative, near Earth, Mars and Jupiter thermal vacuum-solar electromagnetic radiation environments; thus enabling the generation of microbiological data that would facilitate the determination of planetary quarantine requirements for a mission.

The viability of microorganisms in a space environment has been of concern to microbiologists since the initiation of recent space programs. Since we at JPL have been primarily concerned with one-way space journeys, by unmanned spacecraft, to planets within the local solar system, it has not been possible to measure the die-off rate of microorganisms that have "stowed away". Retrievable balloon flights (Ref. 1), as well as manned probes (Refs. 2 and 3), have returned experimental samples of various organisms exposed to the solar electromagnetic radiation of space; however, these studies have not lent themselves to the experimental manipulation achievable through ground based simulations.

Our main object then was to provide a chamber of suitable dimensions, capable of maintaining a clean vacuum, in which we could expose microbial samples to representative solar electromagnetic space environments.

Method of Procedure

1. Vacuum Chamber

The vacuum chamber (Fig. 1) used in this study had a 30" diameter and was 80" long. Its function was to provide the required vacuum (1.33×10^{-4} n/m²) and, in combination with the microbiological test fixture, temperature (-125 to +70°C) conditions.

A closed cylindrical copper shroud (27" diameter and 70" long) was positioned within the chamber. The shroud was plumbed to accept LN₂ and painted black: all to enhance deep space environmental simulation. To facilitate thermal isolation, the shroud rested within the chamber on Teflon standoffs. In operation, the shroud temperature was -185°C.

Utilities were fed to their respective inputs. LN₂ to the temperature control system and baffles for the diffusion pumps. Water for diffusion pumps and accessory cooling. GN₂ for backfilling the chamber and purging water lines. Electricity for chamber and accessory operation. All items were carefully monitored for safety aspects and flow control.

2. Solar Simulator

The solar simulator (Fig. 2) provided a uniform light intensity ($\pm 2\%$) of 0.1 to 1.0 solar constant over a 12" diameter target plane located 30" from the vacuum penetration lens. A solar constant was defined as a beam intensity, at the plane of irradiance, of 0.54 mW cm^{-2} in the wavelength interval from 200 to 270 nm.

The simulator was of a closed cabinet design and purged constantly with dry filtered GN₂ at a rate of 2 SCF/hr. Because of the nitrogen purge, no oxygen was

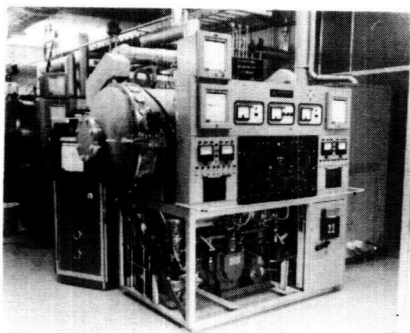


Fig. 1—Thermal vacuum system

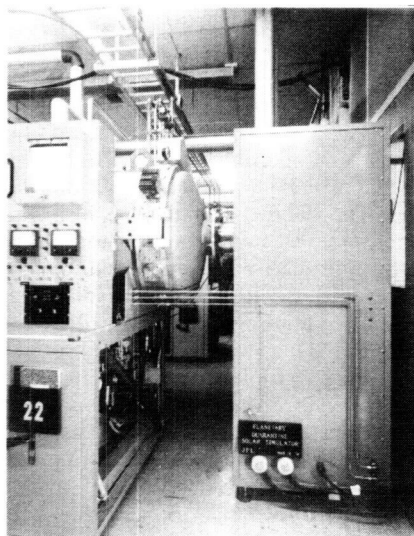


Fig 2—Solar simulator

present and therefore no ozone was ever produced. The radiant energy was produced by a Hanovia 2.5 kW xenon compact short arc lamp; because of the UV requirement it had a Suprasil quartz envelope to permit UV transmission.

Intensity control of the beam was accomplished with a variable fan shutter mechanism placed between the lamp and the turning mirror (Fig. 3). With the output of the lamp set at a constant current of 60 amps, the angle of the 12 bladed "pie" shutter was varied to obtain all of the required intensities. The uniformity was obtained by passage of the beam through a water-cooled, double integrator system consisting of nineteen Suprasil elements in each cluster. The beam douser was located between the optical integrator assemblies, and downstream of the photo-cells that were used for sensing beam output for servo control of the variable shutter.

The separate elements of the optical integrator focused at slightly different locations at the target plane. Therefore, to bring all images into coincidence, a "tipping lens" was installed after the integrator assembly. It was this lens that formed the vacuum interface seal for the chamber adapter flange. This lens, as with the integrator elements, was made from Suprasil Quartz.

3. Test Fixture and Temperature Control

The target area within the vacuum chamber was set at a distance of 30" from the vacuum flange interface. This distance gave a beam diameter of 12" with an incident beam half angle of 27° . Since the chamber is some 80" in length, and chamber access is from the opposite end to the solar simulator position, fixture mounting could be made quite difficult. In order to overcome the long reach into the chamber, and also allow for flexibility for other test sample distances, an optical

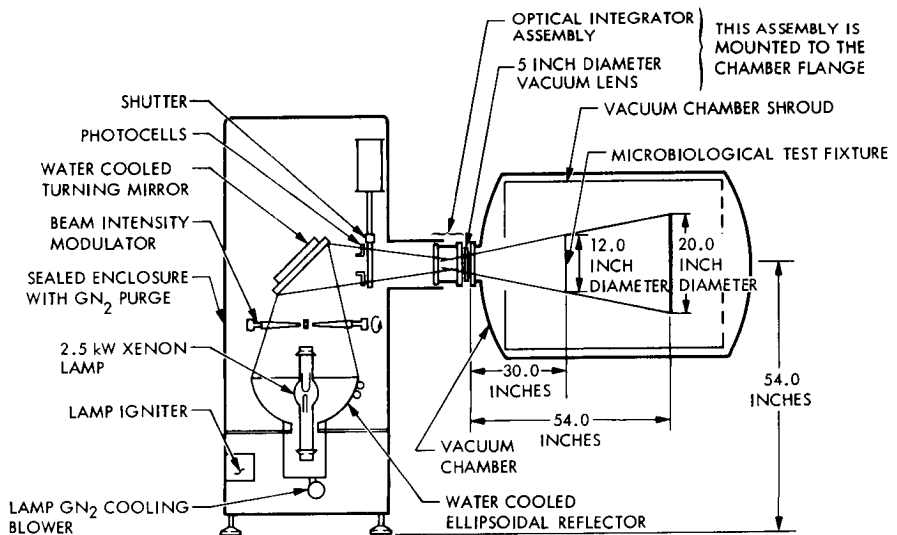


Fig. 3—Schematic of UV solar simulator

bench type of run was installed (Fig. 4). The run consisted of two stainless steel tubes, each 2" D., running the length of the chamber and a little over 8" apart.

A tiltable platform on which the test fixture could be easily mounted and slid along the runners was made on an A-frame basis. All contact surfaces were Teflon coated to permit a smooth movement and thermal isolation.

The 12" D. test fixture (Fig. 5) was made of 6061 aluminum; the surface of which was polished (Ref. 4) to a mirror finish to de-couple it from solar energy absorption and also to simulate a spacecraft type finish. The microbiological stages (Fig. 5) were also made of polished 6061 aluminum, and loaded to the support plate by attachment to the opposite side of the plate with a nut torqued to 15 in-lb. The opposite side of the support plate (Fig. 6), which during tests faced away from the solar radiation beam, had Kapton film heaters bonded to its surface that were painted black to maximize emitted radiant energy to the vacuum chamber's cold wall. For each organism tested, three inoculated stages were placed on the polished side (sun side) and three on the painted (dark) side. These served as test and control samples, respectively. In addition, nine thermocoupled stages were torqued to the test fixture (Fig. 6).

Temperature control of the test fixture was accomplished by the Kapton film heaters on the back surface of the test support plate and/or the LN₂ heat exchanger system of the vacuum chamber. For test requiring below ambient temperatures, the fixture temperature was controlled by the latter. This necessitated activation of the LN₂ cold wall well in advance of irradiation (approximately 12 h for -125°C tests and 6 h for -15°C).

Solar Simulator Irradiation and Test Operation

Once the preparation of cultures (pure cultures of spores and nonspore-formers) was complete, the stages were inoculated and mounted to the support plate.

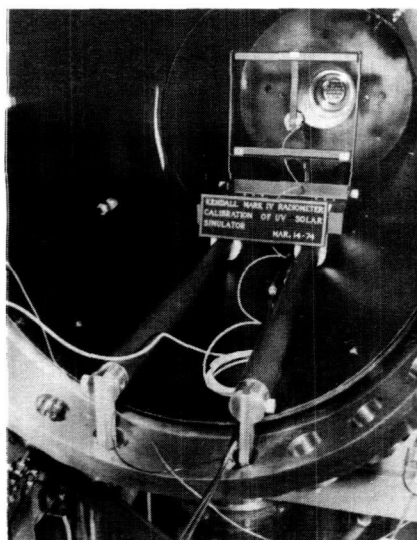


Fig. 4—Optical bench set-up in vacuum chamber

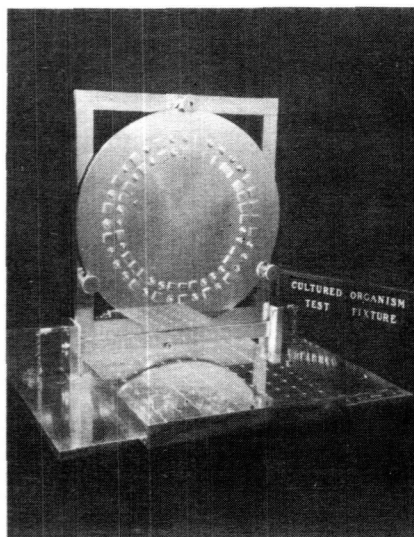


Fig. 5—Irradiation side of test article support plate

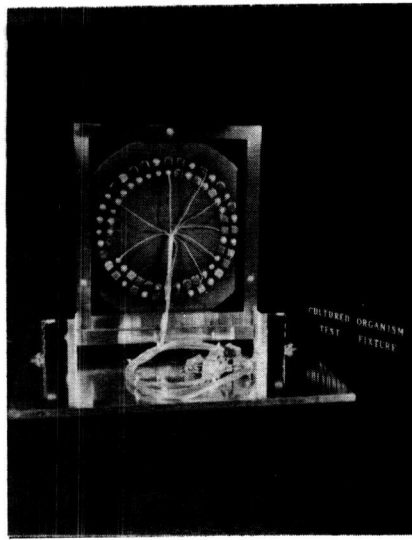


Fig. 6—Dark side of test article support plate (showing thermocouple stages)

The support plate was attached to the tiltable frame in the vacuum chamber (Fig. 7). The support plate attached to the tiltable frame by three peripheral and equidistant standoffs made of Teflon. The three standoffs also served as convenient feet for the loading of the stages to the support plate. The tiltable frame was swung from the horizontal to the vertical position, pushed along the Teflon-coated rails and locked in position. Thermocouples and heaters were connected to a recorder and power source, respectively. The recorder provided continuous readout of the fixture temperature throughout each test.

After placement of the test fixture within the vacuum chamber, the LN_2 cold wall backplate was connected. A cryogenic "cold finger" consisting of $1/2$ " D. copper tubing was installed along the inside wall of the chamber shroud to capture any contaminants that could prove detrimental to consistent testing; i.e., occlude the inoculated stages or the vacuum penetration lens to UV (Fig. 7). The chamber door was closed and the vacuum pumpdown commenced.

The vacuum level obtained under these conditions was 2.7×10^{-4} n/m² (2×10^{-6} torr). Because of long stabilization times, the vacuum system was allowed to pump overnight. With stabilization obtained, the solar simulator was turned on and allowed to operate for a period of 30 minutes before exposure of the micro-organisms. As previously stated, the N_2 purge to the solar simulator cabinet was continuous. The simulator control panel (Fig. 8) contained interlocks for water flow, N_2 purge and an internal cooler fan. Once lamp ignition had taken place, the current to the lamp was set at 60 amps. The shutter remained closed and the potentiometer set-point (controlling the servo mechanism to the variable fan blades) was set to a predetermined number. This number would correspond to a calibrated solar constant (see Calibration). With the test article, test vacuum and solar simulator all satisfying a stabilized condition, the simulator shutter was opened and the

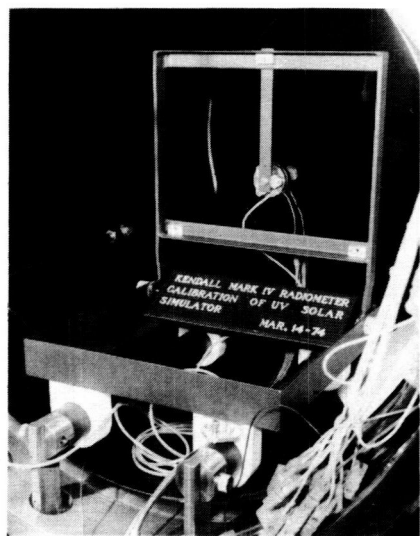


Fig. 7—Kendall radiometer mounted to tiltable frame

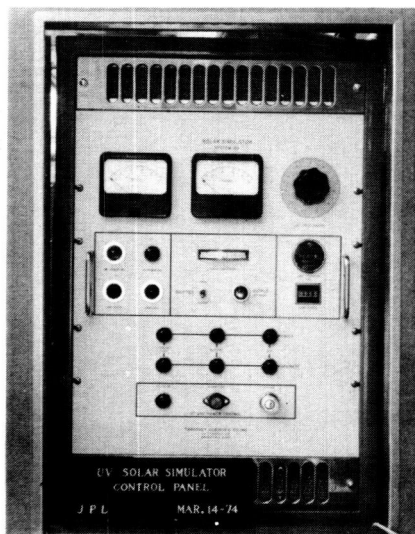


Fig. 8—Simulator Control panel

microbiological samples irradiated for a carefully timed exposure. After exposure, the test fixture was slowly brought back to ambient conditions and removed from the chamber. Backfill of the chamber was made with GN_2 and the samples were transported to a GN_2 environment to the microbiology laboratory for assay.

CALIBRATION

Because of the sensitivity of microbiological responses to UV, it was imperative to remove as many of the variables as possible from the test system. It was therefore extremely important that measurement and calibration of the solar simulator beam was accurate. Quality, intensity, uniformity and degradation were prime.

Spectral distribution measurements were conducted at the plane of irradiance (for our purposes, this was set at 30" from the vacuum flange interface). Measurements were made at an intensity of approximately one sun. Optical readings (Ref. 5) were taken with a McPherson UV monochrometer which utilized a 1200 line/mm grating, blazed for $0.15 \mu\text{m}$ in the first order. The dispersion radiation was detected using photomultiplier tubes and a Keithley 610 CR electrometer.

Table I shows the results of a typical spectral analysis of the solar electromagnetic beam. The integrated radiant flux density from 200 to 270 nm was used as a reference point in the definition of the required dose rates. Periodic spectral analysis, by this method, ensured that any degradation of the beam would be detected.

In order to calibrate the overall intensity output necessary to achieve the required dose levels, a Kendall Mark IV cone radiometer (Ref. 6) was used, *in situ*, to measure total irradiance at the plane of the microbiological test fixture (Fig. 7).

Table I—Spectral analysis of the solar simulator beam

Wavelength Interval, nm	Radiant Flux Density, $\mu\text{W cm}^2$ (10 nm)	Wavelength Interval, nm	Radiant Flux Density, $\mu\text{W cm}^2$ (10 nm)
200 - 210	14	350 - 360	549
210 - 220	19	360 - 370	566
220 - 230	37	370 - 380	557
230 - 240	59	380 - 390	590
240 - 250	108	390 - 400	646
250 - 260	167	400 - 410	677
260 - 270	217	410 - 420	659
270 - 280	263	420 - 430	680
280 - 290	317	430 - 440	687
290 - 300	377	440 - 450	728
300 - 310	407	450 - 460	789
310 - 320	438	460 - 470	864
320 - 330	488	470 - 480	986
330 - 340	522	480 - 490	891
340 - 350	533	490 - 500	898
Integrated radiant flux density (200 - 270 nm) = 0.62 mW cm^2 ($\pm 20\%$)			
Integrated radiant flux density (400 - 500 nm) = 7.9 mW cm^2 ($\pm 15\%$)			
Radiometer measurements made at the same distance indicated a total radiant flux density of 84.4 mW cm^2			

Table II shows the settings for the variable fan shutter as obtained by this method and in the correct relationship of $1 \text{ sun} = 0.54 \text{ mW cm}^{-2}$ in the interval, 200 to 270 nm.

Since the critical parameter in the definition of a solar constant was the irradiance interval from 200 to 270 nm, measurements of the beam were made on a routine basis using an ultraviolet dose rate meter (Ref. 7) high in sensitivity to far UV and low, to infrared. Due to the small percentage of UV in the beam relative to infrared, it was necessary to make measurements with and without a band-pass filter between the Solar Source and the detector. Resultant readings were then obtained by the subtractive method. The routine use of the meter served to indicate any impairment in the system that may have led to a reduction or loss in the far UV portion of the solar simulator source.

Uniformity measurements of the beam were made outside of the vacuum chamber because of the dimensions of the scanning set-up. A Hewlett-Packard

Table II—UV Solar Simulator System 140 Calibration using
Kendall Cone Radiometer Mark IV

Ultraviolet Intensity (Based on 0.54 mw/cm ² 0.2 to 0.27 μ = 1 sun)	Total Intensity mw/cm ²	Tamarack Variable Shutter Setting	
		Warm Wall	Cold Wall
0.1 Solar Constant	8.4	36	36
0.2 Solar Constant	16.8	68	67
0.3 Solar Constant	25.2	102	103
0.4 Solar Constant	33.6	137	137
0.5 Solar Constant	42.2	174	174
0.6 Solar Constant	50.4	213	213
0.7 Solar Constant	58.8	254	255
0.8 Solar Constant	67.2	299	300
0.9 Solar Constant	75.6	350	350
1.0 Solar Constant	84.4	404	404

135 mw/cm²
125 w/ft² = 1 solar constant

Lamp setting 60 amps at 24 volts

Vacuum chamber at 7×10^{-5} torr

Target plane 30" from simulator flange interface

Radiometer temperature 17°C (15° Cold wall)

With variable fan closed as much as possible, leakage = 4.3 mw/cm²

Full opening on variable shutter = 169.6 mw/cm²

pin-diode mounted to an electro-mechanical arm was drawn across the diameter of the beam at target distances of 30" and 54". These measurements were taken in the vertical and horizontal modes. The pin-diode was sensitive to the complete spectrum and acted like a radiometer in its readout. The x-y plot of such a uniformity measurement made with 0.5 solar constant irradiation at 30" and 54" from the vacuum flange, can be seen in Fig. 9.

Further Studies

Current indications are that the ultraviolet portion of the solar electromagnetic spectrum accounts for the most significant lethal effect. Inherent in microbiological studies of UV is the problem of attenuation by viable and nonviable particles. This situation is present in studies of both pure cultured and naturally occurring (uncultured) microbial populations. In order to provide a conservative estimate of the resistance of naturally occurring microbial populations it was decided to

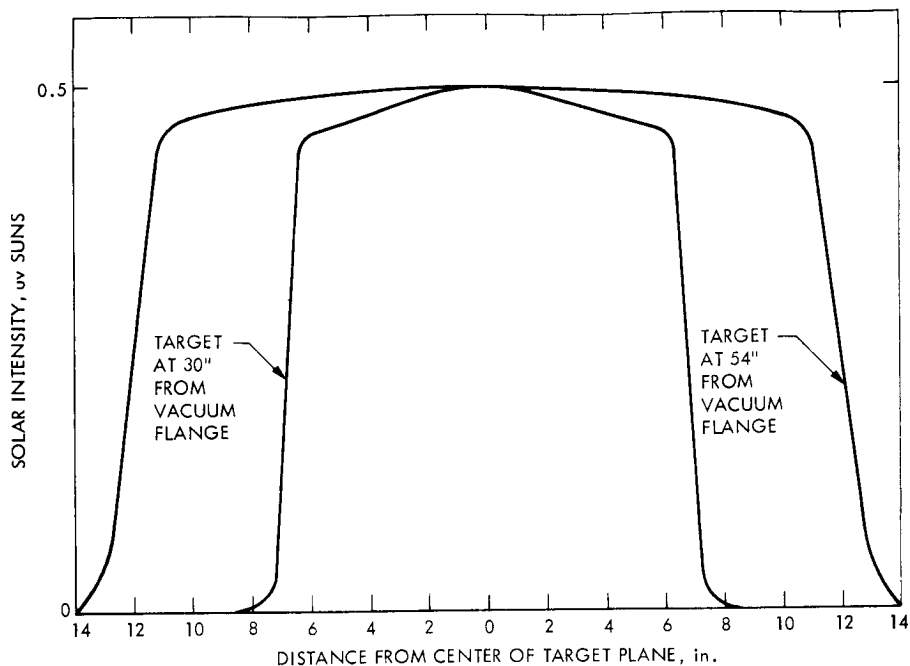


Fig. 9—Horizontal uniformity of solar beam

select as test surfaces, flight type solar panels. These panels have electrical leads and a labyrinth of crevices that contribute to the attenuation of incident UV by shielding and particle layering.

The solar panel test fixture for naturally occurring populations (Fig. 10) was composed of a 6061 aluminum base plate, 35.56 cm square and 0.635 cm thick, to which solar cell test pieces were attached. Kapton film heaters, 34.29 cm square, were bonded to the backside (nonirradiated side) of the plate and painted black. Five thermocouples were attached to the plate to monitor and profile temperature. To the front of the base plate were attached nine 10.16 cm square, 0.318 cm thick, 6061 aluminum pieces to which were bonded solar cells. The configuration of the solar cells, as bonded to the aluminum, was identical to that of their functional mode; i.e., electrical connection, spacing and topography were duplicated.

The collection of naturally occurring populations was accomplished by exposing initially sterile solar cells to a spacecraft component test environment for 5 to 7 days. After exposure the pieces were loaded to a base plate (nine per plate) and held in place by twelve stainless steel screws each torqued to 15 in-lbs. The assembled test fixture was then placed in the simulator.

A solar beam 20" in diameter was required for this test fixture configuration. It was found that at a distance of 54" from the vacuum flange a beam of 20" D. with the same uniformity characteristics as at 30" was obtainable. Of course, the power drop-off was significant so that with a variable fan setting of 732 we were able to obtain 0.5 solar constant. Settings somewhat beyond 732 proved to be a saturation point for the photocells in the servo system loop. All tests, as made with the solar panels were made at the 0.5 solar constant level.

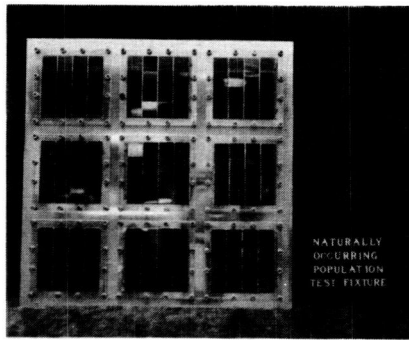


Fig. 10—Solar cell test array for naturally occurring microorganisms

Results to Date

The test system has been used for the irradiation of pure cultured populations at dose rates of 0.1, 0.5 and 1.0 sun under temperature conditions of -125, -15 and +70°C, respectively. Studies were also conducted on naturally occurring microorganisms under 0.5 sun, +65°C conditions. The system provided reliable data that attributed significant reductions in the microbial populations investigated to broad spectrum solar electromagnetic radiation.

Future Studies

This simulator system will be used to further define the resistance of pure cultured and naturally occurring microorganisms to solar electromagnetic radiation as a function of dose, dose rate, organism type and temperature. Collateral experimentation will be initiated to define the effect of viable and nonviable particulate shielding on survival. In addition, studies will be conducted on the photoreactivability of naturally occurring microbial populations.

Acknowledgements

The technical support of J. Barengoltz, A. Ferreira and J. Smith in the development of the simulator system is deeply appreciated. The technical support of C. Fea in the operation of the simulator and of J. Farber, G. Simko and S. Yamada in the microbiological assays is gratefully acknowledged.

This work presents the results of one phase of research carried out at the Jet Propulsion Laboratory, California Institute of Technology, under contract No. NAS 7-100, sponsored by the National Aeronautics and Space Administration.

REFERENCES

1. Hotchin, J.P.: The Microbiology of Space, Journal of British Interplanetary Society, Vol. 21, June 1968, pp. 22-130.
2. Gerald R. Taylor, et al: Proceedings of the Microbial Response to Space Environment Symposium, NASA Lyndon B. Johnson Space Center, Sept. 1972, NASA TM X-58103 May '73.
3. Hotchin, J.P.; Lorenz, P.; Hemenway, C.L., The Survival of Terrestrial Micro-Organisms in Space at Orbital Altitudes During Gemini Satellite Experiments, Life Sciences and Space Research VI, North-Holland Publishing Co. (Amsterdam) 1968, pp. 108-114.
4. Phillips, K.L.: "Buffering Aluminum Alloys – Detail Specification for" Spec. No. FS500627, Rev. B., Jet Propulsion Laboratory 1967 (JPL internal document).
5. Carlson, R., U.S.C. Physics Dept., Los Angeles, Calif.
6. Kendall, J. SNR, JPL Instrumentation Section, Pasadena, Calif.
7. Ultra-Violet Products Inc., San Gabriel, Calif., Blak-Ray Ultraviolet Intensity Meter.

LIFE SCIENCES LABORATORY BREADBOARD SIMULATIONS FOR SHUTTLE

S. T. Taketa,* R. C. Simmonds,* and P. X. Callahan,* *Ames Research Center, Moffett Field, Calif. 94035*

ABSTRACT

Breadboard simulations of life sciences laboratory concepts for conducting bioresearch in space were undertaken as part of the agency's Concept Verification Testing (CVT) Program.

INTRODUCTION

The Life Sciences discipline, which represents a broad, multisubdisciplinary scientific community involved in biomedical and biological research and technology, has a requirement unique among all scientific disciplines to launch and maintain living organisms with a wide range of life-support, environmental control, and waste management requirements in space for experimental use.

The NASA Office of Life Sciences, recognizing the need to resolve the many potential problems associated with the development of shuttle-supported, life sciences payloads, is engaged in payload definition, integration, and simulation studies. This paper deals with Test II of laboratory breadboard simulations to test concepts of and scope problems associated with bioresearch support equipment and facility requirements and their operational integration for conducting manned research in earth orbital missions. Test II, which was considerably more complex than Test I (1,2), emphasized requirements, functions, and procedures for candidate research on crew members (simulated) and subhuman primates and on typical radioisotope studies in rats, a rooster, and plants. The test was conducted as part of the agency's CVT Program in collaboration with Marshall Space Flight Center (MSFC) and Johnson Space Center (JSC) and the programmatic support of the NASA Office of Life Sciences and the Spacelab Program Office. The simulation was conducted first at ARC, then at MSFC. The emphasis at ARC (with input from JSC) was on science and payload integration and, at MSFC, on engineering to interface the payload with the simulator subsystems (3). (The candidate

*STT, Project Manager, and RCS, Project Veterinarian; in addition, all the authors were payload specialists (simulated).

experiments used in these simulations are not to be construed as having been selected for actual flight experiments. They were selected as examples of research activities and requirements for conceptual testing and planning only. Henceforth, candidate experiments are referred to as experiments.)

CONCEPTS TESTED

The concepts tested or emphasized in Test II, including those developed in NASA Life Sciences payload planning activities (4,5), were: 1) three categories of equipment and facility- (a) common operations research equipment (CORE, a matrix of research support equipment and facilities that serves a broad spectrum of experimental areas), (b) supplemental instrumentation and facilities for research support, and (c) experiment-specific equipment; 2) modular rack-mounted equipment; 3) modular organism housing units; 4) methods for collecting, preparing, and preserving biological materials (for analysis on ground after recovery rather than onboard); 5) role of payload specialists (trained scientists) in performing onboard research activities; 6) research support role of a mission specialist (an onboard engineer); 7) a hooded unit for either a general purpose work-bench or a surgical table (hereafter referred to as HWB/ST); 8) sink drainage by vacuum into a storage tank; and 9) pressure-forced rodent watering system - the latter two being independent of gravity action.

In addition to the aforementioned concepts, the following requirements and procedures were evaluated: 1) data recording, handling, and telemetering of physiological measurements; 2) control of animal odor and radioisotope hazards; 3) influence of crew activity on organisms; 4) interaction among different organisms; and 5) logistics of handling visiting scientists and their research support requirements and of transporting organisms and equipment between ARC and MSFC.

TEST PROCEDURE

The test-related activities were performed by in-house personnel except for the involvement of a few university scientists. The participating scientists provided detailed, time-lined experimental protocols; sketches depicting equipment configuration, interfaces, dimensions and power requirements; organisms; supplies; and data recording and experiment-specific equipment. The laboratory (lab) supplied the CORE, modular organism housing and HWB/ST breadboards, and utilities. Procedures and techniques applicable for use in the weightless environment of space were implicit considerations but were not firm requirements.

The test duration was 5 days and the daily testing period was 8 hr. The experiment time-lines and equipment/facility

requirements were used to schedule daily activities and to plan the lab layout to optimize functional integration and to avoid conflict of crew operations. At ARC, dry (practice) runs were conducted by the involved investigators during the week preceding the test run to familiarize themselves with the payload layout and operations, to firm up the experimental protocol timing requirements and the operational integration of the payload, and to train the payload specialists (simulated; hereafter referred to as payload specialists). Briefings were held before the dry and test runs, debriefings after.

After simulation at ARC was completed, the equipment was transported to MSFC on a NASA-10 aircraft; some of the bulky and heavy equipment was shipped by truck. The simulation at MSFC was 2 months later to allow sufficient time to install and check out equipment and organism housing units. Having observed the installation procedures and interface requirements at ARC, the MSFC personnel were able to proceed rapidly and without difficulty with the installation at MSFC. The organisms, equipment, and ancillary supplies provided by the involved investigators were shipped from ARC to MSFC accompanied by the ARC veterinarian on the NASA-10 aircraft about a week preceding the simulation at MSFC. Upon arrival at MSFC, the equipment was installed in the simulator and the organisms were transported in a temperature-controlled van to the organism-holding facility where they were kept until they were installed in the simulator and checked out the day before the five-day test.

Within a few days after completion of the simulation at MSFC, the organisms and some of the sensitive equipment were shipped back to ARC on the NASA-10 aircraft accompanied by an ARC scientist; the remaining equipment was returned by truck.

Simulator

The MSFC-supplied ARC simulator was a low-cost functional mock-up similar in dimension and configuration to the more sophisticated one used at MSFC, the lower deck of the z-floor, double deck-configured General Purpose Laboratory (GPL) Simulator. The configuration and dimensions are illustrated in Figure 1, which also shows the Test I lab layout. Figure 2 is the exterior view.

Candidate Experiments

The 10 candidate experiments used in the test are identified in Table 1 by experiment code; investigator (experiment proposer), his institution and ARC Technical Monitor (for ARC-supported research contracts or grants); short title; organism (test subject); and measurements. The work stations associated with the experiments have been described (3).

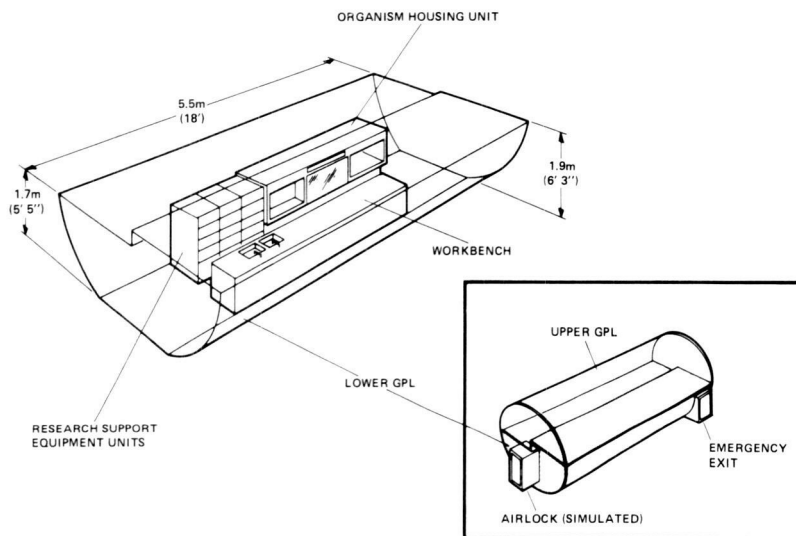


Fig. 1—Sketch of ARC Bioresearch Laboratory Simulator (lower GPL) with Test I breadboard layout and (in insert) z-floor, double deck-configured MSFC General Purpose Laboratory (GPL) Simulator.

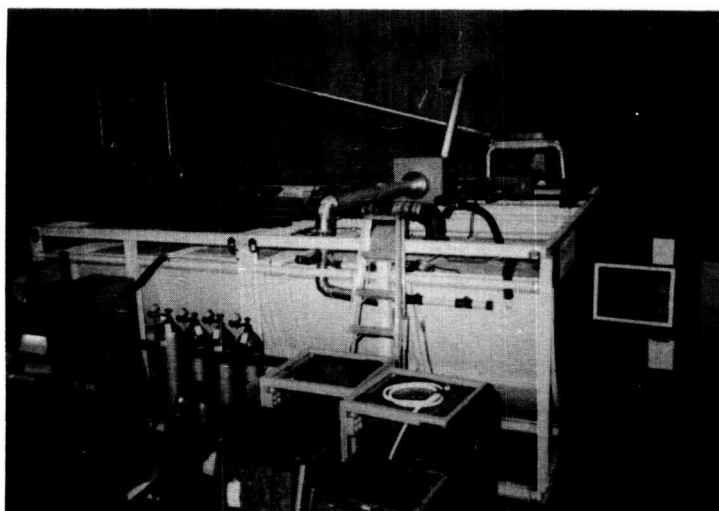


Fig. 2—Exterior of ARC Bioresearch Laboratory Simulator.

Table 1 – ARC BIORESEARCH LAB BREADBOARD TEST II CANDIDATE EXPERIMENTS FOR CVT

EXP. CODE	INVESTIGATOR/ INSTITUTION (ARC TECHNICAL MONITOR)	SHORT TITLE	ORGANISM	MEASUREMENTS
MEDICAL STUDIES				
H1	H. Sandler, M.D., & R. Lee, E.E. ARC	Cardiac Function	Crew	ONCE DAILY: Cardiac dimensions
H2	T. Decker, Ph.D./Baylor U. R. Haines, Ph.D./ARC L. Loner, Ph.D./JSC	Visual Function	Crew	ONCE DAILY: Visual acuity, binocular stereoscopic acuity, accommodation, fusal reserves
SUBHUMAN PRIMATE STUDIES				
P1	Nello Pace, Ph.D. U.C. Berkeley (B.D. Newsom, Ph.D.)	Metabolic & Cardiovascular Studies in Monkey in OG	<i>M. nemestrina</i> (logrolled monkey)	ONCE DAILY: Automated water/food intake, respiratory gases IO ₂ , CO ₂ , N ₂ /water vapor, excrement collection/preservation ONCE IN 2 DAYS: HR/BP responses (telemetered) to LBNP
P2	C. M. Winget, Ph. D. ARC	Photoperiod Effects on CNS & Physiological Biorhythms in Monkey in OG	<i>C. albifrons</i> (cetus monkey)	ONCE PER 6 MIN: Telemetered ECG, EEG, body temperature & activity signals ONCE DAILY: Feeding, watering & excrement collection/preservation
P3	C. M. Winget, Ph.D. & J. V. Danelis, Ph.D. ARC	Physiologic Cost in Monkey of Repeated Shuttle Sorties	<i>C. albifrons</i> (cetus monkey)	ONCE PER HR: Telemetered ECG & body temperature ONCE DAILY: Food/water intake & excrement collect/preservation
P4	G. H. Bourne, M.D. Emory U. (C.M. Winget, Ph.D.)	Effect of Long-term OG on Histopathology & Histochimistry of Monkey	<i>M. mulatta</i> (Rhesus monkey)	ONCE DAILY: Telemetered ECG & waste management ONCE EVERY OTHER DAY: Manual blood withdrawal, cell counts & plasma preservation WATER & FEED: Automated & at lib
RADIOISOTOPE TRACER STUDIES				
R1	H. A. Leon, Ph.D. ARC	Hemolytic Rate of Rat RBC in OG	Rat	¹⁴ C 2-Glycine • RBC → Expired ¹⁴ CO
R2	S. Ellis, Ph.D. & Consortium ARC	Plutitary Function, Plasma Enzymes & Bone Metabolism in OG	Rat	¹⁴ C Proline → Collagen • Urinary ¹⁴ C Hydroxyproline; Blood/plutitary hormones; Plasma fibrinogen, Renin, Angiotensin, Femur Ca, P, Collagen
A1	J. R. Bellan, M.D. U.C. Davis (C.M. Winget, Ph.D.)	Quantitation of Calcium Dynamics in OG	Rooster	⁸⁵ Sr, ⁴⁵ Ca → Bone → Blood/excreta. Bone density/ Fracture repair rate; EKG, Body temp/Wt., Hematology
B1	C. H. Ward, Ph.D. & Consortium Rice U. (S. T. Taketa, Ph.D.)	Metabolism & Energetics in Hypogravity in a Higher Plant	Higher Plant (Marigold)	¹⁴ C Labeled Amino Acids • ¹⁴ CO ₂ Starch granules, Pigments, Amino acid pathway, Enzyme/Hormone activity, Lignification, Minerals, Respiration/Photosynthesis

Briefly, in H1 (see Table 1 for identification of experiments), the left ventricular dimensions were measured in crew members using an ultrasonoscope with a built-in 28-V battery. An ultrasonic transducer was held against the chest in the third intercostal space along the left sternal border in reclining subjects. Echograms were recorded by the experimenter with a polaroid camera attached to the window of the oscilloscope portion of the ultrasonoscope.

In H2, visual functions were measured in crew members using a haploscope. The experimenter initiated the computerized visual function test by typing a programmed message into a teletype; the subject, viewing the test through a binocular eyepiece, responded by actuating a hand-held switch. The response was automatically recorded on the teletype printout.

For P1, the measurements listed in Table 1 were made in a monkey subject seated and restrained in a pod, which had a device for imposing lower body negative pressure (LBNP) as one of the experimental procedures. The research support equipment requirements were extensive and included, in addition to the monkey pod, a mass spectrometer, four calibrated compressed cylinder gases for instrument calibration, pen recorders with capacity for 10 channels, two consoles for control panels, and a vacuum used at ARC for the LBNP (the simulator-supplied vacuum was used at MSFC). For simulations at both ARC and MSFC, the recorder units and gas cylinders were placed outside the simulator to accommodate P4 requirements.

The P2 test monkey was housed in a unit from which external light was eliminated, for it required continuous exposure to a constant source of built-in light for the 5-day test period.

Both P2 and P3 animals were implanted with transmitters for telemetering physiological data; the electronics for receiving and recording the telemetered data were rack-mounted on top of the P4 monkey cage plywood envelope that covered all except the cage front and caster-mounted bottom.

The P4 monkey, a large rhesus, required a relatively large squeeze cage. For drawing blood from a saphenous vein in the lower extremity, the animal was squeezed to the front of the cage and anesthetized.

The R1 rats were individually maintained in airtight rodent metabolism (gas exchange) chambers through which air flowed under constant low pressure; the expired ^{14}CO was collected and preserved for later analysis to measure hemolysis (red blood cell destruction). The animals were transferred daily from their soiled chambers to clean chambers through transfer tunnel provided with air lock-type gate valves to prevent changes in internal gas pressure and composition.

The R2 rats were housed individually in wire mesh bottom rodent metabolism cages — each equipped with a urine-feces separation/collection funnel, food tray, and a conceptual automated, air pressure-forced watering system that would function and measure water consumption in the absence of gravity. The

regularly used pulverized dry rodent feed (meal) was mixed in inert agar for simulated OG usage to prevent spillage or dropping which commonly occurs during consumption when untreated meal is used. Daily measurements were made of animal weight and food and water intake; daily collections of urine and fecal droppings were measured and preserved in the freezer. In addition, on the fifth day, blood was drawn from the animals by heart puncture, then centrifuged, and the plasma preserved in the freezer; the animals were subsequently sacrificed and various tissues and organs were removed, weighed, and frozen.

The A1 organism (rooster) was restrained off the cage floor by means of a "saddle." A gamma-ray Geiger detector, mounted through the cage top for *in vivo* radioactivity measurement, was connected to a pulse height analyzer that interfaced with a teletype printer shared with H2. The radioactivity counts were recorded daily on the teletype.

The B1 (plant) module was partitioned into upper and lower compartments. The upper compartment contained a small growth chamber (simulated) for maintaining 20 plants at standard conditions (296°K, 75% relative humidity, 1000-ft-c light intensity at the surface of the upper leaves, and 500-cc/min air flow) for experimental use and a time-lapse camera for photographing rhythmical leaf movement and epinasty (bending of leaves toward the base). The lower compartment was used to collect $^{14}\text{CO}_2$ expired from ^{14}C -glutamic acid injected plants. The collections were preserved in a freezer. Equipment for measuring O_2 and CO_2 to calculate photosynthesis and respiration was located adjacent to the B1 module and consisted of a gas exchange chamber enclosed in a light-tight box with a built-in light source and interfaced by tubings to O_2 and CO_2 analyzers which were wired to pen recorders for online recording. Four cylinders of calibrated, compresses gases with differing composition were required for instrument calibration. In addition, one of the gases (340 ppm CO_2 and the balance in N_2) was required to continuously purge the gas exchange chamber at 500 cc/min during the daily 1-hr test period. All test plant materials were trimmed, weighed, measured, and frozen in liquid nitrogen and preserved.

Payload Specialists

Three to four candidate experiments were assigned to each of three ARC scientists who simulated the role of Payload Specialists as follows: S.T. Taketa (H1, H2, P1), R.C. Simmonds (P2, P3, P4, A1), and P.X. Callahan (B1, R1, R2). The experiment assignments were based in general on the training and/or experience of the involved scientists.

Laboratory Breadboard

The layout is illustrated in Figure 3 and the refurbished interior is shown in Figure 4. The design of the hardware/

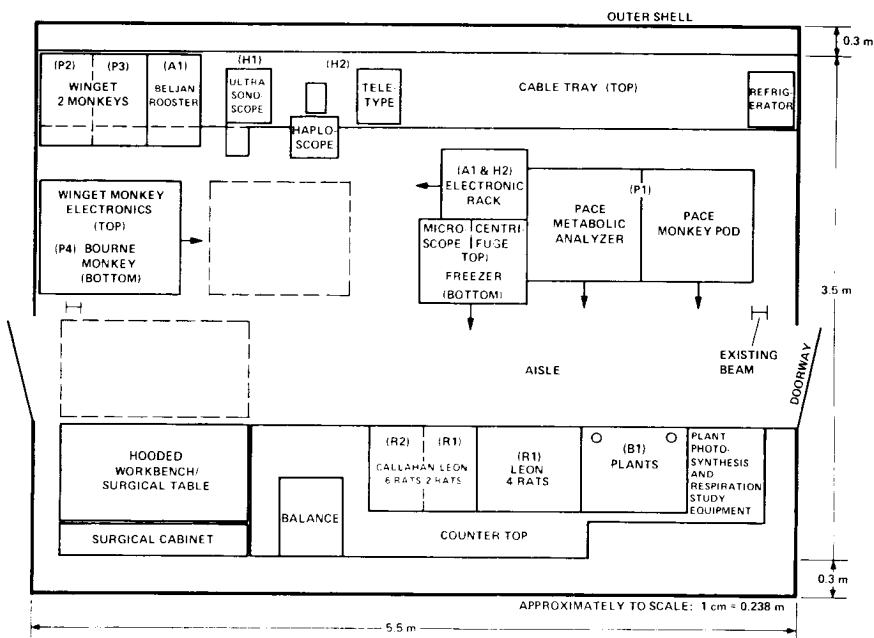


Fig. 3-ARC Bioresearch Laboratory Breadboard Test II layout (arrows indicate fronts of respective units).

work station layout took into account the research support and work area requirements of the experiments such as the area required for the portable reclining chair for H1 subjects (Fig. 5), the HWB/ST unit required for the B1, R1, R2, and P4 experiments (e.g., Fig. 6(a)), and the shared usage of the teletype for A1 and H2.

The limited lab space was optimized for experimental use by providing for two large mobile items — the HWB/ST unit (on rollers) and the P4 housing module (on casters) — as required to accommodate research requirements. For example, H1 (Fig. 5), H2, and P4 tests were conducted daily and the HWB/ST unit was used in the workbench mode (Fig. 6(a)) while the HWB/ST and P4 units were in the normal stowed positions as indicated by solid lines in Figure 3. For the P4 waste management (accessible from the back) and for access to A1, P2, and P3 modules, the P4 unit was moved to the position indicated by the dashed lines in Figure 3. For use in the surgical mode, the HWB/ST unit was moved into the aisle as shown by dashed lines in Figure 3. This permitted access to the surgical table from both sides as demonstrated in Figure 6(b). Both ends of the HWB/ST unit were provided with glove ports for additional accessibility and assistance as might be required for surgical procedures or for handling hazardous materials with long-sleeved gloves.

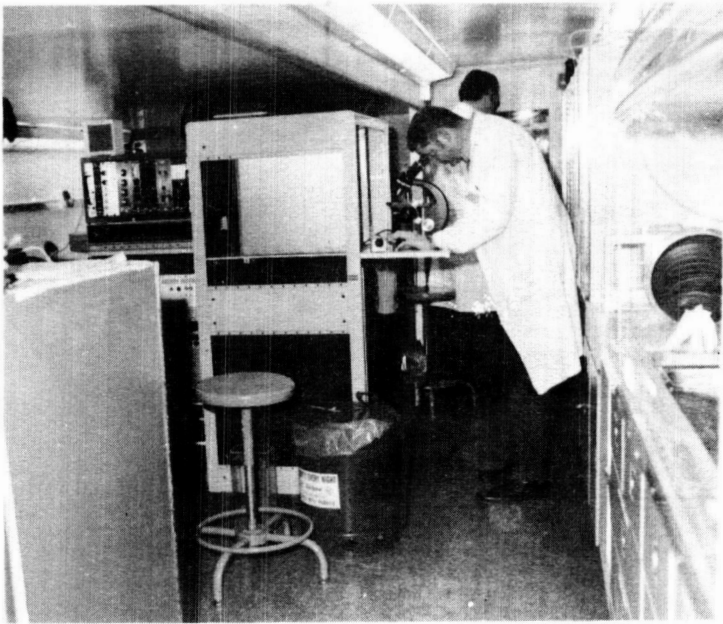


Fig. 4—Interior of simulator refurbished for Test II (RCS at microscope work station and, in background, PXC at B1 work station).

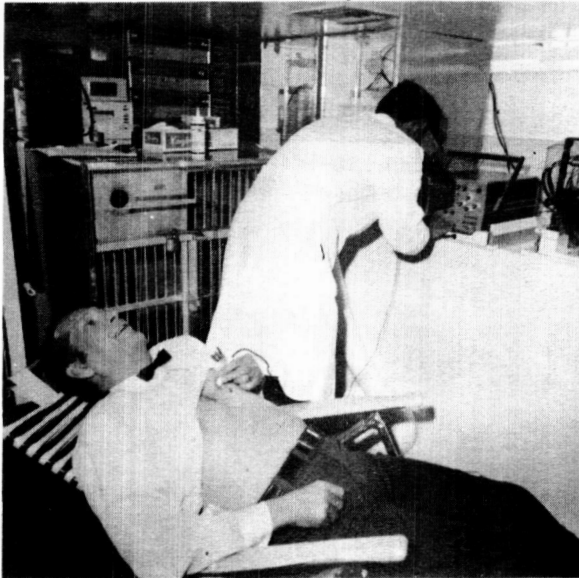


Fig. 5—H1 work station (STT at ultrasonoscope measuring cardiac dimension on subject, PXC) with A1, P2, P3, and P4 organism housing breadboards and P2 and P3 electronics in background.

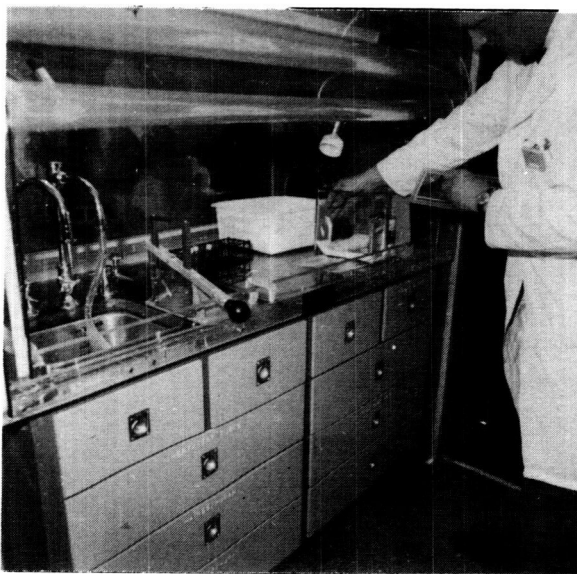


Fig. 6(a)—Hooded workbench/surgical table unit in workbench mode (PXC preparing to sacrifice R2 rats).



Fig. 6(b)—Hooded workbench/surgical table unit in surgical mode (PXC and STT demonstrating use of table from both sides).

Other provisions in the conceptual HWB/ST unit (0.7×1.4 -m table surface) were drawers, a sink, and all utilities including a radioisotope-rated exhaust system and two high-intensity light fixtures with flexible tubing for surgery and other procedures requiring high illumination. Sink drainage was by vacuum into a storage tank — a procedure that made draining independent of gravity; control of water flow was accomplished by air-flow entrainment.

All but two of the subhuman test organisms were housed in standard size units $76 \times 76 \times 61$ cm in height, width, and depth, respectively, or a half portion thereof. For example, the A1 rooster occupied half a standard unit and the P2 and P3 monkeys shared a standard unit partitioned into two as did two R1 rats with six R2 rats. The R2 metabolism cages in the out-mode are shown in Figure 7. The P1 and P4 monkeys were housed in non-standard units because of the unique and large size requirements, respectively. Figure 8 shows a payload specialist at the P1 work station.

The CORE compound microscope, table model centrifuge, and freezer were rack-mounted on a single rack (Fig. 4). A small refrigerator was mounted on top of the cable tray. The ancillary supplies for the experiments were stowed in drawers and cupboards. Separate containers were provided for regular and radioactive waste disposal.

For the test at MSFC, the air flowing through the organism housing modules under negative pressure was filtered, scrubbed, and recirculated into the lab.

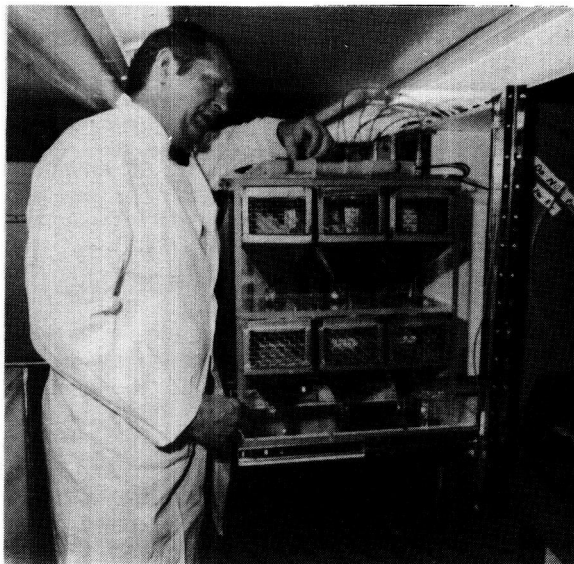


Fig. 7-R2 work station with metabolism cages in the out-mode (PXC measuring water consumption).

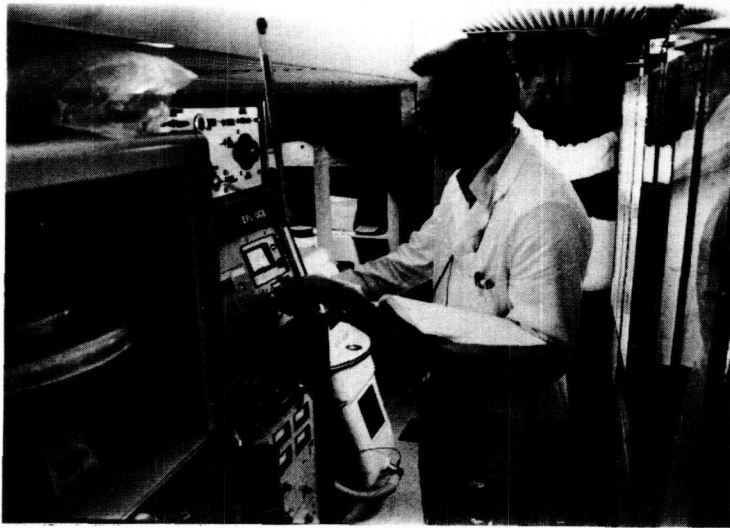


Fig. 8—PI work station (STT making mass spectrometer measurements and, in background, PXC at B1 work station).

RESULTS AND DISCUSSION

The simulations at ARC and MSFC were highly successful with respect to test objectives. Admittedly, the activities would have been more meaningful and realistic had they been related to an actual flight payload and had a Spacelab-configured simulator been used. Nevertheless, the problems encountered and the experience gained from such conceptual payload breadboard simulation activities will be extremely valuable in planning and developing flight payloads.

Our simulation experience indicates that an economical, functional volume and configuration simulator of a payload carrier such as the one used at ARC can be an extremely valuable, low-cost tool for integrating, testing, and iterating payloads. The prior payload integration and testing at ARC significantly reduced the problems associated with payload installation and test activities at MSFC. Having the simulator at ARC stimulated the interest and participation of scientists in simulation activities at the center and increased their awareness of the problems that could be encountered with payload requirements and operations. Use of a Spacelab-configured simulator with a larger floor area and volume would undoubtedly have made the lab layout and operations easier than in the z-ceiling configured simulator. However, the now-defined Spacelab configuration was not known nor was a simulator with such a configuration available when the test was planned. Future simulations should utilize the Spacelab configuration.

Even under the seemingly crowded condition of the z-ceiling simulator, the test activities were carried out efficiently and smoothly in a professional manner by the involved payload specialists, thereby demonstrating the importance of proper pre-planning of the lab layout and scheduling of the payload specialists' activities to avoid conflict of movement and of equipment/facility usage. Upon receiving their experiment assignments, the payload specialists further integrated their respective activities and increased their efficiency with experience. While the involved investigators were required to submit evaluations of the test activities, they were not required to write reports of their respective experiments. However, in most of the test experiments, the accumulated data were of sufficient quantity and quality to provide the basis of reports (e.g., 6,7). The involved investigators were unanimous in their support of the concept that payload specialists carry out their respective experiments. The involved payload specialists, as a result of their interaction with the mission specialist during simulation at MSFC, felt that a highly motivated and properly trained mission specialist could provide valuable assistance to the payload specialists in carrying out their research activities. Mission specialists should be discipline-oriented in training (e.g., for Life Sciences, an engineer with training in biology or physiology).

No apparent problems were encountered in integrating and conducting studies on crew members along with those on lower forms of organisms in the same confined lab. However, there is a need to control or minimize the potential influence of crew- or organism-induced noise or perturbation (such as the intermittent crowing of the rooster and the shaking of the cage by a monkey which were experienced in the test) on other onboard species, e.g., those involved in biorhythm, behavioral, and telemetered physiological studies. The possibility exists that, in the unnatural weightless environment of space, the animals may become hypersensitive and react to perturbations that might normally be ignored on the ground.

The use of modular, rack-mounted research support equipment in Tests I and II presented no apparent problems and was endorsed by the involved payload specialists. Perhaps similar rack-mounted equipment might be used in ground-based research laboratories to reduce their size, hence construction costs.

Although our experience is limited to Tests I and II simulations, we believe that the concept of using standard-sized organism housing modules is sound, practical, and worthy of further study for use in space. It could be cost effective to design and mass-produce an appropriate-sized module, an environmental control system (ECS) with adjustable controls, and readily exchangeable inserts with species-peculiar cages or accommodations and life-support system (LSS) to fulfill the requirements of commonly used species of laboratory organisms for both minilab and dedicated lab missions. Replicates of such a module with an appropriate insert, ECS, and LSS would be used to house ground

control and flight organisms of a given experiment during the various phases of the flight experiment (i.e., preflight ground testing in the investigator's lab, ground transportation, inflight and postflight, where appropriate). Provisions for negative pressure unidirectional air flow and for inserting tubings and wirings are essential for the organism housing modules.

Neither animal odor nor radioisotope hazards were experienced in the simulations, indicating that they can be effectively controlled by proper air flow, filtration, and scrubbing techniques and, in addition, with radioisotopes by use of well-established handling procedures.

The conceptual HWB/ST unit (conceived by one of the authors, S.T. Taketa, as a result of his experience in Test I (1,2) and developed by P.X. Callahan) showed considerable promise as a practical and versatile hardware item for the Life Sciences Space-lab. In addition to fulfilling the functions of three research support hardware in Test I — the portable glove boxlike unit, long workbench, and chemical hood — the HWB/ST unit in the surgical table mode provides for research procedures that involve two or three operators.

Using an agency aircraft to transport experimental organisms and research support equipment between ARC and MSFC greatly facilitated the logistics and reduced the apprehensions and potential problems (such as delays, uncertainty of delivery, environmental conditions, etc.) generally associated with modes of transportation not under user control. However, the organisms, not having been transported in modules with ECS/LSS, were exposed to variations in environmental conditions experienced by the aircraft. Since it is scientifically essential to maintain the organisms under similar controlled-environment conditions during transport as in organism housing modules during experimentation, there is a need to develop suitable organism transport modules containing features identical to those in the organism housing modules as discussed earlier.

PROBLEMS

One of the objectives of the simulations was to scope the problems associated with payload activities. Accordingly, the major problems encountered are discussed candidly and constructively.

1. All personnel assigned to the simulation activities at ARC had other major nonsimulation-related work assignments, hence their efforts were not fully directed to the simulation. For conducting science simulation activities as at ARC, we feel that a management team consisting minimally of the following members assigned on a full-time basis is required: a project manager, an assistant, a project engineer, and a mission scientist, who could double as the test conductor. Additional personnel requirements are scientists to assume the role of payload specialists, an electronic specialist familiar with the discipline electronics,

and other specialists as required — whose major, if not sole, responsibilities for the period before and during the actual testing are directed to the simulation activities.

2. The short (1-month) lead time for modification of the simulator at ARC to accommodate Test II requirements forced a rescheduling of simulation tests at ARC and MSFC. The problems associated with such a rescheduling could be avoided by providing a longer lead time (e.g., 3 months). The use of a Spacelab-configured simulator with skids for rack-mounting of equipment should reduce the lead time necessary for test-to-test lab modifications.

3. The lack of cooperation of a few of the involved scientists during planning and testing caused problems in accommodating their experiments. Since the active participation of involved scientists is especially important in fulfilling their requirements, the criteria for selecting experiments should include a provision to ensure the active involvement of the selected investigators.

4. The equipment supplied for installation by one of the investigators was significantly larger than the dimensions that he had given during the planning phase; this forced a marked change in the planned lab layout. The lesson learned is to recheck and substantiate each investigator's equipment specifications including dimensions, power, weight, etc. during planning.

5. The limiting factor for the number of experiments that can be accommodated in a dedicated Life Science Spacelab mission, based on our simulation experience, would undoubtedly be the equipment and/or organism requirements rather than the workload on the payload specialists. To accommodate 10 experiments in Test II, sample numbers of organisms rather than the numbers specified in the experiment protocols were used. If the numbers of organisms specified were used, only about five experiments could have been accommodated because of the large organism requirements.

6. Considerable time and effort were spent in locating two government furnished instruments for university scientists involved in Test II — a pen recorder with a Biotach coupler for P1 and a CO₂ analyzer of sufficient sensitivity for online measurement of plant-evolved CO₂ for B1. Apparently, specifying equipment requirements by manufacturer, model number, and specification are, in some cases, insufficient unless the specific equipment is found or the parties involved (e.g., the electronics specialists at both ARC and MSFC in the case here) are sufficiently familiar with the instrument to discuss alternates and make necessary modifications in an alternative instrument to satisfy user requirement (as was done with the pen recorder at MSFC by an ARC electronics specialist). For the CO₂ analyzer, we learned, unfortunately too late for the test at ARC, that the instrument specified was modified to the investigator's unique requirements, consequently none like it was available. (The investigator furnished his unique CO₂ analyzer for the test at MSFC.) It is quite evident

from this experience that there are user requirements sufficiently unique even in commonly used instruments as pen recorders and CO₂ analyzers to cause unforeseen problems.

7. The lack of built-in ECS in the organism housing modules caused considerable problems in maintaining the desired temperature and humidity levels in the modules, especially at MSFC where the temperature and humidity were high. The obvious solution would be to have self-contained ECS in each module.

8. The high-frequency breakdown of cordless microphones worn by the payload specialists to communicate with the outside during simulation at MSFC caused significant disruptions in communication. Since cordless microphones would not hinder the movement or operations of payload specialists, they would be preferred over fixed or wired microphones provided the breakdown problem is solved.

CONCLUSION

The experience and observations from low-cost simulation (as reported here) provide valuable background for subsequent testing of payload concepts in a Spacelab-configured simulator and enhance the development of actual flight payloads. The observations made could form the basis of a useful approach for developing preflight integration and testing of flight payloads and their logistics.

RECOMMENDATIONS

1. Use a Spacelab-configured simulator for subsequent concept verification simulations of payloads.

2. Assign a full-time management team composed minimally of a project manager, an assistant, a project engineer, and a mission scientist for simulation activities such as conducted at ARC.

3. Make the utilization of procedures and techniques applicable for use in weightlessness firm requirements for subsequent simulations.

4. Provide mission specialists with science discipline-oriented training in addition to his training to fulfill his primary engineering role.

5. Provide an organism-holding facility with adequate environmental control to maintain organism at life sciences payload integration center and launch site.

6. Determine the feasibility of designing and developing a standard-sized organism-housing module with a built-in ECS with adjustable controls and readily exchangeable inserts with species-peculiar cages or accommodations and LSS to accommodate most of the commonly used lab organisms in the investigator's lab, for ground transportation and inflight. Include provisions for negative pressure unidirectional air flow and for insertion of tubings and wirings.

7. Provide for controlling animal odor and potential radioisotope hazards in the design and development of the Space-lab ECS and LSS.

8. Design and develop the hooded workbench/surgical table unit for Spacelab use.

9. Improve the quality of cordless microphones for use onboard Spacelab.

10. Provide an aircraft to be at the disposal of the user for long-distance transport of experimental organisms and research support equipment for shuttle missions.

ACKNOWLEDGMENT

We gratefully acknowledge the valuable contributions made by the participating scientists, engineers, and support personnel at both ARC and MSFC. We owe special thanks to the university scientists for their enthusiastic involvement, to Mr. Robert Johnson, Mr. Peter Haro, and Mr. Gerald Hall and associates of the ARC Research Support Directorate for their dedicated and untiring support, and to Mr. William Brooksbank, Jr., Mr. Jack Rowan, Mr. Robert McBrayer, Mr. Robert Shurney, Mr. Ken Smith and associates of MSFC for their wonderful cooperation in all phases of the simulation activities.

REFERENCES

1. McBrayer, R.O.; and Steadman, J.D.: CVT/PCS Phase I Integrated Testing. NASA TM X-64770, 1973.
2. Taketa, S.T.: Shuttle Bioresearch Laboratory Breadboard Simulations. Proc. Amer. Astronaut. Soc., Advances in Astronaut. Sci., Vol. 32, Part II, Paper 75-257, 1975.
3. Shurney, R.E.; Cantrell, E.; Maybee, G.; and Schnitt, S.: CVT/GPL Phase III Integrated Testing. NASA TM X-64909, 1975.
4. Anon.: Reference Earth Orbital Research and Applications Investigation (Blue Book), Preliminary ed., NHB 7150.1, Vol. III, Life Sciences, Jan. 15, 1971, NASA, Washington, D.C.
5. Anon.: Final Report of the Space Shuttle Payload Planning Working Groups, NASA TM X-66842, Vol. 4, 1973.
6. Rahlmann, D.F.; Kodama, A.M.; Mains, R.C.; and Pace, N.: Results from the EPL Monkey-Pod Experiment Conducted as Part of the 1974 NASA/Ames Shuttle CVT-II, EPL 64-1, Environ. Physiol. Lab., University of California, Berkeley, June 10, 1974.
7. Rahlmann, D.F.; Kodama, A.M.; Mains, R.C.; and Pace, N.: Results from the EPL Monkey-Pod Experiment Conducted as Part of the 1974 NASA/MSFC CVT/GPL III, EPL 74-2, Environ. Physiol. Lab., University of California, Berkeley, Oct. 15, 1974.

METABOLIC RATE CONTROL DURING EXTRAVEHICULAR ACTIVITY SIMULATIONS AND MEASUREMENT TECHNIQUES DURING ACTUAL EVAs

David J. Horrigan, *NASA, Johnson Space Center, Houston, Texas*

ABSTRACT

A description of the methods used to control and measure metabolic rate during ground simulations is given. Work levels attained at the Space Environment Simulation Laboratory of the L. B. Johnson Space Center are presented. The techniques and data acquired during ground simulations are described and compared with inflight procedures.

Data from both the Skylab and Apollo Programs are utilized and emphasis is given to the methodology, both in simulation and during flight. The basic techniques of work rate assessment are described. They include oxygen consumption, which was useful for averages over long time periods, heart rate correlations based on laboratory calibrations, and liquid cooling garment temperature changes. The relative accuracy of these methods as well as the methods of real-time monitoring at the Mission Control Center are discussed. The advantages and disadvantages of each of the metabolic measurement techniques are discussed. Particular emphasis is given to the problem of utilizing oxygen decrement for short time periods and heart rate at low work levels.

A summary is given of the effectiveness of work rate control and measurements; and current plans for future EVA monitoring are discussed.

INTRODUCTION

Plans for extravehicular activity (EVA) in the Apollo Program raised questions with regard to the physical costs to the crewmen, and the physical

capabilities of the crewmen. This information was important to those planning consumable usage and crew tasks. It was also significant in crew training and simulations to be able to control workloads to mission related levels. As we completed the Apollo flights and initiated the Skylab Program, a large amount of inflight data became available for use in mission planning and crew training. The metabolic rates established for Skylab training in the space suit were partially based on previous data although the null gravity experience with EVA was not as great as the 1/6-g experience.

Measurement Methods

Heart Rate - As discussed above, the heart rate method was based on a preflight correlation between heart rate and metabolic rate. During the Skylab Program, this correlation was determined inflight by utilizing the most recent metabolic experiment run (M171) which provided an updated correlation of heart rate and metabolic rate. This provided a correction for any changes which might have occurred in the crewman's physiological state since his preflight calibration. The heart rate method generally is less reliable than the other two methods in the low heart rate range (<100 beats per minute). It is also adversely affected by psychogenic tachycardia.

Oxygen Decrement - Metabolic rate was determined from an analysis of the oxygen bottle pressure decrement per unit time. A predetermined pressure suit leakage was included in the input to the program for each crewman. Because of the resolution required for this data, a 15 psia drop was required before the program would provide an update. This prevented false high readings and improved the accuracy of the method. However, metabolic rate determinations for short-term activities were not feasible. The oxygen consumption method assisted in confirming the results of the LCG thermodynamics method.

Liquid Cooling Garment (LCG) - A correlation was set up for LCG ΔT as a function of metabolic rate assuming a predetermined water flow rate. This method proved to be an excellent indicator of total metabolic production. If the crewmen were to sweat, it would cause a lag time in the appearance of BTUs as the sweat evaporated. However, this did not prove to be a problem. The garment can suppress sweating at work rates as high as 500 Kcal/hr.

These methods were selected because standard metabolic rate measurement techniques would have

broken pressure suit integrity. However, it is interesting to note the similarity of the LCG method to the classical method of direct calorimetry where body heat output was recorded by measurement of the temperature change of water flowing through the walls of a small chamber (1).

Ground Training in the Space Suit

One of the principal locations for training in the pressure suit for the Apollo and Skylab flights was the Space Environment Simulation Laboratory (SESL) at the Johnson Space Center. The man-rated chamber at this facility was utilized for work in the space suits in a vacuum environment at preselected metabolic rates. The crewmen were first calibrated in the laboratory to correlate their heart rates with metabolic rates. Then, during the vacuum runs, an auditory pulse timer was set to preselected rates to prompt the crewman as to how often he had to step up on a stand to elicit the desired workload. An example of the laboratory calibration is shown in Figure 1. An estimate was then made of the number of times per minute the crewman would have to step up on the 6-inch step to elicit a heart rate which would correspond to the preselected metabolic rates.

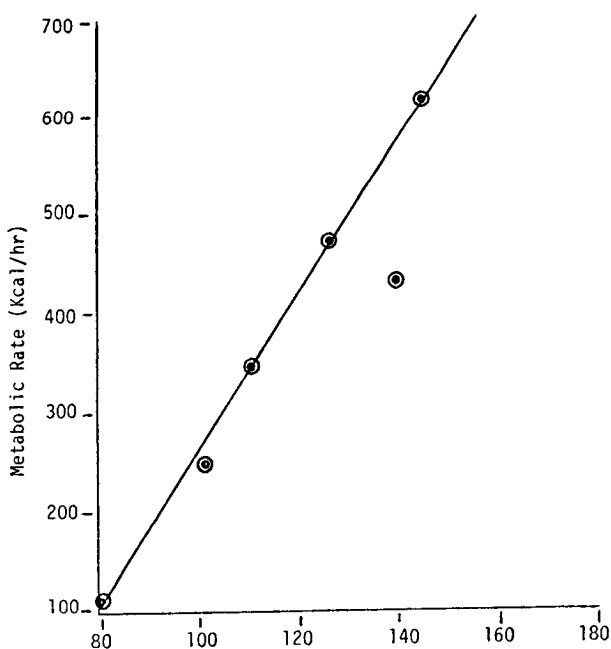


Fig. 1-Step test calibration

Table I shows a typical protocol during the training of the Skylab crews. This protocol was designed to give the Skylab crewman experience in pressure suit activities similar to those expected during the actual flights. During these activities an attempt was made to control the metabolic rates to levels typical of previous suited operations in space. Work was first performed with the suit in the unpressurized state to simulate those operations conducted prior to pressurizing the suit for EVA or intravehicular activities (IVA). After pressurizing the suit, work rates of 200 Kcal per hour and 300 Kcal per hour were performed. Then the cooling water to the suit was shut off and a work rate of 200 Kcal per hour was done without cooling. This was to simulate an anticipated IVA without cooling. The chamber was then depressurized to 3 psia and then back up to 5 psia as EVA work rates of 300, 400, and 500 Kcal/hr were accomplished. Again cooling was terminated and work rates of 400 and 500 Kcal/hr were repeated. The same frequency of stepping was used and elicited similar heart rates even with the temporary lack of cooling.

In addition to monitoring the heart rate to control work rates, parameters related to metabolic rate were monitored through a real-time computer program similar to that used during actual space flights. Thus, the LCG data was a check on the heart rate data. Since the Skylab oxygen supply was via an umbilical system, it was not feasible to use the oxygen decrement program which was used on Apollo. General agreement was obtained between the heart rate and LCG data with the exception, of course, of those segments of the protocol during which liquid cooling was not used.

Table I
A Typical Protocol During EVA Training

Heart Rate Beats/ Min	Metabolic Rate Kcal/ hr	Duration of Work Periods (Min)	Predicted Step Inter- val (Sec)	Actual Step Interval (Sec)
(Chamber at 5 psia; suit unpressurized)				
83	200	3	10	14
104	300	3	6	10
(Suit pressurized - IVA training)				
83	200	3	14	18
104	300	2	8	14
83*	200	4	14	18
(Chamber decompressed to 3 psia, back to 5 psia, down to vacuum)				

Table I (cont.)
A Typical Protocol During EVA Training

Heart Rate Beats/ Min	Metabolic Rate Kcal/ hr	Duration of Work Periods (Min)	Predicted Step Inter- val (Sec)	Actual Step Interval (Sec)
104	300	3	8	14
123	400	5	6	7
143	500	4	5	5
123*	400	2	6	8
143*	500	2	5	6
(Repressurize to 5 psia, back to vacuum, repressurize to ambient)				
94	250	5	12	18
*No Cooling Water				

Ground-based metabolic rates were also monitored during the training at Kennedy Space Center (KSC) prior to the lunar missions.

Table II lists the ground-based training metabolic rates as compared to the rates during actual lunar activity. As would be expected, the 1/6-g provided a considerable reduction in work. The one-g training was valuable in assessing the validity of measurement techniques, but of only limited value in predicting actual workloads on the lunar surface and during free-space EVAs. The term "overhead" was used to group together tasks such as egress, setup of equipment, ingress and stowage of lunar samples.

Table II
Metabolic Rate Measurement During Training
and Inflight

Activity	KSC Training (Kcal/hr)	Inflight Data (Kcal/hr)	Percent Decrease
Overhead	379	275	27
Station Activity	445	228	49
LRV	203	123	39
Average	393	230	41

Real-Time Monitoring

During the lunar EVAs, the analysis of the work rate was accomplished by the same basic mechanisms as were utilized during training - namely heart rate, oxygen decrement, and temperature change in the LCG. These methods were selected because standard metabolic rate measurement techniques would have broken pressure

suit integrity. The data available from the crewmen during the lunar EVAs consisted of voice, electrocardiogram (ECG), oxygen bottle pressure, liquid cooled garment water entry temperature, and the change in this temperature after flowing through the suit. After the Apollo 11, 12, and 14 missions, the sublimator feedwater which remained in the Portable Life Support System (PLSS) was poured into a bag and weighed. During the later missions, the sublimator feedwater was carried in two tanks to meet the requirements of extended EVA periods. When the first tank was emptied, an alarm sounded and the crewman switched to the second tank manually. This allowed for a check on the feedwater usage rate and the heat removed from the pressure suit could be calculated and compared with the LCG metabolic program.

During the Apollo Program, frequent EVA simulations were conducted with the support of the real-time computer complex at the Mission Control Center. The displays on the cathode ray tubes were identical to those during actual EVAs, and an electrocardiogram was also displayed on a strip chart. All three methods of estimating metabolic rate were utilized during the simulations. The data gathering, analysis, and real-time simulated anomalies provided a high quality of training and resulted in effective operations during the actual missions.

During the EVAs of the Apollo Program, real-time data was available throughout the entire length of the activity. By utilizing all three programs, a "best estimate" of crewman workload for each activity was reported to the Flight Surgeon in the Mission Operations Control Room. A typical list of workloads for selected activities is shown in Table III. During the Skylab EVAs, real-time monitoring was feasible only when the crew were in contact with a ground station. The fragmented data permitted only a partial analysis of crew workload during the real-time operations. The complete data was acquired later from a tape dump. The oxygen decrement method of metabolic rate assessment was not used since the crew were on the open loop umbilical system.

Table III
Metabolic Expenditures for Selected
Events of a Typical Skylab EVA

Events	Duration Min	Metabolic Rate Kcal/hr
Pre-egress operations	12	374
Egress	8	412
LRV traverse	26	122
Station 1 activities	18	246
Photography and traverse preparation	5	333
Solar wind composition experiment deployment and EVA termination	13	406

Effectiveness of Work Rate Control and Measurements

Work Rate Control - The protocol described in Table I was a training function in the chamber, and the step test with a timer was useful and effective in controlling metabolic rates at the desired levels. This is only useful if real-time measurements are available to permit adjustments during the protocol and to provide a validation of the proper workloads.

Measurements - When direct laboratory methods were not feasible, the use of more than one technique of acquiring and analyzing work rates was useful in providing assurance of correct information. The heart rate method was not used for overall averages, but was the only method that could provide analyses of short-term activities. The oxygen decrement method had a slow update programmed in because of a resolution problem, but was very accurate for long periods. The LCG method provided reliable analysis during steady-state conditions, but was not as accurate in the event of sweating or of frequent changes of the flow selector valve.

Future EVA Monitoring - As an activity becomes more common and hence more predictable, the need for a large variety of monitoring sensors is not seen as necessary or desirable. The question of the quantity and type of biomedical monitoring during the EVAs of the Shuttle era has not been worked out in detail. Electrocardiogram data will probably be utilized as a check on stress and medical status rather than as a basis for a comprehensive metabolic rate analysis.

Shuttle EVAs are expected to be facilitated by the development of a manned maneuvering unit.

REFERENCES

1. Bell, Davidson, and Scarborough: Textbook of Physiology and Biochemistry, 7th ed. Livingstone, 1969.
2. National Aeronautics and Space Administration, Lyndon B. Johnson Space Center (JSC-08006) Test Report-Skylab 3 and 4 Crew Training Test, April 1973.
3. Waligora, J. M. et al.: Apollo Experience Report - Assessment of Metabolic Expenditures, NASA Technical Note (JSC-07484), September 1974.
4. Waligora, J. M. and D. J. Horrigan: Apollo Biomedical Experience Report, Sec. II Crew Health and Inflight Monitoring During Apollo EVA Periods, Chapter 4, Metabolism and Heat Dissipation During Apollo EVA Periods. (In Press)

THE USE OF A MODEL OF HUMAN THERMOREGULATION DURING THE APOLLO AND SKYLAB PROGRAMS

James M. Waligora, NASA, Johnson Space Center, Houston, Texas

ABSTRACT

A model of thermoregulation in man was used operationally during the Apollo and Skylab programs. The evolution of this description of thermoregulation is discussed as well as the supporting research programs that led to its growth in representational detail and operational accuracy. A discussion of the operational use of the model is presented as well as future applications of the model.

INTRODUCTION

A mathematical model of thermoregulation in man was used throughout the Apollo and Skylab programs and had a significant impact on the programs in a number of ways.

It was used to set heat tolerance limits in pressure suits and cabins, to size life support cooling systems, to predict water generation in spacecraft, to predict drinking requirements in pressure suited operation, to predict comfort limits in spacecraft, and to evaluate adequacy of temperature control of crewmen during extravehicular activities. The model also contributed to the assessment of metabolic rate of crewmen during extravehicular activity and to the evaluation of the medical data collected by the Skylab medical experiments.

The use of this model in the space program was probably the most extensive use of a model of a physiological system in man as an operational tool in a major engineering program. A description of the use of the model may be useful to those using models of this nature for similar purposes.

Model Development

Early in the Apollo program when liquid cooling was being considered to support a crewman working on the lunar surface and when the level of work required

to walk on the lunar surface was speculation; analytical programs were being constructed representing suit and cabin environmental control systems. Physiological limits had not been firmly set and it became clear that representation of the thermal responses of man was the weak link in a thermal balance assessment of several environmental control system problems.

Accordingly, an effort was undertaken to produce a method to predict thermal responses to any environment. Thermal limits available in aviation and occupational health programs were examined for their applicability in predicting thermal response. These standards were not well suited to the need. The indices were either empirical in nature or stated in terms of a physiologic response (refs. 1, 2, 3). If they did use a heat balance approach, they considered the man as a constant temperature source and did not represent thermoregulatory responses (refs. 4 5). Therefore, a simple set of heat balance equations and empirical thermal responses was prepared to be used by the thermal analysis group. Although this set of equations was not thought of as a model, it was in fact a simple model. It had a mass and a surface area but no shape or internal detail. The model was programmed but was never used before it was replaced by a more sophisticated model. This model was a two-node analog model in use by Dr. Hardy and Dr. Stolwijk of the John B. Pierce Foundation Laboratory and it was obtained from them in early 1965. This model was converted to digital form at the Johnson Space Center (JSC) and was used for a considerable period of time. For resting steady-state conditions, the model could provide very good whole-body simulation. Starting in 1965, an active research program was sponsored at the Pierce Foundation investigating thermoregulation in man utilizing modeling as a tool in the definition of thermoregulatory mechanisms. As a result of this research, a series of models were developed. A six-node analog model was developed in 1966, a 13-node digital model was generated in 1968, and a 25-node model in 1970 (refs. 6, 7, 8). The increased definition of the later models permitted more accurate representation of levels of metabolism encountered during physical work and permitted representation of dynamic situations where metabolism and environmental parameters change within a time frame of a few minutes.

The models were made available to the thermal analysis group at JSC. They converted the analog models to digital, added environmental interfaces to the model and developed a model of ventilation in the pressure suit (ref. 9). Additional nodes were added to the models at JSC to allow bilateral representation of the arms and legs.

Utilization

The first use of the model was in predicting latent and sensible heat loss avenues for sizing cabin environmental control systems (ECS). It soon became apparent that the model could be used to assure compliance with the heat storage limits that were being used in sizing pressure suit cooling systems. A 75-Kcal heat storage limit was selected as a tolerance limit based on interpretation of an Air Force tolerance criteria (ref. 5). This criteria was based on tests with a maximum duration of 2 hours in an environment quite different from that of the pressure suit, and the subjects were at rest. Although the 75-Kcal heat storage limit was established as a conservative limit, a test program was initiated to verify the limit at higher work rates and under conditions more representative of the pressure suit environment (ref. 10). This data and the data of other investigators indicate that the tolerance limits selected were applicable. Although the average tolerable heat storage of a population increased with exercise, the minimum tolerance point did not.

The model was used as a part of the evaluation of many thermal environments. Some were simple and some were quite complex. The complexity of the environment determined the extent to which empirical data was required to validate model predictions for a specific environment. Where the model was used to predict heat storage under conditions of very limited physical heat removal, as in the case of the pressure suit emergency ventilation, the accuracy of the model in predicting thermoregulatory response was not as critical, because the thermoregulatory response could not be effective. In such a case, the difference between metabolic rate and the maximum heat removal was the rate of heat storage and tolerance was a function of time. In other cases where the limiting factors were as much physiological as physical (for instance a gas cooled suit at high flow rates) the representational accuracy of the model was quite critical and updates to the model changed assessments of the tolerance of a given contingency.

Although the decision to provide a liquid cooling system in the pressure suit was made before the model was available, the model showed clearly the necessity for liquid cooling. To use the program to represent a man wearing a liquid cooling garment, data was collected which would allow such an interface. Tests conducted at JSC using high metabolic rates and low coolant temperatures defined heat transfer coefficients

which allowed representation of the liquid cooled garment in the model (ref. 11). Data collected later at the Naval Air Crew Equipment Laboratory (ref. 12) indicated that different heat transfer coefficient had to be used to properly represent the liquid cooling garment at high coolant temperatures and lower metabolic rates. This data defined the maximum heat removal capability of the spacesuit coolant system and allowed evaluation of heat balance during the lunar walks. The contingency system for the pressure suit employed limited gas cooling. The maximum distance a crewman could walk away from the lunar landing module or the lunar rover was constrained by analysis with the model of heat storage using the contingency cooling system at assumed walking speeds and metabolic rates.

The thermoregulatory program was also used to contribute to an assessment of metabolic rate during the extravehicular activities on both Apollo and Skylab. The heat removal of the liquid cooling garment at given coolant temperatures and at comfortable body temperatures was specific for each metabolic rate. Data generated by the model made possible the development of a simple operational program to output metabolic rate from engineering measurements telemetered from the backpack cooling system. This data in combination with O_2 pressure data and heart rate data telemetered from the backpack allowed real-time evaluation of metabolic rate during each of the extravehicular activities.

In the early planning of the Skylab mission, the spacecraft was to be an active fuel tank prior to occupancy. The initial estimations of the environment indicated a change in temperature of about $40^{\circ} F$ during each orbit. The evaluation of this environment led to the definition of a thermal comfort and tolerance design criteria in 1967 (ref. 13). This document was updated in 1968 and again in 1970. The document stated thermal comfort and tolerance limits in terms of steady-state heat storage as predicted by the thermoregulatory program and as bounded by specific limits for individual parameters. The comfort limits in the criteria were based on research done at Kansas State University using very large subject populations and in which the primary measurements were comfort votes and a numerical scale (refs. 14, 15). The recommended comfort environmental ranges determined by this research were input into the thermoregulatory model and minimum and maximum heat storage values were output and used as comfort limits. In this manner, the heat balance technique could be used to evaluate comfort in an unusual environment in space flight where convection was reduced at 5.0 psia and where cycles in temperature or substantial differences between air temperature and mean radiant

temperature were potential problems.

The model predicted a 2 to 3 degree shift of the comfort band as a result of the lower pressure and reduced convection in Skylab. Clothing, air motion, and metabolism conditions that resulted in a 70° to 80° F permissible range at 14.7 psia led to a 67° to 78° F range at 5.0 psia. A program was initiated at the Naval Air Crew Equipment Laboratory to verify this shift (ref. 15). The shift was verified at least qualitatively by these tests, by tests done at the Marshall Space Flight Center and by Skylab flight experience. A comfort box generated by the model became the comfort specification for Skylab and contractors were given the computer model and the design criteria to allow them to do their own analysis of specific environmental conditions.

As a result of more rapid diffusion of water vapor in the 5.0 psia pressure of the Apollo and Skylab vehicles, low humidity was more of a problem as far as discomfort (ref. 17). The thermoregulatory program includes prediction of sweat loss and evaporative heat loss from the lungs and this capability in the model was used to size the humidity control system in Skylab.

Using a heat balance technique the model can be used to compare dissimilar but stressful thermal environments by comparing the predicated strain they impose on the crewmen. Figure 1 shows predicted heat storage generated by the model from environmental parameters measured during a lunar extravehicular activity performed on Apollo 15. Figure 2 shows heat storage predicted by the model from more conventional environmental conditions while the same work rate is imposed.

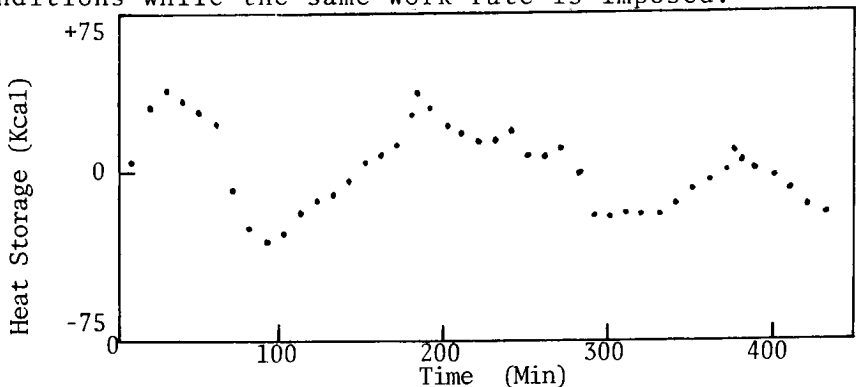


Fig. 1 - Heat storage as predicted by the thermoregulatory model for the CDR in the pressure suit environment during the second lunar walk on Apollo 15. The average metabolic rate was 250 Kcal/hr.

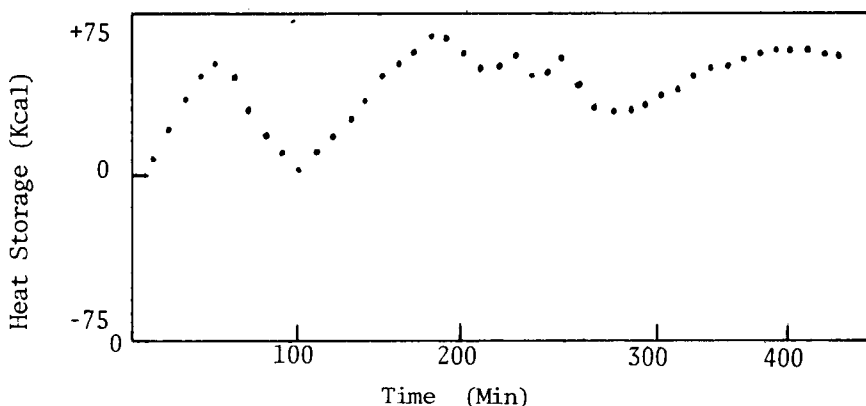


Fig. 2 - Heat storage as predicted by the thermoregulatory model for a man dressed in gym trunks and T-shirt in a 65° F gymnasium; exercising at the metabolic rate profile experienced by the Apollo 15 Commander during the second lunar walk.

Although no physiological parameters that would allow direct calculation of heat storage were measured during the lunar walk, the model allows a comparative assessment of thermal strain to be made and indicates that the Apollo crewman was closer to thermoneutrality than a man working at the same rate under more conventional environmental conditions.

SUMMATION

There is some resistance to the operational use of a physiological model. Some of this resistance stems from the fear that the model will be used instead of empirical data. There is also concern by those doing modeling that a model might be used without familiarity with the details of the model and, therefore, without an appreciation of the limitations of the model.

The model is properly understood as a hypothesis of the mechanism of operation of a physiological system. As such it is valid only to the extent that it has been challenged and verified by empirical data.

The successful use of the model at JSC is a result of cooperation among scientists, bioengineers, and programmers from several sources outside the NASA and from different organizations within NASA. This effort included development and verification of the basic model at the Pierce Foundation Laboratory, research

required to adapt the model to its operational use, modification of the model to apply it to the spacecraft and pressure suit environments, verification of the modified model and verification of specific model predictions for unusual environments.

The model served to define areas requiring investigation and provided preliminary answers until empirical information became available. The framework of a criteria outlining limits within which the model is applicable served to eliminate improper use of the model. The model and the thermal criteria have received wide distribution and it is possible that it could be misused, however, that is the case with any design guide. By its nature a limit based on a model, particularly when it is well documented, provides more information to a user as to its applicability to an operational problem than a simple empirically determined environmental limit, and is more likely to be properly used.

Recent research at the Pierce Foundation has improved definition of the interactive effects of the respiratory and cardiovascular system with the thermoregulatory system. Research has also improved the definition of the circulatory response to thermoregulatory control as opposed to the evaporative and metabolic responses which have been more intensively studied. Future investigations will be directed to increasing the accuracy of prediction of a specific group within a population or of an individual by definition of thermoregulatory set points and gains either by population description or by definitive test procedures on individuals. This capability is particularly desirable to deal with the wide population variation that may be acceptable as Shuttle passengers.

The thermal model is presently being used to define inputs to Shuttle design requirements. It is anticipated that a whole-body algorithm being developed to help analyze the Skylab medical data will allow similar operational use of models of other physiological systems.

REFERENCES

1. Houghten, F. C. and C. P. Yaglou: Determining Equal Comfort Lines. Trans Amer Soc Heat and Ventil Engrs 29:163, 1923.
2. Bedford, T.: Environmental Warmth and Its Measurement. Medical Research Council War Memorandum No. 17, His Majesty's Stationary Office, London, 1946.

3. Beldin, H. S., T. F. Hatch: Index for Evaluating Heat Stress in Terms of Resulting Physiologic Strains. Heating Piping and Air Conditioning 27:129-136, 1955.
4. Gagge, A. P.: Standard Operative Temperature, A Generalized Temperature Scale, Applicable to Direct and Partitional Calorimetry. Am J Physiol 131:92-102, 1940.
5. Blockley, W. V., J. W. McCutchan, C. L. Taylor: Prediction of Human Tolerance for Heat in Aircraft. A Design Guide, WADC-TR-53-346, May 1954.
6. Stolwijk, J. A. J., J. D. Hardy: Temperature Regulation in Man - A Theoretical Study. Pfluegers Arch 291:129-162, 1966.
7. Stolwijk, J. A. J., D. J. Cunningham: Expansion of a Mathematical Model of Thermoregulation to Include High Metabolic Rates. Final Report-A NAS-9-7140, 1968.
8. Stolwijk, J. A. J.: A Mathematical Model of Physiological Temperature Regulation in Man. Final Report NAS-9-9531, NASA CR-1855, 1970.
9. Morgan, L. W., G. Collete, D. W. Cook: Computer Program Documentation - 41-Node Transient Metabolic Man Program, J196, 1970.
10. Blockley, W. V., H. P. Roth: Limits of Endurance for Heat Stress Arising From Work While Totally Insulated. Final Report NAS-9-8871, 1970.
11. Waligora, J. M., E. L. Michel: Application of Conductive Cooling for Working Men in a Thermally Isolated Environment. Aerospace Med 39:485-487, 1968.
12. Santa Maria, L. J.: Determination of Skin Temperature Under Comfort - Controlled Liquid Cooled Garment in Exercising Subjects. NADC-CS-7118, 1971.
13. Waligora, J. M.: Thermal Comfort and Tolerance Design Criteria, BRO DB-57-6R, Change B, 1970.
14. Nevins, R. G., F. H. Rohles, W. Springer, A. M. Feyerherm: A Temperature-Humidity Chart for Thermal Comfort of Seated Persons. ASHRAE Journal 55, April 1966.
15. McNall, P. E., I. Jax, F. H. Rohles, R. G. Nevins, W. Springer: Thermal Comfort (Thermally Neutral)

Conditions for Three Levels of Activity. ASHRAE Trans.
73, 1967.

16. Santa Maria, L. J.: Effects of Reduced Ambient Pressure Conditions on Thermal Comfort in Mildly-Active Subjects. NADC-73064-40, 1973.

17. Carleton, W. M. B. E. Wesh: Flued Balance in Artificial Environments: Role of Environmental Variables. NAS-CR-114977, 1971.

EVALUATION OF THE GRAVITY INDEPENDENT MINIATURE ANALYTICAL SYSTEM

Larry D. Wallace,† Carolyn S. Leach, and C. B. Lassiter,† NASA, L. B. Johnson Space Center, Endocrine and Biochemistry Laboratories, Houston, Texas

ABSTRACT

The gravity independent Fast Analyzer System evaluated in this communication was designed for the National Aeronautics and Space Administration by Oak Ridge Laboratories. The system consists of a 17 place rotor type spectrophotometer and computerized data acquisition system weighing only 30 pounds and occupying a volume of 1 cubic foot.

INTRODUCTION

The miniature fast analyzer is an automated, analytical instrument developed for NASA primarily for potential use for biochemical analyses conducted in space flight. Instruments based on the concept conceived by Dr. Norman Anderson in 1968 were initially developed by members of his staff at Oak Ridge National

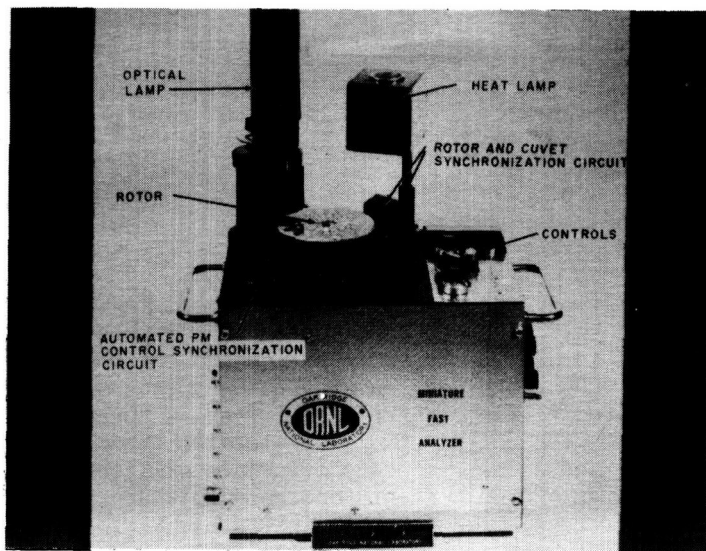


Fig. 1 - Miniature fast analyzer

Laboratory under the directions of the National Institute of General Medical Sciences and the U.S. Atomic Energy Commission.

RESULTS

The miniature fast analyzer is a compact, bench-top instrument occupying one cubic foot of space and weighing only 30 pounds, whereby, it can easily be moved or stored.

The primary function of the analyzer is to spin a 17-cuvet rotor through a stationary optical system at speeds ranging from 100 to 5000 rpm with 1000 rpm being the normal speed to determine the transmittance through the solution being analyzed. The optical system consists of a quartz-iodine tungsten light source mounted in a movable housing above the rotor, interference filter and a miniature photomultiplier (PM) tube. The six interference filters (340, 400, 415, 485, and 620 nm) are contained in a movable wheel which is mounted directly under the rotor housing. The appropriate filter is manually placed in the optical light path using the filter selector switch. The signals generated by the PM tube can be displayed conveniently on an oscilloscope. Since the rotors contain 17 individual cuvetts, the resulting display has 17 signals corresponding to the light transmittance of the solution contained in each cuvet. By defining the signal from cuvet 1 to represent 100% transmittance, the relative percent transmittance of the individual cuvetts can be determined, converted to absorbance values and used in the calculation of results.

The rotor is placed into its housing and indexed by matching slots in the rotor with two offset indexing pins that ensure a single orientation of the rotor in its holder. The rotor and its housing are driven by a dc servomotor, located in the instrument cabinet, in conjunction with a tachometer generator. A 4-position switch marked Auto, Stop, Run, and Accelerate is provided to control the rotor. In the accelerate position, the rotor is rapidly accelerated to the speed set by a potentiometer (POT). In the run position, the rotor is spun at a speed set by the rotor speed pot located directly above the 4-way switch. At any speed, the rotor may be abruptly stopped simply by setting this switch to stop. A meter indicating rotor speed is conveniently located on the upper right corner of the cabinet top.

In actual practice, the loaded rotor is placed in its housing with the speed switch set at stop and the rotor speed at zero. The switch is then turned to the run position and the rotor slowly accelerated to 1000 rpm by dialing the rotor speed using a previously calibrated setting. After the switch is turned to the accelerate position, the rotor rapidly accelerates to 4000 rpm, a speed previously set. This sequence of events will ensure quantitative transfer of the contents of the sample and reagent cavities into their respective cuvetts. Thorough mixing of the contents within the cuvetts is achieved by alternately braking and accelerating the rotor. When the rotor switch is placed in the auto position and the run switch located on the data printer is

actuated, the acceleration and braking sequence is automatically performed.

The rotor housing also contains a set of synchronization apertures located on the peripheral edge of the rotor holder. Synchronization signals for the computer and analog display scope are provided by the cuvet and rotor synchronizing photometric detectors through which the peripheral edge of the spinning rotor housing passes. Thus, during rotation, the synchronization apertures pass through these detectors and allow light to impinge on a photodiode. The resultant signals are used to synchronize the analyzer with its scope and data system.

A third photometric detector is used to provide a signal indicating that cuvet number 1 is in the light path. An automated control circuit then obtains the photomultiplier voltage signal produced by the light transmission peak of the solution contained in cuvet number 1 and maintains this value at constant voltage by varying the high voltage supplied to the photomultiplier. This modification eliminates the need to adjust manually the photomultiplier voltage supply each time a different filter is placed in the optical light path. This feature becomes quite advantageous when performing multi-chemistry analyses which require sequential and repetitive filter changes.

Instrumentation utilized in a biochemistry laboratory to determine enzymatic reactions must be capable of maintaining a precise temperature to ensure that the proper reaction rate will occur. To measure the temperature of the rotor, a calibrated thermistor is embedded in a copper-tipped, stainless steel pin. This pin is mounted on the rotor holder of the analyzer and also serves as one of the two indexing pins. Once a rotor is in place, the measuring section of the pin contacts the center portion of the rotor midway between two cuvetts. The resulting signal from the thermistor is transmitted from the rotor holder through a pair of slip rings and brushes to an operational amplifier circuit. Which, in turn, provides a meter display of the rotor temperature.

The thermistor output is also used with an additional operational amplifier circuit as a proportional controller to maintain the cuvet temperature at a constant level. The output from the controller powers the output of an additional lamp, which, when mounted above the rotor, serves as an infrared heat source for the rotor. The rotor temperature can be maintained from somewhat above ambient temperature to 37.5°C. Typically it is controlled at $30.0^{\circ}\text{C} \pm 0.2^{\circ}\text{C}$ in an ambient temperature of $25^{\circ}\text{C} \pm 1^{\circ}\text{C}$.

The primary component of the analyzer is a 17-cuvet rotor, a multi-functional device in which samples and reagents can be loaded either dynamically or discretely. Solutions can be injected into the center of a spinning rotor and split into aliquots by vanes, and simultaneously transferred into their respective cuvetts; or samples and reagents can be loaded discretely into either of two concentric series of cavities, these samples and reagents are transferred to their respective cuvetts when rotation begins.

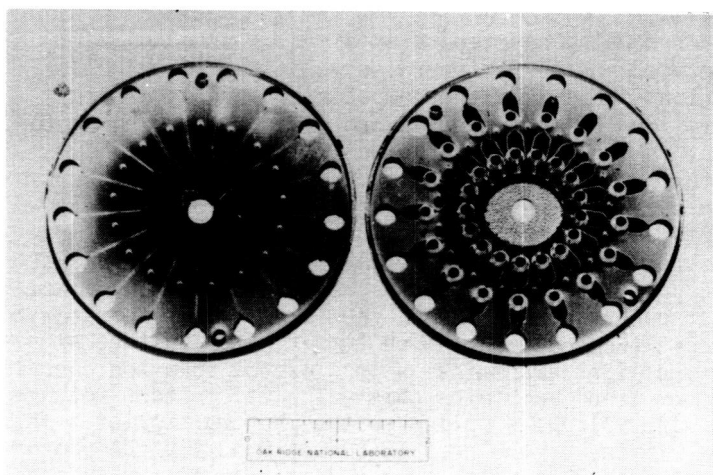


Fig. 2 - 17-Cuvet rotor

The volume capacities of these rotors are quite low. For example, the sample volume per cuvet range from 1 to 10 μ l and are assayed in a total reaction volume of only 130 μ l.

An unassembled rotor consists of three separate parts -- a body and two windows, which are all sealed together to produce a finished rotor. The rotor components are fabricated by means of a computer-controlled machining method. Black acrylic plastic, 0.5 cm thick, and 3.2 mm thick ultraviolet-transmitting (UVT) acrylic plastic are used for the body and windows respectively. Using the UVT as the window material allow the rotors to be used for analyses in the 300 - 700 nm region of the energy spectrum. The rotor components are assembled using a silicone adhesive.

"The data system is composed of a PDP-8/E computer (Digital Equipment Corp., Maynard, Mass.) with 8192 words of core memory, a 1200- Hz line-frequency-based clock, an ARS 33 Teletype, a Sykes cassette-tape unit (Sykes Datatronics Inc., Rochester, N.Y.), and the necessary analog and digital interfaces for coupling the analyzer to the computer hardware". (1)

The high-level FOCAL language (registered trade name, Digital Equipment Corp.) has been modified and expanded to accept data under real-time control of the line-frequency clock. Subprograms have been altered and added to allow program and data storage on and recovery from the cassette tape. Data from several analyses may be stored for later study and correlation. (1)

An operating program has been developed for the routine system. This program contains an executive file which requires the operator to respond to a series of questions to initiate the daily operation by loading the computer core automatically. (1)

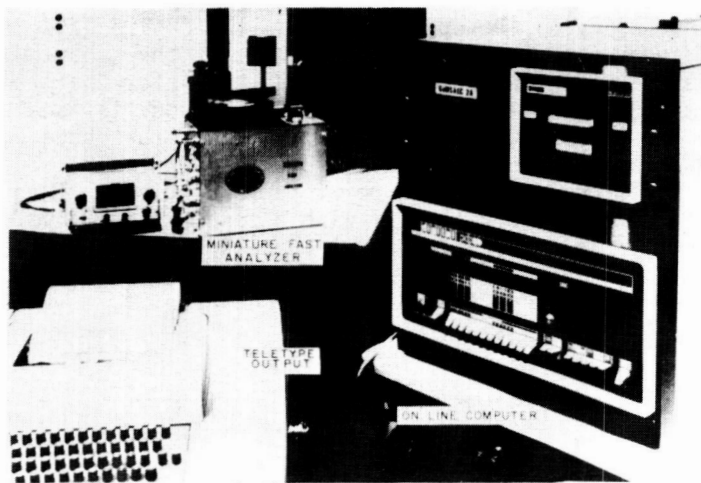


Fig. 3 - Miniature Fast Analyzer and PDP/8E computer

An example of this program is shown in Figure 4 with operator responses shown underlined.

```

Day 147 Time 10 : 0 : 9
DO YOU WISH TO CALIBRATE A ROTOR (YES OR NO): NO
TO SELECT A CHEMICAL PROCEDURE ENTER ONE OF THE FOLLOWING CODES:
CODE      CHEMICAL PROCEDURE
108-      CHOLESTEROL
401-      GLUCOSE (FASTING)
402-      GLUCOSE (1 HOUR)
403-      GLUCOSE (2 HOUR)
404-      GLUCOSE (TOLERANCE)
411-      GLUCOSE
405-      URIC ACID
408-      ALKALINE PHOSPHATASE
409-      SGOT
410-      LDH-L
412-      TRIGLYCERIDES-KINETIC ASSAY
700-      TRIGLYCERIDES-EQUILIBRIUM ASSAY
800-      TERMINATE RUN
900-      RESTART
ENTER DESIRED CODE: 409
                      SGOT ASSAY
DAY 147 TIME 10 : 2 : 27
OPERATOR: LW
GEMSAEC UNIT: 17.2
ROTOR NUMBER: 40
READY!

```

Fig. 4 - NASA-ORL Miniature Analyzer results

The first response the program asks for may be answered yes or no. If no is given, the operator enters the desired code from the list of chemistry procedures. An example of the question: answer format is given for the SGOT procedure. After the proper entries have been made, the computer system is ready for analysis.

At the present time, there are 13 procedures that have been developed for application on the miniature fast analyzer. These procedures are either rate or end point type reactions. The sample volume ranges from 2 to 20 μ l with a total reaction volume of 130 μ l. See Table 1 for the list of these procedures.

Table 1 - Fast Analyzer procedures

Procedure	Sample Size(μ l)	Reagent Size(μ l)	Temp C	Type Reaction
Alkaline Phosphatase	10	20	30	Rate
Acid Phosphatase	10	20	30	Rate
Aspartate transaminase	10	20	30	Rate
Alanine transaminase	10	20	30	Rate
Lactate dehydrogenase	10	20	30	Rate
Creatine kinase	10	20	30	Rate
2,3-Diphosphoglycerate	10	20	30	Rate
Glucose	2	20	30	End point
Blood urea nitrogen	2	20	30	End point/ Rate
Triglycerides	20	80	30	Rate/Equil- ibrium
Calcium	10	75	30	End point
Creatinine (serum & urine)	10	20	30	End point/ Rate
Total Protein	10	100	30	End point

An evaluation of the instrument and procedures was carried out by the Biochemistry Laboratory at Johnson Space Center. The linearity of the fast analyzer was determined using different concentration of co-enzyme solutions. Results are shown in Figure 5. The percent coefficient of variation was determined on each procedure using normal and abnormal control serum. The results are presented in Table 2.

Fluid handling in zero gravity with presently designed rotors and loading techniques would be a major problem during space flight. Therefore, NASA-Johnson Space Center and Oak Ridge National Laboratory are considering alternative methods. One possibility is a whole blood rotor containing lyophilized reagent within the cuvetts. The concept is to reconstitute the reagents by dynamically adding a predetermined quantity of water to the rotor. The vanes of the rotor will be so designed to ensure that the water goes directly into the cuvetts. Then a predetermined amount of whole blood will be added dynamically while the rotor is spinning at 1000 rpm. The blood will quantitatively be collected

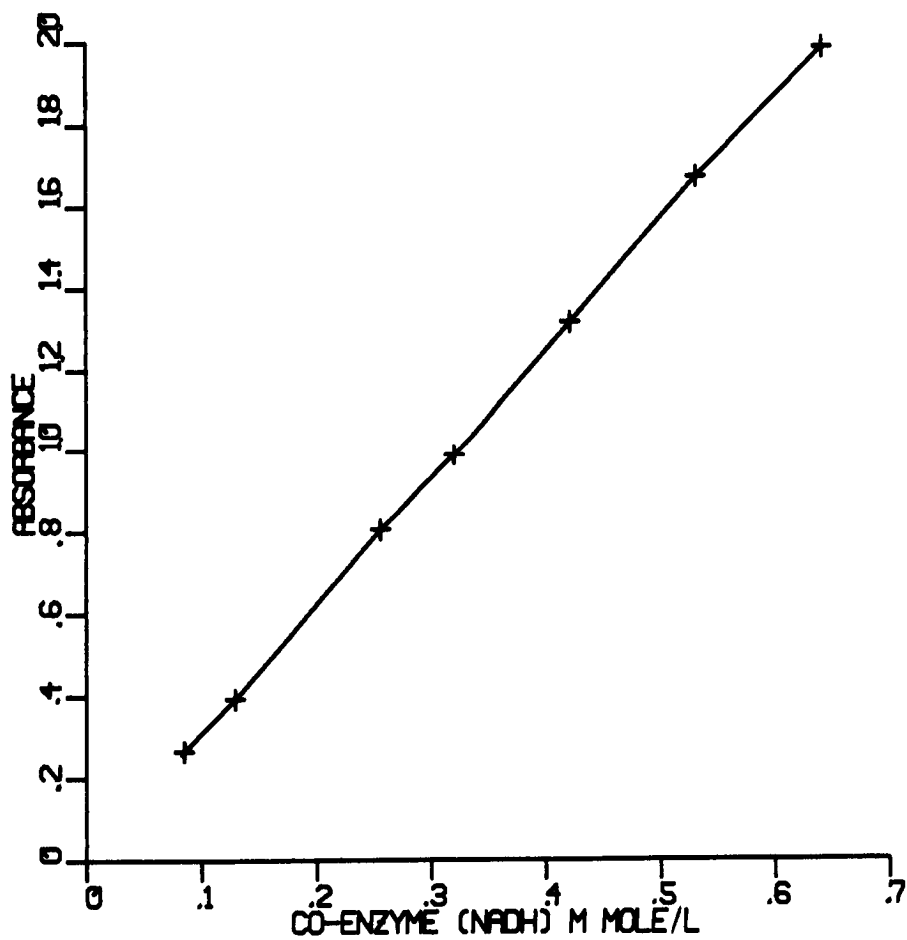


Fig. 5 - Linearity of Fast Analyzer

within a network series of capillary vanes. A second dynamic injection of heavy oil separates the cellular material from the clear plasma. The oil forces the displacement of the plasma into another network of capillary vanes. After this sequence has been completed, the rotor is stopped and removed from the rotor housing. The bottom portion of the rotor containing the oil and cellular material is removed and discarded. The rotor now contains only the sample and reagent and can be processed using the standard method.

Table 2 - Instrument variability

Procedure	N	\bar{X}	S.D.	C.V. % ^c
ALP ^a	48	31.0 I.U.	0.53	1.70
ALP ^b	48	49.6 I.U.	0.71	1.42
LDH-L ^a	48	57.0 I.U.	1.49	2.63
LDH-L ^b	48	269.4 I.U.	3.72	1.38
SGPT ^a	48	21.2 I.U.	0.81	3.81
SGPT ^b	48	42.1 I.U.	0.59	1.40
SGOT ^a	32	14.5 I.U.	0.97	6.65
GLUCOSE ^a	48	84.6 mg/dl	2.19	2.59
GLUCOSE ^b	48	282.6 mg/dl	3.62	1.28
BUN ^a	48	24.2 mg/dl	1.25	5.17
BUN ^b	48	9.9 mg/dl	0.32	3.17
TRIGLYCERIDES ^a	48	117.4 mg/dl	3.77	3.21
TRIGLYCERIDES ^b	48	112.3 mg/dl	4.11	3.66

a - Calbiochem normal control; b - Calbiochem abnormal control.

c - With the exception of blood urea nitrogen determination, the coefficients of variance obtained from the data in Table 2 are indicative of a five-fold increase in reproducibility using the Miniature Fast Analyzer; compared to routine clinical instrumentation. The coefficients of variance obtained from the blood urea nitrogen determination, using either method, are approximately equal.

The Miniature Fast Analyzer was the primary instrument in the Clinical Diagnostic System for the first Life Sciences Payloads Test. This seven day test was held at Johnson Space Center in September 1974. Blood samples were taken on days 2, 3, and 4 of the test. These samples were separated and aliquoted into two portions, one for real time analysis and the other for postflight analysis. Four enzymes, SGOT, SGPT, CPK, and LDH-L, all rate type reactions, were selected for analysis.

Rotors were loaded using the rotor loading station and then passed into the simulated space laboratory on the day of analysis. Thus the crew added the serum sample to the simulated pre-packed rotors. This was done by drawing the sample into a 50 μ l syringe and dispensing 10 μ l per test. This procedure was performed on

each crewman. Results of real time assays are in the following table.

Table 3 - Multi-enzyme analysis performed with 50 μ l syringe

	Enzyme activity (U liter ⁻¹ min ⁻¹)			
	SGOT	SGPT	CPK	LDH-L
Mission day 2				
P.S.	15.8	13.6	23.1	26.2
M.S.	18.4	22.0	53.7	39.0
Mission day 4				
P.S.	11.7	13.1	24.0	29.5
M.S.	14.1	18.0	47.1	39.0
Mission day 6				
P.S.	14.1	19.4	28.9	40.3
M.S.	17.0	22.4	49.3	44.3
P.S. - Payloads Specialist; M.S. - Mission Specialist				

Post-flight analysis was performed on three of the four enzymes using the rotor loading station to load the 10 μ l of sample to the rotor instead of the 50 μ l syringe. Results are shown in the following table.

Table 4 - Multi-enzyme analysis using rotor loading station

	Enzyme activity (U liter ⁻¹ min ⁻¹)		
	SGPT	CPK	LDH-L
Mission day 2			
P.S.	11.7	23.7	39.9
M.S.	17.2	63.0	66.6
Mission day 4			
P.S.	10.3	28.2	36.9
M.S.	13.9	47.1	55.4
Mission day 6			
P.S.	11.8	24.5	42.3
M.S.	11.6	40.2	50.8
P.S. - Payloads Specialist; M.S. - Mission Specialist			

The greatest difference between postflight and real-time data occurred in the LDH-L procedure. It is felt that this deviation was caused by reagent evaporation from within the rotor. This problem will be eliminated however, by utilizing sealed,

lyophilized reagents for flight. The much smaller difference observed in the other tests, may best be explained by variations in the methods of sample loading and storage phenomenon.

CONCLUSION

In conjunction with the pre-pack whole blood rotor the Miniature Fast Analyzer, because of its size and weight, offers a unique diagnostic system for real-time analysis during space flight. The versatility of the instrument also offers other investigators an analytical tool for experiments not necessarily related to a medical protocol. As demonstrated in the first Life Sciences Payloads Test, the instrument can be operated with only a minimal amount of training. Therefore, the utilization of the Miniature Fast Analyzer in space to perform real-time analysis will meet a critical need of the physician in health care of the space flight crewmen as well as the Scientist in his study of physiological changes caused by the weightless environment.

LITERATURE CITED

Burtis, C. A., Development of an analytical system based around a miniature fast analyzer. Clin. Chem. 19, 895 (1973)

[†] Northrop Services, Inc., Houston, Texas

PROPOSED APPLICATIONS OF LOWER BODY NEGATIVE PRESSURE TO CARDIOLOGY

E. V. Schmidt, R. F. DeBusk, R. L. Popp, *Division of Cardiology, The Biomedical Technology Transfer Team, Stanford University School of Medicine*

ABSTRACT

With the advent of long duration space-flights, the time-dependent cardiovascular deconditioning effects of weightlessness on NASA astronauts became increasingly apparent. Tilt-table testing of Gemini astronauts revealed consistent losses of orthostatic tolerance after flights as brief as three days. In order to further study the effects of zero gravity on the cardiovascular system, lower body negative pressure (LBNP) testing was included in the pre- and post-flight evaluations of Apollo astronauts. Because LBNP testing does not require the presence of gravitational force, it was also extensively applied to in-flight evaluations of Skylab crews. LBNP has had extensive successful application by NASA in spaceflight related astronaut evaluation and it now appears that this unique physiological tool will have further applications in non-space related areas.

The purpose of this paper is to present some of the potential medical applications of lower body negative pressure to the evaluation and treatment of cardiac patients. The essential features of an LBNP unit and the basic cardiovascular physiology of LBNP testing are described. Some of the results of previous NASA spaceflight experiences and bedrest studies conducted at the NASA-Ames Research Center are summarized. The deconditioning effects of weightlessness experienced by orbiting astronauts are compared with the effects of bedrest restrictions prescribed for convalescing cardiac patients. The potential of LBNP for evaluating both pharmacological and physical activity regimens is examined, particularly in relation to post-myocardial infarction and coronary

artery bypass patients. Applications of LBNP to the cardiac catheterization laboratory and the out-patient follow-up of cardiac patients are proposed. Finally, some preliminary results of LBNP studies conducted at the Stanford University Cardiac Rehabilitation Laboratory are presented.

INTRODUCTION

NASA has assumed responsibility not only for manned space missions but also for insuring that the technological advances resulting from the space program are fully utilized for the public benefit. To provide an effective mechanism for transferring aerospace technology to the biomedical field, four Biomedical Application Teams (BATEams) have been established by NASA. Their purpose is to identify, test, and disseminate aerospace technological advances which could have significant impact on biomedical research and clinical medical practice. Each BATEam has programs focusing on specific problem areas in medicine. The team at Stanford operates through the Division of Cardiology of the Stanford University Medical School. Thus, it emphasizes NASA developments and techniques which have direct application to the diagnosis and treatment of cardiac disease.

During the past year Richard L. Popp, M.D., head of the Stanford Cardiology Noninvasive Laboratory, has participated in simulated space flight studies conducted at the NASA-Ames Research Center, Moffett Field, California. His primary role in these studies was to perform and analyze echocardiograms as part of the cardiovascular evaluation of the effects of prolonged bedrest on young normal male and female subjects. During these studies, Lower Body Negative Pressure (LBNP) provided an orthostatic tolerance stress test for evaluating the deconditioning effects of simulated spaceflight.

Both because of this experience with space flight simulation and because of the extensive background NASA has had using LBNP to evaluate astronauts, Stanford University cardiologists are investigating the responses of cardiac patients to LBNP. The chief purpose of these studies is to determine if the unique cardiovascular stress of LBNP is useful in evaluating the left ventricular function of cardiac patients and determining the time course of cardiovascular deconditioning and recovery of patients convalescing after acute myocardial infarction and coronary artery bypass surgery.

PHYSIOLOGICAL PRINCIPLES

Lower body negative pressure is the application of a reduced pneumatic pressure to that portion of the body surface below the level of the iliac crests. When the lower body is placed in a negative pressure chamber at 20-80 mm Hg less than atmospheric pressure a sequence of physiological events begins. Within 1-2 minutes, a fraction of the normally circulating blood volume becomes pooled in the lower extremities and pelvis. The volume of blood thus removed from the central circulation has been estimated at 0.5-1.5 liters, depending on the level of LBNP as well as differences in individual physiologic responses (1). As a consequence of this pooling of blood, the venous return to the heart from the lower body is significantly reduced. In response to the acute cardiovascular stress caused by the decreased venous return, complex neurocirculatory and humoral reflexes are activated to attempt continued perfusion of the heart and brain. The heart beats faster in an attempt to maintain cardiac output and blood pressure. Peripheral blood vessels constrict, manifested by increased systemic vascular resistance, in order to conserve central blood volume (2,3,4).

In spite of the compensatory tachycardia and peripheral vasoconstriction, stroke volume and cardiac output usually continue to decline. Just prior to syncope, heart rate, blood pressure, and cardiac output fall precipitously (Figure 1). At negative pressures from

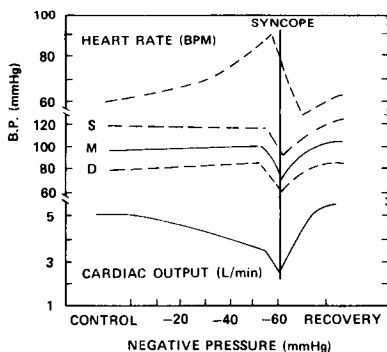


Fig. 1 NORMAL RESPONSE TO LOWER BODY NEGATIVE PRESSURE

-60 to -80 mm of mercury, most normal young subjects will develop pre-syncope episodes and faint if the stress is continued. In essence, as the LBNP chamber pressure is lowered, the subject's cardiovascular system is challenged to an increasing stress.

LBNP offers several advantages over other forms of

orthostatic stress. During negative pressure testing the subject rests passively in the supine position. Since active movement is not required, motivational factors do not effect the physiological responses. Accessory instrumentation is easier to apply and maintain and physiological signals remain more stable. This is particularly advantageous for the clinical studies planned which require echocardiography. Unlike tilt-table testing, the degree of stress applied can be readily controlled by regulating the amount of negative pressure applied and the magnitude of the stress is not limited by gravity. General physiological conditioning does not have the same significance it has in ECG treadmill testing. Thus, patients who would be physically unable to undergo treadmill ECG testing can be evaluated using the controlled stress of LBNP. In addition, the stress caused by LBNP can be rapidly relieved by venting the unit or turning off the vacuum pump (Figure 2).

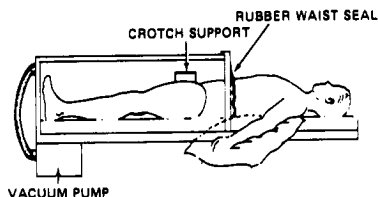


Fig. 2 SIDE VIEW OF SIMPLIFIED LBNP CHAMBER

THE LBNP UNIT

A simple LBNP device consists of a rigid air-tight chamber connected to a vacuum pump. An adjustable waist aperture (5) provides a nearly air-tight seal. A variable position crotch support is used so that the negative pressure does not move the subject toward the foot end of the chamber. A plywood device on loan from the NASA-Ames Research Center is presently being used in preliminary evaluations of out-patients at the Stanford University Cardiac Rehabilitation Laboratory. Refinements in the basic design to increase patient acceptance, safety, and reliability will be incorporated into units for use in this medical center. An artist's conception of a unit for the Cardiac Catheterization Laboratory (Figure 3) is shown below.

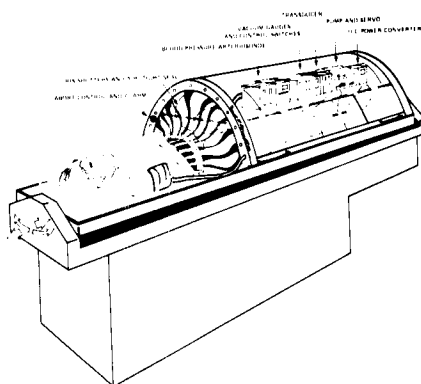


Fig. 3 CATH LAB LBNP UNIT

BEDREST EVALUATIONS

Prolonged bed rest has been used extensively in previous aerospace studies to simulate weightlessness (6,7,8). During recently completed studies at the NASA-Ames Research Center, 8 male and 12 female volunteers were subjected to two weeks of total bed rest. Orthostatic tolerances were evaluated using LBNP at -50 mm Hg for 15 minutes. Echocardiograms, blood pressure, heart rate, and leg volumes were obtained before (control) and immediately following the period of bed rest.

Analysis of echocardiograms revealed a significant decrease in end diastolic volume in all subjects after 2 weeks of bed rest compared to the control values. In addition, significant decreases in stroke volume and cardiac output were found in the female group (Table 1).

TABLE 1

	PULSE	SV	CO	EDV	ESV
MALES:					
CONTROL	69	77 ± 13	5.37 ± 1.3	123.6 ± 18	46.5 ± 9
REST	65	73 ± 11	4.72 ± 0.9	111.9 ± 15	39.4 ± 8
FEMALES:					
CONTROL	74	69.4 ± 13	5.06 ± 1.4	98.2 ± 14	28.9 ± 6
REST	76	53.5 ± 8	4.14 ± 0.7	83.5 ± 12	29.7 ± 8

Evaluation of changes in tolerance to LBNP pre- and post-bed rest and assessment of the relative roles of central cardiac effects versus peripheral vascular responses is currently in progress in this laboratory.

SPACE FLIGHT LBNP EVALUATIONS

Lower body negative pressure was used extensively to evaluate the function of the cardiovascular system of astronauts in the Apollo and Skylab missions (Figure

4). During longer duration space flights, the time dependent deconditioning effects of weightlessness on NASA astronauts became increasingly apparent. After space flight as brief as three days, some astronauts were experiencing symptoms of fainting on their return to earth and experiencing the full effect of gravity. For longer duration space flights, astronauts were required to wear G-suits on landing to prevent syncope on leaving their space capsules.



Fig. 4 SKYLAB LBNP DEVICE

In order to study the deteriorative effects of zero gravity on the cardiovascular system, NASA engineers designed prototype LBNP devices for use in pre- and post-flight evaluation of Apollo astronauts. Post-flight reduction in orthostatic tolerance during LBNP testing (compared to pre-flight results) was manifested by significant elevations in heart rate and decreases in systolic and pulse pressures (9). The ability to detect these changes encouraged the continued use of LBNP for cardiovascular evaluations aboard the subsequent Skylab flights.

The Skylab missions provided an opportunity for detailed studies of the cardiovascular system during prolonged exposure to weightlessness. Skylab studies showed that fluid volume redistribution during the first four-five days of weightlessness created marked alterations in cardiovascular function and impaired orthostatic tolerance. The increased heart rate during LBNP tests were generally shown to be the best single index in the assessment of orthostatic tolerance. In-flight data from the LBNP Skylab experiments was useful in predicting the status of early post-flight ortho-

static tolerance and assessing the health of the crew (10).

CARDIAC CATHETERIZATION LABORATORY STUDIES

Based on the space program related successful applications of LBNP as an effective orthostatic stress, Stanford University cardiologists are planning to apply this unique tool to the evaluation of patients in the cardiac catheterization laboratory. The objective of these studies is to develop a noninvasive method for assessment of left ventricular function by combining the circulatory effects of LBNP with echocardiographic analysis of ventricular volume. These results will then be compared with those obtained using standard invasive techniques.

Presently, cardiologists are able to evaluate ventricular function by plotting left ventricular work (LVW) as a function of either end diastolic pressure (EDP) or end diastolic volume (EDV) (Figure 5). To de-

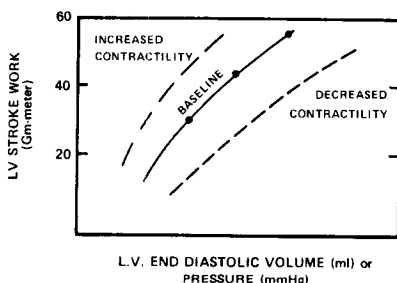


Fig. 5 VENTRICULAR FUNCTION CURVES

termine LVW by standard techniques, cardiac output is measured by either dye or thermal-dilution techniques requiring intravascular catheterization.

Obtaining values for intravascular pressure also requires an indwelling line. Measurement of volume (without echocardiography) requires injection of radio-opaque dye for cineangiography, but angiographic dye itself is known to affect contractility thus changing the parameter which is to be studied. Several points on the ventricular function curve can be obtained by expanding fluid volume in serial increments to increase EDV (or EDP). Contrast material from the preceding angiograms however, reduces the reliability of the measurements. Thus, conventional methods of measuring ventricular function involving indwelling catheters and injection of radio-opaque material have inherent inadequacies.

The combination of echocardiography and LBNP allows

a totally noninvasive approach to determining left ventricular function. Since ventricular volume correlates well with the cube of the left ventricular diameter (11) stroke volume (SV) is obtained echocardiographically by subtracting ESV from EDV. Left ventricular stroke work (LVSW) can be calculated using the formula $LVSW = SV \times LVP \times \text{conversion factor}$, where LVP stands for left ventricular mean systolic pressure (12). An approximation to LVSW is obtained by substituting peak brachial artery systolic pressure (obtained with a blood pressure cuff) for mean left ventricular systolic pressure. A left ventricular function curve is obtained by plotting SW against EDV. Reducing the lower body pressure decreases venous return to the heart and reduces end diastolic volume, thus creating a continuum of points on the ventricular function curve.

The feasibility of such a noninvasive approach has been demonstrated in space simulation bed rest studies previously described and in pre- and post-flight ventricular volume studies of Skylab 4 astronauts (13). Thus, it should be possible to generate ventricular function curves in patients totally noninvasively and without requiring the elaborate facilities of a cardiac catheterization laboratory.

Besides correlating with cardiac disease states such as coronary artery insufficiency, assessment of ventricular function using LBNP should prove useful in analyzing the effect of various pharmacological therapeutic agents. Administration of Beta adrenergic compounds such as Isuprel, Levophed or the still investigational Tazolol, increase cardiac contractility producing a ventricular function curve showing a higher performance level. Other drugs such as the Beta blocking agents, used in treating angina and various arrhythmias decrease contractility and ventricular function. Thus, for a particular cardiac disease a family of ventricular function curves can be generated indicating the effect of specific drugs on cardiac contractility.

Validating the assessment of ventricular function of patients in the Catheterization Laboratory could lead to the routine use of this noninvasive technique on the hospital wards with a mobile LBNP unit (Figure 6). In addition to evaluating ventricular function, a mobile LBNP unit could have applications in the intensive care units in treating acute pulmonary edema (14, 15). Also, it has been proposed that LBNP could be profitably used in titrating antihypertensive medications particularly in those patients who have had previous hypotensive episodes (16).

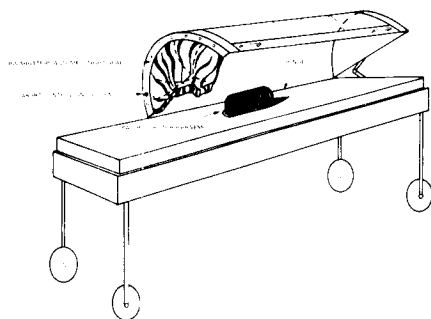


Fig. 6 MOBILE LBNP UNIT

PROPOSED CLINICAL CARDIOLOGY APPLICATIONS

Apollo and Skylab LBNP evaluations have shown that negative pressure testing was a useful approach to evaluating the cardiovascular deconditioning resulting from the absence of gravitational forces. Periods of prolonged bed rest and limited activity are frequently prescribed in the convalescent management of patients recovering from acute myocardial infarction and coronary artery bypass surgery. It is therefore reasonable to expect that LBNP might be a useful approach to characterizing the time course of cardiovascular deconditioning and reconditioning of heart patients following these events. To investigate this hypothesis, a program of LBNP testing has been recently begun at Stanford University Medical School in the Cardiac Rehabilitation Laboratory under the direction of Robert F. DeBusk, M.D.

Patient Selection

Three groups of patients will be evaluated. The first group will be patients with chest pain syndromes undergoing evaluation, including exercise electrocardiography to determine functional capacity. These patients must meet the following criteria for inclusion in the LBNP protocol: freedom from congestive heart failure, no major ventricular arrhythmias, and stable cardiovascular status. These studies will provide initial experience with application of LBNP to coronary patients. LBNP tolerance data, not previously documented in patients with coronary artery disease, may provide a more useful index of cardiovascular deconditioning than has been available in the past, especially in individuals whose functional capacity is limited by coronary heart disease.

The second group will be composed of patients who

have recently had coronary artery bypass surgery. These patients will undergo LBNP testing on five occasions: during hospital admission for coronary angiography, on the day prior to the surgery, immediately prior to hospital discharge (10-14 days), and at four and eight weeks postoperatively. Better understanding of the deteriorative effects of bed rest on postoperative patients may lead to more rapid mobilization and ambulation of such patients, and thereby to preservation of their functional capacity.

The third group will consist of patients convalescing from myocardial infarction. They must be free from unstable angina, congestive heart failure, and major arrhythmias. They will undergo LBNP testing at three, five, seven and eleven weeks post-infarction.

Procedure

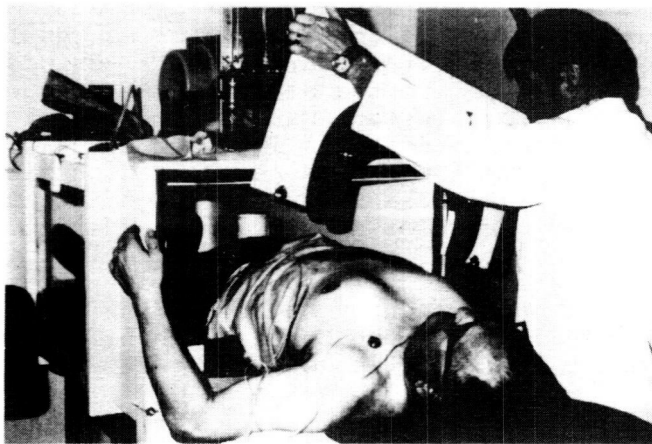


Fig. 7 CARDIAC REHAB LBNP UNIT

Following a thorough physical examination the patient is assisted into the LBNP unit (Figure 7). A protocol similar to that used aboard Skylab is followed. Baseline recordings of blood pressure, heart rate, and electrocardiogram are taken for five minutes followed by sequential lowering of chamber pressure to 20, 40, and 60 mm mercury below atmospheric pressure (Figure 8). Five minutes are allowed for equilibration at each pressure level followed by a five minute recovery period. ECG is continuously monitored and semi-automatic blood pressure recordings are made at 60 second intervals. Other noninvasive concurrent measurements which can be included are echocardiography, phonocardiography, and measurement of arterial flow velocity. Patients are

continuously attended by a physician who can terminate the procedure if any of the following events occur: 1) increase in heart rate of 50-75% over baseline; 2) decrease in systolic blood pressure of 20% below baseline; 3) inappropriate bradycardia, ST segment depressions, or frequent PVC's; 4) presyncopal symptoms or chest pain. Although the responses to LBNP of relatively young, normal individuals is well documented in aerospace publications and other medical literature, there have been only two published studies using LBNP in patients with congestive heart failure and no published works on patients with documented coronary artery disease.

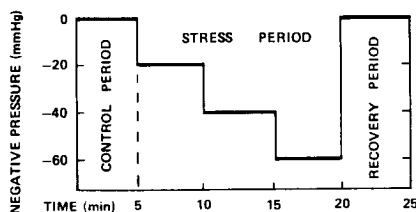


Fig. 8 THE LOWER BODY NEGATIVE PRESSURE PROTOCOL USED FOR EVALUATING PATIENTS WITH CORONARY ARTERY DISEASE

Because exercise electrocardiograms are concurrently administered it will be possible to compare the results of this active stress test with the passive cardiovascular stress of the LBNP. A better understanding of the deteriorative effects of bed rest in post-myocardial infarction and post-bypass surgery patients may lead to more rapid mobilization and ambulation, with a consequent shortening of hospital stay.

Figure 9 shows some preliminary results obtained from 4 sedentary, normal control subjects age 45-63 (average 53). Repeat evaluation showed excellent reproducibility especially when data were averaged for the group. Qualitatively, the pattern of changes in blood pressure and heart rate seen in this older group is similar to that observed for younger subjects. Comparison of the magnitude of changes in the young normals with older subjects may not be valid unless the effects of indwelling instrumentation are considered (2,17). These reports indicate that only identically instrumented (or non-instrumented) groups should be compared.

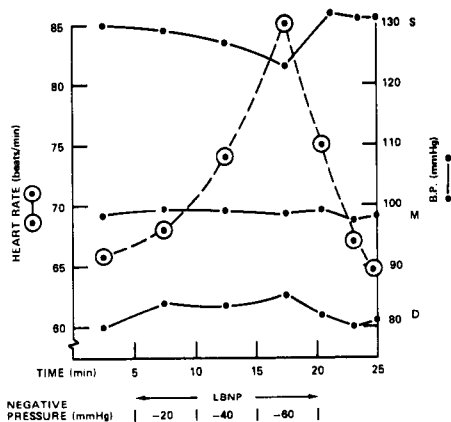


Fig. 9 LBNP IN OLDER NORMALS

SUMMARY

Both simulated and actual space flight experiences have shown LBNP to be an effective stress test of the cardiovascular system. It appears that LBNP will also have applications to the noninvasive evaluation of left ventricular function of cardiac patients. Cardiologists at Stanford University Medical School are implementing LBNP in the determination of baseline ventricular performance in various cardiac disease states, evaluating the effects of pharmacological agents on ventricular function, and characterizing the time course of cardiovascular deterioration and recovery from acute myocardial infarction and coronary artery bypass surgery.

ACKNOWLEDGEMENTS

It is a pleasure to acknowledge the support provided by Donald C. Harrison, M.D, Chief of the Division of Cardiology, Stanford University School of Medicine and Ernest McCutcheon, M.D., Biomedical Research Division, NASA-Ames Research Center. (This work is being supported by the Stanford University Biomedical Applications Team through NASA Grant NGR-05-020-634).

REFERENCES

1. Balakhovskii, I.S., Virovets, O.A., and Voloshin, V.G.: Changes in the circulating blood volume during lower body negative pressure exposure. *Kosmicheskaja Bio. i Med.* 4:27, 1970.

2. Stevens, P.M.: Cardiovascular dynamics during orthostasis and the influence of intravascular instrumentation. *Am. J. Card.* 17:211, 1966.
3. Stevens, P.M. and Lamb, L.E.: Effects of lower body negative pressure on the cardiovascular system. *Am. J. Card.* 16:506, 1965.
4. Wolthius, R.A., Bergman, S.A., and Nicogossian, A. E.: Physiological effects of locally applied reduced pressure in man. *Physiol. Rev.* 54:566, 1974.
5. Wolthius, R.A., Hoffler, G.W., and Baker, J.T.: Improved waist seal design for use with lower body negative pressure (LBNP) devices. *Aerospace Med.* 42:461, 1971.
6. Graveline, D.E., and McCally, M.: Body fluid distribution: Implications for zero gravities. *Aerospace Med.* 33:1281, 1962.
7. Miller, P.B., Johnson, R.L., and Lamb, L.E.: The effects of four weeks of absolute bed rest on circulatory function in man. *Aerospace Med.* 35:1199, 1964.
8. Stevens, P.M., Miller, P.B., Gilbert, C.A., et al: Influence of long-term lower body negative pressure on the circulatory function of man during prolonged bed rest. *Aerospace Med.* 37:357, 1966,
9. Hoffler, G.W., Wolthuis, R.A., and Johnson, R.L.: Apollo space crew cardiovascular evaluations. *Aerospace Med.* 45:807, 1974.
10. Johnson, R.L., et al: Lower Body Negative Pressure: Third Manned Skylab Mission. Proc. Skylab Life Sci. Symp., August 27-29, 1974, Lyndon B. Johnson Space Center, Vol. II. JSC-09275. NASA TMX-58154, 1974.
11. Feigenbaum, H., Wolfe, S.B., Popp, R.L., et al: Correlation of ultrasound with angiocardiology in measuring left ventricular diastolic volume. *Am. J. Card.* 23:111, 1969.
12. Yang, S.S., et al: From Cardiac Catheterization Data to Hemodynamic Parameters, Chapter 10, page 157, F.A. Davis Co., Philadelphia, 1972.
13. Henry, W.L., et al: Effects of prolonged space flight on cardiac function and dimensions. *Am. J. Card.* 35:143, 1975 (ABSTRACT).

14. Potanin, C.: Lower body decompression in left heart failure. *Lancet* 2:241, 1967.
15. Murray, R.H., et al: Hemodynamic effects of hypovolemia in normal subjects and patients with congestive heart failure. *Circulation* 39:55, 1969.
16. Wolthuis, R.A., Bergman, S.A., and Nicoszossian, A.E.: Physiological effects of locally applied reduced pressure in man. *Physiol. Rev.* 54:566, 1974.
17. McCutcheon, E.P., and Sandler, H.: Effect of Venipuncture on Cardiovascular Responses to Lower Body Negative Pressure. *Proc. Aerospace Med. Assoc. Meeting, San Francisco, Calif., April 28-May 1, 1975.*

CALIBRATION SOURCE FOR REMOTE SENSORS

J. T. McLean and A. McCulloch, *Goddard Space Flight Center*
E. I. Mohr, *Columbia Union College (Retired)*

ABSTRACT

A wide angle diffuse source used for the calibration of the Multi-spectral Scanner (MSS) flown on ERTS (Landsat) satellite has been developed.

INTRODUCTION

The source described below was developed as a calibration target for the Multispectral Scanner (MSS) which was flown on the Earth Resources Technology Satellite A (ERTS A) now known as Landsat 1. The wavelength region of interest covered the four (4) MSS bands extending from 0.5 to 1.1 micrometers (μm), although the target was calibrated from 0.32 to 2.5 μm .

The following characteristics for the target were required:

1. large aperture, sufficient to accommodate an instrument with a 9 inch (23 centimeters (cm)) aperture and $2\frac{1}{2}^\circ$ field of view (fov).
2. highly diffuse energy from target.
3. high spatial uniformity across aperture area of source.
4. spectrally calibrated in absolute units.
5. stable output over long periods of time (1-2 yrs).
6. rugged, yet portable enough to be easily transported long distances without detrimental effects on the operational capabilities of the target.

Two approaches were considered: (a) a thirty (30) inch (76 cm) diameter integrating sphere with a twelve inch (30.5 cm) exit port, or (b) the use of one hemisphere of a 76 cm sphere in conjunction with a Kodak Ektolite Screen. The screen has the property of reflecting back uniformly into a well defined area the majority of the light received. Thus the radiation coming from the lamps in the hemisphere would be reflected back into the hemisphere, and finally, after a number of reflections, to the exit port of the hemisphere, creating at least a partial integrating effect.

After some preliminary trials it seemed that the 76 cm sphere would give the most satisfactory results.

THE SPHERICAL INTEGRATOR

General Discussion

The spherical integrator target assembly consists of two (2) parts, namely: (1) a 76 cm diameter sphere and (2) an electronic control unit which provides power and allows the monitoring of the lamp's power.

The sphere consists of two (2) spun aluminum hemispheres which are mounted on a support frame (see Fig. 1). An exit port of 30.5 cm diameter is located at the midpoint of one of the hemispheres. Inside the sphere, twelve (12) 45 watt quartz-line lamps, General Electric #6.6A/T2 1/2/1CL, are mounted symmetrically around the exit port (see Fig. 2). Aluminum baffles are used to prevent the lamps from being viewed directly from outside the sphere. The interior surface of the sphere and the baffles are covered with several coats of barium sulfate integrating sphere paint.

To eliminate any temperature variations which may affect the calibration, a small fan mounted at the top of the sphere is used to insure temperature uniformity. This also helps maintain the inside surface of the sphere at a temperature at which minimal radiation is emitted in the near infrared.

The electronic control unit consists of three (3) current regulated power sources, readout devices, elapsed time meters, and associated circuitry to control the operation of the sphere.

The 45-watt quartz-halogen lamps are operated @ 6.5 ampere current at approximately 6.8 volts. The lamps are operated in three banks of four lamps each. The four lamps in a given bank are in series.

Different calibrated intensity levels are obtained from the source by varying the number of lamps being utilized at any one time.

Hence, a switching arrangement is used which allows any one or all of the lamps in a given bank to be turned off. Since there would be a considerable decrease in load on the power supply for a given bank if one or more lamps in the bank were turned off, each lamp which is turned off is automatically replaced by an equivalent resistive load outside of the sphere. This load consists of a 7.07 ampere, 100 watt Ohmite Dividohm adjustable power resistor adjusted to give a resistance of 1.033 ± 0.010 ohms. It is located in the control rack so that the dissipated power does not contribute to the total flux in the sphere.

THEORY OF THE SPHERICAL INTEGRATOR

The principle of spherical integration which has been discussed elsewhere (Refs. 3, 5, 12, 13) was proposed by Sumpner in 1892 (Ref. 4). He showed that if a source of light is placed inside a hollow sphere which is coated internally with a perfectly diffusing coat, the luminance of any portion of the surface due to the light reflected from the rest of the sphere is everywhere the same and is directly proportional to the total flux emitted by the source.

It is easy to show (Ref. 5) that the theoretical expression for this relation in terms of the reflectance ρ of the perfectly diffusing coat of the sphere wall due to an infinite number of reflections is given by

$$\Phi = \frac{F}{4\pi r^2} \frac{\rho}{1 - \rho}$$

where Φ is the total radiant flux reaching unit area of the spherical surface by reflection, F the total flux emitted by the source and r the radius of the sphere. In this derivation it is assumed that ρ is constant, that the surface is a perfect diffuse, the sphere is empty and that it has no ports. However, the reflectance ρ of the coating varies with wavelength and there is no perfect diffuser so that Lambert's cosine law does not hold accurately. In addition, the sphere has sources, shields and ports, all of which affect the total radiant flux. Moreover, the spectral dependence of the reflection can modify considerably the spectral distribution of the flux streaming from

the port of the sphere. In spite of these uncertainties, one can calibrate the output of the sphere against a known standard for use as an absolute calibration source.

The sphere paint is composed of high purity barium sulfate pigment suspended in a polyalcohol to facilitate its use in a spray gun and also make it adhere well to the inside wall of the sphere. The reflectance of this paint was determined by comparing it with freshly smoked magnesium oxide in the range $0.2\ \mu\text{m}$ to $2.5\ \mu\text{m}$ by means of a Cary 14 Double Beam Spectrophotometer. For the range $2.5\ \mu\text{m}$ to $10\ \mu\text{m}$ the reflectance of the paint was compared with a calibrated aluminum mirror as a standard by means of a Cary-White 90 Double Beam Spectrophotometer. The resulting data are given in Table 1 and plotted in Figure 3. The data are shown only for the range $0.25\ \mu\text{m}$ to $3.0\ \mu\text{m}$ since the reflectance drops rapidly beyond $2.5\ \mu\text{m}$.

CALIBRATION OF SPHERICAL INTEGRATOR

Relative Spectral Distribution

Since the spectral output of the sphere is not the same as that of the lamps, due to the reflectance characteristics of the paint, a one to one calibration of the individual lamps against an irradiance standard cannot be made. It is necessary, therefore, to compare the spectral distribution of the output of the sphere with that from a standard of spectral irradiance. Tests have shown that the number of lamps used in the sphere has no effect on the spectral distribution of the output within the limits of experimental accuracy (Ref. 1), hence twelve lamps were used to calibrate the sphere in order to get a satisfactory flux intensity.

The measurements of the spectral distribution of the sphere were made with a Perkin-Elmer Double-Pass Monochromator Model 99. The slit of the monochromator was positioned about 20 cm from the port of the spherical integrator. The slit width and gain were held at the smallest values possible in order to have the best resolution consistent with good signal-to-noise. For the wavelength range from 0.45 to $2.7\ \mu\text{m}$ a Reeder thermocouple detector with quartz window was used. A photomultiplier detector 1P28 was used in the range from 0.32 to $0.75\ \mu\text{m}$. The spectral distribution for both ranges was automatically recorded by means of a Leeds and Northrup Speedomax G.

The data for the relative spectral distribution of the sphere was obtained by recording a short run at a fixed wavelength setting of the monochromator in order to obtain a reliable average value at that wavelength. This was repeated for additional wavelength settings at every one tenth micrometer or less from $0.32\ \mu\text{m}$ to $2.70\ \mu\text{m}$. This procedure was repeated two or three times to obtain the average value of the radiation at each wavelength measured.

To calibrate the sphere output two Eppley Laboratories standards of spectral irradiance were used. For a given trial one of these lamps was positioned about 2.6 meters in front of the slit of the monochromator and aligned with its axis. The spectral distribution of each lamp was obtained under the same conditions of slit width and amplifier gain as those which were used to get the spectral distribution of the output of the sphere.

The average recorder deflections $D_{\text{sr}\lambda}$ obtained for the output of the sphere were divided by the corresponding average recorder deflections $D_{\text{rl}\lambda}$ obtained for each of the standard lamps. This was done at one-tenth micron intervals or less over the entire spectral range which was scanned. This gave the relative ratio of the spectral distribution of the sphere to a specific lamp. The ratio $k_{\text{r}\lambda} = D_{\text{sr}\lambda}/D_{\text{rl}\lambda}$ at each wavelength was determined separately for each of the standard lamps used.

Absolute Spectral Distribution

The spherical integrator as a source of radiant flux has a different spatial configuration from that of an approximate point source such as a standard quartz-halogen lamp. In order to obtain an absolute calibration by comparing the spectral distribution of the sphere with that of the standard lamp it is necessary to eliminate the effects of this difference. Since "the role of a diffusely reflecting surface is to obliterate the past history of the incident radiation" (Ref. 9), a 30.5 cm spherical integrator was mounted on the front of the Perkin-Elmer Monochromator. This small sphere consists of two aluminum hemispherical shells painted on the inside with the same type of barium sulfate paint used on the 76 cm sphere. The two hemispheres were bolted together and rigidly fastened to the monochromator so that a 1.8 cm diameter exit port was centered in front of the monochromator slit. The second hemisphere has a 3.7 cm diameter entrance port designed (a) to be positioned at the exit port of the 76 cm integrator so that it is on the inside curvature of the 76 cm integrator and thus receive flux from all parts of the large sphere, or (b) so as to be in line with the standard quartz-iodine lamp located at a known distance (about 18 cm) from this port and thus receive the flux from the standard lamp. Using the small sphere in this way, the monochromator alternately saw the flux emitted by the 76 cm integrator or from the standard lamp at a known distance after the flux had been integrated by the small sphere.

Using a given slit width of the monochromator and gain of the recorder a direct comparison was made between the total flux which the small sphere received from the 76 cm integrator and from the standard lamps which had been used to derive the relative ratios as described above. This was done using the photomultiplier detector 1P28 at the following wavelengths: 0.50, 0.55, 0.60 μm . This procedure was repeated using the Reeder thermocouple detector at the following wavelengths: 1.1, 1.2, 1.3 μm . Each measurement was repeated a number of times. The data obtained from these measurements were utilized in the following manner.

Let $D_{sa\lambda}$ be the recorder deflection of the monochromator at one of the above-mentioned wavelengths when the small sphere receives flux from the 76 cm integrator, and $D_{la\lambda}$ the deflection at the same wavelength when it receives flux from one of the standard lamps placed at a known distance from the entrance port. Then $k_{a\lambda} = D_{sa\lambda}/D_{la\lambda}$ is the absolute ratio of the flux from the 76 cm integrator to that of the standard lamp at this wavelength. The average value obtained at three wavelengths was chosen as the true value for $k_{a\lambda}$. The absolute ratios for all wavelengths measured was obtained by normalizing the relative ratios $k_{r\lambda}$ to this absolute ratio $k_{a\lambda}$.

When the small sphere, mounted on the monochromator, has its entrance port located at the exit port of the 76 cm integrator, the flux incident on the entrance port is obviously the same flux which is incident on the corresponding portion of the exit port of the thirty inch integrator. Since this flux comes from all parts of the inside surface of the integrator by diffuse reflection, each elemental area of the inside surface of the small sphere receives flux from an equivalent fractional portion of the inside surface of the integrator which is on the line of sight through the port with that of the small sphere. This means that the small sphere receives completely diffuse radiation from the 76 cm integrator.

In order to determine the total flux received by the small sphere, one must evaluate it in terms of the flux incident at the exit port of the integrator which has come from all parts of the diffusing surface of the integrator. Let $F_{s\lambda}$ watts \cdot cm $^{-2}$ μm^{-1} be diffusely reflected into the solid angle 2π . (See Fig. 4.) Then the diffuse

spectral radiation in the normal direction is $F_{s\lambda}/\pi$. The spectral radiant flux from the diffusely reflecting surface of the spherical segment of area dA_s which is incident at the effective area of the exit port, and hence of the area A of the entrance port of the small sphere is equal to

$$A dW_s = \frac{F_s}{\pi} \times \frac{dA_s \times \cos 1/2 \theta \times A \cos 1/2 \theta}{d^2}$$

where d is the distance between the element of area dA_s and the port, and $1/2 \theta$ is the angle between the line of sight propagation from this area and the inner normal to the sphere at the same point on dA_s . Since $d = 2r \cos 1/2 \theta$, and $dA_s = 2\pi r^2 \sin \theta d\theta$, the element of spectral radiant power at the entrance port of the small sphere is

$$dP_{s\lambda} = A dW_{s\lambda} = \frac{F_{s\lambda}}{\pi} \times \frac{2\pi r^2 \sin \theta d\theta \cos^2 1/2 \theta A}{4r^2 \cos^2 1/2 \theta}$$

Upon simplification this becomes $dP_{s\lambda} = 1/2 F_{s\lambda} A \sin \theta d\theta$. Thus the spectral radiant power at the port of the 76 cm integrator and hence at the entrance port of the small sphere is

$$P_{s\lambda} = 1/2 F_{s\lambda} A \int_0^\theta \sin \theta d\theta = 1/2 F_{s\lambda} A (1 - \cos \theta) \quad (2)$$

Since θ varies essentially from 0° to 156.4° because of the size of the port and the relative positions of the ports of the two spheres Equation 2 becomes

$$P_{s\lambda} = W_{s\lambda} A = 0.958 F_{s\lambda} A \text{ watts/micron} \quad (3)$$

This diffuse flux from the 76 cm integrator was integrated by the small sphere so that the radiant emittance at the exit port of the small sphere is given by Equation 1 as

$$W'_{s\lambda} = \frac{W_{s\lambda} A}{4\pi r_1^2} \frac{\rho_\lambda}{1 - \alpha\rho_\lambda} \quad (4)$$

where $\alpha\rho$ is the area weighted average reflectance of the wall of the small sphere. α is the fraction of the flux reflected from the wall (excluding hole losses) of the small sphere by the first reflection and is incident on the wall for a second reflection. r_1 is the radius of the small sphere and ρ_λ is the spectral reflectance of the sphere paint. This flux was viewed by the monochromator. The resulting recorder deflection $D_{sa\lambda}$ was proportional to the integrated flux $W'_{s\lambda}$ and hence to the spectral radiant emittance $W_{s\lambda}$ of the 76 cm integrator.

On the other hand when the small sphere, mounted on the monochromator, receives flux from the standard lamp, it comes from approximately a point source. Let $J_{\ell\lambda}$ watts/steradian/ μm be the spectral radiant intensity of the standard quartz-iodine lamp. Then the spectral irradiance per unit area at the port of the small sphere due to the standard lamp is given by

$$H_{\ell\lambda} = C J_{\ell\lambda} / r^2 \text{ watts/cm}^2 / \mu\text{m} \quad (5)$$

where r is the distance from the lamp to the entrance port and C is a correction factor to correct for inverse square failure (Ref. 2). The spectral radiant power received by the small sphere from the standard lamp is given by

$$P_{\ell\lambda} = H_{\ell\lambda} A \text{ watts}/\mu\text{m} \quad (6)$$

where A is the area of the entrance port of the small sphere.

As mentioned previously, the flux received by the small sphere from the 76 cm integrator is diffuse radiation. The flux from the standard lamp, however, comes from approximately a point source and falls on a relatively small area of the inside of the small sphere after which it is diffusely reflected. Thus the flux from the standard lamp only becomes comparable to the diffuse radiation received from the 76 cm integrator after it has undergone a single diffuse reflection. Hence the effective radiant power from the standard lamp which will be integrated by the small sphere is obtained by multiplying Equation 6 by the spectral reflectance of the sphere paint ρ_λ so that

$$P_\ell = \rho_\lambda \times H_{\ell\lambda} A \text{ watts}/\mu\text{m} \quad (7)$$

This effective flux was integrated by the small sphere. Hence the spectral radiant emittance at the exit port of the small sphere which is viewed by the monochromator is found by Equation 1 to be

$$W_{\ell\lambda} = \frac{\rho_\lambda \times H_{\ell\lambda} A}{4\pi r_1^2} \times \frac{\rho_\lambda}{1 - \alpha\rho_\lambda} \text{ watts}/\text{cm}^2/\mu\text{m} \quad (8)$$

where r_1 is the radius of the small sphere. The corresponding recorder deflection $D_{\ell a\lambda}$ was proportional to the emittance $W_{\ell\lambda}$ and thus to the effective flux $\rho_\lambda \times H_{\ell\lambda}$ received from the lamp after a single diffuse reflection.

It is therefore possible to compare the spectral radiant emittance which the small sphere received from the 76 cm integrator with the spectral intensity from the standard lamp after a single diffuse reflection in terms of the corresponding deflections of the record as seen by dividing Equation 4 by Equation 8, or

$$\frac{W'_{s\lambda}}{W_{\ell\lambda}} = \frac{\frac{W_{s\lambda} A}{4\pi\lambda_1^2} \times \frac{\rho_\lambda}{1 - \alpha\rho_\lambda}}{\frac{\rho_\lambda H_{\ell\lambda} A}{4\pi\lambda_1^2} \times \frac{\rho_\lambda}{1 - \alpha\rho_\lambda}} = \frac{W_{s\lambda}}{\rho_\lambda H_{\ell\lambda}} \quad (9)$$

As stated before, the monochromator deflections are proportional to the intensity of the flux seen by the monochromator if the gain and the slit width are held constant. Hence the absolute ratio of the recorder deflections is equal to the ratio given by Equation 9, or

$$k_{a\lambda} = D_{sa\lambda}/D_{\ell a\lambda} = W'_{s\lambda}/W_{\ell\lambda} = W_{s\lambda}/\rho_\lambda H_{\ell\lambda}$$

Thus one obtains

$$W_{s\lambda} = \rho_\lambda H_{\ell\lambda} D_{sa\lambda}/D_{\ell a\lambda} \text{ watts}/\text{m}^2/\text{micrometer} \quad (10)$$

for the spectral radiant emittance (exitance) of the 76 cm integrator.

Using Equation 10 the diffuse spectral emittance (exitance) of the 76 cm integrator was determined every tenth of a micrometer or less from 0.32 to 2.7 μm for each standard lamp separately. The resulting data in the case of standard lamp EPI-1155 is given in Table 2. The wavelength is in micrometers. The second column gives the spectral irradiance of the standard lamp EPI-1155 at 17.7 cm (in milliwatts/ $\text{cm}^2/\text{micrometer}$). The third column gives the spectral radiance after a single reflection by the small sphere. The fourth column gives the absolute ratios of the recorder deflections. The fifth column gives the diffuse spectral radiant emittance (exitance) of the 76 cm integrator when twelve lamps are operating. Table 3 gives the mean spectral radiant emittance (exitance) of the integrator as determined by means of the standard lamps EPI-1154, and EPI-1155. Figure 5 shows the spectral distribution of the 76 cm integrator at the port as determined by the use of the standard lamps, as well as points from the solar spectrum as reported by Johnson.

INTEGRATOR EMITTANCE VERSUS NUMBER OF LAMPS

In order to use the spherical integrator to calibrate radiometers it is necessary to vary the magnitude of the spectral radiant emittance. To permit such a change in intensity the source, the circuit design permits one to turn on or off any one of the lamps independently. Thus, any number of lamps from one to twelve may be used as the source in the integrator.

The linearity of the source for different intensity levels was tested at several wavelengths. Twelve levels were obtained from the sphere by operating different numbers (0 to 12) of lamps at any one time. The outputs from the sphere were measured with a Perkin-Elmer Model 99 Monochromator with quartz thermocouple. The ratios obtained by dividing the deflection for N lamps by the deflection for 12 lamps are used to fix the intensity levels. The mean of the ratios for three trials are given on the calibration data sheet. The spectral radiant emittance for ten lamps may be obtained by multiplying the spectral radiant emittance for twelve lamps by the ratio of the intensity of ten lamps to that of twelve lamps and similarly for any number of lamps from one to eleven.

ANALYSIS OF RESULTS

An examination of the spectral curves in Figure 5 reveals several significant facts. First, it will be observed that the peak value of the integrator emittance is 1.41 times the peak value of the irradiance of the standard lamp at 20 cm. Secondly, the maximum intensity of the integrator emittance is located at approximately 0.90 μ for the sphere as well as the lamp. Thirdly, for those wavelengths for which the reflectance of the sphere paint is high, the sphere enhances the emitted power, while for the wavelengths for which the reflectance is low, the emitted power of the sphere is less than that of the source.

A comparison of the spectral distribution of the integrator emittance as determined by the two standard lamps shows that the results are reasonably consistent. The greatest difference at a given wavelength between the two sets of data is usually less than three percent except in the ultraviolet where it is about 15%. The variation between the data for several trials with the same lamp was two percent or less for the absolute calibration data and three percent or less for the relative calibration data. The National Bureau of Standards (NBS) reports that the calibration of the standard lamps has an uncertainty of 8% in the ultraviolet and one of 3% in the visible and the

infrared (Ref. 10).^{*} The data for the calibration of the sphere which was obtained by the use of the two standard lamps differ by approximately the same amount.

There are a number of possible sources of error. First, there is some uncertainty in the reflectance of the sphere paint. The recording on the chart may be read to within 0.5%. In reversing the two samples of freshly smoked MgO in the Cary 14 spectrophotometer while determining the reflectance of the sphere paint, the difference in reflectance was found to be less than 0.5% at most points. The data for the reflectance of MgO which has been reported by various observers differ somewhat. It seems to depend on the nature of the surface, the thickness of the layer and the age. Thus the uncertainty in the reflectance of the MgO standard is probably less than 1% in the spectral range where the quartz-Halogen lamp is most intense, while in the near infrared this uncertainty may be as high as 5%.

Secondly, there is a variation in the voltage across the 45 watt lamp in the integrator. This variation has been found to be 1% or less. This would represent a variation in the flux of the lamps and hence of the sphere of about two percent.

Among other sources of error may be mentioned the monochromator slit which may be set within 0.2%. The chart which records the magnitude of the flux at various wavelengths can be read within 0.5%. It has been observed that there may be a decrease in the 0.1 microvolt test signal as shown by the corresponding recorder deflections at the beginning and the end of a run. This change was usually less than 1% when sufficient time was allowed to warm up and stabilize the amplifier and recorder electronics.

Some of these errors may compensate for each other. The end product of this experiment consists of taking the ratio of two sets of data which were obtained under nearly identical experimental conditions. It is reasonable to expect certain systematic errors to cancel out.

For the errors that are random and assumed independent, the most probable error may be calculated (Ref. 11). Consider Equation 10,

$$W_{s\lambda} = \rho_{\lambda} H_{\ell\lambda} \left(\frac{D_{sa\lambda}}{D_{\ell a\lambda}} \right) \equiv F(\rho H D_s D_{\ell})$$

The error in W ,

$$e_w^2 = \sum_n \left(\frac{\partial F}{\partial n} \right)^2 e_n^2$$

where n refers to the number of quantities which contribute to the error in W .

$$e_w^2 = \left(H \frac{D_s}{D_{\ell}} \right)^2 e_{\rho}^2 + \left(\rho \frac{D_s}{D_{\ell}} \right)^2 e_H^2 + \left(\frac{\rho H}{D_{\ell}} \right)^2 e_{D_s}^2 + \left(- \frac{\rho H D_s}{D_{\ell}^2} \right)^2 e_{D_{\ell}}^2$$

Dividing by W^2 , we get probable error

$$\epsilon_w = \left(\frac{e_w^2}{W^2} \right)^{1/2} = \left(\frac{e_{\rho}^2}{\rho^2} + \frac{e_H^2}{H^2} + \frac{e_{D_s}^2}{D_s^2} + \frac{e_{D_{\ell}}^2}{D_{\ell}^2} \right)^{1/2}$$

^{*}Standards of spectral irradiance with accuracy of 3% in the ultraviolet and 1% in the visible and near infrared are now available from NBS.

- The components of the probable error is treated in the same manner as that for ϵ_w . That is, the root mean square of the components are taken resulting in fractional errors:

in ρ — 5.05% (max)

H — 8.02% (max)

D_s, D_ℓ — 1.6% each

Hence $\epsilon_w = (25.50 + 64.32 + 2.56 + 2.56)^{1/2} \sim 9.75\%$. Thus, max uncertainty in $W_{s\lambda}$ is estimated to be less than 10%.

CONCLUSIONS

The present arrangement of the 76 cm spherical integrator provides a satisfactory extended source for the calibration of radiometers and other optical devices used to measure radiation in the near UV, visible and near IR wavelength regions. A check on the angular dependence of the exitance of the spherical integrator showed a 1% variation over a 12° angle about the normal to the center of the aperture. An analysis of the errors in this experiment indicate a maximum probable error of 9.75%. This number is considered conservative since worst case data was used.

REFERENCES

1. NASA/GSFC Final Report of the Workshop Program 1964, p. A-17.
2. NASA/GSFC Final Report of the Workshop Program 1965, p. B-23.
3. NASA/GSFC Final Report of the Workshop Program 1966, p. 399.
4. W. E. Sumpner, Physics Society Proceedings, Vol. 12, p. 10, 1892.
5. J. W. T. Walsh, Photometry, London, Constable and Co., 1958, p. 258
6. A. C. Hardy and O. W. Pineo, Journal of the Optical Society of America, Vol. 21, p. 502, 1931.
7. E. G. Zubler and F. A. Mosby, Illumination Engineering, Vol. 54, p. 734, 1959.
8. J. A. Moore and C. M. Jolly, General Electric Company Journal, Vol. 29, p. 99, 1962.
9. E. M. Sparrow and R. D. Cess, Radiation Heat Transfer, Belmont, Calif., Brooks/Cole Publ. Co., 1966, p. 52.
10. Ralph Stair, W. E. Schneider and J. K. Jackson, Applied Optics, Vol. 2, p. 1151, 1963.
11. Cook, Rabinowicz, Physical Measurement & Analysis, Addison-Wesley, 1963.
12. M. W. Finkel, Optics Communications, Vol. 2, Number 1, p. 25-28, May/June 1970.
13. W. B. Fussell, NBS Technical Note 594-7, "Approximate Theory of the Photometric Integrating Sphere," March 1970.

Table 1
Spectral Reflectance of BaSO₄ Sphere Paint (MS125-4)
(λ in microns)

λ	ρ_{λ}	λ	ρ_{λ}	λ	ρ_{λ}
0.25	0.898	0.70	0.962	2.10	0.859
0.26	0.923	0.75	0.960	2.20	0.867
0.27	0.935	0.80	0.960	2.30	0.853
0.28	0.946	0.90	0.960	2.40	0.850
0.29	0.961	1.00	0.960	2.50	0.826
0.30	0.967	1.10	0.959	2.60	0.802
0.32	0.960	1.20	0.953	2.70	0.727
0.35	0.962	1.30	0.950	2.80	0.368
0.37	0.964	1.40	0.943	2.90	0.225
0.40	0.951	1.50	0.926	3.00	0.208
0.45	0.955	1.60	0.924		
0.50	0.964	1.70	0.921		
0.55	0.960	1.80	0.912		
0.60	0.962	1.90	0.893		
0.65	0.961	2.00	0.876		

Table 2
Spectral Radiant Exitance of Spherical Integrator by Use of Lamp EPI-1155

λ	H_λ	$\rho_\lambda H_\lambda$	$D_{s\lambda a}/D_{\ell\lambda a}$	$W_{s\lambda}$
0.32	2.613	2.509	0.4006	1.005
0.35	5.927	5.702	0.5626	3.208
0.37	9.145	8.816	0.6178	5.446
0.40	15.882	15.104	0.7376	11.14
0.45	35.04	33.46	0.7561	25.30
0.50	58.03	55.94	0.8281	46.33
0.55	84.00	80.64	0.8808	71.04
0.60	109.4	105.3	0.9145	96.26
0.65	137.8	132.4	0.9373	124.1
0.70	160.1	154.0	0.9550	147.1
0.75	178.2	171.1	0.9730	166.4
0.80	191.8	184.2	1.026	189.0
0.90	199.3	191.3	1.182	226.1
1.00	194.4	186.7	1.072	200.0
1.1	178.3	171.0	1.023	175.0
1.2	164.4	156.7	1.004	157.3
1.3	148.9	141.5	0.9817	138.9
1.4	132.8	125.2	0.9091	113.8
1.5	117.4	108.7	0.7852	85.37
1.6	103.0	95.16	0.8010	76.22
1.7	89.26	82.21	0.8140	66.92
1.8	77.16	70.37	0.7509	52.85
1.9	66.69	59.56	0.7097	42.27
2.0	57.95	50.76	0.4784	24.29
2.1	50.23	43.15	0.5029	21.70
2.2	44.20	38.30	0.5101	19.54
2.3	39.33	33.55	0.4978	16.70
2.4	35.74	30.38	0.4008	12.18
2.5	32.75	27.05	0.3274	8.856
2.6	26.90	21.58	0.2886	6.228
2.7	23.77	17.28	0.2058	3.556

Table 3

Spectral Radiant Exitance of Thirty-Inch Spherical Integrator
 (λ in microns; W_λ in milliwatts $\text{cm}^{-2} \mu^{-1}$; W'_λ in watts $\text{m}^{-2} \mu^{-1} \text{sr}^{-1}$)

λ	W_λ	W'_λ	λ	W_λ	W'_λ
0.32	0.920	2.92	1.1	173.9	553.5
0.35	2.989	9.51	1.2	155.2	494.0
0.37	5.056	16.09	1.3	136.8	435.4
0.40	10.49	33.39	1.4	112.8	359.1
			1.5	84.51	269.0
0.45	25.53	81.26	1.6	75.25	239.5
0.50	46.83	149.1	1.7	65.72	209.2
0.55	71.65	228.1	1.8	51.90	165.2
0.60	97.99	311.9	1.9	41.78	133.0
0.65	124.6	396.6	2.0	23.82	75.82
0.70	146.6	466.7	2.1	21.35	67.96
0.75	165.9	528.0	2.2	19.21	61.15
0.80	187.5	596.7	2.3	16.44	52.33
0.90	221.6	705.5	2.4	12.10	38.52
1.00	194.6	619.3	2.5	8.820	28.07
			2.6	6.234	19.84
			2.7	3.625	11.54

Table 4

Ratio of Intensity of N Lamps to 12 Lamps
 in Spherical Integrator

No. of Lamps	$W_{\lambda n}/W_{\lambda 12}$
12	1.0000
11	0.9183
10	0.8350
9	0.7513
8	0.6684
7	0.5840
6	0.5014
5	0.4184
4	0.3364
3	0.2507
2	0.1663
1	0.0837

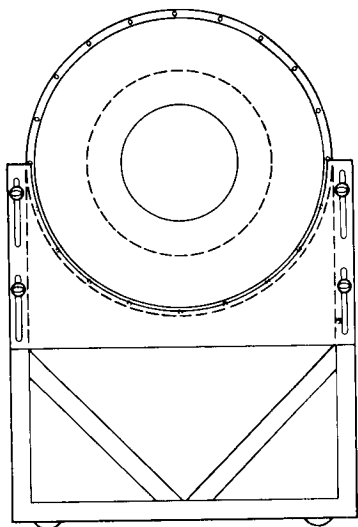


Figure 1. Front view of the 30 inch sphere and support. The height of the sphere is adjustable. The twelve inch port is shown by the circle at the center. The lamps are mounted in the sphere along the dashed circle.

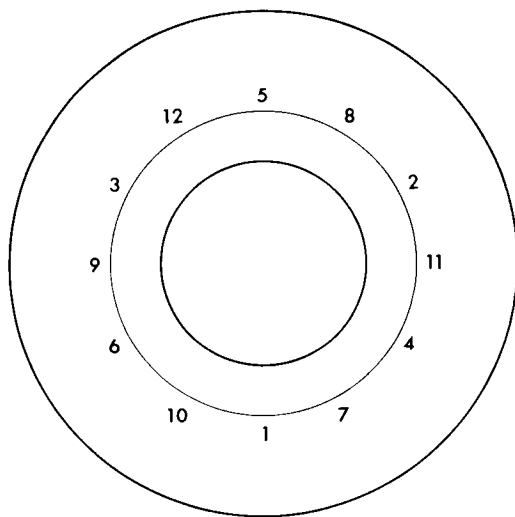


Figure 2. Lamp Placement in the Thirty-Inch Spherical Integrator (Inside View)

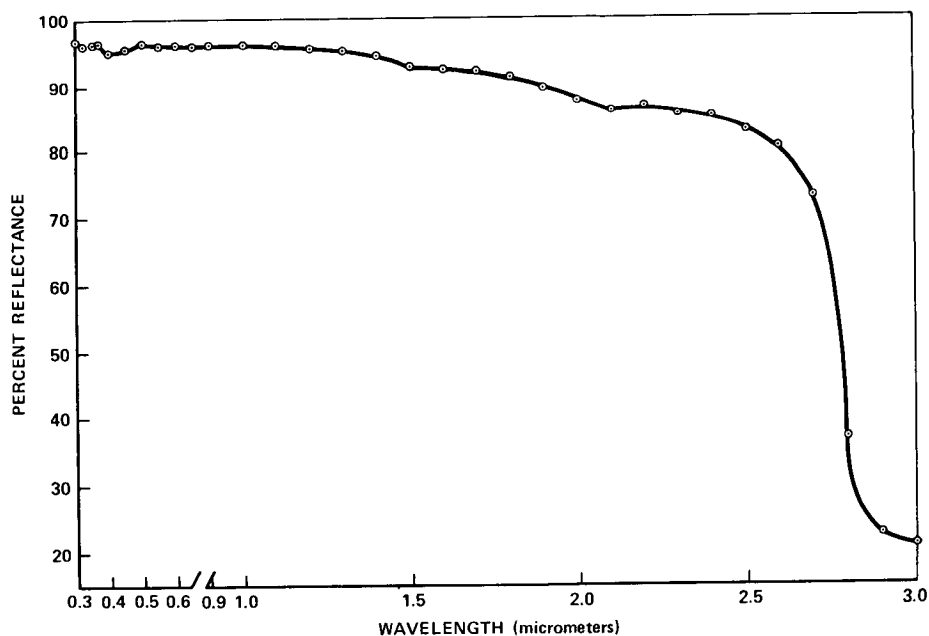


Figure 3. Spectral Reflectance

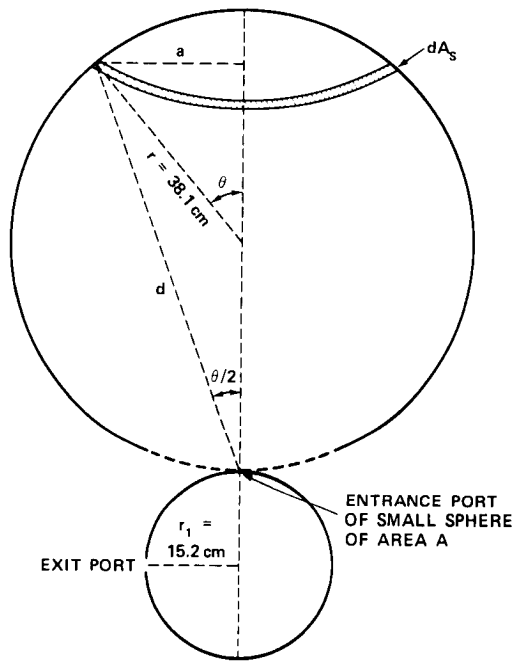


Figure 4. Cross Section of Large and Small Spheres Showing Data Used to Derive Equations 2 and 3

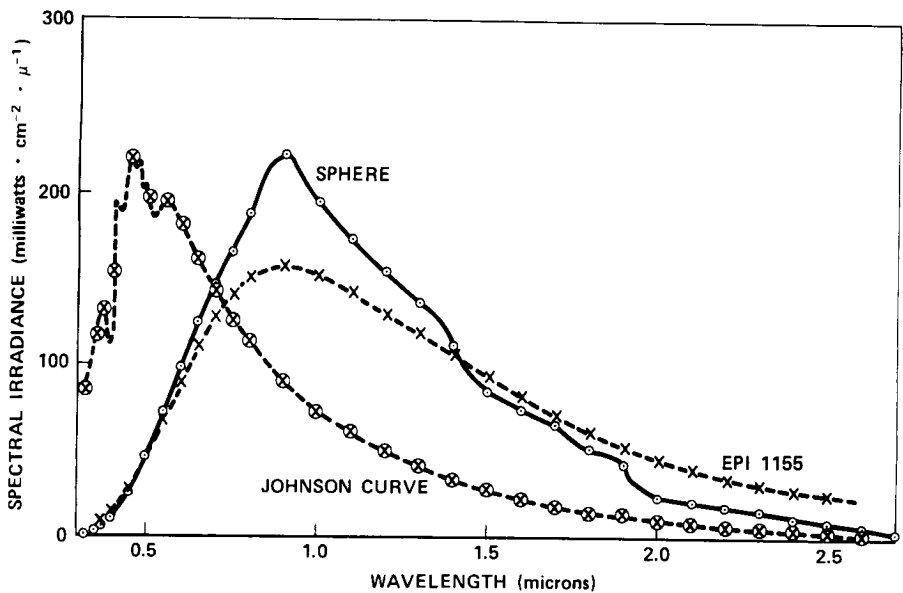


Figure 5. Spectral Irradiance

THE STATUS OF THE MEASUREMENT AND TRANSFER OF THE ABSOLUTE SPECTRAL RESPONSE OF SILICON PHOTODIODES

Edward Zalewski, *National Bureau of Standards, Washington, D.C. 20234*

ABSTRACT

NBS is presently completing a cw laser facility that will enable absolute spectral response characterizations of silicon photodiodes to be accurately based on electrically calibrated pyroelectric detectors. As part of the program to disseminate these characterizations, we are conducting an intercomparison to assess the capability of several laboratories to perform transfer measurements between different detector response functions. The detector characterization procedure and the results obtained from the intercomparison will be presented and the implication regarding the status of this measurement system will be discussed.

CURRENT STATUS AND FUTURE PLANS FOR NBS RADIOMETRIC SOURCE STANDARDS

Henry J. Kostkowski, *National Bureau of Standards, Washington, D.C.*

ABSTRACT

The accuracy and long-term stability of currently available NBS radiometric source standards will be described. Current research efforts and expected results in this area will be outlined.

There are over ten NBS radiometric source standards currently available or under development that might be of interest for solar measurements or for remote sensing of the earth. In addition there are several very stable sources used in establishing these standards that have not been widely used outside NBS but may be very useful for some of these applications. The standards and sources will be classified and described, in the current paper, in terms of the radiometric quantities they represent -- spectral radiance, spectral irradiance and irradiance.

SPECTRAL RADIANCE STANDARDS

The NBS standards and stable sources of spectral radiance currently available or under development are listed in Table I. Most of the standards are calibrated by spectral comparison with a high-quality blackbody whose temperature has been accurately measured. Exceptions are the deuterium lamp* and the low-temperature blackbody. Deuterium lamps are compared to a wall-stabilized hydrogen arc which can be radiometrically characterized by the equilibrium equations of the arc and the atomic properties of hydrogen. The lamps have also been compared to blackbody-derived standards. The low-temperature blackbody is calibrated with an electrically calibrated blackbody radiometer

*This NBS standard is provided by Dr. W. Wiese's Plasma Spectroscopy Section. All the others discussed in this paper are provided by the Optical Radiation Section.

operating at about 2 K.

Only the highest accuracy standards in Table I will be discussed in detail in this paper.

The tungsten ribbon gas-filled lamp has been available as an NBS standard of spectral radiance for over 15 years. During this time its uncertainty has been reduced by a factor of about three [1]. There are three major factors contributing to the current uncertainty of this standard. They are:

- (1) Uncertainty of realizing the Thermodynamic Temperature Scale
- (2) Uncertainty of realizing the International Practical Temperature Scale (IPTS)
- (3) Instability of the lamps.

Each of these factors contributes about equally to the spectral radiance uncertainty. At 650 nm this contribution is about $\frac{1}{2}\%$ * and varies approximately inversely with wavelength. In addition, at the longer wavelengths the signal-to-noise ratio and instrumental polarization effects contribute significantly to the uncertainty.

Efforts now under way at NBS are expected to reduce the first two components of the uncertainty significantly within a few years. The $\frac{1}{2}\%$ radiance uncertainty due to the Thermodynamic Temperature Scale is largely caused by the uncertainty of the melting point of gold. Considerable progress has been made by Guildner at NBS in establishing a new state of the art in thermodynamic temperature measurements from 0 K to about 700 K via gas thermometry. This work is continuing to higher temperatures with an improvement of the gold point by a factor of ten considered realistic. The uncertainty of realizing the IPTS in the neighborhood of 2500 K, temperatures of interest for the spectral radiance standards, have been largely limited by the instability at 650 nm of the tungsten ribbon lamps used as brightness temperature standards. We now think it is possible to significantly reduce the effect of this instability by attaching a silicon photodiode rigidly to a lamp and using the diode current rather than lamp current to monitor the brightness temperature. Preliminary experiments indicate that a 0.1%

*The uncertainty due to all these factors is therefore somewhere between $\frac{1}{2}\%$ and $1\frac{1}{2}\%$ depending on the signs of the corresponding errors. It has become common practice to combine such independent components in quadrature to obtain an estimate of their combined uncertainty. For 650 nm the uncertainty in percent would be $\sqrt{(.5)^2 + (.5)^2 + (.5)^2} = \sqrt{.75} \approx 0.9$.

correlation between spectral radiance and diode current is realizable, and a lamp-detector system is now being developed as a new standard of high brightness temperature. Such a standard is expected to make possible the development of techniques for realizing the IPTS to an uncertainty in terms of the spectral radiance of a blackbody at 2500 K of about 0.2%.

The instability of the tungsten ribbon lamps used as spectral radiance standards should also be improved by the use of a silicon photodiode. However, experience has shown that even when such lamps are stable in the visible they may vary significantly below 300 nm. So at this time, it appears that the uncertainty of tungsten ribbon spectral radiance standards could very well be reduced within a few years by a factor of about three at wavelengths greater than 300 nm but only about a factor of two at shorter wavelengths.

The major component to the uncertainty of the 500 K - 800 K blackbody spectral radiance standards is the long-term drift and instability of the commercially available blackbodies used for these standards. We believe these blackbodies could be developed so that they are monitored with a platinum resistance thermometer and have a long-term instability of much less than 0.1%. It would not require extensive development at NBS to provide a calibration service for such blackbodies with an uncertainty of as little as 0.2%. A graphite-copper core blackbody would be used with the temperature being determined with a standard platinum resistance thermometer. Thus if there is a need for infrared spectral radiance standards in this temperature range with an uncertainty significantly less than the 1% now available, they could be provided.

Several sources that are used in realizing the IPTS or checking the NBS 500 K to 800 K variable temperature blackbody should be mentioned because of their unique stability. These are the metal (gold [2], zinc and tin) freezing-point blackbodies and the Quinn-Lee vacuum tungsten lamp [3].

Gold-point blackbodies have been used in defining and realizing the practical temperature scale above 1336 K for many years. In the past 15 years we have built a variety of gold-point blackbodies at NBS and the spectral radiances at 650 nm of all of them have agreed to 0.01% or better. Though it is felt that zinc and tin freezing-point blackbodies are potentially as good as the gold-point blackbody, they have only been checked for a few years in the 1.5 μm to 3.0 μm region and only with an imprecision of about 0.1%.

Quinn and Lee found that by taking special precautions in cleaning and outgassing the tungsten and the glass bulb and in aging the tungsten [3], vacuum

lamps could be produced with significantly better stability than previously available. These lamps typically drift by 0.1% or less per 1000 hours of use and have hysteresis effects not exceeding about 0.05%. To achieve this type of stability, however, the lamps must be used at brightness temperatures at 650 nm of below about 1800 K.

SPECTRAL IRRADIANCE STANDARDS

There are only two standards of spectral irradiance currently available from NBS. These are a 1000-watt tungsten-halogen quartz lamp and a special red LED source. As indicated in Table II there is also a deuterium lamp standard currently under development for use in the ultraviolet.

NBS tungsten halogen lamp standards of spectral irradiance have been available for about thirteen years. As with the spectral radiance standards from which they are usually derived, their uncertainties have been reduced by a factor of about 3 over this time period. These uncertainties are primarily due to the spectral radiance uncertainties and the instability and positional imprecision of the lamp. The previously discussed improvement in spectral radiance standards, the use of silicon photodiodes for monitoring purposes and the use of ground quartz envelopes for more uniform irradiance fields should reduce the uncertainty of these standards by a factor of at least two.

The LED standard listed in Table II has only been available for about one year so there has been little experience with it. However, such solid state devices are expected to have a long-term stability much greater than high-temperature tungsten sources. And since highly stable gold-point blackbodies or Quinn-Lee type lamps could be used as spectral radiance standards for calibrating them, a 0.1% uncertainty should be possible in a few years. Thus if high-accuracy spectral irradiance standards in the red with levels 10^{-2} to 10^{-3} that of the 1000-watt lamps are desired, LED's should be considered.

In addition to the standards listed in Table II, blackbodies in the 500 K to 800 K range listed in Table I have been combined with an accurately measured aperture system to serve as spectral irradiance standards. The best available have an uncertainty of about 1% provided the apertures are not so small that diffraction effects become significant.

IRRADIANCE STANDARDS

The NBS irradiance standards presently available

are listed in Table III. The two highest level standards are based on an electrically calibrated thermopile radiometer (ECTR) and the two lowest on blackbodies. The uncertainty of the latter two is expected to be reduced to about 1% within a year by using an electrically calibrated pyroelectric radiometer (ECPR) now under development. In addition, with the ECPR, it should be possible to extend the standards to irradiance levels at least a factor of ten lower. Uncertainties approaching 0.1% appear feasible with the ECPR but considerable additional effort would be required to achieve this within a few years. One of the major advantages of the ECPR relative to the ECTR is that the responsivity of the ECPR is not proportional to its temperature but to the rate of change of its temperature. This makes its response time much shorter, even with large detectors, and permits chopping at a convenient frequency. The major current problems in realizing 0.1% with ECPR's are the non-uniformity of the responsivity over the entire target area and insufficient knowledge of the optical properties of its black coating as a function of wavelength.

SUMMARY

The best NBS source standards currently available for spectral radiance, spectral irradiance and irradiance have uncertainties of about 1%. Improvement to about ½% is anticipated within a few years with the lamp instability limiting much further improvement unless a major breakthrough occurs in lamp development. At lower levels where blackbody standards below 800 K or light-emitting diodes can be used, a 0.1% uncertainty can be realistically expected if a strong demand for such accuracy develops. Irradiance standards or measurements based on electrically calibrated pyroelectric radiometers also appear to have a potential of achieving an uncertainty of 0.1%. However, considerably greater effort would have to be placed on this particular application of the ECPR than is currently planned.

REFERENCES

1. Advances in Geophysics, 14, (Academic Press, 1970), p. 111.
2. Metrologia, 2, 150 (1966).
3. Temperature, Its Measurement and Control in Science and Industry (Instrument Society of America, Pittsburgh, 1972), Vol. 4, Part 1, p. 395.

TABLE I. SPECTRAL RADIANCE STANDARDS

Standard	Estimated Availability	Typical Electrical Requirements	Radiometric Magnitude or Temperature ($W\text{ cm}^{-3}\text{ sr}^{-1}$)		Wavelength Range	Uncertainty	Estimated Drift or Instability per 100 hrs
Tungsten ribbon lamp	Now	40A, 12VDC	225 nm-7	225 nm	225 nm-2%	2%	2% @ 650 nm
			1000 nm-2 $\times 10^5$	to	1000 nm-0.7%		
			2400 nm-4 $\times 10^4$	2400 nm	2400 nm-0.6%		
Pyrometer lamp-detector system	June 76	40A, 12VDC	.25 to 2×10^5	650 nm	Predicted to be 0.7%	Predicted to be 0.1%	
Medium temp. blackbody	Now	6A, 120VAC	500 K - 800 K	1.5 μm to 15 μm	1%	1% at 2 μm	
Deuterium lamp	Now	.3A, 300VDC	170 nm-8 $\times 10^4$ 250 nm-3 $\times 10^4$ 350 nm-7 $\times 10^3$	170 nm to 350 nm	10%	10%	
Low temperature blackbody	Dec. 75	.5A, 5VDC	200 K - 500 K	(Total radiance)	Predicted to be 5%	Not available	
Large area source	June 76		250 K - 350 K	8 μm to 12 μm	Predicted to be 5%	Not available	

TABLE II. SPECTRAL IRRADIANCE STANDARDS

Standard	Estimated Availability	Typical Electrical Requirements	Radiometric Magnitude at 50 cm ² (W cm ⁻³)	Wavelength Range	Uncertainty	Estimated Drift or Instability per 100 hrs
Quartz-halogen tungsten lamp	Now	8A, 110VDC	250 nm-0.2 1000 nm-250 1600 nm-130	250 nm to 1600 nm	250 nm-2.6% 555 to 1.2% 1600 nm	2%
LED	Now	.1A, 1.5VDC	Peak value of 0.01	600 nm to 725 nm	2.5%	1%
D ₂ lamp	Nov. 75	.3A, 300VDC	200 nm-.9 350 nm-0.06	200 nm to 350 nm	Predicted to be 10%	Not available

TABLE III. IRRADIANCE STANDARDS
(mW/cm²)

Quartz-halogen tungsten lamp	Now	8A, 110VDC	30 at 50 cm	1%	1%
Quartz-halogen tungsten lamp with reflector	Now	8A, 110VDC	130 at 40 cm	0.5%	2%
Airway beacon lamp	Now	5A, 110VDC	3 at 100 cm	2%	Not available
Microscope Illumination lamp	Now	1A, 110VDC	0.6 at 100 cm	2%	Not available

SOLAR RADIATION MEASUREMENTS BY THE ACTIVE CAVITY RADIOMETER — PAST, PRESENT AND FUTURE

R. C. Wilson, *Jet Propulsion Laboratory, California Institute of Technology, Pasadena, California 91103*

ABSTRACT

The active cavity radiometer (ACR) is an accurate state-of-the-art pyrhelimeter, capable of defining the absolute radiation scale in terms of S.I. units. In a series of ground based experiments beginning in 1968 and extending to the present a 2.2% ($\pm 0.4\%$) systematic error in the International Pyrhelimetric Scale (IPS) has been discovered. ACR's are currently being used in the First International Comparison of Absolute Radiometers at Davos, Switzerland to determine the precise value of this error. ACR's were used in high altitude balloon experiments in 1968 and 1969 to make the first high altitude (36 km) measurements of the solar constant by absolute pyrhelimeters. A value of $H_0 = 136.6 \pm 0.7 \text{ mw/cm}^2$ was derived from the 1969 experiment. Direct comparison of the ACR with Murcray's IPS-referenced balloon flight instrumentation in 1970 increased his average solar constant value to 137.3 mw/cm^2 on the absolute scale, referenced to S.I. units by the ACR, thus reconciling their solar constant value and ours to within the bounds of experimental error. A design study is being conducted at present to define an ACR satellite experiment to monitor the solar constant on a long term basis with an absolute uncertainty of less than $\pm 0.1\%$ and a resolution of one part in 10^6 .

PRECEDING PAGE BLANK NOT FILMED

1 N 76-11177

INITIAL SOLAR RADIATION MEASUREMENTS FROM ERB

J. R. Hickey and F. J. Griffin, *The Eppley Laboratory, Inc., Newport, Rhode Island* and
D. T. Hilleary, *NOAA/NESS, Suitland, Maryland*

ABSTRACT

Some preliminary comments on the results of the solar radiation measurements from the Earth Radiation Budget Experiment of the NIMBUS 6 satellite are discussed.

INTRODUCTION

The Earth Radiation Budget Experiment is one of the subsystems aboard the NIMBUS 6 Satellite. The satellite was launched on June 12, 1975 from the Western test range. It attained a nearly perfect circular solar orbit with an inclination of 99.9640° and a period of 107.23 minutes. The solar radiation channels were protected by a door during a decontamination period which lasted until July 2nd. The first solar measurements were made during Orbit 273 with the data being relayed to earth during the Orbit 274 Alaska interrogation.

At the time of this writing detailed analysis of all solar data has not been completed. Preliminary results are given below.

The ERB Radiometer Package

The Earth Radiation Budget subsystem is shown in Figure 1. It comprises ten channels for solar measurement, four channels for direct earth flux measurement and eight channels which measure earth radiance by scanning the earth's disc. The experiment has been described in the previous IES document (1). The calibration has been discussed by Hickey and Karoli in reference (2) and the solar measurement capability by Hickey, et al. (3). Table I contains pertinent channel characteristics for the solar channels.

PRECEDING PAGE BLANK NOT FILMED

The solar radiation in the bands from $<.2$ to $>50\mu\text{m}$ is measured by Channel 3 as shown in the Table. Channels 1 and 2, which are redundant, measure in the band $.18$ to $4.0\mu\text{m}$. Channel 5 covers the range from $.698$ to $3.0\mu\text{m}$. These particular bands match those of the fixed earth flux channels with Channel 3S corresponding to 11E and 12E, Channels 1S and 2S corresponding to Channel 13E and Channel 5S corresponding to Channel 14E. During the polar orbit the solar radiation impinges on these earth flux channels during both the satellite night/day and day/night transitions which occur near the South and North Poles, respectively. The direct solar measurements are made at the southern terminator crossing. The measurement of direct solar radiation by the earth flux channels acts as a check on the direct solar measurements, while also acting as a mutual consistency check between these two measuring capabilities. This type of intercomparison is being examined at the time of this writing.

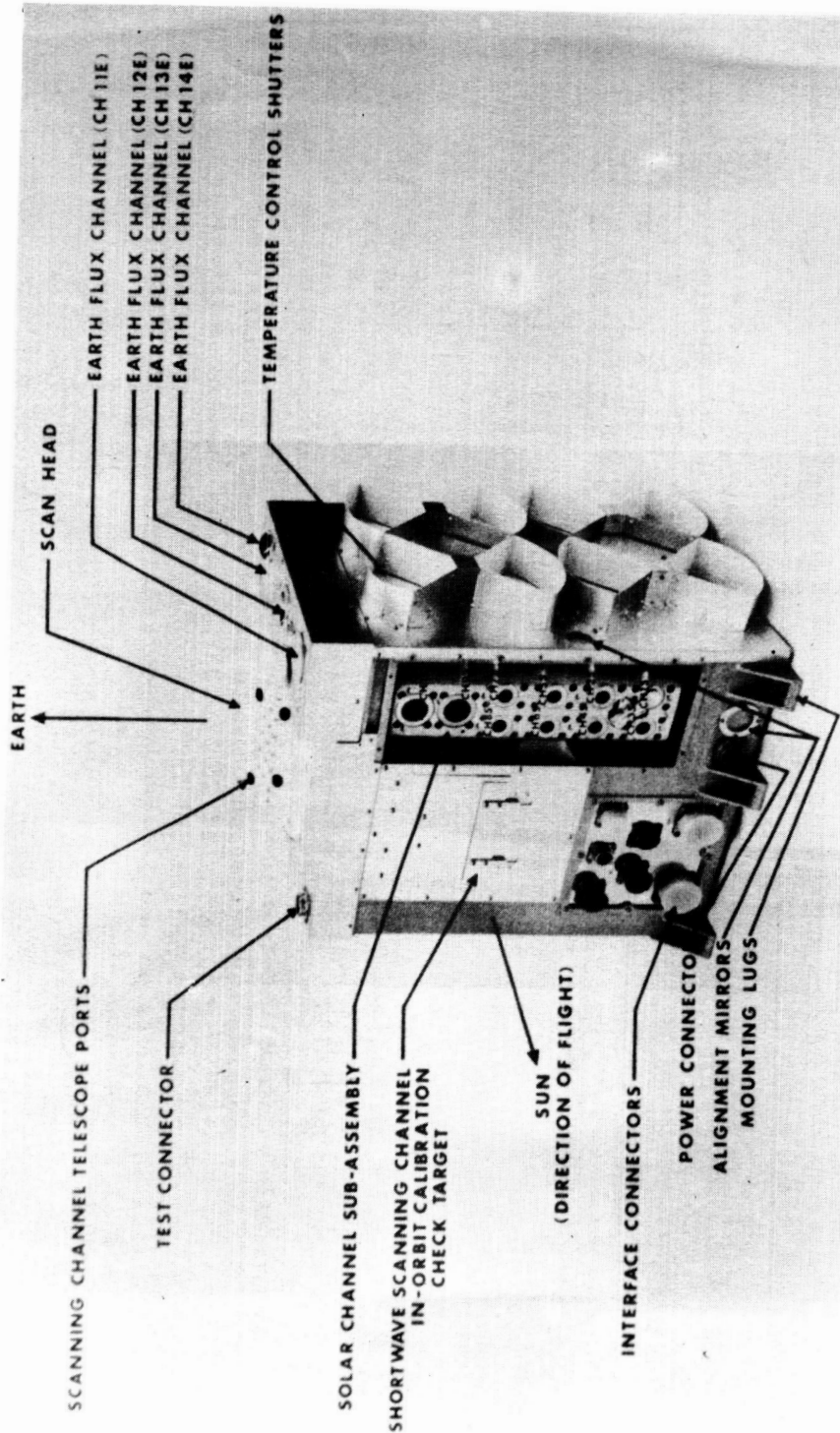
Initial Radiation Values

The initial values of the solar radiation in Channel 1, 2 and 3 regions appears to be somewhat higher than anticipated from the results of previous measurements, (4,5,6). The total radiation value at this time is 1394 Wm^{-2} while that for the $.18$ to $4\mu\text{m}$ region is 1369. The accuracy assigned to these values at this early stage is $\pm 1\%$. The values are corrected to mean earth-sun distance. The calibration is referenced to the cavity or absolute radiation scale as embodied in a PACRAD instrument (7) maintained by the Eppley Laboratory, which has been included in a number of intercomparisons at Table Mountain and elsewhere.

The results from the other solar channels are under study. They will be reported on November 5 at the Symposium. In general, results from the interference filter channels are in closer agreement with values reported by Labs and Neckel than those included in NASA SP-8005 (8).

Measurement Stability

It had been anticipated that the change in mean earth-sun distance should be used as a quality control tool in assessing the performance of the solar



Earth Radiation Budget Subsystem - Fig. 1

Table I. ERB Solar Channel Characteristics

Channel	Wavelength Limits (μm)	Gain	Sensitivity ² (Counts/ Wm^{-2})	On-Axis Signal for early orbits (counts)
1S	.18 - 4.0	606	1.272	1681
2S	.18 - 4.0	660	1.310	1733
3S	.2 - 50	606	1.227	1636
4S	.524 - 3	923	1.822	1708
5S	.698 - 3	1214	2.525	1655
6S	.395 - .508	7959	7.745	1541
7S	.344 - .460	17197	9.789	1552
8S	.300 - .410	21060	12.60	1328
9S	.0275 - .360	9081	33.12	1828
10S	.252 - .324	32125	51.98	1348

- Notes:
- (1) Channel 1S is normally shuttered and is redundant to Channel 2S.
 - (2) Sensitivity values pertain to on axis solar radiation at 25°C and must be adjusted for temperature and orbital differences.
 - (3) Channel 3S has no optical elements, windows or filters.
 - (4) Channels 9S and 10S require correction for thermal transient response.

channels. Since the solar measurements started close to earth aphelion there has been an insufficient change at the time of this writing to assess this matter, since there has been less than 0.1% predicted variation. However, the stability of all channels over the first 70 orbits of measurement has been noted, with the broad channels varying less than two counts in 1700. This indicates that fears concerning degradation due to contaminants being irradiated by UV has not been a problem up to this time. The narrow band channels are exhibiting similar low variations for their peak signals in the order of 3 to 5 counts on 1500 to 1800 total counts depending upon the channel. This situation exists when the scan head is in operation which induces a small amount of noise in the high gain channels. We have requested that the scan head be turned off periodically during ERB operation times so that the no-noise variability of these channels can be established.

The Reference Sensor Model

As described in the reference there is a matching instrument to the ERB subsystem called the reference sensor model. This instrument is an exact duplicate with regard to the protoflight instrument which is now in orbit. During each stage of the calibration and test program the reference sensor model was exposed or tested in a similar manner to the flight instrument. This was to assure that any anomalies determined during testing or in orbit could be studied after-the-fact with a radiometer of the same quality. At this time the RSM is undergoing recalibration. It was released for this purpose at the time of the launch. Any changes found in the calibration of the RSM may necessitate adjustments to the response values of the flight instrument. Also, some angular response data which could not be obtained experimentally earlier in the program is being studied using the RSM.

Summary

Initial solar radiation measurements from the ERB experiment indicate that the total radiation is somewhat higher than anticipated. Assuming that the previous X-15 results of 1360 Wm^{-2} had been properly

referenced to the IPS scale and knowing that the relationship of the present cavity standard to the previously used Angstrom standard is $2.0 \pm 0.3\%$ then the expected value for the solar constant would be approximately 1387 Wm^{-2} . Our initial value from ERB is 0.5% higher than this anticipated value. The low UV channels 9 and 10 are in closer agreement to the values of Labs and Neckel than with NASA SP-8005. However, these values are undergoing correction for thermal effects in the high gain channels. The consistency of the measurements from orbit to orbit is of the order of 0.1% for the broad band channels and in the order of 0.3% for the narrow band channels.

It is anticipated that further analysis of these data will allow final values to be presented at the November meeting.

References:

1. Hickey, J.R., Chapter 5 of "The Extraterrestrial Solar Spectrum" edited by A.J. Drummond and M.P. Thekaekara, Institute of Environmental Sciences, Mount Prospect Illinois, 1973.
2. Hickey, J.R. and Karoli, A.R., Applied Optics, 13, 523, March 1974.
3. Hickey, J.R., Hilleary, D.T. and Maschhoff, R.H., Proceedings of the Symposium on Solar Radiation Measurements and Instrumentation, Smithsonian Institution, Nov. 1973, (in press).
4. Drummond, A.J., Hickey, J.R., Scholes, W.J. and Lane, E.G., Nature, 218, 5138, April 20, 1968, pp.259-261.
5. Willson, R.C., Proceedings of the Symposium on Solar Radiation Measurements and Instrumentation, Smithsonian Institution, Nov. 1973, (in press).
6. Labs, D. and Neckel, H., Proceedings of the Symposium on Solar Radiation Measurements and Instrumentation, Smithsonian Institution, Nov. 1973, (in press).
7. Kendall, J.M. Sr., NASA Technical Report 32-1396, Jet Propulsion Laboratory, July 15, 1969.
8. Anonymous, NASA SP-8005, Solar Electromagnetic Radiation, Revised May 1971.

QUANTITATIVE DETERMINATION OF SMOKE AND TOXIC PRODUCT POTENTIAL OF MATERIALS WITH THE AMINCO® NBS SMOKE DENSITY CHAMBER

Samuel Greenberg, *Applications Engineer, American Instrument Co., Silver Spring, Maryland*

ABSTRACT

Quantitative measurements of smoke obscuration produced by standard area samples under high energy pyrolysis both with and without an ignition source, using a collimated vertical light beam in conjunction with an ultra-linear photomultiplier microphotometer are obtainable with an apparatus first developed at NBS. Results are expressed in dimensionless Specific Optical Density permitting usage calculations in accordance with geometric relationship:

$$D_s = D \times \frac{V}{A \times L}$$

HISTORICAL BACKGROUND

The introduction of plastics and other man-made synthetics required new techniques and equipment for fire fighting since their behavior under conditions normally encountered in fire situations was directly contrary to the material behavior of non-synthetics. The principal emphasis by the researcher and scientist was to improve the inherently poor flame spread and ease of ignitions characteristics of most of these synthetics. In many cases materials which evolved relatively low levels of smoke and toxic gasses were changed to dangerously high smoke and toxic gas sources by the addition of additives intended to lower the flaming hazards.

During the past twenty-five years, industry strides in inhibiting the flammability of both the new synthetics and even some of natural materials has permitted the use of many materials previously considered too dangerous for general use. This has usually been achieved by modification of physical and chemical structure usually by use of additives as antioxidants.

Unfortunately, safety and insurance officials now note that over half the injuries and fatalities in fires are due to smoke of toxic products produced in spite of the reduced flammability of the materials involved. Insurance authorities in the United States have stated that property damage is now approximately 25% for fire and 75% for smoke-related claims, in-

cluding the high rate of corrosion on metals and machinery. With the increased use of Teflon and other fluorinated plastics, the loss to properties and life has further increased due to the evolution of HF and Hydrofluoric Acid.

This concern with the increased hazards from smoke and toxic effluents caused the U.S. Federal Housing Authority to commission the U.S. National Bureau of Standards to investigate and develop test methods to better evaluate the hazard potential of currently used materials. The parent department, the U.S. Department of Commerce, the Federal Aviation Agency responsible for commercial aviation safety and the U.S. Department of Housing and Urban Development joined in these investigations. One of the principle benefits of the investigation was the development of an apparatus and test procedure for evaluating the smoke potential of materials subjected separately to radiant flux without a flame source and to the same radiant flux with an ignition source. The heat flux selected was 2.5 watts/cm^2 a severe exposure and the same average heat flux provided by the internationally accepted Radiant Test Panel method for flame spread measurements. Several authorities in the United States now specify the Radiant Panel for determining flame spread and the NBS Smoke Chamber for smoke obscuration. Since the entire product evolved during the test (smoke, steam and gas) are accumulated in the chamber, to be later exhausted, the test chamber is gaining increased usage as a means of producing and containing gasses for further analysis and study. Since the area of material exposed, the volume and the heat flux are constant and reproducible, the accuracy and reproducibility of gas analyses from the chamber approach those obtainable for smoke criteria.

Other recognized agencies have also studied the smoke hazards including full scale tests by the National Research Council of Canada, the Los Angeles, California, Fire Department, the Underwriters Laboratories and the Fire Department of Paris, France. In 1958 the National Research Council of Canada, conducted full scale burns on several houses to be destroyed for the new St. Lawrence Waterway. Their report concluded with the statement: "With reference to the survival of occupants, it was found that all dwellings became smoke-logged within 6 minutes of ignition. In all but one case the criterion for decrease of visibility was exceeded before the other criteria for survival - the carbon monoxide concentration, reduction of oxygen and temperature. The smoke criterion relates principally to possible unaided escape of occupants in contrast to the lethal effects of carbon monoxide and high temperatures, upon which survival depends more directly and without regard for subsequent rescue."

The Los Angeles tests comprised 55 separate test fires in an attempt to correlate the data with the 7.6 meter (25 ft) Steiner or ASTM E-84 Tunnel, concluded with the following: "The smoke itself does not contain a high concentration of dangerous gasses to be lethal in the early

stages of a fire. However the untenable smoke, by its irritant properties, and its obscuration of normal visibility, does immobilize the occupants within the area of the building where they happen to be located. They are then 'trapped' within the building and unless rescued promptly, may be killed by the lethal heat and gasses which follow shortly."

The 1963 tests in Paris on a new 22 story apartment house resulted in the following conclusions:

1. Where evacuation of the occupants is of prime concern, the principal danger is from the elevated temperature of the smoke.
2. Cool smoke tends to diffuse while hot smoke tends to stratify.
3. Optical density of the smoke decreases as the smoke temperature increases. The carbon monoxide hazard becomes significant when the temperature reaches a point where evacuation is difficult.
4. Choking, irritating and lachrymating elements of combustion products made the test room untenable before various dangerous temperatures of toxic gas levels were reached.

TEST METHODS AVAILABLE

Various test methods are available in the United States for measuring smoke properties of materials, but except for the method under discussion, the NBS Smoke Density Chamber test, they are mainly restricted to the flaming mode and provide only qualitative data based on an arbitrary standard of measurement. These include:

1. The ASTM E-84, a tunnel which is based on the original Steiner Tunnel used primarily to measure flame spread with a rather insensitive light meter used to record the smoke evolved while under a 73 m/min (240 ft/min) air flow through the tunnel.
2. The ASTM E-286, 2.4 m tunnel, developed by the U.S. Forest Products Laboratory is primarily used for flame spread and fuel contribution studies. It varies from the E-84 test in employing a radiant energy source, and a small ignition source, enabling non-flaming tests if desired. The smoke obscuration is by means of horizontal phototube optical system in the exhaust.
3. The Rohm and Haas XP-2 chamber is primarily intended to determine the extent to which plastics are likely to smoke under conditions of active burning and decomposition in the presence of flame. The smoke obscuration is measured by the rising smoke intercepting a horizontal light path .3 m long located at mid-height in the .9 m high chamber.
4. The ASTM E-162 Radiant Panel Test, also recognized as an ISO procedure for flame spread determinations, provides two relatively sim-

ple smoke measuring systems; a glass disc located in the exhaust, which is weighed before and after the test and a relatively simple photometric system in the exhaust duct.

5. The Monsanto Tunnel in which the effluent from a plastics flammability test bar is drawn through a filter paper which is then weighed.
6. The Aminco-NBS Smoke Density Test Chamber, herein described, provides several unique features including:
 - A. A fixed volume chamber in which the total smoke and effluent is accumulated during the test.
 - B. Each test specimen provides equal surface exposure to the radiant source at an average radiant heat flux of 2.5 watts/cm^2 , both under non-flaming and flaming exposures.
 - C. The cumulative smoke obscuration measurements are made using a collimated, vertical light beam approximately 1 meter long, using an incandescent light source operating at constant voltage and spectral output and measured by a photomultiplier microphotometer system capable of linear readout to an Optical Density of 7, (.0001% of the original transmitted light).
 - D. All measurements are in Specific Optical Density, a quantitative value which can be factored to estimate the smoke potential of the material under conditions of actual usage in accordance with the established geometrical relationship of:

$$\text{Specific Optical Density} = \frac{\text{Optical Density} \times \text{Volume}}{\text{Surface Area} \times \text{Light Path Length}}$$

- E. Provides a means of retaining the melted sample in the zone of radiant flux and flame impingement and therefore contributes to the total measurement. All other methods show reduced values with melting and dripping materials.

It must be realized that although the NBS Smoke Density Chamber provides a measure of the obscuration by the smoke, that vision will never be as good as the photometric determination, because of sensitivity of the eye to the alkaline and acid forming gasses which may be present in the smoke. The reflex reactions to an irritated eye can be so severe that little freedom is provided for normal vision. Thus a light, highly transparent smoke with high chemical irritant content may limit vision much more severely than a more dense but chemically inert smoke. Nevertheless, there is ample evidence that even in the absence of toxic or irritating elements, dense smoke presents a real hazard. In addition to ingested solid particles from the smoke, the limitation of vision can be a major cause for alarm and panic with resulting disorientation. While the measurement of smoke through its light attenuation may not provide the ideal fire gas indicator it does provide a useful measure of some compo-

nents of the hazard associated with fire gasses.

SPECIFIC OPTICAL DENSITY

Specific Optical Density has been used in chemical photometric practice but is uniquely applied to the measurement of smoke with the NBS Chamber. It is based on Bouguer's Law and permits reporting smoke development based on the area of the specimen involved, the volume of the space in which the smoke is accumulated and the length of the light path. The property is without dimensions but must be recognized as relating to the specimen thickness. Figure 1 shows a chart from ASTM STP 422 which demonstrates this quantitative and geometrical relationship. The cross hatched area indicates the approximate limit of visibility of a strong light by eyes protected from contact with smoke. The Specific Optical Density determination is expressed as D_s and the maximum measured over a maximum period of 20 minutes is expressed as D_m . Some existing regulations express either a maximum average D_m as determined for both the radiant-flaming and the radiant-(non-flaming) exposures, or a maximum D_m for either exposure. Other requirements which have been promulgated include: time to attain D_{s16} (25% obscuration), time to attain 90% of D_m , and a maximum D_s attained within a specified period of time. Some U.S. authorities have also suggested a Smoke Obscuration Index (SOI) which is a combination of D_m , D_{s16} and rate of smoke evolution.

The ability of individuals to escape from smoke-filled areas without assistance is dependent upon the visual distance to the exit and the smoke density. This, too, will differ with visual threshold response of different individuals; therefore, data must be based on broad based tests with different age levels, and different types of smoke. Perhaps the most authoritative data is derived from: "Visibility Through Fire Smoke", Jin, T., Report of Fire Research Institute of Japan, 31, 33 (1971). This relationship of apparent density of smoke may be expressed as:

$$D/L$$

where: D = Optical Density of the Smoke

L = Visual Distance

The data from the Aminco-NBS Smoke Density Chamber is used directly by either using the Optical Density equivalent of the Optical Transmission value as indicated by the Microphotometer or using the following formula to convert the maximum Specific Optical Density (D_m):

$$D/L = D_m \times A/V$$

where: A = Exposed area of test sample 42.2 cm^2 (6.54 in^2)

V = Volume of test chamber 0.51 m^3 (18 ft^3)

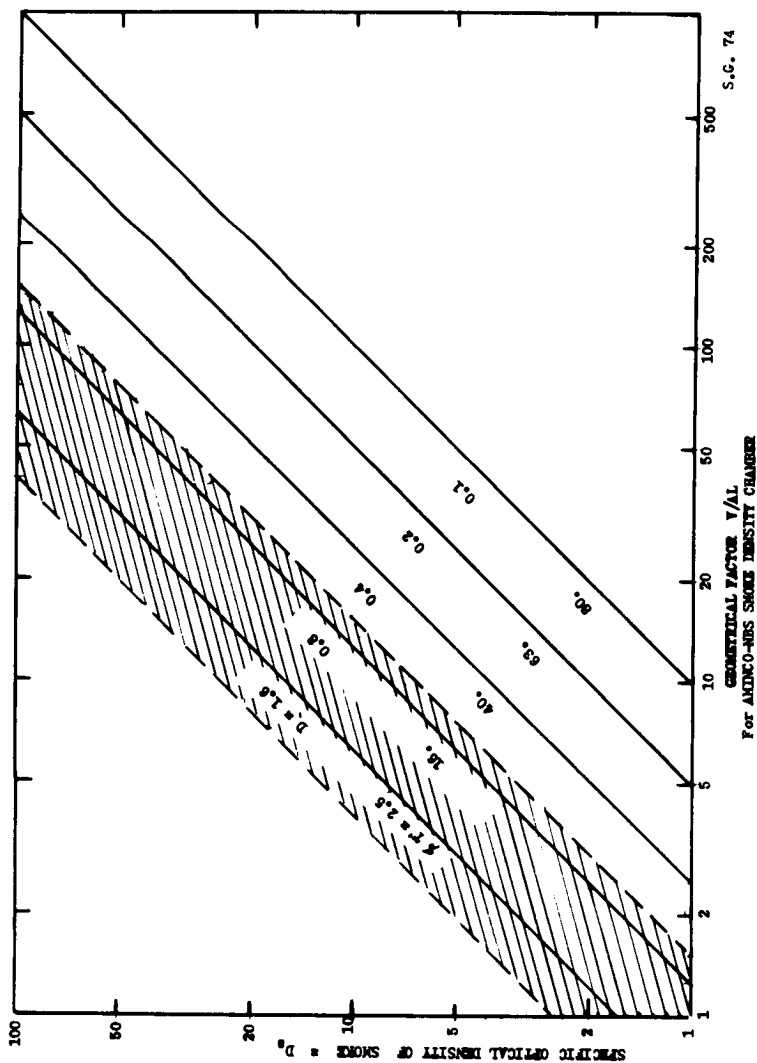


Figure 1. Specific Optical Density versus Geometrical Factor for 5 selected light transmission values. The hatched area represents the approximate limit of visibility of a bright light.

Figure 2 derived from "The Smoke Density Chamber Method for Evaluating the Potential Smoke Generation of Building Materials", NBS Technical Note 757 by T.G. Lee, January 1973, shows a practical application of the data to determine "Visual Thresholds vs Smoke Density". This graph is, of course, based on observations without the presence of smoke or other eye irritants which might reduce the visual capacity of the individual. The use of this data must therefore consider this added reduction in the Visual Threshold in the presence of smoke.

APPLICATION OF AMINCO-NBS SMOKE DENSITY CHAMBER

For meaningful application of the Aminco-NBS Smoke Density Chamber test, the following must be considered:

1. Any requirement limiting the maximum D_m value must, to be valid, be based on the assumed area of the material which would be likely to be exposed to fire.
2. In any application of the D_m value, it must be recognized that the value derived is not a material property or characteristic which can be generally applied. The derived value from the NBS test is a specimen property and representative of the product in the thickness and assembly upon which the test conditions were imposed.
3. The data derived from the test is only valid for the conditions of test. Any other variables in the heat-flux, or ambient conditions may drastically affect the values obtained.

The Aminco-NBS Smoke Density Chamber is the commercial version of the original apparatus developed by the U.S. National Bureau of Standards and reported on at the A.S.T.M. Symposium on Fire Test Methods - Restraint and Smoke, 1966, ASTM STP 422, 1967, p166. Many improvements in range, accuracy, reproducibility and ease of operation have been incorporated in the commercial model. At the time of writing, there were over 170 chambers in use both in the United States and abroad.

The apparatus is designed for ease of operation, portability and clean-up. The caster-mounted cabinet is intended to be connected by means of flexible lines to sources of compressed air and propane as well as to an exhaust system or chemical hood. The self-contained exhaust blower which is activated when the floor damper is opened, after completion of the test and removal of gas samples if desired, is capable of exhausting the test product to the laboratory exhaust system through a flexible hose no longer than 8 feet long. Full interior visibility is provided through the front door tempered glass window. To optical density 4 (0.01% transmission) no cover is usually required on the window, but for more dense smoke, light scattering can produce a false value of D_s . The interior is fabricated from porcelainized steel on all flat surfaces

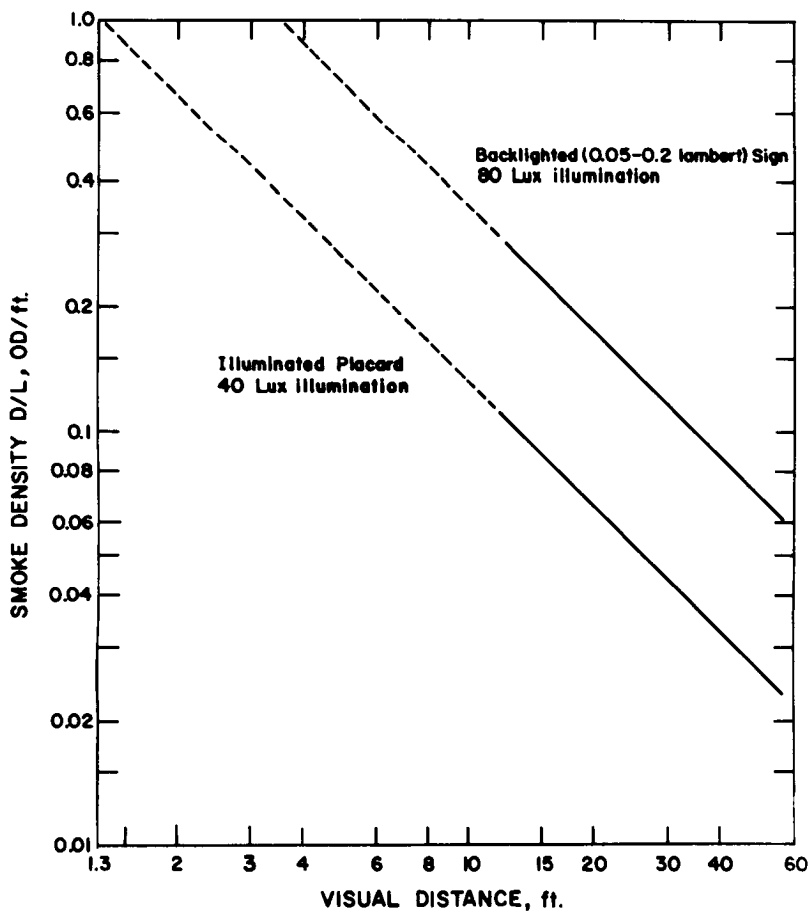


Figure 2. Apparent Smoke Density D/L versus Visual Distance for Front and Backlighted Placards

with the hardware of epoxy steel, and austenitic stainless steel trim. Orientation of the furnace, samples and the calibration radiometer are assured through the use of a furnace fixture with adjustments for furnace alignment, and two support rods with adjustable stops to support and align the sample holders and radiometer. The precision sample holders with and without a trough for containing any sample melt, are provided with alignment and support features to assure that each sample is exactly aligned with the furnace while permitting ease of positioning and removal while hot. The Radiometer which was especially designed for this test procedure by NBS scientists is based on the Gardon heat-flux transducer used primarily in the space program. It is designed to fit on the same rods as the sample holder and with the stops properly set is accurately and rapidly centered to determine the heat flux to which samples will be subjected. Each radiometer is accurately calibrated in accordance with an NBS procedure assuring that each furnace in use will be operating at 2.5 watts/cm^2 plus or minus 0.25 watts/cm^2 . The radiometer is provided with quick disconnect lines to a source of compressed air used to maintain the body at 93.3°C and a shielded low loss line to a potentiometric read-out of T_d output. The quick-disconnect features provide for ease in removal after calibration with minimal chance of damage to the device. The current models incorporate a pull-knob below the door which enables the operator to move expended samples from in front of the furnace, minimizing the final correction required for aerosol fall-out on the optical window. Roof-mounted fittings are provided to connect devices, to sample the effluents, measure and indicate internal pressures or insert tubing or wiring without the need for reducing the sealing properties of the chamber. Although the effluents are often corrosive and dirty, the chamber is capable of containing all of the product and then exhausting it through the flexible hose to be installed and furnished by the user. Most chambers in the United States are operated in modern air-conditioned laboratories without the need for special safety precautions or excessive maintenance of the chamber or the environ. The solid state microphotometer incorporates four decades of direct read-out and in conjunction with a permanently installed but movable Neutral Density 2 filter in the optical system provides an additional two decades of operation without fatiguing the Photomultiplier Tube. The system also features a full range dark current blank adjust eliminating the need for correction calculations and compensations for aging of either the Photomultiplier or light source. The original NBS prototype permitted adjustment of the light source voltage to provide the base illumination. Round-robin tests among 22 users indicated that the change in voltage changed the spectral characteristics and the obtained data. All chambers, therefore are operated at a constant light source voltage of 4 plus or minus 0.4 volts in conjunction with 9 graded neutral density filters. In calibration procedures the user selects one or more of the 9 and installs the same in the optical system to compensate for differences in luminous sensi-

vity of the Photomultiplier Tube.

The U.S. National Bureau of Standards offers standards for sale for both the non-flaming, radiant mode (Alpha-Cellulose) and the flaming-radiant mode (A.B.S.). These may be procured from the Office of Standard Reference Materials. No other similar standards exist for any other smoke test.

Early in 1974 the National Fire Protection Association, a leading code writing group in the fire technology field voted to adopt the NBS Smoke Density Chamber and its procedure as NFPA 258T-74. This tentative designation will hold for one or two years to permit amendment and modification before achieving permanent status.

On July 29, 1974, the Assistant Secretary of Health for the United States Department of Health, Education and Welfare signed into law a revision of the existing regulations for Construction of Hospitals and Health Facilities requiring NBS Smoke Density Tests for all finish materials, including wall coverings and carpeting to be tested with the Aminco-NBS Smoke Density Chamber.

The smoke density chamber has gained ever increasing acceptance both in the United States and abroad and is presently under consideration as the primary apparatus for the determination of smoke potential of materials and material systems. In addition the number of technical articles and publications dealing with both the basic apparatus and with various modifications indicates an ever increasing potential for both quality assurance and research in conjunction with various existing and contemplated accessories.

One source of possible misunderstanding is the lack of a single reference to the Aminco-NBS Smoke Density Chamber. Various documents and specifications have used any of the following to identify the commercial apparatus being marketed by the American Instrument Company:

- ASTM STP 422: ASTM Special Technical Publication of the seminar at which the original NBS Smoke Density Chamber was described by Gross, Robertson and Loftus from the Fire Technology Section at the National Bureau of Standards.

NOTE

This reference is not a preferred designation since the prototype device described has been vastly improved in the commercial apparatus, which varies in several areas from the apparatus described.

- NBS TECHNICAL NOTE 708 - APPENDIX II: "Test Method for Measuring the Smoke Generation Characteristics of Solid Materials", by T.G. Lee of NBS, updating the original apparatus description to essentially include the modifications incorporated in

2-10
the commercial chamber.

- NFPA 258-T-74: "Tentative Standard Test Method for Smoke Generated by Solid Materials", describing the test procedure and apparatus as approved by the National Fire Protection Agency in May 1974, essentially conforming with NBS Tech Note 708 preceding with additional background and reference information.

In addition to the preceding there have also been references to several specifications requiring the test apparatus, including:

- New York Port Authority, or Fire Advisory Board of the New York City Fire Department, August 1971
- MIL-P-36816, Amended February 1973
- MIL-C-24500 (Ships) 24 May 1974
- MIL-P-15280G 24 May 1974
- MIL-STD-1623A (Ships) 20 May 1974, Fire Performance and Approved Specifications for Interior Finish Materials and Furnishings (Naval Shipboard Use)

As of the date of this paper there are several other documents in process which may be referenced incorrectly as identifying the apparatus. These include:

- Proposed Test Method, ASTM Committee E-5, presently in a 3rd Round-Robin series of tests to establish the reproducibility prior to ballot by the sub-committee E5.04 and then by the main committee.
- Proposed Test Method, ASTM Committee F7.06, includes specialized procedures specific for commercial aerospace interiors and a special wire insulation test, currently in ballot by the subcommittee. This essentially conforms with the proposed Rules by the F.A.A. announced in the Federal Register of February 12, 1975.
- Proposed Interim Federal Specification TT-P-1932 for Fire Retardant Latex Paints, being proposed by G.S.A.
- Proposed Rules, Department of Transportation, F.A.A., Federal Register dated December 30, 1974 to require toxic effluent analyses after testing in the NBS Smoke Density Chamber.
- Proposed Rules, Department of Transportation, F.A.A., Federal Register dated February 12, 1975 requiring the specialized procedure for aerospace interior materials and wire insulation essentially the same as the ASTM F7.06 document above.
- H.E.W. Publication HRA74-4000, amended to require the Smoke Density Test for all interior finish materials used in the construc-

tion of federal funded hospital and medical facilities.

- OPERATION BREAKTHROUGH, U.S. Department of Housing and Urban Development, Fire Protection - Smoke Criteria, establishing minimum smoke levels under flaming and non-flaming pyrolysis for interior and exterior materials used in pre-fabricated housing units.

Unfortunately all of the preceding where smoke values are stated do not appear to recognize the unique feature of this procedure, an established geometric relationship of:

$$D_s = D \times \frac{V}{A \times L}$$

The original paper and subsequent publications by others establish this relationship which would enable an engineer or architect to predetermine the level of visibility to be expected using a certain material based on the value obtained from the test, the volume of the space, area exposed and the visible distance required. Figure 3 illustrates the application of this relationship. These data in Figure 3 can only be used with the standard test as presently described in the various referenced documents. With the horizontal (Meister) test to be described or any other procedure where a different area of exposure is to be used will require revision of both Figures 1 and 3, since the $V/AL \times D$ value will no longer be $D_s = 132$ at $D = 1$.

Several noteworthy investigators have either developed in-house modifications or have cooperated with us to produce prototype modifications which might likely be used for further amplifying the application of the NBS Smoke Density Chamber.

The University of Utah, Flammability Research Center under the leadership of Professor Irving N. Einhorn, working closely with a multi-discipline team continue to be the leaders in such modifications. Working closely with Dr. Leo Parts of the Monsanto Corporation, James Gaskill of the University of California, Dr. M. M. Birky of the National Bureau of Standards and other outside investigators they have presented or published about 15 papers describing various smoke chamber modifications. Their most recent report, "Smoke Measurement In a Modified NBS Smoke Density Chamber", by W.P. Chien and Dr. J.D. Seader, Chairman of the Department of Chemical Engineering, describes the major modifications incorporated in the first of two they presently use in their investigations. These include:

1. Revise the sample handling features to incorporate a water-cooled force transducer to permit simultaneous TGA under essentially isothermal mode together with the normal measurement of smoke obscuration.

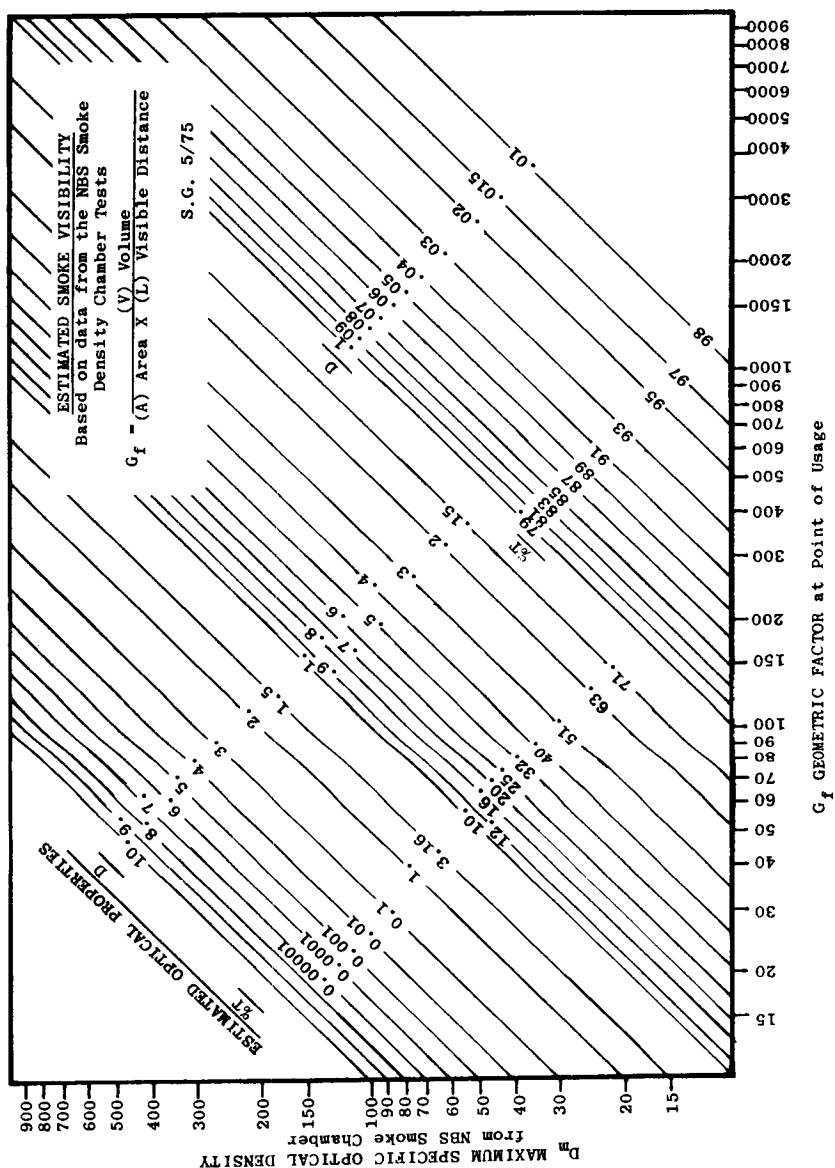


Figure 3. Estimated Smoke Visibility

2. Replacement of the standard furnace with a high-energy-flux furnace and controlled by a sensitive thermocouple controller with the junction located within 3 to 4 millimeters of the heating element.
3. The addition of an interference filter into the optical path to make the light beam being measured essentially monochromatic with a central wavelength at 5468 Å.
4. Adding a technique for determining the concentration of smoke particulates.
5. Adding a technique for determining the smoke particulate size.
6. Identification and measurement of the toxic components in the effluents produced in the procedure.

A second smoke chamber at the University of Utah is presently equipped with an Aminco Exposure Module Accessory in which several small test animals can be placed, monitored and observed while conducting normal smoke tests. This work is directly under the leadership of Dr. Stephen Packham working with Dr. Einhorn and the medical associates in the investigation.

Dr. Mart Meister, a Research Associate at the National Bureau of Standards on leave from the Celanese Research Corporation has developed a prototype horizontal test fixture incorporating an Aminco built frame. This was developed to provide a facility for high melt materials which might not readily be tested in the standard vertical sample holder and for research on basic materials and components. The arrangement incorporates two standard furnaces inclined at about 60° to provide a clear smoke passage and a water cooled force transducer. For those not requiring the simultaneous continuous weight loss values a platform will be provided permitting net weight loss values to obtain the overall MOD (Mass Optical Density). This is based on the same measurement first suggested by Dr. Leo Parts and Dr. J.D. Seader and in the authors opinion is an improvement over the original concepts.

T.G. Lee, the author of several papers on the smoke chamber at NBS, has developed a multi-pass aspirator for use with up to 6 colorimetric gas analysis tubes and we have based our design of a 4 pass unit for use with future chambers, especially when the F.A.A. toxic product rules are finally established.

Almost all of the high energy furnaces used at the University of Utah and by others investigating the procedure under higher heat flux values have been produced by a heater company in Colorado. We have found that the heat pattern and the variability between furnaces exceeds our tolerances. We are working with several leading furnace manufacturers both here and abroad to develop suitable furnaces for both the standard 2.5 watts/cm² and up to 7.5 watts/cm² with a longer life expectancy than that presently available. There is pressure to provide 10 watts/cm² and

even high heat-flux but we believe that 7.5 watts/cm² has reached the limit for Kanthal A-1 or even Super Kanthal within the existing furnace frame.

Preliminary discussions have been held with Dr. Alex Robertson of the NBS and John Blair, Senior Consultant, Plastics Tests at DuPont as to the development of a Heat Release Rate Calorimeter Accessory which might derive these valuable data with samples identical to that involved in the present standard tests.

With continued interest both here and abroad in this apparatus by leading authorities from industry, research, education and government its applications and acceptance for quantitative analysis of smoke and effluent products of either mode of pyrolysis will be certain to establish the NBS Smoke Density Chamber as perhaps the most widely used and referenced apparatus in the fire technology field.

REFERENCES

ASTM D20.22 Subcommittee on Cellular Plastics, "Rigid Cellular Plastics and Flammability", a paper presented at a seminar, Los Angeles, Calif. (1972)

ASTM, Task Group Committee E-5, "The Control of Smoke in Building Fires - A State-of-the-Art Review", Materials, Research and Standards, ASTM, 11, 4, 16-24 (1971)

Auticu, J., Toxicology Aspects of Flammability and Combustion of Polymeric Materials", Fire and Flam., 239-268 (July 1970)

Birky, M.M., Chien, W.P. and Dinger, B.G., "Comparison of Combustion Product Toxicity of Nomex and Nylon Carpets" UTEC-MSE 74-054, Flammability Research Center, University of Utah, (1974)

Birky, M.M., Einhorn, I.N. and Seader, J.D., "The Effects of Fire Retardants on the Combustion of Rigid-Urethane Foams", JFF/Fire Retardant Chemistry, 1, 31, p55 (1974)

Braun, E., "Fire Tests on an AM-General Metro Bus", report of special tests preformed by the Center for Fire Research, NBS for Washington D.C. Metropolitan Transit Agency, (May 1975)

Brenden, J.J., "Usefulness of a New Method for Smoke Yield from Species and Panel Products", Forest Prod. J21, 23-8 (1971)

Chien, W.P., Seader, J.D. and Birky, M.M., "Monitoring Weight Loss in an NBS Smoke Density Chamber", Fire Technology, 9, 285-298 (1973)

Chien, W.P. and Seader, J.D., "Smoke Development at Different Energy Flux Levels in an NBS Smoke Density Chamber", Fire Technology, 10, 187-196 (1974)

- Chien, W.P. and Seader, J.D., "Smoke Measurement in a Modified NBS Smoke Density Chamber", UTEC 75-055, Flammability Research Center, University of Utah, (1975)
- Christian, W.J., and Waterman, T.E., "Ability of Small-Scale Tests to Predict Full Scale Smoke Production, Fire Tech. 7, 4, 332-344 (Nov. 1972)
- Comeford, J.J., "The Spectral Distribution of Radiant Energy of a Gas-Fired Radiant Panel and Some Diffusion Flames", Combustion and Flame, 18, 125-132 (1972)
- Comeford, J.J., and Birky, M., "A Method for the Measurement of Smoke and HCl Evaluation from Poly(vinyl-chloride)", Fire Tech. 8, 2, 85-90, (May 1972)
- Einhorn, I.N., Birky, M.M., Grunnet, M.L., Packham, S.C., Petajan, J.H., and Seader, J.D., "The Physiological and Toxicological Aspects of Smoke Produced During the Combustion of Polymeric Materials", Annual Report FRC/UU-12, Flammability Research Center, University of Utah (1973) also NBS SP 411 (1974)
- Einhorn, I.N., "Mechanism of Combustion in Polymeric Materials", a paper presented at Polymer Conference Series, University of Utah, (1974)
- Gaskill and Veith, "Smoke Opacity from Certain Woods and Plastics", Fire Technology 4, 3, 185-195, (1968)
- Gaskill, "Smoke Development in Polymers During Pyrolysis of Combustion", J. Fire and Flammability, 1, 183-216, (1970)
- Gaskill, J.R., "How Plastics Smoke", SPE Journal 28, 43-49, (Oct. 1972)
- Gaskill, J.R., "Smoke Hazards and their Measurement, A Researcher's Viewpoint", J. Fire and Flammability, 4, 279-298, (1973)
- Greenberg, S., "Quantitative Determination of Smoke and Toxic Product Potential of Materials with the Aminco-NBS Smoke Density Chamber", paper presented at the Seminar Electrical Research Association, Flammability and Smoke Testing Techniques, London, England, (6 February, 1974) and the Colloquium, Flammability of Materials, Centre Nation De La Prevention Et Protection, Paris, France, (20 November, 1974)
- Gross, D., Loftus, J.J., and Robertson, A.F., Method for Measuring Smoke from Burning Materials, ASTM STP 422, pp166-204
- Gross, D., Loftus, J.J., and Robertson, A.F., "Method for Measuring Smoke from Burning Materials, Fire Test Methods - Restraint and Smoke" ASTM STP No. 422 (1967)

- Gross, D., Loftus, J.J., Lee, T.G., and Gray, V.E., "Smoke and Gasses Produced by Burning Aircraft Interior Materials", NBS Bldg. Sci. Series BSS 18, U.S. Govt. Printing Office, Washington, D.C. (Feb. 1969)
- Hebert, R.V., "Steel and Fire Safety", Canadian Steel Industries Construction Council, p28, (April 1975)
- Hilado, C.J., "Flammability Handbook for Plastics", Technomic, Stanford, Conn. (1969)
- Hilado, C.J., "Smoke from Cellular Polymers", Fire Tech. 5, 2, 130-139, (May 1969)
- Hilado, C., "The Effect of Chemical and Physical Factors on Smoke Evaluation from Polymers", Fire and Flam. 1, 217-238, (July 1970)
- Jin, T., "Visibility Through Fire Smoke (Part 2, Visibility of Monochromatic Signs Through Fire Smoke)", Report of Fire Res. Inst. of Japan, No. 33, 31-48 (1971)
- King, T.Y., "Smoke and Carbon Monoxide Generation from Burning Selected Plastics and Red Oak", NBS Special Publication 411, Fire Safety Research, Proceedings of a Symposium held at NBS, (1974)
- Lee, T.G., "Interlaboratory Evaluation of Smoke Density Chamber", NBS Tech. Note 708 (Dec. 1971)
- Lee, T.G., "The Smoke Density Chamber Method for Evaluating the Potential Smoke Generation of Materials", NBS Tech. Note 757 (Jan. 1973)
- New York City, Transit Authority and Fire Advisory Board, "Specifications Governing the Flammability and Smoke Developed Rating of Carpets", (Aug. 1971)
- NFPA, "Tentative Standard Test Method for Smoke Generated by Solid Materials" NFPA-258T, (May 1974)
- Parker, W.J., and Long, M.E., "Development of a Heat Release Rate Calorimeter at NBS", ASTM STP 502, pp135-151, (1972)
- Parts, L., "Smoke Formation Associated with the Burning of Polymers", paper presented at the Polymer Conference Series, University of Utah (1972)
- Rashbash, D.J., "Smoke and Toxic Products Produced at Fires", Trans. J. Plastics Inst., 55-61 (Jan. 1967)
- Robertson, A.F., "Tests Indicate Venting Increases Smoke Production from Some Polymeric", Fire Engineering 126, 9, 97-8, (Sept. 1973)
- Seader, J.D., and Chien, W.P., "Smoke Density Studies With a Modified NBS-Aminco Chamber", UTEC 73-208, paper presented at Polymer

Conference, University of Utah

Seader, J.D., and Chien, W.P., "Quantification and Measurement of Smoke", paper presented at the Polymer Conference Series on Flammability Characteristics of Materials, University of Utah, (1973)

Seader, J.D., and Chien, W.P., "Mass Optical Density as a Correlating Parameter For The NBS Smoke Density Chamber", Journal Fire and Flammability, 5, 1515-163, (1974)

Seader, J.D., and Chien, W.P., "Physical Characteristics of Smoke Development", paper presented at the 106th Meeting of the Rubber Division of the American Chemical Society, Philadelphia, Pa., (1974)

Seader, J.D., and Chien, W.P., "Factors Affecting Smoke Development and Measurement", paper presented at the International Symposium on Physiological and Toxicological Aspects of Combustion Products, University of Utah (1974)

Silversides, R.G., "Measurement and Control of Smoke in Building Fires", ASTM STP 422, pp125-166, (1967)

Smith, E.E., "Heat Release Rate of Building Materials", ASTM STP 502, pp119-134

U.S., Department of Defense, Air Force, MIL-P36816, "Litter Pads" Amended February, 1973

U.S., Department of Defense, Navy, Bureau of Ships, "MIL-STD-1623A, Fire Performance and Approved Specifications for Interior Finish Materials and Furnishings", (May 1974)

U.S., Department of Health Education and Welfare, "Minimum Requirements of Construction and Equipment for Hospital and Medical Facilities", HEW publication No. HRA 74-4000, Revision 16; Section 7.28 and Table 2; Section 8.16 and Table 7; Section 9.9 and Table 10 and Section 10.27 and Table 13

U.S., Department of Housing and Urban Development, "Operation Breakthrough, Smoke Generation Criteria, B.4.3.1, C.4.3.1, D.4.3.1, E.4.3.1, F.4.5.1, and L.4.2.1"

FIRE-RESISTANT AIRCRAFT MATERIALS DEVELOPMENT AND EVALUATION PROGRAM

Richard W. Bricker and Robert N. Stuckey, *Johnson Space Center, Houston, Texas*

ABSTRACT

An aircraft flammability program has been undertaken to utilize spacecraft developed fire-resistant materials to improve passenger safety and decrease losses from unattended fires in commercial aircraft.

INTRODUCTION

Commercial aircraft provide a safe means of transportation, but when accidents do occur, sometimes fires are involved that result in loss of human life, destruction of the aircraft, or both. A 1967 review of commercial jet incidents and accidents (ref. 1) revealed that fires caused or contributed to passenger deaths in 12 of 16 impact-survivable aircraft accidents occurring from 1958 to 1966. All 12 accidents involved external fuel fires that resulted in interior cabin fires in 11 cases. Several additional accidents resulting in loss of life because of fire or toxic products have occurred since 1967 (ref. 2). Fires in unattended aircraft have also resulted in gutted aircraft interiors (ref. 3). These accidents illustrated the need for improved fire-resistant materials for aircraft interiors.

Since the early 1960's, the manufacturers of commercial aircraft and the airlines, aided by the Federal Aviation Administration (FAA), the Aerospace Industries Association of America, Inc. (AIA), the Air Line Pilots Association, and the National Fire Protection Association have sought fire safety improvements by screening, testing, and using improved nonflammable and fire-resistant materials. Test programs included full-scale mockup flammability tests of aircraft interiors (refs. 1 through 7). Experience has shown that full-scale mockup tests are necessary. Individual materials that self-extinguish in laboratory tests may when used in a final configuration with other materials develop synergistic reactions to the ignition source, configuration geometry, and environmental conditions that result in a large fire.

As a result of the Apollo fire in 1967 and the ensuing investigations related to the Apollo and Skylab Programs, new materials having excellent fire-resistant qualities in an oxygen-enriched environment have been developed. The oxygen enrichment creates more stringent conditions than those for present commercial aircraft. Some of these new promising materials were selected for

installation on four NASA aircraft (Gulfstreams) and subsequently for full-scale flammability tests in a 737 fuselage.

This paper presents the results of a total of five full-scale tests performed in the 737 fuselage.

PROGRAM OBJECTIVES

The overall objective of the program is to provide a more fire-resistant commercial aircraft interior. Secondary objectives are to reduce smoke and toxic gas production of the materials and meet the end item use requirements pertaining to wearability, color fastness, and aesthetic appeal.

MATERIALS REQUIREMENTS

Physical Properties

Standard physical properties, such as tensile strength, elongation, tear strength, et cetera, were determined in the laboratory. Other properties important and pertinent to aircraft cabin interiors were determined during actual usage conditions by installing the selected materials in four NASA Gulfstream aircraft. These properties included wearability, cleanability, and maintenance of aesthetic and decorative appearance.

Weight was controlled by selecting the lightest high strength materials.

Fire-Resistance and Related Chemical-Thermal Properties

The LOI (Limiting Oxygen Index) was adopted for determining the flammability properties of materials rather than the bunsen burner tests. The LOI is expressed as a number that is the percent oxygen in a mixture of oxygen and nitrogen below which a material will not sustain combustion. A value of 30 was established at JSC as the LOI screening requirement for all newly acquired and developed aircraft cabin materials.

Smoke production is measured by optically determining the reduction in visibility. The value is given numerically in terms of DSM or Ds (Specific Optical Density). A value of 50 has been established at JSC as the criterion for the DSM of aircraft cabin materials, which is more stringent than the proposed FAA value of 200.

Evaluation of the offgassing and toxicity of the gases evolved from materials during pyrolysis and combustion is a task performed by the JSC environmental health branch. Concurrent with these tests a thermal stability requirement of 477K (400° F) determined by TGA (Thermogravimetric Analysis) in air was established as an offgassing screening test. Materials that do not offgas toxic products at temperatures up to 477K (400° F) would provide additional evacuation time should a fire occur.

Costs

Because many of the new improved materials cost more than those currently in use, there has been a continuing effort to reduce costs through the use of fillers, economical substrates, and materials selection.

EXPERIMENTAL PROGRAM

Tests

Five full-scale flammability tests were performed in a Boeing 737 fuselage (fig. 1). For test 1, conducted to provide a base-line for subsequent tests, materials were used that were the same as those installed in aircraft before the 1968 issuance of more stringent Federal Air Regulations on flammability of aircraft cabin materials.

Tests 2 and 3 were performed to determine the benefits derived from materials having improved fire-resistant characteristics (New Materials "A"). These materials were representative of interior materials installed in two NASA Gulfstream aircraft for in-use evaluation. Also included were some spinoff materials from the Apollo and Skylab programs.

Materials for tests 4 and 5 (New Materials "B") consisted of newer developed materials, and modifications of materials tested previously in tests 2 and 3. Some of the materials evaluated in tests 4 and 5 were replacements for the materials configured in the four NASA aircraft that failed to meet the serviceability and maintainability requirements for aircraft cabin interior materials.

Table I lists the materials used in the five full-scale tests, along with their applications and comparative costs, and figures 2, 3, and 4 show the pretest configuration for the tests.

Test Setup

A 4.6-meter (15-foot) long section of a Boeing 737 fuselage was furnished to simulate the passenger cabin of a commercial jet transport. Sidewalls, windows, ceiling panels, hatracks, passenger service units, and three rows of triple seats were installed along one side of the fuselage section.

The ignition source for tests 1, 2, and 4 consisted of one quart of JP-4 aircraft fuel contained in a 30.5 X 30.5-centimeter (1 X 1 foot) pan and having a burning time of five minutes. For tests 3 and 5, 1.18 (1.25) and 1.47 liters (1.55 quarts), respectively, of a smokeless fuel (50 percent acetone/50 percent methanol) were used so the only smoke produced would be from the materials. For test 5, the fuel pan dimensions were increased to 38.1 X 38.1 centimeter (15 X 15 inches). The additional fuel was used to compensate for the lower energy content per unit mass of the smokeless fuel.

The fuel pan was placed under the outboard seat of the middle row of seats and the fuel ignited electrically. For all five tests, an airflow rate of 5.7 m³/min. (200 ft³/min.) was provided through the test section.

Instrumentation

Instrumentation was provided to measure temperatures, cabin pressure, smoke density, and heat flux. In addition, two separate systems were used to take gas samples every 30 seconds for subsequent analyses of the products of combustion. Color and infrared movies were taken during the tests and still photographs before and after each test.

RESULTS AND DISCUSSION

Pre-1968 Materials (Test 1)

Smoke was observed immediately after ignition of the JP-4 fuel in test 1. This initial smoke appeared to come mainly from the JP-4 ignition source; however, smoke was also observed coming from the outboard seat cushion as it was ignited by the JP-4 fire. Visibility of the fire was lost to observers, TV monitors, and motion picture cameras at approximately 60 seconds elapsed time as black smoke filled the cabin. Temperatures in the test section increased slowly until 60 seconds; then, the temperatures increased more rapidly as the fire spread and more materials were ignited. Apparently, a flash fire, which is a rapid burning of accumulated hot combustible gases, began at approximately 95 seconds because of an accumulation of such gases along the ceiling of the cabin interior. Indicative of the flash fire phenomenon was a rapid increase of cabin temperatures (fig. 5) followed by oxygen depletion to a concentration of less than 5 percent (fig. 6). In addition, the concentration of nonhydrolyzable products of combustion (carbon dioxide and carbon monoxide) increased rapidly as the oxygen was depleted (figs. 7 and 8).

Thermocouple (TC) data indicate that the flash fire originated beneath the hatrack, spread to the ceiling and to the seats, and propagated beneath the hatrack for the full length of the test section.

At 140 seconds, as the flash fire progressed, the maximum radiant heat flux measured at standing head level in the center aisle (fig. 9) was between 5.7×10^4 and 6.8×10^4 W/m² (5 and 6 Btu/ft² -sec). Reduction of visibility, as illustrated in figure 10, occurred rapidly with loss of visibility of the fire at 60 seconds and 83 percent smoke density measured at the ceiling smoke detector. Severe fire damage occurred during test 1, as shown in figures 11 and 12.

New Materials "A" (Test 2)

Test 2 also began with an immediate indication of smoke coming mainly from the JP-4 ignition fuel and the outboard seat cushion above the fuel fire. The fire slowly increased in size until, at approximately 45 seconds elapsed time, it intensified as the fire-resistant materials decomposed and released flammable gases. Unlike the materials used for test 1, however, the fire-resistant materials burned or decomposed only where exposed to the JP-4 fuel fire and did not allow the fire to propagate. Apparently the amount of combustible gases liberated during test 2 was insufficient to produce a flash fire.

After ignition, the smoke density increased, and visibility of the fire was lost at approximately 150 seconds as smoke filled the cabin. In addition, cabin temperatures slowly increased, peaked at approximately 150 seconds, and then began to decrease (fig. 13). Temperatures measured at the sidewall and seat armrest above the fuel pan reached 950K (1250° F); however, motion pictures revealed that the TC at these locations were partly subjected to direct flame impingement from the ignition source, both during this test and during tests 1 and 3. The gradual decrease in oxygen (fig. 6) and the gradual increase in carbon monoxide (fig. 8) indicate a typical open fire and absence of a flash fire. A typical open fire would gradually cease as the oxygen content of the air reached approximately 15 percent (ref. 2). Examination of figures 6 and 13 shows that the temperatures began decreasing as the oxygen content approached 15 percent. Maximum heat flux measured during test 2 (fig. 9) was less than $0.57 \times 10^4 \text{ W/m}^2$ ($0.5 \text{ Btu/ft}^2 \text{-sec}$) at 140 seconds after fuel ignition.

Far less material damage occurred in test 2 than in test 1 and propagation of the fire was limited (figs. 14 and 15). A comparison of ceiling temperatures indicated a maximum temperature of 505K (450° F) for test 2, whereas during test 1 the temperature at the same location was more than 1033K (1400° F). Temperatures at other locations were also significantly lower in test 2 than those measured in test 1. Maximum heat flux levels in test 2 were only one-fifteenth as high as in test 1 (fig. 9). The levels of carbon monoxide and carbon dioxide were significantly lower in test 2 than in test 1 (figs. 7 and 8). Also, the loss of visibility because of smoke density occurred significantly later in test 2 than in test 1 (fig. 10).

In general, the concentrations of the products of combustion (figs. 16, 17, and 18) produced during JSC test 2 were much lower than the concentrations found in JSC test 1. An important factor indicated by these data should be noted. Although large quantities of fluoroelastomers were present in test 2, the measured fluoride concentration was relatively low (fig. 16). A fluoride absorber (or scavenger) had been compounded into the fluorel formulation to capture and convert the reactive fluorine species to a solid ash, which results in reduced amounts of evolved toxic fluorides.

Analysis of the comparative results of tests 1 and 2 indicates that more time would be available to combat and extinguish an inflight cabin fire or an unattended ground fire in an aircraft refurbished with the improved materials.

New Materials "A" with Smokeless Fuel (Test 3)

During test 3, it was observed and later verified by motion pictures that the smokeless fuel (acetone and methanol) did not produce a fire as dynamic as the JP-4 aircraft fuel. Consequently, cabin temperatures increased slowly to a maximum value of 533K (500° F) (at the sidewall adjacent to the fuel pan, at window level) at 200 seconds elapsed time, and then decreased slowly (fig. 19). Smoke production was slight (fig. 10) until 80 seconds, when the smoke began to increase slowly. A loss of visibility of 55 percent was measured at the ceiling smoke detector 240 seconds after ignition. The test 2 level was 94 percent at this point. Damage to the seat above the fuel fire was almost identical to test 2 but sidewall damage was less severe. Ceiling damage was less severe. Generally, major damage was sustained only by the seat directly above the fuel fire; thus, lower cabin temperatures, less radiant heat, and smaller concentrations of combustible products resulted.

Because identical materials were used in tests 2 and 3, the differences in visibility (94 and 55 percent, respectively) at 240 seconds elapsed time (fig. 10) resulted mainly from the additional smoke produced by the JP-4 fuel. Some differences undoubtedly were due to the smaller fire and less burning of materials that occurred in test 3. This information indicates that a significant portion of the reduction in visibility within the cabin for tests 1 and 2 was caused by the smoke produced by the JP-4 ignition source. However, even after considering the smoke contribution of the JP-4 fuel in these two tests, the smoke produced by the materials of test 1 would still be considerably greater than that produced by the materials of test 2.

New Materials "B" (Test 4)

The initial smoke appeared to come mainly from the burning JP-4; however, small amounts of light colored smoke appeared to come from the seat materials. The fire slowly increased in size until about 60 seconds at which time the fire intensified and flames reached seat-top height. The intensification was augmented by flammable gases released as the fire-resistant materials decomposed; however, the amount of combustible gases released during test 4 was apparently insufficient to result in a flash fire.

After ignition, the smoke density increased (fig. 20) and visibility of the fire was lost at approximately 140 seconds as smoke filled the cabin. Cabin temperatures increased, reaching a peak of about 755K (900° F) (at the top of the seat armrest, above the fuel pan) at 160 seconds after ignition, and then rapidly decreased to an average of about 422K (300° F) at 200 seconds

(fig. 21). At 320 seconds the temperatures again increased, peaked at 350 seconds, and then decreased to lower levels at about 400 seconds. Two additional significant temperature increases occurred, with one peak at 460 seconds and the last at about 600 seconds. The maximum heat flux measured at standing head level in the center aisle (fig. 22) was less than $0.28 \times 10^4 \text{ W/m}^2$ ($0.25 \text{ Btu/ft}^2 \text{ -sec}$) at about 150 seconds elapsed time.

The material damage in test 4 (figs. 23 and 24) was similar to test 2 (ref. 8 and figs. 14 and 15), except that more ceiling and sidewall damage occurred during test 2. Although the material damage was comparable to test 2, the ceiling temperature of test 4, which reached a maximum of approximately 450K (350° F) (fig. 21) was about 311K (100° F) lower than for test 2. In general, the concentrations of the major combustion product in test 4 were similar to those obtained in test 2 (figs. 7, 8, 16, 17 and 18).

New Materials "B" with Smokeless Fuel (Test 5)

The smokeless fuel ignition source resulted in a much larger fire and higher cabin temperatures than did test 4, although the TC beneath the seat bottom (above the fuel pan) indicated a lower fuel flame temperature than measured during test 3 or test 4.

Smoke was not observed until approximately 15 seconds elapsed time and then increased slowly until approximately 150 seconds, at which time the smoke production increased at a significant rate to a maximum value at 240 seconds (fig. 20). Cabin temperatures (fig. 25) increased at a slow rate after ignition, similar to the rate of increase measured for test 3 (fig. 20), until approximately 165 seconds, then the temperatures increased more rapidly as the fire intensified. Prior to this, at 80 seconds the armrest material was observed to be burning, and at approximately 130 seconds a piece of burning material fell from the seat into the fuel pan. By 150 seconds, flames were at seat top height and at 180 seconds flames had reached the bottom of the hatrack. The fire continued to intensify, reaching a peak at 210 seconds of approximately 1033K (1400° F) at the seat armrest above the fuel pan and about 575K (575° F) at the ceiling. Also, at 210 seconds, burning material was observed falling next to the sidewall in front of the seat above the fuel pan. Temperatures began to decrease rapidly shortly after 240 seconds, and loss of visibility occurred at 255 seconds. Except for a minor peak of 0.8 W/m^2 ($0.7 \text{ Btu/ft}^2 \text{ -sec}$) at 265 seconds, the radiant heat flux for test 5 averaged approximately $0.68 \times 10^4 \text{ W/m}^2$ ($0.6 \text{ Btu/ft}^2 \text{ -sec}$) from 210 seconds until 240 seconds. The fire did not propagate, although the seat above the fuel pan and the adjacent sidewall sustained major damage.

Test 5 resulted in a much larger fire and more damage (figs. 26 and 27) than test 2, 3, or 4. Although the smokeless fuel resulted in a smaller fire and less damage for test 3 than test 2 using the same materials, the greater quantity of smokeless fuel and larger fuel pan used for test 5 exposed more materials to direct flame impingement.

In addition to the increased damage, the cabin temperatures of test 5 were higher than tests 2, 3, or 4. However the peak temperatures occurred approximately 60 seconds later in test 5 than in tests 2 and 4.

An event that had not been observed during previous JSC tests of fire-resistant materials was the direct impingement of flames on the underside of the hatrack. This occurred at approximately 180 seconds, along with a rapid increase of cabin temperatures (fig. 25), heat flux (fig. 22), and smoke production (fig. 20).

Despite the larger ignition source in test 5 and the direct flame impingement on the hatrack panels, neither burnthrough or delamination of the panels occurred. Furthermore, the fire did not propagate from the seat. Primarily damage occurred only in the region having direct flame impingement from the ignition source. Although there was more local damage in this test than in the previous tests of fire-resistant materials, this was due to the larger heat source.

Most of the measured gaseous combustion products of test 5 increased sharply between 160 seconds and 200 seconds and oxygen content decreased. This coincides with the rapid increase in cabin temperatures and smoke production as the fire intensified.

The significance of test 5 is that despite the severe fire resulting from the larger fuel source, the fire-resistant materials effectively limited fire damage and prevented propagation.

Cost Comparisons

Fire-resistant materials are generally more expensive than the materials they replace. Comparative cost ratings for the materials used in the five tests, with the materials of test 1 assigned a value of one, are given in Table I. The materials used in tests 2 and 3 were, in most cases, considerably more expensive than those in test 1. The materials selected for tests 4 and 5 were generally more economical than those used in tests 2 and 3 but still exceeded the costs of the pre-1968 materials used in test 1.

CONCLUDING REMARKS

Five full-scale aircraft flammability tests were performed to evaluate the effectiveness of improved fire-resistant materials by comparing their burning characteristics with those of pre-1968 aircraft materials.

In test 1, pre-1968 materials were tested to provide a baseline for subsequent tests. The test resulted in significant fire propagation, rapid loss of visibility, evidence of flash fire (characterized by rapid oxygen depletion and temperature increase), significant quantities of toxic gases, and high temperatures. Major fire damage was sustained throughout the test section.

Test 2, in which newer improved fire-resistant materials were tested, resulted in less fire propagation, lower temperatures, a longer time lapse before loss of visibility, and a significant

reduction of toxic gas concentrations because of the much smaller fire. No flash fire occurred and therefore, minimum oxygen depletion, and fire damage was limited.

In test 3, using the same materials as used in test 2, the JP-4 aircraft fuel ignition source was replaced with a smokeless fuel (acetone/methanol). The result was an even greater reduction in temperatures, smoke, toxic gas production, and fire damage than observed in the previous test of the newer materials. The results of test 3 documented the significance of the smoke produced by the JP-4 aircraft fuel in reducing cabin visibility and also permitted an evaluation of the smoke produced by the fire-resistant materials.

Test 4, in which a second generation of improved materials were installed, resulted in fire propagation, fire damage, cabin temperatures, radiant heat flux, and toxic gas production similar to, or less than the results reported for test 2.

In test 5, using the same materials as in test 4, and utilizing a larger quantity of a smokeless fuel (acetone/methanol) and a larger fuel pan than those for tests 1 through 4, the result was a larger fire and more material damage than experienced during any previous JSC tests of new fire-resistant materials (tests 2 through 4). One result not occurring in previous tests was the melting of the metal seat structure above the fuel pan. Another was the impingement of the flames on the bottom of the hatrack because of the more expansive fire resulting from the increased amount of fuel and larger fuel pan. Even though the ignition source for this test was considerably more severe than in the previous tests, damage was limited to the regions receiving direct flame impingement. The fire did not propagate from the seat above the ignition source to adjacent seats. The hatrack underside that was exposed to direct flame impingement did not burn through or delaminate and despite higher temperatures as compared to previous tests with improved materials, a flash fire did not occur. Test 5 showed that the new materials are effective in limiting fire damage and preventing fire propagation.

Many of the materials of tests 2 and 3 were too costly, not durable, and not aesthetically acceptable. The fire-resistant materials of tests 4 and 5 are, in general, economically feasible and meet the end use requirements.

REFERENCES

1. Anon.: Fire Suppression, and Smoke and Fume Protection. Rep. AIA CDP-2 (restricted distribution), Aerospace Industries Association of America, Inc. (Washington, D.C.), July 1968.
2. Lucha, G.V.; Robertson, M.A.; and Schooley, S.A.: An Analysis of Aircraft Accidents Involving Fires. NASA CR-137690, May 1975.
3. Anon.: Aircraft Interior Fire Protection Systems. 1971 NFPA Technical Committee Reports. Vol. I, pp. 52-79. National Fire Protection Association, 1971.
4. Marcy, John F.: Air Transport Cabin Mockup Fire Experiments. Rep. FAA-RC-70-81, Federal Aviation Administration, Dec. 1970.
5. Brenneman, James J.; and Heine, Donald A.: The Cleveland Aircraft Fire Tests - June 30 and July 1, 1966. Air Line Pilots Association (Chicago, Illinois).
6. Brenneman, James J.; and Heine, Donald A.: The Cleveland Aircraft Fire Tests - July 24 and 25, 1968. Air Line Pilots Association (Chicago, Illinois).
7. Sarkos, Constantine P.: Titanium Fuselage Environmental Conditions in Post-Crash Fires. Rep. FAA-RC-71-3, Federal Aviation Administration, March 1971.
8. Stuckey, Robert N.; Supkis, Daniel E.; and Price, L. James: Full-Scale Aircraft Cabin Flammability Tests of Improved Fire-Resistant Materials. Rep. TMX-58141, National Aeronautics and Space Administration, June 1974.

REPRODUCIBILITY OF THE
ORIGINAL PAGE IS POOR

TABLE I. - TEST MATERIALS

Part description	Pre-1968 materials (test 1)	New materials "A" (test 2 and 3)	New materials "B" (tests 4 and 5)
Ceiling panels	Tedlar coated vinyl-covered paper-core/wood-edged fiberglass sandwich	Fiberglass coated with white Fluoral L-3203-6, overcoated with Kel-F FX703, applied to identical ceiling panels of pre-1968 materials test (test 1) * (4.0-1)	FX resin on Nomax or fiberglass honeycomb with skins of FX resin on fiberglass, and a decorative layer of white Kel-F 2401D on fiberglass applied to honeycomb panels with 3M EC-4715 adhesive. (2.0-1)
Dado (lower wall) panels	Tedlar coated vinyl/aluminum laminate	Durette 400-5 coated with Fluoral L-3203-6, overcoated with Kel-F FX703, applied to aluminum sheet (5.0-1)	Blue Kel-F 2401B on nylon, applied to aluminum sheet with 3M EC-4715 adhesive. (2.0-1)
Window panels	Tedlar coated vinyl/aluminum laminate	Durette 400-5 coated with Fluoral L-3203-6, overcoated with Kel-F FX703, applied to aluminum sheet (5.0-1)	Kynar Decorative Laminate, applied to aluminum panel with 3M EC-4715 adhesive. (2.0-1)
Windows	None used	Epoxy-Boroxine (developed by Ames Research Center) (7.0-1)	Epoxy-Boroxine (developed by Ames Research Center) (7.0-1)
Upper wall panels	Tedlar coated vinyl/aluminum laminate	Durette 400-5 coated with Fluoral L-3203-6, overcoated with Kel-F FX703, applied to aluminum sheet (5.0-1)	White Kel-F 2401D on fiberglass, applied to aluminum sheet with 3M EC-4715 adhesive. (2.0-1)
Window shades	Tedlar vinyl laminate	Fiberglass coated with white Fluoral L-3203-6 and overcoated with Kel-F FX703 (4.0-1)	White Kel-F 2401D on fiberglass. (2.0-1)
Floor covering	None used	Wool carpet/high resilience foam padding treated with ADP (Ammonium dihydrogen phosphate and overcoated with Fluoral L-3203-6 (\$12.00/yd)	Nomex pile carpet, and pad of Mobay resilient foam 115014-6 treated with ADP (ammonium dihydrogen phosphate) and coated with Fluoral L-3203-6. (\$12.00/yd)
Hetrack	Paper-core/aluminum-edged fiberglass sandwich, underside of AMS-3570 foam covered with supported vinyl	Paper-core/aluminum-edged fiberglass sandwich, underside of treated high-resilience foam, covered by fiberglass coated with white Fluoral L-3203-6, overcoated with Kel-F FX703 (1.5-1)	Paper-core/aluminum-edged fiberglass sandwich (original Boeing 727 part), underside a mixture of treated Scott high-resilient foam and treated Mobay resilient foam 115014-6, covered by fiberglass coated with Kel-F 2401D. (1.1-1)
Passenger service unit (PSU)	Polysulfone	PRD-49 felt impregnated with 6113 resin and painted with white Fluoral L-3203-6 (1.5-1)	Polysulfone (Stilan) glued to the simulated PSU used for tests 2 and 3 with 3M EC4715 adhesive, and coated with white pigmented Kel-F FX703. (1.5-1)
Seats	AMS-3570 polyurethane foam	Scott Foam treated with ADP and coated with Fluoral L-3203-6 (9.0-1)	Mobay resilient foam 115014-6 treated with ADP and coated with Fluoral L-3203-6 (the seat back padding for test 5 was treated Scott high-resilient foam). (9.0-1)
Cushions			
Ticking	None used	None used	Modacrylic/Polyester Weframatic fabric, style 6186. (\$1.50/yd)
Upholstery fabric	Nylon-wool rayon combination	Proban wool (2.0-1)	100% Nomax, Anchorage II blue 69/1211 (2.0-1)
Armrests	Foam rubber covered with natural leather	Durette 400-5 coated with blue Fluoral L-3203-6, overcoated with Kel-F FX703 (1.7-1)	Blue Kel-F 2401B on nylon. (0.8-1)
Seatbelt	Nylon	Nomax (2.5-1)	Nomex S/WNX 1856 (2.5-1)
Seat tray	ABS	PRD-49 felt impregnated with 6113 resin and painted with white Fluoral L-3203-6 (15.0-1)	Polyethylene (Stilan) (15.0-1)
Headrest cover	None used	Fire retardant nonwoven cellulosic S/AMK 770 (50.01 EACH)	Fire retardant nonwoven cellulosic S/AMK 770. (50.01 EACH)

*THE NUMBERS IN PARENTHESES ARE COMPARATIVE COST RATINGS, WITH THE MATERIALS OF TEST 1 ASSIGNED A VALUE OF ONE. PRICES ARE GIVEN IF KNOWN.

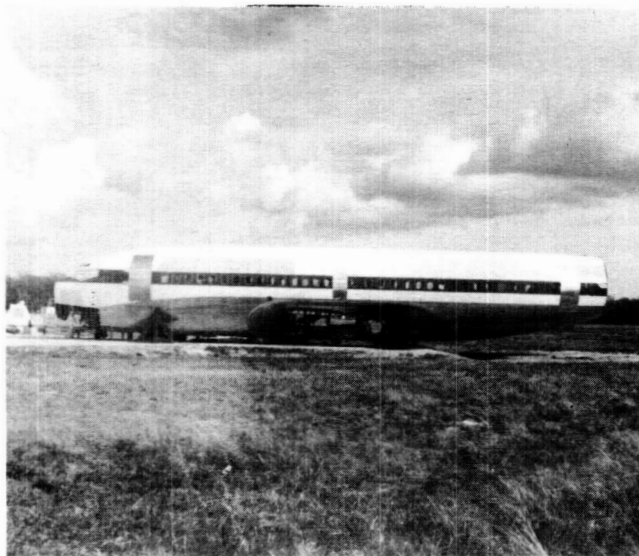


Fig. 1 - Boeing 737 Test Fuselage

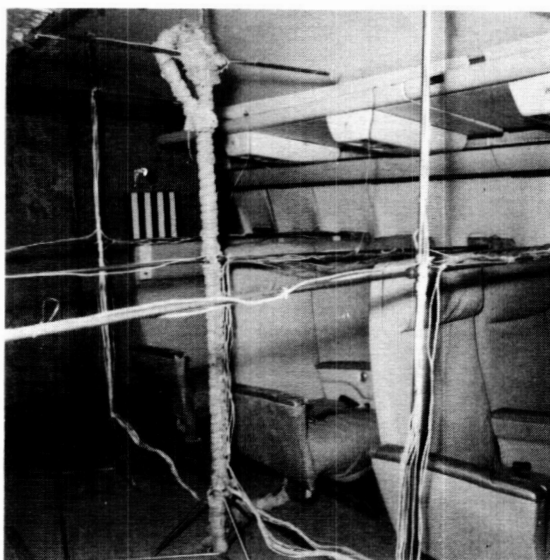


Fig. 2 - Test Configuration for Test 1 using
Pre-1968 Materials

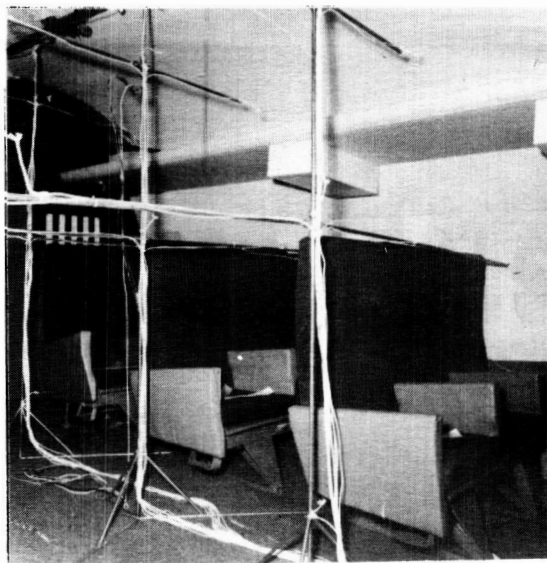


Fig. 3 - Test Configuration for Tests 2 and 3
using New Materials "A"

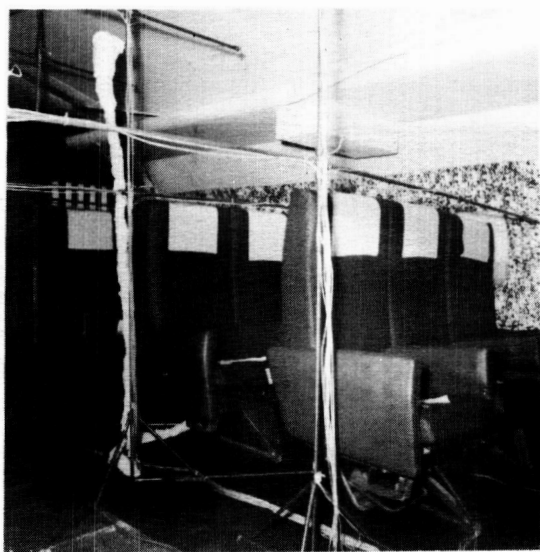


Fig. 4 - Test Configuration for Tests 4 and 5
using New Materials "B"

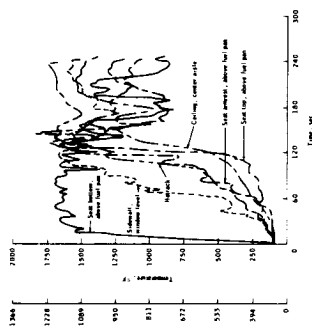


Fig. 5 - Temperatures at Center of Test Section, pre-1968 Materials

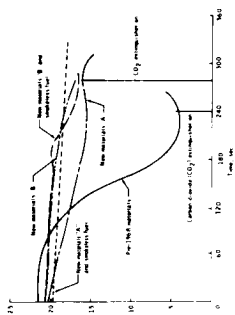


Fig. 6 - Oxygen Concentration

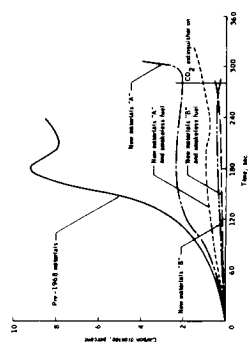


Fig. 7 - Carbon Dioxide Concentration

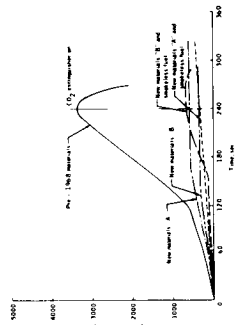


Fig. 8 - Carbon Monoxide Concentration

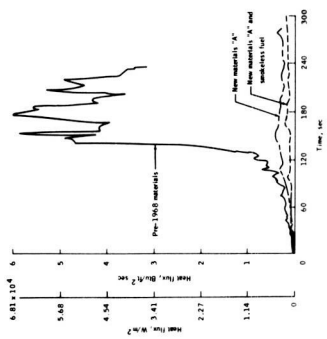


Fig. 9 - Heat Flux at Center of Test Section, Center Aisle

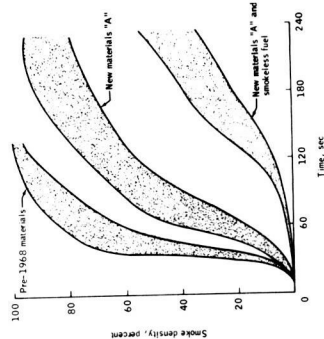


Fig. 10. - Minimum and Maximum Smoke Density Levels

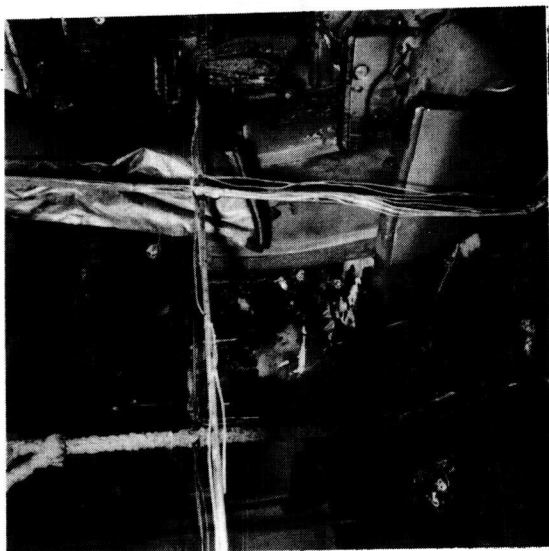


Fig. 11 - Fire Damage for Test 1 using Pre-1968 Materials



Fig. 12 - Fire Damage for Test 1 using Pre-1968 Materials

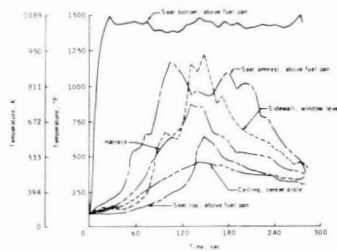


Fig. 13 - Temperatures at Center of Test Section, New Materials "A"

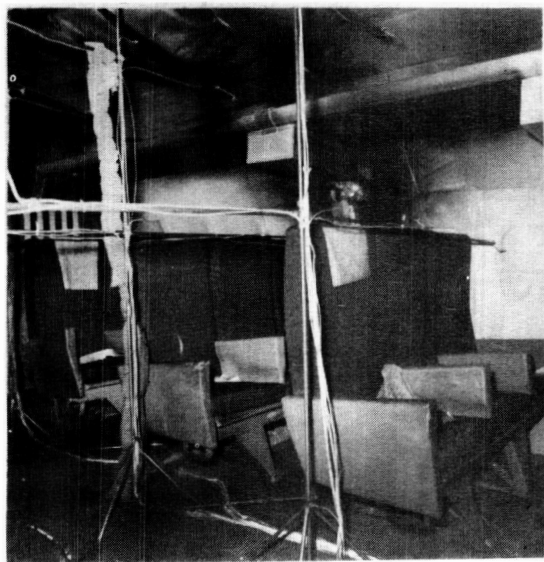


Fig. 14 - Fire Damage for Test 2 using New Materials "A"

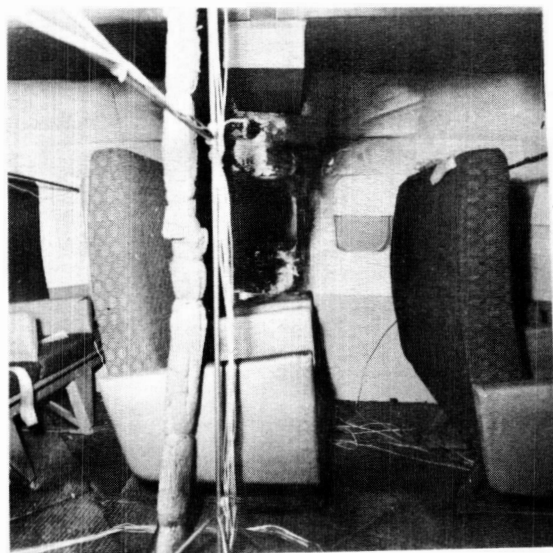


Fig. 15 - Fire Damage for Test 2 using New Materials "A"

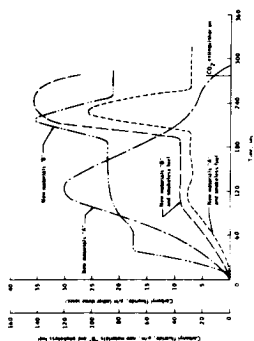


Fig. 16 - Fluoride (As Carbonyl Fluoride) Concentration

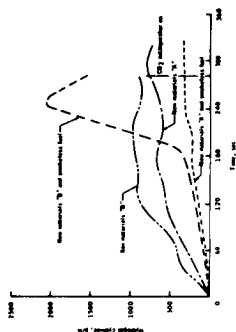


Fig. 18 - Cyanide (As Hydrogen Cyanide) Concentration

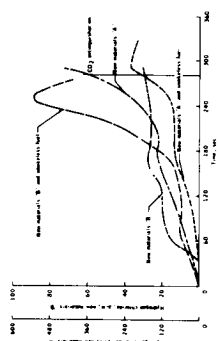


Fig. 17 - Chloride (As Hydrogen Chloride) Concentration

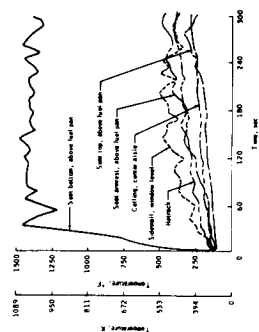


Fig. 19 - Temperatures at Center of Test Section, New Materials "A" and Smokeless Fuel

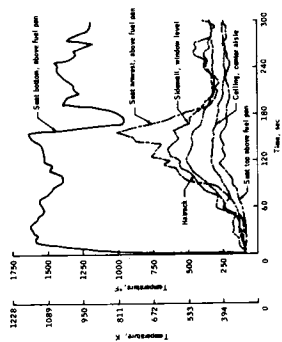


Fig. 21 - Temperatures at Center of Test Section, New Materials "B"

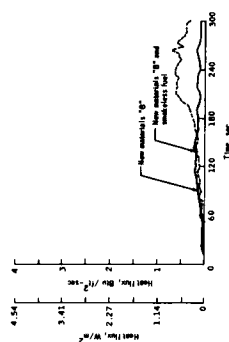


Fig. 22 - Heat Flux at Center of Test Section, Center Aisle

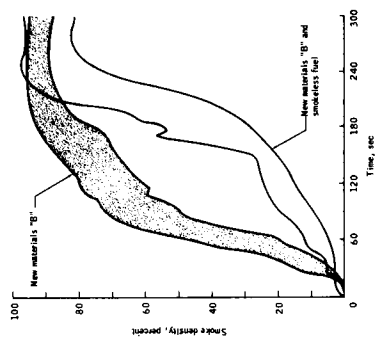


Fig. 20 - Minimum and Maximum Smoke Density Levels

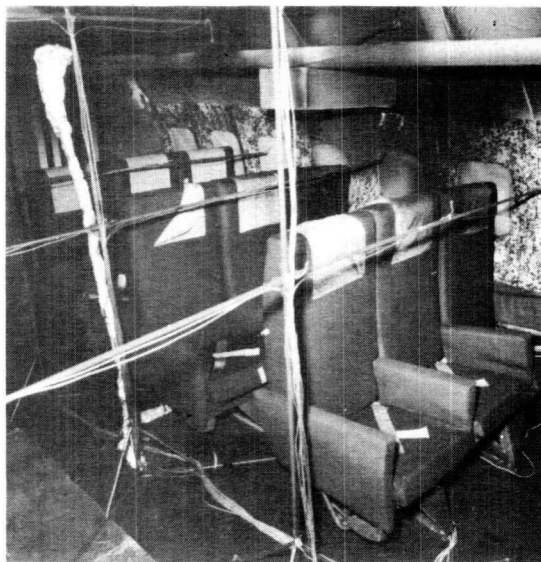


Fig. 23 - Fire Damage for Test 4 using New Materials "B"

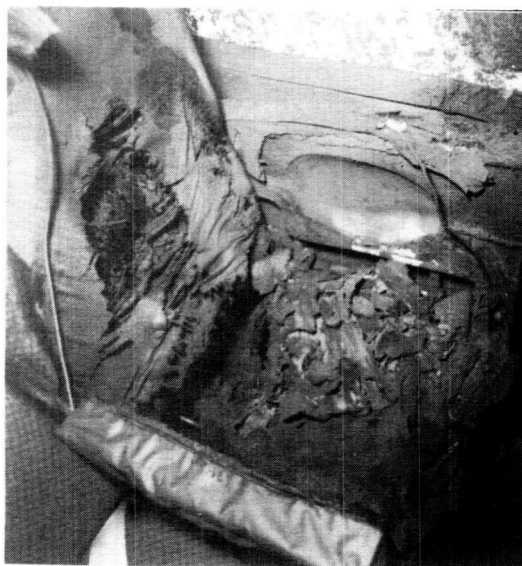


Fig. 24 - Seat Fire Damage for Test 4 using New Materials "B"

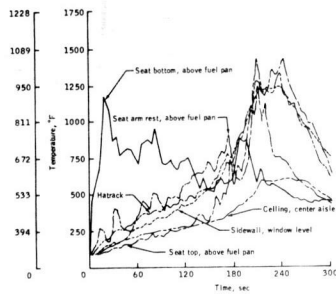


Fig. 25 - Temperatures at Center of Test Section, New Materials "B" and Smokeless Fuel

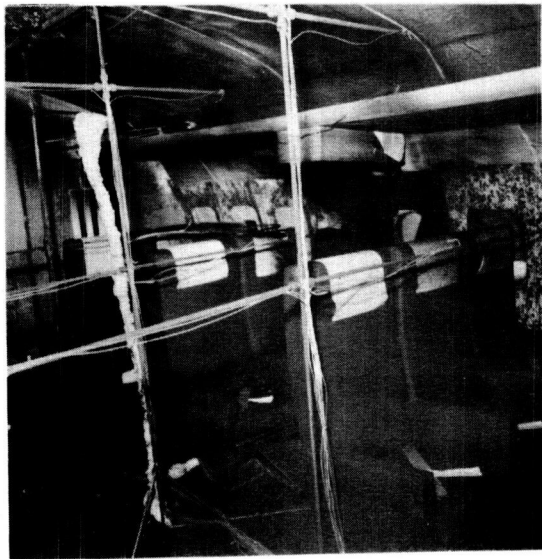


Fig. 26 - Fire Damage for Test 5 using New Materials "B"

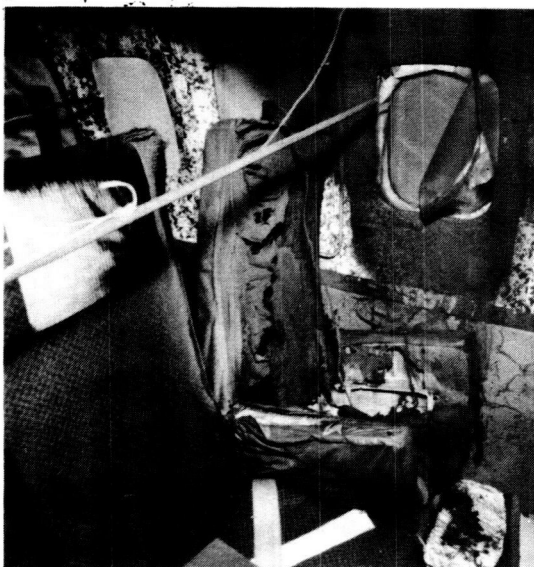


Fig. 27 - Seat and Sidewall Fire Damage for Test 5
using New Materials "B"

REPRODUCIBILITY OF THE
ORIGINAL PAGE IS POOR

DEVELOPMENT OF FIRE RESISTANT ELECTRONIC CONFIGURATIONS FOR USE IN OXYGEN ENRICHED ENVIRONMENTS

F. J. Smith, *Martin Marietta Aerospace, Denver, Colorado 80201*

ABSTRACT

The flammability requirements of the various manned space programs have required development of electronic configurations that would eliminate any flammability hazard to crews or missions.

Initial test and development efforts were directed at the development of nonflammable or self-extinguishing materials. It was soon realized that a more relevant approach in eliminating flammability hazards was to consider materials as to their application and configuration.

Design concepts for electronic black boxes and modules were tested in oxygen enriched atmospheres, and it was found that various types of sealed configurations would generally eliminate any flammability hazard. The type of configuration and its construction was found to be of more importance in the elimination of flammability hazards in electronic configurations than the types of materials utilized in them.

The design concepts developed for fire hazard free electronic configurations for use in manned space programs are applicable for the design of electronic hardware for any use or environment.

Manned spacecraft developed under the direction of the National Aeronautics and Space Administration from the Mercury spacecraft through the Skylab Program have utilized oxygen enriched reduced pressure breathing atmospheres, typically seventy percent oxygen and thirty percent nitrogen at a pressure of 6.2 psia. The need for comprehensive flammability requirements and control of materials and configurations was emphasized by the tragic Apollo Command Module fire in 1967, in which three astronauts lost their lives. This fire is thought to have been initiated by electrical wiring in the spacecraft. Because of the fire, all non-metallic materials, materials applications and configurations were rigorously screened to eliminate possible future ignition sources. As a result of this screening, it was soon obvious that most of potential ignition sources in the spacecraft were found in the electronic/electrical system. Principle

sources were wire and cable harnesses, circuit breakers, terminal strips, switches, and electronic "black boxes." Considerable flammability testing was then performed on the materials used in electrical/electronic configurations and the configurations themselves in order to eliminate any flame hazard to the crew and mission.

Initial test and development efforts were directed at the development of non-flammable or self-extinguishing materials. As a result, most of the non-metallic materials used in electrical applications were found to be flammable not only in oxygen enriched atmosphere, but in air itself when tested as individual materials. With this experience, it was readily seen that it would be more relevant if materials were tested in their intended application and, if possible, as part of a major configuration. As examples, the thin "TFE Teflon" insulation used on wire and cable will burn (decompose) when tested as an individual material in an oxygen atmosphere of 6.2 psia,⁽¹⁾ "the same material will at times support combustion in the same atmosphere when tested in its application as a wire insulation in an unprotected wire bundle,⁽²⁾ but is relatively non-flammable when tested in wire bundles protected with fire breakers (non-flammable lacing tape or clamps) or non-flammable sheathing.⁽³⁾ Also a polyurethane conformal coating which will burn in air if tested unsupported or when applied to a non-fire retardant printed circuit board, but will offer no flame hazard when tested in a hermetically or environmentally enclosed configuration.⁽⁴⁾

With the above in mind, it seemed more logical to qualify electronic materials for flammability requirements by testing mockups of large configurations of actual hardware. During the Skylab Program Martin Marietta tested in oxygen enriched atmospheres through NASA/JSC, mockups of several "worst case" electronic configuration in order to qualify its electronic/electrical hardware for the flammability requirements imposed on the program.

Among these designs included control and display panels, tape recorders, power supply, wire and cable assemblies, and a number of different electronic black box assemblies. These configurations included hermetically and environmentally sealed units. While testing closure methods, the only failure occurred where a tight open-metal screen was employed as a vent device.⁽⁵⁾ This failure was caused by an accumulation of burning polyurethane coating on the interior of the screen melting it and blowing it

-
- (1) NASA/JSC, "Non-Metallic Design Guidelines & Test Data Handbook; Rev. G JSC02681, Test Report DEN-0136, pp 367, 1974
 - (2) Ibid, Test Report PLN-4037, pp 367
 - (3) Ibid, Test Report 71-2614, pp 415
 - (4) Ibid, Test Report 73-4172, pp 105
 - (5) NASA/WSTF, Flammability Test 70-1912, October 22, 1970

out. After this vent failure, the fire in the interior of this assembly died out for the lack of oxygen. As a result of this failure, a number of vent devices and configurations were tested (6) including differential pressure valves, baffles/screens, hole patterns, and a "Beta-Cloth" cover. All of these were successful in containing fires generated with electronic configurations. The only material related failures occurred when a high energy ignition source (such as a 20 AWG nichrome wire) was buried in a material such as a polyurethane closed cell foam placed in a closed container with an oxygen enriched atmosphere and the ignitor initiated. In these cases, the heat from the ignition source decomposed the material, causing a build up of volatile gases within the configuration and then the ignitor became exposed to this volatile gas/oxygen mixture, the result was a violent explosion. In one particular case, (7) a mock-up of the Skylab Earth Resources Experiment Control and Display assembly was tested. This assembly mock-up was environmentally sealed, vented with a pattern of small holes, and tested in an oxygen enriched atmosphere at 6.2 psia with the following results. Three separate ignitors placed on the surface of internal components of the assembly were fired individually and the assembly opened after each ignition examined, resealed, and re-pressurized with the test atmosphere. Each of these ignitors, which were placed on the surface of the materials with the assembly, burned for a very short time (until the available oxygen was gone), and did little material damage and no structural damage. However, shortly after an ignitor that was buried in approximately 125 grams of a polyurethane foam inside the control and display assembly was fired, a catastrophic explosion resulted. This explosion ruptured the assembly structure. The resulting fire reduced the interior of the assembly to ash and melted areas of the 0.1 inch aluminum alloy structure. As a result of this testing, logical design concepts for the production of non-flammable and/or self-extinguishing configurations were developed. These concepts briefly follow in general terms.

1. Choose the best available, least flammable material possible that will meet the functional requirements of the application.
2. Where possible, enclose electronic assemblies in hermetically sealed assemblies with inert atmospheres and non-flammable structure.
3. If hermetically sealed assemblies are not practical, then utilize an environmentally sealed assembly containing pressure relief devices such as a small pattern of holes or a pressure differential valve in

(6) NASA/WSTF; Test Ibid

(7) NASA/WSTF; Flammability Test Report 70-2189
Document #TR-CR-001; February 5, 1971

the assembly shell.

4. If sealed containers are not practical for thermal reasons, then it would be necessary to provide flammability protection at points of possible ignition. These protective devices could include flame retardant coatings, fire breaks, heat sinks, and/or flame-proof sub-containers.
5. Avoid potting or containing ignition and/or heat source with materials that decompose or release flammable or explosive atmospheres as they are treated and which might create a flammability, explosive and/or toxicity problem.

The design concepts developed for fire hazard free electronic configurations for use in manned space programs are applicable for the design of electronic hardware for any use or environment. Systems that might benefit from such design concepts include military and commercial aircraft, transit system, ships, in-ground facilities, and submersibles.

A RELATIVE TOXICITY RANKING OF THERMALLY DECOMPOSED AIRCRAFT INTERIOR MATERIALS

Joe C. Spurgeon, *DOT/FAA/NAFEC, Atlantic City, N.J.*

ABSTRACT

The existence of a relationship between animal toxicity and the quantity of hydrogen cyanide released by 9 aircraft interior materials when thermally decomposed has been investigated. Relative toxicities of the 9 materials were established by observing times-to-incapacitation for male Sprague-Dawley rats which were exposed to the decomposition products formed by heating the materials in a tube furnace to 600° C. The coefficient of correlation between times-to-incapacitation and the amounts of hydrogen cyanide released by the materials is 0.93. The ability of a combined approach involving both gas analysis and animal toxicity tests to identify materials which produce uniquely toxic decomposition products has been demonstrated.

Although this paper is not available for publication at this time, copies will be made available at the conference.

NATIONAL AERONAUTICS AND SPACE ADMINISTRATION
WASHINGTON, D.C. 20546

OFFICIAL BUSINESS
PENALTY FOR PRIVATE USE \$300

SPECIAL FOURTH-CLASS RATE
BOOK

POSTAGE AND FEES PAID
NATIONAL AERONAUTICS AND
SPACE ADMINISTRATION
451



POSTMASTER: If Undeliverable (Section 158
Postal Manual) Do Not Return

"The aeronautical and space activities of the United States shall be conducted so as to contribute . . . to the expansion of human knowledge of phenomena in the atmosphere and space. The Administration shall provide for the widest practicable and appropriate dissemination of information concerning its activities and the results thereof."

—NATIONAL AERONAUTICS AND SPACE ACT OF 1958

NASA SCIENTIFIC AND TECHNICAL PUBLICATIONS

TECHNICAL REPORTS: Scientific and technical information considered important, complete, and a lasting contribution to existing knowledge.

TECHNICAL NOTES: Information less broad in scope but nevertheless of importance as a contribution to existing knowledge.

TECHNICAL MEMORANDUMS: Information receiving limited distribution because of preliminary data, security classification, or other reasons. Also includes conference proceedings with either limited or unlimited distribution.

CONTRACTOR REPORTS: Scientific and technical information generated under a NASA contract or grant and considered an important contribution to existing knowledge.

TECHNICAL TRANSLATIONS: Information published in a foreign language considered to merit NASA distribution in English.

SPECIAL PUBLICATIONS: Information derived from or of value to NASA activities. Publications include final reports of major projects, monographs, data compilations, handbooks, sourcebooks, and special bibliographies.

TECHNOLOGY UTILIZATION PUBLICATIONS: Information on technology used by NASA that may be of particular interest in commercial and other non-aerospace applications. Publications include Tech Briefs, Technology Utilization Reports and Technology Surveys.

Details on the availability of these publications may be obtained from:

SCIENTIFIC AND TECHNICAL INFORMATION OFFICE

NATIONAL AERONAUTICS AND SPACE ADMINISTRATION
Washington, D.C. 20546